JOURNAL OF THE ELECTROCHEMICAL SOCIETY

ELECTROCHEMICAL
SCIENCE AND TECHNOLOGY

SOLID-STATE
SCIENCE AND TECHNOLOGY

REVIEWS AND NEWS
Call for Papers
Boston, Massachusetts, Meeting

VOL. 132, NO. 11 NOVEMBER 1985

JESOAN 132 (11) 2521-2816, 441C-464C

FUTURE MEETINGS

BOSTON, MASSACHUSETTS—MAY 4-9, 1986—HEADQUARTERS AT SHERATON BOSTON HOTEL

See the detailed Call for Papers published in the July-November 1985 issues of **This Journal.** Final program to be published in the March 1986 issue of **This Journal**.

SAN DIEGO, CALIFORNIA—OCTOBER 19-24, 1986—HEADQUARTERS AT THE TOWN AND COUNTRY HOTEL

The detailed Call for Papers will be published in the December 1985-April 1986 issues of **This Journal**. Final program to be published in the August 1986 issue of **This Journal.**

Planned symposia for the San Diego Meeting include the following Divisions, Groups, Subcommittee, and subjects. **Battery**—Lithium Battery; Stored Hydrogen Batteries; Sodium-Sulfur Battery; General Session. **Battery/Physical Electrochemistry**—Electrochemical and Thermal Modeling; Fuel Cell Electrochemistry and Electrolysis. **Corrosion**—Surfaces, Sorption, and Inhibition (Norman Hackerman 75th Birthday Symposium); Corrosion Protection by Organic Coatings; General Session. **Corrosion/High Temperature Materials**—Corrosion of Aerospace Materials. **Dielectrics and Insulation/Electronics**—Isolation Technology; Sixth Symposium on Plasma Processing; Multilevel Interconnect and Contact Technology. **Dielectrics and Insulation/Electronics/High Temperature Materials**—Silicon Nitride and Silicon Dioxide Thin Films. **Electrodeposition**—Electrodeposition Technology—Theory and Practice in Different Industries; General Session. **Electrodeposition/Physical Electrochemistry**—Electrosolidification and Crystallization. **Electronics**— Entrepreneurship in the Semiconductor Industry. **Electronics/Dielectrics and Insulation**—State-of-the-Art Program on Compound Semiconductors V; Silicon Process Physics and Modeling; Ion Implantation of Compound Semiconductors; Joint General Session; Joint Recent News Papers Session. **Electronics/Luminescence and Display Materials**—Microstructured Silicon Sensors. **Energy Technology**—Electrolyte Management in Electrochemical Energy Systems; Thermodynamic Analysis of Energy Systems; Protonic and Hydroxyl Electrolytes for Use in Electrochemical Devices; Mechanical Properties of Photovoltaic Device Structures; General Session. **Energy Technology/Physical Electrochemistry**—Semiconductor-Electrolyte Interfaces. **High Temperature Materials/Corrosion/Dielectrics and Insulation/Electrodeposition**—Protective Coatings at Elevated Temperatures. **High Temperature Materials/Physical Electrochemistry/Electronics**—Electrical Properties and Applications of Amorphous Materials. **Industrial Electrolytic**—Industrial Processes for the Production of Organic and Specialty Chemicals. **Industrial Electrolytic/High Temperature Materials**—Industrial Electrolysis of Fused Salts. **Luminescence and Display Materials**—Physics and Chemistry of Lamp Phosphors; Lamp Manufacture and Performance; Light Modulation in Optical Processing; X-Ray Imaging; Picosecond and Faster Phenomena in Luminescence; General Session; Recent News Papers Session. **Luminescence and Display Materials/Dielectrics and Insulation**—Materials and Fabrication Techniques for Display Devices. **Luminescence and Display Materials/Electronics**—Sensors for Robot Applications. **Luminescence and Display Materials/Electronics/New Technology Subcommittee**—Robotics for Use in Manufacture of Electronic Devices. **Physical Electrochemistry**—General Session. **Physical Electrochemistry/High Temperature Materials/Battery**—Solid Electrolytes.

PHILADELPHIA, PENNSYLVANIA—MAY 10-15, 1987—HEADQUARTERS AT ADAM'S MARK HOTEL

The detailed Call for Papers will be published in the July-November 1986 issues of **This Journal**. Final Program to be published in the March 1987 issue of **This Journal.**

Planned symposia for the Philadelphia Meeting include the following Divisions, Groups, Subcommittee, and subjects. **Corrosion**—General Sessions. **Corrosion/Energy Technology**—Electrochemistry of Coal Slurries. **Dielectrics and Insulation**—Coatings and Media for Magnetic Recording; Nonblodgett Monomolecular Films. **Dielectrics and Insulation/Electronics**—Fourth International Symposium on VLSI Science and Technology; Semiconductor Manufacturing Science and Clean Room Technology; Contactless Testing of Semiconductor Devices; State-of-the-Art Program on Compound Semiconductors VI; Interconnects and Contacts for Compound Semiconductors; Joint General Session; Joint Recent News Papers Session. **Energy Technology**—General Session. **Energy Technology/Industrial Electrolytic**—Application of Fuel Cell Electrodes in Electrolytic Industries. **Energy Technology/Physical Electrochemistry/Electrodeposition**—Electrochemistry and Tribology. **Energy Technology/Physical Electrochemistry/Organic and Biological Electrochemistry**—Applications of Macromolecules in Energy Conversion. **High Temperature Materials**—Rapidly Solidified Materials. **High Temperature Materials/Battery/Corrosion**—Materials and Processing for Solid Oxide Fuel Cells. **High Temperature Materials/Corrosion/Dielectrics and Insulation/Physical Electrochemistry**—*in situ* Nonelectrochemical Techniques. **High Temperature Materials/Dielectrics and Insulation**—Chemical Interactions in Ceramic Composites; Laser-Induced Chemical Reactions. **Industrial Electrolytic**—General Session. **Industrial Electrolytic/Physical Electrochemistry**—Electrochemistry in Mineral and Metal Processing II. **Physical Electrochemistry**—The Electrical Double Layer, Quantum Effects in Electrochemistry; General Session. **Physical Electrochemistry/Battery**—Nonaqueous Electrochemistry. **Physical Electrochemistry/Battery/Energy Technology**—Electrode Materials and Processes for Energy Conversion and Storage. **Physical Electrochemistry/New Technology Subcommittee**—Magnetic Effects in Electrochemistry.

THE ELECTROCHEMICAL SOCIETY BOOKS IN PRINT

Society Proceedings Series
1980-1985

The following softbound proceedings volumes are sponsored and published by The Electrochemical Society, Inc., 10 South Main Street, Pennington, NJ 08534-2896. Orders filled at the list price given, subject to availability. Enclose payment with order.

Electronic and Optical Properties of Polycrystalline or Impure Semiconductors and Novel Silicon Growth Methods. K. V. Ravi and B. O'Mara, Editors. A 1980 symposium. 280 pages, **$15.00.**

Electron and Ion Beam Science and Technology, Ninth International Conference. R. Bakish, Editor. A 1980 symposium. 672 pages, **$28.00.**

Lithium Nonaqueous Battery Electrochemistry. E. B. Yeager, B. Schumm, Jr., G. Blomgren, D. R. Blankenship, V. Leger, and J. Akridge, Editors. A 1980 workshop. 328 pages, **$18.00.**

Ion Exchange: Transport and Interfacial Properties. R. S. Yeo and R. P. Buck, Editors. A 1980 symposium. 396 pages, **$15.00.**

Materials and New Processing Technologies for Photovoltaics. J. A. Amick, E. Sirtl, P. Rai-Choudhury, and J. P. Dismukes, Editors. A 1980 symposium. 368 pages, **$14.00.**

Lithium Batteries, H. V. Venkatasetty, Editor. A 1980 symposium, 516 pages, **$26.00.**

Semiconductor Silicon 1981. H. R. Huff, R. J. Kriegler, and Y. Takeishi, Editors. A 1981 symposium. 1064 pages, **$25.00.**

Electrocrystallization. R. Weil and R. G. Barradas, Editors. A 1981 symposium. 352 pages, **$13.00.**

Corrosion and Corrosion Protection. R. P. Frankenthal and F. Mansfeld, Editors. A 1981 symposium. 304 pages, **$10.00**

Third International Symposium on Molten Salts. G. Mamantov, M. Blander, and G. P. Smith, Editors. A 1981 symposium, 600 pages, **$23.00.**

Second International Symposium on Molten Salts. J. Braunstein and J. R. Selman, Editors. A 1978 symposium. 420 pages, **$16.00**

High Temperature Materials Chemistry. D. D. Cubicciotti and D. I. Hildenbrand, Editors. A 1981 symposium. 498 pages, **$21.00.**

Electrocatalysis. W. E. O'Grady, P. N. Ross, Jr., and F. G. Will, Editors. A 1981 symposium. 428 pages, **$18.00.**

Photoelectrochemistry: Fundamental Processes and Measurement Techniques. W. L. Wallace, A. J. Nozik, S. K. Deb, and R. H. Wilson, Editors. A 1981 symposium. 736 pages, **$35.00**

The Nickel Electrode. R. G. Gunther and S. Gross, Editors. A 1981 symposium. 324 pages, **$15.00.**

Semiconductor Technology. D. A. Doane, D. B. Fraser, and D. W. Hess, Editors. A 1982 symposium. 264 pages, **$18.00.**

Plasma Processing. J. Dieleman, R. G. Frieser, and G. S. Mathad, Editors. A 1981 symposium. 528 pages, **$25.00.**

VLSI Science and Technology. C. J. Dell'Oca and W. M. Bullis, Editors. A 1982 symposium. 392 pages, **$20.00.**

Materials and New Processing Technologies for Photovoltaics. J. P. Dismukes, E. Sirtl, P. Choudhury, and L. P. Hunt, Editors. A 1982 symposium. 544 pages, **$25.00.**

Inorganic Resist Systems. D. A. Doane and A. Heller, Editors. A 1982 symposium. 320 pages, **$15.00.**

Transport Processes in Electrochemical Systems. R. S. Yeo, T. Katan, and D-T. Chin, Editors. A 1982 symposium. 288 pages, **$18.00.**

Corrosion in Batteries and Fuel Cells and Corrosion in Solar Energy Systems. C. J. Johnson and S. L. Pohlman, Editors. A 1981 symposium. 554 pages, **$22.00.**

Electron and Ion Beam Science and Technology, Tenth International Conference, R. Bakish, Editor. A 1982 symposium. 474 pages, **$30.00.**

Membranes and Ionic and Electronic Conducting Polymers. E. B. Yeager, B. Schumm, Jr., K. Mauritz, K. Abbey, D. Blankenship, and J. Akridge, Editors. A 1982 symposium. 380 pages, **$22.00.**

Aggregation Phenomena of Point Defects in Silicon. E. Sirtl and J. Goorissen, Editors. A 1982 symposium. 216 pages, **$15.00.**

Corrosion in Fossil Fuel Systems. I. G. Wright, Editor. A 1982 symposium. 522 pages, **$20.00.**

Electrochemical Process and Plant Design. R. C. Alkire, T. R. Beck, and R. D. Varjian, Editors. A 1982 symposium. 288 pages, **$20.00.**

High Temperature Materials Chemistry II. Z. A. Munir and D. Cubicciotti, Editors. A 1983 symposium. 480 pages, **$30.00.**

Silicon Nitride Thin Insulating Films. V. J. Kapoor and H. J. Stein, Editors. A 1983 symposium. 522 pages, **$25.00.**

Defects in Silicon. W. M. Bullis and L. C. Kimerling, Editors. A 1983 symposium. 660 pages, **$30.00.**

Plasma Processing. G. S. Mathad, G. C. Schwartz, and G. Smolinsky, Editors. A 1983 symposium. 660 pages, **$35.00.**

Materials and New Processing Technologies for Photovoltaics. J. A. Amick, V. K. Kapur, and J. Dietl, Editors. A 1983 symposium. 512 pages, **$25.00.**

Electroplating Engineering and Waste Recycle—New Developments and Trends. D. D. Snyder, U. Landau, and R. Sard, Editors. A 1982 symposium. 428 pages, **$22.00.**

III-V Opto-Electronics Epitaxy and Device Related Processes. V. G. Keramidas and S. Mahajan, Editors. A 1983 symposium. 289 pages, **$25.00.**

Lithium Batteries. A. N. Dey, Editor. A 1983 symposium. 460 pages, **$35.00.**

Fourth International Symposium on Molten Salts. M. Blander, D. S. Newman, M-L. Saboungi, G. Mamantov, and K. Johnson, Editors. A 1983 symposium. 776 pages, **$35.00.**

Fundamental Aspects of Corrosion Protection by Surface Modification. E. McCafferty, C. R. Clayton, and J. Oudar, Editors. A 1983 symposium. 364 pages, **$25.00.**

Advances in Battery Materials and Processes. J. McBreen, R. S. Yeo, D-T. Chin, and A. C. C. Tseung, Editors. A 1983 symposium. 320 pages, **$26.00.**

The Electrochemistry of Carbon. S. Sarangapani, J. R. Akridge, and B. Schumm, Editors. A 1983 symposium. 648 pages, **$32.00.**

Ninth International Conference on Chemical Vapor Deposition. McD. Robinson, C. H. J. van den Brekel, G. W. Cullen, J. M. Blocher, Jr., and P. Rai-Choudhury, Editors. A 1984 symposium. 824 pages, **$36.00.**

VLSI Science and Technology/1984. K. E. Bean and G. A. Rozgonyi, Editors. A 1984 symposium. 520 pages, **$30.00.**

Porous Electrodes: Theory and Practice. H. C. Maru, T. Katan, and M. G. Klein, Editors. A 1982 symposium. 492 pages, **$18.00.**

Equilibrium Diagrams; Localized Corrosion. R. P. Frankenthal and J. Kruger, Editors. A 1984 symposium. 611 pages, **$36.00.**

Electrochemistry in Mineral and Metal Processing. P. E. Richardson, S. Srinivasan, and R. Woods, Editors. A 1984 Symposium. 677 pages, **$30.00.**

Advances in the Chlor-Alkali and Chlorate Industry. M. M. Silver and E. M. Spore, Editors. A 1984 Symposium. 374 pages, **$18.00.**

The Chemistry and Physics of Electrocatalysis. J. D. E. McIntyre, M. J. Weaver, and E. B. Yeager, Editors. A 1983 symposium. 684 pages, **$27.00.**

Molten Carbonate Fuel Cell Technology. J. R. Selman and T. D. Claar, Editors. A 1982 Symposium. 533 pages, **$15.00.**

Advances in Lead-Acid Batteries. K. R. Bullock and D. Pavlov, Editors. A 1984 Symposium. 548 pages, **$28.00.**

Plasma Processing. G. S. Mathad, G. C. Schwartz, and G. Smolinsky, Editors. A 1984 symposium. 636 pages, **$40.00.**

High Temperature Lamp Chemistry. E. G. Zubler, Editor. A 1985 symposium. 340 pages, **$25.00.**

Computer Aided Acquisition and Analysis of Corrosion Data. M. W. Kendig, U. Bertocci, and J. E. Strutt, Editors. A 1984 symposium. 276 pages, **$17.00.**

Manganese Dioxide Electrode Theory and Practice for Electrochemical Applications. B. Schumm, Jr., R. L. Middaugh, M. P. Grotheer, and J. C. Hunter, Editors. A 1984 symposium. 696 pages, **$40.00.**

VLSI Science and Technology/1985. W. M. Bullis and S. Broydo, Editors. A 1985 symposium. 572 pages, **$35.00.**

Electromigration of Metals/Multilevel Metallization and Packaging. J. R. Lloyd, R. A. Levy, J. Pierce, and R. G. Frieser, Editors. A 1984 symposium. 201 pages, **$16.00.**

Silicon Molecular Beam Epitaxy. J. C. Bean, Editor. A 1985 symposium. 455 pages, **$36.00.**

The Chemistry and Physics of Composite Media. M. Tomkiewicz and P. N. Sen, Editors. A 1985 symposium. 373 pages, **$35.00.**

Materials and New Processing Technologies for Photovoltaics. V. K. Kapur, J. P. Dismukes, and S. Pizzini, Editors. A 1984 symposium. 432 pages, **$27.00.**

10/85

JOURNAL OF THE

EDITOR
Norman Hackerman
Jackie Bourne, Assistant to the Editor

DIVISIONAL AND GROUP EDITORS

BATTERY
R. J. Brodd
Elton J. Cairns
Eugene G. Gagnon
G. F. Nordblom
Darrel Untereker

CORROSION
J. W. Faust, Jr.
R. P. Frankenthal
H. S. Isaacs
Barry R. MacDougall
Florian Mansfeld
Ken Nobe
W. H. Smyrl

DIELECTRICS AND INSULATION
Robert S. Alwitt
Rudolf G. Frieser
Dennis Hess
Vikram J. Kapoor
S. P. Murarka
George L. Schnable
Alan W. Swanson

ELECTRODEPOSITION
Ugo Bertocci
Huk Y. Cheh
Y. Okinaka
Mordechay Schlesinger

ELECTRONICS
John M. Andrews
Ted F. Ciszek
George R. Cronin
James S. Harris
Subhash Mahajan
David L. Nelson
Bertram Schwartz
Thomas O. Sedgwick
Don W. Shaw
Ben Streetman
C. C. Wang
P. Wang
J. M. Woodall

ENERGY TECHNOLOGY GROUP
A. R. Landgrebe
S. Srinivasan
M. Tomkiewicz

HIGH TEMPERATURE MATERIALS
William A. Adams
E. D. Cater
J. V. Cathcart
Daniel Cubicciotti
Lee P. Hunt
Peter J. Meschter
Zuhair A. Munir
T. A. Ramanarayanan
David A. Shores
Donald R. Vissers
Gene F. Wakefield

INDUSTRIAL ELECTROLYTIC
Richard C. Alkire
Ronald L. Dotson
Scott Lynn

LUMINESCENCE AND DISPLAY MATERIALS GROUP
Harry G. Brittain
Simon Larach
Melvin Tecotzky

ORGANIC AND BIOLOGICAL ELECTROCHEMISTRY
Martin Blank
Glenn Dryhurst
John H. Wagenknecht
Stanley Wawzonek

PHYSICAL ELECTROCHEMISTRY
Gregory C. Farrington
David S. Ginley
Adam Heller
Nathan S. Lewis
Joseph T. Maloy
Gleb Mamantov
Barry Miller
William E. O'Grady
Robert A. Osteryoung
C. W. Tobias
Ronald H. Wilson

News Editor—Jack H. Westbrook

JOURNAL OF THE
ELECTROCHEMICAL SOCIETY
(USPS 284-140)
ISSN 0013-4651

The JOURNAL OF THE ELECTROCHEMICAL SOCIETY (USPS 284-140) is published monthly by The Electrochemical Society, Inc. at 215 Canal St., Manchester, NH 03108. The address for the Executive Offices, Editorial and Advertising Office, and Circulation Department of The Electrochemical Society, Inc., is 10 South Main St., Pennington, NJ 08534-2896. Subscription to members as part of membership service; subscription to nonmembers $135.00 plus $15.00 for postage outside U.S. and Canada. Single copies $7.00 to members, $12.00 to nonmembers. © Copyright 1985 by The Electrochemical Society, Inc. Second Class Postage paid at Pennington, New Jersey and at additional mailing offices.

POSTMASTER: Send address changes to THE ELECTROCHEMICAL SOCIETY, INC., 10 South Main St., Pennington, NJ 08534-2896.

November 1985

ELECTROCHEMICAL SCIENCE AND TECHNOLOGY

TECHNICAL PAPERS

Recharge Kinetics of the Porous Lead Dioxide Electrode. I. The Effect of Structural Changes
P. Ekdunge, D. Simonsson 2521

Recharge Kinetics of the Porous Lead Dioxide Electrode. II. The Effect of Sulfuric Acid Concentration
P. Ekdunge, D. Simonsson 2529

The Influence of Composition and Microstructure on the Corrosion Behavior of Pb-Ca-Sn Alloys in Sulfuric Acid Solutions
D. Kelly, P. Niessen, E. M. L. Valeriote 2533

Characteristics of Sulfolane-Based Electrolytes for Rechargeable Lithium Batteries
Y. Matsuda, M. Morita, K. Yamada, K. Hirai 2538

Effect of EDTA on the Cathodic Reduction of Oxide Films on Iron in Sodium Hydroxide Solution
Z. Szklarska-Smialowska, T. Zakroczymski, C.-J. Fan 2543

Activation of the Iron Surface to Hydrogen Absorption Resulting from a Long Cathodic Treatment in NaOH Solution
T. Zakroczymski, Z. Szklarska-Smialowska 2548

Formation and Breakdown of Passive Oxide Films on Nickel in Halide Solutions
B. MacDougall, M. J. Graham 2553

Polarization and Corrosion of Electrogalvanized Steel—Evaluation of Zinc Coatings Obtained from Waste-Derived Zinc Electrolytes
M. Dattilo 2557

Transpassive Dissolution of Ni in Acidic Sulfate Media: A Kinetic Model
M. Keddam, H. Takenouti, N. Yu 2561

An Improved Accelerated Test Chamber for Electrolytic Metal Migration and Corrosion
J. J. Steppan, W. R. Seebaugh, J. A. Roth, L. C. Hall 2567

Electroreduction of Chromium (VI) in Aqueous Acid Solutions
A. F. Diaz, D. Schermer 2571

Electrochemical and Metallurgical Aspects of Laser-Enhanced Jet Plating of Gold
M. H. Gelchinski, L. T. Romankiw, D. R. Vigliotti, R. J. von Gutfeld 2575

Mechanisms of Electroless Metal Plating. II. Formaldehyde Oxidation
P. Bindra, J. Roldan 2581

Plasma-Sprayed Semiconductor Electrodes: Photoelectrochemical Properties of TiO_2
L. Parent, J. P. Dodelet, G. G. Ross, B. Terreault, S. Dallaire 2590

On the Thermal Characteristics of Electrolytic Cell
Y. Ogata, S. Kainuma, M. Yasuda, F. Hine 2594

Gas Permeation in SPE Method. II. Oxygen and Hydrogen Permeation Through Nafion
Z. Ogumi, T. Kuroe, Z.-i. Takehara 2601

Oxidation of Phenol with AC Electrolysis
D-T. Chin, C. Y. Cheng 2605

Modification of Titanium Electrodes for Detection of Biological Substances
I. Nakabayashi, T. Tomida, K. Kawashiro 2611

Laser Interferometry of Pulsed Galvanostatic Deposition of Polycarbazole
R. N. O'Brien, K. S. V. Santhanam 2613

Ionic Conductivity in Glass and Glass-Ceramics of the $Na_3YSi_3O_9$ and $Na_3YSi_4O_{12}$ Type Materials
E. Banks, C. H. Kim 2617

ELECTROCHEMICAL SOCIETY

Vol.132 • No. 11

Light-Generated Electrodics-Rotating Dual Electrodes
.....B. Miller, J. M. Rosamilia 2621

Extension of DC Transient Techniques to the Nonlinear Current Density-Overpotential Range and the Limitations of Linearized Approximations
.....Z. Nagy, R. H. Land, G. K. Leaf, M. Minkoff 2626

A Systematic Approach to the Determination of Possible Reaction Mechanisms of Oyxgen Reduction of Platinum in Alkaline Medium
.....J. L. Valdes, H. Y. Cheh 2635

Underpotential Deposition of Copper on Gold and the Effects of Thiourea Studied by AC Impedance
.....J. C. Farmer 2640

On the Evolution of Concepts Concerning Events at the Semiconductor/Solution Interface
.....J. O'M. Bockris, S. U. M. Khan 2648

The Effects of Surface Energetics on the Cyclic Voltammetry of Metallocenes at Nonilluminated n-InP Electrodes
.....C. A. Koval, R. L. Austermann 2656

TECHNICAL NOTES

Influence of pH on the Charge Storage Behavior of Thermally Prepared MnO_2 Film
.....L. D. Burke, M. J. Ahern 2662

Electrochemical Behavior of Thin Platinum (111) Films Deposited on Mica Surfaces
.....H.-Y. Liu, F.-R. F. Fan, A. J. Bard 2666

Hydrogen Insertion of a Vanadium Pentoxide Cathode
.....S. J. Hibble, A. M. Chippindale, P. G. Dickens 2668

The Electrochemical Deposition of Conducting Poly(3-Methyl-2,5-Thienylene) Films from Aqueous Media
.....A. Czerwinski, H. Zimmer, C. V. Pham, H. B. Mark, Jr. 2669

SOLID-STATE SCIENCE AND TECHNOLOGY

TECHNICAL PAPERS

Deep Levels in Semi-Insulating LEC GaAs Before and After Silicon Implantation
.....S. Dindo, I. Abdel-Motaleb, K. Lowe, W. Tang, L. Young 2673

Chemical Vapor Deposition of Ruthenium and Ruthenium Dioxide Films
.....M. L. Green, M. E. Gross, L. E. Papa, K. J. Schnoes, D. Brasen 2677

Thermal Oxidation of Silicon in Dry Oxygen: Growth-Rate Enhancement in the Thin Regime. Experimental Results
.....H. Z. Massoud, J. D. Plummer, E. A. Irene 2685

Thermal Oxidation of Silicon in Dry Oxygen Growth-Rate Enhancement in the Thin Regime. II. Physical Mechanism
.....H. Z. Massoud, J. D. Plummer, E. A. Irene 2693

Polyimide Adhesion. Mechanical and Surface Analytical Characterization
.....R. G. Narechania, J. A. Bruce, S. A. Fridmann 2700

Electrical Properties of Silicon Dioxide Films Fabricated at 700°C. III. High Pressure Thermal Oxidation
.....L. P. Trombetta, R. J. Zeto, F. J. Feigl, M. E. Zvanut 2706

Formation of Silicon-On-Insulator Structures by Implanted Nitrogen
.....L. Nesbit, S. Stiffler, G. Slusser, H. Vinton 2713

Sidewall-Tapered Oxide by Plasma-Enhanced Chemical Vapor Deposition
.....G. C. Smith, A. J. Purdes 2721

Precipitation and Diffusivity of Arsenic in Silicon
.....R. Angelucci, G. Celotti, D. Nobili, S. Solmi 2726

Ultrafine Aerosol Particles in Semiconductor Cleanrooms
.....R. P. Donovan, B. R. Locke, C. M. Osburn, A. L. Caviness 2730

DIVISION AND GROUP OFFICERS

Battery Division

Sidney Gross, Chairman
Eugene Gagnon, Vice-Chairman
James McBreen, Secretary-Treasurer
Brookhaven National Laboratory
DAS Building 815
Upton, NY 11973

Corrosion Division

Edward McCafferty, Chairman
Robert A. Rapp, Vice-Chairman
Ronald B. Diegle, Secretary-Treasurer
11515 Manitoba NE
Albuquerque, NM 87111

Dielectrics and Insulation Division

Laura Rothman, Chairman
Robert B. Comizzoli, Vice-Chairman
D. L. Flowers, Treasurer
J. P. Dismukes, Secretary
Exxon Research & Engineering Company
Clinton Township
Route 22 East
Annandale, NJ 08801

Electrodeposition Division

Mordechay Schlesinger, Chairman
David S. Lashmore, Vice-Chairman
Uziel Landau, Secretary-Treasurer
Department of Chemical Engineering
Case Western Reserve University
Cleveland, OH 44118

Electronics Division

Patricia L. Castro, Chairman
W. Murray Bullis, Vice-Chairman (Semiconductors)
Howard R. Huff, Vice-Chairman (New Electronic Technologies)
Kenneth E. Bean, Treasurer
Stella W. Pang, Secretary
Massachusetts Institute of Technology
Lincoln Laboratory
244 Wood St.
Lexington, MA 02173

Energy Technology Group

V. K. Kapur, Chairman
H. Maru, Vice-Chairman
V. Jalan, Treasurer
D. S. Ginley, Secretary
Sandia National Laboratories
P.O. Box 5800
Albuquerque, NM 87185

High Temperature Materials Division

Wayne L. Worrell, Chairman
Zuhair A. Munir, Senior Vice-Chairman
Vishu D. Dosaj, Junior Vice-Chairman
David A. Shores, Secretary-Treasurer
Corrosion Research Center
151 Amundson Hall
421 Washington Ave. SE
Minneapolis, MN 55455

Industrial Electrolytic Division

Robert S. Karpluk, Chairman
W. Bruce Darlington, Vice-Chairman
Marino Y. C. Woo, Secretary-Treasurer
930 Brown Road
Bridgewater, NJ 08807

Luminescence and Display Materials Group

C. W. Struck, Chairman
R. O. Petersen, Vice-Chairman
W. M. Yim, Secretary-Treasurer
RCA Laboratories
David Sarnoff Research Center
Princeton, NJ 08540

Organic and Biological Electrochemistry Division

P. Zuman, Chairman
D. Evans, Vice-Chairman
G. Dryhurst, Secretary-Treasurer
Dept. of Chemistry
University of Oklahoma
620 Parrington Oval
Norman, OK 73019

Physical Electrochemistry Division

Larry R. Faulkner, Chairman
Barry Miller, Vice-Chairman
Rolf H. Muller, Secretary-Treasurer
30 High Gate Rd.
Berkeley, CA 94707

SOCIETY OFFICERS AND STAFF

Richard C. Alkire, President
Dept. of Chemical Engineering
University of Illinois
Urbana, IL 61801

Ronald E. Enstrom, Vice-President
RCA Laboratories
Princeton, NJ 08540

Fritz G. Will, Vice-President
General Electric Company
Research and Development Center
Schenectady, NY 12301

Bruce E. Deal, Vice-President
Fairchild Camera & Instrument Corporation
Palo Alto, CA 94304

James A. Amick, Secretary
Exxon Research & Engineering Company
Clinton Township
Route 22 East
Annandale, NJ 08801

Jerome Kruger, Treasurer
Department of Materials Science and Engineering
Johns Hopkins University
Baltimore, MD 21218

V. H. Brenneky, Executive Secretary
The Electrochemical Society, Inc.
10 South Main Street
Pennington, NJ 08534-2896

Roque J. Calvo, Assistant Executive Secretary
The Electrochemical Society, Inc.
10 South Main Street
Pennington, NJ 08534-2896

PUBLICATION STAFF

Sarah A. Kilfoyle, **Director of Publications**
Hugh P. Molloy

PUBLICATION COMMITTEE

Robert P. Frankenthal, **Chairman**
James A. Amick
Norman Hackerman
Bertram Schwartz
Lee P. Hunt
Rolf H. Muller
Boone B. Owens
Klavs F. Jensen

Manuscripts submitted to the JOURNAL should be sent in triplicate to the Editorial Office at 10 South Main Street, Pennington, NJ 08534-2896. They should conform to the revised "Instructions to Authors" available from Society Headquarters. Manuscripts so submitted, as well as papers presented before a Society technical meeting, become the property of the Society and may not be published elsewhere in whole or in part without written permission of the Society. Address such requests to the Editor.

The Electrochemical Society does not maintain a supply of reprints of papers appearing in its JOURNAL. A photoprint copy of any particular paper may be obtained from University Microfilms, Inc., 300 N. Zeeb St., Ann Arbor, MI 48106.

Inquiries regarding positive microfilm copies of issues should be addressed to University Microfilms, Inc., 300 N. Zeeb St., Ann Arbor, MI 48106.

Walter J. Johnson, Inc., 355 Chestnut St., Norwood, NJ 07648, have reprint rights to out-of-print volumes of the JOURNAL, and also have available for sale back volumes and single issues with the exception of the last two calendar years.

The JOURNAL OF THE ELECTROCHEMICAL SOCIETY combines the JOURNAL and TRANSACTIONS OF THE ELECTROCHEMICAL SOCIETY. Statements and opinions given in articles and papers in the JOURNAL OF THE ELECTROCHEMICAL SOCIETY are those of the contributors, and The Electrochemical Society, Inc. assumes no responsibility for them.

Claims for a missing issue should be reported within 60 days of normal delivery date to the Circulation Dept., The Electrochemical Society, Inc., 10 South Main Street, Pennington, NJ 08534-2896.

Notice of a change in address should be sent to the Circulation Dept., The Electrochemical Society, Inc., 10 South Main Street, Pennington, NJ 08534-2896. Include the mailing label or the number from the mailing label from your previous issue of the JOURNAL to ensure proper identification.

SOLID-STATE SCIENCE (Cont.)

Potential-Enhanced Doping of Si Grown by Molecular Beam Epitaxy
R. A. A. Kubiak, W. Y. Leong, E. H. C. Parker **2738**

Rapid Thermal Annealing in GaAs IC Processing
S. J. Pearton, K. D. Cummings, G. P. Vella-Coleiro **2743**

Lateral Epitaxial Growth over Oxide
L. O. Wilson, G. K. Celler **2748**

The Analysis of Diffusion Data by a Method of Moments
R. Ghez, J. D. Fehribach, G. S. Oehrlein **2759**

Comparisons of GaAs, Tungsten, and Photoresist Etch Rates and GaAs Surfaces Using RIE with CF_4, CF_4 + N, and SF_6 + N_2 Mixtures
N. Susa **2762**

Electrodeposition of Cadmium Telluride Using Phosphine Telluride
A. Darkowski, M. Cocivera **2768**

Thermodynamic Properties of Potassium Polyphosphide KP_{15}
H. S. Marek, C. G. Michel, J. A. Baumann, M. A. Kuck **2771**

Lift-Off Patterning of Sputtered SiO_2 Films (LOPAS) and Its Application to Recessed Field Isolation
T. Yachi, T. Serikawa **2775**

Kinetics and Mechanism of Selective Tungsten Deposition by LPCVD
Y. Pauleau, Ph. Lami **2779**

A Diffusion Model for Electron-Hole Recombination in Zn_2SiO_4: (Mn,As) Phosphors
D. J. Robbins, N. S. Caswell, Ph. Avouris, E. A. Giess, I. F. Chang, D. B. Dove **2784**

TECHNICAL NOTES

Backgating in Ion-Implanted GaAs MESFET
W. C. Tang, K. S. Lowe, I. Abdel-Motaleb, L. Young **2794**

Precipitation in Fe-Doped Semi-Insulating InP Epitaxial Layer Grown by Metalorganic Chemical Vapor Deposition (MOCVD)
S. N. G. Chu, S. Nakahara, J. A. Long, V. G. Riggs, W. D. Johnston, Jr. **2795**

Color and Efficiency of Neodymium Iodide Discharges
W. A. McAllister **2798**

COMMENTS **2801**

ACCELERATED BRIEF COMMUNICATIONS

***In Situ* Raman Spectroscopy for the Study of Iron Passivity in Relation to Solution Composition**
A. Hugot-Le Goff, C. Pallotta **2805**

The Analysis of Silver in Germanium Selenide Photoresist by Anodic Stripping Voltammetry
B. G. Huggett, J. Greenaway, M. L. Hitchmen **2807**

Alkenylsilane Sulfone Copolymers and Terpolymers as Electron-Beam-Sensitive Positive Resists for Two-Layer Systems
A. S. Gozdz, H. G. Craighead, M. J. Bowden **2809**

Microphotoelectrochemical Etching of n-GaAs Using a Scanned Focused Laser
R. D. Rauh, R. A. LeLievre **2811**

Elimination of Flux Transients in Molecular Beam Epitaxy
P. A. Maki, S. C. Palmateer, A. R. Calawa, B. R. Lee **2813**

A Measurement of the Effect of Intrinsic Film Stress on the Overall Rate of Thermal Oxidation of Silicon
J. K. Srivastava, E. A. Irene **2815**

REVIEWS AND NEWS

NEWS **445C**

Instructions to Authors **453C**

Call for Papers—Boston, Massachusetts, Meeting **459C-464C**

JOURNAL OF THE ELECTROCHEMICAL SOCIETY

ELECTROCHEMICAL SCIENCE AND TECHNOLOGY

NOVEMBER 1985

Recharge Kinetics of the Porous Lead Dioxide Electrode

I. The Effect of Structural Changes

Per Ekdunge and Daniel Simonsson

Department of Chemical Technology, The Royal Institute of Technology, S-100 44 Stockholm, Sweden

ABSTRACT

The changes in structure and kinetics during charge of the porous PbO_2 electrode have been studied by means of electrochemical and structure characterizing methods. It was found that the potentiostatic charge current after an initial period of growth, due to nucleation and growth of PbO_2, is proportional to the decreasing amount of remaining lead sulfate. The polarization curves have a Tafel slope of about 60 mV/decade at overvoltages lower than 0.1V and about 180 mV/decade at higher overvoltages. The form of these curves can be explained by a mechanism with two consecutive single-electron transfer reactions. The results from these specific studies of the positive electrode and charge experiments with complete lead-acid cells show that the fastest way to charge lead-acid batteries is to charge at a constant cell voltage of a value just below that which leads to unacceptable gassing rates.

In spite of its great age, the cheap and reliable lead-acid battery is still the single most used battery in the world. Consequently, it has been and still is the target of intensive research. The research area has been reviewed by Burbank *et al.* in 1971 (1) and by Rüetschi in 1977 (2). Vinal's classic textbook (3) on the subject from a technological point of view has been succeeded by Bode's "Lead-Acid Batteries," published in 1977 (4). In comparison to the discharge process, less scientific interest has been paid to the charge process. This topic has more often been approached with the technological aim of finding the optimal method of charging or procedures for very rapid charging. One of the results of these studies of black-box character is the classical rule of thumb which goes by the name of the ampere-hour law and states that a battery can accept as much current (in amperes) as it needs in capacity (in ampere-hours) until it reaches full charge.

On the other hand, fundamental studies have been made of specific phenomena in the electrodes of the lead-acid battery. Studies have thus been reported on the electrocrystallization of lead dioxide from lead sulfate formed on smooth electrodes of electrodeposited lead dioxide or lead (5-8).

A lot of research has also been devoted to the electrode kinetics of the lead dioxide electrode (*e.g.*, 9-13), but it has been mainly with simplified systems with a plane electrode and where the sulfuric acid has been substituted with an electrolyte which does not give a solid product such as lead sulfate. A real battery electrode deviates significantly from the majority of systems used in these studies. A main difference is its porous structure, which introduces the additional complexities of current distribution and concentration gradients in the pores. The porous structure is in itself of decisive importance for the electrode kinetics. Specific surface area and pore size distribution are important structural parameters. These parameters are not constant in the porous lead dioxide electrode because of the structural transformations that occur between the two solid phases: lead dioxide and lead sulfate. These structural changes have been studied in optical and scanning electron microscopes (14-19) and with structure characterizing methods (19-20).

The overall kinetic behavior of the porous lead dioxide electrode as a result of the mutual dependences of intrinsic kinetics, structural changes, current distribution, and concentration changes is still waiting to be explored, especially with regard to the anodic process. The aim of the present work was to determine the relative importance of various structural and kinetic parameters for the rate at which lead-acid batteries can be charged. This is a question of high practical importance, not least in the application as a power source in electric vehicles. The interest was focused on the positive electrode since in most systems this is generally the limiting one, both at discharge and charge.

Experimental

The investigations were performed with commerical battery electrodes from Noack, Sweden, with a thickness of 2.0 mm. The lead grid was alloyed with 2.4-2.6% antimony and lesser amounts of arsenic (0.09-0.11%), tin (0.03-0.04%), and selenium (0.02%). Electrodes for the investigations were cut into the size 60 × 60 mm^2. The working electrode was placed centrally in a Plexiglas cell. Two lead electrodes were used as counterelectrodes. The electrolyte was 5.0*M* H_2SO_4 in large excess. The electrode potential was measured relative to a Hg/Hg_2SO_4 reference electrode. The potentiostatic experiments were performed with a Wenking 68TS10 potentiostat. In order to obtain a uniform lead sulfate distribution in the electrodes, they were discharged with a low current density (−20 A/m^2) in the standard case. The discharge was interrupted at a potential of 0.9V. The electrode was at rest for 2h before the charge.

For comparisons, recharge experiments were also performed with complete lead-acid cells with electrodes of the full size. Six cells were assembled; each with three positive and four negative plates. In five of these cells, the distance between the electrodes was 5 mm and was controlled by vertical separator tubes of the type used for tubular electrodes. In one cell, the electrodes were closely packed with ordinary separators between them. The cells were made of Plexiglas. They were closed and gastight; evolved gases were allowed to escape from the cell through an outlet connected to an oxygen sensor (Servomex OA250). The gas evolution rate was measured volumetrically with a graduated tube. The temperature was measured with a thermometer inserted through the lid via a sealing rubber stopper. A thermostat bath was used to

control the temperature in runs at nonambient temperature.

In all experiments, the charges were recorded by electronic coulometers simulataneously with the overvoltage or current.

The structural changes were followed by visual observations with SEM (Jeol JSM2) and by measuring the changes in specific surface area according to the BET method (Micromeritics Accusorb 2100 E) and pore size distribution by means of mercury porosimetry (Aminco 5-7118). Samples taken for these observations were washed according to a special procedure in order to avoid large concentration gradients which can cause redistribution of the lead sulfate in a bipolar process driven by the concentration elements thus created. The samples were placed in a beaker filled with a stirred $5M$ H_2SO_4 solution. This solution was then progressively diluted with distilled water, which was added continuously with a rate adjusted so that all the sulfuric acid had been washed out overnight. In this way, the concentration gradients within the porous electrode were limited to small values.

The changes in effective conductivity of the pore electrolyte were determined from the ohmic voltage drop required to pass a given current through the unloaded electrode. An x-ray diffraction analysis showed that the active mass of the fully charged positive electrode consisted almost entirely of β-PbO_2.

Results

Galvanostatic and potentiostatic charges.—Charging with a constant current gave the overvoltage-time curves shown in Fig. 1 and 2. In these curves the Ri-free overvoltage has been plotted against a nominal state of charge defined as

$$q = q_d + \int_0^t i\,dt \qquad [1]$$

where q_d is the charge output in the previous discharge. The general form of these curves can be interpreted by formally distinguishing four different regions. When the constant current is applied to the fully discharged electrode, the potential immediately rises to a peak value. The overvoltage then rapidly decreases to a flat minimum at about 10-20% charge. In a third region, the overvoltage increases monotonically until it finally reaches the plateau corresponding to the oxygen evolution reaction on the fully charged electrode.

The potential peak decreases with the decreasing discharge capacity at increasing discharge current. The minimum, on the other hand, first decreases with increasing discharge current density and then increases at very large discharge currents.

Figure 2 shows that the charge curve is flatter at lower current densities. The recharge of a partially discharged electrode requires a lower overvoltage than a fully discharged electrode which has been recharged to the same state of charge. It can also be noted that the inflection point of curve 3 in Fig. 2 is at an overvoltage of approximately the same value as the minimum in the recharge curve (curve 1) of the fully discharged electrode.

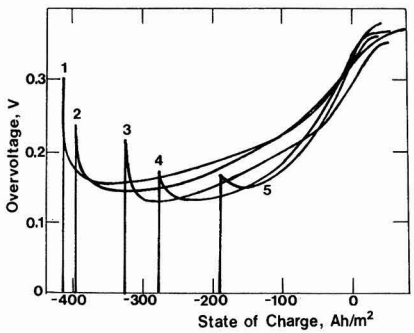


Fig. 1. Overvoltage-time curves at galvanostatic charge with 200 A/m² of an electrode discharged with −30 (curve 1), −100 (curve 2), −200 (curve 3), −500 (curve 4), −1000 A/m² (curve 5).

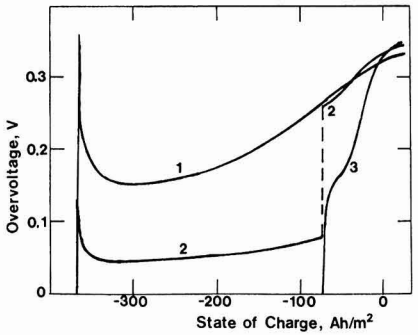


Fig. 2. Overvoltage-time curves at galvanostatic charge of fully discharged (curve 1) and partially discharged (curve 3) PbO_2 electrodes. Current density = 200 A/m². Curve 2: charge with 20 A/m² to 80%, followed by charge with 200 A/m².

The potentiostatic charge curves (Fig. 3) can be interpreted in the corresponding way. The falling potential after the initial peak value at the galvanostatic charge has its correspondence in a rising current at potentiostatic charge. After a maximum (corresponding to the minimum in the galvanostatic charge curve), the current decays almost linearly with the state of charge. Since the current efficiency is somewhat less than 100%, especially at higher overvoltage, the nominal state of charge (q) is somewhat higher than the true state of charge. The curves therefore do not level off at the oxygen evolution current until q assumes positive values. Figure 4 shows that the current density at potentiostatic charge is not a state function with respect to the $PbSO_4/PbO_2$ composition. The maximum current was roughly the same (within 20%) irrespective of whether the electrode had been discharged to 100, 70, or only 20% (curves 1-3 in Fig. 4). When the electrode had been discharged with a high current density (−1000 A/m²), the potentiostatic charge current was somewhat higher.

The rising transients in Fig. 3 and 4 and the falling overvoltage in Fig. 1 and 2 can be ascribed to nucleation and growth of lead dioxide. This process governs the kinetics only up to 10-20% charge. The amount of charge consumed in this region is independent of the current or the potential. An initial galvanostatic charge with low current

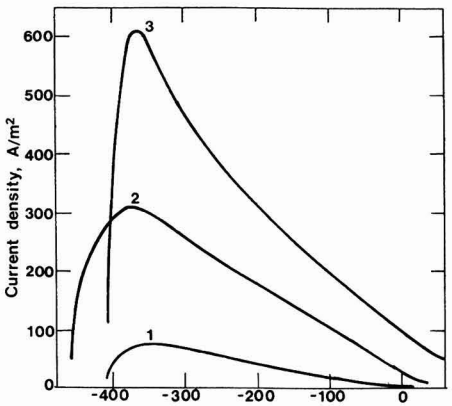


Fig. 3. Potentiostatic charge of a PbO_2 electrode at different overvoltages: 100 (curve 1), 200 (curve 2), 266 mV (curve 3).

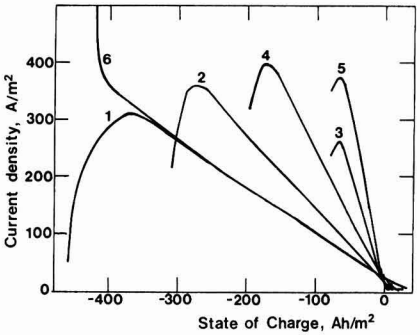


Fig. 4. Potentiostatic charge of an electrode discharged under different conditions. Curves 1-3: discharged with −20 A/m² to 100 (curve 1), 70 (curve 2), and 20% (curve 3). Curves 4, 5: discharged with −1000 A/m² to 100 (curve 4), and 40% (curve 5). Curve 6: discharged with −20 A/m² to 100% and recharged galvanostatically with 20 A/m² to 10%.

density (20 A/m²) to 10% followed by a potentiostatic charge resulted in a monotonically decreasing current coinciding with the decreasing current of the complete potentiostatic charge curve (Fig. 4). The initial deviation between the two curves can probably be explained by the differences in electrolyte concentration profiles. The rising transients were also observed at the potentiostatic charge of only partially discharged electrodes, although its relative importance decreases with decreasing discharge.

The dependence of overvoltage on current density at different states of charge is shown in Fig. 5. These curves were obtained by applying different constant currents of short duration at three different states of charge (20, 50, and 80%), while the electrode was otherwise charged with a low constant current density in order to avoid nonuniform current distribution and the establishment of concentration gradients. The overvoltage was corrected for the contribution from the increasing acid concentration gradient by extrapolation back to time zero. The anticipated linear decrease in current density with the increasing state of charge indicated by the potentiostatic oxidations was tested by a rate equation of the form

$$i = S_m j_0 L\,(q/q_d)\exp\left(\frac{\alpha n \mathbf{F}}{RT}\eta\right) \qquad [2]$$

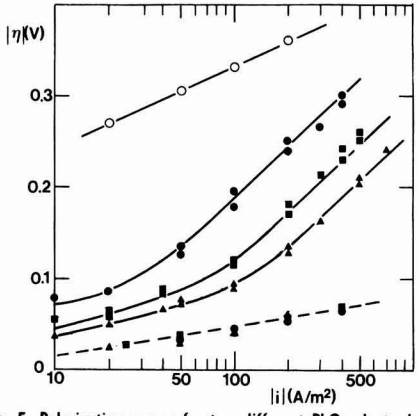


Fig. 5. Polarization curves for two different PbO_2 electrodes fully discharged with −20 A/m² and recharged with 20 A/m² to 20 (triangles), 50 (squares), 80 (filled circles), and 120% (open circles) (oxygen evolution). Solid lines: anodic current. Dashed line: cathodic current. The anodic polarization curves drawn for the partial charges are fits to the relation $i = S_m j L q/q_d$ where j is given by Eq. [12] with α_r = 0.32, $S_m 2j_{0,r}L$ = 47 A/m², $j_{0,r}/j_{0,o}$ = 25, and α_o = 0.5.

at higher overvoltage, where the back reaction can be neglected. Piecewise fits of this expression are in good agreement with the experimental points in Fig. 5. At lower overvoltage, $\alpha n \approx 1$ and $S_m j_0 L \approx 3$ A/m². The Tafel slope increases abruptly at an overvoltage of 0.1V. Above this value, αn = 0.32 and $S_m j_0 L$ = 47 A/m². Calculations with a rate equation derived from Eq. [2] showed that the current density distribution in the porous electrode was practically uniform at all current densities. When the overvoltage approaches a value of 0.3V, the side reaction of oxygen evolution becomes significant. The Tafel slope of 95 mV/decade found for this electrode reaction is in agreement with the results of Rüetschi *et al.* (21). Figure 5 also shows the cathodic overvoltage measured in the same way at different states of charge during the recharge process.

Charging of full-size cells.—Preliminary experiments with potentiostatic charge of lead dioxide and lead electrodes, respectively, showed that the positive electrode was the limiting one both at discharge and at charge. The behavior of the lead-acid cell would then be controlled mainly by its positive electrode. Experiments with complete cells with full-size electrodes were therefore undertaken in order to compare the behavior observed for the single lead dioxide electrode with that of the complete cell. Comparisons were made between charging with constant current (*I*), constant voltage (*U*), and constant current followed by constant voltage (*IU*), respectively. The voltage-time curves at charging with constant current are shown in Fig. 6 together with the total volume of evolved gases. The common feature of the different charge curves is a continuously increasing voltage up to a state of charge where the voltage rises abruptly to a much higher level while simultaneously the gassing rate increases rapidly. A cell voltage of, *e.g.*, 2.6V is reached after 71, 79, and 90% charge at 150, 100, and 50 A/m², respectively. The fraction remaining to be charged into the battery is thus approximately proportional to the current density. This is in accordance with the first-order dependence on lead sulfate as expressed in Eq. [2]. The galvanostatic charge curves in Fig. 6 exhibit a steeper rise in overvoltage than those of a single PbO_2 electrode in Fig. 1.

Charging with constant current until the cell voltage reaches 2.50V followed by charging at constant voltage gave the results shown in Fig. 7. Compared to charging with constant current, this procedure has the advantage that excessive gassing is automatically avoided by not allowing the voltage to increase above a prescribed value. According to Fig. 7, the charging current decays exponentially during the period of constant voltage. The

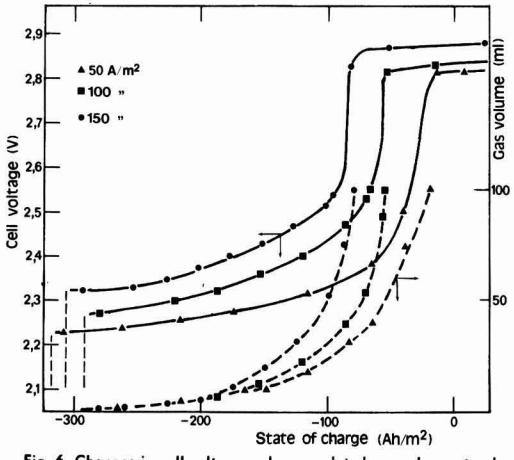


Fig. 6. Changes in cell voltage and accumulated gas volume at galvanostatic charge at different current densities. Discharge current density = −120 A/m².

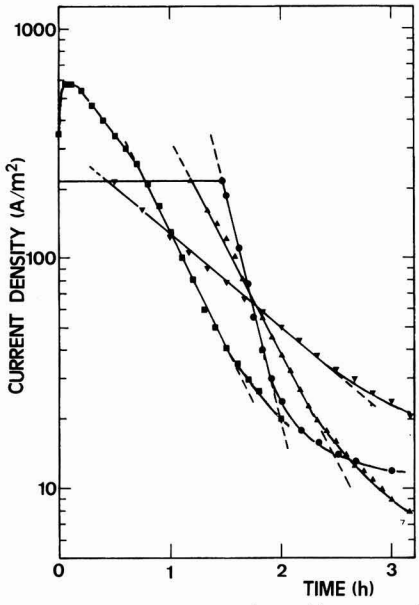


Fig. 7. Current density vs. time at a charge with constant cell voltage = 2.50V (squares), 22°-29°C, and *IU* charging with current limitation to 22A at different temperatures: 3.5°C (nablas), 25°C (triangles), and 52°C (circles).

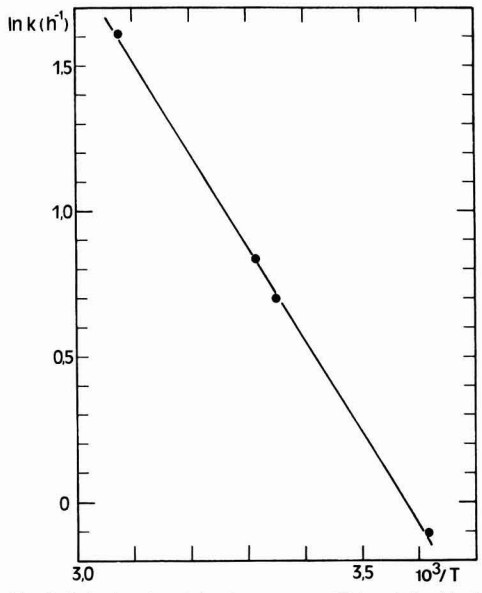


Fig. 8. Arrhenius plot of the charge rate coefficient defined by Eq. [4].

experimental curves deviate from the straight ln i-t lines at lower current densities, since the electrochemical gas evolution becomes a progressively higher fraction of the total, decreasing current. The disadvantage of *IU* charging is obviously that it does not take full advantage of the high charge acceptance in the beginning. Charging at constant voltage utilizes this possibility of high initial currents. The curve for charging at a constant cell voltage of 2.50V in Fig. 7 is somewhat convex after the maximum. This is due to a temperature rise from 22° to 29°C. In the linear portion of the curve, the temperature varies only between 29° and 28°C.

When Eq. [1] and [2] are combined, we obtain the variation of current density with time

$$i = i_1 \exp\left[-k\,(t - t_1)\right] \qquad (\eta \approx \text{const}) \qquad [3]$$

where index 1 denotes the time after which Eq. [2] is valid, and

$$k = S_m j_0 L \exp\left(\frac{\alpha n \mathbf{F} \eta}{RT}\right)/(-q_0) \qquad [4]$$

The coefficient k is a rate coefficient which can be determined from the slopes of the linear portions of the curves in Fig. 7. The temperature dependence of k at constant cell voltage follows an Arrhenius relation (see Fig. 8).

Structural changes.—The morphological changes during charge were followed by taking out samples at different states of charge for visual observations by means of a scanning electron microscope. These observations showed that larger lead sulfate crystals were formed at lower rates of discharge (Fig. 9 and 10). The size of the lead sulfate crystals could, furthermore, be related to the volumetric restriction imposd by the porous structure. On the exterior surface, where there are no such restrictions, the lead sulfate can grow to large, closely packed crystals (Fig. 9 and 10). This also holds for larger voids in the porous electrode (Fig. 11), while otherwise the lead sulfate crystals were smaller and randomly dispersed in the porous structure (Fig. 12). In most cases, no firm conclusions could be drawn as for the mechanism of the structural transformations: occasionally, we could observe how lead sulfate crystals were transformed into lead dioxide with the macrostructure preserved (Fig. 13). This type of transformation has earlier been observed by Simon *et al.* (14, 16). Interesting observations were made concerning the structural transformations of the larger lead sulfate crystals formed on the exterior surface at low discharge rates. The lead dioxide formed during charge was held within the dimensions of the original lead sulfate crystals. A dense microcrystalline wall of lead dioxide was formed which eventually was ruptured at excess charge and revealed an inside growth of small lead dioxide crystals into the form of a compact kernel (see Fig. 10 and 14-17).

The changes in specific surface area are of great importance when attempting to explain the changes in electrode kinetics. Although the BET method does not distinguish between the surface areas of PbO_2 and $PbSO_4$, important conclusions can be drawn when combined

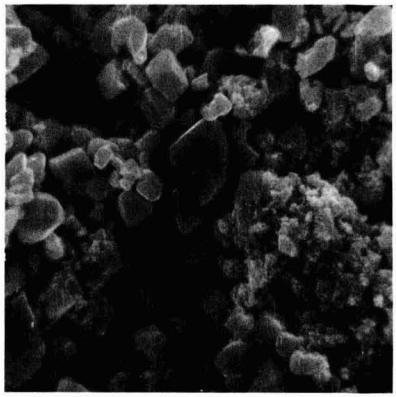


Fig. 9. Lead sulfate crystals formed on the exterior surface of the electrode at a discharge with −200 A/m² to −320 Ah/m².

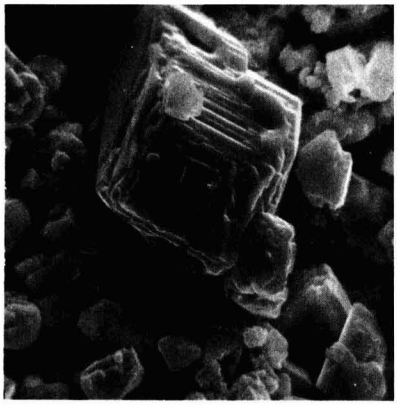


Fig. 10. Lead sulfate crystals formed on the exterior surface at a discharge with -30 A/m^2 to -410 Ah/m^2.



Fig. 11. Formation of dense agglomerates of lead sulfate crystals in a larger void. Electrode discharged with -30 A/m^2.



Fig. 12. Morphology of the interior of the electrode. Discharge with -30 A/m^2 to -350 Ah/m^2.

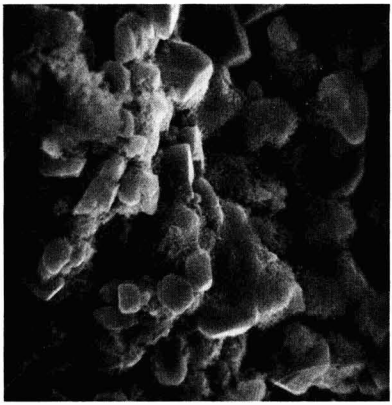


Fig. 13. Formation of microporous lead dioxide within the dimensions of the original lead sulfate crystals formed during discharge. Electrode discharged with -30 A/m^2 and recharged with 200 A/m^2 to -48 Ah/m^2.

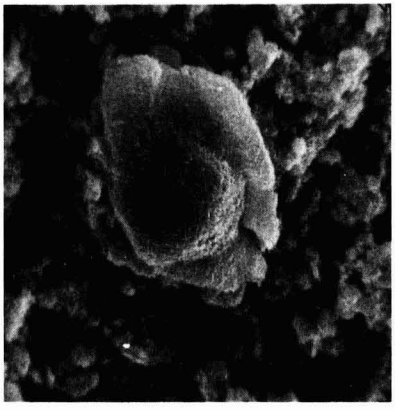


Fig. 14. SEM micrograph showing the beginning of the transformation of large lead sulfate crystals into microcrystalline lead dioxide in the form of shell and kernel.

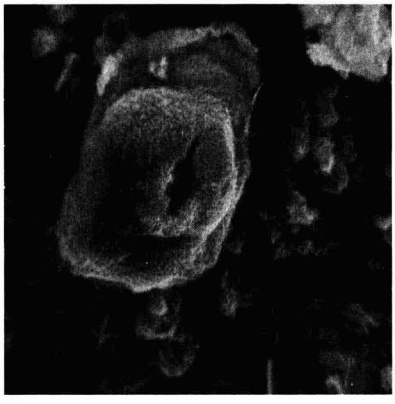


Fig. 15. SEM micrograph showing the transformation of large sulfate crystals into microcrystalline lead dioxide in the form of shell and kernel.

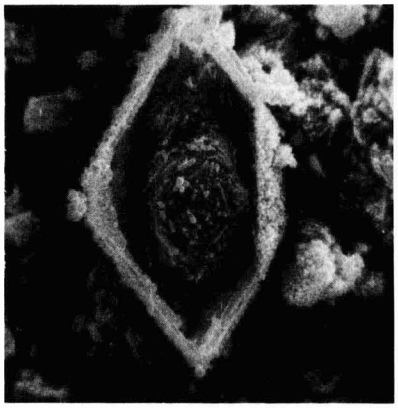


Fig. 16. SEM micrograph of large sulfate crystals transformed into microcrystalline lead dioxide in the form of shell and kernel.

with other pieces of information. The changes in specific surface area during charge are illustrated in Fig. 18. The fully discharged electrode has a specific surface area which is almost three times smaller than that of the fully charged. The latter is 6.4 m^2/g, which according to the geometric relationship for spherical particles

$$S\rho = 6/d_p \qquad [5]$$

corresponds to a mean particle diameter of 0.1 μm. The mean particle diameter of the fully discharged electrode can, in the same way, be calculated to be 0.4 μm. These values can be compared to those estimated from micrographs, which are about 0.1 μm for the lead dioxide and 1-10 μm for the lead sulfate. The specific surface area of the fully discharged electrode must, therefore, to a major extent, be attributed to residual lead dioxide which has not been covered with $PbSO_4$ but is either electrically insulated or electrochemically nonactive. The dashed line in Fig. 18 represents the change in specific surface area of the lead dioxide only according to a structural model assuming spherical particles shrinking uniformly during discharge. The measured surface area of the fully discharged electrode is lower than that predicted by this model. This is also to be expected since microscopy studies have revealed that much of the PbO_2 remaining at the end of discharge have been encapsulated within $PbSO_4$ crystals (14, 16). The initially rapid growth of specific surface area during charge can thus be attributed to the uncovering of this encapsulated PbO_2, while at the same time a large inner surface area of $PbSO_4$ is created inside the $PbSO_4$ crystals as they dissolve. Although residual PbO_2 may act as nuclei for the lead dioxide formed during charge, new nuclei will probably be formed in parallel at the high initial overvoltage. These new PbO_2 crystals will give an additional contribution to the surface area. After the initially rapid growth of surface area, the continued increase is much slower because the surface area of PbO_2 grows slower than linearly with the amount of charge, while the surface area of $PbSO_4$ decreases.

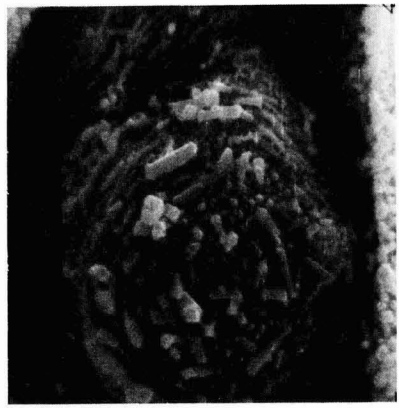


Fig. 17. Detail of Fig. 16

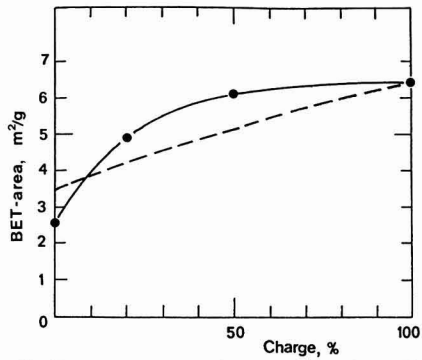


Fig. 18. Changes in specific surface area during charge. The surface area is given in the unit of square meter per equivalent gram of PbO_2.

The changes in pore size distribution are plotted in Fig. 19. The fully charged electrode had a total porosity of 56%, including closed pores and pores smaller than 0.035 μm, and a mean pore diameter of but 0.15 μm. Using a cylindrical pore model, the porosimetry data can also be used to estimate the specific surface area. The values obtained in this way were 40-50% lower than the corresponding values measured by the BET method. Besides the inaccuracy of the cylindrical pore model, part of this discrepancy can be attributed to pores smaller than 0.035 μm, which contribute little to the pore volume but appreciably to the specific surface area.

The changes in the porosimetry curves in Fig. 19 also reflect the fact that the molar volume of lead sulfate (48.9 cm^3/mol) is almost twice that of lead dioxide (25.5 cm^3/mol). The plugging effect of the lead sulfate in the pores affects the effective transport coefficients for diffusion and migration. The changes in effective conductivity are plotted in Fig. 20. As expected, the effective conductivity increases during charge, due to the opening up of pores, but then reaches a flat maximum at about 80% charge. The labyrinth factor $\lambda = \kappa_{eff}/\kappa_{free}$ of the fully charged electrode is 0.15 including the effect of the grid and about 0.19 after correction for the grid, which occupies about 20% of the total projected electrode area.

Discussion and Conclusions

The results should be interpreted with respect to both the individual factors and their mutual dependence. It can thus be concluded that the initial part of the charge process is governed by the formation of electrochemically active PbO_2 surface. As already discussed, Fig. 18 indicates that this occurs not only by nucleation and growth of new PbO_2 crystals, but also by the uncovering of encapsulated or covered residual lead dioxide. This hypothesis is also supported by the observation that the duration of this process is independent of current density or overvoltage and that it does not affect the later period of the recharge.

The rising potentiostatic transient reaches a maximum after recharge to only 10-20%. While this first, shorter period is controlled mainly by the available surface area of lead dioxide, the major portion of the charge process

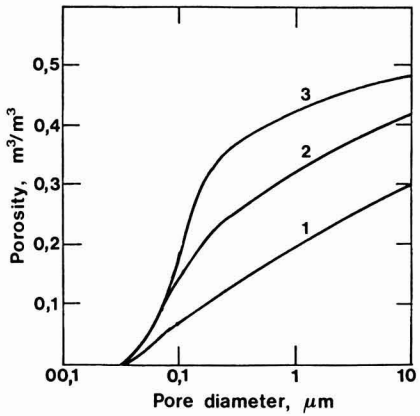


Fig. 19. Pore size distribution of a porous PbO_2 electrode. 1: Fully discharged. 2: 50% charged. 3: Fully charged.

seems to be controlled by the availability of lead sulfate. It is obvious that the anodic and cathodic reactions are different in their dependence on the structural changes and cannot be microreversible at the current densities employed. The cathodic polarization curves in Fig. 5 do not differ significantly from each other, which indicates that the working surface area of the active lead dioxide is relatively constant after a recharge to 20%. This is in agreement with the results from the surface area measurements (Fig. 18) when recalling that the main fraction of this total specific surface area can be attributed to the lead dioxide.

Contrary to this, the anodic reaction is apparently first order with respect to the amount of remaining lead sulfate. The charge reaction, therefore, seems to be confined to a zone very close to the surface of the lead sulfate crystals. An evident explanation would be that the reaction proceeds through a solid-state mechanism. On the other hand, it is more commonly believed that the transformations between lead sulfate and lead dioxide occur via a dissolution precipitation mechanism involving dissolved Pb^{2+} ions. Vetter (22) has shown that such a mechanism is possible in the lead dioxide electrode, and that the volumetric diffusion rate of Pb^{2+} ions over the microscopic distances is sufficiently high to allow an efficient utilization of the whole PbO_2 surface. According to this mechanism, the oxidation reaction can be formally written as

$$PbSO_4\,(s) \rightarrow Pb^{2+} + SO_4^{2-} \qquad [6]$$

$$Pb^{2+} + 2H_2O \rightarrow PbO_2\,(s) + 4H^+ + 2e \qquad [7]$$

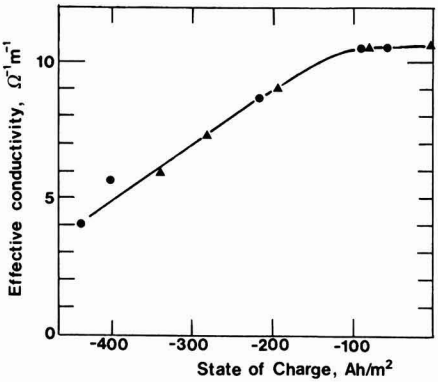


Fig. 20. Changes in effective conductivity during charge. Two different electrodes.

where the latter reaction in turn is composed of several elementary steps. Vetter's analysis can be extended by taking into consideration the interplay of diffusion and intrinsic electrode kinetics in a rate equation. Assuming first-order, purely consecutive reactions, the kinetic equation at high overvoltage for this scheme would be of the form

$$i = \frac{S_2 j_0 \exp\left(\frac{\alpha n \mathbf{F}}{RT}\eta\right)}{1 + \frac{S_2 j_0}{2\mathbf{F}}\left(\frac{1}{k_0 S_1} + \frac{L}{D c_{eq} S_{1,2}}\right)\exp\left(\frac{\alpha n \mathbf{F}}{RT}\eta\right)} \qquad [8]$$

Equation [8] takes into account the dissolution rate of $PbSO_4$ and the diffusion of Pb^{2+} ions over a characteristic distance L and across a mean cross section $S_{1,2}$, which is some weighted average of the surface areas of $PbSO_4$ (S_1) and PbO_2 (S_2). When the dissolution and diffusion rates are high in comparison to the charge transfer rate, the second term in the denominator vanishes and the current is proportional to the surface area of lead dioxide. It is only at the limiting current density, when the reaction rate is controlled by the dissolution and/or diffusion, that the current is proportional to the surface area of lead sulfate. Equation [8] thus predicts η-i curves for different states of charge which approximately coincide at low current densities, diverge at higher current densities, and finally reach their different limiting values appearing as vertical lines in the η-i diagram. The different curves in Fig. 5 obviously do not follow this pattern. The curves at different states of charge do not coincide until very close to the equilibrium potential, and no distinct limiting currents can be observed at higher overvoltages.

An alternative kinetic model takes into account that diffusion of Pb^{2+} ions and their reaction occur in parallel as well as in consecutive steps. The physical picture is then similar to that in a heterogeneous catalyst particle (23). An order of magnitude calculation shows, however, that even in this case, the diffusion rate of lead ions is sufficient to balance their consumption rate in the charge reaction.

The switch from a low to a high Tafel slope in Fig. 5 can be explained by a mechanism with two consecutive single-electron transfer reactions. This case has been treated by Vetter (24) for the general scheme

$$S_r \rightleftarrows S_m + e^- \qquad [9]$$

$$S_m \rightleftarrows S_o + e^- \qquad [10]$$

$$S_r \rightleftarrows S_o + 2e^- \qquad [11]$$

Writing down the rate equation for each step and eliminating the concentration of the intermediate S_m between the two equations give the following relation between current density and overvoltage

$$j = 2j_{0,r} \cdot \exp\left(\frac{\alpha_r \mathbf{F}}{RT}\eta\right) \frac{1 - \exp\left(-\frac{2\mathbf{F}}{RT}\eta\right)}{1 + \frac{j_{0,r}}{j_{0,o}} \cdot \exp\left(-\frac{1 + \alpha_o - \alpha_r}{RT}\mathbf{F}\eta\right)} \qquad [12]$$

where $j_{0,r}$ and $j_{0,o}$ are the exchange current densities and α_r and α_o are the charge transfer coefficients of reactions [9] and [10], respectively. At high anodic overvoltages, Eq. [12] is simplified to

$$j = 2j_{0,r}\exp\left(\frac{\alpha_r \mathbf{F}}{RT}\eta\right) \qquad [13]$$

The geometric current density of the porous electrode at uniform current distribution would then be

$$i = S_m L\,(q/q_d)\,2j_{0,r}\exp\left(\frac{\alpha_r \mathbf{F}}{RT}\eta\right) \qquad [14]$$

which is similar to Eq. [12]. The values of the charge

transfer coefficient α_r and the pre-exponential factor can thus be explicitly determined from the slope and intercept of the Tafel line at overvoltages higher than 0.1V. The obtained value of the charge transfer coefficient, $\alpha_r = 0.32$, is rather low and indicates an unsymmetrical energy barrier. Assuming that $\alpha_o = 0.5$ and using the quotient $j_{0,r}/j_{0,o}$ as a fitting parameter, the complete polarization curve can be constructed from Eq. [12] multiplied by $S_m L(q/q_0)$. The fitted curves are drawn as solid lines in Fig. 5 with a fitted value of $j_{0,r}/j_{0,o} = 25$.

The reality corresponding to the formal Eq. [9] and [10] is not possible to elucidate from current density overvoltage curves only. Several possible mechanisms can be proposed, but the discrimination between these requires further information, for example, about electrochemical reaction orders.

The situation is more complicated when the cathodic Tafel-line in Fig. 5 is taken into consideration. It is remarkably straight in spite of the fact that the current distribution in this case with a low Tafel slope would become successively more nonuniform with an increasing current density, thus leading to an increasing Tafel slope. It has a slope of about 30 mV/decade, which is consistent with results obtained on plane electrodes (25). This slope is consistent with a rate-determining chemical step after both electrons have been transferred. One thinks, on the first hand, of the precipitation of lead sulfate. The observed value of the cathodic transfer coefficient is not consistent with the transfer coefficients obtained for the anodic reaction. The value of the parameter $S_m j_0 L$, obtained from the intercept with the log i axis is about 3 A/m², which is in approximate agreement with the value of $j_{0,o}$ obtained for the anodic reaction. On the other hand, the exchange current density j_0 obtained on a flat electrode of electrodeposited β-PbO_2 is of the order of 0.1 A/m² (24). With $S_m = S_2 \approx 10^7$ m^{-1} and $L = 10^{-3}$m, this value of j_0 gives an estimated value of $S_m j_0 L = 10^3$ A/m². Even after a correction for the roughness factor of the plane electrode, this value is orders of magnitude higher than that obtained for the porous electrode.

The inconsistency between the anodic and cathodic branches at higher overvoltages is difficult to explain in view of the reversiblity of the lead dioxide electrode. Probably, a change in mechanism occurs in the region of lower anodic overvoltages: for example, a change from a solid-state to a dissolution precipitation mechanism. This hypothesis is partly supported by the SEM micrographs, from which the latter mechanism seems to be the more probable at the cathodic reaction, while the first-order dependence on lead sulfate at anodic overvoltages above 30 mV is in favor of a solid-state mechanism.

The SEM micrographs, unfortunately, do not give an unequivocal discrimination between these two mechanisms at recharge. The formation of the core-shell structure in Fig. 16-17 evidently requires transfer of lead species via the solution, while the structure in Fig. 13 is more consistent with a solid-state reaction.

In conclusion, the experimental results can be combined to give an understanding of the effect of the structural changes on the electrode kinetics of the porous lead dioxide electrode. During discharge, the cathodic reaction is distributed (although not uniformly) over the entire PbO_2 surface. As the discharge proceeds, the $PbSO_4$ crystals grow larger, overlap, and merge into larger but fewer crystals. The total surface area of $PbSO_4$ will then grow only slowly. This explains why in Fig. 4 approximately the same maximum current is obtained at potentiostatic charge of fully and partially discharged electrodes.

At the same time, the amount of lead dioxide decreases and thus a successively larger amount of charge is needed for the formation of new lead dioxide in the electrocrystallization process. The rising transients in Fig. 4, therefore, have a longer duration after a deeper discharge. The morphology of the lead sulfate crystals formed during discharge, especially the larger crystal size in larger voids and on the exterior surface, indicates that the cathodic reaction proceeds via a dissolution-precipitation mechanism. The Tafel slope even indicates that the precipitation of lead sulfate from Pb^{2+} and SO_4^{2-} ions might be the rate-determining step at sufficiently high current densities.

Acknowledgments

This work was financially supported by the National Swedish Board for Technical Development (Project no. 83-3262). The SEM studies were performed by Mats Hällberg.

Manuscript submitted Dec. 5, 1984; revised manuscript received May 21, 1985. This was Paper 22 presented at the New Orleans, Louisiana, Meeting of the Society, Oct. 7-12, 1984.

The Royal Institute of Technology assisted in meeting the publication costs of this article.

LIST OF SYMBOLS

c_{eq}	equilibrium concentration of Pb^{2+} ions (mol/m³)
D	diffusion coefficient of Pb^{2+} ions (m²/s)
d_p	particle diameter (m)
i	geometric current density (A/m²)
i_0	apparent geometric exchange current density (A/m²)
j	true current density (A/m²)
j_0	true exchange current density (A/m²)
k	charge rate coefficient (h^{-1})
k_0	rate constant for the dissolution of $PbSO_4$ (mol/m²/s)
L	thickness of one symmetric half of the porous electrode (m)
n	number of electrons transferred in the electrode reaction
q	amount of charge remaining to be recharged (Ah/m²)
q_d	charge output in the previous discharge (Ah/m²)
S	specific surface area (m²/kg)
S_m	specific active surface area (m^{-1})
S_1	specific surface area of $PbSO_4$ (m^{-1})
S_2	specific surface area of PbO_2 (m^{-1})
$S_{1,2}$	mean specific cross-section area for the diffusion of Pb^{2+} ions

Greek Letters

α	charge transfer coefficient
η	charge transfer overvoltage (V)
ρ	density of electrode material (kg/m³)

Subscripts

r	first electron transfer step
o	second electron transfer step

REFERENCES

1. J. Burbank, A. C. Simon, and E. Willihnganz, in "Advances in Electrochemistry and Electrochemical Engineering," Vol. 8, P. Delahay, Editor, p. 157 (1971).
2. P. Rüetschi, *J. Power Sources*, **2**, 3 (1977/1978).
3. G. W. Vinal, "Storage Batteries," 4th ed., John Wiley and Sons, New York, (1955).
4. H. Bode, "Lead-Acid Batteries," Wiley-Interscience, New York (1977).
5. M. Fleischmann and H. R. Thirsk, *Trans. Faraday Soc.*, **51**, 71 (1955).
6. S. G. Canagaratna, P. Casson, N. A. Hampson, and K. Peters, *J. Electroanal. Chem.*, **79**, 281 (1977).
7. P. Casson, N. A. Hampson, and K. Peters, *ibid.*, **83**, 87 (1977).
8. N. A. Hampson, S. Kelley, and K. Peters, *J. Appl. Electrochem.*, **10**, 261 (1980).
9. D. Spahrbier, Dissertation, Technische Hochschule Stuttgart, Stuttgart, Germany (1960).
10. N. A. Hampson, P. C. Jones, and R. F. Phillips, *Can. J. Chem*, **45**, 2045 (1967).
11. N. A. Hampson, P. C. Jones, and R. F. Phillips, *ibid.*, **46**, 1325 (1968).
12. N. A. Hampson, P. C. Jones, and R. F. Phillips, *ibid.*, **47**, 2171 (1969).
13. H. Ogura and T. Sekine, *Denki Kagaku*, **41**, 638 (1973).
14. A. C. Simon, C. P. Wales, and S. M. Caulder, *This Journal*, **117**, 987 (1970).
15. A. C. Simon, S. M. Caulder, and J. T. Stemmle, *ibid.*, **122**, 461 (1975).
16. A. C. Simon and S. M. Caulder, in "Power Sources 5,"

D. H. Collins, Editor, p. 109, Academic Press, London (1975).
17. S. Hattori, M. Yamaura, M. Kohno, Y. Ohtani, M. Yamane, and H. Nakashima, in "Power Sources 5," D. H. Collins, Editor, p. 139, Academic Press, London (1975).
18. P. Casson, N. A. Hampson, K. Peters, and P. Whyatt, *J. Electroanal. Chem.*, **93**, 1 (1978).
19. P. Reinhardt, M. Vogt, and K. Wiesener, *J. Power Sources*, **1**, 127 (1976/1977).
20. W. Kappus and A. Winsel, *ibid.*, **8**, 159 (1982).
21. P. Rüetschi, J. B. Ockerman, and R. Amlie, *This Journal*, **107**, 325 (1960).
22. K. J. Vetter, *Chem.-Ing.-Tech.*, **45**, 213 (1973).
23. C. N. Satterfield, "Mass Transfer in Heterogeneous Catalysis," Chap. 3, M.I.T. Press, Cambridge, MA (1970).
24. K. J. Vetter, "Elektrochemische Kinetik," Springer Verlag, Berlin (1961).
25. D. Simonsson, *This Journal*, **120**, 151 (1973).

Recharge Kinetics of the Porous Lead Dioxide Electrode

II. The Effect of Sulfuric Acid Concentration

Per Ekdunge and Daniel Simonsson

Department of Chemical Technology, The Royal Institute of Technology, S-100 44 Stockholm, Sweden

ABSTRACT

Anodic polarization curves for partially recharged porous lead dioxide electrodes have been recorded at different sulfuric acid concentrations. These curves can be fitted by the rate equation for two consecutive single-electron transfer reactions. The dependence of the two exchange current densities on the sulfuric acid concentration is strongly negative. The apparent electrochemical reaction order for the first transfer step approaches −3 as the sulfuric acid concentration approaches 7*M*. The polarization curves also depend on the acid concentration during the previous discharge. At the same current density, the overvoltage at recharge in 5*M* H_2SO_4 was much higher when the electrode had been discharged in 1*M* H_2SO_4 compared to a discharge in 5*M* H_2SO_4. This effect can probably be attributed to the larger lead sulfate crystals formed at lower sulfuric acid concentrations.

In the previous paper (1), the recharge kinetics of the porous lead dioxide electrode in 5.6*M* H_2SO_4 was studied with regard to the effects of structural changes. The present paper deals with the effects of changes in sulfuric acid concentration. Although of great importance, this parameter has not been studied often before. Many investigations of the electrode kinetics of the PbO_2 electrode have been made with electrolytes giving soluble Pb (II) species, *e.g.*, $HClO_4$ and $NaClO_4$ (2-5) or HNO_3 (6), since this is the only way to vary the concentrations of Pb^{2+} and H^+ independently and at a constant ionic strength. The results of these studies are not directly applicable to the positive electrode in the lead-acid battery in which the electrolyte is sulfuric acid with a concentration of generally 4.5-5*M*. The concentration decreases during discharge and increases during charge. Due to the concentration gradients required for the diffusion process, the sulfuric acid concentration in the interior of the electrode may deviate significantly from that in the free electrolyte. The acid concentration affects not only the electrode kinetics, but also the maximum utilization of the active material of the electrode (7-9).

The complexity of sulfuric acid as the electrolyte in the porous lead dioxide electrode is due to not only its two dissociation steps and the low solubility of lead sulfate, but also to the fact that sulfate ions are specifically adsorbed on the lead dioxide surface (10, 11).

The goal of the experimental studies reported here was to investigate the effect of sulfuric acid concentration on the recharge kinetics and as a specific result obtain a practically useful rate expression, which relates current density to charge transfer overvoltage and includes parameters taking into account the effects of changes in composition of both the solid electrode and the electrolyte. A kinetic expression of this form is of great use in mathematical models for analyzing and predicting the electrochemical behavior of the porous lead dioxide electrode.

Experimental Procedure

The electrochemical measurements were performed in two different cells, one of which has been described earlier (1). The other cell was designed with the porous lead dioxide electrode as a flow-through electrode (Fig. 1). This cell design with its two symmetrical Luggin capillaries was also suitable for the determination of the effective conductivity and for diagnosing the current distribu-

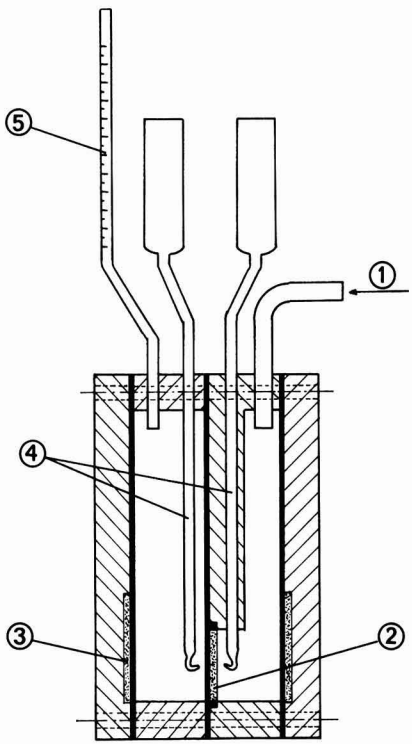


Fig. 1. Experimental cell with the porous PbO_2 electrode as a flow-through electrode. 1: Electrolyte flow from a peristaltic pump. 2: Porous lead dioxide electrode. 3: Lead electrode. 4: Luggin capillaries. 5: Graduated tube.

tion by measuring the electrode potential both at the front and the back of the electrode under current load from one side only (12). All experiments were performed at room temperature (22°C) according to procedures described in the previous paper (1).

Experimental Results

The effect of sulfuric acid concentration on the electrode potential during galvanostatic recharge with 200 A/m² is shown in Fig. 2. The overvoltage (with respect to the equilibrium potential at the actual concentration) evidently increases with an increasing acid concentration. While the change in overvoltage is relatively small when going from 5.0 to 6.0*M*, the increase is much greater when going from 6.0 to 7.5*M*. Charging in 10.0*M* H_2SO_4 made the potential go directly into the oxygen evolution region at the actual current density.

The results illustrated in Fig. 2 were obtained with the electrode always discharged in 5.0*M* H_2SO_4. Figure 3 shows that the acid concentration during discharge is also of a great importance. At the same recharge conditions, the overvoltage is much higher when the electrode has been discharged in a more diluted acid. In addition, at the low discharge current used (−20 A/m²), the discharge capacity was somewhat higher (about 10%) in 1*M* than in 5*M* H_2SO_4.

The influence of the sulfuric acid concentration on the electrode kinetics is demonstrated in the form of polarization curves in Fig. 4 for electrodes previously recharged to 20%. All curves in Fig. 4 have the same general form, with a low slope at overvoltages below about 0.1V and a much higher slope at higher overvoltages. The slopes of the lines for the different sulfuric acid solutions are parallel to each other in both regions of overvoltage. At the same charge transfer overvoltage, the current density is approximately twice as high in 1.0*M* H_2SO_4 as in 5.0*M* H_2SO_4, although the electrode potential is more than 0.1V lower. This somewhat unexpected result leads to the question which of the ions has the greatest effect. A solution was therefore prepared with the composition of 1.0*M* H_2SO_4 and 4.0*M* $HClO_4$. This solution has approximately the same hydrogen ion activity and ionic strength as 5*M* H_2SO_4 and approximately the same Pb^{2+} and HSO_4^- ion concentration as 1*M* H_2SO_4. The results with this electrolyte fell between those of 1*M* H_2SO_4 and 5*M* H_2SO_4, respectively, but with a higher slope, especially in the high overvoltage region. This indicates that not only the hydrogen ion, but also the anion, is of importance for the kinetics, especially in the low overvoltage region. At higher overvoltage, the curve for 4*M* $HClO_4$/1*M* H_2SO_4 approaches the one for 5*M* H_2SO_4. Between 5 and 7*M* H_2SO_4,

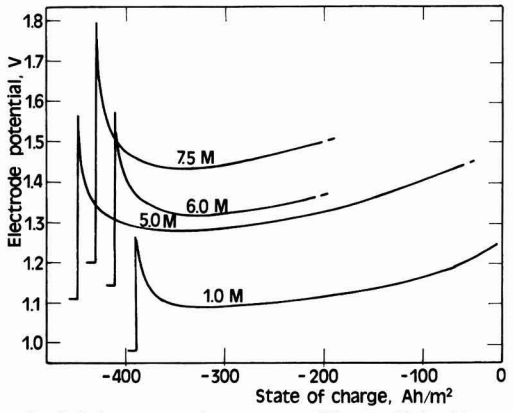


Fig. 2. Galvanostatic recharge curves at different sulfuric acid concentrations. Current density = 200 A/m². The previous discharges were all made in 5.0M H_2SO_4 at −20 A/m². The electrode potential was measured relative to a Hg/Hg_2SO_4 electrode.

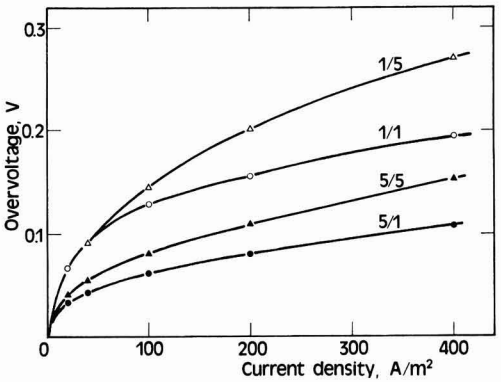


Fig. 3. Overvoltage vs. current density at 1.0 and 5.0M H_2SO_4, respectively. The notation 1/5 means discharge in 1M and recharge in 5M H_2SO_4, etc. Current load from one side only. Electrode fully discharged with −20 A/m² and recharged with 20 A/m² to 20%.

the charge transfer overvoltage is fairly independent of the concentration, especially in the low overvoltage region. For 8*M*, the polarization curve is very close to those for 5 and 7*M* in the low overvoltage region. At higher overvoltages, the working electrode potential in this solution enters into the oxygen evolution region, and the measurements at overvoltages approaching 200 mV were therefore made at significant gas evolution. This may explain the increasing deviation from the curves obtained at lower concentration. The current density at these high overvoltages is not simply the sum of the independent predictions of the partial currents for oxygen evolution and $PbSO_4$ oxidation. In view of the lowered current densities, the effect of oxygen evolution seems rather to be antagonistic.

Exchange current densities for the different electrolytes can be obtained by extrapolation of the linear portions of the polarization curves in the high overvoltage region to

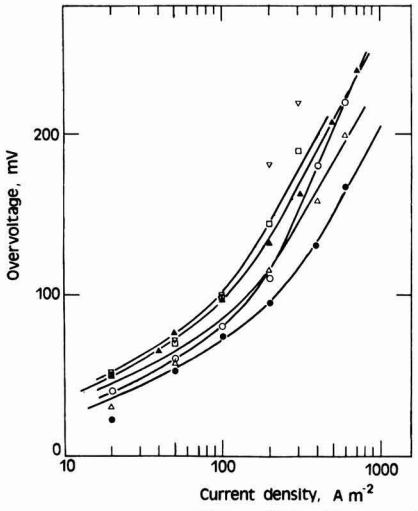


Fig. 4. Polarization curves at different sulfuric acid concentrations: • 1.0M; △ 3.0M; ▲ 5.0M; □ 7.0M; ▽ 8.0M H_2SO_4; and ○ 4.0M $HClO_4$/1.0M H_2SO_4. Electrode fully discharged with −20 A/m² and recharged with 20 A/m² to 20% in 5.0M H_2SO_4. The lines are predictions for all concentrations but 8M by means of Eq. [1], with exchange current densities for the first electron transfer step taken as the intercepts with the X-axis (see Fig. 5). $\alpha_r = 0.32$ (0.26 for 4M $HClO_4$/1M H_2SO_4), $\alpha_o = 0.5$, and $j_{0,r}/j_{0,o} = 25$.

their intercepts with the i-axis. These straight lines were drawn with the same slope for the curves for 1-7M H_2SO_4. The exchange current densities obtained at the different sulfuric acid concentrations are plotted in a bilogarithmic form in Fig. 5.

During charge, the acid concentration in the pores increase continuously due to a limited diffusion rate. It is therefore of great interest to establish the relative importance of this concentration gradient. In Fig. 6, a comparison is made between galvanostatic recharge curves obtained with and without forced electrolyte flow. With regard to the great effect of concentration on the electrode potential, both thermodynamically and kinetically, its resulting effect on the total overvoltage is fairly small.

Evaluation of a Kinetic Equation

At the previous studies with a constant concentration of sulfuric acid, the kinetics could be successfully described by the rate equation for two consecutive electron transfer reactions (1)

$$i = S_m L(q/q_d)^2 j_{0,r} \exp\left(\frac{\alpha_r \mathbf{F}}{RT}\eta\right) \frac{1 - \exp\left(-\frac{2\mathbf{F}}{RT}\eta\right)}{1 + \frac{j_{0,r}}{j_{0,o}} \exp\left(-\frac{1 + \alpha_o - \alpha_r}{RT}\mathbf{F}\eta\right)} \quad [1]$$

The overvoltage, η, in Eq. [1] is defined as the difference between the working electrode potential and the equilibrium potential of the electrode in the actual solution. The effect of structural transformations is explicitly taken into account by the factor (q/q_d), the extent of discharge. The validity of Eq. [1] is restricted to extents of discharge lower than 0.8-0.9 (1). The effect of sulfuric acid concentration should manifest itself as a functional dependence of the two exchange current densities, $j_{0,r}$ and $j_{0,o}$, on the concentration.

The variation of $j_{0,r}$ with the sulfuric acid concentration can be directly obtained from Fig. 5, since $j_{0,r}$ is the exchange current density obtained by extrapolation of the Tafel lines in the high overvoltage region. The simplest way to express in mathematical terms the variation of $j_{0,r}$ with the sulfuric acid concentration, c, is by a power function

$$j_{0,r} = kc^{-0.43} \quad [2]$$

The maximum error is then about 10%, which is acceptable for most practical applications of Eq. [1]. The value of $j_{0,o}$ determines the potential region where the polarization curve shifts from a lower to a higher slope and can only be determined by curve-fitting of the experimental data in Fig. 4. Since all polarization curves in Fig. 4 bend at approximately the same charge transfer overvoltage, the quotient $j_{0,r}/j_{0,o}$ was in a first attempt taken to be constant and equal to 25, which is the value estimated earlier (1). The values of the charge transfer coefficients, $\alpha_r = 0.32$ and $\alpha_o = 0.5$, were also taken from this work. The theoretically predicted polarization curves with these input data are drawn as solid lines in Fig. 4. The fit is fairly good, and a possible further improvement by finding optimal values of $j_{0,r}/j_{0,o}$ and α_o for each curve individually would not outweigh the additional complexity of Eq. [1].

At lower overvoltages, below about 50 mV, the predicted curves deviate signficantly from the experimental points. This may be explained by the fact that Eq. [1] is valid only for the anodic process at sufficiently high overvoltages. In the previous work, it was thus found that the cathodic polarization curves were not consistent with Eq. [1] either with respect to the structural dependence or with respect to the values of α_o and α_r. It must, therefore, be concluded that the mechanism changes at some lower anodic overvoltage. From a practical point of view, these deviations at lower overvoltages are no real problem since charging at these conditions is far from the optimal strategy. Restricting the validity of Eq. [1] to charge transfer overvoltages higher than 50 mV also means that the exponential term in the numerator can be neglected. Introducing this approximation and the estimated values of the parameters in Eq. [1] then leads to the final useful form

$$i = i_o c^{-0.43}(q/q_d) \exp(0.32\eta')/(1 + 25 \exp[1.18\eta']) \quad (q/q_d < 0.8;\ \eta' = \eta\mathbf{F}/RT \geq 2) \quad [3]$$

where i_o has the form of an apparent, geometric exchange current density which depends on the value of $j_{0,r}$ and the total active surface area per projected area unit. This quantity, therefore, varies with the thickness and overall activity of the electrode. The other parameters are of a more fundamental electrochemical nature, and can thus be expected to be valid for most lead-acid positive electrodes.

Finally, it should be remarked that Eq. [1] and the interpretations of the measured polarization curves have been based upon the implicit assumption of a uniform current distribution within the porous electrode. This assumption was checked by using Eq. [1] together with Ohm's law for the ionic current density in a numerical calculation of the current distribution (13). The deviation of the current density at the front of the electrode from the average value was then found to be of the order of 10% at the current densities employed. The uniform current distribution can be attributed to the high Tafel slope, especially at higher current densities.

Discussion

The main objective of this study was to evaluate a rate equation, which can be used as a vital part in a mathemat-

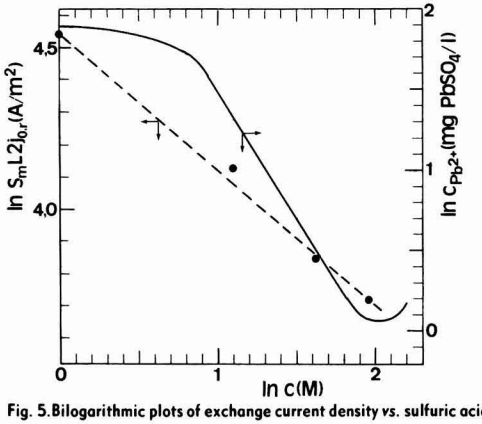


Fig. 5. Bilogarithmic plots of exchange current density vs. sulfuric acid concentration (experimental points) and solubility of lead sulfate vs. sulfuric acid concentration (solid line) according to Ref. (16).

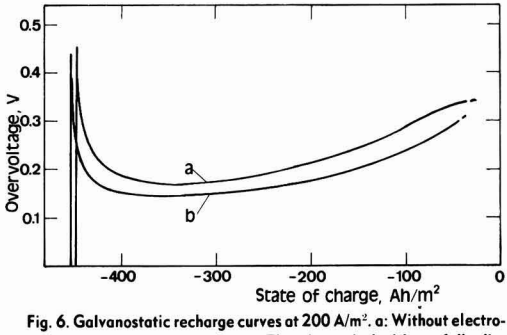


Fig. 6. Galvanostatic recharge curves at 200 A/m². a: Without electrolyte flow. b: With electrolyte flow. The electrode had been fully discharged with −20 A/m².

ical model for the recharge of the lead-acid battery. The experimental conditions were therefore chosen as close as possible to those in real lead-acid batteries. Although the results thus obtained are not suitable for a precise evaluation of fundamental electrochemical parameters, they give valuable hints as regards the mechanism of the electrode process. One very interesting aspect is the strongly negative influence of the sulfuric acid concentration on the recharge kinetics. According to the theory of electrochemical kinetics (14), the exchange current density $j_{0,r}$ in Eq. [1] should be a function of the concentrations according to the expression

$$j_{0,r} = k_r \pi c_j^{z_{r,j}} \cdot \exp\left(\frac{\alpha_r \mathbf{F}}{RT}\,\epsilon_0\right) \qquad [4]$$

where the exponent $z_{r,j}$ is the electrochemical reaction order with respect to component j. Taking first the logarithm of Eq. [4] and then the derivative with respect to the logarithm of sulfuric acid concentration gives

$$\frac{\partial \ln j_{0,r}}{\partial \ln c} = z + z_{Pb^{2+}} + \frac{\partial \ln c_{Pb^{2+}}}{\partial \ln c} + \frac{\alpha_r \mathbf{F}}{RT}\,\frac{\partial \epsilon_0}{\partial \ln c} \qquad [5]$$

The term on the left-hand side can be evaluated from Fig. 5 or Eq. [2]. The second term on the right-hand side takes into account the implicit effect of changes in Pb^{2+} concentration with changes in sulfuric acid concentration. The derivative $\partial(\ln c_{Pb^{2+}})/\partial \ln c$ can be graphically determined from the solubility curve in Fig. 5. Two extreme cases can be distinguished. In the first case, we assume that the mechanism involves soluble Pb^{2+} ions and that the electrochemical reaction order with respect to Pb^{2+} is equal to one. In the second case, we assume a solid-state mechanism where soluble Pb^{2+} ions play no role and $z_{Pb^{2+}} = 0$.

The last term on the right-hand side accounts for the dependence of the equilibrium potential on the sulfuric acid concentration. The derivative of this term can be estimated from, *e.g.*, the correlation given in Ref. (15). When going from 1 to 7*M* H_2SO_4, the electrochemical reaction order with respect to sulfuric acid, *z*, was found to vary from about −0.4 to −3 using the assumption of $z_{Pb^{2+}} = 1$ and from approximately −1 to −3 with $z_{Pb^{2+}} = 0$. The extreme value of −3 was in both cases obtained for 7*M* H_2SO_4, at which concentration the solubility of $PbSO_4$ passes a minimum and then starts to increase with a further increase in acid concentration.

Regardless of the role of the Pb^{2+} ions, the reaction order with respect to sulfuric acid concentration is clearly highly negative. An explanation of this effect might be that a protonation equilibrium is established before the first electron is transferred. For example, the mechanism proposed by Hampson *et al.* for acid perchlorate electrolytes (4) involves as the first step

$$Pb(II) + 2H_2O \rightleftharpoons Pb(OH)_2 + 2H^+ \qquad [6]$$

Here Pb(II) stands for either dissolved Pb^{2+} in the case of a dissolution-precipitation mechanism, or solid lead sulfate in the alternative case of a solid-state mechanism. At equilibrium, the activity of $Pb(OH)_2$ is proportional to $[H_2O]^2/[H^+]^2$. If then $Pb(OH)_2$ is the electroactive reactant in the first charge transfer step, the current density should be proportional to this quantity at higher overvoltage where the reverse reaction can be neglected. The activity coefficient of water decreases, and the mean activity coefficient of sulfuric acid increases strongly with increasing acid concentration in the range 1-7*M* (16). The electrochemical reaction order with respect to the hydrogen ion concentration may thus be as high as −3. Assuming that the sulfuric acid can be considered as a 1,1 electrolyte which dissociates almost completely in H^+ and HSO_4^- ions (17) means that the concentration of H^+ is equivalent to the sulfuric acid concentration.

The discussion above has so far been restricted to the first anodic charge transfer step, which is rate determining at overvoltages higher than 100 mV. The lower Tafel slope at lower overvoltages is governed by the denominator in Eq. [1]. The effect of the sulfuric acid concentration is implicit in the quotient $j_{0,r}/j_{0,0}$. According to theory (14)

$$j_{0,r}/j_{0,0} = k_r^-/k_0^- \exp\left(-\frac{1 + \alpha_0 - \alpha_r}{RT} - \mathbf{F}\epsilon_0\right) \qquad [7]$$

The equilibrium potential ϵ_0 increases with the sulfuric acid concentration. With $\alpha_0 = 0.5$ and $\alpha_r = 0.32$, this equation predicts that a change in sulfuric acid concentration from 1 to 5*M* with $\Delta\epsilon_0 \approx 130$ mV should make $j_{0,r}/j_{0,0}$ decrease by a factor of several hundreds. In view of this, the constancy of this quotient found in our experiments is very puzzling, and Eq. [3] is in this respect hard to give a mechanistic explanation for.

A more direct evaluation of the influences of the Pb^{2+} and H^+ ions would be possible by a comparison of the polarization curves for 5*M* H_2SO_4 and 1*M* H_2SO_4/4*M* $HClO_4$, respectively. The hydrogen activity is nearly the same in these two solutions, whereas the Pb^{2+} ion concentration is approximately four times higher in the latter. The results show, however (Fig. 4), that such a direct comparison is not possible. The Tafel slope for the $HClO_4/H_2SO_4$ solution is higher than for the pure H_2SO_4 solutions, which demonstrates that the kind of anion also affects the electrode kinetics, probably due to adsorption. This fact rules out the possibility of making more exact kinetic-mechanistic studies of the porous lead dioxide battery electrode by varying the concentrations of H^+, Pb^{2+}, HSO_4^-, and SO_4^{2-} ions at a constant ionic strength by the addition of perchlorate salts. The value of $\alpha_r = 0.26$ for the $HClO_4/H_2SO_4$ solution in the high overvoltage region is comparable to that obtained by Hampson *et al.* (4) for acid perchlorate electrolytes, $\alpha_r = 0.21$-0.24. This value and that for sulfuric acid solutions, $\alpha_r = 0.32$, are both unusually low in comparison to a generally expected value around 0.5. A probable explanation is again the effect of adsorption of the anions.

The effect of the sulfuric acid concentration at discharge on the subsequent recharge (Fig. 3) can be explained by the first-order dependence on the amount of lead sulfate (1). It is well known that the size of the lead sulfate crystals increases with a decreasing sulfuric acid concentration (7-9), which also explains the higher discharge capacity obtained in 1*M* H_2SO_4. The lower recharge current at the same amount of lead sulfate indicates that the total surface area of the lead sulfate crystals is the determining factor. While in the case of a single particle size this would imply that the potentiostatic current varies during recharge proportionally to the amount of lead sulfate raised to two thirds, a crystal size distribution gives a higher dependence and may explain the established first-order dependence. Since order of magnitude calculations show that a limiting mass transfer rate of the Pb^{2+} ions is less probable, this result is in favor of a solid-state mechanism.

Acknowledgment

This work was financially supported by the National Swedish Board for Technical Development (Project no. 83-3262).

Manuscript submitted Feb. 7, 1985; revised manuscript received May 21, 1985.

The Royal Institute of Technology assisted in meeting the publication costs of this article.

LIST OF SYMBOLS

- c sulfuric acid concentration (*M*)
- i geometric current density (A/m²)
- i_0 apparent geometric exchange current density in 1.0*M* H_2SO_4 (A/m²)
- j_0 true exchange current density (A/m²)
- L thickness of one symmetric half of the porous electrode (m)

q amount of charge remaining to be recharged (Ah/m²)
q_d charge output in the previous discharge (Ah/m²)
S_m specific surface area (m^{-1})
z electrochemical reaction order

Greek characters

α charge transfer coefficient
ϵ_o equilibrium electrode potential (V)
η charge transfer overvoltage (V)
η' dimensionless overvoltage [$\eta F/(RT)$]

Subscripts

r first electron transfer step (anodic direction)
o second electron transfer step (anodic direction)

REFERENCES

1. P. Ekdunge and D. Simonsson, *This Journal*, **132,** 2521 (1985).
2. D. Spahrbier, Dissertation, Technische Hochschule Stuttgart, Stuttgart, Germany (1960).
3. N. A. Hampson, P. C. Jones, and R. F. Phillips, *Can. J. Chem.*, **45,** 2045 (1967)
4. N. A. Hampson, P. C. Jones, and R. F. Phillips, *ibid.*, **46,** 1325 (1968).
5. N. A. Hampson, P. C. Jones, and R. F. Phillips, *ibid.*, **47,** 2171 (1969).
6. H. Ogura and T. Sekine, *Denki Kagaku*, **41,** 638 (1973).
7. S. Hattori, S. Tosano, and O. Kuzuoka, *ibid.*, **44,** 109 (1976).
8. D. B. Matthews, M. A. Habib, and S. P. S. Badwal, *Aust. J. Chem.*, **34,** 247 (1981).
9. K. Asai, M. Tsubota, K. Yonezu, and K. Ando, *J. Power Sources*, **7,** 73 (1981).
10. I. G. Kiseleva and B. N. Kabanov, *Dokl. Akad. Nauk SSSR*, **122,** 1042 (1958); *ibid.*, **108,** 864 (1956).
11. G. A. Kokarev, V. A. Kolesnikov, and M. Ya. Fioshin, *Elektrokhimiya*, **19,** 196 (1983).
12. L. G. Austin and E. G. Gagnon, *AIChE J.*, **17,** 1057 (1971).
13. J. Newman and C. Tobias, *This Journal*, **109,** 1183 (1962).
14. K. J. Vetter, "Elektrochemische Kinetik," Springer Verlag, Berlin (1961).
15. D. Simonsson, *J. Appl. Electrochem.*, **3,** 261 (1973).
16. H. Bode, "Lead-Acid Batteries," Wiley-Interscience, New York (1977).
17. H. S. Harned and B. B. Owen, "The Physical Chemistry of Electrolytic Solutions," Reinhold Publishing Corporation, New York (1958).

The Influence of Composition and Microstructure on the Corrosion Behavior of Pb-Ca-Sn Alloys in Sulfuric Acid Solutions

D. Kelly and P. Niessen

Department of Mechanical Engineering, University of Waterloo, Waterloo, Ontario, Canada N2L 3G1

E. M. L. Valeriote*

Cominco Limited, Product Research Centre, Sheridan Park, Mississauga, Ontario, Canada L5K 1B4

ABSTRACT

The corrosion behavior of selected Pb-Ca-Sn alloys after various thermal treatments has been studied. Alloys with high tin content or high tin:calcium ratios had lower rates of intergranular corrosion but were susceptible to intergranular stress corrosion cracking. A low tin:calcium ratio promotes discontinuous precipitation, which produces an interlocking grain structure. This structure is very resistant to stress corrosion. It is experimentally shown that during corrosion of these alloys, stresses are produced across boundaries by the intergranular corrosion products.

In recent years, lead-calcium-tin alloys have become established alternatives to lead-antimony alloys for grids in automotive batteries. Although much research has been done on the Pb-Ca-Sn alloys, some aspects of their behavior, particularly in the corrosive environment of the lead-acid battery, are not fully understood. Valeriote (1) extensively studied weight loss and integrity of various Pb-Ca-Sn alloys under open-circuit and anodic polarization conditions. His work provided a basis for selecting suitable alloy compositions, but some of his results remain unexplained. For example, he found that, for grids made from expanded continuously cast strip, a Pb-0.09Ca-0.3Sn alloy retained its structural integrity in the corrosive environment better than a Pb-0.06Ca-0.6Sn alloy.

Prengaman (2) has reported that the microstructures as well as the compositions of Pb-Ca-Sn alloys influence their corrosion behavior. He claimed that for alloys which have partially transformed by a slow discontinuous precipitation mechanism, resulting in coarse lamellar or rod-like precipitates, grid life is considerably shortened by "deep penetrating corrosion." Other researchers (3-8) have also claimed that corrosion properties are influenced by alloy composition. However, there is no agreement on what compositions provide the best grid integrity or on how composition influences the corrosion behavior of the Pb-Ca-Sn alloys.

*Electrochemical Society Active Member.

The present study was undertaken to provide a better understanding of the relationships between alloy composition, microstructure, and corrosion behavior.

Alloy Selection

Three alloys were obtained for testing in the form of strip samples, prepared by Cominco Limited (Sheridan Park, Ontario, Canada), using a commercially established continuous casting process (9). These were selected on the basis of work by Borchers and Assmann (8), who found that at the weight ratio of tin:calcium = 8.83:1 (ratio of 3:1 atomic per cent) there is a marked change in both the microstructure of the alloy and in the precipitation strengthening mechanism. Below this ratio, lead-calcium-tin alloys are strengthened by fine Pb_3Ca particles which are formed by a discontinuous precipitation hardening reaction involving extensive movement of the grain boundaries. [For a more complete discussion of the discontinuous precipitation mechanism, the reader is referred to recent review articles by Williams and Butler (10) and by Gust (11)]. Above the 8.83:1 ratio, the strengthening occurs by the more common continuous precipitation mode in which no boundary movement takes place. Subsequent to the continuous precipitation, a slow, and therefore coarse, discontinuous precipitation reaction can occur. In this reaction, the existing continuously precipitated Pb_3Ca particles are transformed into coarse rod-like particles. This slow reaction is accompanied by a sharp decrease in hardness and strength.

In order to produce a wide range of microstructures, the three alloys used in this study were selected to have Sn:Ca ratios well below, well above, and close to the critical ratio. Alloy compositions and corresponding Sn:Ca ratios are given in Table I.

Experimental Procedures

Specimens of each alloy were cut from 1 mm thick strip to dimensions of 25 × 150 mm. These were solution treated for 60s in a molten salt bath approximately 3°C below their experimentally determined solidus temperatures. Subsequently, specimens were subjected to each of the following aging treatments: (*i*) air cool to 180°C, hold for 20 min, air cool to room temperature; (*ii*) air cool to 100°C, hold for 20 min, air cool to room temperature; and (*iii*) air cool to 50°C, hold for 11 days, air cool to room temperature.

These treatments were selected to evaluate the effects of a high temperature aging treatment, to simulate the thermal history of a continuously drum-cast strip which is coiled and left to cool (12), and to simulate long-term aging at room temperature. Specimens were stored in liquid nitrogen until the start of corrosion testing.

Corrosion testing was carried out at 50°C, in 1.27 ± 0.02 specific gravity (sp gr) sulfuric acid, at a constant anodic overpotential of 200 mV. In order to monitor corrosion, 81 coupons were examined, nine from each alloy/aging treatment combination. These were removed from the corrosion cell at various corrosion times from 21 to 92 days. Each coupon was examined metallographically to determine the mode and extent of corrosive attack. The depths of both intergranular corrosion and surface corrosion were measured on sections perpendicular to the sample surfaces using a calibrated optical microscope. The maximum depth of intergranular corrosion was measured at ten randomly selected sites on each specimen.

To show that stresses are produced by the corrosion product, two further experiments were designed in which corrosion was greater on one surface of a specimen than the other. It was reasoned that these stresses would cause an initially straight specimen to take on curvature with time.

One experiment was done by thinning a 1 mm thick strip of 903 alloy to 0.5 mm using a chemical polish and then coating one surface of the sheet with Teflon. (This alloy was selected for its large grain boundary area in order to accelerate testing.) The coupon was then placed in a 1.25 sp gr H_2SO_4 solution at room temperature and anodized for five days at a cell voltage of about 3V with a current density of 8 mA/cm^2.

The second experiment, which more closely approximated normal battery overcharge conditions, was carried out by corrosion of 1 mm thick strip coupon samples of drum-cast Pb-0.18Ca-0.26Sn-0.012Al (1803) at 50°C and 200 mV anodic overpotential (1.347 ± 0.002V with respect to a Hg/Hg_2SO_4/1.275 sp gr H_2SO_4 reference electrode at room temperature) for 70 and 90 days in a 1.280 sp gr (at 15°C) sulfuric acid solution. These samples were chosen for their unusual duplex microstructure, as will be discussed later. Samples of expanded and of gravity cast grids of other compositions were included in the same corrosion cell (13), but the 1803 samples were tested as coupons because they lacked sufficient ductility for expansion.

Results

Microstructure.—As expected, the alloy/heat-treatment combinations produced a range of different microstructures. Alloy 609, aged at 50°C, had the relatively large

Table I. Alloy compositions and Sn:Ca ratios

Alloy	Composition (w/o) Ca	Sn	Sn:Ca ratio Atomic	Weight
903	0.087	0.33	1.3	3.8
606	0.058	0.56	3.3	9.7
609	0.051	0.89	5.9	17.5

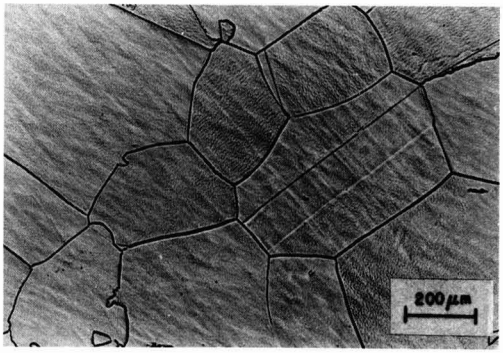


Fig. 1. Equiaxed grain structure of alloy 609

equiaxed grains shown in Fig. 1. During the course of the corrosion experiments, regions of the coarse discontinuous precipitation reaction were observed, increasing in size and number with time. These were also observed, although less frequently, in alloy 606. Figure 2a shows the complex interlocking grain structure of alloy 903 aged at 180°C. To emphasize the interlocking structure, the perimeter of one of the grains has been traced in Fig. 2b. The complexity of the microstructure increased from that of Fig. 1 to that of Fig. 2 with decreasing Sn:Ca ratios and to a lesser extent with increasing temperature.

The complex shape of the grains in Fig. 2 prevents a meaningful determination of grain size. Because of this, the relative grain boundary area of each sample is reported as the number of grain boundaries crossed by a 1 mm linear transverse on the sample surface. The grain boundary data summarized in Table II with respect to alloy and heat-treatment are average values based on a minimum of five measurements.

Corrosion.—Very early in the corrosion tests, it became clear that all alloys were preferentially attacked at grain boundaries, but there was also a general corrosive attack over the surface of the samples. After 75 days of testing, the surface corrosion product on the 609 alloy was 17 μm thick, while on the 606 and 903 alloys the layer was 24 μm.

The influence of the various alloy/heat-treatment combinations on the intergranular corrosion was determined by performing an analysis of covariance with alloy and heat-treatment as independent variables, depth of corrosive penetration as the dependent variable, and time as the covariate. This showed, with a high level of confidence (>99%), that each of the three alloys has a different time *vs.* depth-of-intergranular-corrosion relationship. There was no evidence that the heat-treatments used had a significant effect on the rate of intergranular penetration. Because of this, the curves in Fig. 3 indicate the depth of corrosive penetration for each alloy averaged over the three heat-treatments. It should be noted here that although the heat-treatment does not influence the rate of intergranular corrosion, it does affect the micro-

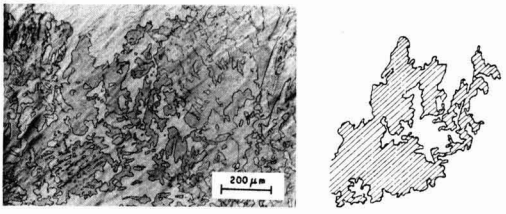


Fig. 2. a: Irregular microstructure typical of alloy 903 aged at 180°C. b: To better illustrate the interlocking of the grains, the perimeter of one of the grains in a has been traced at the same magnification as a.

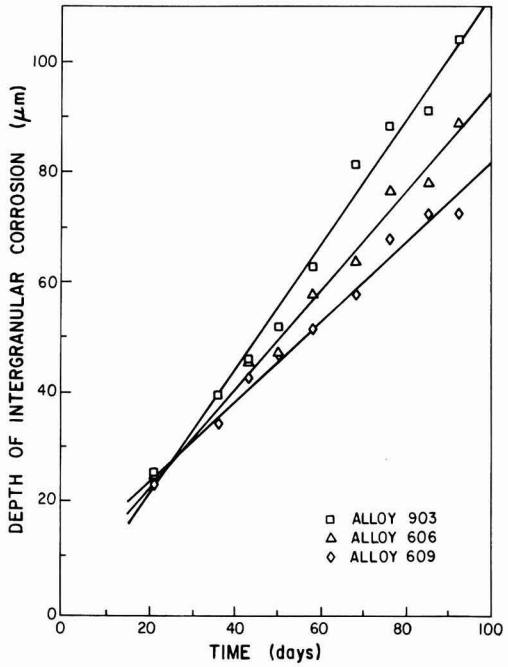


Fig. 3. Depth of intergranular corrosion as a function of time. The rate of intergranular corrosion decreases with increasing tin:calcium ratio and/or increasing tin content.

structure, which, as will be shown later, does play a significant role in the overall corrosion behavior. The results of linear regression analysis for each alloy are summarized in Table III. The rates of corrosive penetration for the 606 and 609 alloys were, respectively, 80 and 64% of that for the 903 alloy.

The linear regression analysis of the data produced lines with nonzero intercepts. However, it must be recognized that the equations represent the line of best fit through the data points. In fact, the 95% confidence limits for the regression line include the origin for alloys 903 and 606. The larger positive intercept for alloy 609 may be indicative of a different corrosion rate at short times.

In several specimens, boundaries which had sustained much more than typical damage were sometimes observed. For example, the average depth of penetration for alloy 609 after 75 days was 64 μm; however, the boundary shown in Fig. 4 has been penetrated to a depth of 240 μm. (The measurements for very deeply penetrated boundaries represented samples from a different population and were, therefore, excluded from the averages because of their anomalous behavior.) These were observed most frequently in alloy 609, to a lesser extent in alloy 606, and not at all in alloy 903. Also, as shown in Table IV, for alloy 609 the depth and frequency of the deeply penetrated boundaries increased as the heat-treatment temperature decreased. No correlation was found between the time in the corrosion test cell and either the frequency of occurrence or the depth of this "deep penetration."

Metallographic examination of the intergranular corrosion gave no indication that grain boundaries associated with the coarse discontinuous precipitation reaction were penetrated at a faster rate than were other boundaries. The only difference in the corrosion which was associated with the regions of coarse discontinuous precipitation was in regard to the lateral spread of the intergranular corrosion, *i.e.*, the widening of the corrosive wedge. This widening occurred at a faster rate into the regions which contained the coarse rod-like precipitates than into the regions of submicroscopic precipitates.

In the experiment showing the effects of corrosion which was restricted to one surface of the strip, the effect of the intergranular corrosion was clear after 5 days of testing. As expected, the initially straight specimen had become curved with the bare lead alloy on the convex side and the Teflon on the concave side. The radius of curvature was found to be 400 mm after 1 day, 275 mm after 2 days, and 175 mm after 5 days. The increasing curvature of the specimen confirms the existence of substantial forces exerted by the corrosion products on the parent metal.

Table II. Summary of effects of alloy content

Alloy	Heat-treatment temperature (°C)	Grain boundaries (mm^{-1})[a]
903	180	33.0
	100	18.5
	50	20.5
606	180	9.2
	100	5.0
	50	4.0
609	180	2.7
	100	2.3
	50	1.7

[a] Average of five measurements.

Table III. Summary of linear regression analysis of depth of intergranular corrosion vs. time for each alloy

Alloy	Intercept	Slope		Correlation coefficient
		Estimate	Percentage of 903	
903	−1.19	1.135	100	0.993
606	4.17	0.905	80	0.993
609	9.05	0.728	64	0.992

Table IV. Depth and frequency of deeply penetrating grain boundaries for alloy 609

Aging temperature (°C)	Number of sites of deep penetration observed	Average depth of deep penetration (μm)
180	9	262
100	14	290
50	38	375

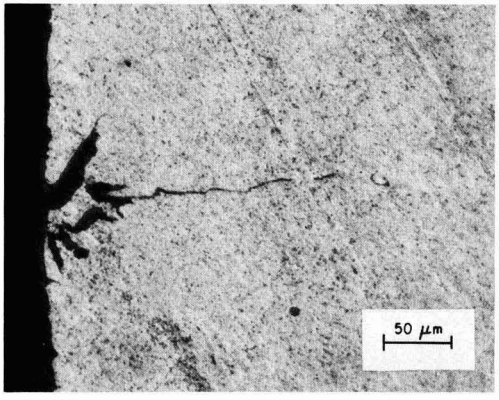


Fig. 4. Deep penetration of grain boundary in alloy 609. Although the average depth of intergranular corrosion is 64 μm after 75 days of testing, this boundary has been penetrated to a depth of 240 μm.

This result was confirmed even more dramatically in the second accelerated corrosion experiment. The samples for this experiment were chosen because of their highly unusual duplex microstructure (Fig. 5), which is not found in cast strip of conventional compositions. Only a small difference in calcium content could be determined between the "drum" side of the strip (0.176% Ca) and the "air" side (0.183% Ca), but the microstructures were very different. Although some transformation of the grain boundaries (similar to that seen in Fig. 2) is evident, the microstructure on the drum side (top of Fig. 5) still indicates the effects of nucleation on the cooled drum casting surface and consequent growth of columnar grains during solidification. On the air side, however, the structure is extremely fine and many coarse primary precipitate inclusions, which appear to have nucleated in the melt, have been incorporated into this side of the strip, which solidified last and under very different cooling conditions than the drum side.

As expected (13), weight losses for the 1803 coupons were very high after 70 days (112 mg/cm^2) compared to a 903 expanded cast-strip grid in the same cell (42.5 mg/cm^2) (13), an 803 (Pb-0.08Ca-0.3Sn) expanded cast-strip grid containing aluminum (39.6 mg/cm^2) (14), and 903 gravity cast grids, with and without aluminum [37.6 and 25.6 mg/cm^2, respectively (13)]. Weight loss for the 1803 grid at 90 days was 178 mg/cm^2, indicating an accelerating corrosion rate, as previously observed for other Pb-Ca alloys (1). Metallographic examination indicated a much more uniform attack on the fine-grained air side than on the drum side of the coupon, where the attack penetrated more deeply, apparently associated with the straight columnar grain boundaries.

Substantial growth of the coupons accompanied the corrosion. The radius of curvature at the bottom of the coupons (Fig. 6) was about 100 mm after 70 days and 20 mm after 90 days. At the midpoint of the 90 day sample, where it was most warped, the radius of curvature was only 16 mm. The air side became convex and the drum side concave during corrosion, indicating greater horizontal growth on the fine-grained air side. This also suggests that the corrosion rate was greater on the fine-grained air side than on the drum side, assuming that both growth and corrosion are grain-boundary-related phenomena (13).

Discussion

It has been shown that changes in alloy composition and aging treatments produced a wide range of microstructures. The various aging treatments had no effect on the corrosion rate for a particular alloy, but there were significant differences in the rates of corrosion of the alloys studied. This indicates that composition has a significant influence on the corrosion properties of Pb-Ca-Sn alloys, while the temperature of heat-treatment appears to have little effect. Considering the composition effect, if only the level of calcium had affected the corrosion, there would have been little difference in behavior between the 606 and 609 alloys. Since the high tin alloy, 609, had a lower corrosion rate than the 606 alloy, it appears that an increase in either the tin content or in the tin:calcium ratio reduces the rate of intergranular corrosion. Further studies will be required to determine which is more important: the Sn:Ca ratio or only the Sn level.

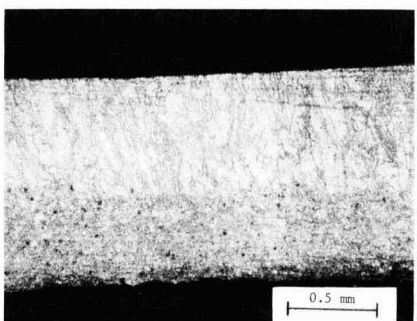


Fig. 5. Novel duplex structure in cross section of etched 1803 alloy cast strip. Top is drum-cast surface; bottom is air side of cast strip.

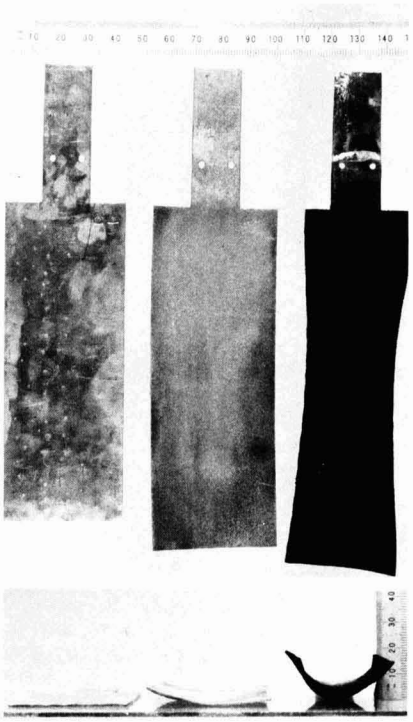


Fig. 6. Corrosion test coupons as prepared (left), after 70 days corrosion and chemical stripping (center), and after 90 days corrosion (right) at 50°C, η_i = 200 mV. Top photograph is a vertical view illustrating growth; lower photograph is a bottom view illustrating curvature.

Increasing the tin:calcium ratio decreased the intergranular corrosion rate, the number of grain boundaries, and the general surface corrosion. Therefore, if weight loss were used as the criterion for selection of grid material, one would expect alloy 609 to be the best material.

This, however, does not consider the influence of the deeply penetrating cracks observed, particularly in alloy 609, on the overall corrosion behavior. To understand the effect of the deep penetrating cracks, it is important to understand their origin. The authors believe they result from stress corrosion (15), and the following mechanism is proposed.

Most commonly, stress corrosion mechanisms involve accelerated rates of cracking in the presence of an applied stress and a corrosive environment. The mechanism in this study is somewhat different since the applied stress results directly from the formation of the corrosion product. A similar mechanism has been observed in stainless steels (16). For Pb-Ca-Sn alloys, it is known that the corrosion product, containing primarily lead oxides, has a larger specific volume (17) than the lead matrix. As a result, the intergranular corrosion product is under compressive stresses due to the physical constraints of the bulk material. This produces tensile stresses which are concentrated across the grain boundary at the tip of the intergranular corrosion. The effect of the stresses pro-

duced by this wedging action of the corrosion product will vary depending on microstructure of the alloy. If alloy 609, with its relatively straight immobile grain boundaries, is considered, it is evident that as the corrosion continues the stresses will increase until, at a critical stress level, an intergranular fracture will be initiated, as shown in Fig. 4. Once a crack exists, more electrolyte will be able to flow to the crack tip, leading to more corrosion and continued crack propagation. This mechanism will likely lead to rapid failure of a grid wire because the increasing volume of corrosion product will cause higher loads, which must be carried by the reduced cross-sectional area of the grid wire. These two factors combine to produce increasing stresses across the boundary and an accelerating rate of crack propagation.

The behavior of alloy 903 (or 1803) under the same stresses will be quite different than that of alloy 609 because crack propagation is impeded by the interlocking of the grains (recall Fig. 2). This forces the intergranular corrosion, or an intergranular crack, to follow a very irregular path. Even though the stresses may be sufficient, very little cracking occurs because there are only short lengths of boundary which are oriented with respect to the applied load such that crack propagation will occur. Thus, the irregular shape of the grain boundaries in alloy 903 prevents the stress corrosion mechanism from occurring.

The results in Table IV are consistent with this mechanism. The higher aging temperatures result in more extensive discontinuous precipitation and hence more irregular grain boundaries. The irregularities can either prevent the initiation of a crack or arrest its propagation. Thus, both the frequency of occurrence and the depth of penetration are reduced as aging temperature is increased.

This proposed mechanism is supported by our previous experimental results (1). Grids made from alloy 606 (and 909) fell apart during grid integrity tests, but those made from alloy 903 retained their integrity.

Subsequent testing (14) on grids made from alloy 609 indicated that they too suffered a loss of grid integrity. Thus, of the three main alloys studied, only alloy 903 with its irregular boundaries resists intergranular separation. The above mechanism is based on the premise that corrosion product produces tensile stresses across the grain boundaries.

The experiments in which one side of the corrosion sample corroded preferentially to the other and thereby produced warping also illustrate the generation of these tensile stresses and show that they are related to grain boundary density.

If, for alloys with relatively straight grain boundaries, these stresses cause grain boundary cracking leading to early failure as was shown by differences in grid integrity (1, 14), this mechanism may also account for Prengaman's "deep penetrating corrosion" (2). Although he associated this phenomenon with the coarse discontinuous precipitation, it was observed in our metallographic studies that the grain boundaries between the areas of coarse precipitation and the matrix are relatively straight. These boundaries are therefore susceptible to the stress corrosion mechanism. Prengaman also states that the deep penetrating corrosion is not observed in alloys in which the entire structure has been transformed by the fine discontinuous precipitation reaction, *i.e.*, those alloys which the present work has shown to exhibit irregular microstructures. The proposed stress corrosion mechanism is accordingly consistent with his observations.

The existence of stresses induced by the corrosion product also suggests an explanation of the grid growth often observed in Pb-Ca-Sn alloy grids. It is probable that the same intergranular stresses which cause cracking in alloys such as 609 will result in creep of coupons or grid wires in alloys such as 903. Because the stresses act along the length of the grid wires, they will increase in length regardless of their orientation in the grid. Furthermore, wires of thin cross section will see higher stresses and therefore will have higher creep (growth) rates. For the 1803 alloy, the nonuniformity of the growth, due to the nonhomogeneous microstructure, also causes warpage to occur.

Conclusions

1. For the alloys studied, there is an increase in the rate of intergranular corrosion with decreasing tin content or decreasing tin:calcium ratio.
2. Since both the rate of intergranular attack and the grain boundary area increase with decreasing tin:calcium ratio, corrosive weight loss will also increase with decreasing tin:calcium ratio.
3. The measurement of integranular corrosion rate or weight loss is not sufficient for selecting Pb-Ca-Sn alloys best suited for use in battery grids. It is also necessary to consider the microstructure and its influence on the overall corrosion behavior.
4. The grain boundary cracking observed in Pb-0.06Ca-0.6Sn (606) and Pb-0.05Ca-0.9Sn (609) alloys has been explained by a stress corrosion mechanism. Internal tensile stresses result from the intergranular corrosion product, which has a larger specific volume than the uncorroded metal. These stresses act across the grain boundary and can result in intergranular fracture.
5. Alloys which have irregular grain structures are resistant to the stress corrosion fracture mechanism because the shape of the boundaries impedes crack propagation. However, the stresses caused by the corrosion product do lead to creep of the alloy, particularly along grid wires, giving rise to grid growth in batteries.
6. If the grain size within a battery grid wire or casting is not uniform, the resultant unbalanced tensile stresses arising from intergranular corrosion can lead to warpage of grids or fracture of grid wires.

Acknowledgments

Useful discussions with J. A. Brown and assistance with the corrosion experiments by M. J. Dewar, J. Sklarchuk, and K. Cowan are gratefully acknowledged.

Manuscript submitted Dec. 26, 1984; revised manuscript received July 13, 1985.

Cominco Limited assisted in meeting the publication costs of this article.

REFERENCES

1. E. M. L. Valeriote, *This Journal*, **128,** 1423 (1981).
2. R. D. Prengaman, in "Edited Proceedings, 7th International Lead Conference, Madrid, May 11-14, 1980," pp. 34-47, Lead Development Association, London (1980).
3. J. Perkins and G. R. Edwards, *J. Mater. Sci.*, **10,** 136 (1975).
4. A. M. Howard and E. Willihnganz, *Electrochem. Technol.*, **6,** 370 (1968).
5. G. W. Mao, J. G. Larson, and P. Rao, *This Journal*, **120,** 11 (1973).
6. J. A. Young and J. B. Barclay, in "Proceedings of the 85th Convention of Battery Council International," pp. 37-51, San Francisco, CA, May 1-3, 1973.
7. J. A. Young, in "Proceedings of the 87th Convention of Battery Council International," Hollywood, FL, April 8-10, 1975, pp. 127-134.
8. H. Borchers and H. Assmann, *Z. Metallkd.*, **69,** 43 (1978).
9. Canadian Pat. 978 324 (1975).
10. D. B. Williams and E. P. Butler, *Int. Metals Rev.*, **26,** 153 (1981).
11. W. Gust, in "Phase Transformations," Vol. 1, pp. II 27-68, Institution of Metallurgists, Spring Residential Conference, April, 1979, Chameleon Press, London (1979).
12. P. C. Coghlan, Cominco Ltd., Product Research Centre, Sheridan Park, Ontario, Canada, Private communication.
13. E. M. L. Valeriote, J. Sklarchuk, and M. S. Ho, in "Advances in Lead-Acid Batteries," K. R. Bullock and D. Pavlov, Editors, p. 224, The Electrochemical Society Softbound Proceedings Series, Pennington, NJ (1984).

14. E. M. L. Valeriote, Unpublished data.
15. D. E. Kelly, M.A.Sc. Thesis, University of Waterloo, Waterloo, Ontario, Canada (1980).
16. H. W. Pickering, M. G. Fontana, and F. H. Beck, *Corrosion*, **18**, 230t (1962).
17. H. Bode, "Lead-Acid Batteries," p. 13, R. J. Brodd and K. V. Kordesch, Translators, John Wiley and Sons, Toronto (1977).

Characteristics of Sulfolane-Based Electrolytes for Rechargeable Lithium Batteries

Yoshiharu Matsuda,* Masayuki Morita, Kazuhiro Yamada, and Kohji Hirai

Department of Industrial Chemistry, Faculty of Engineering, Yamaguchi University, Tokiwa-dai, Ube, Yamaguchi 755, Japan

ABSTRACT

The utility of sulfolane (S)-based electrolytes has been studied for rechargeable lithium batteries. Electrolytic conductivities of $LiClO_4$, $LiBF_4$, and $LiPF_6$ were measured in the mixed system of S with 1,3-dioxolane (DOL), tetrahydrofuran (THF), or 1,2-dimethoxyethane (DME). Vapor pressure, viscosity, and relative permittivity of the mixed solvents and/or the electrolytic solutions were also measured, and the results were discussed in connection with the solution conductivity. Conductivity maxima were observed in the mixed solutions containing 60-90 mole percent ethers. The conductivity of S-DME (1:9 by volume)/$LiPF_6$ (1*M*), being the highest of all examined, was 1.5×10^{-2} S-cm^{-1}. The Li cycling characteristics were mainly investigated in the S-ether (1:1) mixed solutions. Efficiencies on the Ni substrate in the S-DME solutions varied less with cycling than those in S-DOL and S-THF. The average efficiency of Li cycling in S-DME increased in the order of $LiClO_4 < LiBF_4 < LiPF_6$. The Li cycling characteristics in the S-ether solutions are discussed from the standpoints of ionic behavior in the solution and chemical reaction at Li-solution interface.

In the course of the development of ambient temperature, rechargeable lithium (Li) batteries, it has been noted that the choice of an electrolyte system is of special importance in the cycling performance of the Li electrode (1, 2). Up to the present, the electrolyte systems in which high Li cycling efficiency has been obtained have been 1,3-dioxolane (DOL)/$LiClO_4$ and 2-methyltetrahydrofuran (2-MeTHF)/$LiAsF_6$ (3). The Li electrode characteristics in these electrolytes are sufficient to realize a practical rechargeable battery, but some problems such as detonation susceptibility of DOL/$LiClO_4$ (4) and relatively low conductance of 2-MeTHF/$LiAsF_6$ (5, 6) remain to be solved. Thus, various solvent-salt systems as the electrolytes of the rechargeable Li batteries are still under investigation (3, 7).

Sulfolane (S) is one of the promising solvents for the electrolytes of the rechargeable Li batteries (8, 9). It has high relative permittivity (dielectric constant) and high resistance to electrochemical oxidation or reduction (10). Because of its high melting point (mp) of 28.86°C (10), however, S is not easy to use as the solvent of the ambient temperature cell. To avoid this inconvenience of S, the use of 3-methylsulfolane (3-MeS), whose mp is relatively low (~ 0°C), has also been attempted (11). On the other hand, the mp of the solvent can be lowered by blending S with low viscosity ethers. This attempt was first made by an EIC group (12), but no quantitative data have been presented yet.

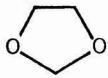
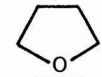
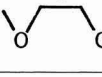
We have examined the S-based electrolytes for the ambient temperature Li batteries. The solvent mixing effects on the electrolytic conductivity and on the electrode characteristics have already been proved in the propylene carbonate (PC)-ether (13, 14) and ether-ether mixed systems (15, 16). In this paper, DOL, tetrahydrofuran (THF), and 1,2-dimethoxyethane (DME) were used as the cosolvent of S. Table I shows the selected physicochemical properties of S, DOL, THF, and DME. The ethers have low viscosity and also relatively high donicity (17). (The donicity of DOL has not been reported, but it should be comparable with those of the other ethers.) The latter implies that some interaction between the ether solvents and cations would be produced in the electrolytic solutions of the S-ether mixed systems. For the present work, the electrolytic conductivity of some Li salts were measured in the mixed solvents, and the mixing effects of the ethers on the conductivity were investigated. The Li electrode characteristics were studied in the S-ether mixed electrolytes. Differences in the Li cycling behavior between the cosolvent ethers and anion effects of the electrolytes will be discussed in connection with the results of conductivity measurements.

Experimental

The purification of ethers, or DOL (Tokyo Kasei Kogyo), THF (Toyo Soda Manufacturing), and DME (Mitsubishi Yuka Fine Chemicals), was carried out as described previously (14, 16). S (Tokyo Kasei Kogyo) was dehydrated by P_2O_5 and distilled under reduced pressure at 95°-110°C (18). The electrolytic salts, $LiClO_4$ (Ishizu Pharmaceutical) and $LiBF_4$ (Morita Chemical Industries), were used after drying under a vacuum at appropriate temperatures (14, 15). $LiPF_6$ (Morita Chemical Industries) was used as received because it had been sealed under a dry Ar atmosphere and tends to decompose by heating.

The electrolytic conductivity, the relative permittivity, and the viscosity of the solvents and the solutions were

Table I. Viscosity (η), relative permittivity (ϵ_r), donicity (DN), and acceptor number (AN) of the solvents

Solvent	Structure	$\eta/10^{-3}$ Pa-s (30°C)	ϵ_r (30°C)	DN[a]	AN[a]
S		9.87	42.5	14.8	19.0
DOL		0.58	6.79	—	—
THF		0.46	7.25	20.0	8.0
DME		0.40	6.92	24	—

*Electrochemical Society Active Member.

[a] From Ref. (17).

measured by the same methods as in the previous work (16). The vapor pressure was measured by a static method (19, 20). These measurements were carried out at controlled temperatures (20° or 30°C).

Li cycle efficiency was determined by a galvanostatic charge-discharge test (21), which is an accelerated test for brief evaluation of secondary Li electrode in the electrolyte under consideration. A beaker-type glass cell (volume = 100 cm^3) was used for the measurement. The substrate of the test electrode was a Ni sheet (0.95 cm^2) mounted on a Teflon holder. The counterelectrode was a Li sheet (2.5 × 3.0 cm) with a Ni mesh current collector. The reference electrode was a Li piece on the tip of a Ni wire (Li/Li^+). It was connected to the test electrode through a Luggin capillary. The plating and stripping current densities (i_p, i_s) were usually 2 mA/cm^2, and the plated charge (Q_p) was 0.2 C/cm^2. The cycle efficiency was defined as $(Q_s/Q_p) \times 100$ [%], where Q_s is stripped charge (15, 22). The plated charge of 0.2 C/cm^2 is much lower than those to be cycled in a practical full cell (> 10 mAh/cm^2) (6). However, even under the present conditions, the results will give an outline of the Li cycling behavior in the electrolyte under consideration, especially in the initial stage of the cycle (21).

Polarization behavior of Li in the S-based electrolytes was also studied on the Ni substrate by using the same apparatus as described above. The polarization curves were potentiostatically measured. At first, the electrode potential was stepwise changed from the rest potential to a cathodic (charging) one, and then the potential changed in the anodic (discharging) direction. The values of current density were recorded after 2 min of the potential setting. These electrochemical measurements were carried out in a dry Ar atmosphere at room temperature (18°-22°C).

Results and Discussion

Conductivity and related properties of S-based electrolytes.—Vapor pressure of an electrolytic solution is of technical interest because it relates to the storage performance of the cell containing that electrolyte. It is also used for interpreting the thermodynamic behavior of the mixed electrolyte solution (20). The vapor pressure of a real mixed solvent is given by Eq. [1]

$$P = P_A^0 x_A \gamma_A + P_B^0 x_B \gamma_B \quad [1]$$

where P, P_A^0, and P_B^0 are the vapor pressures of the mixed solvent and the pure solvents, A and B, respectively. The x's and γ's are the molar fractions and the activity coefficients of the components, respectively. If the mixed solvent is an ideal liquid, Eq. [1] will be identical with Raoult's equation, where γ_A and γ_B are unity.

Figure 1 shows the vapor pressure of the S-ether mixed systems at 20°C as a function of the ether concentration (mole percent [m/o]). The vapor pressure of the mixed solvent increased in the order S-DME < S-DOL < S-THF. Some deviation in the positive direction from the straight line indicates $\gamma > 1$, or the mixed solvents' being nonregular solutions. A certain association of the S molecules in the pure solvent would be weakened by addition of the ether. At that time the S=O bond of S can interact more effectively with noncyclic structure of DME without steric hindrance as compared with those of DOL or THF. The vapor pressure of the S-DME solution containing 1*M* (mol/dm^3) $LiBF_4$ decreased about 20%, compared with that of the parent S-DME solvent. This was also the case for the solutions of S-DOL/$LiBF_4$ and S-THF/$LiBF_4$. The lowering of vapor pressure in the 1*M* $LiBF_4$ solutions is largely explained on the basis of the depression of vapor pressure by dissolving the salt. An interaction between the Li^+ ion and the solvent, binding solvent molecules to Li^+, would also take part in the lowering of vapor pressure.

Conductance of an electrolytic solution is much affected by the relative permittivity of the solvent and the viscosity of the solution (23). Table II shows the viscosity (η) of the mixed S-ether solutions, and Fig. 2 shows the

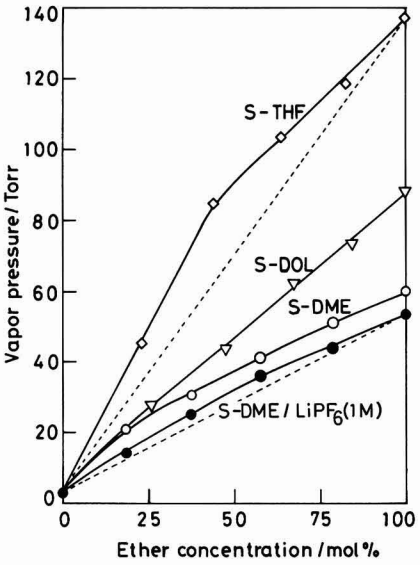


Fig. 1. Vapor pressure of S-ether mixed solvents and S-DME/$LiBF_4$ (1M) solution.

relative permittivity (ϵ_r) of the mixed solvents. The neat ethers have ϵ_r's and η's similar to one another. Therefore, ϵ_r's and η's of the mixed S-ether solutions were also comparable to one another. The ϵ_r's varied almost linearly with a change in the volume percent of each ether, but in the systems of S-THF and S-DOL the variation of ϵ_r against mole percent of the ether revealed a slight positive deviation from an additive property, as shown in Fig. 2. This suggests that there would be some difference in the solvent-solvent interaction between S and the ethers. The variation of η with solvent composition in the S-ether mixed systems was similar to those in the mixed systems with combinations of high and low viscosity solvents such as PC-ether systems (14, 24).

Figure 3 shows the electrolytic conductivity (κ) of the 1*M* $LiBF_4$ solution as a function of the solvent composition. The conductivity became maximum at about 70 m/o ether in every S-ether system. This conductivity enhancement would result from a favorable combination of high permittivity of S and low viscosity of the ether (14, 24). The maximum conductivities (κ_{max}) of 1*M* $LiBF_4$ were 3.3, 3.7, and 5.0 × 10^{-3} $S\text{-}cm^{-1}$ in S-THF, S-DOL, and S-DME,

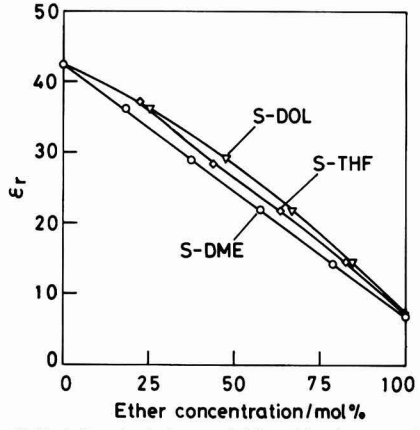


Fig. 2. Variation of relative permittivity with ether concentration for S-ether mixed solvents.

Table II. Viscosity of S-ether mixed solvent (η_0) and S-ether/$LiBF_4$ (1M) mixed solution (η^*) at 30°C

Solvent composition (v/o of ether)	S-DOL $\eta_0/10^{-3}$Pa-s	S-DOL ($\eta^*/10^{-3}$Pa-s)	S-THF $\eta_0/10^{-3}$Pa-s	S-THF ($\eta^*/10^{-3}$Pa-s)	S-DME $\eta_0/10^{-3}$Pa-s	S-DME ($\eta^*/10^{-3}$Pa-s)
100	0.58	(1.00)	0.46	(1.29)	0.40	(0.71)
80	0.81	(1.43)	0.72	(1.33)	0.65	(1.21)
60	1.22	(2.17)	1.17	(2.41)	1.07	(2.14)
40	2.08	(4.12)	2.09	(4.68)	1.99	(4.15)
20	3.98	(8.75)	4.17	(10.04)	3.98	(8.92)
0	9.87	(23.29)	9.87	(23.29)	9.87	(23.29)

respectively. The critical distance for ion-pair formation, or Bjerrum's q value (25), at the solvent composition providing κ_{max} ($\simeq$ 70 m/o) was estimated to be 1.25-1.53 nm from ϵ_r at that solvent composition. It is reasonable that ionic association takes place in the solution with such a large q (14, 24). Thus, ionic association is responsible for the low conductance of the solution with higher ether concentration than about 70 m/o.

Differences in the conductivity among the different ethers to be mixed with S are at least partly attributable to differences in the solution viscosity. Walden products ($\Lambda\eta$) for 1M $LiBF_4$ are shown in Fig. 4. In spite of the appreciable differences in the conductivity, the Walden products are almost the same at given ether concentrations. The monotonous decrease in $\Lambda\eta$ with increasing ether concentration, however, means that the Walden rule fails in each S-ether system even at the lower concentration of the ether. This means that ionic association takes place in the solutions of high ether concentration.

Figure 5 shows the conductivity dependence on the DME concentration for 1M solutions of $LiBF_4$, $LiClO_4$, and $LiPF_6$ in S-DME. Solubility of $LiPF_6$ was rather low in S-DME. It was lower than 1M at DME concentration below 40 m/o or above 95 m/o. Thus, the conductivities of $LiPF_6$ solutions at such solvent compositions refer to those of saturated (< 1M) solutions (closed squares in Fig. 5). The conductivity increased in the order $LiBF_4$ < $LiClO_4$ < $LiPF_6$, and the κ_{max}'s were 5.0, 7.1, and 15.1 ($\times 10^{-3}$ S-cm^{-1}) for $LiBF_4$, $LiClO_4$, and $LiPF_6$, respectively. The DME concentration at which the conductivity reached κ_{max} also depended on the electrolyte salts. These results show that the anions of the salts greatly affect the electrolytic conductance in this system. The Stokes radii of ClO_4^-, BF_4^-, and PF_6^- are comparable to one another in PC-DME (20), which is an analogous mixed-system to present S-DME. It is, therefore, reasonable that there is no great difference in the size among these three anions in S-DME. The difference in the conductance behavior among the solutions of $LiClO_4$, $LiBF_4$, and $LiPF_6$ might be attributable to differences in some anion-cation or anion-solvent(s) interaction in S-DME. For example, the formation of ion-pair and triple ions would be responsible for the conductance behavior. The formation in the $LiBF_4$ solution is probably high, and, therefore, it lowers conductivity. In the $LiPF_6$ solution, the larger crystallographic size and lower charge density of the PF_6^- ion would minimize Li^+-PF_6^- interaction and, hence, higher conductivity would be achieved. Unfortunately, this trend in the conductance behavior, as shown in Fig. 5, could not be proved in S-THF or S-DOL. As $LiPF_6$ liberates free PF_5, which is a strong Lewis acid, its THF or DOL solution polymerizes under Lewis acid-catalyzed oxidation (26). Because of this polymerization accompanying an increase in the solution viscosity, no accurate conductivity was obtained for the $LiPF_6$ solutions of S-THF and S-DOL.

Charge-discharge behavior of Li in S-based electrolytes.—Anodic and cathodic current-potential relations were measured by a potentiostatic polarization method. The polarization curves of Li at Ni substrates in S-DME (1:1 mixture = 48 m/o DME) are shown in Fig. 6. The curves were first measured in the cathodic direction from the rest potentials. Li was deposited on the Ni substrate during this cathodic polarization. Then, the measurements were carried out in the anodic direction from −2.0 to +1.5V (*vs.* Li/Li^+). The anodic currents (from 0 to +1.5V) are based on the dissolution of Li which has been deposited on the Ni substrate during the preceding cathodic polarization.

A hysteresis observed on each cathodic curve in the solution of $LiBF_4$ or $LiClO_4$ seems to originate from a

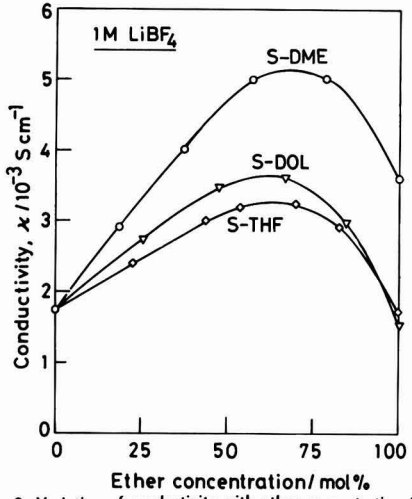


Fig. 3. Variation of conductivity with ether concentration for 1M $LiBF_4$ in S-ether mixed systems.

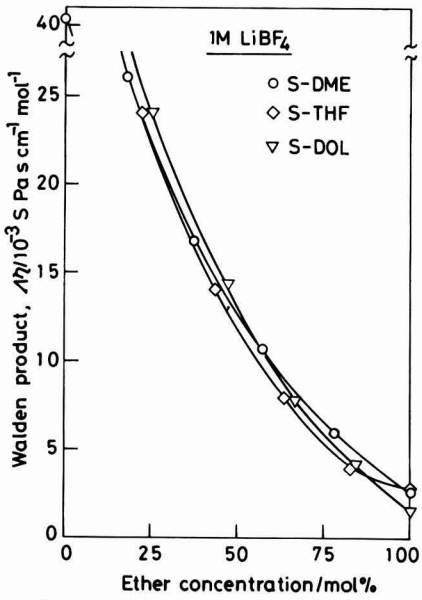


Fig. 4. Variation of Walden product with ether concentration for 1M $LiBF_4$ in S-ether mixed systems.

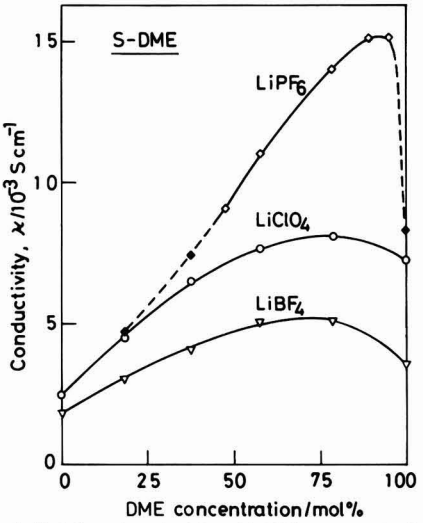


Fig. 5. Variation of conductivity with DME concentration for 1M $LiClO_4$, $LiBF_4$, and $LiPF_6$ in S-DME.

change in the real surface area of the electrode by continuous Li deposition during the measurement. The hysteresis was hardly observed in the $LiPF_6$ solution. In the potential region away from 0 V, the current densities at given potentials increased in the order $LiClO_4 < LiBF_4 < LiPF_6$. That is, the polarization in the $LiPF_6$ solution was smallest of the three. The anodic current in the $LiClO_4$ solution dropped at anodic potentials of 0.5V or greater. Active Li remained on the Ni substrate after this anodic polarization in the $LiClO_4$ solution. Thus, the current drop at about 0.5V is probably due to passivation of Li deposited during cathodic charge.

Variations of Li cycling efficiency in 1*M* $LiBF_4$ solutions are shown in Fig. 7. In this case, 1:1 (by volume) mixtures were used as the mixed solvents for convenience. The actual mixing ratios are 58, 54, and 48 m/o ethers for S-DOL, S-THF, and S-DME, respectively. The efficiency in S/$LiBF_4$ was about 60% for the initial cycles but decreased with repeated cycles. The reason for this lowering in the efficiency is not clear, but it might be related to passivation of Li or formation of isolated, inactive

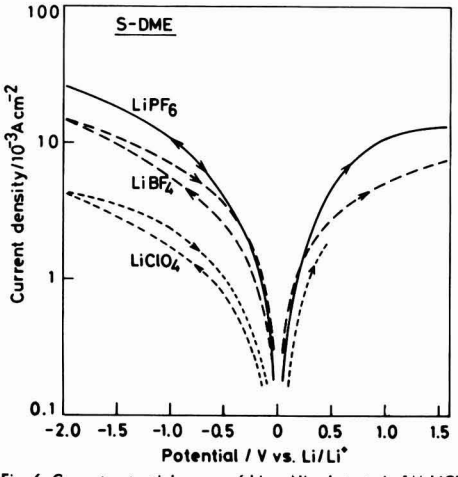


Fig. 6. Current-potential curves of Li on Ni substrate in 1M $LiClO_4$, $LiBF_4$, and $LiPF_6$. Solvent: S-DME (1:1 by volume = 48 m/o DME).

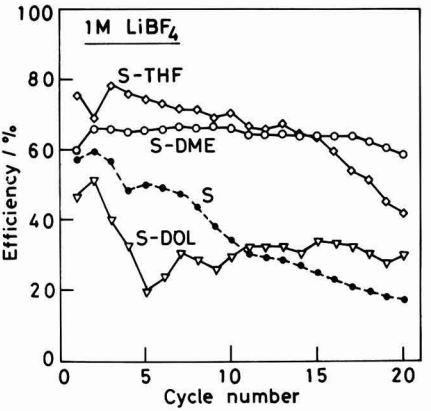


Fig. 7. Variation of efficiency with cycle number in 1M $LiBF_4$ solutions. $i_p = i_s = 2.0$ mA/cm². $Q_p = 0.2$ C/cm².

Li as in the case of PC-based electrolytes (27). The efficiency was little improved by mixing DOL with S.

On the other hand, the use of THF or DME as a cosolvent of S brought relatively high efficiency. This was probably caused by two effects. The one is lowering the polarization of Li during the charge-discharge cycles. The other is coordination of THF and DME to the Li^+ ions. The former mainly results from the improvement of electrolytic conductivity (or ionic mobility) by mixing S with low viscosity THF or DME. The lower polarization should lead to the reduction in the rates of side reactions (*e.g.*, decomposition of the electrolyte solution), which causes the efficiency loss in the cycle. The latter effect, coordination of the ethers, would also contribute to the reduction in the decomposition rate of solvents. In PC-based electrolytes, the interaction between PC and Li^+ accelerates the decomposition of the solvent (28). This would also be the case for S-based electrolytes, although S has a higher resistance to electrochemical reaction than PC has. Isolation of Li^+ from solvent S by coordination of the ether to Li^+ would minimize the reaction rate. Furthermore, it is difficult to rule out the possibility that the added ethers play a part in the superior Li deposition. Such a Li film formed in the ether containing solutions might be different from the film deposited from the solution consisting of neat S.

The cycle efficiency in S-THF was relatively high initially but gradually decreased. In S-DME, however, variation of the efficiency with cycling was rather small. The average cycling efficiency from the first to twentieth cycles on the Ni substrate was 64.2% in S-DME/$LiBF_4$.

In Fig. 8, the cycle efficiencies in the S-DME solutions with different electrolytes were compared with one another. The average efficiency in the $LiPF_6$ solution was 77.1% and was the highest of all. Relatively low efficiencies were observed in the $LiClO_4$ solution, which would be related to the results of the current-potential measurements. These differences in the cycle efficiency among the three electrolytes are based on the differences in the electrochemical stability of the solution, which depend on the magnitude of polarization during the charge-discharge process. The morphology of Li deposited on Ni and the electrochemical properties of the film which might be formed on Li would also affect the cycling characteristics. In the $LiBF_4$ and $LiPF_6$ solutions, liberation of Lewis acids (BF_3 and PF_5), whose amounts might be different to each other, can also affect the cycling efficiency. Furthermore, the structures of the electrical double layers with different anions might influence the charge-discharge characteristics of the Li electrode. Details of these differences in the cycling behavior between the electrolytic salts are now under consideration.

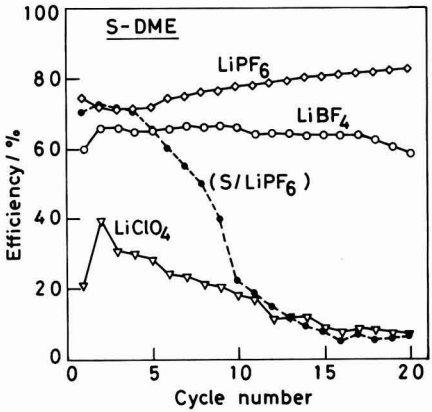


Fig. 8. Variation of efficiency with cycle number in 1M $LiClO_4$, $LiBF_4$, and $LiPF_6$. Solvent: S-DME (1:1 by volume = 48 m/o DME).

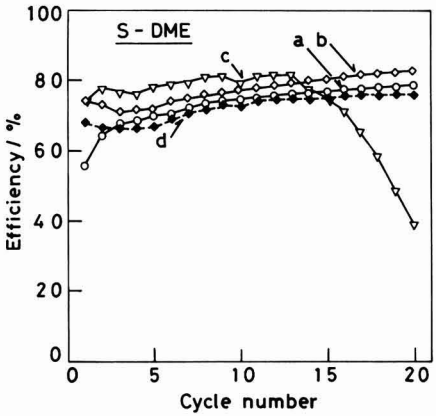


Fig. 10. Variation of efficiency with cycle number in S-DME/$LiPF_6$. Solvent: 1:1 by volume (a-c), 1:9 by volume = 89 m/o DME (d). i_p (= i_s): 1 mA/cm² (a), 2 mA/cm² (b, d), and 5 mA/cm² (c). Q_p: 0.2 C/cm².

The efficiencies in S/$LiPF_6$, which contains no ether, were as high as those in S-DME/$LiPF_6$ for few initial cycles, but a marked decreasing of the efficiency was observed, especially after the tenth cycle. Therefore, DME mixed with S apparently functions to keep the efficiency in S/$LiPF_6$ high.

When the cycles were further extended in S-DME/$LiPF_6$, about 80% of the efficiency was reproducibly observed up to the fortieth cycle or so. However, the efficiency at additional cycles varied with less reproducibility. Figure 9 shows the potential-time curves during the charge-discharge cycles in S-DME/$LiPF_6$. Up to the fortieth cycle, the potential variation with time in each cycle was similar to one another. The polarization (potential difference from 0 V) during the charge and discharge increased with continued cycling after the fortieth cycle. The shape of the discharge curve also varied with the cycle. These changes in polarization behavior seem to be associated with the efficiency variation. Repetition of the charge-discharge cycle leads to accumulation of inactive Li which is electrically isolated from the substrate (27). This seems to be the cause of the changes in cycling characteristics at the extended cycles.

Figure 10 shows the effects of current density and mixing ratio of the solvents on the cycling efficiency in S-DME/$LiPF_6$. Average efficiency during the first ten cycles increased with increasing i_p. As Q_p was kept constant at 0.2 C/cm², increasing i_p implied decreasing the plating (charging) time. Thus, the lower i_p and i_s were, the longer the deposited Li contacted the solution. This would lead to the result that the Li deposited under low i_p is not effectively utilized because of an inert film formed on Li. However, the dependence of the average efficiency on the current density was rather small, compared with that in ether-ether mixed systems (22). Therefore, the film formation or production of isolated, inactive Li might proceed with relatively slow rate. On the other hand, cycling at higher i_p and i_s (5 mA/cm²) led to a marked decrease of efficiency after the thirteenth cycle. The polarization of the electrode becomes high when plating is done at high current density. Some side reaction such as cathodic reduction of the solvents might occur during the charge. This results in the efficiency loss with repeating the cycle.

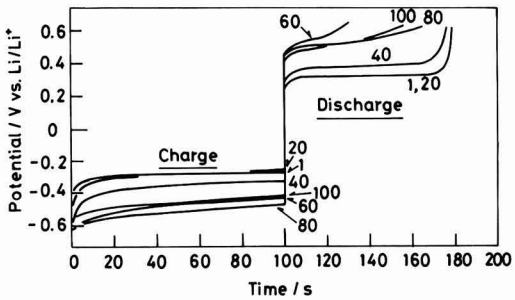


Fig. 9. Potential-time curves of Li on Ni substrate during charge-discharge cycles.

The Li cycle efficiencies were measured in the S-DME/$LiPF_6$ solutions with various solvent compositions. In Fig. 10, the solvent mixing ratio of 1:9 (by volume) is equivalent to 89 m/o DME in S-DME. The electrolytic conductivity of 1*M* $LiPF_6$ in S-DME (1:9) was about 1.5 times of that in S-DME (1:1). The increase in the conductivity brought little improvement to the cycling characteristics. Values of efficiency similar to that in S-DME (1:1) were obtained in the solutions with other mixing ratios (30-90 m/o DME).

Summary

Some properties of the electrolytic solutions consisting of sulfolane (S)-ether mixed solvents were investigated for rechargeable lithium batteries. The results are summarized as follows.

1. Vapor pressure of the mixed solvent increased in the order S-DME < S-DOL < S-THF, and it deviated from the Raoult rule in the positive direction for every system. Relative permittivity of the mixed solvent and viscosity of the electrolytic solution were little dependent on the added ether.

2. Maximum conductivities were obtained in the solutions consisting of the mixed solvent. The conductance behavior varied markedly with the electrolytic salt and cosolvent ether. The highest conductivity of all examined was observed for S-DME (1:9)/$LiPF_6$ (1*M*).

3. The polarization of Li on the Ni substrate in S-DME increased in the order $LiPF_6$ < $LiBF_4$ < $LiClO_4$, and the average efficiency of Li cycling increased in its opposite order. The cycling in S-DME/$LiPF_6$ showed the highest efficiency of all examined.

Acknowledgments

We wish to thank Dr. Y. Takasu for measurements of vapor pressure. We also thank Mr. F. Tachihara for conductivity measurements.

Manuscript submitted April 18, 1985; revised manuscript received July 23, 1985.

Yamaguchi University assisted in meeting the publication costs of this article.

REFERENCES

1. J. O. Besenhard and G. Eichinger, *J. Electroanal. Chem.*, **68,** 1 (1976).
2. V. R. Koch, *J. Power Sources*, **6,** 357 (1981).
3. K. M. Abraham and S. B. Brummer, in "Lithium Batteries," J. P. Gabano, Editor, p. 371, Academic Press, New York (1983).
4. G. H. Newman, R. W. Francis, L. H. Gaines, and B. M. L. Rao, *This Journal*, **127,** 2025 (1980).
5. J. L. Goldman, R. M. Mank, J. H. Young, and V. R. Koch, *ibid.*, **127,** 1461 (1980).
6. K. M. Abraham, J. L. Goldman, and D. L. Natwig, *ibid.*, **129,** 2404 (1982).
7. S. B. Brummer, in "Lithium Battery Technology," H. V. Venkatasetty, Editor, Chap. 7, p. 159, John Wiley and Sons, New York (1984).
8. B. J. Carter, S. P. S. Yen, D. H. Shen, R. M. Williams, and R. B. Somoano, Abstract 72, p. 179, The Electrochemical Society Extended Abstracts, Vol. 81-2, Denver, CO, Oct. 11-16, 1981.
9. J. S. Foos and L. M. Rembetsy, Abstract 73, p. 117, The Electrochemical Society Extended Abstracts, Vol. 83-2, Washington, DC, Oct. 9-14, 1983; J. S. Foos and L. M. Rembetsy, in "Lithium Batteries," A. N. Dey, Editor, pp. 413-421, The Electrochemical Society Softbound Proceedings Series, Pennington, NJ (1984).
10. H. V. Venkatasetty, in "Lithium Battery Technology," H. V. Venkatasetty, Editor, Chap. 1, p. 7, John Wiley and Sons, New York (1984).
11. S. P. S. Yen, D. H. Shen, R. P. Vasquez, B. J. Carter, and R. B. Somoano, Abstract 74, p. 119, The Electrochemical Society Extended Abstracts, Vol. 83-2, Washington, DC, Oct. 9-14, 1983.
12. DOE Project, *J. Power Sources*, **11,** 212 (1984); J. S. Foos, L. M. Rembetsy, and S. B. Brummer, Final Report on Department of Energy Contract no. DE-AC03-76SF00098, Subcontract no. 4514810 (1984).
13. H. Ikeda, S. Ueno, T. Saito, S. Nakaido, and H. Tamura, *Denki Kagaku*, **45,** 391 (1977).
14. Y. Matsuda, M. Morita, and K. Kosaka, *This Journal*, **130,** 101 (1983).
15. Y. Matsuda, M. Morita, and K. Takata, *ibid.*, **131,** 1991 (1984).
16. Y. Matsuda, M. Morita, and T. Yamashita, *ibid.*, **131,** 2821 (1984).
17. V. Gutmann, *Electrochim. Acta*, **21,** 61 (1976).
18. M. D. Monica, L. Jannel, and U. Lamanna, *J. Phys. Chem.*, **72,** 1068 (1968).
19. E. Koizumi and S. Ouchi, *Nippon Kagaku Zasshi*, **91,** 510 (1970).
20. Y. Matsuda, H. Nakashima, M. Morita, and Y. Takasu, *This Journal*, **128,** 2552 (1981).
21. V. R. Koch and S. B. Brummer, *Electrochim. Acta*, **23,** 55 (1978).
22. K. Takata, M. Morita, Y. Matsuda, and K. Matsui, *This Journal*, **132,** 126 (1985).
23. R. Jasinski, in "Advances in Electrochemistry and Electrochemical Engineering," Vol. 8, P. Delahey and C. W. Tobias, Editors, p. 253, Interscience, New York (1971).
24. Y. Matsuda, M. Morita, and K. Kosaka, *Denki Kagaku*, **51,** 119 (1983).
25. N. Bjerrum, *K. Danske Vidensk. Selk.*, **7,** No. 9 (1926); R. A. Robinson and R. H. Stokes, "Electrolyte Solutions," p. 16, Elsevier, New York (1966).
26. G. H. Newman, in "Lithium Nonaqueous Battery Electrochemistry," E. B. Yeager, B. Schumm, Jr., G. Blomgren, D. R. Blankenship, V. Leger, and J. Akridge, Editors, pp. 143-157, The Electrochemical Society Softbound Proceedings Series, Princeton, NJ (1980).
27. E. Peled, in "Lithium Batteries," J. P. Gabano, Editor, p. 43, Academic Press, New York (1983).
28. E. B. Yeager, in "Lithium Nonaqueous Battery Electrochemistry," E. B. Yeager, B. Schumm, Jr., G. Blomgren, D. R. Blankenship, V. Leger, and J. Akridge, Editors, pp. 1-12, The Electrochemical Society Softbound Proceedings Series, Princeton, NJ (1980).

Effect of EDTA on the Cathodic Reduction of Oxide Films on Iron in Sodium Hydroxide Solution

Z. Szklarska-Smialowska, T. Zakroczymski,[1] and C.-J. Fan

Department of Metallurgical Engineering, The Ohio State University, Columbus, Ohio 43210

ABSTRACT

Simultaneous electrochemical and ellipsometric investigations of the behavior of iron in 0.05 NaOH solution (pH 12) with and without the addition of EDTA showed that EDTA did not affect the passive film formation but drastically enhanced cathodic reduction of the passive film. Cathodic reduction of the passive film in EDTA-free 0.05*M* NaOH resulted in the formation of an unreducible porous layer on the iron surface. This layer grew progressively in thickness when periodic passivation-reduction cycles were applied but did not influence the passive film formation. The cathodically formed layer probably consisted of some kind of iron hydroxide and elemental iron. In contrast, when EDTA was added to 0.05*M* NaOH, the cathodic reduction and removal of the passive film was complete and occurred very rapidly. Cathodic polarization of passive iron carried out potentiostatically in the presence of EDTA was found to provide reliable data on the charge consumed for reduction of the passive film.

In two other studies of ours (1, 2), it was found that the formation of passive films on iron in NaOH and NaOH + NaCl solutions (pH 12.0) resulted in a release of iron cations into the surrounding electrolyte starting in about 2s of the anodic polarization. In addition, it was noticed that after passivation and successive cathodic reduction in both NaOH and NaOH + NaCl solutions, the optical parameters did not return to their initial values before passivation, suggesting that some film still existed on the metal surface. Huang and Ord (3) reported that during cycling of iron in NaOH solution between anodic and cathodic potentials, the thickness of the unreducible film increased during each consecutive cycle. This film had a very low index of refraction and was probably FeOOH. Therefore, it seemed interesting to assess whether the addition of a complexing agent would interfere with the formation and reduction of oxide films on iron. The ethylenediaminetetra-acetic acid (EDTA) has been chosen to be studied here, because this chelating agent is known to dissolve magnetite in acid and neutral solutions at 50°C and higher temperatures (4). On the other hand, EDTA added to the alkaline electrolyte in iron batteries has been found (5) to increase their capacity.

Experimental

The material used and the experimental procedure were the same as in the two aforementioned studies (1, 2).

Results of Electrochemical and Ellipsometric Measurements

Polarization curves.—Anodic polarization curves measured at a potential sweep rate (PSR) of 0.01 V/s in 0.05*M* NaOH without and with the addition of either 0.001 or

[1] Permanent address: The Institute of Physical Chemistry, Polish Academy of Sciences, Kasprzaka 44/52, 01-224 Warsaw, Poland.

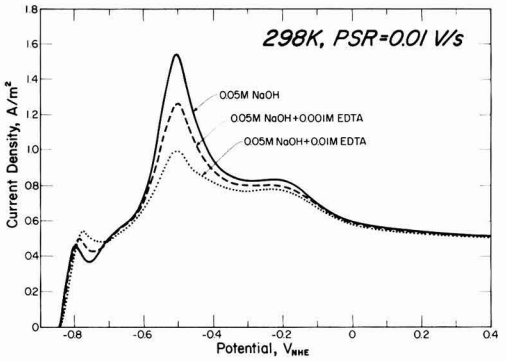


Fig. 1. Anodic polarization curves for iron in 0.05M NaOH containing different amounts of EDTA.

0.01*M* EDTA are shown in Fig. 1. In the presence of EDTA, a slight decrease of the critical current for passivation occurred, with no effect on the current density in the passive state. It appeared, therefore, that there were no changes in the protective properties and quality of the film grown on iron in either the presence or absence of EDTA in 0.05*M* NaOH solution.

Current decay curves.—Figure 2 depicts variations of the anodic current density with time at a constant potential of 0.550V, resulting from a rapid (PSR = 80 V/s) change of the electrode potential from −0.950 to 0.550V. Also in this case, no significant effect of EDTA on the anodic current density was observed, suggesting that EDTA added to 0.05*M* NaOH did not affect the passive film growth on iron. This conclusion was supported by the results of ellipsometric measurements in 0.05*M* NaOH + 0.01*M* EDTA which did not differ from those obtained in 0.05*M* NaOH (anodic part of the first cycle in Fig. 3).

Passivation-reduction cycling.—Contrary to the anodic polarization, there was a significant effect of EDTA on the course of the cathodic reduction. In 0.05*M* NaOH, the cathodic polarization of a passivated iron electrode did not permit the optical parameters Δ and ψ to return to their initial values observed for nonpassivated iron. Furthermore, repeated passivation-reduction cycles carried out with the same electrode resulted in an additional irreversibility of optical parameters, so that each consecutive $-\delta\Delta$ *vs.* t, $\delta\psi$ *vs.* t, or $\delta\psi$ *vs.* $-\delta\Delta$ curve was shifted relative to the preceding one (Fig. 3 and 4). In contrast, in the presence of EDTA, the film reduction was fast and complete, and numerous repeated passivation-reduction cycles had the same run.

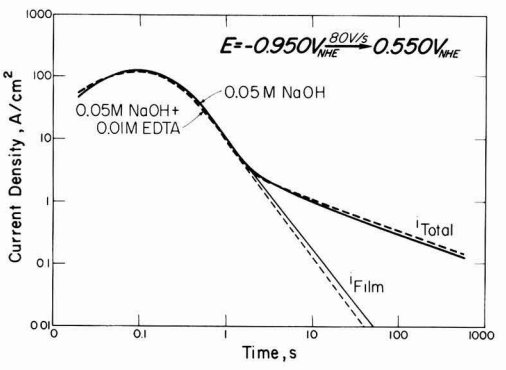


Fig. 2. Changes in current density with time for iron in 0.05M NaOH with and without EDTA and at 0.550V. The extrapolated fine lines correspond to the current consumed for film growth ($t > 2$s).

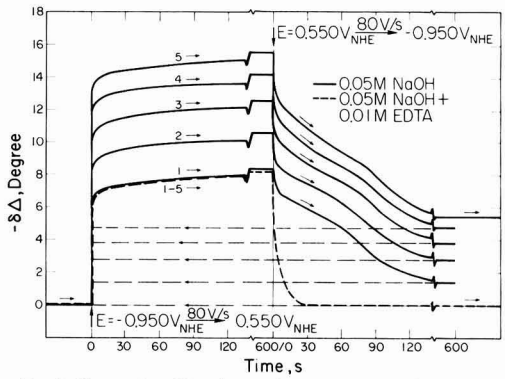


Fig. 3. Changes in $-\delta\Delta$ with time during consecutive five cycles of film growth and film reduction in 0.05M NaOH with and without EDTA.

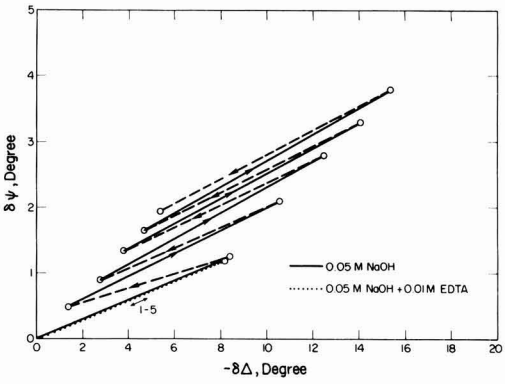


Fig. 4. Relationship between $-\delta\Delta$ and $\delta\psi$ during consecutive cycles of film growth and film reduction in 0.05M NaOH with and without EDTA.

Figure 5 shows changes in $-\delta\Delta$ and $\delta\psi$ in relation to the number of passivation-reduction cycles obtained in two similar experiments. In the first experiment, which was performed in 0.05*M* NaOH without EDTA, 20 consecutive cycles between −0.950 and 0.550V were applied, with both potentials maintained each time for 600s. Values of Δ and ψ were taken after a successive reduction at −0.950V; their changes are marked as $(-\delta\Delta)_{red}$ and $(\delta\psi)_{red}$, respectively. After 20 cycles, the metal surface was covered with a yellow-brown deposit. In the second experiment, after

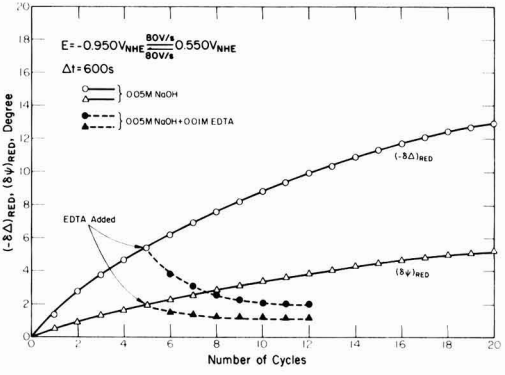


Fig. 5. Changes in optical parameters obtained after successive cathodic polarization of the passivated iron in 0.05M NaOH and the effect of the addition of EDTA.

five passivation-reduction cycles in 0.05*M* NaOH, EDTA was added at −0.950V. At this potential, no significant changes in the optical parameters were observed (even for times longer than 600s). However, during the successively repeated passivation-reduction cycles, a partial restoration of the optical parameters was observed (solid characters in Fig. 5).

In contrast to the optical parameters, both the anodic (at 0.550V) and the cathodic (at −0.950V) current densities were not significantly affected by passivation-reduction cycling in either EDTA-free or EDTA containing 0.05*M* NaOH. The magnitude and the changes of the anodic current density with time shown in Fig. 2 are the same for many cycles.

Since both the *p*H and kind of anion can play significant roles in the film formation and film reduction processes, additional passivation-reduction cycling experiments were carried out using NaOH, borate, and phosphate solutions of different *p*H. Figure 6 indicates that in all applied solutions of high *p*H (> 12), without EDTA the reduction of the passive film in a successive cycle led to a gradual increase of $(-\delta\Delta)_{red}$, whereas in the presence of EDTA the restoration of Δ was complete. In turn, Fig. 7 shows that at *p*H 9, the passive film was removed in spite of the absence of EDTA.

Reduction and removal of the passive film.—Additional information regarding the influence of EDTA on the reduction of passive films on iron in 0.05*M* NaOH is provided in Fig. 8, showing changes in $-\delta\Delta$ under various passivation and reduction conditions. When both the passivation and reduction were conducted in the absence of EDTA, restoration of Δ during reduction was slow and not complete; the longer passivation time was employed, the slower restoration was. Moreover, irreversibility was more pronounced when the passivation time was longer. When the passive film grew in 0.05*M* NaOH and was then reduced in the presence of EDTA, Δ returned to its initial value before passivation. This occurred at a rate which also was passivation-time dependent, but much faster than in the EDTA-free 0.05*M* NaOH solution. Identical results were obtained when both the passivation and reduction occurred in the presence of EDTA, once again indicating the EDTA did not affect passivation but decisively enhanced the reduction of passive films on iron and caused a full restoration of the optical parameters.

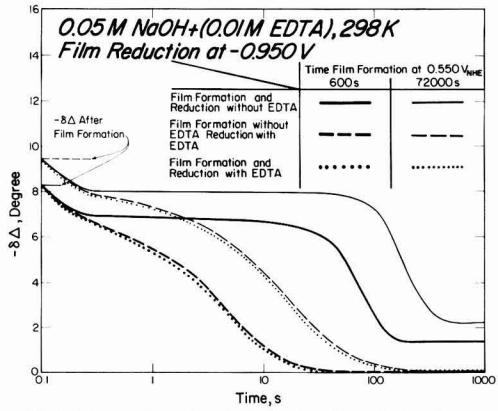


Fig. 8. Changes in $-\delta\Delta$ with time during the cathodic reduction of films grown in 0.05M NaOH with and without EDTA.

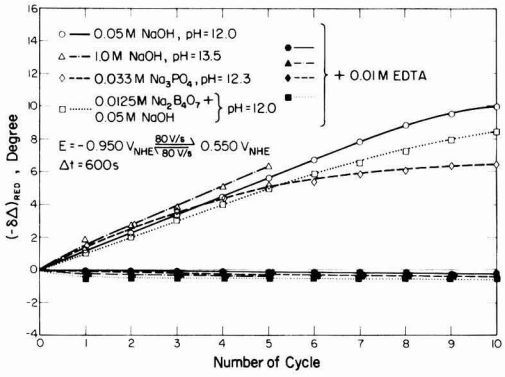


Fig. 6. Changes in $-\delta\Delta$ obtained after successive cycling from anodic to cathodic polarization of iron in solutions containing different anions, with and without EDTA (high *p*H).

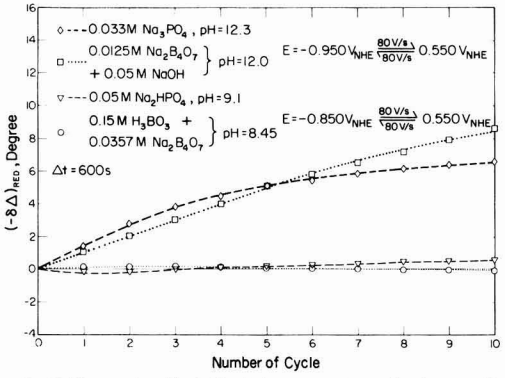


Fig. 7. Changes in $-\delta\Delta$ obtained after successive cycling from anodic to cathodic polarization of iron in borate and phosphate solutions of different *p*H.

Determination of the film charge density.—Since the cathodic reduction method is often used to determine the charge consumed for the reduction of a passive film and to measure its thickness, additional experiments aimed at assessing the influence of EDTA on the results of film charge measurements have been performed. Relationships between the electrode potential and $-\delta\Delta$ *vs.* time of galvanostatic reduction are shown in Fig. 9 and 10, respectively. In both those figures, the value of q_{film} = 67.5 C/m² is marked on the charge density scale. This value was obtained by integration of the curve i_{film} plotted in Fig. 2. It was expected that the same q_{film} value could be obtained on the basis of the reduction experiment. Unfortunately, this proved to be impossible because there was no characteristic point on the potential-time curve (Fig. 9)

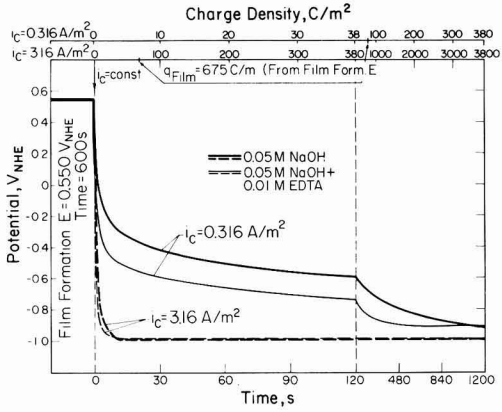


Fig. 9. Variation in potential with time during galvanostatic reductions of the passive film in 0.05M NaOH with and without EDTA.

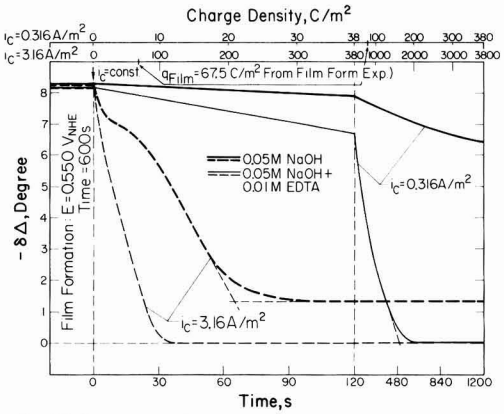


Fig. 10. Changes in $-\delta\Delta$ with time during galvanostatic reductions of the passive film in 0.05M NaOH with and without EDTA.

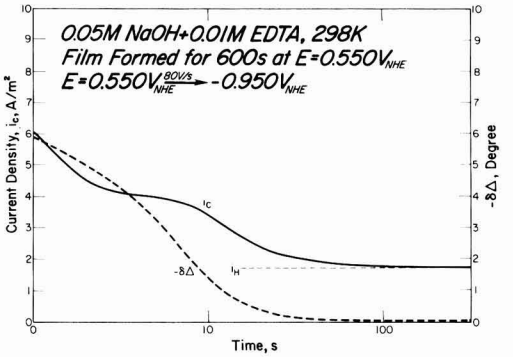


Fig. 11. Changes in current density and $-\delta\Delta$ with time during cathodic reduction of the passive film in 0.05M NaOH + 0.01M EDTA at −0.950V.

which could permit differentiation of the film reduction charge from the hydrogen evolution charge. Attempts to evaluate q_{film} taking into account the time after which Δ returned to its initial value ($-\delta\Delta = 0$) in the presence of EDTA or to a constant value in the absence of EDTA (see Fig. 10) were also unsuccessful. However, the q_{film} value obtained in the presence of EDTA at a high current density was about 90 C/m² and hence not very far away from the previously determined value of 67.5 C/m².

In the next series of experiments, the cathodic reduction of the passive film was conducted in 0.05*M* NaOH under controlled potentiostatic conditions at −0.950V. It was assumed that the reduction of the film ended when $-\delta\Delta$ was constant and that i_c also is constant and associated with the hydrogen evolution reaction (i_H). Another assumption was that during the cathodic reduction the evolution of hydrogen occurred at a constant rate. This was a very rough simplification, because in the initial reduction stage the hydrogen evolution reaction probably was overwhelmed by that of film reduction. Based on these assumptions, the charge consumed for hydrogen evolution, q_H, could be calculated. Finally, q_{film} could be obtained by substracting q_H from q_{total}. The results of these calculations showed that, again, the q_{film} value was still too high relative to that obtained in the film formation experiments.

The results of measurements taken under the same conditions as above but in the presence of EDTA are much more promising; see Fig. 11 and 12. The obtained value of q_{film} is only 4% lower than the one sought. This difference could be caused by the simplified assumption concerning the constancy of i_H. From those considerations, it follows that potentiostatic measurements conducted in the presence of EDTA in alkaline solutions may lead to reliable data of the charge consumed for the passive film reduction on iron.

Discussion

It was expected that EDTA, which is a potent complexing agent for iron ions, could reduce the propensity to passivation of iron in NaOH. However, neither the course of anodic polarization curves (Fig. 1) nor those of decay curves (Fig. 2) or ellipsometric data (Fig. 3 and 4) support the above expectation. In fact, passive film grown on iron in either EDTA-free or EDTA containing 0.05*M* NaOH solution exhibit the same protective and optical properties. This fact can be explained by the high ability of iron to be passivated by alkaline solutions.

The most significant finding to be discussed here is the appearance of a layer on the surface of iron after its anodic oxidation, followed by cathodic reduction in 0.05*M* NaOH. This layer does not, however, appear when the cathodic reduction is conducted in 0.5*M* NaOH containing EDTA. The question arises whether this layer consists of a residue of the previous passive film or results from a certain, heretofore unknown, cathodic reaction. The first option seems to be likely, since it is generally accepted that a complete reduction of the passive film on iron is hard to attain in alkaline solutions. However, the presence of some passive film residue on iron would influence its next anodic behavior, which is not observed. In all the repeatedly conducted passivation-reduction cycles, the current density was the same, and both $-\delta\Delta$ and $\delta\psi$ increased a little with increasing cycle number (Fig. 3 and 4).

These observations show that the new passive film formed during each successive passivation does not substantially differ from that formed during the previous passivation. It is obvious, therefore, that the surface layer resulting from the cathodic reduction of passive iron in 0.05*M* NaOH does not consist of an unreducible residue of the previous passive film.

The above conclusion was supported by the following additional experiment. A fresh iron electrode was pretreated cathodically at −0.950V and kept in 0.05*M* NaOH under open-circuit condition for 20h. Both the corrosion potential and optical parameters varied with time, showing that slight passivation occurred; namely, after 20h, the potential attained about −0.4V and $-\delta\Delta$ was 5.4°. Then, the electrode was polarized to 0.550V and kept at this potential for 600s, during which $-\delta\Delta$ increased to 8.3°, *i.e.*, to a value close to that characterizing the passive state of iron after its passivation in one stage from −0.950 to 0.550V (Fig. 3). The charge consumed for the potential shift from −0.4 to 0.550V was less than that consumed from −0.950 to 0.550V, indicating that the presence of a

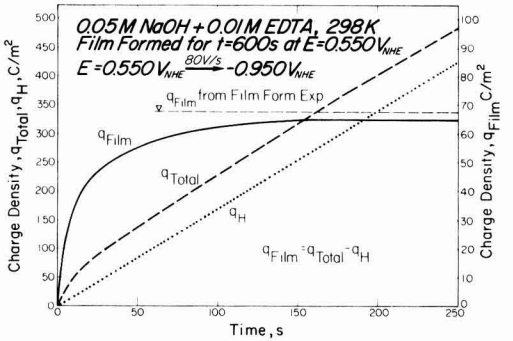


Fig. 12. Effect of time on the total charge density during cathodic reduction of the passive film and on the charge densities consumed for film reduction and hydrogen evolution in 0.05M NaOH + 0.01M EDTA at −0.950V.

passive film residue does not interfere with the next passivation but assists its attainment.

The layer that forms on iron during the cathodic polarization in 0.05*M* NaOH has a very low refractive index. The n and k values obtained from the $(\delta\psi)_{red}$ *vs.* $(-\delta\Delta)_{red}$ relationship are about 1.4-1.6 and 0, respectively. None of the known iron oxides exhibit such low n and k values. The thickness of the cathodic layer increases with the number of passivation-reduction cycles applied and may attain several hundred angstroms. It can be supposed, therefore, that this layer is porous and that its refractive index, as measured, is immaterial. Because of its porosity, the layer is nonprotective and does not affect the next passivation.

Another question to be asked regards the origin of the cathodic layer. Two possibilities can be taken into account: first, that this layer is a result of the cathodic reduction of the pre-existing passive film; second, that ferric ions released from the film during passivation undergo reduction and iron is electrodeposited during the next cathodic polarization. To check the latter possibility, the following auxiliary experiment was performed. After 600s of cathodic polarization of an iron electrode at −0.950V in 0.05*M* NaOH, ferric ions at a concentration of 1×10^{-5} mol/liter were added and ellipsometric parameters were recorded. Although the concentration of ferric ions added was much higher than that which could be produced by dissolution of a pre-existing passive film, the optical parameters did not change during a few hours of cathodic polarization. Consequently, the first alternative appears to be more probable.

The above considerations do not provide a clear solution to the crucial question regarding the nature of the cathodic layer. One possibility is that during cathodic polarization, the passive film, probably FeOOH (1), is reduced to iron in the form of a porous layer. In the presence of this layer, at a constant cathodic potential of −0.950V, the optical parameters do not change in either EDTA-free or EDTA containing 0.05*M* NaOH solution. This indicates that under these conditions the cathodic layer does not undergo any change. However, optical parameters are decreased by cycling between anodic and cathodic potentials in EDTA containing 0.05*M* NaOH (Fig. 5), suggesting that by such a procedure the porous layer becomes partly removed. When EDTA is added to the electrolyte after passivation but before application of the first cathodic reduction, *i.e.*, when the iron electrode is covered by the sole passive film, cathodic polarization results in a complete removal of the passive film and there is no porous layer formation. The optical parameters return to their initial values before passivation.

The exact part played by EDTA in the above processes is not quite clear. Since EDTA is a complexing agent of iron cations, it might be supposed that the charge density consumed for the passive film reduction should be less than that for passivation (Fe° → FeOOH). In reality, however, the charge used for film removal was close to that corresponding to the reduction of FeOOH into Fe° (Fig. 12). This suggests that in this process, the effect of EDTA was nonexistent or neglibible. Therefore, another possibility regarding the nature of the cathodic layer has to be considered. It can be presumed that cathodic polarization of the passive film leads to the formation of porous iron in a highly active state in which it is able to react chemically with water at high *p*H, producing some compound of unknown composition, say $Fe_x(OH)_y$. During the next anodic polarization, a new passive film might grow beneath the porous layer, and processes of this kind occur alternately during each successive passivation-reduction cycle. Presumably, in the cathodic layer, $Fe_x(OH)_y$ predominates in its outer part and Fe° in its inner one, *i.e.*, in the one adjacent to the electrode. EDTA might be supposed to react with $Fe_x(OH)_y$ according to the following reaction

$$Fe_x(OH)_y + xL^{-4} \rightarrow xFeOHL^{-3} + (y - x)OH^-$$

where L is an EDTA molecule

The results presented in Fig. 7 reveal the essential role of *p*H in the passive film reduction process. Namely, at high *p*H (> 12) in the absence of EDTA, cathodic polarization leads to the formation of a porous layer which does not form at lower *p*H values. The presence of this layer was found on the surface of passivated iron after its cathodic treatment in all the studied solutions of high *p*H, irrespective of the kind of anion. In solutions of lower *p*H (8-9), as in those containing EDTA, there is no cathodic film formation at either high or low *p*H values. There is, however, a different reason for the absence of the cathodic layer in EDTA-free low *p*H solutions and in solutions of high *p*H containing EDTA. Namely, $Fe_x(OH)_y$ does not form at *p*H 8-9, but at high *p*H, EDTA removes the cathodic layer by binding $Fe_x(OH)_y$.

Conclusions

1. EDTA added to 0.05*M* NaOH has no effect on passive film formation on iron during its anodic polarization.

2. The passive film formed on iron in 0.05*M* NaOH during anodic polarization as well as at corrosion potential can be completely reduced and removed when cathodic polarization in the presence of EDTA is applied.

3. The cathodic reduction of the passive film in EDTA-free 0.05*M* NaOH (*p*H 12) leads to the formation of a porous surface layer which presumably consists of some kind of iron hydroxide, say $Fe_x(OH)_y$, and elemental iron. This layer has the following properties. It cannot be removed during cathodic polarization in either EDTA-free or EDTA containing 0.05*M* NaOH. It undergoes partial oxidation when anodic polarization is applied, and then it can be partly dissolved by cathodic polarization in the presence of EDTA. It achieves a significant thickness when periodic passivation-reduction cycles in the absence of EDTA are applied. It is porous, has no protective properties, and therefore does not influence the passive film formation. In solutions of lower *p*H (≃ 8-9), there is no porous layer formation.

4. Summing up, the course of events that probably occurs on the surface of an iron electrode during its anodic and cathodic polarization in the absence or presence of EDTA in 0.05*M* NaOH might be described as follows.

Electrolyte: 0.05M NaOH.—During the first anodic polarization, passive film formation occurs. During the first cathodic polarization, reduction of the passive film to iron and chemical interaction of the freshly formed porous iron with water molecules occur, producing $Fe_x(OH)_y$.

Successive cycles of anodic and cathodic polarization.—In anodic polarization, a new passive film grows mainly at the interface between solid metal and porous layer formed in previous cathodic treatment. In cathodic polarization, the newly formed passive film is reduced to active iron which reacts chemically with water molecules, forming $Fe_x(OH)_y$, mainly in the outer layer of the newly formed and reduced passive film. Periodic cycling between anodic and cathodic potentials results in gradually increasing thickness of the porous layer.

Electrolyte: 0.05M NaOH + EDTA.—In each of the successive cathodic and anodic polarization cycles, passive films form at anodic potentials and are reduced to Fe° at cathodic potentials. Fe° reacts chemically with water molecules, forming $Fe_x(OH)_y$, but EDTA removes the latter, producing $FeOHL^{-3}$.

5. Because EDTA assists the reduction of passive films on iron, cathodic polarization conducted potentiostatically in the presence of EDTA can provide reliable data about the charge consumed for passive film reduction.

Acknowledgment

This investigation was supported by The National Science Foundation under Contract no. DMR-8213905.

Manuscript submitted March 16, 1985; revised manuscript received July 5, 1985.

Ohio State University assisted in meeting the publication costs of this article.

REFERENCES

1. T. Zakroczymski, C-J. Fan, and Z. Szklarska-Smialowska, *This Journal*, To be published.
2. T. Zakroczymski, C-J. Fan, and Z. Szklarska-Smialowska, *ibid.*, To be published.
3. Z. Q. Huang and J. L. Ord, *This Journal*, **132,** 24 (1985).
4. EPRI Report, NP-2815 "Cleaning Steam Generators Off-Line (Soaking) with Chelants" Electric Power Research Institute, Palo Alto, CA (1983).
5. T. Yabumoto and K. Ohsawa, *Jpn. Kokai*, **75,** 45, 243.

Activation of the Iron Surface to Hydrogen Absorption Resulting from a Long Cathodic Treatment in NaOH Solution

T. Zakroczymski[1] and Z. Szklarska-Smialowska

Department of Metallurgical Engineering, The Ohio State University, Columbus, Ohio 43210

ABSTRACT

Electrochemical measurements of the permeation rate of hydrogen through pure iron cathodically polarized in 0.1*M* NaOH, together with ellipsometric and optical observations of the electrode surface, were performed. A long, uninterrupted charging caused disintegration of a subsurface metal layer and, as a result, the metal surface became more prone to both hydrogen absorption and corrosion. The permeation rate through activated iron membranes was controlled by the cathodic current density. An addition of EDTA into 0.1*M* NaOH increased the activity of the iron surface by removing from it some oxidized products of the chemical reaction of iron with water. Therefore, at the same charging current density, the hydrogen permeation rate through iron membranes was much greater in the presence than in the absence EDTA. On the contrary, a layer of palladium on the input surface impeded the entry of hydrogen.

In a previous paper by one of the authors (1), it was found that a sufficiently long (100-200h) cathodic polarization of ARMCO iron membranes in a dilute NaOH solution resulted in a surprisingly high permeability of the metal to hydrogen. Interruption of the charging current followed by its switching on caused the hydrogen permeation rate to decrease transiently, before the previous permeability was restored. It was supposed that, upon the exposure of the iron to NaOH, a barrier layer formed at the metal/electrolyte interface, hindering the entry of hydrogen into the metal bulk. This barrier could be removed by a sufficiently long, uninterrupted cathodic polarization, leading to a very high permeability level.

In another paper by the authors (2), it was shown that passive films formed on iron in NaOH and then subjected to cathodic reduction in the same electrolyte could not be completely removed. After such a treatment, some unreducible porous layer remained on the iron surface. However, in the presence of EDTA (ethylenediaminotetraacetic acid) in NaOH, the cathodic removal of the passive film on iron was complete.

Therefore, it was deemed interesting to compare the properties of the barrier layer which hindered the entry of hydrogen into iron with those of the porous layer remaining on the surface of iron after passivation followed by reduction in NaOH, and also to check if EDTA would influence the permeation rate of hydrogen through iron.

Experimental

Hydrogen permeation measurements, ellipsometry, and microscopic observations were performed. The classical electrochemical permeation technique (3) was used for permeability measurements, and the nonsteady-state diffusion method (4, 5) was used for diffusivity determination (see Appendix).

The base electrolyte was aqueous 0.1*M* NaOH. Additional experiments were conducted in the presence of ethylenediaminetetra-acetic acid (EDTA) or in that of both EDTA and As_2O_3. The test membranes, 0.001m thick, were of high purity 99.998% iron (Puratronic iron of Johnson Matthey Chemicals Limited). For all permeability measurements, the input surfaces of membranes were mechanically polished with diamond paste to a 1 μm finish. The output surface of each membrane was coated with a thin layer of Pd. Palladium electroplating was performed in aqueous solution 0.8g $PdCl_2$/liter + 60g NaOH/liter and at current densities of 200 A/m^2 during the first 30s and 100 A/m^2 during the next 270s. Some permeability measurements were taken in the presence of a Pd layer on the input surface as well. For ellipsometry, a different kind of pure iron, 99.991% Fe (product of Material Research Corporation) was used. These specimens were in the form of slices cut off from a 0.0064m diam rod; they were polished in the same way as the membranes. A manual ellipsometer, Type 436 of Rudolph Research, and a mercury light source of 546.1 nm wavelength were used. The angle of incidence was 71°. Directly measured polarizer and analyzer angles were converted into relative changes of phase (Δ) and amplitude (ψ), respectively. All experiments were carried out at 24° ± 1°C.

[1] Permanent address: The Institute of Physical Chemistry, Polish Academy of Sciences, Kasprzaka 44/52, 01-224, Warsaw, Poland.

Results

Permeability measurements.—Figure 1a shows three examples of hydrogen permeation rate (i_p) *vs.* time (t) curves obtained for iron membranes in either pure 0.1*M* NaOH solution or in that containing 0.01*M* EDTA. The entry side of one of these membranes [marked Fe(Pd)] was covered with Pd. These results were obtained during the first 200s of cathodic polarization at a current density of 90 A/m^2. As a rule, in this initial charging period, the H permeation rate was relatively small. The addition of EDTA to the electrolyte caused a substantial increase of permeability, whereas the presence of Pd on the input surface of iron had an opposite effect.

Analyses of the first build-up transients as depicted in Fig. 1a are given in Fig. 1b. Because the log ($i_p \cdot t^{1/2}$) *vs.* t^{-1} relationships were not linear, only mean values of their slopes and, consequently, mean values of the effective diffusivity of hydrogen (D) could be estimated. As in the case of permeability, EDTA increased and Pd decreased the effective diffusivity. All calculated D values were much lower than those reported in literature for the lattice diffusivity of hydrogen in pure iron at room temperature. This suggests that, during the above initial period of cathodic polarization, the permeability was controlled not by diffusion of H in the metal but by some kinetic impediments acting on the input surface. The present results differ from those found for gas phase diffusion (6, 7) in

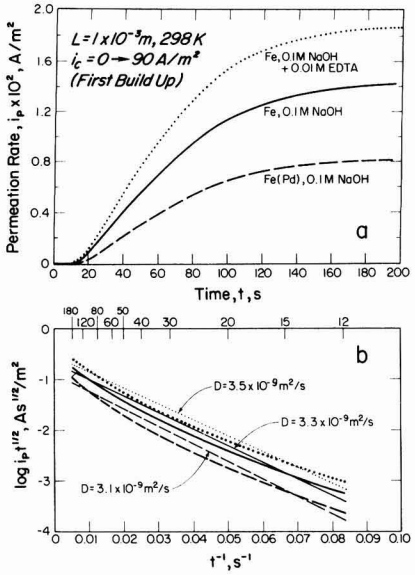


Fig. 1. Build-up transients (a) and their evaluation (b) for nonprecharged membranes. Experimental curves are marked by thick lines, dashes, and dots (compare 1a), while thin marks correspond to averaged straight lines from which the average *D* values (indicated by arrows) are calculated.

that the presence of palladium did not eliminate permeation control by surface processes.

Figure 2 shows relationships between the hydrogen permeation rate and the square root of cathodic current density for freshly prepared (*i.e.*, not precharged) membranes of the same type as in Fig. 1a, exposed to the same two solutions for 200s. From Fig. 2 it follows that permeability increased with input current density, increasing up to some 20 A/m², but did not at higher currents.

A quite different picture was obtained when the cathodic polarization was continued for 50h or more. As shown in Fig. 3, for both the nonpalladized membranes the permeability increased quite rapidly within, approximately, the 20-50h range, after which a nearly constant permeation rate was obtained; its level was much higher in the presence of than in the absence of EDTA in 0.1*M* NaOH. Here again, a Pd layer on the input side of the membrane had a significant impeding effect on H permeation. In the presence of EDTA, after about 50h of

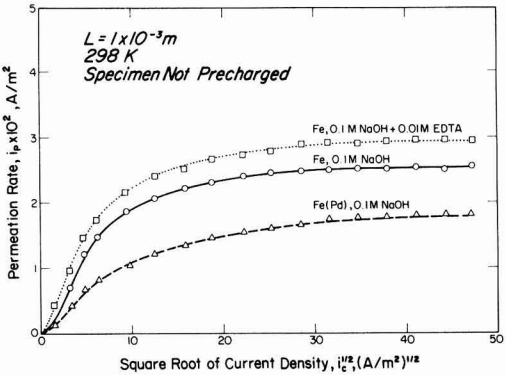


Fig. 2. Relationships between hydrogen permeation rates and the square root of cathodic current density for nonprecharged membranes at t = 200s.

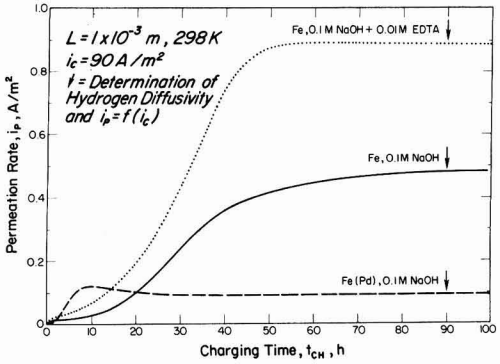


Fig. 3. Changes of hydrogen permeation rate with time

uninterrupted charging, the permeability attained an approximately constant level of 0.9 A/m², *i.e.*, about 50 times that observed after the first 200s. When As_2O_3 was added to the EDTA containing solution after the above steady-state permeability was achieved, the permeation rate still increased up to about 1.8 A/m².

After 90h of interrupted cathodic charging (at times marked in Fig. 3 by arrows), the permeation decay and build-up transients were measured by a rapid variation of the current from 90 to 30 A/m² and then back to the previous value of 90 A/m². An example of decay and build-up permeation transients is plotted in Fig. 4a and the result of their analysis in Fig. 4b. By this method, the true diffusivity of hydrogen was determined (4, 5).

There was a very good agreement between the hydrogen diffusivity values calculated from either the permeation decay or the build-up transient recorded in both EDTA-free (Fig. 4) and EDTA containing electrolyte. In the EDTA-free solution, D was a little greater (8.20×10^{-9} m²/s) than in the remaining one (7.57×10^{-9} m²/s). Both were independent of the concentration of hydrogen and close (especially D obtained in EDTA-free solution) to literature data for the lattice diffusivity of hydrogen in pure iron at room temperature (8, 9). In contrast, for membranes coated on the entry side with Pd, nonlinear rela-

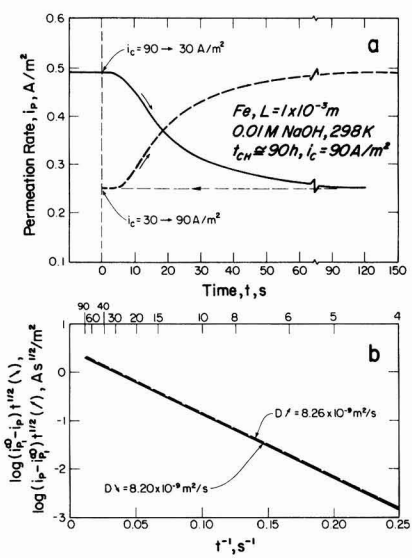


Fig. 4. Permeation decay and build-up transients (a) and their evaluation (b) for precharged iron membrane in 0.1M NaOH.

tionships (similar to those in Fig. 1b) and lower diffusivity values were obtained (~5 × 10^{-9} m^2/s).

Effects of the cathodic current density on the permeation rate of hydrogen through precharged membranes are shown in Fig. 5. In this case, the permeation rate was a linear function of the square root of cathodic current density over its whole applied range, *i.e.*, up to 2250 A/m^2. The most striking result was again obtained in the EDTA containing solution, where the permeability reached 5 A/m^2, *i.e.*, a value corresponding to $i_p \times L = 3.12 \times 10^{16}$ H at./m^2-s. (Concentration of diffusive hydrogen in the metal beneath the input side was equal to 4.87 × 10^{-5} at. H/at. Fe.) Fluxes of such a high intensity are hard to obtain in acid, poison-free solutions.

On the entry surface of membranes in which permeabilities higher than about 1 A/m^2 were obtained, blisters appeared. They were not numerous and covered only a small part of the surface. They did not detectably influence the permeability.

Ellipsometry and observations of the electrode surface.—Changes in $-\delta\Delta$ with time for iron specimens polarized cathodically in 0.1*M* NaOH at three different current densities are shown in Fig. 6, and the respective relationships between $-\delta\Delta$ and $\delta\psi$ are depicted in Fig. 7. As a rule, cathodic polarization resulted in significant changes of the ellipsometric parameters. The greater the current density applied, the larger the change in Δ and ψ.

Effects of EDTA and Pd on ellipsometric parameters are shown in Fig. 8 and 9. In the presence of EDTA, the increase of $-\Delta$ was less pronounced than that of ψ. The palladized specimen exhibited relatively small changes in both $-\Delta$ and ψ with time.

In more advanced stages of the cathodic treatment, a brownish layer appeared on the surface of all the electrodes. Depending upon the composition of the electrolyte and time, the color of that layer changed from golden or yellow-brown to almost black. Optical and scanning electron microscopic observations revealed that it had a finely dispersed porous structure. Its thickness reached several hundred nanometers.

Evolution of hydrogen bubbles at the cathode surface also changed with time. In the initial charging stage, only a few sites on the metal surface were engaged in this process. Later on, more sites became available for H_2 evolution. Finally, a multitude of very small bubbles was seen to take off rapidly from the whole metal surface. These events developed with time rather slowly and depended equally upon the presence of EDTA in the electrolyte and of Pd on the electrode; hence, they were related to the observed changes in H permeability.

Discussion

In contrast to the behavior of fresh (nonprecharged) iron membranes, where a linear dependence of hydrogen permeation on the square root of cathodic current density was held over a narrow range of low cathodic current densities (Fig. 2), for all the precharged (activated) membranes the above linear relationship was seen up to very high applied currents (2250 A/m^2, Fig. 5). This indicated that in the former case some barrier layer existed on the input surface but was absent in the later case. However, despite that same supply of hydrogen to the cathodic surface, in the three experiments referred to in Fig. 5 the hydrogen permeation rate was different, indicating differences in either the state of surface or partial pressure of the atomic hydrogen supplied.

Ellipsometry revealed the formation of some alien layer on the surface of iron treated cathodically in NaOH. After about 24h of cathodic treatment, this layer became visible to the unaided eye. The longer the cathodic polarization was, the thicker the layer was. It was supposed, therefore, that by a long cathodic polarization with simultaneous hydrogen evolution in NaOH, disintegration of a thin subsurface iron layer occurred. The disintegrated iron particles probably were highly active and, because of the high pH at the cathode, could react chemically with water molecules and produce an oxidized iron compound.

It was found previously (2) that passive films formed on iron in NaOH and then subjected to a cathodic treatment in the same electrolyte could not be completely removed because some unreducible porous layer remained on the iron surface. It was assumed that this layer consisted of some kind of iron hydroxide [$Fe_n(OH)_n$] and elemental iron.

It is believed that the nature of the porous layer formed on iron by cathodic treatment in NaOH is identical with that formed on iron by passivation and then reduction in NaOH. It can be predicted that such an oxidized layer

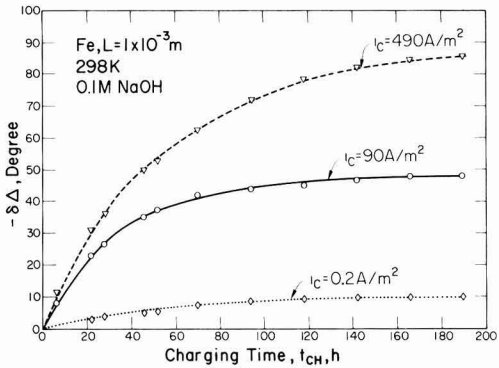


Fig. 6. Changes in $-\delta\Delta$ with time during cathodic polarization of iron in 0.1M NaOH at different current densities.

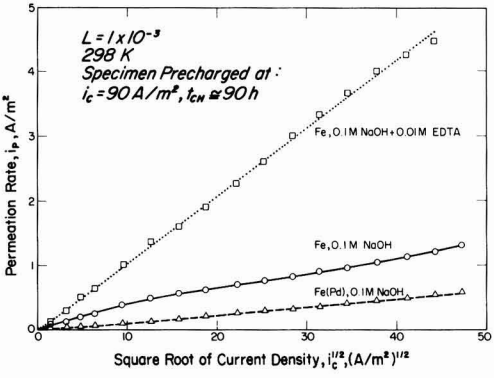


Fig. 5. Relationships between hydrogen permeation rates and the square root of cathodic current density for precharged specimens.

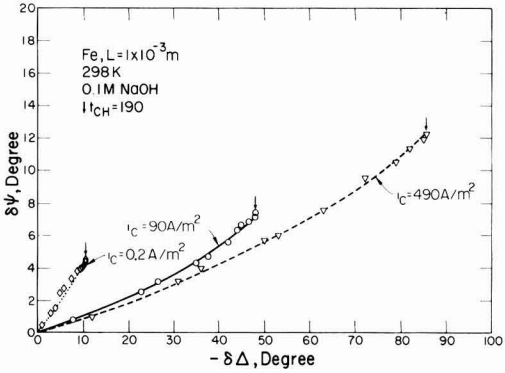


Fig. 7. Relationships between $-\delta\Delta$ and $\delta\psi$ for iron cathodically polarized in 0.1M NaOH at different current densities.

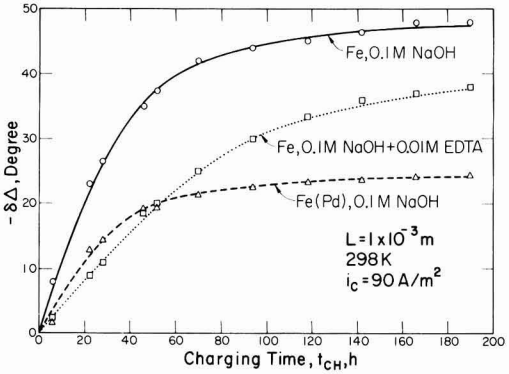


Fig. 8. Changes in $-\delta\Delta$ with time during cathodic polarization of iron in EDTA-free and EDTA containing 0.1M NaOH and of Pd-coated iron in 0.1M NaOH.

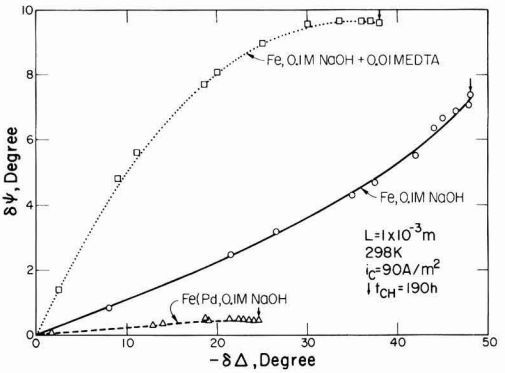


Fig. 9. Relationships between $-\delta\Delta$ and $\delta\psi$ for cathodically polarized iron in EDTA-free and EDTA containing 0.1M NaOH and for Pd-coated iron in 0.1M NaOH.

would deactivate the iron surface for the absorption of hydrogen, since the access of H atoms to the bare metal surface would be more difficult. At the same time, however, the presence in that layer of disintegrated iron particles of very high areas could make the metal surface more accessible to hydrogen. Consequently, the permeation rate of hydrogen through precharged membranes was greater than through fresh membranes.

In a previous work (2), it was also found that in the presence of EDTA in NaOH cathodic reduction of the passive film was complete, and if no prolonged cathodic treatment was applied, the iron surface was free of any alien layer. Obviously, EDTA removed $Fe_x(OH)_y$ forming soluble complexes. However, after a long cathodic treatment of iron in EDTA containing NaOH, a porous layer of iron always was present; being evidently free of any oxidized product of the chemical reaction of iron with water, it increased the surface area of the cathode. As a result, in EDTA containing NaOH, the permeation of hydrogen through precharged membranes was much faster than in EDTA-free NaOH (Fig. 3 and 5).

In the presence of Pd on the input side of membranes the hydrogen permeation rate during the first approximate 2-15h of charging was greater than that observed for uncoated Fe, but it diminished then to a much lower, approximately constant value (Fig. 3). The former event could be caused by the fact that, initially, H dissolved in Pd, forming the α phase in which the transport of hydrogen is known to be faster than in the β phase that exists at high H concentrations. Another reason for the later decrease of permeability could be the greater recombination rate of hydrogen on Pd than on Fe, resulting in a decrease of the supply of H atoms to the cathode.

The presence of a layer of Pd on the entry side of the membrane does not prevent disintegration of the subsurface iron layer. This is clearly demonstrated by ellipsometric results shown in Fig. 8, where $-\delta\Delta$ for Fe(Pd) changes with charging time in a way similar to that for unpalladized iron.

Determination of the diffusivity of hydrogen based on decay and build-up transients recorded in NaOH with and without EDTA led to correct values of the diffusion coefficient of hydrogen in iron (Fig. 4). Contrary to expectations, for membranes coated on the input side with Pd, it was impossible to obtain correct diffusivity values using the method of successive permeation transients; the D values obtained were low. Apparently, Pd coatings retarded both the desorption and absorption of hydrogen during decay and build-up transients, respectively. As is known, under cathodic charging conditions, Pd forms a hydrogen-rich beta phase, the formation and decomposition of which is relatively slow. As a result, the relaxation time necessary to establish new boundary conditions was too long to permit application of the nonstationary diffusion equations.

Conclusions

1. The absorption of hydrogen by iron during the first several hours of its cathodic polarization in 0.1M NaOH occurred relatively slowly and was controlled by the applied current only within a narrow range of low current densities.

2. A long, uninterrupted cathodic polarization of iron in NaOH solutions caused disintegration of a thin subsurface metal layer. As a result, the working surface of the cathode increased and became activated, *i.e.*, more prone to both hydrogen absorption and corrosion.

3. Over the whole range of the applied charging currents (up to 2250 A/m²), the permeation rate of hydrogen through activated iron membranes was controlled by the cathodic current density, *i.e.*, the rate of which the hydrogen atoms were supplied to the metal surface.

4. Disintegration of iron at its interface with NaOH solution led to the formation of a thin porous layer which was probably composed of disintegrated iron and of some oxidized iron compound. Because of its porosity, this layer did not hinder the absorption of hydrogen.

5. EDTA increased the activity of the iron surface by removing from it some oxidized products of its reaction with water at high pH values.

6. A layer of palladium on the input surface impeded the entry of hydrogen into iron.

7. Despite the presence of blisters on the input side of iron specimens and the very large hydrogen fluxes obtained in NaOH with EDTA, the permeation of hydrogen through iron was controlled in these experiments by lattice diffusion.

Acknowledgment

The authors are grateful for the support of this research by the National Science Foundation under contract no. DMR-8213905.

Manuscript submitted March 16, 1985; revised manuscript received July 5, 1985.

Ohio State University assisted in meeting the publication costs of this article.

APPENDIX

Principles of the Nonsteady-State Diffusion Method of Hydrogen Diffusivity Determination

In contrast with the steady-state diffusion, where the rate of hydrogen entry into a flat membrane is balanced by an equal rate of hydrogen exit from the opposite surface of the membrane, in the nonsteady state of diffusion these rates differ from one another. For materials in which the hydrogen diffusion coefficient (D) is independent of the hydrogen concentration, Fick's second law applies, and D can be precisely determined on the basis of build-up or decay permeation transients when the following initial and boundary conditions are fulfilled (4)

$$C = 0;\ 0 < x < L;\ t < 0 \qquad [A\text{-}1]$$

$$C = C_o;\ x = 0;\ t = 0 \qquad [A\text{-}2]$$

$$C = 0,\ x = L;\ t \geqslant 0 \qquad [A\text{-}3]$$

where C is the concentration of hydrogen at a chosen distance x from the entry side, C_o is the concentration of hydrogen in the first layer of metal atoms beneath the entry surface, L is the membrane thickness, and t is the time. These conditions mean the following.

1. Before charging, the whole membrane is free of hydrogen.

2. When cathodic charging begins at $t = 0$, a constant H concentration C_o corresponding to the applied current density settles immediately beneath the entry surface ($x = 0$); this is also true of any other change in the state of the cathodic current density.

3. At the exit side of the membrane (*i.e.*, at $x = L$) the concentration of hydrogen at any t is 0; this is assumed by coating the exit surface with a thin layer of palladium and maintaining it at an appropriate anodic potential at which all the oncoming hydrogen is immediately ionized.

In this work, the following equations were used to calculate the effective diffusivities of hydrogen on the basis of build-up and decay permeation transients

decay

$$\frac{i_p - i_{p_2}^{\infty}}{i_{p_1}^{\infty} - i_{p_2}^{\infty}} = 1 - \frac{2}{\sqrt{\pi\tau}}\, e^{-1/4\tau} \qquad [A\text{-}4]$$

buildup

$$\frac{i_p - i_{p_1}^{\infty}}{i_{p_2}^{\infty} - i_{p_1}^{\infty}} = \frac{2}{\sqrt{\pi\tau}}\, e^{-1/4\tau} \qquad [A\text{-}5]$$

where $i_{p_1}^{\infty}$ is the initial steady-state permeation rate settled at a chosen cathodic current density $i_{c_1}(t < 0)$, $i_{p_2}^{\infty}$ is the final permeation rate settled at i_{c_2} ($t = \infty$), i_p is the actual permeation rate at a chosen time $t > 0$, and τ is a dimensionless parameter equal to Dt/L^2.

Equations [A-4] and [A-5] can be converted into more convenient forms

decay

$$\log (i_{p_1}^{\infty} - i_p)\sqrt{t} = \log \frac{2\mathbf{F}\sqrt{D}\,(C_1 - C_2)}{\sqrt{\pi}} - \frac{L^2 \log e}{4D} \cdot \frac{1}{t} \qquad [A\text{-}6]$$

buildup

$$\log (i_p - i_{p_1}^{\infty})\sqrt{t} = \log \frac{2\mathbf{F}\sqrt{D}\,(C_2 - C_1)}{\sqrt{\pi}} - \frac{L^2 \log e}{4D} \cdot \frac{1}{t} \qquad [A\text{-}7]$$

where C_1 and C_2 are hydrogen concentrations in the metal directly beneath the entry surface, corresponding to i_{c_1} and i_{c_2}, respectively, and $\mathbf{F}$ is Faraday's constant. The slopes of linear relationships, $\log (i_{p_1}^{\infty} - i_p)\sqrt{t}$ *vs.* $1/t$, and $\log (i_p - i_{p_1}^{\infty})\sqrt{t}$ *vs.* $1/t$, permits calculation of $D\downarrow$ and $D\uparrow$ values for decay and buildup, respectively. The linearity of these relationships, symmetry of build-up and decay transients, and equality $D\downarrow = D\uparrow$ all indicate that the permeation of hydrogen is controlled by diffusion and that the boundary conditions for nonsteady-state of diffusion are strictly fulfilled. Nonlinearity, asymmetry, or difference between $D\downarrow$ and $D\uparrow$ indicate that the permeation rate is controlled by some other events, most probably by either trapping or kinetic impediments on the entry surface, or jointly by both these events. However, the trapping of hydrogen in iron is a fast process which usually (especially for a thin membrane) ceases within several minutes after a constant cathodic current is applied, *i.e.*, when all traps present in the volume of the membrane are filled with hydrogen to a content related to the input fugacity of the external hydrogen source. Therefore, when deviations from linearity, symmetry, or equality continue for hours under constant charging conditions, evidence is given that the permeation is affected by some spurious surface effects.

REFERENCES

1. T. Zakroczymski, *Scrip. Metall.*, **19,** 521 (1985).
2. Z. Szklarska-Smialowska, T. Zakroczymski, and C.-J. Fan, *This Journal*, **132,** 2543 (1985).
3. M. A. V. Devanathan and Z. Stachurski, *Proc. R. Soc. London, Ser. A*, **270,** 90 (1962).
4. J. McBreen, L. Nanis, and W. Beck, *This Journal*, **113,** 1218 (1966).
5. T. Zakroczymski, *Corrosion (Houston)*, To be published (1985).
6. A. J. Kumnick and H. H. Johnson, *Met. Trans. A*, **6,** 1087 (1975).
7. G. M. Pressouyre, Ph.D. Thesis, Carnegie-Mellon University, Pittsburgh, PA (1977); also cited in "Advanced Techniques for Characterizing Hydrogen in Metals," p. 89, TMS-AIME, Warrendale, PA (1982).
8. H. G. Nelson and J. E. Stein, NASA Report TND-7265, NASA, Ames Research Center, Moffett Field, CA (1973).
9. N. R. Quick and H. H. Johnson, *Acta Metall.*, **26,** 903 (1978).

Formation and Breakdown of Passive Oxide Films on Nickel in Halide Solutions

B. MacDougall* and M. J. Graham

Division of Chemistry, National Research Council of Canada, Ottawa, Ontario, Canada K1A 0R9

ABSTRACT

The influence of Cl^-, Br^-, and F^- on the passivation of nickel in pH 3.0, 0.15*N* Na_2SO_4 has been studied. The presence of Cl^- and Br^- only temporarily delays the establishment of passivity; in contrast, F^- has little short-term (< 1s) influence, but a considerable long-term effect with the anodic current falling to only ~ 1 mA-cm^{-2}. To study the influence of the different halide ions, passive oxide films were formed on nickel in pH 3.0 Na_2SO_4, and then subjected to potentiostatic polarization in 0.08*M* Cl^-, Br^-, or F^- solutions. In Cl^- and Br^- solutions, the anodic current remains very low but increases abruptly with pit initiation. The breakdown results in F^- solution are completely different, with the measured anodic current increasing gradually with time of polarization; the rate of current increase is at first very low, but then increases with time and eventually slows as passivity breakdown approaches completion. While the kinetics of passivity breakdown depend on both the prior passivation treatment and the conditions existing in the F^- solution, the results generally give S-shaped curves, suggesting that the breakdown process is one of nucleation and lateral growth of "holes" in the passive oxide film. This mechanism of film breakdown in F^- is confirmed by replica electron microscopy of the surface at various stages in the breakdown process, with local attack initiating at selected sites and then gradually spreading over the entire surface. The difference in behavior between F^- and Cl^- and Br^- is discussed in terms of the adsorption characteristics of the ions.

Metals and alloys such as nickel, iron, and the stainless steels have the ability to form thin, passive oxide films which are susceptible to either general or local breakdown in the presence of aggressive halide ions. The exact role of these anions, and therefore the fundamental mechanism of passivity breakdown, is still under discussion with various theories proposed to explain the influence of Cl^- and Br^- on pit initiation (1-12). It has been argued that these ions can rupture or break the passive oxide film (12, 13), *e.g.*, by adsorption on the surface, so that underlying metal is exposed to the aggressive environment at potentials high enough to cause pitting. Another suggested mechanism involves direct incorporation of the halide ion into the oxide film with a subsequent increase in pitting susceptibility. The halide ion may, however, initiate passivity breakdown by simply interfering with local film repair, *i.e.*, the oxide may experience continual local breakdown-repair events and the halide ion merely influences the efficiency of local repassivation.

Unlike the highly localized attack observed with Cl^- and Br^- ions, F^- ion has been found to cause an overall breakdown of passivity and general metal dissolution (14-17). At present, however, neither the kinetics and mechanism of F^--induced passivity breakdown nor the influence of F^- on the formation and development of an oxide film are well known. In this work, the influence of F^- on both the establishment and breakdown of passivity is studied. With regard to the latter, a variety of passive oxide films are formed in non-F^- solutions and then exposed to F^- containing solutions for breakdown of the previously established passivity. In this way, the influence of both prior passivation treatment and conditions in the aggressive F^- solution on the breakdown of passivity is studied. Replica electron microscopy has been used to follow the initiation and propagation of passivity breakdown. The results are analyzed in terms of the nucleation and lateral growth of holes at breakdown sites in the passive oxide film. The behavior of F^- as an aggressive anion is contrasted with that of Cl^- and Br^-.

Experimental

Polycrystalline nickel specimens and Ni(111) single crystals were prepared as described previously (18). Potentials are referred to the saturated calomel electrode, Hg/Hg_2Cl_2. Experiments were conducted at 25°C in deaerated pH 3.0 solutions of 0.15*N* Na_2SO_4 either with or without added NaF, NaCl, and NaBr. To determine the influence of the various anions on the establishment of passivity, electropolished nickel electrodes were cathodically reduced at 20 μA-cm^{-2} for 5 min (to obtain oxide-free starting surfaces), and the potential was then stepped to a value in the passive region. The resulting current-time transients were obtained on a high speed Brush recorder (risetime < 8 ms) and integration gave the passivation charge. Nickel electrodes were also passivated in F^--free solutions and then transferred through the air to deaerated 0.08 or 0.01*M* F^- solution for passivity breakdown. Results from previous work indicate that such air exposure has no influence on the state of the passive oxide film (19). To determine the extent and type of passivity breakdown in the presence of F^-, the surface of a passivated (111) single crystal was examined by replica electron microscopy after treatment in F^- solution.

* Electrochemical Society Active Member.

Results and Discussion

Influence of halide ions on anodic passivation.—Figure 1 shows the influence of 0.08*M* concentrations of the various halide ions on the *i-t* profile upon stepping the potential into the passive region. Cl^- and Br^- ions substantially increase the short-term anodic charge passed in establishing passivity, indicating that they interfere with the passivation process; the extent of interference is greater for Cl^- than for Br^- (Fig. 1 and Table I). In contrast, F^- ion appears to have little influence on the initial stages of passivation, the *i-t* profile during the first 0.5s being similar to that obtained in its absence. The results are consistent with the expected strong interaction of Cl^- and Br^- ions with the nickel surface, an interaction which should block at least part of the surface for oxide formation. However, the apparently stronger interaction of Cl^- than Br^- is not in agreement with predicted strengths of adsorption of these ions (20-23). The anticipated weak interaction of F^- ion should cause little interference with passivation, as observed.

Although the Cl^- and Br^- ions strongly interfere with the initial surface oxidation (Fig. 1), passivity eventually

Table I. Anodic charge passed during the first 1s after stepping the potential to 0.2V in pH 3.0 Na_2SO_4 solution containing no halide and 0.08M of the various halide ions. Electrode pretreatment was electropolishing and cathodic reduction at 20 μA-cm^{-2} prior to the potential step

Halide ion present	Anodic charge (mC-cm^{-2})	Percentage of background charge
—	2.8	100
F^-	3.5	130
Cl^-	18.3	670
Br^-	8.8	320

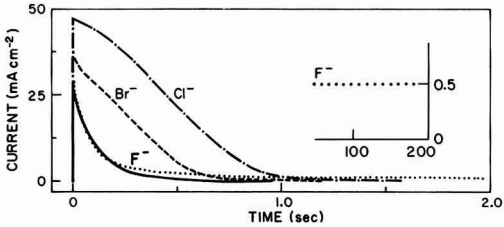


Fig. 1. Current-time transients, obtained on oxide-free nickel in pH 3.0 Na_2SO_4, upon stepping the potential to 0.2V (solid line). Also shown are transients in solutions with 0.08M Cl^- (dot-dash line), Br^- (dashed line), and F^- (dotted line). The inset indicates the steady current of 0.5 mA-cm^{-2} observed after 200s at 0.2V in 0.08M F^-.

occurs and the anodic currents fall to very low values. Indeed, the currents measured 60s after the potential step are only *ca.* 10-15% higher than in the absence of halide ions. The behavior with F^- is completely different in that the current stops falling a few seconds after the potential step and reaches a steady value of ~0.5 mA-cm^{-2} (Fig. 1, inset). Such a high anodic current indicates that passivity has not developed beyond the most elementary stages which is in sharp contrast to the initial (< 0.5s) lack of influence of F^- on passivation. This result could be due to F^- either (*i*) influencing the nature of the passive film and therefore its stability toward dissolution or (*ii*) increasing the aggressiveness of the solution. Whatever the reason, it is clear that normal passivity cannot be achieved for nickel in a pH 3.0 Na_2SO_4 solution containing 0.08*M* F^-.

Galvanostatic charging of nickel in halide ion solutions.—Figure 2 shows a series of galvanostatic charging profiles for electropolished nickel at 4 μA-cm^{-2} in pH 3.0 Na_2SO_4 solutions with different halide ions present. In the absence of halide ion, the potential increases from the immersion value of −0.04V to the oxygen evolution region at 0.96V with no indication of film breakdown or pitting (24). In the presence of 0.08*M* Br^- or Cl^-, the galvanostatic charging curve is the same as in halide-free solution until the potential is high enough for pitting to occur. This is manifested as a sharp reversal of the potential as the passive oxide film locally breaks down; rapid metal dissolution at the breakdown sites results in the observed anodic depolarization. Thus, neither Cl^- nor Br^- has any apparent influence on the galvanostatic development of the passive oxide film until pitting begins at the higher anodic potentials. This is certainly not the case with F^-, where passivity breakdown begins as soon as the electrode is immersed at 4 μA-cm^{-2} and continues until passivity has completely broken down a short time later. Galvanostatic charging in F^- gives rise not to pitting but rather to an overall loss of passivity with corresponding general metal dissolution, which is again in contrast to the localized attack by Cl^- and Br^-.

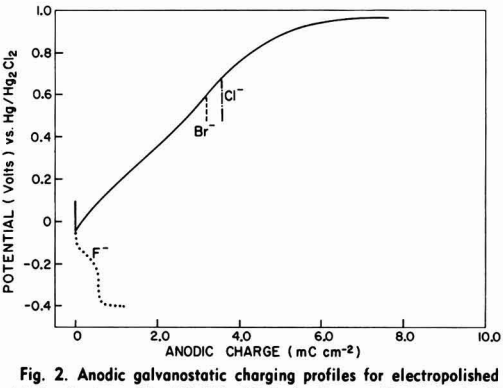


Fig. 2. Anodic galvanostatic charging profiles for electropolished nickel at 4 μA-cm^{-2} in pH 3.0 Na_2SO_4 in the absence of halide ion (solid line), and in solutions containing 0.08M Cl^- (dot-dash line), Br^- (dashed line), and F^- (dotted line).

Potentiostatic breakdown of passivity in F^- solutions.—It is well known that, when prepassivated nickel is exposed to a Cl^- or Br^- solution above the pitting potential, the measured anodic current remains almost constant but then abruptly increases when pit initiation occurs [see, *e.g.*, Ref. (25)]. The time required for the sharp current increase, referred to as the induction time (τ_{ind}) for pit initiation, varies exponentially with the potential of the pitting experiment. In the present work, similar experiments were performed in the presence of F^- both to compare the results with those obtained in Cl^- and Br^- and to understand the nature of passivity breakdown in F^-.

Figure 3 shows the current response for a film preformed in pH 3.0 Na_2SO_4 at 0.6V for 1h and then polarized at 0.2V in 0.08*M* F^-. The current is initially quite low (< 0.1 μA-cm^{-2}) but after ~ 5 min it begins to increase, at first slowly but then more rapidly. The rate of change of current increases with time during about the first 18 min, but then begins to decrease and a steady state is eventually reached after ~ 23 min. During this time, the current increases by over four orders of magnitude indicating a massive breakdown of passivity. The eventual constant current is actually somewhat higher than that obtained when electropolished and cathodically reduced nickel is polarized at 0.2V in the F^- solution (Fig. 1); this is probably due to the increased surface roughness associated with breakdown in F^- (see below, especially Fig. 7). The results thus suggest that complete breakdown of passivity occurs in F^- after a certain time of exposure. The breakdown results shown in Fig. 3 are reproducible from experiment to experiment to within ±2%. This high degree of reproducibility means that the increase of anodic current can be used to carefully study the kinetics of passivity breakdown in F^- as a function of condition of formation of the prior passive film as well as the conditions in the breakdown solution.

If the current, *i*, at any time, *t*, in F^- solution is a measure of the extent of passivity breakdown, then the ratio $\alpha = (i_{max} - i)/i_{max}$ is the fraction of the surface still covered by the passive film. The term $(1 - \alpha)$ is therefore a measure of the extent of passivity breakdown; $[(1 - \alpha) = i/i_{max}]$. When the results from Fig. 3 are plotted in the form of $(1 - \alpha)$ *vs.* *t*, an S-shaped curve is obtained (Fig. 4). Passivity breakdown is initially slow and then accelerates, eventually slowing again towards the end of breakdown.

Influence of electrode pretreatment on F^--induced film breakdown.—To investigate the influence of state of pas-

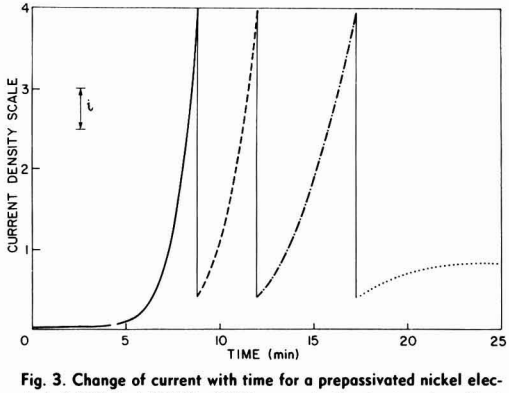


Fig. 3. Change of current with time for a prepassivated nickel electrode in 0.08M F^- (pH 3.0) at 0.2V; prepassivation treatment was 1h at 0.6V in pH 3.0 Na_2SO_4. The current marker, i, represents 0.5 μA-cm^{-2} (solid line), 5.0 μA-cm^{-2} (dashed line), 50 μA-cm^{-2} (dot-dash line), and 500 μA-cm^{-2} (dotted line).

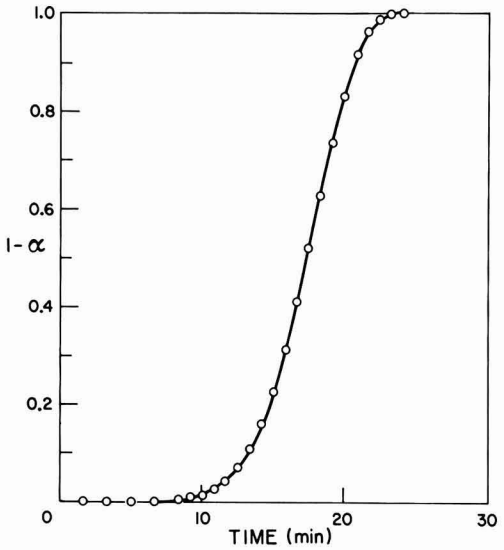


Fig. 4. Results of Fig. 3 plotted in terms of $(1 - \alpha)$ vs. time where $\alpha = (i_{max} - i)/i_{max}$.

sivity on the rate of film breakdown in F^-, $(1 - \alpha)$ *vs.* t profiles were obtained for electropolished nickel (EP Ni) and nickel prepassivated in pH 3.0 Na_2SO_4 at 0.6V for 3 min and 16h and at 0.2V for 1h. The results, shown in Fig. 5, indicate that the rate of passivity breakdown at 0.2V in 0.08*M* F^- is highly dependent on the prior state of the film. Both the potential and time of anodization have a major influence on the stability of the film toward F^--induced breakdown. Either a higher passivation potential or a longer passivation time gives an increase in the induction time before measurable breakdown occurs as well as a slower rate of activation after breakdown has begun. The order of resistance of these films toward attack by F^- is the same as that previously observed for open-circuit breakdown in slightly acid sulfate solutions (26), with the film on EP Ni being the least stable. In that previous work, an increase in the open-circuit film stability was shown to be associated with a decrease in the density of film defects rather than any change in film thickness.

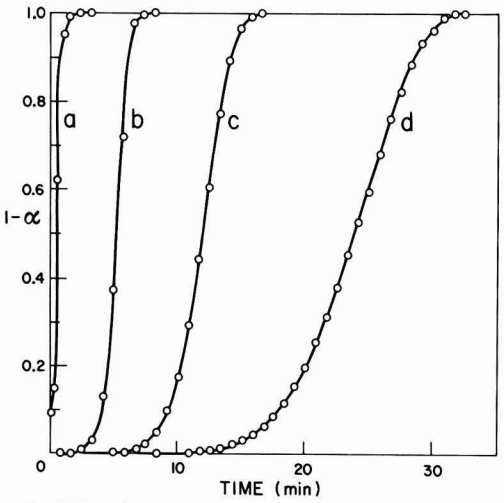


Fig. 5. $(1 - \alpha)$ vs. time profiles for different oxide films formed in pH 3.0 Na_2SO_4 and broken down at 0.2V in 0.08M F^- (pH 3.0). Prepassivation treatments are: electropolishing (a); 1h at 0.2V (b); 3 min at 0.6V (c); and 16h at 0.6V (d).

Influence of breakdown conditions in F^- solutions.—Figure 6 shows the influence of potential of breakdown in F^- solution on the $(1 - \alpha)$ *vs.* t profile for a standard passive film, *i.e.*, one formed at 0.6V for 1h in pH 3.0 Na_2SO_4. The film breakdown kinetics are highly dependent on the applied potential in the F^- solution, the rate of passivity breakdown increasing dramatically with increasing anodic potential (*cf.* profiles a and b). Both the induction time and the rate of subsequent breakdown are strongly influenced by the breakdown potential. The kinetics of passivity breakdown are also dependent on the $[F^-]$ in solution, the breakdown time being much longer in 0.01*M* F^- solution in comparison to 0.08*M* F^-, all other conditions being constant (*cf.* profiles c and a). The lower $[F^-]$ more than compensates for a high potential, so that breakdown is slower than at 0.1V in 0.08*M* F^- solution (*cf.* profiles c and b). These results indicate that by a proper selection of the conditions in F^- solution, breakdown of even the most defective oxide films (*e.g.*, the film on EP Ni) can be studied in detail.

Mechanism of passivity breakdown in F^- solutions.—While the above results demonstrate which parameters influence passivity breakdown in F^-, questions remain concerning the breakdown mechanism. The most probable modes of attack by F^- are either general layer-by-layer thinning of the oxide film with time (27) or local attack at specific sites with a gradual spreading of this attack across the surface. To distinguish between these two possibilities, replica electron micrographs of a Ni (111) surface were obtained at various times during breakdown in F^-. The Ni (111) electrode was prepassivated at 0.6V for 1h and then transferred to a 0.08*M* F^- solution for breakdown at 0.2V. The $(1 - \alpha)$ *vs.* t. profile is very similar to that shown in Fig. 4 for a polycrystalline electrode, *i.e.*, an intital induction period is followed by a rapid increase in $(1 - \alpha)$ with an eventual slowing down as a steady state is approached. The micrograhs associated with three extents of breakdown, having $(1 - \alpha)$ values of 0.5, 10, and 99%, are shown in Fig. 7a, 7b, and 7c. It is apparent that the F^- attack begins at a few specific points on the surface (Fig. 7a) and that both the number of attack sites and their radii increase as the attack progresses (Fig. 7b). Eventually, the attack spreads over most of the surface as new sites of attack appear and the existing sites spread laterally (Fig. 7c); by this time, close to complete passivity breakdown has occurred. This form of attack is in sharp contrast to that observed when electropolished and cathodically reduced nickel is polarized at 0.2V in 0.08*M* F^- solution (Fig. 7d). In this case, there is no evidence of local attack since there was no passive oxide film to break down. A general attack is observed with uniform roughening of the metal surface. Similar surface features are observed after F^- breakdown of the oxide film on EP Ni. Since dissolution of this highly defective oxide is very rapid (Fig. 5a), there is little time for localized attack to develop. The almost immedi-

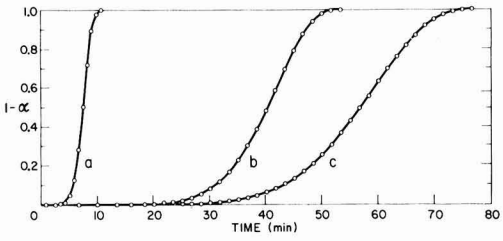


Fig. 6. $(1 - \alpha)$ vs. time profiles for an oxide film formed at 0.6V for 1h in pH 3.0 Na_2SO_4 and broken down under different conditions in pH 3.0 F^- solution. Breakdown conditions are: 0.4V in 0.08M F^- (a); 0.1V in 0.08M F^- (b); and 0.4V in 0.01M F^- (c).

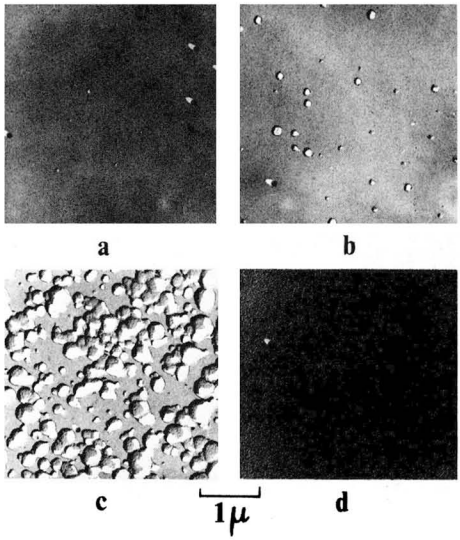


Fig. 7. Replica electron micrographs of a Ni(111) single crystal prepassivated at 0.6V for 1h in pH 3.0 Na_2SO_4 and then exposed to 0.08M F^- (pH 3.0) at 0.2V for times required to give $(1 - \alpha)$ values of 0.5% (a), 10% (b), and 99% (c). d: The micrograph obtained after electropolishing, cathodic reduction, and passivation at 0.2V in 0.08M F^-. Shadowed spheres are 900Å polystyrene balls.

ate disappearance of the oxide film thus gives rise to the same general dissolution features observed in the absence of an oxide film.

The results presented for the breakdown of passivity in F^- suggest that the process is one of nucleation and lateral growth, *i.e.*, local breakdown of the oxide film is nucleated, perhaps at defect sites in the film, and the attack then spreads laterally across the surface. The mechanism is akin to that discussed in detail by Evans (28) for nucleation and growth of new phases (with the generation of S-shaped kinetics) and analogous to the more recent computer modeling work of Kozlowska *et al.* (29) for the cathodic removal of thin oxide films on platinum. In this later work, initial oxide removal was considered to be the result of a nucleation process at specific sites on the surface giving rise to "lakes" or "holes" in the film. Continued cathodic reduction occurred at the periphery of the established holes, and the rate of reduction increased with the extent of reduction until the holes began to overlap. The potential had a strong influence on the reduction rate since it determined the density of sites where holes would be nucleated. In the present work, local breakdown of the passive NiO film in F^- solution results in its replacement by a poorly passivating film characteristic of the particular potential. The resulting local high rates of metal dissolution give rise to the local surface attack which is seen by electron microscopy. The rate of passivity breakdown will be determined by both the density of breakdown sites and their rate of radial growth. The dependence of the breakdown rate on the prior passivation treatment is easy to understand since this prior treatment determines the defect density of the oxide film and therefore the number of sites susceptible to breakdown. The increase in breakdown rate at higher potentials in F^- could be due to an increase in the number of film defects at which breakdown is nucleated as well as to a change in the lateral growth rate of developing holes. Electron microscopy indicates that the nucleation is progressive, as opposed to instantaneous, since the number of breakdown sites increases with time (Fig. 7). This local breakdown of oxide by expanding holes and newly appearing nuclei eventually results in complete removal of the passive film with subsequent general metal dissolution. At that point, the passive oxide has been replaced by a poorly inhibiting film.

The precise mechanism by which F^- locally breaks down passivity and destroys the film is still open to question. It is known that F^- forms stable complexes with transition metal cations (rather than metal atoms) so it has more effect on the metal oxide film than on the metal itself (30-33). This fact may explain the different behavior of F^- *vs.* Cl^- and Br^- (Fig. 1 and 2). There is a suggestion in the literature that F^- forms a surface complex with passive oxide films on nickel and iron which enhances the rate of cation transfer from the oxide lattice into solution (14, 15). However, it may be that F^- in solution does not directly influence the initial breakdown of the passive oxide film at all but simply influences local repair after breakdown has occurred. Breakdown occurs even in the absence of F^-, and its extent is determined by the state of perfection of the film and the aggressiveness (pH) of the solution.

Whatever the precise mechanism of F^--induced breakdown of passivity, the present results clearly show that the attack is initially localized at a few sites on the surface. With long exposure to F^- solution, the eventual general breakdown of passivity is a result of the spreading of this local attack, as well as attack occurring at new sites. There appears to be a direct correlation between the defect state of the oxide film and its resistance to breakdown in F^-, the defects in the film likely being the sites of attack by F^-. While F^- is quite different from Cl^- and Br^- in terms of its ability to eventually cause a general breakdown of passivity, it appears that breakdown is initiated in much the same way as by Cl^- and Br^-, *viz.*, by a highly localized attack at a few specific sites on the surface.

Mansucript submitted Feb. 27, 1985, revised manuscript received *ca.* July 8, 1985.

The National Research Council of Canada assisted in meeting the publication costs of this article.

REFERENCES

1. Z. Szklarska-Smialowska, *Corrosion (Houston)*, **27,** 223 (1971).
2. T. P. Hoar and W. R. Jacobs, *Nature (London)*, **216,** 1299 (1967).
3. T. P. Hoar, D. C. Mears, and G. P. Rothwell, *Corros. Sci.*, **5,** 279 (1965).
4. C. L. McBee and J. Kruger, in Proceedings of U. R. Evans International Conference on Localized Corrosion, 1971," p. 252, NACE, Houston (1974).
5. J. R. Galvele, *This Journal*, **123,** 464 (1976).
6. H. H. Strehblow and B. Titze, *Corros. Sci.*, **17,** 461 (1977).
7. B. MacDougall, *This Journal*, **126,** 919 (1979).
8. N. Sato, *Electrochim. Acta*, **16,** 1683 (1971).
9. M. Janik-Czachor, *Werkst. Korros.*, **30,** 255 (1979).
10. K. E. Heusler and L. Fischer, *ibid.*, **27,** 551 (1976); *ibid.*, **27,** 697 (1976).
11. M. Janik-Czachor, *This Journal*, **128,** 513C (1981).
12. H. H. Strehblow, *Werkst. Korros.*, **27,** 792 (1976).
13. T. P. Hoar, *Corros. Sci.*, **7,** 341 (1976).
14. H. H. Strehblow, B. Titze, and B. P. Lochel, *ibid.*, **19,** 1047 (1979).
15. H. H. Streblow and B. P. Lochel, in "Proceedings of the Fifth International Symposium on Passivity," Bombannes, France, M. Froment, Editor, p. 379, Elsevier, Amsterdam (1983).
16. A. Cakir and J. C. Scully, in "Passivity of Metals," R. P. Frankenthal and J. Kruger, Editors, p. 385, The Electrochemcials Society Corrosion Monographs Series, Princeton, NJ (1978).
17. B. MacDougall, in "Proceedings of the Ninth International Congress on Metallic Corrosion," Toronto, Ont., Canada, Vol. 2, p. 168, National Research Council of Canada, Ottawa, Ont., Canada (1984).
18. B. MacDougall and M. Cohen, *This Journal*, **121,** 1152 (1974).
19. B. MacDougall and M. Cohen, *ibid.*, **123,** 191 (1976).
20. M. W. Breiter, *Electrochim. Acta*, **8,** 925 (1963).
21. M. Jesionek and Z. Szklarska-Smialowska, *Corros. Sci.*, **23,** 183 (1983).

22. W. Paik, M. A. Genshaw, and J. O'M Bockris, *J. Phys. Chem.*, **74**, 4266 (1970).
23. Y-C. Chiu and M. A. Genshaw, *ibid.*, **73**, 3571 (1969).
24. B. MacDougall and M. J. Graham, *Electrochim. Acta*, **27**, 1093 (1982).
25. B. MacDougall, in "Proceedings of the Fifth International Symposium on Passivity," Bombannes, France, M. Froment, Editor, p. 275, Elsevier, Amsterdam (1983).
26. B. MacDougall and M. Cohen, *This Journal*, **124**, 1185 (1977).
27. J. J. Kelly, *Electrochim. Acta*, **24**, 1273 (1979).
28. U. R. Evans, *Trans. Faraday Soc.*, **41**, 365 (1945).
29. H. Angerstein-Kozlowska, B. E. Conway, and J. Klinger, *J. Electroanal. Chem.*, **87**, 301, 320 (1978).
30. C. C. Seastrom, *Corrosion*, **20**, 179t (1964).
31. K. Azuma and H. Kametari, *Trans. Metall. Soc. AIME*, **230**, 835 (1964).
32. M. J. Pryor and U. R. Evans, *J. Chem. Soc.*, **71**, 3330 (1949).
33. S. Ahrland, J. Chatt, and N. R. Davies, *Quart. Rev.*, **12**, 265 (1958).

Polarization and Corrosion of Electrogalvanized Steel—Evaluation of Zinc Coatings Obtained from Waste-Derived Zinc Electrolytes

M. Dattilo

U.S. Department of the Interior, Bureau of Mines, Rolla Research Center, Rolla, Missouri 65401

ABSTRACT

The corrosion of electrogalvanized 1070 steel wire has been investigated in molar quiescent ammonium chloride and ammonium sulfate under near-neutral conditions. Zinc coatings obtained from waste-derived electrolytes were evaluated *vs.* coatings from relatively pure zinc electrolytes. The waste source of zinc was brass smelter flue dust. Corrosion rates were measured by Tafel line extrapolation and the polarization resistance technique. Values of the Tafel slopes and the corrosion currents were also compared with those for pure zinc (99.999%). Corrosion rates were found to be affected by the medium employed, pH, and bimetal diameter reduction (drawing). Drawn electrogalvanized steel displays higher values of the Tafel slopes than do the as-plated samples. The Tafel slopes are different from those obtained on pure zinc. This is assumed to be due to inhomogeneous surface features obtained from additive adsorption (during plating) and residual lubricants used in the drawing process as well as surface structure. The corrosion rates of electrogalvanized samples plated in the waste-derived zinc electrolytes were similar to the corrosion rates of samples plated in relatively pure zinc electrolytes. Therefore, wastes are a potential source of zinc for electrogalvanizing.

Large quantities of zinc bearing waste materials exist; therefore, the Bureau of Mines is investigating processes that can benefit from using this resource. Previous Bureau work has shown that zinc coatings obtained in waste-derived electrolytes are comparable to coatings from relatively pure electrolytes when evaluated in salt spray tests (1). Most uses for zinc require high purity material; and since wastes normally contain other metals which coextract with zinc, they are less suitable for the production of primary cathode zinc. Zinc electrowinning is accomplished in pure electrolytes. Cathode current densities for this process range from 20 to 100 mA/cm^2, and the plating times from 18 to 48h. This allows buildup of impurity levels that lower cell efficiency as well as cathode purity. Removal of these impurities involves several process steps (2-3) requiring greater cost to the producer. In electrogalvanizing, however, high current densities (200-600 mA/cm^2) and short plating times (minutes) are employed, thus allowing higher impurity levels in the plating electrolyte (4-5).

Electrogalvanizing is accomplished in a continuous process. The steel substrate is cleaned, plated, and subjected to multiple diameter reductions (drawing) in the case of wire products. This working of the metal surface causes a change in its structure and corrosion properties. It also allows better adherence of materials such as rubber or polymer for structural applications.

There is a considerable amount of reported data on zinc corrosion in acid, alkaline, neutral, and near-neutral media (6-13), and corrosion rates are highly influenced by the medium employed. Normally, electrogalvanized steel is evaluated in aerated NaCl; however, it has been shown that the corrosion rates measured electrochemically are in error because of two competing cathodic reactions and corrosion products on the surface. Deaerated ammonium salt solutions appeared to be an excellent choice for a corrosion medium because of reproducible electrochemical measurements and suppression of oxide film formation (11).

This report deals with the corrosion of electrogalvanized steel obtained by plating in a brass dust-derived zinc electrolyte. Evaluation of these coatings was necessary *vs.* coatings obtained from industrial-type electrolytes to determine if wastes are viable sources of zinc for electrogalvanizing.

Experimental

Electrolytes and plating.—Synthetic zinc electrolytes were prepared by dissolving French process zinc oxide (prepared from zinc metal) in reagent-grade sulfuric acid. Reagent-grade NH_4Cl and H_3BO_3 were added as desired for conductivity and buffering. Waste electrolytes were obtained by extraction of brass smelter flue dust (64.6% zinc) with 180 g/liter sulfuric acid. This yielded an impure electrolyte containing ~120 g/liter zinc and ~1 g/liter copper. Copper was removed by addition of 2 g/liter zinc dust at 75°C for 30 min. A thorough account of this procedure has been given in a previous report (1). Compositions of the electrolytes are shown in Tables I and II along with the additions.

Steel wire 1070 (0.234 cm diam) was prepared for plating by first degreasing with trichloroethylene and then electrocleaning in 600 g/liter H_2SO_4 using a current density of 400 mA/cm^2 (1). Wires were then rinsed and plated at constant cathode current density of 600 mA/cm^2 for 30s at 40° and 60°C over a pH range of 2-5. The wire was rotated during plating at 105 rpm. The anode in the plating cell was a 99.999% zinc rod so as to maintain constant zinc concentration. Cathode area was 7 cm^2, and the anode area was > 10 cm^2 in all cases.

Drawing.—Bimetal drawing was accomplished on wire plated as above. The samples were ~10 cm long and were

Table I. Synthetic zinc electrolyte compositions (g/liter)

Electrolyte	Zn	NH_4Cl	H_3BO_3	Licorice
P-1	120-145	18	12	0.3
P-2	120-145	18	12	0
P-3	120-145	18	12	0.1
P-4	120-145	18	12	0.5

Table II. Waste zinc electrolyte compositions (g/liter)

Electrolyte	Zn	Cd	Cl	Cu	Ni	NH_4Cl	H_3BO_3	Licorice
W-1	120-130	0.002	2.1	0.003	0.003	18	12	—
W-2	120-130	0.01	1.11	< 0.001	0.002	18	12	—
W-3	120-130	0.002	2.1	0.003	0.003	18	12	0.1

drawn through a hard die to reduce the diameter ~10% in the first pass. (Samples drawn twice were reduced 20% on the second pass.) Industrial dies and lubricant were used. The dies used were 6° conical type.

Corrosion media.—The electrolytes for this corrosion study were 1*M* NH_4Cl and 1*M* $(NH_4)_2SO_4$. Analytical reagent-grade salts were dissolved in distilled water. The *p*H was adjusted to 6 ± 0.1, except in specific experiments, by small additions of NH_4OH, H_2SO_4, or HCl. Prior to immersion of samples, the solutions were deaerated with oxygen-free nitrogen. Polarization measurements were performed at 25° ± 2°C.

Solutions were analyzed by atomic absorption for zinc content during weight loss tests.

Sample preparation.—Samples were prepared by degreasing in boiling trichlorethylene followed by rinsing with absolute ethanol and distilled water. The surface was then dried in a filtered air stream. 1 cm^2 surface area was used in all measurements.

In the solution analysis (weight loss) experiments, 5.6 cm^2 area was used.

Measurements were made after the simple degreasing preparation so as to retain the characteristic surface of electrogalvanized steel. Zinc rods (99.999% pure) were machined to give a flat face and polished with 600 grit SiC, then etched in 50% HCl and degreased.

Polarization measurements and cell.—The cell used was a commercially available 1-liter glass vessel. The counterelectrode was platinum mesh, and the reference a saturated calomel electrode. The reference electrode was placed in an electrolyte bridge tube with fritted glass tip designed for low leakage and minimum IR drop. All measurements were made with a scanning potentiostat, and current and potential were constantly monitored by digital electrometers.

The sample was placed in the corrosive medium and allowed to equilibrate which takes ~15 min, and then the corrosion potential (E_{corr}) was measured. Next the polarization resistance (R_p) was determined. The potential was adjusted to 5 mV cathodic of E_{corr} and the scan was begun in the anodic direction at a rate of 0.1 mV/s, and stopped at a value 5 mV anodic of E_{corr}.

Following the measurement of R_p, the electrode was allowed to stabilize again at E_{corr}. The cathodic scan was then obtained from E_{corr} scanning at 0.25 mV/s. After completion of the cathodic scan, the corrosion potential was redetermined and the anodic scan was initiated at the same sweep rate (0.25 mV/s). All measurements were made in quiescent electrolytes.

Results

Polarization data.—Anodic and cathodic polarization curves of 99.999% zinc in 1*M* NH_4Cl and 1*M* $(NH_4)_2SO_4$ are shown in Fig. 1 and 2, respectively. Typical polarization curves of electrogalvanized steel in 1*M* $(NH)_4)_2SO_4$ and 1*M* $(NH_4)Cl$ are shown in Fig. 3 and 4. These figures show both as-plated and drawn samples. The current-potential relationships are similar to pure zinc, but close inspection shows intrinsic differences. In Fig. 3 [$(NH_4)_2SO_4$], the anodic branch shows an inflection at ~ −1.05V. In NH_4Cl (Fig. 4), a similar current-potential relation is obtained. The inflection in the anodic portion suggests more than one anodic reaction.

These curves were obtained at *p*H 6 ± 0.1. At lower *p*H values, there is a considerable shift of the corrosion potential to more anodic values. Figure 5 shows the polarization curve of drawn electrogalvanized steel at *p*H 6 and 4.

Table III. Corrosion of pure (99.999%) zinc

	i_{corr}^E (μA/cm²)	b_a	$-b_c$	E_{corr}	i_{corr}^R (μA/cm²)
1*M* $(NH_4)_2SO_4$	16.8	41	125	−1.154	17.1
1*M* NH_4Cl	10.5	30	174	−1.133	—

The current is increased at lower *p*H and it is difficult to determine a cathodic Tafel slope; therefore, *p*H 6 was chosen for all measurements given in this report.

Calculation of corrosion rates.—The values obtained for the corrosion rates of electrogalvanized steel (EG) samples and 99.999% zinc are given in Tables III-V. Arithmetic mean values are listed in the tables at the 95% confidence level. Corrosion currents were measured by Tafel line extrapolation of the anodic portion to give i_{corr}^E (11). Both the anodic and cathodic Tafel slopes were measured directly from the polarization curve.

Corrosion currents were also calculated using the polarization resistance technique. The well-known Stern-Geary equation was used to calculate i_{corr}^R (14-16)

$$i_{corr}^R = \frac{b_a b_c}{2.303\,(b_a + b_c)R_p} \qquad [1]$$

Values of the Tafel slopes for the anodic (b_a) and cathodic (b_c) reactions are also listed in the tables.

Polarization resistance measurements yield a straight line about E_{corr} for zinc (10-11). Because of the widespread knowledge of this method, no curves are given.

Corrosion rates measured by atomic absorption analysis of test media during immersion tests are given in Table VI. The data is for as-plated wire in 1*M* $(NH_4)_2SO_4$ calculated from Faraday's law (17).

Discussion

The results were determined according to the mixed potential theory of coupled corrosion reactions developed by Wagner and Traud (17) and the assumption of a charge transfer-controlled process using the Stern-Geary equation (15-16). Pure zinc yielded values of the Tafel slopes and corrosion rates in good agreement with those deter-

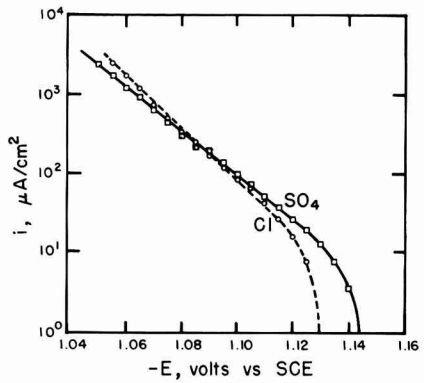


Fig. 1. Anodic polarization of zinc in 1M NH_4Cl and $(NH_4)_2SO_4$ at *p*H 6.

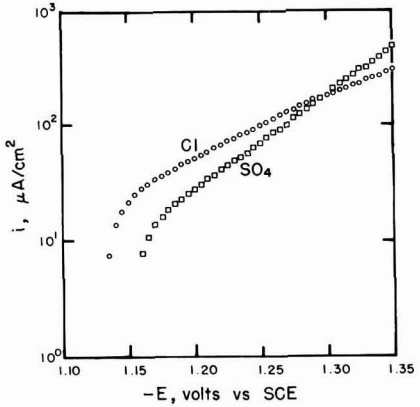


Fig. 2. Cathodic polarization of zinc in 1M NH_4Cl and $(NH_4)_2SO_4$ at pH 6.

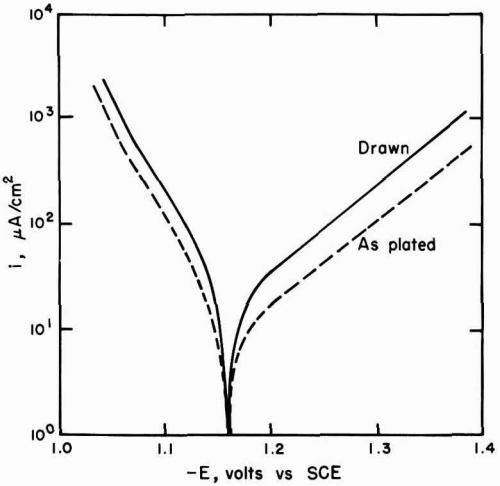


Fig. 3. Polarization of as-plated and drawn electrogalvanized steel in 1M $(NH_4)_2SO_4$ at pH 6.

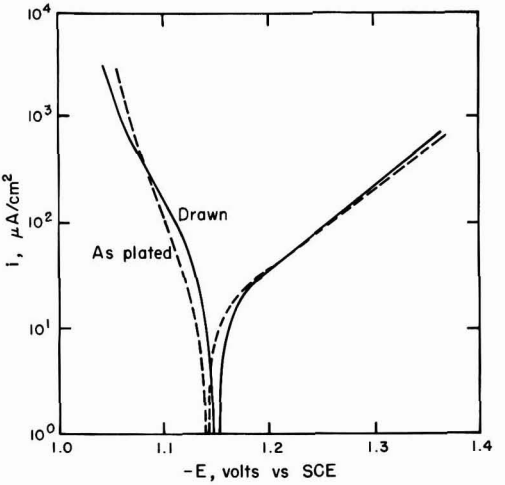


Fig. 4. Polarization of as-plated and drawn EG steel in 1M NH_4Cl at pH 6.

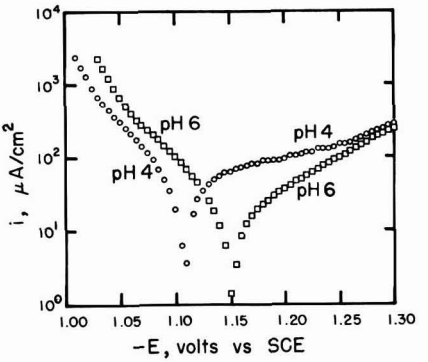


Fig. 5. Comparison of polarization of drawn EG steel in 1M $(NH_4)_2SO_4$ at pH 4 and 6.

mined by other investigators (11). Electrogalvanized (EG) steel displayed different values of the Tafel parameters, b_a and b_c, for the anodic and cathodic reactions, respectively. This implies differences in the processes of corrosion according to some authors (11, 14, 18).

On the average, drawn EG steel corrodes more rapidly than does the as-plated material. This is certainly related

Table IV. Corrosion rate data for measurements in 1M $(NH_4)_2SO_4$

Plating electrolyte	b_a (mV)	E_{corr} (V)	$-b_c$ (mV)	i_{corr}^E (μA/cm^2)	i_{corr}^R (μA/cm^2)	N[a]	Surface condition
P-1	71 ± 4	−1.157 ± 0.004	124 ± 5	21.9 ± 5.6	24.6 ± 5.1	9	Drawn
W-2	82 ± 5	−1.159 ± 0.003	119 ± 4	21.6 ± 6.6	18.6 ± 4.1	11	Drawn
P-1	55 ± 5	−1.155 ± 0.005	148 ± 10	12.5 ± 4.9	12.9 ± 3.0	7	As-plated
W-2	51 ± 7	−1.158 ± 0.005	149 ± 12	5.4 ± 2.2	9.8 ± 2.5	6	As-plated
P-2	77 ± 24	−1.157 ± 0.003	120 ± 3	11.7 ± 3.3	14.1 ± 5.0	4	Drawn
P-3	78 ± 9	−1.150 ± 0.014	125 ± 22	21.2 ± 14.5	20.9 ± 11.7	4	Drawn
P-4	70 ± 3	−1.151 ± 0.005	118 ± 7	16.2 ± 8.4	17.1 ± 8.9	4	Drawn

[a] Number of determinations.

Table V. Corrosion rate data for measurements in 1M NH_4Cl

Plating electrolyte	b_a (mV)	E_{corr} (V)	$-b_c$ (mV)	i_{corr}^E (μA/cm^2)	i_{corr}^R (μA/cm^2)	N[a]	Surface condition
P-1	56 ± 3	−1.145 ± 0.007	132 ± 7	24.0 ± 12.4	23.9 ± 7.6	4	Drawn
P-1	35 ± 2	−1.138 ± 0.004	135 ± 13	10.5 ± 5.6	11.9 ± 4.0	3	As-plated

[a] Number of determinations.

Table VI. Corrosion rates of as-plated electrogalvanized wire in deaerated 1M ammonium sulfate (Factor for calculating i_{corr} in microamperes per square centimeter from solution analysis: $F = 34.2$)

Plating electrolyte	Test	i_{corr} ($\mu A/cm^2$)	t (h)
P-1	1	14.5	25.2
		24.6	49.2
		21.8	73
P-1	2	17.2	4.3
		22.1	21
P-1	3	22.4	18.6
W-2	1	10.4	24
		19	48
		24	71
	2	4.7	24
		7.7	48
		13.5	72

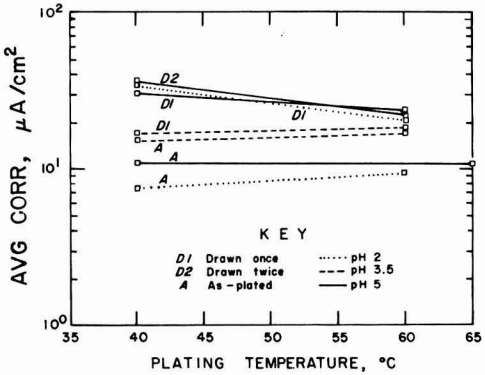


Fig. 7. Average corrosion current densities of as-plated and drawn EG steel plated in pure electrolyte P-1.

to surface structural changes incurred in the deformation of the malleable zinc coating. Figure 6 shows that the as-plated and drawn surfaces are distinctly different. The zinc coating from the synthetic electrolyte P-1 (Fig. 6A) shows larger grains than the waste electrolyte-derived deposit (Fig. 6B). The drawn surface (Fig. 6C) shows a relatively smooth surface with "die" lines. X-ray analysis shows perturbation of the crystallographic orientations upon drawing the as-plated surface as expected.

As-plated wire was also evaluated by weight loss (solution analysis) and the results show that zinc is dissolved at a rate consistent with electrochemical measurements under the assumption given above.

Waste-derived EG steel corrodes at a rate slightly lower than does the EG coating from a relatively pure zinc electrolyte. This result is presumably due to the finer-grained coating from the waste electrolyte. Salt spray corrosion tests yielded the same result: the waste coating outlasted the coatings from electrolytes prepared from French process zinc oxide (1).

Electrogalvanized wire used for evaluation was plated at two different temperatures, 40° and 60°C, representing the range normally used to produce this type of product. Also, a pH range of 2-5 was evaluated since various processes require different acid contents. Figures 7 and 8 depict the affects that plating temperature and electrolyte pH have on electrogalvanized steel corrosion rates. The corrosion currents are averages of the extrapolated and polarization resistance values. It can be seen that, in general, the higher plating temperature (60°C) yields the more corrosion-resistant product, especially after the wire is drawn.

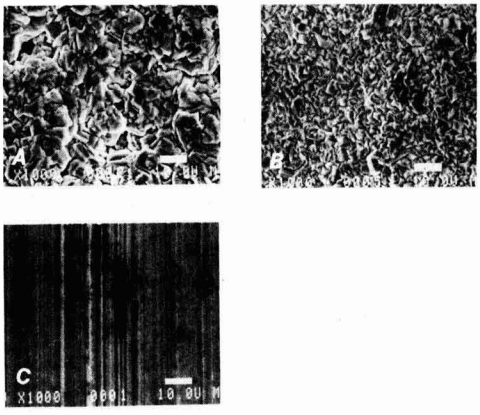


Fig. 6. SEM photographs of as-plated EG steel plated in synthetic (A), waste-derived zinc electrolytes (B), and drawn EG steel (C).

Another process variable that was evaluated was the affect of the licorice additive concentration in the pure electrolyte and the drawn wire corrosion properties. Results given in Table IV for drawn wire plated in electrolytes P-1 through P-4 show that no licorice and 0.5-g/liter licorice yield results for the final product that are better than those with intermediate licorice content. Licorice is a common additive for acid zinc plating.

The observation of the inflection in the anodic Tafel curves in Fig. 3-5 during active corrosion of the EG steel deserves comment. Tafel slopes for the dissolution of zinc on EG steel are larger than those obtained when corroding pure zinc. This is assumed to be caused by the affects of additives in the plating electrolyte and embedded drawing lubricants in the case of the drawn surface. Battery alloy zinc shows a similar inflection in the anodic polarization curve (11), so that competing anodic processes due to inhomogeneities appear to be the cause (16).

Electrogalvanized steel appears to corrode by a simple charge transfer process since the correlation between weight loss and the electrochemical techniques is acceptable. Because the medium for corrosion was deaerated, hydrogen evolution is the cathodic process coupled with anodic zinc dissolution. The use of an ammonium salt provides an increase of the rate of the cathodic hydrogen evolution process, and these media were sufficiently aggressive in their attack without the problems of surface films observed in aerated salt solution. Because electrogalvanized steel is covered with paint, rubber, or polymer in actual service and the corrosion processes are determined by real environments subject to numerous variables, the choice of medium is somewhat arbitrary.

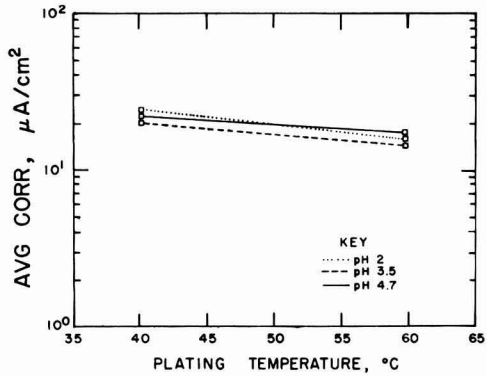


Fig. 8. Average corrosion current densities of drawn EG steel plated in waste-derived electrolyte W-2.

Conclusions

It has been shown that electrogalvanized steel plated in waste-derived zinc electrolytes corrode at rates similar to those of pure electrolyte coatings. Electrogalvanized steel displays different Tafel parameters than does pure zinc because of surface differences. The correlation between the weight loss determined by solution analysis and the electrochemical techniques of Tafel line extrapolation and polarization resistance is excellent for as-plated steel wire in ammonium sulfate solution. This allows a rapid evaluation of corrosion performance.

Because of the increased use of electrogalvanized steel for automotive application, rapid analysis is needed for process monitoring which is not provided by salt spray and performance testing. Other process variables such as plating temperature, pH, and additive concentrations can also be evaluated as to their effect on corrosion.

If wastes are to be used as raw materials in industrial processes, the final product must meet the requirements specified. Electrochemical techniques provide a means of determining corrosion rates in a short time and have been used to show that wastes are a viable source of zinc for electrogalvanizing.

Manuscript submitted Nov. 19, 1984; revised manuscript received July 1, 1985. This was Paper 6 presented at the Cincinnati, Ohio, Meeting of the Society, May 6-11, 1984.

REFERENCES

1. M. Dattilo, E. R. Cole, and T. J. O'Keefe, *Conserv. Recycl.*, **8**, 399 (1985); presented at Federation of Materials Recycling Conference, July 18, 1984, Proceedings to be published.
2. V. R. Miller and D. L. Paulson, *Resourc. Conserv.*, **9**, 95 (1982).
3. J. B. Stephenson, E. R. Cole, and D. L. Paulson, *ibid.*, **6**, 203 (1981).
4. E. H. Lyons, *Trans. Electrochem. Soc.*, **78**, 317 (1940).
5. E. H. Lyons, *ibid.*, **80**, 387 (1941).
6. H. Leidheiser, Jr., Y. Momose, and R. D. Granata, *Corrosion*, **38**, 178 (1982).
7. J. J. Podesta, R. C. V. Piatti, and A. J. Arvia, *ibid.*, **38**, 599 (1982).
8. R. F. Ashton and M. T. Hepworth, *ibid.*, **24**, 50 (1968).
9. R. D. Armstrong and G. M. Bulman, *J. Electroanal, Chem.*, **25**, 121 (1970).
10. L. M. Baugh, *Electrochim. Acta*, **24**, 657 (1979).
11. L. M. Baugh, *ibid.*, **24**, 669 (1979).
12. K. Boto and L. F. G. Williams, *J. Electroanal. Chem.*, **77**, 1 (1977).
13. K. Boto and L. F. G. Williams, *This Journal*, **124**, 656 (1977).
14. J. O'M. Bockris and A. K. N. Reddy, "Modern Electrochemistry," Vol. 2, Plenum Press, New York (1970).
15. M. Stern and A. L. Geary, *This Journal*, **104**, 56 (1957).
16. M. Stern, *ibid.*, **104**, 645 (1957).
17. C. Wagner and W. Traud, *Z. Elektrochem.*, **44**, 391 (1938).
18. J. O'M. Bockris, B. E. Conway, E. Yeager, and R. E. White, "Comprehensive Treatise of Electrochemistry," Vol. 4, p. 2, Plenum Press, New York (1981).

Transpassive Dissolution of Ni in Acidic Sulfate Media: A Kinetic Model

Michel Keddam, Hisasi Takenouti, and Ning Yu

LP0015 CNRS "Physique des Liquides et Electrochimie," associé à l'Université Pierre et Marie Curie, 75230 Paris Cedex 05, France

ABSTRACT

The transpassive dissolution of Ni in acidic sulfate media, including the influence of crystallographic orientation, was investigated. The surface plane had low index values, that is (100), (110), and (111). This study was largely based on the analysis of complex impedance. (100) and (110) specimens showed identical electrochemical behaviors, whereas the (111) specimen showed a current density about 20% lower. A reaction mechanism describing the dissolution of the passive film was proposed. This dissolution step was postulated to be catalytic, in the sense that the passive film transformed into a soluble species by anion was not consumed by the transpassive dissolution itself. Calculated polarization curves as well as electrode impedances at various polarization points were in a good agreement with experimental results.

Beyond the passivity range and preceding the oxygen evolution reaction, Ni electrode in an acidic sulfate medium exhibits a transpassive dissolution followed by a secondary passivity. A very marked intergranular dissolution which is to be directly related to localized corrosion of austenitic stainless steel immersed in an oxidizing medium is observed in this potential range (1).

This paper is aimed at a better understanding of the transpassive dissolution of Ni, including the influence of the crystallographic orientation which is likely to play an important role in the course of localized attack. Of major interest may be the interaction of the crystallographic orientation with the electrochemical behavior of the passive layer. Nickel single crystals with low index surface plane (100), (110), and (111) were investigated along with a polycrystalline specimen. The use of single crystals also avoids, to a large extent, complications due to poorly defined surface area and potential distribution within intergranular grooves and crevasses (2). This study was largely based on complex impedance measurements which yield a far more realistic picture of the reaction mechanism.

A mechanism of transpassive dissolution, based on potential decay experiments (3), was first proposed by Sato and Okamoto in 1963

$$Ni + H_2O \rightleftarrows NiOH_{ad} + H^+ + e^-$$

$$NiOH_{ad} \rightarrow NiOH_{sol}^+ + e^-$$

where the subscripts "ad" and "sol" indicate, respectively, a species adsorbed on the electrode surface and one that dissolved in the solution bulk. This dissolution mechanism is close to that proposed by Bockris *et al.* for the active dissolution of iron (4). The sole difference is the use of H_2O molecule as reactant instead of OH^- for the iron dissolution. The valency of transpassive dissolution was reported by many authors to be equal to two (5-7).

Osterwald observed that when a polarization device was switched from potentiostat to galvanostat, nearly sine wave potential oscillations took place (8, 9). On the basis of the stability theory, he deduced the existence of two time constants (second-order dynamical system) associated with a negative resistance in the frequency response. This prediction was experimentally verified by Epelboin and Keddam (10).

In 1975, on the basis of impedance data, Jouanneau *et al.* proposed a very general model for Ni dissolution cov-

ering the whole range from activity to oxygen evolution including transpassivity (11). They remarked, furthermore, that the transpassive dissolution is highly dependent on anion. Hence, they introduced reaction paths implying anion in addition to hydroxyl ion. The skeletal model includes ten adsorbed intermediate species and 12 reaction paths besides two dissolution processes and two oxygen evolution reactions. Nevertheless, the model does not distinguish explicitly the active and the transpassive dissolution. In other words, it includes no dissolution process of the passive film. Therefore, the transpassive dissolution is preceded by the reduction of bivalent passive film to a monovalent intermediate species at potentials more anodic than the passivity range. This unlikely feature seems to be an important weakness in consistency of this model. Furthermore, the model is much too intricate to be checked by numerical simulations or to fit experimental data with enough reliance. This is why we devised a new reaction mechanism.

Experimental

Electrode.—Single-crystal specimen rods, 9 mm diam, prepared by Bridgman or Czochralski method, were supplied by Cristal-Tec (France). The purity was evaluated to be 99.95%. The specimen rods were mounted in a stainless steel shaft to form a rotating disk electrode. The specimen was then covered by a thin heat curing epoxy-phenolic resin at 200°C under pressure (3.5 bar). This particular preparation of electrode allowed us to avoid any underlying attack between metal and insulating material.

The electrode surface was then polished on emery paper under water flow up to 1200 grade, and then electrochemically polished in 10% perchloric acid in ethyleneglycol monobutyl-ether at 5°C. The misorientation with respect to the corresponding index plane was kept to less than 1°.

Electrolyte.—The electrolyte was prepared by mixing dilute sulfuric acid and sodium sulfate solutions to obtain the desired pH value at different total concentrations of sulfate ions. The electrolyte was deaerated by Ar bubbling before and during experiments. The solution temperature was kept at 25° ± 0.2°C.

Cell.—A cylindrical glass cell contained about 0.35 liter solution. The working electrode, rotated at about 1200 rpm, was set at the center. This rotation speed was high enough to avoid control by mass transport. A platinum gauze counterelectrode, *ca.* 200 cm^2, was set around the cell wall. The reference electrode, located halfway between these two electrodes, was mercurous sulfate in saturated K_2SO_4 (SSE). The potential given in this paper was corrected for ohmic drop due to the electrolyte resistance determined by the high frequency limit of electrode impedance and dc current.

Measurements.—dc and ac measurements were performed potentiostatically with the Schlumberger-Solartron equipment (1186-1172 TFA). The electrode impedance was measured under sine-wave perturbation of small amplitude (ΔE < 5 mV) at various dc polarization points.

Calculations.—Numerical simulations were performed using FORTRAN-77 language with double precision (*i.e.*, 16 bytes for a complex variable) on a Gould 32/27 computer. A reaction model was first translated into a set of differential equations corresponding to the mass and charge balances. Then this set of equations was solved for steady-state and linearized nonsteady-state conditions yielding mathematical expressions of the dc current and the frequency dependence of the impedance at any given potential. A detailed description of the procedure has been given elsewhere (12). Specific equations relevant to the model of transpassive dissolution of Ni are shown below.

Numerical simulations were performed by varying the values of the kinetic parameters. No fitting program was used, but the values were adjusted manually for each run to approach sufficiently to the experimental data. Models able to reproduce neither analytically nor numerically the experimental results were discarded. The steady-state polarization curve was first simulated. At this stage, a certain number of kinetic parameters had little or no influence on the calculated curve. Then the impedance diagrams at various polarization points were tried to be reproduced by numerical calculations.

Results and Discussion

In Fig. 1, the steady-state polarization curve of the transpassive dissolution of (111) single-crystal Ni in 1*M* H_2SO_4 is shown. This curve exhibits a fairly well-defined Tafel relationship spreading over two orders of magnitude, in agreement with Ref. (5). The steady state was reached within a few minutes at a given potential for single-crystal specimens. This contrasts to the case of a polycrystalline specimen on which the steady state was reached only after 10-15 min of polarization, due probably to the formation of grooves and crevasses at grain boundaries. The current maximum can be seen near 1.0V, due to the secondary passivation process. Beyond 1.1V, the oxygen evolution reaction sets in, leading to a further current increase.

The influence of crystal plane on the polarization curve is illustrated in Fig. 2. Except for the full passive range (13), (100) and (110) specimens showed identical polarization curves. On the contrary, the current density of (111) specimen is about 20% lower in the transpassive dissolution range, and roughly half at the current maximum. The results were highly reproducible, and the difference observed was significantly greater than the experimental error. The same difference was also observed in the polarization curves obtained in other solutions. On the contrary, no significant difference can be seen in the oxygen evolution range.

Figure 3 depicts different impedance diagrams obtained at the polarization points labeled A to F in Fig. 1 on the (111) specimen. Over the entire transpassive dissolution range, in addition to the high frequency capacitive loop related to the double-layer capacitance and the

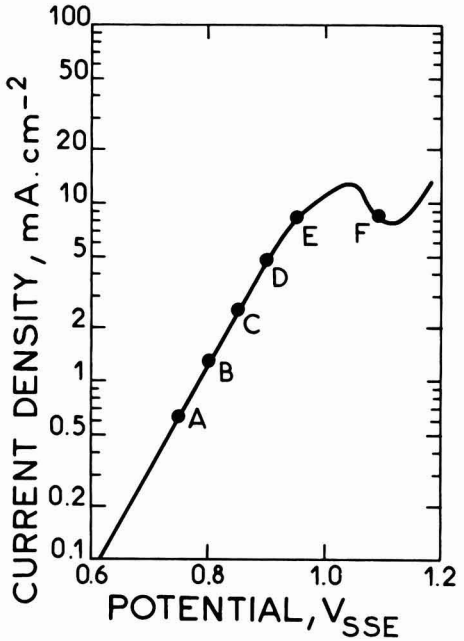


Fig. 1. Steady-state polarization curve of the transpassive dissolution; (111) Ni single crystal in deaerated 1M H_2SO_4 at 25°C. A to F correspond to the diagrams given in Fig. 3.

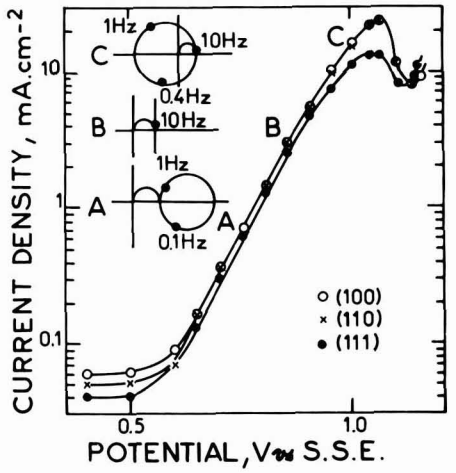


Fig. 2. Polarization curves for different crystal planes. Diagrams A to C illustrate schematically the evolution of electrode impedance with potential.

charge transfer resistance, two loops, one capacitive and another inductive, can be seen. Hence, the impedance diagram intersects the real axis at a frequency ranging from 0.1 to 0.4 Hz, depending upon the electrode potential. At a potential near 0.88V, the impedance becomes infinite at this frequency (wave-trap circuit). At potentials less anodic than this critical value, the real part of impedance remains always positive. On the contrary, at more anodic potentials, the real part of the impedance exhibits a negative contribution. This change of the impedance diagrams is illustrated in Fig. 2. The impedance diagram above the critical potential is in fact stable under potential but unstable under current regulation (14), as correctly predicted by Osterwald (9).

The impedance diagrams of (100) and (110) specimens are quite similar to those shown in Fig. 3. A slight difference in the observed impedance modulus can be related to the difference of the dc component. The similarity of the polarization curves, and more significantly of the complex impedances, exhibited by these three specimens indicates that the electrode kinetics is not clearly dependent on the crystallographic plane.

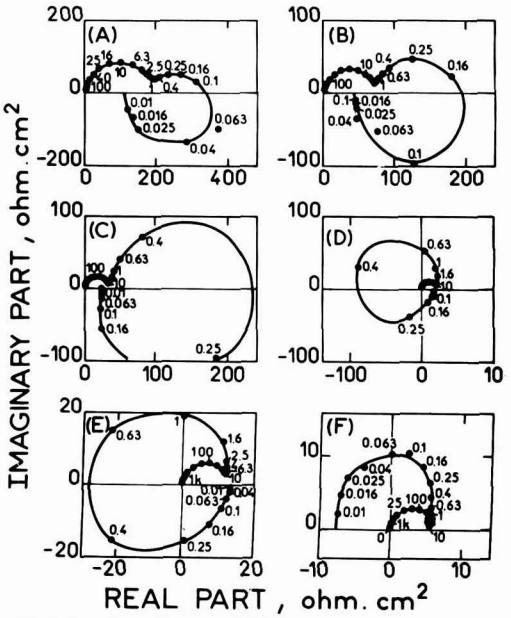


Fig. 3. Impedance diagrams of (111) Ni single crystal. A to F are measured at dc points labeled on Fig. 1.

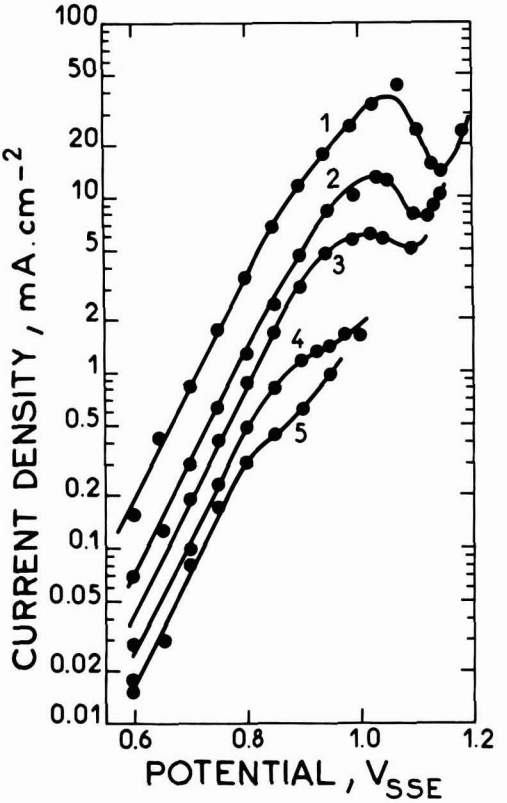


Fig. 4. Influence of solution pH on polarization curves: (111) Ni in 2M H_2SO_4 (curve 1) and in a molar SO_4^{--} of various pH. Curve 2: pH 0.0. Curve 3: pH 0.6. Curve 4: pH 1.6. Curve 5: pH 3.

In order to obtain additional data about the reaction mechanism, the solution pH and the total sulfate concentration were independently varied. Figure 4 depicts the influence of solution pH on the polarization curve for (111) single-crystal specimen. When the solution pH increases, the dissolution current decreases. The apparent reaction order of dissolution rate with respect to H^+ concentration is *ca.* 0.25. That is, the influence of solution pH is small. Furthermore, its increase seems to enhance the passive state instead of the dissolution, as in active Fe dissolution. These two points contrast definitively with the consecutive dissolution mechanism proposed by Bockris *et al.* (4) for active Fe.

Figures 5 and 6 illustrate the influence of total sulfate concentration at a constant pH. At a low pH value (0.35), as can be seen in Fig. 5, no clear relationship between the dissolution current and the sulfate concentration can be established. It may be worth noting that, at this pH, sulfate anions are mainly HSO_4^-. At pH 3.0, on the contrary, the major solution anion is SO_4^{--}, for which the results are shown in Fig. 6. Somewhat more significant change than at pH 0.35 can be seen. The apparent reaction order with respect to the total sulfate concentration is 0.2. That is, the influence of sulfate concentration is small for a weakly acid and negligible in a strongly acid medium in spite of the fact that the very nature of anion plays a crucial role in transpassive dissolution (11). This strongly

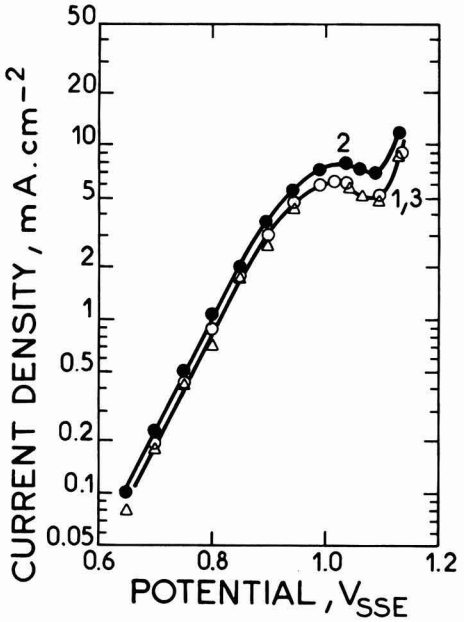


Fig. 5. Influence of sulfate concentration on polarization curves: (111) single-crystal Ni. 1: 0.5M H_2SO_4. 2: 0.5M H_2SO_4 + 0.5M Na_2SO_4. 3: 0.5M H_2SO_4 + 1M Na_2SO_4. Solution *p*H: 3.5.

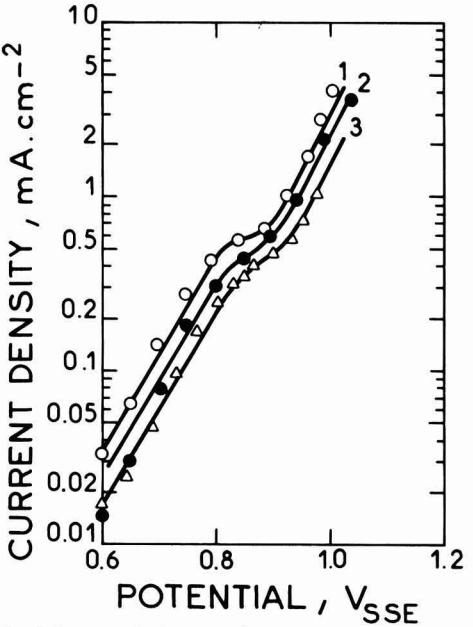


Fig. 6. Similar to Fig. 5 with *p*H 3 solution at total sulfate concentration 1M (1), 0.1M (2), and 0.01M (3).

suggests a catalytic effect of anion on the dissolution of the passive layer, as established recently in the case of F^- by spectroscopic and electrochemical techniques (15).

In this potential range, the metal surface is completely covered by a bivalent passive layer. At high enough anodic potentials, SO_4^{--} and/or HSO_4^- are assumed to attack the passive film and to transform it into a soluble species. The secondary passivity is to be explained by another type of passive film such as $Ni(OH)_3$. This concept contrasts drastically with those proposed in the literature, in which the transpassive dissolution is considered to be similar to the active dissolution (3, 11).

Reaction Model

The impedance data clearly put forward a far more intricate mechanism than the single charge transfer step expected in Ref. (5) from the Tafel law obeyed over a large range of current densities. Neither polarization curves nor electrode impedances allow us to determine the chemical nature of reaction intermediate species, but only allow some guess about their potential and time dependence. Therefore, a skeletal reaction model was preferably used without expliciting reaction chemistry but only on the valency state of intermediate species

$$\begin{array}{ccccccc} & & K_1 & & K_3 & & K_5 \\ \mathrm{Ni} & \underset{K_{-1}}{\rightleftarrows} & \mathrm{Ni(II)_{ad}} & \underset{K_{-3}}{\rightleftarrows} & \mathrm{Ni(II)^*_{ad}} & \underset{K_{-5}}{\rightleftarrows} & \mathrm{Ni(III)_{ad}} \\ & & \downarrow K_2 & \swarrow K_4 & & & \downarrow K_6 \\ & & \mathrm{Ni(II)_{sol}} & & & & \mathrm{O_2} \end{array} \qquad [\mathrm{I}]$$

The reaction step [I] depicts the formation of the passive film. Since the potential range of interest in this work is far anodic to the active dissolution, the latter process is discarded from the reaction scheme. The K_2 step is the chemical dissolution process of the passive film which determines the constant current density in the full passive range. The K_3 step denotes the transformation of the passive film into a somewhat more soluble species, likely containing anion, leading to the transpassive dissolution itself (K_4 step). The K_5 step accounts for the secondary passivity, whereas the K_6 step describes the oxygen evolution reaction. This reaction is assumed to take place on top of the secondary passivity adsorbate since its contribution is detectable only after the current maximum. This model implies three intermediate species sharing simultaneously the electrode surface. The fractional coverage of Ni(II), Ni(II)*, and Ni(III) are, respectively, denoted by θ_1, θ_2, and θ_3.

In spite of this formalism, the model validity can be extended to a situation where the kinetics is partly controlled by depth profiles of potential and/or concentration within a film. In this range of potential, the electrode surface must be considered as completely covered by the passive film and no bare nickel is allowed to contact electrolyte. Therefore, K_1/K_{-1} step can be considered as the transfer of Ni(II) across the film from the metal to a surface site on the passive layer. A high field migration is consistent with an exponential dependence on the applied potential. Adsorption states are assumed to be located at the film/electrolyte interface.

The mass balance of the three intermediate species given above can be expressed by

$$\beta\frac{d\theta_1}{dt} = K_1\Sigma - (K_{-1} + K_2 + K_3)\theta_1 + K_{-3}\theta_2 \qquad [1]$$

$$\beta\frac{d\theta_2}{dt} = K_3\theta_1 - (K_{-3} + K_5)\theta_2 + K_{-5}\theta_3 \qquad [2]$$

$$\beta\frac{d\theta_3}{dt} = K_5\theta_2 - K_{-5}\theta_3 \qquad [3]$$

where $\Sigma = 1 - \theta_1 - \theta_2 - \theta_3$ and β stands for the surface concentration (4.0×10^{10} mol-cm^{-2}) of adsorbed species at $\theta_1 = 1$. These equations indicate that K_4 and K_6 steps do not intervene in the mass balance. In a preliminary work, it was found that experimental data cannot be accounted for by the K_4 dissolution step obeying usual electrochemical kinetics. Though not demonstrated analytically, a catalytic process seems to be needed to simulate the experimental results on the basis of this reaction scheme. Furthermore, the formation of a catalytic surface species is also in agreement with a small dependence of the reaction rate on anion concentration. Such a reaction can be represented for instance by

$$\text{Ni(II)}^* + \text{Ni} \overset{K_4}{\rightleftarrows} \text{Ni}^{2+} + \text{Ni(II)}^* + 2e^-$$

This particular mechanism allows us to separate the relaxation time constant from the current flow through the electrode interface. In fact, in this reaction scheme, the dissolution of Ni(II)* is not accompanied with its consumption. The consequence of such a reaction from the viewpoint of electrode impedance was described in detail in the case of Fe dissolution (12). For oxygen evolution reaction, the secondary passive species Ni(III) also plays a catalytic effect, but these kinetics are introduced only to simplify the mass balance equation. In fact, this reaction is beyond the scope of this work and is introduced merely to explain the current increase due to the oxygen evolution. The reaction process may be explicited for instance as

$$\text{Ni(III)} + \text{H}_2\text{O} \overset{K_6}{\rightleftarrows} \text{Ni(III)} + 2\text{H}^+ + \frac{1}{2}\,\text{O}_2 + 2e^-$$

The charge balance dQ/dt, that is, current flow I, can be written as follows

$$I = \mathbf{F}[2K_1\Sigma - 2K_{-1}\theta_1 + (2K_4 + K_5)\theta_2 - (K_{-5} - 2K_6)\theta_3] \quad [4]$$

where $\mathbf{F}$ is the Faraday.

The Tafel law and the Langmuir-type isotherm are postulated to describe the potential dependence of K_i

$$K_i = K_{i0} \exp(b_i E) \quad [5]$$

where K_{i0} and b_i are independent of θ, K_i is expressed in mol-s^{-1}-cm^{-2}, and the unit of b_i is V^{-1}. For an equilibrium reaction, $(b_i + b_-) = RT/n\mathbf{F}$. This condition was found much too drastic to fit experimental results over a wide range of experimental conditions. This implies that K_1/K_{-1}, K_3/K_{-3}, and K_5/K_{-5} cannot be considered as true elementary equilibrium processes but depict merely an overall reaction reversibility. Furthermore, the K_{-1} value in the transpassive dissolution range is so small that this process may be considered as practically irreversible.

The steady state is defined by $d\theta_i/dt = 0$, hence from Eq. [1]-[4] one yields the steady-state polarization current $\bar{J}$

$$\bar{J} = 2\mathbf{F}(K_2\bar{\theta}_1 + K_4\bar{\theta}_2 + K_6\bar{\theta}_3) \quad [6]$$

where

$$\bar{\theta}_1 = K_1K_{-3}K_{-5}/D;\ \bar{\theta}_2 = K_1K_3K_{-5}/D;\ \bar{\theta}_3 = K_1K_3K_5/D$$

and

$$D = (K_1 + K_{-1} + K_2)K_{-3}K_{-5} + K_1K_3(K_5 + K_{-5})$$

$\bar{\theta}$ indicates the steady-state value of fractional coverage. The faradaic impedance Z_F is to be derived from the Taylor expansion of Eq. [1]-[4] limited to the first order. The result of this straightforward calculation is given below

$$\frac{1}{Z_F} = \frac{1}{R_t} - \mathbf{F}[2(K_1 + K_{-1})\frac{d\theta_1}{dE} + (2K_1 - 2K_4 - K_5)\frac{d\theta_2}{dE} + (2K_1 + K_{-5} + 2K_6)\frac{d\theta_3}{dE}] \quad [7]$$

where

$$\frac{1}{R_t} = \mathbf{F}\{[2(b_1 - b_{-1})K_{-1} + b_1K_2]\bar{\theta}_1 + [2b_4K_4 + (b_5 - b_{-5})K_5]\bar{\theta}_2 + 2b_6K_6\bar{\theta}_3\}$$

$$\frac{d\theta_1}{dE} = \frac{X_1Z_2Z_3 - X_1K_3K_{-5} - (K_1 - K_{-3})(X_2Z_3 + K_{-5}X_3) - K_1(X_3Z_2 + X_2K_5)}{Z_D}$$

$$\frac{d\theta_2}{dE} = \frac{Z_1X_2Z_3 + X_1K_3Z_3 + Z_1X_3K_{-5} - K_1K_3X_3}{Z_D}$$

$$\frac{d\theta_3}{dE} = \frac{Z_1Z_2X_3 + (K_1 - K_{-3})K_3X_3 + Z_1X_2K_5 + X_1K_3K_5}{Z_D}$$

Table I. Kinetics parameters used in simulation calculation

$K_1 = 1 \times 10^{-8} \exp(5E)$	$K_4 = 5 \times 10^{-11} \exp(10E)$
$K_{-1} = 2.8 \times 10^{-7} \exp(-5.5E)$	$K_5 = 3 \times 10^{-13} \exp(10E)$
$K_2 = 5 \times 10^{-12} \exp(7E)$	$K_{-5} = 3 \times 10^{-8} \exp(-4.5E)$
$K_3 = 2 \times 10^{-13} \exp(5E)$	$K_6 = 2 \times 10^{-14} \exp(12.5E)$
$K_{-3} = 7.6 \times 10^{-9} \exp(-4.5E)$	

with

$$Z_D = Z_1Z_2Z_3 + (K_1 - K_{-3})K_3Z_3 - Z_1K_5K_{-5} + K_1K_3K_5$$

$$X_1 = [(b_1 - b_{-1})K_{-1} + (b_1 - b_2)K_2 - (b_3 - b_{-3})K_3]\bar{\theta}_1$$

$$Z_1 = K_1 + K_{-1} + K_2 + K_3 + j\omega\beta$$

$$X_2 = [(b_3 - b_{-3})K_{-3} - (b_5 - b_{-5})K_5]\bar{\theta}_2$$

$$Z_2 = K_{-3} + K_5 + j\omega\beta$$

$$X_3 = (b_5 - b_{-5})K_{-5}\bar{\theta}_3$$

$$Z_3 = K_{-5} + j\omega\beta$$

ω is the angular frequency (rad-s^{-1}) and $j = \sqrt{-1}$.

It is assumed that the double-layer capacitance C_d (= 100 μF-cm^{-2}) is linked in parallel with the faradaic impedance, and hence the overall electrode impedance is expressed by

$$\frac{1}{Z} = \frac{1}{Z_F} + j\omega C_d \quad [8]$$

By a trial-and-error method, a set of kinetic parameters shown in Table I was found to simulate suitably the experimental results on (111) single-crystal specimen in 1M H_2SO_4. The polarization curve obtained by numerical calculation is shown in Fig. 7. The calculated curve is in fairly good agreement with experimental results.

In the same figure, the changes of fractional coverage by Ni(II), Ni(II)*, and Ni(III) are shown. This figure illustrates that the electrode is practically completely covered ($\theta_1 + \theta_2 + \theta_3 \simeq 1$), and the passivating species θ_1 decays in the transpassive range and undergoes a transformation into the soluble transpassive species θ_2. The fractional coverage of this species remains rather small in the whole potential range, and shows a maximum near $E = 0.88$V, corresponding to the critical potential.

From calculated results, at the foot of the transpassive range, Ni dissolution through K_2 path is still significant, but, beyond $E = 0.7$V, the K_4 path prevails in the whole range of transpassive nickel dissolution.

Figure 8 shows the impedance diagrams obtained by simulation according to the model at various dc polarization points labeled A′ to F′ in Fig. 7. The change in the diagram shape with potential is well reproduced by the model. In particular, the critical potential beyond which the negative real part is observed is seen to be well simulated. On the contrary, at potentials close to the current maximum, experimentally, the impedance diagram again takes a shape similar to Fig. B′ or C′. This was not successfully reproduced by the kinetic parameters given in Table I. Another discrepancy with the model is the R_t value. Calculated charge transfer resistance is a few times smaller than that measured experimentally for high cur-

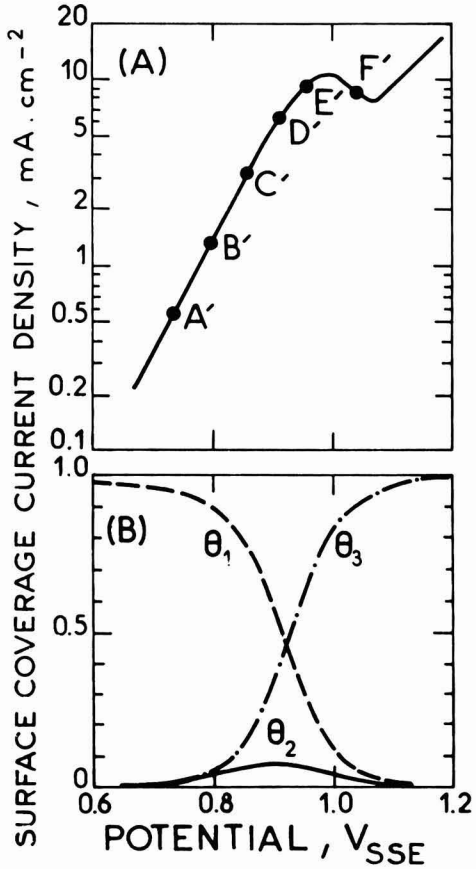


Fig. 7. A: Calculated polarization curve of the transpassive dissolution of Ni (cf. Fig. 1). B: Fractional surface coverage by Ni(II) (θ_1), Ni(II)* (θ_2), and Ni(III) (θ_3).

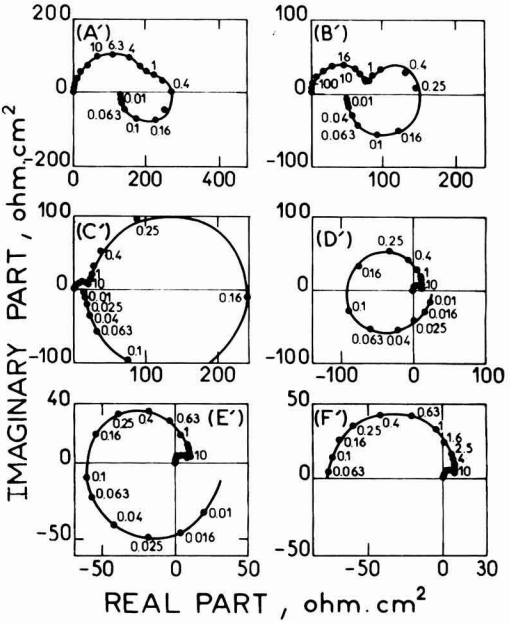


Fig. 8. Calculated impedance diagrams at dc polarization points labeled on Fig. 7A by corresponding letters.

rent densities. However, it is reasonably hoped that these points can be improved by the choice of a better set of kinetic parameters.

Conclusion

Experiments on the transpassive dissolution of Ni in acidic sulfate media were performed with single-crystal specimens having three different orientations (100), (110), and (111). The polarization curves, as well as the impedance diagrams, of (100) and (110) are identical, whereas (111) showed a slightly lower dissolution current.

The dissolution rate is weakly dependent on the solution pH. The lower the pH value, the faster the dissolution rate. This experimental observation contrasts to the influence of solution pH on the active dissolution of Fe in an acidic medium. The influence of sulfate concentration is also weak or negligible, although the anion plays a crucial role in the very existence of transpassive dissolution. These experimental data led us to consider the transpassive dissolution as a catalytic dissolution of the passive film.

A reaction model for the transpassive dissolution and the secondary passivity, implying three adsorbed species and two dissolution paths, is proposed. A numerical simulation of this model reproduces the experimental results with a satisfactorily good agreement in the case of (111) Ni specimen in 1*M* H_2SO_4.

Consideration of the role of OH^-, HSO_4^-, and SO_4^{--} in the framework of the model will constitute the next step of this work.

Acknowledgment

One of the authors (N.Y.) gratefully acknowledges the Ministry of Education of the People's Republic of China for providing his fellowship.

Manuscript submitted Oct. 22, 1984; revised manuscript received April 14, 1985. This was Paper 258 presented at the New Orleans, Louisiana, Meeting of the Society, Oct. 7-12, 1984.

CNRS assisted in meeting the publication costs of this article.

REFERENCES

1. L. Beaunier, M. Froment, and C. Vignaud, *J. Electroanal. Chem.*, **119,** 125 (1981).
2. R. de Levie, in "Advances in Electrochemistry and Electrochemical Engineering," Vol. 6, P. Delahay, Editor, p. 239, John Wiley and Sons, New York (1967).
3. N. Sato and G. Okamoto, *This Journal*, **110,** 605 (1963); *ibid.*, **111,** 897 (1964).
4. J. O'M. Bockris, D. Drazic, and A. R. Despic, *Electrochim. Acta*, **4,** 321 (1961).
5. K. Arnold and K. J. Vetter, *Z. Elektrochem.*, **64,** 407 (1960).
6. K. Schwabe, U. Ebersbach, and W. Leimbrock, *Electrochim. Acta*, **17,** 957 (1972).
7. M. Turner, G. E. Thompson, and P. A. Brook, *Corros. Sci.*, **13,** 985 (1973).
8. J. Osterwald and H. G. Feller, *This Journal*, **107,** 473 (1960).
9. J. Osterwald, *Electrochim. Acta*, **7,** 523 (1962).
10. I. Epelboin and M. Keddam, *ibid.*, **17,** 177 (1972).
11. A. Jouanneau, M. Keddam, and M. C. Petit, *ibid.*, **21,** 287 (1976).
12. M. Keddam, O. R. Mattos, and H. Takenouti, *This Journal*, **128,** 257, 266 (1981).
13. C. J. Mauvais, R. M. Latanision, and A. W. Ruff, Jr., *ibid.*, **117,** 902 (1970).
14. I. Epelboin, C. Gabrielli, M. Keddam, and H. Takenouti, in "Comprehensive Treatise of Electrochemistry," Vol. 4, J. O'M. Bockris, B. E. Conway, E. Yeager, and R. E. White, Editors, p. 151, Plenum Press, New York (1981).
15. H. H. Strehblow and B. P. Löchel, in "Passivity of Metals and Semiconductors," Vol. 4, M. Froment, Editor, p. 379, Elsevier, Amsterdam (1983).

An Improved Accelerated Test Chamber for Electrolytic Metal Migration and Corrosion

J. J. Steppan*

Department of Chemical Engineering, Vanderbilt University, Nashville, Tennessee 37235

W. R. Seebaugh

Department of Mechanical and Materials, Vanderbilt University, Nashville, Tennessee 37235

J. A. Roth

Department of Chemical Engineering, Vanderbilt University, Nashville, Tennessee 37235

L. C. Hall

Department of Chemistry, Vanderbilt University, Nashville, Tennessee 37235

ABSTRACT

Many accelerated electrolytic metal migration and corrosion investigations have been performed in accelerated test chambers with unknown gas concentration and flow characteristics. This paper outlines the development of a well-characterized accelerated test chamber. The length (mean flow path) to hydraulic diameter ratio of the closed-circuit rectangular flow channel is 20. Velocity and concentration measurements showed minimal horizontal or vertical gradients in the test section. The range of standard deviations (m/s) for the velocity profiles in the test section was 0.0037-0.16 at mean velocities of 0.11-2.9 m/s, respectively. Similarly, the range of standard deviations [ppm(vol.) SO_2] for the SO_2 concentration profiles was 1.0-1.2 for a standard gas mixture of 102 ± 1.1 ppm SO_2 in the air. The effect of gas velocity upon the rate of metal migration was demonstrated in the described test chamber using a new accelerated test in an SO_2 environment. This test, the PEG-400 drop test, is a moderate accelerated test with metal migration rates that are less than the water-drop test but greater than a temperature humidity bias test with or without pollutants. The gas velocity was found to have a significant effect upon the rate of copper migration.The effects of gas velocity, humidity, and pollutant concentrations upon the metal migration and corrosion rates can be investigated in this accelerated test chamber.

Accelerated life tests are performed on electronic components to predict the actual lifetime and reliability of these components. Electrolytic metal migration and corrosion are common reliability problems encountered in the microelectronics industry. Accelerated metal migration and corrosion investigations are performed in test chambers in which the temperature, humidity, pollutant concentration, air velocity, and applied bias can be varied or cycled. Typically, little attention is paid to velocity or concentration profiles and gradients in these chambers. Most accelerated metal migration and corrosion laboratory tests are performed in test chambers which have unknown or uncontrolled velocity and concentration gradients.

The accelerated test chambers used in metal migration and corrosion studies can be classified as one of three types: flow-through chambers (1-11), commercial humidity cabinets (12-16), and sealed containers (17-20). The flow-through chambers are usually constructed of glass, Plexiglas, or Teflon and are best suited for studies using humidified air with or without pollutant gases. Some investigators using a flow-through chamber (1-6) mix humidified air and pollutants in the test chamber, which does not provide consistent pollutant and water concentrations in the chamber. Other investigators (7-11) mix the humidified air and pollutant gas streams before introductions into the test chamber.

Most flow-through chambers are rectangular. Rectangular chambers exhibit velocity gradients, stagnant regions in the corners, and eddy currrents at the entrance and exit (21). Antler and Dunbar (22) observed different corrosion rates on copper coupons in different locations within their accelerated test chamber. This was attributed to nonuniformity of velocity and water vapor and SO_2 concentrations, especially at the entrance and exit of the test chamber.

*Electrochemical Society Student Member.

It has been shown that the rates of corrosion of silver (23-25), of copper (25), and of copper migration (21) are dependent upon the gas velocity past the specimens. Sharma *et al.* (26) include a velocity term in their acceleration corrosion rate expressions. Other investigators do not discuss velocity effects.

The majority of metal migration and corrosion studies reported in the literature apply only to the specific system in which the accelerated tests were performed. It is difficult to establish the significance of comparisons between accelerated test results obtained using uncalibrated test chambers. Accelerated test chambers have not been standardized. Thus, investigators must standardize or characterize their test chambers so that comparisons with other experimenters and field tests can be made. This is essential for the development of acceleration factors used to predict electronic machine life under actual conditions.

The accelerated test of interest was first devised by Carbone and Corl (27). It involves placing a drop of 400 average molecular weight polyethylene glycol (PEG-400) between a pair of biased electrodes. The PEG film absorbs water and gaseous pollutant species from the ambient environment. These species ionize in the PEG or PEG-water film, causing an increase in the electrical conductivity of the film. Copper ions are formed at the anode and migrate to the cathode where they are reduced, producing dendrites. When the dendrites form a continuous filament between the electrodes, the device shorts. The time for the electrode system to short (t_s) is a measure of the relative rate of metal migration. The metal migration rates for this accelerated test (PEG-400 drop test) are moderate. The short times are longer than the water-drop test, but shorter than exposing dry electrodes to a temperature-bias-humidity test with or without pollutants.

The first objective of this paper is to outline the development of a well-characterized test chamber suitable for

accelerated metal migration and corrosion studies. The second objective is to determine the effect of velocity upon the rate of copper migration for the PEG-400 drop test in an SO_2 environment.

Apparatus and Experimental Methods

Two conceptual approaches to the design of the accelerated test chamber were considered. The principal goal was to obtain a steady, reproducible flow at the test section. Generally, this may be accomplished by (*i*) providing sufficient entrance length upstream of the test section to provide a fully developed velocity profile across the test section or (*ii*) by minimizing the length of the upstream to provide a nearly uniform flow across the test section.

The velocity profile in a duct becomes fully developed at a certain distance from the entrance to the duct. For laminar flow in circular tubes (28), the approximate entrance length is given by

$$\frac{x_l}{D} = 0.05\ \mathrm{Re} \qquad [1]$$

where x_l is the entrance length, D is the tube diameter, and Re is the flow Reynold's number (ratio of the product of linear-flow-velocity, test-medium-density, and tube-diameter to the test-medium-viscosity). Similarly, the entrance length for turbulent flow (28) is given by

$$\frac{x_l}{D} = 4.4\ \mathrm{Re}^{1/6} \qquad [2]$$

For a desired velocity variation 0.11-2.9 m/s (Reynold's number range of approximately 1,100-29,000 for a 0.15m diam tube), the entrance length is 8.3-16m for laminar flow (0.11-0.20 m/s) and 2.4-3.7m for turbulent flow. These lengths are not practical for an accelerated test chamber, since the laminar entrance length must be used as the upstream length for investigations covering both the laminar and turbulent regimes.

Alternative designs were considered, since it was desirable to limit the overall size of the test chamber while obtaining reproducible and constant velocity and concentration profiles at the test section. Steady, nearly uniform flow at the test section with a minimum duct length can be achieved by careful design. This may be accomplished by either accelerating flow through a short nozzle or interrupting the flow by a pressure reducing device that occupies the duct a short distance upstream of the test section. The flow is stabilized just ahead of the test section using either of these methods.

The second option, use of a flow restrictor, was selected. A closed-circuit test chamber was constructed of clear acrylic plastic to permit use of flow visualization aids. The rectangularly configured flow channel design is advantageous, since the size of the chamber is small (0.91 × 0.91 × 0.15m) and the pollutant gas is recycled, requiring only a small make-up stream. The ratio of total length of flow channel (mean flow path) to hydraulic diameter is 20 for this chamber. The flow restrictor is a bundle of polyethylene straws held in the duct by a polyvinylchloride screen. Flow visualization studies were conducted using Dry Ice vapor to observe the air flow patterns. Vanes were installed at the two corners of the chamber between the drive fan and the flow restrictor to eliminate stagnant regions. The final configuration of the accelerated test chamber is shown in Fig. 1.

Velocity profile measurements.—Air velocity measurements were made at multiple locations in the test section with a Flow Corporation Model 55 air velocity meter. The (x, y, z) coordinate system (see Fig. 2) was used to define these locations. The $x = 0$ plane is the exit side of the air distributor. The air velocity was varied from 0.11 to 2.9 m/s by varying the fan speed.The velocity measurements were taken in the $z = 0.013$, 0.064, and 0.11 planes of the test section.

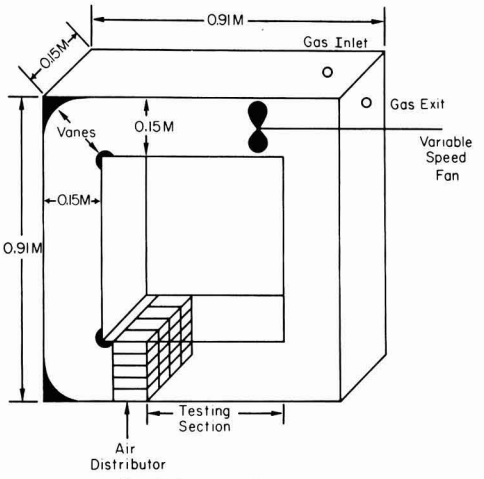


Fig. 1. Accelerated test chamber

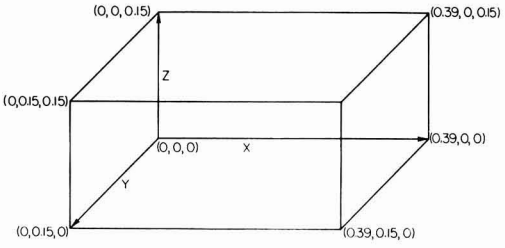


Fig. 2. Coordinate system for velocity measurements

Concentration profile measurements.—A Matheson Certified Standard gas mixture of 102 ppm (vol.) SO_2 in air was introduced into the accelerated test chamber with the fan creating a velocity of approximately 1.0 m/s. Gas samples (5.0×10^{-7}m^3) were taken from locations in the test section after steady state was reached (approximately 1800s). The SO_2 concentrations were determined with a Tracor Model 565 gas chromatograph equipped with a Hall 700A electrolytic conductivity detector. Gas samples were taken in the $z = 0.11$ plane to determine the horizontal concentration gradient, if any. Samples were also taken at $x = 0.30$, $y = 0.076$, and $z = 0.025$, 0.091, and 0.11 to determine vertical concentration gradients. Gas samples taken directly from the cylinder were used as standards for comparison with samples taken from the accelerated test chamber.

Copper migration measurements.—The test specimens for the copper migration investigation consist of copper electrodes (approximately 5.0×10^{-5}m thick) on a substrate of nonfire retardant epoxy reinforced with woven Fiberglas cloth. The "point-to-plane" electrode configuration was manufactured by a vendor using a lithographic technique. Figure 3 shows the point-to-plane electrode design. The electrode pairs used in this investigation had spacing of approximately 2.2-2.5 × 10^{-4}m between the point and plane. There was some inconsistency in initial electrode spacings and condition due to problems inherent with the manufacturing process.

The test specimens were cleaned to remove residual photoresist and manufacturing fluxes in order to obtain a reproducible electrode surface. The electrode cleaning procedure appears in Table I. This cleaning procedure produced visually clean electrodes at 60 times magnification with long blank short times compared to accelerated short times, *i.e.*, $\frac{t_s(\text{accelerated})}{t_s(\text{blank})} << 1$. Care was taken

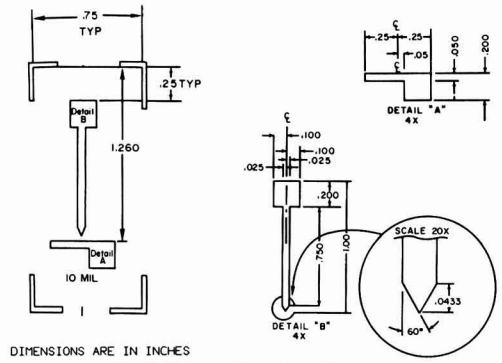


Fig. 3. Point-to-plane electrode design

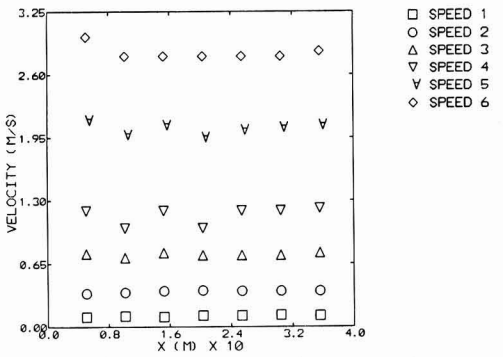


Fig. 4. Longitudinal velocity profiles in test section

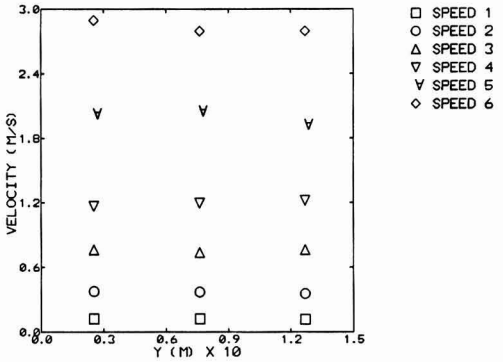


Fig. 5. Transverse velocity profiles in test section

not to touch the copper metallurgy, and latex gloves were worn when handling the specimens.

After the specimens were cleaned, two electrode pairs were placed in a Plexiglas holder and the electrode spacings were measured using a calibrated eyepiece micrometer at a magnification of 60 times. The sample holder was then placed in the test chamber and electrical connections were made to the electrodes with alligator clips. The plane was biased negatively and was located upstream of the point (+). Unreproducible results were obtained when the bias was reversed in preliminary metal migration investigations involving PEG-water drops doped with ammonium perchlorate. The applied potential was measured to ensure good electrical contacts and was then turned off. The chamber was sealed and the fan was turned on. The velocity across each specimen was measured prior to the introduction of the SO_2. The fan motor was located on the floor and drove the fan blade by means of a flexible shaft in order to eliminate any vibrations. The samples were then covered with a polyethylene cover to prevent the SO_2 environment from coming in contact with the copper electrodes before steady state was reached. The chamber was then resealed and the 104 ppm SO_2-air mixture was introduced. The SO_2 concentration was monitored by gas chromatography using a ten-port gas sampling valve to compare the feed and test chamber concentrations. Once steady state was reached, the polyethylene cover was removed through a septum in the chamber wall and a 6.0 μliter drop of PEG-400 was placed between each electrode pair, and a potential of 9.0V was applied. The leakage current of each electrode pair was monitored as a function of time. The time until short (t_s) was determined at several gas velocities in the laminar and transition flow regimes. A short is defined as a surge in leakage current, typically 1.0-10 μA, and visual observation of a dendritic structure bridging the electrodes. Upon completion of the short time runs, the fan speed was increased to 5.7 m/s [minimum velocity for reproducible psychrometric measurements (30)] and the relative humidity was determined by psychrometry.

Results and Discussion

The Dry Ice vapor (CO_2) flow patterns qualitatively showed a reproducible velocity profile with no eddy currents or stagnant regions in the velocity range from 0.11 to 2.9 m/s. This velocity range corresponds to a Reynold's number range of approximately 1,100-29,000.

Velocity profile results.—Figure 4 shows the velocity profile along the center of the accelerated test chamber at z = 0.064m. Figure 5 shows the velocity profiles across the chamber at the same height. The mean velocity values and their standard deviations appear in Table II.

The velocity profile results show no organized patterns, but some scatter in the transverse and longitudinal directions in the test section of the accelerated test chamber. The range of standard deviations (m/s) in the test section was 0.0037-0.16 at mean velocities of 0.11-2.9 m/s, respectively.

The introduction of test specimens and electrical connections disturbs the velocity profile downwind of the

Table I. Copper electrode cleaning procedure

1. Dip card in hot (50°-60°C) HNO_3 [25% (by volume)] for 60s or longer if copper lines are not clean after 60s.
2. 15s rinse with deionized water.
3. Ultrasonicate in hot (50°-60°C) HCl [25% (by volume)] for 1800s.
4. 15s rinse with deionized water.
5. 15s rinse with isopropanol.
6. Ultrasonicate in isopropanol for 900s.
7. Store cards in isopropanol until ready for use (do not store for more than 24h).
8. Dry card with nitrogen before using.

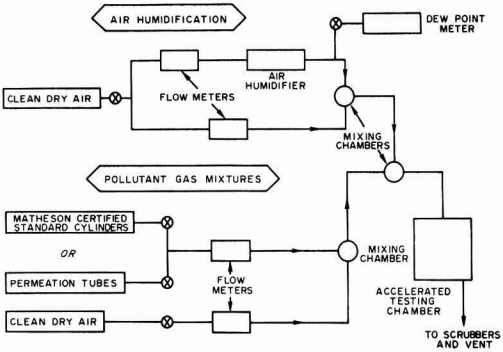


Fig. 6. Gas mixing system

Table II. Velocity results in test section

Mean velocity (m/s)	Standard deviation (m/s)
z = 0.013m plane	
(x = 0.051-0.36m; y = 0.025-0.13m)	
0.13	0.016
0.38	0.0060
0.81	0.035
1.2	0.092
2.1	0.079
2.9	0.16
z = 0.064m plane	
(x = 0.051-0.36m; y = 0.025-0.13m)	
0.11	0.0083
0.36	0.014
0.75	0.030
1.1	0.092
2.0	0.056
2.8	0.081
z = 0.11m plane	
(x = 0.051-0.36m; y = 0.025-0.13m)	
0.11	0.012
0.36	0.018
0.72	0.022
1.0	0.080
1.9	0.056
2.6	0.060
x = 0.30m plane	
(y = 0.0039-0.055m; z = 0.013-0.11m)	
0.11	0.0037
0.36	0.012
0.72	0.036
1.0	0.10
1.9	0.082
2.6	0.093

samples. Thus, it is important to design a sample holder with a small cross-sectional area. The sample holder used in this accelerated test holds two test specimens. Both specimens have identical velocity profiles across them.

Concentration profile results.—Replicate samples of standard 102 ppm (vol.) SO_2-air mixture were analyzed by gas chromatography with a maximum standard deviation of 1.1 ppm. The standard deviation of the vertical point concentration analyses in the test section was 1.2 ppm. Similarly, the standard deviation of the horizontal point concentration analyses was 1.0 ppm. The concentration profile results show that there are minimal horizontal and vertical concentration gradients in the test section.

The gas mixing system shown in Fig. 6 can be used to prepare humidified air-pollutant mixtures for accelerated testing of electronic components. The effects of velocity, humidity, and pollutant concentrations upon the rate of metal migration or corrosion can be investigated singly or in combination.

Copper migration results.—The effect of velocity upon the relative rates of copper migration was investigated by varying the velocity while holding the SO_2 concentration [104 ± 1 ppm (vol.)], relative humidity (20.0-31.6%), electrode spacing (2.2-2.5 × 10^{-4}m), and applied potential (9.0V) constant. The time until a short occurred (t_s) was determined at each velocity. The Q test (31) was used to eliminate outlier points at the 90% confidence level. Figure 7 shows the relationship between the short time (t_s) and velocity (V) in the laminar and transition flow regimes. The decrease in short time with increased velocity indicates that the diffusion of pollutants and water from the gas phase to the PEG-film significantly contributes to the rate of copper migration. This relation is easily explained by transport phenomena or hydrodynamic theory (26, 32). The higher the velocity past the PEG-400 film, the thinner the diffusion (boundary) layer, and thus, the rate of gas-liquid mass transfer of SO_2 increases. Ishino *et al.* (23) report that the diffusion of pollutants to metal surfaces is the controlling step of corrosion processes in the field. The sudden break in the t_s-V relationship in the transition region is predicted by hydrodynamic theory for any process which is significantly affected by velocity.

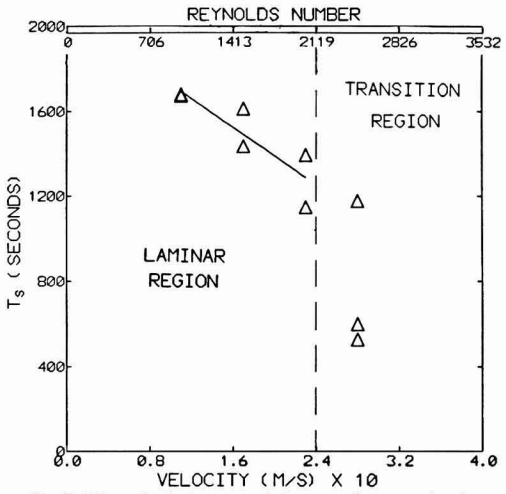


Fig. 7. Effect of velocity upon relative rate of copper migration

Thus, the break in the t_s-V relationship supports the idea that the gas-liquid mass-transfer step, and therefore the velocity significantly affects the rate of copper migration.

Conclusions

An accelerated test chamber has been developed with reproducible velocity and concentration profiles with minimal velocity and concentration gradients. The length to hydraulic diameter ratio of the chamber is 20. This chamber provides a constant and reproducible atmosphere in which the rates of electrolytic metal migration and corrosion can be determined as a function of pollutant concentration and humidity at constant velocities.

The results of PEG-400 drop tests performed in the described accelerated test chamber show that the velocity significantly affects the rate of copper migration. This velocity effect agrees with hydrodynamic and diffusion theories.

Acknowledgments

The work upon which this paper is based was supported by a contract from IBM (project number MR201). The assistance of Maureen Steg with the velocity profile measurements is acknowledged.

Manuscript submitted Nov. 13, 1984; revised manuscript received July 2, 1985.

REFERENCES

1. W. H. Abbott, *IEEE Trans. Parts, Hybrid, Packag.*, **php-10,** 24 (1974).
2. L. G. Feinstein and N. L. Sbar, *IEEE Trans. Components, Hybrids, Manuf. Technol.*, **chmt-2,** 159 (1979).
3. F. N. Fuss, C. T. Hartwig, and J. M. Morabito, *Thin Solid Films*, **43,** 189 (1977).
4. M. Iannuzzi, *IEEE Trans. Components, Hybrids, Manuf. Technol.*, **chmt-6**, 191 (1983).
5. M. Iannuzzi and R. P. Kozakiewicz, *ibid.*, **chmt-5,** 345 (1982).
6. D. W. Rice, P. Peterson, E. B. Rigby, P. B. P. Phipps, R. J. Cappell, and R. Tremoureux, *This Journal*, **128,** 275 (1981).
7. N. L. Sbar, *IEEE Trans. Parts, Hybrids, Packag.*, **php-12,** 176 (1976).
8. N. L. Sbar and L. G. Feinstein, *ibid.*, **php-13**, 208 (1977).
9. N. Schwartz and D. D. Bacon, *This Journal*, **125,** 1487 (1978).
10. E. S. Sproles, Jr., and S. P. Sharma, *IEEE Trans. Components, Hybrids, Manuf. Technol.*, **chmt-6,** 343 (1983).
11. O. A. Svedung, L. G. Johansson, and N. G. Vannerberg, *ibid.*, **chmt-6,** 349 (1983).
12. G. DiGiacomo, in "20th Annual Proceedings of the Reliability Physics Symposium," pp. 27-33, San

Diego, CA, March 30-April 1, 1982, IEEE, New York (1982).
13. M. Iannuzzi, *IEEE Trans. Components, Hybrids, Manuf. Technol.*, **chmt-6,** 181 (1983).
14. H. M. Naguib and B. K. MacLaurin, *ibid.*, **chmt-2**, 196 (1979).
15. N. L. Sbar and R. P. Kozakiewicz, *IEEE Trans. Electron Devices*, **ed-26,** 56 (1979).
16. S. P. Sharma, *This Journal*, **125,** 2005 (1978).
17. P. J. Boddy, R. H. Delaney, J. N. Lahti, E. F. Landry, and R. C. Restrick (Part 1) and R. H. Delaney and J. N. Lahti, (Part 2) in "14th Annual Proceedings of the Reliability Physics Symposium, 108-117, April (1976).
18. J. N. Lahti, R. H. Delaney, and J. N. Hines, in "17th Annual Proceedings of the Reliability Physics Symposium, 39-43, April, (1979).
19. D. J. Lando, J. P. Mitchell, and T. L. Welsher, in "17th Annual Proceedings of the Reliability Physics Symposium, 51-63, April (1979).
20. J. C. Williams and D. B. Herrmann, in *"IRE Trans. Reliab. Qual. Control."* pp. 11-20, February (1956).
21. J. J. Steppan, M. S. Thesis, Vanderbilt University, Nashville, TN (1983).
22. M. Antler and J. J. Dunbar, *IEEE Trans. Components, Hybrids, Manuf. Technol.*, **chmt-1**, 17 (1978).
23. M. Ishino, M. Kishimoto, K. Matsui, and M. Shoichi, *ibid.*, **chmt-3**, 63 (1980).
24. J. A. Lorenzen, in "17th Annual Proceedings Inst. Envir. Sciences, pp. 110-116 (1971).
25. F. N. Fuss, R. F. Leach, and W. H. Yocum, *Proceedings of the 1979 International Microelectronics Symposium*, 325-330 (1979).
26. S. P. Sharma, J. H. Thomas, III and F. E. Bader, *This Journal*, **125,** 2002 (1978).
27. S. P. Carbone, and E. A. Corl, in "Atmospheric Corrosion," W. H. Arbor, Editor, pp. 173-175, John Wiley and Sons New York (1982).
28. F. M. White, "Fluid Mechanics," pp. 312-313, McGraw Hill Book Company, New York (1979).
29. B. J. W. Tuin, M.S. Thesis, Vanderbilt University, Nashville, TN (1984).
30. J. H. Arnold, *Physics* (NY), **4,** 334 (1933).
31. R. B. Dean, and W. J. Dixon, *Anal. Chem.*, **23,** 636 (1951).
32. R. B. Bird, W. E. Stewart, and E. N. Lightfoot, "Transport Phenomena," John Wiley and Sons, Inc. New York (1960).

Electroreduction of Chromium (VI) in Aqueous Acid Solutions

A. F. Diaz* and D. Schermer

International Business Machines Corporation, General Products Division, San Jose, California 95193

ABSTRACT

The cyclic voltammogram of chromium (VI) in aqueous acid solution shows a reduction peak at 0.3-0.4V when a platinum electrode is used *vs.* Na SCE. The reaction is electrochemically irreversible, and, with phosphoric acid in the solution, the voltammogram is different than with any other acid because an insoluble chromium (III) phosphate film is formed on the electrode. This film is insulating and forms in a self-healing manner. Although it passivates the electrode towards further Cr(VI) reduction, it remains active to protons and oxygen. The film is very tight, and the diffusion of small molecules such as ferrocene across the film is significantly reduced. In aqueous sulfuric acid, the Cr(VI) reduction reaction is diffusion limited with no indications of adsorption on the electrode surface either before, during, or after the reaction.

Chromium conversion coatings (1-4) are used commercially on aluminum surfaces to provide a protection layer. The coating process is a galvanic process which proceeds spontaneously upon contact of the aluminum substrate with the aqueous acid solution containing chromium (VI). The driving force for the reaction is *ca.* 2.5 eV (5). Therefore, the reaction is controlled kinetically and has no thermodynamic limitation. The chemistry is complicated and involves electron transfer between aluminum, which is oxidized to aluminum (III) and chromium (VI), which is reduced to chromium (III). The net reaction is shown in Eq. [1]

$$Al + H_2Cr(VI)O_4 + 6H^+ \rightarrow Al(III) + Cr(III) + 4H_2O \quad [1]$$

The chromate solutions contain phosphoric acid, which precipitates Cr(III) as chromium phosphate, the protective layer. Therefore, the resulting protective film is a composite of chromium phosphate and mixed aluminum oxide-fluoride salts. Initially formed films are gelatinous and soft, but they become insoluble, hard, and strongly adherent when dried.

The chromate phosphate process works quite well when relative thick coatings are desired (several microns thick) because the coating covers the aluminum completely. However, the coating is not uniform in thickness on a microscopic level. The thickness of the film is difficult to control because the Cr(VI) species must penetrate the aluminum oxide layer and come in near contact with the aluminum metal in order for electron transfer to occur. Therefore, variations in the protective layer thickness will result from differences in the oxide layer and the corresponding diffusion rates along the aluminum surface. In addition, the chromium phosphate films are subject to disruption due to the diffusion of ions and hydrogen gas evolution. As a result, the quality of the thin film coatings is noticeably poor. They are very irregular, and areas of the substrate are often left uncoated.

The overall process is quite complicated, and it is not clear how the quality of the thin films is influenced by the quality of the aluminum surface and by the inherent nature of the chromium reaction. Therefore, as an approach, the reduction of chromium (VI) was studied under conditions which would permit us to understand the reaction in the absence of complications due to the chemistry of the aluminum surface. The reaction was probed electrochemically using a platinum surface in both sulfuric and phosphoric acid solutions. The reaction is electrochemically irreversible and limited by diffusion of the electroactive species in solution. In sulfuric acid solution, the reaction produces soluble products, whereas in phosphoric acid an insoluble chromium (III) phosphate film is produced which insulates the electrode surface.

Experimental

The electrochemical equipment used in this study was available from previous studies (6). Most of the measurements were made using a 0.2 cm^2 platinum working electrode, a gold wire counterelectrode, and a saturated sodium chloride standard calomel reference electrode. A 0.156 cm^2 gold working electrode was also employed. The solutions were prepared using either Baker "Analyzed" reagent-grade chromium trioxide and mineral acids or using commercially available Alodine 407 which contains 4.4*M* phosphoric acid and 2*M* chromic oxide. Reagent-grade ferrocene from Aldrich Chemicals was recrystallized before use. Burdick acetonitrile and tetraethylammonium tetrafluoroborate were used without further purification.

* Electrochemical Society Active Member.

The electron micrographs were measured with a Hitachi S405A scanning electron microscope. The films were coated with a 100Å film of gold prior to the measurement in order to improve the resolution of the micrograph. The ESCA analyses were performed with a Hewlett-Packard 5950B ESCA spectrometer. The energy reference for the instrument is set for Au at 84.0 eV.

Results and Discussion

Chromium (VI) on Pt in aqueous sulfuric acid.—The reduction of 0.01*M* chromium (VI) in aqueous sulfuric acid (0.18*M*) was studied by cyclic voltammetry using a platinum electrode. As shown in Fig. 1, the scans were initiated at 0.6V, which is a potential near the open-circuit potential. Better reproducibility was obtained when the voltage was swept to 1.2V before sweeping in the cathodic direction. The cyclic voltammogram shows a peak for the Cr(VI) to Cr(III) reaction at 0.3V. The nature of the electroactive species in aqueous dilute sulfuric acid can be approximated from the magnitude of the various equilibrium constants. Chromium (VI) is primarily in the form of the dissociated ions of chromic acid, H_2CrO_4, and chromium (III) is in the form of dissociated hydrated ions, $Cr(H_2O)_6^{3+}$ (7). The peak heights scale approximately linearly with the square root of the sweep rate as anticipated for a diffusion-controlled process. This relationship is also plotted in Fig. 1. The plot is not truly linear. Only the first three points extrapolate to the origin, and the points for the faster scan rates deviate down from linearity. Considering the points at the slower scan rates which extrapolate to the origin, a value for $i/Av^{1/2}$ equal to 0.042 A/cm^2 (V/s)$^{1/2}$ is calculated. This provides a value for $n(\alpha nD)^{1/2}$ equal to 14.1 × 10^{-3} cm/s$^{1/2}$ using the Randles-Sevcik equation for an irreversible reaction (8). With n equal to 3, αD is calculated to be 0.74 × 10^{-5} cm^2/s.

The reaction is electrochemically irreversible, and the products remain soluble with no evidence of change in the activity of the electrode surface as a result of the formation of an insulating film. In the anodic sweep, there is a small anodic peak at 1.0-1.2V which must be due in part to the oxidation of chromium (III) which is formed while the electrode is resting at 0.6V before the scan is initiated, plus the oxidation of the platinum surface. The oxidation of the platinum surface is a relatively unimportant reaction in these conditions. For example, the voltammogram measured using an aqueous sulfuric acid solution, containing no chromium (VI), does not show a peak at 0.6V (anodic scan); it shows only a gradual increase in the current. Furthermore, the reduction peaks, which appear at 0.25 and 0.47V, are 15-20 times smaller. Finally, in the potential region cathodic of 0.0 V (not shown in Fig. 1), the cathodic current increases rapidly, owing to the reduction of protons and oxygen in the electrolyte solution. The reactions occurring in this voltage range were not investigated further. The results obtained with the platinum electrode/sulfuric acid solution could be reproduced with a gold electrode or a hydrofluoric acid solution.

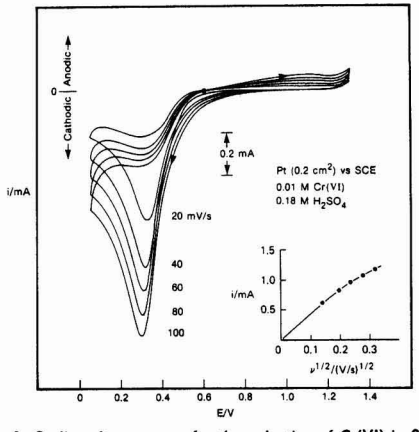


Fig. 1. Cyclic voltammogram for the reduction of Cr(VI) in 0.18M aqueous sulfuric acid using a platinum electrode. The inset shows a plot of the peak current *vs.* the square root of the sweep rate.

Chronocoulometry of the platinum electrode/sulfuric acid solution reconfirms that the reaction is diffusion limited. As seen in Fig. 2, the consumption of charge is linear in $t^{1/2}$. For these measurements, the potential was stepped from 0.6 to 0.2, 0.0, and −0.2V, respectively. The same slope was obtained in every case, and a value for $nD^{1/2}$ equal to 9.63 × 10^{-3} cm/s$^{1/2}$ is calculated using the integrated form of the Cottrell equation (8). With n equal to 3, the diffusion coefficient for the chromium (VI) reaction is 1.03 × 10^{-5} cm^2/s. To the extent that there may be some reduction of platinum oxide, the linearity in the chronocoulometric plots suggests that it is not very important under these conditions. When the potential was stepped to values cathodic of −0.3V, the current response was no longer linear with $t^{1/2}$ due to the concurrent reactions of oxygen and protons at the electrode surface.

The electrochemical stoichiometry of the reaction has been assumed equal to 3 F/mol. The same stoichiometry, 3.03 F/mol of chromate, is observed for the electrochemical reduction of Cr(VI) in aqueous ammonium-buffered solution (9) and of $CaCrO_4$ (<0.04*M*) in LiCl-KCl eutectic melt (10). In the report by Delnick and McCarthy (10), the cyclic voltammogram of the melt solution is described as having a single irreversible wave at −0.45V *vs.* Ag/Ag$^+$ reference electrode. The reaction is a one-step process yielding $LiCrO_2$ exclusively. The stoichiometry also varies with the reaction conditions and is different in aprotic solvent (11). In acetonitrile, the first reduction reaction of chromate on a dropping mercury electrode is a one-electron reversible reaction. The log(*i*) *vs.* *E* plot for this reaction has a slope of 16.7 (11) with n = 1 and α = 0.98. However, under the same conditions but using a solid gold electrode, the reaction is again irreversible and produces mainly Cr(II) and Cr(O) (11).

A comparison of D (1.03 × 10^{-5} cm^2/s) from the chronocoulometry experiment with αD (0.74 × 10^{-5} cm^2/s) from the cyclic voltammetry experiment provides a value for α equal to 0.72. This value can be determined experimentally from the low current levels at the initial part of the reduction peak. The voltammogram is shown in Fig. 3 along with the log(*i*) *vs.* *E* plot (inset). The measurement was made using a slow sweep rate, 4 mV/s, between 0.7 and 0.4V. Log(*i*) is linear with *E*, and the slope of the line ($n\mathbf{F}/RT$) is 13.1. From the slope, αn is estimated to be equal to 0.77, which does not fit for α equal to 0.72 and n equal to three. This gross discrepancy between the two values cannot be reconciled unless the peak shown in Fig. 1 envelopes several peaks and the stoichiometry changes from one in the initial part of the peak to three as the scan progresses through the voltage range of the peak.

Chromium (VI) on Pt in aqueous phosphoric acid.—The results obtained using solutions prepared from commer-

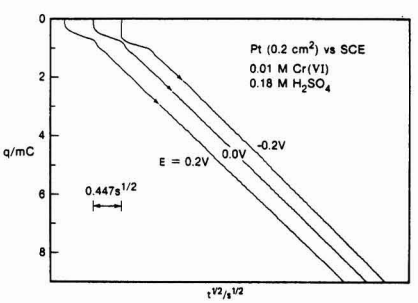


Fig. 2. Q-$t^{1/2}$ plot for the reduction of Cr(VI) in 0.18M sulfuric acid using a platinum electrode. The curves correspond to separate measurements where the potential was stepped from 0.6V to 0.2, 0.0, and −0.2V, respectively.

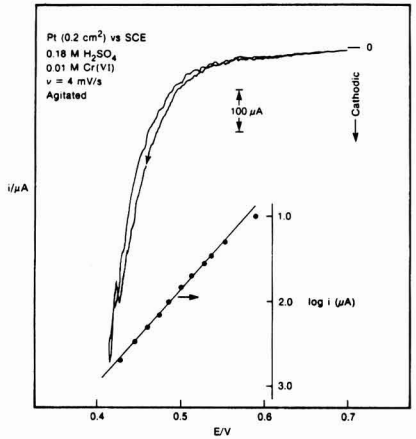


Fig. 3. Current-voltage plot at the foot of the wave for the reduction of Cr(VI) in 0.18M aqueous sulfuric acid using a platinum electrode. The measurement was made using a sweep rate of 4 mV/s and with agitation of the solution. The inset shows a plot of log *i* vs. V.

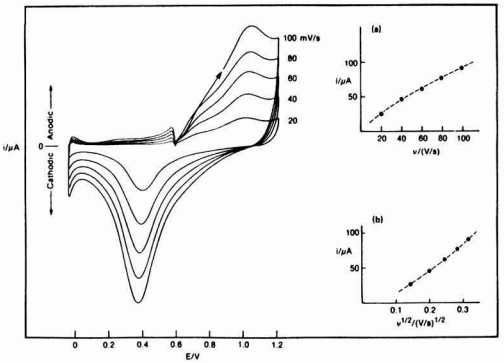


Fig. 4. Cyclic voltammogram for the reduction of Cr(VI) in 0.022M aqueous phosphoric acid solution using a platinum electrode. The insets show a plot of the peak current vs. the sweep rate (a) and square root of the sweep rate (b).

cially available Alodine 407 are quite different. The Alodine solution was diluted 1 to 200 with distilled water and used directly for analyses. This solution consists of 0.01*M* Cr(VI) and 0.022*M* phosphoric acid. The chemical nature of Cr(VI) can be estimated in this acid solution by considering the various equilibria for the proton dissociation of phosphoric (log $K = -2$) and chromic acid (log $K = 0$) plus the condensation of chromic acid to form the mixed anhydride with phosphoric acid (log $K = 0.95$) and with dihydrogen phosphate (log $K = 0.48$) (7). Using these values, it can be calculated that the Cr(VI) species exists primarily in the anhydride form where the equilibrium mixture is 0.0075*M* $H_2CrPO_7^-$ and 0.0025*M* $HCrPO_7^=$.

The measurements were more difficult to make with this solution because the reaction product, chromium (III) phosphate (log $K_{sp} = -17$ to -23) (7), precipitates on the electrode surface. It is essential that the potential applied to the electrode be swept anodically to 1.2V before the excursion in the cathodic direction in order to oxidize away the deposit. Without this treatment, reproducible voltammograms are not obtained, where, in the subsequent sweeps, the peak becomes considerably smaller and displaced. Repeated scanning over this potential range without cleaning the electrode causes the electrode to become completely passivated. Finally, cleaning the electrode by the anodic sweep treatment is successful only with freshly formed films. Electrodes which were removed from the electrochemical cell and whose film had dried had to be cleaned by abrasion.

The scan for the voltammetric analysis of this solution was initiated at 0.6V, scanned anodically to 1.2V, and then cathodically to 0.0 V. Two oxidation waves appear in the initial anodic scan at *ca.* 0.8 and 1.0V and are due to the oxidation of chromium (III) phosphate which is formed on the electrode during the short time that the cell is at rest before the scan is initiated, plus the oxidation of the platinum electrode. As can be seen in the voltammogram shown in Fig. 4, the change in the electrolyte from sulfuric to phosphoric acid causes the peak to shift to 0.38V and reduces the current response by an order of magnitude even though the Cr(VI) concentration is similar in both solutions. Thus, the effective surface area is only *ca.*. 10% of the geometric area of the electrode. The peaks have a more symmetrical shape, are much broader, and still increase with the sweep rate. The increase in the peak height is more closely linear with the rate (inset a) but is not truly linear with either the rate or the square root of the rate (inset b). These characteristics suggest a shift in the mechanism to a surface-localized reaction occurring in the absence of diffusion. However, the peak width at half-height is approximately 0.3V and much larger than the expected value of $93/n$ mV. Thus, the electroreduction reaction is much more complicated in the presence of phosphoric acid and is strongly influenced by the chromium phosphate deposit on the electrode surface.

Although definite conclusions cannot be drawn from this data, the characteristics of the voltammogram may result from the gradual decrease in the effective electrode area during the scan caused by the formation of the passivating layer. A continuous decrease in the area will cause the current to drop off faster than is expected for a diffusion-controlled reaction, thus giving the peak a symmetrical appearance. The surface does not fully passivate during the time of a single scan with the sweep rates used, and the film is easily penetrated by protons and oxygen. As a result, the current in the cathodic sweep increases at *ca.* 0.0V.

The oxidation and reduction of the platinum surface is important with these conditions. For comparison, voltammetric analyses were made of an aqueous 0.03*M* phosphoric acid, with no chromic acid present, and using the same potential limits and scan rates as above. The voltammogram shows a gradual increase in the anodic current during the initial anodic sweep. In the cathodic scan, the cathodic current increases gradually, starting at *ca.* 1.0V, and the peak appears at 0.2V. The current response is comparable to the case with chromic acid present. Thus, with the chromic acid/phosphoric acid solution (Fig. 4), the anodic current resulting from the oxidation of the surface in the initial anodic scan must lie under the peaks observed at 0.8-1.0V. And, in the cathodic scan, the presence of the prewave at 0.6V is due to the reduction of the platinum surface (12). The peak at 0.2V does not appear when chromic acid is present.

From the chronocoulometric measurements, it is seen that the surface is readily passivated and maximum current levels are quickly attained. For these measurements, the applied voltage was stepped from 0.6 to 0.2V, and the amount of charge consumed was measured with time. The results are plotted in Fig. 5, where it can be seen that the charge is linear with neither time nor the square root of time, but continually decreases as the electrode becomes passivated. The current levels off after approximately 20s, and the amount of charge consumed is approximately 3 mC/cm², which corresponds to approximately five monolayers of chromium phosphate.

Finally, the voltammogram for chromium (VI) in phosphoric acid solution can be changed to resemble the voltammogram observed in solutions containing only sulfuric acid by the addition of sulfuric acid. With the addition of 0.18*M* sulfuric acid to the above solution, the voltammogram changes and resembles the one measured in aqueous solution containing only sulfuric acid. The re-

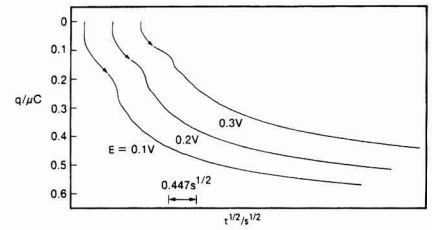


Fig. 5. Q-$t^{1/2}$ plot for the reduction of Cr(VI) in 0.022M aqueous phosphoric acid using a platinum electrode.

duction peak is shifted cathodically from 0.38 to 0.33V at 20 mV/s, and the size of the peak recovers. In addition, there now appears a slight cathodic depression at *ca.* 0.3V in the anodic sweep.

Concentrated chromium (VI) solution.—The results with the dilute solutions are very different from those reported using a high concentration (2.5M) of chromic acid (13, 14). As can be seen in Fig. 6, the voltammogram is much more complicated and is consistent with the voltammogram published by Hoare (12, 13). Analysis of this concentrated solution is not straightforward since the electrode is easily contaminated. As a result, we observed wide variations in both the size of the signal and the reproducibility of the results between runs. As before, the reproducibility was improved when the voltage was scanned anodic to 1.4V before scanning cathodically. The most striking difference is in the size of the signals. The peaks are *ca.* ten times smaller than the peak produced by the dilute solution even though the solution is 250 times more concentrated, suggesting again that the electrode surface is heavily contaminated by an insulating film. In addition, the oxidation of the platinum surface strongly interferes with the analysis of these solutions. The film that is formed probably results from the chemical reaction between platinum and chromate, and consists of the oxides of these metals (12, 13). The peak at 0.3V observed with the dilute solutions is now shifted to 0.4V, and two additional reduction peaks appear in this voltage range, one at 0.6V and one at 0.9V. With these solutions, the oxidation peaks in the range 1.0-1.2V, corresponding to the oxidation reactions of Cr(III) and the platinum surface, are considerably larger.

The decrease in current density with increasing concentrations of chromate has been reported by Wallace (14). In the concentration range 0.2-1.0M chromate, the current density for the reduction reaction on a nickel-plated steel surface was found to be lower at the higher concentrations (14).

Passivating chromium phosphate films.—Films of chromium phosphate were prepared at constant potential, 0.2V, and using the dilute solution 0.01M chromic acid and 0.022M phosphoric acid. Films prepared using *ca.* 1 mC/cm^2 were too thin, and no information was obtained about the topology or the presence of cracks or defects from scanning electron microscopy using 40,000 magnification. ESCA analysis was only semiquantitative because of the limited amount of material. The ESCA spectrum shows a small signal for chromium (575 eV) and phosphorus (189 eV) in the ratio of 1 to 2.

Since the SEM analysis was not helpful for determining the integrity of the film, measurements of the diffusion of ferrocene across the film were made. For these determinations, films on the platinum electrode were mounted as a working electrode in a cell containing 0.001M ferrocene in acetonitrile. The voltammogram of this solution shows a signal for the oxidation of ferrocene which is *ca.* 50 times smaller and has a distinctively different shape than the peak observed on bare platinum (see Fig. 7). This measurement could be repeated with no obvious damage to the film. Films prepared in this way were quite reproducible where the variation in the current response was 10-30% between films. From the size and the shape of the peak in Fig. 7, it is clear that the film covers the platinum electrode completely. There are no open areas, cracks, or defects. If the current was due to the reaction of ferrocene occurring at exposed areas of the electrode provided by cracks or defects, the shape of the voltammogram would resemble that for a clean electrode surface and the size of the signal would depend on the extent of exposure.

The film does permit some level of diffusion, and the current levels observed permit us to estimate the diffusion of ferrocene across the chromium film. The diffusion velocity (D/u) is 2×10^{-4} cm/s, and was estimated using the equation provided by Lacaze for a process where there is limited diffusion across an insulating thin film on the electrode surface (15), $i_{lim}/A = n\mathbf{F}CD/u$. This equation was derived from the case where there is no selectivity for ion migration from the solution into the film and there is a linear concentration gradient of the electroactive species across the thin film. The concentration of the electroactive species is zero at the metal film interface and equal to the bulk concentration at the film solution interface. For this calculation, n is 1, $\mathbf{F}$ is Faraday's constant, C is the concentration of ferrocene, D is the diffusion coefficient for ferrocene across the film, and u is the thickness of the film. Considering that the film is 20-25Å thick, the diffusion constant for ferrocene in the film is 0.5×10^{-10} cm^2/s. The chromium phosphate films

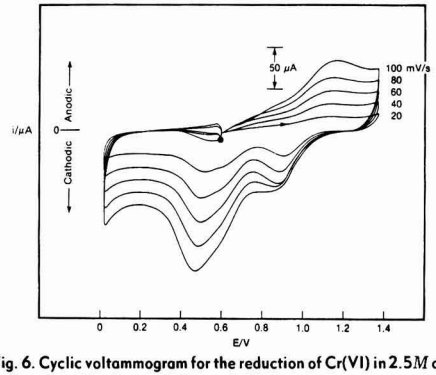


Fig. 6. Cyclic voltammogram for the reduction of Cr(VI) in 2.5M aqueous chromic acid using a platinum electrode.

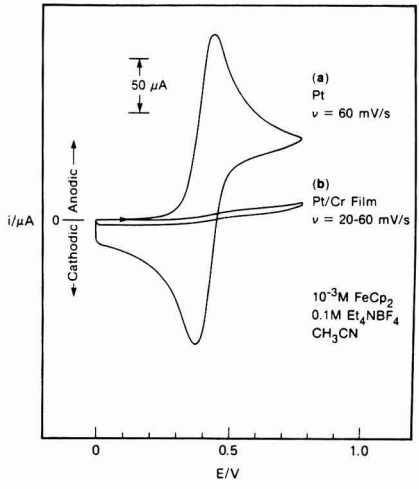


Fig. 7. Cyclic voltammogram for the oxidation of ferrocene in acetonitrile solution containing 0.1M tetraethylammonium tetrafluoroborate. a: Bare platinum electrode. b: Platinum electrode coated with chromium phosphate film.

are quite stable on the electrode in the acetonitrile electrolyte and can be used repeatedly. For example, with the thicker films of chromium phosphate, the electrode was totally insulated from the solution and no current response was observed in the voltammogram, even with repeated scanning between 0 and 1.0V. In contrast with the behavior in aprotic solvent, they are not stable in aqueous solution containing ferrocyanide ion. Electrochemical analysis of this solution with the coated electrodes resulted in the destruction of the film during the anodic scan.

The diffusion of ferrocene across the chromium phosphate film is much slower than has been observed with passivating organic films on electrode surfaces. Diffusion through the organic thin films (600-30,000Å) varies with the structure of the polymer (16). The smallest diffusion coefficients have been observed with polysilanes which have values of 5×10^{-10} cm²/s. The hydrocarbon polymers have values in the range 14-1300 $\times 10^{-10}$ cm²/s.

Conclusions

The electrochemical reduction of Cr(VI) is well behaved in dilute acid solutions. The reaction is electrochemically irreversible and diffusion limited. In aqueous sulfuric acid with low concentrations of Cr(VI), soluble Cr(III) products are formed. In concentrated solutions, the electrode is partially passivated by the formation of insoluble Cr(III) salts. In solutions containing phosphoric acid, insoluble chromium phosphate is formed on the electrode even at dilute Cr(VI) concentrations. The film insulates the total surface very efficiently, and the diffusion of molecules, such as ferrocene, across the film is significantly reduced.

Acknowledgments

The authors wish to thank R. Galwey, A. Tuason, V. H. Le, and L. Van Ness for their technical assistance, and M. Henneberg, R. Balanson, M. Bergkamp, and T. Tilbury for their support of this project.

Manuscript submitted Feb. 4, 1985; revised manuscript received July 15, 1985.

IBM Corporation assisted in meeting the publication costs of this article.

REFERENCES

1. C. W. Ostrander, in "Electroplating Engineering Handbook," 3rd ed., A. K. Graham, Editor, p. 437, Van Nostrand Reinhold Company, New York (1971).
2. S. Wernick and R. Pinner, "The Surface Treatment and Finishing of Aluminum and Its Alloys," 4th ed., Vol. 1, p. 263, Robert Draper Ltd., London (1972).
3. F. A. Lowenheim, "Electroplating," 3rd ed., p. 442, McGraw-Hill Company, New York (1974).
4. B. Laszlone, *Gepgyartastechnologia*, **12,** 495 (1972).
5. W. M. Latimer, "Oxidation Potentials," 2nd ed., Prentice Hall, Inc., New York (1952).
6. A. Diaz, J. I. Castillo, W. Lee, and J. A. Logan, *J. Electroanal. Chem.*, **129,** 115 (1981).
7. "Stability Constants of Metal Ion Complexes," The Chemical Society Special Publication 17," The Chemical Society, London (1964).
8. R. N. Adams, "Electrochemistry at Solid Electrodes," Marcel Dekker, New York (1969).
9. J. Matysik and M. Korolczuk, *J. Electroanal. Chem.*, **88,** 421 (1978).
10. F. M. Delnick and D. K. McCarthy, *This Journal*, **130,** 1875 (1983); see references therein for earlier work on the electrochemical reduction of chromates in molten salt solutions.
11. M. Otto, R. Wagner, and H. Hennig, *Inorg. Chim. Acta*, **64,** L11 (1981).
12. J. P. Hoare, *This Journal*, **130,** 1475 (1983).
13. J. P. Hoare, *Plat. Surf. Finish.*, **71,** 50 (1984).
14. A. J. Wallace, Jr., *ibid.*, **67,** 66 (1980).
15. M. Delmar, M. C. Pham, P-C. Lacaze, and J-E. Bubois, *J. Electroanal. Chem.*, **108,** 1 (1980).
16. A. Diaz and R. D. Miller, *This Journal*, **132,** 834 (1985).

Electrochemical and Metallurgical Aspects of Laser-Enhanced Jet Plating of Gold

M. H. Gelchinski, L. T. Romankiw,* D. R. Vigliotti, and R. J. von Gutfeld*

IBM T. J. Watson Research Center, Yorktown Heights, New York 10598

ABSTRACT

Experimental results for a new plating technique using a laser in combination with a pressurized jet are described. Electrochemical and hydrodynamic parameters affecting the gold deposits are discussed. Scanning electron micrographs of the deposited gold surfaces indicate increased smoothness and decreased nodularity as well as disappearance of voids with increasing laser power density. A marked decrease in voids with increasing laser power is also observed in cross-sectioned samples. At the highest laser power densities used, with a 0.5 mm diam nozzle, plating rates of up to 12 μm/s have been observed. In general, the rate increases with increasing laser power density. Measurements of the Knoop hardness of the deposits gave values in the range characteristic for soft gold.

The development and potential benefits of the laser-enhanced plating (LEP) technique have been described in several previous publications (1-8). Investigations of the experimental parameters, mechanisms, and applications were carried out for laser-enhanced copper plating (1-4) and more recently for laser-enhanced gold plating (5-7). High quality gold deposits, at plating rates of approximately 1 μm/s, were obtained. Recently, it was suggested that the plating rate of LEP is limited by the substrate heat conductivity (10). Based on experimental and theoretical considerations, it is claimed in Ref. (10) that the application of a thin layer of a relatively poor heat conducting material may lead to a higher local heat increase and significantly improved plating rate and selectivity of gold deposits.

We have demonstrated (6, 8) that plating rates in LEP are limited by the concentration of ions in solution and the supply of ions into the plating region. Dendritic or powdery depositions were obtained when plating was carried out from a commercially available plating solution containing as much as 32.4 g/liter (4 tr oz Au/gal) at plating rates greater than 1 μm/s. An attempt to avoid operation at the limiting current density region by using high concentration solutions in conjunction with a higher power laser did not substantially increase the plating rate, though a larger volume per second could be deposited by defocusing the laser to a larger spot size.

To improve the mass transport and consequently the plating rate, we developed a new technique, laser-enhanced jet plating (LEJP) (9), which combines the earlier LEP technique with a free-standing jet of electro-

* Electrochemical Society Active Member.

lyte to achieve localized high speed, resulting in gold-plated spots and lines of high metallurgical quality. The principal advantage of the free-standing jet is its ability to provide a rapid resupply of fresh ions into the region of plating to overcome the mass transport limitation. In addition, the jet stream limits the region of plating without the use of masks. In the present application, the jet stream also acts as an optical waveguide or light pipe for the laser beam. This paper reports the electrochemical and metallurgical aspects of LEJP of gold deposits.

General Concept—Total Internal Reflection

When a light beam emerges from a medium of higher refractive index, such as water, into a lower index medium, such as air, at a finite angle, it is bent away from the normal to the interface as it enters the lower index medium (air). When the incident angle for a water-air interface is greater than 49°, the beam will undergo total internal reflection in the water with the angle of reflection being equal to the angle of incidence. In our experiments, the laser is directed collinearly through an optical window into a free-standing jet of plating liquid. In such a configuration, the jet both resupplies the ions and acts as an optical waveguide to contain the laser beam by reflecting diverging light from the jet periphery-air interface. The waveguide also tends to homogenize the power density in the radial direction.

Experimental Setup and Procedure

The experimental setup is shown in Fig. 1. A CW argon laser beam with maximum output power of 25W was passed through a beam expander prior to entering the cell and focused approximately at the center of the jet orifice with a 50 mm focal length lens. The flow system is comprised of a solution container, a pump which recirculates the electrolyte after impingement on the cathode, and the jet cell. The components of the flow system are connected with polypropylene and tygon tubes. The pump is equipped with 316 stainless steel bearings. The jet cell, shown schematically in Fig. 2, is a hollow Lucite cylinder, consisting of an inlet chamber, maintained under pressure with the jet nozzle. The nozzle is made from a section of capillary tube glassed onto a flat Pyrex plate. The end plates of the cell are quartz windows. A platinum wire serves as an anode and is inserted into the fluid chamber. Air bubbles trapped in the fluid chamber are eliminated by a bleeder valve. A nozzle orifice of 0.5 mm diam is used, giving rise to gold spots of similar diameter. To maintain a constant current, we used a PAR 173 potentiostat set to operate galvanostatically. The cathode is attached to a microprocessor-controlled X-Y-Z table via an extension arm. The Anorad microprocessor also controls the on-off gating of the argon laser and can be made to operate the on-off controls of the potentiostat. Programs we use move the cathode to a desired position, followed by gating on both the laser and potentiostat simultaneously while the jet runs continuously. In several experiments, the potentiostat was controlled manually. Plating takes place only when the current and the laser beam are on.

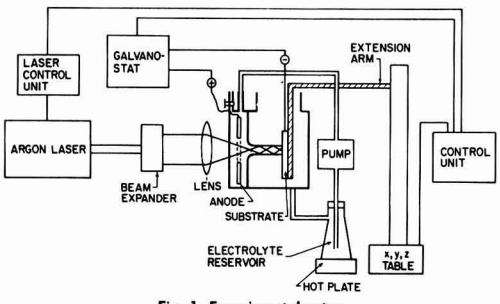


Fig. 1. Experimental setup

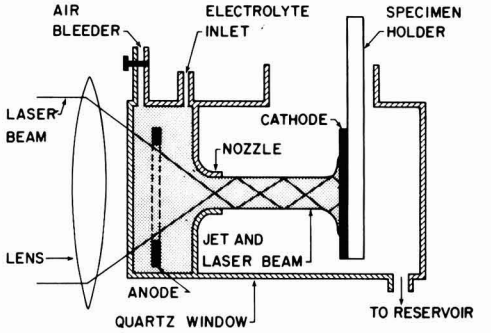


Fig. 2. Schematic representation of the jet cell and the waveguide effect

In either mode of operation, the height of the deposit was measured from the time the sample was moved into position for the particular dwell time programmed with the potentiostat supplying constant current.

For all electroplating runs, we used a high speed cyanide acid solution (Sel-Rex Autronex 55 GV without addition of the cobalt complex) containing 4 tr oz/gal of metallic gold. The electrolyte was preheated to 60°C. The linear flow velocity was 1.0×10^3 cm/s, which corresponds to a Reynolds number of 5.5×10^3 at the nozzle orifice. The nozzle-cathode spacing was typically 0.5 cm.

For metallurgical cross sectioning, the samples were nickel plated prior to mounting in epoxy to preserve the original profile of the deposit during the metallurgical sectioning. After sectioning, the potted samples were polished, etched to reveal the structure, and examined by an optical microscope. Scanning electron microscopy was used to study the morphology of the deposits. Thickness was measured from the photographs of the cross-sectioned samples under the optical microscope. These values agreed with those measured with a Talysurf prior to potting in epoxy.

Results

Jet plating.—Morphology of jet plating deposits at high current densities.—Initial studies were conducted with the jet system without laser irradiation in order to compare the jet-plated gold to LEJP gold under otherwise the same plating conditions. The substrates used were 200 μm (8 mil) thick beryllium-copper, plated with approximately 1 μm nickel from a sulfamate plating bath. To prevent contamination of the gold solution, the substrate was precleaned in acetone and methanol. This cleaning proce-

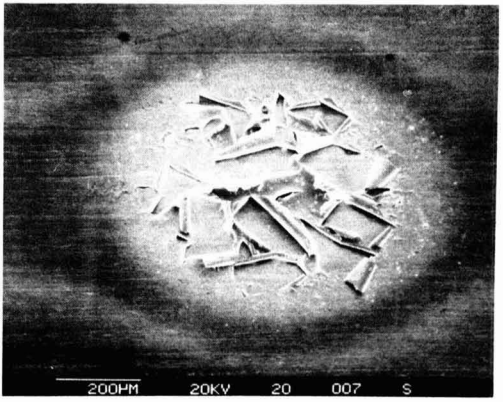
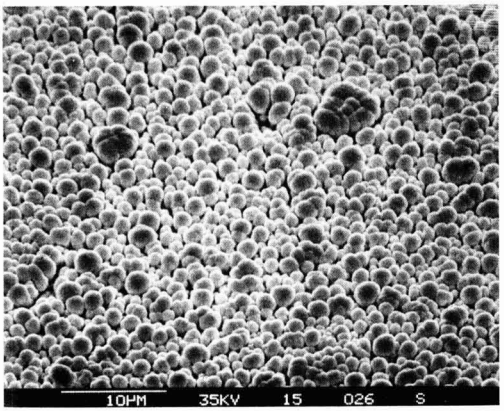


Fig. 3. SEM micrograph of a jet-plated (no laser) gold spot plated at room temperature. Current density ~10 A/cm². (Note that deposition is badly cracked and peeled due to stresses and residual nickel oxide on the substrate.)

dure, however, was insufficient to dissolve the thin native nickel oxide layer usually present on plated nickel.

Plating at room temperature with the aforementioned cleaning procedure at current densities above 5 A/cm² resulted in a cracked deposit which peeled off very easily (Fig. 3) owing mainly to high internal stresses and poor adhesion. Increasing the electrolyte temperature to 60°C resulted in a nodular deposit, shown in Fig. 4a-4b, composed of small, isolated nodules separated by large voids. Cross sections of these deposits are shown in Fig. 5a-5c. One observes large voids throughout the deposit irrespective of film thickness, indicating that the voids initiate at the nickel-gold interface apparently due to a combination of the presence of nickel oxide on the surface (with a resulting low density of nucleation sites) and very high local current density. This type of columnar deposit with columns physically separated from each other is typical of metal deposition resulting from a low density of nucleation sites in combination with plating near or at the limiting current density.

Laser-enhanced jet plating.—Effect of laser power on morphology.—The effect of laser power on the morphological structure of laser-enhanced jet deposits is demonstrated in the scanning electron microscope (SEM) micrographs of Fig. 6a-6d. The deposits were plated for 0.5s at a current density of 12.5 A/cm². Figure 6a shows that deposits obtained with a relatively low laser power result in a nodular microstructure. This surface is composed of uniform, small, isolated nodules separated by open voids which penetrate deeply into the deposit. This morphology is similar to the structure obtained with jet plating without laser irradiation, as shown in Fig. 4. This implies that 10W of laser power (an incident power density of $\sim 5 \times 10^3$ W/cm²) is insufficient to alter the microstructure of the deposit for these particular plating conditions.



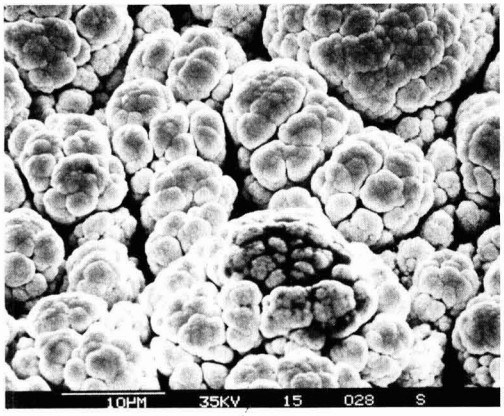


Fig. 4. SEM micrographs of jet-plated (no laser) gold spots plated at 60°C. The current density is 12.5 A/cm². a: Plating time = 1s; thickness ~3 μm. b: Plating time = 10s; thickness ~25 μm.

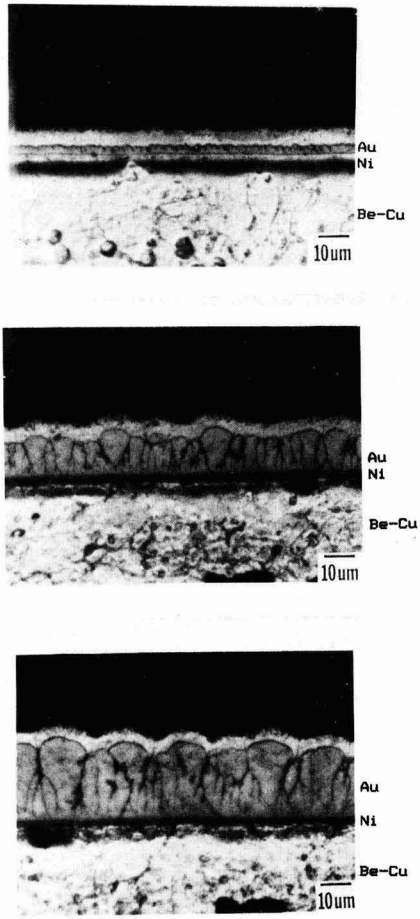


Fig. 5. Cross section of jet-plated gold spots without the use of laser power during deposition. The current density is 11 A/cm². Plating times and resulting thickness are: 1s, 3 μm (a), 5s, 12.5 μm (b), and 10s, 25 μm (c). Note that the voids and pores appear throughout the deposits, irrespective of film thickness.

Increasing the laser power to 15W still resulted in a somewhat nodular deposit (Fig. 6b) although the nodules are larger and more connected. A substantial morphological change occurred when the laser power was raised to 20W (1×10^4 W/cm²), Fig. 6c. This power was sufficient to produce a visually bright, smooth deposit with very few surface cracks and nodules. When the laser power was increased to 25W, a more continuous morphology was produced (Fig. 6d).

The morphological changes caused by the laser illumination in LEJP are more pronounced when thick deposits are produced, as illustrated in Fig. 7a-7d. These deposits were plated for 5s at a current density of 12.5 A/cm². Figures 7a-7c show that the nodules become larger (suggesting large crystallites or grains) as the laser power increases from 10 to 20W. With 10W of laser power, a nodular deposit was obtained. This deposit appears to contain two types of morphologies: small nodules with distinct, tight boundaries which form larger nodules separated by deep voids. At 15W, the number of voids decreases (Fig. 7b). One can also see that the surface of the deposit became smooth. Increasing the laser power to 20W leads to

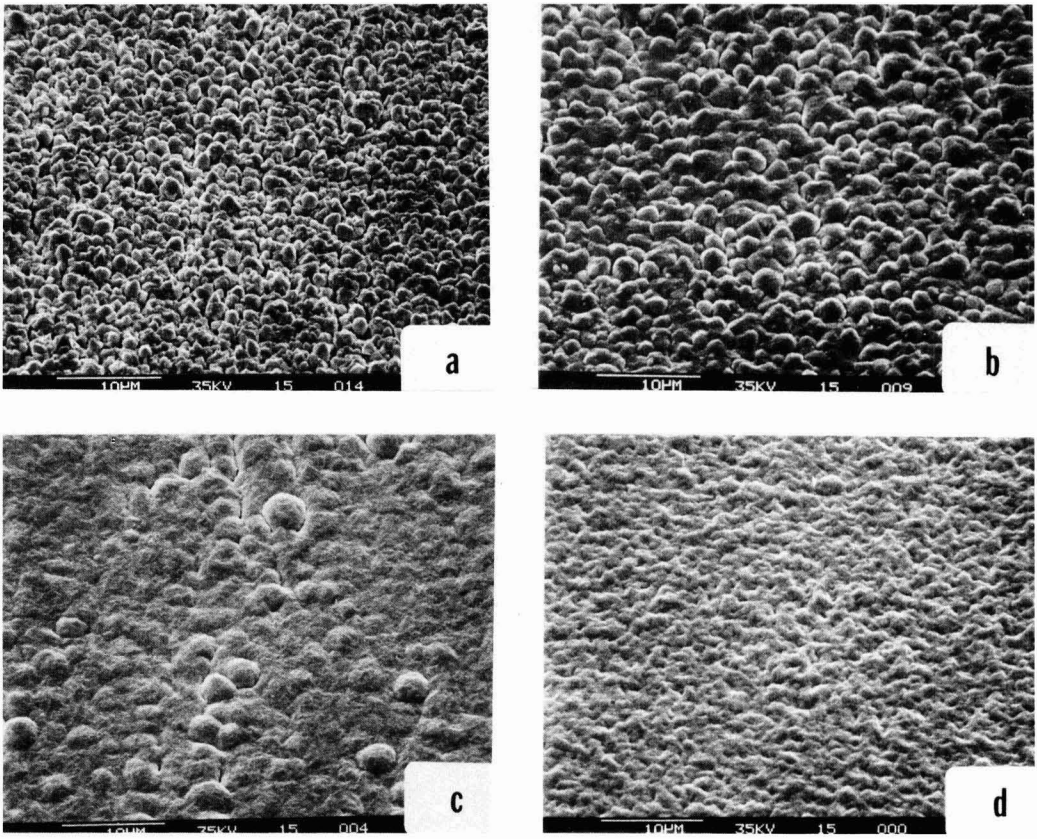


Fig. 6. Effect of laser power on the morphology of LEJP of gold deposits as shown in SEM. The current density is 12.5 A/cm². Plating time = 0.5s. Laser power: 10W (a), 15W (b), 20W (c), 25W (d).

a pronounced morphology modification as shown in Fig. 7c. Here, the structure appears to be that of large crystallites (~10 μm) without voids or cracks. Finally, at 25W, a smooth deposit is produced (Fig. 7d).

Cross-sectioned samples of laser-jet plated gold spots are shown in Fig. 8a and 8b. These deposits were plated at a current density of 12.5 A/cm² in conjunction with 25W of laser power. Examination of their morphology indicates dense deposits consisting chiefly of small crystallites, free of cracks and voids. Upon electroetching, the samples were found to possess a columnar structure, typical of pure soft gold deposits. We have observed a similar behavior in the morphology of gold laser-jet deposits on both copper and beryllium-copper substrates with increasing laser power.

Effect of laser power on plating rate.—The effect of the laser power on the plating rate was measured for deposits plated at a constant current density of 12.5 A/cm². Figure 9 shows the variation of the plating rate as a function of laser power. The curve of Figure 9 is divided into two regions which have two different slopes. The first region, extending from 0 to 15W, results in only a moderate enhancement in the plating rate. Above 15W the rate enhancement due to the laser illumination is significant and reaches ~10 μm/s at 25W, compared to 2.5 μm/s without the laser. This increase in plating rate can be explained in terms of an increase in plating efficiency described in more detal in the Discussion section.

Effect of current density on plating rate and microhardness.—The plating rate, in conjunction with 20W of laser power, increases linearly with the current density, as demonstrated in Fig. 10. This indicates that deposition is carried out at potentials below the limiting current density at a constant plating efficiency.

Microhardness was measured on polished cross sections using a Leitz Miniload microhardness tester with a 25g load. The results of the variation of microhardness with current density are shown in Fig. 11. The Knoop hardness number at a 25g load decreases slightly with increasing current density. Microhardness testing indicates that LEJP from a pure gold solution results in a soft gold deposit, *i.e.*, Knoop values ranging from 70 to 90 kg/mm². The low Knoop values of LEJP deposits are indicative of a high purity deposit and large crystallites, consistent with the morphological findings. It is important to mention that these morphological results are also a function of jet velocity, jet diameter, ambient bath temperature, as well as plating solution parameters.

Discussion

Two factors are probably responsible for the production of the rough, dull, and porous deposits obtained for jet plating, without laser illumination, at high current densities. First, plating was performed near or at the limiting current density. Second, the substrate was covered with a thin native oxide layer. In general, plating at the limiting current density yields a rough nodular or powdery deposit (11, 12) due to the depletion of the ions and due to OH formation at the cathode. For jet-plated deposits, the long voids between the columns are found to occur throughout the film irrespective of thickness, apparently initiating at the nickel-gold interface. This indicates that an oxide layer greatly reduces the number of nuclea-

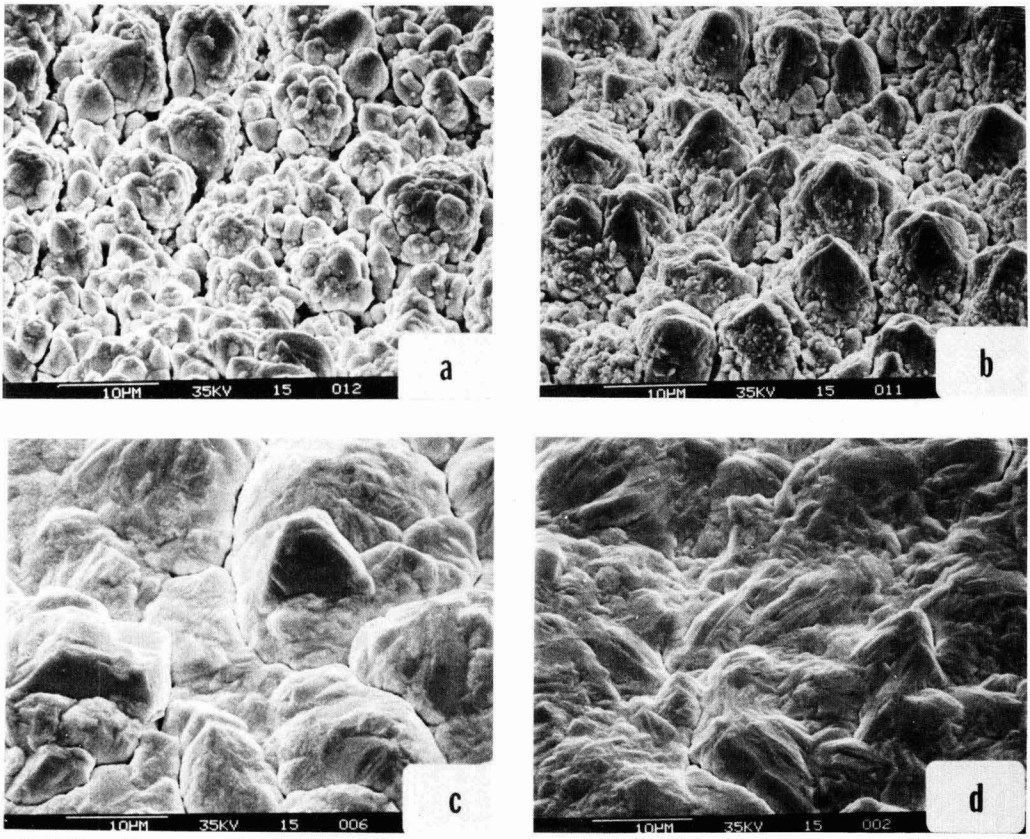


Fig. 7. Effect of laser power on the morphology of LEJP of thick gold deposits as shown by SEM. The current density is 12.5 A/cm^2. Plating time = 5s. Laser power: 10W (a), 15W (b), 20W (c), 25W (d).

tion sites. Because of the very fast deposition rate, the surface mobility of Au ions is insufficient to quickly backfill the voids. This forces the fast growing grains to grow in columns perpendicular to the substrate without making connections in the lateral direction thereby giving rise to voids. Our beryllium-copper substrates have a very thin nickel film so that acid etching was not possible. Based on our previous work, there is evidence that the laser dissolves thin oxides so that elaborate precleaning is not generally required for laser-enhanced plating.

Introducing the laser into the jet system substantially improves the morphology of the deposit and enhances the plating rate. Three major factors may contribute to the enhanced plating rates observed when laser light is absorbed by an electrode: (*i*) an increase in the kinetic rate due to locally higher temperature, (*ii*) increased rates of mass transport due to microstirring arising from locally steep thermal gradients in and around the region of the laser absorption, and (*iii*) a shift in the equilibrium potential to more positive values due to locally higher temperatures. From this study, it appears that there is an increase

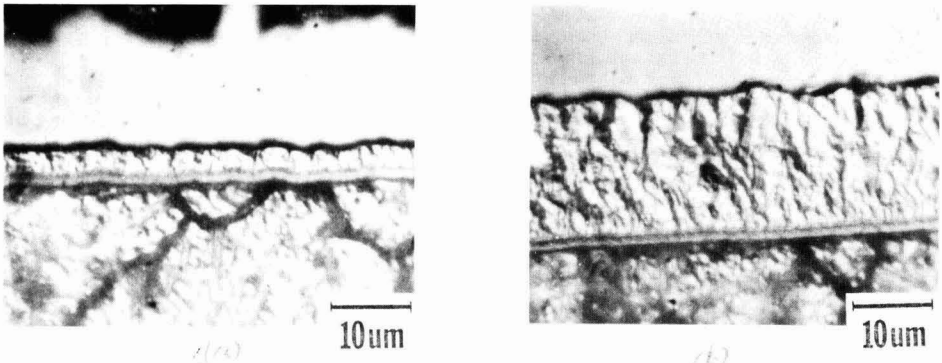


Fig. 8. Cross sections of laser-jet plated gold spots (LEJP) on nickel-plated Be-Cu substrates. The current density is 12.5 A/cm^2. Laser power = 25W. Laser-jet plating times and resulting thicknesses are: 0.5s, 42 μm (a), 2.5s, 18μm (b).

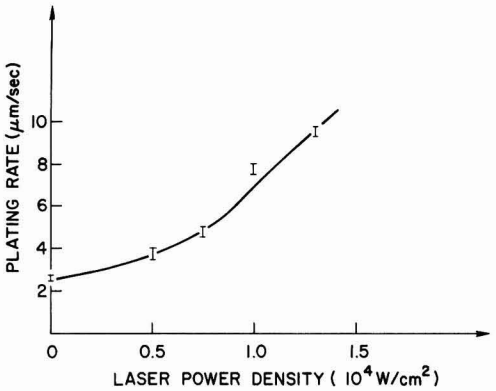


Fig. 9. Influence of laser power density on plating rate of LEJP. The current density is 12.5 A/cm^2.

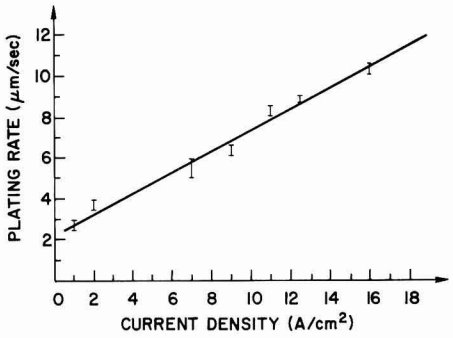


Fig. 10. Effect of current density on LEJP plating rate. The laser power is 20W. (Laser power density = 1.0×10^4 W/cm^2.)

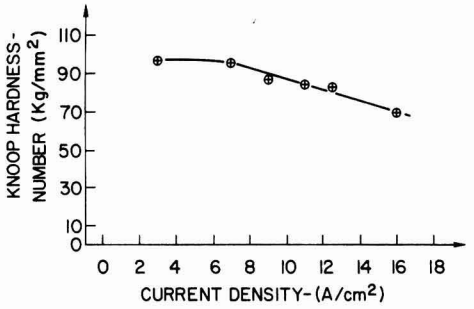


Fig. 11. Effect of current density on LEJP deposit microhardness. Films were deposited at a laser power of 25W. Hardness was measured on the cross-sectioned area with a 25g load.

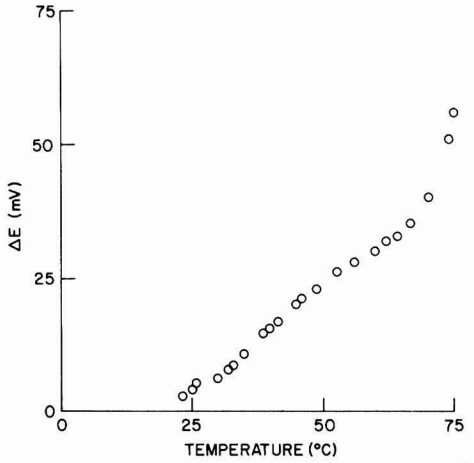


Fig. 12. Shift of the rest potential with temperature for the Sel-Rex Autronex 55 GV solution in absence of cobalt.

in plating efficiency with an increase of the laser power (see Fig. 9).

Figure 12 shows the shift in rest potential in Sel-Rex Autronex 55GV solution used in our experiments as a function of temperature. This shift is approximately 1 mV/°C over the range investigated. This is probably due to a weakening of the gold complex. The laser irradiation shifts the current-voltage curve to more positive potentials. This shift and an increase in surface mobility of Au leads to a dramatic change observed in the morphology of the laser-enhanced deposit.

From the point of view of the morphology of the deposits, without laser irradiation, a typical I-V curve for gold can be divided into two regions: (*i*) a low current density region (low overpotentials) where normally dense deposits are obtained and the plating rate is reasonably efficient, and (*ii*) high current density region where simultaneous hydrogen evolution reaction is substantial. This results in nodular, dendritic, and even powdery deposits at the highest current densities because of the very high rate of hydrogen evolution that occurs simultaneously. At these high current densities, we estimate the plating efficiency from our results to be ~15-20% in the absence of laser radiation and approximately 60% under otherwise the same plating conditions but utilizing 25W of laser power. Due to the shift of the I-V curve to the more positive potentials and an increase in Au surface mobility, it is possible to obtain dense Au deposits in the LEJP plating, while at similar current densities in the absence of laser irradiation, the deposits are nodular and/or powdery. The higher the laser power density, the greater the shift to more positive rest potentials and accompanying decrease of the hydrogen evolution rate. This shift seems adequate to account for the changes observed in the morphology at different laser powers as is seen in Fig. 6a-6d and 7a-7b. We also believe that the laser-heated solution dissolves the nickel oxide on the substrate, creating a clean surface for electrocrystallization. On such a surface, lateral crystallite growth becomes less inhibited. This results in denser deposits. In addition, the dissolution of oxide greatly improves adhesion of the deposit.

The potential shift caused by the laser irradiation can also be used to explain the differences in the plating rates obtained by jet plating and LEJP, at similar current density. Plating at more positive potentials means less hydrogen evolution, *i.e.*, less current consumed for side reactions.

LEJP of gold from a commercial solution (without cobalt complex) possesses a columnar microstructure typical of soft pure gold. The slight decrease in microhardness with the increase of current density cannot be explained at this time.

Acknowledgments

We are grateful for the technical assistance of C. F. Aliotta in obtaining the scanning electron micrographs and for the helpful technical discussions with Dr. D. A. Smith, Dr. R. E. Acosta, and Dr. J. M. Locarnini.

Manuscript submitted Nov. 28, 1984; revised manuscript received *ca.* March 4, 1985.

IBM Corporation assisted in meeting the publication costs of this article.

REFERENCES

1. R. J. von Gutfeld, E. E. Tynan, R. L. Melcher, and S. E. Blum, *Appl. Phys. Lett.*, **35**, 651 (1979).
2. R. J. von Gutfeld, E. E. Tynan, and L. T. Romankiw, Ab-

stract 472, p. 1185, The Electrochemical Society Extended Abstracts, Vol. 79-2, Los Angeles, Oct. 14-19, 1979.
3. J. Cl. Puippe, R. E. Acosta, and R. J. von Gutfeld, *This Journal*, **128**, 2539 (1981).
4. R. J. von Gutfeld, R. E. Acosta, and L. T. Romankiw, *IBM J. Res. Dev.*, **26**, 136 (1982).
5. R. J. von Gutfeld, M. H. Gelchinski, and L. T. Romankiw, Paper 663 RNP presented at the Denver, CO, Meeting of the Society, Oct. 11-16, 1985.
6. M. H. Gelchinski, L. T. Romankiw, and R. J. von Gutfeld, Abstract 131, p. 206, The Electrochemical Society Extended Abstracts, Vol. 82-2, Detroit, MI, Oct. 17-21, 1982.
7. R. J. von Gutfeld, M. H. Gelchinski, and L. T. Romankiw, in "Proceedings of the SPIE Conference on Laser Processes of Semiconductor Devices," SPIE 385, p. 118 (1983).
8. L. T. Romankiw, M. H. Gelchinski, R. E. Acosta, and R. J. von Gutfeld, in "Electroplating Engineering and Waste Recycle—New Developments and Trends," D. D. Snyder, U. Landau, and R. Sard, Editors, p. 66, The Electrochemical Society Softbound Proceedings Series, Pennington, NJ (1983).
9. R. J. von Gutfeld, M. H. Gelchinski, L. T. Romankiw, and D. R. Vigliotti, *Appl. Phys. Lett.*, **43**, 876 (1983).
10. H. K. Kuiken, F. E. P. Mikkers, and P. E. Wierenga, *This Journal*, **130**, 554 (1983).
11. N. Ibl, in "Advances in Electrochemistry and Electrochemical Engineering," Vol. 2, P. Delahay and C. W. Tobials, Editors, p. 49, Interscience, New York (1962).
12. A. R. Despic and Y. I. Popov, in "Modern Aspects of Electrochemistry," Vol. 7, p. 199, Plenum Press, New York (1972).

Mechanisms of Electroless Metal Plating

II. Formaldehyde Oxidation

Perminder Bindra* and Judith Roldan

IBM Corporation, Thomas J. Watson Research Center, Yorktown Heights, New York 10598

ABSTRACT

A detailed investigation of the decomposition of formaldehyde was carried out to account for the fact that formaldehyde decomposition on Group VIII metals, *e.g.*, palladium, occurs without simultaneous hydrogen generation, while on Group IB metals, *e.g.*, copper, formaldehyde decomposition is accompanied by hydrogen evolution. It was found that, in principle, metals may be divided into three main classes: (*i*) metals with positive free energy of hydrogen adsorption, (*ii*) metals with free energy of hydrogen adsorption close to zero, and (*iii*) metals with negative free energy of hydrogen adsorption. In the case of class (*i*) metals, formaldehyde oxidation is accompanied by hydrogen evolution. For class (*ii*) metals, there is no simultaneous hydrogen evolution. Class (*iii*) metals show low catalytic activity for formaldehyde oxidation. Hence, formaldehyde cannot be used as a reducing agent for electroless plating of class (*iii*) metals.

In electrolytic metal deposition, the electrons required for the reduction of the metal ions are supplied by an external current source. In electroless metal deposition, on the other hand, the electrons required for reduction are supplied by the catalytic or electrocatalytic oxidation of a reducing agent. The electrocatalytic oxidation of reducing agents such as methanol has been widely studied (1). Relatively little work has been done on the oxidation of formaldehyde, an important reducing agent for electroless copper deposition (2). It is generally agreed, however, that the oxidation of both of the organic molecules proceeds via dissociative adsorption leading to dehydrogenation as the precursor reaction. The oxidation of formaldehyde in acid media has been shown (3) to proceed as follows

$$HCHO + H_2O \rightarrow CO_2 + 2H_2 \quad [1]$$

In alkaline media, two types of behavior are observed. On Group VIII metals, such as platinum and palladium formaldehyde oxidation occurs without simultaneous hydrogen generation (4), while on Group IB metals, such as copper, silver, and gold, formaldehyde oxidation is accompanied by hydrogen evolution (1a). One of the objectives of this investigation is to account for this behavior. To this end, a quantitative study of the kinetics and mechanism of formaldehyde oxidation on one metal from each group, namely, platinum and copper, has been carried out and the overall stoichiometries of the oxidation reaction on each metal determined.

The second objective has been to determine the effect of the nature of the metal on the electrocatalytic oxidation of formaldehyde. This is a qualitative study in which the catalytic activities of several metals were compared by cyclic voltammetry. The measurements were performed in both acid and alkaline media and the data are plotted in the form of the so-called volcano plots proposed by Balandin (5) for gas phase heterogeneous catalytic reactions and by Parsons (6) and Gerischer (7) for electrocatalytic (electrochemical) reactions.

Experimental

The electrochemical measurements were performed in a standard three-compartment cell. The auxiliary electrode chamber and the reference electrode chamber were separated from the working electrode chamber by sintered glass frits. The potential of the working electrode was monitored via a Luggin capillary with its tip placed 1 mm from the working electrode. Formaldehyde concentrations were estimated using standard quantitative analysis equipment. It is noted that in aqueous (acid) solution formaldehyde exists mainly as a hydrate, methylene glycol, while in alkaline solution the predominant species is methylene glycolate anion (8).

All the solutions were prepared with water purified by running deionized water through a Milli-Q water purification system, Continental Water Systems. Perchloric acid and sodium hydroxide were ultrapure Baker products and were diluted without further purification. Formaldehyde solutions were prepared by dissolving solid paraformaldehyde in pure water to the required concentration and determining the concentration iodometrically (9). Iodine and thiosulfate solutions were also prepared from Baker chemicals by the methods described by Vogel (10). Solutions were deaerated by continuous bubbling with purified argon.

Pine Instruments rotator and electrodes were used for all rotating disk measurements. The electrodes, which had a geometric area of 0.458 cm^2, were polished to a near mirror finish on a wheel using successively finer grades of alumina abrasive. The electrodes were then degreased with alcohol and thoroughly rinsed with purified water before each measurement.

The counterelectrode was a large (10 cm^2) gold foil, and the reference electrodes were Hg/HgO (1*M* NaOH) for

*Electrochemical Society Active Member.

measurements in alkaline solution and Hg/Hg_2SO_4 for measurements in acid solutions, respectively. The electrode potentials are referred to the reversible hydrogen electrode (RHE) at the solution pH.

Cyclic voltammetry and current-potential curves were obtained with a PAR 173 potentiostat in conjunction with a PAR 175 universal programmer. The curves were recorded on a Yokogawa Model 3033 X-Y-t recorder. The charge passed during the formaldehyde decomposition efficiency measurements was recorded with the help of a PAR 179 coulometer. pH values were measured on a Beckman-Altrex pH meter, with a pH electrode designed for measurement at high pH.

Results

Cyclic Voltammetry

Formaldehyde oxidation on noble metals such as Au, Pt, Pd, Rh, and Ir in 1*M* $HClO_4$ was compared by the cyclic voltammetry technique. In 1*M* NaOH solution, the list of metals was extended to include Ag, Cu, and Ni. Cyclic voltammograms for formaldehyde oxidation on some of these metals are described below, and the voltammograms for the other metals are also included but will be described elsewhere (11).

Platinum.—A typical cyclic voltammetry curve for Pt in 0.1*M* HCHO + 1*M* $HClO_4$ is shown in Fig. 1, together with the curve obtained in the base electrolyte. The general features of this voltammogram are similar to the voltammogram for Pt in HCOOH + 0.5*M* sulfuric acid (12). In each case, three peaks occur in the anodic scan, though in the case of formaldehyde the first peak occurs at 0.7V *vs.* RHE instead of at 0.5V *vs.* RHE as for formic acid. This peak is attributed to a simple charge transfer step

$$H_2C(OH)_2 \rightarrow \overset{x}{H}C(OH)_2 + H^+ + e^- \quad [2]$$

where $\overset{x}{H}C(OH)_2$ represents an adsorbed radical occupying a single site on the substrate. The first anodic peak is followed by a "passive" region (as opposed to an "inhibitive" region in the case of formic acid) before the onset of the second oxidation peak. In the second anodic peak, the strongly adsorbed intermediates of the type $\overset{xxx}{C}OH$ are removed from the substrate by oxidation reactions such as

$$\overset{xxx}{C}OH + Pt(OH) \rightarrow \overset{xx}{C}(OH)_2 + Pt \quad [3]$$

$$\overset{xx}{C}(OH)_2 + Pt(OH) \rightarrow \overset{x}{C}OOH + Pt + H_2O \quad [4]$$

$$\overset{x}{C}OOH + Pt(OH) \rightarrow CO_2 + Pt + H_2O \quad [5]$$

With the removal of the strongly adsorbed intermediates, more Pt(OH) sites are created and solution phase formaldehyde is oxidized sequentially to give the following overall stoichiometry

$$H_2C(OH)_2 + 4Pt(OH) \rightarrow CO_2 + 4Pt + 4H_2O \quad [6]$$

It is not clear whether the decrease in current after the second anodic peak is due to the formation of inactive PtO (13) or due to self-poisoning of the formaldehyde oxidation reaction by some sort of a secondary disproportionation reaction (14). In any case, oxidation of formaldehyde does not totally cease after the second anodic peak as in the case of formic acid. At around 1.1V, the current increases rather abruptly, and this increase in current is attributed to the reaction of a $PtO(O)_{ad}$ species with formaldehyde. At 1.25V, the potential scan was reversed.

In the cathodic scan, a broad anodic peak spread over 0.4V is observed. This peak has substructure which indicates two peaks at 0.8 and 0.6V, and the familiar shoulder also observed in the case of formic acid is observed at 0.4V. The peak at 0.8V occurs at approximately the same potential as the first anodic peak and is attributed to the formation of the weakly bound intermediate $\overset{x}{H}C(OH)_2$ via the charge transfer reaction described in Eq. [2]. At more cathodic potentials, the weakly bound $\overset{x}{H}C(OH)_2$ undergoes a disproportionation reaction to give the strongly bound and "poisonous" species $\overset{xxx}{C}OH$ and the current decreases until it reaches zero at ~0.3V.

The cyclic voltammetry curves obtained with and without formaldehyde in alkaline solution are shown in Fig. 2. There is a clear difference in the voltammograms obtained in acid and alkaline media, and it is almost certain that this difference is due to the fact that at pH = 14 the active species in the electrolyte is the methylene glycolate anion, $H_2C(OH)O^-$, while at pH = 0 the active species is the formaldehyde hydrate or methylene glycol, $H_2C(OH)_2$. The fact that surface oxidation on Pt in acid electrolyte commences at 0.8V and in alkaline electrolyte at 0.6V does not seem to have much effect. Formaldehyde oxidation currents are much higher in 1*M* NaOH than in 1*M* $HClO_4$, suggesting that the reaction is base catalyzed. There is no evidence of strongly adsorbed intermediates either in the hydrogen region or in the double-layer region. Inhibition of the oxidation reaction first begins at 0.7V. This may be due to the formation of inactive PtO or a self-poisoning reaction described earlier. The peak at 1.0V in the anodic and cathodic scans is probably due to the formation of $PtO(O)_{ads}$ which is able to react with formaldehyde. The reaction totally ceases at 1.5V. It is tempting to suggest that this is due to the formation of inactive PtO_2 even though it is inconsistent with the results of Biegler *et al.* (15) which show that a complete PtO_2 layer forms at much more anodic potentials.

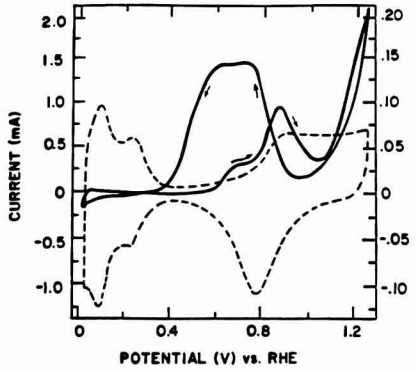


Fig. 1. Cyclic voltammetry curves for Pt in 1M $HClO_4$ (dashed curve, scale on right) and 1M $HClO_4$ + 0.1M HCHO (solid curve). Ar saturated; electrode area = 0.458 cm^2; scan rate = 0.1 V/s; temperature = 25°C.

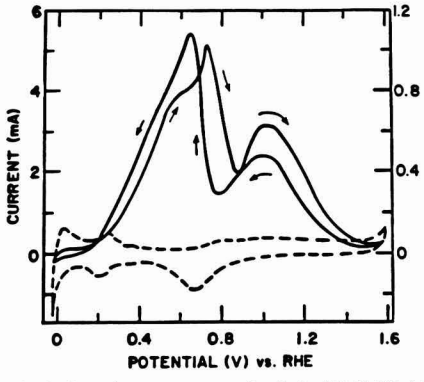


Fig. 2. Cyclic voltammetry curves for Pt in 1M NaOH (dashed curve, scale on right) and 1M NaOH + 0.1M HCHO (solid curve). Ar saturated; electrode area = 0.458 cm^2; scan rate = 0.1 V/s; temperature = 25°C.

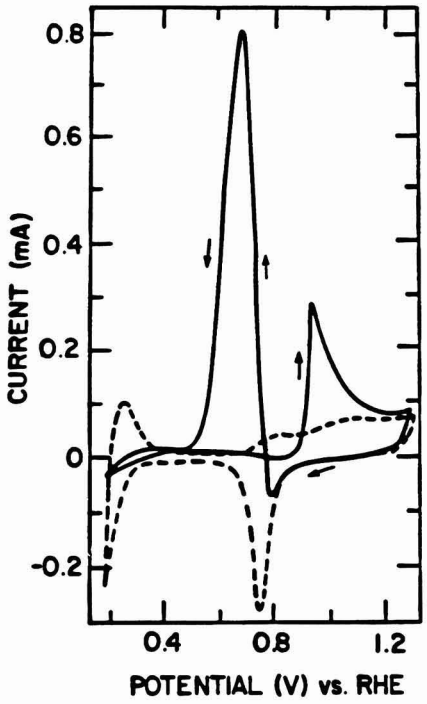


Fig. 3. Cyclic voltammetry curves for Pd in 1M $HClO_4$ (dashed curve) and 1M $HClO_4$ + 0.1M HCHO (solid curve). Ar saturated; electrode area = 0.458 cm^2; scan rate 0.1 V/s; temperature = 25°C.

Palladium.—Figures 3 and 4 show the cyclic voltammetry curves for Pd in the presence and absence of formaldehyde in 1*M* $HClO_4$ and 1*M* NaOH, respectively. In acid solution, there is only one anodic peak in the anodic scan which occurs at 0.95V. Hydrogen adsorption on Pd is suppressed in the presence of formaldehyde in the electrolyte, indicating the presence of strongly adsorbed intermediates on the surface. Between 0.4 and 0.7V, the anodic current in the presence and absence of formaldehyde has the same value. From 0.7V until the anodic peak at 0.95V, the current in the presence of formaldehyde is much lower than the base electrolyte current. This confirms the presence of strongly adsorbed intermediates which prevent the formation of Pd(OH) or PdO. At 0.95V, there is an abrupt increase in current and an asymmetrical peak is observed. This peak is most likely due to the reaction between $PdO(O)_{ads}$ and the poisonous intermediates as well as bulk phase, $H_2C(OH)_2$, just as in the case of Pt in acid solution. The current due to formaldehyde oxidation ceases around 1.2V, presumably due to the formation of inactive PdO_2.

In the cathodic scan, one large anodic peak is observed. This peak commences at the threshold of oxide reduction on Pd. The acceleration of oxide reduction by strongly adsorbing organic intermediates has been described by Capon and Parsons (12). The oxidation peak, however, is rather narrow, suggesting langmuirian adsorption of the intermediate.

The voltammogram obtained in alkaline solution (Fig. 4) is quite different from that obtained in acid solution. It is clear from Fig. 4 that the anodic and the cathodic scans show some hysteresis, though the general formaldehyde oxidation characteristics are the same. In the anodic scan, the first anodic peak occurs at 0.5V. This peak is attributed to the first charge transfer reaction of the type described in Eq. [2]. The reduction in current following the peak is due to surface coverage by strongly adsorbed intermediates. The large peak at 0.85V is, as in the case of Pt in alkaline solution, due to the interaction of Pd(OH) with formaldehyde. The reduction in current is due either to the formation of inactive PdO or a self-poisoning secondary reaction. In the cathodic scan, there is one large anodic peak at 0.7V and two shoulders at 0.65 and 0.4V. The anodic peaks in the cathodic and anodic scans are of approximately the same magnitude. The cyclic voltammetry curves for formaldehyde oxidation in 1*M* NaOH on Pt and Pd are quite similar. The catalytic activity is slightly greater for Pd.

Nickel.—The cyclic voltammetry curves obtained with and without formaldehyde in 1*M* NaOH solution are shown in Fig. 5. In the base electrolyte, only one peak is observed during the anodic scan. This peak occurs at 0.55V and is attributed to the chemisorption of an OH layer to form NiOH or $Ni(OH)_2$. The rapidly increasing current at potentials exceeding 0.8V is due to the formation of phase oxide. In the cathodic scan, the phase oxide reduction appears reproducible but there is no complimentary peak for the desorption of the OH layer. This suggests that a breakdown of the adsorbed layer is required in order to nucleate the growth of the phase oxide.

In the presence of formaldehyde, hydrogen adsorption on Ni is suppressed. The anodic peak at 0.55V due to the adsorption of OH is no longer there as the surface is pre-

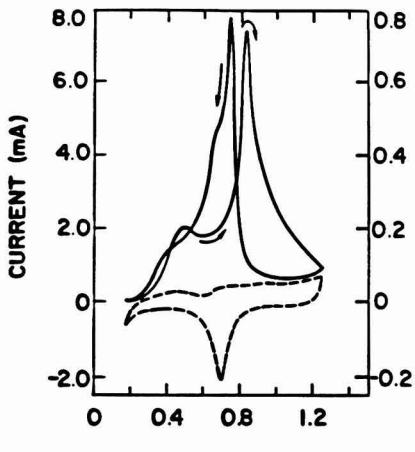


Fig. 4. Cyclic voltammetry curves for Pd in 1M NaOH (dashed curve, scale on right) and 1M NaOH + 0.1M HCHO (solid curve). Ar saturated; electrode area = 0.458 cm^2; scan rate = 0.1 V/s; temperature = 25°C.

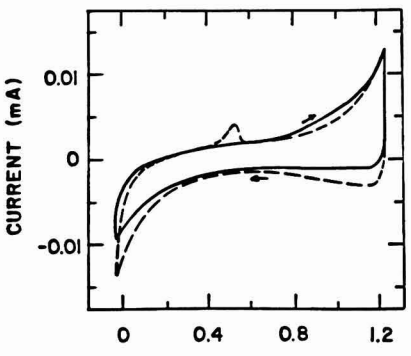


Fig. 5. Cyclic voltammetry curves for Ni in 1M NaOH (dashed curve) and 1M NaOH + 0.1M HCHO (solid curve). Ar saturated; electrode area = 0.458 cm^2; scan rate = 0.1 V/s; temperature = 25°C.

ferentially covered by carbonaceous radicals. Oxidation of such radicals or of methylene glycolate anion occurs at potentials greater than 0.6V. There is suppression of the phase oxide formation until the adsorbed species have been oxidized from the surface. Clearly, Ni is not a very good catalyst for formaldehyde oxidation. Hence, formaldehyde is not used as a reducing agent in electroless Ni plating solutions even though the decomposition potential is favorable for such an application.

Copper.—The cyclic voltammetry curve for copper in 1*M* NaOH + 0.1*M* HCHO is given in Fig. 6 together with the background curve. The first anodic peak in the background curve is attributed to the formation of Cu_2O. At slow scan rates (dv/dt < 10 mV/s), this peak is preceded by a prepeak at 0.55V due to $Cu(OH)_2^-$ formation. The current between 0.8 and 1.0V increases as $Cu(OH)_2$ is formed and decreases when the passivating species CuO forms. There is some evidence of film dissolution in this potential range. At around 1.2V the anodic current increases again, probably due to the reaction Cu(II) → Cu(III) (16). The background curve shows a cathodic peak at 0.5V. This peak is due to the reduction of Cu_2O. The cathodic peak which starts at around 0.2V is due to the reduction of a surface layer by consisting of more than one species. The Cu/NaOH system is very complex and requires more work for full interpretation than expended in this study.

In the presence of formaldehyde, the first anodic peak occurs at 0.55V as a result of the reaction of formaldehyde on the freshly reduced Cu surface. This peak has been used for the volcano plots and other analysis. Cu_2O is not catalytically active. The interaction of formaldehyde with $Cu(OH)_2$ causes a large increase in the anodic current at 0.8V. The current decreases at 0.9V as a result of the formation of inactive CuO. Once the inactive CuO has been removed via dissolution (16) or the conversion of Cu(II) to Cu(III), a large anodic current due to the oxidation of formaldehyde on the fresh Cu surface appears again. During the cathodic sweep, the curve in the presence of formaldehyde coincides with the background curve until 0.25V when a large cathodic current due to formaldehyde reduction is seen.

Silver and gold.—The cyclic voltammogram for Ag in 1*M* $HClO_4$ (Fig. 7) is essentially featureless. There is hardly any evidence of hydrogen adsorption prior to hydrogen evolution at around 0 V. In the anodic scan, oxide formation is immediately proceeded by Ag dissolution. A peak due to oxide reduction and/or Ag deposition is seen at 0.7V in the cathodic scan. In the presence of formaldehyde in the acid solution, the cyclic voltammogram is hardly affected. There is suppression of the hydrogen adsorption/evolution current and oxide formation is somewhat inhibited, but there is no clear evidence of formaldehyde adsorption or oxidation. In alkaline solution (Fig. 8), the base electrolyte curve on Ag shows evidence for the formation and stripping of "Ag-oxides," but the currents are very small. In the presence of formaldehyde, there is an abrupt increase in the anodic current at around 0.2V. A broad oxidation peak is observed which is asymmetrical and has the maximum at 0.4V. Between 0.4 and 1.1V, the anodic current is due to the oxidation of adsorbed as well as solution phase formaldehyde. As the solution phase formaldehyde is depleted in the vicinity of the electrode, the oxidation current comes down. This also accounts for the decreasing current in the cathodic scan.

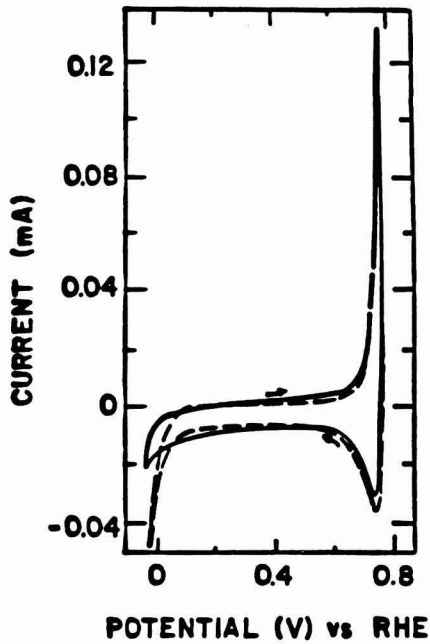


Fig. 7. Cyclic voltammetry curves for Ag in 1M $HClO_4$ (dashed curve) and 1M $HClO_4$ + 0.1M HCHO (solid curve). Ar saturated; electrode area = 0.458 cm^2; scan rate = 0.1 V/s; temperature = 25°C.

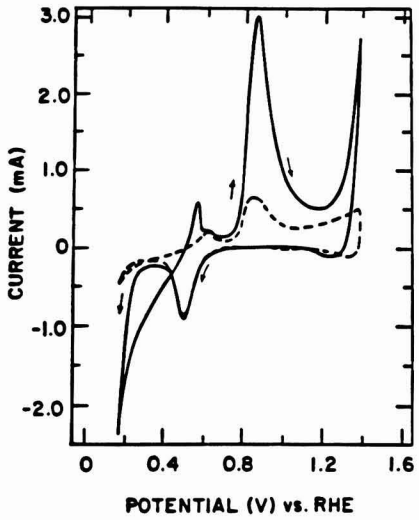


Fig. 6. Cyclic voltammetry curves for Cu in 1M NaOH (dashed curve) and 1M NaOH + 0.1M HCHO (solid curve). Ar saturated; electrode area = 0.458 cm^2; scan rate = 0.1 V/s; temperature = 25°C.

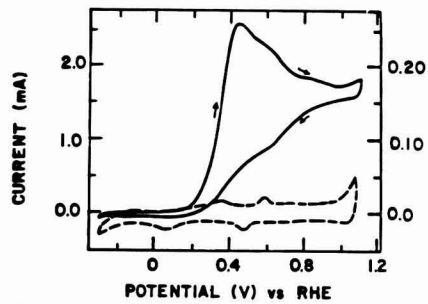


Fig. 8. Cyclic voltammetry curves for Ag in 1M NaOH (dashed curve, scale on right) and 1M NaOH + 0.1M HCHO (solid curve). Ar saturated; electrode area = 0.458 cm^2; scan rate = 0.1 V/s; temperature = 25°C.

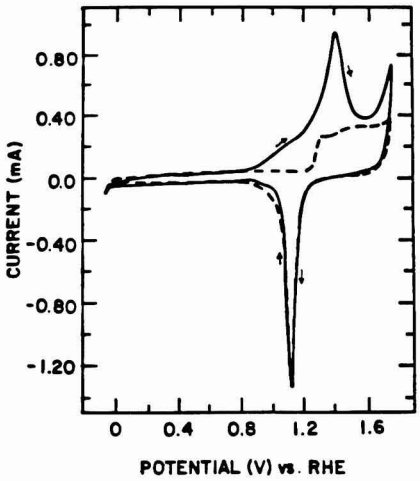


Fig. 9. Cyclic voltammetry curves for Au in 1M $HClO_4$ (dashed curve) and 1M $HClO_4$ + 0.1M HCHO (solid curve). Ar saturated; electrode area = 0.458 cm^2; scan rate = 0.1 V/s; temperature = 25°C.

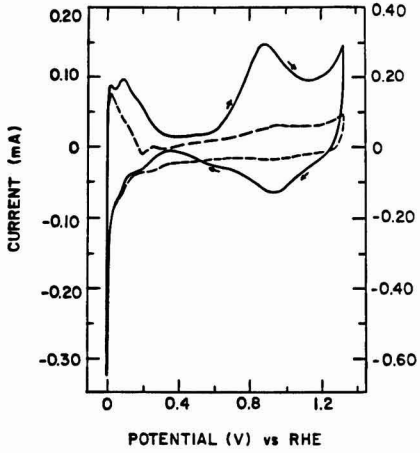


Fig. 11. Cyclic voltammetry curves for Ir in 1M $HClO_4$ (dashed curve) and 1M $HClO_4$ + 0.1M HCHO (solid curve). Ar saturated; electrode area = 0.458 cm^2; scan rate = 0.1 V/s; temperature = 25°C.

The cyclic voltammetry curve obtained in the presence and absence of formaldehyde in acid and alkaline electrolytes on Au are shown in Fig. 9 and 10, respectively. In acid solution, the double-layer region on gold is extensive and OH adsorption commences at 1.2V. There is hardly any evidence of formaldehyde oxidation at room temperature. At slightly elevated temperature, three peaks due to formaldehyde oxidation are observed in the anodic scan. This suggests that the activation energy for formaldehyde adsorption on Au is rather low. Each of the anodic peaks is associated with the adsorption of −OH species on the Au surface, suggesting once again that −OH catalyzes the formaldehyde oxidation reaction. In alkaline solution, −OH adsorption on Au occurs around 0.7V. However, this does not seem to affect the formaldehyde oxidation reaction which begins at 0.2V in the anodic scan. There is an anodic peak at 0.4V and some structure between 0.4 and 0.8V; otherwise, there is a steady oxidation current until 1.2V. At 1.2V, the formation of AuO or Au_2O_3 passivates the gold surface and formaldehyde oxidation current is gradually reduced. In the cathodic scan, there is evidence of the oscillatory phenomena observed for carbonaceous reducing agents on solid electrodes. The anodic peak at 1.1V during the cathodic sweep is attributed to this oscillatory behavior. This peak potential is a function of the sweep rate.

Iridium and Rhodium.—Figures 11 and 13 show the cyclic voltammetry curves for Ir and Rh in 0.1*M* HCHO + 1*M* $HClO_4$, respectively. The base electrolyte curves show that the "double-layer" regions for Ir and Rh are much smaller than the "double-layer" region for Pt. The oxide reduction peak on Rh occurs at ~0.4V *vs.* RHE, while for Ir there is no distinct oxide reduction peak but the cyclic voltammogram is symmetrical about the potential axis in the oxygen adsorption region. In the case of Rh, there is clear evidence that during the anodic scan, OH adsorption on the metal is suppressed in the presence of formaldehyde in the solution. This is followed by a large asymmetrical peak due to formaldehyde oxidation,

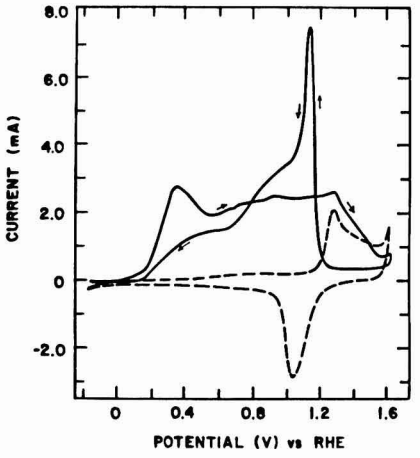


Fig. 10. Cyclic voltammetry curves for Au in 1M NaOH (dashed curve) and 1M NaOH + 0.1M HCHO (solid curve). Ar saturated; electrode area = 0.458 cm^2; scan rate = 0.1 V/s; temperature = 25°C.

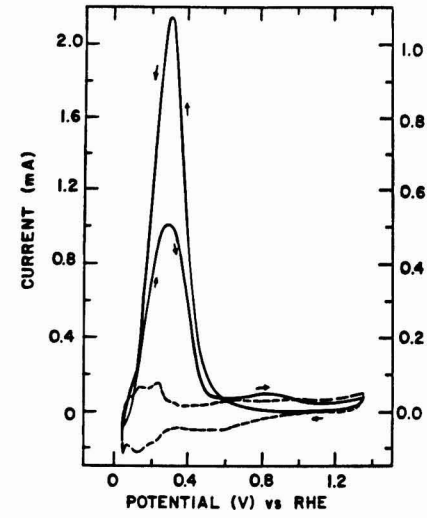


Fig. 12. Cyclic voltammetry curves for Ir in 1M NaOH (dashed curve) and 1M NaOH + 0.1M HCHO (solid curve). Ar saturated; electrode area = 0.458 cm^2; scan rate = 0.1 V/s; temperature = 25°C.

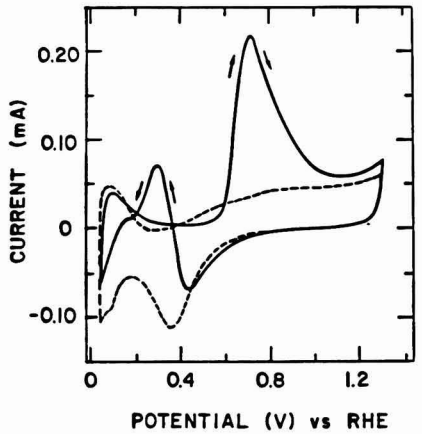


Fig. 13. Cyclic voltammetry curves for Rh in 1M $HClO_4$ (dashed curve) and 1M $HClO_4$ + 0.1M HCHO (solid curve). Ar saturated; electrode area = 0.458 cm^2; scan rate = 0.1 V/s; temperature = 25°C.

demonstrating that formaldehyde oxidation is catalyzed by Rh(OH) species. The decrease in current is due to the formation of inactive RhO or Rh_2O_3. In the cathodic scan, an anodic peak at 0.3V and a shoulder at 0.2V are observed. The anodic peak is attributed to the first dehydrogenation reaction (Eq. [2]) leading to the formation of weakly bound $\overset{x}{H}C(OH)_2$ species and the shoulder is due to the disproportionation of this species. In general, the behavior of formaldehyde in acid electrolyte on Rh resembles its behavior on Pt.

For Ir, in the presence of formaldehyde there are several peaks during the anodic scan. In this case, hydrogen adsorption is not suppressed; in fact, there are two peaks due to formaldehyde oxidation in the hydrogen adsorption/desorption region. The current begins to rise again at 0.6V and a broad peak appears at around 0.9V, indicating that the adsorption of OH on Ir also catalyzes formaldehyde oxidation. During the cathodic scan, there is further evidence of formaldehyde oxidation between 0.4 and 0.2V.

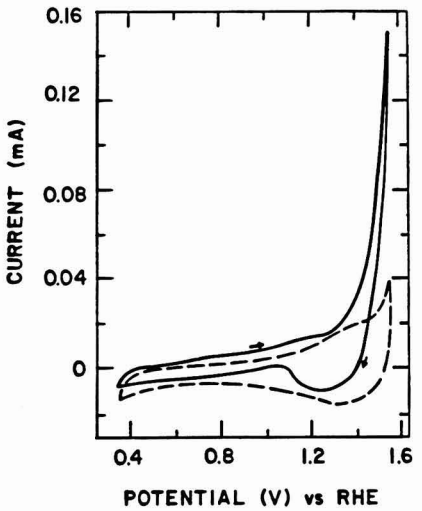


Fig. 14. Cyclic voltammetry curves for Rh in 1M NaOH (dashed curve) and 1M NaOH + 0.1M HCHO (solid curve). Ar saturated; electrode area = 0.458 cm^2; scan rate = 0.1 V/s; temperature = 25°C.

Figures 12 and 14 show the cyclic voltammetry curves for Ir and Rh in the presence and absence of formaldehyde in 1*M* NaOH, respectively. Rh shows a fairly featureless curve in the base electrolyte. In the presence of formaldehyde, there is a dramatic increase in current at ~1.3V *vs.* RHE. Ir shows a somewhat broadened hydrogen adsorption region in alkaline solution. In the presence of formaldehyde, there is an abrupt increase in current in the hydrogen region leading to a broad peak at 0.3V. In the cathodic scan, the current due to formaldehyde oxidation begins to set at 1.0V, long before oxide reduction is complete. The anodic peak in the cathodic scan also occurs at 0.3V and is at least twice the magnitude of the anodic peak during the anodic scan. Data not published here have shown that these peaks are a function of temperature and that at high temperatures the two peaks are of the same magnitude. Clearly, formaldehyde oxidation of Ir is quite complex and has been described in detail in a subsequent publication (11).

Kinetic Parameters

Tafel slopes.—A potential step method was used to obtain Tafel plots on platinum substrates free from strongly adsorbed intermediates. The technique involved pretreatment of the electrode at an anodic potential (1.0V *vs.* RHE) where the strongly adsorbed intermediates are oxidized, prior to stepping the potential into the potential region where oxidation of formaldehyde first begins. Currents are measured on electrodes rotated at 1600 rpm, at a standard time interval of 1s after the application of the potential step. Hardly any hysteresis was observed when the potential was retraced. No corrections for the IR drop were made, as the measurements were performed in the region of low current densities where this correction was found to be insignificant. The Tafel plots on copper electrode were constructed from polarization data obtained by the potentiodynamic method. The potential scan rate was 100 mV/s. Tafel plots for formaldehyde oxidation on platinum and on copper are shown in Fig. 15. These plots yield Tafel slopes of 150 ± 5 and 180 ± 5 mV/decade for platinum and copper, respectively.

Reaction orders.—Reaction orders were ascertained with respect to formaldehyde and hydroxide ion only. The reaction order for the reduction of the formate ion, while desirable, is difficult to measure and therefore was not attempted.

Formaldehyde.—Peak currents for the large cathodic peak at varying concentrations of formaldehyde yielded a reaction order of 0.9 ± 0.15 for platinum. Confirmation of first order was obtained from rotating disk data which yielded linear plots of $1/i$ *vs.* $1/\sqrt{\omega}$ (17). The complete rotating disk electrode data will be given elsewhere (11). In the case of copper electrode, the first anodic oxidation peak current was plotted as a function of formaldehyde concentration. Figure 16 shows that the reaction order with respect to formaldehyde on copper is similar to that on platinum and has a value of 0.9 ± 0.1.

Hydroxide ion.—The pH dependence of formaldehyde oxidation was examined over the range 12.0-13.7 by adding varying amounts of concentrated $HClO_4$ to 0.1*M*

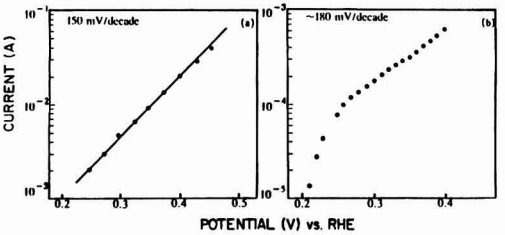


Fig. 15. Tafel plot for HCHO oxidation in 1M NaOH. Ar saturated; electrode area = 0.458 cm^2. a: Platinum. b: Copper. Temperature = 25°C.

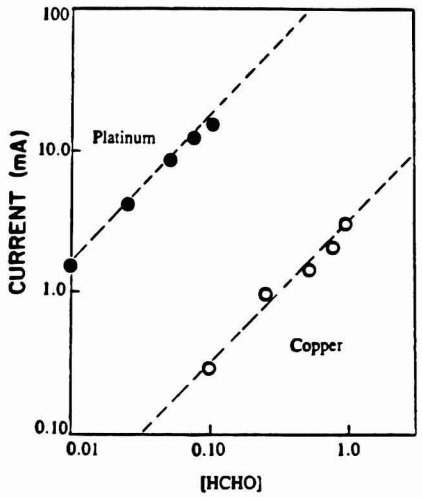


Fig. 16. Reaction order for oxidation of HCHO in Ar-saturated 0.1M HCHO + 1M NaOH. Electrode area = 0.458 cm^2; scan rate = 0.1 V/s; temperature = 25°C.

HCHO in 1*M* NaOH. Plots of peak currents against *p*H (the large cathodic peak for platinum and the first anodic peak for copper) yielded a reaction order of 0.5 in hydroxide ion for Cu and of 0.0 for Pt. These plots are displayed in Fig. 17. A fractional reaction order implies participation of the hydroxide ion via an adsorbed state, thus confirming that in the case of Cu substrate the anodic peak is due to catalysis by $Cu(OH)_2^-$. A reaction order of 0, as in the case of Pt, implies that the reaction is independent of hydroxide ion concentration in the solution.

Stoichiometric number ν.—The stoichiometric number, ν, is generally evaluated either by the activation polarization resistance method (18) or from the anodic and cathodic transfer coefficients (19). These methods could not be applied here because neither the current-potential curves for formaldehyde oxidation at low overpotentials nor the transfer coefficient for formate reduction could be measured. ν was therefore evaluated by applying the Allen and Hickling (20) graphical treatment to the general equation for a multistep reaction (21). This equation has the form

$$i = i_o \left\{ \exp\left[\left(\frac{n-\vec{\gamma}}{\nu} - r\beta \right) \frac{\mathbf{F}\eta}{RT} \right] - \exp\left[-\left(\frac{\vec{\gamma}}{\nu} + r\beta \right) \frac{\mathbf{F}\eta}{RT} \right] \right\} \quad [7]$$

where η is the overpotential, $\vec{\gamma}$ is the number of electrons transferred before the rds in the electronation reaction or the number of electrons transferred after the rds in the de-electronation reaction, n is the number of electrons involved in the overall reaction, β is the symmetry factor of the rds, and r is the number of electrons involved in the rds. The graphical treatment of Allen and Hickling (20) gives a linear plot of $\log \{i/1 - \exp(-n\mathbf{F}\eta/\nu RT)\}$ against η for the appropriate value of ν. Plots of $\nu = 1$ and $\nu = 2$ are shown in Fig. 18 for platinum and for copper. It is evident from Fig. 18 that $\nu = 1$ for platinum and $\nu = 2$ for copper. The slope of these plots is $[(n - \gamma)/\nu - r\beta]\, RT/\mathbf{F}$. The numerical values observed in Fig. 18 are 150 mV/decade for platinum and 180 mV/decade for copper, similar to the Tafel slopes observed in Fig. 15.

Discussion

Reaction mechanisms.—The mechanism of formaldehyde oxidation on Pt and on Cu in alkaline media is discussed in this section. Under Langmuir adsorption conditions, the transfer coefficient obtained from the Tafel plot is equal to the transfer coefficient yielded by the Allen-Hickling analysis (Fig. 18), *i.e.*

$$\alpha_a = \frac{n - \vec{\gamma}}{\nu} - r\beta \quad [8]$$

Equation [8] is solved for $\vec{\gamma}$ by inserting the appropriate values for the other parameters. n was evaluated by measuring the coulombic efficiency for formaldehyde oxidation of Pt and Cu (see Fig. 21), while the value of ν on each metal was obtained from the Allen-Hickling plots. The values of r and β were assumed to be 1 and 0.5, respectively, for each substrate. $r = 0$ is rejected because a symmetry factor is needed for an electron transfer step, and $r = 2$ is improbable, as a two-electron transfer would require very high activation energy. The values of the kinetic and mechanistic parameters are collected in Table I.

It is clear from Table I that the Tafel slope for formaldehyde oxidation on both platinum and on copper is $RT/\alpha\mathbf{F}$ with α values substantially less than 0.5. This indicates specific adsorption of reacting species or intermediates (22) and suggests an ihp mechanism in which the first electron transfer is rate determining. The data given in Table I are compatible with the following sequence of steps.

$$H_2C(OH)O^- \rightleftarrows [H_2C(OH)O^-]_{ads} \quad [i]$$

$$[H_2C(OH)O^-]_{ads} + OH^- \xrightarrow{rds} HCOO^- + H_2O + \underset{M}{H} + e^- \quad [ii]$$

$$\underset{M}{H} + OH^- \rightleftarrows M + H_2O + e^- \quad [iii]$$

or

$$2\underset{M}{H} \rightleftarrows 2M + H_2\uparrow \quad [iv]$$

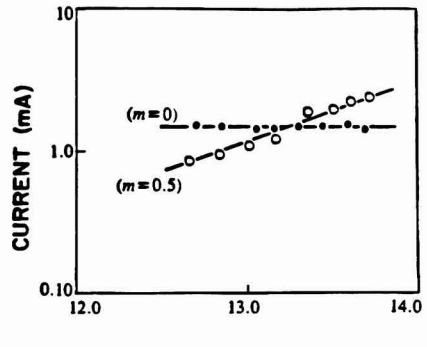


Fig. 17. Dependence of HCHO oxidation on *p*H for (solid circles) Pt and (open circles) Cu in Ar-saturated 1M NaOH + 0.1M HCHO. Electrode area = 0.458 cm^2; scan rate = 0.1 V/s; temperature = 25°C.

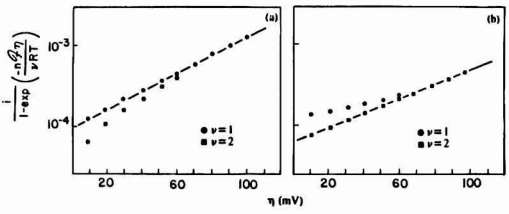


Fig. 18. Allen and Hickling type plots for stoichiometric number determination at Pt (a), and Cu (b).

Table I. Kinetic and mechanistic parameters

	$\frac{\partial V}{\partial \log i}$	$\frac{\partial \log i}{\partial \log C_F}$	$\frac{\partial \log i}{\partial \log C_{OH^-}}$	α_a	n	ν	τ	β	γ
Platinum	150 ± 5	1	0	0.4	2	1	1	0.5	1
Copper	180 ± 5	1	0.5	0.33	1	2	1	0.5	0

M in the above reaction scheme represents the substrate. Steps (*i*), (*iii*), and (*iv*) are in quasi-equilibrium.

The rate equation for the reaction on platinum, based on the data in Table I, is

$$\vec{i} = \vec{k}\,\mathbf{F}C_F(1-\theta_F-\theta_H)\exp(i-\beta)\frac{\mathbf{F}E}{RT}\exp-(1-\delta)(r_F\theta_H + r_M\theta_M) \quad [9]$$

where C_F = concentration of formaldehyde, θ_F and θ_M are the coverages of methylene glycol anion (MGA) and hydrogen, respectively, and r_F and r_M are the interaction coefficients for adsorbed MGA and hydrogen, respectively. δ represents the activation coefficient in the case of charge transfer from the adsorbed state and is given by $0 \leq \delta \leq 1$. In the case of platinum, Table I shows that $\vec{\gamma} = 1$, *i.e.*, one electron is transferred before the rds in the cathodic reaction, or, in this case, the anodic rds is followed by a reversible electron transfer step so that the complete stoichiometry of the reaction on Pt is obtained by adding steps (*i*), (*ii*), and (*iii*), *i.e.*

$$H_2C(OH)O^- + 2\,OH^- \rightarrow 2HCO_2^- + 2H_2O + 2e^- \quad [10]$$

The mechanism described in Eq. [10] is similar to that proposed by Buck and Griffith (3) for formaldehyde oxidation on Pt in 1*M* KOH.

In the case of copper, the oxidation current is obtained by multiplying the right-hand side of Eq. [9] by $C_H^{0.5}$, as in this case $\partial i/\partial C_H = 0.5$ (Table I). The stoichiometry number is 2, so that the overall stoichiometry of formaldehyde oxidation on Cu is obtained by adding steps (*i*), (*ii*) and (*iv*)

$$2H_2C(OH)O^- + 2\,OH^- \rightarrow 2HCO_2^- + 2H_2O + H_2\uparrow + 2e^- \quad [11]$$

This mechanism is in agreement with the proposal of Lukes (4).

Volcano plots.—Volcano plots provide a useful means for comparing the electrocatalytic activities of metals or alloys toward certain reactions. True volcano curves are obtained by plotting the actual catalytic activities as a function of the free energy of adsorption of the reactant or a reaction intermediate (6). Capon and Parsons (12) have shown that, for the electrochemical oxidation of formic acid on various noble metals, a plot of the relative catalytic activity against the formate heat of formation, obtained via gas phase measurements by Sachtler *et al.* (23), gives a volcano-type plot. Such a plot therefore suggests that HCOO-M is a likely intermediate in the HCOOH oxidation pathway.

In this investigation, the relative catalytic activities of various metals toward formaldehyde oxidation were obtained from cyclic voltammograms by the Capon and Parsons (12) method. When these approximate catalytic activities are correlated with the formate heats of formation, volcano-type curves are obtained as shown in Fig. 19 and 20. In acid media (Fig. 19), the convex relation obtained is quite similar to the curve obtained by Capon and Parsons for HCOOH oxidation. It is therefore logical to assume that HCOO-M is also the weakly bound intermediate in the formaldehyde oxidation pathway. Under the circumstances, formaldehyde oxidation in acid media may simply be described as

$$H_2C(OH)_2 \rightarrow HCOOH \rightarrow CO_2 \quad [12]$$

In alkaline media, there is little doubt that $HCOO^-$ is an intermediate. In fact, on metals such as Pt, a larger overpotential is necessary to oxidize the $HCOO^-$ further to CO_3^{2-} (1a). It is therefore quite appropriate that Fig. 20 should show a volcano-type correlation. The shapes of the volcano curves are, however, not very helpful in determining the reaction mechanism (6). Consequently, Fig. 20 does not explain why on certain metals such as Ag and Cu formaldehyde oxidation is accompanied by hydrogen evolution while on metals such as Pt and Pd formaldehyde oxidation proceeds without simultaneous hydrogen generation. An explanation for this behavior can be found by examining the detailed mechanism of formaldehyde oxidation on the two types of metal described in the previous section. On Pt, the dehydrogenation reac-

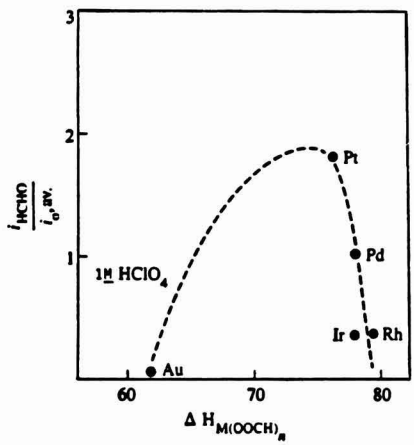


Fig. 19. Plot of the relative catalytic activity for HCHO oxidation in 1M $HClO_4$ as a function of enthalpy of formation of metal formate.

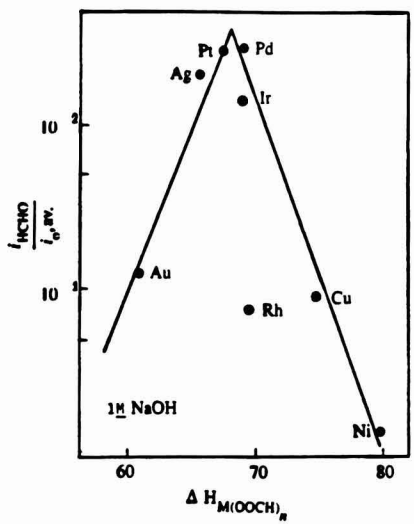


Fig. 20. A plot of HCHO oxidation currents in 1M NaOH vs. enthalpy of formation of metal formate.

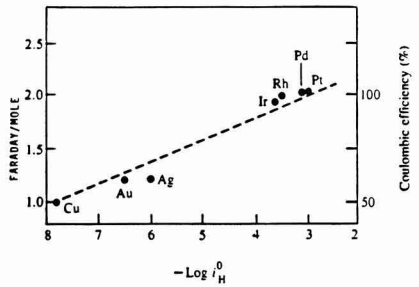


Fig. 21. Plot of coulombic efficiency for HCHO oxidation in 1M NaOH against i_H^0 on various metals.

tion and rds are followed by a hydrogen ionization reaction (reaction scheme [*i*]-[*iv*]). At the potentials at which formaldehyde oxidation on Pt occurs, the hydrogen oxidation reaction is entirely possible. On copper, the rds occurs twice, and this is then followed by hydrogen radical recombination reaction. Presumably, at the potential at which formaldehyde oxidation on copper takes place, hydrogen recombination and evolution is kinetically more favorable than hydrogen ionization, though thermodynamically at these potentials hydrogen ionization is the favored reaction. This suggests that whether formaldehyde oxidation on a substrate is accompanied by hydrogen evolution or not depends entirely on the catalytic activity of the substrate toward the hydrogen ionization reaction, *i.e.*, on the free energy of adsorption of hydrogen on the substrate. This is verified in Fig. 21, which shows a linear relationship between the coulombic efficiency of the formaldehyde oxidation reaction on various metals (or the number of electrons realized per formaldehyde molecule decomposed), and $-\log i_H^0 \cdot i_H^0$ is the exchange current density for the hydrogen reaction on these metals and is taken to represent the free energy of adsorption for hydrogen (24). The correlation between simultaneous hydrogen evolution during formaldehyde oxidation and the heat of adsorption for hydrogen on the metals was first suggested by van den Meeraker (25); but the heat of adsorption for hydrogen was erroneously calcuated by the Eley-Stevenson (26, 27) method for both transition and sp metals. It has been shown by Trasatti (28) that while this method can give satisfactory results for transition metals, it does not hold at all with sp metals. The correct parameter to be used for the reactivity scale toward hydrogen of the various metals (transition and sp metals) is i_H^0. This parameter relates to the free energy of adsorption for hydrogen in the presence of the solvent and the field in the double layer.

It is interesting to note in Fig. 21 that the Group IB metals or the sp metals such as Cu, Au, and Ag show low coulombic efficiency even though Ag exhibits approximately the same catalytic activity for formaldehyde oxidation as Pt and Pd (*cf* Fig. 20). The Group VIII metals or metals with unfilled d bands exhibit high coulombic efficiency giving two electrons per formaldehyde molecules oxidized. Clearly, according to the data in Fig. 21, metals may in principle be divided into three main classes: (*i*) metals with positive free energy of hydrogen adsorption, (*ii*) metals with free energy of hydrogen adsorption close to zero, and (*iii*) metals with negative free energy of hydrogen adsorption. In the case of class *i* metals, formaldehyde oxidation is accompanied by hydrogen evolution. For class *ii* metals, there is no simultaneous hydrogen evolution during the formaldehyde oxidation. Class *iii* metals, such as Ni, showed very low catalytic activity for formaldehyde oxidation to allow accurate measurements of the coulombic efficiency.

Manuscript submitted Feb. 19, 1985; revised manuscript received June 19, 1985.

IBM Corporation assisted in meeting the publication costs of this article.

REFERENCES

1. (a) W. Vielstich, "Fuel Cells," Revised English ed., Interscience, New York (1978); (b) M. W. Breiter, "Electrochemical Processes in Fuel Cells," Springer-Verlag, New York (1969); (c) "From Electrocatalysis to Fuel Cells," G. Sandstede, Editor, Washington University Press, St. Louis, MO (1972).
2. O. A. Khazova, Yu. B. Vasiliev, and V. S. Bagotskii, *Electrokhimiya*, **1,** 82 (1965).
3. R. P. Buck and L. R. Griffith, *This Journal*, **109,** 1005 (1961).
4. R. M. Lukes, *Plating*, **51,** 1066 (1964).
5. A. A. Balandin, *Adv. Catal.*, **19,** 1 (1969).
6. R. Parsons, *Trans. Faraday Soc.*, **54,** 1053 (1958).
7. H. Gerischer, *Bull. Soc. Chim. Belg.*, **67,** 506 (1958).
8. R. J. L. Martin, *Aust. J. Chem.*, **7,** 4000 (1954).
9. J. F. Walker, "Formaldehyde," 3rd ed., Reinhold, New York (1964).
10. A. Vogel, "Textbook of Quantitative Inorganic Analysis," ed. IV, Langman (1978).
11. P. Bindra and J. Roldan, To be published.
12. A. Capon and R. Parsons, *J. Electroanal. Chem.*, **44,** 239 (1973).
13. O. G. Tyunikova, N. B. Miller, A. A. Yakovleva, and V. I. Veselovski, *Electrokhimiya*, **7,** 690 (1971).
14. A. Capon and R. Parsons, *J. Electronal. Chem.*, **45,** 205 (1973).
15. T. Biegler, D. A. J. Rand, and R. Woods, *ibid.*, **29,** 269 (1971).
16. J. Ambrose, R. G. Baradas, and D. W. Shoesmith, *ibid.*, **47,** 65 (1973).
17. V. G. Levich, "Physicochemical Hydrodynamics," Prentice Hall, Englewood Cliffs, NJ (1962).
18. K. J. Vetter, "Electrochemical Kinetics," English ed., Academic Press, New York (1967).
19. R. Parsons, *Trans. Faraday Soc.*, **47,** 1332 (1951).
20. P. L. Allen and A. Hickling, *ibid.*, **53,** 1626 (1957).
21. J. O'M Bockris and A. K. N. Reddy, "Modern Electrochemistry," Vol. 2. Plenum Press, New York (1970).
22. D. S. Gnanamuthu and J. V. Petrocelli, *This Journal*, **114,** 1036 (1967).
23. J. Fahrenfort, L. L. Van Reyen, and W. M. H. Sachtler, in "The Mechanism of Heterogeneous Catalysis," J. H. DeBoer, Editor, Elsevier, New York (1960).
24. S. Trasatti, *J. Electroanal. Chem.*, **39,** 163 (1972).
25. J. E. A. M. van Den Meeraker, *J. Appl. Electrochem.*, **11,** 387 (1981).
26. D. D. Eley, *Disc. Faraday Soc.*, **8,** 34 (1950).
27. E. P. Stevenson, *J. Chem. Phys.*, **23,** 203 (1955).
28. S. Trasatti, *J. Chem. Soc. Faraday 1*, **68,** 229 (1972).

Plasma-Sprayed Semiconductor Electrodes: Photoelectrochemical Properties of TiO_2

L. Parent, J. P. Dodelet,* G. G. Ross, and B. Terreault

INRS-Energie, Varennes, Québec, Canada J0L 2P0

S. Dallaire

Institut de Génie des Matériaux, Boucherville, Québec, Canada J4B 6Y4

ABSTRACT

TiO_2 photoanodes have been prepared by the plasma spray technique on titanium, graphite, and alumina substrates. 25-30 μm thick coatings display a good adhesion to the substrate and a highly textured surface. Dark and photoelectrochemical properties of the photoanodes have been measured in oxygen-saturated solutions of NaOH at pH 13. It is shown that the performances of the electrodes are quite insensitive to the plasma power or to the TiO_2 powder granulation but are very sensitive to the purity of the spraying material, to the substrate, and also to a heat-treatment (H_2 or Ar at 800°C followed by a rapid quenching in air). The maximum quantum yield is obtained at 300 nm for heat-treated TiO_2. It is about 40% on alumina and 70% on the titanium. The heat-treatment affects the conductivity, σ, and the surface density of hydroxyl groups, N_{OH}, of the coatings. For heat-treated TiO_2, typical values are $\sigma = 2.4\ (\Omega\text{-cm})^{-1}$ and $N_{OH} = 2.8 \times 10^{15}\ cm^{-2}$. For untreated TiO_2, typical values are $\sigma = 30.6\ (\Omega\text{-cm})^{-1}$ and $N_{OH} = 2.1 \times 10^{16}\ cm^{-2}$. The J-V curves of heat-treated TiO_2 sprayed on alumina extend anodically up to 9.5V (*vs.* SCE), where film breakdown occurs. For the same film sprayed on titanium and graphite, the anodic dark behavior is similar to that observed for the bare substrates. It is concluded that polycrystalline TiO_2 coatings, produced by the plasma spray technique, can display photoelectrochemical and dark characteristics similar to the ones obtained with single-crystal material.

Polycrystalline n-TiO_2 has been largely studied as a semiconducting electrode in photoelectrochemical cells. Several techniques for the preparation of the photoanodes are found in the literature, namely, thermal oxidation (1-8), anodic oxidation (8-16), chemical vapor deposition (8, 9, 14, 17-21) and plasma-enhanced chemical vapor deposition (22), sputtering (23, 24), pressed and sintered powders (2, 25, 26), and screen printing (27).

An industrial coating technique, plasma spraying, has also been used to produce polycrystalline electrodes from TiO_2 powders of unspecified purity sprayed on titanium (28) and from raw rutile sprayed on alumina (29). The latter investigation reports an unusual anodic flatband potential ($V_{FB} \simeq -0.6$V SCE) at the pH used (10*M* NaOH) and a large potential dependence of the photocurrent below 0.4V. At higher anodic potentials, a rapid rise in dark current is attributed by Wang and Henager (29) to the presence of impurities (Si, Fe, Cr, Ni, Mn) in the raw rutile. TiO_2 was again recently sprayed on titanium (30). The obtained results were similar to the ones reported by Wang and Henager except that anodic dark currents, in 0.1*M* NaOH, rise quickly at potentials higher than ~0.7V *vs.* SCE.

In the present work, it will be shown that the current voltage (J-V) characteristics of plasma-sprayed n-TiO_2 photoanodes are largely dependent on the purity of the powder and on the nature of the substrate.

Using this technique, it is possible to produce large surfaces of polycrystalline TiO_2 photoanodes displaying J-V characteristics like the ones observed with monocrystals. On alumina substrates, J-V curves can be obtained up to 9.5V.

Experimental

Powder preparation.—TiO_2 powders were obtained from three different sources. Two of them [Metco 102 ($\leq$44 μm) and H. C. Starck (5-12 μm)] had the appropriate size distribution for direct feeding of the torch and were used without modifications. X-ray diffraction showed that these powders had the rutile structure. The third one, a high purity anatase powder (99.9%, A. D. MacKay Chemicals), had a particle diameter which was too small ($\leq$5 μm). It was agglomerated before plasma deposition by atomization in a spray dryer. The atomization was realized from a suspension prepared by mixing demineralized water (30 weight percent [w/o]), polyvinyl alcohol (0.5 w/o; J. T. Baker, 88-89% hydrolized), polyethylene glycol (2 w/o; Carbowax, Fisher Laboratories), and TiO_2. All the organic components were eliminated during the sintering of TiO_2 performed in an alumina crucible at 1200°C in air. This temperature treatment also induces the transformation of the initial anatase form of TiO_2 into the rutile form. Finally, the desired size of powders was sieved with an air jet sieve classifier (Alpine, Augsburg) and the distribution of particles having a diameter smaller than 32 μm was measured with a particle size analyzer (PA-720, Pacific Scientific).

Spraying system.—Plasma spraying was performed with a plasma spray system (Plasmadyne). Three plasmas were used for the production of the coatings: (*i*) Ar/He (2:1) 30 kW, (*ii*) Ar/He (2:1) 40 kW, and (*iii*) Ar/H_2 (20:1) 30 kW. TiO_2 was introduced in the plasma at a constant rate of about 9 g-min^{-1} and projected in subsonic mode on three different substrates: titanium foils (99.7% from Alfa), alumina disks (99.8% Coors), and graphite slices. Fused silica was also tried out as a substrate but was abandoned because of the poor adhesion of the coating. The distance between the torch and the substrate was always 7.5 cm, and the speed of X-Y sweeping was set to obtain coatings 25-30 μm thick [measured with a Surtronic 3 profilometer (Taylor and Hobson)]. The surface texture of the films was quite sensitive to the particle size distribution. Coatings obtained with powders having a diameter ranging from 32 to 63 μm are rougher than those made with powders of 4-20 μm, but their exposed surface is smaller. With all powders used in this investigation, gray coatings were always obtained.

Hydrogen or argon treatment.—The photoelectrochemical properties of the TiO_2 films were investigated either directly after plasma spraying or after a hydrogen or argon treatment at temperatures up to 800°C. This treatment usually consisted in leaving the electrode for 15 min in a 0.3 liter-min^{-1} flow of hydrogen or argon. The samples were always introduced in the furnace under argon atmosphere at the temperature of the treatment; upon removal, they were quenched at room temperature.

Photoelectrochemical measurements.—In order to perform electrochemical measurements on the TiO_2-coated electrodes, ohmic contacts were established by directly attaching a lead to the conducting substrates (C, Ti). On alumina, the ohmic contact was obtained with a Ga/In eu-

* Electrochemical Society Active Member.

tectic. All the nonphotoactive parts of the electrode were afterwards covered with silicone rubber to avoid corrosion, leaving an active area of 1.5 cm^2.

The electrochemical measurements were performed in a three-electrode cell equipped with a quartz window, using a NaOH solution at pH 13 (~0.1*N*) saturated with oxygen at atmospheric pressure. The counterelectrode was a 15 cm^2 Pt foil, and a standard calomel electrode was used as reference.

The working electrode was illuminated with white light from a high pressure 300W Xe lamp equipped with a 10 cm water filter. The maximum UV power (up to 400 nm) incident on the working electrode was 30 mW-cm^{-2} (uncorrected for the reflection). Neutral density filters were used to vary the light intensity. Monochromatic light for quantum yield determination was obtained by interference filters having a 10 nm bandwith. At 300 nm, the incident power on the working electrode is 0.150 mW-cm^{-2}. The light intensity was measured with a Photodyne 44 XL radiometer. The J-V curves were performed with a Princeton Applied Research Model 173 potentiostat and a Model 175 programmer. The scanning rates were always 10 mV-s^{-1}. The quantum efficiencies were obtained in a two-electrode configuration using a Keithley 614 electrometer. All the measurements were performed at room temperature.

Conductivity measurements.—The van der Pauw technique (31) was followed to perform the conductivity measurements on TiO_2 sprayed on alumina. For these measurements, a Keithley 225 current source and a Hewlett-Packard 3455 A digital voltmeter were used.

Hydrogen depth profiling.—A novel, quantitative, nondestructive, nuclear microanalysis technique (32) called elastic recoil detection was used to detect the presence of hydrogen in the top layer of plasma-sprayed TiO_2. This technique uses a 350 keV $^4He^+$ beam incident under vacuum (10^{-7} torr) on the material to probe the hydrogen concentration to a depth of 600Å. The sensitivity is 1 H atom percent (a/o).

Results and Discussion

Surface aspect of TiO_2 coatings.—Figure 1 is a scanning electron microscope (SEM) picture showing the surface texture of the TiO_2 coating. Irregularities of the surface introduce a much larger actual area as compared to the geometrical one. The surface texture is a function of the size of the sprayed particles and the power of the plasma.

The largest exposed surfaces are obtained with the smallest particles (4-20 μm) and with the highest plasma power (40 kW). In this case, the melted particles leave the torch with a large kinetic energy resulting in a bigger splash upon arrival on the substrate. The electrode surface depicted in Fig. 1 is an intermediate between a flat surface and a colloid.

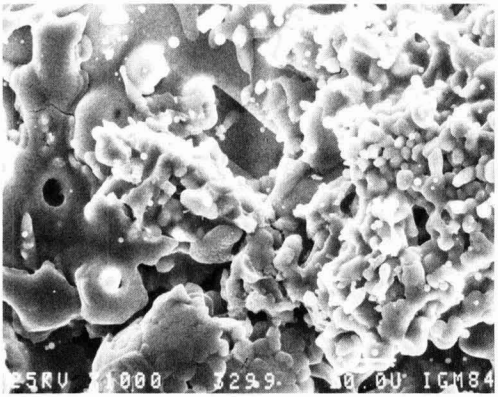


Fig. 1. SEM picture of the surface of a plasma-sprayed TiO_2 electrode

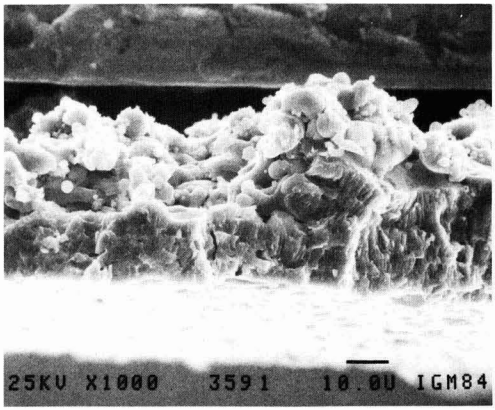


Fig. 2. SEM picture of a fracture of a plasma-sprayed TiO_2 coating removed from its substrate.

No bare spots were detected in the coatings by SEM. However, there are small cracks and pores on the surface through which the electrolyte could eventually penetrate and reach the substrate.

Figure 2 is a SEM picture showing a fracture of a TiO_2 coating removed from its substrate. This picture confirms the film thickness (25-30 μm) measured with the profilometer. The more regular surface seen at the bottom of the picture was the surface in contact with the substrate. This film is typical of plasma-sprayed coatings which always show a vertically oriented crystallization.

Purity of TiO_2 powders and plasma characteristics.—Figure 3 presents the J-V curves obtained for TiO_2 coatings on Ti using three powders having different impurity contents. All these coatings were heated in H_2 at 800°C, and the UV power ($\lambda \leq 358$ nm) incident on the electrodes is 9 mW-cm^{-2}. The smallest photocurrent densities were obtained with TiO_2 from Starck (dash-dotted curve) followed by TiO_2 from Metco (dotted curve). The highest photocurrent densities were obtained with TiO_2 from Mackay (full curve). Chemical analysis of these powders is presented in Table I. The Al content, which is known to improve the quantum yield of TiO_2 (33), is about the same for the three powders. However, the amounts of Cr and Fe, which are known to decrease the UV quantum yield (34), are smaller in the MacKay powder.

The influence of the plasma powder and its type on the photocurrent densities has also been analyzed. No significant differences were observed when the power of the plasma was changed from 30 to 40 kW and when He was replaced by H_2. Within experimental error, there were no significant differences due to variation in the size of the feeding particles from 4-20 to 32-63 μm. Cooling the

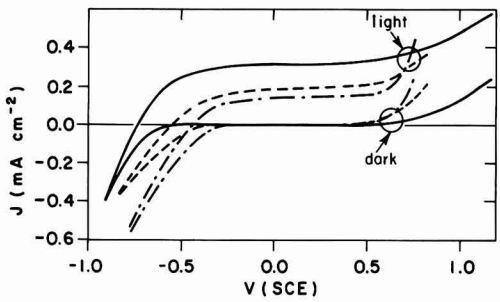


Fig. 3. J-V curves for plasma-sprayed TiO_2 coatings (H_2 treated at 800°C) on titanium using three powders having a different impurity content.

Table I. Chemical analysis of the three TiO_2 powders used in this work (in weight percent)

Elements	Starck	Metco	MacKay[a]
Si	0.015	0.035	0.02
Mn	0.001	0.002	0.001
Cr	0.02	0.002	0.002
Fe	0.05	0.14	0.01
Al	0.02	0.015	0.016
Ni	0.001	0.001	0.001

[a] After agglomeration and sintering.

substrate with Dry Ice during coating also has no effect. In light of these results, the experiments that follow were performed exclusively on coatings made with TiO_2 from MacKay by using a 30 kW Ar/He plasma to melt the powders.

Quantum yields and coating conductivities.—Figures 4A and 4B depict the quantum yields, ϕ, for TiO_2 sprayed on titanium and alumina, respectively. When graphite is used as a substrate, the obtained quantum yields are similar to the ones measured for TiO_2 on titanium. The full points represent the values obtained directly after plasma spraying. The open points, on the other hand, are obtained after treating the plasma-sprayed TiO_2 at 800°C in H_2. All these action spectra are corrected for a constant photon flux (3.4×10^{14} photon-s^{-1}-cm^{-2}) using the following relation

$$J_{sc} = kI^{\gamma} \quad [1]$$

where J_{sc} is the short-circuit photocurrent in the two-electrode configuration used for the quantum yield determination, k is a proportionality constant, and γ is the light power exponent. A value of $\gamma = 0.80$ was found for both untreated and H_2-treated TiO_2. The maximum quantum yield is obtained at about 300 nm and reaches values as high as 70% for H_2-treated TiO_2 on titanium. This value compares favorably with the quantum yields reported in the literature (8, 22, 33, 35).

An increase in the quantum yield is always observed for plasma-sprayed TiO_2 electrodes treated in H_2 at temperatures higher than 300°C with a maximum effect at temperatures above 600°C. A similar effect on ϕ is found when the electrodes are treated in Ar. The H_2 or Ar treatment above 600°C induces a reduction of the coating conductivity, σ. Typically, $\sigma = 30.6\ (\Omega\text{-cm})^{-1}$ for untreated samples and $\sigma = 2.4\ (\Omega\text{-cm})^{-1}$ for H_2- or Ar-treated samples at 800°C. As the treatment of the electrode in either H_2 or Ar atmosphere has the same effect on the conductivity of TiO_2, the formation of Ti—H bonds, resulting in a decrease of the charge carrier density N, may not be invoked to explain the decrease of the conductivity of the H_2- or Ar-treated electrodes. It is, however, possible that the quenching of the electrode in air after H_2 or Ar treatment might decrease, by reoxidation, the amount of triply ionized interstitial titanium and doubly ionized oxygen vacancies, which, according to Kofstad (36), are responsible for the semiconducting character of TiO_2. The oxidation effect is quite critical since an electrode left for 15 min in air at 800°C becomes so resistive that no photocurrent can be detected afterwards. A shorter oxidation time generates intermediate quantum yields tending toward the maximum value obtained after the H_2 or Ar treatment. In the remainder of the text, plasma-sprayed TiO_2 heated at 800°C in Ar in H_2 for 15 min and then quenched in air will be referred to as heat-treated electrodes.

Surface hydroxyl group densities.—Figure 5 shows the hydrogen profile, in atom percent, obtained by the nuclear microanalysis technique, for untreated (full line) and heat-treated (broken line) plasma-sprayed TiO_2 before any contact with the electrolyte solution. Even if the probed depth is 600Å, the detected hydrogen probably originates exclusively from the TiO_2 surface. This can be understood in terms of surface irregularities, as depicted in the insert of Fig. 5, where five surface analyzing conditions are illustrated. In case 1, H^+ ejected from the surface by the impact of 350 keV $^4He^+$ will be detected as having the maximum energy. It will be identified correctly as belonging to the surface of the sample (0 Å depth). In cases 2 and 3, even if the hydrogen also originates from the actual TiO_2 surface it will be measured by the detector as originating from a certain depth because of the energy loss in traversing the matter. The surface hydrogens represented by cases 4 and 5 will not be detected by the technique because they are shielded from $^4He^+$ by a too large thickness of material or the ejected H^+ stops in the layer of TiO_2 before being able to be detected. Another indication that the hydrogen is located mostly on the surface is that the profile of Fig. 5 shows a definite surface peak whose width has the theoretical resolution of the technique.

Taking into account the rutile density (4.25 g-cm^{-3}) and a sensitivity limit of 1 a/o of H, one obtains $2.1\ 10^{16}$ H cm^{-2} for untreated TiO_2 and $2.8\ 10^{15}$ H cm^{-2} for heat-treated TiO_2. The actual area of the coating is not known, but these results indicate that there is a difference of nearly one order of magnitude between both hydrogen surface

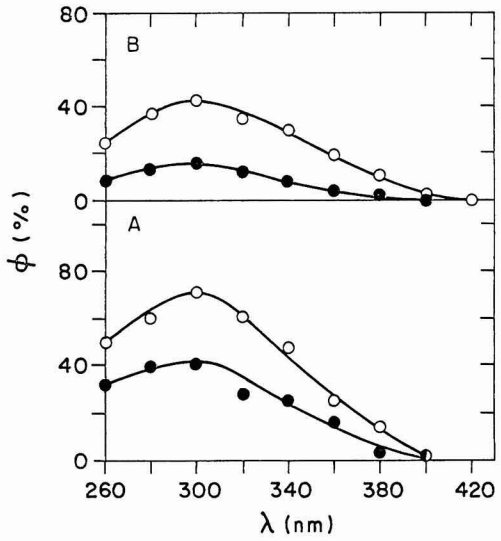


Fig. 4. Quantum yield, ϕ, for H_2- or Ar-treated (open symbols) and untreated (dark symbols) TiO_2 sprayed on titanium (A) and on alumina (B), as a function of the wavelength.

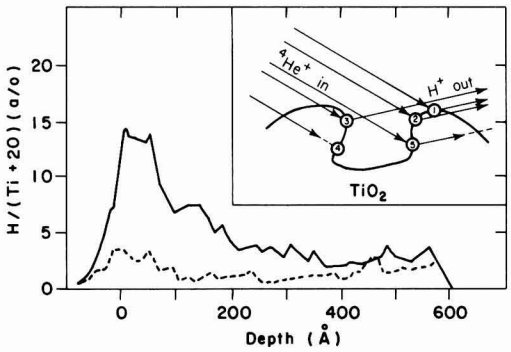


Fig. 5. Depth profiles of hydrogen content (in atom percent) for H_2- or Ar-treated (broken line) and untreated (full line) TiO_2 coatings obtained by nuclear microanalysis. The insert illustrates five analyzing conditions encountered on irregular surfaces.

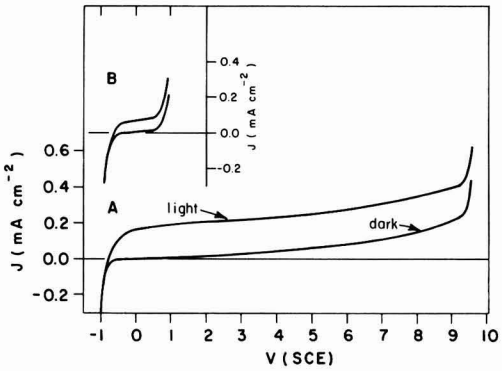


Fig. 6. TiO_2 sprayed on alumina. J-V curves obtained in oxygen-saturated NaOH (pH 13) for H_2- and or Ar-treated TiO_2 (A) and untreated TiO_2 (B) electrode.

densities. A similar ratio was found for the conductivities of untreated and heat-treated TiO_2, with the most conducting coating having the largest surface hydrogen density. Surface hydrogen probably belongs to hydroxyl groups chemisorbed on the surface as the result of the interaction of atmospheric water vapor and TiO_2 (37).

TiO_2 substrate and breakdown potential.—Figure 6A displays the J-V curves obtained in NaOH at pH at 13 for heat-treated TiO_2. The breakdown potential of the film happens at 9.5V. When heat-treated TiO_2 of the same purity is sprayed on Ti, a rapid increase of the dark oxidation current is observed for applied voltages >0.5V (full curve in Fig. 3). It demonstrates that the breakdown observed for TiO_2 sprayed on Ti is not characteristic of the heat-treated sprayed film. It is the oxidized titanium surface of the titanium substrate, in contact with the electrolyte through cracks and pores of the sprayed film, which is responsible for the dark J-V behavior. J-V curves obtained in the dark for bare Ti (always covered by a native oxide layer) in contact with NaOH at pH 13 corroborate this interpretation. These curves are similar to the dark J-V curve displayed in Fig. 6B for untreated TiO_2 sprayed on alumina. The dark anodic behavior of TiO_2 films sprayed on graphite is also dominated by the dark characteristics of the graphite substrate in alkaline solutions.

Conclusion

This work demonstrates that the plasma spray technique is well suited for the production of TiO_2 semiconductor electrodes. The photoanodes are characterized by a highly textured surface and are able to show, after being submitted to a suitable heat-treatment, dark and photoelectrochemical properties comparable to those measured for monocrystalline TiO_2. This technique would be particularly well suited for large-scale production. The photocatalytic performances of these coatings are now under investigation.

Acknowledgments

This work has been supported by NCR Contract no. RSD.31950-4-0008. We wish to thank D. Spino for his help with the coating production, G. Gobeil for operating the 350 keV accelerator, and Dr. C. H. Langford for his helpful suggestions.

Manuscript submitted Feb. 4, 1985; revised manuscript received July 11, 1985. This was Paper 591 presented at the Toronto, Ontario, Canada, Meeting of the Society, May 12-17, 1985.

INRS-Energie assisted in meeting the publication costs of this article.

REFERENCES

1. A. Fujishima, K. Honda, and K. Kohayakawa, *This Journal*, **122,** 1487 (1975).
2. G. Mavroides, D. I. Tchernev, J. A. Kafalas, and D. F. Kolesar, *Mater. Res. Bull.*, **10,** 1023 (1975).
3. J. F. Houlihan and D. P. Madacsi, *ibid.*, **11,** 1191 (1976).
4. L. A. Harris and R. H. Wilson, *Ann. Res. Mater. Sci.*, **8,** 99 (1978).
5. H. R. Sprünken, R. Schumacker, and R. N. Schindler, *Discuss. Faraday Soc.*, **70,** 55 (1980).
6. K. J. Hartig, J. Lichtscheild, and N. Getoff, *Z. Naturforsch.*, **36a,** 51 (1981).
7. V. Antonucci, N. Giordano, and J. C. J. Bart, *Int. J. Hydrogen Energy*, **7,** 769 (1982).
8. K. J. Hartig, N. Getoff, and G. Nauer, *ibid.*, **8,** 603 (1983).
9. J. Keeny, D. H. Weinstein, and G. M. Hass, *Nature*, **253,** 719 (1975).
10. H. Gerischer, *J. Electroanal. Chem.*, **82,** 133 (1977).
11. J. F. McAleer and L. M. Peter, *Discuss. Faraday Soc.*, **70,** 67 (1980).
12. J. C. Manchenoir, J. P. Loup, and J. Masson, *Thin Solid Films*, **66,** 357 (1980).
13. K. J. Hartig, N. Getoff, K. D. Kotchev, and St. Kanev, *Solar Energy Mater.*, **9,** 167 (1983).
14. S. E. Lindquist, B. Finnström, and L. Tegner, *This Journal*, **130,** 351 (1983).
15. P. Clechet, C. Martelet, R. Olier, J. P. Thomas, and M. Fallavier, *ibid.*, **130,** 1795 (1983).
16. P. Miller, S. Mamiche-Afara, M. J. Dignam, and M. Muskovits, *Chem. Phys. Lett.*, **100,** 236 (1983).
17. K. L. Hardee and A. J. Bard, *This Journal*, **122,** 739 (1975).
18. K. L. Hardee and A. J. Bard, *ibid.*, **124,** 215 (1977).
19. C. Stalder and J. Augustynski, *ibid.*, **126,** 2007 (1979).
20. R. Schumacker, R. H. Wilson, and L. A. Harris, *ibid.*, **127,** 96 (1980).
21. Y. Takahashi, K. Tsuda, and K. Sugiyama, *J. Chem. Soc., Faraday Trans. 1*, **77,** 1051 (1981).
22. L. M. Williams and D. W. Hess, *Thin Solid Films*, **115,** 13 (1984).
23. A. A. Soliman and H. J. Seguin, *Can. J. Phys.*, **59,** 1674 (1981).
24. M. F. Weber, L. C. Schumacker, and M. J. Dignam, *This Journal*, **129,** 2022 (1982).
25. J. Gautron, P. Lemasson, and J. F. Marucco, *Discuss. Faraday Soc.*, **70,** 81 (1980).
26. P. Salvador, *This Journal*, **128,** 1895 (1981).
27. C. Blaauw, H. M. Naguib, A. Ahmad, and S. M. Ahmed, *Solar Energy Mater.*, **7,** 331 (1982).
28. W. Gissler, P. L. Lensi, and S. Pizzini, *J. Appl. Electrochem.*, **6,** 9 (1976).
29. R. Wang and C. H. Henager, Jr., *This Journal*, **126,** 83 (1979).
30. M. Takeuchi, F. Shimizu, F. Kaneko, and H. Nagasaka, in "Proceedings of the International Ion Engineering Congress," p. 927 (1983).
31. L. J. van der Pauw, *Philips Res. Rep.*, **13,** 1 (1958).
32. G. G. Ross, B. Terreault, G. Gobeil, G. Abel, C. Boucher, and G. Veilleux, *J. Nucl. Mater.*, **128-129,** 730 (1984).
33. A. K. Ghosh and H. P. Maruska, *This Journal*, **124,** 1516 (1977).
34. H. P. Maruska and A. K. Ghosh, *Solar Energy Mater.*, **7,** 237 (1979).
35. D. Laser and A. J. Bard, *This Journal*, **123,** 1027 (1976).
36. P. Kofstad, *J. Less-Common Metals*, **13,** 635 (1967).
37. W. J. Lo, Y. W. Chung, and G. A. Somorjai, *Surf. Sci.*, **71,** 199 (1978).

On the Thermal Characteristics of Electrolytic Cell

Y. Ogata, S. Kainuma, M. Yasuda,* and F. Hine*

Nagoya Institute of Technology, Nagoya 466, Japan

ABSTRACT

Mathematical analysis of the heat balance of electrolytic cell was investigated. Experimental results with a vertical-type water electrolysis cell under normal conditions agreed with calculation. The water vaporization is a major factor of heat loss from the cell and, hence, it must be reduced. The thermal behavior of a water electrolysis cell was simulated under normal and pressurized conditions with the equations proposed. It was clarified that the heat loss from the cell could be reduced by increasing the operating pressure because the water vaporization was a large factor of heat dissipation at high temperatures. The effects of the thermal insulation and the emissivity of the cell wall were also discussed.

Electrochemical processes consume much more electric energy than the thermodynamic requirement to proceed the reaction under discussion. A part of excess energy is of course utilized to cover the entropy and the heat loss from the system, although it must be minimized as small as possible. The heat transfer through the cell wall is generally a major factor of these losses. In practice, the operating temperature is kept constant by balancing the Joule heat, the heat losses, and the external source such as the heat exchanger if any. Beck and Ruggeri have investigated the heat balance of several electrochemical processes (1). They point out that the diaphragm-type chlor-alkali cell and the chlorate cell dissipate some 15 and 32% of the electricity supplied, respectively, through the cell wall. The heat loss can be reduced by utilizing improved insulation, whereby the operating temperature is affected.

The energy balance of electrochemical processes has been studied by several authors. Fahidy has published the general description emphasizing the heat loss through the cell wall (2-6). These evaluations of the thermal behavior of the electrochemical system under discussion are useful for reducing the energy requirement and hence further improvement of the process economy. Use of the selected electrode materials and separators, minimization of the electrode gap, operation at high temperatures, and other factors must be considered to reduce the cell voltage and generation of unwanted Joule heat. In fact, many electrochemical cells generate excess heat over the minimum requirement. However, it might be possible to equalize the heat generation with the heat loss if the cell is operated at a certain temperature.

As Kawashima (7) and LeRoy (8, 9) state, the cell voltage decreases, but the thermal balance voltage increases when the operating temperature rises. As a result, the cell could be operated with no external heat at a temperature t_{NT}, where the cell voltage is equal to the thermal balance voltage, depending on the cell design and the operating conditions such as the cell current.

This paper deals with a basic formulation for evaluating the thermal characteristics of the electrochemical cell filled with aqueous solution operated under both steady-state and nonsteady-state conditions. A vertical-type water electrolysis cell was used as an example.

Heat Balance of Electrolytic Cell

The heat accumulation Q_A results from a balance of the heat generation by electrolysis Q_E, the heat coming from the external source Q_{EX}, the heat losses due to the solution flow and vaporization of water Q_S and Q_V, respectively, and the heat transfer through the cell wall Q_L

$$Q_A = Q_E + Q_{EX} - Q_S - Q_V - Q_L \quad [1]$$

$$Q_A = mC_{ps}\frac{dt_s}{d\theta} \quad [2]$$

$$Q_E = 0.86I(V - \mathbf{E}_d) - 0.86I\left(\Sigma|\eta| + \Sigma IR - \frac{T_s\Delta S_r}{n\mathbf{F}}\right) \quad [3]$$

*Electrochemical Society Active Member.

$$Q_S = GC_{ps}(t_s - t_i) \quad [4]$$

$$Q_V = w\Delta H_v \quad [5]$$

and

$$Q_L = \Sigma UA(t_s - t_a) \quad [6]$$

where $\mathbf{E}_d$ is the enthalpic voltage ($\Delta H_r/n\mathbf{F}$) (8). It is well known that the specific heat of aqueous solution is large in comparison with that of the cell components. Therefore, it is assumed that the product of the mass and the specific heat of the cell hardware is negligible to mC_{ps} in Eq. [2] in general, or in the case under discussion at least. Of course, the heat capacity of hardware must not be avoided when the cell consists of a narrow channel so that the solution volume is small for example. Both Q_E and Q_{EX} under given conditions must be minimized as small as possible in order to save energy requirements. Of these, reduction of Q_E or the cell voltage V is a main subject for research and development which includes development and utilization of high performance electrodes, separators, and other cell components, and minimization of the ohmic voltage drop between two electrodes. On the other hand, Q_{EX} can be decreased by adequate design of the hardware and utilization of the construction materials, especially thermal insulators. The operating conditions such as the electrolyte flow rate and the temperature are also important factors.

Now let us consider the factors represented by Eq. [1]-[6]. The heat generation Q_E is decreased by increasing the operating temperature because the resistivity of electrolyte, the electrode overvoltages, and the resistance of separators decrease at high temperatures. The solution IR drop is the largest factor of the excess Joule heat, especially at large amperages in most cases. The contribution of $T_s\Delta S_r$ is relatively small at medium temperatures, and its sign, of course, depends on the reaction proposed.

The heat losses, Q_S, Q_V, and Q_L increase with the operating temperature. The flow rate G on the right side of Eq. [4] is given by the cell current and the conversion of feedstock. The heat loss with vaporization of water is relatively small at low temperatures, but it increases significantly at high temperatures close to the boiling point of the electrolytic solution.

The heat loss through the cell wall Q_L depends on the hardware design and the construction materials as well as the operating conditions. The solution temperature is of course a major factor.

The external heat Q_{EX} varies with the operating temperature, as stated above. At t_{NT}, the heat generation is balanced with the dissipated heat, and hence no external heat is required. Its steady-state temperature moves to the high direction when the heat dissipation from the cell is reduced. When Q_{EX} is negative, the excess heat of the cell could be recovered. In fact, it is wasted in most cases because it is inferior to use [see Fig. 7 and 8 in Ref. (9)].

A vertical-type, undivided laboratory cell for water electrolysis with dilute caustic soda solution was operated under normal atmospheric pressure so as to evaluate the heat balance on Eq. [1]. For simplicity, assume that electrolytic solution is not circulated externally. However, the

solution is agitated and circulated extensively in the cell by electrolytic gas lift. Under such conditions, Eq. [7] is obtained

$$\left[m_0 - \frac{18 \times 10^{-3}}{2\mathbf{F}}\left(1.0 + \frac{1.5\ p_{H_2O}}{1.0 - p_{H_2O}}\right) I\theta\right] C_{ps}\frac{dt_s}{d\theta} = 0.86I(V - \mathbf{E}_d) - \frac{18 \times 10^{-3}}{2\mathbf{F}}\left(\frac{1.5\ p_{H_2O}}{1.0 - p_{H_2O}}\right)\gamma_{H_2O} I - \Sigma UA(t_s - t_a) \quad [7]$$

It is assumed that the gas bubbles leaving the cell are saturated with water vapor at the solution temperature t_s. The second term in the brace on the left side of Eq. [7] shows the water consumption due to electrolysis and vaporization.

The left side of Eq. [1], Q_A, is equal to zero under the steady-state conditions. In this case, the temperature t_{ST} was obtained by means of the iteration method. Under nonsteady-state conditions, on the other hand, the temperature varies with time and is evaluated by a Runge-Kutta method.

The cell voltage is represented by Eq. [8]

$$V = E_d^0 + \frac{RT_s}{2\mathbf{F}} \ln (1.0 - p_{H_2O})^{1.5} - \eta_a + |\eta_c| + K\frac{l_e I}{A_e \kappa_s} \quad [8]$$

The activity of water was assumed to be unity. A coefficient K consists of the bubble effects, the current distribution on the working electrodes, and other factors (10-12). The overvoltages of the anode and cathode also vary with time because of deactivation and changes of the working surface (13). Since there was concern about discrepancies between calculation and experimental results caused by these factors, the terminal voltage was measured and used in the calculations.

The overall heat-transfer coefficient of a wall U is as follows

$$\frac{1}{U} = \frac{1}{h_s} + \frac{l_p}{k_p} + \frac{1}{h_a} \quad [9]$$

where h_s and h_a are the heat-transfer coefficients of the solution side and of the air side next to the cell wall, respectively, k_p is the thermal conductivity, and l_p is the thickness of the cell wall. Of these factors on the right side of Eq. [9], the first term $1/h_s$ is negligible to other factors, since solution in the cell is circulated vigorously by gas lift and hydrodynamic boundary layer on the cell wall with the exception of the cell top is sufficiently thin (14). Therefore, we have

$$\frac{1}{U} \simeq \frac{l_p}{k_p} + \frac{1}{h_a} \quad [10]$$

Since there is a gas phase at the cell top in most cases, the heat-transfer coefficient of its phase, similar to h_a, must be added in the calculation. Of course, Eq. [10] is valid for the top wall when the cell is filled up with electrolyte.

The heat-transfer coefficient h_a consists of two factors: natural convection and radiation as shown by Eq. [11]

$$h_a = h_c + h_r \quad [11]$$

The coefficient with respect to convection of air along the wall, h_c, is represented by a dimensionless term, the Nusselt number, Nu, which is a function of the Prandtl number, Pr, and the Grashof number, Gr. For the vertical wall, Nu is represented by Eq. [12a] and [12b]. For other cases, the equations can be found in the reference books such as Ref. (15)

$$\mathrm{Nu} = 0.13(\mathrm{Pr\ Gr})^{1/3} \qquad \text{for Pr Gr} \geq 10^9 \quad [12a]$$

and

$$\mathrm{Nu} = 0.59(\mathrm{Pr\ Gr})^{1/4} \qquad \text{for Pr Gr} \leq 10^9 \quad [12b]$$

where

$$\mathrm{Nu} = \frac{h_c H}{k_a} \quad [13]$$

$$\mathrm{Pr} = \frac{C_{pa}\mu_a}{k_a} \quad [14]$$

and

$$\mathrm{Gr} = \frac{\rho_a^2 \beta_a g H^3 (t_{pa} - t_a)}{\mu_a^2} \quad [15]$$

where β_a is the volume expansion of air and g is the gravity acceleration. The coefficient with respect to radiation, h_r, is shown by the Stefan-Boltzmann equation

$$h_r = \sigma\epsilon \frac{T_{pa}^4 - T_a^4}{T_{pa} - T_a} \quad [16]$$

This equation is applicable to calculating the heat-transfer coefficient for radiation (h_r) from the cell wall in a large room (16). Table I shows the factors employed for

Table I. Physicochemical properties used

Terms	Unit	Equation	Temp. (°C)	Ref.
Enthalpic voltage	$\mathbf{E}_d$ (V)	$\mathbf{E}_d = 1.4850 - 1.490 \times 10^{-4} t_s - 9.84 \times 10^{-8} t_s^2$		(8)
Vapor pressure of water	p_{H_2O} (atm)	$\log \frac{218.617}{p_{H_2O}} = \frac{\chi}{T_s}\left(\frac{3.2437814 + 5.86826 \times 10^{-3}\chi + 1.1702379 \times 10^{-8}\chi^3}{1 + 2.1878462 \times 10^{-3}\chi}\right)$ where $\chi = 647.27 - T_s$	10-150	(17)
Latent heat of water vapor	γ_{H_2O} (kcal/kg)	$\gamma_{H_2O} = 596.25 - 0.5654 t_s$	35-100	
Specific heat of air	C_{pa} (kcal/kg-K)	$C_{pa} = 0.241$	20-100	
Viscosity of air	μ_a (kg/m-h)	$\mu_a = 6.198 \times 10^{-2} + 1.655 \times 10^{-4} t_f$	0-100	
Thermal conductivity of air	k_a (kcal/m-h-K)	$k_a = 1.840 \times 10^{-3} \frac{T_f^{1.5}}{T_f + 125}$	−191-212	(18)
Density of air	ρ_a (kg/m³)	$\rho_a = \frac{1.2932}{1 + 3.67 \times 10^{-3} t_f}$		(19)
Thermal conductivity of acrylic resin	k_p (kcal/m-h-K)	$k_p = 0.18$		
Emissivity of acrylic resin	ϵ	$\epsilon = 0.90$		
Specific heat of water	C_{ps} (kcal/kg-K)	$C_{ps} = 1.0007 - 1.226 \times 10^{-4} t_s + 1.903 \times 10^{-6} t_s^2$	20-100	

calculation. Those factors having the reference number in the last column were quoted from the publications, and others were obtained from the handbooks and the like.

The emissivity of the cell wall was estimated, since its availability was limited. The water vapor pressure and the specific heat of the solution employed were nearly the same as of water, since the caustic soda concentration was sufficiently low.

Experimental Procedure

Three vertical cells equipped with Type 304 stainless steel (SS) electrodes were used. Cell A was a rectangular-type SS cell 100 mm wide, 100 mm deep, and 1000 mm high, with one side open where a Lucite resin plate of an adequate thickness was flanged as a heat-transfer wall (see Fig. 1). A Lucite plate 10 mm thick was normally used. The copper-constantan thermocouples were embedded in the resin plate perpendicular to the wall and measured to estimate the heat flux passing through the plate. Besides the resin wall, the cell was thermally insulated with cotton of *ca.* 100 mm thick. A pair of the SS plate electrodes 40 mm wide and 700 mm high were positioned at the center of the cell, and the electrolysis gap was 10 mm. This cell was capable of 100A while most experiments were carried out at the amperage up to 60A, or 2100 A/m^2.

Cell B was a plate-and-frame type cell made of Lucite resin and was 90 mm wide, 43 mm deep, and 450 mm high. The experimental setup with this cell was almost the same as with cell A. However, a pair of thermocouples were inserted into the thermally insulated wall to estimate the heat loss from this side as well as the plastic plate on the front.

Cell C was composed of a Lucite resin cylinder of 110 mm id, 120 mm od, and 600 mm height. Two SS rods of 8 mm diam were located at the center of the cell in parallel as the electrodes. The center-to-center distance was 50 mm. The thermocouples were located along the vertical electrode to determine the temperature distribution in the solution.

Dilute caustic soda solution (0.2*m* NaOH) was electrolyzed. Oxygen and hydrogen were liberated at the anode and the cathode, respectively, and these gases were mixed together in the cell since there was no separator between two electrodes in these cells.

Although most experiments were conducted in the batch-wise manner, cell A was also operated under forced circulation of electrolytic solution, *i.e.*, the solution was pumped from the reservoir to the cell bottom and was recycled from the cell top to the reservoir by gravity. The solution was heated by an electric heater in the reservoir.

Results and Discussion

Verification of the thermal behavior.—Experimental results with cell A under various conditions are shown in Fig. 2. The ordinate is the temperature difference between solution and environment under steady state.

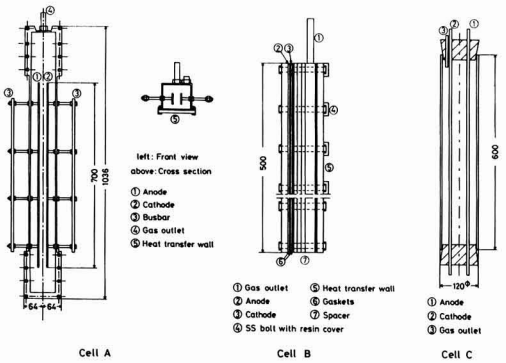


Fig. 1. Electrolytic cells

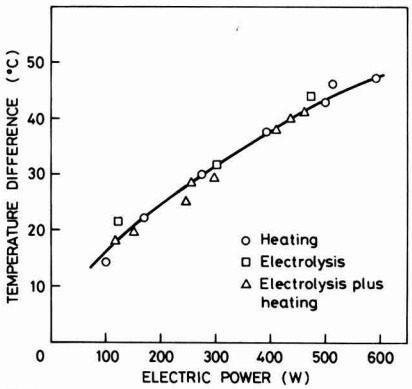


Fig. 2. Temperature difference, $t_s - t_a$, as a function of the electric power supplied to the system.

Since the enthalpic voltage $\mathbf{E}_d$ is consumed to proceed electrolysis under a given temperature, the effective voltage as the heat source is $V_{eff} = V - \mathbf{E}_d$, and hence the corresponding electric power is $I \times V_{eff}$, where I is the cell current. Also, the electrolyte is heated by an electric heater in the reservoir as stated above. The abscissa of this figure shows $I \times V_{eff} + W_{heater}$, where W_{heater} is the wattage supplied to the heater.

First, the solution was circulated between the reservoir and the cell without electrolysis, so that the heater in the reservoir was only a heat source (circular points). Second, electrolysis was conducted with no outside heater, *i.e.*, the Joule heat by electrolysis is a single source of heating (rectangular points). Finally, electrolysis was conducted with solution heating by using the heater in the reservoir (triangular points). It is clear that three cases agree well, and hence Eq. [3] is considered to be applicable for calculating the heat generation of electrolytic cell. Heat was dissipated from the piping to some extent, but no differ-

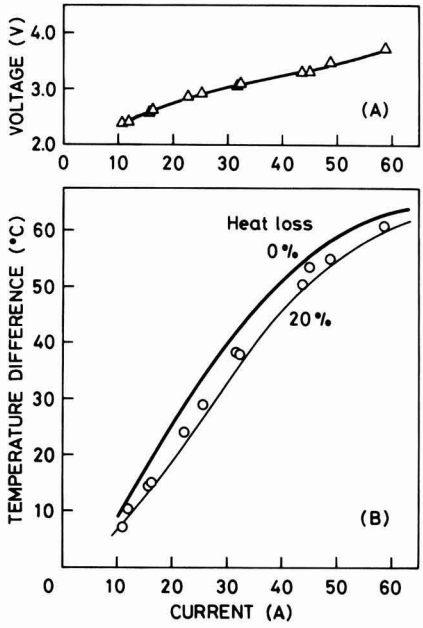


Fig. 3. Cell voltage (A) and temperature difference, $t_s - t_a$, (B) of cell A as functions of the electrolytic current. Wall thickness = 10 mm. Electrode gap = 10 mm.

ence exists among three cases. Therefore, the results shown in Fig. 2 are not affected.

Figure 3 illustrates the experimental results obtained with cell A without solution circulation. The electrolysis gap was 10 mm, and the Lucite resin wall was 10 mm thick. The solution temperature depends on the cell current. According to a preliminary experiment with cell B, the heat loss through the thermally insulated wall was some 20% of the total heat in the range 35°-80°C. The thick and thin lines in draft B illustrate the temperature calculated with assumptions of 0 and 20% of the heat loss, respectively. Almost all the experimental results locate between two curves, so that the heat loss through the insulated wall of cell A is assumed to be 15-20%. While the solution temperature rises with the increase of the cell current up to a temperature difference of 50°C, the slope of the curve decreases because the water vaporization becomes significant at high temperatures.

Although the configuration of cell C was unrealistic as practice, its simple cell design was useful to avoid the heat-transfer problems through the insulated wall as in the cases of cells A and B. The experimental results shown by the circular points in Fig. 4 agreed well with calculation using Eq. [12b] shown by the solid line, since the heat transfer was uniform along the cell wall.

Figure 5 shows the Joule heat with electrolysis, the heat loss through the wall, and the heat loss caused by water vaporization as functions of the electric current passing through cell C. It is clear that the last factor increases greatly with increases of the cell current and, hence, the solution temperature as stated above with cell A.

To investigate the effects of the emissivity of the cell wall on the heat balance, a small cell C was used. That is, the outside surface of the resin cylinder was covered with an adhesive aluminum foil to change the emissivity. Air voidage between the resin and the aluminum foil was negligible and, hence, did not affect the heat transfer. The open points and the closed points in Fig. 6 show the experimental results obtained with and without aluminum foil, respectively. The solid lines illustrate the results of calculation with 0.45 and 0.90 for ϵ. An aluminum foil employed here had a relatively large ϵ shown above against expectation since its surface was coated with synthetic polymer. The emissivity of bright aluminum is said to be less than 0.1. The solution temperature of the cell with aluminum foil is high. In consequence, the emissivity of the cell wall is a large factor of the heat balance of the electrolyzer rather than the thickness of the thermal insulator (see Fig. 12 and its description).

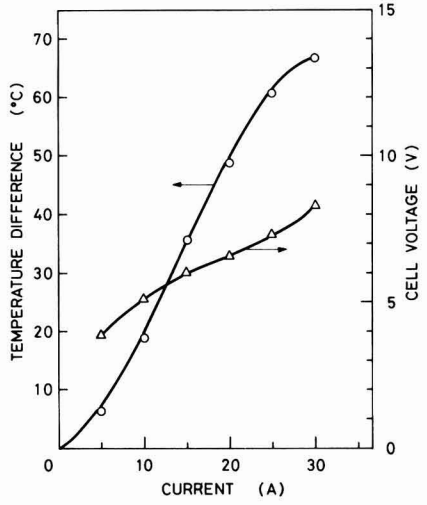


Fig. 4. Temperature difference, $t_s - t_{ii}$, and voltage of cell C under steady-state conditions as functions of the electrolytic current.

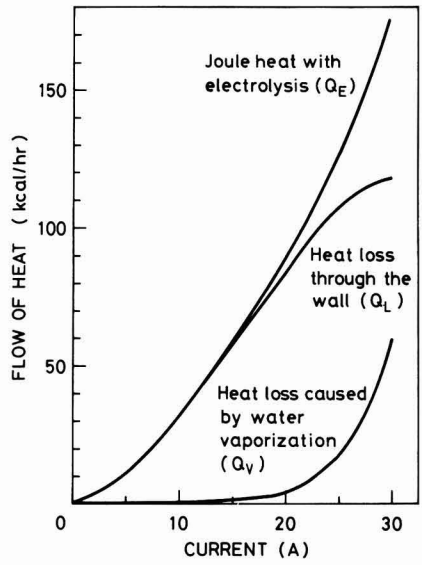


Fig. 5. Flow of heat *vs.* amperage of cell C

Figure 7 is an example of the solution temperature *vs.* time curves during electrolysis. The solid lines illustrate the results of calculation with Eq. [7] under respective conditions. The experimental results agree with calculation. Pickett (20) reported, however, disagreement of experiment with theory, probably due to variation of the solution temperature within his cell.

Since calculation described above is feasible to simulate the thermal characteristics of the cell having a simple configuration, the solution temperature in the electrochemical system consisting of the electrolyzers, the solution circulation pumps and reservoir, and other auxiliaries could be calculated exactly if the structure and geometry of hardware, the operating conditions, and the physicochemical properties of materials and electrolyte are given. Also, it is applicable to calculate the thermal

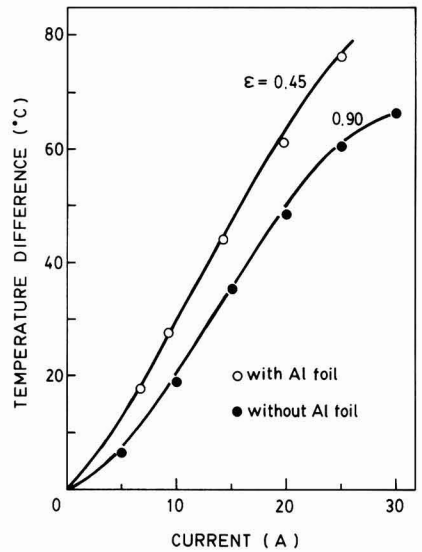


Fig. 6. Effect of the emissivity on the temperature difference, $t_s - t_{ii}$, *vs.* current curve of cell C. Plots = experimental. Curves = calculated.

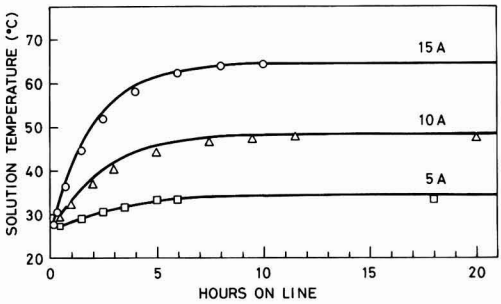


Fig. 7. Transient curves of the solution temperature of cell C. Plots = experimental. Curves = calculated.

behavior of complex systems if the overall heat-transfer coefficient for those systems is available.

Mathematical simulation of the thermal behavior of water electrolysis cell.—Tilak *et al.* have illustrated a useful diagram showing the material and energy balances of a monopolar, tank-type cell for water electrolysis [see Fig. 7 in Ref. (21)]. Calculation of the heat balance of this system operated under normal conditions shown in Table II was conducted to evaluate applicability of the mathematical treatment discussed above.

Assume that the electrolyzer is operated at a given temperature t_s. The cell voltage is V, and the amperage is I. Excess heat is removed by the heat exchanger and the like. Purified water is fed to the cell at the temperature t_i. A part of heat is dissipated from the cell wall by radiation and convection. Hydrogen and oxygen are generated at the cathode and the anode, respectively, and these gases are saturated with water vapor at the cell temperature. They also contain entrainment of electrolytic solution to some extent. The gases are cooled by the respective heat exchangers to the temperature t_c and brought to the gas holder. A small amount of water may go out with hydrogen and oxygen; instead, the condensate is sent back to the cell.

The heat balance of the water electrolysis cell under steady-state conditions is represented by Eq. [17]

$$0.86I(V - \mathbf{E}_d) - \frac{18 \times 10^{-3}}{2\mathbf{F}}\left(\frac{1.5p_{H_2O}}{p - p_{H_2O}}\right)\gamma_{H_2O}I - \Sigma UA(t_s - t_a) - \frac{18 \times 10^{-3}}{2\mathbf{F}}\left(1 + \frac{1.5p_{H_2O}'}{p - p_{H_2O}'}\right)(t_s - t_i)I - \frac{18 \times 10^{-3}}{2\mathbf{F}}\left(\frac{1.5p_{H_2O}}{p - p_{H_2O}} - \frac{1.5p_{H_2O}'}{p - p_{H_2O}'}\right)(t_s - t_c)\,I + Q_{EX} = 0 \quad [17]$$

The fourth and the fifth terms on the left side of this equation are the heats required for water feed and condensate, respectively. The cell voltage V is as follows

$$V = \mathbf{E}_d + \eta_a + |\eta_c| + \frac{il_c}{\kappa_s} \quad [18]$$

Table II. Operating conditions of a water electrolysis cell

Electrolyzer:	1.6m wide, 1.2m deep, and 1.2m high, fabricated with carbon steel plate 5 mm thick, equipped with 20 pairs of the electrodes. For carbon steel, k_p = 45 kcal/m-h-K and ϵ = 0.8.	
Electrodes:	Anodes = nickel-electroplated carbon steel plate. Cathodes = bare carbon steel plate. Size = 1.0m wide and 1.0m high. Electrode spacing = 20 mm.	
Electrolyte:	28% KOH (6.93m)	
Temperatures: (°C)	Feed water	30
	Condensers	40
	Ambience	30

Table III. Parameters employed for calculating the thermal behavior of the water electrolysis cell

Decomposition voltage (V)	$E_d = E_d^\circ + \frac{RT_s}{2\mathbf{F}} \ln\left(\frac{p_{H_2O}^\circ\,(p - p_{H_2O})^{1.5}}{p_{H_2O}}\right)$
Standard decomposition voltage (V)	$E_d^\circ = 1.5184 - 1.5421 \times 10^{-3}T_s + 9.523 \times 10^{-5}T_s \ln T_s + 9.84 \times 10^{-8}T_s^2$
Anodic overvoltage (V)	$\eta_a = 0.062 \log i + 0.164$
Cathodic overvoltage (V)	$\eta_c = -0.160 \log \lvert i \rvert + 0.146$
Solution conductivity (1/Ω-m)	$\kappa_s = 26.112 + 1.5451t_s - 1.6271 \times 10^{-3}t_s^2$
Water vapor pressure on solution (atm)	$\ln p_{H_2O} = 0.016214 - 0.13802m + 0.19330m^{0.5} + 1.02391 \ln p_{H_2O}^\circ$ (m = 6.93 at 28% KOH)

In this equation, both the diaphragm resistance and the coefficient K in Eq. [8] have been neglected for simplicity. Although the standard decomposition voltage and the overvoltages were found in the published papers (8, 13), the temperature coefficient of the overvoltage was unavailable. The water vapor pressure on the solution and the solution conductivity κ_s were quoted from Ref. (21) and (22), respectively. The relationships of these factors are shown in Table III. Some heats are dissipated from the cell cover and the side wall by radiation and convection, and for simplicity these surfaces are assumed to be flat. Also, conduction from the cell bottom is neglected.

Equation [12a] is employed for calculating convection from the cell cover as well as the vertical surface with a different coefficient 0.14 instead of 0.13 for the vertical surface (15).

Figure 8 shows the results of calculation of the thermal characteristics of a water electrolysis cell operated under normal pressure. Drafts A, B, and C show the solution temperature, the cell voltage, and the three components of heat losses, respectively, as functions of the current density. As is shown in draft A, the solution temperature rises with the increase of current density and becomes asymptotic to the boiling point. The cell voltage is almost a straight line with the current density, except with the range lower than 1000 A/m² where the superficial resist-

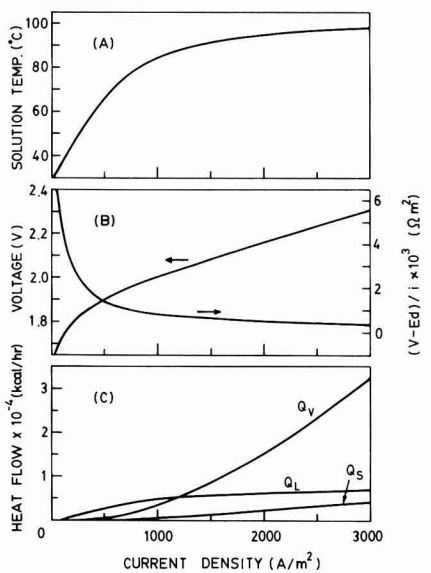


Fig. 8. Solution temperature (A), cell voltage (B), and flow of heat (C) as functions of the current density under normal pressure.

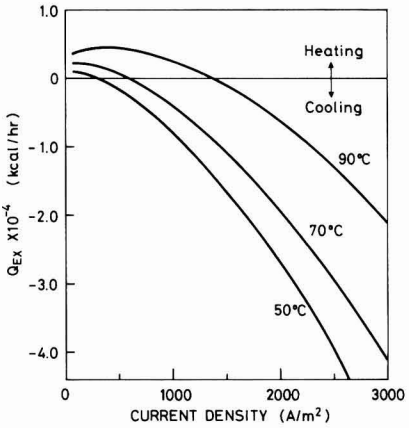


Fig. 9. External heat as a function of the current density of a cell operated under various temperatures and normal pressure.

ance $(V - E_0)/i$ decreases steeply with the increase in amperage as illustrated in draft B.

Although the heat loss through the wall Q_L is the largest factor at low current densities, the electrolytic cell is cooled mainly by water vaporization Q_V when the solution temperature rises at high current densities. The sensible heat of the feedstock Q_S is also a small factor (see draft C).

The ordinate of Fig. 9 represents the heat supply heated from an outside source for electrolyzing under given temperatures. The electrolytic cell requires some heat when operated at low current densities. On the other hand, the excess heat generated by electrolysis at high current densities must be removed. At the current density at $Q_{EX} = 0$, the heat generation is equal to dissipation so that no extra heating or cooling is required. This current density increases when the low overvoltage anode and/or cathode are employed with a minimum gap between them; thereby, the Joule heat generation is minimized. Also, Fig. 8 and 9 indicate that improvement of thermal insulation, and hence decreasing the current density at the break-even thermal conditions, is useless for minimizing the heat loss from the cell wall unless the Joule heat is reduced, since, otherwise, water vaporization is rather stimulated.

The cell operation under high pressures might be favorable for minimizing water vaporization at high temperatures, resulting in high energy efficiency. Reduction of the water content in the cell gas is an additional advantage in practice.

Figure 10 illustrates the heats as functions of the operating pressure at 2000 A/m^2 evaluated by the same manner as of the cell operated under normal pressure discussed above. However, some data necessary for the calculation were estimated by means such as extrapolation, since availability was limited. It is clear that the heat dissipation accompanied water vaporization. Q_V is decreased greatly by increasing the pressure, while the heat loss from the wall Q_L increases. The sensible heat Q_S and the Joule heat by electrolysis Q_E are almost unchanged.

Figure 11 shows the solution temperature as a function of the current density under constant pressures. The solution temperature is limited to *ca.* 100°C under atmospheric pressure (1 atm). On the other hand, the cell can be operated at the temperatures higher than 200°C when it is pressurized at 50 atm, and hence a significant reduction of the cell voltage or the energy requirement is anticipated. Miles *et al.* report a voltage saving of some 0.5V at 3000 A/m^2 by changing the operating temperature of the water electrolysis cell filled with 50% KOH from 80° to 208°C (23). According to our calculation, however, the voltage reduction by increasing the operating pressure from 1 to 50 atm, which correspond to 98° and 215°C, respectively, is only 0.1V. This disagreement might be caused by limited data and inadequate extrapolation. Thus, further experiments to obtain the physicochemical properties of electrolyte and the electrode kinetics necessary for the calculation must be conducted.

Figure 12 shows the energy requirement from the outside source as a function of the emissivity of the cell wall (A) and the thickness of the thermal insulator around the cell (B). Although the emissivity of the cell wall is difficult to change in a wide range, minor modification of the hardware surface could be possible. As is shown in Fig. 12A, the external heat supply is decreased considerably by decreasing the emissivity, especially at high cur-

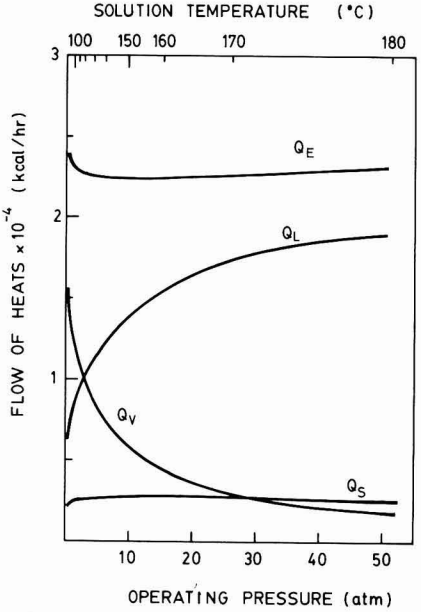


Fig. 10. Breakdown of the flow of heat as a function of the operating pressure of a cell at 2000 A/m^2.

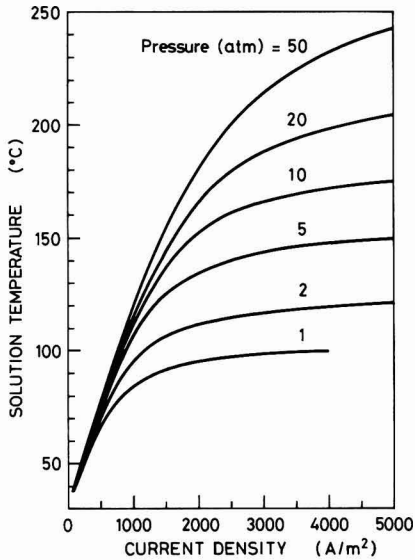


Fig. 11. Solution temperature vs. current density curves under different pressures.

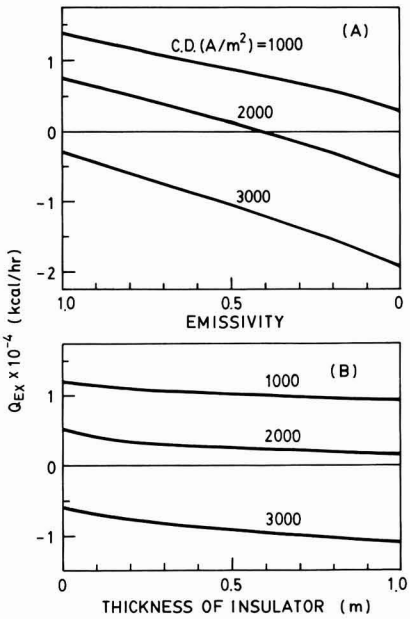


Fig. 12. External heat as a function of the emissivity of the cell wall (A) and the thickness of the thermal insulator (B) of a cell operated at 50 atm and 200°C. For the thermal insulator, k_p = 0.15 kcal/m-h-K and ϵ = 0.95.

rents. On the other hand, the reduction of the external heat is not fully accomplished by increasing the thickness of the insulator as shown in Fig. 12B. An insulator thickness 1m thick is impractical for industrial cells.

In conclusion, the heat balance in the electrolytic cell was discussed by using an alkali water electrolysis cell as an example. Experiments were carried out to obtain the results useful for calculation. A vertical-type, rectangular cell *ca.* 1m high was operated under normal pressure to determine heat transfer through the cell wall. Experimental results were referred to calculation, and they agreed well in both steady-state and nonsteady-state conditions.

It is concluded that a mere increase of the thickness of the thermal insulator around the cell is not beneficial because it causes the rise of the solution temperature, and the water vaporization is stimulated extensively, resulting in the loss of heat. Any component of the Joule heat such as the electrode overvoltage and the solution IR drop must be reduced as well.

It was clarified that the emissivity of the cell wall was a large factor of the heat loss, even at relatively low temperatures. The decrease of the emissivity through any surface modification might help to improve the heat balance of electrolytic cells significantly.

Operation under high pressures and temperatures will minimize unwanted vaporization of water from the electrolysis cell.

Mathematical treatment for water electrolysis under pressurized conditions was carried out with limited physical data, and the energy saving was demonstrated. Further experiments must be conducted to acquire all necessary data needed for calculation.

Acknowledgments

The authors appreciate T. Isobe and T. Sanno for their laboratory work. A part of this study was supported by the Japan Soda Industry Association and the Asahi Glass Foundation for Industrial Technology.

Manuscript submitted March 19, 1985; revised manuscript received *ca.* July 12, 1985.

Nagoya Institute of Technology assisted in meeting the publication costs of this article.

LIST OF SYMBOLS

- A surface area of the cell wall (m^2)
- A_e area of the working electrode (m^2)
- C_{pa} specific heat of air (kcal/kg)
- C_{ps} specific heat of solution (kcal/kg)
- E_d decomposition voltage (V)
- E_d° standard decomposition voltage (V)
- $\mathbf{E}_H$ enthalpic voltage (V)
- $\mathbf{F}$ Faraday's constant (kcal/V-eq)
- g gravity acceleration (m/h^2)
- G mass flow rate of solution (kg/h)
- Gr Grashof number
- ΔG_r free energy change for electrode reaction (kcal/mol)
- H height of the cell wall (m)
- ΔH_r enthalpy change for electrode reaction (kcal/mol)
- ΔH_v heat of vaporization (kcal/kg)
- h_a heat-transfer coefficient of the air side (kcal/m^2-h-K)
- h_c coefficient for convective heat transfer (kcal/m^2-h-K)
- h_r coefficient for radiative heat transfer (kcal/m^2-h-K)
- h_s heat-transfer coefficient of the solution side (kcal/m^2-h-K)
- I current for electrolysis (A)
- i current density (A/m^2)
- K correction factor
- k_a thermal conductivity of air (kcal/m-h-K)
- k_p thermal conductivity of the cell wall (kcal/m-h-K)
- l_e electrode gap (m)
- l_p thickness of the cell wall (m)
- m mass of solution (kg)
- m molality (mol/kg H_2O)
- m_0 initial mass of solution (kg)
- Nu Nusselt number
- n number of charge transfer
- Pr Prandtl number
- p operating pressure (atm)
- p_{H_2O} water vapor pressure on the solution (atm)
- $p_{H_2O}^\circ$ vapor pressure of pure water (atm)
- p_{H_2O}' water vapor pressure at t_c (atm)
- Q_A heat accumulation (kcal/h)
- Q_E heat generation by electrolysis (kcal/h)
- Q_{EX} heat from the external source (kcal/h)
- Q_S heat loss accompanied with feedstock (kcal/h)
- Q_L heat loss through the cell wall (kcal/h)
- Q_V heat loss caused by water vaporization (kcal/h)
- R resistance (Ω)
- R gas constant (kcal/mol-K)
- ΔS_r entropy change for electrode reaction (kcal/mol-K)
- t_a and T_a temperature of surroundings (°C and K, respectively)
- t_c temperature of condenser (°C)
- t_f and T_f film temperature, $t_f = (t_{pa} + t_a)/2$ (°C and K, respectively)
- t_i temperature of inflow (°C)
- t_{pa} and T_{pa} temperature of the cell wall at the air side (°C and K, respectively)
- t_s and T_s solution temperature (°C and K, respectively)
- t_{ST} steady-state temperature (see third paragraph) (°C)
- U overall heat-transfer coefficient (kcal/m^2-h-K)
- V cell voltage (V)
- V_{eff} part of the cell voltage effective to heat generation (V)
- W_{heater} wattage supplied to the heater (W)
- w rate of vaporization (kg/h)
- β_a volume expansion of air (1/K)
- γ_{H_2O} latent heat for water vaporization (kcal/kg)
- ϵ emissivity
- η overvoltage (V)
- θ time (h)
- κ_s conductivity of electrolytic solution (1/Ω-m)
- μ_a viscosity of air (kg/m-h)
- ρ_a density of air (kg/m^3)
- σ Stefan-Boltzmann's coefficient

REFERENCES

1. T. R. Beck and R. T. Ruggeri, in "Advances in Electrochemistry and Electrochemical Engineering," Vol. 12, H. Gerischer and C. W. Tobias, Editors, p. 263, Wiley-Interscience, New York (1981).
2. T. Z. Fahidy, *Appl. Math. Model.*, **4,** 59 (1980).
3. T. Z. Fahidy, *This Journal*, **129,** 953 (1982).
4. T. Z. Fahidy, *ibid.*, **131,** 1054 (1984).
5. T. Z. Fahidy, *J. Appl. Electrochem.*, **14,** 231 (1984).
6. T. Z. Fahidy, *Electrochim. Acta*, **29,** 1321 (1984).

7. N. Kawashima, *Ryuan Gijutsu*, **7,** 9 (1954).
8. N. L. LeRoy and C. T. Bowen, *This Journal*, **127,** 1954 (1980).
9. R. L. LeRoy, *ibid.*, **130,** 2158 (1983).
10. F. Hine, M. Yasuda, R. Nakamura, and T. Noda, *ibid.*, **122,** 1185 (1975).
11. F. Hine and K. Murakami, *ibid.*, **127,** 292 (1980).
12. F. Hine, S. Yoshizawa, and S. Okada, *ibid.*, **103,** 186 (1956).
13. R. L. LeRoy, M. B. I. Janjua, R. Renaud, and U. Leuenberger, *ibid.*, **126,** 1674 (1979).
14. R. B. MacMullin, K. L. Mills, and F. N. Ruehlen, *ibid.*, **118,** 1582 (1971).
15. R. H. Perry and C. H. Chilton, "Chemical Engineers' Handbook," 5th ed., Section 10, McGraw-Hill, New York (1973).
16. J. P. Holman, "Heat Transfer," 5th ed., p. 337, McGraw-Hill, New York (1981).
17. R. B. MacMullin, *This Journal*, **116,** 416 (1969).
18. S. Kamei, "Kagaku Kikai no Riron to Keisan" (Principles and Calculation of Chemical Process Equipments), p. 542, Sangyo Tosho Publishers, Tokyo (1959).
19. "Kagaku Binran" (Handbook of Chemistry), 2nd ed., p. 667, Chemical Society of Japan, Maruzen Publishers, Tokyo (1975).
20. D. J. Pickett, "Electrochemical Reactor Design," p. 355, Elsevier, Amsterdam (1979).
21. B. V. Tilak, P. W. T. Lu, J. E. Colman, and S. Srinivasan, in "Comprehensive Treatise of Electrochemistry," Vol. 2, J. O'M. Bockris, B. E. Conway, E. Yeager, and R. E. White, Editors, Chap. 1, Plenum Press, New York (1981).
22. W. Yang, Unpublished work.
23. M. H. Miles, G. Kissel, P. W. T. Lu, and R. Srinivasan, *This Journal*, **123,** 332 (1976).

Gas Permeation in SPE Method

II. Oxygen and Hydrogen Permeation Through Nafion

Zempachi Ogumi,* Tohru Kuroe, and Zen-ichiro Takehara*

Department of Industrial Chemistry, Faculty of Engineering, Kyoto University, Kyoto 606, Japan

ABSTRACT

The permeation of hydrogen and oxygen through Nafion® of different water contents was investigated by an electrochemical monitoring technique utilizing SPE composite electrodes. For both gases, the solubility, c^0, was very high compared with the value in aqueous solutions and was on the order of 10^{-2} mol-dm^{-3}. The diffusion constant, D, was on the order of 10^{-7} cm^2-s^{-1}. While D increased with increasing exchange capacity, c^0 was independent of the capacity. D and c^0 were almost independent of the water content of the Nafion. Hydrophobic cations, R_4N^+, decreased D. It was concluded that the permeation of gases through Nafion takes place in the intermediate region, which consists of the flexible amorphous part of the polytetrafluoroethylene backbone.

Recently, electrolyzers employing solid polymer electrolyte (SPE) have undergone extensive investigation for applications such as water electrolysis (1), brine electrolysis (2), and electro-organic syntheses (3-5). In gas evolving electrolyzer systems, gas permeation through SPE materials results in decreases in current efficiencies. This has been observed in Kolbe-type reactions using a "both-sides" SPE method as well as in water electrolysis. Similar decreases in efficiencies probably are also observed in SPE fuel cells (6).

Nafion perfluorinated cation exchange membranes are used widely in many electrochemical systems (7-9), including SPE technologies, because of their chemical and thermal stabilities and their high ionic conductivities. The structure of Nafion has attracted the interest of many workers and has been the subject of considerable investigation. An ionic cluster model by Gierke *et al.* (10-12) has been basically accepted widely. This model satisfactorily explains Nafion's mechanical properties (10) and transport behavior (11-15). Yeager and Steck have modified the spherical ionic cluster model and have proposed a model based on irregular ionic clusters, composed of three regions, *viz.*, a hydrophobic backbone, aqueous ionic clusters, and intermediate regions (16).

The present authors have investigated oxygen permeation through Nafion 120 using an electrochemical monitoring technique and have reported previously the diffusion coefficient and the solubility of oxygen (17). The very high solubility of oxygen was briefly discussed, and the influence of the polytetrafluoroethylene backbone was inferred to explain the high solubility.

In the present work, solubilities and diffusion coefficients of hydrogen and oxygen have been examined in detail for different counterions and water contents. Based on the results obtained, the permeation of these gases through Nafion is discussed with reference to the model by Yeager and Steck.

* Electrochemical Society Active Member.

Experimental

Chemicals.—All chemicals, with the exception of hydrazine, were reagent grade. Hydrazine was chemical pure grade. All chemicals were used without further purification. Hydrogen, nitrogen, and argon were of purity higher than 99.9%, oxygen of 99.8%.

Membranes and deposition of platinum.—Nafion 125 (nominal exchange capacity of 0.83 meq/g-dry polymer and thickness of 0.125 mm), Nafion 120 (0.83 meq/g-dry polymer, 0.250 mm), and Nafion 117 (0.91 meq/g-dry polymer, 0.175 mm) were chosen for this study. Nafion is known to change its water content depending on the treatment conditions, such as boiling time and counterions, and the electrolyte concentration of the soaking solutions (18). The membranes were pretreated in the manner of Yeager and Steck (19). Platinum was deposited on one side of the membranes after boiling membranes in the H^+ form for 3h. The prepared SPE composite electrode, referred to as Pt-Nafion, was soaked in a solution containing a given M^+ ion for more than 36h at 25°C for equilibration. These composites are referred to as M-type membranes. Solutions containing M^+ were prepared from M_2SO_4 and distilled water at 0.5 mol-dm^{-3} for alkali metal ion solutions and from R_4NCl at 1 mol-dm^{-3} for tetraalkylammonium ion solutions. Some of the Nafion membranes were treated according to a different procedure in which they were boiled in the Na^+ form in water for 0.5 or 3h, followed by deposition with platinum. The prepared Pt-Nafion then was soaked in M^+ ion solutions as described above. Composites prepared thus are referred to as M^a-type (0.5h boiling) and M^b-type (3h boiling) membranes. Platinum deposition was carried out by utilizing a previously described electroless plating method using hydrazine as a reductant (3, 17). The resistivity of the prepared Pt-Nafion was less than 4Ω at 2 cm distance on the surface and it did not increase beyond 6Ω after repeated permeation measurements.

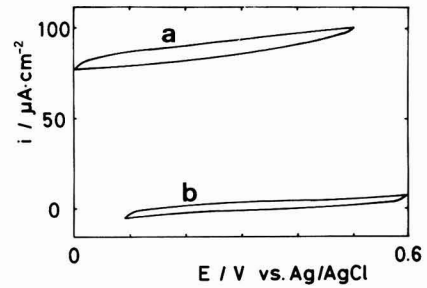


Fig. 1. Polarization curves on Pt-Nafion of K[a]-type membrane. Sweep rate: 0.1 mV-s^{-1}. Curve a: hydrogen. Curve b: nitrogen in the gas compartment. 0.5M K_2SO_4 in the solution compartment.

Electrolysis cell and permeation measurement.—The experimental cell was constructed as described elsewhere (17). The solution compartment was filled with solution of the same composition as used previously for soaking and equilibration, in order to prevent the membrane from changing its water content during the measurements. Permeation measurements were carried out in the same manner as in Ref. (17).

Results

E-i relationships.—Figure 1 shows the results from a set of polarization experiments on Pt-Nafion using K[a]-type Nafion 125. Curve a was obtained using 100% hydrogen, and curve b 100% nitrogen. A hysteresis was observed between the forward and reverse sweep in spite of the very slow sweep rate of 0.1 mV-s^{-1}. This hysteresis can be ascribed to the large capacity of the electrodes, which were deposited on the Nafion in a form similar to platinum black. An almost constant current due to hydrogen oxidation was observed at 0-0.5V *vs.* Ag/AgCl, which was controlled by hydrogen mass-transfer limitation through the membrane. With nitrogen, the observed current was very small and was regarded as a residual current. During all the hydrogen permeation experiments, the potential of the SPE composite electrodes was set at 0.25V *vs.* Ag/AgCl in order to oxidize hydrogen under diffusion limiting conditions. The obtained currents were corrected for the residual current. In all experiments for oxygen reduction, the potential was set at −0.25V *vs.* Ag/AgCl according to our previous results (17).

Permeation results.—All permeation transients for hydrogen oxidation and oxygen reduction showed the small second step following the large first step in both buildup and decay curves as described by curve a in Fig. 2, which was measured for hydrogen oxidation on Na-type Nafion 125. The first large step corresponds to a main fast permeation pass, and the second small one to a slow permeation pass. $J_{1\infty}$ and $J_{2\infty}$ are the steady-state currents for the fast pass and the (fast + slow) pass, respectively. The first step was replotted as curve b in Fig. 2, neglecting the second step. Curve b agrees very well with the theoretical curve for fickian diffusion shown by the broken line in the figure. Although the slow pass was replotted neglecting the fast pass, the resulting curves did not show agreement with the theoretical curve. In this study, only the fast permeation is treated neglecting the slow permeation.

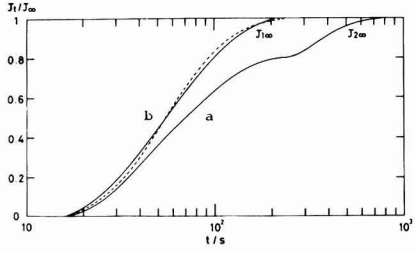


Fig. 2. Hydrogen permeation transient currents through Na-type Nafion 125 at 25°C in 0.5M K_2SO_4. Solid line a: full transient. Solid line b: transient until $J_{1\infty}$ of curve a. Broken line: theoretical curve.

Both the buildup and decay curves for hydrogen permeation through Li-type Nafion 125 did not agree well with the theoretical curve. This poor agreement leads to diffusion coefficients and solubilities of a limited reliability for hydrogen permeation through Li-type Nafion 125.

Evaluation of diffusion coefficients, D, and solubilities, c^0.—In order to evaluate diffusion coefficients, D, and solubilities, c^0, using the transient technique, the membrane thickness, l, must be known (17); $D = 0.138\ l^2/t_{1/2}$ and $J_\infty = nFDc^0/l$ [see Ref. (17) for details]. Since Nafion without reinforcement is known to change its dimension isotropically by swelling (18), the thickness can be calculated from the volume change at swelling. The thicknesses of Li, Na, K, and Cs types were calculated using the reported water content by Yeager *et al.* (19). The water content in swollen Nafion was also estimated by using the following empirical equation (18, 20) with the above membranes

$$V_w = 2.4AB \exp(3980/EW)$$

The differences between values from the two methods were less than 10%. The thicknesses of membranes of types other than the above four were estimated by using the empirical equation. The results obtained from the permeation experiments are summarized in Table I and Table II for hydrogen and oxygen. Each value is the average of more than three measurements.

Both dry and wet gases were used in the experiments for oxygen permeation using Na-type membranes. Both results were the same within experimental error. This coincidence means that the conditions of the gases are less important than those of the solution contacting the membrane.

Discussion

Solubilities.—Table III summarizes the solubilities of O_2 and H_2 in several media. Both hydrogen and oxygen solubilities are much higher in liquid perfluorocarbon and polytetrafluoroethylene (PTFE), which comprises the backbone chain of Nafion, than in aqueous solutions. Hydrogen and oxygen dissolved 40 and 20-30 times more in PTFE, respectively, than in aqueous solutions. The solubilities in Nafion shown in Tables I and II are as high as in PTFE. In addition to high solubilities, similarity in the solubility ratio of the two gases is observed between Nafion and PTFE. These facts show that the dissolution of both gases in the hydrophobic backbone of Nafion (which has a structure similar to PTFE) is preferred to dissolution in the ionic cluster. In Fig. 3 and Fig. 4, the solubilities of hydrogen and oxygen, respectively, are plotted against the water content of swollen Nafion. The solubilities of both gases are scattered, and it is difficult to find any dependency on the water content. The solubilities of both gases were comparable to each other in the same types of membranes. Table IV lists the solubili-

Table I. Permeation parameters of hydrogen through Nafion 125 of different ionic types at 25°C

	K[a]	K[b]	Cs	K	Na	Li
Water content	9.2*	9.5	9.9	12.0	18.6	22.2
mol H_2O/mol SO_3^-	**		11.3	13.3	18.4	22.3
$J_{1\infty} \times 10^6$ (A-cm^{-2})	83.1	84.0	71.0	82.8	92.0	69.7
$D \times 10^7$ (cm^2-s^{-1})	8.02	5.66	4.68	6.03	5.06	4.65
$c^0 \times 10^2$ (M)	0.75	1.03	1.09	0.97	1.36	1.18

[a] Using empirical equation.
[b] By Yeager *et al.*

Table II. Permeation of oxygen through Nafion 125 (A) and Nafion 117 (B) of different ionic types at 25°C

		R'_4N^a	R''_4N^a	K^a	R''_4N	Cs	K	Na	Li	
A	Water content mol H_2O/mol SO_3	8.7	9.0	9.2		9.9 11.3	12.0 13.3	18.6 18.4	22.2 22.3	b c
	$J_{1x} \times 10^6$ (A-cm^{-2})	50.1	68.2	80.1		59.8	72.1	94.9	108.8	
	$D \times 10^7$ (cm^2-s^{-1})	1.39	1.73	2.16		1.88	2.42	2.61	2.62	
	$c^0 \times 10^2$ (M)	1.27	1.38	1.31		1.14	1.09	1.37	1.60	
B	Water content				15.6		15.9	24.6	29.3	b
	$J_{1x} \times 10^6$ (A-cm^{-2})				76.9		89.2	68.4	101.5	
	$D \times 10^7$ (cm^2-s^{-1})				3.59		4.32	4.29	4.24	
	$c^0 \times 10^2$ (M)				1.10		1.07	0.86	1.34	

[a] R′ = C_2H_5; R″ = CH_3.
[b] Using empirical equation.
[c] By Yeager *et al.*

ties, c'^0, referred to the volume of the hydrophobic backbone of Nafion, which was calculated by subtracting the volume of the swelling water from the apparent total volume. In this estimation, the partial molar volume of the swelling water was assumed to be equal to that of ordinary free water. The solubility, c'^0, was almost constant within experimental error except for Li- and Na-type Nafion. It is known that gases do not dissolve in the crystalline region but in the amorphous region when they dissolve in polymers (23). The crystalline region of Nafion decreases in the order $-SO_2F$ form (XR resin, the precursor polymer of Nafion) > dry H^+ form > wet H^+ form. An increase in the exchange capacity decreases the crystalline region (24).

The above discussion of solubility leads to the expectation that gases are dissolved preferentially in the hydrophobic backbone region of Nafion.

Diffusion coefficients.—Figures 5 and 6 show the diffusion coefficients of hydrogen and oxygen in Nafion, D_H and D_O, against $V_p/1 - V_p$, where V_p is the polymer fraction of the swollen membrane. The double circles and

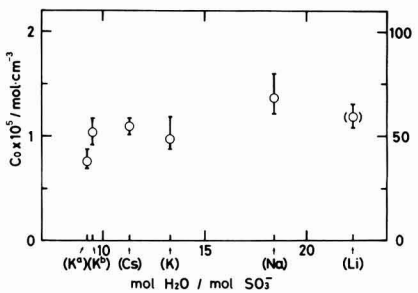


Fig. 3. Hydrogen solubility in Nafion 125 of different ionic types at 25°C.

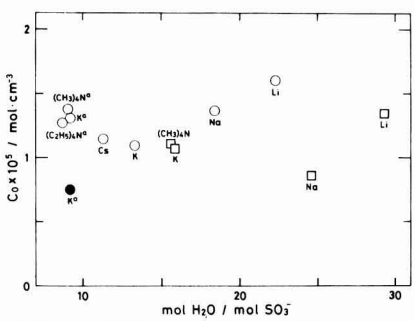


Fig. 4. Oxygen solubility in membranes of different ionic types at 25°C. Open circles: Nafion 125. Closed circles: Nafion 120. Squares: Nafion 117.

Table III. Solubilities of oxygen and hydrogen in several media in $c \times 10^3$ (mol-dm^{-3})

Medium	Temp. (°C)	H_2	O_2	Ref.
K-type Nafion 125		9.7	10.9	
K-type Nafion 117			10.7	
Nafion 120	25	24.5		(32)
H_2O	25	0.78	1.3	(17)
0.5M H_2SO_4	25	0.72		(17)
0.5M K_2SO_4	25		0.85	(17)
n-C_7F_{16}	25	6.8	26.8	(21)
n-C_8F_{18}	25		23.2	(21)
PTFE	20	31.3	26.8	(22)

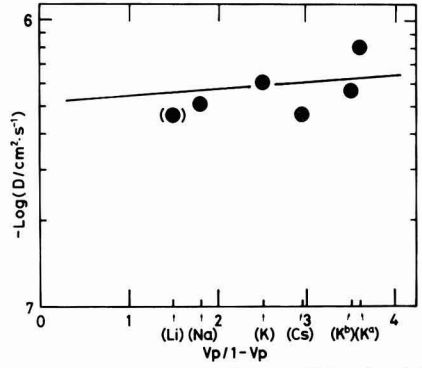


Fig. 5. Dependence of hydrogen diffusion coefficient through Nafion at 25°C.

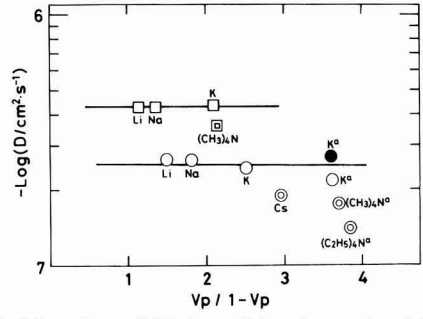


Fig. 6. Dependences of diffusion coefficient of oxygen through Nafion 125 (circles, double circles), Nafion 120 (closed circle), and Nafion 117 (squares, double square) at 25°C.

Table IV. Solubilities, c'^0, of hydrogen and oxygen in polymer part of Nafion. $c'^0 \times 10^2$ (mol-dm^{-3})

		$(C_2H_5)_4N^a$	$(CH_3)_4N^a$	K^a	K^b	$(CH_3)_4N$	Cs	K	Na	Li
H_2	Nafion 125			0.96	1.32		1.46	1.35	2.11	1.97
O_2	Nafion 125	1.60	1.75	1.67			1.53	1.52	2.13	2.67
	Nafion 117					1.61		1.58	1.49	2.52

double square designate the results obtained by using ions which are known to exist in the intermediate region between the hydrophobic backbone and ionic cluster regions (16). The unit $(V_p/1 - V_p)$ of the abscissa was introduced by Yasuda *et al.* in order to describe the transport phenomena of small particles through polymer materials bearing a fixed charge (25). In the case of diffusion through the aqueous part of a swollen polymer, theoretically, log D decreases against $V_p/1 - V_p$. Yeager *et al.* obtained straight lines of negative slopes for H_2O and Na^+ transport through swollen Nafion using the above plots. On the other hand, they obtained a constant value of log D against changing $V_p/1 - V_p$ for Cs^+ transport through the identical membrane. These results allowed them to propose a structural model of Nafion and to conclude that, while H_2O and Na^+ permeate through the ionic cluster region, Cs^+ permeates through the intermediate region which is not affected by the change in water content (16).

IR (26) and NMR (27) measurements have revealed the existence of the interaction of water with perfluorocarbon backbone. Hydrophobic interaction of large hydrophobic cations in Nafion has been recognized in addition to electrostatic interaction with the fixed anion (28-30).

Taking these reported observations into consideration, the results shown in Fig. 5 and 6 that D_H and D_O are independent of $V_p/1 - V_p$ and small in the presence of cations existing in the intermediate region lead to the conclusion that the main diffusion region is not the ionic cluster but the intermediate region. This conclusion is consistent with the discussion in the section on solubility. Yeager *et al.* considered that the intermediate region of Nafion consists of an aqueous part. The region, however, might be too small to satisfy the high solubility and large diffusion coefficient observed in the present work. It is reasonable to assume that the intermediate region available for dissolution and permeation of gases includes the amorphous part of the perfluorinated backbone. It is known that unhydrolyzed precursor polymer ($-SO_2F$) comprises ~40% of the crystalline portion of dry polymer (24) and Nafion of exchange capacity 0.83 meq/g-dry polymer and 0.93 meq/g-dry polymer 5 ~ 10%. This means that most parts of the backbone are of a flexible structure and are available for gas permeation in the permeation model through the amorphous part of the hydrophobic perfluorocarbon backbone of Nafion.

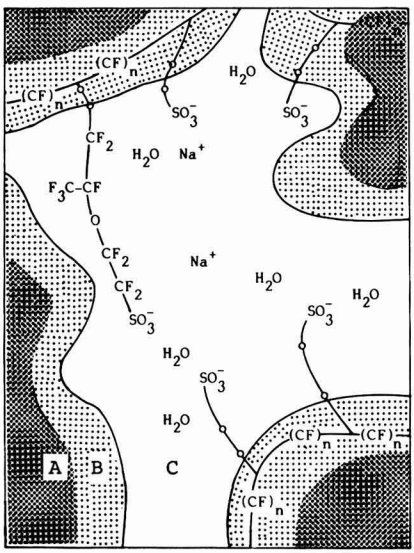


Fig. 7. Schematic model of the permeation region through Nafion. Region A: rigid hydrophobic backbone. Region B: flexible perfluorocarbon where gases permeate. Region C: ionic cluster region containing water similar to bulk water.

The flexible hydrophobic part is expected to show properties similar to PTFE, which dissolves much hydrogen and oxygen as shown in Table III. This was confirmed by the solubility results.

It is expected also that the cation existing in the intermediate region will interfere with the diffusion of gases there. This was proved in the diffusion measurements through membranes with $(CH_3)_4N^+$, $(C_2H_5)_4N^+$, and Cs^+ ions, which are considered to have hydrophobic interactions, as shown in Fig. 6 with double circles and the double square. Larger D_O's were obtained with Nafion 117 than with Nafion 125 and 120. This is because the former should have a larger amorphous part available for the permeation than the latter, because of the higher exchange capacity.

Based on the above discussion, it can be concluded that the permeation of gases through Nafion takes place in the intermediate region of the structural model of Yeager *et al.*, which consists mainly of the flexible amorphous part of perfluorocarbon backbone of Nafion. This is illustrated in Fig. 7.

Of course, this discussion does not exclude permeation through an ionic cluster, although the contribution from such permeation is estimated to be small.

Permeability.—Permeability, P, which is the product of the diffusion coefficient and the solubility, often is used to describe the transport of gases through polymers. Table V contains values of P calculated from D and c'^0. Except for hydrophobic ion-type membranes, P changes with c'^0 because D was almost constant. High water content causes an increase of the intermediate region at the cost of the crystalline part of Nafion to produce an increase in P. Hydrophobic R_4N^+ interferes with the permeation and decreases P.

The ratio P_H/P_O is almost constant, and is similar to the value for PTFE. This similarity supports the concepts of gas permeation through Nafion discussed in the above sections.

Summary

The permeation of hydrogen and oxygen through Nafion of different water content was investigated by an electrochemical monitoring technique using SPE composite electrodes.

Table V. Permeability, P, through Nafion 125 of different ionic types in $P \times 10^{12}$ (cm^2-s^{-1}) mol-cm^{-3} Nafion

Ion	R'_4N^a	R''_4N^a	R''_4N	K	K	Cs	K	Na	Li
H_2				7.70	7.47	6.83	8.14	10.68	9.16
O_2	2.22	3.03		3.61		2.88	3.68	5.56	7.00
O_2 [b]			5.78				6.83	6.39	10.68
$\frac{H_2}{O_2}$				2.13		2.37	2.21	1.92	1.31

[a] R′ = C_2H_5; R″ = CH_3.
[b] Through Nafion 117; *cf.* H_2: 8.13, O_2: 3.73 through PTFE.

The solubility and diffusion coefficient were almost independent of the water content of the membrane. While the high solubility was almost independent of the exchange capacity, the diffusion coefficient of oxygen was higher in Nafion 117 of higher exchange capacity than in Nafion 125 of lower exchange capacity. Hydrophobic cations, R_4N^+, decreased the diffusion coefficient of oxygen because such ions could intrude and block the diffusion pass. The results lead to the conclusion that gases permeate mainly through the intermediate region, which consists of the flexible amorphous part of the polytetrafluoroethylene backbone of Nafion. The permeability ratio P_H/P_0 through Nafion was similar to the ratio in PTFE. This similarity strongly supports the discussion on the permeation pass.

Acknowledgments

Special thanks are due to Professor F. Foulkes of the University of Toronto for his helpful discussions. The authors also wish to thank E. I. du Pont de Nemours and Company for providing membrane samples.

Manuscript submitted April 1, 1985; revised manuscript received June 5, 1985.

Kyoto University assisted in meeting the publication costs of this article.

REFERENCES

1. P. W. T. Lu and S. Srinivasan, *J. Appl. Electrochem.*, **9,** 269 (1979).
2. A. P. Laconti, Japan Tokkyo Kokai, 54-112398 (1979).
3. Z. Ogumi, K. Nishio, and S. Yoshizawa, *Denki Kagaku*, **49,** 212 (1981).
4. Z. Ogumi, K. Nishio, and S. Yoshizawa, *Electrochim. Acta*, **26,** 1779 (1981).
5. Z. Ogumi, H. Yamashita, K. Nishio, Z. Takehara, and S. Yoshizawa, *ibid.*, **28,** 1687 (1983).
6. H. A. Liebhafsky and E. J. Cairns, "Fuel Cells and Fuel Batteries," John Wiley and Sons, New York (1968).
7. R. S. Yeo, J. McBreen, G. Kissel, F. Kulesa, and S. Srinivasan, *J. Appl. Electrochem.*, **10,** 741 (1980).
8. D. Bergner, *ibid.*, **12,** 631 (1982).
9. R. S. Yeo and D-T. Chin, *This Journal*, **127,** 549 (1980).
10. R. S. Yeo and A. Eisenberg, *J. Appl. Polym. Sci.*, **21,** 875 (1977).
11. T. D. Gierke, Paper 438 presented at The Electrochemical Society Meeting, Atlanta, GA, Oct. 9-14, 1977.
12. R. S. Yeo, *This Journal*, **130,** 533 (1983).
13. H. L. Yeager and B. Kipling, *J. Phys. Chem.*, **83,** 1836 (1979).
14. H. L. Yeager, B. O'Dell, and Z. Twardowski, *This Journal*, **129,** 85 (1982).
15. C. Fabiani, G. Scibona, and B. Scuppa, *J. Membr. Sci.*, **5,** 16 (1983).
16. H. L. Yeager and A. Steck, *This Journal*, **128,** 1880 (1982).
17. Z. Ogumi, Z. Takehara, and S. Yoshizawa, *ibid.*, **131,** 769 (1984).
18. W. G. Grot, G. E. Munn, and D. N. Walmsley, Paper 154 presented at The Electrochemical Society Meeting, Houston, TX, May 7-11, 1972.
19. A. Steck and H. L. Yeager, *Anal. Chem.*, **52,** 1215 (1980).
20. E. I. du Pont de Nemours & Co., Inc., E-05569, 2/76 (catalog).
21. M'H. A. Hamza, G. Serratrice, M-J. Stebe, and J-H. Delpuech, *J. Am. Chem. Soc.*, **103,** 3733 (1981).
22. T. K. Gibbs and D. Pletcher, *Electrochim. Acta*, **25,** 1105 (1980).
23. A. S. Michaels and H. J. Bixler, *J. Polym. Sci.*, **50,** 393 (1961).
24. T. D. Gierke, G. E. Munn, and F. C. Wilson, *J. Polym. Sci. Polym. Phys. Ed.*, **19,** 1687 (1981).
25. H. Yasuda, C. E. Lamaze, and L. D. Ikenberry, *Makromol. Chem.*, **118,** 19 (1968).
26. M. Falk, *Can. J. Chem.*, **58,** 1495 (1980).
27. N. Sivashinsky and G. B. Tanny, *J. Appl. Polym. Sci.*, **26,** 2625 (1981).
28. P. C. Lee and D. Meisel, *J. Am. Chem. Soc.*, **102** 5477 (1980).
29. D. A. Buttry and F. C. Anson, *ibid.*, **105,** 685 (1983).
30. C. R. Martin and H. Freiser, *Anal. Chem.*, **53,** 902 (1981).
31. N. G. Boyle, V. J. McBrierty, and D. C. Douglas, *Macromolecules*, **16,** 75 (1983).
32. R. S. Yeo and J. McBreen, *This Journal*, **126,** 1682 (1979).

Oxidation of Phenol with AC Electrolysis

D-T. Chin* and C. Y. Cheng

Department of Chemical Engineering, Clarkson University, Potsdam, New York 13676

ABSTRACT

The method of alternating voltage (AV) modulation has been used to determine the effect of alternating current on the polarization behavior of the oxidation of phenol on platinum in aqueous sulfuric acid electrolyte. The study was made with sinusoidal, square, and triangular AV over a range of frequency from 20 to 6000 Hz, and a range of magnitude from 0 to 500 mV rms. A batch electrochemical cell operated on a potentiostatic mode was used to evaluate the conversion of phenol, anode current efficiency, yield of hydroquinone, and energy consumption of the process. The results indicate that AV strongly modified the shape of the polarization curve. It caused a shift in the rest potential toward the negative direction, and increased the dc current density for both the anodic and cathodic reactions. The rate of conversion of phenol increased with increasing magnitude of AV and decreased with increasing AV frequency.

Recently, the rising cost of petrochemical feedstocks and environmental considerations have generated a renewed interest in electro-organic reactions (1). The disadvantages of electro-organic synthesis as compared to the chemical synthetic methods are the slow reaction kinetics, high capital investment of electrolytic cells, and high energy consumption for the electrolysis. The purpose of this work is to improve the reaction rate of electro-organic reactions with an alternating current (ac) electrolysis. Previous investigations in this laboratory on the ac corrosion processes (2-9) have shown that ac enhances the apparent reaction kinetics of electrochemical reactions by improving the exchange current density and transport of reacting ions to the electrode surface. The application of ac to electro-organic reactions has an advantage that there is no need to modify the electrochemical cell, and no catalysts and additives are used, thus avoiding the contamination of reaction products.

Superimposition of an ac component in electrolysis shifts the rest potential and lowers the overpotential of electrode reactions. This property may be used to isolate a desired product, which would be otherwise destroyed at higher overpotentials. Reitlinger (10) has found that ac affected the selectivity of the electro-organic reaction. Ethyl alcohol was oxidized to acetaldehyde without being further oxidized to acetic acid with an alternating current. He also reported that with ac electrolysis p-benzaldehyde sulfonic acid could be obtained from p-tolune-sulfonic acid. Kappana *et al.* (11) applied the ac electrolysis to the oxidation of glucose to calcium gluconate. They showed

*Electrochemical Society Active Member.

that the current efficiency increased with increasing ac current density and with decreasing ac frequency. Noguchi (12) applied 0.8-2*M* Hz ac (below 100V) to two Ag-plated electrodes in soy sauce, synthetic vinegar, whiskey, sake, and perfume to decrease the time required for the aging process. He also found that green tea lost its flavor, persimmons lost their bitterness, coffee and cocoa extracts lost their taste, and acrylic ester was polymerized by applying high frequency ac. Polymerization of methylmethacrylate in aqueous solutions of H_3PO_4 and H_2SO_4 was initiated by ac on a platinum electrode (13). The degree of polymerization depended on the type of electrolyte, concentration, and ac current density. Korchinskii (14) found that ac increased the adsorption of acetate ions on a platinum electrode. Nadebaum *et al.* (15) obtained a rate equation for the oxidation of aqueous ethanol to carbon dioxide and ethane when the cell was modulated with a rectangular alternating voltage (AV). Nitskanskii (16) exposed eggs to high frequency sinusoidal ac during incubation. The total protein and albumin content increased, and γ-globulin content decreased. Kikuchi and Ueyama (17) found that the electrolysis of a mixture containing N-vinylcarbazole, $LiClO_4$, and ethyl ether or methylcyanide at −22° to 30°C gave low molecular weight poly(N-vinylcarbazole) in the anode compartment by superimposing a rectangular ac. The yield of the polymer increased with decreasing temperature, and the molecular weight of the polymer produced with the rectangular-wave ac was greater than that with only dc. Florequin *et al.* (18) found that the use of anodic rectangular current pulses restored the activities of a platinized Pt electrode for the reduction of dimethylacetone and butanone to alkane. Bhadani (19) passed sinusoidal ac through a styrene solution containing sodium tetraphenylboron, and a high molecular weight polystyrene was formed. The yield and molecular weight of polystyrene decreased with increasing ac frequency. Tamura (20) and his co-workers found that superimposed AV at 50 Hz increased the formation of β-type crystals of vinylindene fluoride. Kawahara (21) mixed soybean milk with an acidic medium containing oxalic acid, or lactic acid and $CaHPO_4$, and treated the solution with a sinusoidal ac (0.25 A/dm²) to make Tofu. Alkire and Tsai (22) prepared propylene oxide by electrolysis of propylene in a sodium bromide solution with sinusoidal ac. They obtained a 22% current efficiency at 1 Hz and an ac current density of 175 mA/cm² on a platinum electrode. Adzic *et al.* (23) investigated the oxidation of formic acid to carbon dioxide and water on platinum with a superimposed rectangular alternating voltage. The oxidation rate was higher than that of the constant dc potential electrolysis.

In this study, the method of alternating voltage (AV) modulation (6-9) has been used to determine the effect of sinusoidal, square, and triangular wave ac on the polarization behavior of the oxidation of phenol to benzoquinone

$$C_6H_5OH + H_2O \rightarrow C_6H_4O_2 + 4H^+ + 4e^- \quad [1]$$

The oxidation of phenol was first reported by Fichter (24), and its industrial importance is reflected by numerous patents (25-31). In an undivided cell, the benzoquinone produced at the anode is subsequently reduced to hydroquinone at the cathode

$$C_6H_4O_2 + 2H^+ + 2e^- \rightarrow C_6H_4(OH)_2 \quad [2]$$

A bench-scale electrochemical cell operated on a potentiostatic mode was used to evaluate the effect of superimposed ac on the conversion, chemical yield, current efficiency, and energy consumption of the process.

Experimental

An alternating voltage (AV) modulation was used in the present investigation. In this method, a constant AV is superimposed onto a dc potential and the resulting composite potential wave is applied between working and reference electrodes through a potentiostat. The resulting dc and ac current densities are then measured as a function of dc potential and applied AV. The details of the experimental technique are described in Ref. (6-9), and will not be repeated here.

Electrolyte and cell setup.—The electrolyte used in this work consisted of 0.01-0.1*M* phenol in 1*M* sulfuric acid in a temperature range of 23°-50°C. A platinum rotating disk electrode mounted on a rotator (Pine Instruments ASR2) and having a surface area 0.458 cm² exposed to the electrolyte was used for the polarization measurement. A stationary platinum foil of 12.5 cm² surface area was used for the potentiostatic batch cell electrolysis of oxidation of phenol. A 1 liter Pyrex glass jar immersed in a constant temperature bath was used as a single-compartment cell. The counterelectrode was a platinum screen, and a saturated calomel electrode (SCE) connected to a Luggin capillary tube was used as the reference electrode.

Polarization measurement.—The platinum rotating disk electrode was used for the polarization measurement. For each run, the electrode was cleaned with methanol and was cathodically activated at −3.0V for 2 min in 1*N* NaOH solution followed by rinsing in distilled water. The clean electrode was quickly transferred into the cell and installed on the rotator. The potential difference between the working and reference electrodes was controlled by a potentiostat with a built-in sweep generator (Pine Instrument RDE3). The superimposed AV was supplied to the potentiostat from an ac signal generator (Hewlett-Packard 2311A), and the dc potential of the working electrode was swept between 0 and 1500 mV at a sweep rate of 5 mV/s. The dc current was converted to a voltage signal by passing the current through a precision resistor (10-1000Ω) connected in parallel to a capacitor (16,800 mF). The voltage drop was fed to a logarithmic converter (Linseis N46), and the output of this converter was fed to a X-Y recorder (Hewlett Packard 7044A) for plotting dc current *vs.* dc potential. The ac current was determined with a multimeter (Keithley 177) by measuring the ac voltage drop across a second precision resistor; the output from the multimeter was fed to a second X-Y recorder (Linseis 1700) for plotting ac current *vs.* dc potential. In this way, the dc and ac currents *vs.* dc potential curves were obtained with the test electrolytes for a range of superimposed sinusoidal, square, and triangular AV varying from 0 to 500 mV rms, and the AV frequency from 20 to 6000 Hz. The experiments were carried out in a temperature range 23°-50°C.

Batch electrolysis experiment.—After the polarization measurement, a potentiostatic batch electrolysis was carried out for the oxidation of phenol with the stationary platinum electrode at selected dc potentials superimposed with a constant AV. During the electrolysis, the dc current, ac current, dc cell voltage, and ac cell voltage were recorded as functions of electrolysis time. Electrolyte samples were also withdrawn from the cell at selected time intervals, and the concentration of phenol was analyzed with a bromination and iodometric titration method. At the end of the run, the yield of hydroquinone was determined by an oxidimetric titration with a ceric sulfate solution. The details of the chemical analytical methods used are given in Ref. (32).

Results and Discussion

DC polarization curves without superimposed AV.—To establish the basis for comparing with AV modulation, the dc polarization curves were first obtained for the platinum rotating disk electrode in the test electrolytes without any superimposed AV. It was found that the speed of rotation had no effect on the anodic polarization curves for the oxidation of phenol, and all the data were collected at a rotational speed of 2400 rpm.

The effect of phenol concentration (0-0.1*M*) on the dc polarization curves at 50°C is shown in Fig. 1. The anodic curves are for the oxidation of phenol, and the cathodic curves correspond to the reduction of surface oxides and dissolved oxygen on the platinum surface. The arrows in the figure indicate the location of rest potentials. The

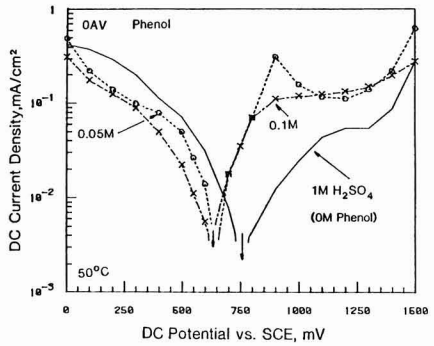


Fig. 1. DC polarization curves without superimposed AV for the oxidation of phenol on a platinum rotating disk electrode in 1M H_2SO_4 at 50°C. The data are given for three phenol concentrations: 0, 0.5, and 0.1M. The arrows indicate the rest potentials. The platinum electrode was rotating at 2400 rpm.

cathodic current density decreased with increasing phenol concentration. This was due to the adsorption of phenol on platinum, which blocked the active sites for the oxygen reduction reaction. For the anodic curves, the blank run with only 1*M* H_2SO_4 exhibited two potential regions: the curve between 750 and 1250 mV *vs.* SCE corresponded to the formation of a platinum oxide, and the curve above 1250 mV *vs.* SCE corresponded to the oxygen evolution reaction on the platinum surface (33). Addition of phenol to the sulfuric acid supporting electrolyte increased the anodic current density and shifted the rest potential to a more negative value of 620 mV *vs.* SCE. The phenol concentration did not seem to affect the anodic current in the low overpotential regime of 620-900 mV *vs.* SCE. At the potentials more positive than 900 mV *vs.* SCE, the adsorption of the oxidation product, benzoquinone (34), on the electrode surface caused the current to decrease with a further increase in potential for the run with 0.05*M* phenol. This adsorption phenomenon was found to be more pronounced at low phenol concentrations (0.01-0.05*M*) and at low temperatures (23°C). At the potentials above 1250 mV *vs.* SCE, the oxygen started to evolve and the current density increased again with increasing potential.

Effect of sinusoidal AV on dc polarization curves.— Figures 2-3 show the typical dc polarization curves for the oxidation of phenol on platinum in 0.1*M* phenol plus 1*M* sulfuric acid at 50°C when the electrode was superimposed with sinusoidal AV at the frequencies of 60 and 200

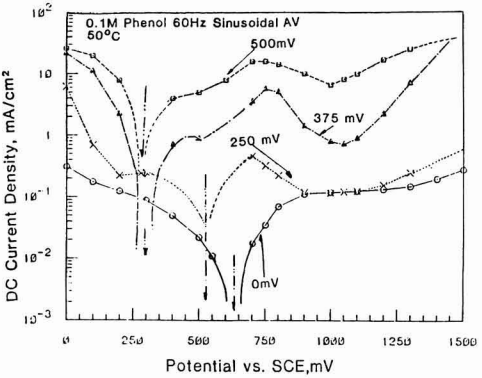


Fig. 2. DC polarization curves with 60 Hz sinusoidal AV for the oxidation of phenol on a platinum rotating disk electrode (2400 rpm) in 0.1M phenol and 1M H_2SO_4 at 50°C. The magnitude of superimposed AV varied from 0 to 500 mV rms as indicated in the figure. The arrows refer to the position of the rest positions.

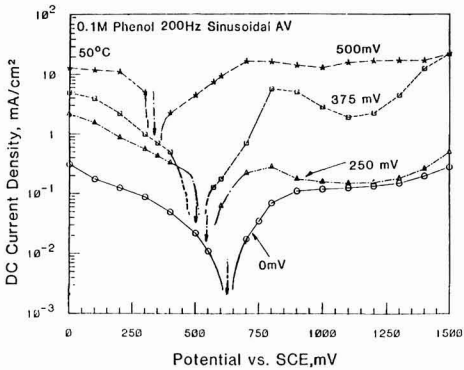


Fig. 3. DC polarization curves with 200 Hz sinusoidal AV for the oxidation of phenol on a platinum rotating disk electrode (2400 rpm) in 0.1M phenol and 1M H_2SO_4 at 50°C. The magnitude of superimposed AV varied from 0 to 500 mV rms as indicated in the figure. The arrows indicate rest potentials.

Hz. The magnitude of AV varied from 0 to 500 mV rms. The dc polarization curves covered both the cathodic and anodic potential regimes, and the arrows in the figures indicate the rest potentials. The results indicate that AV caused an increase in the dc current density for both the anodic and cathodic processes. The rest potential was shifted by the AV toward the negative direction. For the anodic process, the rate of oxidation of phenol was enhanced when the magnitude of AV was greater than 250 mV rms, and the dc current density increased with increasing magnitude of AV. At 60 Hz, for example, the greatest dc enhancement for the anodic process occurred near the dc potential of 750 mV *vs.* SCE. At this potential, the dc current with 500 mV rms AV was two orders of magnitude greater than the dc current without AV. This rate enhancement can be partly explained by an increase in the apparent electrokinetics under the superimposed AV conditions. Consider an electrode process whose current-potential relation under the activation control is described by the Butler-Volmer equation of the type

$$i = i_o \left\{ \exp\left(\frac{\phi - \phi_o}{\beta_a}\right) - \exp\left(\frac{\phi_o - \phi}{\beta_c}\right) \right\} \qquad [3]$$

where i_o and ϕ_o are the exchange current density and the rest potential without superimposed AV, respectively, and β_a and β_c are the anodic and cathodic Tafel slopes based upon ϕ *vs.* ln i plot. When the electrode is polarized with a dc potential, ϕ_{dc}, plus a superimposed sinusoidal AV, then

$$\phi = \phi_{dc} + V \sin \omega t \qquad [4]$$

where V is the peak AV potential, ω is the AV frequency in radians per second, and t is the time. Under this condition, the current density flowing across the electrode/solution interface will be composed of a time-averaged dc component, i_{dc}, and a periodic ac component, i_{ac}

$$i = i_{dc} + i_{ac} \qquad [5]$$

Substituting Eq. [4] and [5] into Eq. [3] and carrying out the time average on both sides of the resulting equation, one has

$$i_{dc} = i_o \left\{ \exp\left(\frac{\phi_{dc} - \phi_o}{\beta_a}\right) \overline{\exp\left(\frac{V}{\beta_a} \sin \omega t\right)} - \exp\left(\frac{\phi_o - \phi_{dc}}{\beta_c}\right) \overline{\exp\left(-\frac{V}{\beta_c} \sin \omega t\right)} \right\} \qquad [6]$$

The time-averaged quantities in the above equation are given as

$$\overline{\exp\left(\frac{V}{\beta_a}\sin\omega t\right)} = \frac{1}{2\pi}\int_0^{2\pi}\exp\left(\frac{V}{\beta_a}\sin\omega t\right)d(\omega t) \quad [7]$$

$$\overline{\exp\left(-\frac{V}{\beta_c}\sin\omega t\right)} = \frac{1}{2\pi}\int_0^{2\pi}\exp\left(-\frac{V}{\beta_c}\sin\omega t\right)d(\omega t) \quad [8]$$

These two quantities are always greater than one, and may be considered as the enhancement factors for the anodic and cathodic current under the superimposed AV condition. The numerical calculation for the current enhancement by AV is given in Ref. (6), and it has been shown that it is possible to enhance the dc current density by a factor of 100-1000 with a peak AV of 5-10 β_a.

In addition, the AV had the ability to breakdown the adsorption layer on the platinum surface in a way similar to the breakdown of passive film by AV in the corrosion of iron and stainless steels (5, 7, 9). The phenomenon was similar to the reactivation of the platinum fuel cell electrode by the application of alternate anodic and cathodic potential pulses (35, 36). Thus, the function of AV was to continuously activate the platinum electrode, thus enabling the oxidation of phenol to proceed at a rate higher than that of the steady-state dc electrolysis.

When the frequency of AV was increased, the effect of AV became less obvious. At 6000 Hz, there was no significant increase in the dc current density over a range of AV from 0 to 500 mV rms (32). This was caused by the fact that the double-layer impedance became smaller at high frequencies, and the application of AV was used for the charge and discharge of the electric double layer at the electrode-solution interface.

Figure 4 shows the rest potential of the polarization curves against the magnitude of superimposed AV for a range of AV frequencies from 20 to 6000 Hz. The rest potential was shifted to the negative direction by the applied AV. The reason for this is that the cathodic Tafel slope was larger than anodic Tafel slope, and, according to an analysis by Chin *et al.* (4-5), the rest potential would be shifted toward the negative direction because of an unsymmetric behavior between the anodic and cathodic polarization of the present reaction system.

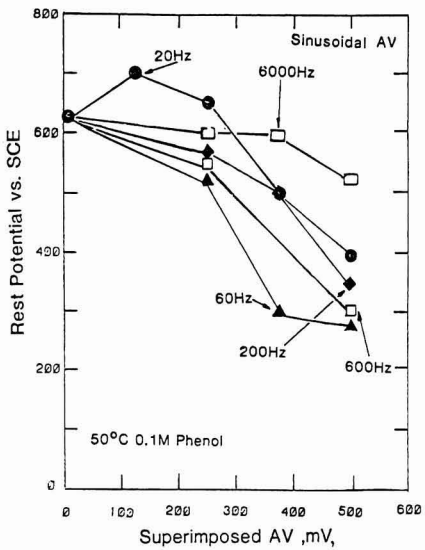


Fig. 4. Apparent rest potential of a platinum rotating disk electrode (2400 rpm) as a function of the root-mean-square of superimposed sinusoidal AV for 0.1M phenol and 1M H_2SO_4 at 50°C. The AV frequency varied from 20 to 6000 Hz as indicated in the figure.

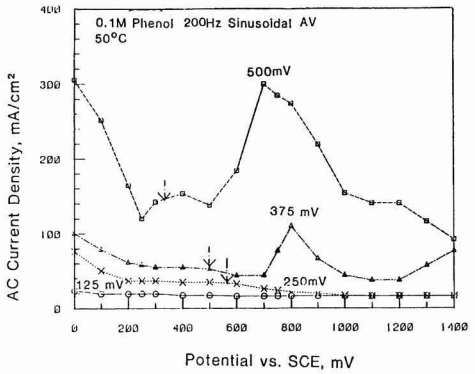


Fig. 5. AC current density vs. dc potential when 200 Hz sinusoidal AV was superimposed on a platinum rotating disk electrode (2400 rpm) in 0.1M phenol and 1M H_2SO_4 at 50°C. The AV magnitude varied from 125 to 500 mV rms as indicated in the figure. The arrows refer to the position of the rest potentials where the dc current density became zero on the electrode.

AC current density vs. dc potential.—The typical ac current density *vs.* dc potential curves at 200 Hz are given in Fig. 5 for a range of sinusoidal AV from 125 to 500 mV rms. The measurements were made with a platinum rotating disk in a solution containing 0.1*M* phenol and 1*M* H_2SO_4 at 50°C. The ac current density increased with increasing AV at a given dc potential. For a given root-mean-square of AV, the ac current density increased with AV frequency. The ac current was also a function of dc potential. For the AV less than 250 mV rms, the ac current at the cathodic dc potentials was higher than that in the anodic regime (the arrows in the figure indicate the rest potentials). However, as the magnitude of AV increased beyond 375 mV rms, the ac current density *vs.* dc potential curves exhibited a maximum within the dc potential range investigated. The maximum ac current occurred approximately at 750 mV *vs.* SCE, and the height of the maximum increased with increasing AV. The phenomenon is similar to that of ac polarography (34). Accordingly, the dc potential where the maximum ac occurred was in the vicinity of the half-wave potential for the oxidation of phenol.

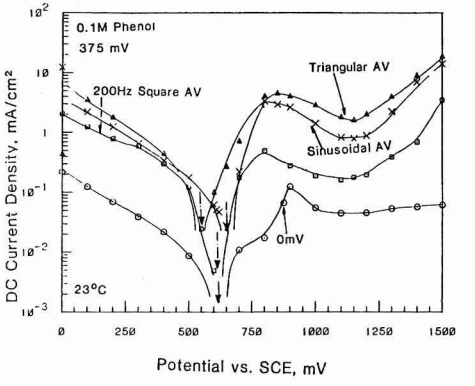


Fig. 6. Effect of AV waveforms on the dc polarization curves of a platinum rotating disk electrode (2400 rpm) in 0.1M phenol and 1M H_2SO_4 at 23°C. The data are given for the 200 Hz sinusoidal, square, and triangular wave AV as indicated in the figure. The AV magnitude was kept at 375 mV rms. For comparison, the polarization curve without any superimposed AV is also given (open circles).

Effect on AV waveforms.—In order to investigate the effect of AV waveforms on the oxidation of phenol, a set of runs was made by superimposing 200 Hz triangular and square-wave AV onto the platinum electrode in 0.1*M* phenol + 1*M* H_2SO_4 at 23°C. Figure 6 shows the resulting dc polarization curves for a set of sinusoidal, square, and triangular AV at a constant AV magnitude of 375 mV rms (200 Hz). For comparison, the dc polarization without AV is also shown in the figure. It is seen that the triangular wave resulted in the largest increase in the dc current density for both the anodic and cathodic reactions. This was followed by the sinusoidal and square wave according to the sequence

$$\text{triangular AV} > \text{sinusoidal AV} > \text{square AV} \qquad [9]$$

The trend was similar to that of previous mass-transfer studies in ac electrolysis (37-38), where the triangular wave was shown to have the largest limiting ac current density, followed by the sinusoidal and square wave ac. This sequence may be explained by the fact that, for a given root-mean-square value, the triangular wave possesses the highest peak voltage, causing the severest destruction of the adsorbed layer on the platinum surface. Qualitatively, all the three waveforms had the same effect on the oxidation of phenol on the platinum electrode. Distinctions can be made only by the extent of enhancement in the dc current density. All the AV waveforms shifted the rest potentials toward the negative direction, as shown in Fig. 4.

Results of batch electrolysis.—The batch electrolysis experiment was carried out in a single-compartment cell at 50°C with 0.01*M* phenol in 1*M* sulfuric acid. In this experiment, phenol was oxidized to benzoquinone on a stationary platinum anode, and the benzoquinone was further reduced to hydroquinone on a platinum screen cathode having a surface area much larger than that of the anode. The cell was operated with a potentiostat by controlling the potential of the anode with respect to a saturated calomel reference electrode. The operating condition was dc potential, 750 mV *vs.* SCE, and 60 Hz sinusoidal AV varying from 0 to 375 mV rms. This condition was chosen from the polarization curves shown in Fig. 2-3. To manifest the effect of AV frequency on the batch electrolysis, a superimposed AV of 250 mV rms in a range of AV frequency from 20 to 600 Hz was also used. The conversion of phenol (mole converted per mole of phenol charged at the beginning of electrolysis) and the yield of hydroquinone (mole formed per mole of phenol converted) were obtained with a chemical analysis. The dc current I, ac current $\tilde{I}$, dc cell voltage E, and ac cell voltage $\tilde{E}$ were recorded on a strip chart recorder. The number of dc coulombs passing the cell was obtained by integrating the dc current with respect to the time, and the anodic current efficiency for the oxidation of phenol was calculated according to Faraday's law. The consumption of electric energy during the electrolysis was calculated by

$$W = \int_0^t [E(t)I(t) + \tilde{E}_{rms}(t)\tilde{I}_{rms}(t)]dt \qquad [10]$$

where W is the electric energy in joules, t is the time in seconds, and the subscript rms refers to the root-mean-square values.

Figure 7 shows the results for the dc current as a function of time when the cell as superimposed with 60 Hz sinusoidal AV varying from 0 to 375 mV rms. The dc current increased with AV. At 375 mV AV, the dc current was 1000 times greater than that without any superimposed AV. The results imply that the applied AV increased the reaction rate. The conversion of phenol is presented in Fig. 8 as a function of time for various applied AV. The figure shows that the conversion increased with increasing AV. However, the slopes of the curves decreased with time because of the loss of current efficiency. Figure 9 shows the effect of AV frequency on the conversion of phenol when 250 mV rms sinusoidal AV was superimposed onto the anode potential. The conver-

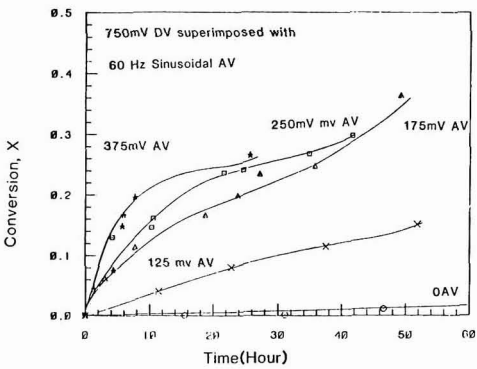


Fig. 8. Conversion of phenol as a function of time for a potentiostatic batch electrolysis with a stationary platinum electrode in 0.01M phenol and 1M H_2SO_4 at 50°C. The potential of the platinum anode was maintained at 750 mV vs. SCE, and was superimposed with 60 Hz AV with a magnitude varying from 0 to 375 mV rms as indicated in the figure.

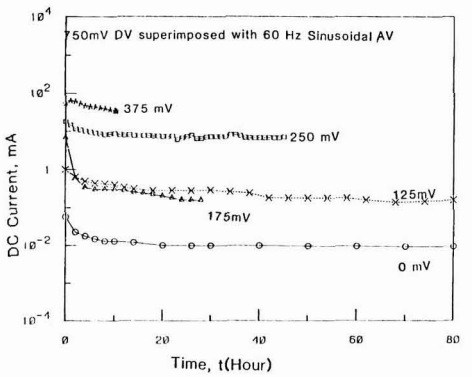


Fig. 7. DC current as a function of time for a potentiostatic batch electrolysis of the oxidation of phenol on a stationary platinum electrode (12.5 cm^2 surface area) in 0.01M phenol and 1M H_2SO_4 at 50°C. The potential of the platinum anode was maintained at 750 mV vs. SCE and was superimposed with 60 Hz sinusoidal AV with a magnitude varying from 0 to 375 mV rms as indicated in the figure.

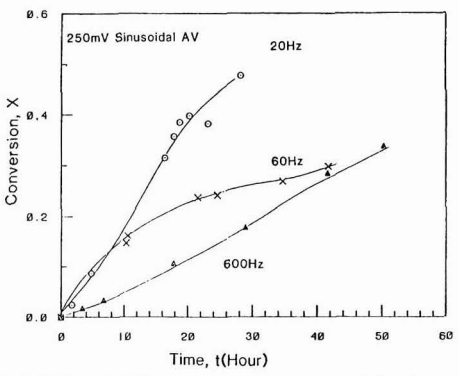


Fig. 9. Effect of AV frequency on the conversion of phenol in a potentiostatic batch electrolysis with a stationary platinum electrode in 0.01M phenol and 1M H_2SO_4 at 50°C. The data are given for three frequencies of sinusoidal AV: 20, 60, and 600 Hz. The magnitude of the superimposed AV was 250 mV rms, and the dc potential of the platinum anode was maintaind at 750 mV vs. SCE.

Table I. Results for the oxidation of phenol with a potentiostatic batch electrolysis

	Experimental conditions	Time (h)	DC (C)	Conversion (%)	Current efficiency (%)	Yield (%)	Energy consumption $\left(\frac{J}{\text{kg-mol phenol}}\right)$
Present work (12.5 cm^2 Pt)	0 AV	172	6.2	—	—	—	—
(0.01*M* phenol) (50°C)	125 mV rms 60 Hz AV	116	91.5	42		29.4	2.9×10^8
	250 mV rms 60 Hz AV	45	1278	29.7	65	19.9	1.65×10^9
(DC potential 750 mV *vs.* SCE)	375 mV rms 60 Hz AV	10.3	1699	26.5	44	4.1	2.82×10^9
	250 mV rms 20 Hz AV	43.9	2104	55.3	28.6	48.8	3.84×10^9
	250 mV rms 600 Hz AV	68	58	25.9	30.2	16.8	3.17×10^{10}
Covitz (28) (154 cm^2 PbO_2) (0.32*M* phenol) (30°C)	80 A/dm^2	0.5		40.3	35	61.2	1.49×10^{10}

sion of phenol decreased with increasing AV frequency. After 30h electrolysis, the run with 20 Hz AV had 50% conversion, whereas only 25 and 18% conversion were obtained with the 60 and 600 Hz AV, respectively. The dc current with 20 Hz AV was also proportionally greater than those at the higher frequencies.

Table I summarizes the results of the potentiostatic batch electrolysis experiments shown in Fig. 7-9. All the values in the table were obtained at the end of each run. The electric energy consumption was determined by integrating the product of dc current and dc cell voltage, and of ac current and ac cell voltage with respect to the time, and the result is expressed in joules per kilogram-mole of phenol converted at the end of the electrolysis. For the run with only dc potential, the cell current was so small that only 6.2C of electricity were passed after 172h electrolysis, and the conversion of phenol was negligible. With superimposed AV, the dc current increased and the electrolysis time was shortened. The rate of oxidation of phenol increased with increasing magnitude of AV and with decreasing AV frequency. However, as the dc current increased by AV, the anodic current efficiency decreased. The yield of hydroquinone appeared to increase with decreasing AV frequency and to decrease with increasing magnitude of superimposed AV. For comparison, the results of a galvanostatic dc electrolysis using a lead dioxide anode as reported by Covitz (28) are also listed in Table I. The present results for the conversion of phenol, anode current efficiency, and yield of hydroquinone were comparable to those of Covitz's dc electrolysis. On the other hand, the energy consumption of the potentiostatic ac electrolysis (except for the run with 600 Hz AV) was about one order smaller than Covitz's value. This is because AV served as a depolarizer and reduced the electrode overpotential and dc cell voltage by continuously activating the electrodes during the electrolysis. A large portion of the total energy requirement in the present work was caused by the passage of ac current and ac cell voltage.

Conclusions

A study has been made of the effect of AV on the oxidation of phenol on platinum in aqueous sulfuric acid electrolyte. The effects of AV waveforms (sinusoidal, square, and triangular waves), frequency, and magnitude were also examined. The results indicate that, within the frequency range of 20-600 Hz, AV increased the dc current density for the anodic and cathodic processes and shifted the rest potential toward the negative direction. The magnitude of dc enhancement increased with increasing root-mean-square of superimposed AV, and decreased with increasing frequency. The results of a potentiostatic batch electrolysis in an undivided cell revealed that superimposed AV increased the dc current and shortened the electrolysis time. The rate of conversion of phenol increased with increasing AV. The anodic current efficiency, and yield of hydroquinone decreased with increasing AV. The electric energy consumption was smaller than that of a galvanostic dc electrolysis reported in the literature.

Acknowledgment

Acknowledgment is made to the donors of the Petroleum Research Fund (Grant 14330-AC5-C), administrated by the American Chemical Society, for the support of this research.

Manuscript submitted March 7, 1985; revised manuscript received July 16, 1985.

The Petroleum Research Fund assisted in meeting the publication costs of this article.

REFERENCES

1. R. Jansson, *Chem. Eng. News*, **62,** 43 (Nov. 19, 1984).
2. D-T. Chin, in "Proceedings of the 9th International Congress Metallic Corrosion, Toronto, Canada," Vol. 4, pp. 96-103, National Research Council, Ottawa, Ont., Canada (1984).
3. S. R. Pookote and D-T. Chin, *Mater. Perf.*, **17** (3), 9 (1978).
4. D-T. Chin and T. W. Fu, *Corrosion*, **35,** 514 (1979).
5. S. Venkatesh and D-T. Chin, *This Journal*, **128,** 2588 (1981).
6. D-T. Chin and S. Venkatesh, *ibid.*, **126,** 1908 (1979).
7. D-T. Chin and P. Sachdev, *ibid.*, **130,** 1714 (1984).
8. R. Sethi and D-T. Chin, *J. Electroanal. Chem.*, **160,** 79 (1984).
9. J. L. Wendt and D-T. Chin, *Corros. Sci.*, To be published.
10. O. Reitlinger, *Z. Electrochim.*, **20,** 261 (1914).
11. A. N. Kappanna and K. M. Joshi, *J. Ind. Chem. Soc.*, **29,** 69 (1952).
12. I. K. Noguchi, *Res. Rep. Nagoya Ind. Sci. Res. Inst.*, **1,** 19 (1949); *ibid.*, **2,** 32 (1950); *ibid.*, **5,** 26 (1952); *ibid.*, **6,** 20 (1953).
13. N. S. Tsvetkov and E. P. Kovalchuk, *C.A.*, **64:** 5213e (1966).
14. G. A. Korchinski and E. F. Fedorov, *Elektrokhimiya*, **2,** 1395 (1966).
15. P. R. Nadebaum and T. Z. Fahidy, in "Symposium on Electrochemical Engineering," Vol. 1, J. D. Thronton, Editor, p. 145, Institute of Chemical Engineers, London (1973).
16. S. G. Nitskanskii, O. S. Khristeva-Strizhen, and I. I. Nitskanskaya, *C.A.*, **81:** 117281 (1983).
17. Y. Kikuchi and T. Ueyama, *Nippon Kagaku Kaishi*, **5,** 981 (1974).

18. P. Florequin, H. Larmuseau, and X. De Hemptinne, *Ann. Soc. Sci. Bruxelles. Ser. 1*, **88**, 241 (1974).
19. S. N. Bhadani, *Ind. J. Technol.*, **12**, 570 (1974).
20. M. Tamura, K. Ogasawara, N. Ono, and S. Hagiwara, Japan Pat. 7,744,593 (1977).
21. M. Kawahara, Japan Pat. 80,111,767 (1980).
22. R. C. Alkire and J. E. Tsai, *This Journal*, **129**, 1157 (1982).
23. R. R. Adzic, K. I. Popov, and M. A. Pamic, *Electrochim. Acta*, **23**, 1191 (1978).
24. F. Fichter and E. Brunner, *Z. Electrochem.*, **19**, 781 (1913).
25. N. H. Vagenius and R. J. King, U.S. Pat. 2,135,368 (1938).
26. G. C. Jones and R. H. Meen, U.S. Pat. 4,035,253 (1977).
27. G. C. Jones and D. A. Payne, U.S. Pat. 3,994,788 (1976).
28. F. H. Covitz, U.S. Pat. 3,509,031 (1970).
29. F. H. Covitz, U.S. Pat. 3,616,323 (1971).
30. F. H. Covitz and R. V. Carruba, U.S. Pat. 3,616,324 (1971).
31. I. N. Sorokin, U.S.S.R. Pat. 489,525 (1972).
32. C. Y. Cheng, Ph.D. Dissertation, Clarkson University, Potsdam, New York (1983).
33. K-L. Hsueh, E. R. Gonzalez, S. Srinivasan, and D-T. Chin, *This Journal*, **131**, 823 (1984).
34. H. Breyer and H. Bauer, "Alternating Current Polarography and Tensammetry," pp. 203-205, Interscience, New York (1963).
35. S. Schuldiner and T. B. Warner, *This Journal*, **112**, 212 (1965).
36. S. Gilman, in "Electroanalytical Chemistry," Vol. 2, A. J. Bard, Editor, pp. 111-192, Marcel Dekker, New York (1967).
37. C. Y. Cheng and D-T. Chin, *AIChE J.*, To be published.
38. C. Y. Cheng and D-T. Chin, *Chem. Eng. Commun.*, To be published.

Modification of Titanium Electrodes for Detection of Biological Substances

Ichiro Nakabayashi, Tahei Tomida, and Katsuhiro Kawashiro

Faculty of Engineering, The University of Tokushima, Minamijosanjima, Tokushima 770, Japan

ABSTRACT

Several modifications of the surface structure and texture of electrode substrate (titanium) were carried out by the treatments of rolling, heating, and ion bombardment to develop electrodes to detect biological substances. These electrodes were chemically modified with trypsin or aprotinin (trypsin inhibitor). The electric response measured in a specific reaction system of trypsin-aprotinin depended on the characteristics of surface of the electrode substrate as well as the concentration of the biological substances. The ion bombardment in H_2O vapor was found to be more effective in modifying electrodes for biosensors of this type.

Chemically modified electrodes have been developed to detect biological substances such as antigens, antibodies, enzymes, etc. (1-3). Yamamoto *et al.* (1, 2) have proposed a new electrical method using a titanium electrode modified chemically with the counterpart of a biologically active substance described above. This electrical method is expected to have wide applications because of its simplicity, high specificity, and sensitivity.

On the other hand, it is known that the proteins to be modified should be immobilized by the hydroxyl group on the surface of electrodes. It is therefore important to increase the hydroxyl group on the electrode surface.

In this study, several modifications of the surface structure and texture of electrode substrates (titanium) were tried by rolling treatment, heat-treatment, and ion bombardment. With these electrodes, the relation between electric responses and surface properties was also studied for an aprotinin-trypsin system.

Experimental

Preparation of electrode.—Titanium wires (1ϕ × 35 mm) were used as the electrode substrates. Each wire was modified separately by a different treatment as follows: a was heated at 600°C in the air atmosphere for 5 min; b was rolled by length of 50% with a dental roller and then oxidized at 600°C for 5 min; c was treated like b and then annealed at 1300°C in 6.7×10^{-3} Pa for 30 min and further oxidized at 600°C in air for 5 min; with d, the substrate of c was exposed to ion bombardment (20 Pa of H_2O vapor) with an energy of 200 eV. The ion bombardment was carried out by the usual radio frequency (RF) diode sputtering method described elsewhere (4).

After these various treatments, these electrode substrates were chemically modified with trypsin or a trypsin inhibitor (aprotinin) by the conventional cyanogen bromide method (5). The chemically modified electrode with bovine serum albumin (BSA) was used as the reference electrode. The chemicals of trypsin (type III), aprotinin (type I-S), and BSA were procured from Wako Pure Chemicals Company Limited and Sigma and Seikagaku Kogyo Company Limited, respectively. Aqueous solution of barbital sodium (0.1*M*) served as the buffer solution at *p*H 8.6. This particular *p*H was adjusted by 1*M* hydrochloric acid.

Electrical measurement.—The electric circuit is shown in Fig. 1. A potential difference between the working and reference electrode immersed in a sample solution (18 ml) at 35°C was measured with a vibrating reed electrometer (Takeda Riken Company Limited). The sample solution was stirred with a Teflon stirrer piece at an appropriate speed. The whole system of measurement was set in the dark box shielded electrically with aluminum foil.

Results and Discussion

The electrode potential between the working (aprotinin) and the reference electrode shifted exponentially toward the positive after the addition of trypsin solution (2 ml). On the other hand, the electric response changed in the negative direction by the trypsin electrode-aprotinin solution. The response direction (positive, negative) and the voltage change observed have been well explained by the reasonable assumption of the dipole moment upon the formation of the complex of trypsin-aprotinin (6). This potential shift is attributed to the specific reaction between aprotinin and trypsin at the electrode surface as described by Yamamoto *et al.* (1).

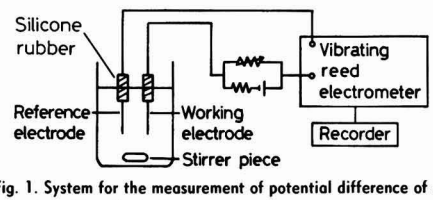


Fig. 1. System for the measurement of potential difference of reference and working electrodes.

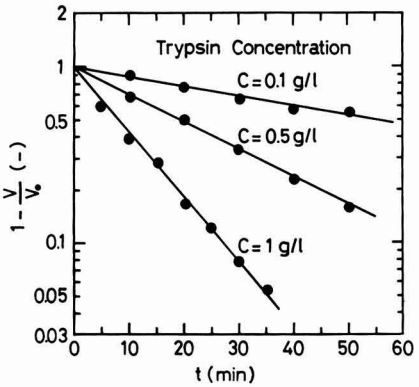


Fig. 2. Semilog plots of potential *vs.* time for electrode of original titanium wire.

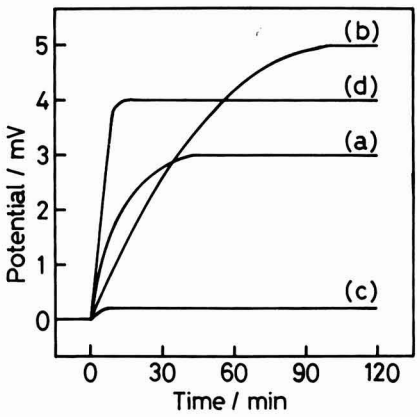


Fig. 3. Effects of surface treatment on electric response. a: Original titanium wire. b: Titanium plate rolled wire. c: Titanium plate rolled and then annealed at 1300°C in 6.7 × 10^{-1} Pa. d: Titanium plate annealed at 1300°C and then bombarded in 20 Pa of H_2O vapor.

Figure 2 shows the semilog plots of potential *vs.* time. The slope of each curve in the figure was proportional to the trypsin concentration, and potential shift could be expressed by the equation

$$V = V_u [1 - \exp(-kCt)]$$

where V_u is the terminal potential shift, which depends on the amount of couplings, and C is the concentration of an additive. In this case the additive is trypsin.

Figure 3 shows the effect of different surface treatments for substrates on electric responses. The rolled electrode (treatment b) gives a higher potential shift but longer delay time than that of the original titanium wire (treatment a). This may be due to the thick porous oxide layer produced on the electrode surface by the rolling, resulting in the increase of hydroxyl group attached to the surface, and so the long time is needed for the additive to diffuse through the porous layer to the binding sites. Also, the heat-treatment of rolled plate (treatment c) decreases the potential significantly. This is due to the decrease in the hydroxyl group or aprotinin immobilized, owing to the high crystallinity of TiO_2 (rutile) and titanium metal. This was confirmed by x-ray diffraction analysis. The decrease in roughness of the surface and grain boundaries broadened by heat-treatment were also observed in the photograph of scanning electron microscope (SEM).

The response obtained from the H_2O-bombarded electrode (treatment d) was very rapid and sensitive as compared with curves a, b, and c corresponding to the non-bombarded electrodes. The potential *vs.* time behavior of the variously treated electrodes was expressed by the equation described above, except for the data on the high temperature-annealed substrate (c) in Fig. 3, which shows very small potential change. The value of k for the bombarded electrode is about seven times that of the non-bombarded one (a). The effect of the ion bombardment may contribute to increase in the hydroxyl group on the electrode surface. This was confirmed by the detection of the sulfur atoms in the trypsin molecules attached to the hydroxyl group on the surface of electrode.

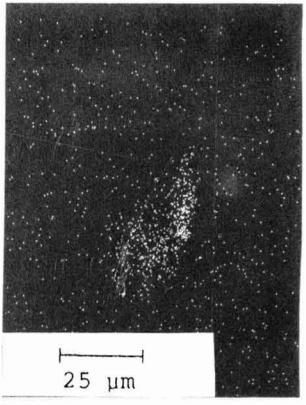
Figure 4 shows the photographs of the secondary electron image and S-Kα radiation profile with an electron probe microanalyzer (EPMA). In the ion-bombarded substrates, a small amount of sulfur was found to be uniformly distributed. On the other hand, only a trace of sulfur was detected in the original or annealed substrate.

X-ray diffraction studies were conducted for the above substrates. It was observed that, for all substrates treated below 600°C, no peaks corresponding to titanium oxide were found in the x-ray patterns. On the other hand, TiO_2 (rutile) crystal was detected in all substrates treated above 600°C. From the x-ray and SEM analyses of rutile crystal which was treated by the ion bombardment in H_2O vapor, no change was observed in its surface texture or crystal structure. However, a thin amorphous layer of titanium

Fig. 4. Texture of trypsin electrode surface and sulfur distribution on it by EPMA.



Secondary electron image



S-Kα radiation profile

oxide is assumed to be formed due to the displacement of atoms in the surface layer from their regular sites. In the similar technique employed for Zn_2SiO_4, this analogy is already established (4). This thin amorphous layer could have a large amount of hydroxyl group in a similar manner as silica gel or porous glass (5).

These results show that the response of potential in the trypsin inhibitor (aprotinin)-trypsin system depends on the characteristics of electrode substrate surface which are modified by the various surface treatments such as rolling, heating, and ion bombardment. Above all, the ion bombardment in H_2O vapor was found to be more effective in modifying electrodes for biosensors of this type.

Acknowledgments

The authors wish to acknowledge their gratitude to Professor O. Tada of the Department of Electronic Engineering, the University of Tokushima, for suitable discussions that led to the development of the modifying electrode. We also would like to thank Mr. Y. Itsuki, K. Itoh, and A. Ugai for their experimental assistance.

Manuscript submitted Feb. 20, 1985; revised manuscript received May 17, 1985.

The University of Tokushima assisted in meeting the publication costs of this article.

REFERENCES

1. N. Yamamoto, S. Shuto, and H. Tsubomura, *Nippon Kagaku Kaishi*, 1562 (1980).
2. N. Yamamoto, Y. Nagasawa, S. Shuto, M. Sawai, T. Sudo, and H. Tsubomura, *Chem. Lett.*, 245 (1978).
3. J. Janata, *J. Am. Chem. Soc.*, **97,** 2914 (1975).
4. O. Tada, K. Tominaga, T. Kondo, and K. Ichinomiya, *This Journal*, **131,** 1365 (1984).
5. H. H. Weetall and C. C. Detar, *Biotechnol. Bioeng.*, **17,** 295 (1975).
6. N. Yamamoto, Y. Nagasawa, M. Sawai, T. Sudo, and H. Tsubomura, *J. Immunol. Meth.*, **22,** 309 (1978).

Laser Interferometry of Pulsed Galvanostatic Deposition of Polycarbazole

R. N. O'Brien*

Department of Chemistry, University of Victoria, Victoria, British Columbia, Canada V8W 2Y2

K. S. V. Santhanam

Tata Institute of Fundamental Research, Bombay 400 005, India

ABSTRACT

The galvanostatic deposition of polycarbazole was conducted by pulsing the current in the frequency range from 0.1 to 500 Hz in solutions of N,N-dimethylformamide containing carbazole and tetra-n-butyl ammonium perchlorate. Compared with its dc deposition, the results obtained here indicated a smooth deposit (pinhole free) and with greater binding to the substrate surface. The SEM studies demonstrate that the range of pulsed frequencies and the potential drop across the electrodes control the deposition process. An advantage of the unsymmetrically pulsed current deposition was the selective reduction of the unpolymerized free radicals at the electrode-solution interface resulting in increasing the surface concentration of the monomer. The development of concentration gradients in the pulsed electrolysis has been followed by laser interferometry, and it shows frequency-controlled growth at the electrode/solution interface.

While the organic synthetic metals have prospective usage as electrodes in fuel cells and in rechargeable batteries (1-3), a key problem in their development has been associated with their stability. One factor which is responsible for this instability, especially with polycarbazole-type electrodes, is caused by the pinholes (nonsmooth deposits) and weakly adhering nature of the deposits produced during their electrodeposition. Problems such as fine-grained and "burned" deposits during electrodeposition of metals, such as Ni, Au, Ag, etc., arise but can be avoided by using a high c.d. pulsed at a low frequency (4) to enhance the metal ion concentration in the diffusion layer (5-7). The effect of pulsed electrolysis has been to increase the allowable rate of deposition. As the mechanism of the electrodeposition of real metals differs from others (synthetic metals), an investigation has been undertaken to study the effect of pulsed current on the deposition of polycarbazole. The results obtained in this study suggest that a smooth deposition can be obtained at moderate frequencies (higher than that employed in the conventional depositions), *i.e.*, < 1 Hz. The need for using higher frequencies than those employed in conventional metal depositions is attributed to two factors: (*i*) as the synthetic metals are produced by an initial electrochemical oxidation of the electroactive species generating the radical cation for propagating the polymer chain, the reduction of the nonpolymerized radical at the electrode during galvanostatic (current pulsed anodic on/off, anodic/cathodic, or anodic/off/cathodic/off) pulsed electrolysis results in the enhancement of the surface concentration of the electroactive species (carbazole), and (*ii*) the negligible destruction of the deposits in the pulsing mode (the polymer is reduced at $E^0 \approx 0.0$ V).

The pulsed electrodeposition of polycarbazole has been followed by laser interferometry, and the diffusion gradients that exist in the pulsed electrolysis are discussed here.

Experimental

The solutions for the electrodeposition of carbazole were prepared in anhydrous N,N-dimethylformamide (DMF, MCB reagent grade). Tetra-n-butyl ammonium perchlorate (South Western Analytical Chemicals) was dried at 100°C for 24h in a drying piston under vacuum before using it as the supporting electrolyte. The dried sample was stored in a dessicator before use in the experiments.

The electrodes employed in this study were of two types. In one type (for multiple beam laser interferometry), glass disks were cut in half and the cut edges were sputtered with Au about 3000-5000Å thick. The sputtering was done for about 10 min.

The glass disks were cleaned in alcoholic KOH solution before carrying out the sputtering. In the second type (for SEM studies and holographic interferometry), rectangular glass plates (0.8 cm wide and 8.5 cm long) were covered with vacuum-deposited Au. The thickness of the film was measured with a profilometer and was estimated at

3000Å. The two electrodes were widely separated in the interferometric cell (separation of 5-10 mm).

The experimental arrangement for laser interferometry has been described previously (8-10). The Au plated glass disk electrodes were mounted into the Teflon cell in a parallel configuration. The optical glass flats were placed on either side of the electrodes and clamped in a brass cell holder. A He-Ne laser (1 mW) was used for producing the interference fringes. The fringe movements were videotaped on a Hitachi video recorder (VTR Model VT-7A) and were displayed on a 20 in. Hitachi color television. An RCA CC 030 microprocessor-controlled camera was used to follow the fringes.

The pulsed electrolysis experiments were carried out using a Keithley constant current source (Model 220) in combination with a Wavetek Model III function generator or Data Royal Corporation F210B waveform generator. The cell voltages were followed using a Tektronix Type 561A oscilloscope with Type 3A6 dual-trace amplifier and Type 3B3 time base. A few experiments were carried out with a Harrison power supply-amplifier 6824A with ±50V and ±1A suitably modified to generate the pulsed currents.

Results and Discussion

The electrodeposition of polycarbazole was conducted at c.d.'s ranging from 0.06 to 3.5 mA-cm^{-2} with galvanostatic pulsed frequencies ranging from 0.5 to 500 Hz. The galvanostatic pulsed current amplitude oscillates symmetrically from the positive to negative direction. Figure 1 shows the potential drop across the electrodes plotted as a function of the applied c.d. during the electrolysis of carbazole. The magnitude of the observed changes in the cell voltage is larger at lower c.d.'s (< 0.3 mA-cm^{-2}) owing to the smaller extent of polarization at the electrodes. The interfacial concentration of carbazole or its radical is expected to change periodically (as is the double-layer capacitance, which must charge with the solution resistance) as the potential of the system is changed. At the anode (when the current magnitude is positive), the oxidation of carbazole to a free radical occurs, and at the cathode, reduction of carbazole to its anion with its follow-up reaction will occur (11). The extent to which these reactions proceed is dependent on the imposed c.d. and the actual potentials attained by the electrodes during the electrolysis. Thus, at both the electrodes, the onset of background electrolysis occurs after a long time (several minutes). In the electrolysis conducted at lower frequencies (< 10 Hz) due to the factors discussed earlier, the oscillating potential range [the maximum (V_{max}) and minimum (V_{min}) potential drop across the electrodes] spans a wider range with V_{min} reaching negative values relative to the V_{max} and relative to V = 0. Figure 2 describes the V_{max} and V_{min} distribution as a function of the

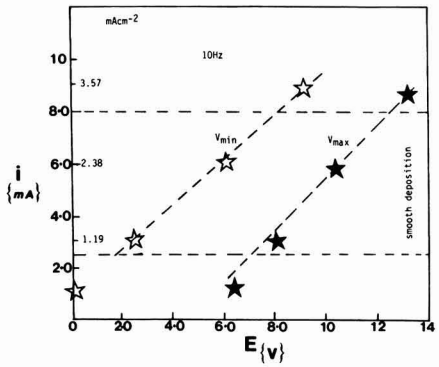


Fig. 1. Current-voltage curves for the electrolysis of 60 mM carbazole and 0.1M $(C_4H_9)_4NClO_4$ in DMF under 10 Hz pulsing. V_{max} represents the maximum cell voltage, and V_{min} represents the minimum voltage. Dotted lines indicate the smooth deposition of polycarbazole.

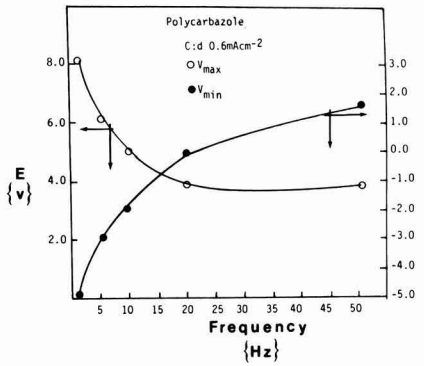


Fig. 2. The effect of frequency upon pulsed electrolysis of 60 mM carbazole. The V_{max} and V_{min} attained during the electrolysis is given in the figure.

pulsing frequency during the electrodeposition of polycarbazole in a laser interferometric cell.

The onset of concentration profiles during the pulsed electrolysis of carbazole follows a pattern similar to that of dc electrolysis (12); a smooth down turn of the fringes was observed at the anode, indicating a decrease in refractive index of the medium in that region of the electrolyte. Due to the pulsing current density, the electrode polarity changes with the result that these fringe bendings show a reversal. The fringe shifts at the anode during the progress of the electrolysis show a frequency dependency; at 500 Hz, pulsed electrolysis at a c.d. of 0.30 mA-cm^{-2} fringe shifts of 0.85 (240s) and 1.07 (360s) were obtained. At a lower frequency, 50 Hz, a fringe shift of 0.53 (240s), 0.67 (360s), and at an intermediate frequency of 100 Hz a fringe shift of 0.75 (240s) was estimated during the progress of the electrolysis. This decreasing trend was maintained to the lowest frequency, that is, 0.5 Hz. With a view to understanding this fringe shift behavior, we monitored the potentials V_{max} and V_{min} during the course of the electrolysis. At the highest frequency examined (500 Hz), the V_{min} value differed from the V_{max} by about 0.20V, and at the lowest frequency of 0.5 Hz this difference widens to 12.0V. In the latter situation, the potential drop across the electrodes (V_{min}) moves to the negative region. In the experiments that were conducted with 500 Hz pulsing, the V_{max} and V_{min} were both in the positive region. Based on these results, it is possible to postulate two sets of reactions, one set of reactions when both V_{max} and V_{min} are well into the positive region of potentials and another set of reactions when the cell voltage oscillates from positive to negative values (relative variations). We wish to suggest that (at the electrode which is usually the anode) these reactions are the reduction of the free radical cation on the surface of the electrode (produced after the initial oxidation of carbazole) and the redox reaction of the polymerized product. A cyclic voltammetric study of the polycarbazole in background solutions of DMF containing $(C_4H_9)_4NClO_4$ reveals such a reduction of polycarbazole at E_{pc} = 0.0 V (13, 14) and a drawn-out oxidation wave of the product at about +0.20V. These reactions are possibly responsible for the differences in the observed fringe shifts.

The effect of pulsed electrolysis on the concentration gradients is much more pronounced at higher c.d.'s (> 1 mA-cm^{-2}). This point is illustrated in Fig. 3. Note the developments of concentration gradients in the frames 1 through 4. The fringe bending occurs smoothly up to 60s of electrolysis of carbazole, and thereafter the fringe distortions occur until destroyed at times greater than 900s. An important feature of the high c.d. electrolysis is the stronger distortions of the fringes at the initially cathodically polarized electrode. The sequence of fringe distortions are much more easily seen on the videotapes where hydrodynamic contours are clearly discernible on the television screen. Since in pulsed electrolysis the polarities

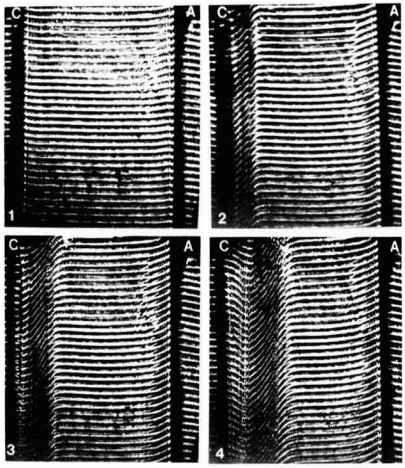


Fig. 3. Laser interferograms obtained during high c.d. electrodeposition of polycarbazole. i_0 = 16.6 mA-cm^{-2}. f = 1 Hz. 1: At 60s of electrolysis. 2: 180s. 3: 240s. 4: 360s. The anode is a Au plated glass electrode on the left side, and the cathode is another Au plated glass electrode.

of the electrodes are continuously reversed, one would expect a similar development of fringe distortions at the anode (the other electrode). It is, however, not observed in these experiments. The occurrence of fringe distortions at the cathode is being ascribed to the $(C_4H_9)_4N+$ reduction (background electrolysis) and the cleavage of the neutral radical produced to the corresponding amine and N_2. This process occurs more efficiently on the Au cathode than on the polymer-covered Au anode. These results suggest differences in the electrocatalytic behavior of the polymer and Au electrodes.

A more detailed analysis of the concentration gradients and the concentration-distance profiles at the anode can be done by using a holographic interferometric cell,[1] where the distance between the electrodes is larger, 10 mm compared with the 3 mm in multiple beam laser interferometry. The development of these profiles during the electrolysis is shown in Fig. 4 and 5.

The smoothness of the pulsed electrolytic deposition of polycarbazole at a c.d. of 0.30 mA-cm^{-2} with a pulsed frequency of 10 Hz is shown in Fig. 6. The fringes are well developed during the progress of the electrolysis, and the frames in Fig. 6 should be compared with those shown in Fig. 3 for the development of distorted coutours.

[1] These profiles are obtained from holographic interferometry by using a 5 mW He-Ne laser in combination with a beam splitter. The analyzing beam is attenuated by using a neutral density filter. The details of the experimental arrangement are described in Ref. (14) and (15).

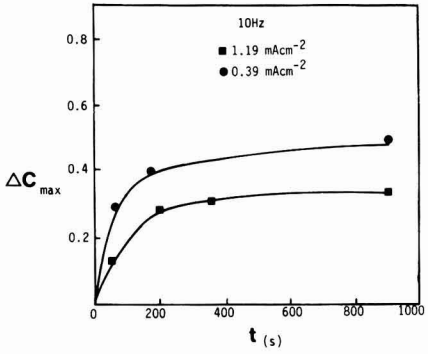


Fig. 4. Holographic interferometry of electrodeposition of polycarbazole under pulsed conditions. f = 10 Hz. The development of concentration gradients during electrolysis at two different c.d.'s are shown.

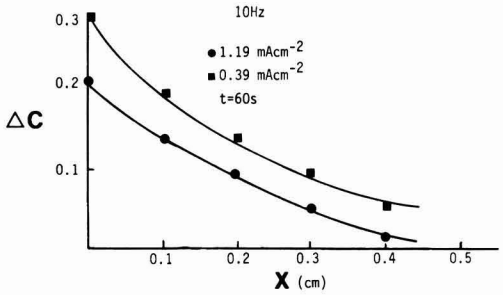


Fig. 5. Holographic interferometry of the electrodeposition of polycarbazole. The development of concentration-distance profiles are indicated at two different c.d.'s. f = 10 Hz.

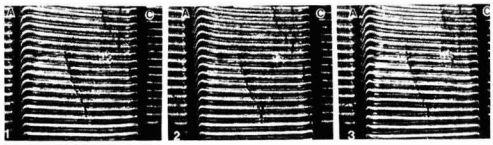


Fig. 6. Laser interferograms of pulsed electrolytic deposition of polycarbazole. 1: 60s. 2: 240s. 3: 360s. f = 10 Hz. i_0 = 1.66 mA-cm^{-2}.

The experiments were also conducted by using unsymmetrical timings in the pulsing circuits but with the same overall frequency. By this method, we would have the oscillating potential spanning different potential regions; however, the frequency of the pulsed electrolysis is maintained at the same value. These experiments would provide a support to the hypothesis (conclusions reached earlier) that the oscillating potential plays a critical role in the development of concentration gradients. For this purpose, a comparison of a symmetrical 10 Hz (t_f = 50 ms and t_r = 50 ms) with an unsymmetrical pulsing (t_f = 60 ms and t_r = 40 ms) gives differences in the potential excursions of +8.00 to −2.00V and +8.00 to +4.00V, respectively; correspondingly, the gradients are different for the same superimposed frequency. This difference in concentration gradients is shown in Fig. 7.

The conductivity of the polycarbazole films have been measured (10 to 100 Ω^{-1}-cm^{-1}) (12). The stability of the film has also been measured. An interesting aspect of the pulsed electrolysis is in the morphological developments that appear on the polycarbazole deposits. For these experiments, two Au sputtered-glass plates were used as

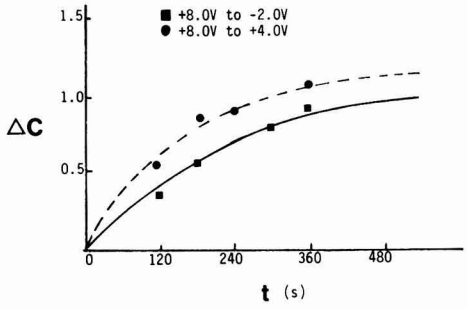


Fig. 7. Differences in the buildup of concentration gradients under symmetrical and unsymmetrical pulsed electrolysis of carbazole. f = 10 Hz. c.d. = 1.66 mA-cm^{-2}.

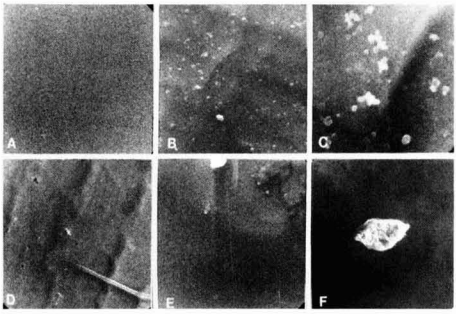


Fig. 8. SEM photographs of the polycarbazole deposits under different conditions. A: 10 Hz, 0.39 mA-cm^{-2}. B: 10 Hz, 1.19 mA-cm^{-2}, magnification of 550 times. C: 10 Hz, 1.19 mA-cm^{-2}, magnification of 2100 times. D: 1 Hz, 0.39 mA-cm^{-2}, magnification of 550 times. E: 100 Hz, 1.19 mA-cm^{-2}, magnification of 550 times. F: 1.19 mA-cm^{-2}, 100 Hz, magnification of 550 times of edge region.

electrodes in the holographic cell; during these depositions, holographic fringes were monitored. The results of these are given in the earlier section. The pulsed electrolysis was carried out at different c.d.'s in the range of 0.30-3.57 mA-cm^{-2} with the pulsing frequencies operating at 1-100 Hz. Films made with current densities of 1-3.0 mA-cm^{-2} (10 Hz) are remarkably rugged. They were active over a period of two weeks, as indicated by the SEM and the electrochemical oxidations of organics. The film continued to be active over a period of six months. The anode was washed well with DMF and dried after the experiment. It was then examined under a scanning electron microscope at different magnifications up to 4000 times. A representative set of data on polycarbazole is shown in Fig. 8. The frame A in the figure was obtained at 10 Hz, 0.39 mA-cm^{-2} pulsed electrolysis. The next frame, B, was the deposit obtained at the 10 Hz, 1.19 mA-cm^{-2} electrolysis, and the following frame, C, was the observation of the deposit under a higher magnification (3900 times). In these frames, one can see the crude deposits on the underlying bumpy deposits. The unevenness is much more visible at still higher c.d.'s, 3.57 mA-cm^{-2}, and the deposits tend to peel off from the glass surface. Frame D shows the deposit obtained at the 0.39 mA-cm^{-2}, 1 Hz electrolysis; the develpment of cracks on the electrode is visible in the frame. Frame E in Fig. 8 shows the deposit obtained when pulsing at 100 Hz. At these frequencies, the electrode edges develop uneven growth. A magnified view of the edge deposit is shown in frame F. The higher c.d.'s such as 3.57 mA-cm^{-2} do not yield good adherent deposits even though the cell voltage under pulsed (10 Hz) conditions varies from +12.0 to +9.0V. This is believed to be because of the onset of the background electrolysis at these thicker deposits of polycarbazole.

Acknowledgments

The authors wish to acknowledge the support for this work by National Sciences and Engineering Research Council of Canada and the help of Teddy Gathright of Triumpf, and D. R. Bapat and Jack Dietrich for their help in gold sputtering and in SEM studies.

Manuscript submitted March 19, 1985; revised manuscript received July 3, 1985.

The University of Victoria assisted in meeting the publication costs of this article.

REFERENCES

1. T. Nagatome, T. Honma, C. Yamamoto, K. Negishi, and D. Omoto, *J. Appl. Phys.*, **22,** L275 (1983).
2. P. Bernier, A. El-Khodary, F. Maurice, C. Fabre, P. Mirebeau, and A. M. Ledunois, *J. Phys. C*, **3,** 583 (1983).
3. M. Armand, *ibid.*, **3,** 559 (1983).
4. H. Y. Cheh, *This Journal*, **118,** 551 (1971).
5. A. Hickling and H. P. Rothbaum, *Trans. Inst. Met. Finish.*, **34,** 53, 199 (1957).
6. N. Ibl, *Metalloberflache Agnew Elektrochem.*, **33,** 51 (1979).
7. T. Z. Fahidy, *This Journal*, **130,** 296 (1983).
8. K. S. V. Santhanam and R. N. O'Brien, *J. Electroanal. Chem.*, **160,** 377 (1984).
9. R. N. O'Brien and K. S. V. Santhanam, *This Journal*, **129,** 1266 (1982).
10. R. N. O'Brien, *Rev. Sci. Instrum.*, **35,** 803 (1964).
11. K. S. V. Santhanam, R. N. O'Brien, and A.D. Kirk, *Can. J. Chem.*, **47,** 1355 (1969).
12. R. N. O'Brien, N. S. Sundaresan, and K. S. V. Santhanam, *This Journal*, **131,** 2028 (1984).
13. N. S. Sundaresan, V. Swayambunathan, and K. S. V. Santhanam, *Trans., SAEST*, **19,** 85 (1984).
14. R. N. O'Brien and K. S. V. Santhanam, in "Interfinish '84," p. 255 of the World Congress on Metal Finishing, Jerusalem, 1984.
15. V. S. Srinivasan, in "Advances in Electrochemistry and Electrochemical Engineering," Vol. 9, P. Delahay and C. W. Tobias, Editors, John Wiley and Sons, New York (1973).

Ionic Conductivity in Glass and Glass-Ceramics of the $Na_3YSi_3O_9$ and $Na_5YSi_4O_{12}$ Type Materials

Ephraim Banks* and Chy Hyung Kim

Department of Chemistry, Polytechnic Institute of New York, Brooklyn, New York 11201

ABSTRACT

The ionic conductivities in glass and glass-ceramics were studied for $Na_{3.2}M_{0.7}Si_{2.9}P_{0.1}O_{8.7}$ (M = Er, Y, Ho, Dy, Gd, Eu, and Sm) compounds. The results showed comparable conductivity values, in the range of 10^{-4} $(\Omega\text{-cm})^{-1}$ at 280°C, with the glasses being somewhat better conductors. Compounds of the type $Na_5MSi_4O_{12}$ (M = Fe, In, Er, Y, Gd, and Sm), which yielded highly conductive phases in the crystalline ceramic form, were also studied in glassy and glass-ceramic states. In compositions of the latter type, the glasses showed lower conductivity than that in the glass-ceramic or the conventional ceramic phase. However, glass-ceramic samples with M = Er, Y showed lower activation energies (4.0-4.4 kcal/mol) compared with those in the conventional crystalline phase prepared by Shannon *et al.* (1). The greater conductivity of the glass-ceramic state in the $Na_5MSi_4O_{12}$ phases, compared to the glassy state, is understood in terms of the favorable structure for ionic transport in the crystalline state.

Glasses containing alkali ions are well known as good conductors of electricity. The processing involved in forming glasses and glass-ceramics can eliminate the porosity usually associated with sintered ceramics, and can permit the production of thinner sections, which would decrease the series resistance of a cell. The feasibility of forming ceramics was investigated using known solid electrolyte compositions to yield a highly conductive phase.

Since the compounds of the type $Na_3YSi_3O_9$ were prepared (2), it has been reported that ionic conductivity was improved by the addition of more sodium with a combination of phosphorus substitution and reduction of Y^{3+} content, such as $Na_{3.2}Y_{0.7}Si_{2.9}P_{0.1}O_{8.7}$ (3).

The hydrothermal synthesis of $Na_5YSi_4O_{12}$ and its crystal framework was reported by Maksimov *et al.* (4). Since 1977 and 1978 (5, 6), those materials have been known as good superionic conductors owing to the existence of large channels in the structure, which facilitate ionic transport. However, the study of glassy and glass-ceramic forms of these materials has not yet been investigated.

In this work, preparation of $Na_{3.2}M_{0.7}Si_{2.9}P_{0.1}O_{8.7}$ (M = Er, Y, Ho, Dy, Gd, Eu, and Sm) and $Na_5MSi_4O_{12}$ (M = Fe, In, Er, Y, Gd, and Sm) glasses and glass-ceramics was attempted, and comparisons of their ionic conductivities were made.

Experimental

Appropriate amounts of reagent-grade Na_2CO_3, M_2O_3, SiO_2, and $NH_4H_2PO_4$, according to the composition, were mixed in an agate mortar. The ground mixture was placed into a platinum crucible and heated in a furnace to about 1200°-1250°C for $Na_{3.2}M_{0.7}Si_{2.9}P_{0.1}O_{8.7}$ samples and 1300°-1350°C for $Na_5MSi_4O_{12}$ samples for 2-3h until no air bubbles were found in the fused material. Weight loss measurements showed no appreciable loss by vaporization. Pouring the molten glass into a stainless steel mold before it solidified allowed preparation of disk specimens of 1.25-1.35 cm diam. The disk-shaped glass was then annealed in the furnace from room temperature to 550°C for $Na_{3.2}M_{0.7}Si_{2.9}P_{0.1}O_{8.7}$ and 600°C for $Na_5MSi_4O_{12}$ to relieve the strain in the quenched glass and to prevent cracking. It was held at that temperature for 1-2h, and then cooled to room temperature at the natural cooling rate of the furnace. X-ray powder diffraction of the glasses revealed no crystalline structure. The x-ray patterns were obtained on a Philips diffractometer using Cu Kα radiation. The glass disks were cut to thinner sizes using a diamond saw, and were subsequently polished with emery papers (180, 320, 400, and 600). Finally, they were polished with alumina powder (3 μm) on a polishing wheel and then washed with acetone.

For the production of glass-ceramic materials, the same general process was applied except that the molten glasses were poured into a stainless steel plate instead of a mold and pressed to form thin disk specimens. These were placed on a graphite plate to prevent adhesion to the steel plate at high temperature and heated in a furnace from room temperature to 845°-920°C for $Na_{3.2}M_{0.7}Si_{2.9}P_{0.1}O_{8.7}$ (845°C for M = Sm; 890°C for M = Ho, Er, Eu, Gd; and 920°C for M = Y, Dy); and 890°-1000°C for $Na_5MSi_4O_{12}$ (890°C for M = Sm, 920°C for M = Er and Gd, and 1000°C for M = Y) materials. No measurements of glass transition temperatures were made. However, the annealing temperatures listed above were determined empirically for each composition, approaching them by tests taken at successively higher temperatures. Microscopic examination showed a polycrystalline structure, with no evidence of a glassy intercrystalline phase.

The glasses were held at that temperature for 2-3h and then cooled to room temperature overnight. These glass-ceramics were polished with emery papers and alumina powder using the technique previously described. The

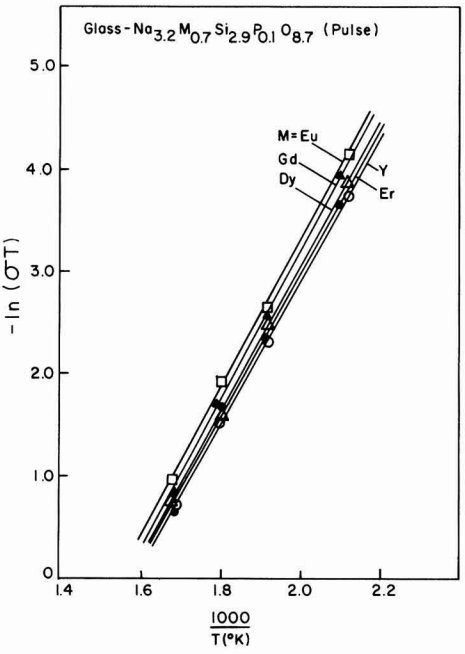


Fig. 1. Arrhenius plots of ionic conductivity for glass $Na_{3.2}M_{0.7}Si_{2.9}P_{0.1}O_{8.7}$.

*Electrochemical Society Active Member.

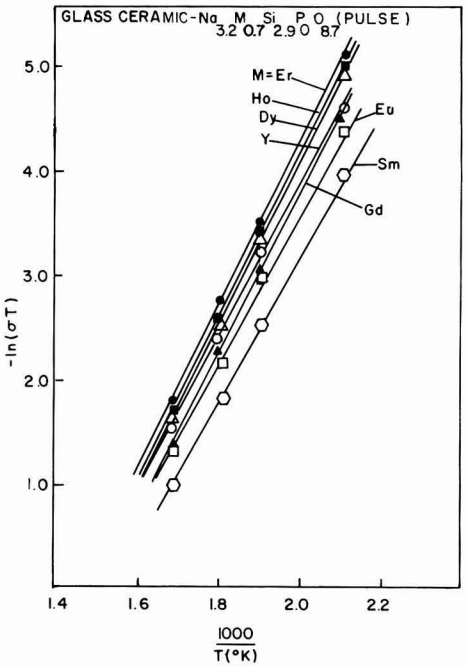


Fig. 2. Arrhenius plots of ionic conductivity for glass-ceramic $Na_{3.2}M_{0.7}Si_{2.9}P_{0.1}O_{8.7}$.

x-ray diffraction patterns for the glass-ceramic $Na_{3.2}M_{0.7}Si_{2.9}P_{0.1}O_{8.7}$ revealed the same sharp crystalline patterns as the corresponding samples prepared by pressing and sintering. For the glass-ceramic $Na_5MSi_4O_{12}$, the x-ray patterns showed traces of the $Na_3MSi_3O_9$ phase, except for the case of yttrium, which showed only the

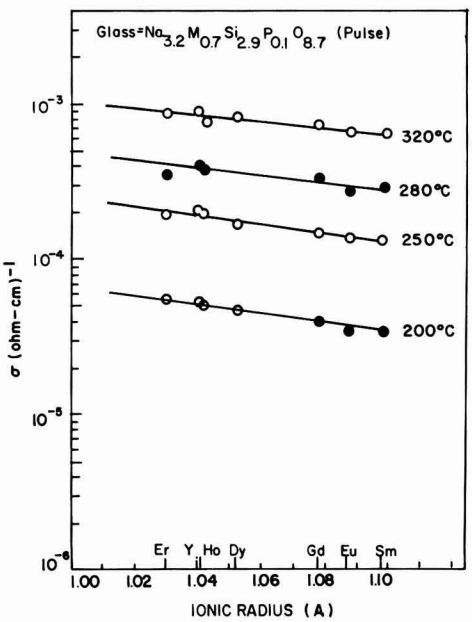


Fig. 3. Variation of ionic conductivity with M^{3+} radius for glass $Na_{3.2}M_{0.7}Si_{2.9}P_{0.1}O_{8.7}$.

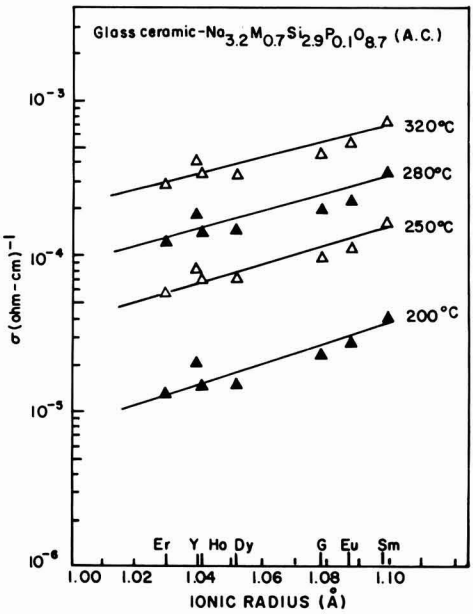


Fig. 4. Variation of ionic conductivity with M^{3+} radius for glass-ceramic $Na_{3.2}M_{0.7}Si_{2.9}P_{0.1}O_{8.7}$.

$Na_5YSi_4O_{12}$ phase. No detectable crystalline phases were found by x-ray diffraction of the glassy materials.

The polished disk-shaped samples were coated with chromium (~400Å) followed by gold to about 2000Å in thickness by vacuum evaporation, forming irreversible blocking electrodes. Their relative density varied from

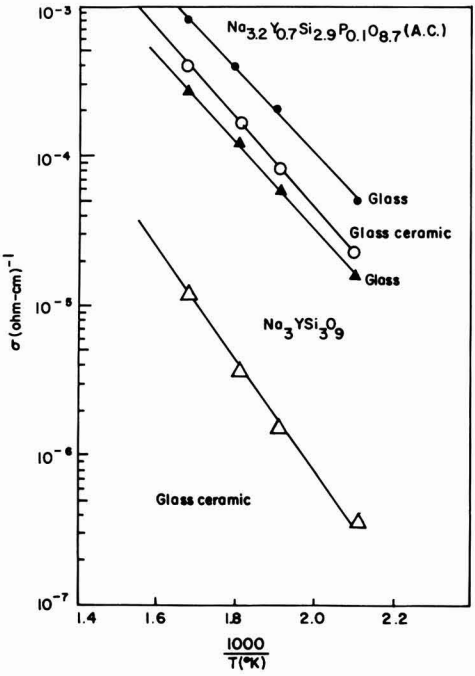


Fig. 5. Ionic conductivity *vs.* $1/T$ for $Na_3YSi_3O_9$ and $Na_{3.2}Y_{0.7}Si_{2.9}P_{0.1}O_{8.7}$.

98-100% in glass-ceramic $Na_{3.2}M_{0.7}Si_{2.9}P_{0.1}O_{8.7}$ to 90-99% in the glass-ceramic $Na_5MSi_4O_{12}$. The existence of pores in the glasses was negligible as observed microscopically. Two conductivity measurement techniques, a pulse method and a two-terminal ac method, were used at 200°, 250°, 280°, and 320°C. The pulse method was combined with a dc method which permitted the separation of ionic and electronic contribution to the conductivity. The pulses generated were 80 μs with 200 μs between pulses, but for the glass-ceramic $Na_5MSi_4O_{12}$ a shorter pulse width of 8 μs and a longer pulse repetition time of 1000 μs were chosen to eliminate the polarization effect occurring due to high ionic mobility in those materials. Pulse heights varied from 1 to 8V. For the dc measurement, a constant 0.5V was applied in the circuit, but the electronic contribution was negligible when the known series resistance was 5-10 kΩ. Two-terminal ac measurements were performed at 10^2-10^5 Hz and at 1V using a Hewlett-Packard 4274A Multifrequency LCR meter.

Results and Discussion

The glasses produced were transparent. The rigid glasses were devitrified to produce glass-ceramics. A major goal of this study was to compare the ionic conduction of the same composition in glasses and glass-ceramics. Usually, a glass will be a better conductor than a ceramic of the same composition. In this case, the effort was to compare crystalline phases of two materials with their glassy phases, one material being a good superionic conductor and the other being a relatively poor conductor.

$Na_{3.2}M_{0.7}Si_{2.9}P_{0.1}O_{8.7}$.—Figures 1 and 2 display the plot of $-\ln(\sigma T)$ *vs.* $1/T$ for the glass and glass-ceramic samples (curves for M = Ho and Sm are omitted in Fig. 1 due to the close spacing between lines). Tables I and II show the conductivities and energies of activation in the glass and glass-ceramic phases by the pulse and ac method at four temperatures. The magnitudes of the conductivities were in the order of 10^{-4} $(\Omega\text{-cm})^{-1}$ at 250°C in glass and at 280°C in glass-ceramic phases. Activation energies were in the range of 13.5-15.5 kcal/mol and not very different from those of the corresponding conventional polycrystalline phases (3). The results by the pulse and ac measurement were in good agreement.

Figures 3 and 4 show the dependence of conductivity upon the ionic size of six-coordinate M^{3+}. Most of the radii given here are "crystal radius" radii derived by Shannon (7). As can be seen in Fig. 3, the larger the size of M^{3+} in the glassy state, the lower the conductivity. It might be expected that the sodium ion motion in the amorphous state would be somewhat disturbed by the M^{3+} around the sodium ion and that the degree of disturbance depends on the size of M^{3+}. On the other hand, the conductivity in the glass-ceramic showed a different tendency from the case of glass, as can be seen in Fig. 4. The larger the ionic size of M^{3+}, the greater the conductivity. This result was same as that observed in corresponding conventional ceramic materials (3). When the glass-ceramic has recrystallized, ordering occurs and the position of each type of ion in the structure becomes fixed in the same way. The amount of space for the ionic motion is determined by the size of M^{3+}, which results in different cell volumes. The magnitudes of the conductivities in both glasses and glass-ceramics were comparable. Except when M = Sm, the other rare earth compounds showed higher sodium ion conductivities in glasses than in glass-ceramics.

Comparison of $Na_3YSi_2O_9$ and $Na_{3.2}Y_{0.7}Si_{2.9}P_{0.1}O_{8.7}$.—Figure 5 shows the results by ac method. The glassy state

Table I. Ionic conductivity of glass-$Na_{3.2}M_{0.7}^{III}Si_{2.9}P_{0.1}O_{8.7}$, pulse (ac) methods

M^{III}	Ionic conductivity $(\Omega\text{-cm})^{-1}$ 200°C	250°C	280°C	320°C	E_a (kcal/mol)
Er	5.40×10^{-5} (5.20×10^{-5})	1.90×10^{-4} (1.88×10^{-4})	3.52×10^{-4} (3.56×10^{-4})	8.61×10^{-4} (7.99×10^{-4})	14.05 ± 0.10 (13.90 ± 0.02)
Y	5.15×10^{-5} (5.06×10^{-5})	2.00×10^{-4} (2.00×10^{-4})	4.00×10^{-4} (3.94×10^{-4})	8.69×10^{-4} (8.23×10^{-4})	14.24 ± 0.02 (14.11 ± 0.02)
Ho	4.94×10^{-5} (5.00×10^{-5})	1.95×10^{-4} (1.88×10^{-4})	3.80×10^{-4} (3.70×10^{-4})	7.50×10^{-4} (7.88×10^{-4})	13.71 ± 0.11 (13.92 ± 0.03)
Dy	4.55×10^{-5} (4.53×10^{-5})	1.70×10^{-4} (1.66×10^{-4})	3.75×10^{-4} (3.31×10^{-4})	8.13×10^{-4} (7.39×10^{-4})	14.36 ± 0.07 (14.06 ± 0.02)
Gd	4.00×10^{-5} (3.90×10^{-5})	1.49×10^{-4} (1.47×10^{-4})	3.30×10^{-4} (3.00×10^{-4})	7.36×10^{-4} (6.50×10^{-4})	14.98 ± 0.06 (14.49 ± 0.04)
Eu	3.35×10^{-5} (3.36×10^{-5})	1.40×10^{-4} (1.30×10^{-4})	2.72×10^{-4} (2.60×10^{-4})	6.41×10^{-4} (5.96×10^{-4})	14.61 ± 0.05 (14.37 ± 0.02)
Sm	3.36×10^{-5} (3.32×10^{-5})	1.36×10^{-4} (1.30×10^{-4})	2.85×10^{-4} (2.65×10^{-4})	6.28×10^{-4} (6.20×10^{-4})	14.80 ± 0.05 (14.76 ± 0.02)

Table II. Ionic conductivity of glass-ceramic $Na_{3.2}M_{0.7}^{III}Si_{2.9}P_{0.1}O_{8.7}$, pulse (ac) methods

M^{III}	Ionic conductivity $(\Omega\text{-cm})^{-1}$ 200°C	250°C	280°C	320°C	E_a (kcal/mol)
Er	1.30×10^{-5} (1.32×10^{-5})	5.73×10^{-5} (5.70×10^{-5})	1.20×10^{-4} (1.23×10^{-4})	2.80×10^{-4} (2.80×10^{-4})	15.28 ± 0.03 (15.20 ± 0.05)
Y	2.10×10^{-5} (2.10×10^{-5})	7.80×10^{-5} (8.22×10^{-5})	1.65×10^{-4} (1.81×10^{-4})	3.75×10^{-4} (3.98×10^{-4})	14.54 ± 0.03 (14.96 ± 0.06)
Ho	1.44×10^{-5} (1.58×10^{-5})	6.43×10^{-5} (6.82×10^{-5})	1.39×10^{-4} (1.40×10^{-4})	3.14×10^{-4} (3.25×10^{-4})	15.41 ± 0.07 (15.11 ± 0.04)
Dy	1.54×10^{-5} (1.60×10^{-5})	6.71×10^{-5} (6.93×10^{-5})	1.50×10^{-4} (1.49×10^{-4})	3.32×10^{-4} (3.26×10^{-4})	15.37 ± 0.08 (15.09 ± 0.07)
Gd	2.24×10^{-5} (2.30×10^{-5})	9.19×10^{-5} (9.56×10^{-5})	1.90×10^{-4} (1.91×10^{-4})	4.35×10^{-4} (4.45×10^{-4})	14.94 ± 0.02 (14.83 ± 0.03)
Eu	2.70×10^{-5} (2.80×10^{-5})	1.12×10^{-4} (1.14×10^{-4})	2.20×10^{-4} (2.27×10^{-4})	4.63×10^{-4} (5.10×10^{-4})	14.31 ± 0.08 (14.52 ± 0.02)
Sm	4.11×10^{-5} (4.17×10^{-5})	1.58×10^{-4} (1.66×10^{-4})	3.12×10^{-4} (3.38×10^{-4})	6.50×10^{-4} (7.47×10^{-4})	14.00 ± 0.05 (14.57 ± 0.02)

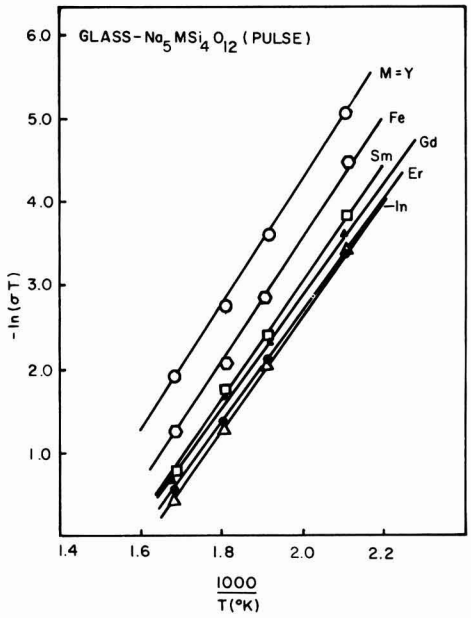


Fig. 6. Arrhenius plots of ionic conductivity for glass $Na_5MSi_4O_{12}$.

has higher conductivities than those of the glass-ceramic state in both materials. Larger conductivity differences between glass and glass-ceramic states were observed in $Na_3YSi_3O_9$. The conductivity of $Na_{3.2}Y_{0.7}Si_{2.9}P_{0.1}O_{8.7}$ was always higher than that of $Na_3YSi_3O_9$ in the glassy and glass-ceramic states. The activation energy of glass-ceramic $Na_3YSi_3O_9$ was higher (19.8 kcal/mol) than that of $Na_{3.2}Y_{0.7}Si_{2.9}P_{0.1}O_{8.7}$ (14.5 kcal/mol), but in glass the values for both materials were comparable. This is consistent with the view that the conduction mechanism in glass is largely determined by the structure of the glass network and relatively independent of the number of large network modifying ions.

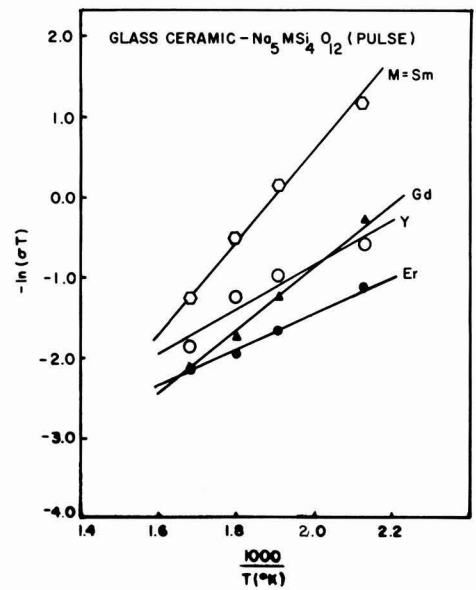


Fig. 7. Arrhenius plots of ionic conductivity for glass-ceramic $Na_5MSi_4O_{12}$.

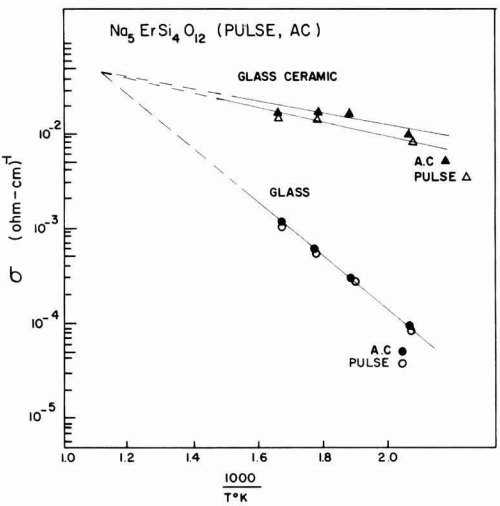


Fig. 8. Ionic conductivity vs. $1/T$ for $Na_5ErSi_4O_{12}$

$Na_5MSi_4O_{12}$ compounds.—Figures 6 and 7 indicate Arrhenius plots for the glasses and glass-ceramics of composition $Na_5MSi_4O_{12}$. The glasses show similar activation energies. However, in the case of glass-ceramics, the energies of activation were somewhat different depending on the nature of M^{3+}. Activation energies estimated for glass-ceramics with M = Er, Y were lower than those of the corresponding polycrystalline materials prepared by conventional techniques (6) (see Table III). It is thought that this may be an effect of the smaller radii of these ions on the anisotropic nucleation of the $Na_5MSi_4O_{12}$ crystals in the glass. This point should be investigated more systematically.

Figure 8[1] shows the results of measurements on glassy and glass-ceramic $Na_5ErSi_4O_{12}$. The glass-ceramics gave

[1]In contrast to earlier Arrhenius plots, Fig. 8 shows the logarithm of the conductivity, rather than its negative, in order to emphasize the higher conductivity and lower activation energy of the glass-ceramic phase.

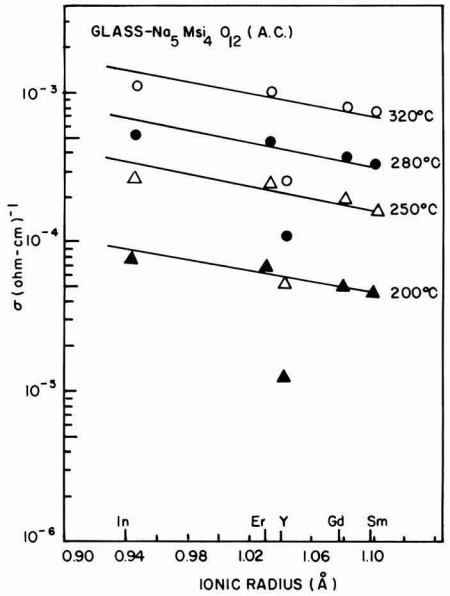


Fig. 9. Ionic conductivity vs. M^{3+} radius for glass $Na_5MSi_4O_{12}$.

Table III. Activation energy (kcal/mol) for $Na_5MSi_4O_{12}$

	M			
	Er	Y	Gd	Sm
Glass-ceramic[a]	4.0	4.4	7.5	11.1
Crystalline	7.5	7.1	6.5	7.3

[a] Average of two measurements.

much better conductivities than the glasses, with lower activation energies. This may be explained by the fact that the large open channels (4, 6) in the glass-ceramic structure would not be disturbed as in the case of the amorphous state, and that this may help the motion of mobile sodium ions. It should be noted that all lines cross at a value of $1/T \sim 10^{-3}$, close to zero. The pre-exponential factor is 4×10^{-2} $(\Omega\text{-cm})^{-1}$.

The relation between the conductivity and ionic size of M^{3+} in glassy $Na_5MSi_4O_{12}$ is displayed in Fig. 9. The same tendency found in glassy $Na_{3.2}M_{0.7}Si_{2.9}P_{0.1}O_{8.7}$ resulted; the larger the ionic size of trivalent metal, the lower the conductivity, with some deviation when M = Y. The same explanation given for the glasses $Na_{3.2}M_{0.7}Si_{2.9}P_{0.1}O_{8.7}$ may be used for this phenomenon in glassy $Na_5MSi_4O_{12}$. The larger ions evidently interfere more with the motion of the mobile sodium ions in the disordered glass.

The result of this comparison of glass and ceramic phase of the same composition appears to confirm the suggestion that compounds with crystal structure having channels for rapid ion migration will have their conductivity decreased in a disordered state, while compounds whose structure is not conducive to rapid transport and that depend primarily on defect migration for their conductive properties will have higher conductivities in the glassy state, where the defect concentration is increased relative to the crystalline state. This work has also demonstrated the feasibility of forming ceramic solid electrolytes by glass forming techniques without degrading the intrinsic conductivity properties of the crystalline phase, and perhaps even enhancing them.

Acknowledgments

The authors thank Mary Eschwei of the Department of Physics, Polytechnic Institute of New York, for the preparation of electrodes on the samples. This research was supported by the Polytechnic Institute of New York via a teaching assistantship of C. H. Kim. This paper is part of a dissertation submitted to the Polytechnic Institute of New York by C. H. Kim in partial fulfillment of the requirements for the degree of Doctor of Philosophy.

Manuscript submitted Feb. 19, 1985; revised manuscript received July 5, 1985.

REFERENCES

1. R. D. Shannon, B. E. Taylor, T. E. Gier, H.-Y. Chen, and T. Berzins, *Inorg. Chem.*, **17,** 958 (1978).
2. R. D. Shannon, T. E. Gier, C. M. Foris, J. A. Nelen, and D. E. Appleman, *Phys. Chem. Miner.*, **5,** 245 (1980).
3. C. H. Kim, B. Y. Qiu, and E. Banks, *This Journal*, **132,** 1340 (1985).
4. B. A. Maksimov, Y. A. Kharitonov, and N. V. Belov, *Sov. Phys. Dokl.*, **18,** 763 (1974).
5. R. D. Shannon, H.-Y. Chen, and T. Berzins, *Mater. Res. Bull.*, **12,** 969 (1977).
6. R. D. Shannon, *Acta Crystallogr, Sect. A*, **32,** 751 (1976).

Light-Generated Electrodics—Rotating Dual Electrodes

B. Miller* and J. M. Rosamilia

AT&T Bell Laboratories, Murray Hill, New Jersey 07974

ABSTRACT

The generation of current for solution redox reactions below the mass-transport limiting current at semiconductor electrodes has been shown to be spatially controllable by light-beam dimension and placement. Thus, a localized electron or hole transfer surface can be created at a semiconductor-redox electrolyte junction by means of a focused laser beam. Such a spot was scanned over a semiconductor disk in a series of experiments within a rotating ring-disk electrode geometry to test the transit and collection properties of the local reaction products. By comparison to related theory for the given geometries, the predicted disk and ring currents as a function of electrode size and location were quantitatively confirmed. These microelectrodes ought to have the enhanced radial transport and reduced resistive losses associated with their micrometallic counterparts, but with flexible manipulation of the geometric parameters. Other results include mapping the generation of selected products over the surface of the semiconductor material and establishing the possibility of detecting kinetic processes by monitoring the collection and transit parameters as a function of radial origin.

It is well appreciated that electrode geometry and mass-transport mode are of primary concern in the various forms of voltammetry (1). Schemes in which a detecting electrode monitors a generating one (*e.g.*, rotating ring-disk electrodes) take further advantage of geometry and mass transport to great effect. Our purpose here is to explore the possibilities inherent in "generator" electrodes whose location and dimensions can be defined by light beams rather than limited to conventional mechanical shaping or masking.

To describe this approach, we refer first to the recent thrust of electrodic studies to semiconductor photoelectrochemistry. Extensive development has been made of the energy conversion possibilities in the light stimulated formation of electron-hole pairs and their separation to initiate photoanodic (n-type) or photocathodic (p-type) processes. These reactions of minority carriers proceed in the direction forbidden in the dark by the rectifying barrier associated with the existence of a bandgap in the semiconductor whose edges straddle the levels of the relevant redox potentials. For our present aim, light activation under proper electrode potential control creates an electron-transfer surface defined geometrically by the incident light flux (only restricted diffusive spreading of charge in the solid exists parallel to the interface).

We have applied the above concepts to making spatially controllable electrode surfaces by focusing light spots onto a semiconductor surface through a redox electrolyte. Since laser light can be readily concentrated to form disk profiles of FWHM (full width at half maximum) sizes in the micrometer region, an immediate possibility is the generation of very small electrodes for the ordinarily (dark) current blocking direction. Such electrodes could have the advantages of enhanced radial transport and low relative losses ascribed to such "ultramicro" electrodes (2, 3), could the effective electrode area be restricted to light spot dimensions. Thin rings are another useful pattern readily accessible to light beam definition.

* Electrochemical Society Active Member.

In this initial report, however, we concentrate on the more physically complex arrangement of generator-detector electrode pairs where the generator electrode is that defined by light and semiconductor junction properties. Existing theory allows us in this way to demonstrate our facile control of the features of variable electrode size and location and the useful properties that emerge from this capability. Future work will treat the single electrode possibilities we have alluded to above.

Our experiments employ rotating dual electrodes whose collection characteristics are theoretically related to those of the well-known rotating ring-disk and ring-ring electrodes. With some graphic visualizations and quantitative tests, we demonstrate here that electrodes of defined small dimensions with predictable properties can be produced. The quantitative aspects refer to the collection and transit time features of electrode pairs in the convective diffusion regime.

We first discuss the theoretical and practical considerations necessary for partially illuminated semiconductor electrodes. The collection properties of rotating generator-detector dual electrodes of our geometry are treated by means of dual ring electrode theory (4). The transit time relations for localized generating electrodes to a fixed ring are calculated from the previous treatments for rotating ring-disk electrodes (5, 6).

Semiconductor junctions.—The flux of photons to a given semiconductor area (A) can produce a flow of minority carriers to the interface up to its equivalent current density, i^*/A, should all photons be absorbed and each generate a hole-electron pair. If i^*/A is less than the mass-transfer-limited flux of an appropriate redox species to the interface with current density, i_l/A, then the interfacial potential of the localized redox reaction at cell current $i \cong i^*$ will be fixed (7, 8).

Consider all the photocurrent generated at only a small area, A (small meaning $A << A_D$, where A_D is the area of the entire electrolyte-exposed semiconductor). The photocurrent produced over A is in parallel with the "dark" current of the unilluminated area. In order to detect a process occurring at the illuminated small spot, this dark current must be significantly less than the light-generated value when the electrode is reverse-biased (*i.e.*, held a few tenths of a volt positive of flatband for a n-type material). This situation can be readily achieved for a FWHM spot size ≤ 100 μm, as we will show, even where A_D/A ratios are of order 2×10^3, as in our typical electrodes.

The diffusion length of minority carriers in the semiconductor crystals employed in our experiments is <10 μm. Further, the flux of redox species to the illuminated spot to accept the photogenerated carriers is kept from being limiting by the use of sufficient concentrations (0.1M). Diffusive spreading of the carriers outside of spot sizes in the work below can be neglected. Also, the fact that the profile of intensity across the beam is gaussian, rather than rectangular, is not taken into account in the geometric considerations below.

Collection properties of dual electrodes.—The experiments are performed on rotating ring-disk electrodes (semiconductor disks, gold rings). The collection property in the absence of any localization of the reaction within the disk area is expressed by $N = |i_R/i_D|$, where i_R is the ring current (change) produced by disk current, i_D. The calculation of N from the electrode radii is well known (9). Following Matsuda (10, 11) and Albery and Bruckenstein (9), Filinovskii *et al.* (4) have also derived the collection efficiency, $N_r = |i_{ro}/i_{ri}|$ for a rotating dual ring electrode, where subscripts o and i refer to outer and inner ring, respectively.

Consider all the product generated at current i arises from a spot on the disk for detection at a limiting current level (collection) at a fixed ring. The collection efficiency, $N_s = |i_R/i|$, for this case will approximate that of a dual ring system with radii r_0, $r_1 = r_0 + \Delta$, r_2, and r_3; r_0 is the distance from the inner edge of the spot to the center of the disk, Δ is the diameter of the spot, and r_2 and r_3 are the inner and outer radii of the fixed ring, respectively.

For the dual ring system, N_r is given by (4)

$$N_r = \left(\frac{r_3^3 - r_2^3}{r_1^3 - r_0^3}\right)^{2/3} G\left(\frac{r_1^3 - r_0^3}{r_2^3 - r_1^3}\right) + G\left(\frac{r_3^3 - r_2^3}{r_2^3 - r_1^3}\right) - \left(\frac{r_3^3 - r_0^3}{r_1^3 - r_0^3}\right)^{2/3} G\left[\left(\frac{r_1^3 - r_0^3}{r_2^3 - r_1^3}\right)\left(\frac{r_3^3 - r_2^3}{r_3^3 - r_0^3}\right)\right] \quad [1]$$

where

$$G(Z) = \frac{\sqrt{3}}{4\pi} \ln \frac{1 + Z}{(1 + Z^{1/3})^3} + \frac{3}{2\pi} \arctan\left(\frac{2Z^{1/3} - 1}{\sqrt{3}}\right) + \frac{1}{4} \quad [2]$$

The collection efficiencies, N_s, for the current generated at a spot were calculated from Eq. [1] and [2], using the radii defined above.

Transit time.—Another mode of defining location of electrode reaction under these hydrodynamic conditions is through the interval from generation to detection of the reaction at the spot. The transit time, τ, from initiation of a light-activated pulse of current somewhere on the disk to its detection at the inner edge (r_2) of a ring is the quantity of interest. Bruckenstein *et al.* (5, 6) found this transit time in seconds from the generation of a step of current at a disk of radius r_1 to its detection at the ring to be given by

$$w\tau = (43.1)\left(\frac{\nu}{D}\right)^{1/3} (\log r_2/r_1)^{2/3} \quad [3]$$

w is speed in revolutions per minute and ν/D is the Schmidt number, Sc, the ratio of the kinematic viscosity of the solution to the diffusion coefficient of the electroactive species. Prater and Bard (12, 13), with slightly different assumptions about particle trajectories, found a numerical factor of 34.2 rather than 43.1.

This relation should approximate the transit time associated with the transport of photogenerated species from a small spot of diameter Δ. The variation of τ with r_1 in this case can be tested against Eq. [3] by applying light pulses and measuring the transit time oscilloscopically.

Experimental

Acetonitrile (CH_3CN) from Burdick and Jackson was not further purified. Ferrocene $Fe(Cp)_2$ was obtained from Aldrich, and tetrabutylammonium fluoroborate (TBAFB) from Eastman Kodak Company. Redox electrolyte solutions of 0.1M $Fe(Cp)_2$/1.0M TBAFB/CH_3CN (14) were stored over activated Linde 3Å molecular seives. Amborane 345 polymeric reductive resin (Rohm & Haas) was used to reduce the level of $Fe(Cp)_2^+$ that might be present in the stock solution.

Rotating ring-disk electrodes (RRDE's) consisted of either n-InP or n-GaAs disks and Au rings. The geometric values of r_1, r_2, and r_3, respectively, were 2.35, 2.47, and 3.11 mm for the n-InP RRDE and 2.37, 2.45, and 3.11 mm for n-GaAs. Collection efficiencies for the n-InP and n-GaAs electrodes are 0.384 and 0.398, respectively. Rotation was provided by a Pine Instruments MSR rotator/controller. The n-InP and n-GaAs electrodes were etched for 3s in concentrated HCl or 1:1 H_2SO_4/H_2O_2, respectively. The etchant procedure for each was repeated until a constant light limited current profile, *i.e.*, current independent of position, was established across the semiconductor disk for a scanned beam. The disk and ring currents were measured using a Pine Instruments Model RDE3 bipotentiostat using graphite rods as reference and counterelectrodes. Potentials are thus reported *vs.* solution redox level.

A block diagram of the instrumentation employed for rastering the RRDE is shown in Fig. 1. A He-Ne laser beam is deflected 90° using a 45° mirror mount and focused to a spot size of about 100 μm on the electrode surface using a 10× microscope objective. A Servo-Tek motor in an assembly equipped with silver-graphite electrode contacts and the RRDE are mounted on an X-Y

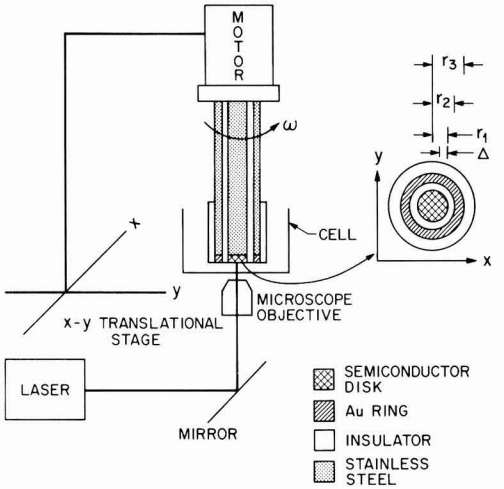


Fig. 1. Schematic of the laser-RRDE scanning system with fixed optics and translated electrode. Insert of electrode face shows fixed disk and ring radii and programmable spot diameter, Δ.

translational stage driven by a Newport Corporation 855C programmable controller system. This arrangement allows the laser beam and an optical flat-bottom cell to be fixed in space while the electrode itself is displaced in X-Y coordinates (the plane of the disk).

Two-dimensional (line) scans were monitored by both a Y1-Y2-t recorder and a microcomputer. The microcomputer provided digital data for analysis of N. The electrode was scanned in the X direction at a fixed Y location at a rate of 0.06 mm/s. Three-dimensional and contour plots were obtained with the same mapping procedures as in Ref. (15), substituting the electrode for the photovoltaic cell.

The only physical modification needed in the above apparatus to measure transit times was adding a controllable shutter in the path of the laser beam to provide a 50 ms pulse of light. A step pulse of disk current is correspondingly generated, followed by a rise in ring current as the product is detected. The i_D and i_R $vs.$ time relations were measured on an oscilloscope, and τ values were determined from these traces (5, 6). The laser beam was moved across the electrode in 0.2 mm steps.

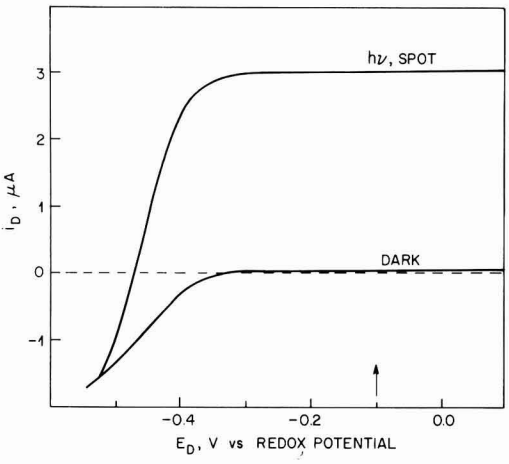


Fig. 2. i_D and E_D curves in dark and with ~100 μm laser spot, at a rotating n-InP disk electrode in 0.1M $Fe(Cp)_2$/1.0M TBAFB/CH_3CN. ω = 1600 rpm. Scan rate = 7.5 mV/s.

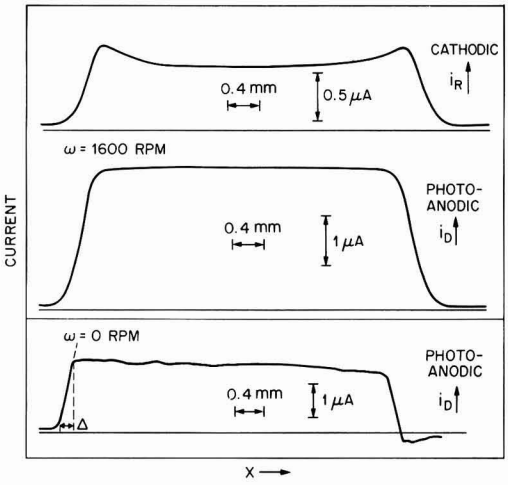


Fig. 3. Two dimension line scans of i_D (photoanodic) and i_R (cathodic) for ω = 1600 rpm, and i_D (photoanodic) for ω = 0 rpm as a function of light spot position, x, across a diameter of the n-InP electrode. E_D fixed at −0.1V vs. redox potential. E_R fixed at −0.2V [limiting current region for $Fe(Cp)_2^+$ reduction].

The laser beam spot size was determined by monitoring a Metrologic Radiometric Si detector in conjunction with a 10 μm pinhole attached directly to an X-Y translational stage in front of the detector head. The pinhole is positioned at the focus corresponding to electrode experiments and is scanned across the beam at 0.006 mm/s. The power output as a function of distance traveled is recorded and the corresponding peak width at 50% (FWHM) and 25% of peak height is measured.

Results and Discussion

The i-E curves for the n-InP disk, first in the dark and then with the addition of a laser beam focused on area A (anywhere on its surface area A_D) are shown in Fig. 2. The solution used throughout is 0.1M $Fe(Cp)_2$/1.0M TBAFB/CH_3CN. Although the A_D/A ratio is at least 2×10^3, the reverse (residual) current at the dark crystal is still very small compared to the photoanodic component generated over the small area. At these ferrocene concentrations, the results are independent of rotation speed. The current density, i/A, in the illuminated spot is about 0.4 mA/cm².

If the disk electrode potential is held in the range indicated by the arrow on the abscissa of Fig. 2 while the electrode face is scanned across the beam, virtually all current is attributable to the light source. Such a scanning experiment is shown in Fig. 3. When the electrode was ro-

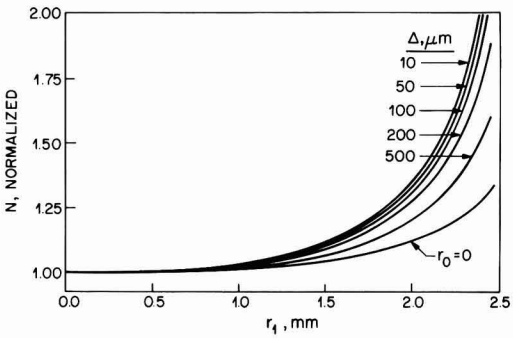


Fig. 4. Theoretical curve of normalized collection efficiency vs. r_1 for several values of Δ and for r_0 = 0. Ring diameters r_0 and $r_0 + \Delta = r_1$.

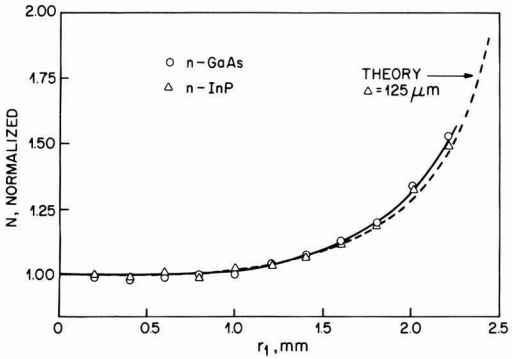


Fig. 5. Experimental curve of normalized collection efficiency vs. r_1 for both n-GaAs (circles) and n-InP (triangles) disk-Au ring electrodes. Values are obtained from i_R vs. X scans as shown in Fig. 2. Theoretical relationship of N vs. r_1 for $\Delta = 125\,\mu m$ (Δ from Fig. 2) is the dashed line.

tated at 1600 rpm, the ring current for the reduction of ferrocenium species was simultaneously monitored. The i_D profile is constant across the disk once the entire spot is on the semiconductor surface. The ring current trace shows the anticipated higher collection for product generated nearer the disk edge where it has less chance of escape before detection. A scan across a stationary disk is also shown under the same beam conditions. The profiles of disk current are essentially flat across the bulk of the disk, independent of rotation rate, under these local light-limited current conditions.

The profiles of rotated and stationary electrode disk currents differ materially only at the edge. The stationary electrode, for any scanned diameter, shows a sharper rise to its constant value since there is no eccentricity attributable to rotation and circular imperfections to broaden this distance. The scan traverse from edge (initial rise) to flat current, as indicated in Fig. 3, is a measure of Δ, the spot diameter. A more direct measure of spot diameter has been made by pinhole profiling under the same focus conditions. The FWHM was ~70 μm, and the width at 25% peak was ~90 μm. These values are consistent with the measurements of Δ from the stationary disk current profiles.

A set of theoretical curves calculated from Eq. [1] and [2] for spot collection is shown in Fig. 4. They are plotted normalized to the limiting collection of 0.315 for a small disk at the center of rotation where it becomes independent of spot size. This limiting collection efficiency was obtained using $r_2 = 2.45$ and $r_3 = 3.11$ mm. The plot for $r_0 = 0$ is identical with the set of calculated ring-disk collection efficiencies (9). As the spot becomes smaller, collection for spots near the disk edge becomes relatively larger (r_2 and r_3 fixed). The sensitivity to Δ can be used as a test of the localization of current as defined by $r_1 = r_0 + \Delta$.

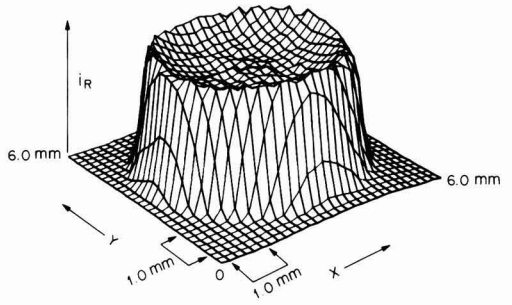


Fig. 6. Three-dimensional surface of i_R as a function of spot location on disk. Experimental conditions as in Fig. 3.

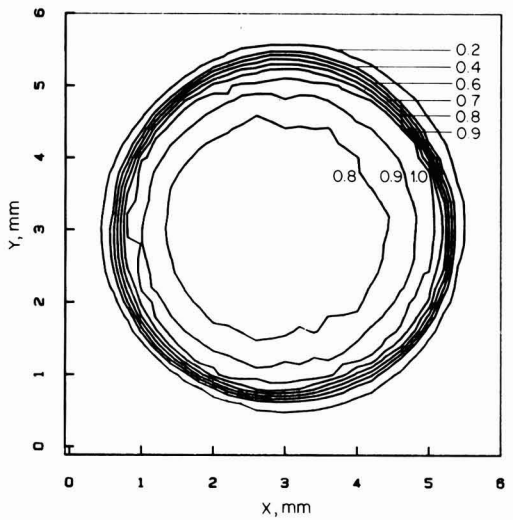


Fig. 7. i_R contour plot projected on disk surface. The maximum ring current is normalized to 1.0. Contour values of 0.2, 0.4, 0.6, 0.7, 0.8, 0.9, and 1.0 are indicated.

In Fig. 5 are plotted the experimental determinations of the function in Fig. 4 from the analysis of data obtained, as in Fig. 3, by a disk scan across a diameter. The theoretical curve for the Δ value obtained from the edge effect for a stationary electrode scan is also plotted in Fig. 5. There is good agreement of predicted and experimental curves. The sensitivity of normalized collection efficiency to the value of Δ is, however, largest at the edge where the difficulty of having perfect geometry and no eccentricity is highest.

The results of the two-dimensional experiments in Fig. 3 and 5 can be expanded to a three-dimensional representation of an X-Y collection (i_R) scan over the full disk area, as shown in Fig. 6. The corresponding i_D map is a flat topped mesa; it is not shown. In principle, the entire disk area is observed through rotation during a single radial scan. Rotationally synchronized data acquisition could give a point-by-point i_R map, rather than the radially averaged one of Fig. 6. The damping imposed by the spiral trajectory and the finite transit time precludes effective use of this fact.

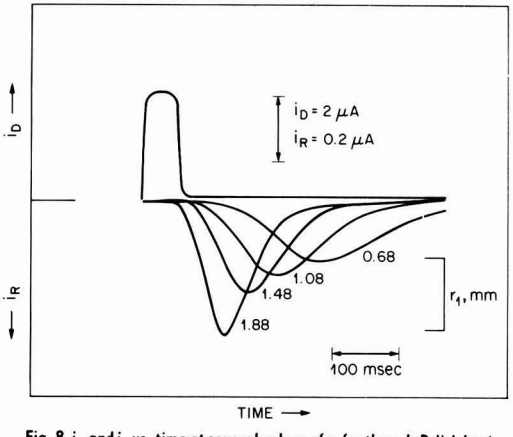


Fig. 8. i_D and i_R vs. time at several values of r_1 for the n-InP disk having $r_2 = 2.47$ mm. $\omega = 1600$ rpm. The laser spot originates from a 50 ms pulse.

Besides the visualization of the collection efficiency as a surface over the moving radial origin of disk current, the X-Y scans allow more facile determination of what is a true radial direction scan. For example, curves shaped as in Fig. 3 can be obtained even though one may be missing the center of the disk in the scan. A radial scan, as opposed to that of any other chord, will, of course, give the largest abscissa in a Fig. 3 experiment. A contour display of the three-dimensional experiment, normalized to unity at the high (near-edge) values, is given in Fig. 7.

This plot offers the information of a two-dimensional scan averaged over the whole disk electrode. The drawing of radii across the disk contours allows one to make Fig. 5 plots with a fuller estimate of the range of reproducibility. In the contours of Fig. 7, the ring residual current has been linearly corrected for any changes in each X-direction scan noted before and after crossing the active disk surface. Step increments are treated as Y-direction.

The transit time experiments were accomplished by producing an i step with a pulse of light controlled by the shutter drive, then monitoring both i_D and i_R on a dual-beam storage oscilloscope. If sufficient time is allowed for the i_R response to return to the residual (dark disk) value, repetitive pulses produce successively coincident i and i_R traces when appropriately triggered by either the shutter pulse or i.

A sequence of i_R traces produced by the same i timing, but for different radial positions at constant rotation speed, is shown in Fig. 8. The i_R traces are extrapolated by a tangent line on the steeply rising part of the peak to a time intercept on the extrapolated residual line. Maximum transit time is obtained at the disk center.

A similar set of traces was obtained for a point near a $r_1/2$ position as a function of rotation speed. These two experiments in which $w\tau$ is obtained as a function of r (constant w) and w(constant r_1) are plotted in Fig. 9. The quantity $(\log r_2/r_1)^{2/3}$ arising from Eq. [3] is plotted as the radial abscissa (lower), as is w(upper).

Using the tangent method, the $w\tau$ vs. $(\log r_2/r_1)^{2/3}$ line is straight but extrapolates through a finite $w\tau$. Since this extrapolation should be zero (point of origin and detection coinciding), the intercept value of $w\tau$ was used as a correction in the $w\tau$ as $f(w)$ plot. When corrected in this manner, $w\tau$ is a constant at all w, as predicted and found for fixed geometry ring-disk electrodes (5, 6). However, the way τ is chosen can be reflected in the value of the $w\tau$ product (12).

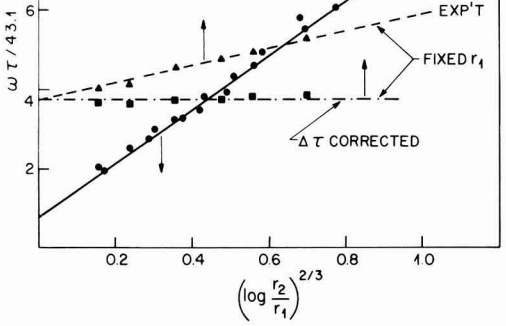


Fig. 9. Plot of $\omega\tau$/43.1 vs. $(\log r_2/r_1)^{2/3}$ at fixed ω = 1600 rpm (solid line) and ω at fixed $(\log r_2/r_1)^{2/3}$ = 0.569 (dashed line). Plot of the corrected values $\omega(\tau - \Delta\tau)$/43.1 vs. ω is shown by the dash-dotted line where $\Delta\tau$ is obtained from the Y-intercept of the solid line.

Table I. Summary of $Sc^{1/3}$ values

		$Sc^{1/3}$	$\overline{Sc^{1/3}}$	$Sc^{1/3}$	$\overline{Sc^{1/3}}$
A	$w\tau$ vs. $(\log r_2/r_1)^{2/3}$	6.51[a]		8.20[b]	
		5.42[a]	6.5	6.83[b]	8.2
		7.54[a]		9.50[b]	
B	$w\tau$, fixed r_2/r_1	7.03[a]		8.86[b]	
			6.8		8.6
		6.60[a]		8.32[b]	
C	Δi_L at $p = 0.05/\Delta i_L$ at $p = 0.5$	8.32			
D	i_L vs. $w^{1/2}$	8.81			

[a] Numerical factor of 43.1 from Ref. (5) was used in Eq. [3].
[b] Numerical factor of 34.2 from Ref. (12) was used in Eq. [3].

A summary of $Sc^{1/3}$ values obtained from the slope of three sets of $w\tau$ vs. $(\log r_2/r_1)^{2/3}$ experiments and from two sets of constant $w\tau$ product at fixed r_2/r_1 is given in Table IA and IB. An Sc value for this solution was further estimated independently in two ways. A Levich plot of limiting current vs. $w^{1/2}$ was determined for a known ferrocene concentration, and D was calculated using the kinematic viscosity of 1.0M TBAFB/CH_3CN measured with a Cannon-Fenske viscometer. The frequency response of hydrodynamic modulation of the limiting current was measured for two ratios, p, of modulation frequency/rotational frequency. This two-point method (16, 17) gives a value for Sc independent of concentration. The data are summarized in Fig. 10.

The modulation current ratio for p = 0.05 and 0.5 of 0.341 corresponds to a $Sc^{1/3}$ as given in Table IC. $D = 1.2 \times 10^{-5}$ cm^2-s^{-1} calculated from the Levich equation (i_L vs. $w^{1/2}$ plots) using $\nu = 8.3 \times 10^{-3}$ cm^2-s^{-1} gives the $Sc^{1/3}$ value in Table ID, which ought to be the most reliable. The consistency of the $Sc^{1/3}$ measurements by all four procedures is adequate within the experimental limits of the $w\tau$ repeatability and assumptions for the numerical constant.

Conclusions

The generation of current at locally selected areas of semiconductor (disk) electrodes has been shown to be spatially controllable by light-beam placement and dimension. The quantitative confirmation comes from two properties (transit time and collection) of rotating ring-disk systems for which theoretical relations may be adapted to the local generation problem. By both of the methods the current stimulated by the light beam can be shown to originate in the area fixed by a diameter corresponding to that determined through beam profile and disk edge crossing effects. The properties of the laser

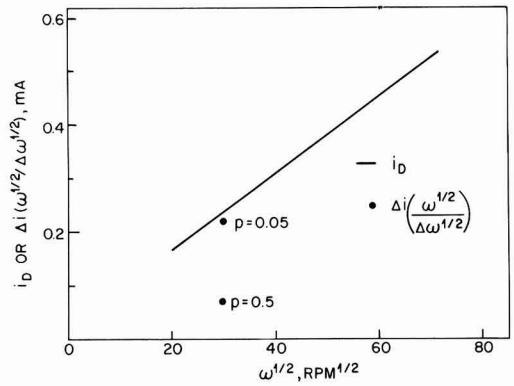


Fig. 10. Plot of i_D vs. $\omega^{1/2}$ for 1.6 × 10^{-3}M $Fe(Cp)_2$ in 1.0M TBAFB/CH_3CN at a Au disk electrode held at 0.6V vs. SCE. The points represent the Δi response for p = 0.05 and 0.5 employing $\omega^{1/2}$ = 30 $rpm^{1/2}$ and $\Delta\omega^{1/2}$ = 2 $rpm^{1/2}$.

scanned beam have been extended to a three-dimensional representation of the collection characteristic of the entire surface.

Two general points are intended by these demonstrations. First, directly from the experiments discussed, the flexible localized control of reaction generation in dual electrode systems leads to new schemes of kinetic measurement where a geometric, as well as a hydrodynamic (rotation speed), factor can be a primary variable. An example of this would be in chemical follow-up reactions (EC mechanisms) where the collection as a $f(r)$ would be altered. Another in this category is the use of the r variable to increase sensitivity in the detection of adsorption via the transit-time experiment (6). The illustrated mapping of a surface with respect to collection of ring current from that area is a geometric extension that adds the discrimination of selective product detection to the mapping of photocurrent (18) or differential power efficiency (15) over surfaces of semiconductors. Thus, corrosion current or redox transfer efficiency can be determined over a locally heterogeneous disk, averaged in this case over a radial position.

The second emphasis relates to producing small electrodes of selected shapes in regions of controlled mass transport. Such properties are currently under study. The use here in the context of exposed semiconductor surfaces is limited because of the competitive photocorrosion reactions, through another means to study that competition. The use of buried junctions and "noble" overlayers to augment controlled passivation must overcome, by appropriate design, the lateral spreading of carriers in the overlayer. Such electrodes, if successfully constructed, could allow localized reaction at a choice of surfaces not restricted to semiconductors while retaining the advantageous geometric control properties that cannot now be obtained with metals.

Manuscript submitted March 28, 1985, revised manuscript received May 3, 1985. This was Paper 445 presented at the Las Vegas, Nevada, Meeting of the Society, Oct. 13-18, 1985.

AT&T Bell Laboratories assisted in meeting the publication costs of this article.

REFERENCES

1. A. J. Bard and L. R. Faulkner, "Electrochemical Methods," John Wiley and Sons, New York (1980).
2. A. M. Bond, M. Fleischmann, and J. Robinson, *J. Electroanal. Chem.*, **172,** 11 (1984).
3. R. M. Wightman, *Anal. Chem.*, **53,** 1125A (1981).
4. V. Yu. Filinovskii, I. V. Kadija, B. Z. Nicolic, and M. B. Nakic, *J. Electroanal. Chem.*, **54,** 39 (1974).
5. S. Bruckenstein and G. A. Feldman, *ibid.*, **9,** 395 (1965).
6. S. Bruckenstein and D. T. Napp, *J. Am. Chem. Soc.*, **90,** 6303 (1968).
7. S. Bruckenstein and B. Miller, *This Journal*, **129,** 2029 (1982).
8. S. Bruckenstein, J. M. Rosamilia, and B. Miller, *J. Phys. Chem.*, **89,** 677 (1985).
9. W. J. Albery and S. Bruckenstein, *Trans. Faraday Soc.*, **62,** 1920 (1966).
10. H. Matsuda, *J. Electroanal. Chem.*, **15,** 109 (1967); *ibid.*, **16,** 153 (1968).
11. H. Matsuda, *ibid.*, **35,** 77 (1972).
12. K. B. Prater and A. J. Bard, *This Journal*, **117,** 207 (1970).
13. A. J. Bard and L. R. Faulkner, "Electrochemical Methods," p. 307, John Wiley and Sons, New York (1980).
14. C. M. Gronet and N. S. Lewis, *Appl. Phys. Lett.*, **43,** 115 (1983).
15. J. M. Rosamilia and B. Miller, *Solar Cells*, To be published.
16. K. Tokuda, S. Bruckenstein, and B. Miller, *This Journal*, **122,** 1316 (1975).
17. J. M. Rosamilia and B. Miller, *Anal. Chem.*, **56,** 2410 (1984).
18. T. E. Furtak, D. C. Canfield, and B. A. Parkinson, *J. Appl. Phys.*, **51,** 6018 (1980).

Extension of DC Transient Techniques to the Nonlinear Current Density-Overpotential Range and the Limitations of Linearized Approximations

Z. Nagy* and R. H. Land

Argonne National Laboratory, Chemical Technology Division, Argonne, Illinois 60439

G. K. Leaf and M. Minkoff

Argonne National Laboratory, Mathematics and Computer Science Division, Argonne, Illinois 60439

ABSTRACT

The applicability of the dc relaxation techniques for the measurement of kinetics of fast electrode reactions has been limited generally to the linear current density-overpotential (i-η) range by the mathematical difficulties in obtaining a closed-form solution of the differential equations describing the system, confining the measurements to the vicinity of the equilibrium potential. Evaluation of the experimental data with numerical curve-fitting procedures offers a possibility for the extension of these techniques into the nonlinear i-η range. The feasibility of such extension was demonstrated by a curve-fitting data-evaluation method with a nonlinear multidimensional least squares minimization package coupled to a software package designed to solve systems of nonlinear partial differential equations. The main advantage of this approach is that measurements can be made at high enough overpotentials to avoid signal-to-noise ratio problems without introducing linearization errors in the data evaluation. The error of the linearized i-η relation is not negligible under many experimental conditions. A quantitative evaluation of this error has been made as a function of three dimensionless parameters: $\alpha\nu/n$, $C_0D_0^{1/2}/C_RD_R^{1/2}$, and $\eta n\mathbf{F}/RT$. The error in the exchange current density determination, with the assumption of linear i-η relation, will be at least as large as the error of the linearized equation.

The applicability of the dc relaxation techniques for the measurement of kinetics of fast electrode reactions has been limited generally to the linear current density-overpotential range by the mathematical difficulties in obtaining a closed-form solution of the differential equations describing the electrode system (1). It would be highly desirable to extend the applicability of the relaxation techniques to the nonlinear range because the linearization is valid only within a few millivolts polariza-

*Electrochemical Society Active Member.

tion around the equilibrium potential; this limit is very restrictive for both practical and theoretical purposes. Measurements at low overpotentials are often difficult because of signal-to-noise ratio problems. Furthermore, the assumption that the kinetics and mechanisms of the electrode reaction are independent of potential is often incorrect; therefore, extrapolation from the linear range to higher overpotentials is generally questionable. Evaluation of the experimental data with numerical curve-fitting procedures offers a possibility for using these techniques in the nonlinear current density-overpotential range. It has been shown previously (2-6) that numerical curve-fitting, using nonlinear, multidimensional least squares calculation, is the best data evaluation method for all dc relaxation techniques in the linear range. The curve-fitting program does not require a closed form solution of the diffusional equations: all it requires is a user-supplied subroutine to provide a set of numerical values for the relaxation curve, calculable with parameters supplied by the curve-fitting program, and a set of numerical values for the derivatives of the relaxation curve with respect to all parameters to be determined (the jacobian matrix). These numerical values were calculated with the help of the closed form solutions of the diffusional equations for the linear range (2-6), but the numerical values for the relaxation curve could be equally well calculated, in principle, using a numerical differential equation software package, and the jacobian matrix can be calculated by a forward difference approximation. This approach is reported in the present communication.

The linearized current density-overpotential relation, which, in the past, has been generally used for the calculation of kinetic data from the results of the relaxation techniques, places a restriction on the experiments because the linearized relation is valid only for sufficiently low overpotentials. The meaning of "sufficiently low" is still a matter of some controversy, which is yet another subject of this communication. Generally, 5 mV has been considered a limiting value, although it was shown some time ago (7, 8) that the value of the overpotential alone is not sufficient to set the limit of applicability of the linearization because it will be influenced also by the transfer coefficients of the reaction and the concentrations of the reactants and products. The linearized and full current density-overpotential relations themselves can be directly compared. Kooijman *et al.* (8) used such a comparison and concluded that, under some conditions, overpotentials much less than 5 mV are needed to limit the error of the linearization to less than 1%. On the other hand, the diffusional differential equations must be solved numerically to compare the relaxation curves calculated with the linearized and full relations. Such calculations were carried out for the coulostatic (9) and the galvanostatic single-pulse (10) relaxation techniques, and it was concluded, in contradiction to Kooijman's results, that the error of the linearization was smaller than previously assumed; *e.g.*, an error of less than 2% was found at overpotentials up to 25 mV for the coulostatic technique. However, in the latter calculations, the transfer coefficients were assumed to be 0.5, and this may limit the validity of the conclusion since there is a controversy about the effect of the transfer coefficients (8, 11-13). The effect of the concentrations of the reactants and products is also controversial, especially in the extreme case where the concentration of one species remains constant during the course of the reaction as is the case in metal deposition-dissolution reactions (11-13). Our numerical calculation methods were also useful for determining the error and, consequently, the limitations of the data evaluations based on the linearized current density-overpotential relation and for resolving the above controversies.

Theory of DC Relaxation Techniques

Only a brief outline of the theory of the relaxation techniques will be given here, mainly to define the terms and to enumerate all basic assumptions; detailed reviews are available (1, 14, 15). Experimentally, the techniques involve the application of a perturbing current (or potential) pulse and the resulting potential (or current) relaxation is observed. A redox reaction, $O + ne = R$, or a metal deposition-dissolution reaction, $M^{+n} + ne = M$, is under investigation, with, in the simplest case, only three processes to be considered. These processes are: (*i*) the reaction at the electrode surface, (*ii*) the diffusion of the reactant and product to and from the surface, and (*iii*) the charging of the double-layer capacitance. The reaction can take place in any number of elementary electrochemical and chemical steps; it is assumed that one of these steps is rate determining and that none of the reaction intermediates is lost by diffusion into the bulk solution. The rate-determining step can occur ν times for each occurrence of the overall reaction, where ν is the stoichiometric number of the reaction mechanism. The uniform flux of the reactant to the electrode surface, being equal to the flux of the product away from the electrode, is assumed to be completely supplied by semi-infinite, linear diffusion in the presence of excess supporting electrolyte. This flux is equivalent to the faradaic current density. The double-layer capacitance is assumed to be independent of potential and concentrations within the limits of the experiment. Adsorption and double-layer effects are neglected.

The relaxation process is described by a set of partial differential equations for diffusion, coupled with an ordinary differential equation for the overpotential. The diffusion equations are

$$\frac{\partial C_j^s(x, t)}{\partial t} = D_j \frac{\partial^2 C_j^s(x, t)}{\partial x^2} \qquad [1]$$

with the following initial and boundary conditions

$$C_j^s = C_j \text{ for } t = 0,\ x \geq 0 \qquad [2]$$

$$C_j^s \to C_j \text{ for } t > 0,\ x \to \infty \qquad [3]$$

$$\left[\frac{\partial C_j^s(x, t)}{\partial x}\right]_{x=0} = \pm \frac{i_f(t)}{n\mathbf{F}D_j} \qquad [4]$$

where j can stand for O or R, and in Eq. [4] the positive sign corresponds to R and the negative to O. The last condition expresses the equivalence of the faradaic current density and the diffusion flux. The faradaic current density in Eq. [4] is related to the overpotential and the concentrations of the species at the electrode surface[1]

$$i_f = i_0\left\{\left[\frac{(C_R^s)_{x=0}}{C_R}\right]^{1/\nu} \exp\left(\frac{\alpha_a \mathbf{F}}{RT}\eta\right) - \left[\frac{(C_O^s)_{x=0}}{C_O}\right]^{1/\nu} \exp\left(-\frac{\alpha_c \mathbf{F}}{RT}\eta\right)\right\} \qquad [5]$$

where the overpotential is the sum of the charge transfer (activation) and mass-transport (concentration) overpotential terms

$$\eta = \eta_{ct} + \eta_{mt} \qquad [6]$$

and

$$\alpha_a + \alpha_c = n/\nu \qquad [7]$$

At low overpotentials, Eq. [5] can be approximated by the linearized expression[2]

$$\eta' = \frac{\nu RT i_f}{n\mathbf{F}i_0} + \frac{RT}{n\mathbf{F}}\left[\frac{(C_O^s)_{x=0}}{C_O} - \frac{(C_R^s)_{x=0}}{C_R}\right] \qquad [8]$$

The ordinary differential equation for the overpotential is

[1]Equation [5] can be obtained by adjusting the generalized, multistep Butler-Volmer equation (16, 17) for surface concentration changes by a method equivalent to that used for single-step reactions (18). It is to be emphasized that the transfer coefficients are not equal to, although are functions of, the symmetry factor of a single-step reaction.

[2]Equation [8] is obtained from Eq. [5] by assuming that $\alpha\mathbf{F}/RT\,\eta << 1$; and, consequently, that $(C_j^s)_{x=0}/C_j \approx 1$ (see Eq. [17]).

$$i(t) = i_f(t) + c\frac{d\eta(t)}{dt} \quad [9]$$

with an initial condition of $\eta(0) = 0$, indicating that the total current is the sum of the faradaic and capacitive currents. The overpotential in Eq. [9] is related to the measured potential by Eq. [10], indicating that the measured potential includes the overpotential and the uncompensated potential drop in the solution between the working and reference electrodes

$$E(t) = \eta(t) + i(t)R_s \quad [10]$$

For the galvanostatic and coulostatic (current impulse) techniques, $i(t)$ is controlled and $E(t)$ is measured and vice versa for the voltage and potential step techniques. The kinetic and mechanistic parameters to be calculated from the experimental results are: the exchange current density (i_o), the transfer coefficients (α_c, α_a), and the stoichiometric number (ν). Additionally, there are five more parameters which may have to be determined from the relaxation experiment if their values are not available from independent measurements. These are the double-layer capacitance (c), the diffusion coefficients (D_O, D_R), the uncompensated solution resistance (R_s), and the total number of electrons exchanged during the overall reaction (n). The following parameters are usually known: the perturbing signal (i or E), the concentrations (C_O, C_R), and the temperature (T).

A closed-form solution of the differential equations can be obtained using the linearization shown in Eq. [8], and this is the basis for the evaluation of the experimental data taken at potentials near the equilibrium value. Equation [5] is the basis for the data evaluation procedure proposed in this work, making it possible to carry out the experimental measurement at any potential.

Computational Procedures

Curve-fitting data evaluation methods.—Two methods were tested for the data evaluation in the nonlinear range. Both methods are similar in that they involve the numerical solution of Eq. [1] and [9] and the use of numerical optimization techniques to determine the kinetic and mechanistic parameters described above.

Numerical simulation of electrochemical kinetics-diffusion models such as Eq. [1] and [9] have previously been dealt with by finite difference approximation; see, for example, Feldberg (19, 20), Sandifer and Buck (21), and Britz (22). More recently, in an effort to achieve greater accuracy, spline approximation techniques have been combined with collocation methods by Pons (23) and with Galerkin's method by Franceschetti and Macdonald (24). Our approach also uses a spline-based Galerkin procedure as implemented in the software package DISPL2 (25). We, however, combine this numerical simulation with optimization techniques to extend the curve-fitting evaluation of the dc transient techniques to the nonlinear current density-overpotential ranges, for which range closed-form solutions do not exist for the diffusional differential equations.

In the first method, the curve-fitting was accomplished with subroutine LMDIF from the MINPACK-1 package developed at Argonne National Laboratory (26) for nonlinear multidimensional least squares minimization using a modified Levenberg-Marquardt algorithm (27). The same program package was used previously for data evaluation in the linear range (2-6). The subroutine LMDIF requires the user to supply only the function values from which the jacobian matrix is calculated by a forward difference approximation. This means, however, that for an N parameter fitting, the function value has to be calculated $N + 1$ times for each new guess of the parameters. The function values were calculated by solving Fick's diffusion equations numerically using the software package DISPL2 developed at Argonne National Laboratory (25). This package is designed to solve systems of nonlinear partial differential equations in one- and two-dimensional geometries. The numerical approximation is based on the use of Galerkin's procedure combined with the use of a B-spline basis set in order to reduce the system of partial differential equations to a system of ordinary differential equations. The latter system is solved by means of an ordinary differential equation software package for stiff systems based on the use of multistep time differencing with local error control (28).

The problem was treated as a system of two partial differential equations for C_R^s and C_O^s coupled with an ordinary differential equation for η. The equations were integrated to the full pulse length, t_f, with output at selected intermediate times. The half-axis, $x \geq 0$, was truncated at $x_\infty = 5\sqrt{Dt_f}$, where D was the mean value for D_R and D_O. The spatial domain was subdivided by a nonuniform spatial mesh, and the B-spline basis used corresponded to piecewise quadratic polynominals with continuous first derivatives to approximate the spatial distribution of $C_j^s(x, t)$. The time integration error was controlled by the local error control in the multistep stiff ordinary differential equation solver, and the spatial discretization was controlled by the number of points and their distribution in the spatial grid.

The second method also used the DISPL2 software package to solve Fick's diffusion equations. However, instead of employing a nonlinear least squares approach, use was made of a general constrained optimization approach implemented in subroutine VMCON1 developed at Argonne National Laboratory (29). To understand the strengths and weaknesses of these two approaches to the data evaluation problem, the differences in the optimization problems, methods, and techniques for generation of jacobian matrices are summarized below.

1. The first method specifically treats the unconstrained nonlinear least squares problem. That is, for m observations y_i and a model $f(X, t_i)$ where X is an N-component vector of parameters, we wish to select X so that

$$\sum_{i=1}^{m} [f(X, t_i) - y_i]^2 \quad [11]$$

is minimized. The second method solves the problem: minimize $f(X)$, subject to

$$c_j(X) \leq 0;\ j = 1, \ldots, k$$
$$c_j(X) = 0;\ j = k + 1, \ldots, l \quad [12]$$

That is, a general function (not specifically of the form used in Eq. [11]) is minimized subject to constraints which may be inequality or equality constraints. Thus, the second approach allows for constraints on the problem but treats a more general optimization function.

2. The first method uses a modification of the Levenberg-Marquardt algorithm to solve the problem. This algorithm exploits the structure of the nonlinear least squares problem and uses a combination of the steepest descent and the Gauss-Newton methods. The steepest descent method is globally reliable but slow. The Gauss-Newton method is locally reliable and fast. The Levenberg-Marquardt algorithm adaptively combines these two methods to obtain a fast, reliable algorithm. The second method uses an iterative quadratic programming technique developed by Powell (30). This algorithm generates quadratic programming subproblems, *i.e.*, quadratic functions minimized subject to linear equality and inequality constraints. These subproblems can be solved without requiring function evaluations. This second method is essentially a constrained Newton technique and converges quite rapidly. When compared to other constrained optimization methods, the iterative quadratic programming technique requires relatively few function evaluations (31). This is important since the DISPL2 computation is quite time consuming. Nevertheless, this second method does not exploit the structure of the nonlinear least squares function and thus is not likely to be as efficient as the first method. In particular, the first method uses the structure of the sum-of-squares function,

Eq. [11], to obtain approximations of the second derivative of the function in terms of first derivative approximations (the Gauss-Newton method). The second method treats Eq. [11] as a general function and, therefore, cannot provide second derivative estimates as easily.

3. The first method uses a derivative-free version of the Levenberg-Marquardt algorithm. As in most optimization techniques, both methods require the derivatives of the optimization function with respect to the variables. In the first method, this reduces to the jacobian which is obtained by forward-difference approximation. These differences, however, require N additional evaluations of the partial differential equation system. In the second method an attempt was made to obtain the derivatives without resorting to finite differencing. These derivatives can often be obtained in terms of additional ordinary and partial differential equations. As an example, if α_c is a parameter in the curve-fit, the necessary information for the derivatives can be assembled if we can obtain an ordinary differential equation for $d\eta/d\alpha_c$. Such an equation can be derived by differentiating Eq. [9] with respect to α_c and using the initial condition $(d\eta/d\alpha_c)_{t=0} = 0$. In deriving the additional equations needed for the jacobian, some terms were neglected for the sake of practicality. In particular, in deriving the equation for $d\eta/d\alpha_c$ there is an indirect dependence on $\partial C_i^s(x, t)/\partial\alpha_c$. If we seek to calculate these terms in the numerical simulation, two additional partial differential equations are generated. The computational cost of calculating the jacobian via this combined system would be as great as using finite-difference methods for the jacobian (and the computer storage cost would be much greater as well). We, therefore, compromise by neglecting the dependency which leads to the additional partial differential equations. Thus, while we avoid the additional N evaluations of the finite-difference approach, the analytic derivatives obtained have an inherent error.

To summarize, there are two areas of difference between the methods: the numerical method and the jacobian estimate. The first method treats the specific form of Eq. [11] but cannot handle constraints such as [12]. When constraints are necessary (as, for example, to control the range of parameters used for the simulation) other methods should be used. The second method handles constraints but treats a more general minimization function. Therefore, the numerical approach of the second method does not take advantage of the mathematical form of Eq. [11]. Ideally, the first method with the capability of handling constraints should be used. The second area of difference between the methods deals with the jacobian calculation. The first method uses finite-difference estimates to build up the jacobian. The second method adds a differential equation for $d\eta/d\alpha_c$ to estimate the derivatives directly. Either of these jacobian calculation methods could be used with either of the optimization methods. The second approach to estimate the jacobian can lead to considerable savings in computation time when compared with the finite-difference approach. However, it can also lead to larger simulation problems because of the use of approximations to the derivatives.

Evaluation of the curve-fitting methods.—Primarily because of the long computational times required, and also because of the large number of variables involved, it was not practical to carry out a full error analysis and to develop applicability digrams and compare to those calculated for the linear cases (2-6). The main purpose of this work was to show that it is feasible to extend the relaxation techniques to the nonlinear current density-overpotential range. This could be done by a small number of calculations using representative conditions. For similar reasons, the calculations were carried out only for the galvanostatic single-pulse technique.[3] Extension to other techniques is expected to be straightforward. The calculation procedure was similar to that used in the error analysis for the linear range (2-6). It consisted essentially of three steps.

1. Synthetic data were generated, with the use of DISPL2, for a set of parameter values. The relaxation curves were defined by 25 points, equally spaced in time. The pulse length was selected to include the time period containing the most kinetic information (3).[4] Then, to simulate practical conditions, random measurement errors were introduced by rounding off the calculated potential values, creating data sets with either ±5 or ±50 μV errors (3).

2. This set of points was then treated as experimental data, and a curve-fitting calculation was carried out. The number of parameters to be determined was varied from two to seven; the other parameters were assumed to be known from independent measurements. Measurement errors were introduced for the known parameters to simulate practical conditions by using 0.1 or 1.0% different values in the data evaluation than were used in the data generation. The stoichiometric number was treated differently than other parameters because it is an integer parameter, a restriction that the curve-fitting subroutine was not equipped to handle. It was treated as a known parameter but a series of calculations was carried out with different values assigned to it in search of the best fit. The total number of electrons exchanged, another integer parameter, was always considered known. Were this not the case, it could be treated similarly to the stoichiometric number. The transfer coefficients are interrelated through Eq. [7], and only one of them needs to be determined. All parameters were restricted to positive values by a square root transformation, that is, the parameters calculated by the curve-fitting were the square roots of the parameters to be determined. The curve-fitting routines need a starting guess for each parameter to be determined; ten times the actual value of the parameter was usually used, except for the transfer coefficient, which was started from 0.5. Previous work on curve fitting in the linear current density-overpotential range has shown that good results are obtained with guesses not more than one order of magnitude off the true values, except at the very edges of the applicability fields (2-6).

3. Finally, the calculated parameter values were compared to the known values (used in the data generation) and a percent error was calculated. These errors and the standard deviations of the calculated results (33) were used to evaluate the curve-fitting methods.

Determination of linearization errors.—The following procedure was used to evaluate the errors and the limitations of the linearized approximation. Relaxation curves were calculated using both the full current density-overpotential relation, Eq. [5], and the linearized relation, Eq. [8], and the maximum deviation between the two relaxation curves was determined. The differential equations were solved using the DISPL2 software package (25). Closed-form solutions were available for the linearized cases (2-5). Calculations were carried out for all dc relaxation techniques, the galvanostatic (single and double pulse) techniques, the coulostatic (current impulse relaxation) technique, and the potential and voltage step techniques. A large variety of conditions (exchange current density, transfer coefficients, concentrations, diffusion coefficients, overpotential, etc.) were used to cover the whole field of applicability of each technique (2-6). Selection of all experimental conditions (*e.g.*, pulse lengths, pulse amplitudes) were also made in accordance with procedures described in the above-mentioned references. Two extreme cases were also considered: the charge transfer-controlled system ($\eta_{ct} >> \eta_{mt}$) and the mass-

[3]This technique involves a simple current step perturbation of the electrode. To allow for the finite risetime of the pulse generator, the current was taken to rise linearly from zero to the desired value. The correction for this risetime was found to be important for the linear approximation case (3, 32).

[4]The selection of the proper pulse length for an unknown system by the use of a statistical sensitivity analysis of the parameters determined by the curve-fitting data evaluation was discussed earlier for the linear current density-overpotential range (33). A similar technique can also be used for the nonlinear range.

transport-controlled system ($\eta_{ct} << \eta_{mt}$). All calculations were carried out for both anodic and cathodic polarizations and also for the case of a cell containing two identical working electrodes, one being polarized anodically and the other cathodically; in the latter case, η stands for the total overvoltage of the cell.

An additional series of calculations was carried out to determine the deviations between the full and linearized current density-overpotential relations themselves, rather than those of the relaxation curves, for the extreme cases of pure charge transfer- or mass-transport-controlled systems. For $\eta_{ct} >> \eta_{mt}$, the Butler-Volmer equation can be written in the form of

$$i_f = i_o\{\exp(P_1P_2) - \exp[-(1 - P_1)P_2]\} \quad [13]$$

where $P_1 = \alpha_a\nu/n$ $(= 1 - \alpha_c\nu/n)$ and $P_2 = (n\mathbf{F}/\nu RT)\,\eta_{ct}$. Equation [13] can be linearized to

$$i_f = (n\mathbf{F}i_o/\nu RT)\eta'_{ct} \quad [14]$$

if the exponents in Eq. [13] are small. Since every term in the expansion of Eq. [13] is a function only of P_1 and P_2, the deviation between η_{ct} and η'_{ct} will obviously be a function of two dimensionless parameters: $\alpha\nu/n$ and $n\mathbf{F}\eta_{ct}/\nu RT$, where α can stand for either α_a or α_c.

The deviations between Eq. [13] and [14] were calculated as a function of these dimensionless parameters in two ways. At constant current density, the error can be represented as

$$\epsilon_\eta = \frac{100(\eta' - \eta)}{\eta} \quad [15]$$

Alternatively, one can keep the overpotential constant and calculate the current densities needed to produce the same overpotential with the full and linearized equations; an error, ϵ_i, can be defined analogously to Eq. [15]. The two errors are interrelated by

$$\epsilon_i = -\frac{100\epsilon_\eta}{100 + \epsilon_\eta} \quad [16]$$

which can be demonstrated by a geometric consideration of the deviations between the linear and the full equations.

For the case of $\eta_{ct} << \eta_{mt}$, the Nernst equation expresses the overpotential as a function of surface concentrations, which, in turn, are dependent on the faradaic current density and time

$$\eta_{mt} = \frac{RT}{n\mathbf{F}} \ln\left[\frac{(C_O^s)_{x=0}}{C_O} \cdot \frac{C_R}{(C_R^s)_{x=0}}\right] \quad [17]$$

This can be linearized to

$$\eta'_{mt} = \frac{RT}{n\mathbf{F}}\left[\frac{(C_O^s)_{x=0}}{C_O} - \frac{(C_R^s)_{x=0}}{C_R}\right] \quad [18]$$

if $(C_j^s)_{x=0}/C_j \approx 1$. Equations [17] and [18] are not in convenient form because the surface concentrations of the species are generally not known. The mass-transport overpotential can, however, be expressed in terms of measurable parameters by using the relation

$$(C_O^s)_{x=0}D_O^{1/2} + (C_R^s)_{x=0}D_R^{1/2} = C_OD_O^{1/2} + C_RD_R^{1/2} \quad [19]$$

which can be shown to be true for all relaxation techniques considered here (34). This leads to

$$\frac{(C_1^s)_{x=0}}{C_1} = \frac{1 + \dfrac{C_2D_2^{1/2}}{C_1D_1^{1/2}}}{1 + \dfrac{(C_2^s)_{x=0}D_2^{1/2}}{(C_1^s)_{x=0}D_1^{1/2}}} \quad [20]$$

where the indexes 1 and 2 can stand for O and R. The fraction in the denominator of the right-hand side of Eq. [20] can be expressed, with the help of Eq. [17], as

$$\frac{(C_O^s)_{x=0}D_O^{1/2}}{(C_R^s)_{x=0}D_R^{1/2}} = \frac{C_OD_O^{1/2}}{C_RD_R^{1/2}} \exp\left(\frac{n\mathbf{F}}{RT}\,\eta_{mt}\right) \quad [21]$$

Therefore, η_{mt} and η'_{mt}, and the deviation between them, can be expressed in terms of the dimensionless parameters $P_3 = C_OD_O^{1/2}/C_RD_R^{1/2}$ and $P_4 = n\mathbf{F}\eta_{mt}/RT$, both of which are known for a given experiment

$$\eta_{mt} = \frac{RT}{n\mathbf{F}} \ln\left[\frac{1 + P_3\exp(P_4)}{P_3 + \exp(-P_4)}\right] \quad [22]$$

and

$$\eta'_{mt} = \frac{RT}{n\mathbf{F}}\left[\frac{1 + P_3}{P_3 + \exp(-P_4)} - \frac{1 + P_3}{1 + P_3\exp(P_4)}\right] \quad [23]$$

In conclusion, the error of the linearization can be expressed in terms of dimensionless parameters for both the charge transfer- and the mass-transport-controlled cases.

The deviations between Eq. [17] and [18] were calculated in two ways: (*i*) as a function of $(C_j^s)_{x=0}/C_j$ and (*ii*) as a function of $C_OD_O^{1/2}/C_RD_R^{1/2}$ and $n\mathbf{F}\eta_{mt}/RT$. The calculations were carried out at constant current (or, more precisely, using the same surface concentrations for both equations), and ϵ_η was obtained. Equation [16] is also valid for the mass-transport-controlled case.

Error of exchange current density measurements due to linearization.—The following procedure was used to calculate the error in the exchange current density determination caused by measurement in the nonlinear i-η range coupled with data evaluation assuming a linear i-η relation. Relaxation curves were generated using both the linear and the nonlinear $i = \eta$ relations and the maximum deviation between the two curves was determined (see above). The curve generated with the nonlinear relation was used as input data for a curve-fitting data evaluation assuming a linear i-η relation (2-5), and the calculated exchange current density was compared to the exchange current density used in the generation of the synthetic data. To ensure that the results reflect only the error caused by the linearization of the i-η relation, no other measurement errors (current density and potential) were introduced into these data sets. The calculations were carried out for a series of overpotential values keeping all other parameters constant.

Results and Discussion

Curve-fitting in the nonlinear i-η range.—Initial calculations have demonstrated that both calculation methods described above give satisfactory results, but we found that the second method requires significantly more computational effort than the Levenberg-Marquardt method (2.5 times more in one case). It is likely that the ability of the Levenberg-Marquardt method to exploit the structure of the nonlinear least squares problem, its use of a hybrid of steepest descent and Gauss-Newton techniques, and the approximating aspects of the analytic jacobian combine to cause the second approach to be relatively slow. We decided to abandon the constrained method for the remainder of this study. (A constrained Levenberg-Marquardt approach would provide the positive features of both methods and may be a subject of further work.) All the results discussed below were obtained with the Levenberg-Marquardt method.

Satisfactory results were obtained for a variety of electrode reaction parameter values and measurement conditions with the number of parameters determined varying from two to seven. Two typical examples are presented in detail in Tables I-III. Table I shows the conditions, and Tables II and III show the results of the calculations. The results indicate that the parameters can be determined with a few percent error (the maximum error was 6.4% in these examples). The synthetic data were calculated with a stoichiometric number of one, while the evaluations were carried out for $\nu = 1$, 2, and 3. To select the correct ν value, one has to select the best fit based (26, 33) on (*i*)

Table I. System parameters used in the examples

Parameter	Used in Three-parameter fit	Used in Five-parameter fit
Exchange current density (A-cm^{-2})	6.42×10^{-1}	6.42
Concentration, O and R (mol-cm^{-3})	4.21×10^{-5}	4.21×10^{-5}
Diffusion coefficient, O (cm^2-s^{-1})	1.00×10^{-5}	1.00×10^{-5}
Diffusion coefficient, R (cm^2-s^{-1})	1.00×10^{-5}	2.00×10^{-5}
Double-layer capacitance (F-cm^{-2})	2.50×10^{-5}	2.50×10^{-5}
Uncompensated solution resistance (Ω-cm^2)	0.00	0.00
Cathodic transfer coefficient	3.00×10^{-1}	3.00×10^{-1}
Temperature (K)	2.98×10^{2}	2.98×10^{2}
Risetime (s)	1.00×10^{-7}	1.00×10^{-7}
Pulse length (s)	1.00×10^{-5}	5.00×10^{-6}
Pulse current density (A-cm^{-2})	1.44	8.26
Overpotential at the end of the pulse (V)	5.60×10^{-2}	1.73×10^{-1}
Stoichiometric number	1	1
Number of electrons	1	1

Table II. Example of a three-parameter fit

Calculated with a stoichiometric number	Parameter	Percent error of determination	Percent standard deviation	Root mean square residual
1	i_o	1.9	0.15	
	α_c	2.1	0.24	2.44×10^{-5}
	c	0.8	0.08	
2	i_o	136	0.59	
	α_c	−64	2.67	1.09×10^{-4}
	c	−4	0.35	
3	i_o	269	0.73	
	α_c	−85	8.29	1.40×10^{-4}
	c	−5	0.45	

Table III. Example of a five-parameter fit

Calculated with a stoichiometric number	Parameter	Percent error of determination	Percent standard deviation	Root mean square residual
1	i_o	1.4	0.22	
	α_c	−0.9	0.38	
	c	1.1	0.21	2.46×10^{-5}
	D_O	−6.4	0.99	
	D_R	−0.1	0.07	
2	i_o	227	0.33	
	α_c	95	0.16	
	c	−20	0.90	1.51×10^{-4}
	D_O	5,200	12.12	
	D_R	164	0.80	
3	i_o	375	0.37	
	α_c	55	0.24	
	c	−19	1.21	2.01×10^{-4}
	D_O	11,017	12.91	
	D_R	88	0.72	

the standard deviation of the parameters (expressed in the tables as a percentage of the calculated parameter value) and (*ii*) the root mean square residuals (which expresses the overall quality of the fit). In both cases, $\nu = 1$ gives the best fit. These results demonstrate the feasibility of using a combination of a numerical differential equation solver and a least squares minimization software package for the data evaluation of relaxation techniques in the nonlinear i-η range. Numerous calculations were carried out, but, because of the long computational times involved, a complete error analysis could not be carried out. Therefore, an applicability field cannot be defined for this method. Five runs were made under conditions near the diffusion-limited edge of the applicability field calculated for the linearized case (3), and it was concluded that the limitations of the nonlinearized and linearized cases are similar. All calculations were carried out for the galvanostatic single-pulse case; no difficulties are expected in the extension of this data-evaluation method to the other dc relaxation techniques.

The present method of data evaluation, which is not limited to the linear i-η range, has several advantages over the previously used curve-fitting data evaluations. (*i*) Signal-to-noise problems can be minimized by the use of large overpotentials. This is especially important for electrode reaction systems where, in the linear range, one would use very small overpotentials because the error of the linearized equations is large, *e.g.*, when the $\alpha\nu/n$ is far from 0.5 or $C_O D_O^{1/2}/C_R D_R^{1/2}$ is far from unity (see discussion below). (*ii*) Because of freedom from overpotential limitations, the possible potential dependence of the transfer coefficients can be easily detected by making measurements at a number of current densities. (*iii*) The values of the exchange current density and the stoichiometric number can both be individually determined, while in the linear range only i_o/ν is determinable. (*iv*) The transfer coefficients can be directly obtained from the data, while in the linear range they are determinable only from the concentration dependence of the exchange current density. (*v*) The diffusion coefficients are also directly determinable, while in the linear range only the diffusion parameter $(1/C_O D_O^{1/2} + 1/C_R D_R^{1/2})$ is determinable.

The disadvantage of the method is that it requires considerable computational time, about one to two orders of magnitude more than similar calculations using the linearized approximations. All calculations were carried out with a Digital Equipment Corporation VAX 11/780 machine; with this computer, a curve-fit in the linearized approximation takes a matter of minutes, while it can take several hours for the nonlinear range. (Equivalent execution times on an IBM mainframe computer are about one order of magnitude shorter.)

Linearization errors.—A comparison of the errors caused by the linearization of the current density-overpotential relation for the dc relaxation techniques revealed that, under comparable experimental conditions, all techniques suffered the same error. Therefore, in the following discussion the individual techniques will not be treated separately and all results apply equally to the single- and double-pulse galvanostatic, the coulostatic, and the potential and voltage step techniques.[5] It was also found that the errors calculated by simply comparing the full and linearized current density-overpotential relations were essentially the same as those calculated from the comparison of the relaxation curves. The deviation between the relaxation curves calculated with the full and linearized i-η relations is not constant but changes with time because some conditions (*e.g.*, surface concentrations) change with time. Therefore, what can be stated is that if the linearized i-η relation is in error by x%, as compared to the full i-η relation, for a given system and at y mV overpotential, then for that system the relaxation curve calculated for any relaxation technique using the linearized i-η relation will have a maximum deviation of x% from an analogous relaxation curve calculated with the full i-η relation (as long as the overpotential never exceeds y mV). It seems prudent, therefore, to use this maximum error to characterize the overall error. These results are presented below in terms of ϵ_η. As expected, the error was found to be a function not only of the overpotential but also of every parameter needed to characterize the electrode reaction system. Because of this, the results of the error analysis can be simply presented only for certain extreme conditions, specifically, for the case of charge transfer control ($\eta_{ct} >> \eta_{mt}$), and mass-transport control ($\eta_{ct} << \eta_{mt}$). For these cases, the results of the er-

[5]However, the use of two working electrodes is not readily applicable for the potential and voltage step techniques because the potential control of the individual electrodes will be lost.

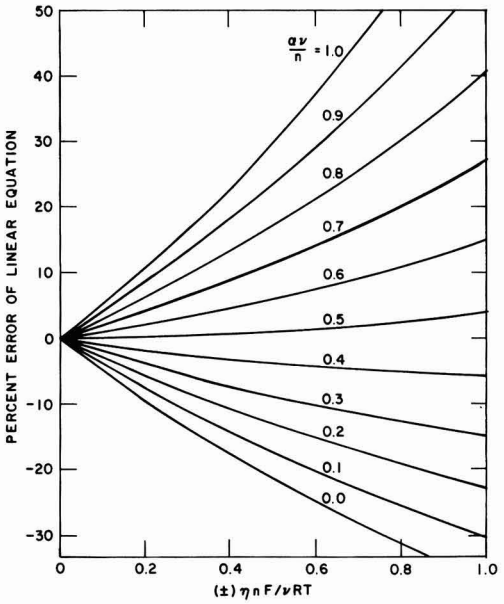


Fig. 1. Error of the linearized i-η relation for the case of charge transfer control ($\alpha = \alpha_a$ for $\eta > 0$; $\alpha = \alpha_c$ for $\eta < 0$).

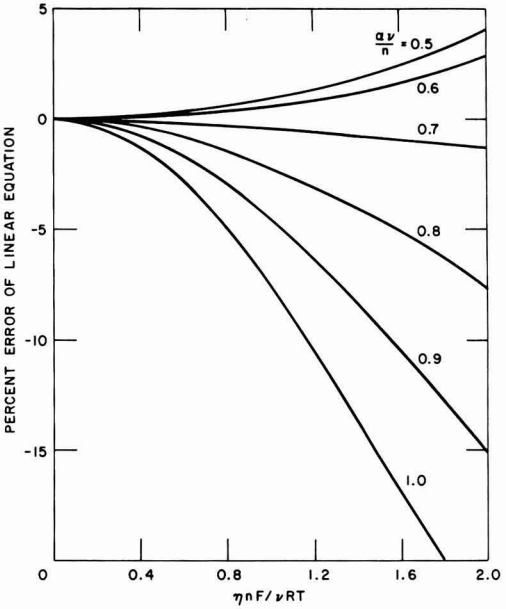


Fig. 2. Error of the linearized i-η relation for the case of charge transfer control and two identical working electrodes. The symbol α stands for the larger of α_a and α_c.

ror calculations can be presented in terms of the dimensionless parameters discussed earlier.

The results for the charge transfer-control case are shown in Fig. 1. The error increases almost linearly with increasing overpotential parameter ($\eta n\mathbf{F}/\nu RT$), and the rate of this increase is a strong function of the transfer-coefficient parameter. The smallest error occurs near, but not exactly at, $\alpha\nu/n = 0.5$ and increases drastically below and above this value.[6] For example, at $\eta n\mathbf{F}/\nu RT = 0.2$, which is approximately 5 mV polarization at room temperature and $n = \nu$, the error is only 1% at $\alpha\nu/n = 0.5$, but increases to 10% under the worst conditions ($\alpha\nu/n = 1$ or 0). One can also express the limitation of the linearized equation as the highest allowed overpotential for the error not to exceed a maximum value. For a 5% error this limit is 30 mV at $\alpha\nu/n = 0.5$ but decreases to 2.5 mV under the worst conditions. Changing the polarity of the current will change the sign of the error; therefore, if two identical working electrodes are used, polarizing one anodically and the other cathodically, much of the error will cancel, as indicated in Fig. 2. This approach to decrease the error of linearization was first suggested by Kooijman *et al.* (8). Considerable error cancellation results at all values of $\alpha\nu/n$ except at 0.5, and the error is close to zero at $\alpha\nu/n \approx 0.65$. The cancellation effect is very significant: the worst-case error at 5 mV polarization decreases from 10% for a single electrode to 2% for the two-electrode case, and the 5% error limit increases from 2.5 to 10 mV at $\alpha\nu/n = 1$ (the worst condition).

The results for the mass-transport-controlled case are shown in Fig. 3. The error increases with increasing overpotential parameter, and the effect is approximately linear. The rate of increase is strongly dependent on $C_0D_0^{1/2}/C_RD_R^{1/2}$, which, for the sake of simplicity, will be called the mass-transport parameter. Zero error occurs near, but not exactly at, a mass-transport parameter of one. Above and below this value, the error increases steeply but reaches asymptotic limits.[7] For example, at $\eta n\mathbf{F}/RT = 0.2$ and mass-transport parameter of one, the error is 1%, but increases to 8% at the asymptotic limit. Alternatively, the maximum allowed overpotential (at room temperature and $n = 1$) for a 5% error is 20 mV at the mass-transport parameter of one but decreases to 2.5 mV at the asymptotic limit. It is to be noted here that for metal deposition-dissolution reactions (the concentration of one species is fixed) the error will always be the asymptotic limit. The sign of the error changes as the sign

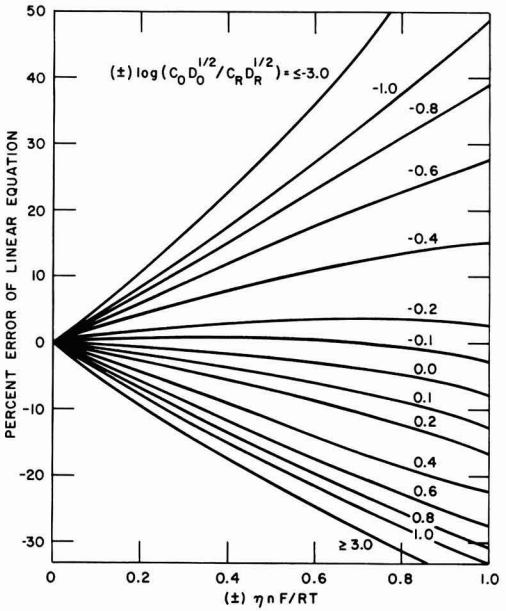


Fig. 3. Error of the linearized i-η relation for the case of mass-transport control.

[6]It is important to emphasize that α, here and throughout this paper, refers to the transfer coefficient of the multistep Butler-Volmer equation (16, 17). The transfer coefficient is equivalent to the symmetry factor only for the case of a single-step reaction with $n = 1$.

[7]The error calculated at the mass-transport parameter of 1000 and 0.001 is within 0.5% relative error of the asymptotic limit.

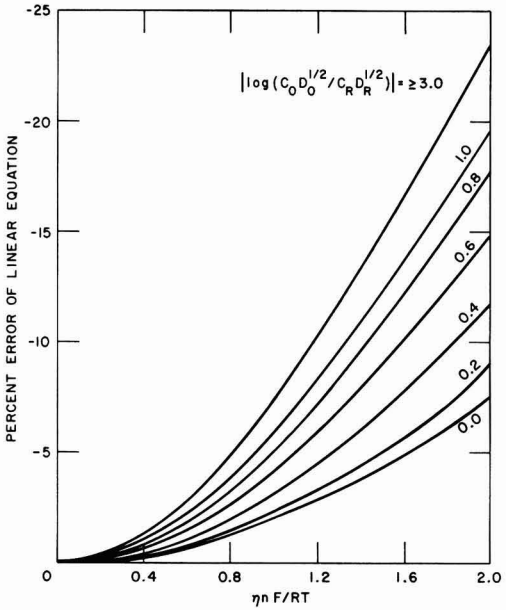


Fig. 4. Error of the linearized i-η relation for the case of mass-transport control and two identical working electrodes.

of the polarization changes; therefore, a cancellation of errors occurs when using two identical working electrodes. This case is shown in Fig. 4. The beneficial effect of this type of measurement is shown by the decrease of the error at the asymptotic limit from 8% for a single electrode to 1.5% for two electrodes; similarly, the maximum allowed overpotential for a 5% error increases from 2.5 to 10 mV.

The error as a function of the $(C_j^s)_{x=0}/C_j$ ratios is shown in Fig. 5. This was calculated by a straightforward

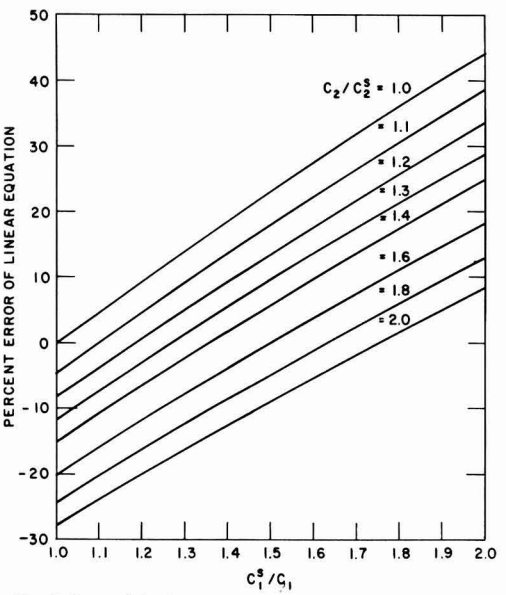


Fig. 5. Error of the linearized i-η relation for the case of mass-transport control as a function of surface concentrations (1 = O and 2 = R for $\eta > 0$; 1 = R and 2 = O for $\eta < 0$).

comparison of Eq. [17] and [18]. These results are instructive, though the figure cannot be used to predict errors for practical situations. The error depends not only on the individual concentration ratios but also on the ratio of the two ratios. This explains the small error near the mass-transport parameter of one and the large error for metal deposition-dissolution reactions.

The error cannot be represented in a simple way for more general cases because it is a function of too many parameters, some of which may be unknown at the time of an experiment. Specifically, one would need to know how the total overpotential is divided into charge transfer and mass-transport overpotentials. One would also need to know the values of the transfer coefficients and the stoichiometric number. If these are known, or at least estimated, the figures presented in this communication can be used to determine the error of the charge transfer and mass-transport overpotentials and the overall error will be their algebraic sum. If the above-mentioned parameters are not known, one can estimate the maximum error by assuming that the reaction is charge transfer or mass-transport controlled, calculating the worst error for both cases and taking the largest of the two. For example, at room temperature and $\nu = n = 1$, at a 5 mV polarization the worst-case error (at $\alpha = 1.0$ and mass-transport parameter at the asymptotic limit) will be 10%. The actual errors will probably be considerably smaller than the maximum error, in part because the parameters will not have extreme values and in part because the errors of the charge transfer and mass-transport overpotentials can have opposite signs resulting in cancellations. Many numerical calculations were carried out for all relaxation techniques confirming the additivity of errors and the cancellation effects.

There is a small discrepancy for the case of the pure mass-transport control between the errors calculated from the two i-η relations and the errors calculated from the relaxation curves. The first error is calculated by assuming the same surface concentration for all species for both the linear and the full equations, while the latter is calculated for a constant current case. The two errors will be identical only when the double-layer capacitance is zero. For a finite double-layer capacitance, a fraction of the current will be consumed for the double-layer charging and this fraction will not be the same for the linearized and the full i-η cases; consequently, the surface concentrations will be unequal at equal total currents. The results shown in Fig. 3 and 4 are for a double-layer capacitance of zero; the deviation from practical conditions will not be large; for example, for $c = 25$ μF-cm^{-2}, the results given in Fig. 3 and 4 are correct within a factor of 1.2. The results given in Fig. 1-4 are expressed in terms of ϵ_η (Eq. [15]); for a potentiostatic case, the error of interest is, of course, ϵ_i, which can be obtained from ϵ_η by using the relation given in Eq. [16].

These results are in general agreement with those of Kooijman *et al.* (8) and emphasize again the importance of the value of the transfer coefficients and concentrations in the limitation of the linearized i-η relation. The controversy surrounding this subject (7-13) can be resolved by stating that it is correct that in the limit of $\eta \to 0$ the linearized relation will be identical to the full relation, independent of the value of other parameters, but the rate of approach to the limit depends on those other parameters. That is, at a given overpotential value, the error of the linearized i-η relation is a function of all system parameters, namely: $\alpha\nu/n$, $C_0 D_0^{1/2}/C_R D_R^{1/2}$, and $\eta n\mathbf{F}/RT$.

Error of the exchange current density determination due to linearization.—A series of calculations was carried out to determine the error in the exchange current density determination by the dc relaxation techniques caused by measurement in the nonlinear i-η range coupled with data evaluation assuming a linear i-η relation. It was found that, if the electrode system is well within the field of applicability of the techniques (2-5), the percent error of the exchange current density determination is approxi-

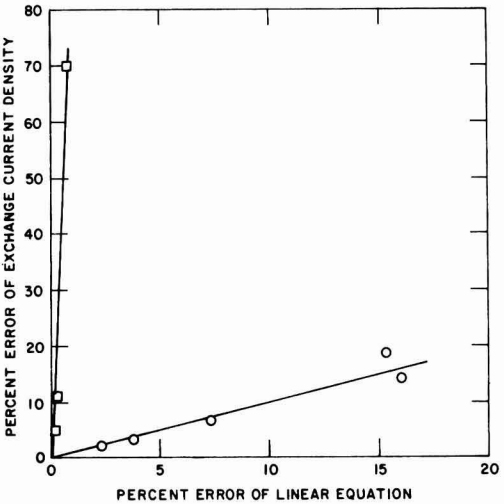


Fig. 6. Error of the exchange current density determination with galvanostatic single-pulse technique assuming linear i-η relation vs. the error of the linearized equation. Circles: electrode reaction well within the field of applicability. Squares: electrode reaction at the edge of applicability.

mately the same as the maximum percent deviation between the relaxation curves calculated with the linear and nonlinear i-η relations. A much larger error in the exchange current density was found at the edge of the applicability fields. This is in agreement with earlier results (2-5) indicating that the limits of applicability of all dc relaxation techniques are sensitive to measurement errors. An example for the galvanostatic single-pulse technique is shown in Fig. 6. The error in the exchange current density determination is plotted against the error of the linearized equation for two electrode reactions: one well within the field of applicability and one at the edge of applicability. [The value of log κ was 3 or 0, while the value of log τ_c was -5 for both cases, see Ref. (3); $\alpha\nu/n$ was 0.3, and the mass-transport parameter was unity.] It can be concluded that the error in the exchange current density determination will be at least as large as the error of the linearized equation.

Summary

The feasibility of the extension of relaxation techniques to the nonlinear current density-overpotential range has been demonstrated. This was accomplished by a curve-fitting data-evaluation method with a nonlinear multidimensional least squares minimization package coupled to a software package designed to solve systems of nonlinear partial differential equations. The main advantage of this approach is that measurements can be made at high enough overpotentials to avoid signal-to-noise ratio problems without introducing linearization errors in the data evaluation. The error of the linearized i-η relation is not negligible under many experimental conditions. A quantitative evaluation of this error has been made as a function of three dimensionless parameters: $\alpha\nu/n$, $C_0D_0^{1/2}/C_RD_R^{1/2}$, and $\eta n\mathbf{F}/RT$. The error in the exchange current density determination, with the assumption of linear i-η relation, will be at least as large as the error of the linearized equation.

Acknowledgments

This work was supported in part by the Division of Materials Science, Office of Basic Energy Sciences, U.S. Department of Energy, and in part by the Applied Mathematical Sciences subprogram of the Office of Energy Research, U.S. Department of Energy, under Contract W-31-109-ENG-38. We are grateful to Dr. V. A. Maroni for his critical reading of the manuscript.

Manuscript submitted July 30, 1984; revised manuscript received May 6, 1985. Parts of this work were presented as Paper 321 at the Detroit, Michigan, Meeting of the Society, Oct. 17-21, 1982.

Argonne National Laboratory, assisted in meeting the publication costs of this article.

LIST OF SYMBOLS

c	capacity of the double layer (F-cm^{-2})
C_j	concentration of species j in the bulk solution (mol-cm^{-3})
C_j^s	concentration of species j near the electrode surface (mol-cm^{-3})
D_j	diffusion coefficient of species j (cm^2-s^{-1})
E	measured potential (V)
$\mathbf{F}$	Faraday constant (C-mol^{-1})
i	total current density (A-cm^{-2})
i_f	faradaic current density (A-cm^{-2})
i_o	apparent exchange current density (A-cm^{-2})
n	total number of electrons transferred in the overall reaction
N	number of optimization variables
O	(index) oxidant
P_j	dimensionless parameter
R	(index) reductant
R	universal gas constant (J-K^{-1}-mol^{-1})
R_s	uncompensated solution resistance between the working and reference electrodes per unit electrode area (Ω-cm^2)
t	time (s)
t_f	pulse length (s)
T	temperature (K)
x	distance from electrode surface (cm)
α_a	anodic transfer coefficient
α_c	cathodic transfer coefficient
ϵ_i	error at constant potential, defined by Eq. [16]
ϵ_η	error at constant current density, defined by Eq. [15]
η	total overpotential (V)
η_{ct}	charge transfer overpotential (V)
η_{mt}	mass-transport overpotential (V)
η'_j	overpotential calculated with the linearized equations (V)
ν	stoichiometric number of the reaction mechanism

REFERENCES

1. J. Kuta and E. Yeager, in "Techniques of Electrochemistry," Vol. 1, Chap. 3, E. Yeager and A. J. Salkind, Editors, Wiley-Interscience, New York (1972).
2. Z. Nagy, *This Journal*, **128,** 786 (1981).
3. Z. Nagy, *Electrochim. Acta*, **26,** 671 (1981).
4. Z. Nagy, *This Journal*, **129,** 1943 (1982).
5. Z. Nagy and J. T. Arden, *ibid.*, **130,** 815 (1983).
6. Z. Nagy, *Electrochim. Acta*, **28,** 557 (1983).
7. P. Delahay, "Double Layer and Electrode Kinetics," p. 160, Interscience, New York (1965).
8. D. J. Kooijman, M. Sluyters-Rehbach, and J. H. Sluyters, *Electrochim. Acta*, **11,** 1197 (1966).
9. J. M. Kudirka and C. G. Enke, *Anal. Chem.*, **44,** 614 (1972).
10. F. H. Beyerlein and R. S. Nicholson, *ibid.*, **44,** 1917 (1972).
11. R. L. Birke and D. K. Roe, *ibid.*, **37,** 450 (1965).
12. D. M. Mohilner, N. Hackerman, and A. J. Bard, *ibid.*, **39,** 1499 (1967).
13. D. K. Roe and R. L. Birke, *ibid.*, **39,** 1501 (1967).
14. P. Delahay, in "Advances in Electrochemistry and Electrochemical Engineering," Vol. 1, Chap. 5, P. Delahay and C. W. Tobias, Editors, Interscience, New York (1961).
15. D. D. Macdonald, "Transient Techniques in Electrochemistry," Plenum Press, New York (1977).
16. J. O'M. Bockris and A. K. N. Reddy, "Modern Electrochemistry," Chap. 9, Plenum Press, New York (1970).
17. J. O'M. Bockris and Z. Nagy, *J. Chem. Ed.*, **50,** 839 (1973); *ibid.*, **51,** 803 (1974).
18. P. Delahay, "Double Layer and Electrode Kinetics," p. 168, Interscience, New York (1965).
19. S. W. Feldberg, in "Electroanalytical Chemistry," Vol. 3, p. 199, A. J. Bard, Editor, Marcel Dekker, New York (1969).
20. S. W. Feldberg, in "Computers in Chemistry and Instrumentation," Vol. 2, p. 185, J. S. Mattson, H. B. Mark, and H. C. MacDonald, Editors, Marcel

Dekker, New York (1972).
21. J. R. Sandifer and R. P. Buck, *J. Electroanal. Chem. Interfacial Electrochem.*, **49,** 161 (1974).
22. D. Britz, "Digital Simulation in Electrochemistry," Lecture Notes in Chemistry 23, Springer-Verlag, New York (1981).
23. S. Pons, in "Electroanalytical Chemistry," Vol. 13, p. 115, A. J. Bard, Editor, Marcel Dekker, New York (1984).
24. D. R. Franceschetti and J. R. Macdonald, in "Electrode Processes," S. Bruckenstein, B. Miller, J. D. E. McIntyre, and E. Yeager, Editors, p. 94, The Electrochemical Society Softbound Proceedings Series, Princeton, NJ (1980).
25. G. K. Leaf and M. Minkoff, in "Advances in Computer Methods for Partial Differential Equations V," p. 429, R. Vichnevetsky and R. Stepleman, Editors, IMACS, New Brunswick, NJ (1984).
26. J. J. More, B. S. Garbow, and K. E. Hillstrom, Argonne National Laboratory Report ANL-80-74 (1980).
27. J. J. More, in "Numerical Analysis," G. A. Watson, Editor, p. 105, Lecture Notes in Mathematics 630, Springer-Verlag, New York (1978).
28. A. C. Hindmarsh, Lawrence Livermore Laboratory Report UCID-30130 (1976).
29. R. L. Crane, K. E. Hillstrom, and M. Minkoff, Argonne National Laboratory Report ANL-80-64 (1980).
30. M. J. D. Powell, in "Numerical Analysis," p. 144, G. A. Watson, Editor, Lecture Notes in Mathematics 630, Springer-Verlag, New York (1978).
31. M. Minkoff, in "Nonlinear Programming 4," p. 519, O. L. Mangasarian, R. R. Meyer, and S. M. Robinson, Editors, Academic Press, New York (1981).
32. Z. Nagy, *This Journal*, **125,** 1809 (1978).
33. Z. Nagy, *Electrochim. Acta*, **29,** 917 (1984).
34. A. J. Bard and L. R. Faulkner, "Electrochemical Methods," p. 161, Wiley, New York (1980).

A Systematic Approach to the Determination of Possible Reaction Mechanisms of Oxygen Reduction on Platinum in Alkaline Medium

J. L. Valdes* and H. Y. Cheh**

Department of Chemical Engineering and Applied Chemistry, Columbia University, New York, New York 10027

ABSTRACT

The reaction mechanisms of oxygen reduction of platinum in alkaline medium are determined once a set of reacting species and elementary reactions is specified. The technique utilized to generate all the possible reaction mechanisms is based upon the principles of combinatorial analysis and linear algebra along with application of the principle of microscopic reversibility. The development of this method by Happel and Sellers has enabled them to study complex mechanisms for some important industrial reactions in heterogeneous catalysis. A preliminary evaluation analysis of the myriad reaction mechanisms for oxygen reduction is accomplished by invoking the concept of a stoichiometric number and a corresponding rate-determining elementary reaction. The number of mechanisms which are consistent with a given experimentally derived stoichiometric number is considerably less. The resulting set of mechanisms forms an important basis for further investigations.

The reduction of molecular oxygen in electrochemical systems has been the subject of many investigations over the past 50 years. It is evident from these studies that a mechanism for this reaction is strongly dependent upon the nature of the electrode material, the surface condition, the composition and purity of the electrolyte, the current density and electrode potential, and the temperature and pressure. Consequently, it is not surprising that the study of mechanisms is rendered difficult, as exemplified by the conflicting accounts which are often found in the literature. The determination of all the possible reaction mechanisms consistent with a given set of elementary steps and chemical species provides a systematic framework for a rigorous theoretical analysis of oxygen reduction. In a continuing effort to develop a clearer understanding of the complex structure of this reaction system, the present study has been undertaken.

In alkaline electrolytes, the reduction of oxygen is primarily considered to proceed through two mechanistic pathways: in one path, a four-electron reduction reaction without the formation of hydrogen peroxide; in the other, an initial electroreduction reaction believed to produce hydrogen peroxide which can be transported to the solution, electroreduced further to water, or catalytically decomposed. The mechanism for oxygen reduction can therefore be envisioned as consisting of a network of various elementary steps interconnecting a set of chemical species. Although this perspective may seem unresolvably complicated at first, the method which is applied here unambiguously determines all the possible mechanisms from a given set of elementary steps and chemical species.

The development of the theory of reaction mechanisms for complex reactions is found in the early work of Horiuti and co-workers (1, 2). The determination of the stoichiometric number by Horiuti in 1948 permitted, to a certain extent, distinctions to be made between the various mechanisms. Horiuti also showed that a chemical reaction mechanism can be described by specifying the number of occurrences required by each of the elementary steps in order for a given overall reaction to take place. The determination of possible reaction mechanisms then amounts to selecting the proper stoichiometric number for each of the elementary steps. Horiuti employed a matrix composed of elementary steps by species to select the stoichiometric numbers and obtain the linearly independent sets or reaction routes. According to Happel and Sellers (3), the concept of linear independence introduced by Horiuti will allow mechanisms to be combined in such a way that certain elementary reaction steps can be cancelled. Although this may be mathematically correct, it is not feasible from a kinetics point of view, since no two mechanisms containing a given elementary step can be equivalent to a third in which that step does not appear. As a result, the procedure developed by Horiuti for determining the possible reaction mechanisms of a simple overall reation is not exhaustive and therefore does not provide a complete set of mechanisms.

Milner (4), aware of the deficiencies encountered in Horiuti's model, developed a systematic method for generating complete sets of reaction mechanisms from a given number of elementary steps and intermediates. Here the concept of direct paths was introduced to emphasize that while such paths may not be linearly independent of one another, they are undoubtedly kinetically distinct and unique in that each path or mechanism cannot be considered to result from a superposition of any of the other members in that set. Milner found that the number of nonzero stoichiometric numbers specifying a direct

* Electrochemical Society Student Member.
** Electrochemical Society Active Member.

path can be no more than one greater than the number of intermediates. This seemingly simple rule, however, does not hold true when multiple overall reactions are considered. Hence, Milner applied these concepts only to systems of electrochemical interest for the case in which there is a single overall reaction.

An efficient method of generating all the possible reaction mechanisms was developed by Sellers (5). This theory of chemical reaction networks was originally used to analyze a single overall reaction, and it was later extended by Happel and Sellers (3) to include the case of multiple overall reactions. In the present study, we have applied their method to the enumeration of all the possible reaction mechanisms for oxygen reduction at platinum. The following section is a brief summary of the important facets of this theory; however, the reader is referred to the original article for a detailed account of the procedures and mathematical proofs involved.

Theoretical

The reduction of oxygen in alkaline medium takes place through a network of intermediates, and the transitions that take place between one species and the other can be represented by a set of elementary steps. According to Boudart (6), a reaction is an elementary step if it takes place in a single irreducible act at the molecular level just the way it is written in the stoichiometric equation for the reaction. The act of reaction is irreducible when no intermediate between reactants and products can be detected by any available technique. Once a set of elementary steps is specified and reaction intermediates are postulated, all the possible reaction mechanisms can be unambiguously determined. Furthermore, it is not necessary to know *a priori* the overall reaction.

This method assumes that the networks of reaction steps can be decomposed into two sets. The first set consists of those steps which when combined yield the overall production and consumption of chemical species. The second set of steps forms cycle reactions in the sense that there is no net change of terminal species. (The terminal species are those which appear in the overall reaction.) Such cyclic reactions violate the principle of microscopic reversibility (7) and therefore cannot be physically realizable.

Consider a steady-state reacting system where the chemical species are represented in the notation

$$a_1, a_2, a_3, \ldots, a_A \qquad [1]$$

and the mechanistic elementary steps

$$s_1, s_2, s_3, \ldots, s_S \qquad [2]$$

Each elementary step in Eq. [2] is composed of certain chemical species and symbolically represents a molecular event whereby these species are transformed into others. Every elementary step has an associated chemical reaction which can be put into the form

$$R(s_i) = \alpha_{i1}a_1 + \ldots + \alpha_{iA}a_A \qquad [3]$$

where the α's are the stoichiometric coefficients of the species in each elementary step and the sign depends on the usual convention (positive for a product and negative for a reactant species). Every step s_i has certain scalar values, σ_i, which can take on any value and are used to form all the possible vectors which constitute a one-dimensional mechanistic vector space. The mechanistic vectors can be written as

$$\sigma_1 s_1 + \ldots + \sigma_S s_S \qquad [4]$$

and the set of all vectors of this form constitutes an S-dimensional vector space and is called the mechanism space. Every mechanistic vector thus has a reaction vector $R(m)$ associated with it where each mechanism m is represented by a mechanistic vector as in Eq. [4]. The set of all possible reaction vectors is called a reaction space, which is of dimension R, corresponding to the maximum number of linearly independent reactions.

The stoichiometric coefficient matrix can be written in the form

$$\begin{matrix} \alpha_{11}, \alpha_{12}, \ldots, \alpha_{1A} \\ \alpha_{21}, \alpha_{22}, \ldots, \alpha_{2A} \\ \cdot \quad \cdot \quad \cdot \\ \cdot \quad \cdot \quad \cdot \\ \cdot \quad \cdot \quad \cdot \\ \alpha_{S1}, \alpha_{S2}, \ldots, \alpha_{SA} \end{matrix} \qquad [5]$$

where the rows correspond to the elementary steps and the columns to the various chemical species. It is then a simple matter to enumerate the possible reaction mechanisms by multiplying the matrix given in Eq. [5] by m. This affords the reaction vectors $R(m)$ in terms of the stoichiometric coefficients and the scalar values, σ_i. Thus, for every mechanistic vector m, a reaction vector $R(m)$ can be found by matrix multiplication. However, the present problem can be considered as the inverse of this, in that the values for σ_i are unknown and we wish to find all the mechanistic vectors which produce a specified reaction vector: namely, the overall reaction vector.

The overall reaction vector consists only of terminal species; hence, the mechanistic vectors which must be determined will have to recycle all the intermediate species. Consequently, a set of mechanistic vectors which regenerates all the species must also be determined. It is evident that such a cycle mechanistic vector affords a reaction which is null and is represented by the equation

$$R(z) = 0 \qquad [6]$$

In any chemical system, there is a unique number of mechanisms which are termed direct mechanisms. These are shown by Happel and Sellers (3) to be the fundamental constituents of any mechanism. The first step in the determination of all the possible direct mechanisms is accomplished by a diagonalization of the stoichiometric coefficient matrix given in Eq. [5]. It is sufficient to note in the present context that the process of diagonalization directly provides one with all the mechanistic vectors which produce a particular independent overall reaction. Furthermore, a cycle matrix is formed where the number of rows, C, corresponds to the number of cycle reactions present in the system and the number of columns is given by the total number of species, A. The mechanistic vectors for each of these cycles are also available if a detailed record is kept of all the column and row manipulations during the diagonalization process. It is clear that this type of management is most efficiently realized through the use of a computer algorithm.

The results of any diagonalization process can be shown in the generalized reduced matrix given in Fig. 1. In this matrix, all entries are zero below the diagonal, nonzero in the outlined boxes, and arbitrary above the diagonal. The space of all the nonsteady-state mechanisms, steady-state mechanisms, and cycles is given by: m_1 to m_H, m_{H+1} to m_Q, m_{Q+1} to m_S, respectively. It is clear that only the terminal species are involved in the steady-state mechanisms, whereas cycles regenerate all the species to form a null reaction according to Eq. [6].

The general expression for any steady-state mechanism can be written as a linear combination of the overall reactions and the cycles

$$m = \mu_{H+1}m_{H+1} + \ldots + \mu_S m_S \qquad [7]$$

The coefficients of the mechanistic vectors, m_{Q+1} through m_S, form the C-by-S cycle matrix. Since the general mechanism is composed of a linear combination of overall reaction vectors and cycles, we must insure that this combination does not lead to any cycles, since this would violate the principle of microscopic reversibility. Thus, in order to find every cycle-free system, we must insure that C columns of the C-by-S cycle matrix add up to zero, which is equivalent to the following matrix equation

$$(\sigma_{H+1} \ldots \sigma_Q) + (\mu_{Q+1} \ldots \mu_S)M = 0 \qquad [8]$$

where the solution to the above equation is given by

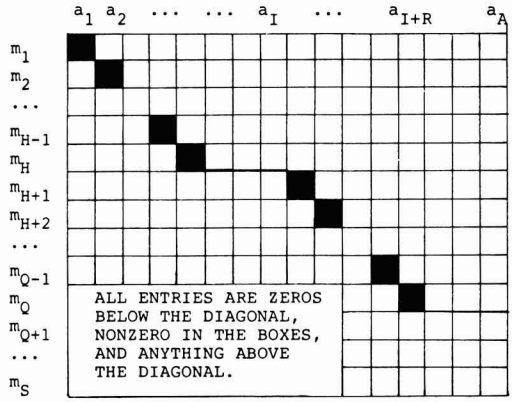


Fig. 1. Generalized reduced matrix

$$(\mu_{q+1} \ldots \mu_s) = -(\sigma_{H+1} \ldots \sigma_q)M^{-1} \quad [9]$$

where M^{-1} is the inverse of the C-by-C cycle matrix. The procedure for enumerating every direct mechanism is simply given by the solution to Eq. [9]. In this case, all the nonsingular C-by-C submatrices of the C-by-S cycle matrix must be considered as viable in generating a direct mechanism. The solution of these sets of linear algebraic equations becomes tedious even for a small cycle matrix, since it is evident that there are at least $S!/[(S - C)!\ C!]$ possible combinations of C-by-C submatrices which can be generated from a C-by-S cycle matrix. A computer algorithm is thus appropriate for this task.

Analysis of Reaction Mechanism

The reduction of oxygen in alkaline solutions is often believed to proceed along two parallel reaction paths. This was the conclusion by Bockris and co-workers (8), using experiments with the rotating ring-disk electrode. In one of these paths, hydrogen peroxide is considered an intermediate which can be partially reduced or electrocatalytically decomposed to water. However, the decomposition reaction of hydrogen peroxide to water is found to take place only in acidic solutions at platinum (9). In the other path, oxygen is reduced to water without hydrogen peroxide as an intermediate. For the purpose of this study, the presence of hydrogen peroxide is included in the reaction scheme. The reason is simply that both pathways will very likely become operable unless "ultra-high" purity solutions are used, which is often difficult to achieve and impractical in most applications.

The overall reaction for the reduction of oxygen in alkaline solutions at platinum is given by the following equation, regardless of whether hydrogen peroxide is formed or not

$$O_2 + 2H_2O + 4e^- = 4\ OH^- \quad [10]$$

Furthermore, two other overall reactions account for the possibility of hydrogen peroxide formation. The following equations apply for alkaline solutions

$$O_2 + H_2O + 2e^- = OH^- + HO_2^- \quad [11]$$

$$HO_2^- + H_2O + 2e^- = 3\ OH^- \quad [12]$$

Note that the preceding reactions do not form an independent set, since Eq. [11] and [12] can be combined to yield Eq. [10].

Any critical assessment of the possible reaction mechanisms of oxygen reduction must necessarily include consistency with certain experimental results. There are at least two ways in which this minimum consistency standard can be met.

The first method involves the deduction of mechanistic indicators and was used by Bockris (10) in evaluating the reaction mechanisms for oxygen reduction. Once a mechanism has been postulated, reaction rate equations are developed. The kinetic expression for a reaction rate depends upon the reaction pathway, upon the behavior of the intermediates, and upon which step is rate determining. The mechanistic indicators obtained reflect how the rest potential changes with logarithm of the current at constant pH, or alternatively, the change of rest potential with pH at constant current. These theoretically derived mechanistic indicators are then compared to experimental results for consistency. Distinction between the various mechanisms is impossible when each is characterized by the same mechanistic indicators, as is often the case. Consequently, this method cannot unequivocally provide conclusive evidence for the existence of one mechanism over the other.

In the present analysis, the stoichiometric number concept is employed as a diagnostic tool for evaluating the reaction mechanisms. The stoichiometric number, originally used by Horiuti in studying mechanisms of single overall reactions, represents the number of times the rate-determining step occurs in order to effect one occurrence of the overall reaction. Partial experimental consistency is obtained by using the cathodic and anodic Tafel slopes, from the polarization curve of the oxygen electrode reaction, in order to calculate the stoichiometric numbers. According to Parsons (11), this can be accomplished from the following expression

$$\nu = \frac{4\mathbf{F}}{RT}(1/b_A - 1/b_C)^{-1} \quad [13]$$

where b_A and b_C are the anodic and cathodic Tafel slopes, respectively. Furthermore, the existence of Tafel line regions for the cathodic reduction of oxygen on platinum strongly indicates that the rate-determining step is electron-transfer related. Hence, the stoichiometric number applied to an electron-transfer rate-determining step provides for an important preliminary screening of the possible reaction mechanisms. This limited set of mechanisms can subsequently be analyzed through the method of mechanistic indicators.

The procedure outlined in the theoretical section can be used to generate all the possible reaction mechanisms once a set of elementary steps and chemical species has been postulated. A review of the literature has revealed that the set of elementary steps listed in Table I may be appropriate in describing the molecular interactions that are likely to take place during the reduction of oxygen at platinum in alkaline solutions.

Although the list of elementary steps given in Table I is not exhaustive, it does comprise a comprehensive set of the most important reactions, which forms a basis for the present systematic study. The intermediate species considered are OH, O, O_2H, O_2^-, and O^-, and the terminal species are OH^-, O_2, H_2O, O_2H^-, and e^-. Although the

Table I. Elementary steps considered in the reduction of oxygen on platinum in alkaline medium

1.			OH^-	=	OH	+	e^-			
2.	OH^-	+	O	=	O_2H	+	e^-			
3.			O_2H^-	=	O_2H	+	e^-			
4.			2 OH	=	O	+	H_2O			
5.	OH	+	O	=	O_2H					
6.			2 O	=	O_2					
7.	OH^-	+	O	=	O_2H-					
8.	O	+	e^-	=	O^-					
9.	OH	+	OH^-	=	O^-	+	H_2O			
10.	OH	+	O_2H	=	O_2	+	H_2O			
11.	O	+	O_2H	=	O_2	+	OH			
12.	O_2H^-	+	O	=	O_2	+	OH^-			
13.	O_2H^-	+	OH	=	O_2H	+	OH^-			
14.	OH^-	+	OH	=	O	+	H_2O	+	e^-	
15.	OH^-	+	O_2H	=	O_2	+	H_2O	+	e^-	
16.	OH^-	+	O_2	=	O	+	O_2H	+	e^-	
17.	O_2H^-	+	OH	=	O_2	+	H_2O	+	e^-	
18.	O_2H^-	+	O	=	O_2	+	OH	+	e^-	
19.			2 OH^-	=	O	+	H_2O	+	$2e^-$	
20.	O_2H^-	+	OH^-	=	O_2	+	H_2O	+	$2e^-$	
21.	O_2	+	e^-	=	O_2^-					
22.	OH	+	O_2H^-	=	O_2^-	+	H_2O			

electron is not usually considered as a species, in order to apply this method it is essential to distinguish between those elementary steps which involve electron transfers.

If we apply the method delineated in the theoretical section, using all the 22 elementary steps proposed, two independent overall reactions are obtained. The overall reactions corresond to those found in the literature and are given previously by Eq. [10] and [12]. In addition, we find that there are 15 cycles. Hence, in order to determine all the possible mechanisms, it is necessary to solve (22!/15!7!) or 179,544 sets of 15 simultaneous linear algebraic equations. This is indeed a great computational effort.

The present situation is ameliorated by inspection of the elementary steps listed in Table I, particularly reactions 19 and 20. Each of these reactions involves the simultaneous transfer of two electrons and is usually not considered to take place in a single molecular interaction. Based on this premise we can exclude reactions 19 and 20 from the original set of 22 elementary steps. Furthermore, although it is possible that the superoxide species O_2^- forms in the outer Helmholtz plane by outer sphere electron transfer, it is unlikely to appear in alkaline solutions and probably contributes insignificantly to the observed current (16). Therefore, it seems reasonable to eliminate the steps in which this species occurs, specifically reactions 21 and 22.

Case study I.—The remaining 18 elementary steps form the basis for case study I. The mechanistic stoichiometric matrix corresponding to this set of reactions is shown in Fig. 2. Each row in this matrix represents an elementary reaction, and the chemical species are arranged by columns. The diagonalization procedure transforms the stoichiometric matrix into the reduced matrix shown in Fig. 3. It is evident that there are two independent overall reactions, consisting only of terminal species, and these are given by Eq. [10] and [12]. The rows in the reduced matrix containing all zero elements belong to the set of cycle reaction mechanisms. These cycle reaction mechanisms are described by an auxiliary *C*-by-*S* matrix which is derived from the diagonalization procedure and is also shown in Fig. 4.

	OH	O	O_2H	O^-	O_2H^-	OH^-	O_2	H_2O	e^-
S_1	1	0	0	0	0	-1	0	0	1
S_2	-1	1	0	0	0	-1	0	1	1
S_3	0	-1	1	0	0	-1	0	0	1
S_4	0	0	-1	0	0	-1	1	1	1
S_5	0	1	1	0	0	-1	-1	0	1
S_6	0	0	1	0	-1	0	0	0	1
S_7	-1	0	0	0	-1	0	1	1	1
S_8	1	-1	0	0	-1	0	1	0	1
S_9	-2	1	0	0	0	0	0	1	0
S_{10}	-1	-1	1	0	0	0	0	0	0
S_{11}	-1	0	-1	0	0	0	1	1	0
S_{12}	1	-1	-1	0	0	0	1	0	0
S_{13}	0	-2	0	0	0	0	1	0	0
S_{14}	0	-1	0	0	-1	1	1	0	0
S_{15}	-1	0	1	0	-1	1	0	0	0
S_{16}	0	-1	0	0	1	-1	0	0	0
S_{17}	0	-1	0	1	0	0	0	0	-1
S_{18}	-1	0	0	1	0	-1	0	1	0

Fig. 2. Mechanistic stoichiometric matrix: case study I

	OH	O	O_2H	O^-	O_2H^-	OH^-	O_2	H_2O	e^-
	1	0	0	0	0	-1	0	0	1
	0	1	0	0	0	-2	0	1	2
	0	0	1	0	0	-3	0	1	3
	0	0	0	1	0	-2	0	1	1
eqn. [10]	0	0	0	0	0	4	-1	-2	-4
eqn. [12]	0	0	0	0	-1	3	0	-1	-2
	0	0	0	0	0	0	0	0	0
	0	0	0	0	0	0	0	0	0
	0	0	0	0	0	0	0	0	0
	0	0	0	0	0	0	0	0	0
	0	0	0	0	0	0	0	0	0
CYCLES	0	0	0	0	0	0	0	0	0
	0	0	0	0	0	0	0	0	0
	0	0	0	0	0	0	0	0	0
	0	0	0	0	0	0	0	0	0
	0	0	0	0	0	0	0	0	0
	0	0	0	0	0	0	0	0	0

Fig. 3. Reduced stoichiometric matrix: case study I

The number of possible reaction mechanisms which are consistent with the prescribed set of 18 elementary steps is found to be 1897. Since this chemical reaction system consists of two independent overall reactions, a "mechanism" is in fact composed of a set of two submechanisms. Each of the two overall reactions is independently described by a submechanism, and furthermore, such a set of submechanisms uniquely defines a mechanism.

A complete analysis of a vast number of alternative reaction mechanisms requires a considerable body of experimental data from which certain mechanistic criteria can be developed. For example, it is possible to explore the reaction order of a mechanism with respect to its dependence on the partial pressure of oxygen, *p*H, and water. The variation in the coverage by intermediates with overpotential and *p*H provides important information on the adsorption of oxygenated species, which plays a major role in determining the kinetics of oxygen reduction. Additional kinetic criteria can include Tafel slopes, the effect of *p*H and the partial pressure of oxygen on the

	S_1	.	.	.	ELEMENTARY STEPS	.	.	.	S_{18}
	1 0 0 0 0 0 0 0 0 0 0 0 0 0 0 0 0 0
	1 1 0 0 0 0 0 0 0 0 0 0 0 0 0 0 0 0
	1 1 1 0 0 0 0 0 0 0 0 0 0 0 0 0 0 0
	1 1 0 0 0 0 0 0 0 0 0 0 0 0 0 0 1 0
OVERALL	2 2 1 0 -1 0 0 0 0 0 0 0 0 0 0 0 0 0
REACTION	-1 -1 -1 0 0 1 0 0 0 0 0 0 0 0 0 0 0 0
MECHANISMS	0 1 0 0 -1 1 -1 0 0 0 0 0 0 0 0 0 0 0
	1 -1 0 0 0 0 1 -1 0 0 0 0 0 0 0 0 0 0
	-1 1 0 0 0 0 0 0 -1 0 0 0 0 0 0 0 0 0
	-1 0 1 0 0 0 0 0 0 -1 0 0 0 0 0 0 0 0
CYCLE	0 0 0 0 0 -1 1 0 0 0 -1 0 0 0 0 0 0 0
REACTION	1 -1 0 0 0 -1 1 0 0 0 0 -1 0 0 0 0 0 0
MECHANISMS	0 -1 1 0 0 -1 1 0 0 0 0 0 -1 0 0 0 0 0
	0 -1 0 0 0 0 1 0 0 0 0 0 0 -1 0 0 0 0
	-1 0 0 0 0 1 0 0 0 0 0 0 0 0 -1 0 0 0
	0 0 1 0 0 -1 0 0 0 0 0 0 0 0 0 -1 0 0
	1 0 0 -1 0 -1 1 0 0 0 0 0 0 0 0 0 0 0
	0 1 0 0 0 0 0 0 0 0 0 0 0 0 0 0 1 -1

Fig. 4. Stoichiometric cycle matrix: case study I

overpotential, the determination of transfer coefficients and the stoichiometric number, and the dependence of reaction rates upon substitution of isotopic atoms. In principle, if all these criteria were to be take into account, the number of possible reaction mechanisms would be drastically reduced. However, such a procedure can be quite involved and many of these criteria are particularly sensitive to the specific system investigated. For these reasons, an analysis of the reaction mechanisms will be performed based on simple kinetic criteria in the form of Tafel slopes and stoichiometric number.

We have shown that with the given set of 18 elementary steps, the reduction of oxygen in alkaline solutions involves two overall reactions. One reaction involves the direct reduction of oxygen to water, while in the other oxygen is reduced to hydrogen peroxide. The stoichiometric number concept as developed by Horiuti strictly applies for the case of a single overall reaction. However, if one of the reaction paths in the reduction of oxygen is predominant over the other, and one of the elementary steps in this path is rate determining, then the Tafel slopes will necessarily be characteristic of that rate-determining step. In the reduction of oxygen near the reversible electrode potential, the path which does not have hydrogen peroxide as an intermediate must predominate (17). Consideration of this case permits the use of the stoichiometric number as a diagnostic criterion in mechanism analysis.

Experiments with the oxygen electrode in alkaline solutions at platinum indicate an anodic Tafel slope of $RT/\mathbf{F}$, at low current densities, while at higher current densities the slope is twice as much (12). This is in accordance with the appearance of oxide formation at the higher anodic overpotentials and is suggestive of a change in the mechanism or a change in the rate-determining step. The cathodic Tafel slopes for the reduction of oxygen in alkaline solutions at platinum have been reported as $-RT/\mathbf{F}$ at low current densities and $-2RT/\mathbf{F}$ for much higher current densities (13-15). Direct substitution of the low current density Tafel slopes into Eq. [13] yields a stoichiometric number of 2.

The results of a diagnostic analysis for case study I using the stoichiometric number concept are shown in Table II. Note that there are 1686 mechanisms which have at least one elementary step with a stoichiometric number of 2. The existence of Tafel lines and the absence of chemical reaction-limited currents indicate that any one of the nine elementary steps which involve electron transfer is likely to be rate determining (18). Consequently, if we consider mechanisms which have a stoichiometric number of 2 associated with an electron-transfer rate-determining step, then the number of possibilities is significantly reduced to 950. The number of mechanisms for this case is also listed separately, according to the particular electron-transfer elementary step. For example, there are 187 possible mechanisms that have a stoichiometric number of 2 in connection with elementary step number 1, which is an electron-transfer reaction. Note that even with these simple criteria we have been able to reduce by one order of magnitude the number of possible mechanisms. However, it is impossible to begin listing all these mechanisms here; thus, a complete list is provided upon request.

Table II. Mechanism diagnostic analysis: case study I

Elementary steps: 18
Terminal species: O_2, H_2O, OH^-, O_2H^-
Intermediate species: OH, O, O_2H, O^-
Total number of mechanisms: 1897

Stoichiometric number $\nu = 2$	Mechanisms
a) Any rds	1686
b) Charge transfer rds	950
Charge transfer elementary step	$\nu = 2$
1	187
2	187
3	143
8	211
14	129
15	157
16	204
17	139
18	187

Table III. Mechanism diagnostic analysis: case study II

Elementary steps: 13
Terminal species: O_2, H_2O, OH^-, O_2H^-
Intermediate species: OH, O, O_2H, O^-
Total number of mechanisms: 315

Stoichiometric number $\nu = 2$	Mechanisms
a) Any rds	277
b) Charge transfer rds	82
Charge transfer elementary step	$\nu = 2$
1	32
2	25
3	23
8	66

Case study II.—In case study II, we examine a set of elementary reactions which excludes those "elementary" steps in which two chemical species and an electron transfer are simultaneously involved. Such reactions tend to have a positive Gibbs free energy of reaction by effecting a concerted mechanism through the presence of three entities at the electrode surface. In this case, elementary steps 14-18, as listed in Table I, will not be considered.

Given the same intermediate and terminal species as in the previous case study, all the possible reaction mechanisms can be determined from the remaining 13 elementary steps. Once again, we find two overall independent reactions. However, unlike case study I, the hydrogen peroxide reaction is given by Eq. [11] instead of by Eq. [12]. Nonetheless, it is important to realize that two independent overall reactions are needed to characterize this chemical reaction system. The results of a diagnostic analysis of these mechanisms based on the stoichiometric number is shown in Table III. The number of possible mechanisms has decreased substantially compared to the previous case. Although simple kinetic criteria like Tafel slopes and the stoichiometric cannot ultimately determine the reaction mechanism, it is an important step in that direction. Furthermore, when these simple kinetic criteria are supplemented with other system-specific experimental data, as previously mentioned, a greater understanding of the mechanism for oxygen reduction is made possible.

Conclusions

A method for generating all the possible reaction mechansims consistent with a given set of elementary steps and chemical species has been applied to the reduction of oxygen under alkaline conditions at platinum. In this study, we have employed the magnitudes of the anodic and cathodic Tafel slopes, through a determination of the stoichiometric numbers, as a major basis for mechanistic interpretations. This procedure establishes a limited set of mechanisms, and other diagnostic criteria can be used to even further reduce these possibilities. We have shown how this method can be used in conjunction with diagnostic criteria, as a powerful and systematic tool in the investigation of the mechanism for the reduction of oxygen.

Manuscript submitted Aug. 28, 1984; revised manuscript received May 24, 1985.

REFERENCES

1. J. Horiuti and T. Ikusima, *Proc. Imp. Acad. Tokyo*, **15,** 39 (1939).
2. J. Horiuti and T. Nakamura, *Z. Phys. Chem. (Frankfurt am Main)*, **11,** 358 (1957).
3. J. Happel and P. H. Sellers, *Ind. Eng. Chem. Fundam.*, **21,** 67 (1982).
4. P. C. Milner, *This Journal*, **111,** 228 (1964).
5. P. H. Sellers, *Arch. Ration. Mech. Anal.*, **44,** 23 (1971).
6. M. Boudart, "Kinetics of Chemical Processes," p. 32, Prentice-Hall Inc., Englewood Cliffs, NJ (1968).
7. W. J. Moore, "Physical Chemistry," p. 332, Prentice-

Hall Inc., Englewood Cliffs, NJ (1972).
8. J. O'M. Bockris, M. A. Genshaw, and A. Damjanovic, *This Journal*, **114,** 1107 (1967).
9. J. O'M. Bockris and L. F. Oldfield, *Trans Faraday Soc.*, **51,** 249 (1955).
10. J. O'M. Bockris, *J. Chem. Phys.*, **21,** 817 (1957).
11. R. Parsons, *Trans. Faraday Soc.*, **47,** 1332 (1951).
12. A. Damjanovic, A. Dey, and J. O'M. Bockris, *Electrochim. Acta*, **11,** 791 (1966).
13. D. B. Sepa, M. V. Vojnovic, and A. Damjanovic, *ibid.*, **26,** 781 (1981).
14. D. B. Sepa, M. V. Vojnovic, and A. Damjanovic, *ibid.*, **25,** 1491 (1980).
15. A. Damjanovic and M. A. Genshaw, *ibid.*, **15,** 1281 (1970).
16. E. Yeager, *This Journal*, **128,** 160C (1981).
17. D. S. Gnanamuthu and J. V. Petrocelli, *ibid.*, **114,** 1036 (1967).
18. F. G. Will, Report no. 76CRD276, p. 34, General Electric Co., Power Systems Laboratory, Schenectady, NY (1976).

Underpotential Deposition of Copper on Gold and the Effects of Thiourea Studied by AC Impedance

Joseph Collin Farmer*

Sandia National Laboratory, Materials Department, Livermore, California 94550

ABSTRACT

This paper reports ac impedance and cyclic voltammetry studies of underpotential deposition (UPD) of Cu on Au in an electrolyte composed of $CuSO_4$ and H_2SO_4. A theoretical kinetic model was developed which fits the experimental impedance spectra over frequencies ranging from 0.001 to 20,000 Hz. Spectra are characterized by a two-time constant process; two capacitive loops were observed in the Nyquist diagrams corresponding to two distinctive peaks in the Bode phase plot. The high frequency time constant is associated with the double-layer capacitance, while the low frequency process is due to relaxation phenomena associated with the charge transfer involved in Cu^{2+} electrosorption. Thiourea is one of the most important organic additives for commercial $CuSO_4$ plating baths. Therefore, the coadsorption of thiourea and UPD Cu on Au was also studied by ac impedance. Adsorbed thiourea was found to have a dramatic effect on the high frequency peak in the Bode phase plot. Measurements such as these are proposed as a means of determining organic additive concentrations in Cu plating and electroforming baths.

Underpotential electrodeposition (UPD) of metal monolayers on foreign substrates offers the electrochemist an opportunity to study electrosorption from a fundamental point of view since coverage can be precisely controlled with potential (1-8). It has been shown that in many cases Langmuir, Frumkin, or Temkin adsorption isotherms govern the equilibrium behavior of UPD films (1, 2). Furthermore, the UPD represents the initial stage of nucleation of an electrodeposit on a foreign substrate, and therefore offers insight into early development of bulk deposits (3). The free energy of electrosorption may be indicative of the bonding (adhesion) between the deposit and substrate.

The UPD of Cu on single-crystal Au electrodes of (111) and (100) orientation were studied by Beckmann *et al.*, who used cyclic voltammetry (CV) and reflected high energy electron diffraction (RHEED) (3). They concluded that deposition of about two-thirds of a Cu monolayer on Au (111) resulted in a $(\sqrt{3} \times \sqrt{3})$ R30 superstructure, and that deposition of bulk Cu on Au (111) resulted in an additional (2×2) superstructure, attributed to a surface alloy of Au_3Cu. Their failure to recover all of the deposited Cu by anodic stripping and the dramatic rearrangement of the Au surface after removal of both UPD and bulk deposits support the alloy concept. They state that these observations are indicative of a deposition process more complicated than simple adsorption and that the probable place exchange between Cu and Au atoms in the surface could result in high kinetic barriers to UPD formation.

AC impedance is a powerful tool for addressing questions regarding the kinetics and mechanism of electrosorption. Recently, ac impedance studies of Pb and Tl UPD formation on Ag single crystals were done by Klimmeck and Juttner (4). Their impedance spectra had a frequency range extending from 0.1 to 10,000 Hz and could be explained by the simple Dolin-Ershler model. Earlier, a dynamic impedance technique was used by Nihei *et al.* to study Cu UPD formation on Pt (5). Unfortunately, the data presented in Ref. (5) were obtained at relatively high modulation frequencies (above 1 Hz). As will be shown here, important features in impedance spectra of electrosorption can only be observed at subhertz frequencies extending to 0.001 Hz. Such data cannot be obtained by dynamic impedance measurements and require fast Fourier transform (FFT) techniques (9) or a single-frequency correlator.

This paper reports ac impedance and cyclic voltammetry studies of UPD of Cu on Au in an electrolyte composed of $CuSO_4$ and H_2SO_4. A theoretical kinetic model was developed which fits experimental impedance spectra over frequencies ranging from 0.001 to 20,000 Hz. Since thiourea significantly effects the morphological properties of Cu electrodeposits and is one of the most important organic additive for commercial $CuSO_4$ plating baths (10, 11), the coadsorption of thiourea and Cu on Au was also studied by ac impedance. Data were collected at various potentials and concentrations.

Experimental

The electrolyte consisted of reagent-grade $CuSO_4$ (0.01-0.1*M*) dissolved in dilute H_2SO_4 (0.1*M*). Distilled, deionized water was used in the preparation. Incremental thiourea additions were then made to this electrolyte (0, 5, 10, 15, and 30 mg/liter). These ranges of concentrations are inclusive of those used in plating baths. Prior to data collection, the electrolyte was stripped with nitrogen and treated by pre-electrolysis at potentials sufficiently cathodic to assure removal of impurities which could interfere with formation of the UPD.

A polycrystalline Au rotating disk working electrode (RDE), a large surface area platinum-sheet counterelectrode, and a double-junction saturated calomel reference electrode (SCE) were used. The cell and RDE rotator were obtained from IBM Instruments (EC/219-1A), and the impedance instrument was obtained from Princeton Applied Research (Model 368). Impedance spectra from 1.3 to 20,000 Hz were obtained using a lock-in amplifier to follow the current response to voltage modulation. At frequencies extending to 0.001 Hz, a fast Fourier transform (FFT) technique was used (9).

*Electrochemical Society Active Member.

Theoretical

In order to interpret impedance spectra for the underpotential deposition of Cu^{2+} on polycrystalline Au, electrosorption mechanisms must be postulated. Then, electrokinetic models and corresponding faradaic impedances are derived based upon these mechanisms. The simplest mechanism is

$$M^{2+} + 2e^- + \theta_v \underset{k_b}{\overset{k_f}{\rightleftarrows}} \theta_M \quad [1]$$

where M^{2+} is the bulk concentration of Cu^{2+}, θ_v represents the fractional vacancies on the electrode surface, θ_M represents the fractional coverage of the electrode surface by UPD Cu, and k_f and k_b are the forward and reverse rate constants, respectively. Note that θ_v and θ_M totaled together equal unity. The kinetic equation which describes the rate of formation of the UPD via the mechanism shown in Eq. [1] is

$$\frac{d\theta_M}{dt} = k_f M^{2+} - (k_f M^{2+} + k_b)\theta_M \quad [2]$$

Based upon Eq. [2], the current involved in the electrosorption process, i, is written as Eq. [3]

$$i = 2\mathbf{F}(\theta_M(k_f M^{2+} + k_b) - k_f M^{2+}) \quad [3]$$

where $\mathbf{F}$ is Faraday's constant. Note that two electrons are involved in the process. In a manner similar to that of Epelboin and Wiart (12), the complex faradaic impedance, Z_f, is then derived from Eq. [3] using Eq. [4]

$$\frac{1}{Z_f} = \left(\frac{\partial i}{\partial E}\right)_{\theta M} + \left(\frac{\partial i}{\partial \theta_M}\right)_E \cdot \frac{\Delta\theta_M}{\Delta E} \quad [4]$$

where E is the electrode potential. The two partial derivatives of current are defined in terms of physically significant quantities by Eq. [5] and [6]

$$\left(\frac{\partial i}{\partial E}\right)_{\theta M} = 2\mathbf{F}(\theta_M(k'_f M^{2+} + k'_b) - k'_f M^{2+}) \quad [5]$$

$$\left(\frac{\partial i}{\partial \theta_M}\right)_E = 2\mathbf{F}(k_f M^{2+} + k_b) \quad [6]$$

Primed rate constants, k'_f and k'_b, represent their respective potential derivatives. The steady-state value of θ_M is required by Eq. [5] and is found by setting the left-hand side of Eq. [2] to zero. The result is

$$\theta_M = \frac{k_f M^{2+}}{k_f M^{2+} + k_b} \quad [7]$$

In addition to Eq. [5] and [6], definition of Z_f requires $\Delta\theta_M/\Delta E$

$$\frac{\Delta\theta_M}{\Delta E} = \frac{k'_f M^{2+} - k_f M^{2+}(k'_f M^{2+} + k'_b)/(k_f M^{2+} + k_b)}{j\omega + k_f M^{2+} + k_b} \quad [8]$$

The total differential of Eq. [2] and the following relationship

$$j\omega\Delta\theta_M = \frac{d}{dt}\Delta\theta_M \quad [9]$$

are used to obtain Eq. [8]; ω is the angular frequency $2\pi f$ (12). Substituting Eq. [5], [6], and [8] into Eq. [4], one finds that Z_f can be written as

$$\frac{1}{Z_f} = \frac{1}{R_p} - \frac{1}{\rho(1 + j\omega\tau)} \quad [10]$$

an impedance identical to that of the equivalent circuit shown in Fig. 1a, a resistor in parallel with a complex capacitive component. Note that this is a special case of Eq. [7] in Ref. (12), where I_1 is greater than $3I_3$. Here, the circuit components R_p, ρ, and τ are defined in terms of Faraday's constant, the electrokinetic rate constants, and the concentration of Cu^{2+} in the bulk electrolyte which are all found in Eq. [3] above

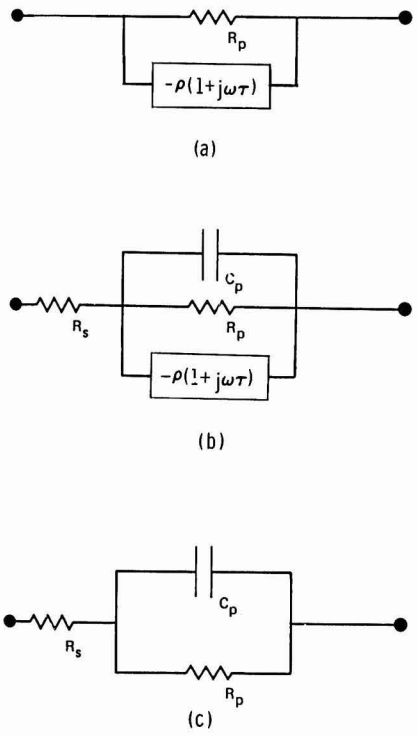


Fig. 1. Equivalent circuit models for the faradaic impedance of electrosorption (a), overall impedance of the electrochemical cell (b), and impedance for the special case of infinite (c).

$$R_p = \frac{1}{2\mathbf{F}(a + b)k_f M^{2+}} + \frac{1}{2\mathbf{F}(a + b)k_b} \quad [11]$$

$$\rho = R_p \quad [12]$$

$$\tau = \frac{1}{k_f M^{2+} + k_b} \quad [13]$$

The constants a and b are from the expressions $k_f = A \exp(-aE)$ and $k_b = B \exp(bE)$. It is also important to note that $R_p = \rho$ in this case. As will be discussed, this equality can be used as a basis of distinguishing between various electrosorption mechanisms.

Bruckenstein *et al.* show that Cu^{2+} can be reduced to form soluble Cu^+ and metallic Cu simultaneously at potentials more cathodic than those required for bulk Cu deposition (13). Bowles presents evidence for formation of Cu^+ on Pt in the UPD region near monolayer coverage (14). As will be discussed here, cyclic voltammetry shows a loss of cathodic charge in the UPD region which is believed to be due to formation of a reduced, soluble species like Cu^+. Therefore, a mechanism is proposed that assumes both the UPD and soluble Cu^+ could form from the same adsorbed intermediate, $Cu_{ads}{}^+$. An additional electron transfer would incorporate this intermediate into the UPD, and its desorption into the electrolyte without charge transfer would yield Cu^+. This mechanism is represented by Eq. [14] and [15]

$$M^{2+} + e^- + \theta_v \underset{k_b}{\overset{k_f}{\rightleftarrows}} \theta_{ads}{}^+ \overset{k}{\rightarrow} M^+ \quad [14]$$

$$\theta_{ads}{}^+ + e^- \underset{K}{\rightleftarrows} \theta_M \quad [15]$$

where $\theta_{ads}{}^+$ represents the fractional coverage of the sur-

face by the intermediate, Cu_{ads}^{+}, and k is the potential independent desorption rate constant. If the second electron transfer shown in Eq. [15] is assumed to be fast relative to all reaction paths shown in Eq. [14], than θ_{ads}^{+} would be in approximate equilibrium with θ_M

$$\theta_M = K\theta_{ads}^{+} \quad [16]$$

where K is the equilibrium constant. The kinetic rate equation for the intermediate is then

$$\frac{d\theta_{ads}^{+}}{dt} = k_f M^{2+} - (k_f M^{2+}(1 + K) + k_b + k)\,\theta_{ads}^{+} \quad [17]$$

and the corresponding current involved in this process is

$$i = \mathbf{F}(\theta_{ads}^{+}(k_f M^{2+}(1 + K) + k_b) - k_f M^{2+}) \quad [18]$$

The complex faradaic impedance, Z_f, is then found by substituting Eq. [18] into Eq. [4]. As in the case of simple adsorption (Eq. [1]), one finds that Z_f can again be represented by Eq. [10] and the equivalent circuit shown in Fig. 1a. However, in the case of the soluble intermediate the equivalent circuit components are redefined

$$R_p = \frac{1}{\mathbf{F}k_f M^{2+}}\left(\frac{k_f M^{2+}(1 + K) + k_b + k}{k_f M^{2+}(K') + k_b(a + b) + k(a)}\right) \quad [19]$$

$$\tau = \frac{1}{k_f M^{2+} + k_b + k} \quad [20]$$

$$\rho = \frac{k_f M^{2+}(1 + K) + k_b + k}{k_f M^{2+}(1 + K) + k_b} R_p \quad [21]$$

From Eq. [12] and [21], it is clear that a simple adsorption mechanism (Eq. [1]) can be distinguished from the mechanism involving formation of a soluble intermediate (Eq. [14] and [15]) by the ratio ρ/R_p; a ratio of unity implies that Eq. [1] is applicable, and a ratio greater than unity implies that Eq. [14] and [15] are applicable, *i.e.*, that k is not zero.

The desorption rate constant, k, has been eliminated in Eq. [22], a ratio derived from Eq. [20] and [21]

$$\frac{R_p}{\tau\rho} = k_f M^{2+}(1 + K) + k_b \quad [22]$$

A plot of this ratio as a function of concentration, M^{2+}, should yield a straight line with a slope of $(1 + K)k_f$ and an intercept of k_b.

The equivalent circuit shown in Fig. 1a does not account for the double-layer capacitance, C_p, and resistance of the electrolyte, R_s. When these effects are taken into consideration, the electrochemical cell has the same electrical response as the circuit shown in Fig. 1b. The overall complex impedance of the electrochemical cell is written as Eq. [23] (12)

$$Z = R_s + \left(\frac{1 + j\omega R_p C_p}{R_p} - \frac{1}{\rho(1 + j\omega\tau)}\right)^{-1} \quad [23]$$

The complex faradaic impedance, Z_f, and the impedance due to C_p are added as circuit components in parallel; then, the result and R_s are added as circuit components in series. The high frequency time constant of the circuit shown in Fig. 1b is proportional to R_pC_p, while the low frequency response is proportional to τ.

The high frequency limit of Eq. [23] is identical to R_s, as shown in Eq. [24]

$$\lim_{\omega\to\infty} Z = R_s \quad [24]$$

The low frequency limit of Eq. [23] gives a useful relationship between ρ and R_p

$$\lim_{\omega\to 0} Z = R_s + \frac{\rho R_p}{\rho - R_p} \quad [25]$$

Based upon Eq. [25], two minima (peaks) are observed in plots of phase angle, ϕ, as a function of frequency (Bode phase plot). One peak appears at intermediate high frequencies, and another at intermediate low frequencies (Fig. 2a, curve A). At intermediate high frequencies,

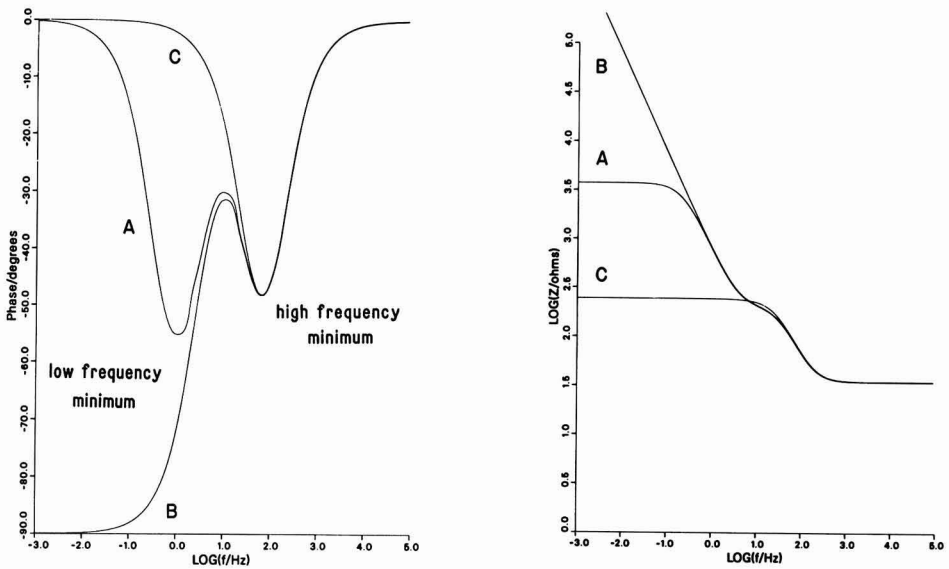


Fig. 2. a (left): Curve A is the Bode phase plot calculated from Eq. [23] and consistent with the electrosorption mechanism shown in Eq. [14] and [15]. Parameter values are: $R_s = 35\Omega$; $R_p = 205\Omega$; $C_p = 30\ \mu F$; $\rho = 229\Omega$; and $\tau = 0.48s$. Curve B shows a case where ρ is changed to a value of 205Ω. Since R_p and ρ are equivalent, curve B is consistent with the mechanism shown in Eq. [1]. Curve C shows a case where it is changed to a value of 10,000Ω and is essentially infinite. b (right): Curves A, B, and C are the Bode amplitude plots corresponding to curves A, B, and C in Fig. 2a, respectively.

$(1 + j\omega R_p C_p)/R_p$ is much greater than $1/(1 + j\omega\tau)$, and the overall impedance given in Eq. [23] is approximately

$$Z = R_s + \left(\frac{1 + j\omega R_p C_p}{R_p}\right)^{-1} \quad [26]$$

Equation [26] can be rewritten as

$$Z = R_s + \frac{R_p}{1 + (\omega R_p C_p)^2} - j\frac{R_p(\omega R_p C_p)}{1 + (\omega R_p C_p)^2} \quad [27]$$

The tangent of the phase angle at intermediate high frequencies, calculated from the ratio of the real and imaginary parts of Eq. [27] is

$$\tan\phi = -\frac{R_p(\omega R_p C_p)}{R_s + R_p + R_s(\omega R_p C_p)^2} \quad [28]$$

The phase angle and its tangent both pass through minima at the same frequency. The point where these minima occur can be found by differentiating Eq. [28] with respect to angular frequency, ω, and setting the result to zero. From Eq. [28], the tangent of the minimum phase angle at intermediate high frequencies and the corresponding angular frequency are $\tan\phi_{min}$ and ω_{min}, respectively

$$\tan\phi_{min} = -\frac{R_p}{2(R_s + R_p)}\sqrt{1 + R_p/R_s} \quad [29]$$

$$\omega_{min} = \frac{1}{R_p C_p}\sqrt{1 + R_p/R_s} \quad [30]$$

These results are consistent with Eq. [15] and [16] given by Mansfeld for a single time constant cell (15).

At intermediate low frequencies, similar approximations are useful. First, it is helpful to rearrange Eq. [23] to the form of Eq. [31]

$$Z = R_s + \frac{\rho R_p(1 + j\omega\tau)}{\rho(1 + j(\omega\tau + \omega R_p C_p) - \omega^2\tau R_p C_p) - R_p} \quad [31]$$

As will be seen, the low frequency time constant, τ, is typically more than three orders of magnitude larger than the high frequency time constant, $R_p C_p$. Thus, at low frequencies ($\omega \leq 1$) all terms in Eq. [31] smaller than $\omega\tau$ are insignificant and Eq. [31] can be written approximately as Eq. [32]

$$Z = R_s + \left(\frac{1}{R_p} - \frac{1}{\rho(1 + j\omega\tau)}\right)^{-1} \quad [32]$$

Then Eq. [33] and [34] are derived for intermediate low frequencies by following the strategy used to develop Eq. [29] and [30]

$$\tan\phi'_{min} = -\frac{R_p(\omega'_{min}\tau)}{(\rho - R_p) + \frac{R_s}{\rho R_p}(\rho - R_p)^2 + (\omega'_{min}\tau)^2\rho\left(1 + \frac{R_s}{R_p}\right)} \quad [33]$$

Table II. Model parameters estimated by approximate equations

E (mV)	Cu^{2+} (M)	T (mg/liter)	R_s (Ω)	R_p(Ω)	C_p(μF)	(Ω)	(ms)
0	0.01	0	35	205	30	217	35
50	0.01	0	36	85	23	86	19
100	0.01	0	37	109	9	109	14
200	0.01	0	37	161	15	161	5
0	0.1	0	49	144	47	183	19
50	0.1	0	49	54	20	57	12
100	0.1	0	49	65	8	66	12
200	0.1	0	49	234	5	236	24
50	0.1	5	49	199	24	238	52
50	0.1	10	49	352	26	381	42
50	0.1	15	49	449	33	486	45
50	0.1	30	49	601	54	651	111

$$\omega'_{min} = \frac{1}{\tau}\sqrt{\frac{1 + R_s/R_p + R_s R_p/\rho^2 - 2R_s/\rho - R_p/\rho}{1 + R_s/R_p}} \quad [34]$$

where $\tan\phi'_{min}$ and ω'_{min} are the tangent of the minimum phase angle and the angular frequency at the minimum, respectively.

The five quantities defined in Eq. [24], [29], [30], [33], and [34] are easily obtained from inspection of experimental impedance spectra similar to curve A in Fig. 2a and 2b. Values of R_s, R_p, C_p, ρ, and τ can all be calculated by substituting the five quantities into Eq. [24], [29], [30], [33], and [34] (Tables I and II). Alternatively, these parameters can be determined numerically by minimizing the sum of squares. The model variance, parameter variances, and parameter confidence intervals can also be calculated (16, 17).

Equation [23] was used to generate three theoretical impedance spectra. These are compared in Fig. 2a and 2b. Curve A represents Eq. [23] for the case where R_p and ρ are not equivalent and shows two minima in the Bode phase plot, Fig. 2a. Parameter values used in this calculation are given in the figure caption and are based upon values measured for underpotential deposition of Cu on Au at 0 mV and 0.01M Cu^{2+}. Note that the adsorption mechanism shown in Eq. [14] and [15] is consistent with this result. In contrast, curve B represents the case where $R_p = \rho$, which is characteristic of the simple adsorption mechanism shown in Eq. [1]. In this case, the phase asymptotically approaches $-90°$ at very low frequencies, while the minimum in phase at high frequency remains unchanged. Curve C shows only one minimum (peak) and corresponds to the special case where ρ is essentially infinite; the circuit shown in Fig. 1b behaves like that shown in Fig. 1c. Such single time constant impedances can result from electrode reactions which occur without the adsorption of reactants. Every minimum observed in Fig. 2a has a corresponding inflection point in Fig. 2b, the Bode amplitude plot.

Table I. Summary of impedance spectra: quantities used to estimate model parameters

			log Z (Ω)		log f (Hz)		Phase minimum (°)	
E (mV)	Cu^{2+} (M)	T (mg/liter)	High frequency	Low frequency	High frequency	Low frequency	High frequency	Low frequency
0	0.01	0	1.54	3.56	1.84	0.00	−48	−51
50	0.01	0	1.56	4.17	2.18	−0.27	−33	−66
100	0.01	0	1.57	5.25	2.53	−0.62	−37	−71
200	0.01	0	1.57	7.07	2.18	−0.93	−43	−71
0	0.1	0	1.69	2.86	1.67	0.55	−37	−28
50	0.1	0	1.69	3.00	2.33	0.35	−21	−43
100	0.1	0	1.69	3.55	2.67	0.14	−24	−55
200	0.1	0	1.69	4.52	2.48	−0.30	−45	−63
50	0.1	5	1.69	3.11	1.88	0.05	−42	−35
50	0.1	10	1.69	3.67	1.69	−0.01	−52	−35
50	0.1	15	1.69	3.77	1.53	−0.03	−55	−35
50	0.1	30	1.69	3.90	1.25	−0.42	−59	−34

Note: The third column contains the thiourea concentration. The fourth and fifth columns contain the log of the amplitude of the complex impedance at the high frequency and low frequency limits. The sixth and seventh columns show the position of the high frequency and low frequency minima in the Bode phase plots, respectively. The last two columns contain the depth of those minima.

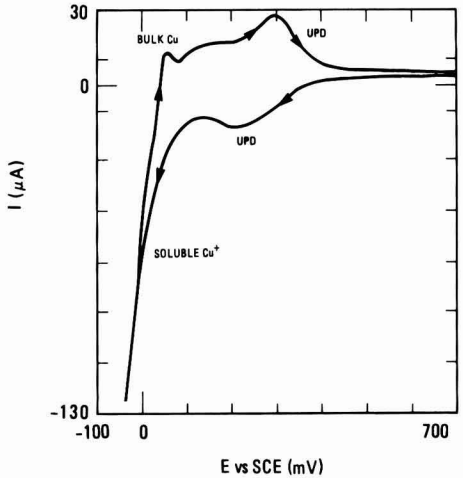


Fig. 3. Cyclic voltammogram of underpotential deposition of Cu on polycrystalline Au rotating disk electrode. The electrolyte consisted of 0.1M H_2SO_4 and 0.1M $CuSO_4$. A sweep rate of 50 mV/s and a rotation speed of 2000 rpm were used.

Results and Discussion

A cyclic voltammogram obtained during underpotential deposition of Cu on Au from an electrolyte consisting of 0.1*M* $CuSO_4$ in 0.1*M* H_2SO_4 is shown in Fig. 3. The potential was swept from 700 to −35 mV, SCE at a rate of 50 mV/s, and the RDE rotation speed was at 2000 rpm. Bulk Cu deposition began at approximately −35 mV and resulted in the small stripping peak centered at 0 mV; the amplitude of this stripping peak increased as the reversal potential was increased in the cathodic direction. The broad anodic peak centered at 300 mV is due to stripping UPD Cu from the Au surface. Approximately 4.61×10^{-4} C/cm^2 of anodic charge was removed from the Au surface during stripping, which corresponds to 1.06 monolayers of Cu. Apparently, surface alloy formation was minimal. However, three times as much charge was passed during the cathodic portion of the potential cycle. The cathodic charge in excess of that required for the UPD is believed to have resulted in formation of soluble Cu^+. Cyclic voltammograms at slower sweep rates, such as those shown in Ref. (3), have more well-defined UPD deposition and stripping peaks; a fast sweep rate was used here to avoid excessive diffusion of Cu into the Au surface (3).

Impedance spectra were obtained at electrode potentials of 0, 50, 100, and 200 mV and at each concentration level of Cu^{2+}. In Fig. 4a and 4b, experimental data obtained at a Cu^{2+} concentration of 0.01*M* and a potential of 0 mV are represented by points and compared to the theoretical model (solid line). This electrosorption process clearly exhibits the characteristics of the mechanism shown in Eq. [14] and [15], which involves formation of Cu^+; the ratio ρ/R_p is greater than unity. Furthermore, the dramatic increase in cathodic current near 0 mV shown in Fig. 1 is attributed to Cu^+ formation; interpretations of impedance spectra and the cyclic voltammogram are consistent. For comparison, data obtained at the same concentration and a more anodic potential, 100 mV, are shown in Fig. 5a and 5b. Changes in potential alter observed impedance spectra of the UPD process dramatically. The ratio of ρ/R_p calculated from Fig. 5a is almost unity.

Figures 6 and 7 show the experimentally determined values of model parameters as a function of electrode potential at Cu^{2+} concentrations of 0.01 and 0.1*M*, respectively. The cell resistance, R_s, is independent of electrode potential, while all other parameters appear to have a strong dependence on this variable. Variations in R_p and ρ with potential are considered to be significant since these parameters have standard deviations of less than 1% of the absolute parameter values. However, variations in C_p and τ with potential have a much larger error associated with them. Consequently, it is inappropriate to use Eq. [22] to calculate rate constants.

Values of ρ are slightly greater than values of R_p over the entire potential range investigated, which is indicative of the mechanism given in Eq. [14] and [15]. However, in some cases the differences are too small to be reflected in tabulated values (Table II). Such differences give rise to two distinct minima observed in spectra such as those

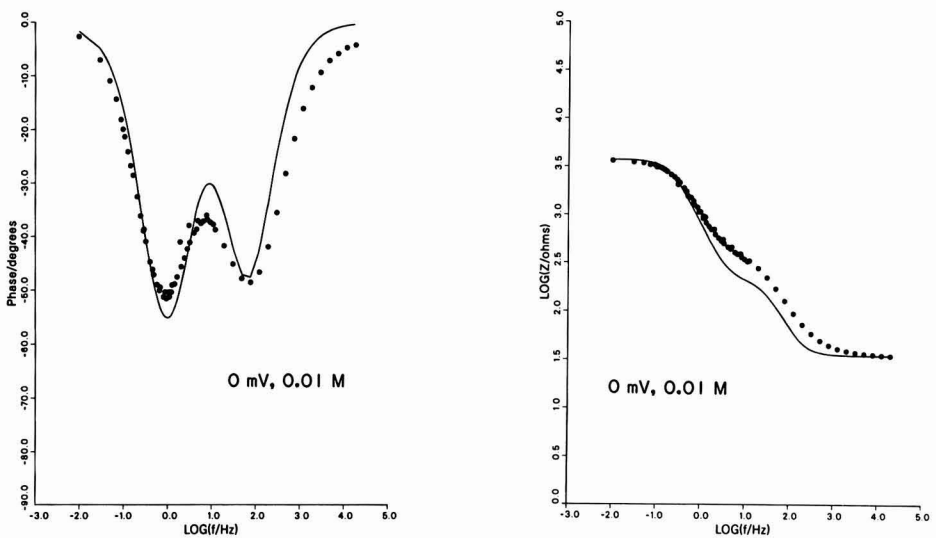
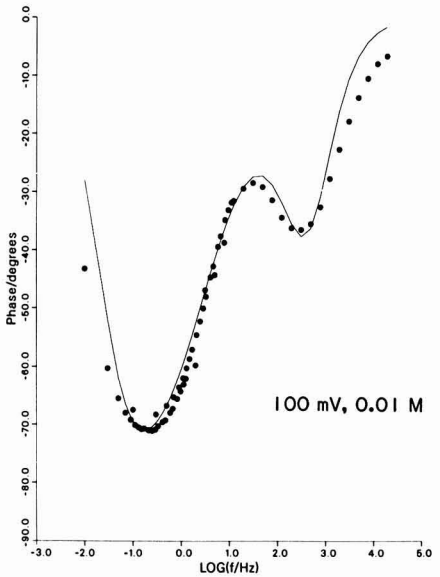


Fig. 4. a (left): A comparison of the theoretical Bode phase plot (solid line) and experimental data (points) for Cu electrosorption on Au at 0 mV. The electrolyte consisted of 0.1M H_2SO_4 and 0.01M $CuSO_4$. Parameter values were $R_s = 35\Omega$, $R_p = 205\Omega$, $C_p = 30\ \mu F$, $\rho = 229\Omega$, and $\tau = 0.048$s. b (right): A comparison of the theoretical Bode amplitude plot (solid line) to experimental data (points) at the same conditions as Fig. 4a.



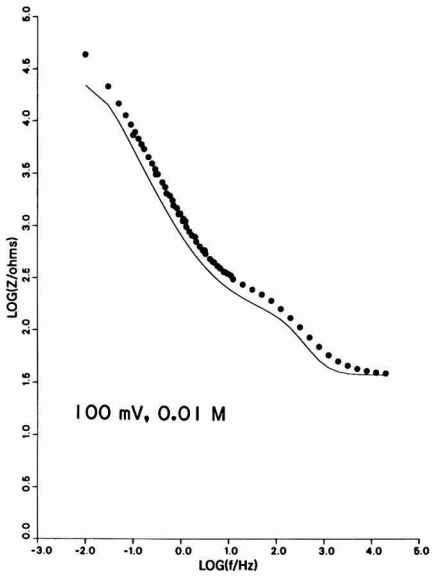


Fig. 5. a (left): A comparison of the theoretical Bode phase plot (solid line) and experimental data (points) for Cu electrosorption on Au at 100 mV. The electrolyte consisted of 0.1M H_2SO_4 and 0.01M $CuSO_4$. Parameter values were $R_s = 35\Omega$, $R_p = 109\Omega$, $C_p = 9\ \mu F$, $\rho = 111\Omega$, and $\tau = 0.078$s. b (right): A comparison of the theoretical Bode amplitude plot (solid line) to experimental data (points) at the same conditions as Fig. 5a.

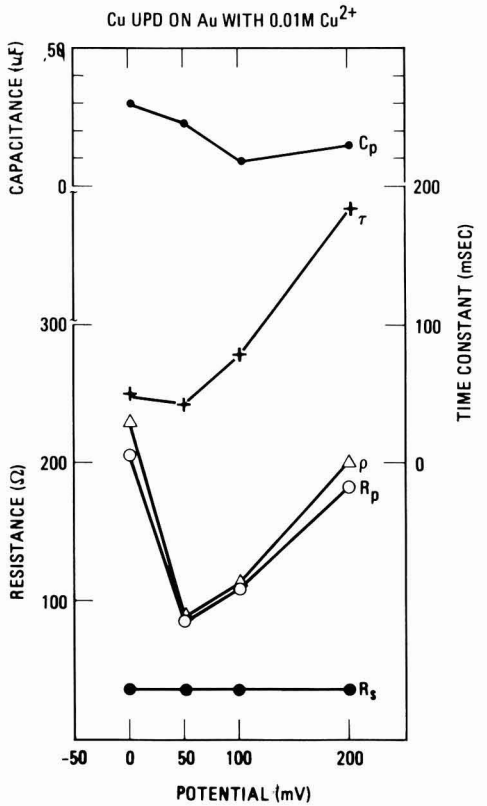


Fig. 6. Potential dependence of impedance model parameters at a $CuSO_4$ concentration of 0.01M.

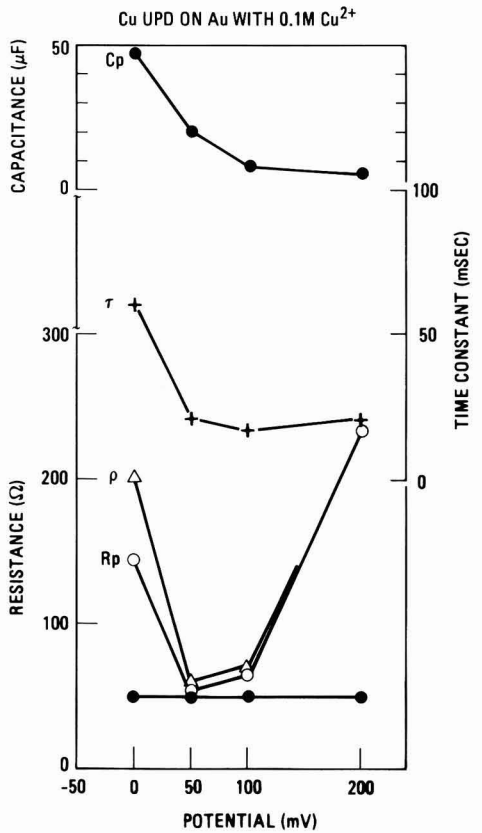


Fig. 7. Potential dependence of impedance model parameters at a $CuSO_4$ concentration of 0.1M.

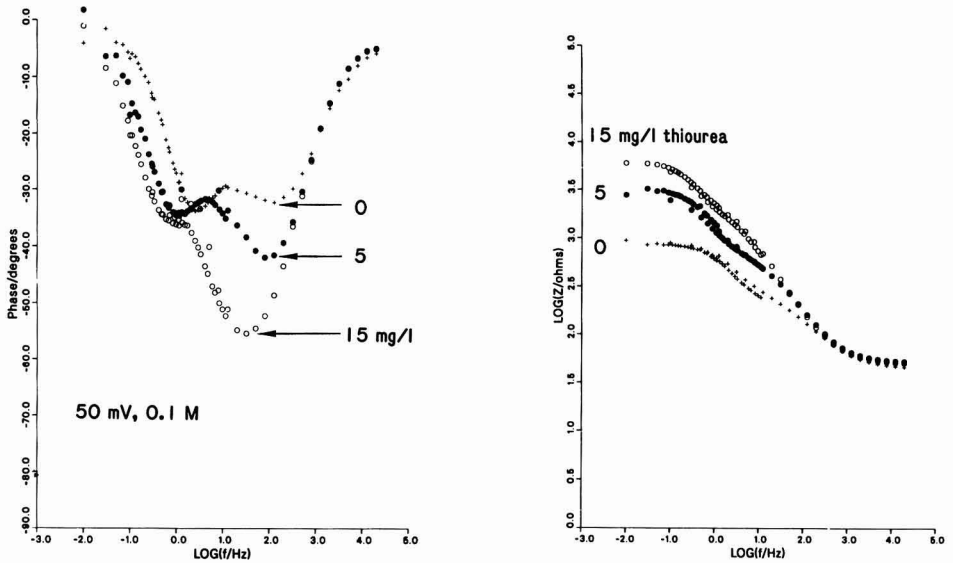


Fig. 8. a (left): Effect of thiourea on impedance spectra (Bode phase plots) at a potential of 50 mV. The electrolyte consisted 0.1M H_2SO_4, 0.1M $CuSO_4$, and thiourea. Data points represent thiourea concentrations of 0 (crosses), 5 (closed circles), and 15 (open circles) mg/liter. b (right): Effect of thiourea on impedance spectra (Bode amplitude plots) at the same conditions as Fig. 8a. Data points represent thiourea concentrations of 0 (crosses), 5 (closed circles), and 15 (open circles) g/liter.

shown in Fig. 4a and 5a. The simple adsorption process given in Eq. [1] cannot account for such spectra or the difference between ρ and R_p. The rate of dissolution of Cu$^+$ responsible for the difference in R_p and ρ would be difficult to detect in a ring-disk experiment (13).

Charge transfer resistances for bulk deposition do not exhibit minima and decrease with increasing cathodic potential (12). However, in the cases of Pb and Tl electrosorption, the observed charge transfer resistances do pass through minima (4). In these cases of simple electrosorption, the reason can be found by inspection of Eq. [11]. At the limit of infinite cathodic potential, k_f becomes infinite while k_b becomes zero. Alternatively, at the limit of infinite anodic potential, k_b becomes infinite while k_f becomes zero. At both extremes, the charge transfer resistance, R_p, approaches infinity and the rate of electron transfer drops to zero. At potentials between these limits, R_p passes through a finite, minimum value. Rationalization of the minima in R_p and ρ are observed in Fig. 6 and 7 near 50 mV is more difficult because of the complexity of Eq. [19]. The equilibrium constant K is assumed to be of

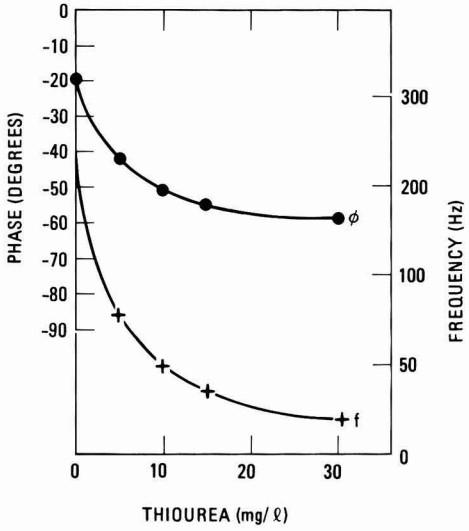


Fig. 9. Empirical effect of thiourea on the high frequency minimum (peak) in the Bode phase plot at the same conditions as Fig. 8a. The depth of the minimum in phase is represented by the curve labeled ϕ and the position of this minimum on the frequency axis is represented by the curve labeled f.

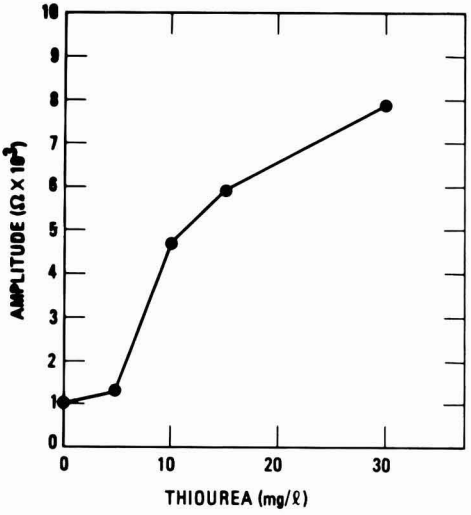


Fig. 10. Empirical effect of thiourea on the impedance amplitude at the low frequency limit. Same conditions as Fig. 8a.

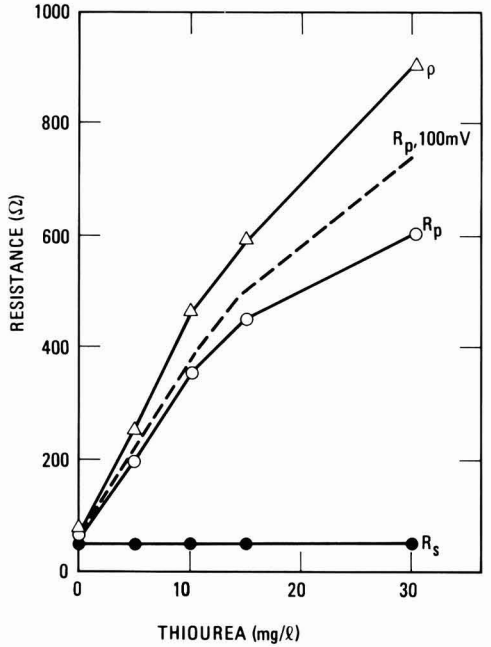


Fig. 11. Effect of thiourea on the impedance model parameters at the same conditions as Fig. 8a. The resistances R_p and ρ increase dramatically with thiourea concentration, while the cell resistance, R_s, remains constant.

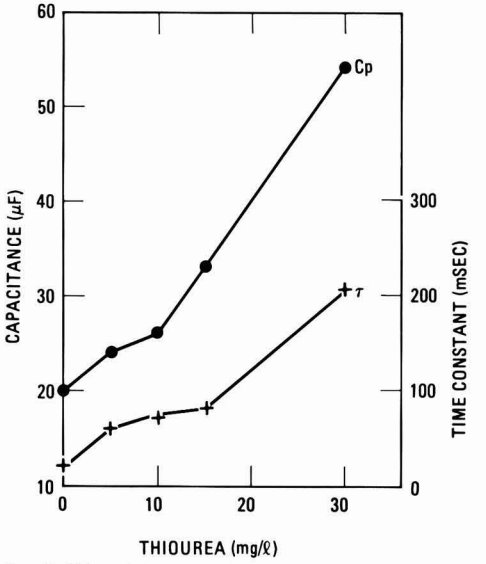


Fig. 12. Effect of thiourea on the impedance model parameters at the same conditions as Fig. 8a.

the form $K = C \exp(-cE)$, so $K' = -cC \exp(-cE)$. Therefore, the denominator of Eq. [19] is proportional to the difference $(a + b)k_h + k - cKk_f M^{2+}$, which becomes zero as the potential increases in the cathodic direction to some limit; at this limit R_p becomes infinite. At intermediate potentials, R_p passes through a finite, minimum value, while at large anodic potentials it approaches infinity.

Impedance spectra showing the effects of thiourea additions to the electrolyte are shown in Fig. 8a and 8b. These data were obtained at a Cu^{2+} concentration of 0.1*M*, thiourea concentrations of 0, 5, and 15 mg/liter, and an electrode potential of 50 mV. Note that thiourea increases the depth and changes the position of the high frequency minimum in the Bode phase plot (Fig. 8a and 9). Furthermore, the amplitude of the complex impedance increases dramatically at the low frequency limit (Fig. 8b and 10). These changes translate into increases in the charge transfer resistances R_p and ρ, as expected (Fig. 11). The rate constants k_f and k_h are proportional to the active area available to discharge metal cations. Coadsorption of thiourea during formation of the UPD would decrease the active area by blocking sites, thereby decreasing the magnitude of rate constants and increasing R_p and ρ. Data also indicate that the double layer capacitance, C_p, and the low frequency time constant, τ, increase with thiourea concentration (Fig. 12). This result for C_p is surprising since organic additives have been shown to decrease the double-layer capacitance during Ni deposition (17) and since it implies that thiourea increases the surface charge density on the electrode.

It is important to note that Cl^- is present in most copper plating solutions at concentrations of about 30 ppm and can effect grain refinement of the electrodeposit significantly. This experimental technique might be useful in understanding the role of Cl^- during electrodeposition. Furthermore, there is strong evidence that thiourea is electrochemically decomposed at the cathode (18). This decomposition results in incorporation of sulfur, but no carbon, into the electrodeposit. Note that thiourea decomposition was not considered in the electrokinetic model presented. However, sulfide formation at the electrode-electrolyte interface could help explain the unexpected increase in double-layer capacitance with increasing thiourea concentration. Such films would exhibit relatively high dielectric strengths.

These measurements suggest that ac impedance could be used as a means of monitoring total organic additive concentration in copper electroplating baths or as a means of verifying electrolyte purity in additive-free copper electroforming baths. Detection of such low levels of thiourea and other surface active organics by spectroscopic means is not practical at the present time.

Summary

Formation of a Cu UPD on Au has been studied by ac impedance. Spectra are characterized by two capacitive peaks in the Bode phase plot. The high frequency peak is associated with both the double-layer capacitance and the resistance to charge transfer which accompanies electrosorption. In contrast, the low frequency time constant is due only to relaxation phenomena associated with charge transfer. Data are consistent with an electrosorption mechanism which involves simultaneous formation of the UPD layer and a soluble intermediate. A method is presented for calculating model parameters from the impedance spectra.

Adsorbed thiourea was found to have a dramatic effect on the high frequency peak in the Bode phase plot. These measurements suggest that ac impedance could be used as a means of monitoring total organic additive concentration in copper electroplating baths or as a means of verifying electrolyte purity in additive-free copper electroforming baths. Detection of such low levels of thiourea and other surface active organics by spectroscopic means is not practical at the present time.

Acknowledgments

This work is supported by the U. S. Department of Energy, DOE, under Contract no. DE-AC04-76DP00789. The support and technical guidance of D. A. Nissen are deeply appreciated.

Manuscript submitted March 12, 1985; revised manuscript received *ca.* June 5, 1985. This was Paper 237 presented at the Las Vegas, Nevada, Meeting of the Society, Oct. 13-18, 1985.

Sandia National Laboratories assisted in meeting the publication costs of this article.

REFERENCES

1. J. C. Farmer and R. H. Muller, *This Journal*, **132,** 39 (1985).
2. S. Swathirajan, H. Mizota, and S. Bruckenstein, *J. Phys. Chem.*, **86,** 2480 (1982).
3. H. O. Beckmann, H. Gerischer, D. M. Kolb, and G. Lehmpfuhl, *Faraday Sympos.*, **12,** 53 (1977).
4. M. Klimmeck and K. Juttner, *Electrochim. Acta*, **27,** 83 (1982).
5. K. Nihei, T. Ohsaka, and K. Anzai, *Denki Kagaku*, **47,** 415 (1979).
6. K. Engelsmann, W. J. Lorenz, and E. Schmidt, *J. Electroanal. Chem.*, **114,** 1 (1980).
7. W. J. Lorenz, H. D. Hermann, N. Wuthrich, and F. Hilbert, *This Journal*, **121,** 1167 (1974).
8. S. Swathirajan and S. Bruckenstein, *J. Electroanal. Chem.*, **146,** 137 (1983).
9. W. Smyrl, in "Electrochemical Corrosion Testing," F. Mansfeld and U. Bertocci, Editors, pp. 199-214, American Society for Testing and Materials, Philadelphia (1981).
10. D. R. Turner and G. R. Johnson, *This Journal*, **109,** 798 (1962).
11. N. J. Spiliotis, in "Metal Finishing Guidebook and Directory," 46th ed., p. 216, Metals and Plastics Publications, Hackensack, NJ (1978).
12. I. Epelboin and R. Wiart, *This Journal*, **118,** 1577 (1971).
13. S. Bruckenstein and G. W. Tindall, *Anal. Chem.*, **40,** 1051 (1968).
14. B. J. Bowles, *Electrochim. Acta*, **15,** 589 (1970).
15. F. Mansfeld, *Corrosion*, **36,** 301 (1981).
16. G. E. P. Box and G. A. Coutie, *Proc. IEE*, **103,** 100 (1956).
17. J. C. Farmer and H. R. Johnson, in "Proceedings of the 11th World Congress on Metal Finishing," pp. 343-355, Jerusalem, Israel, Oct. 21-26, 1984.
18. J. Llopis, J. M. Gamboa, and L. Arizmendi, in "CITCE Meeting Proceedings," pp. 448-458, Paris (1957).

On the Evolution of Concepts Concerning Events at the Semiconductor/Solution Interface

John O'M. Bockris*

Department of Chemistry, Texas A&M University, College Station, Texas 77843

Shahed U. M. Khan*

Department of Chemistry, Duquesne University, Pittsburgh, Pennsylvania 15282

ABSTRACT

The conventional determination of the Fermi level of electrons in solution is found incorrect. One should not utilize the energy corresponding to the redox potential on the vacuum scale to be equal to the energy of the Fermi level of metal or semiconductor at equilibrium. It is activated vibrational states within ions (rather than fluctuations of energy in the ground vibrational state) which should overlap with the electronic states in the semiconductor. Electronic states in solution relevant to an electrode reaction are not gaussian but are boltzmannian. The Schottky model is sometimes (perhaps often) not applicable to the semiconductor/solution interface. Metallic catalysts in photoelectrochemistry are effective by causing a change of rate-determining step to that at the metal/solution interface.

Increasing investigations of the semiconductor/solution interface suggest that there is need to modify some of the classical concepts. It is desired in this paper to discuss the evolution of these concepts.

The Fermi Level in Solution

The equilibrium between a metal, or semiconductor, and a solution can be expressed in various terms. A quite general relationship states that there must be an equality of the electrochemical potentials $\bar{\mu}_i$ for each given entity between the values in the solid phase (m) and the value in the solution (s). Thus

$$\bar{\mu}_i^{sol} = \bar{\mu}_i^{solid} \qquad \bar{\mu}_i^{m} = \bar{\mu}_i^{s} \qquad [1]$$

If one takes the electrons as the species concerned, the advantage is that there is a named concept with which one associates $\bar{\mu}^m$ (m here is taken to mean solid electronic conductor, *i.e.*, it may be a semiconductor as well as a metal). This is the Fermi energy of the electron in the solid.

There is considerable conceptual confusion in relating the meaning of $\bar{\mu}_e^m$ to the concept of the Fermi level energy.

Thus, a simple concept of the Fermi energy, normally given in books in solid-state physics, is to take the approximation that the electron is "free" in the conductivity band. Then, in respect to the bottom of the conduction band, the maximum kinetic energy in the conductivity band is easily shown (7b) to be $n^2h^2/8m_e\lambda^2$, where these quantities have their usual meaning. What is meant by the chemical potential, μ_e^m, is the work done to bring an electron from infinity to this maximum kinetic energy level in the special and unnatural case in which both the surface potential is zero and the charge on the metal is zero. The physical meaning of this μ_e^m (the chemical potential of the electron in the bulk of the metal) for electrons in the conductivity band is the interaction which these electrons have with the surrounding metal atom cores.

The relationship between a kinetic Fermi energy $E_{f,m}$ and $\bar{\mu}_e^m$ (or the corresponding μ_e^m for an unreal case where the metal is uncharged and there is no surface potential) is that the larger the kinetic Fermi energy, the smaller is $\bar{\mu}_e^m$ (see Fig. 1).

In order to express the equilibrium between metal or semiconductor and solution, it is necessary to know the value of the corresponding $\bar{\mu}_e^s$, the electrochemical potential of the electron in solution. In the normal view, accepted up to now, this $\bar{\mu}_e^s$ has been identified with the redox potential (on the vacuum scale) of redox process occurring across the interface.

The origin of this approach relates to a paper by Gerischer (1). In the original derivation, the artificial and unusual case was taken by Gerischer, or perhaps the simplification, that there was a charge-free surface, and also that the solution had a zero value of surface potential, *i.e.*, no dipole potential across the solution-vacuum interface such that $\bar{\mu}_e^s$ becomes equal to μ_e^s. Later, however, such a concept has been utilized for real situation (2, 3) where $\chi_s \neq 0$ and the Fermi level of solution μ_e^s is equated to the negative value of energy corresponding to vacuum-scale redox potential (4, 5), $-n\mathbf{F}V_{redox}$ (vacuum scale).

*Electrochemical Society Active Member.

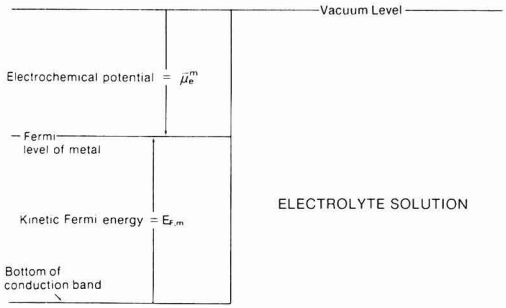


Fig. 1. A schematic diagram to show the kinetic Fermi energy, $E_{F,m}$ and the electrochemical potential of electron, $\bar{\mu}_e^m$, in a metal.

It has been shown (13) that the negative value of energy corresponding to the redox potential in the vacuum scale, $-n\mathbf{F}V_{redox}$ (vacuum scale), is indeed equal to this μ_e^s but not to the $\bar{\mu}_e^s$. The normal practice, from this beginning, is to find out V_{redox} (vacuum scale) (simply done by taking the value of the hydrogen scale and adding to it the value of the hydrogen electrode on the vacuum scale, approximately 4.5 ± 0.3V.

The difficulty comes from the fact that, indeed, solutions neither have zero charge when they are in equilibrium with metals or semiconductors, nor do they have a zero value of the surface potential. Under these circumstances therefore, the identification that $\bar{\mu}_e^s = -n\mathbf{F}V_{redox}$ (vacuum scale) fails. The true identification is that $-n\mathbf{F}V_{redox}$ (vacuum scale) = μ_e^s, not $\bar{\mu}_e^s$.

This matter is one of major importance because of the frequent erroneous use of this $-n\mathbf{F}V_{redox}$ (vacuum scale) in semiconductor photoelectrochemistry to identify as the Fermi level in solution $\bar{\mu}_e^s$ (6-10).

1. Further, the Fermi level in solution must be associated with a "free" movement of electrons within the phase, so that the idea of a "kinetic Fermi energy" can exist.

2. Corresponding to this, it is difficult to conceive of the idea of a Fermi level in a solution in which energy bands for electrons or holes have no real existence.[1]

In applying Fermi level concepts to an ionic solution and the electrons which characterize the electronic states of ions in solution, criteria 1 and 2 do not apply, *i.e.*, there is no kinetic energy of free electrons in ions, since the electrons are in the bound state in the ion and cannot contribute to electronic conductivity in solution; and bands in the normal sense do not arise.

Such considerations must not be confused with the idea of spectral bands in water (11a, 18) which correspond to levels associated with atomic or molecular movements and have a radically different meaning from conduction bands for electrons in water. Such concepts would have no remote relevance even in a solution which contained solvated electrons (11b). The carriers (electrons or holes) have no relevance to the electrons in the orbitals within ions in redox systems where the energy considerations are not band-like.

Thus, in summary, it is, at the least, unrealistic, and, at the most, fundamentally incorrect, to discuss a Fermi level or Fermi energy of electrons and holes in ionic solutions.

3. The idea of the energy of a Fermi level characterizing electronic states in solution, and the equating of it for some electron transfer equilibrium to the energy of a Fermi level in the electrode, goes back to concepts appropriate to the metal/metal and metal/semiconductor interfaces. Here, consideration of equalization of Fermi levels in the two phases is correct, because there are free carriers (electrons or holes) in each phase, and each phase is an electronic conductor. The free electrons from one metal phase to another metal or semiconductor phase can have a conductive flow at the interface. However, the condition which governs the transfer of electrons and holes at metal or semiconductor/solution interfaces is that the transfer is isoenergetic with respect to the particle in transfer and involves an electron transfer reaction. At the metal/metal, or metal/semiconductor, interfaces, there is no transfer from one phase to a single particle, in which specific quantum levels exist. For the metal/metal and metal/semiconductor interfaces, it is a matter of conductive flow (across a gradient of electrochemical potential) in free electron conduction. At the metal/solution and semiconductor/solution interfaces, it is a matter of a reaction between an individual particle in the solution and electrons in the bands of the electronic conductor. The energy states in solution which are relevant and which must be equal to the energy of the carriers in the semiconductor are the energy of vibronic (vibrational and electronic) states in ions in solution when they are activated[2] (for which an activation barrier exists). Hence, electron transfer at the electrode/solution interface occurs in the form of an electron transfer reaction (12), but not as a conductive flow, like that in metal/metal or semiconductor/metal interfaces.

4. Finally, in respect to the value of $\bar{\mu}_e^s$ (which exists, conceptually, for any phase independently of whether, in solution, it should be associated with Fermi level concepts), it has been shown elsewhere (13-15) that for a real interface it should be given by

$$\bar{\mu}_e^s = -n\mathbf{F}V_{redox}(\text{vacuum scale}) - n\mathbf{F}\phi^s = E_{F,redox} \quad [2]$$

where the inner potential of solution, ϕ^s, is not experimentally determinable and is at present not known. Equation [2] clearly proves that one cannot use vacuum-scale redox potential as the Fermi level in solution to equate with that in metal or in semiconductor at equilibrium.

Is the Fermi Level in Solution a Necessary Concept?

In metal-semiconductor contacts, the equilibrium condition is normally regarded as being given by an equality of the Fermi levels. Such a condition provides a reasonable and convenient way of knowing the energy levels in one phase if one knows the energy levels in the other.

The normal approach in electrochemistry is to imitate the situation for the metal-metal and metal-semiconductor systems. Knowing the electrochemical potential in the solid phase, it has been thought convenient to utilize the Fermi level concept in solution (discussed above) in order to assess, or determine, the equilibrium position with respect to electrons in the solid and liquid phases.

The aspect of the validity of applying Fermi-like concepts to solutions (and, if valid, then the question remains about its numerical value) has been dealt with in the previous section. However, there exists a different kind of question, which may be put forward as follows. Let it be assumed that the Fermi level concept applies to solution, and that the difficulty of the numerical determination of it can be overcome (15b); then the question still remains. Is it a useful concept for kinetic and mechanistic electrochemistry where the principal ideas are quantum-oriented and where the thermodynamic states are utilized only as reference to beginning states, but where the transitions concerned are from quantum levels in the electrode to quantum levels in the solution? The most desirable and useful quantities to know are the electronic donor and acceptor energy levels of the ions in solution. To determine these, one needs to know the difference of energy, ΔE_0, between the activated and the ground state of acceptor or donor ions in solution and then to express this with respect to the energy of a clearly defined reference state. The best reference state at present seems to be

[1] Thus, in theoretical work of Williams *et al.* (11a), a conduction level for electrons in water is referred to, but this is almost at the vacuum level.

[2] One should not consider that the activated state is the excited electronic state of the ion, *e.g.*, in a transition metal-ion due, say, to d-d transition. Such a transition involves very high energy, *e.g.*, of the order of 1.5 eV. Activated states in electrochemical reactions correspond to excited vibrational states of the ion-solvent bond in the ground electronic state of the ion.

the stationary electron at infinity in a vacuum. For example, when Fe^{3+} (aq) ion is in solution, one can determine this difference in energy, ΔE_0, by using the following cycle

$$\begin{array}{ccc} Fe^{3+}(aq) + M(e)(soln) & \xrightarrow{\Delta E_0} & Fe^{*2+}\ldots aq \\ \uparrow -\phi^{ec} - \chi^s & & \downarrow -\Delta F^{\#}(2) \\ Fe^{3+}(aq) + e_{vac} & & Fe^{2+}(aq) \\ \uparrow \Delta F_s(3) + 3\chi^s & & \downarrow -\{\Delta F_s(2) + 2\chi^s\} \\ Fe^{3+}(Vac) + e_{vac} & \xleftarrow{I} & Fe^{2+}(Vac) \end{array} \quad [3]$$

Hence

$$\Delta E_0 = \Phi^{ec} + \Delta F^{\#}(2) + \Delta F_s(2) - \Delta F_s(3) - I \quad [4]$$

where $\Delta F^{\#}(2)$ is the free energy of activation of ($Fe^{*2+}\ldots$ aq), and $\Delta F_s(2)$ and $\Delta F_s(3)$ are the free energies of solvation of Fe^{2+} and Fe^{3+} ions, respectively. I is the ionization energy of Fe^{2+} ions and χ^s is the surface potential of solution.

Knowing ΔE_0 and taking the activated electronic level of Fe^{2+}(aq) to be equal in potential energy to the energy of the Fermi level in the electronic conductor, one can calculate the vibronic energies of the ground state of the acceptor ions in solution with respect to the reference level in vacuum, E_0, as (see Fig. 2)

$$E_0 = -\Phi^{ec} + \Delta E_0 \quad [5]$$

Electronic Energy Distribution in Solution

It has been conventional for workers in the field of photoelectrochemistry to follow Russian and German workers in portraying the energy distribution in solution in the form of a gaussian distribution (1, 6-8). Thus, it was thought (16a) that there would be a gap between the vibrational energy levels in solution, as there is a gap between the vibrational energy states of molecules in the gas phase. The energies referred to are those of the electronic states in the ions, as affected by the vibrational-librational levels of the ion-solvent complex (*i.e.*, vibronic states).

It was argued (16a) that the order of the energy difference (*e.g.*, for H_3O^+) between vibrational levels is around 0.5 eV, and, as the energy of the average oscillator in solution is kT, the probability of energy being transferred to levels above the ground-state level must be negligible. Such a concept was originated in the work of Levich (6), since he erroneously avoided the fact that thermal equilibrium between the ion-solvent bond and the surrounding solvent molecules can give rise to sufficient probability of having the required energy of activation.

On the basis of these concepts, the ground-state vibrational level in the first electronic state was the only one which was considered to be relevant to electron transfer processes at electrodes. In order that the range of energies needed in electrochemical reactions could be obtained, it was thought that fluctuations of the energy around the ground state would be necessary. As fluctuations give rise to gaussian distributions, the energy distribution was drawn in the form of a gaussian bell-shaped curve (1-3, 6-8) (see Fig. 3)[3] where the potential energy is considered to vary both around the ground state to an equal degree.

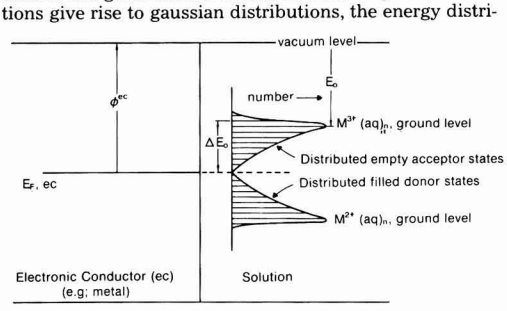


Fig. 2. Maxwellian distribution in solution

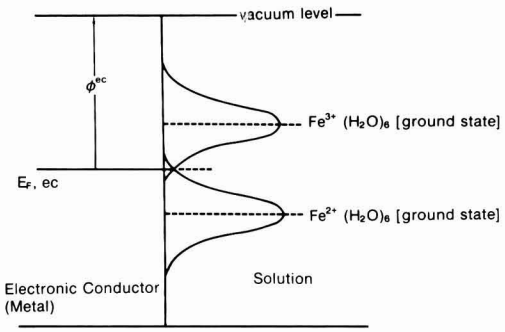


Fig. 3. Gaussian distribution in solution

However, the thing which in fact varies when an ion is in solution and then causes the energy of the central ion to vary is not this ground state and its perturbational fluctuation but the normal boltzmannian distribution of the energy in all the vibrational states of the ion-solvent bonds. This energy is not symmetrically distributed around the central point (*i.e.*, the ground state) but is distributed maxwellianly in the normal way in all presentations of molecular mechanics in solution, except those associated with the Levich-Marcus-Gerischer viewpoint.

Hence, the gaussian concept must now be viewed as nugatory. A very simple and general piece of evidence against an effectively gaussian distribution is that it conforms to the relation (16)

$$\ln i_c = \ln A - \frac{(E_s + e_0\eta_c)^2}{4E_s kT} \quad [6]$$

where A is a constant, E_s is the solvent reorganization energy of the ion, i_c is the cathodic current density, η_c is the cathodic overpotential, and e_0 is the electronic charge. However, the experimental evidence is clear: the current density/overpotential relation usually observed is boltzmannian, *i.e.*

$$\ln i = B - \frac{E_A + \beta e_0 n}{kT} \quad [7]$$

where B is a constant. Equation [7] is not consistent with a gaussian distribution of the relevant energy states of ions in solution but is consistent with the boltzmannian distribution of states in solution (Fig. 2).[4]

[3]Although conceptually, it seems consistent with the literature development as above, it must be mentioned that the gaussian type of energy distribution arises also in a quite different way. Thus, Eq. [6]—which is usually put forward on the basis of some rather complicated considerations of nonequilibrium thermodynamics and even as quantum mechanical concepts (16a)—arises from very simple considerations of the stretching of bonds in an electrode reaction (16b). In fact, the only necessary condition whereby one obtains Eq. [6] is the energy-distance relation of these bonds to be harmonic (*i.e.*, quadratic) and that no more complex and anharmonic relationships should be taken into account.

This is the origin of why Eq. [6] does not give rise to a Tafel equation. To obtain the latter (universally observed), it is necessary to have a more complex energy-distance relationship to have the activated state necessary for electron transfer and their extension from the equilibrium state, and this relationship then gives rise to a non-gaussian distribution. Alternatively (16c), the energy states which are available to electrons in solution are simply regarded as boltzmannian on the basis that they are the normally distributed quantum states in the ion-solvent bond and do not arise due to fluctuations of the ground state.

[4]The evidence for Eq. [7] is overwhelming in terms of very many systems of different types (17a). The counterevidence consists of a paper by Saveant and Tessier (17b) in which results are given for an undefined organic reaction in which, correspondingly, the rate-determining step is unknown.

Gaussian states are essentially error states and represent the deviation from the equilibrium states which are the subject of the boltzmannian distributions. Gaussian distributions are associated with every one of these boltzmannian states.

Treatments in electrode kinetics should not be given in terms of thermodynamic concepts, representing net energy changes.

A gaussian treatment neglects states above the ground vibrational states. There is, in this treatment, basically one state, corresponding to the ground-state vibrational level of the ion-solvent bond: the ground state. The other states are obtained by fluctuating this ground state.

The energy levels in the ion-solvent complexes are likely to represent an energy continuum for electrons, acceptor or donor, which are to be interchanged between the entities in solution and those in the electrode. This is a result of the quasi-continuum nature in respect to energy levels in solution, as indicated by the broadness of the vibrational spectra observed (18, 19).

Apart from bringing of consistency to the situation in respect to energy distribution and generation of activated states, it is desirable to point out that, were fluctuations of the energy of the ground state to be the origin of electronic states in solution, it would seem unlikely that these could occur at a rate sufficient to meet the needs of even the middle range (mA-cm^{-2}) of rates met within chemical reactions. Thus, one could estimate the orders of magnitude for the average rate (*i.e.*, frequency) of activation needed for an ion in solution in the following way.

The number of water molecules which have an energy equal to, say, the activation energy, E_a, of proton discharge on Hg at the reversible potential (0.78 eV) is given by

$$N_{E_a} = N_{E_0} e^{-E_a/kT} = \frac{1}{18} \times 6.0 \times 10^{23} \times e^{-0.78/0.025} = 10^9 \qquad [8]$$

molecules per cubic centimeter (where N_{E_0} is the number of molecules per mole in the ground state energy, E_0).

These activated molecules are, therefore, on the average, 10^{-3} cm apart (since 10^9 activated molecules occupy one cubic centimeter). Hence, in a plane of area 1 cm^2, there will be 10^6 activated molecules. If they have a diffusion coefficient, $D = 2.5 \times 10^{-5}$ cm^2-s^{-1}, the time of diffusion over a distance $\Delta = 10^{-3}$ cm can be obtained as

$$\tau = \frac{\Delta^2}{2D} = 0.02\text{s} \qquad [9]$$

Hence, it is possible to deliver to 1 cm^2 of an electrode surface some 5×10^7 molecules [$= (N_{E_a})^{2/3}/\tau = 10^6/0.02$] with an energy around 0.78 eV in 1s. The number of reactant H_3O^+ ions needed to be available at the activated state per unit time in the reaction plane for an i_0 value of 10^{-12} A-cm^{-2} (a rate which corresponds to the activation energy given) is $i_0 N_A/n\mathbf{F} = (10^{-12}/10^5) \times 6.6 \times 10^{23} = (6.6 \times 10^6$ ion-cm^{-2}-s^{-1}). A sufficient number of appropriately activated molecules can, therefore, be available.[5] Though the calculation is rough in nature, it serves, as an order of magnitude level, to show that the rate of supply of activated ions from solution is not unfeasible by thermal activation. Thus, a Maxwell-Boltzmann distribution of donor and acceptor electronic states (20) (see Fig. 1) in solution is possible.

The Schottky Barrier Model

A dominating thought in the electrochemistry of semiconductors has been the so-called Schottky barrier at the semiconductor/solution interface.

It is traditional in the field of semiconductor/solution photoelectrochemistry to take such a barrier as existing inside the semiconductor only, due to difference between the Fermi level in the semiconductor and that in the solution before the equilibrium is established. However, after the equilibrium is established, it is thought that the Fermi level of the semiconductor coincides with the Fermi level in solution and, thus, gives rise to the enhanced (or reduced) band bending (*i.e.*, the Schottky barrier), depending on the relative positions of the two Fermi levels (see Fig. 4) before the equilibrium is established.[6] Construction of such a barrier at the semiconductor/solution interface is unrealistic, since the existence of a Fermi-like level in solution is doubtful.

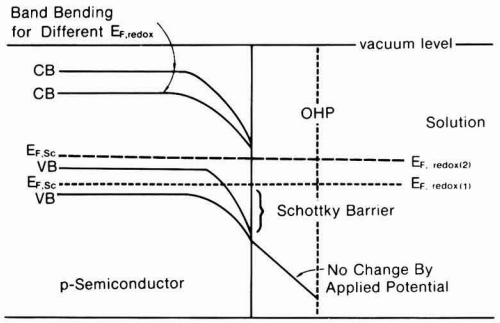


Fig. 4. Schottky barrier model at the interface

Green (21, 22) was the first to question the applicability of Schottky barrier concepts at the semiconductor/solution interface in respect to electrode kinetics. According to the Schottky barrier model, the potential drop inside the semiconductor (*i.e.*, band bending) varies with the externally applied potential, and the other part of the interphasial potential drop is that in the Helmholtz layer in the solution side of the interface which remains (almost) independent of the applied potential (see Fig. 5). The traditional treatments (1-3, 6-8) assume that the above situation nearly always obtains at the semiconductor/solution interface.

Such a treatment leads to a current/potential relationship of the form

$$\frac{\partial V}{\partial \log i} = \frac{RT}{\mathbf{F}} \qquad [10]$$

[6]When one discusses the potential distribution and the corresponding barrier, one talks about classical and equilibrium situation. The nonequilibrium situation gives rise to the fluctuating barrier which is not relevant for electron transfer kinetic studies. This is because the barrier fluctuates slower than the transfer time of electron across the interface. However, under illumination condition the degree of band bending will be less than dark equilibrium situation.

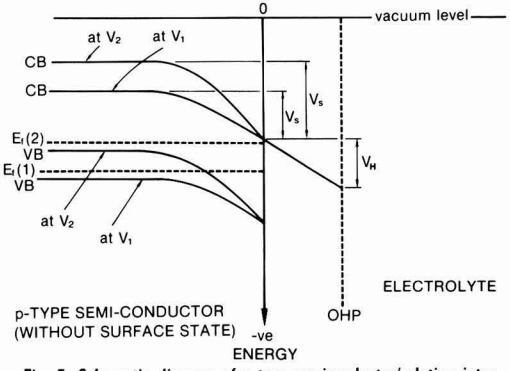


Fig. 5. Schematic diagram of p-type semiconductor/solution interface at two applied potentials, V_2 and V_1. The diagram shows that the potential drop (p.d.) in the Helmholtz layer exhibits no variation with applied potential and the potential varies inside the semiconductor only.

[5]This calculation which has been done here is independent of the value of i_0, i.e., if there were a reaction at an electrode, with an i_0 of 10 mA, where the current needed would be much more, it would not matter, because then the heat of activation would be very much less, and the probability of finding ions with the right energy will be correspondingly greater.

where V is the electrode potential. Green (21, 22) pointed out that the Schottky barrier considerations were dependent upon the absence of a limiting number of surface states. With the semiconductor in equilibrium, if the surface states exceeded about 3% of the total surface occupancy (*e.g.*, 10^{13} cm^{-2} since there will be 3.5×10^{14} sites available for molecular size of 3Å in 1 cm^2 of the surface), the changes in potential would be predominantly in the Helmholtz region and not in the space charge region (21, 22), and the pure Schottky barrier model will fail. Correspondingly, the Tafel slope of the dark reaction at semiconductor/solution interfaces would then become

$$\frac{\partial V}{\partial \log i} = \frac{2RT}{\mathbf{F}} \qquad [11]$$

which indicates a symmetry factor $\beta = 1/2$, as in regular electrode kinetics at metal. Such an observation at semiconductor solution interface indicates the presence of surface states of more than 10^{13} cm^{-2} and, hence, the metallization of the semiconductor. In such situations, variation of the potential will be mainly in the Helmholtz layer. Thus, whether the variation of potential is effective only in the semiconductor side of the interface in the Schottky barrier approximation depends upon the density of occupancy of surface states on the semiconductor.

In situations at the metal/semiconductor interfaces, there is no doubt about the existence of the Schottky barrier to electrons or holes and the variation of band bending (*i.e.*, potential) inside the semiconductor. However, in the case of reactions which are at the semiconductor/solution interface, such a situation may be exceptional. Two events may provoke the existence of surface states in addition to those associated with dangling bonds. One is the specific adsorption of anions and the solvent on the surface of the semiconductor. With hydrogen and oxygen evolution, this is particularly so because the adsorbed intermediate atom on the surface would cause further surface states. The numerical value characterizing the extent of such adsorption is not yet known, but it is reasonable to infer a high degree of adsorption from the published observations of anion adsorption at oxide/solution interfaces (23, 24). The adsorption is higher at nonmetals than in Hg, indicating the formation of charge transfer bonds at the surface. A large extent of specific adsorption at semiconductor/solution interfaces would indicate a high density of surface states and the breakdown of the Schottky barrier approximation. A degree of "metallization" would occur. Correspondingly, the presence of water at the semiconductor/solution interface may give rise to charge transfer bonds between the free antibonding orbitals which exist in oxygen and d-band positions in semiconductor oxides

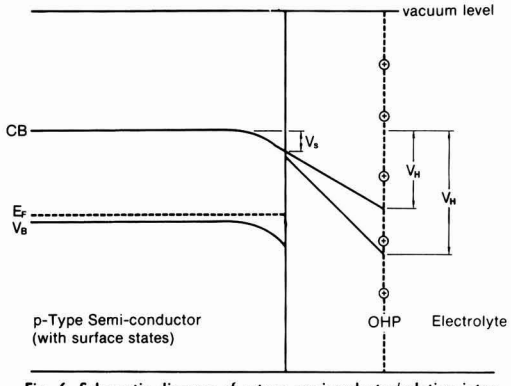


Fig. 6. Schematic diagram of p-type semiconductor/solution interface in presence of high density of surface states. No variation of potential drop (p.d.) inside the semiconductor, V_s, and hence no variation of Fermi level in the semiconductor (pinning); variation of p.d. occurs in the Helmholtz layer, V_H, with applied potential.

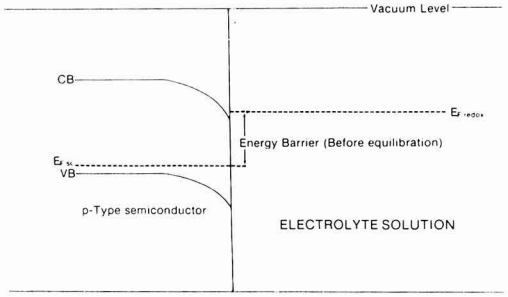


Fig. 7. The barrier for the electron transfer at the interface of semiconductor and redox electrolyte before equilibration of electron of two phases (classical view).

which contain transition metals (24) (*e.g.*, $LaNiO_3$) and, thus, may increase the density of surface states. Such metallization causes the potential to change over the Helmholtz double layer (see Fig. 6), rather than inside the semiconductor across the space charge region. The metallization also occurs if the doping density is very high, $> 10^{19}$ cm^{-3}.

Of course, there must be some p.d. inside all semiconductors; otherwise, they would behave effectively like metals under an applied potential. At present, it seems as though pure Schottky barrier models (25, 26) are applicable to the semiconductor/solution interface as an exception rather than the rule. Recent experiments on the measurement of capacity due to surface states and its dependence on potential even at n-TiO_2 electrodes (27) and other p-type electrodes (28) indicate a high concentration of surface states ($\geq 10^{13}$ cm^{-2}).

Another matter needing discussion is the identity of the so-called "barrier-to-electron passage" at a semiconductor/solution interface.

Thus, work which is normally carried out at the present time, particularly in photoelectrochemistry, normally regards this barrier in the following way. The thought is that, at the moment of immersion of a semiconductor into a solution, before equilibration of the electrons of the two phases has taken place, there will be a situation shown in Fig. 7, where the Fermi levels are at different positions. In this situation, this hypothetical momentary situation, the energy barrier for penetration of carriers outside the semiconductor is indicated in Fig. 7.

At a short time after the contact has been made, equilibration will arise, and the Schottky barrier will change (in the classical concepts) so that the two Fermi levels, that in the semiconductor and that in the solution, are equal.

Thus, in this classical view (in which the basic concept of a Fermi level in solution is taken as an important entity), the nature of the barrier for the electron exit is taken as the extra bending of the Schottky barrier which arises from the original difference of the Fermi levels in the semiconductor and solution before equilibration (see Fig. 4).

Several difficulties inhabit this view, apart from those which are associated with doubts concerning Fermi level concepts in water, with its lack of clarity of defined band structure. Thus, the barrier outlined in Fig. 4 is a barrier for majority carriers. In photoelectrochemistry, however, a p-type semiconductor is a cathode and an n-type semiconductor is an anode, and the photoexcited minority carrier injection from the electrode to the solution would not experience the Schottky barrier as outlined above but rather would be helped by the bending of the band.

It is not the Schottky barrier which is wrong in the concept, but the fact that photoelectrochemistry involves minority carrier transfer (for n-type semiconductor acts as an anode), and hence a different type of barrier would be involved at the photoexcited semiconductor/solution interface. However, it would not be like photoexcited semiconductor-metal junction, since solution does not in any-

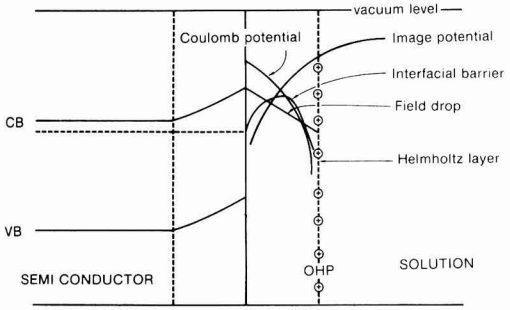


Fig. 8. The schematic diagram of non-Schottky-type barrier at the semiconductor/solution interface (8); the effect of field drop in the Helmholtz layer in solution side and the effect of Coulomb potentials in this layer constitute an extra barrier at the interface.

way behave like metal or semiconductor, which are electronic conductors and have band structure.

However, there is a greater difficulty which pertains to the practices which are present in literature; that is that no account is taken of transfer to quantum states in ions in solution. Thus, the energy barrier which actually exists in an electron transfer reaction is not concerned primarily with the difference of thermodynamic equilibrium states (though this is indeed a basic beginning to the formation of such a barrier), but, as normally conceived in all concepts of kinetic barriers, the height and dimensions of the barriers themselves are concerned with considerations external to the levels of the initial and final states. In particular, in a p-type semiconductor under illumination, electrons exit into solution, and the barrier for the electron is affected by the image forces between the semiconductor and the electron and by the Coulomb interaction between the ion and the electron. The electric field of the interface influences the electron and the height of the barrier in addition to these entities (see Fig. 8). All this has been omitted in the concepts which now exist in the literature. Prior to charge transfer through such an interfacial barrier, the ions in solution need to overcome the activation barrier arising from the potential energy distance relation for the ion-solvent bonds and so forth and attain a suitable distribution of acceptor or donor states such that those states match the electronic states in the electrode to have isoenergetic transfer.

Thus, the conventional treatments which locate the barrier only inside the semiconductor should be revised to take into account the electric potential barrier at the solution side of the interface, along with the activation barrier (Fig. 8) as has been detailed in our recent work (15a).

Fermi Level Pinning

Fermi level pinning has been discussed recently in the photoelectrochemical literature (9, 10) as though it were a new topic.

The idea of Fermi level pinning was introduced into the semiconductor literature in 1953 by Brattain and Bardeen (29). It was Green (21, 22) who introduced the idea in treatments of the semiconductor/solution interface in 1959. The situation was well represented in books discussing semiconductor electrochemistry in the 1960's (30). Fermi level pinning has long been a common and well-known phenomenon in the realm of semiconductor electrochemistry and often has been misused.

Model of Photoelectrocatalysis

Recently, a number of papers have been published (31-37) which show that small metal aggregates on the surface of p-type semiconductors cause a change in the rate of the photoevolution of hydrogen. Two models of photoelectrocatalysis are possible: In one, Model A (36), the function of the catalyst added to the surface (the metal particles in submonolayer amounts) is regarded as speeding up the reaction of electron transfer at the surface to protons in solution in such a way that the surface step becomes nonrate determining and the rate determination (insofar as it varies with the entities on the surface) depends upon factors inside the semiconductor. Thus, interactions at the interface between the metal aggregates and the semiconductor cause a change in reaction rate; since the Fermi level of the semiconductor near the metal aggregates must at equilibrium[7] be equal to that of the catalytic metal, it follows that, when the work function of the metal is lower than that of a p-type semiconductor, the effect of the metal would be to move the Fermi level inside the semiconductor in a more positive direction (on the potential energy scale), thus increasing band bending (Fig. 9) and, correspondingly, augmenting the photoelectrochemical current density (because when the rate-determining step is inside the semiconductor greater band bending would mean a lessened recombination probability and increased drift velocity of electrons towards the semiconductor-metal interface.

In another model, Model B (32, 37a), the rate-determining step is associated with events taking place at the interface between the metal aggregates and the solution, which could be catalyzed, as in the hydrogen evolution reaction, by metal aggregates on semiconductor surfaces.

Recent work has shown the direction of the shift of the midpoint potential in the exponential section of the i_{photo}/potential E curves of metal aggregate-coated p-Si photocathodes, as a function of the presence of a number of individual metals (see Fig. 10). A shift in the positive direction (with respect to the potential of the midpoint for bare Si) implies electrocatalysis of the hydrogen evolution reaction, while a shift in the negative direction implies its inhibition. It has been found that these shifts occur in the order which would be expected if the photoevolution of hydrogen were, in fact, controlled by the kinetics of the dark hydrogen evolution process at the metal/solution interface.

Model A would lead to the expectation that, at a given photoelectrocatalytic rate, the displacement on the potential E axis of the photocurrent/potential curve between the bare and the metal aggregate-covered semiconductor, ΔE, in the positive direction would decrease with increasing work function of the metal.

The trend predicted by Model A is shown by the dashed line in Fig. 11a. The experimental results are represented by the solid line in Fig. 11a. The experimental results show a reverse trend to that predicted by Model A.

To obtain a change in work function so that the direction of change of the photocurrent/potential relations is

[7]Even at nonequilibrium situation under illumination, the band bending varies according to the difference of Fermi energy levels in semiconductor and metal though it may be less than the equilibrium value.

Dependence of band bending on the work functions, Φ_M of metals Ni and Pt.

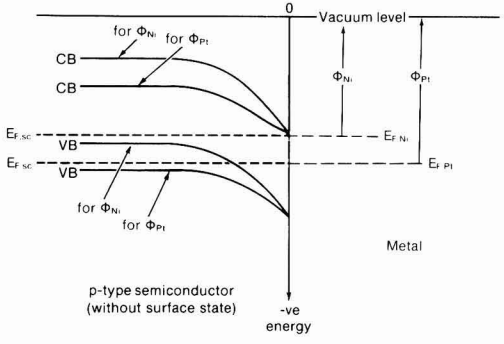


Fig. 9. The dependence of band bending inside the semiconductor on the work function of metal (*e.g.*, Ni and Pt) deposited in the form of islets on the semiconductor surface.

Photocurrent potential dependence for the presence of different metal islets on p-Si electrode.

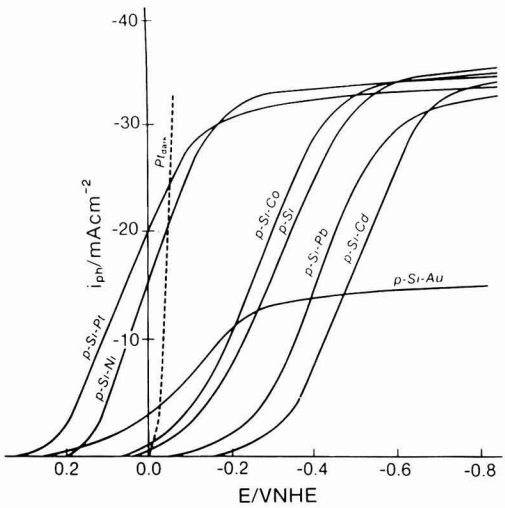


Fig. 10. The photocurrent-potential plot (37a) for various metal islets on p-Si photocathode. p-Si/Pt; p-Si/Ni; p-Si/Au; p-Si/Co; bare p-Si; p-Si/Pb; p-Si/Cd.

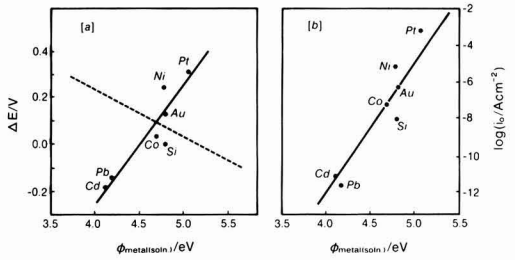


Fig. 11. a: Variation of the potential shift, ΔE, with the work function of the metal pertaining to electrolyte solution, Φ_{metal} (37a). b: The dependence of the log of the exchange current densities, i_o, for hydrogen evolution reaction at various massive metals on the work function of the metals, Φ_{metal} (37b).

consistent with observation on Model A, it was necessary to assume (36) that H would lower the work function of Pt by about 0.8V (Fig. 11a) and raise that of Cd by about the same amount. The observed values are shown in Table I; it is clear that the necessary shifts are not in the needed direction and do not have the appropriate magnitude.

In Model B, the displacement, ΔE, would be proportional to log i_o (see Fig. 12), where i_o is the exchange current density for the hydrogen evolution reaction on massive metal electrodes in the dark (37b). In Fig. 11b, it is

Table I. The values of work functions for different materials in vacuum, ϕ_v, and in solution, ϕ_s, and changes caused by hydrogen, $\Delta\phi_{H_2}$ (40-44)

Material	ϕ_v (eV)	ϕ_s (eV)	$\Delta\phi_{H_2}$ (eV)
Rh	4.9	5.0	+0.3
Ru	4.7	4.8	+0.4
Pt	5.5	5.0	+0.1
Ni	5.1	4.7	+0.4
Au	5.2	4.8	+0.2
Co	4.9	4.7	+0.33
Pb	4.0	4.2	—
Cd	3.9	4.1	—

Dependence of potential shift, ΔE on log i_o, exchange current density for hydrogen evolution on massive metals.

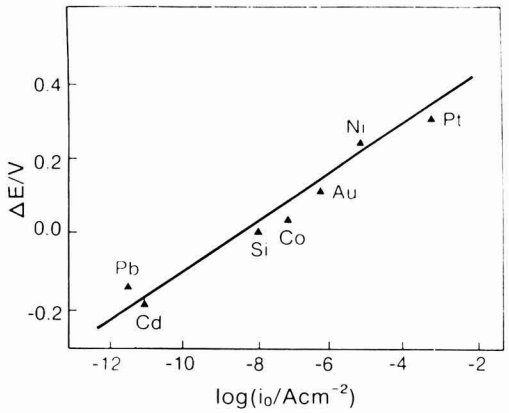


Fig. 12. The dependence of the potential shift, ΔE, with the log of exchange current densities, i_o, at various metal electrodes (37a).

shown that log i_o increases linearly with the work function of the metals when they are in solution (38a). Thus, the experimental results show the trend predicted by Model B.

A clear indication that Heller's Schottky barrier model is not operative has been obtained from the experiment carried out on n-Si electrode in dark with and without metal aggregates on it. Figure 12 shows the similar shift in potential, ΔE, as that in photoelectrochemical situation on p-Si. The shift in potential ΔE in dark and in light correlates well and thus agrees well with log i_o (38b) and with the electrocatalytic model rather than the Schottky model.

These correlations suggest that the rate-determining step in the photoelectrochemical evolution of hydrogen on surfaces decorated with submonolayer quantities of metals of various kinds is one which is rate determined to the metal/solution interface and that interactions at the metal/semiconductor interface do not have a primary influence on the rate of the reaction concerned (except insofar as they make the transition across this interface nonrate determining).

Summary

Traditional and modified views at the semiconductor/solution interface

Concept	Traditional	Modified
Fermi level in solution.	Is equal to redox potential in the vacuum scale.	Must include the inner potential of solution, ϕ^s. No free electron and band structure in solution. Better use of ground state energy of solvated ions.
Electronic energy distribution in solution.	Gaussianly distributed energies of ground state of ions. Fluctuational in nature.	Although such states exist, they seem unlikely to play much part in electrode reactions because they fluctuate too infrequently. Boltzmannian states of ion-solvent bond are origin of relevant states.

Schottky barrier.	Most semiconductor/solution interfaces are like those at the semiconductor/metal interface.	Such (Schottky) barriers are greatly diminished in semiconductor/solution interface. Surface states are always frequent at this interface because of adsorption of species (water, O, H, anions, etc.) from solution.
Relevant interfacial barrier in photoelectrochemical process.	The Schottky barrier.	The principal components controlling the electron exit rate at the semiconductor/solution interface (*i.e.*, the barrier) are activational/stretching or reorientation processes in the ion-solvent complex in the Helmholtz double layer. Interfacial barrier outside the semiconductor surface exists.
Fermi level pinning.	A new (1980) concept in photoelectrochemistry.	Introduced in 1947 (39) and into electrochemistry in 1959 and into photoelectrochemistry in 1978.
Model of photoelectrocatalysis.	Is due to shift of Fermi level in semiconductor due to presence of metal. Hence, band bending $(dV/dx)_{sc}$ changes.	Is due to happenings at metal/solution interface (*i.e.*, electrocatalytic effect).

Acknowledgments

We gratefully acknowledge the financial support of this work by the Robert A. Welch Foundation. The authors acknowledge useful discussion with Professor B. E. Conway, Dr. A. K. Vijh, and Dr. A. Nozik. We gratefully acknowledge the constructive criticism of divisional editor, Dr. R. H. Wilson; it helped to improve the clarity and the strength of the paper considerably.

Manuscript submitted May 17, 1984; revised manuscript received April 29, 1985.

Texas A&M University assisted in meeting the publication costs of this article.

REFERENCES

1. H. Gerischer, *Z. Phys. Chem. N.F.*, **26,** 223 (1960).
2. H. Gerischer, *Surf. Sci.*, **18,** 97 (1969).
3. H. Gerischer, in "Physical Chemistry: An Advanced Treatise," Vol. 9A, H. Eyring, D. Henderson, and W. Jost, Editors, p. 463, Academic Press, New York (1970).
4. J. O'M. Bockris and S. D. Argade, *J. Chem. Phys.*, **49,** 5133 (1968).
5. S. Trasatti, *J. Electroanal. Chem.*, **66,** 155 (1975).
6. H. Gerischer, in "Special Topics in Electrochemistry," P. G. Rock, Editor, p. 235, Amsterdam, The Netherlands (1977).
7. (a) R. Memming, in "Electrocatalysis," M. W. Breiter, Editor, p. 178, The Electrochemical Society Softbound Proceedings Series, Princeton, NJ (1974); (b) S. Trasatti, in "Comprehensive Treatise of Electrochemistry," Vol. 1, J. O'M. Bockris, B. E. Conway, and E. Yeager, Editors, p. 45, Plenum Publishing Company, New York (1980).
8. R. Memming, in "Electroanalytical Chemistry," A. J. Bard, Editor, Vol. 11, p. 1, Marcel Dekker, New York (1979).
9. A. J. Bard, A. B. Bocarsly, F. F. Fan, E. G. Walton, and M. S. Wrighton, *J. Am. Chem. Soc.*, **102,** 3671 (1980).
10. F. F. Fan and A. J. Bard, *ibid.*, **102,** 3677 (1980).
11. (a) F. W. Williams, S. P. Varma, and S. Hillenius, *J. Chem. Phys.*, **64,** 1549 (1966); (b) J. Jortner, *Mol. Phys.*, **5,** 257 (1962).
12. J. O'M. Bockris and D. B. Matthews, *J. Chem. Phys.*, **44,** 298 (1966); *Proc. R. Soc. London, Ser. A*, **292,** 479 (1966).
13. J. O'M. Bockris and S. U. M. Khan, *Appl. Phys. Lett.*, **42,** 124 (1983).
14. S. U. M. Khan and J. O'M. Bockris, in "Photoelectrochemistry: Fundamental Processes and Measurement Techniques," W. L. Wallace, A. J. Nozik, S. K. Deb, and R. H. Wilson, Editors, p. 39, The Electrochemical Society Softbound Proceedings Series, Princeton, NJ (1982).
15. (a) S. U. M. Khan and J. O'M. Bockris, *J. Phys. Chem.*, **87,** 2599 (1983); (b) H. Gerischer and W. Ekardt, *Appl. Phys. Lett.*, **43,** 393 (1983).
16. (a) V. G. Levich, "Physical Chemistry: An Advanced Treatise," Vol. 9B, H. Eyring, D. Henderson, and W. Jost, Editors, Chap. 12, Academic Press, New York (1970); (b) J. Appleby, J. O'M. Bockris, and R. K. Sen, in "MTP International Review of Science," J. O'M. Bockris, Editor, Vol. 6, Butterworths, London (1973); (c) R. W. Gurney, *Proc. R. Soc. London, Ser. A*, **134,** 137 (1931).
17. (a) "Comprehensive Treatise of Electrochemistry," Vol. 7, B. E. Conway, J. O'M. Bockris, E. Yeager, S. U. M. Khan, and R. White, Editors, Plenum Press, New York (1983); (b) J. M. Saveant and D. Tessier, *Faraday Discuss. Chem. Soc.*, **74** (1982).
18. R. E. Moore, O. Ferral, G. W. Koeppl, and A. J. Kresge, *J. Am. Chem. Soc.*, **93,** 1 (1971).
19. K. Nakamoto, "Infrared and Raman Spectra of Inorganic Coordination Compounds," Wiley-Interscience, New York (1978).
20. S. U. M. Khan and J. O'M. Bockris, *J. Appl. Phys.*, **52,** 7270 (1981).
21. M. Green, *J. Chem. Phys.*, **31,** 200 (1959).
22. M. Green, in "Modern Aspects of Electrochemistry," Vol. 2, J. O'M. Bockris and B. E. Conway, Editors, Academic Press, New York (1959).
23. W. K. Paik, M. A. Genshaw, and J. O'M. Bockris, *J. Phys. Chem.*, **74,** 4266 (1970).
24. J. O'M. Bockris and T. Otagawa, *J. Phys. Chem.*, **87,** 2960 (1983).
25. J. F. Dewald, *Bell Syst. Tech. J.*, **39,** 615 (1960).
26. P. J. Holmes, "Electrochemistry of Semiconductors," Academic Press, New York (1962).
27. W. Siripala and M. Tomkiewicz, *This Journal*, **129,** 1240 (1982).
28. P. Janietz, R. Weiche, J. Westfehe, R. Landberg, and R. Dehemlow, *J. Electroanal. Chem.*, **106,** 23 (1980).
29. W. H. Brattain and J. Bardeen, *Bell Syst. Tech. J.*, **32,** 1 (1953).
30. V. Z. Myamlin and L. V. Pleskov, "Electrochemistry of Semiconductors," Plenum Press, New York (1967).
31. J. Nakato, S. Tonomura, and H. Tsubomura, *Ber. Bunsenges. Phys. Chem.*, **80,** 1289 (1976).
32. W. Kautek, J. Brobrecht, and H. Gerischer, *ibid.*, **84,** 1034 (1980).
33. A. Heller and R. G. Vadimsky, *Phys. Rev. Lett.*, **46,** 1153 (1981).
34. A. Heller, R. G. Vadimsky, W. D. Johnston, K. E. Strege, H. J. Leamy, and B. Miller, in "Proceedings of the 15th IEEE Photovoltaic Special Conference," p. 1422, Kissimee, Florida, May 12-15, 1981, IEEE, New York (1981).
35. R. N. Dominey, N. S. Lewis, J. A. Bruce, D. C. Bookbinder, and M. S. Wrighton, *J. Am. Chem. Soc.*, **104,** 467 (1982).
36. A. Heller, E. Aharon-Shalom, W. A. Bonner, and B. Miller, *ibid.*, **104,** 6942 (1982).
37. (a) M. Szklarczyk and J. O'M. Bockris, *Appl. Phys. Lett.*, **42,** 1035 (1983); (b) J. O'M. Bockris, *Discuss. Faraday Soc.*, **1,** 95 (1947); (c) J. O'M. Bockris, S. U. M. Khan, O. J. Murphy, and M. Szklarczyk, *Int. J. Hydrogen Energy*, **9,** 243 (1984).
38. (a) S. Trasatti, *J. Electroanal. Chem.*, **66,** 155 (1975); (b) A. Q. Contractor, M. Szklarczyk, and J. O'M. Bockris, *ibid.*, **157,** 175 (1983).
39. J. Bardeen, *Phys. Rev.*, **71,** 717 (1947).
40. V. V. Gorodetskii, B. E. Nieuwenhuys, W. M. H. Sachtler, and G. K. Boreskov, *Surf. Sci.*, **108,** 225 (1981).
41. G. F. Voronina, L. A. Larin, and T. V. Kalish, *Elektrokhimiya*, **14,** 257 (1978).
42. F. C. Tompkins, in "The Solid-Gas Interface," Vol. 2, E. A. Flood, Editor, p. 765, Marcel Dekker, Inc., New York (1967).
43. R. V. Culver and F. C. Tompkins, in "Advances in Catalysis and Related Subjects," Vol. XI, D. D. Eley, P. W. Selwood, and P. B. Weisz, Editors, p. 67, Academic Press, Inc., London (1959).
44. L. Whatley, B. J. Davis, and R. L. Moss, *Trans. Faraday Soc.*, **66,** 3143 (1970).

The Effects of Surface Energetics on the Cyclic Voltammetry of Metallocenes at Nonilluminated n-InP Electrodes

Carl A. Koval and Robin L. Austermann*

Department of Chemistry, University of Colorado, Boulder, Colorado 80309

ABSTRACT

Electron transfer processes at n-type InP electrodes of moderate to low doping density were investigated by monitoring the cyclic voltammetric dark currents of a series of metallocenes in acetonitrile solutions. The formal reduction potentials of the metallocenes span the bandgap of InP, allowing a comparison of the cyclic voltammetric response as a function of the formal reduction potential and the energetic condition of the electrode surface. The energetic condition of the electrode surface during the cyclic voltammetry experiments was monitored by measurements of the capacitance of the space charge region. A simple chemical etching and electrochemical cycling procedure yielded reproducible surface energetics. The n-InP/acetonitrile interface in the depletion condition responded ideally to changes in electrode potential, as evidenced by linear Mott-Schottky plots, over a range of about 0.9V. It was possible to achieve an accumulation condition at negative potentials, but the interface could not be inverted at positive potentials. The n-InP/acetonitrile interface is less susceptible to surface oxidation than is the p-InP/acetonitrile interface. For each metallocene +1/0 couple, the reversibility of cyclic voltammetric (CV) waves at n-InP was dependent on the doping density of the electrode (N_D) and the proximity of the formal reduction potential ($E^{0\prime}$) to the conduction bandedge (E_{CB}). Couples with $E^{0\prime}$ located negative of E_{CB} displayed nearly reversible CV waves. Couples with $E^{0\prime}$ located in the bandgap were reduced irreversibly at overvoltages of 400-500 mV. A couple with $E^{0\prime}$ located slightly positive of E_{CB} yielded a partially reversible CV wave at moderate N_D, but the wave became irreversible at low N_D. Oxidation of couples with $E^{0\prime}$ positive of −0.5V *vs.* $E^{0\prime}$ for ferricenium/ferrocene was not observed.

The kinetics of electron transfer processes at semiconductor electrode/solution interfaces have not received as much attention experimentally as redox processes at metal electrode/solution interfaces (1-13). We have previously reported our investigation of electron transfer processes at p-InP electrodes in acetonitrile solutions (1). Herein, we extend our study to electron transfer processes at the n-InP/acetonitrile interface.

The purpose of this study is to investigate the ways that heterogeneous charge transfer kinetics at semiconductor electrodes are affected by various combinations of the formal reduction potentials of solution species and the energetic condition of the electrode surface. Our approach has been to measure cyclic voltammetric dark currents in acetonitrile solutions for ferricenium$^+$, cobalticenium$^+$, and a number of their derivatives (Fig. 1) at n-InP electrodes of moderate to low doping density. Abbreviated designations and formal reduction potentials, $E^{0\prime}$, for the metallocenes are listed in Table I. The reasons behind our choices of InP as the electrode material and the series of metallocenes as solution redox probes have been discussed before (1).

The specific knowledge of the energetics of the semiconductor/solution interface that this study requires was derived from measurements of the space charge capacitance taken in the same regions of electrode potential and at scan rates similar to those used in the cyclic voltammetry experiments.

Through these experiments, we have observed a correlation between the dark current flow and the doping density of the electrode, as well as the difference in potential between the conduction bandedge and the formal reduction potential of the solution redox species. The results qualitatively support the Gerischer model of the semiconductor/solution interface (7, 8).

Experimental

Reagents and materials.—Gold-label acetonitrile (Aldrich) was thoroughly dried by refluxing over calcium hydride for 14h in a nitrogen atmosphere.[1] The supporting electrolyte, tetrabutylammonium fluoroborate, $TBABF_4$, (Southwestern Analytical Chemicals, Incorporated) was dried under vacuum for two days at 25°C. Ferrocene, acetylferrocene, 1,1′-diacetylferrocene (Aldrich), and decamethylferrocene (Strem) were purified by sublimation. Cobalticenium hexafluorophosphate (Strem) was used without further purification. 1,2,4,1′,2′,4′-hexamethylferrocene, bis(diphenylphosphinocyclopentadienyl) cobalt hexafluorophosphate, and bis(diphenylphosphinocyclopentadienyl) cobalt molybdenum tetracarbonyl were used as received (14).

Electrochemical measurements.—All electrochemical measurements were performed in a Vacuum Atmospheres controlled-atmosphere glove box containing helium. An opaque, one-compartment cell was used for all electrochemical measurements. The acetonitrile solutions contained 0.5*M* $TBABF_4$ as the supporting electrolyte. The reference electrode was a silver wire immersed in a solution of 0.01*M* $AgNO_3$ and 0.5*M* $TBABF_4$ in acetonitrile, which was contained in a glass tube that was sealed at one end with a Vycor glass disk (Princeton Applied Research). This reference electrode has a potential of 0.29V *vs.* SCE (15). Its potential was monitored daily by comparison with the formal reduction potential, $E^{0\prime}$, of the ferricenium/ferrocene couple, which occurred at approximately 0.1V *vs.* the Ag/Ag$^+$ reference electrode. All potentials herein are reported *vs.* the $E^{0\prime}$ for ferrocene$^{+/0}$ (16). The counterelectrode was a platinum foil.

Cyclic voltammetry, CV, was performed with a Princeton Applied Research Model 175 universal programmer and Model 173 potentiostat/galvanostat. The data were recorded on a Houston Instruments Model 2000 X-Y recorder. In experiments involving InP electrodes, the space charge capacitance of the electrochemical cell was

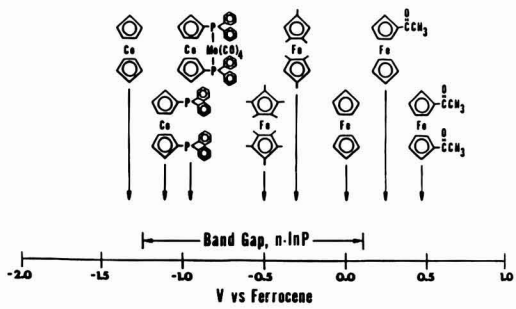


Fig. 1. Formal reduction potentials of the metallocenes in relation to the bandgap of n-InP in acetonitrile solution.

*Electrochemical Society Active Member.

[1]In some of the initial experiments, the acetonitrile was passed through a column of activated alumina prior to solution preparation. This procedure was discontinued because it was found to have no effect on the electrochemical behavior.

Table I. Designations and reduction potentials for the metallocenes

Designation	Metallocene	$E^{0\prime}$ (V *vs.* ferrocene)
FER	Ferrocene	0.00
DFER	Decamethylferrocene	−0.50
HFER	1,2,4,1',2',4'-Hexamethylferrocene	−0.30
AFER	Acetylferrocene	0.24
DAFER	1,1'-Diacetylferrocene	0.47
COB	Cobaltocene	−1.33
PCOB	Bis(diphenylphosphinocyclopentadienyl) cobalt	−1.10
PMCOB	Bis(diphenylphosphinocyclopentadienyl) cobalt molybdenum tetracarbonyl	−0.95

measured by using a Princeton Applied Research Model 5204 lock-in analyzer and a Hewlett-Packard Model 200AB audio oscillator interfaced to a computer acquisition system (17).

The formal reduction potentials of the metallocenes were determined from CV data measured at the platinum electrode as the average of the anodic and cathodic peak potentials. The values of $E^{0\prime}$ so determined (Table I) were within +/- 70 mV of previously reported measurements (14, 18-20). The approximate concentrations of the ferrocene derivatives were estimated by comparing the magnitudes of the CV peak currents obtained at a platinum electrode with peak currents obtained in a solution containing a known concentration of ferrocene. In each CV experiment, the peak current densities obtained at the InP electrode were compared with the peak current densities obtained at a platinum electrode in the same solution. Whenever it was necessary to prepare a solution of the metallicenium$^+$ cation, it was generated electrochemically in a two-compartment cell. One compartment contained the platinum foil working electrode and the reference electrode, and the other compartment contained the platinum wire counterelectrode. The compartments were separated by a Vycor frit.

Electrode pretreatment and characterization.—The platinum disk electrode and n-InP (Varian, Cambridge) electrodes were constructed as described previously (1). Prior to each experiment, the n-InP electrodes were etched for 1 min in a 50/50 solution of CH_3OH/concentrated HCl, rinsed with CH_3OH, and dried in a stream of argon. The areas of the InP electrodes were measured by using a photographic procedure.

The doping densities, N_D, and flatband potentials, E_{FB}, of the InP electrodes were determined from capacitance/potential data by using the Mott-Schottky equation (21)

$$1/C_{sc}^2 = (2/e\epsilon\epsilon_0 N_D)(E - E_{FB} - k_B T/e)$$

where C_{sc} is the capacitance of the space charge region, ϵ_0 is the permittivity of free space, ϵ is the static dielectric of the semiconductor (12.5 for InP), E is the electrode potential, and k_B is the Boltzmann constant. The data were modeled to a series RC circuit, and the total measured capacitance was assumed to be equal to C_{sc} (22). Values of C_{sc} were recorded at 100 mV intervals using a cyclic staircase potential program with the step time equal to 10s, which was superimposed upon an ac signal with a frequency of 5 kHz and an amplitude of 20 mV peak to peak. The X-intercepts of the Mott-Schottky plots for all of the electrodes used in this study and the slopes of the Mott-Schottky plots for all but the electrode of lowest doping density were found to be independent of frequency.

The single-crystal n-InP pieces employed in this study were of moderate or low doping density and had a (100) crystal orientation with both indium and phosphorous atoms exposed. The reproducibility of the voltammetric responses and surface energetics for different electrodes constructed from the same material was quite good. The characteristics of the three electrodes that were used most extensively in this study are summarized in Table II.

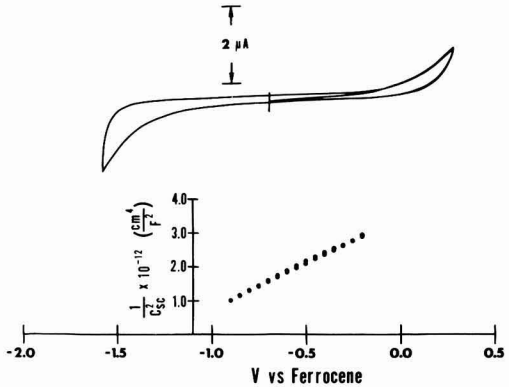


Fig. 2. Cyclic voltammograms for five consecutive cycles and a Mott-Schottky plot for the N18(100) electrode in a solution of 0.5M $TBABF_4$ in acetonitrile. The Mott-Schottky plot shows a forward (negative) and reverse (positive) scan with an ac frequency of 5 kHz.

Results

Surface energetics in the absence of electroactive species.—A cyclic voltammogram for five consecutive cycles of an N18(100) electrode in electrolyte solution exhibited very little current in the region from about −1.1 to −0.2V *vs.* ferrocene (Fig. 2). When the electrode potential was swept positive of −0.2V, an anodic wave appeared, and when the electrode potential was swept negative of −1.1V a cathodic wave appeared that was larger than the anodic wave. Since similar scans in the same solution at a platinum electrode are featureless, these currents can be attributed to oxidation and reduction of the electrode surface rather than to electroactive impurities in the solution. A typical Mott-Schottky plot for this electrode in electrolyte solution is also shown in Fig. 2. The capacitance data were collected in the range of −0.9 to −0.2V, which is within the bandgap of n-InP, where very little faradaic current appeared in the cyclic voltammogram. The plot is linear, with no hysteresis between the forward and reverse scans.

Capacitance data taken in electrolyte solution in the regions where anodic and cathodic faradaic background current appeared in the CV resulted in Mott-Schottky plots like those shown in Fig. 3. When the electrode potential was swept negative of −1.1V, the capacitance became constant and independent of potential. This suggests that negative charge resided at the electrode surface at potentials corresponding to the onset of cathodic current in the corresponding cyclic voltammogram (Fig. 2). This potential-independent capacitance appears at a potential closely corresponding to the position of the conduction bandedge. On the reverse scan, there is a small amount of hysteresis in the Mott-Schottky plot. Compared to similar scans at p-InP (1), these data indicate that the negative scan causes little permanent change of the electrode surface. When the electrode potential is swept positive of −0.2V, the potential corresponding to the on-

Table II. Properties of the n-InP electrodes

Electrode	Area (cm^2)	Orientation	E_{FB} (V)	Doping density (cm^{-3})
N18 (100)A	0.19	(100)	−1.28 +/− 0.04	$(4.1 +/- 0.1) \times 10^{18}$
N18 (100)B	0.13	(100)	−1.23 +/− 0.04	$(2.7 +/- 0.1) \times 10^{18}$
N16 (100)	0.25	(100)	−1.08 +/− 0.04	$(2.3 +/- 0.1) \times 10^{16}$

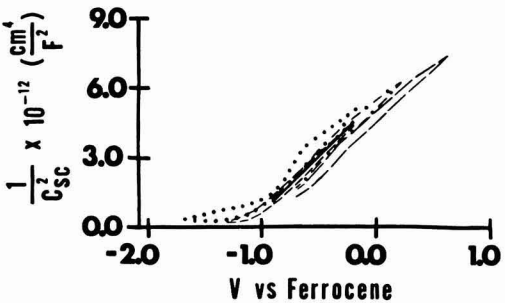


Fig. 3. Mott-Schottky plots for the N18(100) electrode in a solution with 0.5M $TBABF_4$ in acetonitrile. The switching potentials used are: (- - - - -) −0.2 and −1.3V; (· · · · ·) −0.2 and −1.7V (-·-·-) −0.7 and 0.2V; (—— ——) −0.7 and 0.6V.

set of anodic background current in the cyclic voltammogram, the slope of the Mott-Schottky plot decreases slightly, and there is hysteresis in the reverse (negative) scan. The measured capacitance does not become independent of potential in the positive direction.

To determine if cyclic voltammetric scans into regions where cathodic or anodic background current flows cause a permanent change in the position of the band-edges, a series of measurements of the flatband potential were taken as a function of the number of cyclic voltammograms done in a given potential range (Fig. 4). The triangles show that repetitive scans between −0.9 and −0.2V, where very little background current appeared, resulted in a stable value of E_{FB} after a few initial scans. If the electrode potential was scanned between −0.9 and 0.4V, into the range of anodic background current, E_{FB} shifted in a positive direction (squares), but eventually stabilized after about 30 CV scans. When the electrode was swept between −1.6 and −0.2V, into the range of cathodic background current, E_{FB} did shift in a negative direction (circles), but stabilized after about 20 CV scans.

In order to produce a stable E_{FB} before each CV experiment, each freshly etched electrode was cycled five times in electrolyte solution between −0.9 and −0.2V.

Cyclic voltammetry of metallocenes at n-type InP electrodes.—Representative cyclic voltammetric behavior of the metallocenes at n-InP can be shown by presenting the responses of FER^+, $PCOB^+$, and $PMCOB^+$ at the N18(100) and N16(100) n-InP electrodes.

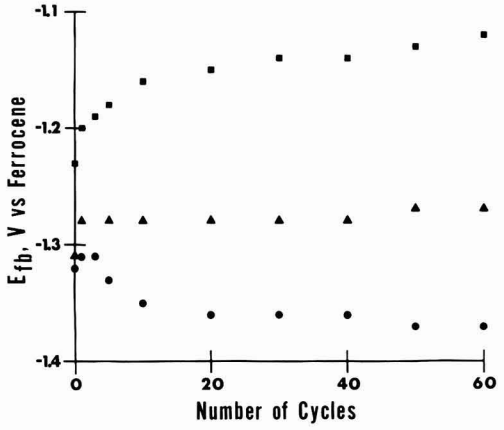


Fig. 4. The flatband potential as a function of the number of cyclic voltammograms done between three different pairs of switching potentials at the N18(100) electrode in a solution of 0.5M $TBABF_4$ in acetonitrile. Switching potentials: (squares) −0.9 and 0.4V; (triangles) −0.9 and −0.2V; (circles) −0.2 and −1.6V.

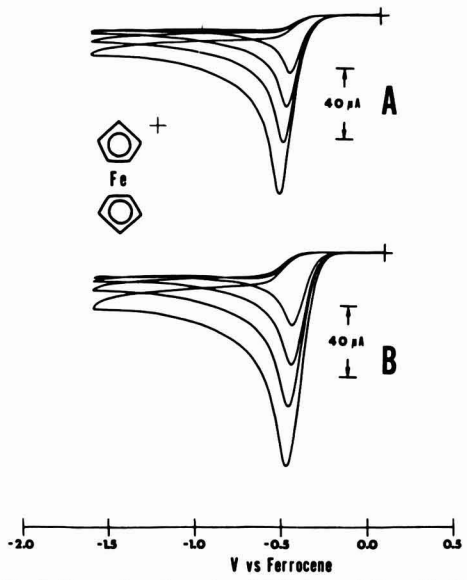


Fig. 5. The cyclic voltammetry of FER^+ in a solution with 0.5M $TBABF_4$ in acetonitrile at: (part A) the N18(100) electrode; (part B) the N16(100) electrode at 200, 100, 50, and 20 mV/s with an initial potential of 0.2V.

Ferricenium$^+$.—Cyclic voltammograms at the N18(100) electrode (Fig. 5A) and at the N16(100) electrode (Fig. 5B) of FER^+ at different scan rates show a diffusion-controlled cathodic wave that appears 450 mV negative of the $E^{0\prime}$ of FER at both electrodes. Neither electrode exhibits an anodic wave on the reverse (positive) scan, even if the electrode potential was swept positive of 1.0V. The cyclic voltammograms of $DFER^+$, $HFER^+$, and $AFER^+$ had a similar appearance to the CV of FER^+, exhibiting only cathodic waves that occurred 450-600 mV negative of their formal reduction potentials (Table III). Anodic waves were not observed on the reverse scans.

Bis(diphenylphosphinocyclopentadienyl) cobalt molybdenum tetracarbonyl.—A cyclic voltammogram of $PMCOB^+$ at the N18(100) electrode (Fig. 6A) and the N16(100) electrode (Fig. 6B) shown at different scan rates also exhibits a diffusion-controlled cathodic wave at both electrodes at less than 100 mV negative of the $E^{0\prime}$ for that compound. The difference in response between the different doping densities lies in the reverse (positive) scan. The N16(100) electrode exhibits no anodic current during the reverse scan, whereas the N18(100) electrode does exhibit a kinetically controlled anodic current during the reverse scan with a magnitude that is less than 60% of the cathodic current.

Table III. Reduction potentials

Compound	Electrode	E_{pc} (V)[a]	E_{onset} (V)[b]	j_o (A/cm^2)	α
$AFER^+$	N18 (100)B	−0.35	−0.05	1.8×10^{-7}	0.44
	N16 (100)	−0.41	−0.20	6.0×10^{-11}	0.71
FER^+	N18 (100)A	−0.48	−0.30	6.7×10^{-7}	0.43
	N16 (100)	−0.45	−0.25	1.6×10^{-11}	1.04
$HFER^+$	N18 (100)A	−0.77	−0.55	2.9×10^{-7}	0.47
	N16 (100)	−0.82	−0.60	4.4×10^{-22}	2.11
$DFER^+$	N18 (100)A	−0.95	−0.60	6.7×10^{-7}	0.46
	N18 (100)B	−0.88	−0.60	3.8×10^{-7}	0.52
	N16 (100)	−0.93	−0.70	3.2×10^{-14}	1.42

[a] At 100 mV/s.
[b] +/− 0.025V.

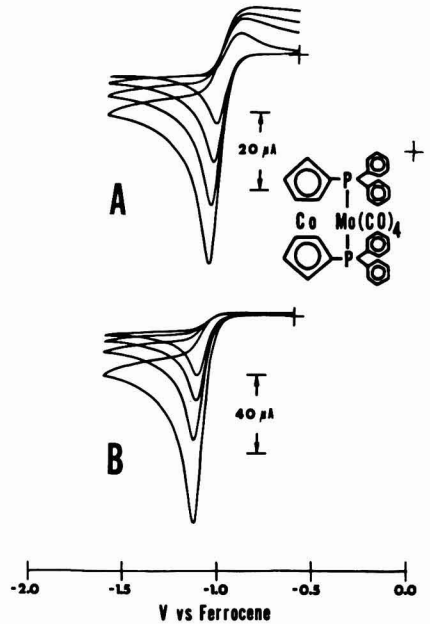


Fig. 6. The cyclic voltammetry of PMCOB$^+$ in a solution with 0.5M $TBABF_4$ in acetonitrile at: (part A) the N18(100) electrode; (part B) the N16(100) electrode at 200, 100, 50, and 20 mV/s with an initial potential of −0.6V.

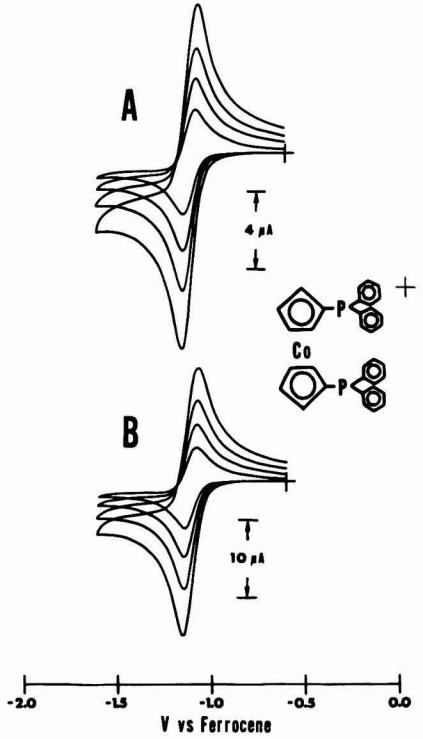


Fig. 7. The cyclic voltammetry of PCOB$^+$ in a solution with 0.5M $TBABF_4$ in acetonitrile at: (part A) the N18(100) electrode; (part B) the N16(100) electrode at 200, 100, 50, and 20 mV/s with an initial potential of −0.6V.

Bis(diphenylphosphinocyclopentadienyl) cobalt.—The cyclic voltammetry of PCOB$^+$ is shown for the N18(100) electrode (Fig. 7A) and the N16(100) electrode (Fig. 7B) at different scan rates. The waves are nearly electrochemically reversible. There is a 62 mV separation between the peak potentials, and the cathodic peak currents are indicative of a diffusion-controlled process. A plot of i_{pc} *vs.* (scan rate)$^{1/2}$ is linear, but a plot of i_{pa} *vs.* (scan rate)$^{1/2}$ is not linear for either electrode, indicating that the anodic waves are not diffusion controlled.

The cyclic voltammetric response of COB$^+$ was similar to that of PCOB$^+$.

1,1′-Diacetylferrocene.—DAFER has a reduction potential that is positive of the valence bandedge of n-InP. No anodic wave appeared on the positive scan for DAFER at the n-InP electrodes. Unfortunately, DAFER$^+$ is not sufficiently stable to allow the electrochemical generation of a solution of the cation at a platinum foil electrode, so it was not possible to see if the reduction of the cation would have occurred at n-InP.

Discussion

The n-InP/acetonitrile interface as a function of electrode potential.—The rates and mechanisms of electron transfer across a semiconductor/solution interface are greatly influenced by the position of the electrode Fermi level with respect to the valence band and conduction bandedges at the electrode surface. The three surface energetic conditions of an ideal, nonilluminated n-type semiconductor/solution interface, which can be achieved by changes in the Fermi level, are shown in Fig. 8. These diagrams represent the electrochemical potential of electronic orbitals as a function of distance into the electrode with respect to redox levels in solution (23). Although dark current flow for each of these energetic conditions has been addressed experimentally and theoretically (10, 13), many questions regarding the interpretation of these currents remain unanswered.

In principle, it should be possible to study faradaic redox processes at semiconductor electrodes under accumulation, depletion, or inversion conditions by adjusting

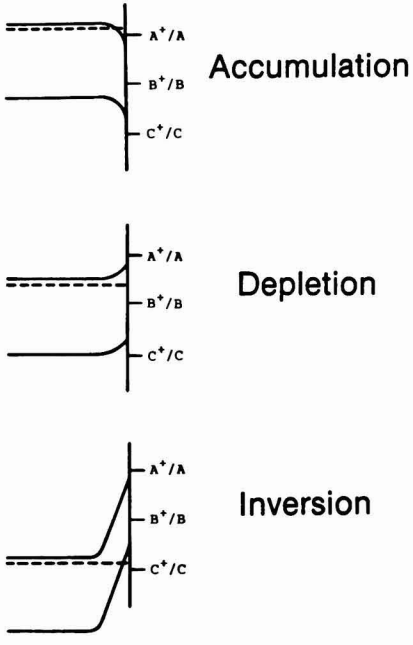


Fig. 8. Accumulation, depletion, and inversion as pictured for the ideal n-type InP/acetonitrile interface in the dark in relation to solution redox levels.

the externally applied potential. Our data indicate that the n-InP/acetonitrile interface responded to changes in the electrode potential in a nearly ideal way if the electrode potential was kept in the range of −1.1 to −0.2V *vs.* ferrocene, which corresponded to having the electrode in a depletion condition (Fig. 2). As the electrode potential was swept negative of −1.1V, the space charge capacitance became independent of potential (Fig. 3). Because the onset of potential-independent capacitance coincides well with the position of the conduction bandedge, we interpret −1.1V as the onset of accumulation at the n-InP electrodes. On the reverse (positive) scan, as the electrode passes from accumulation to depletion, the Mott-Schottky plot shows the same flatband potential as on the forward scan, indicating that little or no negative shift in the position of the conduction bandedge occurred when the electrode was in accumulation.

When the electrode potential was swept positive of −0.2V, the measured capacitance did not become independent of potential, indicating that the inversion condition did not occur (Fig. 3). The observed behavior is characteristic of a semiconductor electrode in deep depletion (9, 24). Deep depletion is a nonequilibrium condition in which minority carriers are consumed at the interface in surface reactions, preventing their accumulation in interface states. This accumulation of minority carriers in interface states is required for inversion. One possible surface reaction is the formation of surface oxide. Surface oxide formation at p-InP caused the bandedges to shift in a positive direction and prevented the electrodes from going into accumulation (1). Although there seems to be much less oxide formation at n-InP than there was at p-InP, it is reasonable that this process is preventing the electrodes from going into inversion by consuming minority carriers.

Since the capacitance measurements and the cyclic voltammograms were done at similar effective scan rates and within the same potential regions, it can be assumed that the changes in the surface energetics just described also occurred during the cyclic voltammetry experiments. Our interpretation of the capacitance data suggests that redox processes negative of −1.1V at n-InP should be indicative of the electrode in accumulation, that is, that metal-like behavior should be observed (10). Redox processes positive of −1.1V at n-InP should be indicative of the electrode in depletion, that is, kinetically controlled currents should be observed (10). Since the capacitance data indicates that inversion does not occur at n-InP, metal-like behavior would not be expected positive of the conduction bandedge.

Interpretation of cyclic voltammograms.—The reduction potentials of $COB^{+,0}$ and $PCOB^{+,0}$ are located negative of −1.1V. It was predicted from the capacitance measurements that the electrode surface would be in accumulation at these potentials. As expected, nearly reversible cyclic voltammograms result for both compounds, regardless of the doping density of the electrode. Kohl and Bard have also observed nearly reversible cyclic voltammograms at n-InP in acetonitrile for redox couples with formal reduction potentials located negative of the conduction bandedge (25).

It is interesting to contrast the cyclic voltammetric behavior of $PCOB^{+,0}$ and $PMCOB^{+,0}$ (Fig. 6 and 7), which have $E^{0\prime}$ values that differ by only 150 mV. The sharp transition from the accumulation condition to the depletion condition, which causes the oxidation waves for PMCOB to become kinetically controlled, is readily apparent from the electrochemistry of these two complexes.

The reduction of $AFER^+$, FER^+, $HFER^+$, and $DFER^+$, which have formal reduction potentials that span a range of 0.75V, could be studied at potentials where the n-InP/acetonitrile interface was in the depletion condition. Each of these couples displayed an irreversible cathodic cyclic voltammetric wave at potentials where the interface was in depletion. Peak potentials and approximate onset potentials for these waves are listed in Table III. Kohl and Bard have also observed irreversible cathodic cyclic voltammetric waves at n-InP in acetonitrile for redox couples with formal reduction potentials within the bandgap (26).

There are several fundamental issues related to the electrochemistry of these complexes. First, since the CV waves are irreversible, the operative electron transport mechanism must be unidirectional. Second, it would be useful to discern whether the reduction currents are due to majority carriers (conduction band electrons) or to injection of minority carriers (holes) from the ferricenium cations into the valence band. Third, the role of surface states in the electron transfer process should be addressed. Fourth, the relative contributions of thermionic emission-diffusion over a Schottky barrier and quantum mechanical tunneling should be assessed (27).

The model that is generally used to discuss current flow at the semiconductor/solution interface is shown in Fig. 9. The figure depicts the energetic situation for $DFER^{+,0}$ as the redox couple in solution. Since the reorganization energies for the various ferrocene redox couples should be similar (1), the energetics for the other couples can be envisioned by vertically displacing the density of states curves to reflect the different values of $E^{0\prime}$.

One mechanism that is consistent with the irreversible CV waves is thermionic emission-diffusion (TED) of conduction band electrons (26). The height of the barrier to reduction of solution species by TED at an n-type electrode is the amount of band bending, approximately $E_{CB} - E_F$. This barrier height influences the concentration and flux of conduction band electrons at the semiconductor/solution interface at the energy of the conduction bandedge. It is possible to change the height of this barrier to reduction by moving the Fermi level with an external potential bias. The height of the barrier to oxidation of solution species by TED at an n-type semiconductor is related to the difference in potential between the conduction bandedge and the formal reduction potential of the solution species, $E_{CB} - E^{0\prime}$. This barrier height determines the concentration of filled states of the solution species at the semiconductor/solution interface at the energy of the conduction bandedge. For a given solution species, assuming that the potential of the conduction bandedge does not change during a CV scan, this barrier height will not change with the electrode potential. The inability to

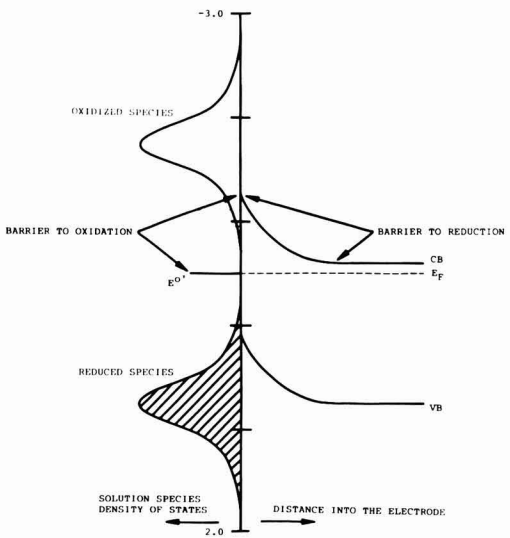


Fig. 9. Illustration of the barriers to oxidation and reduction of solution species at the n-InP/acetonitrile interface. The formal reduction potential shown is for $DFER^{+,0}$. Also shown are the density of states distributions for DFER and $DFER^+$ in solution.

oxidize the ferrocene derivatives in Table III at n-InP can therefore be attributed to a low concentration of filled states at $E_{C.B.}$.

The difficulty with the TED mechanism is that it cannot account for the current densities for reduction of $AFER^+$ and FER^+. Given the high mobility of conduction band electrons in InP (greater than 4000 $cm^2/V\text{-}s$) (26), the peak currents for $HFER^+$ and $DFER^+$, which occur with $|E_F - E_{C.B.}| < 0.5V$, could be attributed to TED. The band bending at E_{pc} for $AFER^+$ and FER^+, however, is greater than 0.7V, which makes a TED process appear unlikely. Since $E^{0\prime}$ for $AFER^+$ and FER^+ lies close to $E_{V.B.}$, reduction of these compounds may be due to minority carrier injection.

Kohl and Bard proposed a model for reductions at depleted n-ZnO, n-CdS, and n-GaP electrodes that involved filling of a surface state that has a redox energy located within the bandgap by conduction band electrons (25). The experimental evidence for this model was a "leveling" effect, that is, the tendency of different couples to be reduced at a common potential. Such a leveling effect is not observed in the present study at n-InP or in the previous study at p-InP. Instead, the data in Table III indicate that reduction of the ferricenium cations occurs over a wide range of potentials and that E_{pc} is related to $E^{0\prime}$. It can be argued that surface states with a variety of energies may be involved; however, it appears that this eventuality would lead to oxidation waves for certain couples. For example, if a surface state with an $E^{0\prime}$ of approximately $-0.3V$ were responsible for the reduction of $AFER^+$, this state should allow oxidation of DFER. In Kohl and Bard's model, it is unclear why current flow should be unidirectional unless the surface states are filled by TED from the conduction band.

Reduction of solution species at depleted surfaces can also occur via quantum mechanical tunneling (QMT) of conduction band electrons through the barrier in Fig. 9. Since the barrier width is inversely proportional to N_D, currents due to QMT depend dramatically on doping density. At semiconductor/metal junctions, currents due to QMT are only important at high doping densities (26). The positions and shapes of the CV waves for the complexes in Table III do depend on N_D. Plots of ln i_{pc} *vs.* $E_{pc} - E^{0\prime}$ were used to estimate exchange current densities, i_o, and transfer coefficients, α, for the redox couples (21). While the use of CV data to obtain these kinetic parameters is questionable (experiments utilizing more reliable methods are in progress), the results tabulated in Table III are intriguing. The exchange current densities and transfer coefficients at the N18(100) electrodes for the different couples are quite similar. A decrease in N_D has the expected effects on these parameters and probably reflects a contribution by QMT to each reduction process. Further evidence for QMT is found in the voltammetry of $PMCOB^{+.0}$ (Fig. 5). The CV wave for this couple occurs at a depleted surface, but close to $E^{0\prime}$. When the electrode potential was swept positive of $E^{0\prime}$ for PMCOB so that oxidation of the neutral species was thermodynamically favorable, no anodic wave appeared at the lower doped electrode. A small, kinetically controlled anodic wave appeared at the moderately doped electrode. The dependence of the current on doping density could indicate that the barrier is thin enough at the moderately doped electrode for electron transfer to occur via quantum mechanical tunneling but too thick at the lower doped electrode for tunneling to be possible.

The formal reduction potentials of acetylferrocene and 1,1′-diacetylferrocene are positive of the valence bandedge. The appearance of anodic waves for the oxidation of these compounds would be an indication that the n-InP electrodes entered the inversion condition under this external potential bias. The absence of anodic waves for either of these compounds is another indication that the n-InP electrodes did not enter inversion, maintaining a deep depletion condition instead.

A comparison of this work to studies of the n-Si/acetonitrile interface.—A study of highly doped n-type silicon in acetonitrile solutions using a series of redox couples that includes metallocenes has been done by Chazalviel and Truong (27). The results of their study show many similarities to our results at InP/acetonitrile interfaces. In their system, the redox couples exhibited cyclic voltammetric waves at small overpotentials, even for redox couples within the bandgap. In addition, all of their redox couples produced an apparently diffusion-controlled cathodic wave on the forward (negative) scan, similar to our results at n-InP. Couples that were located positive of the conduction bandedge had no anodic wave on the reverse (positive) scan, and couples that were located negative of the conduction bandedge had an apparently diffusion-controlled anodic wave on the reverse (positive) scan. Redox couples that were located in the vicinity of the conduction bandedge had a kinetically controlled anodic wave on the reverse (positive) scan. These results were obtained at freshly etched electrodes.

They also did a study of the cyclic voltammetric response as a function of time, in which reversible cyclic voltammograms would evolve into irreversible cyclic voltammograms. The results of their study were similar to the results of our previous study on the effect of anodic switching potential on the cyclic voltammetric response at p-InP (1). They attributed the negative shift in the conduction bandedge that they observed to the oxidation of the electrode surface and the formation of SiO_2. Our data indicate that leaving an n-type electrode in accumulation for an extended period of time can cause the reduction of surface oxide and the subsequent negative shift in the position of the conduction bandedge. Shifting the conduction bandedge negative would increase the height of the barrier to oxidation, which can result in the loss of anodic current as a function of time.

Conclusions

When combined with the data for p-InP from our previous paper (1), these results yield a complete description of the surface energetics and dark currents for the InP/acetonitrile interface. Both studies emphasize the use of metallocenes as effective redox probes and, especially, the use of capacitance data in conjunction with voltammetry experiments. The results for n-InP are summarized in Table IV. The behavior of the n-InP/acetonitrile interface is relatively simple compared to the p-InP/acetonitrile interface (1), because the effects due to surface oxide formation at positive potentials are less extensive for n-InP. This observation is consistent with the fact that the majority carriers in n-InP and p-InP are electrons and holes, respectively. If effects caused by surface oxide for-

Table IV. Summary of results at n-InP

Electrode potential (V *vs.* ferrocene)	Surface energetic condition	Stability of surface energetics	CV dark currents
−1.5 to −1.1	Accumulation	E_{FB} shifts negative. Slight hysteresis in M-S plot.	Nearly reversible waves.
−1.1 to 0.1	Depletion	E_{FB} is stable. Linear M-S plots.	Irreversible waves or reversible waves.
> 0.1	Deep depletion	E_{FB} shifts positive. Hysteresis in M-S plot.	No anodic currents.

mation are considered, the voltammetric responses for metallocenes at n-InP and p-InP can be rationalized qualitatively by using the Gerischer model for electron transfer at semiconductor/solution interfaces (7, 8). In some reports, the predictions of this model are consistent with the theoretical interpretation of current flow across semiconductor/metal junctions (26). One intriguing result of these experiments is that diffusion-controlled CV waves will occur for compounds with formal reduction potentials within the bandgap while the electrode is in depletion, rather than being postponed until the electrode is brought into accumulation or inversion. While deducing the mechanism of charge transport, thermionic emission-diffusion, quantum mechanical tunneling, or a minority carrier process will require additional experiments, the data do not support a mechanism involving surface states.

Acknowledgments

We wish to thank Dan DuBois (Solar Energy Research Institute) for donating samples of the complexes PCOB and PMCOB and Gary Darsey (University of Arizona) for donating a sample of HFER. This project was supported by the Department of Energy (Division of Chemical Sciences) Contract no. DE-FG02-84ER13247.

Manuscript submitted April 18, 1985; revised manuscript received July 23, 1985.

REFERENCES

1. C. A. Koval, R. L. Austermann, J. A. Turner, and B. A. Parkinson, *This Journal*, **132,** 613 (1985).
2. W. J. Albery, "Electrode Kinetics," Clarendon Press, Oxford, England (1975).
3. J. O'M. Bockris and A. K. N. Reddy, "Modern Electrochemistry," Plenum Press, New York (1970).
4. K. J. Vetter, "Electrochemical Kinetics," Academic Press, New York (1967).
5. P. Delahay, "Double-Layer and Electrode Kinetics," Interscience Publishers, New York (1965).
6. A. J. Bard and L. R. Faulkner, "Electrochemical Methods," Chap. 3, 12, John Wiley and Sons, New York (1980).
7. H. Gerischer, *Adv. Electrochem. Electrochem. Eng.*, **1,** 139 (1961).
8. H. Gerischer, *Top. Appl. Phys.*, **31,** 115 (1979).
9. S. R. Morrison, "Electrochemistry at Semiconductor and Oxidized Metal Electrodes," Plenum Press, New York (1980).
10. R. H. Wilson, *Crit. Rev. Solid State Mater. Sci.*, 1 (1980).
11. A. J. Nozik, *Ann. Rev. Phys. Chem.*, **29,** 189 (1978).
12. H. Reiss, *This Journal*, **125,** 937 (1978).
13. R. Memming, *Electroanal. Chem.*, **11,** 1 (1979).
14. G. Darsey (University of Arizona, Tempe, AZ) and D. DuBois (Solar Energy Research Institute, Palo Alto, CA), Personal communication.
15. C. K. Mann, *Electroanal. Chem.*, **3,** 57 (1969).
16. R. R. Gagne, C. A. Koval, and G. C. Lisensky, *Inorg. Chem.*, **19,** 2854 (1980).
17. J. A. Turner, J. Manassen, and A. J. Nozik, *Appl. Phys. Lett.*, **37,** 488 (1980).
18. J. L. Robbins, N. Edelstein, B. Spencer, and J. C. Smart, *J. Am. Chem. Soc.*, **104,** 1882 (1982).
19. D. W. Hall and C. D. Russel, *ibid.*, **89,** 2316 (1969).
20. W. F. Little, C. N. Reilly, J. D. Johnson, and A. P. Sanders, *ibid.*, **86,** 1382 (1964).
21. A. J. Bard and L. R. Faulkner, "Electrochemical Methods," John Wiley and Sons, New York (1980).
22. G. Cooper, J. A. Turner, B. A. Parkinson, and A. J. Nozik, *J. Appl. Phys.*, **54,** 6463 (1983).
23. A. J. Bard and L. R. Faulkner, "Electrochemical Methods," p. 634, John Wiley and Sons, New York (1980).
24. S. M. Sze, "Physics of Semiconductor Devices," p. 371, John Wiley and Sons, New York (1969).
25. P. A. Kohl and A. J. Bard, *This Journal*, **126,** 598 (1979); *J. Am. Chem. Soc.*, **99,** 7531 (1977).
26. S. M. Sze, "Physics of Semiconductor Devices," Chap. 9, John Wiley and Sons, New York (1969).
27. J. N. Chazalviel and T. B. Truong, *J. Am. Chem. Soc.*, **103,** 7447 (1981).

Technical Notes

Influence of *p*H on the Charge Storage Behavior of Thermally Prepared MnO_2 Films

Laurence D. Burke and Michael J. Ahern

Department of Chemistry, University College, Cork, Ireland

It has recently been demonstrated (1) that it is necessary to distinguish between two significantly different forms of oxide. The first is a highly compact, anhydrous form as is found in the rutile phase of thermally prepared IrO_2 (2). The second, involving the same metal oxidation state and usually prepared by wet, nonthermal techniques (*e.g.*, base precipitation and various electrochemical procedures), is a dispersed hydrous oxide (2, 3). The present work is part of a project devoted to a study of the relevance of these ideas, developed mainly from work on noble metal oxide electrochemistry, to the charge storage behavior of the industrially important MnO_2 system. The charge storage behavior of three different types of manganese oxide have been investigated: the first was produced by potential cycling a manganese metal substrate (4); the second by a standard anodic precipitation procedure used commercially to yield battery-grade γ-MnO_2: and the third by thermal decomposition of $Mn(NO_3)_2$ (5).

Experimental

Hydrous manganese oxide layers were generated by potential cycling (−0.40 to 1.65V, 41 mV-s^{-1}, ten cycles) a slab of manganese metal (*ca.* 1 mm thick, Alpha/Ventron, 99.9% pure) sealed into glass—with an exposed polished surface of geometrical area *ca.* 0.1 cm^2—in 1.0 mol-dm^{-3} NaOH at 25°C. Thermal MnO_2 deposits on gold wire of geometrical area *ca.* 0.5 cm^2, sealed into soda glass, were prepared as follows. The wire was degreased in acetone, submerged in boiling aqua regia for 30s, washed with distilled water, and allowed to dry. It was then briefly immersed in a methanol solution containing 1.74 mol-dm^{-3} $Mn(NO_3)_2 \cdot 4H_2O$ and 0.22 mol-dm^{-3} $SnCl_2 \cdot 2H_2O$ and annealed in air after drying (50°C for 15 min) for 3h at 195°-200°C (5). The presence of SnO_2 in this initial mixed oxide layer enhanced the adhesion of the final deposit to the gold substrate; it did not appear to affect the charge storage behavior of the thermal MnO_2—this was checked

by repeating the coating process, leaving out the $SnCl_2 \cdot 2H_2O$ in the case of the second layer (both deposits gave similar voltammograms with higher currents in the case of the two-coated specimen).

To prepare electrodeposited MnO_2, graphite rods were first abraded with emery paper, then coated with a metal etch resist (Kodak, KMER) to leave an exposed geometric area of *ca.* 2 cm^2; after immersion for 1 min in a solution containing 10% H_2SO_4 and 5% H_2O_2 (by volume), these were stored overnight, after washing, in distilled water. MnO_2 was deposited onto the resulting surfaces by anodization at 2.0 mA-cm^{-2} in an aqueous solution containing 0.30 mol-dm^{-3} $MnSO_4 \cdot 1H_2O$ and 0.66 mol-dm^{-3} H_2SO_4 at 80° ± 1°C (raising the deposition temperature to 95°C made little difference to the subsequent voltammetric results) for 25 min. This is a standard procedure for electrodepositing γ-MnO_2 (5, 6). The loading level used was *ca.* 1.4 mg MnO_2-cm^{-2}. X-ray analysis confirmed the presence of β-MnO_2 and γ-MnO_2 as the main bulk constituent in the thermally prepared and electrodeposited material, respectively.

The potentiostatic circuitry has been outlined elsewhere (4). Analar-grade chemicals and triply distilled water were used throughout; the cell temperature was controlled at 25° ± 0.1°C. Experiments involving potential/pH studies were carried out using Michaelis buffer solutions; some problems were encountered due to anion effects, *e.g.*, addition of H_2SO_4, HCl, and H_3PO_4 to the buffer solutions even at high pH tended to dislodge the oxide deposit, and attempts to maintain constant ionic strength by addition of 1.0 mol-dm^{-3} Na_2SO_4 also led to a deterioration (including a certain degree of bleaching) of the oxide coating on the working electrode. Generally, it was found that the oxide deposits were stable at pH values down to *ca.* 9.3.

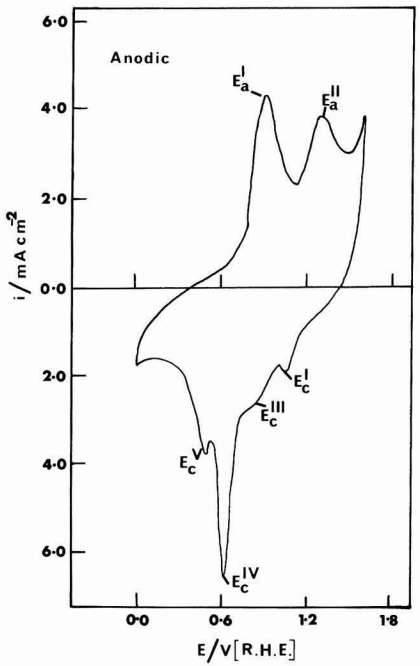


Fig. 2. Cyclic voltammogram for an anodically deposited manganese dioxide layer on graphite; 1.0 mol-dm^{-3} NaOH, 25°C, 0-1.60V, 2 mV-s^{-1}.

Results and Discussion

Preliminary description of the voltammetric behavior.— In basic media, two peaks, E_a^I and E_a^{II}, could be distinguished on the anodic sweep and about four (or five in the case of the thermal oxide) on the cathodic sweep (Fig. 1-3). Approximate peak maximum potential values are

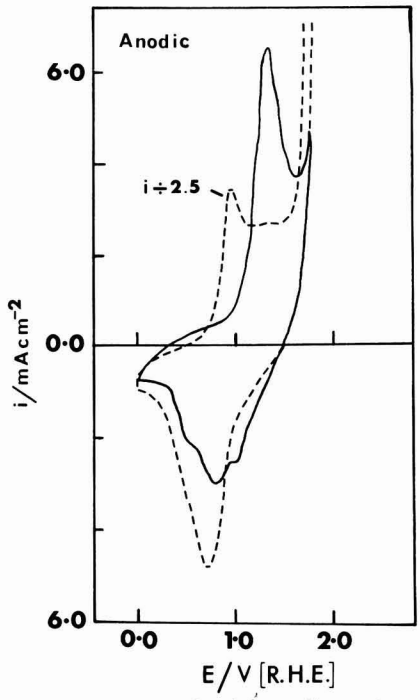


Fig. 1. Cyclic voltammogram for a hydrous oxide coated manganese metal electrode in 1.0 mol-dm^{-3} NaOH (pH = 13.6, dashed line) (a) borate buffer (pH = 9.30, solid line) at 25°C (b); 0-1.75V, 35 mV-s^{-1}.

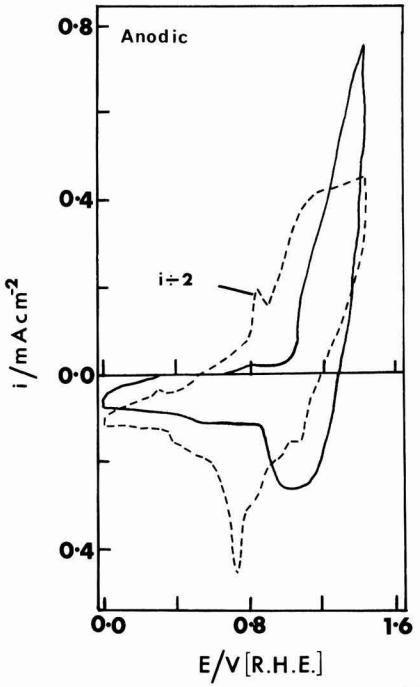


Fig. 3. Cyclic voltammogram for a thermally prepared MnO_2/SnO_2 deposit on gold: 1.0 mol-dm^{-3} NaOH, pH = 13.6 (dashed line); borate buffer, pH = 9.30 (solid line). *T* = 25°C. 0-1.40V; 5 mV-s^{-1}.

Table I. Approximate peak maximum potentials observed in cyclic voltammograms recorded for the three different types of manganese oxide in 1.0 mol-dm^{-3} NaOH at 25°C (RHE scale)

Type of MnO_2 deposit (↓)	E_a^I	E_a^{II}	E_c^I	E_c^{II}	E_c^{III}	E_c^{IV}	E_c^V
(a) Hydrous	0.96	1.37/P	N	N	0.86/P	0.70	0.47/P
(b) Thermal	0.83	1.15/P	1.03/P	0.93/P	0.79/P	0.70	0.39/P
(c) Electro-deposited	0.92	1.32	1.07	N	0.86/P	0.60	0.50

N: not observed.
P: poorly resolved.

listed in Table I; while there seemed to be reasonable agreement between the E_{max} values for the different types of oxide, it is obvious from the original diagrams that most of the peaks are quite broad. In the case of the thermally prepared material, the charge associated with the voltammograms generally increased (Fig. 4) on cycling; evidently, due to some type of rearrangement and hydration process, the depth of charge in this material was increased by this procedure. For most of the present work, the thermal oxide-coated electrodes were pretreated by cycling in 1.0 mol-dm^{-3} NaOH, 15 cycles, 0-1.40V at 28 mV-s^{-1}.

With the hydrous deposit, Fig. 1, only one major anodic and one major cathodic peak was observed. The peak E_a^{II} can be seen much more clearly in the case of the electrodeposited layer (Fig. 2). With all three films, the major feature of the cathodic sweep in base was the peak E_c^{IV} at *ca.* 0.70V.

Effect of pH on the redox response under potential cycling conditions.—Voltammograms are also shown in Fig. 1 and 3 for the oxide films in borate buffer solutions of pH = 9.30. Despite the lower peak current density, the anodic peak for the latter in the case of the hydrous film produced by cycling is clearly at a higher potential than in base. Similarly, for the same system, the main cathodic process occurs over a slightly more anodic potential range at pH = 9.30 than at 13.6; however, the anodic shift observed here on altering the pH is more dramatic for the oxidation as compared with the reduction sweep (see also Fig. 6). These shifts for the hydrous film are not kinetic in origin; this is clear from Fig. 5, where it can be seen that at slow sweep rates (< *ca.* 60 mV-s^{-1}) the peak maximum potentials for the hydrous material are sweep-rate independent. As outlined in Fig. 6, these reversible peak potentials vary in a linear manner with pH, dropping by 137 and 87 mV (anodic and cathodic, respectively) per unit increase in solution pH (pH-independent scale).

It is clear from Fig. 3 that the anodic shift with decreasing pH occurs also in the case of the thermal film. The

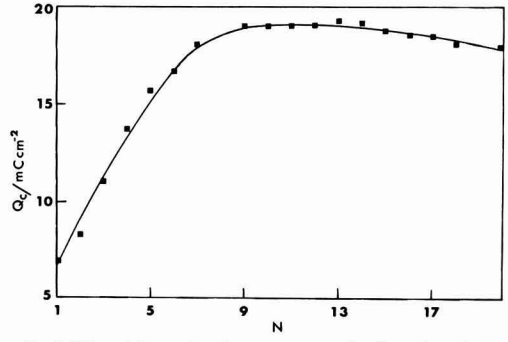


Fig. 4. Effect of the number of pretreatment cycles, N, on the cathodic charge associated with voltammograms (0-1.4V, 28 mV-s^{-1}) recorded for a thermally prepared MnO_2/SnO_2 electrode in 1.0 mol-dm^{-3} NaOH at 25°C.

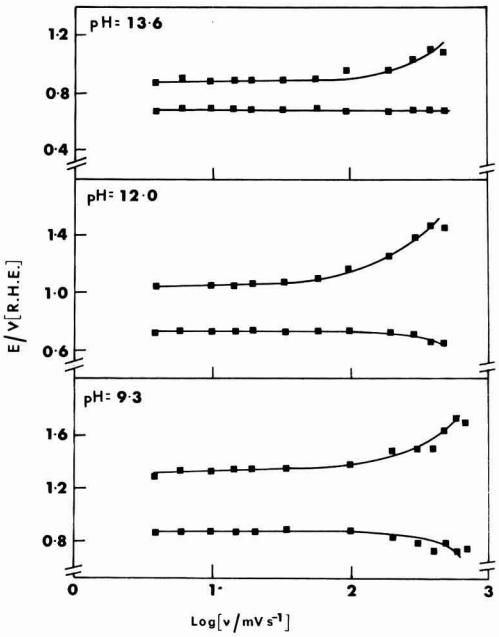


Fig. 5. Effect of sweep rate (ν) on the peak potentials (E_{max}) for the main anodic and cathodic process, at various pH values, for a hydrous film (see Fig. 1).

peaks in this case are not very distinct—especially in the borate buffer solution—but the shift can be illustrated by showing (Fig. 7) the drop in the anodic charge required to attain a given potential under fixed, slow sweep-rate, voltammetric conditions with decreasing solution pH.

The model proposed earlier (1) to explain the redox behavior of hydrous oxide systems—especially their unusual potential/pH dependence—assumes that these materials are loosely cross-linked ion-exchange polymers whose acidity, or ion-exchange capacity, increases with increasing degree of oxidation of the central metal ion. In the case of the material produced by potential cycling (4), the large, apparently sweep-rate independent, potential/pH variation of the anodic peak (*ca.* 137 mV/pH unit, SHE scale) corresponds to a ratio of hydroxide ions/electrons of 2.3/1. An appropriate equation for the oxidation reaction in this case is

$$[Mn_2(OH)_9]^{-3} + 4.6\ OH^- = [Mn_2O_{4.6}(OH)_{4.4}]^{-5.6} + 4.6H_2O + 2e^- \quad [1]$$

The basic reaction involved here is assumed to be Mn(III)/Mn(IV); however, there is evidently significantly greater proton loss from the more oxidized form of the hydroxy complex. The nonintegral values may be viewed in two ways: (*i*) a mixture of anionic products, *e.g.*, $[Mn_2O_5(OH)_4]^{-6}$ and $[Mn_2O_4(OH)_5]^{-5}$, is present in aggregate form, or (*ii*) the hydroxy species given in this equation are simply mean atomic or group ratio values for material present in an extended array. To explain the difference between the anodic and cathodic response (Fig. 6), it is assumed that the highly anionic oxidation product is unstable, decomposing in a postelectrochemical step as follows

$$[Mn_2O_{4.6}(OH)_{4.4}]^{-5.6} + 4.6H_2O = 2[Mn(OH)_6]^{2-} + 1.6\ OH^- \quad [2]$$

This decomposition is assumed to yield the required starting material for the subsequent cathodic process [which is identical to that proposed earlier for iridium (1),

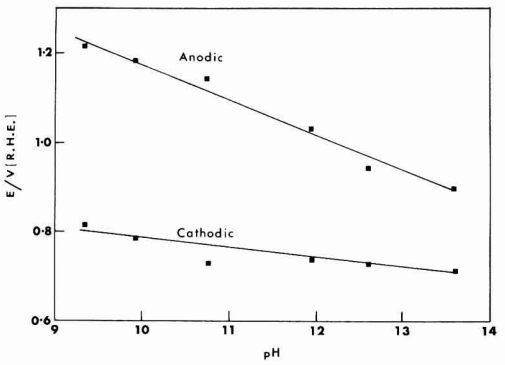


Fig. 6. Effect of pH on E_{max} for the main anodic and cathodic process recorded for a hydrous film at slow sweep rates. Least squares slope values (RHE scale): anodic, −78 mV/pH unit; cathodic, −28 mV/pH unit. T = 25°C.

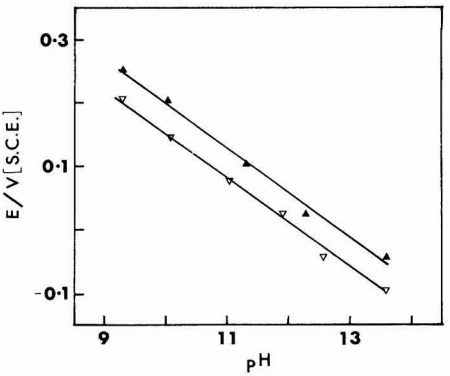


Fig. 8. Effect of pH on the open-circuit potential for a thick (filled triangles) and a thin (open triangles) thermally prepared MnO_2/SnO_2 deposit on gold. Mean least squares slope value (SHE scale): −70.3 mV/pH unit.

where an 87 mV shift was also noted]

$$2[Mn(OH)_6]^{-2} + 2e^- = [Mn_2(OH)_9]^{-3} + 3\ OH^- \quad [3]$$

In the case of the thermally prepared material, it is assumed that only the outer region of the oxide deposit is electroactive; this is also the region which is most likely to be hydrated. The shift of the charge storage reaction to higher potentials on decreasing the solution pH (Fig. 3 and 7) is also similar to that described earlier in the case of hydrous rhodium oxide deposits [Fig. 8 in Ref. (7)]. The pH effect is clearly the dominant factor here; the other anions, *e.g.*, borate (which must be added to the solutions of lower pH if buffering and ionic strength are to be maintained at reasonable levels), affect the charge storage capacity; although they do not, at least to any marked extent, affect the redox potentials [the same type of decrease in redox potential on raising the solution pH is observed in phosphate and sulfate solutions (8)]. Most

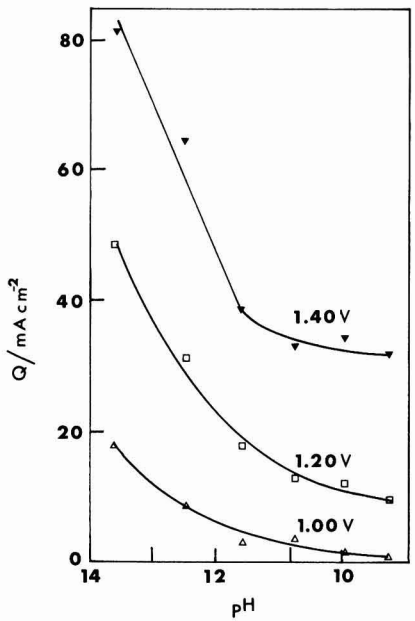


Fig. 7. Effect of pH, in the case of a thermally prepared MnO_2/SnO_2 film, on the anodic charge (above 0.6V) required to reach three specified potentials on the sweep-cyclic voltammetry conditions as outlined in Fig. 3. T = 25°C.

treatments of the manganese dioxide electrode system to date, while briefly mentioning oxide acidity and ion-exchange behavior, have ignored the influence of variation of oxide activity associated with changes in the oxidation state of the central metal ion and, in particular, the influence of such acidity changes on the redox behavior of this type of material. A qualitative treatment of the super nernstian, *i.e.*, > 2.303 $RT/\mathbf{F}$ V/pH unit, shift recorded here may also be given for the case of MnO_2 rather than its hydrated analogs, *e.g.*, $[Mn(OH)_6]^{-2}$ (Eq. [2]) as follows. According to the most recent view of the MnO_2 system, that of Ruetschi (9), this material is a cation vacancy system in which protons replace Mn^{+4} species at certain sites in the oxide, *i.e.*, the latter contains both $O^=$ and OH^- anions and these are related by the equilibrium

$$O^= + H_2O \rightleftharpoons 2\ OH^- \quad [4]$$

Raising the pH or hydroxide ion activity of the solution increases the hydroxide ion activity in the solid, and therefore lowers the metal ion activity. As outlined in the case of gold (10) and iridium (1), this drop is usually greater for material in the hydroxylated or partially hydroxylated state for the oxidized (Mn^{+4}) as compared to the reduced (Mn^{+3}) cationic species. The former tend to be more acidic, anionic, or prone to hydrolysis: one manifestation of this increased acidity is the super-nernstian potential-pH shift; another, for a battery oxide system not very different from MnO_2, is the strong binding of K^+ cations in the oxidized Ni(111) system, *i.e.*, γ-NiO · OH (11).

Open-circuit potential/pH response.—The application of cyclic voltammetry to the study of bulk charge storage reactions in oxides is to date surprisingly limited; the method, however, is extremely useful, as a "spectrum" of the charge/discharge properties of these materials is readily obtained. To eliminate the possibility that the observed super-nernstian shift in the present case is an artifact due to a slow electrochemical or transport step under cyclic voltammetry conditions (though, in view of Fig. 5, this seemed unlikely), the following experiment was carried out with a thermally prepared MnO_2 electrode. The latter, after preliminary cycling in base, was held for a brief period at 0.9V (RHE). It was then transferred to a buffer solution (the order of pH change here with respect to the different buffers was random) and its potential monitored with respect to saturated calomel. Drift was negligible after *ca.* 30 min. The plotted values (Fig. 8) were taken after a period of 1h. From this type of open-circuit experiment, which in fact was carried out at separate times using different electrodes, a mean potential/pH variation of *ca.* 70.3 mV/pH unit (SCE or SHE scale) was recorded.

This super-nernstial response on open circuit is in agreement with the report of other authors (12, 13), whose

work involved the use of battery-type (*i.e.*, γ-) MnO_2. The observed value is lower than that recorded under cyclic voltammetry conditions. A similar effect was again noted in the iridium oxide case (14). The difference is attributed primarily to chemical effects, *i.e.*, the redox processes are rapid, but either the more anionic oxidation product is somewhat unstable (dissociating or rearranging slowly to give a more neutral phase) or the more inert, neutral (*i.e.*, bulk) oxide plays a greater role in the equilibrium value recorded under open-circuit conditions. The potential/pH response observed under cyclic voltammetry conditions may be most relevant to the behavior of MnO_2 under current supply situations in battery systems, *i.e.*, the interaction between oxide acidity and redox behavior seems to be particularly relevant with regard to an interpretation of the charge/discharge characteristics (dynamic as opposed to open-circuit) behavior of MnO_2.

Acknowledgment

The authors are grateful to Dr. P. McSweeney, Mitsui Denman (Ireland) Limited, Little Island, Cork, Ireland, for x-ray data.

Manuscript submitted Dec. 10 1984; revised manuscript received ca. July 8, 1985. This was Paper 68 presented at the New Orleans, Louisiana, Meeting of the Society, Oct. 7-12, 1984.

REFERENCES

1. L. D. Burke and D. P. Whelan, *J. Electroanal. Chem.*, **162,** 121 (1984).
2. L. D. Burke and R. A. Scannell, *Plat. Metals. Rev.*, **28,** 56 (1984).
3. J. D. E. McIntyre, W. F. Peck, and S. Nakahara, *This Journal*, **127,** 1264 (1980).
4. L. D. Burke and M. J. G. Ahern, *J. Electroanal. Chem.*, **183,** 183 (1985).
5. S. Trasatti and G. Lodi, in "Electrodes of Conductive Metallic Oxides, Part A," S. Trasatti, Editor, Chap. 7, Elsevier, Amsterdam (1980).
6. G. W. Nichols, *Trans. Electrochem. Soc.*, **62,** 393 (1932).
7. L. D. Burke and E. J. M. O'Sullivan, *J. Electroanal. Chem.*, **129,** 133 (1981).
8. L. D. Burke, M. E. Lyons, E. J. M. O'Sullivan, and D. P. Whelan, *ibid.*, **122,** 403 (1981).
9. P. Ruetschi, *This Journal*, **131,** 2737 (1984).
10. L. D. Burke, M. E. Lyons, and D. P. Whelan, *J. Electroanal. Chem.*, **139,** 131 (1982).
11. L. D. Burke and T. A. M. Twomey, in "The Nickel Electrode," R. G. Gunther and S. Gross, Editors, pp. 75-95, The Electrochemical Society Softbound Proceedings Series, Pennington, NJ (1982).
12. R. S. Johnson and W. C. Vosburg, *This Journal*, **99,** 317 (1952).
13. P. Benson, W. B. Price, and F. L. Tye, *Electrochem. Technol.*, **5,** 517 (1967).
14. L. D. Burke, J. K. Mulcahy, and D. P. Whelan, *J. Electroanal. Chem.*, **163,** 117 (1984).

Electrochemical Behavior of Thin Platinum(111) Films Deposited on Mica Surfaces

Hsue-Yang Liu, Fu-Ren F. Fan, and Allen J. Bard*

Department of Chemistry, The University of Texas, Austin, Texas 78712

Atomically smooth Pt electrode surfaces are usually prepared from single crystals and are, of necessity, of limited area. It is possible to prepare "smooth" electrode surfaces by mechanical polishing with a fine polishing agent (*e.g.*, 0.1 μm alumina), but such surfaces are only macroscopically smooth (*e.g.*, with asperities >1000Å). An alternative approach is to deposit a thin film onto a smooth substrate such as flat glass or quartz. One problem with this approach is the weak adhesion of a thin metal film to the substrates, especially when the electrode is immersed in liquid and subjected to an applied electrode potential. Mica is a naturally occurring material that can be cleaved to produce an atomically smooth surface. It has been used to prepare epitaxially grown single-crystal films (1-9) for UHV experiments, and films of Ag and Au on mica have been applied to electrochemical measurements (8, 9). Thin Ag(111) films have been prepared to study electroreflectance (9a) and to investigate the migration of complexes (8) at electrode/electrolyte interfaces. Au(111) (9b) films were utilized to examine the hydrogen adsorption isotherm in acidic solutions. In this paper, we report the preparation of smooth Pt(111) films grown on freshly cleaved mica surfaces and the electrochemical behavior of such films in aqueous and nonaqueous solutions.

The thin platinum films were prepared by RF sputtering at 2×10^{-2} torr under Ar flow with a Materials Research Corporation Model MRC 8620 triple shutter RAD sputtering module. Films 1000Å thick were prepared at a deposition rate of 10 Å/s. Before deposition, a thin sheet was first peeled off from a thick mica plate (grade 2, ruby c.c.s. mica sheet, United Mineral and Chemical) in air. Mica has been used frequently for surface studies (1-7), and techniques like multiple beam interferometry (10) can be used to confirm the perfect cleavage and smooth surface.

The crystallography of the resulting platinum film deposited on the mica surface was examined using x-ray diffraction techniques. Figure 1 shows spectra obtained at bare (B) and Pt-deposited (A) mica surfaces. Although the background spectrum (Fig. 1B) due to the bare mica surface is relatively complicated, a peak at $2\theta = 39.5°$ (Fig. 1A) that arises from Pt(111) (ASTM no. 4-0802) can be clearly identified. No peaks associated with other crystal phases were found, so that the crystal phase of the resulting platinum film is clearly (111). Scanning electron microscopy (SEM) was used to check the smoothness of the thin Pt(111) film. There were no distinguishable island features at up to 40,000× magnification. These results indicate that a smooth thin Pt(111) film can be readily prepared on the mica surface (1, 2a).

For electrochemical measurements, the thin platinum film was connected with conductive silver paint (Acme Chemicals and Insulation Company) to a copper wire lead in a glass tube. The electrode surface was masked by 5 min epoxy and silicone rubber cement, except for the area to be examined. The cyclic voltammogram (CV) obtained at the thin platinum film in a solution of 0.5*M* H_2SO_4 is shown in Fig. 2A. The nature of hydrogen adsorption and oxide film formation on platinum single-crystal electrodes have been the subject of many studies (11-16). As shown in Fig. 2A, at the Pt/mica electrode in the hydrogen adsorption region, only a single peak at −0.2V is observed. These results, when compared with those reported previously under similar experimental conditions (11, 13a), show that the thin platinum film used in the present study behaves as a Pt(111) surface. Therefore, the electrochemical results as consistent with the assignment of the Pt(111) surface as deduced from the

* Electrochemical Society Active Member.

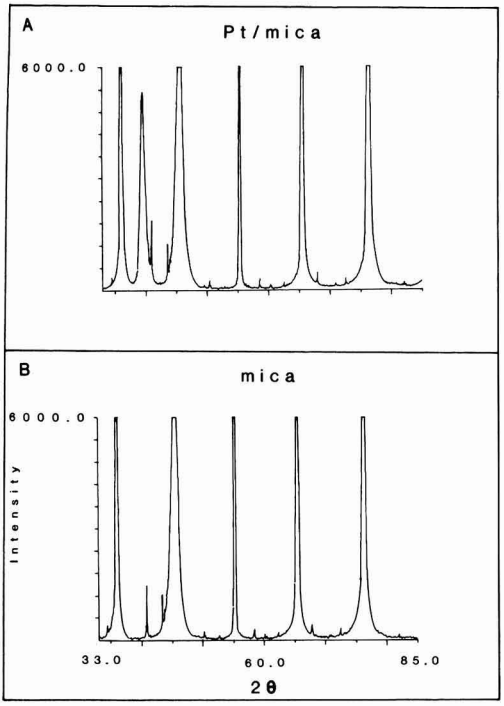


Fig. 1. X-ray diffraction spectra of Pt-deposited mica surface (A) and bare mica surface (B).

x-ray diffraction data. The thin Pt film became flaky if the electrode potential was repeatedly scanned over the hydrogen evolution region. This probably can be attributed to penetration by hydrogen into the platinum lattice.

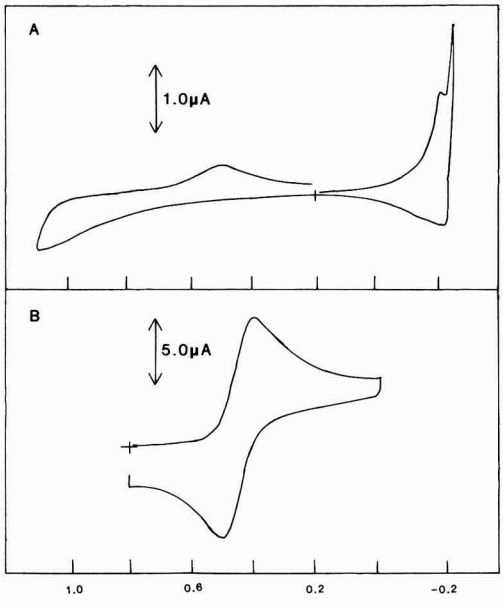


Fig. 2. A: Cyclic voltammetry of thin Pt(111) film in 0.5M H_2SO_4. Electrode area: 0.08 cm^2. Scan rate: 10 $mV\text{-}s^{-1}$. B: Same as A, except the solution containing 1.4 mM $Fe(CN)_6^{3-}$. Scan rate: 50 $mV\text{-}s^{-1}$.

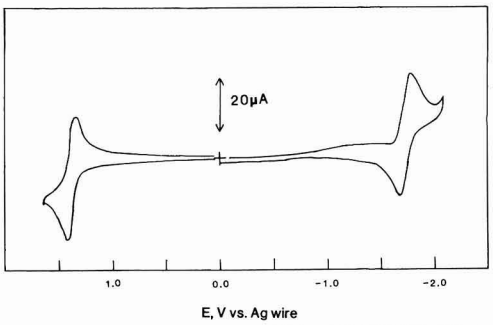


Fig. 3. Cyclic voltammetry of 1 mM DPA in 0.1M TBAF/MeCN solution at 0.12 cm^2 thin Pt(111) film. Scan rate: 100 $mV\text{-}s^{-1}$.

However, this thin film was very stable if the electrode potential was not allowed into the hydrogen adsorption or evolution region. The response of $Fe(CN)_6^{3-/4-}$ at this thin platinum film is given in Fig. 2B. The electrode could be scanned repeatedly over these potentials without loss of Pt from the surface. The observed behavior is similar to that found with bulk Pt electrodes.

To demonstrate the usefulness of this smooth thin Pt(111) film in nonaqueous media, cyclic voltammetry of 9,10-diphenylanthracene (DPA) carried out in MeCN-0.1*M* tetrabutylammonium fluoroborate (TBAF) solution (Fig. 3). Both reversible reduction (DPA → DPA^{-}) and oxidation (DPA → DPA^{+}) reactions were observed. The thin platinum film was stable in the solution on repeated scanning of the electrode potential between +1.65 and −2.1V *vs.* Ag wire. Electrogenerated chemiluminescence (ECL) was also observed with this thin platinum film in the same solution for potential steps (50 ms) between +1.65 and −2.1V. In past studies, we found that Pt films sputtered on glass would peel from the substrate when subjected to such large potential excursions, presumably because of the significant changes of surface tension at the Pt/solution interface.

The possible application of thin Pt films deposited on mica as optically transparent electrodes (OTE) (17) was also examined. A 500Å Pt film on mica is transparent in the visible region with relatively constant absorbance (*ca.* 1.0) with an associated sheet resistance of about 15 Ω/□. These results are comparable to those reported for Pt deposited on quartz (17). However, as demonstrated above, the Pt film on mica appears to show better mechanical stability.

In conclusion, the experiments described here indicate that smooth thin Pt(111) films can be easily prepared on cleaved mica surfaces. Our results also show that these thin films are stable in aqueous and nonaqueous media during electrochemical experiments. Mica surfaces can be used as smooth templates to prepare a wide range of thin film electrodes. We are especially interested in such electrodes for the construction of an ultrathin layer electrochemical cell using mica balance techniques (18). Studies of this application and further characterization of these films are currently under investigation in this laboratory.

Acknowledgment

The support of the National Science Foundation (CHE8402135) and IBM is gratefully acknowledged.

Manuscript submitted June 7, 1985; revised manuscript received Aug. 27, 1985.

The University of Texas assisted in meeting the publication costs of this article.

REFERENCES

1. J. W. Matthews, "Epitaxial Growth, Part B," Chap. 9, Academic Press, New York (1975).
2. (a) R. L. Palmer and J. N. Smith, Jr., *J. Chem. Phys.*, **60,**

1453 (1974); (b) D. G. Welke, M. G. Lagally, and R. L. Palmer, *J. Vac. Sci. Technol.*, **17,** 453 (1980).
3. M. Barkai, E. Grunbaum, and G. Deutscher, *Thin Solid Films*, **90,** 85 (1982).
4. J. Koshy, *ibid.*, **41,** L13 (1977).
5. M. H. B. Stiddard, *ibid.*, **94,** 1 (1984).
6. A. L. Dawar, A. Kumar, R. P. Mail, and P. C. Mathur, *ibid.*, **112,** 107 (1984).
7. J. Caballero, G. Kremer, and L. A. Moraga, *ibid.*, **117,** 1 (1984).
8. (a) R. Waser and K. G. Weil, *J. Electroanal. Chem.*, **150,** 89 (1983); (b) R. Waser and K. G. Weil, *Z. Phys. Chem. N. F.*, **139,** 203 (1984).
9. (a) D. M. Kolb and R. Kotz, *Surf. Sci.*, **64,** 96 (1977); (b) D. A. Scherson and D. M. Kolb, *J. Electroanal. Chem.*, **176,** 353 (1984).
10. S. Tolansky, "Multiple-Beam Interferometry of Surfaces and Films," Oxford University Press, London (1949).
11. A. T. Hubbard, *Acc. Chem. Res.*, **13,** 177 (1980).
12. K. Yamamoto, D. M. Kolb, R. Kotz, and G. Lehmpfuhl, *J. Electroanal. Chem.*, **96,** 233 (1979).
13. (a) W. E. O'Grady, M. Y. C. Woo, P. L. Hagans, and E. Yeager, *J. Vac. Sci. Technol.*, **14,** 365 (1977); (b) A. S. Homa, E. Yeager, and B. D. Cahan, *J. Electroanal. Chem.*, **150,** 181 (1983).
14. (a) F. T. Wagner and P. N. Ross, Jr., *ibid.*, **150,** 141 (1983).; (b) P. N. Ross, Jr., *ibid.*, **76,** 139 (1977).
15. B. E. Conway, H. Angerstein-Kozolowska, and F. C. Ho, *J. Vac. Sci. Technol.*, **14,** 351 (1977).
16. F. Will, *This Journal*, **112,** 451 (1965).
17. W. R. Heineman, F. M. Hawkridge, and H. N. Blount, in "Electroanalytical Chemistry," Vol. 13, A. J. Bard, Editor, Marcel Dekker, New York (1984).
18. (a) J. N. Israelachvili and G. E. Adams, *Nature*, **262,** 774 (1976); (b) J. N. Israelachvili, *J. Colloid. Interface Sci.*, **44,** 259 (1973); (c) J. N. Israelachvili and G. E. Adams, *J. Chem. Soc. Faraday Trans. 1*, **74,** 975 (1978); (d) H. K. Christenson, *J. Chem. Phys.*, **78,** 6906 (1983); (e) P. F. Luckham and J. Klein, *J. Chem. Soc. Faraday Trans. 1*, **80,** 865 (1984); (f) H. K. Christenson and R. G. Horn, *J. Colloid Interface Sci.*, **103,** 50 (1985).

Hydrogen Insertion at a Vanadium Pentoxide Cathode

S. J. Hibble, A. M. Chippindale, and P. G. Dickens

Inorganic Chemistry Laboratory, University of Oxford, Oxford, England OX1 3QR

The galvanostatic discharge of a vanadium pentoxide cathode using 2*M* $ZnSO_4$ as electrolyte at a current density of 50 $\mu A/cm^2$ gives rise to the potential *vs.* charge curve shown in Fig. 1. The discharge curve is in close agreement with that obtained by Shukler and Kuz'min (1) for $V_2O_5/ZnSO_4$ at comparable current densities. The final discharge product was dark green and had a powder x-ray pattern little changed from that of the parent V_2O_5 (Table I), there being no evidence of the characteristic x-ray lines of V_2O_4 or V_2O_3, the reaction products proposed by Shukler and Kuz'min.

It has been previously shown that the reduction of platinized samples of V_2O_5 using "hydrogen spillover" gives rise to a green phase of $H_xV_2O_5$ at low hydrogen contents (x = 0-0.5) with lattice parameters almost identical to those of V_2O_5 (3). Moreover, the IR spectrum of the discharge product (Fig. 2) closely resembles that of the spillover product in that a peak at 928 cm^{-1}, previously assigned as an —OH bend, is clearly visible.

It is therefore proposed that the discharge product is the hydrogen insertion compound, $H_xV_2O_5$, the reaction occurring at the V_2O_5 cathode being

$$V_2O_5 + xH^+ + xe^- = H_xV_2O_5 \qquad [1]$$

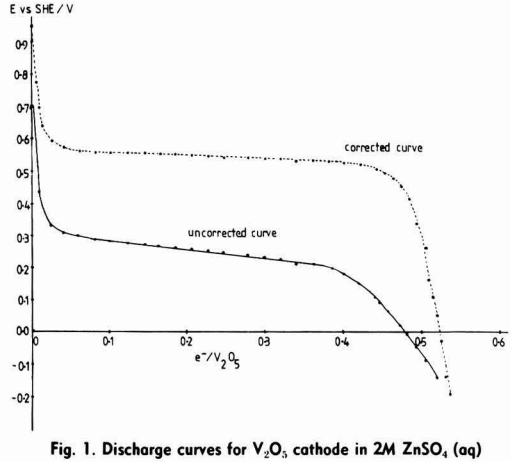


Fig. 1. Discharge curves for V_2O_5 cathode in 2M $ZnSO_4$ (aq)

The plateau in Fig. 1 indicates the coexistence of two solid phases: namely, V_2O_5 and $H_xV_2O_5$. Following the end of the plateau, E varies rapidly with the charge passed and corresponds to the formation of a single phase of $H_xV_2O_5$ with a narrow composition range. The pH of the electrolyte was measured continuously throughout the experiment, and the broken curve shown in Fig. 1 has been corrected to unit hydrogen ion activity using the Nernst equation

$$E_{obs} = E^\circ_{corr} + \frac{RT}{n\mathbf{F}} \log [H^+] \qquad [2]$$

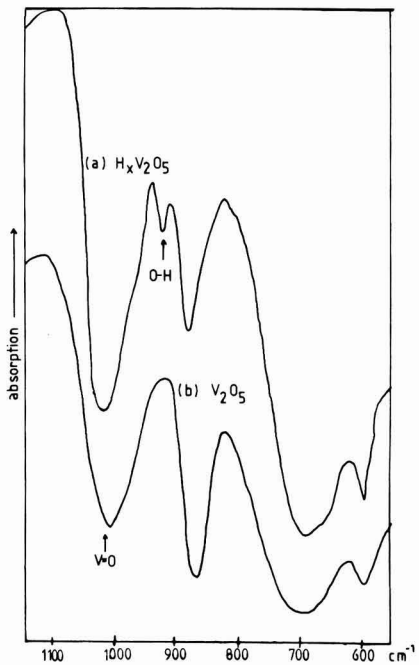


Fig. 2. IR spectra of discharge product (a) and of V_2O_5 (b)

Table I. X-ray powder data for $H_xV_2O_5$

	2θ	d_{obs} (Å)	d_{calc} (Å)	h	k	l
m	15.308	5.787	5.771	2	0	0
s	20.260	4.382	4.368	0	0	1
w	21.729	4.089	4.085	1	0	1
s	26.108	3.412	3.409	1	1	0
m	30.985	2.886	2.886	4	0	0
w	32.429	2.761	2.763	0	1	1
w	33.300	2.690	2.687	1	1	1
wm	34.320	2.613	2.616	3	1	0
w	47.260	1.923	1.924	6	0	0
w	47.981	1.897	1.899	3	0	2
w	48.827	1.865	1.863	0	1	2
w	51.216	1.784	1.784	0	2	0
w	51.888	1.762	1.761	6	0	1

Orthorhombic: Refined lattice parameters: a = 11.544(7), b = 3.568(3), c = 4.368(4) A. Compare refined lattice parameters for V_2O_5 (2): a = 11.51, b = 3.56, c = 4.37 A.

The corrected curve shows $0.45e^-$ passed per V_2O_5 up to the end of the plateau region. The cathode reaction proposed by Shukler and Kuz'min is thus unsatisfactory since $2e^-$ per V_2O_5 would be required for the formation of V_2O_4

$$V_2O_5 + 2H^+ + 2e^- = V_2O_4 + H_2O \quad [3]$$

Our reaction [1] agrees with the expression obtained by Watson and Scott (4) for the pH dependence of the potential of a V_2O_5 cathode in acidic media

$$E = E^\circ - 0.0602pH \quad [4]$$

In conclusion, the cathodic reduction of V_2O_5 in $ZnSO_4$ leads to the formation of the low hydrogen content phase of $H_xV_2O_5$, the lower phase limit being $x = 0.45$.

Acknowledgments

We thank the U.S.A.F. Office of Scientific Research for Grant AFSOR-83-0052. A.M.C. Also thanks the S.E.R.C. for a Research Studentship.

Manuscript received June 25, 1985.

The University of Oxford assisted in meeting the publication costs of this article.

REFERENCES

1. Y. S. Shukler and L. L. Kuz'min, *Shurnal Prikl. Khim.*, **39,** 1327 (1966).
2. ASTM Powder Diffraction File 9-387.
3. P. G. Dickens, A. M. Chippindale, S. J. Hibble, and P. Lancaster, *Mater. Res. Bull*, **19,** 319 (1984).
4. N. V. Watson and A. B. Scott, *This Journal*, **112,** 883 (1965).

The Electrochemical Deposition of Conducting Poly(3-Methyl-2,5-Thienylene) Films from Aqueous Media

Andrzej Czerwinski,[1] Hans Zimmer, Chiem Van Pham, and Harry B. Mark, Jr.*

Department of Chemistry, University of Cincinnati, Cincinnati, Ohio 45221

Diaz *et al.* have published extensively on the characterization of electrodeposited conducting films of poly(pyrrole) (1) and poly(2,5-thienylene) (2) from nonaqueous media. The electrochemical behavior of solution phase redox couples at electrodes consisting of such conducting polymer films have been described also (1-6). There appears to be a certain disagreement about the effect of small amounts of water in the nonaqueous deposition media on the morphological and electrochemical behavior of poly(pyrrole) films deposited by electrochemical oxidation on platinum (3, 4). Although Taurillon and Garnier have done the stability test of poly(3-methyl-2,5-thienylene)[2] in 1:1 CH_3CN/H_2O medium and showed that after 10^3 cycles of anodic-cathodic polarization no degradation of the electrochemical properties of the polymer occurs, (5), there have been no reports of the electrodeposition of polythienylene from aqueous media alone. In spite of the fact that the monomeric, 3-methylthiophene is not significantly soluble in an aqueous media (7), it was found, as reported here, that conducting films of poly-(3-methyl-2,5-thienylene) could be deposited by electrochemical oxidation of aqueous emulsions of the monomer. The procedure for aqueous deposition and the comparison to nonaqueous electrodeposited film are described.

Experimental

The 3-methylthiophene monomer was a commercial sample and was used as is (Aldrich Chemical Company, Milwaukee, Wisconsin). The polymer film was prepared by an electro-oxidation of the monomer in a standard single-compartment cell–three-electrode potentiostat system using both platinum wire working and auxiliary electrodes. A normal calomel electrode (NCE) was used as the reference electrode. As mentioned above, the monomer was essentially water insoluble and the stirred solution was an unstable heterogeneous emulsion. The aqueous phase of the stirred emulsion used for electrodeposition was a 0.1*M* $NaClO_4$ solution. The electrodeposition potentials were either +1.0 or +1.4V *vs.* NCE and the solutions were deaerated prior and during the electrolysis by a constant stream of argon. Prior to use, the platinum working electrodes were pretreated by cyclic polarization using −0.25 and +1.15V *vs.* NCE potential limits in 0.5*M* aqueous H_2SO_4 solution until previously described (8) reproducible cyclic voltammograms were obtained. The chemical and experimental conditions for the background cyclic voltammograms of the aqueous deposited conducting poly(thienylene) films and the ferro/ferricyanide couple are given in the legends of the figures. The photographs of the electrodes surfaces were taken by SEM (Cambridge Stereo Scan 600) and surfaces were analyzed by an attached energy dispersive analyses of x-rays (EDAX) system. The bare Pt electrode and the film-coated Pt electrodes used in these experiments had identical surface areas.

Results and Discussion

Figure 1 shows the scanning electron micrographs obtained for poly(3-methyl-2,5-thienylene) films electrogenerated on Pt wire electrodes at different applied deposition potentials. Figure 1a depicts the surface morphology of a smooth poly(thienylene) film formed on electrogeneration at +1.0 to +1.1V *vs.* NCE. The film appears to the eye as a light yellow color and to be transparent. EDAX shows that the film contains a high concentration of sulfur. The SEM indicates that it is apparently nonporous for the magnification indicated. Physically, the film is strongly adherent to the platinum and cannot be removed by electrochemical or chemical means. A film of a few micrometers in thickness can be obtained after about 60h

* Electrochemical Society Active Member.

[1] On leave from the University of Warsaw, Warsaw, Poland.

[2] The divalent radical derived of thiophene in analogy with the phenylene nomenclature is commonly referred to as thienylene. Thus, the compounds dealt with in this and similar publications from this laboratory are named 2,5-poly(thienylenes) and not 2,5-polythiophenes.

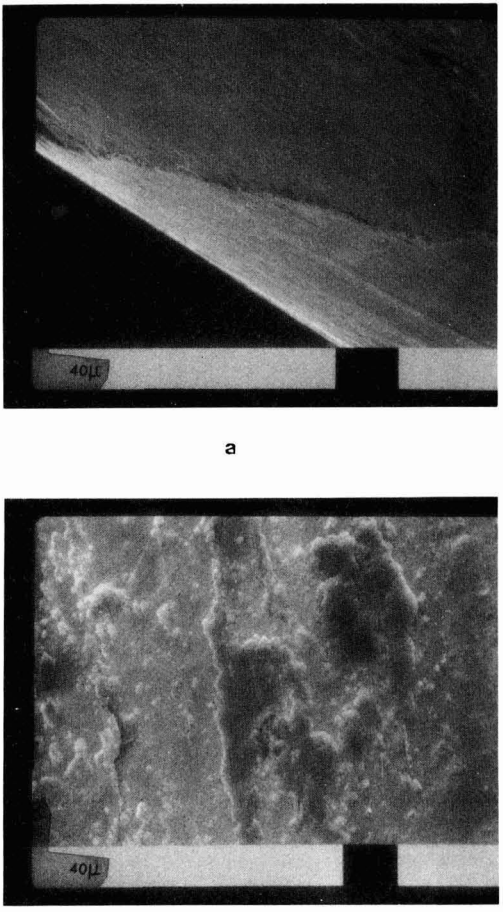


Fig. 1. Scanning electron microscope pictures obtained for the 3-methyl-2,5-poly(thienylene) films. a. Electrodeposited at +1.0V vs. NCE. b. Electrodeposited at +1.4V vs. NCE.

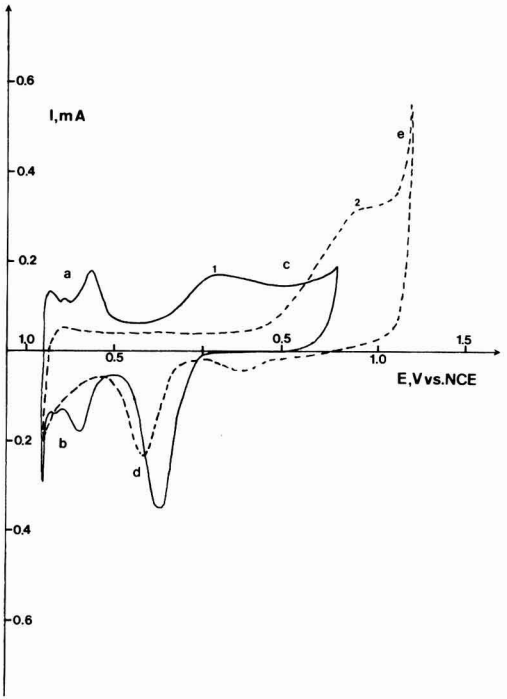


Fig. 2. Voltammogram for Pt electrode film obtained without (curve 1) and with (curve 2) a poly(3-methyl-2,5-thienylene) film obtained in 0.1M $NaClO_4$. Sweep rate = 50 mV-s^{-1}. The electrodeposition potential was +1.0V vs. NCE.

deposition time. Figure 1b shows that the poly(3-methyl-2,5-thienylene) deposited at +1.4V *vs.* NCE is quite rough microscopically as compared to that obtained at +1.0 to 1.1V (Fig. 1a). Furthermore, the film is opaque and appears black to the eye. It also does not adhere strongly to the platinum surface and flakes easily on either electrochemical or mechanical treatment. The SEM suggests that the film is porous. Clearly morphology and chemical nature of the film obtained on electro-oxidative polymerization is highly potential dependent. However, the fact that the film continues to grow with time at both deposition potentials indicates that it is conductive. It should be noted that polymerization under the same conditions for 3-methyl-2,5-dibromothiophene does not occur. It means that when the 2 and 5 positions are blocked by Br atoms the anodic polymerization reaction does not occur. Thus, it is felt that the films obtained on the anodic aqueous oxidation of thiophene results in the 2,5-polymer system.

Figure 2 shows the typical background cyclic voltammetric behavior of an electrodeposited poly(3-methyl-2,5-thienylene) film at +1.0V in a neutral *p*H 0.1*M* aqueous $NaClO_4$ solution. Also shown in Fig. 2 is the typical cyclic voltammogram for the same supporting electrolyte solution at a bare Pt contact electrode. There are marked differences in peak potentials and magnitude of currents, but the currents for polymer-covered Pt electrodes essentially correspond to the same processes as in the bare Pt contact electrode where peaks at negative potentials (a, b in Fig. 2) correspond to the hydronium ion reduction (b) and adsorbed hydrogen oxidation (a) at a platinum electrode surface, and the peaks at positive potentials (c, d) correspond to the formation of oxygen species (c) and their reduction (d) on platinum. The small peak observed at negative electrode polarization (*ca.* 250 mV) subsequent to a positive polarization probably corresponds to reduction of some oxidized moiety of thiophene. It should be noted that there is an increase in the magnitude of the current in the positive applied voltage region, which indicates that both the Pt surface and the polymer oxidation processes are contributing to the total anodic current. Also, the potentials of surface oxidation and oxygen evolution on Pt covered with the thiophene polymer are shifted to more positive potentials than on Pt. At the same time, there is a very significant decrease in the current magnitudes in the corresponding hydrogen-platinum surface redox peaks at negative potentials as compared to the bare Pt electrode. These results suggest that the poly(3-methyl-2,5-thienylene) film is microscopically porous and the redox reactions can occur at both the Pt and poly(3-methyl-2,5-thienylene) surfaces. The results of Tourillon and Garnier (5) showed that poly(thienylene) films deposited from nonaqueous media are fibrillar and also have potential dependent swelling properties. In contrast, the films deposited from aqueous media are not fibrillar and do not exhibit any potential dependent swelling. It is also important to note that there are no observable color changes in the positive and negative polarization regions as noted for the nonaqueous deposited film (6). Similar qualitative results were obtained in 0.5*M* aqueous sulfuric acid electrolyte solutions, as shown in Fig. 3.

As a further test of the electrode response of a +1.0V deposited poly(3-methyl-2,5-thienylene) film from an

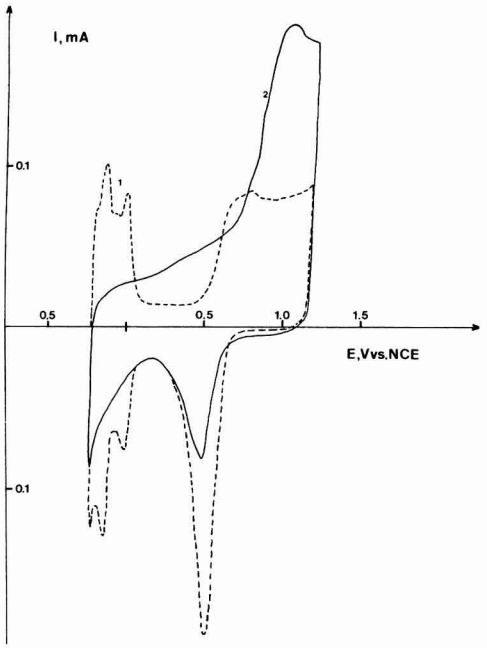


Fig. 3. Voltammograms for Pt electrode without (curve 1) and with (curve 2) a poly(3-methyl-2,5-thienylene) film obtained in 0.5M H_2SO_4. Sweep rate = 50 mV-s^{-1}, and electrodeposition potential was +1.4V vs. NCE.

aqueous media, the background cyclic voltammograms obtained in 0.1*M* acetonitrile solution containing $10^{-3}M$ nitrobenzene and $10^{-3}M$ triphenylamine were examined. Typical cyclic voltammograms are shown in Fig. 4. Again, in the positive potential region of the voltammograms, there is a slight increase in the anodic current (*e.g.*, oxidation reaction of triphenylamine) and a slight decrease in

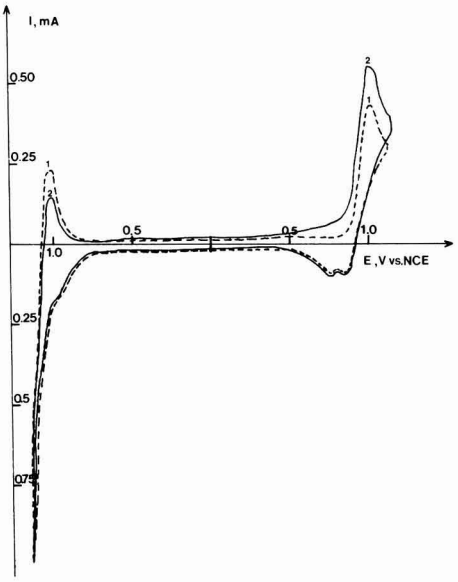


Fig. 4. Cyclic voltammograms of a 0.1 TEAFB/CH_3CN solution containing 10^{-3}M nitrobenzene and 10^{-3}M triphenylamine at 50 mV-s^{-1} vs. NCE. Curve 1 (dotted line): Pt electrode. Curve 2 (solid line): Pt-poly(thienylene) electrode.

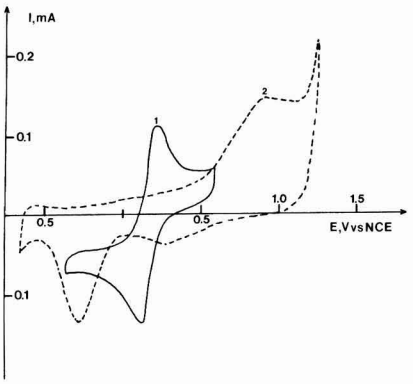


Fig. 5. Cyclic voltammograms for Pt electrode covered by poly-(3-methyl-2,5-thienylene) in 0.1 $NaClO_4$ in the presence of 10^{-2}M $K_3Fe(CN)_6$ (curve 1) and without (curve 2).

peak currents in the negative potential region (*e.g.*, nitrobenzene reduction reaction). This is in contrast to the results reported by Diaz *et al.* (6), which showed that the neutral form of poly(thienylene) in acetonitrile solution exhibited no redox waves for negative polarization and, hence, no conductivity. Again, this indicates a significant degree of porosity of the aqueous deposited poly-(3-methyl-2,5-thienylene) films as compared to the nonaqueous deposited films investigated by Diaz *et al.* (5). It is also interesting to note that electro-oxidation of the monomer when $CuCl_2$ is added to the aqueous $NaClO_4$ solution produces the same polymer film without copper being incorporated. This result is different from that of Tourillon *et al.* (9), who observe that, on oxidation from CH_3CN containing a high concentration of $CuCl_2$, metallic clusters of copper are homogeneously distributed in the polymer matrix. The polymer films obtained on deposition at +1.4V show in all cases significantly more Pt electrode-type behavior or a higher degree of porosity, as suggested by the SEM in Fig. 1b.

Furthermore, the cyclic voltammograms for the ferro/ferricyanide redox systems at an electrode formed with a poly(thienylene) film from an aqueous medium at +1.0V *vs.* NCE are exactly the same in shape as those obtained at a bare Pt electrode, as shown in Fig. 5. However, the magnitude of the peak currents is much lower than that of a bare Pt electrode having the same surface area.

It is clear that the electrodeposition of poly(3-methyl-2,5-thienylene) films from an aqueous emulsion of the monomer produces a conducting film of the polymer which has very different morphology and conducting properties than that produced on electrodeposition from nonaqueous media. It is also clear that the potential of the aqueous electro-oxidation of the monomeric 3-methylthiophene controls the porosity, adherence, etc., of the poly(thienylene) film obtained and a systematic study of the electrochemical and physical nature of the polymer as a function of deposition potential might produce conditions that will yield a nonporous poly(3-methyl-2,5-thienylene) film. Also, a study of films obtained on electro-oxidation from mixed aqueous/nonaqueous solvent systems with variation of the ratio of concentration of the solvents would be interesting. However, no further study of this aqueous electrodeposition is planned in this laboratory.

Acknowledgment

This research was supported in part by the National Science Foundation, Grant no. NSF CHE 8205873, and was also aided significantly by gifts of n-butyl lithium from the Lithium Corporation of America, Bessemer City, North Carolina 28016.

Manuscript submitted Jan. 24, 1985; revised manuscript received May 6, 1985. This was Paper 69 presented at the

Toronto, Ontario, Canada, Meeting of the Society, May 12-17, 1985.

The University of Cincinnati assisted in meeting the publication costs of this article.

REFERENCES

1. A. F. Diaz and J. I. Castillo, *J. Chem. Soc. Chem. Commun.*, 397 (1980); A. F. Diaz, J. I. Castillo, J. A. Legan, and W. Y. Lee, *J. Electroanal. Chem.*, **129,** 115 (1981); E. M. Genies, G. Bidan, and A. F. Diaz, *ibid.*, **149,** 101 (1983); P. Bergmayer and R. W. Murray, *J. Am. Chem. Soc.*, **104,** 6139 (1982); A. F. Diaz, J. M. Vasquez Vallejo, and A. Martinez Duran, *IBM J. Res. Dev.*, **25,** 42 (1981); R. A. Bull, F. F. Fan, and A. J. Bard, *This Journal*, **129,** 1009 (1982); R. Noufi, D. Tench, and L. F. Warren, *ibid.*, **127,** 2310 (1980); R. Noufi, A. J. Frank, and A. J. Nozik, *J. Am. Chem. Soc.*, **103,** 1849 (1981); T. Skotheim, I. Lundstrom, and J. Prejza, *This Journal*, **128,** 1625 (1981); T. Skotheim, L. G. Petersen, O. Inganas, and I. J. Lundstrom, *ibid.*, **129,** 1737 (1982); D. Iganas, T. Skotheim, and I. Lundstrom, *Phys. Scr.*, **28,** 863 (1982); R. A. Simon, A. J. Ricco, and M. S. Wrighton, *J. Am. Chem. Soc.*, **104,** 2031 (1982); G. Cooper, R. Noufi, A. J. Frank, and A. J. Nozik, **295,** 578 (1982); R. Noufi, *This Journal*, **130,** 2126 (1983); A. J. Frank and K. Honda, *J. Phys. Chem.*, **86,** 1933 (1982); K. S. Reddy and A. S. N. Murthy, *Electrochim. Acta*, **28,** 473 (1983); T. Komori and T. Nonaka, *J. Am. Chem. Soc.*, **105,** 5690 (1983); A. F. Diaz, T. J. Castillo, K. K. Kanazava, M. Salmon, and O. Fajardo, *J. Electroanal. Chem.*, **133,** 233 (1982); M. Salmon, A. F. Diaz, J. A. Logan, M. Krounbi, and J. Bargen, *J. Mol. Cryst. Liq. Cryst.*, **83,** 265 (1982); A. F. Diaz, W. Y. Lee, J. A. Logan, and D. C. Green, *J. Electroanal. Chem.*, **108,** 377 (1982); M. Salmon, A. F. Diaz, and J. Goita, in "Chemically Modified Surfaces in Catalysis and Electrocatalysis," J. S. Miller, Editor, p. 65, ACS Symposium Series 192, American Chemical Society, Washington, DC (1981).
2. G. Tourillon and F. Garner, *J. Electroanal. Chem.*, **135** 173 (1982); A. F. Diaz, J. Bargon, and R. Waltmar, in "Membranes and Ionic and Electronic Conducting Polymer," E. B. Yeager, B. Schumm, Jr., K. Mauritz, K. Abbey, D. Blankenship, and J. Akridge, Editors, p. 332, The Electrochemical Society Softbound Proceedings Series, Pennington, NJ (1982); A. Diaz, *Chem. Scr.*, **17,** 145 (1982); G. Garner, G. Tourillon, M. Gazard, and J. C. Dubois, *J. Electroanal. Chem.*, **148,** 299 (1983); R. J. Waltman, A. F. Diaz, and J. Bergen, *This Journal*, **131,** 1452 (1984); *ibid.*, **130,** 2042 (1983).
3. S. Brimmer, Ph.D. Thesis, University of Cincinnati, Cincinnati, OH (1984).
4. A. F. Diaz, Private communication (1984).
5. G. Tourillon and F. Garnier, *J. Electroanal. Chem.*, **161,** 51 (1984).
6. R. J. Waltman, J. Bargon, and A. F. Diaz, *J. Phys. Chem.*, **87,** 1459 (1983).
7. "Handbook of Chemistry and Physics," 61st ed., R. C. Weast, Editor, CRC Press, Inc., Boca Raton, FL (1980).
8. A. Capon and R. Parsons, *J. Electroanal. Chem.*, **65,** 285 (1975).
9. G. Tourillon, E. Dartyge, H. Dexpert, A. Fentaine, A. Jucha, F. Lagarde, and D. E. Sayers, *ibid.*, **78,** 357 (1984).

JOURNAL OF THE ELECTROCHEMICAL SOCIETY

SOLID-STATE SCIENCE AND TECHNOLOGY

NOVEMBER 1985

Deep Levels in Semi-Insulating LEC GaAs Before and After Silicon Implantation

Salam Dindo,* Ibrahim Abdel-Motaleb, Kerry Lowe,**[1] Wade Tang, and Lawrence Young**

Department of Electrical Engineering, University of British Columbia, Vancouver, British Columbia, Canada V6T 1W5

ABSTRACT

The deep trapping levels present before ion implantation of silicon into the semi-insulating LEC GaAs starting material were investigated using optical transient current spectroscopy (OTCS). MESFET channel current deep level transient spectroscopy (DLTS) was used for the implanted material. With a silicon nitride layer used to encapsulate the GaAs for postimplantation annealing and with implantation directly into the GaAs, it was found that of seven or more deep levels seen in the semi-insulating substrate prior to silicon implantation only the level believed to be EL12 remained. On implanting through a thin Si_3N_4 encapsulating layer and annealing under Si_3N_4, only EL2 was found. With a silicon dioxide layer as an encapsulant, two traps remained and two apparently unreported levels appeared.

It is widely, but not universally, accepted (1, 2) that a fabrication process based on the implantation of dopant, often silicon, directly into undoped liquid-encapsulated Czochralski (LEC) GaAs wafers is likely to dominate in the manufacture of high speed digital and analog GaAs integrated circuits. This fabrication process is as opposed to such older methods as the use of doped epitaxial layers for the MESFET channels, or that of implanted semi-insulating "buffer" epitaxial layers deposited on chromium-doped Bridgman or Czochralski wafers. With this fabrication process, some of the problems with deep trapping levels which have been extensively reported in the literature are no longer present. For example, in the earlier work, traps in epitaxial layers and at the interface of the buffer layer and the semi-insulating layer (4-6) were a problem. Naturally, problems associated with chromium or the redistribution of chromium (7-9), which with LEC material is no longer needed to obtain semi-insulating material, are no longer present. Nevertheless, the problems with the newer technology still include those due to the presence or redistribution of deep trapping levels. These levels may be due to impurities or native defects and may be present in the starting material or may be induced by process steps. In addition to problems of deep levels, the distribution of the implanted dopant and its percentage activation are crucial to device characteristics and can depend very significantly on the nature of the starting LEC material as well as on the process steps. With silicon as dopant, a high temperature anneal (at about 850°C) is needed not only to repair damage but also to allow the silicon atoms to find gallium sites on which they act as donors. On arsenic sites, they would act as acceptors. To avoid loss of arsenic, the wafers are sometimes sealed or encapsulated with a layer of SiO_2 or Si_3N_4 (10, 11). These are, of course, nominal formulas; the actual films are nonstoichiometric. Onuma *et al.* (12) have demonstrated that the implanted silicon is redistributed by diffusion during the anneal more with SiO_2 than with Si_3N_4. This was explained as due to the presence of more vacant gallium sites in the GaAs when SiO_2 was used because of increased loss of gallium through the encapsulant film. It is known that gallium can diffuse through SiO_2.

The precise ways in which the details of the growth process of the Czochralski GaAs affect (*i*) the traps initially present, (*ii*) those generated by the processing, and (*iii*) the dopant redistribution and activation process need to be better understood and controlled. The growth and polishing techniques used by suppliers of LEC GaAs wafers are regarded as proprietary. Ingot qualification tests are used by device manufacturers.

There is an extensive literature on deep levels in GaAs (13) and on their effects on device characteristics. Only a few references can be given here. Recent papers which are specifically on deep levels in ion-implanted undoped semi-insulating (SI) GaAs include those by Sriram *et al.* (14, 15), by Rhee *et al.* (16, 17), and by Hickmott (18).

In the present work, we applied optical transient current spectroscopy (OTC)—also known as photoinduced transient spectroscopy (PITS)—(19, 21) to the undoped LEC starting material from various manufacturers and after various surface treatments. Metal semiconductor field effect transistors (MESFET's) were then fabricated on material from one manufacturer using three fabrication procedures. The traps present in the MESFET's were investigated using channel current deep level transient spectroscopy (DLTS) (6, 8, 22).

Experimental Procedures

The test devices for OTCS were of the planar type, *i.e.*, a pair of electrodes were deposited side by side on the one surface. As described previously (25), a constant voltage was applied and a GaAsP LED diode (670 nm) provided pulses of light. The transient current following the termination of the light pulses was sampled at times t_1 and t_2 after the end of the illumination using a boxcar integrator. The temperature of the device was scanned. Peaks were observed at certain temperatures due to the individual traps as their time constants $\tau = \tau_0 \exp(W/kT)$ pass through the observation window. Chromium electrodes were used since these give lower dark current than Au + Ge.

The MESFET used for channel current DLTS were long channel devices ("fat FET's") (23) with a channel width of 180 or 200 μm and a gate length of 100 or 120 μm.

* Electrochemical Society Student Member.
** Electrochemical Society Active Member.
Present address: Bell Northern' Research, Ottawa, Ontario, Canada K1Y 4B7.

The source and drain were Au + Ge alloyed at 430°C for 5 min. The gates were aluminum.

In the first set of devices, the channel was implanted with 3×10^{12} cm^{-2} ^{29}Si at 100 keV through windows etched in a 600 nm RF-sputtered SiO_2 layer. The channel was furnace annealed at 850°C for 20 min using a 170 nm RF-sputtered SiO_2 cap. The second and third set of devices were both made using plasma-enhanced chemical vapor deposition (PECVD) Si_3N_4 films laid down in a Plasmatherm Multiversion machine with NH_3 and SiH_4 in He. The second set (labeled II) had their channels implanted through a thin (40 nm) Si_3N_4 film at 125 keV to 3.38×10^{12} cm^{-2} using ^{28}Si. The Si_3N_4 was thickened to 80 nm before annealing. The implantation of the third set (labeled III) was done directly into the GaAs at 100 keV to 2.25×10^{12} cm^{-2} of Si. 80 nm of Si_3N_4 was deposited before annealing.

The channel current DLTS experiments were performed with a bias of 50 mV applied between drain and source, small enough to be in the linear region. A reverse bias voltage was placed on the gate such that the channel was nearly pinched off. Pulses of voltage taking the gate to near zero bias were applied. The basic idea is that majority carrier traps are filled by carriers which are allowed to enter the previously depleted channel during the positive going gate voltage pulse. When the gate voltage returns to its more negative value the negative charge due to the trapped electrons partially compensates the positive space charge density in the depleted region. To maintain the fixed voltage drop across the region, it must, therefore, become initially wider than before. The channel is therefore narrowed and the drain current is less. As the occupancy of the traps returns to normal, the drain current increases (with the time constant of the trap depopulation emission process). Hole traps (9) give the reverse sign of effect [it is believed (9) that the hole trap occupancy can be changed because the quasi-Fermi level for holes communicated with the gate Fermi level].

Results

Starting LEC material.—Figure 1a shows an OTCS spectrum of a device made on a Cominco wafer from ingot no. 344. The spectrum is considerably different from those of early (lower-numbered) ingots from this manufacturer reported earlier (25), but is very close to that of a device made on a recent Sumitomo wafer (Fig. 2A). A Litton wafer gave the rather different results shown in Fig. 2b. We have no information on how typical these Litton and Sumitomo wafers were. The negative peak P2 has about the same magnitude for the Cominco and Sumitomo wafers. This peak has been related by Oliver *et al.* (24) to the degree of wetness of the B_2O_3 used in the growth process and we have found that the mechanical abrasion can increase its magnitude (25). We have discussed the mechanism by which negative peaks occur elsewhere (25). The EL2 peak P1 is much less pronounced in this current Cominco and Sumitomo material than in the earlier slices from Cominco used to investigate "thermal stability" (of the semi-insulating property) (25).

Figure 1b shows a spectrum for a specimen on a Cominco wafer of a similarly recent era (no. 453) which had been subjected to an etch by Bell Northern Research using H_2O_2 + H_2SO_4. The same specimen, after measurement, was again etched in an H_2O_2 and H_2SO_4 mixture to give the result shown in Fig. 1c. The effect of this process on the Sumitomo specimen in Fig. 2a is shown in Fig. 2c. These results represent a feature of the OTCS method that the effects of surface treatments can be investigated. These treatments should not be assumed merely to remove surface layers and thus reveal a depth profile of traps since a change in surface traps could also affect the result. Surface traps will presumably be populated by the light pulse and could cause some band bending.

All samples show the same set of peaks but with different amplitudes. Arrhenius plots (Fig. 4) were obtained using a range of rate windows for the OTCS sampling and using a total of ten samples made on Cominco wafers

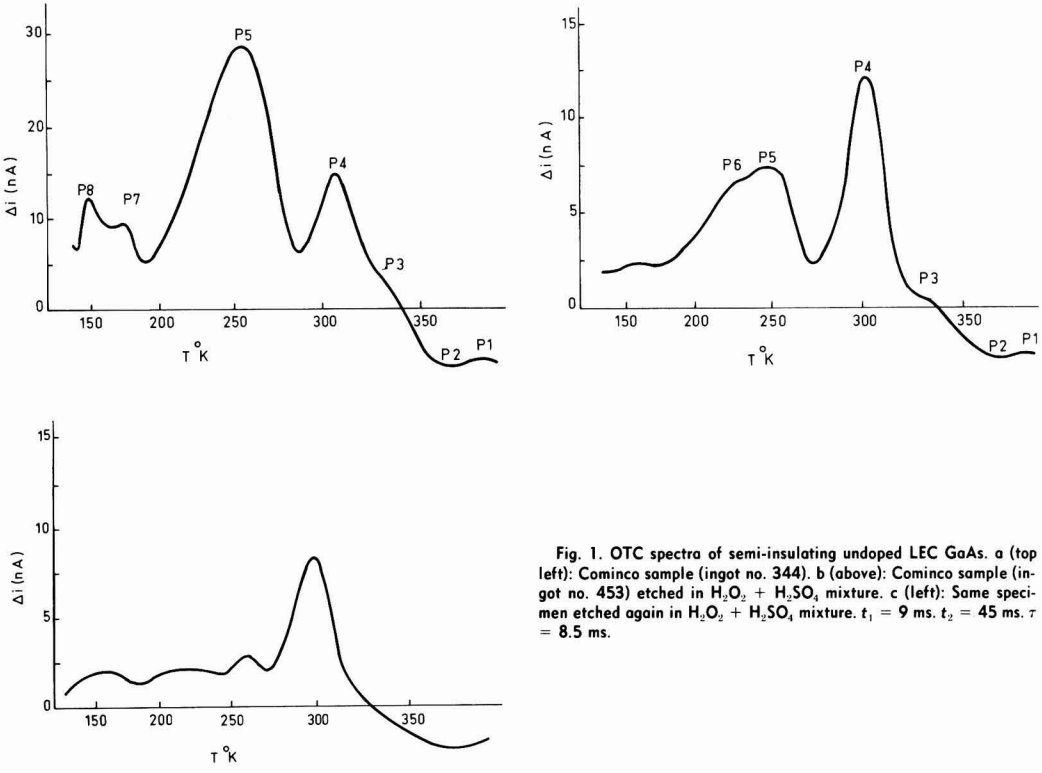


Fig. 1. OTC spectra of semi-insulating undoped LEC GaAs. a (top left): Cominco sample (ingot no. 344). b (above): Cominco sample (ingot no. 453) etched in H_2O_2 + H_2SO_4 mixture. c (left): Same specimen etched again in H_2O_2 + H_2SO_4 mixture. t_1 = 9 ms. t_2 = 45 ms. τ = 8.5 ms.

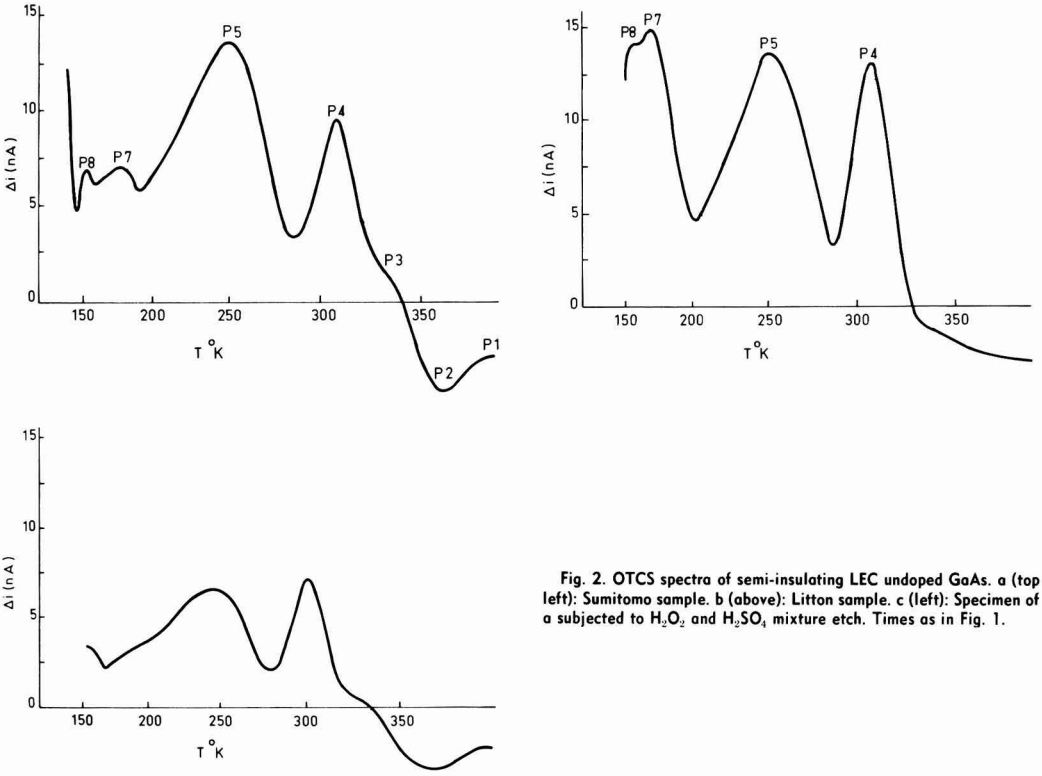


Fig. 2. OTCS spectra of semi-insulating LEC undoped GaAs. a (top left): Sumitomo sample. b (above): Litton sample. c (left): Specimen of a subjected to H_2O_2 and H_2SO_4 mixture etch. Times as in Fig. 1.

(both tail and seed ends). The identifications of the observed peaks with previously reported traps were given in a previous paper (25) and are summarized in Table I for comparison with the channel current DLTS results.

Deep levels in Si-implanted layers.—Channel current DLTS spectra are given in Fig. 3 for MESFET's made from the Cominco material using the three processes above (I: SiO_2 cap. II: Si_3N_4 cap, implantation through Si_3N_4. III: Si_3N_4 cap, direct implantation into the GaAs). Arrhenius plots for the channel current DLTS peaks are given in Fig. 4a, and, for comparison, Arrhenius plots are also given for the OTCS peaks 4b. Table I summarizes the DLTS and OTCS data.

The devices made with a SiO_2 cap gave four peaks. On the basis chiefly of activation energies, two of these, Q1 and Q2, are the same as two peaks found in the starting material by OTCS, P4 and P5. The closest levels in the compilation of Martin *et al.* (26) seems to be EL12 and EL3. The other two levels Q3 and Q4 were not observed in the starting material and are therefore process-induced peaks. The data given are for ingot no. 43, but similar results were obtained for ingots no. 51 and 123.

For devices implanted directly into GaAs and annealed under Si_3N_4, only S1 (0.74 eV) was found. This peak was observed in the starting material by OTCS as P4 and is believed to be EL12. For devices implanted through Si_3N_4 and annealed under Si_3N_4, only R1 (0.85 eV) was observed. This peak was found by OTCS as P1 and is the EL2 of Martin *et al.* (26). The data are for specimens from ingot no. 344, but similar results were obtained for process II with ingot no. 175. Although crystal manufacturers may change their growth procedures from time to time, the above differences are believed to be determined by the choice of process, not the ingot number.

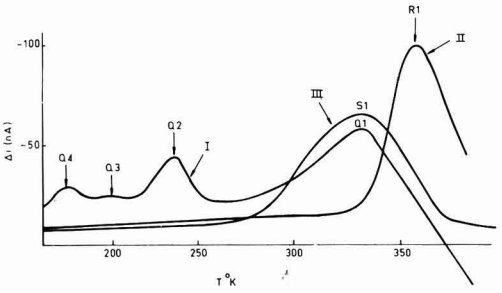


Fig. 3. Channel current spectra for MESFET's using processes I, II, and III. τ = 22.4 ms.

Table I. Activation energies, capture cross sections, and possible identities of the deep levels found using OTCS (P1-8) in semi-insulating, undoped, LEC GaAs, and of deep levels found by channel current DLTS in MESFETs fabricated by three processes (Q1-4, R1, S1)

Label	Activation energy (eV)	Capture cross section (cm^2)	Possible identity
P1	0.87	1.05×10^{-12}	EL2
P2	0.65	3.00×10^{-12}	Negative peak
P3	0.79	3.69×10^{-12}	EL12 ?
P4	0.76	2.12×10^{-12}	EL12 ?
P5	0.59	3.46×10^{-12}	EL3 ?
P6	0.52	2.90×10^{-13}	EL4
P7	0.38	3.20×10^{-14}	EL6
P8	0.32	2.50×10^{-13}	HL6
Q1	0.74	2.67×10^{-13}	P4 and EL12
Q2	0.57	4.47×10^{-12}	P5 and EL3
Q3	0.28	1.66×10^{-16}	—
Q4	0.24	1.45×10^{-16}	—
R1	0.85	4.30×10^{-13}	P1 and EL2
S1	0.74	2.10×10^{-13}	

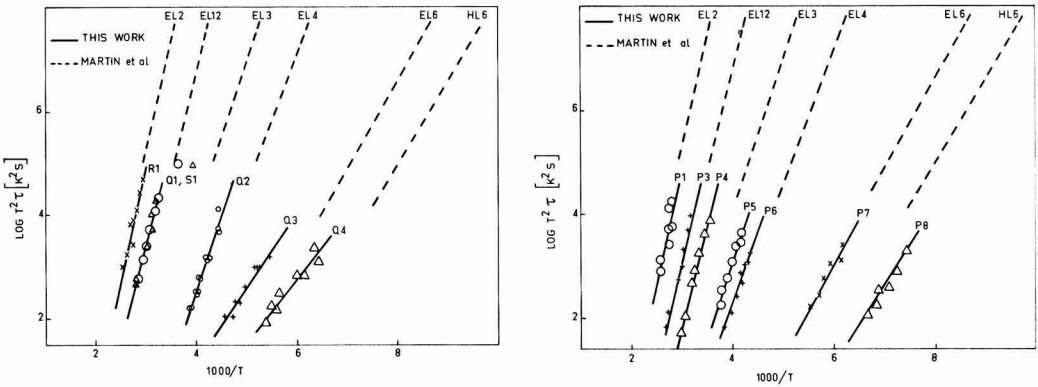


Fig. 4. Signature or Arrhenius plots. a (left): Channel current DLTS data. b (right): OTCS DLTS data.

Relating these results to previous work (Table II), Sriram *et al.* (14, 15) used devices with Si implanted directly into SI LEC GaAs at doses of 2-5.5 × 10^{12} cm^{-2} at 100-325 keV and annealed at 860°C under "phosphorus silicon glass." Using channel current DLTS, they found six levels, of which three were process induced. Their defect A is possibly our level Q4. Rhee and Bhattacharya (16) implanted Si directly into Cr-doped SI LEC GaAs at doses of 10^{12} and 10^{13} cm^{-2} at 100 keV and annealed under SiO_2 (Silox). They found three electron traps, of which one was present in their starting material. In a later paper (17), they found two dominant levels (0.52 eV electron trap and an 0.15 eV hole trap) in directly implanted material, these centers being absent on implantation through Silox. Jervis *et al.* (27) compared the traps produced by implantation (*i*) direct and (*ii*) through Si_3N_4 into epitaxial buffer layers and into Cr-doped semi-insulating wafers. They annealed under Si_3N_4. Using capacitance DLTS with both electrical and optical excitation, they also found an increase in EL2 on implanting through Si_3N_4.

As regards mechanisms for the extra EL2, one might suggest that when implantation is done through Si_3N_4 knock-on nitrogen atoms (28) compete with displaced As atoms for vacant As sites (since nitrogen is also Group 5). The preempted As atoms could adopt vacant Ga sites to produce As_{Ga} which is, or is associated with, EL2 (29).

With SiO_2 as encapsulant, the loss of Ga is to be expected to have some effect on the types of defect produced. Perhaps occupation of the vacant Ga sites by impurities from the SiO_2 cap could be responsible for the two process-induced traps. The fact that two traps present in the starting material disappeared when annealed under Si_3N_4 but not when annealed under SiO_2 surely has to be related to the Ga vacancy concentration.

Table II. Some deep levels in silicon-implanted GaAs reported in the literature

Label	Activation energy (eV)	Capture cross section (cm^2)	Possible identity (Ref.)
A	0.23	1.90×10^{-17}	Unknown (14)
B	0.22	1.17×10^{-15}	EL14
C	0.53	1.60×10^{-12}	EL4
D	0.85	1.00×10^{-9}	New
E	0.64	5.90×10^{-14}	Cr complex
F	0.75	1.50×10^{-14}	EL2
A	0.52 ± 0.01	$(1.20\text{-}1.60) \times 10^{-18}$	(16)
B	0.17 ± 0.01	$(5.20\text{-}5.50) \times 10^{-23}$	
C	0.21	3.10×10^{-21}	
EB2	0.83	2.20×10^{-13}	EL2 (27)
EB3	0.90	3.00×10^{-11}	
EB4	0.71	8.30×10^{-13}	
EB7	0.30	1.70×10^{-14}	
EB6	0.41	2.60×10^{-13}	

Acknowledgments

This work was supported by the British Columbia Science Council and by the Natural Sciences and Engineering Research Council of Canada.

Manuscript submitted April 19, 1985; revised manuscript received Aug. 2, 1985. This was Paper 707 SOA presented at the Toronto, Ontario, Canada, Meeting of the Society, May 12-17, 1985.

The University of British Columbia assisted in meeting the publication costs of this article.

REFERENCES

1. B. M. Welch, Y-D. Shen, R. Zucca, R. C. Eden, and S. I. Long, *IEEE Trans. Electron Devices*, **ed-27,** 116 (1980).
2. "GaAs FET Principles and Technology," J. V. DiLorenzo and D. D. Khandelwal, Editors, Artech House, Inc., Dedham, MA (1982); S. K. Ghandhi, "VLSI Fabrication Principles," John Wiley and Sons, New York (1983).
3. S. Asai, S. Ishioka, H. Kurono, S. Takahashi, and H. Kodra, *J. Jap. Soc. Appl. Phys.*, **42,** Suppl. 71 (1973).
4. N. Yokoyama, A. Shibatomi, S. Ohkawa, M. Fukuta, and H. Ishikawa, *Inst. Phys. Conf. Ser.*, **33b,** 20 (1977).
5. T. Itoh and H. Yanai, *Jpn. J. Appl. Phys.*, **19-1,** Suppl., 351 (1979).
6. T. Itoh and H. Yanai, *IEEE Trans. Electron Devices*, **ed-27,** 1037 (1980).
7. Y. M. Houng and G. L. Pearson, *J. Appl. Phys.*, **49,** 3248 (1978).
8. A. A. Immorlica, D. R. Chen, D. R. Decker, and R. D. Fairman, *Inst. Phys. Conf. Ser.*, **56,** 423 (1981).
9. A. Zylberstein, G. Bert, and G. Nuzillat, *ibid.*, **45,** 315 (1979).
10. K. V. Vaidyanathan, M. J. Helix, D. J. Wolford, G. B. Streetman, R. J. Blattner, and C. A. Evans, *This Journal*, **124,** 1781 (1977).
11. C. W. Farley and B. G. Streetman, *J. Electron. Mater.*, **13,** 401 (1984).
12. T. Onuma, T. Hirao, and T. Sugawa, *J. Appl. Phys.*, **52,** 6128 (1981).
13. U. Kaufmann and J. Schneider, *Adv. Electron. Electron Phys.*, **58,** 81 (1982).
14. S. Sriram and M. B. Das, *IEEE Trans. Electron Devices*, **ed-30,** 586 (1983).
15. S. Sriram, B. Kim, P. K. Ghoush, and M. B. Das, *Inst. Phys. Conf. Ser.*, **63,** 215 (1982).
16. J. K. Rhee and P. K. Bhattacharya, *J. Appl. Phys.*, **53,** 3311 (1982).
17. P. K. Bhattacharya and J. K. Rhee, *This Journal*, **131,** 1152 (1984).
18. T. W. Hickmott, *IEEE Trans. Electron Devices*, **ed-31,** 54 (1984).
19. R. D. Fairman, F. J. Morin, and J. R. Oliver, *Inst. Phys. Conf. Ser.*, **45,** 134 (1979).
20. C. L. Hurtes, M. Boulou, A. Mitonneau, and D. Bois, *Appl. Phys. Lett.*, **32,** 821 (1978).
21. G. M. Martin and D. Bois, in "Semiconductor Characterization Techniques," P. A. Barnes, Editor, p. 32, The Electrochemical Society Softbound Proceedings Series, Princeton, NJ (1978).

22. M. G. Alderstein, *Electron. Lett.*, **12,** 297 (1976).
23. A. A. Immorlica, D. R. Becker, and W. A. Hill, *IEEE Trans. Electron Devices*, **ed-27,** 2285 (1980).
24. J. R. Oliver, R. D. Fairman, and R. T. Chen, *Electron. Lett.*, **17,** 839 (1981).
25. L. Young, W. Tang, S. Dindo, and K. Lowe, Submitted to *This Journal*.
26. G. M. Martin, A. Mitonneau, and A. Mircea, *Electron. Lett.*, **13,** 191, 666 (1977).
27. T. R. Jervis, D. W. Woodward, and L. F. Eastman, *ibid.*, **15,** 619 (1979).
28. R. T. Blunt, R. Sweda, and I. R. Sanders, *Vacuum*, **34,** 281 (1984).
29. J. Lagowski, H. C. Gatos, J. M. Parsey, D. Wada, M. Kaminska, and W. Walukiewica, *Appl. Phys. Lett.*, **40,** 342 (1982).

Chemical Vapor Deposition of Ruthenium and Ruthenium Dioxide Films

M. L. Green,* M. E. Gross, L. E. Papa,[1] K. J. Schnoes, and D. Brasen

AT&T Bell Laboratories, Murray Hill, New Jersey 07974

ABSTRACT

The preparation of Ru and RuO_2 thin films by organometallic chemical vapor deposition and an investigation of the films' properties are reported. Ru is of interest for metallization in integrated circuit fabrication because its thermodynamically stable oxide, RuO_2, also exhibits metallic conductivity. As a result, oxidation during processing of Ru is a less critical concern than in current metallization technology. Taking advantage of the benefits of chemical vapor deposition, such as conformal coverage and low temperature, damage-free deposition, we have deposited Ru, RuO_2, and Ru/RuO_2 by pyrolysis of three organoruthenium complexes. Films of a given phase composition were deposited under a wide variety of conditions and exhibited large variations in electrical resistivity and carbon content. The best Ru film, produced from $Ru_3(CO)_{12}$ at 300°C in vacuum, had a resistivity of 16.9 $\mu\Omega$-cm and exhibited excellent adhesion to Si and SiO_2 substrates. The best RuO_2 film, produced from $Ru(C_5H_5)_2$ at 575°C in O_2, had a resistivity of 89.9 $\mu\Omega$-cm and similarly exhibited excellent adhesion. Rutherford backscattering studies show that Ru and RuO_2 films are effective diffusion barriers between Al and Si up to annealing temperatures of about 550° and 600°C (1/2 h exposure), respectively. Thus, they are significantly better than the currently used W films, which are only effective to about 500°C.

Integrated circuit processing requires the use of conducting films that must maintain their integrity at elevated temperatures. For example, gate electrode metallizations, in addition to being good electrical conductors, must also be resistant to oxidation at temperatures as high as 950°C. Silicides are often chosen for this application. Diffusion barrier films, used to prevent the interdiffusion of Al and Si at source/drain regions (spiking), may be exposed to temperatures as high as 550°C, at which point oxidation, even to a small extent, may degrade the contact resistance between the Al/barrier/Si layers. Tungsten and TiN, currently used as barrier films, are particularly sensitive to oxidation. These examples emphasize the critical concern with the degradation of electrical properties in the film or the film interfaces owing to environmental effects, particularly oxidation.

It is therefore interesting to consider ruthenium as a potential metallization for integrated circuits. Ruthenium dioxide, the most thermodynamically stable oxide of Ru, when formed at temperatures greater than 200°C, is almost as good a conductor as Ru ($\rho_{Ru} = 6.7 \times 10^{-6}$ Ω-cm, $\rho_{RuO_2} = 4.6 \times 10^{-5}$ Ω-cm, where ρ is the resistivity), and is actually as good a conductor as $TaSi_2$($\rho = 5.0 \times 10^{-5}$ Ω-cm) and many other silicides currently used as IC metallizations. In electrical contact applications, the advantages of Ru and RuO_2 are well known (1-3). The use of Ru, therefore, alleviates concern regarding oxidation during processing, since RuO_2 is a good electrical conductor. Other conducting oxides exist, but most are either complex oxides (*e.g.*, $Bi_2Ru_2O_7$, $SrVO_3$) and, therefore, are more difficult to prepare, or are oxides that are thermally unstable with respect to further oxidation [*e.g.*, $2CrO_2$ (conductive) → Cr_2O_3 + 1/2 O_2 (nonconductive)] (4).

This work was undertaken to determine if Ru and RuO_2 films could be prepared by chemical vapor deposition (CVD). Chemical vapor deposition was chosen because of its well-known advantages of conformal step coverage and low deposition temperatures. The properties of CVD Ru or RuO_2 films have not, to our knowledge, been reported before, and only a few references to such films prepared by this method exist (5-7). However, Ru films have been prepared by electrodeposition (8) and sputtering (9). In addition, RuO_2 films have been prepared by sputtering (10) and by oxidation of Ru or decomposition of $RuCl_3$ (2).

Experimental

Three organoruthenium compounds, all sublimable solids, were selected as sources for CVD: ruthenium acetylacetonate, ruthenocene, and triruthenium dodecacarbonyl. Data on these compounds are tabulated in Table I. Vapor pressure data were available only for ruthenocene. The compounds were purchased from Alfa Chemicals and Strem Chemicals and used without further purification.

Film deposition experiments were carried out using the apparatus depicted in Fig. 1. To prevent condensation of the sublimable source materials, all surfaces of the apparatus outside the reaction zone were maintained at temperatures greater than the source sublimation temperature but lower than its decomposition temperature. Placement of the source boat as close as possible to the substrates minimized the condensation problem.

Typically, the deposition process sequence was as follows. The substrates, (100) Si, (100) Si with 1000Å of thermal oxide (SiO_2), or device wafers, were cleaned in 1%

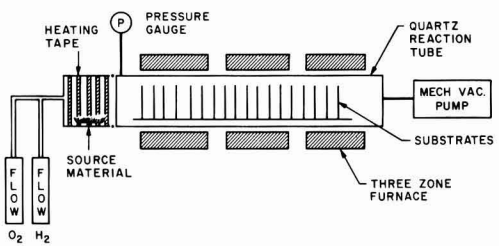


Fig. 1. Chemical vapor deposition apparatus

* Electrochemical Society Active Member.
[1] Present address: IBM Corporation, Charlotte, North Carolina 28201.

Table I. Organoruthenium source materials

Compound	Formula	Ru (w/o)	C (w/o)	H (w/o)	O (w/o)	Form	Vapor pressure	Supplier
Tris-2,4-pentane-dionato ruthenium (III) (ruthenium acetylacetonate)	$Ru(C_5H_7O_2)_3$	25.4	45.2	5.3	24.1	Solid red crystals	Unknown; decomposes at 220°C	Alfa
Bis(cyclopenta-dienyl) ruthenium (ruthenocene)	$Ru(C_5H_5)_2$	43.8	51.9	4.3	—	Solid yellow crystals	~0.01 torr at 85°C	Strem
Triruthenium dodecacarbonyl	$Ru_3(CO)_{12}$	47.4	22.5	—	30.1	Solid red powder	Unknown; decomposes at 150°C	Alfa

HF for 1 min, rinsed in distilled H_2O for 10 min, then dried in a stream of N_2. They were then loaded onto a quartz carrier and positioned vertically in the reaction furnace, which was at 200°C. The furnace was evacuated to about 20 mtorr and then brought up to the deposition temperature while pumping was continued. Once stabilized at this temperature, the gas flow of hydrogen or oxygen, if any, was started. Next, the heating tapes around the source material were turned on and sublimation of the source material was observed to begin. Deposition pressure was monitored with a capacitance manometer. When all the source material had sublimed, gas flow, if any, was stopped, and the furnace was cooled to 200°C. Deposition conditions for various films are listed in Table II.

On removal from the furnace, the samples were subjected to a variety of tests. Sheet resistance was measured with a four-point probe. Film thickness was determined with a mechanical stylus (Dektak II) on steps etched with an aqueous solution containing 5% NaOCl and 3% NaOH. From these two measurements, film resistivity could be determined. Several films, notably those containing RuO_2, could not be etched by this method. The thickness of these films was determined by transmission electron microscopy (TEM), Auger depth profiling (after having determined the Auger sputtering rate for RuO_2 and Ru), or Rutherford backscattering spectroscopy (RBS). Film structure and composition were determined by x-ray diffraction, Auger spectroscopy, TEM, RBS, and x-ray photoelectron spectroscopy.

Results

Selection of source materials.—Selection of source materials for the deposition of thin metal films by organometallic CVD is based on consideration of several factors. The operational considerations are those of vapor pressure sufficient to achieve rapid rates of material transport, and temperatures of sublimation and decomposition that are low, but different enough to prevent reaction of the source before reaching the deposition zone. Coupled with these are the more complex issues of decomposition chemistry and reactions with oxidizing or reducing gases.

The formal oxidation state of the metal atom in an organometallic compound is a useful formalism to consider in terms of the ease and purity of metal deposition, but it is not a physical property. The three organometallic ruthenium compounds that we chose to study as CVD sources in this work contain the metal atom in three formal oxidation states: Ru(0) in $Ru_3(CO)_{12}$, Ru(+2) in $Ru(C_5H_5)_2$, and Ru(+3) in $Ru(C_5H_7O_2)_3$. The reactivity of the complexes and the ease of reduction to a formally zero-valent metal favors the carbonyl complex, in which the ligands can dissociate cleanly without any further reduction of the ruthenium. The deposition of Ru from the other two sources in the absence of reactive gases, however, requires that the organic moieties act as reducing agents for the metal ion. In the process, the ligands oxidize and decompose to leave nonvolatile carbon residues in the films.

Mass spectra of the organometallic species may also offer some clues about the relative ease of ligand dissociation. The most abundant ion in the mass spectrum of $Ru_3(CO)_{12}$ is the bare tri-ruthenium cluster, Ru_3^+ (11). In contrast, the parent ion is the most abundant species in the mass spectrum of $Ru(C_5H_5)_2$ and Ru^+ is among the least abundant ions (12); likewise, for $Ru(C_5H_7O_2)_3$ (13).

Effect of source material on phase structure of film.—Table II summarizes the experimental conditions for the growth of the Ru and RuO_2 films from the various source materials. The phase structure of the films was deter-

Table II. Deposition conditions and phases present for various films

Source	Deposition temperature (°C)	Ambient	Deposition pressure (torr)	Phases present On Si	Phases present On SiO_2	Comments
$Ru(C_5H_7O_2)_3$	500	H_2	1.0	Ru	Ru	
		O_2	0.3-1.0	Ru	Ru	
		Vacuum	0.1 max.	Ru	Ru	
	600	H_2	1.0	Ru, RuO_2	Ru, RuO_2	
		O_2	1.0	RuO_2	RuO_2	
$Ru(C_5H_5)_2$	500-800	H_2	0.5-1.0			No films observed
	500	O_2	1.0	[a]	Ru	Powdery film
	575	O_2	5.0	Ru,[b] RuO_2	RuO_2	
	575	O_2	5.0	Ru	Ru, RuO_2	+900°C/2h postdeposition anneal, in vacuum
	600	O_2	1.0	Ru, RuO_2	Ru, RuO_2	
	500-600	Vacuum				No films observed
$Ru_3(CO)_{12}$	250	H_2	1.0	[a]	Ru	
	300	H_2	1.0	Ru	Ru	
	400	H_2	1.0	Ru	Ru	
	300	O_2	1.0	Ru	Ru	
	250	Vacuum	0.1 max.	[a]	Ru	
	300	Vacuum	0.1 max.	Ru	Ru	
	350	Vacuum	0.1 max.	[a]	Ru	
	400	Vacuum	0.2 max.	[a]	Ru	

[a] Deposition not performed on this substrate.
[b] Minor constituent.

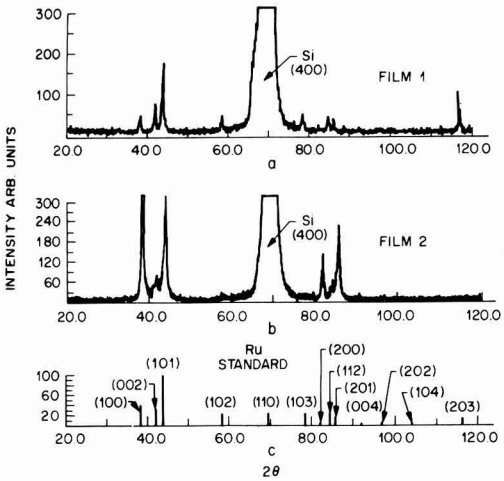


Fig. 2. X-ray diffraction patterns of Ru films: film 1 (acetylacetonate, 500°C, vacuum, on SiO_2) (a) and film 2 (carbonyl, 300°C, vacuum, on Si) (b).

mined by x-ray diffraction. We performed the deposition experiments under a wide range of conditions, with deposition temperatures of 250°-800°C, deposition pressures of 0.1-5.0 torr, and three growth ambients, H_2, O_2, or vacuum. Both Ru and RuO_2 were deposited under a variety of conditions.

Films deposited from the acetylacetonate complex at 500°C contained Ru (hexagonal phase) regardless of the ambient. Note that the thermodynamically favored RuO_2

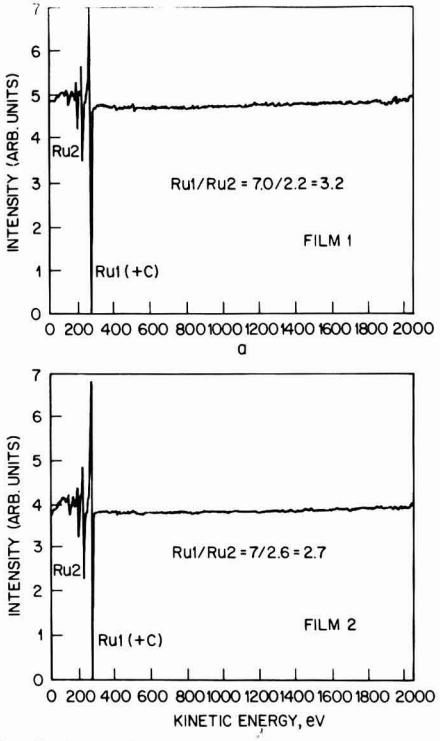


Fig. 3. Auger electron spectroscopy of Ru films: film 1 (acetylacetonate, 500°C, vacuum, on SiO_2) (a) and film 2 (carbonyl, 300°C, vacuum, on Si) (b).

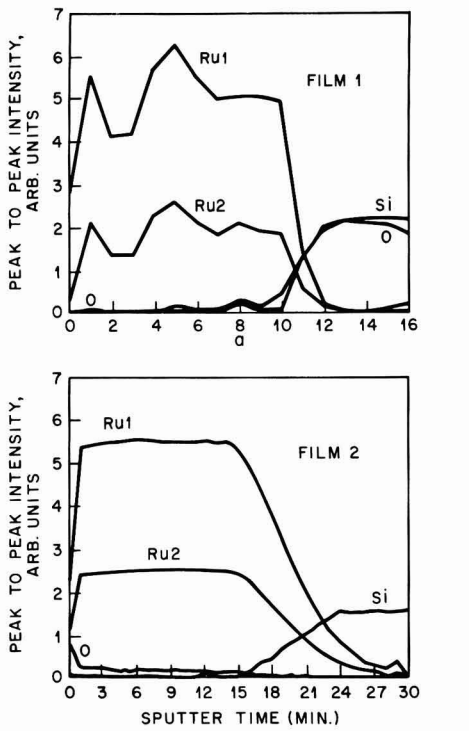


Fig. 4. Auger depth profiles of Ru films: film 1 (acetylacetonate, 500°C, vacuum on SiO_2) (a) and film 2 (carbonyl, 300°C, vacuum, on Si) (b).

did not form in oxygen at that temperature. Films deposited at 600°C began to exhibit RuO_2 (tetragonal phase). In a hydrogen ambient, the oxygen of the RuO_2 could only have originated from the acetylacetonate ligand. Thus, in spite of the reducing ambient, formation of the oxide becomes kinetically, as well as thermodynamically, favored and the ligand serves to oxidize the Ru. Complete oxidation of the Ru at 600°C, however, is only achieved when excess oxygen is present in the ambient.

Films could only be deposited from ruthenocene in an oxygen ambient. At 500°C in oxygen, a Ru film was deposited, although it was porous. When the deposition temperature was raised to 575°-600°C, the RuO_2 phase began to be stabilized. If the oxygen pressure in the reactor is raised to 5.0 torr, films consisting entirely of RuO_2 will result on SiO_2. A RuO_2 film formed in oxygen at 575°C was found to disproportionate when postdeposition annealed in vacuum at 900°C for 2h. According to the reaction

$$2RuO_2 \rightarrow Ru + RuO_4$$

RuO_2 films could decompose, completely or partially, to Ru and RuO_4, a volatile oxide, as observed.

Films deposited from Ru carbonyl consisted entirely of Ru, regardless of the ambient. However, the results for the other two sources show that oxide formation is not kinetically favored below ~575°C under our experimental conditions, and, owing to depletion of the carbonyl source, we could not achieve deposition above 400°C.

Film microstructures and characteristics.—In this section, the physical properties of selected films will be discussed. Several Ru, RuO_2, and mixed Ru/RuO_2 films were chosen for in-depth analysis because they represent different ambient growth conditions. All these films are continuous, specular, and, with one exception, adherent to their substrates.

Ru films.—Figure 2 illustrates the x-ray diffraction patterns for two Ru films, film 1 (acetylacetonate, 500°C, vacuum, on SiO_2) and film 2 (carbonyl, 300°C, vacuum, on Si). Comparison with the stick-figure diffraction pattern of the Ru standard, Fig. 2c, shows that all the observed peaks are attributable to Ru. In addition, whereas comparison of Fig. 2a and 2c shows film 1 to be a randomly oriented polycrystalline film, film 2 has a pronounced texture, as is shown by the high intensity of the (100) peak.

The Auger spectra of these two films, taken at a depth of 300Å into the film with the ion gun on during analysis, are shown in Fig. 3. In the presence of Ru, carbon is not easy to detect by Auger analysis as the C peak overlaps the Ru 1 peak. However, the Ru 2 peak arises only from Ru, and therefore the ratio Ru 1/Ru 2 should be related to the carbon content; specifically, it should increase with increasing carbon content. Auger analysis of a pure Ru sample (bulk) gave a ratio Ru 1/Ru 2 of 2.64, and the same ratio, as measured from the Ru spectra of the Auger handbook (14), is 2.63. Therefore, the carbonyl film, film 2, is pure with respect to carbon, as Ru 1/Ru 2 = 2.7. X-ray photoelectron spectroscopy (XPS) of this sample, a technique that is more accurate for C in Ru than Auger analysis, can detect no difference between it and the Ru standard. On the other hand, the acetylacetonate film, film 1, with its ratio of 3.2, contains much carbon, as is substantiated by XPS and RBS measurements, which show a carbon level of 60 and 62 atomic percent (a/o), respectively.

Figure 4 shows Auger depth profiles for the two films. Film 1 is much less uniform than film 2, a fact that is consistent with the TEM photomicrographs of Fig. 5. The discontinuous appearance of film 1, Fig. 5a, suggests that the carbon may be interspersed between the Ru grains. The high carbon content of this film, combined with its discontinuous microstructure, is responsible for its high electrical resistivity of $\rho = 1940\ \mu\Omega$-cm. On the other hand,

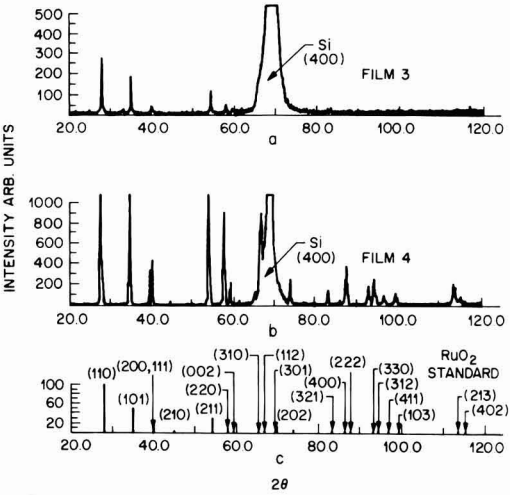


Fig. 6. X-ray diffraction patterns of RuO_2 films: film 3 (acetylacetonate, 600°C, 1.0 torr O_2, on Si) (a) and film 4 (ruthenocene, 575°C, 5 torr O_2, on Si) (b).

film 2, which is uniform and has little, if any, carbon, has $\rho = 16.9\ \mu\Omega$-cm, which is only twice the bulk value of Ru. It is typical for ~1000Å thick films to have higher resistivities than bulk samples, owing to grain size effects and surface electron scattering. Further observations from Fig. 5 are that the grain size range of Ru in film 1 (Fig. 5a) is about 100-400Å, whereas that of film 2 (Fig. 5b) is about 300Å. Neither film shows an interaction with its substrate, based on the planar interfaces ob-

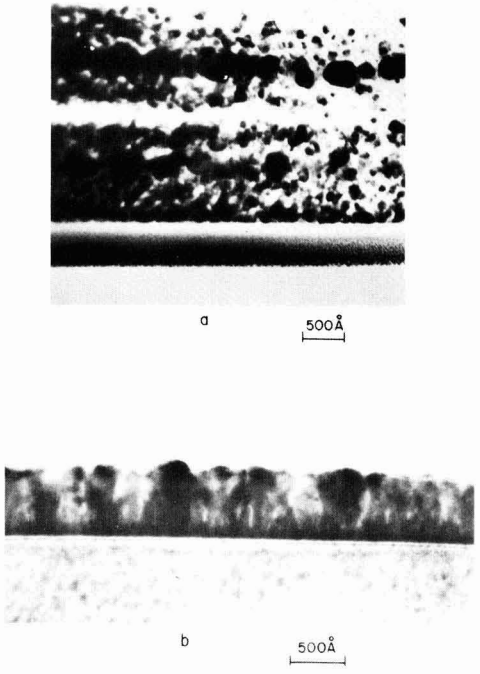


Fig. 5. Transmission electron photomicrographs of Ru films: film 1 (acetylacetonate, 500°C, vacuum, on SiO_2), bright field image (a), and film 2 (carbonyl, 300°C, vacuum, on Si), bright field image (b).

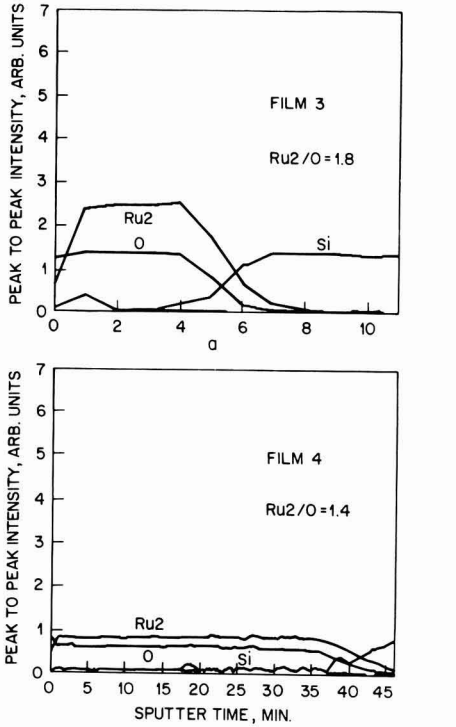


Fig. 7. Auger depth profiles of RuO_2 films: film 3 (acetylacetonate, 600°C, 1.0 torr O_2, on Si) (a) and film 4 (ruthenocene, 575°C, 5 torr O_2, on Si) (b).

Table III. Film properties

Film no.	Source	Deposition temperature (°C)	Deposition pressure (torr)	Ambient	Substrate	Film thickness (Å)	Resistivity ($\mu\Omega$-cm)	Film color	Film adhesion	Carbon content (a/o)	Microstructure
					Ru films						
1	$Ru(C_5H_7O_2)_3$	500	0.12	Vacuum	SiO_2	2500	1940	Metallic	Poor	~60	Grain size ~100-400Å randomly oriented
2	$Ru_3(CO)_{12}$	300	0.09	Vacuum	Si	1029	16.9	Metallic	Excellent	~0	Grain size ~300Å (100) texture
					RuO_2 films						
3	$Ru(C_5H_7O_2)_3$	600	1.0	O_2	Si	1449	643	Metallic, purple-blue	Excellent	<20	Grain size ~100-500Å randomly oriented
4	$Ru(C_5H_5)_2$	575	5.0	O_2	Si	6100	89.9	Blue	Excellent	<20	Grain size ~5000Å randomly oriented
					Ru/RuO_2 films						
5	$Ru(C_5H_7O_2)_3$	600	1.0	H_2	Si	854	521	Metallic, dark	Excellent	~0	Grain size ~300-1000Å (002) texture (Ru)
6	$Ru(C_5H_5)_2$	600	1.0	O_2	SiO_2	707	14.8	Metallic, dark	Excellent	<20	Grain size ~500-750Å (200), (111) texture (RuO_2)

served. This observation is consistent with RBS data that show that little, if any, interdiffusion of the Ru and Si or SiO_2 substrates has occurred.

Table III summarizes the physical properties of the films. Film 2, produced from the carbonyl, is more conductive, contains less carbon impurities, and exhibits better adhesion to its substrate than film 1, produced from the acetylacetonate.

RuO_2 films.—The x-ray diffraction patterns of two typical RuO_2 films are shown in Fig. 6. Film 3 (acetylacetonate, 600°C, 1 torr O_2, on Si) and film 4 (ruthenocene, 575°C, 5 torr O_2, on Si) both show patterns that are completely explainable by referring to the RuO_2 standard (Fig. 6c). Neither film shows any indication of significant texture. The diffraction pattern of film 4 is much more distinct than that of film 3 because, as can be seen in Table III, film 4 is much thicker.

The Auger depth profiles of films 3 and 4 are depicted in Fig. 7. Oxygen is evenly distributed in the films, suggesting that the films are uniform. The apparent oxygen-rich layer on the surface of film 4 is believed to be an artifact of sputtering. The presence of oxygen in these films seems to affect the Auger intensity ratio Ru 1/Ru 2, thereby making it difficult to determine if carbon is present in these films. Whereas for the Ru films, the minimum ratio of Ru 1/Ru 2 is 2.7, the pure Ru value, that ratio for films 3 and 4 is 1.7 and 1.9, respectively. As we had no carbon-free RuO_2 standard to compare these to, the carbon content of these films is not known. However, RBS analysis of film 3 suggests that carbon, if any, is present to the extent of less than 20 a/o, the detectability limit. Based on its similar ratio, the carbon content of film 4 is presumably about the same. The intensity ratio of the Ru 2 and O Auger peaks should, under ideal conditions, be related to the stoichiometry of the RuO_2 phase. However, the ratio Ru 2/O is 1.8 for film 3 and 1.4 for film 4. We believe the variation in this ratio to result from variations in sputtering yields between Ru and oxygen during depth profiling, which is sensitive to grain size and morphology. RBS analysis of film 3 shows that its stoichiometry is RuO_2. The similarity in interplanar spacings observed in the XRD patterns of films 3 and 4 and the RuO_2 standard (Fig. 6c) suggests that film 4 is stoichiometric RuO_2 as well.

The two RuO_2 films are microstructurally different, as is shown in Fig. 8. Film 3 (Fig. 8a) is composed of grains ranging from about 100 to 500Å. Some columnar growth is observable at the Si/RuO_2 interface, but this seems to break down at a thickness of about 700Å, after which the grains appear to be equiaxed. Film 4 (Fig. 8b) is composed of large grains, about 5000Å, that are columnar and well defined. Neither film appears to have interacted to any significant extent with the Si substrate.

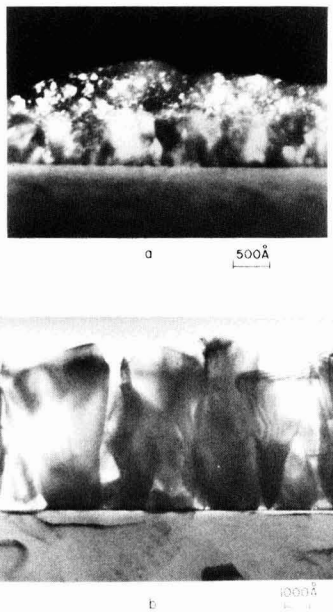


Fig. 8. Transmission electron photomicrographs of RuO_2 films: film 3 (acetylacetonate, 600°C, 1.0 torr O_2, on Si), darkfield image using (110) and (101) reflections (a), and film 4 (ruthenocene, 575°C, 5 torr O_2 on Si), bright field image (b).

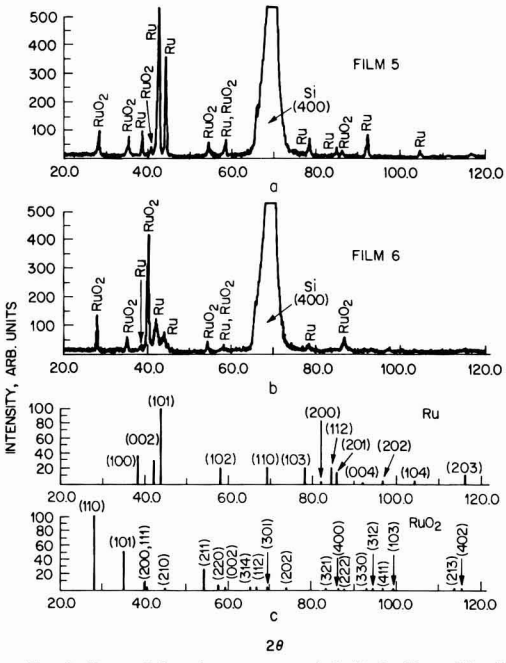


Fig. 9. X-ray diffraction patterns of Ru/RuO_2 films: film 5 (acetylacetonate, 600°C, 1.0 torr H_2, on Si) (a), and film 6 (ruthenocene, 600°C, 1.0 torr O_2, on SiO_2) (b).

The electrical resistivity of film 4 was found to be 89.9 $\mu\Omega$-cm, which is just about twice that of bulk RuO_2. As film 4 is 6100Å thick and is therefore reasonably close to bulk material, one might expect the bulk resistivity to be observed. The increase in resistivity probably results from less than perfect interconnectivity between the RuO_2 grains, as is suggested by Fig. 8b. The resistivity of film 3 is 643 $\mu\Omega$-cm, indicating that the fine grain microstructure, coupled with thin film scattering effects, is probably responsible for this high value. The data for these two films are summarized in Table III.

Ru/RuO_2 films.—Under certain deposition conditions, listed in Table II, films composed of both Ru and RuO_2 phases can be deposited. It is of interest to determine the microstructure of such mixed films. The XRD patterns of two such films are shown in Fig. 9. Film 5 (acetylacetonate, 600°C, 1.0 torr H_2, on Si) is predominantly Ru phase (85% as determined by RBS), whereas film 6 (ruthenocene, 600°C, 1.0 torr O_2, on SiO_2) is predominately RuO_2 phase. Film 5 exhibits a large Ru (002) peak, indicating that the Ru component of the film has some basal plane texture, while the RuO_2 component appears to be of random orientation. The RuO_2 phase of film 6 possesses a texture where the (200) or (111) RuO_2 planes tend to be parallel to the substrate.

Auger depth profile analysis of film 5 (Fig. 10) shows that the sample is Ru rich near the Si interface, and progressively richer in oxygen towards the surface of the film. As this film was deposited in H_2, the only source of oxygen can be from the acetylacetonate radical. Therefore, the Ru-rich layer, first to deposit on Si, seems to catalyze further decomposition into RuO_2. The Auger sample is thinner than the XRD or TEM samples (it is probably from a corner of the wafer). For that reason, Si was able to diffuse to the surface during deposition. Film 5 is also pure with respect to carbon, as the Auger intensity ratio Ru 1/Ru 2 = 2.5. Film 6 has almost the opposite depth profile of film 5. The film is oxygen rich at the SiO_2 interface (Fig. 10b) and Ru rich at the surface. Here, however, the oxygen must be incorporated from the ambient.

Figure 11 illustrates the microstructures of films 5 and 6. Film 5 is composed of equiaxed grains between 300 and 1000Å in diameter. Film 6 is composed of columnar grains between 500 and 750Å in diameter. The resistivity of film 5 is 521 $\mu\Omega$-cm, whereas that for film 6 is 14.8 $\mu\Omega$-cm. The high resistivity of film 5 is probably related to the thinness of the film, its small grain size, and the oxygen-rich surface layer. On the other hand, the low resistivity of film 6 may result from the Ru-rich layer at its surface.

Diffusion barrier properties of Ru and RuO_2 films.—Al-Ru-Si and Al-RuO_2-Si thin film diffusion couples were

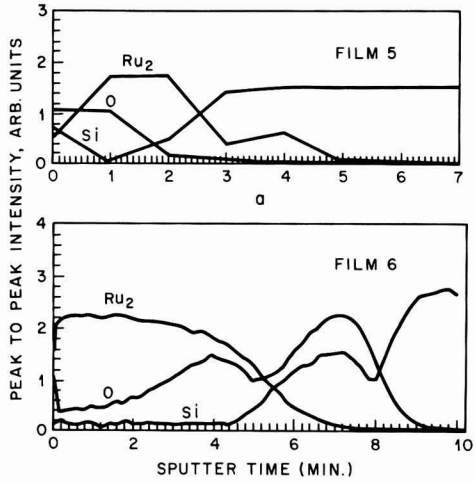


Fig. 10. Auger depth profiles of Ru/RuO_2 films: film 5 (acetylacetonate, 600°C, 1.0 torr H_2, on Si) (a), and film 6 (ruthenocene, 600°C, 1.0 torr O_2, on SiO_2) (b).

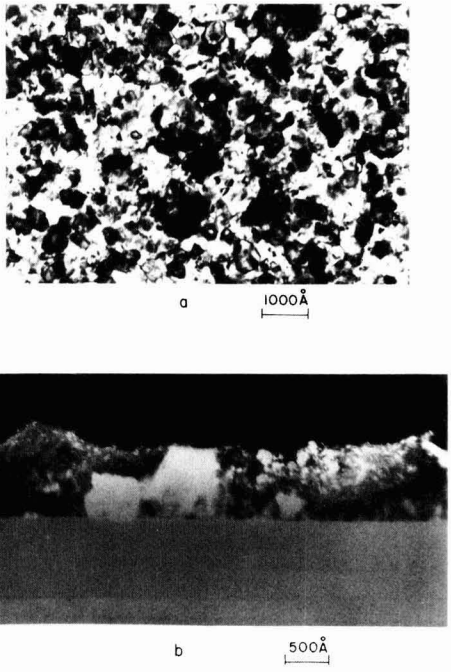


Fig. 11. Transmission electron photomicrographs of Ru/RuO_2 films: film 5 (acetylacetonate, 600°C, 1.0 torr H_2, on Si), bright field image looking through the film (a) and film 6 (ruthenocene, 600°C, 1.0 torr O_2, on SiO_2), darkfield image using (110) and (101) RuO_2 reflections (b).

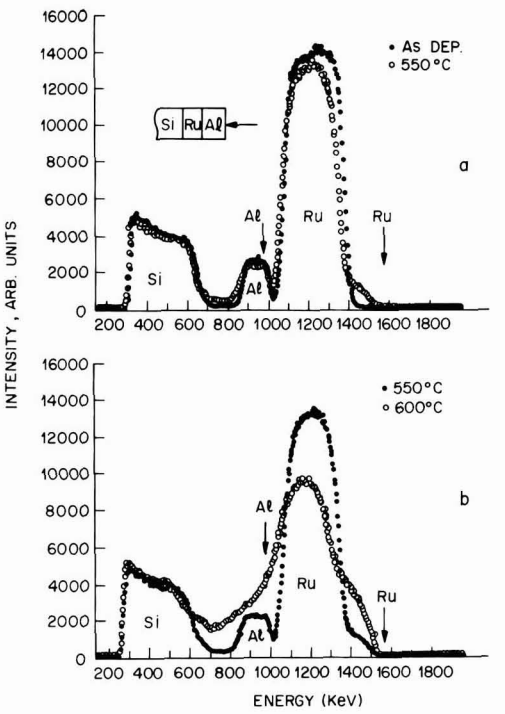


Fig. 12. RBS spectra of an Al-Ru-Si couple (1500Å Al/1029Å Ru/Si substrate), after various heat-treatments. a: Comparison of as-deposited and 550°C(1/2 h, in argon) spectra. b: Comparison of 550°C(1/2 h) and 600°C(1/2 h) spectra. The vertical arrows mark the surface positions of the corresponding elements.

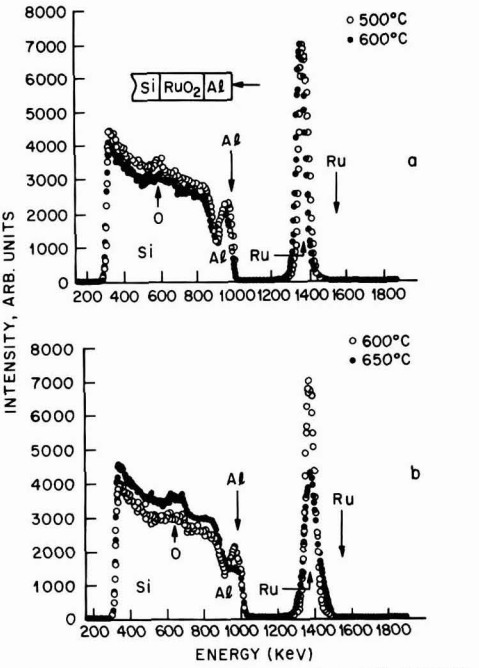


Fig. 13. RBS spectra of an Al-RuO_2-Si couple (1500Å Al/1450Å RuO_2/Si substrate), after various heat-treatments. a: Comparison of 500°C(1/2 h) and 600°C(1/2 h) spectra. b: Comparison of 600°C(1/2 h) and 650°C(1/2 h) spectra. The vertical arrows mark the surface positions of the corresponding elements.

prepared by depositing about 1500Å of evaporated Al on films 2 (Ru) and 3 (RuO_2). The interdiffusion of these couples was studied by RBS as a function of annealing temperature. The ability of Ru or RuO_2 to act as a diffusion barrier between Al and Si would be advantageous for VLSI metallization applications.

Figure 12a compares the RBS spectra of the Al-Ru-Si couple (1500Å Al/1029Å Ru/Si substrate) before (as-deposited) and after a 550°C(1/2 h) anneal in argon. No significant changes in the spectra were noted until 550°C. The interdiffusion of Al and Ru was observed to occur above 550°C, as evidenced by the tail at the leading edge of the Ru peak. This corresponds, however, to only a small amount of Ru in Al. There is some slight evidence for a Ru-Si interaction at this temperature, as the Si leading edge profile has changed to a small extent. Figure 12b illustrates that after a 600°C(1/2 h) anneal the couple has interdiffused significantly. The Al peak is no longer distinguishable, indicating that it has interdiffused with the Ru and possibly the Si. Interdiffusion of Ru and Si has also occurred. XRD of this sample shows the existence of the phases Ru_2Si, Ru_2Si_3, and $RuAl_2$, as well as remnants of the original elemental Si, Al, and Ru.

Figure 13a illustrates the RBS spectra for the Al-RuO_2-Si couple (1500Å Al/1450Å RuO_2/Si substrate) after 500°C(1/2 h) and 600°C(1/2 h) heat-treatments, both in argon. Up to a gon. Up to a temperature of 500°C, no changes in the spectra were observed. After 600°C, a small amount of Al-RuO_2 interdiffusion can be noted, based on the small tail at the Ru leading edge. The general shift of the Ru edges to lower energies after the 600°C anneal probably results from the formation of some Al_2O_3 during the anneal. Also, the difference in Si peak heights (in both Fig. 13a and 13b), is artifactual. Figure 13b shows that interdiffusion is pronounced after a 650°C anneal. The Al peak is smeared out, and the Ru peak is reduced by about 10% (possibly owing to loss by disproportionation of RuO_2 during exposure to air while still hot, see the Effect of source material section). X-ray diffraction of this sample shows the presence of Ru_2Al_3, $RuAl_2$, and Ru_2Si_3, as well as RuO_2, Ru, Al, and Si. The presence of Ru suggests that Al is reducing some of the RuO_2.

Finally, Fig. 14 illustrates, for comparison, RBS spectra of an Al-W-Si sandwich (1500Å Al/1100Å W/Si substrate). The W was deposited by selective chemical vapor deposition via the H_2 reduction of WF_6. LPCVD W is now being considered as a diffusion barrier for VLSI devices (15-17). It can be seen from Fig. 14 that, for the case of LPCVD W, significant interdiffusion takes place during a 550°C(1/2 h) anneal. XRD shows the presence of WSi_2, W(Si, Al)$_2$, W_5Si_3, and WAl_{12}. Therefore, Ru and RuO_2 are

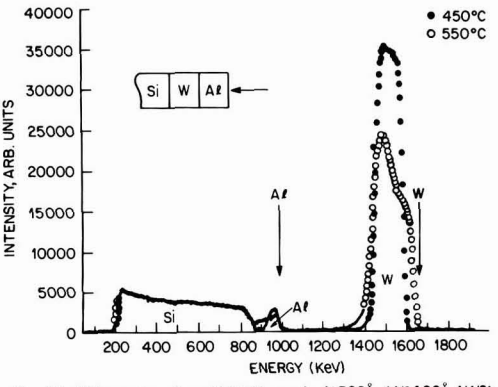


Fig. 14. RBS spectra of an Al-W-Si couple (1500Å Al/1100Å W/Si substrate), after 450°C(1/2 h) and 550°C(1/2 h) heat-treatments. The vertical arrows mark the surface positions of the corresponding elements.

more stable diffusion barriers between Al and Si than LPCVD W by about 50° and 100°C, respectively.

Discussion

Film processing considerations.—Table III shows that Ru, RuO_3, and Ru/RuO_2 films, each with large variations in physical properties, can be produced by varying the experimental conditions. Ruthenium, RuO_2, or Ru/RuO_2 films deposited from the acetylacetonate complex consistently exhibit higher resistivities than the same films deposited from other source materials. The best Ru films are those deposited from the carbonyl at temperatures of about 300°C. An SEM photomicrograph of such a film (Fig. 15) illustrates the excellent conformal coverage typical of LPCVD films. The best RuO_2 films are those deposited from ruthenocene at 575°-600°C.

The deposition of either of these films is consistent with current CVD processing. The fact that both source materials are solids is not in itself a serious drawback, as CVD of Al_2O_3, in which solid $AlCl_3$ is used as a source material, is already in commercial use (18). However, the temperature difference between sublimation and decomposition of the source material should be as large as possible to avoid severe depletion effects in the reactor. This temperature gap appears to be small for the carbonyl (~75°C), but significantly larger for ruthenocene (~300°C).

Device considerations.—Metallization applications in VLSI devices can be classified as interconnects, diffusion barrier layers, contacts, and gates. In this section, we will consider Ru and RuO_2 as potential films for these applications.

As an interconnect, neither Ru nor RuO_2 can compete with Al, if only because of Al's low resistivity (ρ = 2.7 $\mu\Omega$-cm) and ease of deposition. However, as a diffusion barrier and contact between Al and Si at source/drain areas, Ru and RuO_2 may have applications. In particular, Ru has a low Schottky barrier height to Si [0.6 eV to n-type Si (19)], similar to that of Cr, Ni, and W, and should therefore exhibit low contact resistance to Si. This is especially true if the Si is highly doped and tunneling conduction mechanisms are operative. Although the barrier height of RuO_2 is not known, it is assumed that, if some oxidation of the Ru occurred, adequate contact resistance would still be maintained.

Furthermore, Al metallization is compatible with Ru or RuO_2 contacts. Although Al_2O_3 is more stable than RuO_2 at the temperatures of interest (~500°C) (20), our results show that Al does not extensively reduce RuO_2. If Al_2O_3 were formed by this reaction, insulating layers would form. Little is known about Ru-Si interactions that result in silicide formation. At least up to deposition temperatures of 600°C, no silicide formation was observed in our work. As contact metallizations will not see these high temperatures, silicide formation, with its attendant junction erosion and higher contact resistance, is not expected to be a problem. The RBS data of Fig. 12-14 show that Ru and RuO_2 are potentially better diffusion barriers between Al and Si than W.

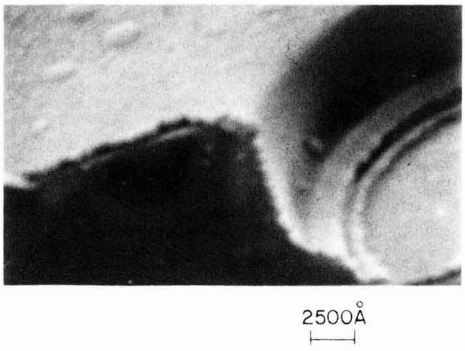


Fig. 15. Scanning electron photomicrograph of a Ru film deposited on a device (film 2, carbonyl, 300°C, in vacuum). The excellent conformal coverage of the film is shown by the film uniformity on the SiO_2 (left) and Si window area (right).

Gate metallizations should have good conductivity and be stable at high temperatures in oxidizing atmospheres. Ruthenium and RuO_2 conductivities are both stable with respect to oxygen, although RuO_2 might disproportionate at higher temperatures (T > 750°C). Furthermore, Ru gates would not interact with SiO_2 gate oxides, as SiO_2 is more stable than RuO_2 (20). Ruthenium might be the more suitable of the two as a gate metallization as its work function is equal to 4.7 eV (21), just about midway between those of N^+ and P^+ silicon. Such midgap metallizations are ideal for CMOS applications where only one gate material, rather than the traditional two, is desired.

In all applications, it should be kept in mind that RuO_2 is thermodynamically unstable in the presence of H_2, even at room temperature (20), and complete reduction to Ru is easily achieved at temperatures greater than about 300°C. Therefore, reducing conditions during heat-treatment are not compatible with the use of RuO_2; vacuum, nitrogen, or inert gas anneals should be used.

A final point should be made about the plasma etchability of Ru and RuO_2. Although no information is available on this subject, it is believed that both materials can be etched in fluoride-based plasmas, as RuF_5 is a low melting and boiling point species (T_{mp} = 101°C, T_{bp} = 250°C).

Conclusions

We have deposited Ru, RuO_2, and Ru/RuO_2 films by organometallic LPCVD, and have extensively characterized these films as potential VLSI metallizations. Ruthenium is of interest to us because its thermodynamically stable oxide, RuO_2, exhibits metallic conductivity. As a result, oxidation during processing of Ru would be a less critical concern than in some current metallization technologies. We have found that films of a given phase composition can be deposited under a wide range of conditions, with large variations in electrical resistivity and carbon content. Ruthenium films with electrical resistivity as low as 16.9 $\mu\Omega$-cm could be deposited from the carbonyl. Ruthenium films deposited from Ru acetylacetonate were found to be mostly carbon and to exhibit high resistivity. Ruthenium dioxide films with electrical resistivity as low as 89.9 $\mu\Omega$-cm could be deposited from ruthenocene. Again, Ru acetylacetonate produced inferior RuO_2 films. Ruthenium/ruthenium dioxide films ranging in resistivity between 14.8 and 521 $\mu\Omega$-cm were also deposited. All films, except the Ru film deposited from the acetylacetonate, were adherent to their substrates (either Si or SiO_2). Ruthenium and RuO_2 films were found, by RBS analysis, to be more effective diffusion barriers between Al and Si than LPCVD W, capable of withstanding about 50° and 100°C higher annealing temperatures before significant interdiffusion, respectively. The advantages of Ru and RuO_2 films may also suggest other applications in VLSI metallization, noting that the deposition processes are compatible with current VLSI processing.

Acknowledgments

We would like to acknowledge S. Abys, R. Frankenthal, and D. Siconolfi for Auger analysis, C. C. Chang for XPS analysis, R. Knoell for the TEM work, and W. D. Reents, Jr., for mass spectrometry of the source materials. Helpful discussions were held with L. C. Feldman.

Manuscript submitted May 7, 1985; revised manuscript received July 15, 1985.

AT&T Bell Laboratories assisted in meeting the publication costs of this article.

REFERENCES

1. D. J. Pedder, "Electrical Components Science and Technology," Vol. 2, pp. 259-261, Gordon and Breach, Ltd., New York (1976).

2. R. G. Vadimsky, R. P. Frankenthal, and D. E. Thompson, *This Journal*, **126,** 2017 (1979).
3. R. D. Lanam and A. R. Robertson, *Res. Dev.*, 102 (1984).
4. V. B. Lazarev and I. S. Shapylgin, *Russ. J. Inorg. Chem.*, **23,** 163 (1978).
5. J. N. Crosby and R. S. Hanley, U.S. Pat. 4,250,210 (1981).
6. J. C. Viguié and J. Spitz, *This Journal*, **122,** 585 (1975).
7. D. R. Rolison, K. Kuo, M. Umana, D. Brundage, and R. W. Murray, *ibid.*, **126,** 407 (1979).
8. T. A. Palumbo, *Plating Surf. Finish.*, **66,** 42 (1979).
9. G. A. Augis and L. L. Hines, *IEEE Trans. Comp. Hyb. Manu. Tech.*, **chmt-1,** 46 (1978).
10. M. C. Canart-Martin, Y. Canivez, R. Declercq, L. D. Laude, and M. Wautelet, *Thin Solid Films*, **92,** 323 (1982).
11. C. R. Eady, B. F. G. Johnson, and J. Lewis, *J. Organometal. Chem.*, **37,** C39 (1972).
12. J. Müller and L. D'Or, *ibid.*, **10,** 313 (1967).
13. W. D. Reents, Jr., Unpublished results.
14. L. E. Davis *et al.*, "Handbook of Auger Electron Spectroscopy," Perkin-Elmer, Eden Prairie, MN (1978).
15. N. E. Miller and I. Beinglass, *Solid State Technol.*, **25** (12), 85 (1982).
16. P. A. Gargini, *Ind. Res. Dev.*, **25** (3), 141 (1983).
17. M. L. Green and R. A. Levy, *This Journal*, **132,** 1243 (1985).
18. S. K. Tung and R. E. Caffrey, *ibid.*, **114,** 275C (1967).
19. S. P. Murarka, *J. Vac. Sci. Technol.*, **17,** 775 (1980).
20. E. A. Brandes, "Smithells Metals Reference Book," Chap. 8, Butterworths, London (1983).
21. D. B. Fraser, in "VLSI Technology," S. M. Sze, Editor, Chap. 9, McGraw-Hill, New York (1983).

Thermal Oxidation of Silicon in Dry Oxygen Growth-Rate Enhancement in the Thin Regime

I. Experimental Results

Hisham Z. Massoud*,[1] and James D. Plummer*

Integrated Circuits Laboratory, Stanford University, Stanford, California 94305

Eugene A. Irene*,[2]

IBM Thomas J. Watson Research Center, Yorktown Heights, New York 10598

ABSTRACT

In many studies of oxidation kinetics, it has been observed that SiO_2 growth in dry oxygen in the thin regime (<500Å) is faster than the classic description of growth in thicker layers by a linear-parabolic relationship. Growth-rate enhancement in the thin regime was studied in the 800°-1000°C range under a variety of substrate doping densities and O_2 partial pressures using *in situ* ellipsometry. The enhancement in oxidation rate is found to decay exponentially with thickness, and its thickness extent is approximately independent of substrate orientation, doping density, and oxygen partial pressure; its oxygen pressure and substrate doping dependence suggest that it is caused by physical mechanisms associated with the substrate. Such mechanisms are discussed in part II of this paper (11).

Thermally grown layers of silicon dioxide have been an integral part of silicon device technology since their first applications in surface protection and selective masking during diffusion (1) and in stabilizing silicon surfaces (2). Silicon dioxide layers found additional applications in device isolation, impurity gettering, masking against impurities, junction passivation, and insulation between metal layers (3-6). Such applications have made silicon oxidation a vital processing step in both bipolar and MOS technologies. Its most important application, however, is the growth of the gate-dielectric material for MOS transistors where SiO_2 layers become an active component. With continued shrinkage of device dimensions, it has been estimated that submicron channel-length VLSI MOSFET's will use oxide layers thinner than 150Å (7). Thin tunnelable oxides are also used in memory devices such as electrically alterable read only memories (EAROM's). These layers must be grown routinely and reproducibly with high yield and long-term reliability and must not be degraded by subsequent processing.

In early studies of silicon-oxidation kinetics, it was observed that growth rates were higher than predicted by linear-parabolic kinetics for layers thinner than 250Å when silicon was oxidized in dry oxygen (8). Available experimental evidence also indicates that such thin layers are different from thicker layers in other properties such as dielectric breakdown and reliability (9) and interfacial optical properties (10). This study focuses on the growth kinetics of SiO_2 layers in the thin regime (<500Å) in order to achieve a better understanding of the oxidation process and to establish a framework within which the difference between thin and thick layers can be better explained.

In this paper, the principles on which the oxidation-rate analysis is based are discussed. The experimental results of the dependence of the growth rate on temperature, substrate orientation, doping density, and oxygen partial pressure in the oxidizing ambient are presented. The rate enhancement is then analyzed quantitatively in the 800°-1000°C range as a function of oxide thickness for lightly doped silicon oxidized in dry oxygen and in oxygen-argon mixtures and for heavily doped substrates oxidized in dry oxygen. The results show that the excess rate decays exponentially with thickness and that it exists under all conditions investigated. The physical mechanisms involved in the early stages of the oxidation of silicon in dry oxygen are discussed in part II of this paper (11).

Experimental Procedures

The thermal growth of silicon dioxide layers on silicon in the thin regime was monitored *in situ* by a high temperature automated ellipsometer. The operation of the automated ellipsometer and the high temperature optical properties of silicon and silicon dioxide are described elsewhere (12, 13). The oxide thickness was measured from the onset of oxidation, where the native oxide is typically 10-15Å, up to ~600Å. The preoxidation cleaning sequence consisted of H_2O_2-based solutions of NH_4OH and HCl with appropriate DI water rinses followed by a dip in dilute HF and a final DI water rinse (14). The wafers were then dried using nitrogen and immediately loaded in the oxidation furnace with argon flowing. Following background intensity measurements, the native oxide thickness was evaluated and was usually found to be in the

*Electrochemical Society Active Member.
[1] Present address: Department of Electrical Engineering, Duke University, Durham, North Carolina 27706.
[2] Present address: Department of Chemistry, University of North Carolina, Chapel Hill, North Carolina 27514.

7-22Å range. The furnace ambient was then switched to the oxidizing ambient of interest. Thickness *vs.* time data in the 800°-1000°C range were obtained for (100), (111), and (110) substrate orientations, with 1.0×10^{15}, 1.8×10^{20}, and 3.2×10^{20} cm^{-3} surface doping concentrations, and in 1.0, 0.1, or 0.01 atm oxygen partial pressure in an oxidizing ambient consisting of mixtures of dry oxygen and argon (15). The lightly doped wafers were either p-type (doped with boron) or n-type (doped with phosphorus). Higher surface doping concentrations were obtained using $POCl_3$ predeposition and drive-in. A typical example of the data obtained is shown in Fig. 1, where thickness *vs.* time results for the oxidation of lightly doped silicon in dry oxygen in the 800°-1000°C range are plotted. It can be seen that, through the use of *in situ* automated ellipsometry, closely spaced data were obtained. This provides a unique opportunity to investigate the underlying physical mechanisms.

The linear and parabolic rate constants, describing the oxidation process beyond the fast initial regime, were first determined as described elsewhere (16). Knowledge of these rate constants is important in accurately determining the magnitude of growth-rate enhancement in the thin regime and the extent of this enhancement in thickness (or the onset of conventional linear-parabolic growth).

Oxidation-Rate Analysis in the Thin Regime

Kinetic growth laws relating oxide thickness and oxidation time may describe distinctly different rate-limiting processes while having the same mathematical form (17). As an example, in the Deal-Grove linear-parabolic model of oxidation (8), linear growth could result if the rate-limiting step were either the flux at the oxide-gas interface or that at the Si-SiO_2 interface. A parabolic growth law could result if the rate-limiting process were either the diffusion of oxygen to the oxide-silicon interface or the diffusion of silicon to the oxide-gas interface. In both situations, additional information obtained from other experiments was essential in identifying the rate-limiting process. Tracer experiments and oxidation results obtained when changing the flow of oxygen over several orders of magnitude (4-6) provided the additional information that helped identify the diffusion of oxygen and the reaction at the Si-SiO_2 interface as the rate-limiting processes in the parabolic and linear regimes, respectively. Investigations of silicon oxidation in dry oxygen in the thin regime were usually limited in the experimental conditions under which the reaction rate was studied. These limitations were subsequently reflected in the multitude of growth laws obtained such as linear, parabolic, linear-parabolic (with different rate constants), logarithmic, and inverse logarithmic (4-6). A comprehensive study of the reaction rate is therefore necessary because knowledge of a rate law under a limited set of experimental conditions is insufficient to determine the reaction mechanism. This is why, in this work, a complete characterization of the dependence of the growth rate on all possible processing conditions was undertaken.

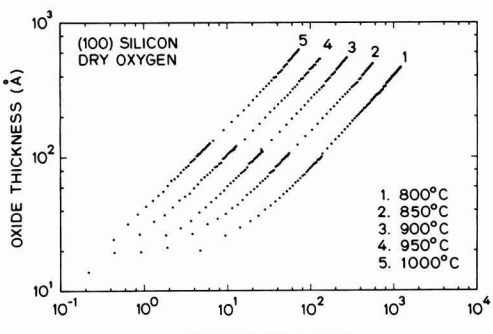


Fig. 1. Oxidation of lightly doped (100) silicon in dry oxygen in the 800°-1000°C range.

To analyze the oxidation process in the early stages of SiO_2 formation, it is important to discuss the assumptions on which the analysis is based. In earlier silicon-oxidation studies, it was shown that the linear-parabolic model is representative of the details of the oxidation process in the thick regime, namely, that oxide growth is the result of the transport of the oxidizing species through an existing layer of oxide and their reaction with silicon atoms at the Si-SiO_2 interface to form SiO_2 (8). Mathematically, this was modeled by three fluxes in series under steady-state conditions—F_1 from the gas to the oxide surface, F_2 through the oxide, and F_3 at the Si-SiO_2 interface.

The resulting growth rate is expressed as (8)

$$\frac{dX_{ox}}{dt} = \frac{B}{(2X_{ox} + A)} \quad [1]$$

where

$$B = \frac{2DC^*}{N_1} \quad [2]$$

and

$$A = 2D\left(\frac{1}{h} + \frac{1}{k_s}\right) \quad [3]$$

and D and C^* are the diffusion coefficient and solubility of the oxidizing species in the oxide, respectively, N_1 is the number of oxidant molecules incorporated into a unit volume of the growing oxide, k_s is the surface reaction-rate constant, and h is the gas phase mass-transfer coefficient.

An oxidation rate higher than predicted by this model could be, in general, the result of additional processes not accounted for in the linear-parabolic model. These processes could be modeled as thickness and/or time dependent, or as a combination of both. Time-dependent processes are in contradiction with the steady-state assumption in the Deal-Grove model (8), and, consequently, silicon oxidation in the initial stages would be treated as a nonsteady-state process. If the oxidation rate increases as the result of additional fluxes, such fluxes would not occur in series with F_1, F_2, or F_3 because that would further reduce the overall oxidation rate if they are the rate-limiting process, or the overall growth rate would remain unchanged if they are not. It is therefore concluded that rate enhancement in the thin regime must be described by processes occurring in parallel with any one of these fluxes or with their entire sequence. In a most general case, the additional processes can be represented by excess fluxes ΔF_1, ΔF_2, and ΔF_3 in parallel with F_1, F_2, and F_3, respectively, and F_4 in parallel with their total sequence, as illustrated in Fig. 2.

Oxidant-species adsorption at the outer surface of the oxide caused by possible field effects on the oxygen species or by the porous structure of SiO_2 at the onset of oxidation is an example of a process that may be represented by ΔF_1. Flux ΔF_2 may be the result of field-aided diffusion of ionized oxygen species or the transport of molecular and atomic oxygen in neutral and ionized states across the oxide. The reaction that forms the oxide at the interface could be the result of the reaction of molecular and atomic oxygen (in neutral and ionized states) with silicon-silicon bonds, partially bonded surface-silicon atoms, or silicon vacancies at the Si-SiO_2 interface. These additional surface fluxes can be modeled by ΔF_3. Flux F_4 possibly represents the transport of oxygen species along microchannels in the oxide to reach the interface and react with the substrate, thereby occurring in its entirety in parallel with the three-flux (F_1-F_2-F_3) process. Some of the details of the oxidation reaction can be altered by stress in the oxidizing structure because of its possible effect on the transport and concentration of oxidizing species in the oxide or on the energy required for the surface reaction.

The expression for the growth-rate increase caused by the additional fluxes follows the same steps used to derive the linear-parabolic relationship, In steady state

$$F = F_1 + \Delta F_1 = F_2 + \Delta F_2 = F_3 + \Delta F_3 \qquad [4]$$

and the total oxidant flux becomes $F + F_4$. If F_1, F_2, and F_3 are expressed as in the Deal-Grove model (8), the growth rate for the modified linear-parabolic model illustrated in Fig. 2 can be written as

$$\frac{dX_{ox}}{dt} = \frac{\frac{2DC^*}{N_1} + \left(\frac{2D}{N_1 h}\right)\Delta F_1 + \left(\frac{2X_{ox}}{N_1}\right)\Delta F_2 + \left(\frac{2D}{N_1 k_S}\right)\Delta F_3}{2X_{ox} + 2D\left(\frac{1}{h} + \frac{1}{k_S}\right)} + \frac{F_4}{N_1} \qquad [5]$$

Based on the definitions of B and A in Eq. [2] and [3], this relationship becomes

$$\frac{dX_{ox}}{dt} = \frac{B + \left(\frac{2D}{N_1 h}\right)\Delta F_1 + \left(\frac{2X_{ox}}{N_1}\right)\Delta F_2 + \left(\frac{2D}{N_1 k_S}\right)\Delta F_3 + \left(\frac{2X_{ox} + A}{N_1}\right)F_4}{2X_{ox} + A} \qquad [6]$$

from which it can be seen that oxidation-rate enhancement in the thin regime can be analyzed as a term added to the parabolic rate constant B in the formulation of the linear-parabolic oxidation rate. It should be noted that the factors multiplying the ΔF_2 and F_4 terms are thickness dependent. Consequently, it can be concluded that, without further assumptions, the above expression does not contribute any additional insight concerning the location of the enhancement process because the dependence of ΔF_1, ΔF_2, ΔF_3, or F_4 on oxide thickness would have to be independently known or assumed. One additional difficulty in delineating the physical processes involved is that, in the initial stages of oxidation, the oxide thickness is so much smaller than A that the linear-parabolic rate becomes approximately thickness independent and equal to the value of B/A. The total growth rate, therefore, can be expressed by two equivalent forms

$$\frac{dX_{ox}}{dt} = \frac{B}{(2X_{ox} + A)} + \Delta R_e(X_{ox}, t_{ox})$$

$$= \frac{B}{A} + \Delta R_e(X_{ox}, t_{ox}) \qquad [7]$$

or

$$\frac{dX_{ox}}{dt} = \frac{B}{(2X_{ox} + A)}[1 + \Delta R_r(X_{ox}, t_{ox})]$$

$$= \frac{B}{A}\left[1 + \Delta R_r(X_{ox}, t_{ox})\right] \qquad [8]$$

where $\Delta R_e(X_{ox},t_{ox})$ and $\Delta R_r(X_{ox},t_{ox})$ are additive "excess" and multiplicative "ratio" rate-enhancement terms, respectively. It is therefore concluded that the oxidation-rate enhancement in the thin regime can be analyzed as either a term added to the linear-parabolic rate or as one that multiplies it. Furthermore, the analysis can be done as a function of oxide thickness or oxidation time. Both analyses were done, and the discussion of the results here will be limited to the analysis as a function of the oxide thickness, which proved to be more physically significant. As the oxidation approaches the onset of linear-parabolic kinetics, the rate-enhancement terms disappear and the expression for the oxidation rate reduces to that of the linear-parabolic model (Eq. [1]).

In this study, the total oxidation rate was obtained by numerically differentiating experimental X_{ox}-t_{ox} data using a five-point differentiation scheme (18). This approach was made possible only because of the use of *in situ* ellipsometry in obtaining closely spaced data points, as illustrated in Fig. 1. Once the total oxidation rate was calculated, the linear-parabolic contribution was subtracted, resulting in the excess in growth rate ΔR_e characteristic of the thin regime, as given by Eq. [7]. Values of B and B/A appropriate to this study were obtained as described in Ref. (16) and are in general agreement with earlier results.

Experimental Results

The dependence of the growth rate on oxide thickness is discussed for lightly doped silicon oxidized in dry oxygen and oxygen-argon mixtures and for heavily doped silicon oxidized in dry oxygen.

Oxidation of lightly doped silicon in dry oxygen.—The dependence of the silicon-oxidation rate on oxide thickness for (100) silicon in the 800°-1000°C range is plotted in Fig. 3. Similar results were obtained for (111) and (110) orientations (15). In every oxidation run, 33 data points were taken at equal time intervals. A first set of experiments covered the oxide growth up to ~600Å. As a result of the fast initial growth at the onset of oxidation, the number of data points in the first 100Å was limited. This

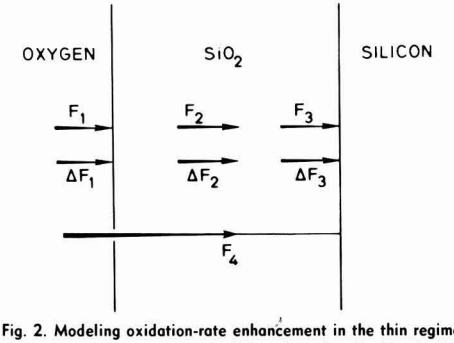


Fig. 2. Modeling oxidation-rate enhancement in the thin regime by adding additional processes in parallel to those described by the linear-parabolic model.

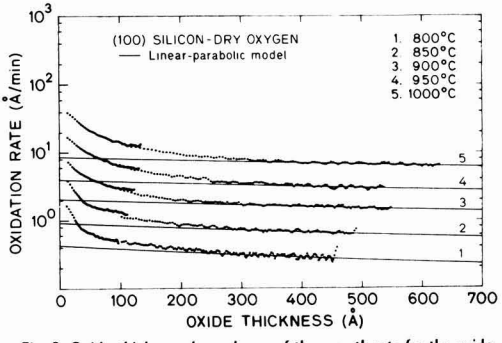


Fig. 3. Oxide-thickness dependence of the growth rate for the oxidation of lightly doped (100) silicon in dry oxygen in the 800°-1000°C range. The solid lines are plots of the linear-parabolic rate.

necessitated that a second set of experiments was carried out in which more closely spaced data points were obtained in the first 100Å.

The oxidation rate expressed by the linear-parabolic model (Eq. [1]) is also plotted as a function of thickness. It is observed that the rate is higher than that predicted by the linear-parabolic model up to 250-350Å and that, beyond this thickness, growth is linear-parabolic. Rate enhancement can be divided into an initial phase extending from the native-oxide thickness up to 40-50Å at 800°C and ~100Å at 1000°C, where the rate rapidly decreases with thickness, and an intermediate phase where it decreases asymptotically to the point of onset of linear-parabolic kinetics. The SiO_2 growth rate on (100) is slower than on (111) and (110) at all temperatures and over the entire thickness range. At all temperatures, the growth rate of SiO_2 on (110) starts higher than in (111) until a certain thickness is reached were this order reverses.

Plots of oxidation-rate enhancement, expressed in the form of an additive term $\Delta R_i(X_{ox})$, for the oxidation of (100) lightly doped silicon oxidized in dry oxygen in the 800°-1000°C range are shown in Fig. 4. These are semilog plots obtained by subtracting the linear-parabolic rate from the total oxidation rate at every oxide thickness. Similar results were obtained for (111) and (100) orientations (15). It can be seen that the excess rate, for all orientations and at all temperatures, has an initial phase extending to ~50Å and an intermediate phase extending from that point to the onset of linear-parabolic kinetics; this suggests that $\Delta R_i(X_{ox})$ can be expressed as the sum of two terms. The parallel straight-line dependence of $\Delta R_i(X_{ox})$ on thickness (on a semilog plot) in the intermediate phase suggests that the fit could be accomplished with a term that exponentially decays with thickness. When $\Delta R_i(X_{ox})$ in the initial phase was calculated and plotted on a semilog plot, it could also be fitted to a second term that decays similarly with thickness. The expression of the total growth rate is then written as

$$\frac{dX_{ox}}{dt} = \frac{B}{(2X_{ox} + A)} + C_1 e^{-(X_{ox}/L_1)} + C_2 e^{-(X_{ox}/L_2)} \quad [9]$$

The following observations apply to the intermediate phase described by C_2 and L_2.

1. The characteristic length L_2 is approximately independent of temperature in the 800°-1000°C range, and its value is 69, 78, and 60Å for (100), (111), and (110), respectively.

2. The constant C_2 has a single activation energy in the Arrhenius-type plot shown in Fig. 5a, where it can be seen that C_2 fits a simple rate expression in the form of

$$C_2 = C_2^0 e^{-(\Delta E_{C_2}/kT)} \quad [10]$$

The pre-exponential constant C_2^0 and the activation energy ΔE_{C_2} are listed in Table I for the three orientations. For (100) and (111), ΔE_{C_2} is nearly the same, while that of

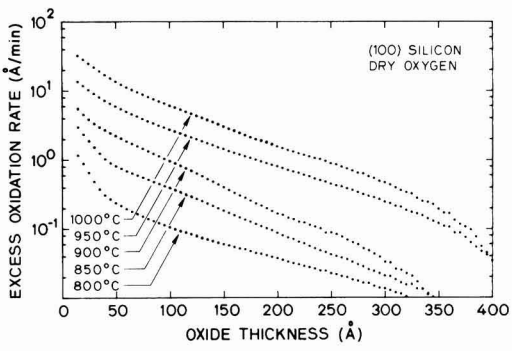


Fig. 4. Oxide-thickness dependence of the excess in growth rate for the oxidation of lightly doped (100) silicon in dry oxygen in the 800°-1000°C range.

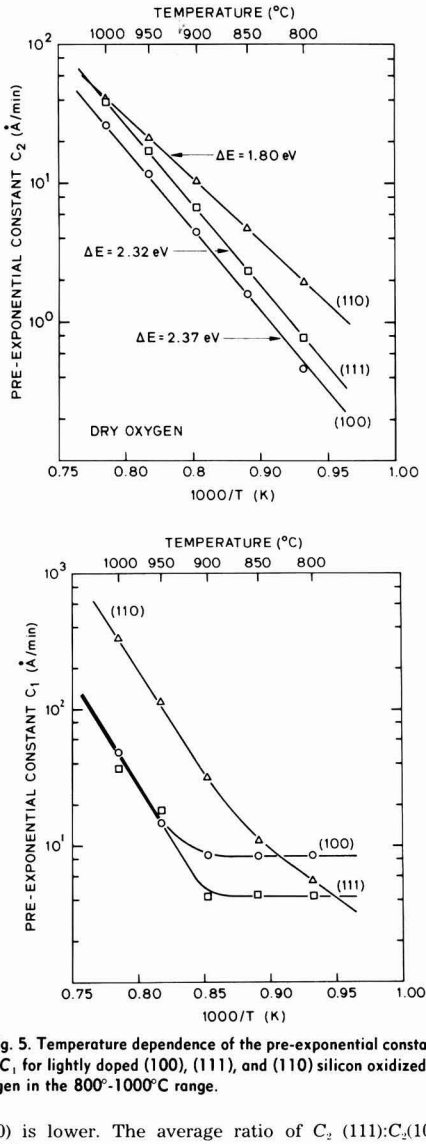


Fig. 5. Temperature dependence of the pre-exponential constants C_2 and C_1 for lightly doped (100), (111), and (110) silicon oxidized in dry oxygen in the 800°-1000°C range.

(110) is lower. The average ratio of C_2 (111):C_2(100) is 1.52:1.

The following observations apply to the initial phase described by C_1 and L_1.

1. The characteristic length L_1 increases slowly from 7.7Å at 800°C to 12.4Å at 1000°C for (100) and from 10.9 to 17.1Å for (111). It has a constant value of 14.7Å for (110).

2. The dependence of C_1 on temperature, shown in Fig. 5b, has a break at ~900°C. For (100) and (111), it is temperature independent below 900°C, and the ratio C_1(100):C_1(111) is 2.0:1; both orientations have similar values above 900°C. For (110), the activation energy in C_1 changes from that of the other two orientations above 900°C to slightly lower below 900°C. Above 900°C, the initial fitted excess rate can be fitted to an expression analogous to Eq. [10] with the values of C_1^0 and ΔE_{C_1} given in Table I. The lack of a well-behaved trend in the temperature dependence of C_1 may be attributed to the fact that it describes the growth of the first few layers of SiO_2 that has been shown to depend on residual traces of impurities remaining on the surface after cleaning and preoxidation procedures. Although this was not verified experimentally, it is suspected that the first exponential contribu-

Table I. Pre-exponential constants C_2° and C_1° and activation energies ΔE_{t_2} and ΔE_{t_1} for the oxidation-rate enhancement in the thin regime of (100), (111), and (110) lightly doped silicon oxidized in dry oxygen

		(100)	(111)	(110)
	C_2° (Å/min)	6.57×10^{10}	5.87×10^{10}	5.37×10^{8}
	ΔE_{t_2} (eV)	2.37	2.32	1.80
T (°C)	C_1° (Å/min)	3.04×10^{10}	4.87×10^{12}	3.21×10^{14}
> 900°C	ΔE_{t_1} (eV)	2.24	2.80	3.03
T (°C)	C_1° (Å/min)	8.49	4.33	3.22×10^{9}
< 900°C	ΔE_{t_1} (eV)	0.00	0.00	1.87

tion to the excess in oxidation rate is closely related to wafer cleaning and surface preparation procedures.

Using the obtained values of C_1, C_2, L_1, L_2, B, and B/A in Eq. [9] and integrating numerically to fit the experimental data, it was found that the first decaying exponential $C_1 \exp(-X_{ox}/L_1)$ affected the fit only slightly at oxide thicknesses up to ~50-100Å. Neglecting this term results in errors of less than 5% in fitting the experimental data. A good empirical expression for the oxidation rate, therefore, could include only the second decaying exponential in addition to the linear-parabolic term.

Oxidation of lightly doped silicon in dry oxygen-argon mixtures.—Based on the steady-state assumption in the linear-parabolic model and the validity of Henry's law, the concentration of oxidizing species in the oxide C^* and the parabolic rate constant B (Eq. [2]) are both directly proportional to oxygen partial pressure in the oxidizing ambient. Consequently, the growth rate, expressed as a function of thickness (Eq. [1]), is expected to have a linear dependence on oxygen pressure because A does not depend on C^* (Eq. [3]). From these considerations, it is concluded that, according to the linear-parabolic model, the oxidation rate should be linearly proportional to the partial pressure of oxygen at any thickness. For this reason, oxygen pressure analysis is done in the form of rate *vs.* thickness plots at different pressures.

Figure 6 plots the dependence of the growth rate on oxide thickness for the oxidation of lightly doped (100) silicon in dry O_2 diluted by argon such that the partial pressure of oxygen in the oxidizing ambient is 0.10 atm. Figure 7 plots the results obtained at 0.01 atm. Here again, similar results were obtained for (111) and (110) orientations (15). These experiments did not cover oxide growth up to 500-600Å because the oxidation rate is reduced at lower oxygen partial pressures and unusually long oxidations would have been necessary. Oxidation time was limited to 5h. As a result, the linear and parabolic rate constants could not be determined with any degree of confidence; however, lower limits on the values of B and upper limits on those of B/A could be obtained. The quantitative analysis of oxidation-rate enhancement in the thin regime at oxygen partial pressures less than 1.0 atm is, therefore, based on the following data analysis and the oxygen-pressure dependence of B and B/A published in the literature.

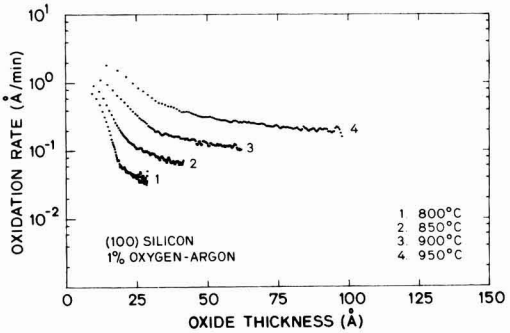


Fig. 7. Oxide-thickness dependence of the growth rate for the oxidation of lightly doped (100) silicon in a dry oxygen-argon mixture corresponding to 0.01 atm of oxygen partial pressure in the 800°-950°C range.

Oxidation rates at 0.10 and 0.01 atm have a thickness dependence similar to that observed at 1.00 atm where the growth is enhanced in the thin regime and two phases are identified. In all three orientations, the initial phase extends from ~ 30 to 80Å at 0.10 atm and from ~ 20 to 40Å at 0.01 atm in the 800°-950°C range. Rate crossover between (111) and (110) occurs at 0.10 atm at all temperatures in the 800°-950°C range where (110) oxidizes faster than (111) below the crossover point. The growth rate of (100) substrates is slowest over the entire thickness range. In contrast, the oxidation of (110) silicon is fastest at 0.01 atm, and crossover is observed between (100) and (111) at 20 and 45Å at 900° and 950°C, respectively. The rate of SiO_2 growth on (111) is higher than on (100) over the entire thickness range at 850° and 800°C.

A comparison of the oxidation rates at 1.00, 0.10, and 0.01 atm is important in determining the dependence of the concentration of oxidizing species in the oxide on the oxygen partial pressure in the ambient. Figure 8 is a plot of the dependence of the oxidation rate of (111) silicon at 950°C on thickness at the three values of oxygen pressure. Past the initial phase, which extends up to ~50-60Å, the growth rates are parallel (or have similar thickness dependence). At any thickness X_{ox} beyond the initial phase, the rate $R_p(X_{ox})$ at any pressure p can be obtained by dividing the growth rate at 1.00 atm, $R_{1.00}(X_{ox})$, by a constant K_0 such that

$$R_p(X_{ox}) = \frac{1}{K_0} R_{1.00}(X_{ox}) \qquad [11]$$

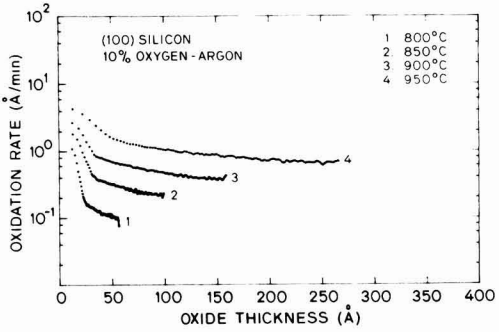


Fig. 6. Oxide-thickness dependence of the growth rate for the oxidation of lightly doped (100) silicon in a dry oxygen-argon mixture corresponding to 0.10 atm of oxygen partial pressure in the 800°-950°C range.

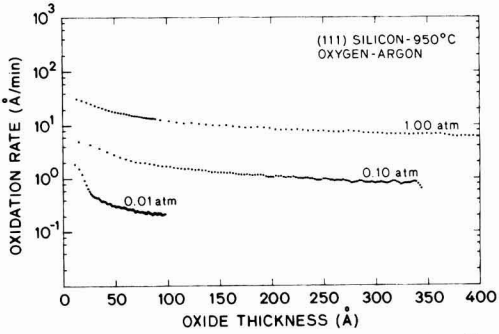


Fig. 8. Oxide-thickness dependence of the growth rate for the oxidation of lightly doped (111) silicon at 950°C in dry oxygen-argon mixtures corresponding to 1.00, 0.10, and 0.01 atm of oxygen partial pressure.

Table II. Temperature dependence of the ratio K_0 of the oxidation rates at 1.00 atm and at 0.10 and 0.01 atm in the 800°-950°C range for (100), (111), and (110) lightly doped silicon oxidized in dry oxygen-argon mixtures

	T_{ox} (°C)	(100)	(111)	(110)
$R_{1.00}/R_{0.10}$	950	6.22	7.45	6.19
	900	6.36	7.16	6.14
	850	6.36	6.05	6.40
	800	6.18	6.17	6.08
$R_{1.00}/R_{0.01}$	950	36.5	57.2	40.6
	900	35.9	48.8	36.2
	850	36.9	35.4	30.2
	800	39.4	33.3	29.6

Values of K_0 for (100), (111), and (110) silicon in the 800°-950°C range are given in Table II.

It can be seen that K_0 is nearly constant at all temperatures and for each value of p. The scatter in the values at 0.01 atm is attributed to the limited thickness range of the experiments. Figure 9 is a plot of the normalized oxidation rate ($R_p/R_{1.00}$ or $1/K_0$) as a function of p. It can be seen that the oxidation rate in the thin regime has a pressure dependence of $\sim p^{0.8}$ which is in agreement with the findings of a high pressure oxidation study in dry oxygen (19) where the linear rate constant B/A was found to have a $p^{0.7}$-$p^{0.8}$ pressure dependence. The variation in K_0 with temperature at 0.01 atm corresponds to a pressure dependence of $\sim p^{0.74}$ at 800°C to $\sim p^{0.88}$ at 950°C. This is shown in Fig. 9 by the spread of the data points towards lower oxygen partial pressures. It is also in qualitative agreement with a pressure dependence of $\sim p^{0.5}$ observed at low temperatures and $\sim p^{1.0}$ at high temperatures in the 700°-1000°C range, for the normalized linear rate constant obtained by Ghez and van der Meulen (20). Variation in the pressure exponent in the two studies is attributed to different approaches to data analysis; oxidation rates are compared in this study, while linear rate constants were extracted using published values of the parabolic rate constants in the earlier study (20).

The analysis of the effect of oxygen partial pressure on the oxidation rate of lightly doped silicon demonstrated that the growth rate beyond the initial phase has a $p^{0.8}$ pressure dependence. An oxidation study at high pressure in dry oxygen (19) has also shown that the linear rate constant has a $p^{0.7}$-$p^{0.8}$ pressure dependence and that the parabolic rate constant is linearly proportional to pressure. Based on these findings, the quantitative analysis of oxidation-rate enhancement in the this study for $p_{O_2} < 1$ atm is based on the assumptions that B is linearly proportional to p and that B/A is proportional to $p^{0.8}$.

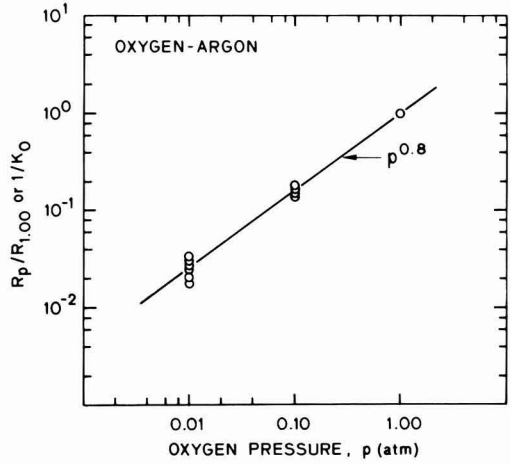


Fig. 9. Dependence of the normalized oxidation rate on the partial pressure of oxygen in the oxidation ambient of (100), (111), and (110) lightly doped silicon in dry oxygen-argon mixtures in the 800°-1000°C range.

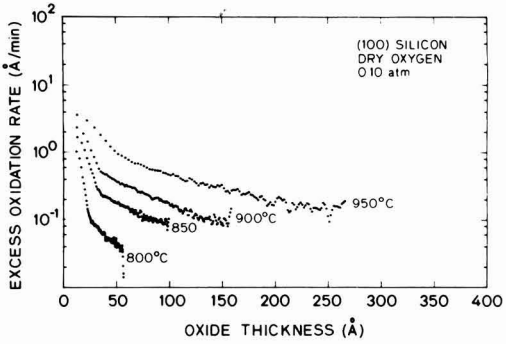


Fig. 10. Oxide-thickness dependence of the excess in growth rate for the oxidation of lightly doped (100) silicon in a dry oxygen-argon mixture corresponding to 0.10 atm of oxygen partial pressure in the 800°-950°C range.

The dependence of the excess growth rate $\Delta R_0(X_{0i})$ on oxide thickness for (100) silicon is plotted in Fig. 10 and 11 for P_{O_2} = 0.10 and 0.01 atm, respectively. Similar results were obtained for (111) and (110) (15). This excess consists of an initial phase that extends up to ~ 30-80Å at 0.10 atm partial pressure and to thinner oxides at 0.01 atm, and an intermediate phase that merges into linear-parabolic kinetics asymptotically. These results are similar to those observed at 1.0 atm. Here, again, the excess rate could be fitted with two terms exponentially decaying with thickness, as in the form of Eq. [9].

The extent of the intermediate phase, as characterized by the decay length L_2, was obtained at 0.10 atm and for 900° and 950°C results at 0.01 atm (where the oxide thickness was large enough at the end of the oxidation to identify the intermediate phase). It was found to have values similar to those obtained at 1.0 atm. The pre-exponential constant C_2 is shown in an Arrhenius-type plot for (100), (111), and (110) in Fig. 12, where it can be fitted with a single activation energy of 1.51, 1.58, and 0.85 eV, respectively. The similar values for the activation energies of (100) and (111) and the smaller value for (110) were also observed at 1.0 atm; activation energies at 0.10 atm are, on the average, ~0.8 eV smaller than at 1.0 atm.

The exponentially decaying term $C_1 \exp(-X_{0i}/L_1)$ represents the fast growth observed at the onset of oxidation and up to ~ 50Å. No well-behaved temperature dependence of C_1 was observed, and the characteristic length L_1 decreased from ~10-20Å at 950°C to ~4-7Å at 800°C. As ob-

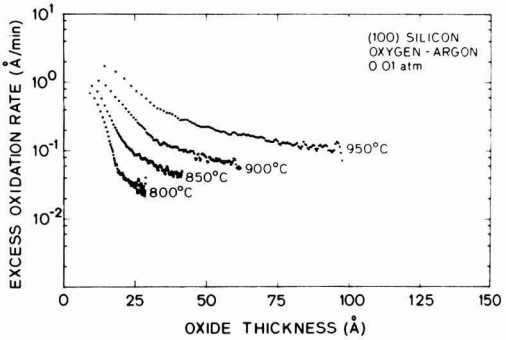


Fig. 11. Oxide-thickness dependence of the excess in growth rate for the oxidation of lightly doped (100) silicon in a dry oxygen-argon mixture corresponding to 0.01 atm of oxygen partial pressure in the 800°-950°C range.

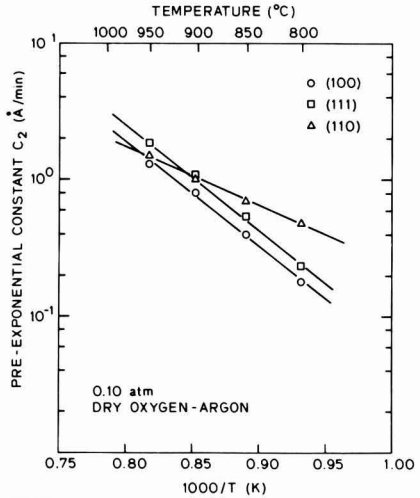


Fig. 12. Temperature dependence of the pre-exponential constant C_2 for the oxidation of lightly doped (100), (111), and (110) silicon in a dry oxygen-argon mixture corresponding to 0.10 atm of oxygen partial pressure in the 800°-950°C range.

served in atmospheric oxidations, this decaying term could also be neglected in the expression of the total oxidation rate with less than 5-7% error in the fit to oxidation data.

The 0.01 atm oxidations were not carried out to oxide thicknesses where the intermediate phase could be quantitatively characterized, except at 900° and 950°C, where the characteristic length of the intermediate phase was found to be similar to 1.0 and 0.10 atm results.

The pressure dependence of the pre-exponential constant C_2 was found to increase monotonically from $p^{0.57}$ at 800°C to $p^{0.88}$ at 950°C for (100), from $p^{0.60}$ at 800°C to $p^{0.93}$ at 950°C for (111), and was nearly constant at $p^{0.83}$ for (110) in the 800°-950°C range. This pressure dependence is similar to that observed for the linear rate constant B/A and discussed earlier.

In summary, oxidation-rate enhancement at lower partial pressures of oxygen has a thickness dependence similar to atmospheric oxidations. The extent of the intermediate phase in oxide thickness is nearly unaffected by oxygen pressure, whereas the activation energy of the pre-exponential constant in the enhancement term is smaller at reduced partial pressures. The pre-exponential constant C_2 was found to have a pressure dependence similar to the linear rate constant B/A.

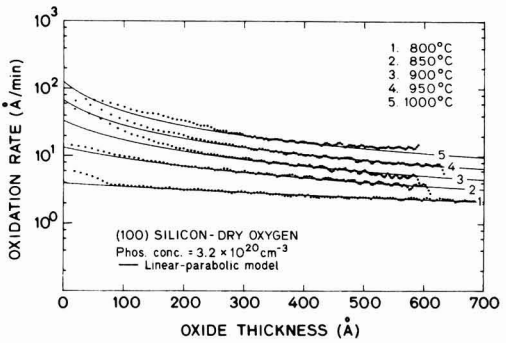


Fig. 14. Oxide-thickness dependence of the growth rate for the oxidation of (100) silicon doped with 3.2×10^{20} cm^{-3} phosphorus, in dry oxygen in the 800°-950°C range.

Oxidation of heavily doped silicon in dry oxygen.—Figures 13 and 14 plot the thickness dependence of silicon-dioxide growth rate on (100) silicon wafers doped with phosphorus at 1.8×10^{20} cm^{-3} (medium doped [MD]) and 3.2×10^{20} cm^{-3} (heavily doped [HD]) oxidized in dry oxygen in the 800°-950°C and 800°-1000°C ranges, respectively. Based on these plots and the results on lightly doped substrates shown in Fig. 3, the oxidation rate increases with doping at all temperatures and over the entire thickness range. Beyond the initial phase (< 100Å), lightly doped (LD) substrates exhibit parallel plots of rate *vs.* thickness in the 800°-1000°C range, whereas, in MD and HD substrates of both orientations, the difference in oxidation rates decreases with increasing thickness. This is expected because, in heavily doped silicon substrates, the linear rate constant B/A is greatly enhanced and the parabolic rate constant B is only modestly enhanced at low temperatures (21, 22); consequently, the transition from linear to parabolic kinetics occurs at a thinner oxide thickness.

The oxidation rate as expressed by the linear-parabolic relationship is also plotted in Fig. 13 and 14 as a function of thickness. The values of B and B/A were determined from the growth data as described elsewhere (16). It can be seen from Fig. 13 and 14 that the growth rate of HD substrates is enhanced during the initial stages of oxidation over a thickness range that decreases from ~ 300Å at 1000°C to ~ 75Å at 800°C. In MD wafers, the rate enhancement extends over a similar thickness range, approaches a constant value at lower temperatures, and its thickness dependence rate is identical for the two orientations; (111) is 1.5 ± 0.1 larger than (100).

The excess in growth rate $\Delta R_v(X_{ox})$ in the oxidation of heavily doped silicon substrates was calculated by sub-

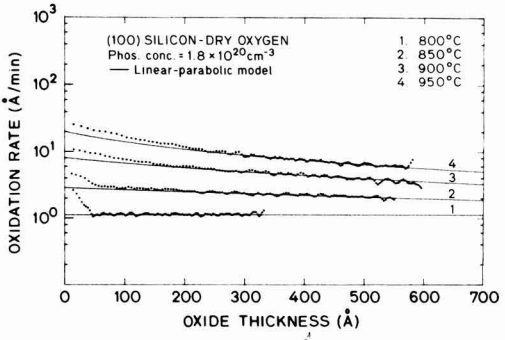


Fig. 13. Oxide-thickness dependence of the growth rate for the oxidation of (100) silicon doped with 1.8×10^{20} cm^{-3} phosphorus, in dry oxygen in the 800°-950°C range.

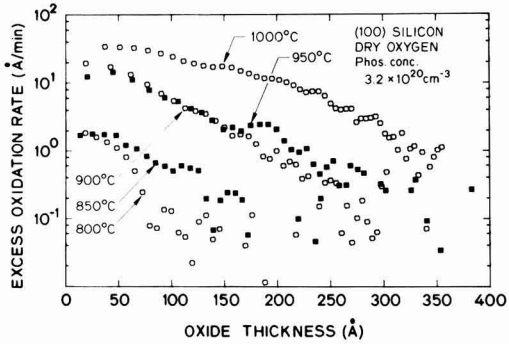


Fig. 15. Oxide-thickness dependence of the excess in the growth rate for the oxidation of (100) silicon doped with 3.2×10^{20} cm^{-3} phosphorus in dry oxygen in the 800°-1000°C range.

tracting the linear-parabolic contribution as before, but with the appropriate doping dependent values of B/A. It is plotted as a function of oxide thickness in Fig. 15 for (100) HD substrates. Similar results were obtained for (111) HD substrates (15). In comparison with lightly doped substrates, which show two distinct phases in the excess rate, $\Delta R_o(X_{ox})$ for HD substrates has only one apparent phase that decays exponentially with thickness, and it accounts for oxidation-rate enhancement from the onset of oxidation. The absence of the initial growth phase (C_1, L_1) observed on lightly doped substrates may be due to the large enhancement in the other rates caused by the high doping levels effectively obscuring it. It may also be related to phase separation and/or precipitation of the dopant into the oxide near the interface, as a limited TEM study of the heavily doped samples revealed small heavily doped silicon inclusions in the oxide at the interface. The total growth rate can be therefore expressed as

$$\frac{dX_{ox}}{dt} = \frac{B}{(2X_{ox} + A)} + C_2 e^{-(X_{ox}/L_2)} \qquad [12]$$

In the heavily doped wafers, an Arrhenius-type plot of the pre-exponential constant C_2 in Fig. 16 indicates a single activation energy ΔE_{t_2} of 1.87 and 1.77 eV for (100) and (111), respectively. It is interesting to note that C_2 is higher for (100) than for (111) and that its activation energy is smaller than in lightly doped substrates, with (100) and (111) again having similar values. The magnitude and thickness extent of the rate enhancement in both HD and LD substrates are similar. It should also be noted that heavy phosphorus doping in the substrate greatly enhances the linear rate constant B/A but increases the excess oxidation rate associated with the thin regime only moderately. It can be concluded that, to a first order, doping does not affect the oxidation enhancement process in the thin regime.

The excess oxidation rate in MD wafers is plotted in Fig. 17 as a function of thickness in (100) silicon. Similar results were obtained for (111) (15). Only one phase that exponentially decays with thickness is observed. The temperature dependence of C_2 is not a singly activated process, and the characteristic length L_2 is also a strong function of temperature, decreasing from ~ 85Å at 950°C

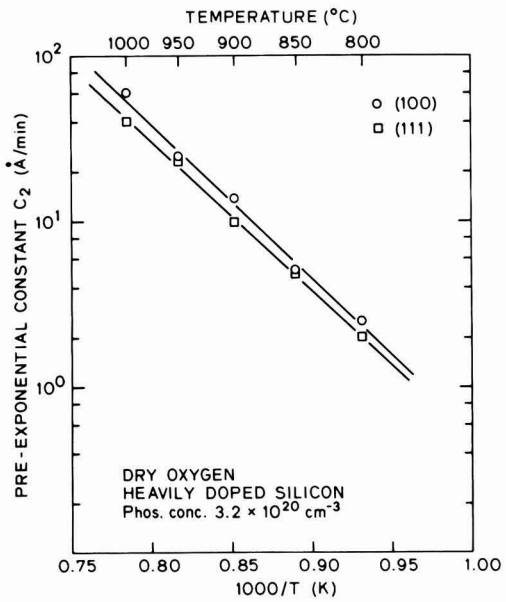


Fig. 16. Temperature dependence of the pre-exponential constant C_2 for the oxidation of (100) and (111) silicon heavily doped with 3.2×10^{20} cm^{-3} phosphorus in dry oxygen in the 800°-1000°C range.

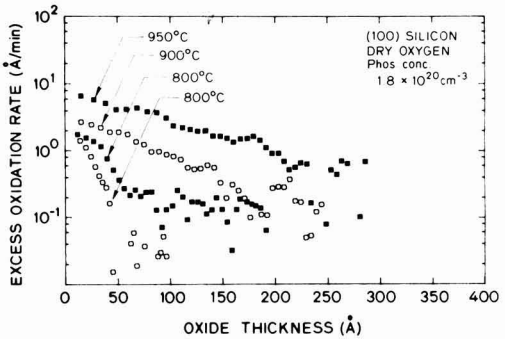


Fig. 17. Oxide-thickness dependence of the excess in the growth rate for the oxidation of (100) silicon doped with 1.8×10^{20} cm^{-3} phosphorus in dry oxygen in the 800°-950°C range.

to ~15Å at 800°C. The enhancement in the excess term when compared to LD substrates is smaller than that in the linear rate constant at high temperatures but is greater at low temperatures. The results should be analyzed in conjunction with the strong phosphorus redistribution occurring during the early stages of oxidation when phosphorus is depleted near the $Si-SiO_2$ interface and the concentration of electrically active species is reduced (23, 24).

In the case of heavily doped substrates, the high concentration of phosphorus is sufficient to maintain the solid solubility level in spite of the redistribution occurring simultaneously. This gives rise to an effectively fixed electrically active surface concentration during the oxidation and, therefore, to well-behaved C_2, L_2, and B/A. This is not the case, however, with moderately doped substrates where the time dependencies of the redistribution process are clearly involved. The variation of C_2 and L_2 in Fig. 17 is therefore not necessarily an indication of a change in the physical mechanisms involved.

In summary, the magnitude of oxidation-rate enhancement in heavily doped samples in the thin regime is only slightly increased by the doping level in the substrate, and its thickness extent is unaffected. This is in contrast with the large enhancement in the linear rate constant. The excess reaction proceeds with an activation energy lower than in lightly doped substrates. These results indicate that, in a first-order analysis, the surface-reaction mechanism in the thin regime proceeds independently of and in parallel with the mechanism enhancing B/A of heavily doped substrates.

Conclusions

Oxidation-rate enhancement during the early stages of the oxidation of silicon in dry oxygen can be modeled by adding a term that exponentially decays with thickness to the rate expression of the linear-parabolic model. This added term has a prefactor that reflects the excess rate at which the reaction proceeds and a characteristic length that represents its extent in thickness. The activation energy of the excess rate was found to be a function of substrate doping density and oxygen partial pressure in the ambient. The characteristic length was observed to be nearly independent of substrate orientation, doping level, and of the partial pressure of oxygen. The oxidation of medium-doped samples during the early stages reflects the transient redistribution of phosphorus near the interface.

Acknowledgments

The authors would like to acknowledge many helpful discussions with Dr. Bruce E. Deal, Dr. C. P. Ho, and Dr. Reda R. Razouk. This study was sponsored by Darpa Contract no. MDA 903-79-C-0257.

Manuscript received April 15, 1985; revised manuscript received July 11, 1985.

Stanford University assisted in meeting the publication costs of this article.

REFERENCES

1. C. J. Frosch and L. Derick, *This Journal*, **104**, 547 (1957).
2. M. M. Atalla, E. Tannenbaum, and E. J. Scheibner, *Bell Syst. Tech. J.*, **38**, 749 (1959).
3. B. E. Deal and J. D. Plummer, in "Integrated Circuits Process Models," J. D. Meindl and K. C. Saraswat, Editors, Prentice Hall, Englewood Cliffs, NJ, In press.
4. R. B. Fair, in "Applied Solid State Science, Supplement 2, Silicon Integrated Circuits, Part B," D. Khang, Editor, Academic Press, New York (1981).
5. W. A. Pliskin and R. A. Gdula, "Materials, Properties and Preparation," S. P. Keller, Editor, Chap. 11, Vol. 3 in "Handbook on Semiconductors," T. S. Moss, Editor, North Holland Publishing Company, Amsterdam (1981).
6. E. H. Nicollian and J. R. Brews, in "MOS (Metal Oxide Semiconductor) Physics and Technology," Chap. 13, Wiley-Interscience, New York (1982).
7. R. H. Dennard, F. H. Gaensslen, H. N. Yu, V. L. Rideout, E. Bassous, and A. R. LeBlanc, *IEEE J. Solid-State Circuits*, **sc-9**, 256 (1974).
8. B. E. Deal and A. S. Grove, *J. Appl. Phys.*, **36**, 3770 (1965).
9. K. Hamano, *Jpn. J. Appl. Phys.*, **13**, 1085 (1974).
10. E. A. Taft and L. F. Cordes, *This Journal*, **126**, 131 (1979).
11. H. Z. Massoud, J. D. Plummer, and E. A. Irene, *This Journal*, **132**, 2693 (1985).
12. Y. J. van der Meulen and N. C. Hien, *J. Opt. Soc. Am.*, **64**, 804 (1974).
13. P. S. Hauge and F. H. Dill, *IBM J. Res. Dev.*, **17**, 472 (1972).
14. W. Kern and D. A. Puotinen, *RCA Rev.*, **31**, 187 (1970).
15. H. Z. Massoud, Ph.D. Thesis, Stanford University, Stanford, CA (1983).
16. H. Z. Massoud, J. D. Plummer, and E. A. Irene, *This Journal*, **132**, 1745 (1985).
17. I. M. Ritchie and G. L. Hunt, *Surf. Sci.*, **15**, 524 (1969).
18. G. Dahlquist and A. Bjorck, "Numerical Methods," Prentice Hall, Englewood Cliffs, NJ (1974).
19. L. N. Lie, R. R. Razouk, and B. E. Deal, *This Journal*, **129**, 2828 (1982).
20. R. Ghez and Y. J. van der Meulen, *ibid.*, **119**, 1100 (1972).
21. C. P. Ho and J. D. Plummer, *ibid.*, **126**, 1516 (1979).
22. C. P. Ho and J. D. Plummer, *ibid.*, **126**, 1523 (1979).
23. S. A. Schwarz, R. W. Barton, C. P. Ho, and C. R. Helms, **128**, 1101 (1981).
24. R. W. Barton, Technical Report no. J701-1, Stanford Electronics Laboratories, Stanford University, Stanford, CA (1981).

Thermal Oxidation of Silicon in Dry Oxygen: Growth-Rate Enhancement in the Thin Regime

II. Physical Mechanisms

Hisham Z. Massoud*[,1] and James D. Plummer*

Integrated Circuits Laboratory, Stanford University, Stanford, California 94305

Eugene A. Irene*[,2]

IBM Thomas J. Watson Research Center, Yorktown Heights, New York 10598

ABSTRACT

In many studies of oxidation kinetics, it has been observed that silicon-dioxide growth in dry oxygen in the thin film regime (<500Å) is faster than predicted by the linear-parabolic description of the growth of thicker layers. Oxidation-rate enhancement in the thin film regime was studied in the 800°-1000°C range for a variety of substrate orientations, doping densities, and oxygen partial pressures using *in situ* ellipsometry. The results were reported in part I of this paper. In this part, the physical mechanisms previously proposed to explain the rate enhancement are discussed. No single model was found to apply under all experimental conditions. A new understanding of the growth-rate enhancement in the early stages of silicon oxidation in dry oxygen is introduced.

Silicon oxidation occurs as a result of the transport of oxidizing species through the existing oxide to react with silicon at the Si-SiO_2 interface and form silicon dioxide. Knowledge of the physical processes that affect thermal oxidation is important in optimizing the applications where SiO_2 plays an essential role and in understanding the interaction between oxidation and other related phenomena, such as defect formation/suppression, impurity gettering, stacking fault growth/shrinkage, and impurity-dopant enhanced/retarded diffusion. This knowledge is vital in growing the highest quality oxides to be used as a gate dielectric material in high performance VLSI MOS circuits. The much-discussed growth-rate enhancement in the early stages of silicon oxidation in dry oxygen was investigated using *in situ* ellipsometry, and its dependence on temperature, substrate orientation, doping density, and oxygen partial pressure was reported in part I of this paper (1). The results indicated that the total growth rate in the thin film regime can be expressed as a term exponentially decaying with thickness added to the linear-parabolic rate. It was also observed that the thickness extent of the initial growth-rate enhancement does not depend, in a first-order analysis, on substrate orientation, dopant density, or oxygen partial pressure and that the pre-exponential constant and its activation energy depend on these experimental parameters.

This paper starts with a summary of the experimental results obtained in this study and reported in part I of this paper (1). The predictions of models already proposed to explain the enhancement in silicon-dioxide growth rate in the early stages of silicon oxidation in dry oxygen are then compared with the experimental results of this study. It will be shown that these models have a limited range of success and could not be applied under all experimental conditions. A possible physical understanding of silicon oxidation in the thin regime which is consistent with all observed experimental results is then introduced.

Summary of Experimental Results

The silicon-dioxide growth rate in the thin regime under a wide variety of experimental conditions (substrate orientation, doping, and oxygen partial pressure) can be expressed as (1)

*Electrochemical Society Active Member.

[1]Present address: Department of Electrical Engineering, Duke University, Durham, North Carolina 27706

[2]Present address: Department of Chemistry, University of North Carolina, Chapel Hill, North Carolina 27514

$$\frac{dX_{ox}}{dt} = \frac{B}{2X_{ox} + A} + C_1 e^{-(X_{ox}/L_1)} + C_2 e^{-(X_{ox}/L_2)} \quad (1)$$

The first term is the linear-parabolic term where B and B/A are the parabolic and linear rate constants, respectively, as defined by Deal and Grove (3). Values for these rate constants used on this study were reported elsewhere (2). The two exponential terms represent the rate enhancement in the thin regime. They are defined in terms of pre-exponential constants C_1 and C_2 and characteristic lengths L_1 and L_2. The first decaying exponential has a characteristic length on the order of 10Å, is nonzero for the first 40-50Å of oxide growth, and vanishes for oxides thicker than 50Å. The second decaying exponential has a characteristic length on the order of 70Å and is present from the onset of oxidation to an oxide thickness of ~250Å, where it decays to zero and where the growth becomes pure linear-parabolic.

In fitting Eq. [1] to oxidation data, it was observed that simplifying the expression of the total oxidation rate to

$$\frac{dX_{ox}}{dt} = \frac{B}{(2X_{ox} + A)} + C_2 e^{-(X_{ox}/L_2)} \quad (2)$$

would result in only 5-7% error. The following observations summarize the experimental results in part I of this paper (1), as expressed by the dependence of the pre-exponential constant C_2 and the characteristic length L_2 on experimental conditions.

1. For lightly doped silicon substrates oxidized in dry oxygen, it was observed that L_2 is independent of temperature in the 800°-1000°C range. Its value (~70 ± 10Å) is, in a first-order analysis, independent of substrate orientation. The pre-exponential constant C_2 is well behaved in its temperature dependence and fits a single activation-energy rate expression. Similar activation energies of 2.37 and 2.32 eV were obtained for (100) and (111), respectively, and a smaller value of 1.80 eV for (110) (1).

2. For lightly doped silicon substrates oxidized in dry oxygen-argon mixtures, the characteristic length L_2 was similar to oxidations in 100% dry oxygen. The pre-exponential constant C_2 was well behaved in its temperature dependence, again fitting a single activation-energy rate expression. Activation energies for the three orientations were on the average 0.8 eV smaller than oxidations in dry oxygen. The pressure dependence of C_2 was found to be $\sim p^{0.8}$, which is the same as the average pressure dependence of the linear rate constant B/A (1).

3. For heavily doped silicon substrates (doped at solid solubility phosphorus) oxidized in dry oxygen, the characteristic length L_2 was unchanged from lightly doped oxidations. The pre-exponential constant C_2 was also well behaved with temperature with similar activation energies of 1.87 and 1.77 eV for (100) and (111), respectively. By comparison with the magnitude of C_2 for lightly doped oxidations, it was observed that heavy doping only moderately affected the amount of oxidation-rate enhancement in the thin regime.

Oxidation-rate enhancement in the thin regime can, in summary, be expressed by a term exponentially decaying with thickness. Its thickness extent is independent of substrate orientation, doping level, and oxygen partial pressure in the oxidizing ambient. Its magnitude has the same pressure dependence as that of the linear rate constant and is only moderately affected by high phosphorus concentrations in the substrate.

Review of Previous Models

An evaluation of the models already proposed to explain the fast initial regime is given here. These models fall into four groups: (*i*) space-charge effects where the enhancement is electrochemical in nature, (*ii*) oxide-structure effects that provide additional oxidant transport, (*iii*) oxide stress effects influencing the diffusivity of oxidizing species in the oxide and the surface-reaction rate constant at the interface, and (*iv*) oxygen-solubility considerations in the oxide where growth would be enhanced due to oxygen concentrations exceeding its solid-solubility limit.

Space-charge effects.—A number of electrochemical mechanisms have been proposed to enhance the oxidation process in the thin regime (3-9). The transport of oxidant species by thermal diffusion has been proposed to be affected by an electric field existing across the oxide in the early stages of growth. Field-assisted oxidant diffusion was originally proposed by Cabrera and Mott (4) to account for metal-oxidation results. This phenomenon was proposed by Deal and Grove (3) to account for silicon-oxidation results in dry oxygen in the thin regime.

Theoretical analyses of the kinetics of metal oxidation emphasize only two types of rate-determining oxidation mechanisms (4). In the first, the oxide thickness is small in comparison to the extent of possible space-charge regions within the oxide, and the growth kinetics are strongly influenced by the voltage drop across the oxide film caused by contact-potential differences. In the second, the diffusion rate of either the oxidizing species or the metal across the oxide determines the oxidation kinetics; the growth is then purely parabolic. The space-charge effect involves electrons readily available in the metal. These electrons penetrate the oxide either by tunneling or by thermionic emission into its conduction band and then fill the surface states provided by the adsorbed gas molecules at the oxide-gas interface. A steady-state condition is then established in which the net electronic current is close to zero, thereby equalizing the surface-state level and the Fermi level of the metal. This process results in a constant contact-potential difference between the two interfaces and an internal electric field. This field is assumed to be strong enough to alter significantly the activation barrier for the diffusion of ions or other charged defects. As a result, field-dependent transport of ionic defects constitutes the rate-limiting step. The model of Cabrera and Mott (4) yielded an inverse-logarithmic growth law.

The rapid initial oxidation regime in dry oxygen and its absence in wet oxygen or steam have been interpreted by Deal and Grove (3) to be a result of space-charge effects. In their interpretation, the oxidizing species is ionic, and oxidation is enhanced until the oxide thickness becomes larger than the extent of the space-charge region within the oxide. This thickness is on the order of the extrinsic Debye length in the oxide

$$L_{D_{ox}} = \sqrt{\left(\frac{kT}{q}\right)\frac{k_{ox}\epsilon_0}{2qC^*}} \quad [3]$$

In dry oxygen, $C^* = 5 \times 10^{16}$ cm^{-3}, $k_{ox} = 3.9$ and, therefore, at 1000°C, $L_{D_{ox}} \cong 150$Å, which corresponds well with the oxide thickness beyond which the rapid initial-growth mechanism stops being effective. In contrast, for wet O_2 at 1000°C, using $C^* = 3 \times 10^{19}$ cm^{-3}, $L_{D_{ox}} \cong 5$Å. Based on the linear pressure dependence of the parabolic rate constant B, Deal and Grove (3) concluded than no dissociation occurs at the oxide-gas interface, which implies that the diffusing species are undissociated molecules of oxygen or water for dry and wet O_2 oxidation, respectively. Coupled with the findings of Jorgensen (5), where an electric field was observed to affect the oxidation of silicon, they suggested that the diffusing species in dry oxygen is a singly ionized oxygen molecule O_2^-. The field created by the space charge of the negatively charged oxygen ions should be directed toward the gas-oxide interface, as illustrated in Fig. 1a.

The transport of the oxidizing species could also be enhanced by a slightly different mechanism (6), illustated in Fig. 1b. Here, it is assumed that as a molecule of oxygen from the gas is adsorbed at the outer surface, and, after entry into the oxide, it dissociates into a negatively charged oxygen molecule O_2^- and a hole. Holes, diffusing more rapidly than O_2^-, move toward the Si-SiO_2 interface and drag the slower oxygen ions with them by the built-in electric field that results from the coupled motion of two

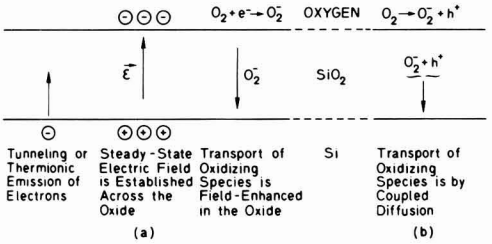


Fig. 1. Enhanced transport of ionized oxidizing species during the initial stages of oxidation in dry oxygen by field enhanced diffusion (a) and by coupled diffusion (b).

charged species with different mobilities. This field aids the motion of the slower species.

Hamasaki (7) proposed that negatively charged oxidant species are prevented from reaching the Si-SiO_2 interface by the oxide field near the interface caused by the positive oxide fixed charge Q_f generated by the oxidation reaction. In this description, electrons reached the outer surface of the oxide by thermionic emission. The initial rapid growth is explained by oxides growing at a fast rate before a sufficient amount of Q_f has been generated by the oxidation reaction. Once formed, the oxide fixed charge establishes an electric field that opposes the transport of negatively charged oxidizing species toward the interface. This description implies that the linear rate constant B/A is a measure of the surface reaction when the oxidizing species are under the influence of the Q_f-induced retarding field. For the same description of the oxidation process, Lu and Cheng (8) further assumed a mathematical form for the distribution of the oxide fixed charge and derived the oxidation rate constants corresponding to the thin (<300Å) and thick regimes

In analyzing the less-than-linear pressure dependence of the linear rate constant B/A, Hu (9, 10) proposed an intermediate oxygen-chemisorption step where chemisorbed molecular oxygen may directly oxidize silicon at a slow rate or dissociate slowly into atomic oxygen which then rapidly oxidizes silicon. The chemisorption isotherm suggested to fit the pressure dependence was the Freundlich isotherm. The extra growth rate in thin regime was proposed to be the result of a possible parallel flux of negatively ionized atomic oxygen (O^-) becoming more important for small thicknesses. Because of its smaller size, O^- ions are expected to diffuse substantially faster than oxygen molecules. The free energy of O^- at 1200 K is 1.1 eV (9). The diffusion of ionized atomic oxygen is argued to be possible only if there is substantial electronic conduction by tunneling through the oxide (9). As a result, this mechanism would stop for oxide thicknesses larger than ~150Å.

The above-mentioned models based on space-charge effects predict an inverse-logarithmic relationship between oxide thickness and oxidation time. The qualitative predictions of such a growth law were successful in explaining the absence of enhancement in wet oxygen in comparison to dry O_2 (3). It should be noted, however, that these models are subject to the following considerations.

1. Space-charge effects rely on the presence of ionized oxygen species in the oxide during growth and are based on Jorgensen's observations of the influence of an electric field on the oxidation rate (5). These observations are, however, the subject of much debate. In a recent investigation of the effect of electric fields and oxygen ion beams on silicon oxidation between 25° and 950°C, Modlin (11) reported results opposite of those of Jorgensen (5). When the surface of the oxide was made positive relative to the silicon substrate, the oxidation rate was enhanced, while for negative potentials it was slightly reduced. In reviewing Jorgensen's experimental setup and results, Modlin (11) concluded that the platinum electrodes used in the earlier experiments may have affected the oxidation process dramatically. Modlin's results indicated that, for diffusion-limited thermal silicon oxidation, the diffusing species is neutral molecular oxygen (11).

2. Goodman and Breece (12) noted that, because the solubility C^* of oxygen in the oxide is weakly dependent on temperature, the Debye length $L_{D_{ox}}$ in SiO_2 would be proportional to the square root of the temperature. If this dependence of $L_{D_{ox}}$ holds down to lower temperatures, it is expected to be 125Å at 600°C; however, at that temperature, the growth rate was observed to become approximately linear with time for oxide thicknesses greater than ~25Å (12). Similar behavior was observed for oxidations in water vapor at 600°C (12). The thickness extent of the initial enhanced regime was found to be nearly independent of temperature in this study (1). These experimental observations (1, 12) are in disagreement with the predicted temperature dependence of the extent of the initial regime as expressed by the Debye length in Eq. [3].

3. Further examination of Eq. [3] shows that $L_{D_{ox}}$ is inversely proportional to the square root of C^*. Consequently, for oxidations at lower partial pressures of oxygen (lower values of C^*), the Debye length should increase as would the extent of the fast initial regime. Results obtained in this study at 0.10 and 0.01 atm (1) indicate that the extent of the fast initial regime has a weak dependence on oxygen pressure and tends to decrease slightly at lower partial pressures. van der Meulen's study of the kinetics in the linear regime also showed that, for (111)-oriented silicon oxidized in 10 and 1% oxygen in nitrogen at 850°C, growth is approximately linear beyond 40 and 25Å, respectively (13). As a result, the experimentally observed extent of the fast initial regime has a trend opposite of that predicted from the dependence of $L_{D_{ox}}$ on C^*.

4. In the above descriptions, the oxidation rate is enhanced because of the effect of the electric field (due to electrons or due to Q_f) on the transport of the ionized oxidizing species toward the Si-SiO_2 interface. Because the oxidation process is, in principle, surface-reaction rate limited in the thin film regime, any process that would result in enhancing the transport of oxidant species through the oxide should have no effect on the growth rate. This is dependent on assuming steady-state conditions for the growth process as defined in the linear-parabolic model (3). Additional transport mechanisms that result in increasing the concentration of oxidizing species in the oxide above the solubility limit would enhance the oxidation rate in the thin film regime. Such a mechanism will be discussed when examining oxygen solubility considerations in the oxide.

It should also be noted that although oxygen ions are attracted to the Si-SiO_2 interface in the Deal-Grove (3) and Hu descriptions (9, 10), they are repelled from it in the Hamasaki model (7). Both claim, however, to have the same effect on the oxidation rate. Further examination of the complete expression of the oxide growth in (7) indicates that, for the same flux of incoming oxidizing species, the net growth rate is reduced in the thin regime as compared with the thick regime as a result of the presence of the electric field. This is intuitively clear because such field would repel the ionized oxidizing species away from the Si-SiO_2 interface.

Based on the previous discussion of the temperature and oxygen partial-pressure dependence of the thickness extent of the fast initial regime, it is concluded, at this time, that space-charge effects are not responsible for oxidation-rate enhancement in the initial oxidation regime in dry oxygen.

Oxide structural effects.—A number of proposals have been made to relate the fast oxidation rate in the thin regime to the oxide structure. Revesz and Evans (14) proposed that SiO_2 films are noncrystalline and may contain structural microheterogeneities, especially microchannels, along which diffusing species may transport preferentially. This is illustrated schematically in Fig. 2. It has been demonstrated (15) that the room temperature gaseous permeability of thermally grown SiO_2 layers can

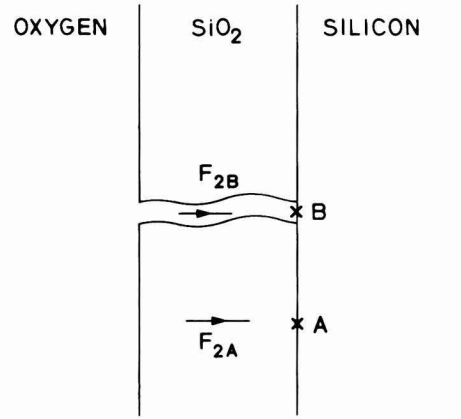


Fig. 2. Micropores in thin oxides affecting the transport oxygen species to the interface.

be considerably higher than in fused silica, and this increase was attributed to microchannels whose diameters are less than 50Å.

The formation of channels has been proposed to be closely related to the mechanism of oxide growth in that both the parabolic rate constant and the extent of the fast initial regime are higher in the (111) than in the (100) orientation of silicon, provided that the H_2O content in the oxidizing ambient is very low (16). This quasi-anisotropic behavior of the SiO_2 film occurs when the channels are aligned perpendicularly to the silicon surface. In dry oxygen, the density of defects, at which interaction between O_2 molecules and SiO_2 occurs, is limited to $\sim 10^{16}$ cm^{-3}. In contrast, the density of SiOH groups resulting from the interaction between H_2O and SiO_2 is on the order of 10^{20} cm^{-3}. As a result, in the noninteractive transport of O_2 in SiO_2, channels may be retained, while the interaction between H_2O and SiO_2 acts against such structural ordering.

Direct experimental evidence of the existence of micropores was reported in a study of 90Å thermally grown SiO_2 layers, using high resolution bright-field transmission electron microscopy (17). Contrast phenomena observed in images of films grown in dry oxygen are consistent with the existence of 10Å pores, typically 100Å apart. Similar, films grown in wet oxygen do not display this contrast. The presence of voids or micropores of 5-8Å diam randomly distributed in dry SiO_2 films were also confirmed by Srivastava and Wagner (18). In a study of the initial regime (up to 200Å), Irene (19) attributed the more parabolic-like behavior of the data produced from H_2O containing ambients to a greater protectiveness of wet oxides. Dielectric breakdown measurements revealed that there are fewer defects in the H_2O-grown thin SiO_2 films, and transmission electron microscopy indicated that these films contain inhomogeneities smaller than 50Å. It was concluded, therefore, that the pore structure differs in dry and wet SiO_2 films, provides a short-circuit path to the Si-SiO_2 interface for oxidant species that do not attack the SiO_2 network (such as dry O_2), and is responsible for the variations in the oxidation data and dielectric breakdown.

In another study of the thermal oxidation of silicon up to 200Å in dry O_2 (20), growth followed a linear-parabolic behavior, but with linear and parabolic rate constants different from those characterizing the growth of thicker oxides (>300Å). Here, B/A was larger and B and X_i were smaller than their corresponding values for thick oxides. Based on these observations and the results of experiments where oxidation was interrupted by a heat-treatment and then reoxidized, Revesz (21) reported that the oxidation of silicon in dry O_2 in the thin regime does not occur under true steady-state conditions because B and B/A change during oxidation. The fast initial regime does not require any special explanation, therefore, because it is a manifestation of the nonsteady-state oxidation process. The structure of thermally grown SiO_2 films, including the Si-SiO_2 interface, is determined by a combination of ordering and disordering effects. Increased ordering enhances the diffusivity of O_2 molecules along structural channels. The presence of H_2O in the oxidizing ambient has a great disordering effect on the structure of SiO_2 because it interacts with SiO_2 more strongly than does O_2 whose behavior is similar to that of inert gases. Revesz concluded that this is the reason no initial fast regime is observed for oxidations in H_2O.

In the above discussion and as illustrated in Fig. 2, growth-rate enhancement occurs as a result of localized points (such as point B) where microchannels or structural defects meet the Si-SiO_2 interface. This is a result of the concentration of oxygen species in contact with silicon at point B being higher than at other interface areas (such as point A) covered with SiO_2. The oxidation rate at these points is enhanced as a result of a localized higher concentration of oxygen in direct contact with silicon rather than a faster transport of oxygen through the oxide which would not affect the oxidation reaction because oxide growth in the linear regime is rate limited by the surface reaction. The lateral transport of high concentrations of oxidant species at the Si-SiO_2 interface, as a result of micropores in the oxide, may be responsible for localized oxidation-rate enhancement around micropores and microchannels in the thin regime.

Stress in silicon dioxide.—Stress measurements in silicon dioxide have been made at room temperature (22, 23) and at growth temperatures (24). Stress in the oxide measured at room temperature is a result of the mismatch between the thermal expansion coefficients of Si and SiO_2, and it develops as the oxidized wafer cools down from the oxidation temperature to room temperature. The oxide was found in a state of compressive stress. Intrinsic stresses resulting from the mismatch in the molar volume of Si and SiO_2 exist at oxide-growth temperatures. For oxides grown in wet O_2 (23), the intrinsic stress was found to depend on temperature. At 950°C and below, a compressive stress on the order of 7×10^9 dyn/cm^2 is generated in the oxide. At 975° and 1000°C, the oxide grows in a stress-free state, with possible small tensile stresses above 1000°C. When present, these intrinsic stresses are large enough to cause plastic deformation of the silicon substrate at growth temperatures. The temperature dependence is explained by viscous flow occurring in both steam- and dry oxygen-grown layers at ~960°C (24). Stress in SiO_2 has been linked to phenomena such as dislocation generation at borders of windows etched in oxide layers, bowing and slip processes of wafers, and impurity segregation and precipitation. The temperature dependence of the linear and parabolic rate constants above and below the viscous flow temperature was discussed elsewhere (2). These results suggested that stress in the oxide affects the transport of oxygen through the oxide and its reaction with silicon at the Si-SiO_2 interface. A new formalism that explains the low and high temperature dependence of the linear rate constant on the intrinsic stress was proposed by Irene (26). Intrinsic stress effects on the surface-reaction rate constant are a possible source of oxidation-rate enhancement in the thin film regime. The appearance of high density thermal oxides grown at low temperatures was also explained in terms of a viscous flow model (27, 28).

In a study of silicon oxidation in dry oxygen in the thin film regime, Fargeix and co-workers (29) suggested that the diffusivity of the oxidizing species is not constant across the oxide layer as a result of the influence of stress in the growing film. They proposed that diffusion through the first hundreds of angstroms of the oxide layer is slowed down due to compressive stresses in the SiO_2 film. The increase in the diffusivity far from the oxidizing interface is presumably related to the relaxation of the stresses. These stresses were assumed to be maximum at the Si-SiO_2 interface and to decrease monotonic-

ally with a characteristic distance (a relaxation length) from the interface and toward the free surface of the oxide. It was found that this relaxation length (which would replace the characteristic length L_2 in this work) is a strong function of temperature, increasing from ~50Å at 980°C to larger than 650Å at 780°C for (100) silicon. This is in contradiction with the experimental results of this study that showed that L_2 is temperature independent. This stress model is also in contradiction with the views of Tiller (30-32) that unless the interface relaxes to become partially incoherent, large amounts of strain energy are stored in the oxide, which results in greatly retarding the oxidation process.

Here again, as in the evaluation of models where the transport of ionized oxidizing species is affected by electric fields, stresses in the oxide, whether they increase or decrease the transport of oxidizing species in the oxide, should have no effect on the oxidation process in a regime where growth is surface-reaction rate limited. It is possible, however, that stress might affect the surface-reaction rate constant, as proposed by Irene (26) for thicker oxides and/or the solubility of the oxidizing species in the oxide.

Oxygen solubility in the oxide.—According to Henry's law, the equilibrium concentration C^* of the oxidant in the oxide is related to the partial pressure p_g of oxidant species in the gas ($C^* = Hp_g$). This relationship holds only in the absence of dissociation or recombination of the oxidant species at the oxide-gas interface and when their chemical potential in the oxide is independent of pressure (dilute case). Increased solubility of O_2 in SiO_2 for very thin layers may be important in describing the fast initial dry oxidation of silicon (33) because it would reflect an increase in the constant of proportionality in Henry's law when the oxide thickness is less than the mean spacing of oxygen solute molecules dissolved in the oxide. For $C^* = 5 \times 10^{16}$ cm^{-3} and 3×10^{19} cm^{-3} in dry and wet O_2 (3), the average spacings are 270 and 32Å, respectively. For thinner dry or wet oxide films, the description of solubility in terms of an equilibrium bulk quantity becomes questionable because of spatial distribution of the solute molecules is nearly two dimensional.

Details of the equilibrium described by Henry's law involve the balance of the fluxes of solute molecules in and out of the gas-solid interface for a given external gas pressure, as illustrated in Fig. 3. It is generally assumed that the solid is semi-infinite and that no reactions inside the solid affect the details of this equilibrium. These assumptions are not valid for oxidation in dry oxygen for thicknesses smaller than the average spacing between the solute molecules, where the flux of oxygen consumed at the nearby oxidizing interface affects the balance of inward and outward fluxes that establishes the equilibrium conditions at the gas-oxide interface.

To obtain a more realistic description of oxides thinner than the average spacing between oxidant molecules, a two dimensional structure, wherein solute molecules are packed, was suggested by Derbenwick and Anderson (33). It is not clear whether the solubility in such films is equal to the bulk equilibrium solubility in thicker films. The oxidation rate is directly proportional to the concentration of oxidizing species at the Si-SiO_2 interface; a higher solubility in dry SiO_2 films thinner than 270Å implies a proportionally faster oxidation rate. A simple model to test this solubility concept was proposed (33) based on the assumption that the effective solubility of oxygen into the oxide decreases exponentially in thin oxides. The oxidation-rate expression based on this assumption was similar to that obtained in part I of this paper (1) and resulted into a growth law of the form (33)

$$X_{ox}(t_{ox}) - X_{ox}(0) - L_o \ln \frac{[C^* + C_o e^{-X_{ox}(0)/L_o}]}{[C^* + C_o e^{-X_{ox}(t_{ox})/L_o}]} = \left(\frac{B}{A}\right) t_{ox} \quad [4]$$

where $X_{ox}(0)$ is the native-oxide thickness at the start of oxidation ($t_{ox} = 0$), C^* the equilibrium bulk solubility, ($C^* + C_o$) the equilibrium concentration at the surface, and L_o a characteristic length related to the equilibrium spacing of the solute molecules. The agreement between this expression and experimental data was good at atmospheric pressure but poor at reduced oxygen pressures (33).

The dependence of the excess rate in the thin film regime on oxygen partial pressure is expected to be the same as that of the linear rate constant because of the concentration of the oxidizing species is expected to affect both by the same amount. Furthermore, for the oxidation of heavily doped substrates, the amount of enhancement in the linear rate constant and in the excess rate should be the same because oxygen in the oxide in excess of the solid-solubility concentration would be common to both the linear-parabolic oxidation process present on lightly doped substrates and the reaction present on heavily doped substrates. This expected behavior in the data analysis of heavily doped substrates was not observed experimentally, as the excess rate in the thin regime was found to be approximately independent of the doping level (1). Until an independent measurement of oxygen solubility in thin oxides unquestionably demonstrates that it is enhanced over its values for thick oxides, such a mechanism is unlikely to be responsible for oxidation-rate enhancement in the thin regime.

In conclusion, all models proposed to interpret oxidation-rate enhancement in the thin regime in dry oxygen, whether based on space-charge effects, oxide structure, oxide stress, or enhanced oxygen solubility in thin oxides, have limited success in accounting for growth-rate enhancement observed experimentally in this study, or have no physical, theoretical, or experimental justification. An understanding of silicon oxidation in dry oxygen based on the above results and discussions is now introduced.

Mechanism of Silicon Oxidation in the Thin Regime

In searching for the physical mechanisms responsible for the oxidation-rate enhancement in the thin regime for

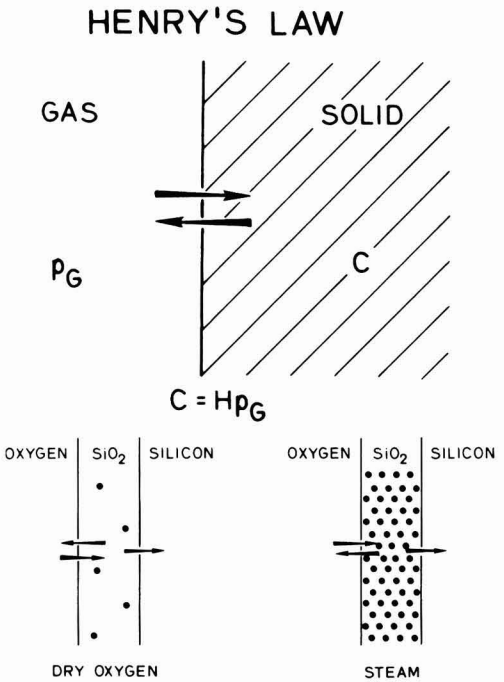


Fig. 3. Henry's law and the equilibrium solid-solubility concentration of oxygen species in the oxide reached through the balance of ingoing and outgoing fluxes at the solid-gas interface, as applied to oxides grown in dry oxygen and in steam.

a surface-reaction rate-limited process, one must investigate the possible ways by which the two components of the surface reaction, namely, the concentration of oxygen species and the contribution of the silicon substrate, can be influenced. In other words, one should investigate the mechanisms that would affect the flux of oxidant species F_3 consumed in the surface reaction at the Si-SiO_2 interface. This flux is expressed as $F_3 = k_S C_i$, where k_S is the surface-reaction rate constant (which represents the contribution of the substrate) and C_i in concentration of oxidizing species at that interface. According to the Deal-Grove model (3), the oxidation is surface-reaction rate limited for thin oxides, and the concentration of oxidizing species is uniformly distributed in the oxide and is at the solid-solubility limit.

The thickness extent of the rate enhancement (as given by L_2) does not depend on substrate orientation, doping density, or oxygen partial pressure. These observations suggest that the oxide might be responsible for the rate-enhancement mechanism, assuming that the films do not retain any relationship to the underlying substrate. This is not, however, in agreement with the observed dependence of the parabolic rate constant at low temperatures on substrate orientation (25), which suggests that oxidant diffusivity and/or solubility depend on the substrate orientation. In other words, oxides under stress were observed to carry a signature of the orientation of the underlying substrate. In addition, the orientation dependence of the enhancement term, as reflected in the pre-exponential constant C_2, indicates that the substrate participates in the reaction during the initial stages. Therefore, it is inconclusive from the results of oxidation of lightly doped substrates as to whether the enhancement mechanism is in the oxide (a process that might affect the concentration of oxygen in SiO_2) or in the substrate (a process by which additional sites at the silicon surface are available for oxidation).

The analysis of the rate enhancement in the thin regime at lower partial pressures of oxygen showed that the pressure dependence of the excess rate is, in a first-order analysis, the same as that of the linear rate constant ($\sim p^{0.8}$). This indicates that, when the oxygen supply to the surface reaction was varied by changing the oxygen partial pressure in the oxidizing ambient, both the linear surface reaction (described in the linear-parabolic model) and the thin film regime surface reaction (responsible for the excess growth rate in thin regime) are affected in the same manner. This result reinforces the fact that oxidation in this thin regime is surface-reaction rate limited, and that the rate enhancement in the thin regime would not be affected by any mechanism that would influence the transport of oxidizing species through the oxide, but by some mechanism that affects the concentration of O_2 at the Si-SiO_2 interface and/or the way in which the silicon substrate contributes to the oxidation reaction. As discussed earlier, oxygen concentrations in the oxide in excess of the solid solubility limit cannot explain the oxidation-rate enhancement of heavily doped wafers and is, therefore, an unlikely mechanism of excess oxidation in the thin film regime. It can be concluded, therefore, that the growth-rate enhancement in the early stages of oxidation is likely a result of an additional surface reaction contributed by the silicon substrate. From these results, however, no conclusion can be made on the nature of this substrate contribution, except that its extent in the substrate is independent of orientation, doping, and oxygen partial pressure.

In heavily phosphorus-doped wafers, it has been observed that the linear rate constant B/A is greatly enhanced by high doping levels in the substrate (34, 35). This observation has been attributed to increased concentrations of silicon vacancies resulting from doping induced shifts in the Fermi level at oxidation temperatures and to the availability of such vacancies at the surface to act as additional sites for thermal oxidation (34, 35). In this study (1), it has been observed that oxidation-rate enhancement in the thin regime is only moderately affected by heavy doping in the substrate. Vacancies may not be responsible for the excess rate because the increase in the linear rate constant with doping is much greater than that in the excess oxidation rate in the thin regime. From this observation, it can be concluded that the thin regime surface reaction is occurring at the Si-SiO_2 interface independently of the surface reaction in heavily doped silicon.

From the above discussion, the understanding of the oxidation process can be summarized as illustrated in Fig. 4. In lightly doped substrates, the reaction at the Si-SiO_2 interface consists of the linear-parabolic reaction [1] and a parallel reaction [2] occurring only in the thin regime. The parallel reaction [2] represents the excess rate term that decays exponentially with thickness. In heavily doped substrates, an additional reaction [3], possibly vacancy related, takes place in parallel with reaction [1] in the thick regime. Reactions [1] and [3] are combined at all thicknesses into a linear-parabolic term where rate constants would reflect their doping dependence. In the thin regime of the oxidation of heavily doped samples, all reactions occur in parallel and the total oxidation rate is the sum of these three fluxes. In this case, the total oxidation rate is the sum of the doping dependent linear-parabolic term and the excess rate term that decays exponentially with thickness. The experimental observations in part I (1) indicate that reactions [2] and [3] are independent.

A number of mechanisms occurring in the substrate could result in increasing the concentration of oxidation sites at the interface. By virtue of its being the surface of an unoxidized silicon substrate, it is expected that some departure from perfect crystallinity would be encountered near the surface. This departure from bulk conditions could be in the form of damage, disorder, bond breaking, bond stretching, surface reconstruction, or vacancies (resulting from band bending caused by surface states pinning down the Fermi level at the surface). This departure from bulk conditions is an inherent property and would exist on any oxide-free surface. Oxidation occurring in a surface zone rather than an oxidizing interface is another possibility. An understanding of the oxidation of silicon based on the availability of additional oxidation sites in a surface layer, the possibility of the oxidation occurring in a surface zone, and the possible interaction of oxygen diffused into the substrate with the surface layer is developed here.

A surface layer in the silicon substrate containing additional sites for oxidation is responsible for the oxidation-rate enhancement in the thin film regime. The concentration of these sites has a profile which decays exponentially with a characteristic length of ~30Å. This decay

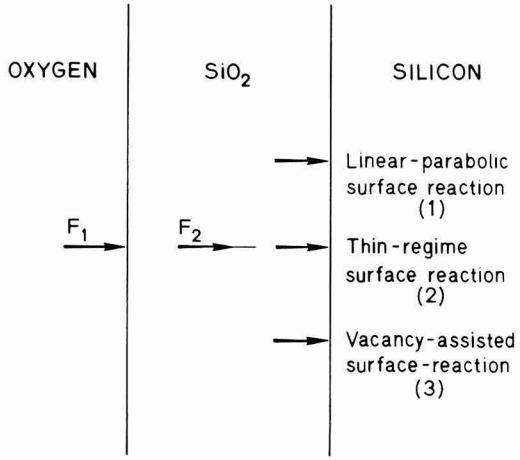


Fig. 4. Components of the interface reaction in the thin regime oxidation of silicon in dry oxygen.

length in silicon corresponds to the average value of ~70Å observed for the characteristic length L_2 in the data analysis as a function of oxide thickness. The nature of the excess oxidation sites in the surface layer is not yet identified; however, if this layer represents the departure from perfect crystallinity expected at any surface, oxidation could be enhanced because Si-Si bonds have changed angles and/or bond energies or are broken in this layer. The orientation dependence of the rate enhancement reflects the influence of substrate orientation on the manner in which departure from perfect crystallinity occurs. This could also explain why the activation energy of the excess rate is orientation dependent. The dependence of the excess rate on oxygen partial pressure is the result of the limited supply of oxygen species at lower partial pressures. The thickness extent of the rate enhancement is the same at lower oxygen partial pressures because the surface layer is a property of the substrate and does not depend on the ambient. The pressure dependence of the excess rate term at lower oxygen partial pressures indicates that the oxygen supply to the linear surface reaction is affected in the same fashion as that to the excess reaction occurring at the additional sites present in the surface layer. The surface layer is only slightly affected by high concentrations of phosphorus in the silicon, and the resulting abundance of silicon vacancies caused by Fermi-level effects in the substrate adds an independent parallel reaction path to the growth rate in the thin regime. The constancy of the thickness extent of rate enhancement is another indication of the additional oxidation sites being a property of the surface layer. The departure from perfect crystallinity at surfaces is intuitive and is not supported by experimental microscopy studies. It should be remembered, however, that this disorder appears in the first few monolayers on the surface, and the experimental techniques used in such a study should have an appropriately high resolution.

In a thermodynamic analysis of thermal oxidation, Tiller (30-32) developed a two-layer model of the oxide in which the thermodynamic driving force partitions itself differently than in a single-layer film. The hypothesis of an interfacial transitional layer enables the incorporation of a broader range of phenomena known to be associated with thermal oxidation into the kinetic model and could be potentially applied to express oxidation as occurring in a zone rather than on an abrupt surface. For this purpose, one might consider the possible influence of oxygen diffused into the silicon substrate at the onset of oxidation of an oxide-free silicon wafer in dry oxygen. In the brief nonsteady-state period at the start of oxidation when the silicon surface comes in contact with a high concentration of oxygen, it is possible for oxygen to diffuse into the silicon substrate. Because the diffusion of oxygen in silicon is accomplished by a one-jump process of interstitial oxygen from one Si-Si bond to an adjacent one (36), it is possible that oxygen which diffused in the substrate would affect the Si-Si bond breaking energy or angle distribution in the first few monolayers of the silicon surface or would have partially oxidized silicon atoms below the surface. Estimates of the time required for oxygen to diffuse to a profile with a diffusion length of ~30Å range from 5 ms at 1000°C to 0.35s at 800°C (36). The lack of orientation dependence of the excess rate in the thin regime is, however, not in disagreement with the orientation-independent diffusion of oxygen in silicon. The orientation dependence of the excess rate in the thin regime can be thought of as reflecting the distribution of Si-Si bond breaking, weakening, or bending processes that might be attributed to the presence of oxygen in the silicon surface layer. This may also explain the difference in the activation energy of the excess term with oxygen partial pressure. The dependence of the excess rate on oxygen pressure is a direct result of the reduction of oxygen diffusing into the silicon substrate at lower pressures. Oxygen diffusion is expected to be only slightly affected by the doping density in the substrate, which explains the weak effect of the substrate doping concentration on the enhancement in the excess rate. This approach can be modeled, in principle, from published data of the diffusion coefficient of oxygen in silicon (36).

Any understanding of growth-rate enhancement in the thin regime has to explain the lack of such a phenomenon when silicon wafers are oxidized in steam or wet oxygen (3). The disordered silicon surface layer is expected to be present on all surfaces irrespective of the oxidizing ambient and, consequently, a growth-rate enhancement should, in principle, be observed in wet oxidations. It is also possible, however, that as water molecules reach the $Si-SiO_2$ interface to yield H_2 molecules and atomic oxygen, the released hydrogen contributes at high temperatures to a reordering of the Si-Si broken-bond or bond-angle distributions in the surface layer resulting in a reduction or total elimination of the additional oxidation sites. It should also be remembered that atomic oxygen resulting from the decomposition of water at the interface is readily consumed in the surface reaction.

Experimental difficulties are expected when attempting to support any physical process proposed to explain oxidation-rate enhancement in the thin regime because the thickness of interest extends for only a few monolayers of silicon. Progress in advancing the limits of detectability, resolution, and accuracy of high resolution experimental techniques will help identify the underlying physical mechanisms in the fast growth rate of SiO_2 during the early stages of oxidation in dry oxygen.

Conclusions

Physical processes (such as space-charge effects, oxide structure, oxide stress, and oxygen solubility in SiO_2) proposed to account for oxidation-rate enhancement in the thin regime were critically analyzed. An understanding of this phenomenon based on the presence of a surface layer, where a distribution of additional sites of oxidation is found, was proposed and is in agreement with all experimental results. This surface layer represents a property of the surface and can be the result of the departure from bulk properties near the surface. The possible interaction with oxygen diffused into the silicon wafer is also in agreement with this understanding. Further investigations of thermal oxidation will help delineate the features of the silicon surface prior to oxidation and will be valuable in defining the nature of the additional oxidation sites.

Acknowledgments

The authors would like to acknowledge many helpful discussions with Dr. B. E. Deal, Dr. C. P. Ho, Dr. C. R. Helms, Dr. W. A. Tiller, and Dr. D. Modlin. This study was sponsored by Darpa Contract No. MDA 903-79-C-0257.

Manuscript submitted April 15, 1985; revised manuscript received July 11, 1985.

Stanford University assisted in meeting the publication costs of this article.

REFERENCES

1. H. Z. Massoud, J. D. Plummer, and E. A. Irene, *This Journal*, **132,** 2685 (1985).
2. H. Z. Massoud, J. D. Plummer, and E. A. Irene, *ibid.*, **132,** 1745 (1985).
3. B. E. Deal and A. S. Grove, *J. Appl. Phys.*, **36,** 3770 (1965).
4. N. Cabrera and N. F. Mott, *Rep. Prog. Phys.*, **12,** 163 (1948).
5. P. J. Jorgensen, *J. Chem. Phys.*, **37,** 874 (1962).
6. A. S. Grove, "Physics and Technology of Semiconductor Devices," Chap. 2, John Wiley and Sons, New York (1967).
7. M. Hamasaki, *Solid-State Electron.*, **25,** 479 (1982).
8. Y. Z. Lu and Y. C. Cheng, *J. Appl. Phys.*, **56,** 1608 (1984).
9. S. M. Hu, *Appl. Phys. Lett.*, **42,** 872 (1983).
10. S. M. Hu, *J. Appl. Phys.*, **55,** 4095 (1984).
11. D. N. Modlin, Ph.D. Thesis, Stanford University, Stanford, CA (1983).
12. A. M. Goodman and J. M. Breece, *This Journal*, **117,** 982 (1970).

13. Y. J. van der Meulen, *ibid.*, **119,** 530 (1972).
14. A. G. Revesz and R. J. Evans, *J. Phys. Chem. Solids*, **30,** 551 (1969).
15. S. W. Ing, R. E. Morrison, and J. E. Sandor, *This Journal*, **109,** 221 (1962).
16. A. G. Revesz, Abstract 350, p. 897, The Electrochemical Society Extended Abstracts, Vol. 80-2, Hollywood, FL, Oct. 5-10, 1980.
17. J. M. Gibson and D. W. Dong, *This Journal*, **127,** 2722 (1980).
18. J. K. Srivastava and J. B. Wagner, Jr., 463 RNP, *ibid.*, **131,** 196C (1984).
19. E. A. Irene, *ibid.*, **125,** 1708 (1978).
20. M. A. Hopper, R. A. Clarke, and L. Young, *ibid.*, **122,** 1216 (1975).
21. A. G. Revesz, Abstract 281, p. 701, The Electrochemical Society Extended Abstracts, Vol. 81-1, Minneapolis, MN, May 10-15, 1981.
22. R. J. Jaccodine and W. A. Schlegel, *J. Appl. Phys.*, **37,** 2429 (1966).
23. P. G. Borden, *Appl. Phys. Lett.*, **36,** 829 (1980).
24. E. P. EerNisse, *ibid.*, **35,** 8 (1979).
25. E. P. EerNisse, *ibid.*, **30,** 290 (1977).
26. E. A. Irene, *J. Appl. Phys.*, **54,** 5416 (1983).
27. H. Z. Massoud, C. P. Ho, J. D. Plummer, E. A. Irene, and E. Tierney, 1982 IEEE 13th Semiconductor Interface Specialists Conference, Dec. 9-11, 1982, San Diego, CA (Unpublished).
28. E. A. Irene, E. Tierney, and J. Angilello, *This Journal*, **129,** 2594 (1982).
29. A. Fargeix, G. Ghibaudo, and G. Kamarinos, *J. Appl. Phys.*, **54,** 2878 (1983).
30. W. A. Tiller, *This Journal*, **127,** 619 (1980).
31. W. A. Tiller, *ibid.*, **127,** 625 (1983).
32. W. A. Tiller, *ibid.*, **127,** 689 (1981).
33. G. F. Derbenwick and R. E. Anderson, Private communication.
34. C. P. Ho and J. D. Plummer, *This Journal*, **126,** 1516 (1979).
35. C. P. Ho and J. D. Plummer, *ibid.*, **126,** 1523 (1979).
36. G. D. Watkins, J. W. Corbett, and R. S. McDonald, *J. Appl. Phys.*, **53,** 7097 (1982).

Polyimide Adhesion

Mechanical and Surface Analytical Characterization

Rajesh G. Narechania, James A. Bruce,* and Sherrill A. Fridmann

International Business Machines Corporation, Essex Junction, Vermont 05452

ABSTRACT

The effects of surface treatments and cure temperature on polyimide to silicon nitride adhesion strength are discussed. Results show the importance of surface cleanliness and the requirement for an adhesion promoter. X-ray photoelectron spectroscopy (XPS) was used to study the mode of failure at different cure temperatures. As the cure temperature is increased, the mode of failure goes from primarily cohesive to a mixed adhesive/cohesive failure, as inferred from the XPS data.

Polyimide is currently being used as an interlevel insulator in semiconductor device manufacturing (1). Poor adhesion of polyimide at an interface will enhance moisture penetration and as a result will promote a loss in its passivation function. To improve polyimide adhesion, a thorough understanding of the chemistry involved is needed. In addition, it is important to know the mode of failure during adhesion testing.

If the failure is adhesive (polyimide separating from an adhesion promoter or adhesion promoter from nitride), then the adhesion can be enhanced by improving the bonding or thermal stability of the interface (*e.g.*, by means of variations in surface treatments, cure temperatures, or adhesion promoters). However, if the failure is cohesive (separation occurring in the polyimide film itself), then changes in the interface would be ineffective in enhancing the adhesion. Rather, the internal mechanical strength of polyimide would have to be improved by making structural changes, such as molecular weight and degree of cross-linking.

The nature of the underlying surface plays a significant role in the adhesion characteristics of polyimide to that surface. Good adhesion of polyimide to an underlying surface (*e.g.*, an oxygen-rich silicon nitride) requires an adhesion promoter such as 3-aminopropyltriethoxysilane (APS). Work done by Linde shows that APS chemically bonds to both the polyimide and the surface (2). The silane portion of the APS bonds to the surface, while the amino portion reacts with the polyimide precursor, polyamic acid (Fig. 1). It may be noted that, since the APS bonds to the surface through surface hydroxyl groups, enrichment of these groups will favor the adhesion process.

A photoresist adhesion promoter, *e.g.*, hexamethyldisilazane (HMDS), is used to improve the wettability of a nitride surface to photoresist (Fig. 2). In semiconductor processing, photoresist can be applied and stripped several times before the application of polyimide. This can leave residual photoresist and/or HMDS on the surface before APS/polyimide is applied. This would prevent the reaction shown in Fig. 1 from occurring as completely as it would on a clean, oxygen-rich nitride surface. Therefore, chemical pretreatments (*e.g.*, plasma cleaning) are needed to assure complete removal of photoresist/HMDS and thereby enhance polyimide adhesion.

Another important factor affecting the bonding (and thus the adhesion) is the cure temperature of the polyimide. The adhesion promoter, APS, has been shown to be thermally unstable at temperatures in excess of 400°C (3). Saiki and Harada have shown a dependence of polyimide adhesion on its cure temperature using a different polyimide with an aminosilane adhesion promoter (4). They found that the temperature dependence of the

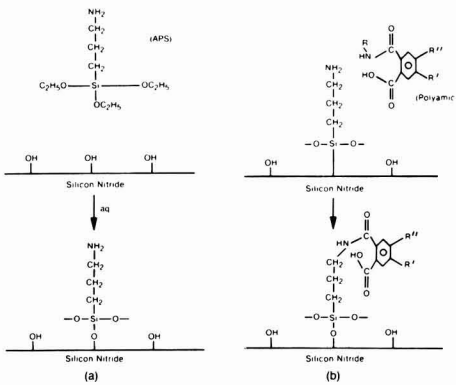


Fig. 1. The reaction of APS with a silicon nitride surface (a) and surface attached APS with polyamic acid (b).

* Electrochemical Society Active Member.

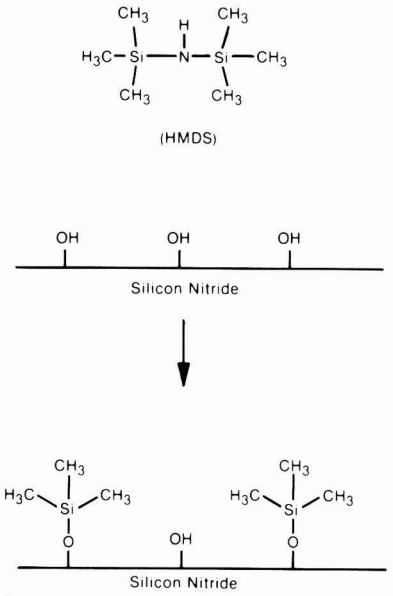


Fig. 2. The reaction of HMDS with a silicon nitride surface

adhesion was due to thermal decomposition of the aminosilane.

It has been shown that a stress of 85°C temperature and 80% humidity can degrade the adhesion of polyimide to a silicon nitride surface (5). Therefore, this test was used as a measure of long-term stability of adhesion to environment.

This paper shows the effects of surface treatment and cure temperatures on polyimide to silicon nitride adhesion strength and investigates the mode of failure during peel testing using x-ray photoelectron spectroscopy.

Methods and Materials

Silicon nitride-deposited wafers were divided into two groups (Fig. 3). In group A, the wafers were oxygen plasma cleaned after applying and removing photoresist and HMDS. This group was divided into two subgroups. In subgroup I, APS was used; in subgroup II, no adhesion promoter was used. The APS was diluted to 0.1% (v/v) with water before puddle-spin application. Polyamic acid was obtained from E. I. du Pont de Nemours and Company, as the amic acid solution of poly(N,N'-(p,p'-oxydiphenylene) pyromellitimide). The commercial equivalent is PI-2540. The polyamic acid was spun onto all the wafers. The wafers in subgroup I were cured in nitrogen at 325°, 350°, 375°, 400°, and 425°C. In group B, no resist was applied on the wafers. This group was divided into two subgroups: plasma clean and no plasma clean. All wafers were then treated with adhesion promoter, spun with polyamic acid, and cured at 400°C.

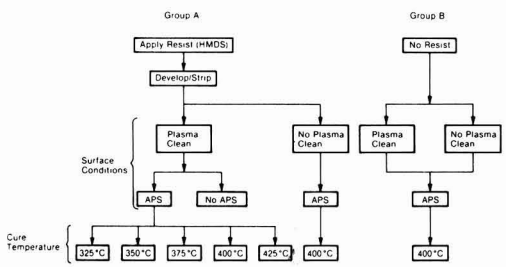


Fig. 3. A flow chart indicating the conditions used to prepare the wafers in group A and group B.

The polyimide-coated silicon nitride substrates were mounted on an X-Y sliding stage. The samples were evaluated by peeling films perpendicularly (Fig. 4) from the nitride surface on the Instron material testing system at a constant rate of 0.2 in./min. A load *vs.* elongation graph was plotted for each peeled sample, and adhesion peel strength in grams per millimeter was computed. The peel test was repeated on samples that were soaked in the temperature-humidity (T&H) chamber (85°C, 80% humidity) for 168h. Each split consisted of a minimum of ten samples, and the reproducibility was in the range of 5-10%.

X-ray photoelectron spectra were obtained using the Hewlett-Packard Model 5950B spectrophotometer. All data were obtained by scanning in the survey mode over the binding energy range of 0-1250 eV. The resolution in the survey scans was ±1 eV. These spectra proved to be adequate for quantifying the elements present on the surface and for distinguishing between two different chemical bonding environments for the nitrogen. Spectra were obtained using an Al Kα x-ray source and a low energy electron flood gun (2 eV, 0.4 mA) to eliminate possible charging of the sample.

Peel Criteria

A definite criterion for defining and computing peel strength was established (Fig. 5a-5c). A complete peel is defined as one during which the polyimide film across the entire width completely debonds from the adhering surface. A partial peel is one during which the polyimide film does not completely debond across the width from the adhering surface, but only from a portion of the width. During a "no-peel" mode, polyimide does not peel at all from the surface, owing to film fracture. A peel strength measurement at no peel, defined as a "minimum peel strength," represents not the actual peel strength but only its lower limit. The minimum peel strength is not a measure of the film tensile strength because the test is performed in a peel test mode. Also, the largest observed no-peel force in this criterion is an estimate of the minimum peel strength provided no handling damage has occurred.

A polyimide film may not peel either because the film is too brittle to support the cleavage stress at the tip of the peel or because handling damage has occurred. The latter situation will be compounded if the film is brittle.

Historically, a no-peel condition is assumed to manifest excellent adhesion. However, this assumption is inaccurate simply because only the lower limit to the peel strength, and not the peel strength itself, is measured. Prior to a steady peeling from the cleavage site, a film must overcome the plastic deformation of the material (6). Therefore, in a no-peel situation, if the adhesion strength is much higher than the plastic strength of the material, then a high load to break the film is obtained. From this, a minimum peel strength can be computed by dividing

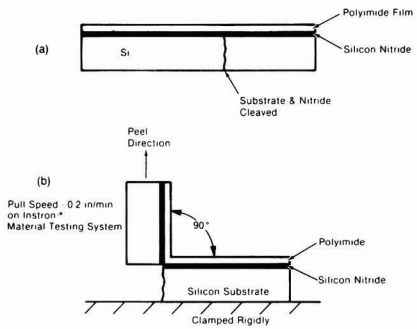


Fig. 4. A cross-sectional representation of a polyimide-coated silicon nitride wafer in which the silicon and the silicon nitride have been cleaved in preparation for the peel test (a) and a sample as it is mounted for the 90° peel test (b).

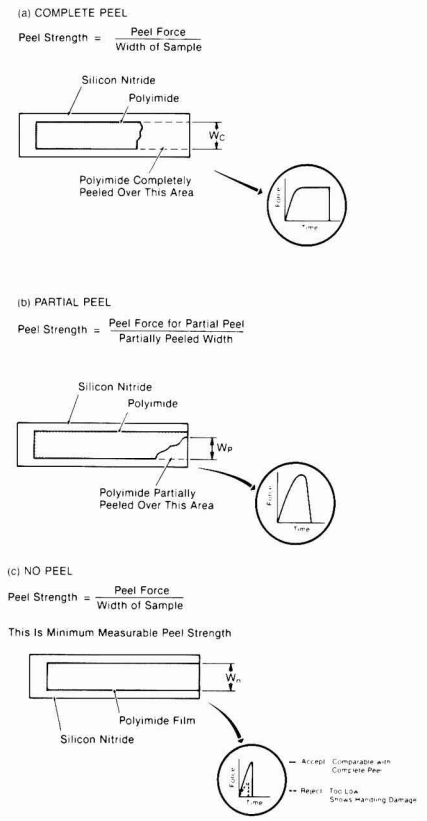


Fig. 5. A representational top view of the polyimide-coated silicon nitride surface after a complete peel (a), a partial peel (b), and no peel (c). A plot of peel force vs. time is shown in the inset for each case.

the load at no peel by the film width. A brittle film will produce a significant load at no peel with high reproducibility if no handling damage is done.

If the minimum peel strength measured in a no-peel situation is within a reasonable limit and comparable to that with complete or partially peeled samples, then the minimum peel strength should be acceptable. However, if the minimum peel strength is significantly lower than when a complete peel is obtained, then the sample tested must be rejected because of the handling damage.

Results

Adhesion strength in all experiments was computed in grams per millimeter according to our peel criteria. All samples were viewed under a microscope to determine the mode of peeling. The results are examined in the three categories below.

Effect of plasma ash conditions on adhesion.—The results in Fig. 6 show that plasma cleaning of HMDS-treated surfaces improved adhesion of polyimide to nitride by 92% for samples not subjected to T&H soak. T&H soaking of plasma-cleaned HMDS-treated samples caused minimal loss of adhesion, whereas those with no plasma clean lost 18% of their adhesive strength.

On the other hand, surfaces not treated with HMDS showed an approximately 40% lower adhesion compared to HMDS-treated samples, whether or not they were plasma cleaned. In addition, these nontreated samples showed adhesion losses of approximately 30% after T&H soak. It is thus evident that adhesion is markedly enhanced by the deposition and subsequent plasma oxidation of HMDS on the surface.

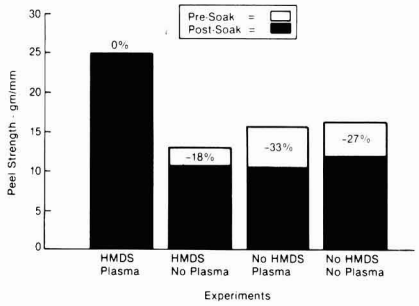


Fig. 6. A comparison of the peel strength before and after the T&H soak for samples prepared with and without plasma clean and HMDS. APS was used in all cases prior to applying polyimide. Polyimide was cured at 400°C.

Effect of APS on the adhesion.—Figure 7 shows that polyimide adhesion strength deteriorated by 40% when adhesion promoter APS was not used. After T&H, the group without APS reduced the adhesion strength to zero. In direct contrast, the group with APS retained adhesion strength after T&H soak.

Effect of cure temperature on polyimide/nitride adhesion.—The peel strengths were computed in this experiment after 168, 336, and 504h of T&H soak (Fig. 8). The results show that after 168h of soak all groups produced a no peel condition, and the minimum peel strength was highest when the polyimide was cured at 425°C. After 336 and 504h of soak, the polyimide cured at 375°, 400°, and 425°C began to peel, whereas those cured at 325° and 350°C produced no peel. Several points may be noted here. (*i*) There is a general tendency for the measured values to increase with T&H soak time. (*ii*) For samples which consistently failed to peel (*i.e.*, those cured at 325° and 350°C), these increases can readily be explained as increases in the fracture toughness of the film caused by plasticization due to the T&H soak. (*iii*) For the samples which consistently peeled at the two longer soak times (*i.e.*, those cured at 375°, 400°, and 425°C), the measurement represents a true adhesive strength.

Surface analytical characterization.—In order to further understand the differences between the various polyimide cure temperatures, XPS was used to examine the silicon nitride surface after peeling. Samples cured at 375°, 400°, and 425°C were peeled after 504h of soak, and then the silicon nitride surface that was exposed by peeling off the polyimide was analyzed by XPS. Samples

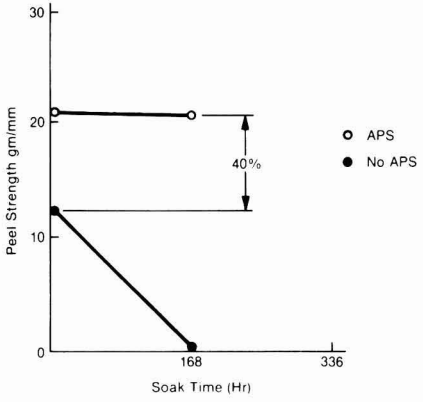


Fig. 7. A plot of peel strength vs. T&H soak time for polyimide-coated silicon nitride wafers prepared with (open circles) and without (closed circles) APS. In both cases, HMDS and plasma clean were used and the films were cured at 400°C.

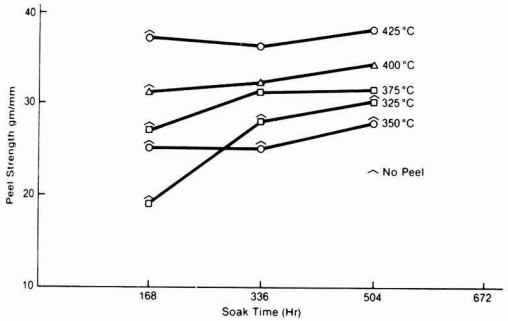


Fig. 8. A plot of the peel strength vs. the T&H soak time for polyimide-coated nitride samples cured at 325°, 350°, 375°, 400°, or 425°C. APS was used in all cases, after HMDS and plasma clean.

cured at 350° and 325°C could not be analyzed because the polyimide did not peel from a large enough area to perform the analysis. Silicon nitride, APS-coated silicon nitride, and polyimide surfaces were analyzed as control samples.

Table I summarizes the results from the XPS analysis. Figure 9 shows survey spectra obtained from some of the samples. Figure 10 shows an expansion of the nitrogen 1s signal from Fig. 9. From Table I and Fig. 9, it can be seen that the silicon signal from the nitride surfaces exposed by peeling increases as the cure temperature increases. There is also a noticeable drop in the carbon content as the cure temperature increases. In all cases, however, the surface exposed by peeling off polyimide does not approach the composition of the silicon nitride surface alone or the silicon nitride plus APS surface.

Table I. Surface composition as determined by XPS

Surface	PI cure temperature (°C)	Surface composition (a/o) C	N	O	Si
Nitride after peel	375	79	5.5	14	1.1
Nitride after peel	400	78	4.5	15	2.7
Nitride after peel	425	70	7.7	15	7.2
Nitride after peel	425	70	6.2	16	7.4
Polyimide	350	78	5.7	16	—
Silicon nitride	—	6.8	37	14	42
APS on nitride	—	17	30	16	37

From Fig. 10, the nitrogen 1s signal shows signs of two different bonding environments (*i.e.*, two overlapping nitrogen signals of different binding energy) for the sample cured at 425°C, as compared to the sample cured at 375°C. The higher binding energy is associated with the imide nitrogen from the polyimide. The lower binding energy is associated with the nitrogen from either the silicon nitride or the APS. These assignments are confirmed by the spectra of the control sample and are in agreement with reported binding energies for polyimide (7), silicon nitride (8), and APS (9).

Scanning electron microscopy was used to analyze the nitride surface after peeling off the polyimide. No differences were found in the surface morphology for samples cured at 375° or 425°C.

Discussion

Plasma ashing enhances polyimide adhesion to HMDS-treated nitride surfaces due to one or all of the following actions: (i) cleaning of or stripping off photoresist resi-

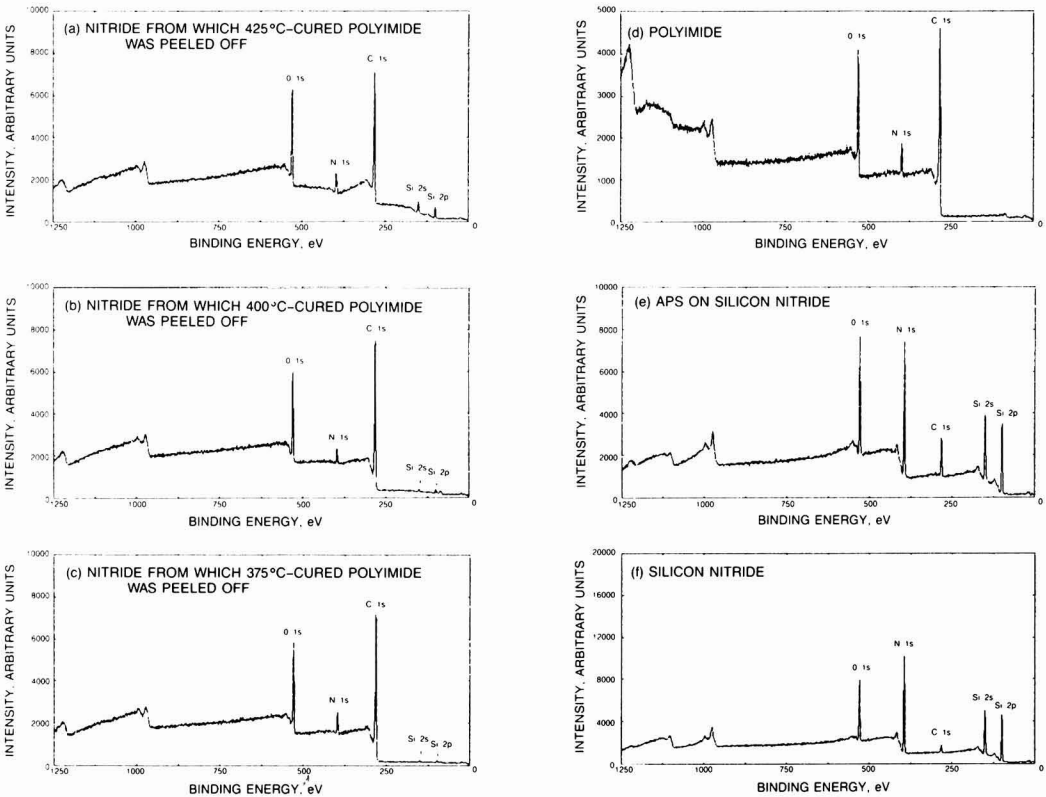


Fig. 9. XPS survey spectra for the nitride surface remaining after peeling off polyimide cured at 425°C (a), 400°C (b), and 375°C (c), as well as the spectra for a polyimide surface (d), a silicon nitride surface coated with APS (e), and an oxygen-rich silicon nitride (f).

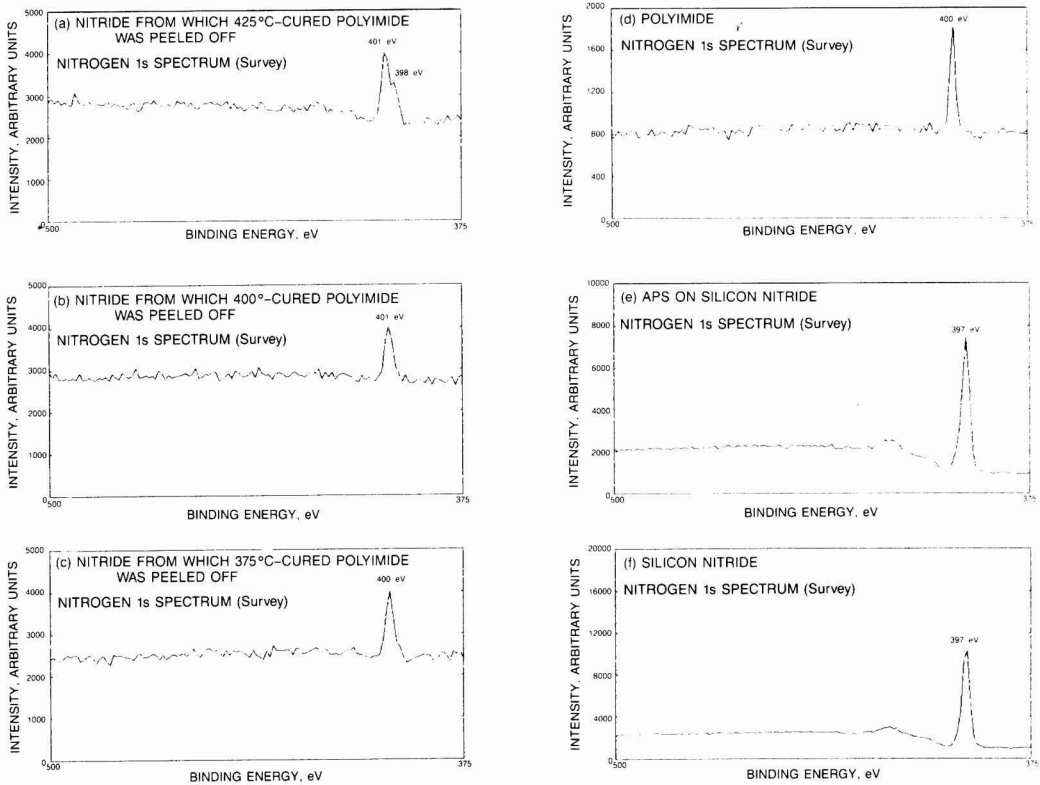


Fig. 10. An expansion of the nitrogen 1s signal from the spectra in Fig. 9

dues and HMDS, (*ii*) oxidation of HMDS, (*iii*) oxidation of nitride, and (*iv*) roughening of the surface. HMDS coating of surfaces enhances adhesion if and only if subsequently plasma cleaned. The omission of HMDS and/or plasma treatment of surfaces results in deterioration in the peel strength post-T&H stress.

APS is a crucial element for polyimide to silicon nitride adhesion. This was previously demonstrated to be true for polyimide to silicon dioxide adhesion (5). Since the silicon nitride surface is oxygen rich, the same chemistry of APS bonding probably occurs on both surfaces.

A higher peel strength at 400° and 425°C than at 350°C is due to the difference in the peel mode: the former values are true adhesive strengths, and the latter are the minimum peel strengths. In order for peel to occur, the tensile strength of the film has to be equal to or greater than the adhesive strength of the bond between film and substrate. This requirement stems from the fact that a certain amount of elastic and plastic deformation of the polyimide must be overcome before peeling can be initiated, given that the adhesion is relatively good (6). However, if adhesion is relatively poor, neither elastic nor plastic deformation is a significant factor. Finally, if the adhesion strength is extremely good, and the plastic deformation of the film is relatively low, then the material can be interpreted as being brittle. This is the case observed in the 325° and 350°C cured polyimide.

The higher cure temperatures produce stronger polyimide than at lower temperatures, but this may not be true for adhesion strength. A higher peel strength at cure temperatures of 375°C and above does not necessarily mean that the adhesion is better than at lower cure temperatures where minimum peel strengths are observed. Higher cure temperatures lead to greater elongation than at lower cure temperatures: hence, high cure temperature superficially shows increased adhesion strength. Our results show that 350°C is the safest cure temperature where both adhesion and plastic properties are adequate.

The XPS data shows that a thin organic film is left on the nitride surface after peeling polyimide. For the sample cured at 375°C, the three following observations can be made. First, the silicon signal is very small. Second, only one binding energy can be detected for the nitrogen. Third, the carbon, nitrogen, and oxygen signals appear almost identical to the spectrum for polyimide. The film remaining on this sample, therefore, is concluded to be polyimide, implying a largely cohesive failure mechanism. For the sample cured at 425°C, three observations can also be made. First, a significant silicon signal can be detected (although it is still much smaller than the signal from nitride or nitride plus APS). Second, two distinct nitrogen signals can be seen. Third, the carbon signal is reduced somewhat in intensity as compared to the polyimide reference. This indicates that the remaining polyimide film is thinner on the average than for the sample cured at 375°C, and that therefore the underlying nitride or APS films can also be detected.

While there is no ambiguity in the fact that the average thickness of the remaining polyimide film decreases with increasing cure temperature, there is uncertainty as to whether the film remains continuous or becomes discontinuous. If the film remains continuous and no underlaying nitride or APS is laid bare, then the failure mode remains cohesive. If, on the other hand, the film becomes discontinuous, *i.e.*, contains microregions where the nitride and/or APS are laid bare, then the failure becomes a mixture of adhesive and cohesive.

Independently of any physical or chemical considerations for the mechanism and mode of adhesion failure, the two extreme situations alluded to above can be quantified from the XPS data. Specifically, for the continuous film case, its thickness may be estimated by

using escape depths. The escape depth of a silicon 2p electron through organic material such as polyimide is about 30Å (10). Using conventional formulas for calculating attenuation of photoelectron signals by overlaying layers (11), and the Si 2p intensities measured in this study, the calculated thickness for the residual polyimide film ranges from 60 to 105Å for cure temperatures ranging from 375° to 425°C, respectively. Alternately, if one assumes that a discontinuous film of polyimide remains on the nitride, the calculated area percent coverage of polyimide ranges from 98% (2% of nitride laid bare) to 89% (11% of nitride laid bare) for cure temperatures of 400° or 425°C, respectively. These calculations assume that nitride is exposed upon peeling. Calculations made assuming that APS is exposed upon peeling would give even lower coverages. Calculations such as these provide some realistic boundaries on the mode of adhesion failure.

As can be seen in Fig. 1b, the polyamic acid chain undergoes scission upon bonding to the APS. This could result in a cohesive failure of the polyimide near the nitride interface, which would be consistent with the cohesive failure mechanism described above. This would not, however, explain an increasingly thinner film remaining after the peel as the cure temperature increases. The chain scission occurs during bonding to APS and is complete at a temperature far below the final cure temperature of the polyimide.

Decomposition of APS could explain this trend. A previous work has shown that the onset of thermal decomposition for the APS/polyimide system occurs in the region of 400°C (3). Any such decomposition occurring at the nitride/polyimide interface would be likely to favor adhesive failure at higher cure temperatures, particularly if these same conditions improve the fracture toughness of the polymer itself.

The fact that no differences were found in the morphology of the nitride surface after peeling for samples cured at 375° or 425°C does not rule out a mixed mode failure mechanism at the higher cure temperatures due to the limited resolution (~100Å) of the SEM.

A mixed mode of failure at higher cure temperatures could be due to inhomogeneities in the nitride/APS/polyimide laminate across the wafer and, therefore, differences in its decomposition behavior in localized areas.

Summary

Our results show the significance of the surface condition of silicon nitride for polyimide adhesion. Surface pretreatments (*e.g.*, plasma cleaning) and adhesion promoters are necessary in order to obtain good polyimide adhesion to silicon nitride. The use of an adhesion promoter plays a crucial role in obtaining and maintaining good adhesion. The cure temperature affects the thermal stability of the interface. At higher cure temperatures, the failure becomes increasingly adhesive in nature due to thermal degradation at the nitride/APS/polyimide interface. All of these results are related to chemical bonding and stability of the nitride/APS/polyimide interface.

Acknowledgments

The authors wish to thank Harold Linde for helpful discussions, Cherie Beach for technical assistance with the peel testing, and Rene Kirby and Tanya Lee for SEM analysis.

Manuscript submitted April 15, 1985; revised manuscript received July 10, 1985.

IBM Corporation assisted in meeting the publication costs of this article.

REFERENCES

1. D. Bergeron, J. Kent, and K. Morrett, in "Proceedings of the 22nd Annual IEEE Reliability Physics Conference," Las Vegas, April 1984, IEEE, New York (1984).
2. H. Linde, *J. Polym. Sci., Polym. Chem. Ed.*, **20,** 1031 (1982).
3. H. Linde, *ibid.*, **22,** 3043 (1984).
4. A. Saiki and S. Harada, *This Journal*, **129,** 2278 (1982).
5. L. Rothman, *ibid.*, **127,** 2216 (1980).
6. A. Crocombe and R. Adams, *J. Adhesion*, **13,** 241 (1982).
7. H. Leary, Jr., and D. Campbell, *Surf. Interface Anal.*, **1,** 75 (1979).
8. H. Leary, Jr., and D. Campbell, *Org. Coat. Appl. Polym. Sci. Proc.*, **46,** 433 (1981).
9. S. Raider, R. Flitsch, J. Aboaf, and W. Pliskin, *This Journal*, **123,** 560 (1976).
10. M. P. Seah and W. A. Dench, *Surf. Interface Anal.*, **1,** 2 (1979).
11. T. A. Carlson, "Photoelectron and Auger Spectroscopy," pp. 261-262, Plenum Press, New York (1975).

Electrical Properties of Silicon Dioxide Films Fabricated at 700°C

III. High Pressure Thermal Oxidation

L. P. Trombetta* and R. J. Zeto*

Electronics Technology and Devices Laboratory (ERADCOM), Fort Monmouth, New Jersey 07703-5302

F. J. Feigl* and M. E. Zvanut

Department of Physics and Sherman Fairchild Laboratory, Lehigh University, Bethlehem, Pennsylvania 18015

ABSTRACT

High quality thermal oxides of silicon have been fabricated on silicon substrates over the oxidation temperature range 635°-1100°C. Dry, high pressure oxidation (DRYPOX) was used to grow oxides at temperatures below 1000°C. The high pressure range investigated was 2-500 atm. Standard capacitance-voltage techniques have been used to characterize these oxides in terms of oxide fixed change (Q_f) and interface trap densities (D_{it}). Additionally, avalanche injection of both electrons and holes has been used to evaluate the charge trapping properties of these films. The electron trapping properties of 685°C, high pressure oxides were compared with "conventional" 1000°C oxides fabricated at 1 atm and with oxides fabricated using low pressure chemical vapor deposition (LPCVD) at 730°C. The results of these experiments were as follows: (*i*) basic electrical properties of high pressure oxides, as well as hole and electron trapping behavior in these oxides, were similar to those of 1000°C conventional oxides; (*ii*) hole trap densities exhibited a broad minimum at an oxidation temperature between 800° and 900°C; and (*iii*) electron trapping behavior in 685°C DRYPOX oxides was markedly superior to that in 730°C LPCVD oxides. The LPCVD oxide required an anneal at 1000°C to produce electron trapping characteristics comparable to those of DRYPOX samples processed entirely at temperatures below 700°C.

The development of low temperature processing techniques within the silicon planar technology is desirable for the development of very large scale integration (VLSI) (1, 2). In particular, low temperature oxidation using high pressure is receiving increased attention (3). Significantly reduced oxidation temperatures have been achieved using thermal oxidation of silicon at elevated pressures of either steam (2, 4, 5) or dry oxygen (1, 6, 7). Additionally, reductions in arsenic and boron diffusion have been demonstrated using high pressure steam to reduce oxidation temperatures (8, 9). A reduction in silicon stacking faults has also been obtained using high pressure steam (10).

High pressure oxidation using dry oxygen (DRYPOX) was first introduced by Zeto *et al.* (11). These authors investigated the kinetics of oxidation in dry oxygen at pressures up to 130 atm. Dry, high pressure oxidation kinetics have also been investigated by Lie *et al.* (1). A comprehensive review of early experiments in high pressure oxidation may be found in the work by Zeto *et al.* (12).

Basic electrical properties and device characteristics of silicon metal-oxide-semiconductor (MOS) devices fabricated using either dry oxygen (1, 6) or steam (2, 5) pressure oxidation for the gate oxide have been reported. To date, however, studies of the electrical behavior of dry, high pressure oxides have been rather select with regard to both the properties investigated and sample preparation conditions. The present work is intended as a more comprehensive survey of the relation between electrical quality and DRYPOX oxide fabrication techniques.

This paper is the third in a series on low temperature oxidation technologies. Parts I and II of this series discussed the use of low pressure chemical vapor deposition (LPCVD) using tetraethoxysilane (TEOS) (13) and dichlorosilane/nitrous oxide (14) deposition, respectively. For the present study, SiO_2 films were prepared by thermal oxidation of silicon at temperatures ranging from 635° to 1100°C and pressures ranging from 1 to 500 atm. The electrical quality of these films was evaluated in terms of the Deal oxide charge classification scheme (15) using aluminum gate MOS capacitors. Measurements were made of oxide fixed charge (Q_f), interface trap densities (D_{it}), and mobile ionic contaminants. In addition to these basic electrical properties, oxide trapped charge (Q_{ot}) produced by avalanche electron and hole injection was studied. An understanding of such oxide charging is important because of the phenomena of hot carrier injection into the gate oxide of short channel field effect devices (16) and of "window closing" in electrically erasable floating gate avalanche injection MOS (E²FAMOS) charge storage devices (17).

The results reported below include a comparison of DRYPOX films with conventional, high temperature (1000° and 1100°C) dry thermal oxide films and with oxide films produced using LPCVD of dichlorosilane and nitrous oxide at 730°C. These comparisons indicate that the electrical characteristics of DRYPOX films are comparable to conventional 1000°C thermal oxides. Additionally, the electron trapping behavior of DRYPOX films produced at 685°C was markedly superior to that of LPCVD films produced at 730°C and equivalent to LPCVD films given a high temperature (1000°C) post-deposition anneal.

Experimental Details

Sample preparation.—High pressure oxidation was performed in the apparatus shown schematically in Fig. 1. This apparatus consisted of an externally heated vessel constructed of a nickel-based alloy (Rene 41) and was pressurized with a Haskel oxygen pump. Gas was supplied to the pump from conventional high pressure cylinders. A Panametrics high pressure hygrometer was used to monitor the moisture content of the oxidation ambient. Under the conditions of the experiment, the moisture content could be maintained at five parts water per million parts oxidation ambient; this value was independent of the ambient pressure. A water content of even a few parts per million may increase oxidation kinetics. However, oxide thicknesses were reproducible to within 10%

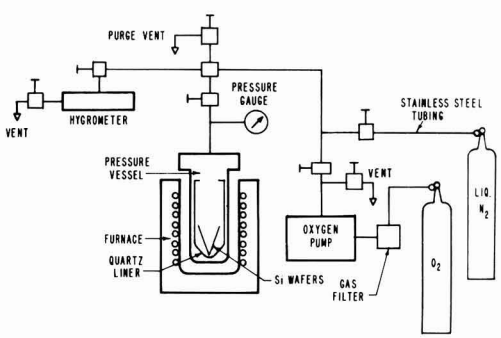


Fig. 1. Schematic diagram of the high pressure apparatus

* Electrochemical Society Active Member.

from run to run, and the moisture content was not considered a problem for the present investigation.

The inside dimensions of the pressure vessel were approximately 1.25 cm diam by 25 cm length. Samples were prepared by dicing polished silicon wafers to dimensions of 0.8 by 2.5 cm and were placed in a quartz test tube prior to insertion into the pressure vessel, as illustrated in Fig. 1. Silicon n-type substrates with phosphorus doping densities of 4-7 $\times$ 10^{15} cm^{-3} (3-5 Ω-cm resistivity) were supplied by Monsanto Company. Lower resistivity n- and p-type substrates with phosphorus and boron doping densities of 5-8 $\times$ 10^{16} cm^{-3} (0.1 Ω-cm resistivity) were supplied by Pensilco Company. The lower resistivity substrates were required for avalanche injection. Samples with resistivities significantly higher than 0.1 Ω-cm are more susceptible to "edge injection" effects produced by electric field enhancement at geometrical irregularities along the gate electrode perimeter [Ref. (18), p. 505]. With the exception of the wafers used for electron injection studies, all substrates were of n-type silicon with (100) crystallographic orientation. Electron injection studies were performed on p-type (100) wafers. Substrate cleaning consisted of a standard, basic peroxide/acid peroxide clean.

Oxidation in the high pressure system was initiated by first raising the external furnace and then pumping to the desired oxygen pressure. Approximately 35 min was required to reach a set temperature of 800°C. The pressurization time was on the order of seconds. Following oxidation, a dynamic postoxidation anneal was obtained by purging dry nitrogen between the source and the purge vent. The furnace was then lowered and the samples allowed to cool overnight in the vessel.

For comparison purposes, a number of dry thermal oxides were prepared in conventional, 1 atm Thermco furnaces at temperatures of 1000° and 1100°C. Following the oxidation, the furnace was flushed and a postoxidation anneal was performed in dry nitrogen. The samples were pulled from the furnace into a quartz "white elephant" end cap and allowed to cool.

MOS capacitors were formed by depositing circular aluminum electrodes (approximately 0.003 cm^2 in area) onto the front oxide surface. To provide substrate contact, the back oxide was stripped using HF and covered with aluminum. The aluminum was deposited using an Airco electron-beam metallization system. A postmetallization anneal (PMA) was found to significantly reduce the net charge in as-oxidized samples and was employed routinely. The PMA was performed at 450°C in dry nitrogen for 30 min. Oxidation conditions used for thermal oxide preparation are listed in Table I.

Program of measurements.—Basic measurement techniques.—The basic electrical properties Q_f (oxide fixed charge) and D_{it} (interface trap density as a function of energy in the silicon bandgap), as well as oxide charging characteristics, were obtained using standard capacitance-voltage measurement techniques. Complete details concerning instrumentation and data reduction are available in Ref. (19).

High frequency capacitance-voltage (HF CV) characteristics were obtained using a Boonton 71D capacitance meter operating at 1 MHz. Ramp-IV, or quasi-static capacitance-voltage (QS CV) characteristics, were obtained using an HP 4140B picoammeter/voltage-source measurement system. Q_f was determined via comparison of the measured flatband voltage with that expected for an ideal capacitor. D_{it} was calculated from a comparison of the experimental HF and QS CV curves (20). Substrate doping densities were determined from measured HF CV curves, using oxide thickness values obtained via ellipsometry.

CV and avalanche injection experiments were executed under computer control, using either an HP 9845B computer with an HP IEEE-488 Interface Bus capability (for hole injection and associated CV measurements) or an Apple II with an Interactive Microwave ADALAB Data Acquisition System (for electron injection and associated CV measurements).

Table I. Sample preparation conditions

T_{ox} (°C)	P_{ox} (atm)	t_{ox} (min)	d_{ox} (nm)	g (nm/min)	t_{POA} (h)
	A. Varying oxidation temperature				
1100	1	35	77.3	2.1	—
1000	1	105	72.5	0.69	—
900	2	165	85.6	0.52	—
800	150	40	72.5	1.8	—
685	500	165	75.9	0.46	—
635	500	540	66.3	0.12	—
	B. Growth rate variation at constant temperature				
800	15	225	86.0	0.4	—
800	73	70	82.0	1.2	—
800	160	40	72.5	1.8	—
800	300	24	79.0	3.3	—
800	500	18	83.0	4.6	—
	C. POA time at constant oxidation temperature				
800	150	40	77.0	1.9	0
800	150	40	65.0	1.6	1.5
800	150	40	66.0	1.6	5
800	150	40	73.0	1.8	10
685	500	165	71.0	0.43	0
685	480	165	75.0	0.45	1.5
685	500	165	75.0	0.45	5
685	490	165	75.0	0.45	10
	D. p-Substrate samples used in electron-injection experiments				
685[a]	500	60	39.8	0.66	0
685[a]	500	60	47.3	0.79	5
685[b]	500	165	90.0	0.54	0
685[b]	500	165	90.0	0.54	5
1000	1	105	79.3	0.75	0
1000	1	105	79.3	0.75	0.5

T_{ox} = Oxidation temperature. P_{ox} = Oxidation pressure. t_{ox} = Oxidation time. d_{ox} = Average sample thickness. g = Average growth rate = d_{ox}/t_{ox}. t_{POA} = Time of postoxidation anneal.
[a] Wet DRYPOX.
[b] Dry DRYPOX. See text for explanation of wet and dry.

Avalanche injection measurements.—Oxide charge trapping kinetics were investigated using constant current avalanche injection techniques. The circuitry used to produce and measure avalanche currents was based on that developed by Nicollian *et al.* for electron injection (21). In this technique, application of a high voltage sinusoidal signal to the sample results in the injection of a dc current of minority carriers into the gate oxide; some fraction of these carriers is trapped as the carriers traverse the oxide film. The injection current is maintained constant using a feedback mechanism which applies a corrective dc voltage to the gate electrode in response to changes in a preset current level. The circuit described by Nicollian *et al.* was modified for the present work by employing a triangular driving waveform, as suggested by Aitken and Young (22).

Oxide charging during avalanche injection was monitored via automatic measurement of the flatband voltage as a function of the cumulative injection fluence. This was accomplished by periodically interrupting the injection to measure the flatband voltage. The flatband voltage measurements generally required 5-10s.

The cumulative injection fluence, $F(t)$, was defined as

$$F(t) = \frac{1}{q}\int_0^t j\,dt \qquad [1]$$

where j is the dc avalanche current density and q is the elementary charge. Typically, hole injections were performed at a dc hole current of 0.125 nA (40 nA/cm^2) and proceeded for 40s between flatband voltage measurements. In all cases presented here, hole currents were set at or below 0.22 nA (70 nA/cm^2). The large corrective feedback voltages necessary to maintain current densities larger than this value were observed to cause electron injection from the gate electrode via Fowler-Nordheim emission (19). As a result of experimental limitations, a

drop in hole current of up to 0.05 nA (16.7 nA/cm²) was observed over the course of the measurement. This drop was accounted for by measuring the hole current and directly calculating the fluence for each data point from Eq. [1].

Current densities during electron injection experiments were typically 20 μA/cm². The electron injection current did not vary by more than 1% from the preset level; therefore, a measurement of the current during each injection cycle, as described for hole injection, was not necessary. The procedure for electron injection and analysis has been described previously (14).

The flatband voltage measured relative to its value prior to charge injection (*i.e.*, the flatband voltage shift) is a measure of the centroid-weighted areal density of charge trapped in the oxide layer. The number density of oxide traps is obtained using the relation

$$N_{ot}(F) = |Q_{ot}(F)|/q = -C_{ox}\Delta V_{FB}(F) \quad [2]$$

where $Q_{ot}(F)$ is the areal oxide charge density, C_{ox} is the oxide capacitance per unit area, A is the electrode area, and ΔV_{FB} is the flatband voltage shift.

Hole trapping analysis.—Flatband voltage shift data were analyzed using a first-order kinetic model for oxide charge buildup. Such a model assumes the presence of one or more types of oxide charge trap, each of which is characterized by a saturated number density $N(\infty)$ and a capture cross section σ. The number density of filled traps as a function of time, $N_{ot}(t)$, is given by

$$\frac{dN_{ot}(t)}{dt} = \frac{1}{q} j\sigma[N(\infty) - N_{ot}(t)] \quad [3]$$

where j is the injected current density.

The hole trapping data of the present work were best fit assuming the presence of two types of hole traps. In this case, the solution to Eq. [3] for constant current density j, and with the initial condition $N_{ot}(t = 0) = 0$ is

$$N_{ot,h}(F_h) = N_{1h}(\infty)\,(1 - \exp(-\sigma_{1h}F_h)) + N_{2h}(\infty)\,(1 - \exp(-\sigma_{2h}F_h)) \quad [4]$$

Equation [4] gives the number density of trapped holes, $N_{ot,h}$, as a function of the cumulative hole injection fluence, F_h. The filling of oxide charge traps by first-order kinetics has been discussed extensively in the literature (14, 23, 24).

An iterative chi-squared curve-fitting procedure was used to fit Eq. [4] to the data, and the best-fit values of the parameters $N_{1h}(\infty)$, $N_{2h}(\infty)$, σ_{1h}, and σ_{2h} were obtained. Additionally, the total saturated hole trap density, $N_h = N_{ot,h}(\infty) = N_{1h}(\infty) + N_{2h}(\infty)$, and the initial hole trapping efficiency, η, were calculated from these parameters. The initial trapping efficiency is defined as the slope of the charging curve extrapolated to zero fluence, and is given by

$$\eta = \left.\frac{dN_{ot,h}}{dF}\right|_{F=0} = \sigma_{1h}N_{1h} + \sigma_{2h}N_{2h} \quad [5]$$

Electron trapping analysis.—During electron injection, an increase in the flatband voltage due to a buildup of negative charge throughout the oxide bulk was observed. In most cases, a subsequent decrease, or "turnaround," in the flatband voltage shift was observed at a fluence dependent upon processing conditions. The turnaround has been interpreted as being due to the generation of donor-like electron trapping centers in the vicinity of the Si-SiO_2 interface (25). These centers are believed to be responsible for the so-called "anomalous positive charge" which has been widely studied (24, 25-27).

Combining the effects of electron trapping in the bulk and the generation of anomalous positive charge at the Si-SiO_2 interface, the net oxide charging is described by the equation

$$N_{ot,e}(F_e) = -N_{ot,b}(f_e) + N_{ot,i}(F_e) \quad [6]$$

where $N_{ot,b}$ and $N_{ot,i}$ are the number density of filled bulk oxide electron traps and interface anomalous positive charge, respectively. Equation [6] gives the number density of net oxide charge, $N_{ot,e}$, as a function of the cumulative electron injection fluence, F_e. The individual charging components are given by

$$N_{ot,b}(F_e) = N_{ot,b}(\infty)\,[1 - \exp(-\sigma_e F_e)] \quad [7a]$$

$$N_{ot,i}(F_e) = N_{ot,i}(\infty)\,[1 - \exp(-\sigma_e F_e)] \quad [7b]$$

where $N_{ot,b}(\infty)$ and $N_{ot,i}(\infty)$ are saturated trap densities and σ_e and σ_e the capture cross sections for bulk electron traps and anomalous positive charge generation, respectively. Equations [6] and [7] were fit to the electron trapping data using a chi-squared fitting routine to obtain the best fit parameters $N_{ot,b}(\infty)$, $N_{ot,i}(\infty)$, σ_e, and σ_e.

Experimental Results

Basic electrical characteristics: Q_f and D_{it}.—In measuring oxide fixed charge densities, between five and ten capacitors from a given wafer were tested. The substrate doping density was 3-5 Ω-cm. Midgap interface trap densities $D_{it,m}$ (*i.e.*, D_{it} taken 0.55 eV above the silicon valence bandedge) were measured on only two or three capacitors per wafer. For both measurements, a standard deviation of 20% was observed on a wafer-to-wafer basis.

Samples were selected periodically throughout the course of these experiments and tested for mobile ion contamination using conventional "bias-temperature-stress" techniques [Ref. (18), p. 428)]. The results of these tests indicated a density of less than 8×10^{10} cm^{-2} mobile ions in all the oxides tested.

Oxide fixed charge and midgap interface trap densities were examined as a function of oxidation temperature in the range 635°-1100°C. The oxidation conditions for this set of oxides are listed in Table IA. Q_f values were in the range 0.9-3 × 10^{11} cm^{-2}, and $D_{it,m}$ values were in the range 1-3 × 10^{11} cm^{-2}-eV^{-1}. No consistent trend in either parameter was observed over the temperature range 635°- 900°C. Oxides grown in conventional furnaces at 1000° and 1100°C had values of Q_f and $D_{it,m}$ which were lower by a factor of approximately 2.

The effect of oxide growth rate at 800°C oxidation temperature was investigated by varying the oxygen pressure. Specific oxidation conditions employed to obtain this growth rate variation are listed in Table IB. Q_f and $D_{it,m}$ as a function of oxide growth rate are listed in Table II. For both properties, a variation of less than a factor of 2 is indicated for an oxide growth rate variation of more than a factor of 10.

Q_f and $D_{it,m}$ were investigated as a function of post-oxidation anneal time between 0 and 10h for wafers oxidized at 800° and at 685°C. The oxidation conditions employed are listed in Table IC. In all cases, the POA was performed at the oxidation temperature. $D_{it,m}$ and Q_f obtained as a function of POA time are listed in Table III. These data indicate a reduction in both Q_f and D_{it} for increasing POA time at both temperatures.

The effect of a 5h POA on oxides fabricated at 685°C on p-type substrates is given in Table IV. This table also contains data obtained on a conventional thermal oxide

Table II. Oxide growth rate investigation

g (nm/min)	Q_f (10^{11} cm^{-2})	$D_{it,m}$ (10^{11} cm^{-2}-eV^{-1})	N_h (10^{12} cm^{-2})
0.4	1.4	1.8	3.0
1.2	1.7	1.5	3.5
1.8	2.1	1.2	4.1
3.3	2.4	1.7	3.1
4.6	1.3	1.8	3.3

As-grown oxide fixed charge Q_f, midgap interface trap density $D_{it,m}$, and total hole trap density N_h as a function of oxide growth rate g. Oxidation temperature is 800°C. Estimated error in Q_f and $D_{it,m}$ is ± 20%; in N_h, it is ± 10%.

Table III. Postoxidation anneal time investigation

T_{ox}/P_{ox} (°C/atm)	t_{POA} (h)	Q_f (10^{11} cm^{-2})	$D_{it,m}$ (10^{11} cm^{-2}-eV^{-1})	N_h (10^{12} cm^{-2})
800/150	0	2.4	0.75	3.2
	1.5	1.7	0.75	3.4
	5	0.8	0.2	3.0
	10	1.2	0.48	3.6
685/500	0	2.5	0.45	4.9
	1.5	0.85	—	4.5
	5	0.6	0.45	4.3
	10	0.27	0.3	—

As-grown oxide fixed charge Q_f, midgap interface trap density $D_{it,m}$, and total hole trap density N_h as a function of POA time. The estimated error in Q_f and $D_{it,m}$ is ± 20%; in N_h, it is ± 10%.

Table IV. Basic electrical properties

Sample/anneals	Q_f (10^{11} cm^{-2})	$D_{it,m}$ (10^{11} cm^{-2}-eV^{-1})
685°C dry DRYPOX		
No POA	2.3	0.7
685°C POA (5h)	−1.1	0.2
685°C wet DRYPOX		
No POA	2.9	1
685°C POA (5h)	0.9	0.7
1000°C 1 atm		
No POA	0.4	0.7
1000°C POA (0.5h)	−0.5	0.5
730°C LPCVD		
No PDA	1	4
1000°C PDA (0.5h)	7	1

Comparison of oxide fixed charge Q_f and midgap interface trap density D_{it} using 685° and 1000°C thermal and 730°C LPCVD oxidation technologies. Estimated error for all entries is ± 20%. See text for definition of anneals.

grown at 1000°C in 1 atm dry oxygen. The POA specified for the thermal oxides refers to a postoxidation anneal at the oxidation temperature. Oxidation conditions are given in Table ID. Table IV also gives Q_f and $D_{it,m}$ values obtained on a 50 nm thick, 730°C LPCVD oxide film (14). The PDA listed for this oxide refers to a 30 min postdeposition anneal. It should be noted that the LPCVD oxides were metallized using a tungsten filament evaporation system rather than the E-beam metallization system used for the DRYPOX and conventional oxides.

Table IV lists data obtained on two sets of 685°C thermal oxides produced under nominally identical conditions. Although Q_f and $D_{it,m}$ values were similar for both the "wet" and "dry" oxides, electron-injection experiments revealed differences in oxide quality. These differences will be discussed below. The similarity in basic electrical quality following POA/PDA treatments is noteworthy.

Avalanche hole injection.—High frequency and quasi-static CV curves obtained before and after a typical hole injection experiment are shown in Fig. 2a for a 685°C DRYPOX oxide. The shift in the capacitance curves to more negative voltage is a result of the buildup of positive charge near the Si-SiO_2 interface.[1] In addition, the distortion in both the high frequency and quasi-static capacitance curves following hole injection is indicative of the generation of interface traps.

Interface trap densities were observed to increase throughout the silicon bandgap with increasing hole injection fluence, as shown in Fig. 2b. These spectra are typical of those obtained on all of the samples examined. Specifically, a nonuniform increase in D_{it} toward the upper half of the bandgap (0.7-0.9 eV above the valence bandedge), and a uniform increase throughout the midgap region (0.2-0.7 eV above the valence bandedge) were observed.

Reproducibility experiments were performed on five wafers processed under nominally identical conditions. The results indicated a variation of 20% in the individual kinetic parameters $N(\infty)$ and σ_h. However, the total hole trap density, $N_h = N_{1h}(\infty) + N_{2h}(\infty)$, displayed a variation of less than 10% on a wafer-to-wafer basis. Variations on a single wafer were observed to be approximately 10% in the individual kinetic parameters and 5% in the total hole trap density.

The only significant variation observed in hole trapping characteristics was as a function of oxidation temperature. This variation is shown in Fig. 3, where the total hole trap density N_h is plotted for oxidation temperatures ranging from 635° to 1100°C. Figure 3 displays a minimum in the total hole trap density at an oxidation temperature between 800° and 900°C. Average values for individual kinetic parameters obtained from several wafers at each temperature, as well as the total hole trap density and initial trapping efficiency η, are listed in Table V. Specific oxidation conditions for these runs are listed in Table IA. Figure 4 shows hole charging curves representative of each oxidation temperature.

Low resistivity substrates (0.1 Ω-cm) oxidized under the conditions listed in Table IB were examined for variations in hole trapping kinetics with varying oxide growth rate at a constant oxidation temperature of 800°C. Total hole trap densities for this set of oxides are listed in Table II. No consistent trend in hole trapping kinetics was observed over the range in growth rate studied.

Low resistivity samples (0.1 Ω-cm) oxidized under the conditions listed to Table IC were examined for the effect of varying postoxidation anneal time on the hole trapping kinetics. Table III lists total hole trap densities obtained from these samples. Evidently, a POA under the conditions investigated has little effect on the hole trapping kinetics.

Aitken (28) has demonstrated that the use of electron beam metallization may introduce neutral traps into the MOS oxide. To investigate this effect in the present work, hole trapping kinetics were compared between two samples, one metallized using electron-beam evaporation techniques, the other using tungsten filament evapora-

[1] A relaxation of the flatband voltage shift following hole injection was observed in all of the samples studied. The post-injection C-V curves of Fig. 2a and the D_{it} spectra of Fig. 2b were measured 300h following hole injection, during which time the flatband voltage shift had relaxed by some 30% of its value immediately following the injection.

Table V. Hole trapping kinetics

T_{ox} (°C)	N_{1h} (10^{12} cm^{-2})	N_{2h} (10^{12} cm^{-2})	σ_{1h} (10^{-15} cm^2)	σ_{2h} (10^{-15} cm^2)	N_h (10^{12} cm^{-2})	η (10^{-3})
635	2.2 ± 1.4	3.8 ± 1.4	9 ± 8	16 ± 0.2	6 ± 0.0	88 ± 5
685	1.4 ± 0.4	3.8 ± 0.5	2.2 ± 0.6	16 ± 7	5.2 ± 0.2	65 ± 3
800	1.2 ± 0.3	2.6 ± 0.5	1.4 ± 0.2	13 ± 2	3.8 ± 0.6	35 ± 8
900	1.2 ± 0.1	2.6 ± 0.4	1.6 ± 0.2	10 ± 2	3.8 ± 0.4	27 ± 10
1000	1.3 ± 0.4	2.8 ± 0.4	2.6 ± 0.6	17 ± 0.4	4.1 ± 0.1	55 ± 12
1100	0.7 ± 0.2	6.8 ± 0.2	2.0 ± 0.4	28 ± 3	7.5 ± 0.4	188 ± 17

Average kinetic parameters for hole trapping as a function of oxidation temperature. Errors indicated for T_{ox} = 685°, 800°, and 1000°C represent one standard deviation about the mean. For the other temperatures, errors indicate the range of values observed.

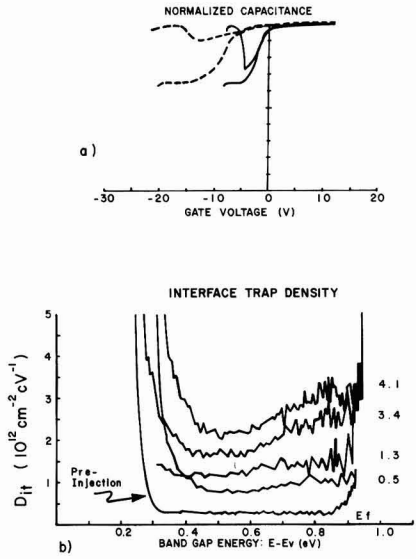


Fig. 2. 685°C DRYPOX oxides. a: High frequency and quasi-static capacitance-voltage characteristics before (solid line) and after (dashed line) avalanche hole injection to a fluence of 3.4×10^{13} cm^{-2}. b: Interface trap densities vs. energy above the silicon valence bandedge (E_v) and following injection to the fluence indicated. Fluences are in units of 10^{13} cm^{-2}.

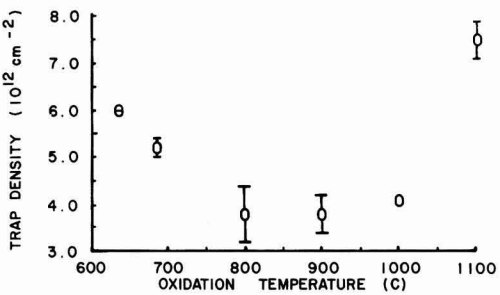


Fig. 3. Total hole trap density as a function of oxidation temperature. No POA was employed. Error bars for T_{ox} = 685°, 800°, and 1000°C represent one standard deviation about the mean. For the other temperatures, the errors bars represent the range of values observed.

tion. The results indicated that (*i*) the hole trapping efficiency was larger by approximately a factor of 2 in samples metallized via electron-beam evaporation, (*ii*) the hole trap density was approximately 20% larger in samples metallized via filament evaporation, and (*iii*) the oxidation temperature dependence of the hole trapping kinetics was the same using either metallization technique (19).

Avalanche electron injection.—Avalanche electron injection was performed on the samples listed in Table ID, as well as on LPCVD oxides deposited at 730°C. Fixed charge densities Q_f and interface trap densities $D_{it,m}$ for all of these samples are presented in Table IV.

Typical high frequency and quasi-static C-V curves obtained before and after electron injection are shown in Fig. 5a for a 685°C DRYPOX oxide. The shift in the capacitance curves to more positive voltage is due to the buildup of negative charge throughout the bulk of the oxide. In addition, the distortion in both the high frequency and quasi-static capacitance curves is indicative of the buildup of interface traps. Interface trap densities determined before and after electron injection are given in Fig. 5b, where D_{it} is compared to samples oxidized at 685°C in

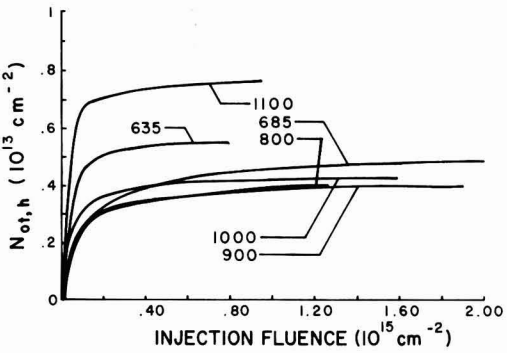


Fig. 4. Hole charging curves with oxidation temperature as a parameter. Oxidation temperatures are shown in degrees centigrade.

500 atm pressure and at 1000°C in 1 atm pressure. Figure 5b demonstrates that D_{it} following electron injection is higher in the 685°C oxide than in the conventional oxide by a factor of approximately 3.

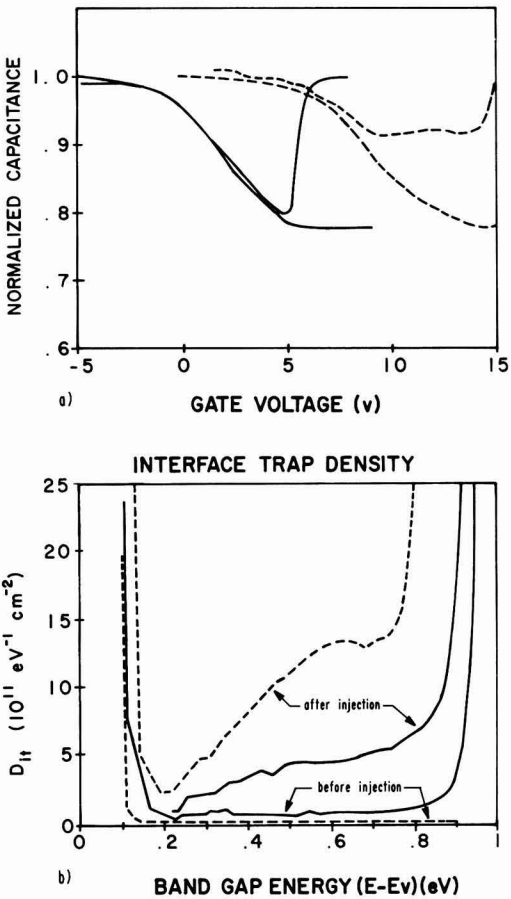


Fig. 5. (a) High frequency and quasi-static capacitance-voltage characteristics and (b) interface trap densities vs. energy above the silicon valence bandedge (E_v) before and after avalanche electron injection to a fluence of 3×10^{18} cm^{-2}. In a, solid lines are before and dashed lines after injection for a 685°C, 500 atm dry DRYPOX oxide. In b, solid lines are for a 1000°C conventional oxide and dashed lines are for a 685°C DRYPOX oxide.

Individual kinetic parameters for electron trapping in 685°C DRYPOX, 1000°C conventional, and 730°C LPCVD oxide films are given in Table VI. This table shows that the dominant capture cross section for bulk electron trapping, σ_c, is a function of sample preparation. In particular, the 1000°C conventional oxides and the "dry" DRYPOX samples had dominant capture cross sections in the range (3-5) $\times$ 10^{-18} cm^2. The "wet" DRYPOX samples exhibited a dominant capture cross section of 1×10^{-17} cm^2. The presence of an electron trap with a capture cross section in the range 10^{-17} cm^{-2} has been associated with water contamination in SiO_2 films (24). Therefore, it is plausible that the DRYPOX films exhibiting the larger electron capture cross section were inadvertently contaminated with water. It was for this reason that the designations "dry" DRYPOX and "wet" DRYPOX were introduced. These assignments are consistent with the larger growth rates observed for the wet oxides (see Table ID).

Differences in electron charging curves between wet and dry DRYPOX samples are evident in Fig. 6. The so-called "flatband voltage turnaround" is evident in the dry oxide at a fluence of 2×10^{18} cm^{-2}, and in the wet oxide at 0.25×10^{18} cm^{-2}. A pronounced turnaround effect has also been associated with water contamination (24, 26). As discussed in the Electron trapping analysis section, the flatband voltage turnaround is due to the buildup of anomalous positive charge at the $Si-SiO_2$ interface, and was modeled by a second trap density and capture cross section. Values for these kinetic parameters are listed in Table VI as $N_{ot,i}$ and σ_c, respectively.

Prior to a PDA, electron trapping in the LPCVD sample was so extensive that oxide breakdown occurred at fluences too low to allow extraction of the trapping parameters. However, this low fluence data did allow accurate determination of the trapping efficiency, η, which was approximately 2×10^{-3}. This value is two orders of magnitude larger than the efficiency exhibited by the unannealed 685°C dry DRYPOX oxides. Following a PDA, the trapping efficiency of the LPCVD oxides were comparable to those of the DRYPOX samples.

Figure 7 compares electron charging curves in dry DRYPOX and 1000°C conventional oxides. The effect of POA on these charging curves is also explored. Figure 7 demonstrates that the oxide-trapped charge density and, consequently, the initial electron trapping efficiency, were greater in the 685°C oxide by a factor of approximately 2. A POA had little effect on the bulk trapping of these oxides, but reduced the turnaround effect in all cases. These results are also evident in the kinetic parameters of Table VI. Due to the limited amount of data, no kinetic parameters for the turnaround process could be extracted for the 1000°C oxides.

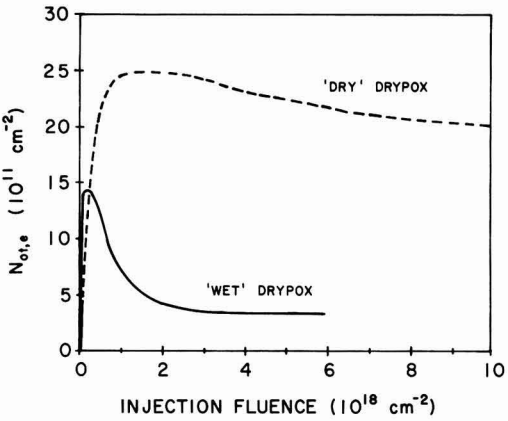


Fig. 6. Electron charging curves for wet and dry DRYPOX oxides

The use of electron-beam metallization may contribute to electron trapping in oxide films (28). No study of electron trapping in DRYPOX oxides metallized by techniques other than electron-beam evaporation was made.

Summary and Discussion

As-grown oxide characteristics.—In general, the levels of oxide fixed charge and interface trap densities found in DRYPOX samples are similar to those reported in the literature (29, 30) for oxides produced using conventional techniques. In particular, oxide fixed charge levels on the order of 10^{11} cm^{-2} were observed, and were found to decrease upon postoxidation annealing. Interface trap densities on the order of 10^{11} cm^{-2}-eV^{-1} were observed following a conventional postmetallization anneal. Variations in oxidation temperature over the range 635°-1100°C and in oxide growth rate at 800°C over the range 0.4-4.6 nm/min had no systematic effect on these properties

Low levels (less than 8×10^{10} cm^{-2}) of mobile sodium contamination were detected in all of the oxides investigated. However, as noted in the Basic electrical characteristics section, values of Q_f and D_{it} were lower in the conventional oxides than in the 1 atm oxides by a factor of approximately 2. Because no dependence of either Q_f or D_{it} on oxidation pressure was observed (recall the oxide growth rate experiments), this difference is believed to be due to systematic differences in cleanliness between the pressure vessel and the conventional oxidation tubes. Specifically, the pressure vessel allowed the oxidation ambient to contact both the silicon wafers and the vessel

Table VI. Electron trapping kinetics

Sample/anneals	$N_{ot,b}$ (10^{11} cm^{-2})	$N_{ot,i}$ (10^{11} cm^{-2})	σ_c (10^{-18} cm^2)	σ_c (10^{-18} cm^2)
685°C dry DRYPOX				
No POA	30	10	4	0.4
685°C POA	30	9	3	0.2
685°C wet DRYPOX				
NO POA	40	30	10	1
685°C POA	20	20	10	1
1000°C 1 atm				
No POA	8	—	5	—
1000°C POA	11	—	4	—
730°C LPCVD				
No PDA	—	—	—	—
1000°C PDA	10	—	10	—

Comparison of electron trapping kinetic parameters using 685° and 1000°C thermal and 730°C LPCVD oxidation technologies. LPCVD data taken from Ref. (14). Estimated error for all entries is ± 20%. See text for definition of anneals.

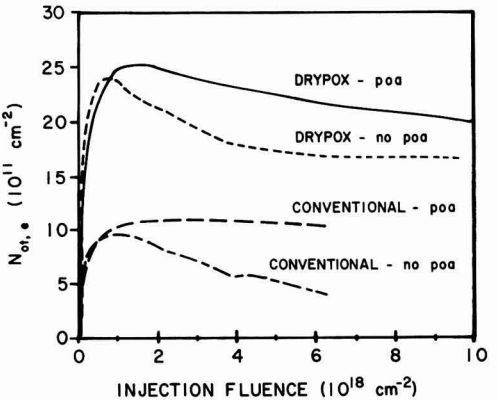


Fig. 7. Comparison of 685°C DRYPOX and 1000°C conventional oxides, with and without a POA at the oxidation temperature.

wall, thereby introducing the possibility of contamination by oxide scale from the vessel wall.

Some differences in the annealing behavior of the low temperature oxides, as compared with conventional oxides, were noted. Specifically, the time required to minimize oxide fixed charge levels was increased with respect to that required at higher temperatures. At anneal temperatures of 1000°C, a minimum in oxide fixed charge has been observed following a POA for approximately 30 min (29). Deal (30) reports a minimum in oxide fixed charge following a POA for 10-20 min at anneal temperatures between 950° and 1100°C. The results of the present work indicate that annealing at 800°C requires an increase of approximately a factor of 10 over these values. After 10h, or an increase of approximately a factor of 20 in POA time, the fixed charge levels observed for a POA at 685°C had not minimized. This behavior is summarized in Table III.

Charge trapping.—Capture cross sections on the order of 10^{-15} and 10^{-14} cm^2 with corresponding trap densities on the order of 10^{12} cm^{-2} were obtained from hole trapping kinetic analyses. Average values for these parameters, obtained as a function of oxidation temperature from 635° to 1100°C, are listed in Table V. Hole trapping kinetic parameters obtained on 1000°C oxides were similar to those reported in the literature (22, 31).

An increase in D_{it} following avalanche hole injection has been observed by Lai (31, 32). Lai reported a uniform increase in fast interface traps throughout the bandgap, with a peak at approximately 0.8 eV above the silicon valence bandedge appearing after the injection and capture of electrons on trapped hole sites. In the present work, a nonuniform buildup of fast interface traps was observed immediately following hole injection, as illustrated in Fig. 2b.

Hole trapping studies have been reported by a number of investigators (22, 33-35). That hole trapping occurs very close to the Si-SiO_2 interface is suggested by etch-back techniques (33) and by photocurrent-voltage measurements (35). A centroid 3-5 nm from the Si-SiO_2 interface is supported by the observation in this work that trapped positive charge decays with time, irrespective of the sign of an applied dc bias, suggesting that quantum mechanical tunneling to the silicon substrate from traps very near the silicon interface is taking place (19, 36). Similar tunneling effects have been observed by other investigators (22).

The most interesting aspect of the hole trapping kinetics obtained in this study is the minimum in total trap density observed between 800° and 900°C. That this effect is due to temperature and not a commensurate change in growth rate was directly demonstrated. A study by Lie *et al.* (1), using dry oxidation at a pressure of 10 atm and over the temperature range 800°-1100°C, suggests a minimum at 900°C in the hole trap density. No analysis of the trapping kinetics was presented by Lie *et al.*

Hole trapping kinetics were unaffected by a post-oxidation anneal for times up to 10h at 800°C and 5h at 700°C. These results are listed in Table III. They differ with the assertion by Lai that a POA below 900°C reduces hole trap densities (31). Hole trapping was also unaffected by a change in growth rate from 0.4 to 4.6 nm/min at an oxidation temperature of 800°C.

The increase in hole trap density observed in this work for oxidation temperatures above 900°C is consistent with a model of hole trapping proposed by EerNisse and Derbenwick (37). These authors suggest that hole traps are produced by viscous flow of the oxide at temperatures greater than 950°C. However, the present work demonstrates that viscous flow is not a necessary condition for the generation of hole traps. Specifically, an increase in the hole trap density is observed for oxidation temperatures below 800°C, where no viscous flow should occur (37, 38).

Another mechanism for the generation of hole traps may be related to the presence of compressive mechanical stress at the Si-SiO_2 interface. A correlation between Si-SiO_2 interface stress and hole trapping has been suggested by other investigators (31, 39). Irene (38) has suggested that oxide stress develops during oxidation at temperatures below 800°C as a result of the inability of the oxide to undergo viscous flow. The magnitude of stress so generated should increase as the temperature is reduced (38).

It is interesting to note that interface stress generation for oxidation temperatures above 900°C has also been investigated. Specifically, Jaccodine (40) has demonstrated that the difference in the thermal expansion coefficients of Si and SiO_2 results in thermal "warping" of an oxidized wafer, and thereby in Si-SiO_2 interface stress which increases with increasing oxidation temperature. Thus, given that oxide stress increases for oxidation temperatures below 800°C (according to Irene's model) and above 900°C (according to Jaccodine's model), the presence of a minimum at 800°-900°C in the hole-trap density is consistent with models in which stress is responsible for hole trapping.

The argument presented above does not preclude viscous flow as a mechanism for the production of hole traps. In fact, Aitken and Young (22) have observed larger hole trap densities in samples annealed for 90 min at 1000°C than in unannealed samples, suggesting that viscous flow contributes to hole trapping. However, if viscous flow indeed plays a role in hole trapping, the results of the POA experiments in the present work show that it is not operative over a time scale of 10h at 800°C.

Weinberg *et al.* (41) have suggested that hole trapping may be due to an oxygen deficiency at the Si-SiO_2 interface. In terms of their model, the increase in hole trapping below 800°C may be interpreted as a depletion of oxygen from this interface at the lower oxidation temperatures. The data of the present work do not allow a distinction to be made among the relative effects of interface stress, viscous flow, and oxygen deficiency.

Values of bulk and interface trapping kinetics determined from electron-injection experiments are also similar to those reported in the literature for conventional oxides (24). The electron trap density and postelectron injection interface trap densities are slightly higher in the low temperature oxides than in the conventional oxides.

Comparison between a dry DRYPOX oxide and an LPCVD oxide fabricated at 730°C indicates that the electron trapping efficiency of the as-deposited LPCVD oxide was 2 orders of magnitude higher than that of the DRYPOX oxide. The LPCVD oxides required a PDA at 1000°C to produce electron trapping characteristics similar to that of the DRYPOX oxides fabricated entirely at temperatures below 700°C.

Conclusions

High quality oxide films have been produced at temperatures which are low compared with conventional processing by using high pressure oxidation in dry oxygen ambients. Characterization of these oxides has demonstrated their electrical properties, as well as the dependence of these properties on process variables, to be similar to those exhibited by higher temperature thermal oxides prepared using more conventional techniques.

Oxide fixed charge and interface trap levels before electron injection were similar among all of the samples studied. As such, it is interesting to note differences in oxide quality which were manifest only upon electron injection. With regard to electron injection, thermal oxides fabricated at 685°C were found to be superior to LPCVD oxides fabricated at approximately the same temperature.

Acknowledgments

Research at Lehigh University was supported by the U.S. Army Research Office under contract DAAG29-81-K-0007. F. J. Feigl was supported in part by the Electronics and Solid State Science Program of the Office of Naval Research, and M. E. Zvanut by a Sherman Fairchild Fellowship.

Manuscript submitted May 8, 1985; revised manuscript received July 29, 1985. This was Paper 64 presented at the

Toronto, Ontario, Canada, Meeting of the Society, May 12-17, 1985.

ERADCOM assisted in meeting the publication costs of this article.

REFERENCES

1. L. N. Lie, R. R. Razouk, and B. E. Deal, *This Journal*, **129,** 2828 (1982).
2. L. E. Katz, B. F. Howells, L. P. Adda, T. Thompson, and D. Carlson, *Solid-State Technol.*, **21** (12), 87 (1981).
3. D. R. Craven and J. B. Stimmel, *Semicond. Intl.*, 59 (June 1981).
4. L. E. Katz and B. F. Howells, *This Journal*, **126,** 1822 (1979).
5. R. R. Razouk, L. N. Lie, and B. E. Deal, *ibid.*, **128,** 2214 (1981).
6. R. J. Zeto, C. G. Thornton, E. Hryckowian, and C. D. Bosco, *ibid.*, **122,** 1409 (1975).
7. R. J. Zeto, C. D. Bosco, E. Hryckowian, and L. L. Wilcox Abstract 82, p. 229, The Electrochemical Society Extended Abstracts, Vol. 77-1, Philadelphia, PA, May 8-13, 1977.
8. P. Deroux-Dauphin and L. P. Gonchond, in "VLSI Science and Technology/1984," K. E. Bean and G. A. Rozgonyi, Editors, p. 311, The Electrochemical Society Softbound Proceedings Series, Pennington, NJ (1984).
9. D. Fuoss and J. A. Topich, *Appl. Phys. Lett.*, **36,** 275 (1980).
10. L. E. Katz and L. C. Kimerling, *This Journal*, **125,** 1680 (1978).
11. R. J. Zeto, E. Hryckowian, C. D. Bosco, G. J. IaFrate, R. W. Brower, and C. G. Thornton, Abstract 206, p. 504, The Electrochemical Society Extended Abstracts, Vol. 74-2, New York, NY, Oct. 13-17, 1974.
12. R. J. Zeto, N. O. Korolkoff, and S. Marshall, *Solid-State Technol.*, **22,** 62 (1979).
13. R. H. Vogel, S. R. Butler, and F. J. Feigl, *J. Electron. Mater.*, **14,** 329 (1985).
14. M. E. Zvanut, F. J. Feigl, S. R. Butler, and S. L. Titcomb, *ibid.*, **14,** 343 (1985).
15. B. E. Deal, *This Journal*, **127,** 979 (1980).
16. T. H. Ning, C. M. Osburn, and H. N. Yu, *J. Electron. Mater.*, **6,** 65 (1977).
17. D. J. DiMaria, K. M. DeMeyer, and D. W. Dong, *IEEE Electron. Device Lett.*, **Edl-1,** 179 (1980).
18. E. H. Nicollian and J. R. Brews, "MOS Physics and Technology," John Wiley and Sons, New York (1982).
19. L. Trombetta, Ph.D. Thesis, Lehigh University, Bethlehem, PA (1984).
20. R. Castagne and A. Vapaille, *Surf. Sci.*, **28,** 557 (1971).
21. E. H. Nicollian, C. N. Berglund, P. F. Schmidt, and J. M. Andrews, *J. Appl. Phys.*, **42,** 5654 (1971).
22. J. M. Aitken and D. R. Young, *IEEE Trans. Nuclear Sci.*, **ns-24,** 2128 (1977).
23. F. J. Feigl, in "VLSI Electronics: Microstructure Science," Vol. 6, N. Einspurch and G. Larrabee, Editors, Chap. 3, pp. 195-204, Academic Press, New York (1983).
24. F. J. Feigl, D. R. Young, D. J. DiMaria, S. Lai, and J. Calise, *J. Appl. Phys.*, **52,** 5665 (1981).
25. D. R. Young, E. A. Irene, D. J. DiMaria, R. F. DeKeersmaecker, and H. Z. Massoud, *ibid.*, **50,** 6366 (1979).
26. R. A. Gdula, *This Journal*, **123,** 42 (1976).
27. S. K. Lai and D. R. Young, *J. Appl. Phys.*, **52,** 4231 (1981).
28. J. M. Aitken, *J. Non-Cryst. Solids*, **40,** 31 (1980).
29. F. Montillo and P. Balk, *This Journal*, **118,** 1463 (1971).
30. B. E. Deal, *ibid.*, **121,** 198C (1974).
31. S. K. Lai, *J. Appl. Phys.*, **54,** 2540 (1983).
32. S. K. Lai, *Appl. Phys. Lett.*, **39,** 58 (1981).
33. R. J. Powell and G. F. Derbenwick, *IEEE Trans. Nuclear Sci.*, **ns-18,** 99 (1971).
34. M. H. Woods and R. Williams, *J. Appl. Phys.*, **47,** 1082 (1976).
35. D. J. DiMaria, Z. A. Weinberg, and J. M. Aitken, *ibid.*, **48,** 898 (1977).
36. S. Manzini and A. Modelli, in "Insulation Films on Semiconductors," J. F. Verweij and D. R. Wolters, Editors, p. 112, Elsevier Science Publishers, New York (1983).
37. E. P. EerNisse and G. F. Derbenwick, *IEEE Trans. Nuclear Sci.*, **ns-23,** 1534 (1976).
38. E. A. Irene, E. Tierney, and J. Angilello, *This Journal*, **129,** 2594 (1982).
39. C. W. Gwyn, *J. Appl. Phys.*, **40,** 4886 (1969).
40. R. J. Jaccodine and W. A. Schlegel, *ibid.*, **37,** 2429 (1969).
41. Z. A. Weinberg, R. D. Young, J. A. Calise, S. A. Cohen, L. C. DeLuca, and V. R. Deline, *Appl. Phys. Lett.*, **45,** 1204 (1984).

Formation of Silicon-on-Insulator Structures by Implanted Nitrogen

L. Nesbit,* S. Stiffler, G. Slusser, and H. Vinton*[1]

IBM General Technology Division, Essex Junction, Vermont 05452

ABSTRACT

The formation of a buried Si_3N_4 by high dose nitrogen ion implantation to form a silicon-on-insulator (SOI) structure is studied by transmission electron microscopy (TEM) and by secondary ion mass spectroscopy (SIMS). Silicon wafers are implanted with a dose of 7.5×10^{17} N^+ ion/cm^2 at an energy of 160 keV at wafer temperatures of 400°, 500°, and 600°C. The wafers are subsequently annealed at 1200°C for 2h to form the buried silicon nitride layer. Both the as-implanted and postannealed microstructures are examined as a function of the implant temperature by TEM cross-sectional analysis. The microstructures of implanted wafers annealed for intermediate times are also examined to elucidate the development of the final microstructure. The as-implanted nitrogen profile and its redistribution during subsequent annealing at 1200°C are studied by SIMS.

The synthesis of silicon-on-insulator (SOI) structures for high density CMOS circuits has received considerable attention in recent years. Various techniques are currently being developed to form SOI structures which will, it is hoped, result in a high quality, thin, single-crystal silicon layer on an insulating layer or substrate (1-3). One of the more promising techniques for forming such a structure is that of ion implantation in which a high dose of a particular atomic or molecular species is implanted into silicon to form a buried insulating compound with silicon upon annealing at an elevated temperature. Most of the interest and research to date has concentrated on the implantation of atomic or molecular oxygen into silicon wafers and then annealing such wafers to form a buried SiO_2 layer. One of the drawbacks to implanting oxygen is that in order to form a sharp Si/SiO_2 interface, an oxygen dose on the order of $2.0\text{-}2.5 \times 10^{18}$ O^+ ion/cm^2 must be implanted into the silicon wafers (4-6). This results in a highly defective top silicon layer after a high temperature anneal, typically at 1150°C. This residual top silicon layer is only 100-400 nm thick (4-6), depending on the implant energy and dose. If this top residual silicon layer is too thin, it may be necessary to grow an epitaxial silicon layer to increase the thickness of the top silicon layer (7, 8).

Implanting nitrogen to form SOI structures has several possible advantages over implanting oxygen (9). First of all, hot filament, high current nitrogen implant sources

*Electrochemical Society Active Member.

[1]Present address: University of Vermont, Burlington, Vermont 05401.

with relatively long lifetimes are easier to construct and maintain than similar oxygen sources. Second, the highly defective layer at the top Si/insulator interface for implanted oxygen is absent in the case of implanted nitrogen. This point will be clearly demonstrated in this paper. Third, annealing of the as-implanted nitrogen distribution at sufficiently high temperatures results in the formation of a top silicon layer sufficiently thick so as to preclude the need for a subsequent epitaxial silicon growth step. Finally, a continuous buried silicon nitride layer may be formed at about 40-50% of the dose necessary to form a buried SiO_2 layer with an abrupt top Si/SiO_2 interface (4, 5). These latter two advantages imply that SOI by implanted nitrogen is a potentially simpler process with greater wafer throughput than SOI by implanted oxygen.

The behavior of high doses of implanted nitrogen is substantially different than that of implanted oxygen, both in the as-implanted state and after subsequent annealing. Maeyama *et al.* (10) have shown that the as-implanted nitrogen profile has a gaussian distribution for doses as high as 1.5×10^{18} N/cm^2 at 150 keV as determined by Rutherford backscattering spectroscopy (RBS). This dose is about 50% in excess of the theoretical dose required for the peak nitrogen concentration to equal that of stoichiometric Si_3N_4. On the other hand, oxygen doses for which the peak oxygen concentration is theoretically in excess of stoichiometric SiO_2 result in the peak oxygen concentration saturating at 66.7 atom percent (a/o) oxygen with the excess oxygen diffusing to the front and back implant tails during implantation (11, 12).

Annealing silicon with a nitrogen dose on the order 1×10^{18} N^+ ion/cm^2 at a sufficiently high temperature (*e.g.*, 1200°C) results in a continuous buried polycrystalline silicon nitride layer. Assuming a silicon nitride density of 3.18 g/cm^3 (13), a dose of 1.05×10^{18} N^+ ion/cm^2 is required at 150 keV for the peak nitrogen concentration to equal that of Si_3N_4. If the dose is too low, a continuous silicon nitride layer will not form, although Tsujide *et al.* (14) found that a dose of 3×10^{17} N^+ ion/cm^2 results in silicon nitride precipitates, albeit not a continuous silicon nitride film. Annealing at temperatures less than 1200°C generally does not result in the crystallization of the silicon nitride, even if the dose is on the order of 1×10^{18} N^+ ion/cm^2.

Implanting nitrogen at temperatures less than 350°C results in an amorphous top silicon layer, which recrystallizes into polycrystalline silicon upon annealing (9, 15). Implanting at temperatures at or in excess of 350°C apparently results in self-annealing of at least part of this top silicon layer during implantation so as to produce a monocrystalline layer after annealing (9, 15).

For relatively low doses of nitrogen (*e.g.*, 1×10^{16} N^+ ion/cm^2), nitrogen readily diffuses in silicon at anneal temperatures as low as 900° and 1000°C. In particular, the nitrogen tends to diffuse toward and pile up at the surface silicon/native oxide interface and at the interface between the heavily damaged and single-crystal silicon layers (16, 17).

The purpose of this paper is to present microstructural and chemical results on the formation of a buried silicon nitride layer in <100> silicon wafers resulting from high dose, high temperature nitrogen ion implantation. The silicon wafers were implanted with a dose 7.5×10^{17} N^+ ion/cm^2 at 400°, 500°, or 600°C. The resulting wafers were then annealed at 1200°C, unless otherwise noted. The microstructure is documented by transmission electron microscopy (TEM) analysis, and the distribution and movement of nitrogen is monitored by secondary ion mass spectroscopy (SIMS).

Experimental Procedure

Silicon wafers of <100> orientation and of p-type doping with a resistivity of 10-12 Ω-cm were first oxidized to grow 25 nm of thermal SiO_2 on the wafer surfaces. The purpose of this oxide layer was to inhibit sputtering and minimize contamination of the underlying silicon surface during implantation. Some thinning of this top oxide layer was observed as a result of the implantation process. The wafers were implanted on an Eaton NOVA NV-10-160 high current ion implanter with a heated end station. The wafers were mechanically scanned and the temperature was monitored and controlled by a calibrated infrared detector. The wafers were preheated in the implanter to within 50°C of the desired implant temperature before initiating the implantation. Once the implantation started, the wafer temperature was maintained at the intended wafer temperature (±20°C) by a combination of ion beam heating, heat from the end station heaters, and compressed air cooling through the heater coils. The ion beam current was about 4.5 mA across an area of 6.5 cm^2, resulting in a localized beam current density of 0.7 mA/cm^2 at the wafer. The wafers were implanted at a 7° tilt at temperatures of 400°, 500°, or 600°C, with 7.5×10^{17} N^+ ion/cm^2 accelerated at a potential of 160 keV. The total implantation time for ten 100 mm wafers at a dose of 7.5×10^{17} N^+ ion/cm^2 was about 12h. Assuming a gaussian as-implanted nitrogen distribution, the peak nitrogen concentration for a dose of 7.5×10^{17} N^+ ion/cm^2 is 3.75×10^{22} N at./cm^3, which is about 69% of the nitrogen concentration of stoichiometric Si_3N_4, assuming a density of 3.18 g/cm^3 for α-Si_3N_4 (13). The wafers were left unannealed or subsequently annealed at 1100° or 1200°C in argon, with most anneals at the latter temperature. Those wafers which were annealed received 125 nm of chemical vapor deposited (CVD) SiO_2 in order to protect the wafer surfaces from possible oxidation during the high temperature anneal. The actual annealing procedure consisted of inserting the wafers into a furnace set at 1000°C, ramping the furnace temperature up to 1100° or 1200°C, annealing for the designated amount of time, ramping the furnace temperature down to 1000°C, and finally pulling the wafers from the furnace. About 50 min was required to ramp the furnace temperature from 1000° to 1200°C or from 1200° to 1000°C. Typical annealing times at 1100° or 1200°C were 2h, although shorter times were also used in order to determine the development of the annealed microstructure. The microstructure of the implanted nitrogen samples was studied by cross-sectional and planer transmission electron microscopy, using a Philips 400T TEM. The defect densities were determined from planer TEM specimens, with an operating g-vector of <400>. SIMS analysis was accomplished on a Cameca IMS-300 with an O_2^+ beam at a current of 500 nA. A 750 μm square was rastered and Si_2N^+ was monitored at a mass of 70 in order to determine the nitrogen profile. An O_2 bleed was supplied at the sample surface in order to minimize artifacts caused by changes in oxygen surface concentration. The lower detection limit of nitrogen in silicon by this SIMS technique was determined to be 6×10^{18} N at./cm^3.

Results

As-implanted structure.—The as-implanted microstructure, as determined by TEM cross-sectional analysis, may consist of as many as four distinct layers or regions, as shown in Fig. 1. The measured thicknesses of the top three layers as a function of implantation temperature are listed in Table I. The top layer consists of defective single-crystal silicon with a high dislocation density. Im-

Table I. As-implanted[a] layer thicknesses

Implantation temperature (°C)	Layer thicknesses (nm) A	B	C	D = B + C	E = A + B
600	165	165	85	250	330
500	150	55	195	250	205
400	170	0	245	245	170

A = Thickness of the top, highly defective single-crystal Si layer.
B = Thickness of the mottled single-crystal Si layer.
C = Thickness of the amorphous layer.
[a] Wafers were implanted with 7.5×10^{17} N^+ ion/cm^2 at 160 keV at the designated temperature.

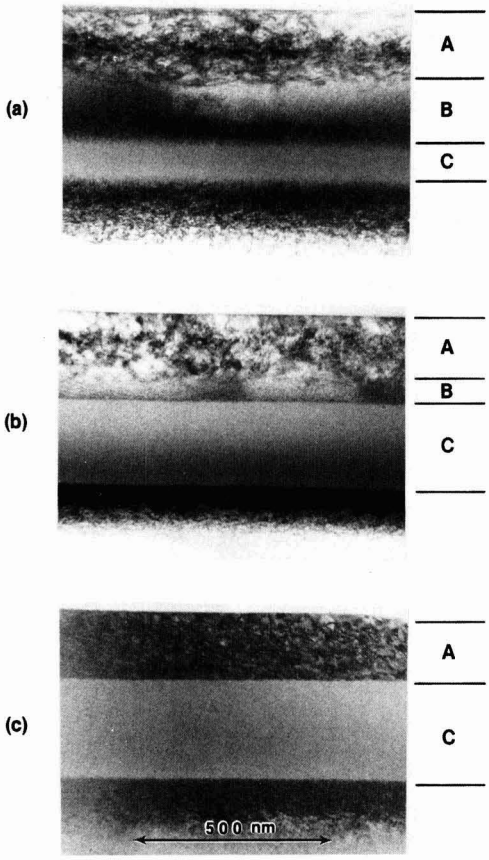


Fig. 1. TEM cross sections of silicon as implanted with 7.5×10^{17} N^+ ion/cm^2 at 160 keV and 600°C (a), 500°C (b), and 400°C (c). The letters next to the micrographs correspond to the column designations in Table I.

mediately under this top layer is a second layer, which has a mottled or textured appearance, particularly at or near the interface between this layer and the third layer, which is amorphous. Below the amorphous layer is a fourth layer consisting primarily of highly defective single-crystal silicon, although Fig. 1a indicates the presence of some of the mottled microstructure in the fourth layer next to the amorphous layer. This fourth layer is approximately 150 nm thick, regardless of the implant temperature, and corresponds to the lower tail of the implanted nitrogen profile.

The thickness of the top, highly defective single-crystal silicon layer is about 150-175 nm and is designated by the letter A in Table I and Fig. 1. The thickness of this top silicon layer is not a definitive function of the implantation temperature, as indicated in column A of Table I. The density of defects in this layer is on the order of 10^{10}-10^{11} dislocation/cm^2 and appears to be independent of the implantation temperature.

The second layer, designated by the letter B, is basically single-crystal silicon as determined by electron diffraction and various other electron microscopy techniques. Despite the mottled appearance of this layer, it contains no classical linear or planer defects, such as dislocations or stacking faults. Lattice imaging of one set of {111} planes in this layer reveals that these planes extend throughout this layer to the completely amorphous layer, except for small, included regions of amorphous material about 1-3 nm diam (see Fig. 2). These small amorphous regions are undoubtedly silicon with a high

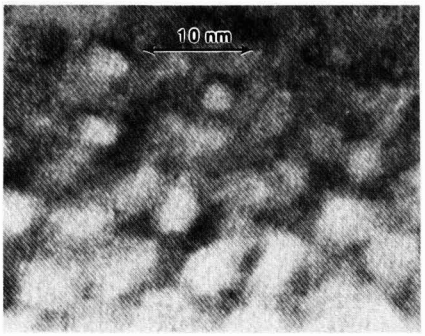


Fig. 2. TEM cross section of silicon as-implanted with 7.5×10^{17} N^+ ion/cm^2 at 160 keV and 600°C. One set of silicon {111} planes is imaged in the second layer near the interface between single-crystal layer and the buried amorphous layer.

concentration of nitrogen, although this hypothesis could not be quantitatively substantiated. The measured periodicity of the mottled microstructure is approximately 5 nm, as determined from micrographs similar to Fig. 1a. The approximate periodicity of the amorphous regions as observed in Fig. 2 is 5-7 nm. Thus, the mottled appearance of this layer in Fig. 1a and 1b is apparently due to the inclusion of small regions of amorphous material in a matrix of single-crystal silicon.

In the electron diffraction pattern corresponding to this layer, the silicon fundamental spots are surrounded by nearly symmetrical halos or rings of diffuse scatter as shown in Fig. 3. The diameters of these rings of diffuse scatter are indicative of a repeated structure with a periodicity of 5-7 nm. These numbers correspond to the periodicity of the mottled microstructure (Fig. 1a) and to the periodicity of the amorphous regions (Fig. 2). Thus, the nearly periodic nature of the mottled microstructure layer gives rise to diffuse scatter about the silicon fundamental spots in electron diffraction.

Below this mottled second layer is a completely amorphous layer, designated by the letter C in Fig. 1 and Table I. As indicated in column C of Table I, the thickness of the totally amorphous layer increases as the implantation temperature decreases. Conversely, the mottled single-crystal silicon layer becomes thinner and ultimately nonexistent at 400°C (Fig. 1c). Examination of column D of Table I indicates that the sum of the mottled and amorphous layer thicknesses is nearly constant as a function of the implantation temperature. Thus, as the implant temperature decreases, the thickness of the amorphous layer increases at the expense of the thickness of the mottled silicon layer. Also, as the implant temperature decreases, the interface between the amorphous layer and the above single-crystal layer becomes more abrupt (*cf.* Fig. 1a-1c).

SIMS analysis of the as-implanted nitrogen distribution indicates that the nitrogen profile is slightly nongaussian with a higher concentration nitrogen tail toward the surface of the silicon wafer than toward the bulk of the wafer

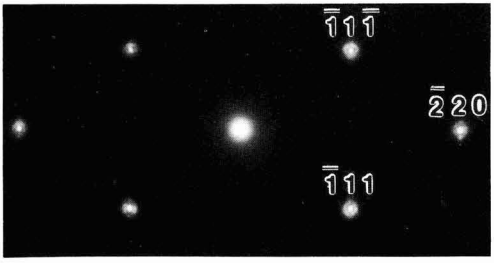


Fig. 3. Silicon <110> diffraction pattern corresponding to the mottled, second layer in Fig. 1a. Rings of diffuse scatter are observed around the fundamental spots.

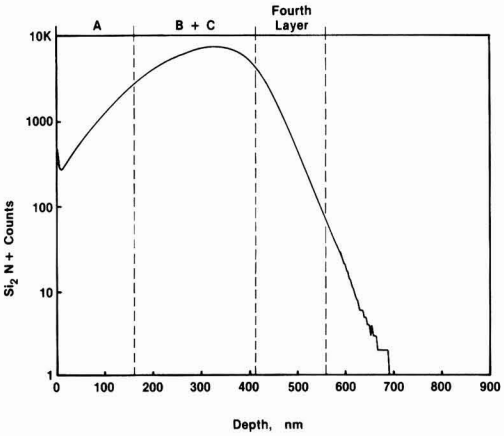


Fig. 4. Nitrogen profile in a <100> silicon wafer implanted with a dose of 7.5×10^{17} N^+ ion/cm^2 at 160 keV. The approximate thicknesses of the various layers observed in the as-implanted microstructures are indicated by the dotted lines. See Table I for an explanation of letters A, B, and C. The "fourth layer" is the highly defective layer below the amorphous layer.

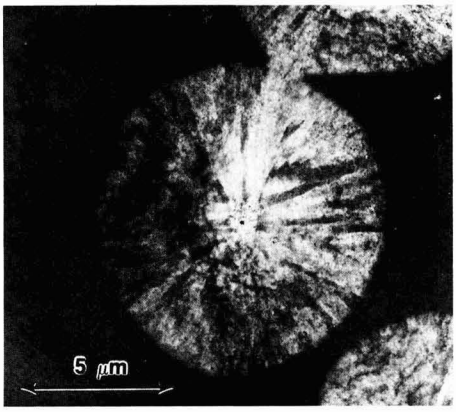


Fig. 5. Planer view of the partially crystallized Si_3N_4 layer in silicon implanted with 7.5×10^{17} N^+ ion/cm^2 at 160 keV and 600°C. The specimen has been annealed at 1200°C for 10 min in argon. Low angle grain boundaries are present between the grains emanating from a common nucleation site. A large angle grain boundary has formed where grains from two adjacent nucleation sites have impinged upon each other.

(see Fig. 4). The general shape of this distribution is typical of a light element implanted at high energies into a heavier element target in which the primary mechanism of ion stopping is electronic interactions between the ions and the atoms. A Si_2N^+ count value of 10K in Fig. 4 corresponds to an approximate nitrogen concentration of 3×10^{22} N at./cm^3. As can be seen in Fig. 4, the as-implanted nitrogen peak concentration is less than that predicted by a strictly gaussian distribution. This discrepancy is obviously due to skewness of the nitrogen distribution and to the slight nitrogen pile up at the SiO_2/Si interface. The nitrogen profiles are virtually identical for wafers implanted at 600° and 400°C, implying that the as-implanted nitrogen profile is not a function of the implant temperature. Also, there is no substantial diffusion of nitrogen at 600°C for implantation times as long as 12h. The approximate locations of the various layers tabulated in Table I, as well as the location of the highly defective fourth layer, are indicated in Fig. 4.

Development of the annealed structure.— Upon annealing the as-implanted silicon wafers at 1200°C for 2h a continuous layer of buried, polycrystalline α-Si_3N_4 forms under a single-crystal silicon layer which has a relatively low defect density. Before proceeding on to a detailed examination of the microstructures of the top silicon and the buried silicon nitride layers, it is helpful to see how the final annealed SOI structure develops from the as-implanted structure. In order to ascertain this development, nitrogen-implanted silicon wafers were annealed at 1200°C for times ranging from 10 min to 2h.

The first event to occur is the nucleation and growth of the polycrystalline α-Si_3N_4 phase within the amorphous layer of the as-implanted structure. The particular crystalline phase of silicon nitride was determined by electron diffraction. The α-Si_3N_4 phase nucleates at discrete points and grows in a radial manner out from a given nucleation site within the plane of the buried amorphous layer (see Fig. 5). As a given α-Si_3N_4 nucleus grows within the amorphous layer, it divides into numerous grains separated by low angle grain boundaries, as determined by electron diffraction and microstructural analysis. The low angle grain boundaries appear to form within a few hundred nanometers of the nucleation site. Eventually, Si_3N_4 grains from adjacent nucleation sites impinge upon each other and form high angle grain boundaries at the points of impingement, as shown in the upper portion of Fig. 5.

For wafers implanted at 600°C, the horizontal growth front of the α-Si_3N_4 spans the entire thickness of the amorphous layer. Also, for wafers implanted at 600°C, 20-30% of the amorphous layer is crystallized after 10 min at 1200°C, and the layer has completely crystallized after 2h at 1200°C. The horizontal growth rate of the α-Si_3N_4 phase within the amorphous layer at 1200°C is estimated at 200-400 nm/min. The time necessary to completely crystallize the buried silicon nitride layer depends not only on the growth rate, but also on the nucleation rate of the α-Si_3N_4 phase within the amorphous layer.

After the α-Si_3N_4 phase forms within the amorphous layer, a dendritic structure develops perpendicularly to the plane of the buried nitride layer for implant temperatures of 500° and 600°C. This dendritic structure starts to form a few hundred nanometers behind the growth front of the silicon nitride phase at the interface between the amorphous layer and the mottled layer of the as-implanted structure. The dendritic structure is more pronounced (*i.e.*, the dendrites are longer) along the top Si/Si_3N_4 interface than along the lower interface for reasons which will be discussed later. Also, the dendritic structure is more pronounced for wafers implanted at 600°C than at 500°C. As the silicon nitride dendrites grow into the mottled silicon layer, the mottled microstructure is transformed to that of defect-free single-crystal silicon, as shown in Fig. 6. The growth front of the silicon nitride in the amorphous layer is to the left of the left edge of the micrograph in Fig. 6. Notice that some of the mottled microstructure is still present in the left portion of the micrograph, but is absent in the right portion of the micro-

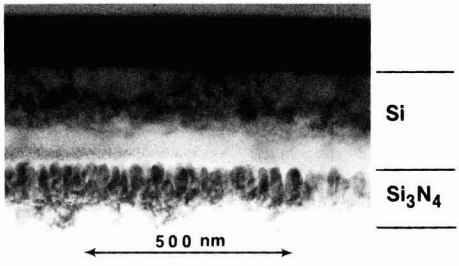


Fig. 6. TEM cross section of silicon implanted with 7.5×10^{17} N^+ ion/cm^2 at 160 keV and 600°C, and subsequently annealed at 1200°C for 10 min in argon. The mottled microstructure just above the α-Si_3N_4 layer is present in the left portion of the micrograph nearest the amorphous-to-crystalline α-Si_3N_4 growth front but is absent in the right portion of the micrograph.

graph. This transformation of the mottled microstructure to that typical of defect-free single-crystal silicon occurs only after the nucleation and growth of the underlying α-Si_3N_4 phase. Thus, in the right portion of Fig. 6 an intermediate microstructure has developed consisting of highly defective top silicon layer retained from the as-implanted microstructure, an intermediate, defect-free single-crystal silicon layer, and a bottom, polycrystalline α-Si_3N_4 layer, with a dendritic or cellular structure prominent along the top interface. Continued annealing at 1200°C results in the elimination of the highly defective top silicon layer and the formation of single-crystal silicon with a substantially lower dislocation density (see Fig. 7).

During the 1200°C anneal, the top silicon layer regrows to form a thin layer of <100>-oriented single-crystal silicon with a dislocation density on the order of 5×10^8 dislocation/cm^2. This dislocation density is nearly independent of the implantation temperature for wafers annealed at 1200°C, but it is much lower than the 10^{10}-10^{11} dislocation/cm^2 in the top silicon layer of the as-implanted specimens. The dislocations in the regrown silicon layer extend from the crystalline nitride layer to the free surface of the silicon layer and are the only observable defects for wafers implanted at 500° or 600°C. Burger's vector analysis indicates that these dislocations are primarily screw in nature.

For the 600°C implant temperature, the α-Si_3N_4 dendrites grow into the mottled silicon layer, but not all of this layer is consumed by the α-Si_3N_4 phase. This is demonstrated by the fact that for the 600°C implant temperature the thickness of the final top silicon layer (column F, Table II) is greater than the thickness of layer A (column A, Table I), but less than the combined thickness of layers A and B (column E, Table I).

For wafers implanted at 400°C and annealed at 1200°C, silicon twins are also observed in the top silicon layer in addition to the dislocations. These twins lie along the silicon {111} planes and begin at about 170 nm below the silicon surface and extend down to the silicon nitride layer. The twins do not extend all the way through the top silicon film. The twin nature of these planar defects in Fig. 7c was confirmed by the observation of {111} twin spots in electron diffraction patterns of the top silicon film.

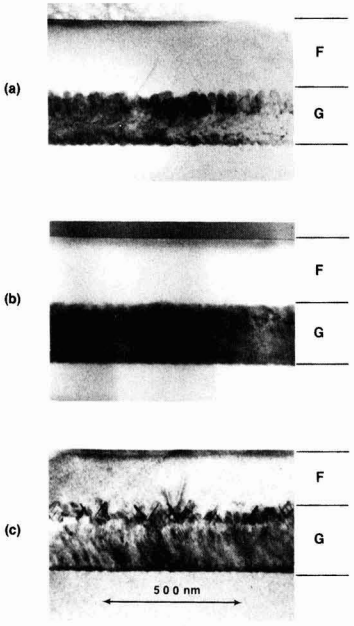


Fig. 7. TEM cross sections of silicon implanted with 7.5×10^{17} N$^+$ ion/cm^2 at 160 keV and 600°C (a), 500°C (b), and 400°C (c), and subsequently annealed at 1200°C for 2h in argon. The letters next to the micrographs correspond to the columnn designations in Table II.

The final microstructure after a 1200°C, 2h anneal consists of a top layer of single-crystal silicon over a buried layer of α-Si_3N_4 for all of the implant conditions investigated. TEM cross sections of silicon implanted at 600°, 500°, or 400°C and subsequently annealed at 1200°C for 2h are shown in Fig. 7a-7c. The thicknesses of the top silicon layer and of the polycrystalline silicon nitride layer are 215-240 and 180-195 nm, respectively (see columns F and G of Table II). These thicknesses do not appear to be dependent on the implantation temperature. However, the overall thickness of the top silicon layer plus the buried silicon nitride layer remains nearly constant with implantation temperature (column H of Table II). Notice that at least for the higher implant temperatures that no highly defective intermediate layer forms just above the buried insulator as in the case of SOI by ion-implanted oxygen (6).

For wafers implanted at 600°C but annealed at 1100°C, the silicon nitride does not crystallize except at gross defects, such as at pits in the top silicon layer. In those scattered instances where the silicon nitride does crystallize, it does so in a manner similar to that at 1200°C. Since the silicon nitride generally does not crystallize at 1100°C, the top silicon layer retains the high density of defects resulting from the nitrogen implantation. These results, along with the above annealing results at 1200°C, indicate that the crystallization of the silicon nitride layer is a prerequisite for the regrowth of the top silicon layer into low defect density silicon.

Nitrogen redistribution.—The redistribution of nitrogen in the silicon as a function of annealing time at 1200°C is shown in Fig. 8. Compare this with Fig. 4. The silicon wafers were implanted with 7.5×10^{17} N$^+$ ion/cm^2 at 160 keV at a temperature of 600°C and subsequently annealed. The ordinate of these graphs is in units of Si_2N^- counts, which is a measure of the nitrogen concentration in the silicon wafer. Again, a value of 10K Si_2N^- counts, approximately corresponds to a nitrogen concentration of 3×10^{22} N at./cm^3.

After annealing for only 10 min, the nitrogen concentration profile in Fig. 8a displays three distinct peaks. A surface nitrogen peak and a high, broad peak corresponding to the buried silicon nitride layer are readily observed. A slight shoulder is observed on this peak towards the surface of the wafer, and this is believed to correspond to the silicon nitride dendritic structure growing towards the wafer surface. As noted above, the silicon nitride begins to crystallize after only 10 min at 1200°C, and the dendritic structure forms immediately behind the crystallization front. Between the surface nitrogen peak and the peak corresponding to the buried silicon nitride layer is a third nitrogen peak. The concentration of nitrogen at the apex of this peak is lower than the as-implanted nitrogen concentration at this depth (*cf.*, Fig. 4 and 8a). This intermediate nitrogen peak results from the diffusion of nitrogen from this region to either the Si/SiO_2 interface at the silicon surface or to the buried polycrystalline silicon nitride layer. This intermediate nitrogen peak decays with annealing time until it is

Table II. Annealed[a] Si/Si_3N_4 layer thicknesses

Implantation temperature (°C)	Layer thicknesses (nm) F	G	H = F + G
600	240	180	415
500	215	195	415
400	215	190	405

F = Thickness of the top single-crystal Si layer.
G = Thickness of the polycrystalline Si_3N_4 layer.
[a] Wafers implanted with 7.5×10^{17} N$^+$ ion/cm^2 at 160 keV and at the designated temperature were annealed at 1200°C for 2h in argon.

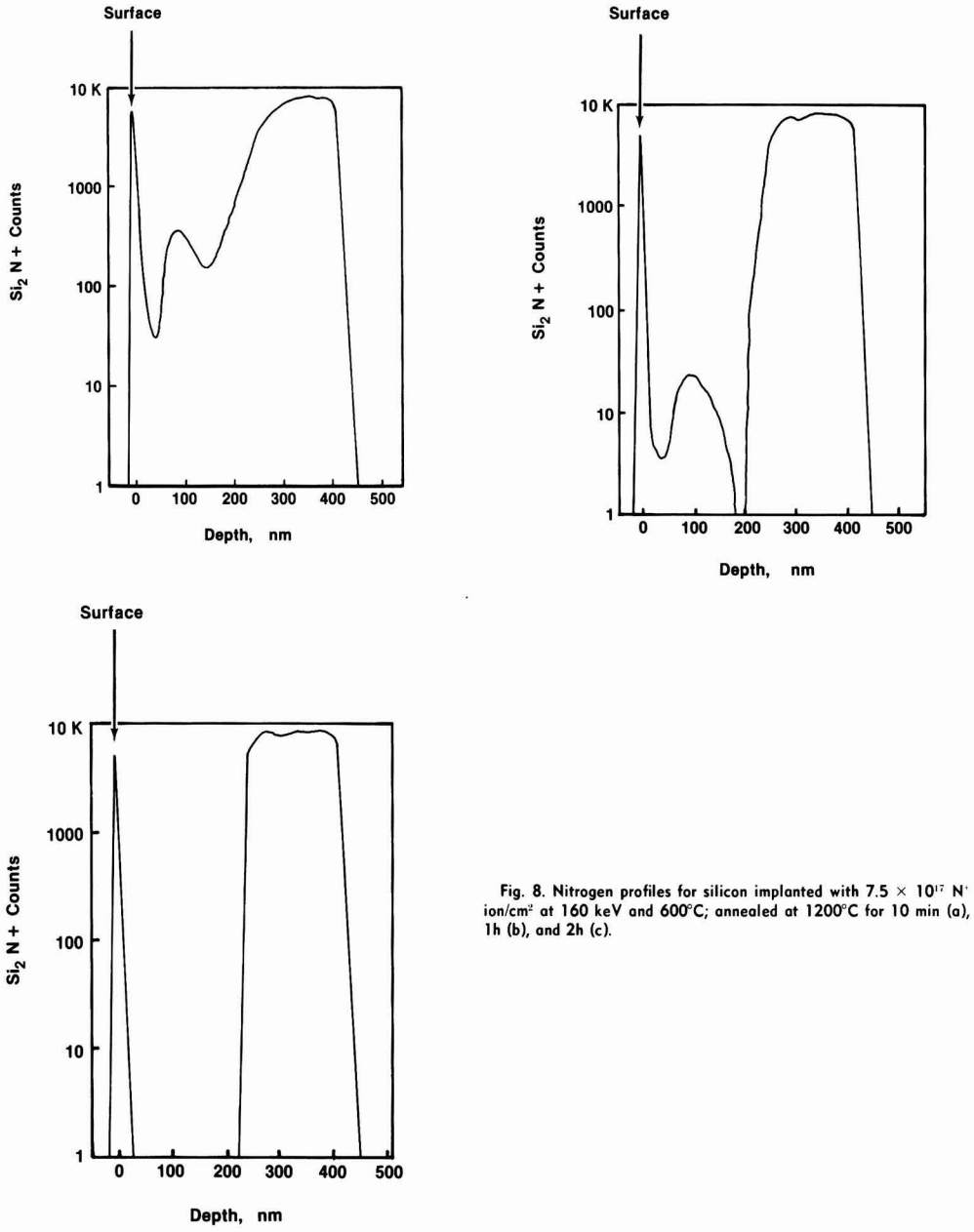


Fig. 8. Nitrogen profiles for silicon implanted with 7.5×10^{17} N^+ ion/cm^2 at 160 keV and 600°C; annealed at 1200°C for 10 min (a), 1h (b), and 2h (c).

less than 6×10^{18} N at./cm^3 (the detection limit of SIMS) for an anneal time of 2h as indicated in Fig. 8c. After a 1h anneal, the nitrogen concentration just above the buried Si/Si_3N_4 interface is substantially lower than the nitrogen concentration in the silicon next to the nitrogen peak at the Si/SiO_2 interface. Thus, the polycrystalline buried nitride layer acts as a better sink for nitrogen than the top Si/SiO_2 interface.

Close examination of the surface of the silicon wafer after a 2h 1200°C anneal did not reveal the presence of any polycrystalline silicon nitride. However, attempts to strip the pyrolytic oxide from the silicon wafers after the 2h anneal required the use of 49% HF for 1-2 min before the wafers would dewet. A solution of five parts NH_4OH to one part HF (5:1 BHF) did not dewet the wafers at 10 min of etching time. These results along with similar results reported by Josquin (13, 14) suggest that an amorphous silicon nitride film forms at the Si/SiO_2 interface.

Discussion

The as-implanted microstructures resulting from the experimental conditions of this investigation basically consist of a buried amorphous layer under a layer of single-crystal silicon for all implant temperatures studied. The formation of an amorphous layer by ion implantation is enhanced by high ion doses, high damage density, low implant temperatures, and by the implantation of a heavier element into a lighter target material (18). A model for amorphizing silicon by ion implantation by Morehead and Crowder (19) predicts that, for an implant

temperature of about 350°C or more, an amorphous layer should not form for any dose of nitrogen in silicon. Their model, however, does not quantitatively consider the effect of dose rate (ion beam current density); nor is the effect of substantial changes in the composition of the silicon resulting from high dose implants considered. They do suggest that higher dose rates will favor the formation of an amorphous layer at higher implant temperatures.

As previously noted, Zimmer and Vogt (9) found for nitrogen doses of 1.3×10^{18} N^+ ion/cm^2 at 150 keV that an amorphous layer extending to the silicon surface forms at implant temperatures below 350°C. Upon annealing such a structure, a top layer of polycrystalline silicon forms. However, if the implant temperature is in excess of 350°C, sufficient self-annealing presumably occurs to maintain a surface layer of monocrystalline silicon from which the remaining silicon recrystallizes during annealing. Based upon Rutherford backscattering data, Bourguet *et al.* (15) suggest that for a dose of 2×10^{17} N^+ ion/cm^2 a buried amorphous layer forms, but that this amorphous layer extends to the surface of the wafer for a dose of 2×10^{18} N^+ ion/cm^2 for an implant energy of 180 keV at or near room temperature.

The results of this study indicate that a buried amorphous layer forms at elevated implant temperatures (400°-600°C) and at a dose of 7.5×10^{17} N^+ ion/cm^2. Since the wafers at all three implant temperatures were implanted at the same dose rate and the nitrogen profiles are identical for wafers implanted at 400° and at 600°C, the differences in the as-implanted microstructures observed in Fig. 1a-1c are due solely to differences in the implant temperature. Clearly, the formation, thickness, and position of the buried amorphous layer is a function of the implant temperature.

For an implant temperature of 400°C, the center of the amorphous layer corresponds to the projected damage peak for nitrogen implanted into silicon at 160 keV as calculated from the model of Sigmund and Sanders (20). Based upon their model, the projected damage peak is at 81% of the projected nitrogen ion range or at about 295 nm for 160 keV. Thus, the center of the amorphous layer at 400°C corresponds to the region of maximum implant damage.

As the implant temperature increases, the amorphous layer appears to become thinner and a single-crystal layer with a mottled microstructure begins to form. This mottled layer forms primarily between the amorphous layer and the top highly defective single-crystal silicon layer, although some of this mottled microstructure also forms below the amorphous layer (Fig. 1a). Examination of the thickness data in column D in Table I indicates that the sum of the mottled and amorphous layer thicknesses is nearly constant as a function of the implant temperature. Thus as the implant temperature increases, the thickness of the mottled layer increases at the expense of the amorphous layer. Since this mottled layer is defect-free single-crystal silicon, except for 1-3 nm diam regions of amorphous material, the elevated implant temperatures apparently promote the *in situ* recrystallization of a portion of the amorphous layer during the nitrogen implantation. At 600°C, the center of the amorphous layer corresponds to the projected range or the peak nitrogen concentration of as-implanted N^+ ions into silicon at 160 keV. Given the asymmetry of the as-implanted nitrogen concentration profile (Fig. 4), and the fact that the mottled microstructure forms predominately above the amorphous layer, the extent to which the mottled layer forms at a given implant temperature appears to be a function of the local nitrogen concentration. In particular, as the implant temperature increases, a higher nitrogen concentration is required to insure the retention of a buried amorphous layer. Conversely, as the implant temperature increases, the mottled layer is capable of incorporating a larger concentration of nitrogen.

The development of the final annealed microstructure proceeds first by the crystallization of the amorphous layer into polycrystalline silicon nitride, and then by the changing of the mottled layer into normal single-crystal silicon with no amorphous pockets (at implant temperatures of 500° and 600°C). Finally, the highly defective top single-crystal silicon layer transforms to single-crystal silicon with a relatively low density of dislocations which span the entire thickness of the top silicon layer. Once the polycrystalline silicon nitride forms, it acts as a sink for the diffusion of nitrogen from the surrounding silicon, particularly for the top silicon layer. As the nitrogen diffuses towards this buried layer, a silicon nitride dendritic structure forms along the Si/Si_3N_4 interface, indicative of morphological instability along this interface. Concurrent with the development of this dendritic structure is the disappearance of the mottled microstructure. This indicates that the 1-3 nm regions of amorphous material may be rich in nitrogen compared to the surrounding silicon matrix. As the nitrogen thus diffuses out of the amorphous pockets in the mottled layer, the silicon lattice relaxes to its perfect state.

For silicon implanted at 600°C and annealed at 1200°C, the dendritic structure is more prominent along the upper Si/Si_3N_4 interface than along the lower interface. This is due more to the lower nitrogen concentration gradient above the amorphous layer than below it, as indicated in Fig. 4. As the silicon nitride crystallizes, the nitrogen in the silicon along the back Si/Si_3N_4 interface of the amorphous layer is rapidly depleted, thus minimizing the development of the dendritic structure. However, along the top Si/Si_3N_4 interface, the dendrites grow into silicon which has a more gradually decreasing nitrogen concentration gradient. Hence, a more prominent dendritic structure develops along this interface. As the implantation temperature increases from 500° to 600°C, the dendritic structure becomes more prominent. This is because the dendritic growth starts at the interface between the amorphous silicon layer and the mottled layer. At higher implant temperatures, this interface is closer to the projected range of the nitrogen and, hence, at a higher nitrogen concentration. Consequently, the dendrites associated with the higher implant temperature start deeper within the silicon and grow farther towards the top surface before the lack of nitrogen inhibits their growth.

In order to understand the development of the various annealed microstructures (Fig. 7a-7c) from their respective as-implanted microstructures (Fig. 1a-1c), it is necessary to examine the pertinent data from Tables I and II as plotted in Fig. 9. In Fig. 9, the total thickness of the top silicon layer for both the as-implanted (Table I, column E) and the annealed (Table II, column F) microstructures is plotted as a function of the implant temperature. For the 600°C implant temperature, the annealed top silicon layer is considerably thinner than the total thickness of the initial single-crystal layers. Consequently, upon annealing,

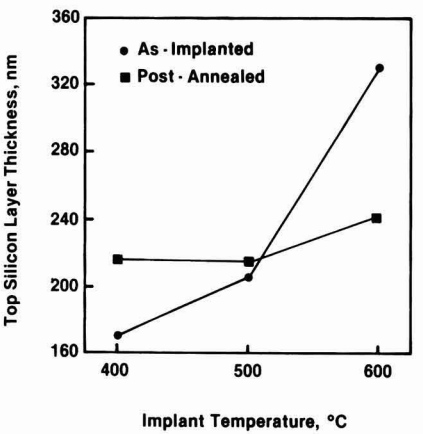


Fig. 9. The total as-implanted and annealed silicon layer thicknesses as a function of the implant temperature.

the α-Si_3N_4 grows dendritically into the mottled layer. For an implant temperature of 500°C, the final silicon layer is of virtually the same thickness as the total top silicon layers in the as-implanted microstructure. As a result, there is virtually no dendritic silicon nitride growth into the mottled silicon layer (see Fig. 7b). For an implant temperature of 400°C, the thickness of the top silicon layer is greater than the thickness of the top silicon layer in the as-implanted microstructure. Consequently, the top silicon layer grows down into the amorphous layer during the anneal. The extent of this silicon growth is about 45 nm, which is approximately the distance of vertical growth of the twins observed in Fig. 7c. Also, the upper extent of the twins in Fig. 7c is located at the position of the interface between the amorphous and single-crystal silicon layers in Fig. 1c. Thus, the regrowth of the top silicon layer for an implant temperature of 400°C and a subsequent anneal at 1200°C is characterized by a twinned microstructure. Based upon this data and the microstructures in Fig. 7, the optimum implant temperature for the studied nitrogen dose and implant energy is about 500°C. At this temperature, the α-Si_3N_4 dendritic growth is minimized and the silicon twins do not form.

The mechanism whereby the final, low dislocation density top silicon film develops is not understood at this time. In particular, the manner in which the high density of defects in the top silicon layer of the as-implanted microstructures (at all implant temperatures) migrate from the silicon is unknown. It is known, however, that the crystallization of the amorphous layer to α-Si_3N_4 is a prerequisite for the formation of the low defect density top silicon layer. Thus the high defect density in the top, as-implanted silicon layer is probably associated with a relatively high concentration of nitrogen in the silicon. As the nitrogen concentration deceases from the top silicon layer, the defect density in this layer correspondingly decreases.

Also unknown at this point is the reason for the formation of the dislocations which form in the top silicon layer and span the entire thickness of this layer. Since the density of these dislocations is independent of the implant temperature, they do not appear to be a function of the as-implanted microstructure for the temperature range of this study. These dislocations could form from the defects in the as-implanted silicon. They could also be due to plastic deformation of the silicon resulting from differences in the thermal expansion coefficients of silicon and alpha silicon nitride. A third possibility is that the dislocations could be due to the difference in the atomic volumes of implanted silicon and the resulting crystalline silicon nitride. Despite their presence, the dislocation density in the top silicon layer of nitrogen-implanted and annealed silicon as described above is relatively low compared to the defect density in the as-implanted microstructure.

The nitrogen profiles as a function of anneal time at 1200°C (Fig. 8) indicate that the implanted nitrogen diffuses to the top Si/SiO_2 interface and to the buried polycrystalline silicon nitride layer. This buried α-Si_3N_4 layer is a better diffusion sink for nitrogen than the nitride layer at the top Si/SiO_2 interface. In particular, the nitrogen profile for implanted silicon annealed at 1200°c for 1h (Fig. 8b) indicates that the equilibrium nitrogen concentration in silicon in contact with crystalline alpha silicon nitride is lower than for the amorphous silicon nitride at the Si/SiO_2 interface. The silicon nitride layer at the Si/SiO_2 interface is amorphous since no polycrystalline material is observed via TEM. Also, it is not known if this nitride is stoichiometric Si_3N_4. However, Josquin (16, 17) has shown that this nitride layer is capable of inhibiting silicon oxidation.

A comparison of the nitrogen in Fig. 4 and 8a indicates that the peak annealed nitrogen concentration is only slightly greater than the peak as-implanted nitrogen concentration. As previously noted, a value of 10K Si_2N^+ counts corresponds to a nitrogen concentration of 3×10^{22} N at./cm³. The fact that the peak nitrogen concentrations are virtually identical implies that the silicon nitride may not be fully dense or that it may have a lower density than anticipated from Ref. (13). This explanation would not be too unreasonable, since the buried nitride has numerous high and low angle grain boundaries. Another explanation for the lower than expected nitrogen concentration in the annealed silicon nitride may by that the nitride has a high solid solubility for silicon, since no silicon precipitates were observed in this layer by electron diffraction.

Conclusions

Both the as-implanted and the postannealed microstructures of silicon implanted with 7.5×10^{17} N^+ ion/cm² at 160 keV are a function of the implant temperature in the range of 400°-600°C. Within this implant temperature range, the as-implanted microstructure consists of a highly defective monocrystalline top silicon layer and a buried amorphous layer.

At implant temperatures of 500° and 600°C, a mottled microstructure forms between the top, highly defective silicon layer and the buried amorphous layer at the expense of the amorphous layer. This mottled layer is single-crystal silicon except for the inclusion of small (1-3 nm) regions of amorphous silicon. The mottled layer apparently results from the recrystallization of the amorphous layer during implantation. The extent to which this mottled layer forms is a function of the implant temperature and of the local nitrogen concentration.

Annealing at 1200°C results in a continuous buried nitride layer and the formation of a top silicon layer with a relatively low density of dislocations. The buried nitride layer forms by the precipitation of a α-Si_3N_4 phase throughout the amorphous layer. This is followed by the dendritic growth of the α-Si_3N_4 phase partially into the mottled silicon layer for silicon implanted at 500° and 600°C. For silicon implanted at 400°C, the top silicon layer grows towards the buried nitride layer, rather than the silicon nitride growing towards the top surface. For all of the above implant temperatures, the final thickness of the top silicon layer is 215-240 nm.

The formation of the polycrystalline silicon nitride layer is a prerequisite for the regrowth of the top layer into low defect density silicon. The high density of defects in the as-implanted top silicon layer migrate out of the silicon as the nitrogen concentration decreases in this layer.

The final annealed top silicon layer is characterized by dislocations which span the entire thickness of the silicon layer. The density of these dislocations is about 5×10^8 dislocation/cm² and appears to be independent of the implant temperature. The regrown silicon resulting from the 400°C implant is characterized by growth twins at the top Si/Si_3N_4 interface, in addition to the dislocations.

From a microstructural viewpoint, the absence of growth twins and the minimization of the silicon nitride dendritic growth imply that 500°C is an optimum implant temperature for the formation of SOI by implanted nitrogen.

Although the as-implanted microstructure is a function of the implant temperature, the actual as-implanted nitrogen distribution is independent of the implant temperature. During the 1200°C anneal, the nitrogen in the top silicon layer diffuses towards the precipitated α-Si_3N_4 layer and towards the top silicon/SiO_2 interface. The silicon nitride layer along this top interface does not crystallize during the 1200°C anneal.

The results of this study also indicate that a nitrogen dose substantially less than predicted for a stoichiometric silicon nitride layer may result in a continuous buried insulator. This is due to the diffusion of part of the nitrogen from the surrounding silicon to the polycrystalline buried silicon nitride.

Acknowledgments

The authors wish to acknowledge S. Kingsland for his work in implanting the wafers and G. Blanchard for conducting the SIMS analysis. The encouragement of J.

Wursthorn and useful discussions with J. Lasky are also appreciated.

Manuscript submitted March 4, 1985; revised manuscript received May 9, 1985.

IBM Corporation assisted in meeting the publication costs of this article.

REFERENCES

1. G. W. Cullen, Editor, *J. Cryst. Growth*, **63,** 429 (1983).
2. H. W. Lam, *1983 IEDM Tech. Dig.*, 348 (1983).
3. "Comparison of Thin Film Transistor and SOI Technologies," H. W. Lam and M. J. Thompson, Editors, Materials Research Society Symposia Proceedings, Vol. 33, Elsevier Science Publishing Co. Inc., New York (1984).
4. C.-E. Chen, T. G. W. Blake, L. R. Hite, S. D. S. Malhi, B.-Y. Mao and H. W. Lam, *1984 IEDM Tech. Dig.*, 702 (1984).
5. D. J. Foster, A. L. Butler, and P. H. Bolbot, *ibid.*, 704 (1984).
6. C. G. Tuppen, M. R. Taylor, P. L. F. Hemment, and R. P. Arrowsmith, *Appl. Phys. Lett.*, **45,** 57 (1984).
7. R. F. Pinizzoto, *J. Cryst. Growth*, **63,** 559 (1983).
8. Y. Homma, M. Oshima, and T. Hayashi, *Jpn. J. Appl. Phys.*, **21,** 890 (1982).
9. G. Zimmer and H. Vogt, *IEEE Trans. Electron Devices*, **ed 30,** 1515 (1983).
10. S. Maeyama and K. Kajiyama, *Jpn. J. Appl. Phys.*, **21,** 744 (1982).
11. T. Hayashi, H. Okamoto, and Y. Homma, *ibid.*, **19,** 1005 (1980).
12. M. R. Taylor, C. G. Tuppen, R. P. Arrowsmith, R. M. Dobson, A. E. Glaccum, M. C. Wilson, G. R. Booker, and P. Hemment, in "Microscopy of Semiconductor Materials Conference," p. 485, Institute of Physics Conference Series 67, Institute of Physics, London (1983).
13. P. Popper and S. N. Ruddlesden, *Trans. Br. Ceram. Soc.*, **60,** 603 (1961).
14. T. Tsujide, M. Nojiri, and H. Kitagawa, *J. Appl. Phys.*, **51,** 1605 (1980).
15. P. Bourguet, J. M. Dupart, E. Le Tiran, P. Auvray, A. Guivarc'h, M. Salvi, G. Pelous, and P. Henoc, *J. Appl. Phys*, **51,** 6169 (1980).
16. W. J. M. J. Josquin, *Nucl. Instrum. Meth.*, **209/210,** 581 (1983).
17. W. J. M. J. Josquin and Y. Timminga, *This Journal*, **129,** 1803 (1982).
18. J. F. Gibbons, *Proc. IEEE*, **60,** 1062 (1972).
19. F. F. Morehead, Jr., and B. L. Crowder, in "Proceedings of the 1st Conference on Ion Implantation." L. Chadderton and F. Eisen, Editors, pp. 25-30, Gordon and Breach, New York (1971).
20. P. Sigmund and J. B. Sanders, in "Proceedings of the International Conference on Applications of Ion Beams to Semiconductor Technology." P. Glotin, Editor, pp. 215-233, Editions Ophrys, Grenoble, France (1967).
21. Y. Yatsurugi, N. Akiyama, Y. Endo, and T. Nozaki, *This Journal*, **120,** 975 (1973).

Sidewall-Tapered Oxide by Plasma-Enhanced Chemical Vapor Deposition

Gregory C. Smith* and Andrew J. Purdes*

Texas Instruments, Incorporated, Semiconductor Process and Design Center, Dallas, Texas 75265

ABSTRACT

Plasma-enhanced chemical vapor deposition (PECVD) was used to deposit SiO_2 layers with tapered sidewalls on silicon-doped aluminum steps. The deposition rates ranged from several hundred to 2000 Å/min. The plasma deposition process was performed in a single-wafer reactor, although the process is compatible with batch processing. The sidewall angles of up to 30° to the vertical are formed by the angular dependence of the sputter etch yield due to ion bombardment. A large negative bias voltage with respect to the plasma is maintained at the substrate during the low pressure process.

The topography of deposited dielectrics has become increasingly important as lateral device dimensions approach, and in some cases become smaller than, the heights of topographical features on VLSI devices. The importance of dielectric surface topography stems primarily from the need to coat the dielectric layer conformally with metal and then to etch the metal cleanly. Dielectric films deposited by sputtering or PECVD without strong ion bombardment have surface topography which can be represented by Fig. 1. This profile is the result of shadowing, which causes low deposition rates at the corners near the bottom of steps relative to the rates at the top (1). This results in the reentrant surfaces and cracks seen in Fig. 1. The deposited dielectric can be planarized by applying resist and etching back to replicate the smoothness of the resist surface in the oxide remaining after etch. However, voids can be opened where the reentrant surfaces had closed on themselves during the deposition. If the dielectric topography of Fig. 1 is not planarized before deposition of the metal by evaporation or sputtering of the metal, conductors will be discontinuous on the reentrant dielectric surfaces as a result of shadowing.

Chemical vapor deposition of the subsequent metal can be successful in producing conformal films on even reentrant dielectric surfaces (2). This solves the open-circuit problem but may result in shorting of adjacent etched conductors because the anisotropic etch of the metallization layers is shadowed by the overhanging dielectric. Hence, regardless of the subsequent metal deposition method, reentrant-deposited dielectric topography is unacceptable.

A well-established method for developing tapered oxide sidewalls during the deposition process is bias sputtering. Bias sputtering of quartz uses sputter etching of the depositing oxide surfaces to tailor the topography of the sputtered film. The sputter etching of the wafers during the deposition is accomplished by providing RF power to the substrate plate from a separate power supply or a power split with the target. Sputter etch rates are maximum for surfaces oriented at about 45° to the incoming ion flux. The steady-state surface topography under sputter etching is either a surface oriented normal to the incoming ion flux or one oriented at a 45° angle to the flux (3, 4). If sputter etching and sputter deposition are done simultaneously, the resulting topography will resemble that of Fig. 2. To completely planarize the oxide, a thick deposition with the topography of Fig. 2 can be made. Then the sputter etch rate is increased so that the net deposition rate on the sloped surfaces is zero, burying the protrusions with a planar film (4). However, planarization can take hours, depending upon the lateral dimensions of the largest circuit feature, and may not be required if the topography of Fig. 2 is acceptable. In these experiments on plasma-deposited films, only tapering of the sidewall was attempted.

* Electrochemical Society Active Member.

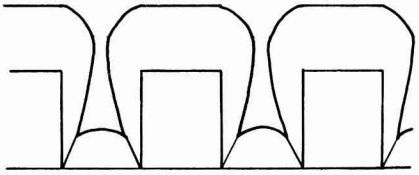


Fig. 1. Breadloafed plasma-deposited oxide over metal steps

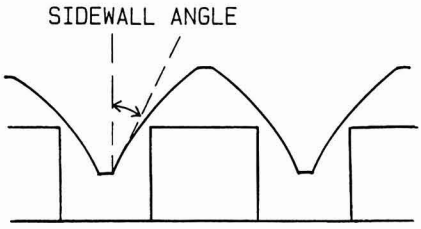


Fig. 2. Sidewall-tapered oxide over metal steps

The topography shown in Fig. 2 has liabilities when compared with conformal film topography or with full planarization. With tapered oxide, the top corner of the underlying metal is isolated from the subsequent metal layer by only a thin insulator, resulting in large capacitance between metal layers and possible reliability problems resulting from film cracking and charge leakage. Also, the bottom of the sidewall is displaced from the underlying metal edge by an amount greater than the average dielectric thickness, consuming valuable chip area. However, unlike planarization, tapering allows contacts cut to the top and bottom of steps to be the same depth. This eliminated the necessity for overetching the contacts to the step tops in order to clear the deep contacts. The problems of poor step coverage and shorts in metal subsequently deposited and etched on conformal oxides will be reduced on sidewall-tapered oxide.

Most of the problems of bias sputtering in producing tapered oxide sidewalls are related to the use of the quartz sputtering target as a source for the deposition. The sodium contaminant levels in quartz targets can be significant, contributing to contamination of the films. Limits on the deposition rate are set by the target. The rate at which the target can dissipate heat limits the allowable target power and thus the deposition rate. For these reasons, experiments were done to determine the feasibility of PECVD tapered oxide as an alternative to bias sputter deposition.

Experimental

The deposition reactor used was a parallel-plate reactive ion etch (RIE) apparatus (Fig. 3). This was chosen because of the highly negative dc bias potentials on the substrate electrode during etch, which enhance the energy of ion bombardment and sputter etch rate. In RIE, the reactor walls and gas inlet plenum are grounded and the plate on which the substrates rest is RF driven, with a blocking capacitor in the matching network. The RF-driven electrode assumes a negative dc potential of large magnitude if the area of the grounded surfaces in contact with the plasma is large compared to the area of the dc floating-RF driven electrode (5). The potential stabilizes when the ion drift current due to the field near the negative substrate electrode equals the diffusion current out of the plasma, which is mostly electron current (6). This ion drift current is used in the present work to sputter etch the surface of the depositing oxide.

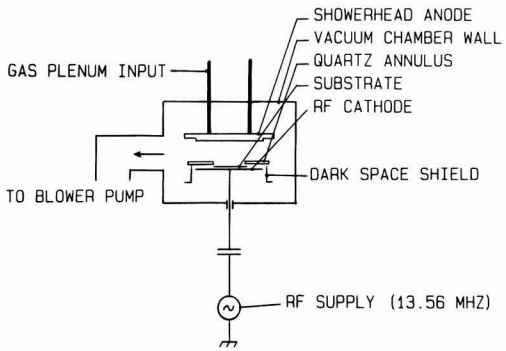


Fig. 3. Deposition reactor for sidewall-tapered plasma oxide

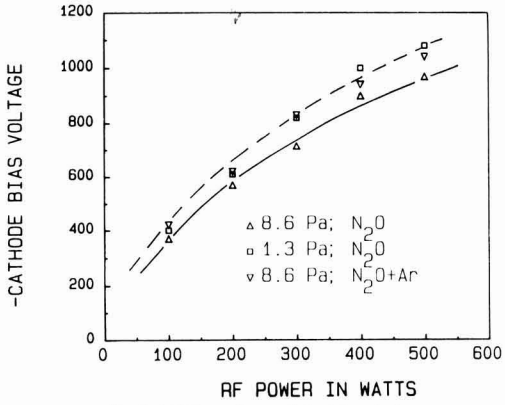


Fig. 4. DC bias voltage of the RF cathode

The RIE reactor used in these experiments had a 15 cm diam substrate electrode and a 25 cm diam grounded anode and gas inlet plenum in a parallel-plate configuration (see Fig. 4). The plasma was observed to completely fill the vacuum chamber for most deposition conditions tried. The chamber walls and gas inlet chamber are grounded and have large area in contact with the plasma compared with that of the capacitively coupled 13.56 MHz RF-driven substrate electrode. This assures that the substrate electrode assumes a negative dc bias voltage of large magnitude.

Vacuum was established and maintained by a Roots-type blower pump for depositions performed at pressures higher than 8.6 Pa. For pressures lower than 8.6 Pa, vacuum was maintained by a diffusion pump backed by a rotary vane pump. Pressure was monitored by a capacitance manometer. Gas flows were established prior to deposition by evacuating and isolating the chamber and then flowing each gas to be used in the run and adjusting the rate of rise of pressure. The rate of pressure rise required had been previsouly calculated from the required flow and the vacuum chamber volume. Flows were controlled during deposition using Brooks Rotameter™ flow tubes.

One p-type 75 mm <100> silicon wafer was used in each deposition run. It was centered on the surface of the substrate electrode. A quartz annulus of 26 cm od, 7.5 cm id, and 0.16 cm thickness covered the substrate electrode with the hole over the wafer. This had the effect of increasing local sputter etch and deposition rates on the wafer. The deposition rate and sputter etch rate with and without the annulus are compared in Table I. All deposi-

Table I. Sputter etch and deposition rates with and without the quartz annulus in angstroms per minute

	Oxide sputter etch rate	Oxide deposition rate (with SiH_4)
With annulus	78	1194
Without annulus	49	1081

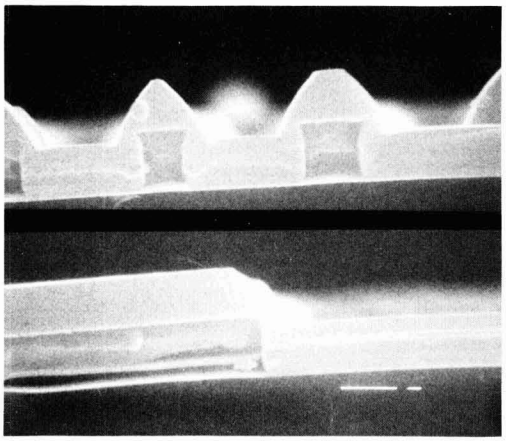


Fig. 5. Topography of plasma-deposited sidewall-tapered oxide. Process: 50 sccm nitrous oxide, 50 sccm argon, 10 sccm silane, 1.3 Pa pressure, 300W RF power, 2.5 cm plate spacing, 30 min.

tion rates, sputter etch rates, and sidewall angle data shown in the Results section were measured on oxides deposited or sputter etched using the annulus. The values quoted in Table I are for 300W, 13 Pa, 100 sccm N_2O sputter etches. The depositions involved the same parameters plus 10 sccm SiH_4 gas flow.

DC bias voltage was measured with a 100× attenuating probe and a 100 MHz oscilloscope. Bias voltage as a function of input power is shown in Fig. 4. The gas ambients used were chosen because they are typical oxidizing ambients in plasma deposition of silicon dioxide. The figure shows that the achieved bias voltages are only weakly dependent on the sputtering ambient or the pressure.

Measurements of oxide thickness were performed with a Nanospec; some measurements were checked with an ellipsometer. SEM samples prepared for measurements shown and plotted in Fig. 5, 11, and 12 were patterned silicon-doped aluminum with 1 μm of oxide deposited on them. They were cleaved at liquid nitrogen temperatures to embrittle the aluminum and stained in potassium hydroxide. In order to compare the topography of films deposited by different deposition processes, a standard underlying topography was used with standard thickness of the tapered oxide deposited upon it. The quality of the oxide topography was defined in the present work as the angle shown in Fig. 2, which will be called the sidewall angle. If this angle is negative the surface is reentrant. The standard underlying topography consisted of 1.0 μm high steps on 3.0 μm pitch. Step and space widths were nominally the same (1.5 μm), but as measured the spaces ranged from 1.5 to 2.2 μm wide. These were then coated with an oxide thickness of about 1 μm for the comparison of sidewall angle.

The sloped oxide shown in Fig. 5 is on the standard topography with space width of 2.2 μm. Widely separated steps exhibit slightly more favorable sidewall topography than do narrowly spaced steps because of less severe shadowing of the deposition. Hence, comparison of the topography of films produced by different deposition processes needs to be performed with consistent underlying topography and deposited film thicknesses, so similar topographic aspect ratios can be compared. The variation of space width from 1.5 to 2.2 μm in the underlying topography in the present work is not believed to be a significant effect on the accuracy of sidewall angle measurements in Fig. 11 and 12.

Results and Discussion

Successful deposition of the sidewall-tapered oxide depends on sputter etching the depositing oxide at a high rate. In order to determine the sputter etch rate of the oxide during deposition, the silane was eliminated from the gas ambient and plasma oxide-coated silicon wafers were used to determine thickness before and after the etch. The sputter etch rates recorded were, of course, for surfaces oriented perpendicular to the ion flux. Maximum sputtering rates of three to five times this value are possible on surfaces oriented at 60°-80° to the ion flux. Figure 6 shows the rates measured in the indicated oxidizing ambients. The rate is apparently independent of ambient and pressure and is proportional to the RF power.

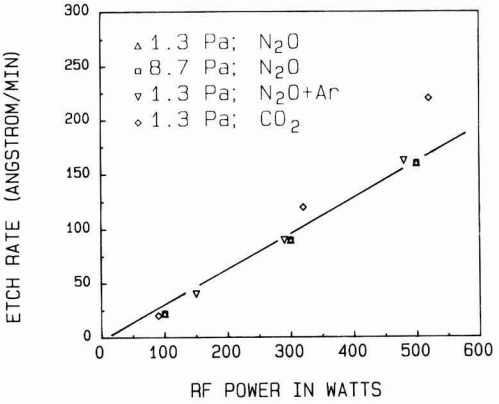


Fig. 6. Sputter etch rates in typical oxidizing gases used for plasma oxide deposition.

An experiment was performed to compare sputter etching in N_2O and reactive ion etching in CF_4 as means for tapering sidewalls of previously deposited, patterned, and anisotropically etched oxide steps. One wafer with oxide steps 1 μm high was sputter etched for 15 min in N_2O at 200W at 1.3 Pa pressure. Another was etched in CF_4 under similar conditions of pressure and power for 5 min. The CF_4 plasma removed 4900Å of oxide (980 Å/min), tapering the oxide sidewalls at a 10° angle. The N_2O sputter etched only 1500Å of oxide (100 Å/min) but tapered the sidewalls at a 19° angle to the vertical, as measured from SEM photographs. From this result, it was decided that sputter etching would be the sidewall tapering method used in this work. For a given rate of taper, the oxide removal was substantially less for sputter etching. In a process involving both deposition and etching, sputter etching to produce the tapered sidewall would reduce the net deposition rate less than RIE etching in CF_4 would. Choosing sputter etching as the tapering method also avoided any coupling which might have resulted between the etch and

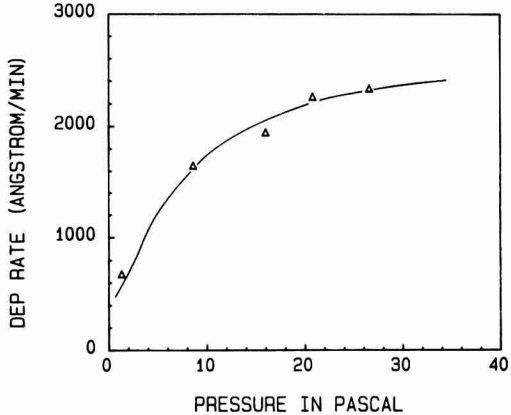


Fig. 7. Dependence of deposition rate on pressure for 10:1 nitrous oxide:silane flow ratio, 500W RF power, 8.7 Pa pressure.

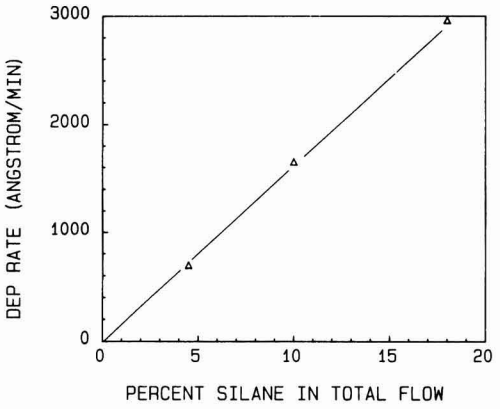


Fig. 8. Dependence of deposition rate on silane fraction at constant 8.7 Pa pressure and 500W power.

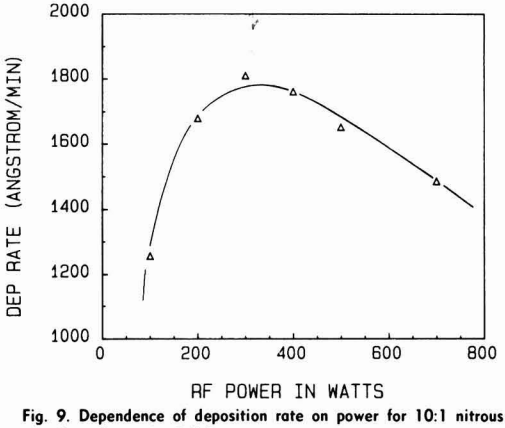


Fig. 9. Dependence of deposition rate on power for 10:1 nitrous oxide:silane flow ratio, 8.7 Pa pressure.

deposition chemistries leading to gas phase nucleation or other undesirable effects. Therefore, the results shown herein are on films tapered by sputter etching.

The net deposition rate of the oxide is plotted as a function of adjustable parameters in Fig. 7-9. Increasing the pressure increases the deposition rate as shown in Fig. 7. Deposition rates of up to 2300 Å/min were achieved at the 10:1 N_2O:SiH_4 ratio, and even higher rates can be achieved with lower ratios. It will be shown later, however, that increasing the deposition rate without an accompanying increase in the sputter etch rate causes degradation of the topography of the deposited oxide.

Figure 8 shows that the deposition rate of the oxide is linearly dependent upon the silane/nitrous oxide fraction at constant total flow. As seen in Fig. 10, there did not appear to be much effect of the silane/total flow ratio on the index of refraction except in those films deposited in a 50:50 nitrous oxide:argon mixture to which the silane was added. Here the ratio of silane to nitrous oxide was twice as high as in the other films. As expected, the index was higher (1.52) at largest silane fraction than the average for the other films (1.46). Not expected was the dip in index at 9% silane in all deposition ambients. This effect was strongest in the N_2O + Ar oxides,.

The dependence of deposition rate on RF power at constant pressure and flows is shown in Fig. 9. As power is increased from 100 to 300W, the reactant utilization increases, causing the rise in deposition rate. Above 300W, however, the net deposition rate falls because of the saturation of reactant utilization and the increase of the perpendicular sputter etch rate. Tapering the sidewalls during oxide deposition required sputter etch rates of one-fifteenth to one-fifth the deposition rate. All sputter etch rates quoted were measured on oxide surfaces normal to the ion bombardment direction.

Plots of sidewall angle as functions of power and pressure are shown in Fig. 11 and 12. The metal coverage at the oxide step bottom in the subsequent deposition increases with the sidewall angle. A 20°-30° sidewall angle indicates favorable topography for subsequent metal deposition. Sidewall angle increases with RF power in all ambients. The high pressure deposition in N_2O + SiH_4 required the highest RF power level to achieve sidewall tapering (angles > 20°). This is because the deposition rate increases with pressure and the sputter etch rate is independent of it. In order to increase the sputter etch rate to taper the sidewalls, the power must increase. Of the low pressure depositions, the CO_2 and N_2O + Ar oxidizing ambients required the lowest RF power levels to taper the oxide sidewalls.

Stress in films deposited in pure N_2O and silane at 1.3 and 8.6 Pa pressure was measured by determining the change in radius of curvature of 2.5 cm diam., 125 μm thick silicon wafers before and after a thick oxide deposition (> 0.5 μm). The results are shown in Fig. 13. Stress was compressive, tending toward lower values as the RF power was increased. The stress in films deposited at 1.3 Pa pressure was higher than in films deposited at 8.6 Pa, except at 300W. The only unacceptably high stress value was the 100W, 1.3 Pa point (5 Gdyn/cm^2). This set of depo-

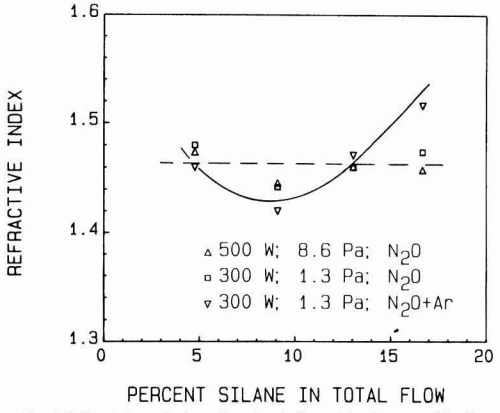


Fig. 10. Variation of the refractive index with nitrous oxide:silane ratio.

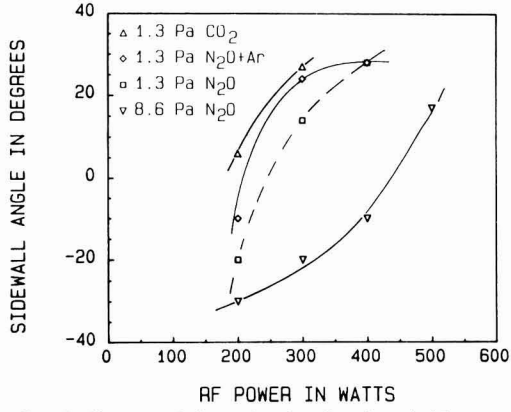


Fig. 11. Variation of the oxide sidewall angle with RF power. Standard topography is 1 μm high aluminum steps on 3 μm pitch.

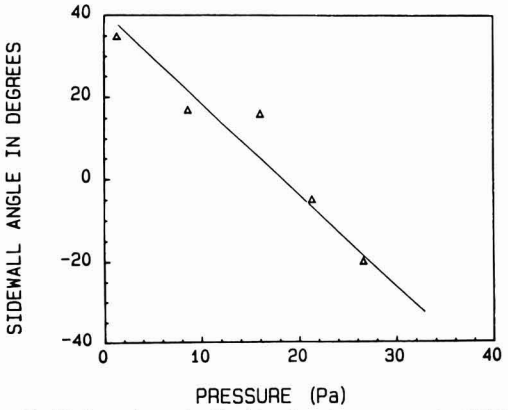


Fig. 12. Dependence of oxide sidewall angle on pressure for 500W RF power, 10:1 nitrous oxide:silane ratio.

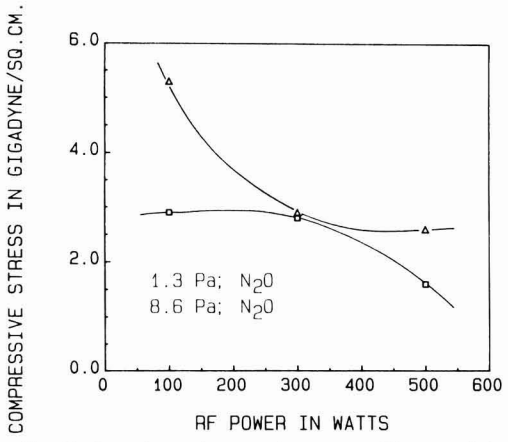


Fig. 13. Dependence of compressive stress on RF power of the deposition

sition conditions does not result in tapered sidewall oxide anyway.

Breakdown strength measurements were made on tapered oxide deposited at 200W and 1.3 Pa in this reactor. Median breakdown fields of 2.6-3.4 MV/cm were obtained on oxides deposited using CO_2 and SiH_4. In an effort to explain these low numbers, x-ray fluorescence was performed on 10,000Å films deposited using the same process. The result was iron contamination levels of 520-852 ppm. The iron is probably from the strongly sputter-etched stainless steel RF cathode and to a lesser degree from the chamber walls. The first approach to eliminating the iron contamination problem will be to use an anodized aluminum RF cathode and, if necessary, an anodized aluminum chamber. The experiments were performed in an environment which lacked particulate control, and this could have made a contribution to the low breakdown fields.

The poor dielectric strength of the tapered oxide films may be tolerable if a standard PECVD film of high breakdown strength can be deposited prior to the tapered oxide deposition, in the same pumpdown. This would provide a low loss capacitor in series with the tapered oxide layer.

Conclusion

A reactive ion etch system has been used to deposit sidewall-tapered oxide by PECVD. The deposition rate is determined by pressure and silane flow for N_2O:SiH_4 ratios of more than 5. The sputter etch rate is independent of pressure and is linear with respect to RF power. These deposition and sputter etch rate parameters are analogous to the target and substrate power in bias-sputtered quartz.

Although sidewall-tapered oxide can be deposited at more than 2000 Å/min, suggesting a single-wafer process, batch processing at lower deposition rates may be a safer approach. This is because of the necessary relationship between the sputter etch rate and the deposition rate in forming the tapered sidewall topography. A high deposition rate requires a high sputter etch rate and, in turn, a large substrate dc bias level. The resulting high energy ion bombardment may be deleterious to the integrity of oxides already on the wafer. Flaking of dielectrics from shielding in a deposition reactor can lead to defects in deposited films. This problem is less serious in batch processing than in single-wafer processing because the thickness of film deposited on the shielding, and therefore the amount of flaking, is less than for a single-wafer process by a factor of the number of wafers in a batch. Lower deposition rates permissible in batch processing are consistent with low sputter etch rates, reduced ion bombardment, and reduced damage to MOS gate oxides already on the wafer.

Although the feasibility experiments for sidewall-tapered plasma oxide were carried out in a parallel-plate RIE-type system, plasma deposition can be performed in a wide variety of ways, offering some flexibility in reactor design. For example, if magnetic fields are used to confine the electrons and increase their ionizing efficiency, increased ion flux to the substrates with smaller biases results. The magnetic field can be used to confine ionizing electrons near the RF-powered substrate as in Ref. (7) or to stabilize a filament-produced high density plasma to which the substrate can be independently biased (8). These approaches may be of use in future attempts to control dc bias and ion bombardment flux independently to reduce damage to the substrates during the tapered oxide deposition.

Acknowledgments

The authors would like to thank Jack Frazier for his help in making most of the measurements.

Manuscript submitted April 15, 1985; revised manuscript received July 8, 1985. This was Paper 413 presented at the New Orleans, Louisiana, Meeting of the Society, Oct. 7-12, 1984.

Texas Instruments, Incorporated, assisted in meeting the publication costs of this article.

REFERENCES

1. R. M. Levin and K. Evans-Lutterodt, *J. Vac. Sci. Technol. B*, **1**, 54 (1983).
2. S. Sachdev, J. A. Fair, C. Fuhs, and W. Coney, Paper presented at the Workshop on Tungsten for VLSI Applications, Albuquerque, NM, Nov. 12-13, 1984.
3. M. J. Nobes, J. S. Colligon, and G. Carter, *J. Mater. Sci.*, **4**, 730 (1969).
4. C. Y. Ting, V. J. Vivalda, and H. G. Schaefer, *J. Vac. Sci. Technol.*, **15**, 1105 (1978).
5. J. W. Coburn and E. Kay, *J. Appl. Phys.*, **43**, 4965 (1972).
6. M. Mitchner and C. H. Kruger, "Partially Ionized Gases," pp. 129-136, John Wiley and Sons, New York (1973).
7. I. Lin, D. E. Hinson, W. H. Class, and R. I. Sandstrom, *Appl. Phys. Lett.*, **44**, 185 (1984).
8. T. D. Mantei and T. E. Wicker, *Solid State Technol.*, **28** (4), 263 (1985).

Precipitation and Diffusivity of Arsenic in Silicon

R. Angelucci, G. Celotti, D. Nobili, and S. Solmi

C.N.R.-Istituto LAMEL, 40126 Bologna, Italy

ABSTRACT

Small angle x-ray scattering measurements were performed on arsenic-implanted laser-annealed silicon slices to investigate the features of precipitation at 900°C for different dopant supersaturations. With decreasing As concentration from 3.2 to 1.1 × 10^{21} cm^{-3}, the size distribution of the precipitates shifts toward larger values and their shape evolves from that of thin platelets, becoming three-dimensional and approaching at last that of a sphere. The high concentration diffusivity of As at 900°C, deduced from the size of the largest precipitates in specimens doped 1 × 10^{21} cm^{-3}, turns out to be 2 × 10^{-14} cm^2-s^{-1}. Determinations of the shift of the carrier concentration profiles and of the junction depth, after heating at 1000°C, show that the diffusivity of As is not affected by the precipitation and, hence, is controlled by the concentration of the dopant.

The physical nature of the electrically inactive As, which is present in Si at high doping levels, is receiving increasing attention, primarily due to the demands of VLSI. Well-known models hypothesize the formation of complex point defects, or "clusters," in thermal equilibrium (1-6).

Previous work (7) performed on ion-implanted and laser-annealed samples, doped with As in a wide composition range, put into evidence that the electrically active concentration depends only on temperature, a finding leading to the conclusion that a two-phase equilibrium takes place.

The formation of a second phase was also indicated by the isochronal heating behavior, typical of a precipitation process. Precipitates were in fact detected in very heavily doped specimens by small angle x-ray scattering (SAXS), a technique which is suitable because of the noticeably different atomic numbers of Si and As. These determinations provided information on the size distribution and shape of these precipitates, which were found to be in the form of thin platelets. These particles should be coherent with the silicon matrix, as suggested by the absence of extra lines or spots in the diffraction patterns.

As an additional result, the displacement of the carrier concentration profiles due to the heat-treatments showed that the diffusivity of the dopant strongly increased with the implanted dose. This effect, which was particularly evident at high temperature, could be attributed either to the increase of As concentration or to the increased amount of precipitates per unit surface, *i.e.*, to lattice defects in excess generated by the precipitation process.

The present work extends SAXS examinations to less heavily doped compositions (a difficult task owing to the small thickness of the implanted layer) with the aim of controlling the occurrence of precipitation at lower dopant concentrations and of getting further information on this process. In addition, it was intended to verify whether the precipitation process can influence the high temperature diffusivity of As.

Experimental

For these experiments, we used (100)-oriented, CZ-pulled, p-type, boron-doped silicon slices of 1 Ω-cm resistivity.

The samples were arsenic implanted at an energy of 100 keV at three different doses, *i.e.*, 1 × 10^{16}, 2 × 10^{16}, and 5 × 10^{16} cm^{-2}. All slices were tilted 7° off axis to reduce ion channeling effects during implantation.

To electrically activate the dopant and to recover the radiation damage, the implanted samples were laser annealed by a 20 ns single pulse delivered by a Q-switched ruby oscillator operating in a multimode regime. An optical guide was used to yield a 16 mm diam light spot with an energy density of 1.8 J/cm^2.

To analyze the influence of dopant concentration on the precipitation and the size distribution of the particles, a set of samples, corresponding to the three implanted doses, was furnace annealed at 900°C for 30 min in nitrogen atmosphere.

A second set of specimens with surface concentration corresponding to the highest dose, but with different amounts of excess dopant per unit surface, was annealed at 1000°C for 10 min, in order to study the effect of precipitation on As diffusivity. The amount of excess dopant was reduced by thinning the laser-annealed wafers using anodic oxidation.

Carrier concentration profiles were determined by a specially designed apparatus which performs automatic anodic stripping followed by incremental sheet resistance and Hall effect measurements (8). The van der Pauw geometry was previously etched on the specimen's surface by a photolithographic process. The thickness of the removed layer was also controlled by Talystep measurements.

The junction depth was evidenced by the standard angle lapping and staining technique using a $CuSO_4$ solution.

The features of the precipitates (size distribution and shape) were studied by small-angle x-ray scattering, using the techniques which were detailed in a previous paper (7). A new Kratky camera was employed for the present observations: the width of the main slit, defining the incident beam, was 80 μm. The sample-to-counter distance was 200 mm, and the scattered intensity was recorded every 50 μm of counter displacement (corresponding to 0.0143° of 2θ) from 300 to 5000 μm (0.086°-1.43° of 2θ), with a fixed counting time of 1000s.

Results and Discussion

Carrier density profiles of our specimens after laser annealing, which corresponds to complete electrical activation of the dopant, are reported in Fig. 1, together with the profiles after 30 min heating at 900°C. The most heavily doped composition presents the lowest carrier concentration in the plateau region (~2 × 10^{20} cm^{-3}), while the more dilute one shows a higher density (~2.6 × 10^{20} cm^{-3}). This indicates incomplete precipitation; in fact, the rate of a precipitation process decreases with decreasing supersaturation.

The carrier concentration values in our profiles are slightly higher (~10%) than those we reported in Ref. (7). This results from more accurate determinations of the thickness of the removed layer.

SAXS examinations were performed only on the specimens doped at 2 × 10^{16} and 1 × 10^{16}, as the most heavily doped composition was the object of previous investigations which were reported in detail in Ref. (7).

A remarkable increase of the intensity scattered at small angles was observed by comparing the experimental SAXS curves after As implantation and laser annealing with those after heat-treatment of the same specimens at 900°C for 30 min.

As it was concluded in our previous paper (7), the occurrence of this small angle scattering is related to the formation of As precipitates. In agreement with this statement, the present experiments show that the amplitude of this effect decreased with decreasing concentration of the dopant.

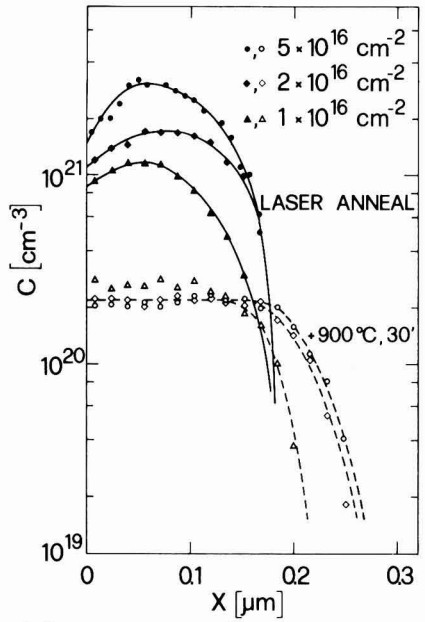


Fig. 1. Carrier concentration profiles of ion-implanted and laser-annealed specimens for three different arsenic doses. Black symbols refer to the initial condition, when all dopant is electrically active, and open symbols to the one after heating 30 min at 900°C.

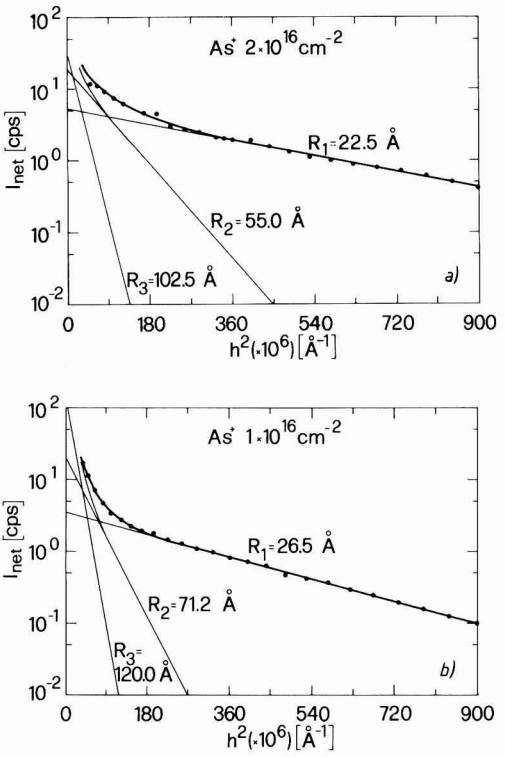


Fig. 2. Guinier plot of the small angle intensity resulting by heating the ion-implanted laser-annealed specimens at 900°C for 30 min. The analysis by the method of the successive less-sloped tangents is also outlined and the proper values of the radii of gyration are indicated. Maximum As concentrations in the profile are (a) 1.7×10^{21} cm^{-3} and (b) 1.1×10^{21} cm^{-3}.

The Guinier plot (log I *vs.* h^2, where $h = (4\pi \text{ sen } \theta/\lambda)$ of the net observed intensity for the specimens implanted with a dose of 2×10^{16} cm^{-2} is reported in Fig. 2a, while the corresponding plot for the less doped specimen (1×10^{16} cm^{-2}) is shown in Fig. 2b. In both cases, it can be observed that the scattered intensity decreases with increasing scattering angle, indicating the absence of particle interference effects.

In addition, the deviation of the graph from a straight line in the very small angle region clearly shows that the radius of gyration of the particles is not unique; *i.e.*, the size of the precipitates is, as expected, distributed over a range of values. Indications of the particle size distributions can be obtained by subtraction of the successive less-sloped tangents (9, 10). With this graphical method, the size distribution is approximated by a set of a few discrete fractions of particles of given volume, and the corresponding radii of gyration can be determined. As is known, the radius of gyration for a particle is defined as the root mean square distance of the electrons from the center of charge.

As is shown in Fig. 2, the distributions can in both cases be approximated by three groups of particles. The corresponding radii of gyration turn out to be larger in the less concentrated solution.

The increase of the radii of gyration with decreasing dopant concentration is put in better evidence considering also the results that we obtained by the same method on specimens implanted with the highest As dose [see Fig. 6 in Ref. (7)].

To get further information on the features of the precipitates as a function of dopant supersaturation, the shape of the particles was investigated by analysis of the SAXS intensity data. Figure 3 reports the theoretical slopes for some elementary shapes in the log I *vs.* log h plot, which permits the derivation of this type of information (11) together with the experimental trends for our specimens. The slope of -5.6 observed in the more dilute solution indicates a shape which approximates that of a sphere. The specimens implanted with 2×10^{16} cm^{-2} show a slope of -4, which still corresponds to three-dimensional particles, probably ellipsoids of revolution with semiaxes a, a, and va, with $v \simeq 0.5$.

By the same method, we determined on samples implanted with 5×10^{16} cm^{-2} [see Fig. 8 in Ref. (7)] a slope of -2.5, which corresponds to platelets having a thickness of the order of an atomic layer.

Consideration of these results puts into evidence that the shape of the precipitates also depends markedly on the concentration of As. The features of As precipitates are summarized in Table I, which includes SAXS results of Ref. (7). For each implanted dose, the maximum dopant concentration C_0 in the profile is indicated, together with the corresponding supersaturation $i = C_0/C_e$, where C_e is the equilibrium solubility of As in silicon at 900°C ($C_e = 2 \times 10^{20}$ cm^{-3}). Besides the shape of the precipitates, we report for each composition the three radii of gyration in the Guinier distribution, together with the corresponding percentage of precipitate in each group. These fractions were calculated from the corresponding Guinier plot, by taking into account the precipitate's shape (10).

A more rigorous determination of the particle size statistical distribution was also obtained in the form of a continuous curve like the one in Fig. 7 of Ref. (7). This analysis confirmed the trend which is shown in Table I.

These results put into evidence that decreasing the concentration of the dopant from 3.2 to 1.1×10^{21} cm^{-3} leads to a remarkable decrease of the population of particles of small size and to a corresponding increase of the fraction of particles with the upper radius. At the same time, the shape of the precipitates evolves from that of a thin platelet, becoming three-dimensional and approaching at last that of a sphere.

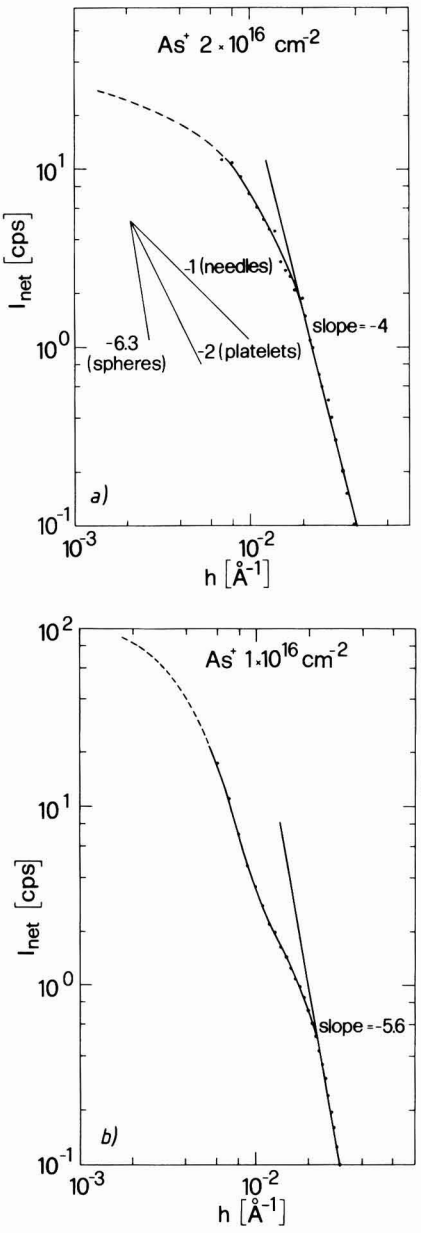


Fig. 3. Experimental slope values providing information on the shape of the precipitates: (a) dose 2×10^{16} cm^{-2}; (b) dose 1×10^{16} cm^{-2}. The theoretical slope values for main limiting cases are reported for comparison.

It seems possible to interpret this behavior on the basis of precipitation kinetics determined by the nucleation process. A growing particle becomes incoherent because the strain energy term increases with size. The very small difference of the tetrahedral radii of Si and As leads to a very small strain energy and, hence, favors a coherent interface between matrix and precipitate. In the case of a coherent boundary, the strain energy is not very dependent on shape; therefore, with decreasing supersaturation, the nuclei evolve toward a spherical shape because this reduces the surface energy term and hence the reversible work ΔG^* for the formation of the critical nucleus.

On the same line, the increase of the size of the precipitate population is explained as due to the decrease of the precipitate density which results from the decrease of the nucleation frequency with decreasing supersaturation.

Following the classical theory, the nucleation frequency depends on $\exp(-\Delta G^*/kT)$, where, at constant temperature, the term $\Delta G^* = \text{const.}/(\ln i)^2$. From the data in Table I, it is easily seen that decreasing the dopant concentration from 3.2 to 1.15×10^{21} cm^{-3} leads to an increase in ΔG^* of a factor of 2.5, a figure which can fully explain a marked decrease of the density of the particles and the consequent increase of the population with the largest radius.

We consider now the diffusivity of the dopant. If the radius of the equivalent sphere available to a particle is sufficiently large, the size of the precipitate will be determined by the diffusivity of the solute. This condition is likely to have been satisfied for the largest group of particles in our dilute solution. These specimens, as it is shown in Fig. 1, are still supersaturated after 30 min heat-treatment.

With the hypothesis that the smaller precipitates (R_1 = 26Å and R_2 = 71Å) depleted the equivalent sphere available for their growth, one obtains for the largest particles (R_3 = 120Å) a radius of the equivalent sphere $r_e \simeq 730$Å, and these regions should be responsible for the residual supersaturation.

With this approximation, the diffusivity of arsenic can be calculated by the diffusion-limited growth model of a spherical particle. By solving the diffusion equation obtained applying the stationary approximation in a finite matrix, one obtains the growth law (12)

$$dr\,(C_p - C_0) = \frac{2(C_p - C_0)\,(r_m^3 - r^3)}{2r_e^3 r - 3r_e^2 r^2 + r^4}\,D\,dt$$

where C_p is the solute concentration in the precipitate, $r_m = r_e\,(C_0 - C_e)/(C_p - C_e)$ is the maximum value of the radius attainable by the particle, and D and t have their usual meanings.

With this model, the growth problem is treated by assuming the particle radius r to be nearly constant and solving the time-independent diffusion equation in the matrix (13). Actually, the high concentration inequality existing in our case between the precipitate and the matrix guarantees that r is a slowly varying function of time. The radius r of the particles was deduced from the corresponding radius of gyration R by the relation valid for a sphere: $r = R\sqrt{5/3}$. The value for the largest particles in our dilute samples turned out to be $\simeq 155$Å. In agreement with the results of Ref. (7) which led to the conclusion that the stoichiometry of the precipitates is SiAs, C_p was assumed to be 2.5×10^{22} cm^{-3}. By using these data, the numerical solution of the above equation gave $D = 2.2 \times 10^{-14}$ cm^2-s^{-1}. It is worth noticing that by using the simple growth model in an infinite matrix (14)

$$r^2 = 2Dt\,(C_0 - C_e)/(C_p - C_e)$$

Table I. Features of arsenic precipitates at 900°C for different dopant concentrations

Implanted dose (cm^{-2})	C_0 (cm^{-3})	i supersaturation	Shape	R_1 (Å)	f_{R_1}	R_2 (Å)	f_{R_2}	R_3 (Å)	f_{R_3}
5×10^{16}	3.2×10^{21}	16	Thin platelets	20	0.80	44	0.17	95	0.03
2×10^{16}	1.7×10^{21}	8.5	Oblate ellipsoids	22	0.77	55	0.18	102	0.05
1×10^{16}	1.15×10^{21}	5.7	Spheres	26	0.60	71	0.17	120	0.23

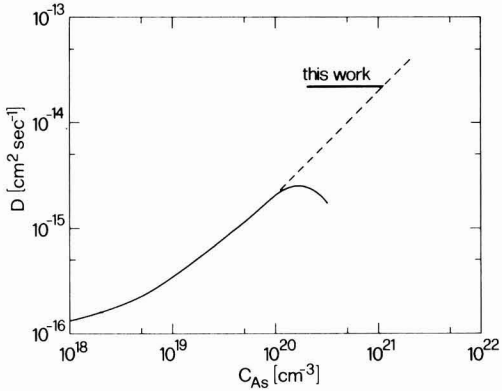


Fig. 4. Diffusion coefficient vs. As concentration at 900°C. The solid line represents the behavior, generally implemented in the simulation programs, which takes into account aggregation phenomena. The dashed line shows the high concentration extrapolation of the model based on the ionized point defects (15). Our experimental value and the corresponding concentration range are also reported.

the diffusivity value turns out to be 1.7×10^{-14} cm^2-s^{-1}, very close to the previous figure.

This comparison puts in evidence that our diffusivity at 900°C, although underestimated as a consequence of the adopted approximations, should be close to the actual value.

This diffusivity represents an average in the concentration range $(2\text{-}10) \times 10^{20}$ cm^{-3} and, as is shown in Fig. 4, is in good agreement with the one obtained by extrapolation of the data reported in literature according to the well-known model of diffusion by ionized point defects (15).

We notice that, to the best of our knowledge, our data are the only experimental values concerning such a high concentration of arsenic in silicon. In fact, the diffusivity data reported in literature refer to concentrations up to about 10^{20} cm^{-3}. They were generally deduced applying the Boltzmann-Matano method to the total arsenic profile and show (see Fig. 4) an apparent reduction of the diffusivity for concentrations exceeding the above-mentioned value (2, 4, 6, 15). This trend is due to the fact that the fraction of the dopant which is present in the form of precipitates (or clusters, according to the authors who proposed this model) is not mobile. Therefore, the solid line with hump shown in Fig. 4 refers to the total As diffusivity, while the solid line with dashed continuation shows the substitutional As diffusivity.

We consider now the influence of precipitation on the diffusivity of arsenic.

Previous experiments performed in the temperature range 850°-1000°C put into evidence that the displacement of the concentration profile with the thermal treatment increases with the implanted dose. This effect, which is also shown in Fig. 1, resulted in better evidence at 1000°C [see Fig. 1 of Ref. (7)].

This phenomenon can be attributed either to the increase of dopant concentration or to the increase of the amount of precipitated dopant per unit surface. The increase of arsenic diffusivity with the concentration is commonly attributed to the increase of the concentration of ionized point defects with rising Fermi level (15). On the other hand, one could attribute to the precipitation process the formation of an excess of point defects enhancing the diffusivity of the dopant.

Previous experiments could not discriminate between these two hypotheses, as both the arsenic concentration and the amount of precipitates increase with the implanted dose.

In order to detect the effect of precipitation on the diffusivity of arsenic, we performed the following experiment on a set of specimens implanted with the highest

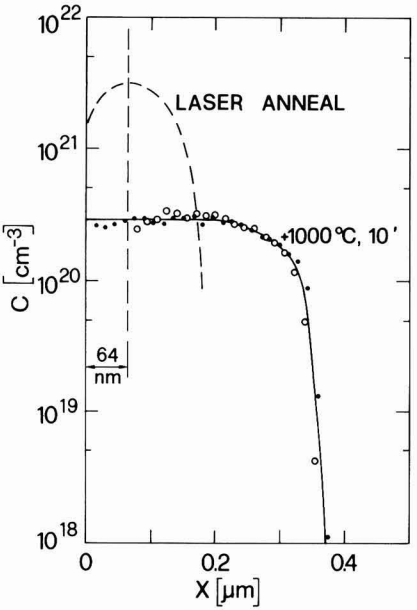


Fig. 5. Carrier concentration profiles of 5×10^{16} As cm^{-2} implanted samples. Dashed curves show the dopant distribution after laser annealing. Dots refer to the profiles after heating for 10 min at 1000°C; the open symbols concern the specimen thinned 64 nm before this thermal treatment. The two profiles, taking into account the shift of the surface, superimpose.

dose: after laser annealing, part of these samples was thinned by anodic oxidation, removing 64 nm of silicon, thus reducing by a factor of 2 the amount of excess dopant per unit surface, still keeping the same value of the dopant surface concentration (3.2×10^{21} cm^{-3}). Both types of specimens were subsequently annealed 10 min at 1000°C.

The results of this experiment are reported in Fig. 5, which shows that the profiles coincide, providing thereby conclusive evidence that at high temperatures the diffusivity is controlled by the concentration and does not depend appreciably on the amount of precipitates. The observation of the junction depth supports the same conclusion. In fact, the optical micrograph shown in Fig. 6, showing a specimen selectively thinned as above by anodic oxidation before the heat-treatment, puts into evidence that the junction depth is the same both in the thinned (left side) and the standard (right side) regions.

Conclusions

SAXS experiments performed on ion-implanted, laser-annealed silicon slices doped with arsenic in the concen-

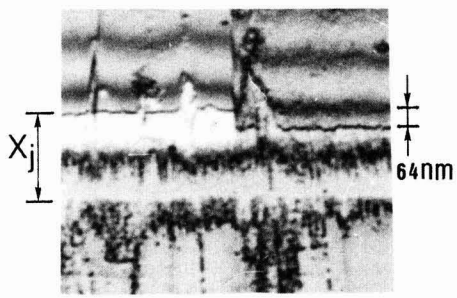


Fig. 6. Optical micrograph taken in a lapped and stained specimen, implanted at 5×10^{16} cm^{-2}, laser annealed and selectively thinned (64 nm) in the left side. After heating for 10 min at 1000°C, the junction depth results are the same in both regions.

tration range 3.2-1.1 × 10^{21} cm^{-3} showed the occurrence of precipitation after heating at 900°C.

The net observed small angle intensity, and hence the amount of the new phase, decreases with decreasing supersaturation of the dopant. Moreover, the size distribution is shifted toward higher values. This implies that, in agreement with the classical theory of nucleation, the density of precipitates decreases with decreasing supersaturation. In addition, the shape of the particles evolves from that of a platelet, becoming three-dimensional and approaching at last that of a sphere.

Consideration of the diffusion-limited growth model for a spherical precipitate, and of the radius (~150Å) of the largest group of particles in the more dilute solution, led to a diffusivity of arsenic at 900°C of about 2 × 10^{-14} cm^2-s^{-1}. This figure, which is an average in the concentration range 2-10 × 10^{20} cm^{-3}, is in good agreement with the one expected on the basis of the well-known model of arsenic diffusion by ionized point defects (15).

The experiments performed by reducing the amount of excess dopant per unit surface, still keeping the same value of arsenic surface concentration, showed that, at high temperature (1000°C), the diffusivity is controlled by the concentration. In fact, the shift of the carrier profile and the junction depth do not depend appreciably on the amount of precipitates.

Acknowledgments

The authors wish to thank A. Armigliato and A. Mazzone for the useful discussion and suggestions.

Manuscript submitted May 27, 1985; revised manuscript received Aug. 10, 1985.

C.N.R.-Istituto LAMEL assisted in meeting the publication costs of this article.

REFERENCES

1. S. M. Hu, in "Atomic Diffusion in Semiconductors," D. Shaw, Editor, p. 217, Plenum Press, London (1973).
2. R. B. Fair and G. R. Weber, *J. Appl. Phys.*, **44,** 273 (1973).
3. M. Y. Tsai, F. F. Morehead, J. E. E. Baglin, and A. E. Michel, *ibid.*, **51,** 3230 (1980).
4. J. Morota, E. Arai, K. Kobayashi, and K. Kudo, *ibid.*, **50,** 804 (1979).
5. E. Guerrero, H. Potzl, r. Tielert, M. Grasserbauer, and G. Stingeder. *This Journal*, **129,** 1826 (1982).
6. S. M. Hu, in "VLSI Science and Technology/1985," W. M. Bullis and S. Broydo, Editors, p. 465, The Electrochemical Society Softbound Proceedings Series, Pennington, NJ (1985).
7. D. Nobili, A. Carabelas, G. Celotti, and S. Solmi, *This Journal*, **130,** 922 (1983).
8. R. Galloni and A. Sardo, *Rev. Sci. Instrum.*, **54,** 369 (1983).
9. R. Hosemann and S. N. Bagchi, "Direct Analysis of Diffraction by Matter," North Holland, Amsterdam (1962).
10. M. H. Jellinek, E. Solomon, and J. Fankuchen, *Ind. Eng. Chem. (Anal. Ed.)*, **18,** 172 (1946).
11. J. C. Grosskreutz, in "Handbook of X-Rays," E. F. Kaelble, Editor, McGraw Hill, New York (1967).
12. O. Simmich and H. Löffler, *Phys. Status Solidi A*, **65,** 153 (1981).
13. S. R. Coriell and R. L. Parker, *J. Appl. Phys.*, **36,** 632 (1965).
14. H. B. Aaron, D. Fainstein, and G. R. Kotler, *ibid.*, **41,** 4404 (1980).
15. R. B. Fair, in "Silicon Integrated Circuits (Part B)," D. Kahng, Editor, p. 28, Academic Press, New York (1981).

Ultrafine Aerosol Particles in Semiconductor Cleanrooms

R. P. Donovan and B. R. Locke

Research Triangle Institute, Center for Aerosol Technology, Research Triangle Park, North Carolina 27709

C. M. Osburn* and A. L. Caviness

Microelectronics Center of North Carolina, Research Triangle Park, North Carolina 27709

ABSTRACT

The fabrication of VLSI chips with high yields on small device geometries requires control of particulate contamination during manufacture. One potential source of particulate contamination is the ambient air of the production facility. Monitoring and control of these ambient aerosol particles require increasingly sophisticated instrumentation capable of measuring smaller and smaller particles. This paper identifies three instrument types capable of sizing ultrafine (≤ 0.1 μm diam) aerosol particles in real time: the integral mobility analyzer, the differential mobility analyzer, and the diffusion battery. All three of these sizing instruments use an independent condensation nuclei counter to count particles in size-separated channels. Two of these combinations, the differential mobility analyzer/condensation nuclei counter and the diffusion battery/condensation nuclei counter, have been used to measure the ultrafine aerosol particle size distribution of various quality semiconductor cleanrooms. The data reduction routines of the differential mobility analyzer/condensation nuclei counter combination break down when ultrafine aerosol particle concentration falls below about 1 particle/cm^3. The diffusion battery/condensation nuclei counter combination functions to below 0.01 ultrafine aerosol particle/cm^3. Data taken by this instrument combination in a state-of-the-art cleanroom at rest show that the peak concentration of ultrafine aerosol particles occurs near 0.1 μm, the cumulative distribution curve being relatively flat below that size.

Device dimensions continue to shrink in the push toward faster, more powerful silicon chips. Processing technology for submicron chip designs is moving from the laboratory to the production floor.

As the size of the modeled device areas decreases, so does the critical size of certain unmodeled device areas, such as surface defects or bulk imperfections. Surface particles that are too small to affect device behavior when minimum device dimensions are in the 2-3 μm range can become important when device dimensions are submicron. An arbitrary rule of thumb that defines the size threshold for surface particles of concern is 0.1 times the minimum device dimensions—devices designed with 5 μm line widths should be built in manufacturing areas in which 0.5 μm particles are monitored and controlled. By this rule, submicron device design and manufacture requires measurement and control of ultrafine particles (size ≦ 0.1 μm). Outdoor measurements indicate very high concentrations of such ultrafine particles in the urban ambient air (Fig. 1).

*Electrochemical Society Active Member.

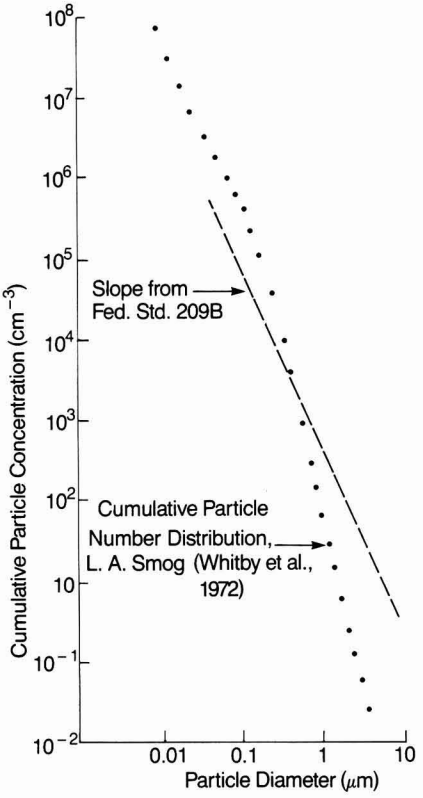


Fig. 1. Cumulative size distribution of ambient urban air (1)

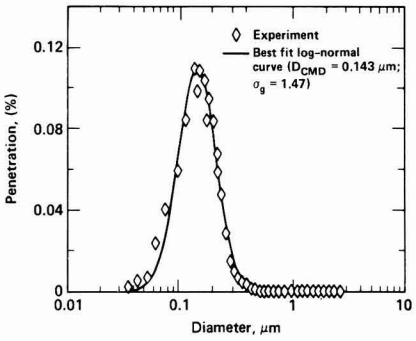


Fig. 2. Particle penetration through a HEPA filter (3)

What is of more direct concern to chip manufacturers is the concentration of ultrafine particles in the semiconductor manufacturing area, typically a cleanroom with air quality rated at Class 100 or better,[1] at least under resting conditions (no people in the clean room). Makeup air entering such a facility not only passes through building humidity and temperature conditioning equipment, but is also filtered through an inlet (high efficiency particulate air (HEPA) filter prior to its introduction to the cleanroom recirculating loop. Typically, makeup air in a cleanroom constitutes only 10-20% of the total air flow so that the bulk of the recirculating cleanroom air passes through the cleanroom HEPA filter bank (inside the cleanroom loop and distinct from the inlet HEPA filter section) many times before discharge. Thus, the recirculating air inside a cleanroom is well filtered and of greatly reduced aerosol particle concentration compared with the ambient air, and is probably of greatly modified aerosol particle size distribution based upon published penetration curves for HEPA filters (3) (Fig. 2). Such curves show very low penetration for both small (< 0.01 μm) and large (> 1 μm) particles. A maximum in penetration occurs between these limits in the transition region between particle collection mechanisms. This filter property could well be expected to suppress the concentration of ultrafine aerosol particles found in cleanrooms.

Data to support this conclusion are scarce. Serious questions have not been raised about this portion of the cleanroom particle spectrum until recently. Even with the growing interest, however, the instrumentation challenges in measuring ultrafine aerosol particles at the ultralow concentrations characteristic of today's cleanrooms have not yet been satisfactorily met. This paper reviews candidate aerosol particle measuring instrumentation, selects certain of these instruments for making cleanroom measurements, and presents both differential and cumulative number distributions of aerosol particles measured in semiconductor cleanrooms having various levels of air cleanliness.

[1]Air quality classifications are defined in Federal Standard No. 209B (2). Figure A-1 is a reproduction of a figure from that standard.

Instrumentation Review and Selection

While many aerosol-particle measuring instruments exist, the number capable of detecting ultrafine aerosol particles is not great and, when the added requirements of single-particle detection in real time or near real time are added, the list becomes very short (Table I). Inertial classifiers operate most efficiently in the 1-10 μm range, well above the ultrafine range of interest here. By reducing the operating pressure below atmospheric, the lower limit of size detection by this principle can be pushed into the ultrafine aerosol particle range, but the lack of real-time analytic capability remains a severe shortcoming. Using a quartz crystal (listed under Miscellaneous types in Table I) as the collection stage does provide real-time readout, but single-particle resolution is possible only for larger particles.

Light scattering instruments, such as the optical particle counter (OPC), popular in the 0.3-3 μm size range because of its real-time readout and single-particle counting capability, lose adequate sensitivity on the fringe of the ultrafine particle regime. New designs, using either two lasers for two-sided illumination of the scattering cavity or shorter wavelength lasers, are claimed to detect aerosol particles as small as 0.05-0.06 μm (4). Instrument noise levels, including signals generated by molecular scattering, match the scattering signal from this size particle so that counting small concentrations of ultrafine aerosol particles is limited by background noise over the lower channels in most laser spectrometers. In practice, this statement means that, although laser spectrometers are very successful at determining size distributions at high particle concentrations, they prove less satisfactory at concentrations typical of a cleanroom. This conclusion applies only to the size range below about 0.3 μm, where sampling flow rates must be reduced so that the entire sample flow can be passed through a small volume illuminated by the laser. Although keeping this volume small reduces molecular light scattering and thus allows detection of small particles, the number of particles counted in a sample remains low because of the small cross section through which all of the sample must flow. For ultrafine particle measurements in the cleanroom, the laser spectrometer is of limited use at present.

The traditional basic instrument design used by aerosol technologists to detect ultrafine aerosol particles is the condensation nuclei counter (CNC) (5). This counter solves the small scattering signal problem of ultrafine particles by converting each ultrafine aerosol particle into an optically huge particle. It does this by passing the ultrafine aerosol stream through a supersaturated vapor

Table I. Candidate methods/instruments for measuring aerosol particle size distributions in a semiconductor cleanroom

Type	Measurement principle/ detection method	Size range (μm)	Real-time analysis	Single particle counting/sizing capability
Inertial classifiers				
Cyclones	Centrifugal fractionation/ weighing	3-30	No	No
Centrifuges		0.1-1.0	No	No
Inertial impactors		0.5-5	No	No
Low-pressure inertial impactors		0.05-5	No	No
Aerodynamic particle sizers	Particle acceleration in gas flow/time of flight	0.5-15	Yes	Yes
Light scattering instruments				
Single-particle optical counters	Light scattering	0.2-5	Yes (size intervals in parallel)	Yes
Laser spectrometers		0.06-3	Yes (size intervals in parallel)	Yes
Electrical mobility analyzers				
Integral samplers	Removal of electrically charged particles in mobility increments	0.01-0.5	Nearly	Sizing but no counting capability
Differential samplers		0.01-1.0	Nearly	
Diffusion batteries	Particle diffusion to a capture surface (*i.e.*, a capillary wall)	0.002-0.3	Nearly	Sizing but no counting capability
Condensation nuclei counters	Particle growth/light scattering after upstream sizing by			
With diffusion battery	Particle diffusion	0.002-0.3	Nearly (size intervals in series)	Yes
With electrostatic classifier (differential mobility analyzer)	Charged particle separation	0.01-1.0	Nearly (size intervals in series)	Yes
Miscellaneous types				
Microscopy (optical; electron)	Imaging	> 0.002	No	Yes
Resistivity	Electrical resistivity change by electrolyte displacement	> 0.5	No	Yes
Quartz X-tal cascade impactor	Frequency change by mass loading of a quartz crystal	0.05-35	Yes	No/Yes (Large particles only)
Triboelectric	Contact charge transfer	No unique size dependence	Yes	No

in which each ultrafine particle serves as a site for vapor condensation. By this technique, ultrafine particles grow into 10 μm or larger particles that are easily detected by a built-in optical counter. A CNC can count aerosol particles as small as 0.01 μm (or even smaller, depending on operator technique and sanguinity). However, it provides little size discrimination—a 0.02 μm particle is counted the same as a 0.2 or a 2 μm particle. To obtain a size distribution requires an upstream size separating device such as an electrical mobility analyzer (6) or a diffusion battery (7). Neither of these devices counts particles; they simply remove a certain aerosol fraction from the total aerosol flow (the integral mobility analyzer or the diffusion battery) or else break out a selected size fraction of the total aerosol flow into a separate airstream that can be counted (the differential mobility analyzer).

Size resolution can be quite good using the differential mobility analyzer (6)—the number of size increments between 0.01 and 1 μm can exceed 30 in the commercial version. Size separation in any mobility analyzer depends on the ability of electric fields to remove charged particles from streamlines, and, in the differential mobility analyzer, aerosol charge is controlled by passing the aerosol stream through highly ionized air, which reduces the particle charge distribution to a Boltzmann equilibrium. However, since the particle fraction actually electrically redirected into a separate countable airstream is primarily just the singly charged, unipolar fraction of any given size-band population, most of the particles in a given size range are discarded. (In Boltzmann equilibrium, the charge distribution on particles in any size range is symmetrical and a maximum at zero charge.) In a cleanroom, the small number of total particles present renders this measuring scheme inappropriate; that the total number of particles counted is only a small fraction of what is only a small concentration to begin with means that this counting technique is less satisfactory than other techniques in which all, or nearly all, particles in a given size range are counted. Thus, techniques with poorer size resolution than the differential mobility analyzer may, in fact, prove better suited for collecting cleanroom size-distribution data in the ultrafine particle size range.

One such alternative is the integral mobility analyzer. This analyzer differs from the differential mobility analyzer in at least two significant features: (*i*) particles entering the analyzer are charged to saturation by ion diffusion (in the differential mobility analyzer, particle-electrical charge is reduced to a Boltzmann distribution by a Kr-85 neutralizer), and (*ii*) only one airstream exits the analyzer; particles removed from that airstream are electrostatically precipitated onto an electrically biased center-rod electrode (in the differential mobility analyzer, two streams exit the analyzer, one containing particles having electrical mobilities that fall within a narrow band, and the other the rest of the airstream; some particles are also precipitated). That all particles are unipolarly charged to saturation means that the electrical force acts on all the particles rather than just on a small fraction as is true in the differential mobility analyzer. Thus, one of the major sources of particle loss in the differential mobility analyzer is absent in the integral mobility analyzer.

The second alternative to the high resolution differential mobility analyzer is the diffusion battery. This instrument operates on an entirely different particle capturing principle than the mobility analyzers. Electrical forces play no role in the designed operation of a diffusion battery, the Brownian motion alone of the ultrafine particles being the mechanism whereby the particles collide with the capture surfaces. By passing the aerosol flow through narrow passageways of varying length and noting the incremental particle removal associated with each path-length, the particle-size distribution of the original aerosol can be reconstructed. Thus, though the boundaries between adjacent size channels are not sharp and the resolution of the separation is relatively crude compared to the differential mobility analyzer, the fact that all particles participate in this statistical removal process means that the technique may be better suited for cleanroom measurements than those techniques that count only a fraction of the total particles present.

Other techniques listed in Table I fall short for one reason or another. Microscopy is excellent by all measures except ease and speed of data reduction. One can examine individual particles in great detail, but deducing concentrations and size distributions from microscopic counting is a tedious technique and one prone to error. The resistivity technique requires particle collection and resuspension into an electrolyte. The triboelectric technique depends on control of subtle surface properties and measures a total charge transfer that is not easily converted to a size distribution.

Based on their size range, single-particle particle counting capability, and compatibility with real-time or near-real-time measurement, the instrument combinations of Table I suitable for sampling ultrafine aerosol particles in cleanrooms consist of the following size separating stages (see Appendix B for a discussion of commercial availability: (*i*) the differential mobility analyzer, (*ii*) the integral mobility analyzer, and (*iii*) the diffusion battery.

Experimental

All the above instruments only separate aerosol particles according to size. A downstream CNC is used as the actual particle counter for all three of these particle separating devices. This paper reports the results of using combinations no. 1 (a differential mobility analyzer/CNC) and no. 3 (a diffusion battery/CNC) plus a single-particle optical counter and a laser spectrometer (see light scattering instruments, Table I) in semiconductor cleanrooms of varying air quality. The integral mobility analyzer/CNC (combination no. 2) was not evaluated, so no data from this combination will be presented. Monitoring cleanrooms of the highest air quality has also included periods in which the ultrafine aerosol particle measurement has been by total CNC count alone without any of the size separating stages. While this approach lumps all ultrafine aerosol particles into a single measurement, this single datum can be added to a conventional cumulative size distribution, as generated by an optical particle counter (OPC) or a laser spectrometer. As indicated in Table I, the smallest particle detectable by most OPC's is about 0.2 μm. Laser spectrometers can measure as low as 0.06-0.09 μm but at a much reduced sample flow rate (1 ft^3/min for the OPC; 0.002-0.01 ft^3/min for the laser spectrometer). The low sampling flow rate of the laser spectrometer generally makes it less suitable for cleanroom measurements than the OPC. However, the laser spectrometer is excellent for calibration of ultrafine aerosol instruments at high particle concentration as discussed next.

Prior to extensive site measurements, the two instrument combinations were cross checked with respect to a laser spectrometer. A lengthy series of comparative measurements was carried out using such test aerosols as freshly generated monodisperse salt, freshly dispersed polystyrene-latex (PSL) spheres, polydisperse ambient room air, and prefiltered room air.

With all these aerosol sources, the aerosol particle concentration greatly exceeded that found in a typical cleanroom. This high concentration aids in establishing instrument measurement consistency but does not necessarily adequately rate instrument suitability for cleanroom use. The latter judgment requires tests at actual cleanroom concentrations, a condition created most readily by cleanrooms themselves. Such tests will be described below.

In the calibration test series of this section, the most extensive comparisons were between a differential mobility analyzer/CNC combination, hereafter called simply the DMPS (see Appendix B), and a laser spectrometer, the PMS Model LAS-X, hereafter referred to as the LAS-X. The size ranges detected by each of these two instruments overlap, both measuring aerosol particles in the 0.09-0.5 μm size bracket. Monodisperse PSL spheres are commercially available in several sizes within this range. Figure 3 plots measurements made of 25 PSL aerosol streams using both the DMPS and the LAS-X. Most of

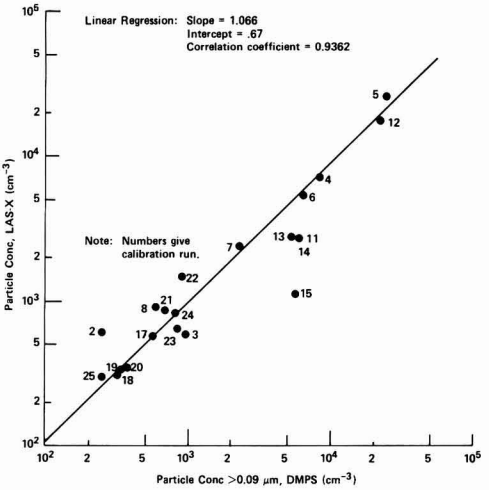


Fig. 3. Concentration measurements of PSL aerosol streams using the DMPS and the LAS-X.

these measurements were made quasi-simultaneously. Since the full range of the DMPS cycle takes 20-30 min and the LAS-X a minute or less at the aerosol particle concentrations generated for the calibrations, the LAS-X count represents the average of many short counting periods spread over the entire DMPS measuring cycle. The regression equation relating the two counts is

$$X = 0.674Y^{1.066}$$
$$r = 0.936 \quad [1]$$

where X is the concentration of particles > 0.09 μm in size as measured by the DMPS (cm^{-3}), Y is the total concentration measured by the LAS-X (cm^{-3}), and r is the correlation coefficient.

Although the DMPS counts fewer particles at low concentration and more at high concentration than the LAS-X, the differences are only about 20% cent over the range of 10-10^4 particle/cm^3. This agreement between the two instruments, each based on completely different sizing principles, is deemed satisfactory for most aerosol particle measurements.

Individual peaks matched reasonably well, as shown in Fig. 4. (The Fig. 4 plot of 0.3 μm PSL spheres is actually the best match among the various PSL comparisons made.) The two LAS-X plots show the value of higher resolution measurements. In one data set, 16 channels span the entire size range of the instrument (0.09-3.0 μm); in the higher resolution setting these same 16 channels span only the range 0.2-0.5 μm. Total concentration varies strongly with size in a monodisperse sample and the high resolution counting mode defines the peak in concentration much better. This high resolution mode of the LAS-X matches the size distribution measured by the DMPS quite well.

In polydisperse aerosol mixtures, aerosol concentration does not vary as much with size as in the monodisperse calibrating aerosols. In this sense, polydisperse aerosol samples represent a less severe test of the aerosol measuring array. However, a polydisperse size distribution more realistically simulates the aerosol found in a cleanroom, especially if it is generated by prefiltering ambient room air. By admitting ambient laboratory air into a closed chamber and then recirculating it continuously through a prefilter, a stable aerosol mixture eventually results that can be used as a source of polydisperse aerosol for instrument array calibration. Figure 5 plots the size distributions measured by the DMPS and the LAS-X

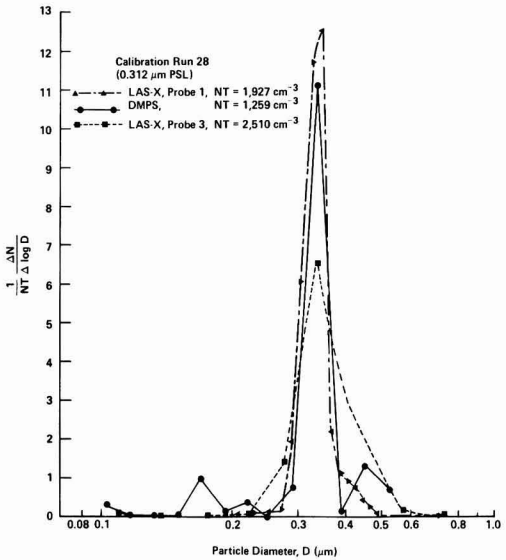


Fig. 4. Differential size distribution of monodisperse 0.3 μm PSL spheres as determined by the DMPS and the LAS-X. NT: particle concentration summed over all sizes. Probe settings on the LAS-X refer to particle size spans.

with such a polydisperse source. Again, the agreement is good in the region of size overlap.

Similar calibration runs with a collimated hole diffusion battery (the CHDB/CNC, see Appendix B) show that it sizes 0.08 μm PSL particles correctly and agrees well with the LAS-X when measuring polydisperse size distributions at particle concentrations above contemporary cleanroom levels. A representative comparison appears in Fig. 6. This plot shows the size distributions measured by both the CHDB/CNC and the LAS-X for air recirculated continuously through an 80% efficient prefilter in a closed box. Particle concentration (size > 0.1 μm) is about 0.1 cm^{-3}, a concentration an order of magnitude lower than the lower concentration limit of the DMPS measuring capability. At this concentration, agreement between the CHDB/CNL and the LAS-X is satisfactory.

Cleanroom Measurements

Four different levels of air quality make up the different cleanrooms sampled as part of this project. In order of decreasing air quality, they were as follows.

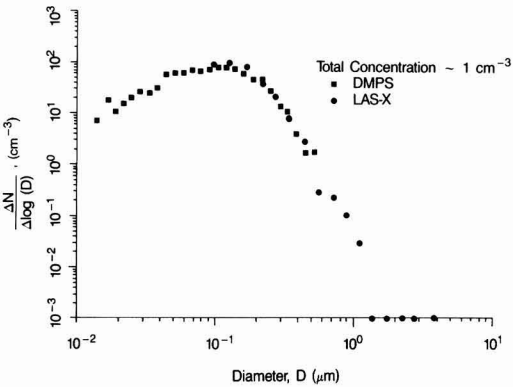


Fig. 5. Differential size distribution of a polydisperse particle mixture as measured by the DMPS and the LAS-X.

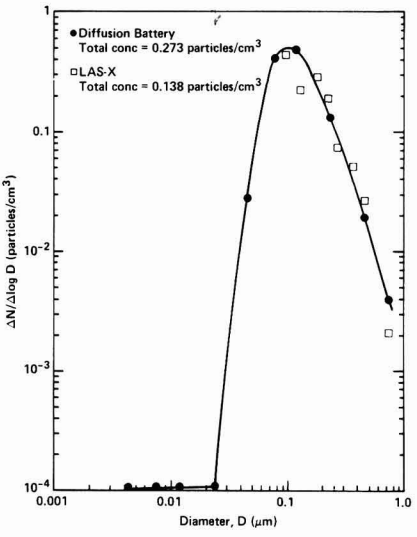


Fig. 6. Differential size distribution of a polydisperse particle mixture (room air recirculated through a prefilter) as measured by the CHDB/CNC and the LAS-X.

1. The future manufacturing area of the Microelectronics Center of North Carolina (MCNC).—This facility was not operational at the time of the air sampling, but all filters had been installed and the recirculating fans had been on for at least 3 months during the earliest sampling periods from which data reported here were collected.

2. A state-of-the-art manufacturing area.—Measurements were made in this facility both while work was in progress and over a weekend shutdown period. However, the sampling site was remotely located with respect to most production activity so that the air sampled is nearer that of a cleanroom at rest than an operational cleanroom.

3. The photoresist room of a university fabrication facility.—This small room is isolated from the main fabrication area and has its own fan and filtration system. Traffic was low during the sampling period.

4. The main fabrication area of the same university facility.—This larger room houses all furnaces and other wafer processing equipment. Its room filtration system is smaller than state of the art, and personnel cleanroom procedures are also less rigid. During the sampling period, the mean concentration of aerosols of size equal to or greater than 0.5 μm was about 300 ft^{-3}.

The DMPS proved capable of measuring size-distribution spectra in only the Class 300 university facility. (See Fig. A-1 for definitions of air-quality classes.) At the other three sites, the particle concentration was too low for significant counting.

The size-distribution data collected at this site (and at the other sites to be reported on in the following paragraphs) are presented in two forms: as differential size-distribution plots and as cumulative size-distribution plots. The latter plot is the type that appears in Federal Standard no. 209B (2) and forms the basis for the various classes of air quality defined in that Standard. The former type of presentation, showing aerosol concentrations at each aerosol diameter, is perhaps more popular among aerosol technologists. Further reflecting this user association, the concentration units used here will be per cubic centimeter for the differential-distribution plots and per cubic foot for the cumulative-distribution plots. The ordinate of the differential-distribution curve in all plots is dN/d (log D), and the abscissa log D, where N is the aerosol concentration and D is the aerosol diameter. The use of a log scale in constructing these plots provides

better coverage of typical aerosol ranges; in the differential plots, the ordinate dN/d (log D) thus is in units of concentration rather than concentration per size increment. Total aerosol concentration as a function of time is the third type of data summary to be presented.

Main fabrication area of a university fabrication facility (DMPS for ultrafine particle data).—Figure 7 presents total aerosol concentration measured by various instruments over the sampling period. The different concentrations measured by each instrument reflect their different size sensitivities. Figures 8 and 9 plot the grand average size distributions as differential and cumulative distributions, respectively. These distributions represent the averages over the entire sampling period depicted in Fig. 7, peaks as well as valleys.

Each datum of the differential number distribution plot (Fig. 8) has error bars corresponding to plus and minus one standard deviation about the mean. In spite of the relatively large error associated with many of the data points, a maximum in the plot clearly occurs in the vicinity of 0.1 μm. In the cumulative-distribution plot (Fig. 9), this peak represents a flattening of the curve and a departure from the extrapolation of the cumulative-size distribution assumed in Federal Standard no. 209B. (The size distributions published in Federal Standard no. 209B [Fig. A-1] abruptly terminate at D = 0.5 μm, so that the distribution below that size is not specified; the curve identified as from Federal Standard 209B in Fig. 9 is thus an extrapolation below 0.5 μm that is drawn with the same slope as that of the distribution above 0.5 μm which is specified in 209B.) Thus, while the total concentration of aerosols measured by the CNC in this university fabrication laboratory exceeds that measured by the optical counters, it is not as high as would be predicted by a simple extrapolation of the 209B size distribution. This conclusion proves true in all the other cleanrooms monitored as well.

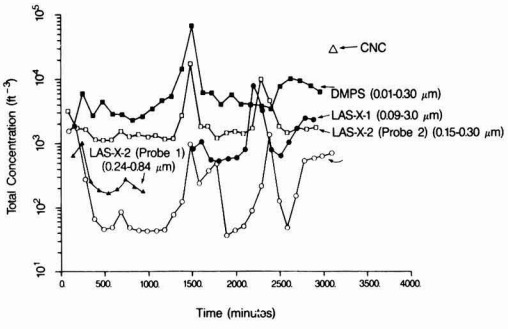


Fig. 7. Total aerosol concentrations, university fabrication laboratory.

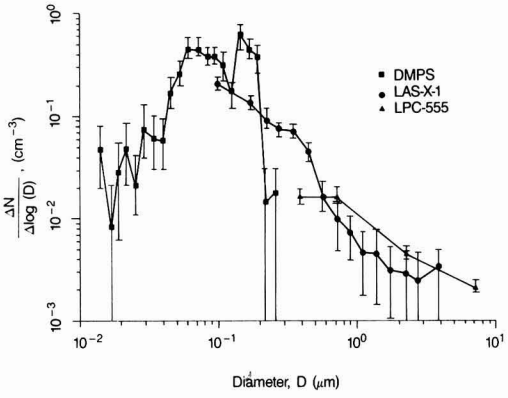


Fig. 8. Grand average differential size distributions, university laboratory.

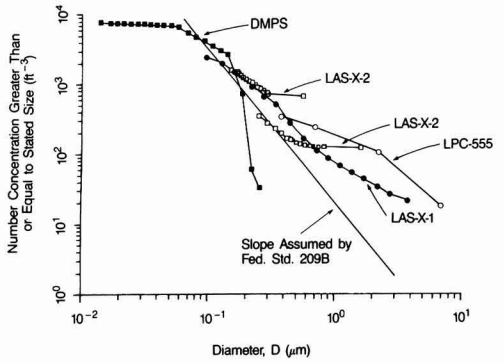


Fig. 9. Grand average cumulative size distribution, university laboratory.

University photoresist room/Class 100 manufacturing area/MCNC (ultrafine particle data by CNC alone).—Detailed size distribution data could not be collected below 0.1 μm in any of these facilities because of the inability of the DMPS to detect a statistically significant number of particles. However, by using the CNC alone, a single data point could be collected in the ultrafine-aerosol regime (Table II) and incorporated into a cumulative-distribution plot (Fig. 10).

The cumulative size distribution plot of Fig. 10 combines one CNC count with four conventional optical particle counter cumulative counts. The CNC total count is plotted at 0.01 μm, which is the size at which the counting efficiency of the CNC falls below about 50% (8). For particles larger than 0.02 μm, the CNC counting efficiency exceeds 90%; for particles smaller than 0.01 μm, counting efficiency decreases rapidly to about 10% at 0.005 μm. Thus, a sub 0.01 μm component may be included in the count plotted at 0.01 μm, but its magnitude should be small. Because of this unknown sub 0.01 μm component, the concentration plotted at 0.01 μm might be larger than the true concentration, but this error is compensated by the reduced counting efficiency between 0.01 and 0.02 μm, making 0.01 μm a reasonable compromise size for plotting CNC data.

By extrapolating the slope used in defining the air-quality classes of Federal Standard no. 209B from the 0.5 μm cutoff of the Standard to the 0.01 μm size in the ultrafine regime, it can be seen that the concentration plotted at 0.01 μm from the CNC count falls well below the concentration predicted by the extrapolation. This result has been universally true for measurements carried out in cleanrooms of various air qualities and in other areas where air quality depends on filtered air (Fig. 11). Figure 11 plots the ratio of the concentration of particles whose size equals or exceeds 0.01 μm (the CNC-determined concentration) to the concentration of particles whose size equals or exceeds 0.3 μm (the lower cutoff of the 1 ft³/min

Table II. CNC and OPC concentrations measured in various cleanrooms

	CNC conc. (ft^{-3})	Concurrent OPC conc. (ft^{-3})
Manufacturing facility	180	3.2
University laboratory		
Fabrication area	27,100	687
Protoresist room	2,860	53

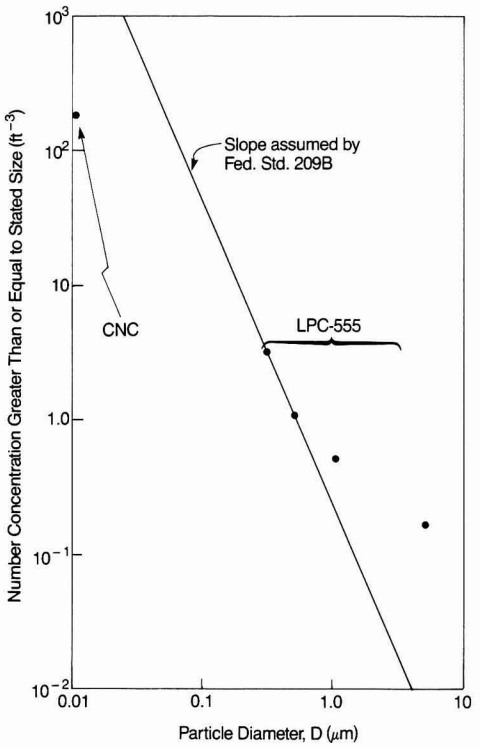


Fig. 10. Cumulative distribution data including that of the CNC alone.

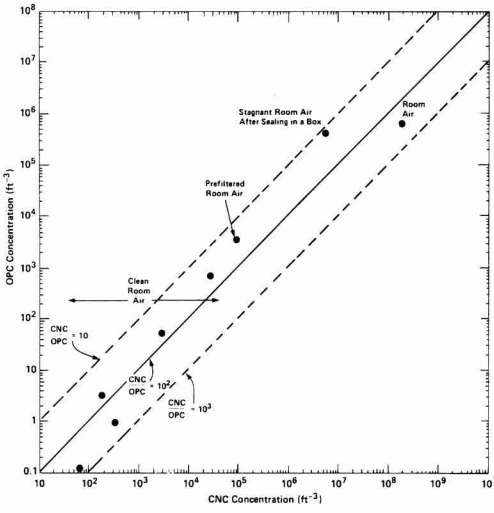


Fig. 11. Comparison of total aerosols counted by the optical particle counter with those counted by the condensation nuclei counter.

OPC [the PMS Model LPC-555] used in these measurements). In Fig. 11, this ratio is written as CNC/OPC. The slope of Federal Standard no. 209B predicts this ratio to be about 1750. The ratios plotted in Fig. 11 all lie between the 10 and 1000 bounds. Interestingly, the highest values of these ratios occur at both the upper and the lower extremes of the concentration range; all the intermediate values are less than 100. No significance or claim of universality is made for this observation or for any of the data points. Virtually all these measurements were carried out in cleanrooms or sheltered areas at rest; they represent measurements made overnight or over weekends during which time activity was either nonexistent or remote to the sampling points. Human activity would be expected to change both the concentration and the size distribution of the aerosols detected. For example, ambient air measurements made in Los Angeles by Whitby *et al.* (1) show the CNC/OPC ratio as defined above to exceed the 1750 predicted by Federal Standard no. 209B, being on the order of 10^4 (Fig. 1).

The CNC/OPC ratios measured in high quality cleanrooms thus support the conclusion that the flattening of the cumulative size distribution below 0.1 μm measured in a low quality cleanroom (Fig. 9) describes the cumulative size distributions of the higher quality cleanrooms as well. Again, this conclusion probably applies only to areas in the cleanroom whose air quality is dominated by the effluent from the HEPA filters rather than emissions from a local source such as equipment or people.

MCNC fabrication area (CHDB/CNC for ultrafine particle data).—The primary purpose of the CHDB/CNC combination was to verify, on a one-time basis, that the flattening of the cumulative size distribution curve below 0.1 μm observed in the Class 300 university fabrication laboratory (Fig. 8) and shown to be consistent with CNC/OPC ratios measured in cleanrooms of higher air quality (Fig. 11) also characterizes the air found in a state-of-the-art cleanroom.

The collimated hole diffusion battery consists of long, cylindrical paths through which the aerosol must pass and along which are access ports that allow CNC measurement of concentrations. The pathlength between the entry port and any access port defines a channel length; the longer the channel length, the greater the particle capture by diffusion to the channel wall. A series of concentration measurements at various channel lengths permits the determination of a size distribution because of the dependence of diffusion coefficient upon particle size. The collimated hole diffusion battery consists of 11 channels, typically measured sequentially by connecting the CNC to each port, one after the other. This measurement technique proved unsatisfactory when using one CNC for all diffusion battery channel measurements in series.

A problem occurred because the long measuring interval used (100 min/port) to obtain sufficient counts in each channel stretched the entire measuring cycle over more than half a day, during which time the cleanroom aerosol concentration changed. Thus, early channels sampled one particle population, while later channels sampled a different population. This instability caused the data inversion process to yield nonsensical distributions.

Two corrective actions were taken: (*i*) a second CNC was added to the instrument combination so that the zero channel concentration (the uncut particle population) was always measured at the same time that a downstream channel was being measured; and (*ii*) only three downstream channels were actually measured, the intermediate channel values being deduced by curve fitting. The first corrective action means that the channel data could be expressed as a fraction of the 0 channel count and thus variations in total aerosol concentration over the measuring cycle could be compensated for. Changes in size distribution, however, are not compensated.

Using this technique produced results such as those shown in Fig. 12. Figure 12 contains two presentations of the same data. The dots (or solid circles) represent the raw data in which the fractional penetration of the three downstream channels, expressed in terms of the mean channel 0 concentration, have been plotted at the size for which the channel penetration is calculated to be 50% as determined by the calibration of the battery. The calculated distribution shown by the squares is that obtained by using the three measured channel values to derive a best fit curve for the penetration from all channels, and

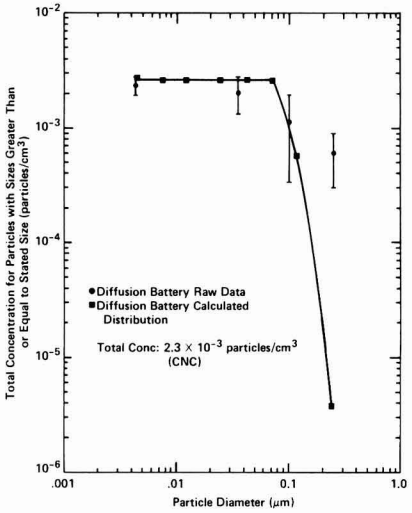


Fig. 12. Cumulative size distribution of ultrafine aerosols in a state-of-the-art cleanroom as deduced from CHDB/CNC measurements.

then substituting this complete set of fitted channel penetration data into published conversion models (9).

This procedure produced a cumulative size distribution having relatively few particles below 0.07 μm for the measuring cycle depicted in Fig. 12. The total mean concentration of condensation nuclei over this measuring period was about 60 ft^{-3}, an impressively low number but one that is typical of state-of-the-art cleanrooms at rest. Other measurement runs yielded similar cumulative size distributions.

Conclusions

The cumulative size distributions of ultrafine particles in resting semiconductor cleanrooms flatten out for particles whose diameters are below about 0.1 μm, as might be deduced from the penetration characteristics of a HEPA filter. The large concentrations of ultrafine particles present in ambient air are effectively removed by these filters, and simple extrapolation of the Federal Standard no. 209B curves leads to overestimation of the ultrafine particle populations below about 0.1 μm.

These conclusions apply to cleanrooms at rest. Particle generating activity within an operational cleanroom can easily dominate the ultrafine aerosol concentration in its vicinity and downwind of it. Ultrafine aerosol concentrations in an operational cleanroom, therefore, like larger aerosols, probably depend on the process and people activity and probably are not limited by the air filters. The condensation nuclei counter, in conjunction with a 1 ft^3/min optical particle counter, is a practical instrument for measuring ultrafine particle concentrations. This combination does not yield size distribution over the ultrafine particle regime. The only instrument combination so far demonstrated to be capable of ultrafine particle size distribution measurements (0.01-0.1 μm) at semiconductor cleanroom concentrations (less than 1000-5000 ultrafine particle/ft^3, for example) is the collimated hole diffusion battery/CNC reported here, and that only with a dual CNC configuration and a modified sampling protocol.

Acknowledgments

Much of the data reported in this paper were collected as part of a research program sponsored by the Semiconductor Research Corporation and the Microelectronics Center of North Carolina.

Manuscript submitted April 8, 1985; revised manuscript received Aug. 8, 1985. This was Paper 474 presented at the New Orleans, Louisiana, Meeting of the Society, Oct. 7-12, 1984.

Research Triangle Institute assisted in meeting the publication costs of this article.

APPENDIX A

Air-Quality Classifications

Figure A-1 is a reproduction of the plot defining classes of air quality in Federal Standard no. 209B (1). The Class 1000 designation, added by a later amendment, has been included in Fig. A-1. Intermediate designations such as 500, 80,000, etc., defined by the 0.5 μm intercept of a curve drawn parallel to those shown, are also defined implicitly. Common usage has been to extend the range of these definitions to include Class 10 and even Class 1 in describing the air quality in contemporary cleanrooms at rest. Note, however, that the Fig. A-1 plot uses a log-log scale so that Class O cannot be defined by this procedure. Under a GSA contract, Committee RP50 of the Institute of Environmental Sciences is currently revising and updating Federal Standard no. 209B. Thus, within the next year or two, a new standard, 209C, should be available for critique and suggestions, prior to promulgation for general use.

APPENDIX B

Commercial Availability of Ultrafine Aerosol Particle Instrumentation

The instruments identified as suitable for ultrafine aerosol particle measurement above have limited commercial availability, being marketed by only one company at present (TSI, Incorporated, St. Paul, Minnesota). Each of the three size separators is discussed separately in the following paragraphs. In the case of the differential mobility analyzer, the complete differential mobility analyzer/condensation nuclei counter combination is commercially available and is described as one unit, the differential mobility particle sizer (DMPS).

1. The differential mobility analyzer.—The only commercial equipment now readily available is the TSI Model DMPS/C 3932 differential mobility particle sizer, which

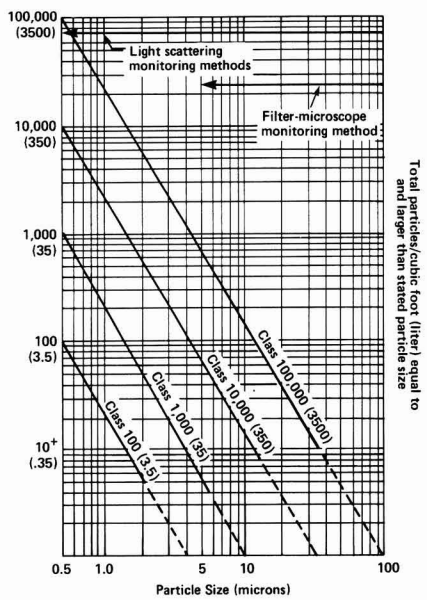


Fig. A-1. Definitions of air quality classes from Federal Standard no. 209B, April 24, 1973, and its Amendment 1, May 30, 1976. Note: Counts below 10 (0.35) particle/ft^3 (liter) are unreliable except when a large number of samplings is taken.

includes a CNC (TSI Model 3020) (8) to measure particles separated by a TSI electrostatic classifier Model 3070 (a differential mobility analyzer), the combination being controlled by an Apple IIe personal computer, which also stores and processes the collected data.

2. The integral mobility analyzer.—The only commercially available apparatus for this measurement is the TSI Model 3030 electrical aerosol size analyzer. To be capable of single-particle detection, it should be modified by replacing the current measuring electrometer with a CNC.

3. The diffusion battery.—The only commercial version is a screen-type diffusion battery (TSI's Model 3040). The diffusion battery used in the measurements presented in this paper, however, used a custom-built collimated hole diffusion battery (CHDB) (7). Any diffusion battery must be followed by a CNC for counting.

4. The continuous flow condensation nuclei counter.—While various commercial versions of the condensation nuclei counter have been on the market for years, these older models all relied on an adiabatic expansion to induce condensation. This mode of operation dictated intermittent operation in which sampling flow had to stop while the expansion, condensation, and counting steps took place. When flow resumed into a chamber of lowered pressure, a pulsed flow occurred. The recent introduction of a continuous flow model (TSI Model 3020) (8) avoids these problems by using a thermoelectrically cooled chamber through which the saturated vapor and aerosol continuously flow.

REFERENCES

1. K. T. Whitby, R. B. Husar, and B. Y. H. Liu, in "Aerosols and Atmospheric Chemistry," G. M. Hidy, Editor, pp. 237-264, Academic Press Inc., New York (1972).
2. Federal Standard no. 209B, "Federal Standard Cleanroom and Workstation Requirements, Controlled Environment," April 24, 1973; Amendment 1, May 30, 1976, General Services Administration, Specification Activity, Printed Materials Supply Division, Washington, DC (1976).
3. W. Bergman, A. Bierman, W. Kuhl, B. Lum, A. Bogdanoff, H. Hebard, M. Hall, U. Banks, M. Mazumder, and J. Johnson, "Electric Air Filtration: Theory, Laboratory Studies, Hardware Development, and Field Evaluations," UCID-19952, Sept. 1983, Technical Information Department, Lawrence Livermore Laboratory, Livermore, CA (1983).
4. R. G. Knollenberg, *J. Environ. Sci.*, **28**, 32 (1985).
5. A. W. Hogan, in "Aerosol Measurement," D. A. Lundgren, M. Lippman, F. S. Harris, Jr., W. E. Clark, W. H. Marlow, and M. D. Durham, Editors, pp. 497-514, University of Florida Press, Gainesville, FL (1979).
6. P. Keady, F. Quant, and G. J. Sem, *TSI Quart.*, **9**, 2 (April-June 1983).
7. D. Sinclair, *AIHA J.*, **33**, 729 (1972).
8. J. K. Agarwal and G. J. Sem, *J. Aerosol Sci.*, **11**, 343 (1980).
9. A. Kapadia, Ph.D. thesis, University of Minnesota, Minneapolis, MN (1980); Particle Technology Laboratory Publication no. 413, Dept. of Mechanical Engineering, University of Minnesota, Minneapolis, MN.

Potential-Enhanced Doping of Si Grown by Molecular Beam Epitaxy

R. A. A. Kubiak, W. Y. Leong, and E. H. C. Parker

Solid State MBE Research Group, Sir John Cass Faculty of Physical Sciences and Technology, City of London Polytechnic, London, England EC3N 2EY

ABSTRACT

Potential-enhanced doping (PED) is a method by which the incorporation efficiencies of certain low sticking coefficient, coevaporated dopants can be enhanced during Si-MBE. PED is implemented by application of a potential to the substrate during deposition. The applied potential is used to control instantaneous dopant incorporation, thereby permitting accurate control over doping levels over a wide dynamic range, as well as offering a powerful method of profile control. PED is especially effective with Sb doping, with enhancements by up to 1000 times being realized, thus permitting doping levels up to the solubility limit to be readily achieved. PED is less efficacious in the case of As doping obtained from III-V compound sources. The electrical, optical, and crystallographic quality of PED:Sb-doped material is comparable to that of bulk Si. Doping transitions of < 50 Å/decade have been obtained for transitions over several decades.

Compared with low energy dopant-ion implantation (1, 2), coevaporation of elemental doping species from thermal sources offers a simple and inexpensive method of doping in Si-MBE. However, not until recently have coevaporative methods, as applied to the preferred MBE dopants Sb, Al, and Ga, proved capable of offering the desired control over doping; these dopants have low, growth temperature-dependent incorporation efficiencies and a propensity to segregate at the growing surface (3-6). Both these factors are severe impediments to obtaining good dopant and profile control. However, two recent developments hold considerable promise in alleviating the limitations of coevaporative doping in Si-MBE. Despite the high temperatures required for evaporation, coevaporated boron behaves as a near-ideal p-type dopant, having a unity incorporation coefficient and being free from any severe surface segregation phenomena (7-9). The second development relates to a method of improved control over dopant incorporation, known as potential-enhanced doping (PED) (8, 10), and is particularly effective in the case of the preferred MBE n-type dopant, Sb (11). This paper reports on PED technique applied to Sb, As, and Ga doping, reports on the material quality obtained, and demonstrates the degree of profile control that can be realized.

Experimental

Epitaxial Si was deposited onto 3 in. diam, (100) Si substrates in a cryopumped three-chamber UHV system described earlier (10, 12). Airco Temescal electron-beam evaporators (Type SFIH-270-2) were used to evaporate semiconductor-grade polycrystalline Si with $\rho > 500$ Ω-cm, at growth rates ranging from 0.5 to 20 μm-h^{-1}, to thicknesses of 0.2-25 μm. Epilayer growth was performed at temperatures in the range 700°-900°C; although the absolute temperature was known only to within ±30°C, reproducibility between experimental runs was better than ±10°C.

Consistent with earlier studies (3-6), elemental species were generally used to obtain Sb and Ga doping. However, III-V compounds were also employed as Group V dopant sources to permit (*i*) comparison of Sb incorporation from Sb_4 (the dominant species generated by elemental Sb) and Sb_2 (the dominant Group V species generated by InSb) and (*ii*) controllable As doping without the attendant problems of severe memory doping effects caused by the high vapor pressure of elemental arsenic (13). The sources used and the resultant fluxes obtained are summarized in Table I. These materials were evaporated from conventional effusion furnaces of the type used in III-V-MBE, with pyrolitic boron nitride crucibles for all the sources except Ga, which was evaporated from a graphite crucible. The positioning of the thermocouple in the source cells used resulted in an underestimate of the source temperature, precluding calculation of the incident dopant fluxes. The Si and dopant source were situated ~28 cm below the substrate plane, in the configuration presented elsewhere (10).

Table I. The coevaporated sources used to achieve Sb, As, and Ga doping. The dominant and secondary evaporated species are listed

Dopant material	Evaporated species Primary	Secondary
Elemental Sb	Sb_4	Sb_2
InSb	Sb_2	In
GaAs	As_2	Ga
InAs	As_2	In
Elemental Ga	Ga	—

The electrical properties of the material were assessed by electrochemical CV profiling (14) and, where appropriate, by Hall measurements. Spreading resistance profiling (SRP), secondary ion mass spectrometry (SIMS), deep level transient spectroscopy, photoluminescence, and Rutherford backscattering (RBS) were further employed on selected samples to evaluate the quality of doped material and the capability for doping control.

Potential-Enhanced Doping

Enhanced incorporation of dopants was induced by application of a voltage (U_s) via a Ta brush in contact with the rotating assembly onto which the substrate is mounted for growth. A schematic representation of the experimental configuration used has been presented elsewhere (10).

The efficacy of PED on dopant incorporation during growth was initially investigated by applying staircase voltage programs of the type shown in Fig. 1a, since the resulting Sb doping profile, as shown in Fig. 1b, is optimized for profile evaluation using the electrochemical-CV method (14). Data obtained for both negative and positive voltages from five epilayers all grown at the same substrate temperature and incident Sb-flux as used in Fig. 1 are presented in Fig. 2. The main features to be noted are (*i*) negative potentials are significantly more effective at sustaining enhancement than positive potentials, and (*ii*) only enhancement obtained under negative potentials was reproducible. As a result, only negative voltage PED will be subsequently discussed.

Figure 3 demonstrates PED enhancement obtained over a wide range of growth temperatures (~730°-850°C) and Sb cell temperatures (315°-390°C), conditions which

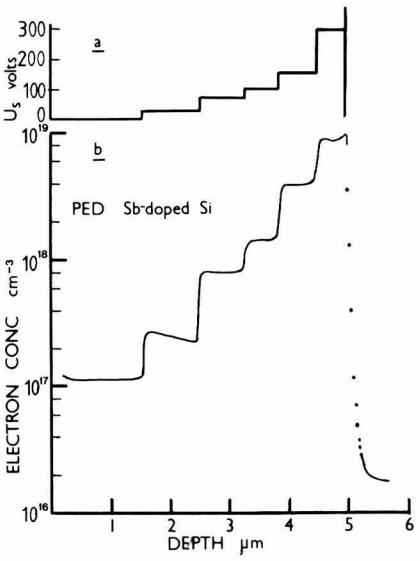


Fig. 1. A typical voltage program (a), and resulting Sb-dopant profile (b), used to establish the efficacy of PED.

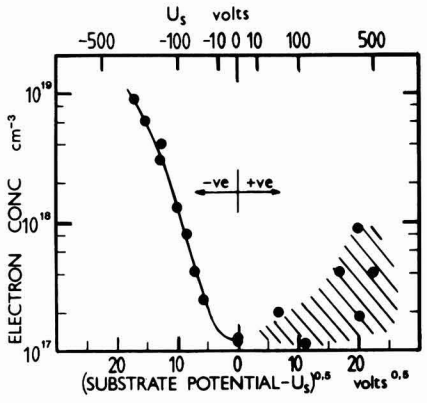


Fig. 2. Variation of Sb doping with applied potential (U_s) obtained from a series of epilayers all grown at the same temperature and Sb flux as used in Fig. 1. For convenience of presentation, the data are presented against the square root of U_s.

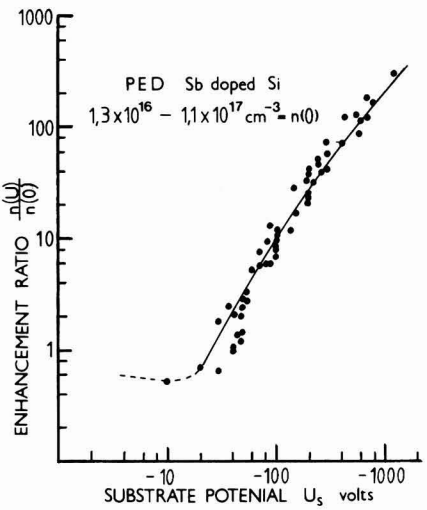


Fig. 3. PED enhancement over a range of growth temperatures and Sb fluxes (generated from elemental Sb and InSb) corresponding to zero potential doping range of 1.3×10^{16} to 1.1×10^{17} cm^{-3}. The ordinate is normalized as an enhancement ratio of doping level at potential U, to that at 0 V: $n(U)/n(0)$.

yielded a zero potential doping range $n(0) = 1.3 \times 10^{16}$ to 1.1×10^{17} cm^{-3}. The ordinate has been normalized as an enhancement ratio of doping level at potential U compared with that at zero volts: $n(U)/n(0)$. It is apparent that PED:Sb doping is highly reproducible. Within the range of growth conditions investigated, a calibration obtained under one set of growth conditions (pertaining to a certain Sb adlayer coverage) can be translated to any other condition. The use of InSb as an Sb_2 source yielded data (10) which coincided with those presented in Fig. 3, indicating that enhanced dopant incorporation was not dependent on the nature of the evaporated Sb species.

Sb forms a two-dimensional surface adlayer with the surface coverage depending on growth temperature and incident Sb flux (5). Based on reported data, the Sb surface coverages obtained under the range of growth conditions employed in this study are considerably less than a monolayer, but still sufficiently high to be detected by Auger electron spectroscopy (AES). Figure 4 shows typi-

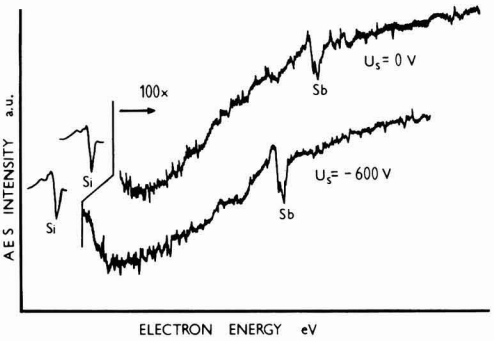


Fig. 4. Auger electron spectra of two epilayers grown under identical growth conditions, except with different applied voltages. The peak heights are identical (within experimental error caused by nonreproducibility of sample positioning), despite a doping level difference of 200.

cal spectra obtained from two epilayers grown at the same temperature and under the same Sb flux, but with differing applied potentials. (The substrate temperature was quenched rapidly immediately on terminating growth to minimize Sb desorption.) Since the measured Sb/Si peak intensity ratio obtained from the two spectra remains practically unchanged, whereas the doping levels differed by a factor of 200, it is surmised that PED enhances incorporation of Sb from the adlayer and does not affect surface coverage (except in a secondary capacity by depletion due to enhanced incorporation). This is consistent with the implication drawn from Fig. 3 that the degree of PED enhancement is independent of adlayer coverage, and hence Sb flux, over the range of growth conditions employed. Although current models for incorporation from dopant adlayers do not distinguish the surface species present, the similarity of enhancement obtained from Sb_2 (InSb source) and Sb_4 (elemental source) suggests a common surface species from which incorporation occurs.

The efficacy of PED:As doping was reported earlier to be less pronounced than in the case of Sb doping (10). Figure 5 shows the enhancement ratio obtained over a range of GaAs source temperatures of 550°-712°C [corresponding to the indicated $n(0)$ doping levels] at a fixed growth temperature of ~810°C. Unlike with PED:Sb doping, Fig. 5 indicates that the enhancement ratio increases with As coverage. This result may indicate either that As adlayer formation is less simple than that of Sb, or, more probably, that the simultaneous presence of a Ga adlayer from the GaAs source affects As incorporation. The latter suggestion is supported by the following observations: (*i*) SIMS profiles have indicated that Ga is also incorporated during doping from the GaAs source, although the relative levels have not been quantified; (*ii*) the increasing enhancement ratio with GaAs source temperature is consistent with the reported thermal decomposition behavior of GaAs, *i.e.*, an increasing As_2/Ga flux ratio with increasing temperature (15); and (*iii*) preliminary investigations using InAs indicate a higher enhancement ratio (factor of ~2) than that obtained from GaAs at a given $n(0)$ coverage, suggesting that In interferes less with As incorporation than does Ga. Although further work is necessary to clarify the effect of the accompanying Group III fluxes obtained from III-V sources, the conflicting responses of the enhancement ratio to arsenide and antimonide sources may imply a shorter surface residence time or a higher spontaneous incorporation efficiency for As compared with that for Sb. Notwithstanding the difficulty in interpreting the effects of the accompanying Group III fluxes from III-V sources, the negligible response of PED:Ga doping (from an elemental source) confirms a species dependence for PED doping (10).

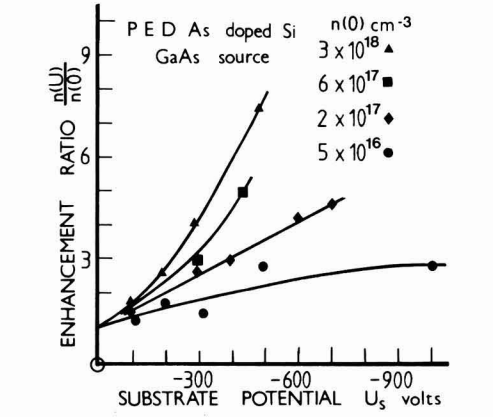


Fig. 5. PED enhancement ratio over a range of As fluxes generated using a GaAs source at constant growth temperature. $n(U)/n(0)$ increases at a given potential with increasing As flux, unlike the case of Sb presented in Fig. 3.

An interesting feature of Sb and Ga doping is that the doping level obtained is independent of growth rate. For example, all the data presented in Fig. 1-3 had no correction applied for growth rate over an experimental range of greater than ten times, and growth of epilayers in which changes in rate were intentionally introduced (with and without PED) confirmed this observation. Although clearly a useful effect, its interpretation in terms of growth step propagation under the adlayer regions (16) requires further study, particularly to account for its occurrence with or without PED. Indeed, this may suggest that spontaneous and enhanced incorporation are dependent on a common mechanism.

Mechanism for PED

The use of electron-beam evaporators for generation of the Si flux also leads to generation of charged particles in the MBE system; secondary (low energy) and backscattered (high energy) electrons are produced, as is a small fraction of low energy Si^+ ions caused by ionizing interactions between the Si flux and the primary electron beam. The application of a potential to the substrate would induce an electrostatic field within the MBE system, which would modify the trajectories of these particles and change the energy with which they impinge on the substrate. The high efficacy of negative potential PED implicates Si^+ ions as the species responsible for the phenomenon, and this is consistent with experiments where dopant incorporation has been enhanced by additional ionization of the Si growth flux by using an electron impact ionizer (17). It is interesting to note that a variety of other effects have been observed (18-21) probably dependent on the same phenomenon.

Enhancement of doping by Si^+ ions would be induced either by attraction of more Si^+ ions to the substrate by the electric field, thus increasing the number of ion-dopant interaction events, or by the increased energy of the ions producing an increased cross section for interaction. To distinguish between these possible mechanisms, an experiment was performed to restrict the flux of Si^+ ions within the MBE chamber to those with direct linear trajectories to the substrate, by using an apertured shroud (22). Since the enhancement ratio of Sb using this procedure was identical to that presented in Fig. 3, we surmise that acceleration of Si^+ ions generated by the evaporators was responsible for the enhancement of incorporation associated with PED.

Jorke *et al.* (17) have proposed that increased Sb incorporation by an applied potential is caused by secondary implantation of the adsorbed Sb atoms by the Si^+ ions. Al-

though such a model is consistent with the PED effect, a better understanding of adlayer chemistry (*e.g.*, the identification of adlayer surface species and the cause for the lack of response of doping level on growth rate), and measurement of experimental parameters such as ion currents, are required to understand the energy dependence indicated in Fig. 3. Alternative mechanisms cannot therefore be discounted at this stage, particularly: (*i*) Si^+ ion-induced activation of the surface dopant species (*e.g.*, decomposition of the adsorbed species to that required for incorporation, or Si^+ ion-induced enhanced surface diffusion of adlayer species), and (*ii*) the formation of Si^+ ion-induced preferential incorporation sites.

Assuming that PED-assisted doping involves direct interactions between Si^+ ions and the adlayer, the observed species dependence between Sb: and Ga:PED doping is consistent with their adlayer properties. Whereas Sb forms a two-dimensional coverage (5) permitting ready access of ion-stimulated Sb to incorporation sites, Ga nucleates as three-dimensional islands (4), thereby (*i*) reducing the cross section for interaction with Si^+ ions by reduced effective surface area and (*ii*) reducing accessibility of ion-stimulated Ga atoms to incorporation sites.

Material Quality

A range of uniformly Sb-doped epilayers was deposited onto 1-10 Ω-cm p-type substrates to facilitate junction isolation of substrate conduction, and resistivity/Hall measurements were performed on cross-shaped samples by using the van der Pauw method (23). The epilayers were sufficiently thick that depletion effects could be ignored (24). Figure 6 shows the measured 300 K mobilities ($\mu = R_H\sigma$) as a function of resistivities of the epilayers; the corresponding carrier concentrations, assuming a Hall factor of unity, are also included. All the epilayers with Sb doping levels greater than 1×10^{17} cm^{-3} were obtained with the aid of PED. Over the experimental doping range 5×10^{15} to 3×10^{19} cm^{-3}, the mobilities agree well with bulk Hall data (25). Comparison of eCV and SRP data (with its inherent assumption of bulk mobility values) confirms bulk-like mobilities at doping levels down to $< 1 \times 10^{15}$ cm^{-3}. By contrast, previous reports of Hall data on Sb-doped Si-MBE material obtained without the aid of PED (5, 26) indicated degraded mobilities and heavily defected material at carrier concentrations above 10^{17} cm^{-3}, caused by the associated requirement for heavy Sb adlayer coverage, which introduces the possibility of cluster incorporation and locally disrupted growth. The upper doping limit obtained in this study (3×10^{19} cm^{-3}) corresponds to the solubility limit of Sb in Si at typical MBE growth temperatures. The corresponding resistivity of 2×10^{-3} Ω-cm compares favorably with values used as n^+ contact regions in device structures, where considerably higher doping levels have to be introduced by ion implantation to achieve the same resistivity due to incomplete electrical activation and degraded mobilities. Extensive comparison between electrical (eCV, Hall, and SRP) and chemical (SIMS) measurements indicates that, to within measurement error, all incorporated Sb and As is electrically active.

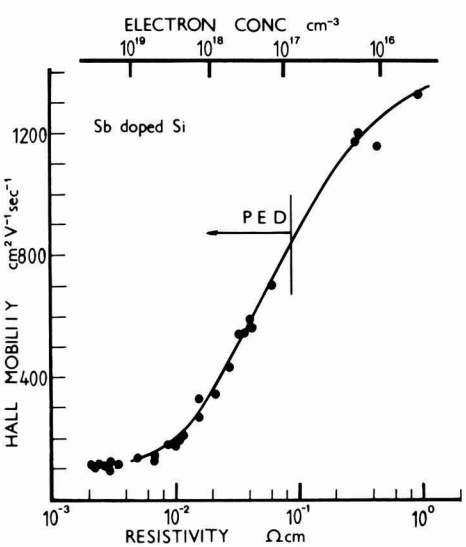


Fig. 6. Room temperature Hall mobility as a function of resistivity (and donor concentration assuming a Hall factor of unity) for uniformly Sb-doped epilayers. Data are superimposed on bulk values (25).

Since PED doping relies on ion irradiation of the epilayers, it is of concern whether any ion-induced damage is present to degrade material quality. To check on the crystalline quality of the material, RBS dechanneling analysis has been applied to an epilayer doped with PED:Sb at ~1 $\times$ 10^{19} cm^{-3} (U_s = −400V). The ratio of random-to-channeled signal, χ_{min}, from the epilayer was 0.03, which compares with values obtained from bulk Si: if significant damage had been introduced by PED causing displacement of the host atoms, considerably higher values of χ_{min} would obtain. It is surmised either that annealing of induced damage occurs at the MBE growth temperatures used or that the damage induced by the relatively low Si^+ fluence is small. RBS dechanneling analysis also indicates no significant fraction of Sb on nonsubstitutional sites, which is consistent with complete electrical activation.

The Sb-doped material was grown over a period of several months, interspersed with other studies, during which time improvements in defect densities were realized (22). Defect etching studies revealed that no additional defects could be specifically attributed to PED:Sb doping, since the material remained comparable with undoped Si grown under similar conditions. Again, this contrasts with earlier studies of Sb doping in MBE-Si without PED, where material became heavily defected at doping levels exceeding 10^{17} cm^{-3} due to high adlayer coverages (26). However, our As-doped epilayers had high dislocation densities when doping levels exceeded ~5×10^{18} cm^{-3}, possibly due to incorporation of Ga. PED:Sb doped Si-MBE material characterized using PL indicates the material to behave as bulk Si (27).

Profile Control

Since PED affects the incorporation efficiency of the dopant species from the adlayer, and not adlayer coverage, control over doping profiles should be readily attainable by using suitable voltage programs. Furthermore, sharp doping transitions should be accessible even at low growth temperatures, provided that equilibrium coverage of Sb has been reached (5). The control that can be realized over doping incorporation is demonstrated in Fig. 1. Further studies were undertaken to establish the doping transition widths obtained, and thereby confirm that PED controls Sb incorporation, and not the adsorption/desorption kinetics. Figure 7 shows a Sb doping profile in which the Si and Sb fluxes were maintained constant throughout the growth run, and three n^+ spikes were introduced by stepping the applied potential between 0 and −800V. This SIMS profile indicates the doping transitions to be extremely sharp; the near-surface doping transition (denoted A) had a measured width of < 50 Å/decade, which compares with the resolution limit of SIMS. The asymmetry of the spike features measured in the SIMS profile, and the gradual slight degradation in the shape of the spikes was established to be due to atomic mixing and segregation effects, since improved symmetry is obtained by profiling such structures at 45° to (rather than along) the sample normal (28). SRP and eCV electrical profiles agree within measurement error with the SIMS values at the dopant peaks. However, lower levels are measured (and indeed expected from the calibration shown in Fig. 3) by the electrical profiling

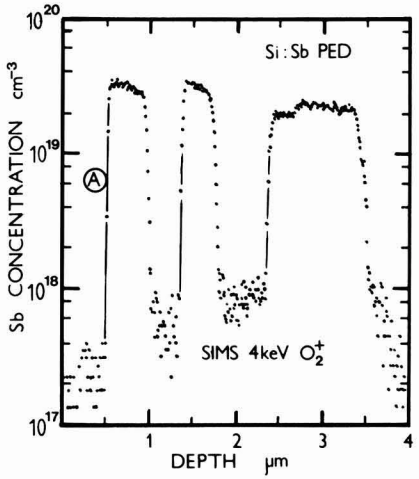


Fig. 7. SIMS profile of an Sb-doped structure grown using PED:Sb. The three n⁺ spikes were introduced by stepping the applied potential from 0 to −800V.

techniques than by SIMS in the n^- valleys due to a mass interference which limits SIMS detection to ^{121}Sb. Comparison of the transition widths obtained by SIMS and SRP indicated similar behavior to that discussed elsewhere for B-doped MBE-Si (9), implying that doping transitions obtained by PED:Sb doping in general exceeded the resolution limit of the three profiling techniques employed.

Conclusions

PED appears to be a powerful method of assisting coevaporation doping in Si-MBE, particularly in the case of n-type Sb. High doping levels are readily and reproducibly obtained using PED:Sb doping without the need for heavy adlayer coverage or low growth temperatures. Bulk-like mobilities up to the solubility limit ($\sim 3 \times 10^{19}$ cm^{-3}) are obtained. PED likely involves the acceleration of Si^+ ions to the substrate, although the exact mechanism for enhanced doping requires further clarification. Despite the influence of these ions, no degradation in crystallinity can be detected by RBS or defect assessment, and photoluminescence indicates the material to be bulk-like. Used in combination with coevaporative B doping as a p-type source (7-9), these methods offer a powerful alternative to dopant-ion implantation in Si-MBE, particularly where introduction of complex profiles involving sharp or controlled doping transitions over a wide dynamic range is required.

Acknowledgments

We wish to thank Dr. M. Pawlik (GEC Hirst Research Centre), Dr. M. G. Dowsett and Dr. D. F. McPhail (CLP), and Dr. E. Maydell-Ondrusz (University of Surrey) for SRP, SIMS, and RBS analyses, respectively, R. Houghton for associated experimental work, and P. Driscoll for technical assistance. The work is performed in collaboration with British Telecom Research Labs (Martlesham, UK) GEC Hirst Research Centre (Wembley, UK), and UG Semicon (East Grinstead, UK).

Manuscript received June 17, 1985. This was Paper 129 presented at the Toronto, Ontario, Canada, Meeting of the Society, May 12-17, 1985.

REFERENCES

1. R. A. Swartz, J. H. McFee, A. M. Voshchenkov, and S. N. Finegan, *Appl. Phys. Lett.*, **40,** 238 (1982).
2. Y. Ota, *J. Appl. Phys.*, **51,** 1102 (1980).
3. G. E. Becker and J. C. Bean, *ibid.*, **48,** 3395 (1977).
4. S. S. Iyer, R. A. Metzger, and F. G. Allen, *ibid.*, **52,** 5608 (1981).
5. R. A. Metzger and F. G. Allen, *ibid.*, **55,** 931 (1984).
6. J. C. Bean, *Appl. Phys. Lett.*, **33,** 654 (1978).
7. R. A. A. Kubiak, W. Y. Leong, and E. H. C. Parker, *ibid.*, **44,** 878 (1984).
8. R. A. A. Kubiak, W. Y. Leong, and E. H. C. Parker, Paper presented at the 3rd International Conference on MBE, San Francisco, 1984: *J. Vac. Sci. Technol. B*, **3,** 592 (1985).
9. R. A. A. Kubiak, W. Y. Leong, and E. H. C. Parker, in "Silicon Molecular Beam Epitaxy," J. C. Bean, Editor, p. 169, The Electrochemical Society Softbound Proceedings Series, Pennington, NJ (1985).
10. R. A. A. Kubiak, W. Y. Leong, and E. H. C. Parker, *Appl. Phys. Lett.*, **46,** 565 (1985).
11. R. A. A. Kubiak, W. Y. Leong, and E. H. C. Parker, in "Silicon Molecular Beam Epitaxy," J. C. Bean, Editor, p. 230, The Electrochemical Society Softbound Proceedings Series, Pennington, NJ (1985).
12. R. A. A. Kubiak, W. Y. Leong, R. M. King, and E. H. C. Parker, *J. Vac. Sci. Technol A*, **1,** 1872 (1983).
13. J. C. Bean, Personal communication.
14. W. Y. Leong, R. A. A. Kubiak, and E. H. C. Parker, in "Silicon Molecular Beam Epitaxy," J. C. Bean, Editor, p. 140, The Electrochemical Society Softbound Proceedings Series, Pennington, NJ (1985).
15. C. T. Foxon, J. A. Harvey, and B. A. Joyce, *J. Phys. Chem. Soc.*, **34,** 1693 (1973).
16. S. S. Iyer, Ph.D. Thesis, University of California, Los Angeles, CA (1982).
17. H. Jorke and H. Kibbel, in "Silicon Molecular Beam Epitaxy," J. C. Bean, Editor, p. 194, The Electrochemical Society Softbound Proceedings Series, Pennington, NJ (1985).
18. T. Itoh, T. Nakamura, M. Muromachi, and T. Sugiyama, *Jpn. J. Appl. Phys.*, **15,** 1145 (1976).
19. T. Narusawa, S. Shimizu, and S. Komiya, *J. Vac. Sci. Technol.*, **16,** 366 (1979).
20. Y. Shiraki, Paper presented at the 3rd International Conference on MBE, San Francisco, 1984; *J. Vac. Sci. Technol. B*, **3,** 725 (1985).
21. F. Arnaud D'Avitaya, Personal communication.
22. R. A. A. Kubiak, W. Y. Leong, R. Houghton, and E. H. C. Parker, in "Silicon Molecular Beam Epitaxy," J. C. Bean, Editor, p. 124, The Electrochemical Society Softbound Proceedings Series, Pennington, NJ (1985).
23. L. J. van der Pauw, *Philips Res. Rep.*, **13,** 1 (1958).
24. S. M. Sze, "Physics of Semiconductor Devices," John Wiley and Sons, New York (1969).
25. F. J. Morin and J. P. Maita, *Phys. Rev.*, **96,** 28 (1954).
26. V. Konig, H. Kibbel, and E. Kasper, *J. Vac. Sci. Technol.*, **16,** 985 (1979).
27. B. Hamilton, Personal communication.
28. M. G. Dowsett, Personal communication.

Rapid Thermal Annealing in GaAs IC Processing

S. J. Pearton, K. D. Cummings, and G. P. Vella-Coleiro

AT&T Bell Laboratories, Murray Hill, New Jersey 07974

ABSTRACT

A variety of annealing steps in GaAs IC processing presently performed in conventional furnaces may be readily transferred to more convenient rapid annealing furnaces. A comparison of the activation characteristics achieved for common implanted species (Si, Se, Be, Mg, and Zn) into semi-insulating GaAs by both annealing regimes is given. The limitations and advantages of the two methods with respect to encapsulation requirements, throughput, and handling are discussed.

The development of GaAs integrated circuits depends upon the routine production of conducting channel and contact regions by ion implantation into semi-insulating substrates. The high temperature annealing step required to activate the implanted ions is crucially important: the activation must be attained with minimal dopant redistribution, and loss of As from the wafer surface must be suppressed. The literature on ion implantation in GaAs has a long and somewhat contradictory history (1, 2), undoubtedly due in large part to the variable quality of substrates available. The need for surface protection, usually achieved by deposition of an encapsulating layer, is also a complicating factor; it is clear that stress induced in the wafer because of differing expansion coefficients (3) and impurities diffusing in from the cap (4), has often been the cause of nonreproducible results reported by many laboratories.

Recent advances in GaAs crystal growing technology, leading to wafers with more uniform properties over a 2 in. diam and better thermal stability, give hope that devices with uniform performance characteristics can be fabricated over large areas (5, 6). Another potential advance in GaAs IC processing comes in the form of rapid thermal annealing (RTA), in which the high temperature cycle is limited to several seconds, rather than 15-20 min as is usual with conventional furnace annealing. The consequent restriction of dopant diffusion (both into the bulk and laterally) is attractive if very small dimension devices are required. Because of the versatility of commercially available rapid annealing furnaces, it also appears feasible to perform other GaAs processing heat-treatments (*e.g.*, contact alloying) in the same furnace. In this paper, we detail experiments to determine the characteristics and suitability of rapid annealing for these heat-treatments.

Experimental

Undoped, semi-insulating (100), LEC-grown wafers were used as substrates for ion implantation. For the production of n or n^+ regions, various doses (2×10^{12}-10^{15} cm^{-2}) of ^{29}Si or ^{78}Se were implanted at energies between 60 and 400 keV. For the fabrication of p or p^+ regions, ^{9}Be, ^{24}Mg, or ^{65}Zn was implanted at energies of 40-100 keV and doses of 3×10^{12}-10^{15} cm^{-2}.

Rapid annealing was performed in a Heatpulse 210T system[1] under a flow of forming gas. The temperature was monitored by a Cr-Al thermocouple embedded in a 3 in. Si substrate on which the GaAs wafers were annealed. All of the high temperature activation steps were preceded by a 60s, 400°C step to warm the tungsten-halogen lamps. This, combined with an appropriate software routine, ensured that sharp temperature profiles were obtained routinely. An example of a typical temperature profile undergone by an implanted wafer is shown in Fig. 1. For comparison to the rapidly annealed samples, wafers were proximity annealed in a conventional As-H_2 furnace for 20 min at 850°C. In this arrangement, a solid source of As is held in a separate, cooler zone of the furnace (410°C), and the resultant As vapor is carried down the main tube of the furnace by a flow of pure hydrogen. This provides an As vapor pressure above the GaAs wafer much higher than the equilibrium value which would be obtained from dissociation of the wafer itself.

To avoid possible complications from encapsulating layers, all rapid annealing was also performed using the proximity technique. Figure 2 shows that it is possible to activate Si implants by this method without degrading the wafer surface.[2] Alternatives, such as placing the wafer on a Si substrate rather than GaAs or leaving the implanted face up during the annealing, lead to surface dissociation at comparatively lower temperatures and shorter times. For routine device production, however, it is clear that encapsulation is required to prevent mechanical damage and baked-on contamination on the implanted face of the wafer.

Electrical activations were determined by C-V profiling using a mercury probe and LCR meter for low dose implants, or a Polaron electrochemical profiler for high dose ($> 10^{13}$ cm^{-2}) implants, and by van der Pauw measurements.

Results

Activation of n-type dopants.—The two most suitable species for the production of n-channel regions by ion implantation are Si and Se. This is evident from the comparison of the characteristics of the various implanted donor ions in GaAs given in Table I. Implants of ^{29}Si (60 keV) or ^{78}Se (100 keV) at two doses (4×10^{12} or 1×10^{13} cm^{-2}) were annealed face down on GaAs substrates for 5s at various temperatures. Figure 3 shows van der Pauw measurements on these wafers; optimum activation is achieved at 950°C for the Si implants at either dose, whereas Se requires a slightly higher temperature (~1000°C), concomitant with the higher degree of damage created by the heavier Se ions. Annealing of either species at still higher temperatures leads to a degradation of electrical properties, owing to site transfer (for the Si) and surface degradation. These optimum activations are essentially identical to those obtained by conventional furnace annealing at 850°C for 20 min.

Electrical profiles of such low dose implants, obtained from C-V measurements, are shown in Fig. 4. The

[1] A. G. Associates, Palo Alto, California 94303.

[2] Some of these data are taken from Kohzu *et al.* (7).

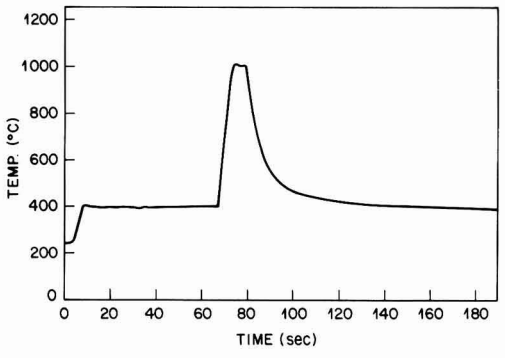


Fig. 1. Typical temperature-time profile for a rapidly annealed wafer

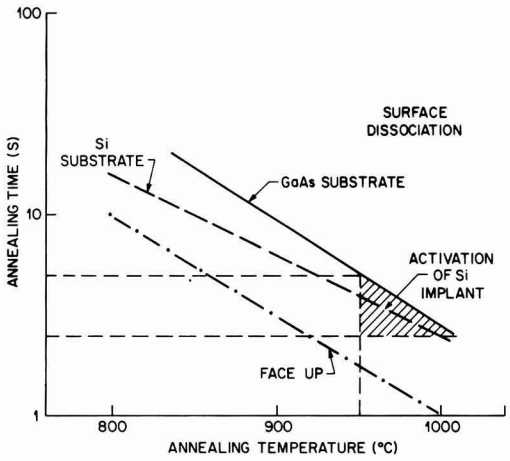


Fig. 2. Surface dissociation of GaAs under RTA. The implanted wafer is placed either face up or face down on a Si or GaAs substrate. Surface dissociation occurs above each line of the plot. Only within the hatched area is good implant activation achieved without surface dissociation of the GaAs wafer. For example, a 1000°C, 5s anneal performed with the implanted wafer face down on another GaAs wafer leads to activation of the Si ions. The same anneal performed with the wafer either face down on a Si substrate or face up leads to surface dissociation of the GaAs wafer.

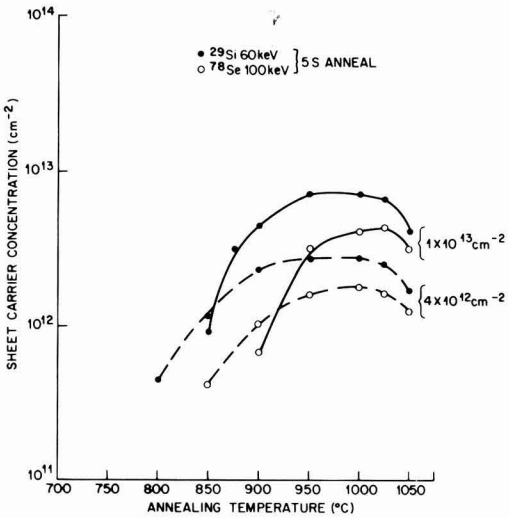


Fig. 3. Donor activation of Si and Se for two doses after 5s anneals at various temperatures.

profiles fit well to those expected from the LSS theory (8). The deviations at the deepest depths are due to two phenomena: first, some channeling of the implanted species during implantation and, second, the increasing series resistance of the sample as pinch off is approached leads to an increasingly inaccurate capacitance determination. There does not appear to be any diffusional broadening during the activation anneal. Although it is not evident from the Se profiles of Fig. 4, it is easier to obtain good activation for deeper (higher energy) implants, presumably because surface effects are less severe than for shallow implants. Once again, the profiles for both Si and Se are similar to those obtained using thermal annealing. The electron mobilities are typically > 3500 cm^2-V^{-1}-s^{-1} for both rapid and thermally annealed regions, with no systematic differences between the two methods.

The production of n^+ regions for contacts are also required in GaAs device fabrication. It is well established that it is apparently impossible to routinely achieve electrical activities above 2-3 × 10^{18} cm^{-3} by direct ion implantation. These values are below that required for the production of an ohmic contact (9) and alloying of various eutectics is used for their fabrication (10). The total contact resistance, however, is still dependent on the resistivity of the underlying GaAs and thus it is necessary to produce the highest possible, regularly achievable doping level. Sheet carrier densities for Si and Se implants as a function of dose after rapid annealing for 5s at 950°C are shown in Fig. 5. The eventual saturation in activity is evident from comparison of the experimental results with the full activation line (*i.e.*, slope of activation *vs.* dose curve equals 1). Amorphization of GaAs for room temperature implants occurs at doses of ~10^{14} cm^{-2} for Si implants and ~5 × 10^{13} cm^{-2} for Se implants, and for device applications it seems clear that amorphization should be avoided, if possible. We have found that the carrier mobilities in recrystallized layers are generally poorer than in those where amorphization was prevented, and it is difficult to completely repair the GaAs lattice. There is generally a high density of dislocation loops left after even high temperature (> 1000°C) annealing of initially amorphous layers. We have also previously seen that for very high dose, room temperature implants, thermal annealing, particularly for heavier ion species, is superior to RTA, presumably because full damage removal is difficult on the time scale of RTA unless higher temperatures are used (11). This, in turn, leads to surface dissociation for capless anneals, or else is a very severe test for encapsulating layers that might be used. Gettering to

Table I. Characteristics of ion-implanted species in GaAs

Ion	Comments
	Donors
Si	Low mass means good activation for RT implant, versatile range.
Se	Good activation for low dose, RT implant.
Te	Poor activation for RT implant.
Ge	Amphoteric species, poor activation, difficult to implant.
S	Diffuses during annealing.
Sn	Amphoteric, diffuses during anneal.
	Acceptors
Be	Very light mass means good activation at low annealing temperature, easy to implant, versatile range, at high concentrations diffuses during anneal.
Mg	Good activation, versatile range, difficult implant source.
Zn	Reasonable activation, at high concentrations diffuses during anneal.
Cd	Reasonable activation, diffuses during implantation at RT, difficult implant source.

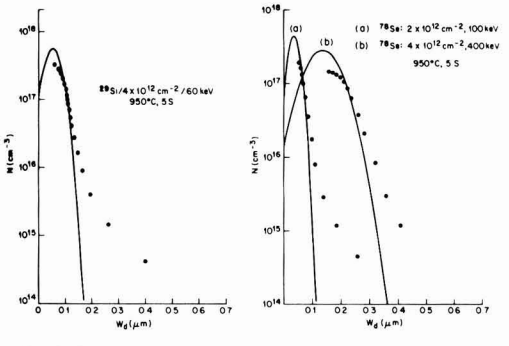


Fig. 4. Electrical profiles for low dose Si and Se implants comparing experimental with theoretically expected profiles. W_d is the depletion depth, and N is the carrier concentration.

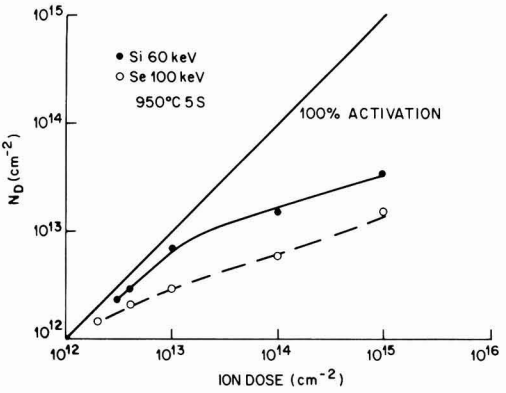


Fig. 5. Activation of Si and Se as a function of implant dose for an anneal of 950°C for 5s.

heavily damaged regions of mobile acceptor impurities such as Mn and Cr also occurs (12), and this will reduce activities and electron mobilities. The point is that if there is little or nothing to be gained electrically by increasing doses above 5-10 × 10^{13} cm^{-2}, then doses should be limited to these values. Elevated temperature implantation of heavy species like Se or Te prevents amorphization and leads to higher electrical activities than room temperature implants (13), but for device production it is simpler to use a lighter ion (Si) and room temperature implantation.

Electrical profiles from dual energy Si-implanted wafers are shown in Fig. 6, comparing results from rapidly annealed and thermally annealed samples. Such structures (n^+/n) are used to simultaneously provide an n^+ region for contact to the electron channel (n-region). There is much less diffusion of the Si in the rapidly annealed wafer, bearing in mind that, in the furnace-annealed samples, annealing was performed after each implant [otherwise the two profiles smear together by diffusion (14)]. While single-energy Si implants display essentially no redistribution during furnace annealing, with dual energy implants there is a marked tendency for the Si ions in the n-channel region to diffuse back into the more heavily damaged n^+ region during the activation anneal (14). The fact that good profiles may be achieved by a single dual-implant-rapid anneal schedule means that a tremendous savings in time and handling can be obtained. This is a clear example of a situation where rapid annealing is superior to furnace annealing.

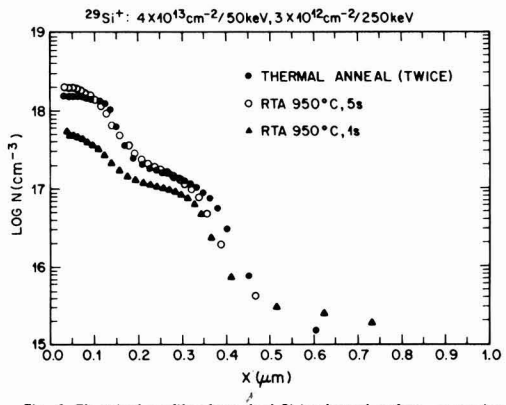


Fig. 6. Electrical profiles from dual Si-implanted wafers, comparing RTA to furnace annealing. The latter was performed after each implant; the former after both implants have been done together.

Activation of p-type implants.—It is widely recognized that p-type implanted regions are activated at lower annealing temperatures than n-type implants (1, 13). In Fig. 7, we show results from rapid annealing of low dose (3 × 10^{12} and 1 × 10^{13} cm^{-2}) implants of ^9Be and ^{65}Zn that would be used for p-channel regions. Maximum (and complete) activation of Be is achieved at 800°C for 5s anneals, while the activation of the much heavier Zn ions is less than complete, and the optimum values occur at higher temperatures (~900°C). Results on Mg implants (mass number 24) follow closely those for Be, with slightly lower activation at the lower temperatures (below 750°C). Above 800°C, essentially complete activation is obtained for Mg as well as Be. Again, at the highest temperatures (~1000°C) there is a degradation in activation because of loss of As and diffusion of the implanted species.

Electrical profiles from low dose Be and Mg implants are shown in Fig. 8. The deviations from the expected LSS profiles are due to the rapidly increasing series resistance of the samples affecting the C-V measurements. While there is some channeling during implantation, it is clear from differential Hall measurements that there is little diffusional broadening of the profiles during annealing for the low doses. The mobilities of rapidly annealed p-channel regions are in the range 220-250 cm^2-V^{-1}-s^{-1} and are always better after annealing at 800°C and above than 750°C annealing, even though the activation is the same. These mobilities are the same as those achieved by thermal annealing at 800°C for 20 min.

The production of high hole concentrations by implantation and thermal annealing is readily achievable in GaAs, in contrast to the case for donor impurities. This is also true for rapid annealing. Figure 9 shows the activation of Be and Zn implants as a function of dose for capless rapid annealing at 950°C for 3s. Essentially complete activation of Be is achieved up to doses of ~10^{14} cm^{-2}, falling to 40% for a dose of 10^{15} cm^{-2}, where amorphization is obvious. Full activation of Zn implants is not achieved at any dose, with 50% activation at 10^{14} cm^{-2} dose, and 28% activation at 10^{15} cm^{-2}.

Electrical profiles obtained by Polaron profiling and differential Hall measurements on high dose Be and Zn implants are shown in Fig. 10. A peak hole concentration of 3 × 10^{19} cm^{-3} was obtained from a 40 keV, 10^{15} cm^{-2} Be implant annealed at 900°C for 1s. Less activation is obtained from Zn implants for equivalent doses. Upon com-

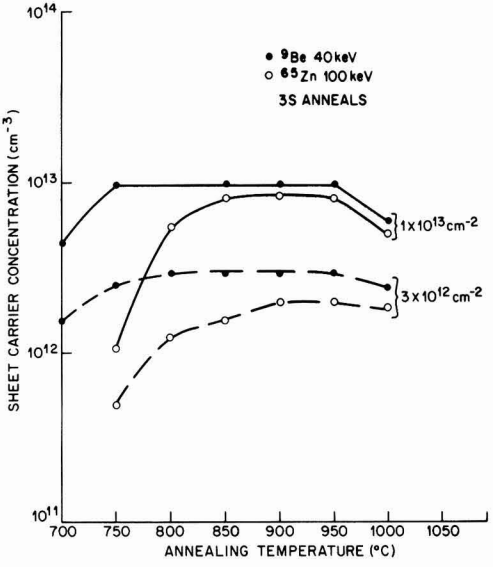


Fig. 7. Acceptor activation of Be and Zn for two doses after 3s anneals at various temperatures.

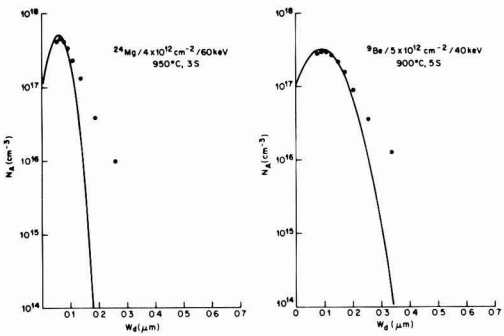


Fig. 8. Electrical profiles for low dose Mg and Be implants after RTA. The deviations from the expected profiles are due to rapidly increasing sample series resistance affecting the C-V data.

parison with the as-implanted profiles (obtained from secondary ion mass spectrometry data), broadening of the profiles during annealing is obvious, particularly for the Be implants. The concentration dependent diffusion of p-type impurities in GaAs is well-documented—thermal annealing usually leads to very broad p' profiles (15), while the much shorter time scale of rapid annealing may limit this diffusion. A number of experimenters have attempted to take advantage of this with a "pulsed" diffusion of Zn from a surface source (16). Our own experiments along this line yield results that are comparable to those obtained by implantation and rapid annealing. Again, from a production viewpoint, implantation is preferable to diffusion. The observed characteristics of the available acceptor species in GaAs after implantation and annealing are shown in the lower part of Table I. It appears Be and Mg are the most useful because of their lower mass and hence more versatile implant depths.

Contact alloying.—The process of alloying various eutectics on GaAs is the standard method of forming ohmic contacts, but the details of the method are still not completely understood (9, 10). Conventional furnace annealing of AuGe-based eutectics on GaAs often leads to undesirable morphological features such as balling up and spiking of the eutectic-semiconductor interface. The shorter time scale of rapid annealing would appear to be ideal for ohmic alloying, and several recent studies have indicated the ability of RTA to provide reproducible, morphologically improved alloy contacts with low specific contact resistance to both n- and p-type layers (17, 18).

Our own experiments on split wafer lots have compared the contact resistances obtained by alloying

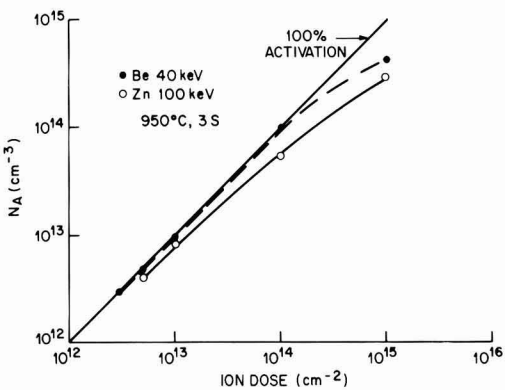


Fig. 9. Activation of Be and Zn as a function of implant dose for an anneal of 950°C for 3s.

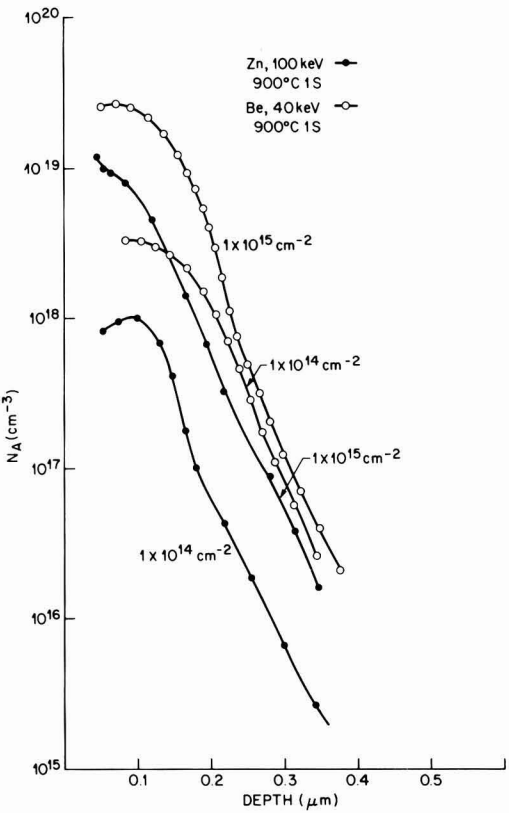


Fig. 10. Electrical profiles of Be and Zn after RTA at 900°C for 1s

AuGeNi to n or n' layers created by Si implantation into GaAs, using either a graphite plate heater, or the Heatpulse RTA system (19). Typical temperature-time profiles from the two annealers are shown in Fig. 11. Contact resistances measured by the transmission line method were obtained at 26 different ohmic test pad positions on the split wafers, and the results from two wafers (n and n') are shown in Table II. The rapidly annealed contacts show 30-50% lower specific contact resistances and are more uniform than those obtained using the graphite heater.

Implant isolation.—To produce highly resistive regions between conducting channels in GaAs, moderate doses (10^{12}-10^{14} cm^{-2}) of protons, helium, boron, or oxygen are implanted to create damage-induced, deep-level compensation of the shallow dopants. The as-implanted resistivity is generally not high enough to achieve effective isolation between neighboring devices, and a low temperature annealing cycle is employed to increase the resistivity to the desired value (20). Obviously, if the temperature is too high, the implant-induced damage is annealed out.

At present, the annealing step is performed in a conventional furnace at 450°-500°C for 10-20 min, but Hall measurements have shown that a much shorter thermal treatment (~20s) in an RTA achieves the same resistivity values for oxygen-implanted wafers. From the production viewpoint, this leads to the attractive scenario of performing all the required heat-treatments for GaAs IC's in a single RTA furnace by cassette-to-cassette loading.

Heterostructure annealing.—A number of experimenters have already demonstrated that normal implant activation annealing in a furnace leads to diffusion of Si ions from the doped AlGaAs layer into the undoped GaAs region of the two-dimensional electron gas (2DEG), with a

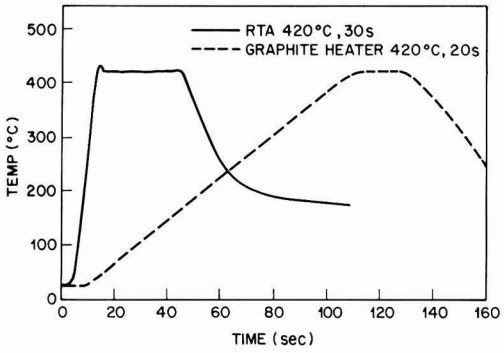


Fig. 11. Temperature-time profiles undergone by wafers during AuGeNi contact alloying in an RTA, compared to a graphite plate heater.

consequent serious degradation of the 77 K electron mobility (21). This falloff, however, is much reduced if a rapid annealing cycle is utilized, and appears to be the only way of annealing heterostructures for device applications without destroying their mobility advantages.

Discussion

The results in this paper demonstrate that the activation and mobility of implanted donor and acceptor species is at least as good using rapid thermal annealing as compared to normal furnace annealing. The uniformity of these properties, which was not discussed in this paper, is also comparable for the two annealing methods, allaying fears that there might be nonuniform heat-transfer to large area (2 in. diam) wafers during RTA (22).

For use as an integral part of device processing, encapsulating layers must be developed capable of withstanding the rapid heating and cooling rates, and the slightly higher annealing temperature of RTA compared to furnace activation. Contrary to the results of some others, we have found that RTA is a more severe test of the encapsulation than is furnace annealing. In particular, the effects of strain or impurities from the cap is most evident on n-channel regions, where an abrupt profile and high electron mobility are essential. The caps which show most promise are AlN (23), Si_3N_4, and PSG (phosphosilicate glass), but a good deal of work remains to be done to get reproducible layers, which can be easily and completely removed after annealing, and which can be deposited in a very uniform manner to allow the use of the through-implantation technique.

The rapid heating and cooling rates during RTA for implant activation are a problem from the viewpoint of slip formation on 2 and 3 in. diam wafers. These morphological features may upset certain subsequent processing steps, notably, photolithography. The slip formation may be reduced or even eliminated by slowing the cooling rate using appropriate software control of the furnace (19). Several Japanese workes have also applied for patents for guard ring structures which prevent slippage of rapidly annealed wafers by eliminating the thermal gradients near the edge of the wafer compared to its center.

Throughput is always a concern from a production viewpoint. This might seem a little strange when talking about rapid annealing, but in the commercially available systems only one wafer can be annealed at a time, while in a tube furnace 20 or 30 can be annealed together. However, even considering the 1 min preheat for each rapidly annealed wafer, and the cooling time required, the throughput is superior to thermal annealing because of the time taken in the latter case with flushing the furnace, backfilling with H_2, heating up the As source, and the reverse sequence when the heat cycle is complete. (The volume of rapid annealing furnaces is much smaller than for a conventional furnace.) Even with manual loading and unloading, the throughput of wafers in a rapid annealer is ~25 h^{-1}, and this should be increased by cassette-to-cassette handling.

There is wide scope for research into novel alloying and solid phase reactions of metals and GaAs using RTA. For the present, the alloying of AuGeNi in an RTA is more uniform and produces lower specific contact resistances than the more conventional graphite strip heating. Similarly, the isolation implant anneal, another relatively low temperature step in GaAs processing, may be conveniently performed for much shorter times than is currently done.

Perhaps the most obvious need for RTA comes with the fact that to be integrated with other devices, and to reduce their own source-to-drain resistance, selectively doped heterostructure transistors need to be able to withstand high temperature implant activation steps. As mentioned above, normal furnace processing leads to an unacceptable degradation in the transport properties of the 2DEG. Using RTA, we have shown this degradation is considerably less even for devices with 20Å buffer layers, and that acceptable implant activation can be achieved without causing unusually low mobilities in the 2DEG (25). This is a case where RTA is not only a superior alternative to furnace annealing, but also the only feasible method of performing a crucial step in the processing of a very promising technology.

All of the above discussion may be summarized quite simply: it appears eminently feasible to perform all the heat-treatments required in GaAs IC processing in a single RTA furnace. The savings in time, space, and handling appear very attractive, and the actual temperature cycle seen by each wafer can be recorded, eliminating the furnace as a source of error if problems occur in device fabrication.

Table II. Specific contact resistance for Au GeNi alloyed contacts on GaAs

Substrate	Annealer	Average r_c (Ω-cm^2)	σ/avg r_c (%)
n^+	RTA	2.1×10^{-7}	33.7
n^+	Graphite	4.8×10^{-7}	40.5
n	RTA	5.5×10^{-7}	33.6
n	Graphite	7.4×10^{-7}	45.5

Conclusions

1. The electrical properties (activation and mobility) of implanted layers following optimum RTA are at least as good as those obtained by furnace annealing.
2. There is less diffusion under optimum RTA conditions than with furnace annealing, with repercussions for the annealing of n^+/n structures and SDHT's.
3. The alloying of metal-semiconductor contacts is more reproducible with RTA than with furnace annealing.

Acknowledgments

The authors acknowledge the contributions to this work by P. K. Chin, J. S. Williams, T. W. Hou, S. P. Hui, B. Schwartz, S. Singh, A. D. Butherus, N. J. Shah, C. W. Tu, L. J. Kroko, D. J. Talley, L. Yesis, S. Tallia, and S. Skunk.

Manuscript submitted May 3, 1985; revised manuscript received July 22, 1985. This was Paper 703 SOA presented at the Toronto, Ontario, Canada, Meeting of the Society, May 12-17, 1985.

AT&T Bell Laboratories assisted in meeting the publication costs of this article.

REFERENCES

1. J. P. Donnelly, *Nucl. Instrum. Meth.*, **182,** 553 (1981).
2. J. S. Williams, "Laser Processing of Semiconductors," J. M. Poate and J. W. Mayer, Editors, p. 283, Academic Press, New York (1982).
3. H. Nishi, S. Okamura, T. Inada, H. Hashimoto, T.

Kabota, and T. Nakumura, *Inst. Phys. Conf. Ser.*, **63,** 365 (1982).
4. C. W. Farley and B. G. Sheetman, *J. Electron. Mater.*, **13,** 401 (1984).
5. D. E. Holmes, H. Kuramoto, C. G. Kirkpatrick, and R. T. Chen, in "Semi-Insulating III-V Materials 1984," p. 204, Shiva, Cheshire, England (1984).
6. H. M. Hobgood, R. N. Thomas, D. L. Barrett, G. W. Eldridge, M. M. Sopira, and M. C. Driver, in "Semi-Insulating III-V Materials, 1984," p. 149, Shiva, Cheshire, England (1984).
7. H. Kohzu, M. Kuzuhara, and Y. Takayama, *J. Appl. Phys.*, **54,** 4998 (1983).
8. J. Linhard, M. Schartt, and H. E. Shiott, *Mat. Fys. Mead. Dun. Vid. Selsk*, **33,** 1 (1963).
9. M. I. Nathan and M. Heiblum, *Solid-State Electron.*, **25,** 1063 (1982).
10. G. S. Marlow, M. B. Das, and L. Tompson, *ibid.*, **25,** 259 (1983).
11. S. J. Pearton, J. S. Williams, J. M. Poate, D. O. Boerma, and D. C. Jacobson, Unpublished data.
12. H. Kanber and M. Feng, *SPIE*, **463,** 67 (1984).
13. F. Eisen, *Rad. Eff.*, **47,** 99 (1980).
14. J. S. Williams and S. J. Pearton, *Proc. Mater. Res. Soc.*, To be published.
15. J. Kashara, H. Sakurai, Y. Kato, and N. Watanabe, *Jpn. J. Appl. Phys.*, **21,** L103 (1982).
16. D. Dobkin and J. F. Gibbons, *This Journal*, **131,** 1699 (1984).
17. S. K. Tiku, J. B. Delaney, N. S. Gabriel, and H. T. Yan, *Proc. Mater. Res. Soc.*, **35,** 486 (1985.
18. R. Zuleeg, Private communication.
19. P. K. Chin and S. J. Pearton, Unpublished data.
20. Y. Kato, T. Shimada, Y. Shiraki, and K. F. Komabsubara, *J. Appl. Phys.*, **45,** 1044 (1974).
21. S. Takuda, T. Inadu, S. Okamura, and S. Hiyamizi, *Jpn. J. Appl. Phys.*, **23,** L147 (1984).
22. K. D. Cummings, S. J. Pearton, and G. P. Vella-Coleiro, *Proc. Mater. Res. Soc.*, To be published.
23. R. Bensalem, N. J. Barrett, and B. J. Sealy, *Electron. Lett.*, **19,** 113 (1983).
24. N. J. Shah, C. W. Tu, and S. J. Pearton, Unpublished data.

Lateral Epitaxial Growth over Oxide

Lynn O. Wilson and G. K. Celler*

AT&T Bell Laboratories, Murray Hill, New Jersey 07974

ABSTRACT

We model numerically formation of thick dielectrically isolated films by recrystallization from the melt. Si films are deposited over oxidized Si wafers, with a regular array of seeding windows opened in the isolation oxide. A stationary radiative heater melts the entire film and crystallization is controlled by the pattern of openings in the SiO_2. The model provides two-dimensional temperature profiles during melting and solidification as well as the shape of the solid-liquid interface and its motion. It also predicts the amount of superheating and undercooling at the buried oxide as a function of the spacing between the windows in the oxide. The computed results are in agreement with the experimental data and clarify the influence of several processing parameters on melting and crystallization.

Controlled crystallization of silicon from the melt has been explored in recent years as an attractive method of forming single-crystalline Si over an insulating substrate (1). The tools for melting range from scanned cw laser beams and electron beams to scanned graphite filaments to extended stationary heaters. Most efforts have been concentrated on forming thin films over oxidized Si wafers using scanned heat sources.

High voltage and high current integrated circuits are an important class of devices requiring dielectric isolation. They are made commercially in crystalline Si segments, 40-60 μm thick, which are isolated by the SiO_2 film from the polysilicon substrate and from each other (2). Fabrication of dielectrically isolated (DI) wafers is complex and expensive; moreover, the polysilicon substrates tend to bow during thermal processing, reducing device yields. Over the last few years, we have developed a method of forming 10-100 μm thick single-crystalline films by uniform melting with an extended stationary heat source (3, 4). The precursor structure consists of polysilicon deposited over oxidized Si wafers, with a regular array of openings in the oxide. These openings provide seeding needed for epitaxial crystallization and impose lateral temperature gradients necessary for lateral epitaxial regrowth. The latter is possible because the thermal conductivity of the oxide is about ten times lower than that of silicon. The fact that molten Si in contact with the amorphous SiO_2 can be undercooled further facilitates lateral crystallization from the seeding windows. Although extensive crystallization over the oxide has been achieved without detailed knowledge of the thermal profiles and the amount of undercooling, a better understanding of temperature distribution, undercooling, and interface dynamics is necessary to optimize melting and crystallization conditions. This paper describes numerical modeling of this process and compares the computed results with the experimental data.

*Electrochemical Society Active Member.

Description of the Process

Melting and crystallization are carried out in a lamp furnace (5) consisting of two rectangular chambers, each 10 × 12.5 in. in lateral dimensions, positioned one above the other and separated by a quartz window. Air-cooled tungsten halogen lamps are suspended under a gold-plated reflector in the upper chamber. Wafers are placed on quartz pins ~0.5 in. above the water-cooled base of the lower chamber. Samples are heated uniformly from the upper side with a broad-band radiative flux emitted by the lamps. At typical settings required for melting, the spectrum is centered at ~1 μm wavelength. At this wavelength, the optical penetration depth is > 100 μm at 20°C, but drops exponentially with temperature to < 1 μm above 1000°C. Cooling is predominantly by blackbody radiation from both the front and back sides of the samples. The presence of the metal base held at a nearly constant temperature < 100°C assures reproducible cooling rates and a gradient across the wafer thickness of the order of 100°C/cm.

Samples for crystallization are prepared by oxidation, photolithography, and deposition of polysilicon and SiO_2 films. (100) starting wafers are cleaned and oxidized in a steam ambient to form the dielectric isolation barrier. The oxide is patterned by photolithography to obtain an array of seeding windows. CVD deposition of polysilicon is carried out at high temperatures in a conventional vertical epitaxial reactor. First, samples are etched briefly with HCl vapor at 1050°C to remove the native oxide from the silicon surface in the seeding windows. Deposition is often done in two steps: (*i*) nucleation and (*ii*) rapid growth. Uniform nucleation of Si over SiO_2 is achieved by decomposition of SiH_4 at 1050°C. After a continuous silicon layer has been formed, the temperature is increased to 1150°C and SiH_4 is replaced with $SiHCl_3$ for a higher, > 1 μm/min, growth rate. The 10-100 μm thick films have columnar grain structure with an average grain diameter > 1 μm and with a surface roughness of 1-3 μm. As a final

step, the surface is capped with a 2 μm layer of LPCVD oxide that is needed to contain molten silicon.

To recrystallize a Si layer on an oxidized Si wafer, the lamps are ramped linearly over 10-30s to a predetermined power setting that exceeds the threshold power for melting, held at that value for 10-100s, and shut off by a linear reduction of electrical power. The sample temperature is monitored with an optical pyrometer that is focused on the back side of the wafer. After a few seconds lag when the power is first applied, the sample temperature increases rapidly until it reaches the melting temperature T_m. This occurs at a power setting of ~ 80 W/cm^2. The onset of melting is easily determined from the pyrometer output even if the absolute temperatures are not known precisely because of some uncertainty in the value of emissivity. The temperature curve has a knee at the melting temperature and its slope is essentially zero for the melt duration. For this reason, no feedback from the pyrometer to the power supply is used in the crystallization experiments. Almost all the absorbed power exceeding the threshold value is taken by the heat of fusion which for silicon is ~ 1810 J/g.

Crystallization of the molten Si starts in the seeding windows and proceeds over the oxide. Upon recrystallization, the entire film is usually single crystalline, and it is free of grain boundaries or subboundaries. The remaining dislocations tend to concentrate where two solidification fronts collide. A cross section of the recrystallized film is shown in Fig. 1.

Since all heating is radiative and the reflectivity of molten metallic Si is roughly twice that of the solid, elongated inclusions of superheated solid are present on the surface of the liquid over a range of input powers, from the threshold for surface melting P_1 to a higher threshold for deep melting P_2 (6). The values of P_1 and P_2 depend on surface preparation. Wafers covered with thick polycrystalline layers deposited by CVD have a characteristic roughness caused by the different rates of growth of randomly oriented Si grains. This rough surface is encapsulated with a 2 μm thick transparent film of SiO_2. Absorptivity of rough surfaces coated with glassy overlayers has been extensively studied for application to solar collectors. Based on calculations of Yablonovitch (7), we have obtained the value of emissivity $\epsilon_S = 0.84$ near the melting temperature $T_m = 1685$ K for a rough Si surface coated with SiO_2. The emissivities of a smooth and encapsulated surface would have been 0.72 and for smooth Si without the cap $\epsilon_S = 0.6$.

The emissivity of molten Si is lower than that of the solid. The initial surface roughness and encapsulation still affect the emissivity value. When a Si surface melts, it becomes more reflective and the input of energy into the irradiated surface is reduced. This causes a melting instability: the heated surface breaks up into an array of solid and molten areas that can coexist indefinitely. Two types of breakup have been observed and described (6, 8). Large-faceted molten areas are formed in defect-free single-crystalline surface layers, and networks of thin solid lamellae appear inside them. In heavily defective layers, faceted melting is absent and the entire surface becomes covered with a lamellar network. The solid inclusions reduce the surface-averaged reflectivity to a value permitting a steady-state heat flow, and only superficial melting is present as long as some solid inclusions exist. In our numerical model, it is assumed that the applied input power exceeds P_2 and that the entire surface is uniformly melted.

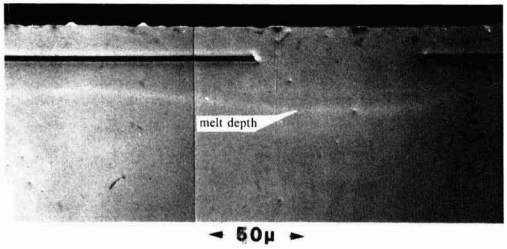


Fig. 1. Optical micrograph of polished cross-section of recrystallized sample after 10s Schimmel etch.

Formulation

The assumptions used in deriving the governing equations have been discussed in Ref. (9) for a one-dimensional model. In brief, heat-transport within the wafer is predominantly due to conduction, heat input from the lamps is modeled through radiative coupling at the top wafer surface, and radiative cooling at the wafer surfaces is the dominant mechanism for heat loss. Effects due to crystalline anisotropy are ignored. The capping layer is not modeled directly; however, its influence is felt via the values used for the emissivity of solid and liquid silicon at the top surface. Since the development of the two-dimensional equations proceeds analogously, we write the equations below in a dimensionless, nearly final, form.

The basic two-dimensional domain, shown in Fig. 2, represents a cross section of a portion of the wafer. The domain is reflected about its left (or, equivalently, right) edge and repeated to give a periodic array. It consists of a silicon substrate of thickness d_1, on top of which lies thermal oxide patterned into alternating islands and windows. Shown are half of an island, with half-width w_1, and half of a window, with half-width w_2. This layer has thickness d_2. On top of this is another layer of silicon of thickness d_3 representing the silicon grown by chemical vapor deposition.

We write the governing equations in a nondimensional form, but present all computational results in a dimensional form. For simplicity, we shall use the same notation for the dimensional quantities d_1, d_2, d_3, w_1, w_2, and for their dimensionless counterparts, when they are divided by a characteristic distance d. Similarly, we use the notation t for time and for dimensionless time, normalized by a characteristic time τ. In practice, this should cause no confusion.

The dimensionless thermal diffusion equation is

$$\mathrm{Pe}\,\frac{\partial T}{\partial t} = \nabla \cdot (K \nabla T) \qquad [1]$$

Here T is the dimensionless temperature and

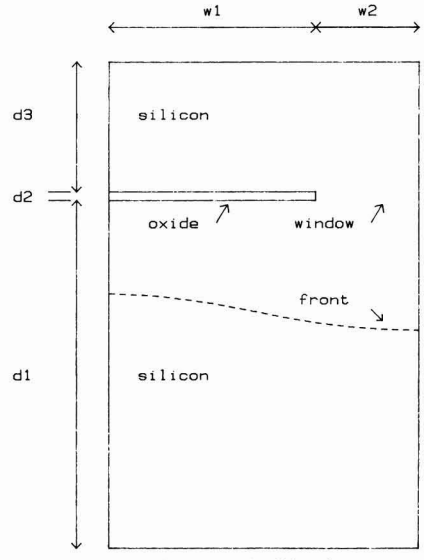


Fig. 2. The computational domain

$$\mathrm{Pe} = \frac{\rho C d^2}{\kappa \tau} \quad [2]$$

is the Péclet number, where ρ, C, and κ represent a characteristic density, heat capacity, and thermal diffusivity, respectively. The dimensionless thermal diffusivity $K(\mathbf{x})$ in Eq. [1] is assumed to take on values $\kappa^{-1}K_S$, $\kappa^{-1}K_L$, and $\kappa^{-1}K_0$ in the solid silicon, liquid silicon, and oxide regions; each of these is constant within its region. The dimensional temperature $\overline{T}$ can be obtained from T by setting

$$\overline{T} = T_m (1 + RT) \quad [3]$$

T_m is the melting temperature of silicon. The radiation number R is given by

$$R = \frac{\sigma d T_m^3}{\kappa} \quad [4]$$

where σ is the Stefan-Boltzmann constant.

Let $\mathbf{n}$ represent the unit outward normal to a surface. By symmetry, no flux crosses the left or right boundary

$$\mathbf{n} \cdot (K \nabla T) = 0 \text{ at } x = 0,\ x = w_1 + w_2 \quad [5]$$

At the top surface, the flux balance is given by

$$\mathbf{n} \cdot (K \nabla T) = \epsilon P(t) - \epsilon (1 + RT)^4,\ y = d_1 + d_2 + d_3 \quad [6]$$

where $P(t)$ is the power input from the lamps, while at the bottom surface we have

$$\mathbf{n} \cdot (K \nabla T) = -\epsilon (1 + RT)^4,\ y = 0 \quad [7]$$

The emissivity ϵ takes on values ϵ_S at the solid top surface, ϵ_L at the liquid top surface, and ϵ_B at the (solid) bottom surface.

Let the position of the melt or solidification front be denoted by $\mathbf{u}(\mathbf{x}, t)$. At the front, the dimensionless temperature is zero

$$T(\mathbf{u}(\mathbf{x}, t), t) = 0 \quad [8]$$

If $\mathbf{n}_f$ represents a unit normal at the front, pointing from the solid to the liquid, the Stefan equation is given by

$$\frac{d(\mathbf{n}_f \cdot \mathbf{u})}{dt} = \frac{R}{\mathrm{PeS}} [\mathbf{n}_f \cdot (K_L \nabla T)|_{\mathbf{u}^-} - \mathbf{n}_f \cdot (K_S \nabla T)|_{\mathbf{u}^-}] \quad [9]$$

S is the Stefan number

$$\mathrm{S} = \frac{L}{C T_m} \quad [10]$$

where L is the latent heat of silicon.

Initially

$$\mathbf{u}(\mathbf{x}, 0) = \mathbf{u}_0(\mathbf{x}) \quad [11]$$

As we discussed in Ref. (9), for typical values of the relevant parameters, $\mathrm{Pe} \approx 2.5 \times 10^{-5}$, so it is reasonable to neglect the left-hand side of Eq. [1] and use the quasi-static approximation

$$\nabla \cdot (K \nabla T) = 0 \quad [12]$$

to decouple partially the system of equations. Furthermore, $R \approx 2.7 \times 10^{-6}$. As we discussed in Ref. (9), for typical wafer thicknesses, the dimensionless temperature T is such that $(1 + RT)^4$ never differs from unity by more than ~2%. Accordingly, we make the approximation

$$(1 + RT)^4 \approx 1 \quad [13]$$

to linearize the boundary conditions [6] and [7].

Finally, we note that $\mathbf{n}_f \cdot \mathbf{u}$ is a function of one, not two, spatial dimensions (*e.g.*, arc length along the front). Mainly for notational simplicity, we make the assumption that $\mathbf{n}_f \cdot \mathbf{u}$ is a single valued function of x and write

$$\mathbf{n}_f \cdot \mathbf{u} = y_f(x, t) \quad [14]$$

in Eq. [9].

These partial differential equations, along with the associated boundary conditions and initial conditions, define a Stefan problem for the position y_f of a moving front and for the temperature T within the domain. The equations are nonlinear because of the coupling between y_f and T. This coupling is reduced, but not eliminated, by means of the quasi-static approximation. The equations are also nonlinear because the material properties differ in the solid silicon, liquid silicon, and oxide. Further nonlinearities due to the radiation boundary conditions have been eliminated via approximation [13].

Note that Eq. [9], with its initial condition [11] and assumption [14], involves time and one spatial dimension. For a given front position, Eq. [12], with boundary conditions [5]-[8] and approximation [13] involves two spatial dimensions.

Parameter Values

In our numerical computations, we used the following parameter values (6, 10, 11)

$$\sigma = 5.672 \times 10^{-12} \frac{\mathrm{J}}{\mathrm{s\text{-}cm^2\text{-}K^4}} \quad [15]$$

$$T_m = 1685 \text{ K} \quad [16]$$

$$\epsilon_S = 0.84,\ \epsilon_L = 0.58,\ \epsilon_B = 0.62 \quad [17]$$

$$K_S = 0.216,\ K_L = 0.64,\ K_0 = 0.02 \text{ W/(cm-K)} \quad [18]$$

$$\rho = 2.41 \text{ g/cm}^3 \quad [19]$$

$$L = 1810 \text{ J/g} \quad [20]$$

$$C = 1.04 \text{ J/(g-K)} \quad [21]$$

Reference (6) details how the values of the emissivity were obtained, taking into account the capping layer on the wafer top and the textures of the surfaces. The density ρ was assumed to be the average of the values for liquid and solid silicon.

For the basic computational subregion (*cf.* Fig. 2), we generally used

$$d_1 = 160\ \mu\text{m},\ d_2 = 4\ \mu\text{m},\ d_3 = 60\ \mu\text{m} \quad [22]$$

$$w_1 = 96\ \mu\text{m},\ w_2 = 48\ \mu\text{m} \quad [23]$$

This represents only a portion of the typical repetition

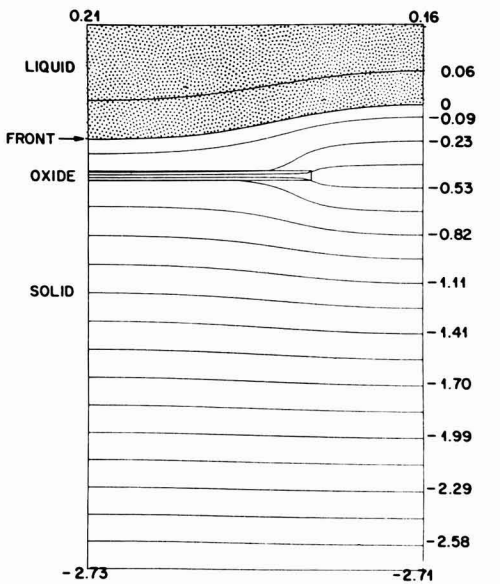


Fig. 3. Typical isotherm distribution when front is above the oxide. Numbers refer to temperature deviation from T_m.

pattern within a wafer. The substrate (d_1) is actually approximately 600 μm thick. The oxide half-width (w_1) varies, but can be as much as several thousand microns. Nevertheless, as will be discussed in more detail later, the dimensions listed above were adequate for most, but not all, considerations. Upon occasion, we used considerably larger values for the oxide half-width or varied the other dimensional parameters.

It is also necessary to specify the power $P(t)$ supplied to the lamps of the furnace. This is a dimensionless function, normalized by σT_m^4. As we observed in Ref. (6), there are two relevant power thresholds

$$P_1 = 1 + \epsilon_H/\epsilon_S \quad [24]$$

$$P_2 = 1 + \epsilon_H/\epsilon_L \quad [25]$$

In our calculations, we omit consideration of the initial ramping stage, during which we suppose that the power has been ramped past the intermediate region $P_1 < P(t) < P_2$ and has been established at a value $P_{max} > P_2$. Starting our time measurement from this point [$\Delta_1 = 0$, in the notation of Ref. (6)], we suppose that the power is held constant at $P = P_{max}$ for Δ_2 seconds, then ramped down linearly to zero over an additional Δ_3 seconds

$$P(t) = P_{max} \qquad 0 \leq t \leq \Delta_2 \quad [26]$$

$$= P_{max}\left(1 - \frac{t - \Delta_2}{\Delta_3}\right) \qquad \Delta_2 \leq t \leq \Delta_2 + \Delta_3 \quad [27]$$

Experimentally, P_{max} appears to be only a few percentage points greater than P_2. For most of our calculations, we used

$$P_{max} = 1.05P_2 \quad [28]$$

We also set

$$\Delta_2 = 17 \quad [29]$$

$$\Delta_3 = 60 \quad [30]$$

To complete the specification of the parameter values for the numerical calculations, we need to define the initial position of the melt front. We assume that it is planar, slightly below (4 μm) the top surface of the wafer

$$y_f(0) = d_1 + d_2 + d_3 - 4 \quad [31]$$

Subsequent computations indicate that the front will quickly readjust itself to a more appropriate shape.

Method of Solution

In this section, we mention some reasons why the Stefan problem we have formulated is particularly challenging numerically. We then sketch the basic method used to solve the problem.

The motion of the front y_f is governed by its initial position (Eq. [11]) and by the difference of the thermal fluxes measured at the two sides of the solid/liquid interface (Eq. [9]). In order to determine the flux difference, it is necessary to know the temperature distribution T within the wafer. This, in turn, is governed by the material properties within the structure (Eq. [12]), the emissivities at the surfaces ([6], [7]), and the position of the front (Eq. [8]). Thus, y_f and T are intricately coupled together.

Notice from parameter [18] that there is more than an order of magnitude range in the size of the thermal conductivities involved. Consequently, we can expect wide variations in the temperature gradients within the structure. These are potentially difficult to compute.

The physical dimensions involved (Eq. [22], [23]) vary considerably. The oxide layer, for example, may be 4 μm thick by several thousand microns long. Since the local computational grid size must be roughly the same as the size of the relevant local dimension, or smaller, a large number of computational grid points is necessarily required.

Note also that the front motion is driven by a thermal flux difference. This presents two computational difficulties. First, the calculation of the temperature gradient (or the flux) is less accurate than the calculation of the temperature itself. Second, we have to take the difference between two fluxes. Since, in the physically relevant operating regime, P_{max} is only slightly greater than P_2, we expect the magnitude of the difference to be small compared with the size of either flux. Hence, the calculation of the thermal flux difference is potentially inaccurate.

When solving the Stefan problem numerically, we can, because of the partial decoupling of the nonlinear equation system via the quasi-static approximation, view Eq. [9] as the primary equation. To evaluate its right-hand side at any instant of time, we need to solve Eq. [12] at that instant, with the appropriate front position and other boundary conditions.

For the computational domain (Fig. 2), we consider the entire liquid Si-solid Si-SiO_2 structure to be a region with a crack in it where the melt/solidification front is. Boundary conditions [5]-[7] are applied at the exterior surfaces; boundary condition [8], that the dimensionless temperature is zero, is applied at the interior surfaces, along the front. If the front does not touch the oxide, the crack goes entirely across the computational domain. The problem then can equivalently be solved on two disjoint domains. If the front touches the oxide (which does not melt), the domain is partially cracked.

Suppose that at some instant of time in the course of the computations the temperature T vanishes along a line which is not connected to the current melt/solidification front boundary (the crack). This situation can occur when the front intersects the oxide. We have a choice of saying either (*i*) that this new line is a new part of the front and melting/solidification proceeds from it as well or (*ii*) that the line is not part of the front. We now make the significant assumption that the new line is not part of the front. This is justified by experimental observations of a substantial nucleation barrier for melting at the silicon-SiO_2 interface. The presence of a similar barrier during solidification is inferred from the behavior of melts other than Si in contact with the amorphous SiO_2. Pyrometric measurements indicate that the temperature can deviate by at least as much as 10° from T_m before the phase transition takes place at the Si-SiO_2 boundary.

This introduces the possibility that regions of the structure may, at times, be superheated or undercooled. Computational and experimental results corroborating this will be presented in the Superheating and Undercooling section.

The basic computational scheme, oversimplified slightly, is as follows. Assume an initial melt front position at time $t = 0$. Solve the diffusion equation [12] and the associated boundary conditions for the temperature T in the "cracked" domain. Evaluate the flux difference at the front. Substitute this into the Stefan equation [9]. Find the front position at the next "instant" of time. Repeat. This concept is a refinement of ideas used earlier to model an oxidation process (12).

The scheme was implemented by means of two large software packages and an intricate driver program which interwove them.

One of the packages, POST, written by N. L. Schryer, is designed to solve a coupled system of nonlinear partial differential equations involving time and one space variable, and associated ordinary differential equations that are a function of time (13). The numerical technique involves Galerkin's method in space, using B splines and a variable order, variable time-step extrapolated backward difference procedure in time. The POST package is based on the PORT library of portable FORTRAN subroutines for numerical mathematics (14). We used POST to solve Eq. [12].

The other package, PLTMGU, is designed to solve a nonlinear elliptic partial differential equation with two space variables. It was adapted from code written by R. K. Smith to do semiconductor device simulation (15, 16). The solution technique is a multigrid finite element procedure with C^0 piecewise linear finite elements. The

computational domain must have a polygonal boundary. The user supplies a (possibly nonuniform) triangulation of the domain; the code refines this triangulation uniformly. PLTMGU is an outgrowth of yet another software package PLTMG, by R. E. Bank and A. H. Sherman, which used a multigrid scheme with adaptive refinement of the triangulation (17). We used PLTMGU to solve Eq. [9].

One of the more interesting things the driver program does is to provide a triangulation of the computational domain which follows the moving solid-liquid interface. It is desirable to have a nonobtuse triangulation with certain additional properties (18). We devised a triangulation such that the interface lies along edges of triangles, there are no obtuse angles, there is a constant number of triangles, and the triangulation changes reasonably smoothly as the front moves (19).

Computations were performed on a Cray-1. The time required to do a complete calculation of melting and crystallization was approximately 200s.

Most computations were concerned with the restricted spatial domain described in the previous section. Sometimes we wanted to do calculations for a considerably larger domain. It turned out to be impossible to track the front motion under those circumstances, since the computational memory requirements considerably exceeded the capacity of the Cray-1.

However, we were able to obtain a partial solution. If, instead of trying to follow the motion of the front, we assumed the front was in a specific position, we were able to calculate the resulting temperature distribution within the wafer.

This amounted to calculating a static "snapshot" solution. We did this by dispensing with all the computational machinery associated with POST and by calculating on a relatively coarsely triangulated domain without refinement, thereby reducing the space requirements significantly.

Isotherms

The temperature distribution in the structure depends upon the position of the melt/recrystallization front, among other things. A number of characteristics of the thermal profile, however, can be identified and discussed in general. We do so here, but exclude from consideration those cases in which the front intersects the oxide layer: they involve superheating or undercooling and will be discussed below.

Figure 3 shows an isotherm plot when the solid/liquid interface is above the oxide layer; Fig. 4 shows a similar plot when the interface is well below the oxide layer. In each such plot, the isotherm lines represent equally spaced temperatures. In addition, the solid/liquid interface, which corresponds to the zero isotherm, is shown. Both isotherm plots were calculated with a power input $P = P_{max} = 1.05P_2$, but the observations here are pertinent to both melting and freezing.

Notice that there is a steep temperature gradient across the oxide. The gradient is less steep in the solid silicon and is least steep in the liquid silicon. The isotherms are compressed in the oxide and expand within the window region. At the wafer top, the temperature is slightly greater over the oxide layer than it is over the window region. The wafer bottom has a nearly uniform temperature. This uniformity is even more pronounced if a deeper substrate (d_1) is used in the calculations.

To quantify these ideas further, in Fig. 5 we plot the dimensional temperature $\overline{T} - T_m$ as a function of the distance from the bottom of the computational domain (*cf.* Fig. 2) at $x = 0$ (left edge) and $x = w_1 + w_2$ (right edge) when the front is at the position shown in Fig. 3. Similarly, in Fig. 6 we plot the temperature profiles corresponding to Fig. 4.

The left-hand edge corresponds to a vertical slice which goes through the oxide layer well away from the window. In both of the figures, the temperature profile at this edge agrees quite closely with that predicted by the one-dimensional theory (6, 9).

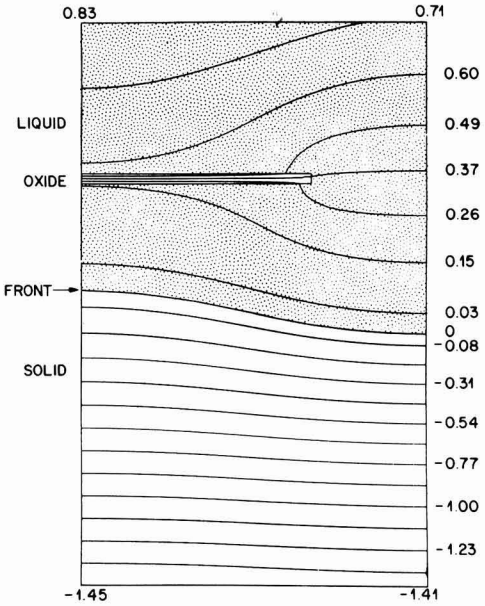


Fig. 4. Typical isotherm distribution when front is below the oxide. Numbers refer to temperature deviation from T_m.

The right-hand edge corresponds to a vertical slice which goes through the center of the seeding window. Here, in the region within a few tens of microns to both sides of the window, the temperature gradient deviates significantly from that predicted by the one-dimensional theory: the effects of the isotherm bunching are still being felt to some extent. It appears that the length characterizing the distance over which the influence of the window can be felt is slightly in excess of 50 μm.

From Fig. 5 and 6, we observe that the temperature changes by ~1.2° over 100 μm of solid silicon, ~0.4° over 100 μm of liquid silicon, and ~0.6° across the 4 μm of isolation oxide.

The facts that the one-dimensional theory holds at the left-hand side and that the isotherms are very nearly uniformly spaced at the bottom of the computational domain indicate that computations on this domain of restricted size give a reasonably good picture of what is happening when the front does not intersect the oxide. This was confirmed also by static calculations on wider, deeper domains.

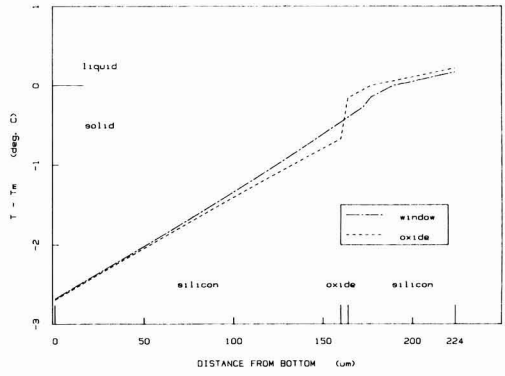


Fig. 5. Deviation of temperature from T_m at the left (dashed line) and right (dot-dashed line) edges of the computational domain as a function of distance from the bottom. Front is above oxide as in Fig. 3.

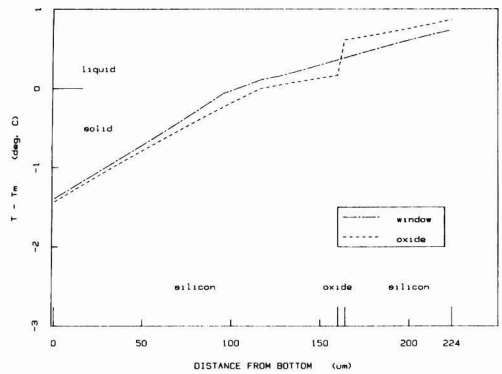


Fig. 6. Deviation of temperature from T_m at the left (dashed line) and right (dot-dashed line) edges of the computational domain as a function of distance from the bottom. Front is below oxide as in Fig. 4.

Motion of the Front

Figures 7 and 8 form composite pictures of the positions of the front at various instants of time during the melting and freezing processes, respectively. The times are not uniformly spaced, since the PDE solver POST automatically adjusts its step size to maintain the desired accuracy. The parameter values used for this calculation are those given in the Parameter section.

Melting.—By assumption, we start with a thin horizontal liquid layer. The melt front quickly readjusts itself so that it is deeper over the oxide. Having done this, it propagates downward toward the oxide with only slight additional steepening. The difference in the heights of the front at the left and right edges of the computational domain is approximately 14 μm.

The melt front contacts the top of the oxide strip at the left-hand edge first (*i.e.*, in the center of the full strip). The point where the front contacts the oxide quickly propagates to the right, toward the window. As it does so, the remaining portion of the front steepens. Superheating may occur on the other side of the oxide, as we discuss in the next section.

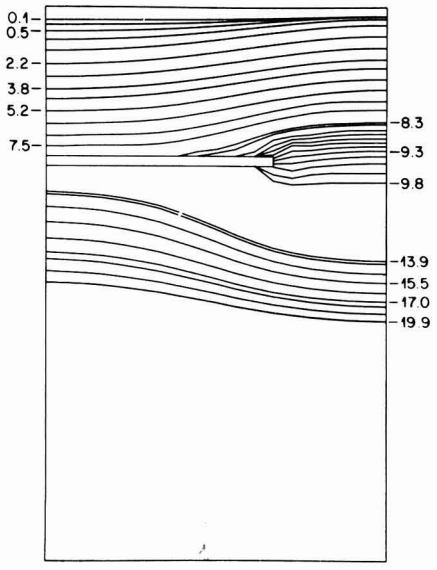


Fig. 7. Calculated melt front positions. Numbers refer to time in seconds.

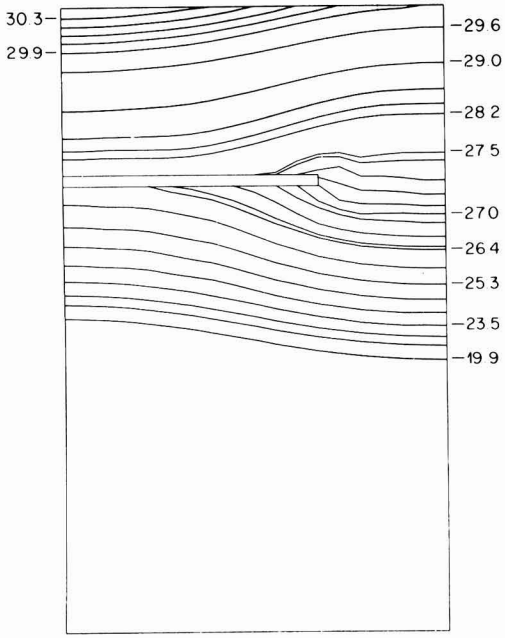


Fig. 8. Calculated solidification front positions. Numbers refer to time in seconds.

Eventually, the front remains only in the window area. Calculations for this regime are extremely difficult to perform accurately. The front flips rapidly, changing its shape from concave downward to concave upward. To some extent, it mimics the general shape of the isotherms which we saw in the preceding section.

Next, the melt front contacts the bottom of the oxide strip at the right-hand edge first, by the window, and moves swiftly to the left. We did not attempt seriously to do calculations for this regime (which involves the reappearance of computational mesh points along the portion of the front which previously disappeared). Nevertheless, we feel that we have an excellent qualitative picture of what is happening.

This type of behavior persists even if the oxide strip is considerably longer than the one used in these calculations. Isotherms, although they may be nearly horizontal over a substantial portion of the region, always have a slight slope which causes the melt contact point to move to the right along the top of the oxide strip and to the left along the bottom of it.

Eventually, the melt front separates completely from the oxide. Since there is a gap in our computations, we had to make an educated guess about the initial front position and starting time for subsequent calculations. Numerical experiments led us to conclude that the height differential of the front is greater when it is just below the oxide layer than when it is above it. In Fig. 7, the differential is approximately 28 μm. As the melt front continues to travel downward, it tends to flatten out.

As the power $P(t)$ is reduced in preparation for freezing, the front rearranges itself slightly. Relative to the shape for higher values of $P(t)$, the part under the oxide descends slightly and the part under the window rises slightly.

In these computations, the final height differential was approximately 12 μm.

Freezing.—When freezing begins, the solidification front moves upward toward the oxide, steepening as it does so. The height differential is not quite as large as it was for melting at a comparable position.

The solidification front contacts the bottom of the oxide at the left-hand edge first, and the contact point

moves rapidly to the right, toward the window. Undercooling may occur, as we discuss below. Again, the remaining portion of the front steepens.

When the solidification front remains only in the window area, it again flips rapidly, changing its shape from concave upward to concave downward. As with the melting flip, these calculations are extremely difficult to perform accurately, as is evidenced by some jaggedness in the curves.

Next, the solidification front contacts the top of the oxide strip at the right-hand side, by the seeding window, and moves rapidly to the left. As with the comparable melting case, we did not attempt to compute this portion of the motion.

Eventually, the front detaches itself from the oxide. Numerical experiments lead us to believe that its shape is quite similar to that which it had when it was melting just above the oxide. The front then moves upward with very little change of shape. In the present calculations, the shape changes very little even after the front intersects the top surface of the device.

Surface freezing.—When the top surface starts freezing, the emissivity of the solidified portion jumps to the value ϵ_S, and more power is able to be coupled into the wafer. This tends to shift the isotherm lines downward in the region directly under the solidified surface or under the solidification front near the point where it contacts the surface. This is illustrated in Fig. 9, which was based on calculations with a hypothetical solidification front in the position indicated and a power input $P = 0.95P_2$, where P_2 is the second power threshold, discussed in the Parameter section. The solid lines represent isotherms for which the emissivity of the solid portion of the surface is ϵ_S and the emissivity of the liquid portion is ϵ_L, as expected. The dashed lines represent what the isotherms would have looked like if both the solid and the liquid portions of the surfaces were assumed to have an emissivity ϵ_L.

Consequently, the motion of the solidification front in the vicinity of the contact point is slowed somewhat by comparison with what it would be if the surface emissivity retained the value ϵ_L everywhere. If the power input $P(t)$ is between P_1 and P_2 when the solidification front

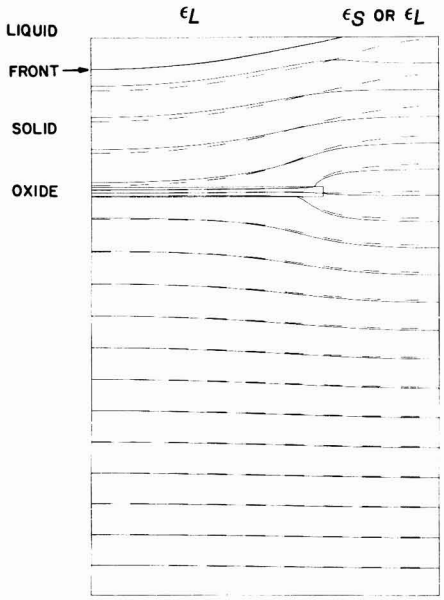


Fig. 9. Effect of emissivity change during surface freezing. Solid lines represent isotherms when solid portion of surface has emissivity ϵ_S, as is true physically. Dashed lines represent isotherms if solid portion were to have emissivity ϵ_L.

reaches the surface, we conjecture that a surface breakup may occur which is similar to the instability present during melting. Small segments of the surface would melt to increase the average reflectivity until there was no net energy gain in the resolidified region. Whether the breakup actually occurs will depend on the size of the resolidified area, its crystalline quality, and the magnitude of $P_2 - P(t)$. Without defects, the surface may tolerate substantial superheating and the excess absorbed power may temporarily halt or even reverse motion of the solidification front if P is held near P_2.

If the power input $P(t)$ is sufficiently small (certainly if it is less than the threshold P_1), this instability will not be present.

We might also note that if the power input $P(t)$ is less than 1, then, from Eq. [6] and [13], the sign of the thermal gradient at the surface changes whether or not the front intersects the surface. Surface cooling is so rapid that freezing might commence at the surface as well as along the solidification front.

In calculating the interface shape and motion, we assumed all physical properties to be isotropic. In fact, melting and freezing exhibit directional anisotropy, with interface velocity lowest along the <111> crystalline axes. This often leads to faceting since the growing phase expands more rapidly in directions other than the <111> until it is bounded by the (111) planes. It is likely that the solidification front instead of assuming the shapes shown in Fig. 8 aligns itself partially or completely with the (111) plane, *i.e.*, makes an angle of ~55° with the surface. This could imply more lateral freezing than obtained from our calculations. At the present time, we have no means of testing experimentally the actual shape of the interface.

Rate of movement of front.—We now return to the time-dependent calculations and discuss further the motion of the front, illustrated previously in Fig. 7 and 8. We plot in Fig. 10 the position of the front, measured at the left and right side of the computational domain, as a function of time. Computations were done in segments: melting above the oxide, melting when the front touches the oxide, melting below the oxide, etc., with educated guesses about the time intervals between the computational segments.

Although we do not expect the one-dimensional theory (9) for the front position y_f as a function of time to hold exactly for the two-dimensional problem, it is interesting to compare our results semiquantitatively with it. With a few notational changes, the theory gives, in dimensional form

$$y_f(t) = y_0 - \beta\left(\frac{P_{max}}{P_2} - 1\right)t \qquad 0 \le t \le \Delta_2$$

$$= y_0 - \beta\left(\frac{P_{max}}{P_2} - 1\right)t + \frac{\beta P_{max}(t - \Delta_2)^2}{2\Delta_2 P_2} \qquad \Delta_2 \le t \qquad [32]$$

with

$$\beta = \frac{(\epsilon_L + \epsilon_H)\sigma T_m^4}{\rho L} \qquad [33]$$

where distance is measured in microns and time in seconds.

Consider first the notion of the front at the right-hand side of the domain, through the seeding window. After an initial adjustment period, the position of the melt front varies nearly linearly with time. The velocity is approximately 6 μm/s, consistent with the one-dimensional theory. The parameter values are those given in the Parameter section. In the vicinity of the oxide layer, say 20 μm above and below it, the velocity of the melt front considerably exceeds that given by the one-dimensional theory. When the melt front gets outside that region, its position again decreases linearly with time at approximately the same rate as it did before being influenced

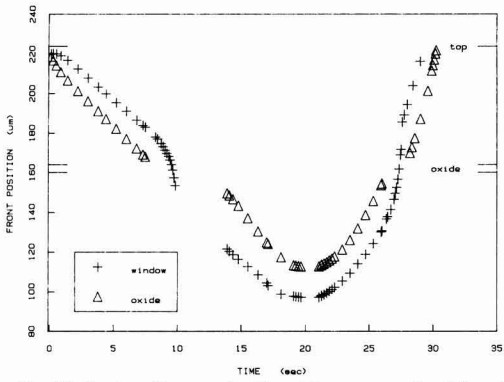


Fig. 10. Front position as a function of time, measured at left and right sides of the computational domain.

significantly by the oxide layer. As the power $P(t)$ is ramped down, the position *vs.* time curve forms a parabola for a while, again reasonably consistent with the one-dimensional theory. In the vicinity of the oxide layer, the velocity of the solidification front increases significantly as the oxide is felt, then decreases again as its influence diminishes.

Next, consider the motion of the front at the left-hand side of the domain, through the middle of the full oxide strip. Above the oxide, the melt front velocity is nearly constant and is nearly the same as that of the front at the right-hand side. The front at this position then disappears for a few seconds, while the remainder of the melt front is doing its flip through the seeding window. When it reappears below the oxide strip, its velocity is nearly constant while the power input is constant, but is slightly larger in magnitude than that of the melt front through the seeding window. When the power is ramped down, the parabolic nature of the position *vs.* time curve is again evident. Again, the front disappears for a while as the solidification front does its flip through the seeding window.

Superheating and Undercooling

When the melt or solidification front is in contact with the oxide strip, the temperature profiles in the structure may change radically. This is particularly true as the front passes through the seeding window. A critical parameter is P/P_2, which gives a measure of the amount by which the power P exceeds, or is less than, the power threshold P_2 for which the global energy balance is in equilibrium.

Suppose, for example, that $P/P_2 > 1$, so that melting is taking place, and that the melt front is going through the seeding window. Power in excess of P_2 applied to the wafer surface directly above the seeding window, or within a few tens of microns directly above it, affects the advancement of the melt front. However, power applied still further away from the window will have an insignificant effect on the front. If we assume that melting below the oxide layer cannot be initiated at a position unattached to the present melt front, the power in excess of P_2 will go into superheating of a portion of the structure below the oxide layer. The longer the oxide strip is, the greater the amount of superheating will be.

Conversely, if $P/P_2 < 1$, some of the silicon above the oxide layer will become undercooled.

Most of the computations discussed in this section are solutions to static problems. They were done with the "snapshot" version of the code, mentioned in the Method of Solution section, for which the position of the front is assumed, not calculated. We assumed that the front was planar and was located in the seeding window. For the superheating calculations, we positioned the melt front level with the bottom of the oxide layer, at $y = d_1$. For the undercooling calculations, we positioned the solidification front level with the top of the oxide layer, at $y = d_1 +$

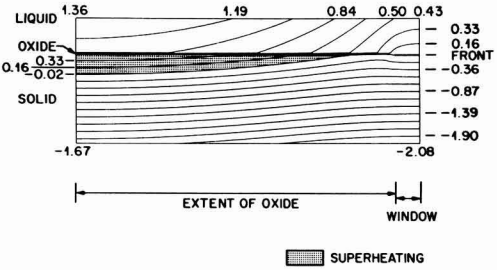


Fig. 11. Isotherms during superheating. The half-width w_1 of the oxide is 600 μm.

d_2. Details concerning the precise shape of the front are not expected to affect the thermal profile far from the window, which is what we are primarily interested in here.

We first discuss superheating and undercooling results for a computational domain with $w_1 = 600$ μm, w_2, d_1, d_2, d_3 as before. That is, the domain is similar to that used earlier, except that the oxide strip is made much longer. After that, we discuss the consequences of varying the dimensions of the structure and the power input. Finally, we sketch what happens dynamically as the melt or solidification front moves.

Superheating.—In Fig. 11, we show the isotherms calculated with the configuration described above and a power input $P/P_2 = 1.05$. Note that there is a region directly under the oxide strip which is superheated and that the amount of superheating increases with horizontal distance from the window. This can be better quantified by means of the following two figures. Figure 12 indicates the dimensional temperature profile $T - T_m$ along the bottom of the oxide strip. It dips slightly near the window, then increases rapidly with distance away from it, leveling out at the center of the oxide strip ($x = 0$) as required by symmetry conditions. In Fig. 13, we plot the temperature at the left-hand edge of the computational domain as a function of the distance from the bottom of the domain. This corresponds to a vertical slice which goes through the center of the full oxide strip. As expected (*cf.* Fig. 3 and 4), the thermal gradients are constant in each of the solid silicon, oxide, and liquid silicon regions.

Undercooling.—Figure 14 depicts the isotherms when the power input $P/P_2 = 0.95$ and the solidification front is planar, at the top of the seeding window. In this instance, there is a region directly over the oxide strip which is undercooled, and the amount of undercooling increases with horizontal distance from the window. In Fig. 15, we

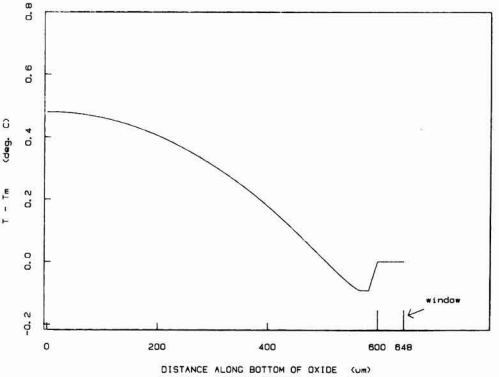


Fig. 12. Deviation of temperature from T_m at the bottom of the oxide strip during superheating.

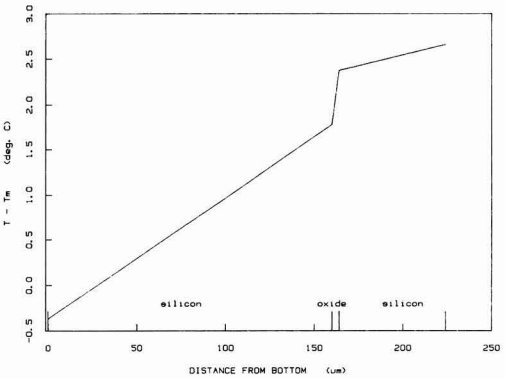


Fig. 13. Deviation of temperature from T_m at the left edge of the computational domain during superheating.

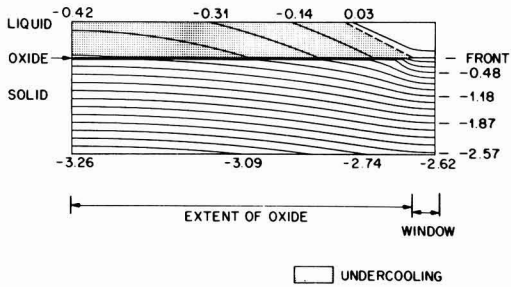


Fig. 14. Isotherms during undercooling. The half-width w_1 of the oxide is 600 μm.

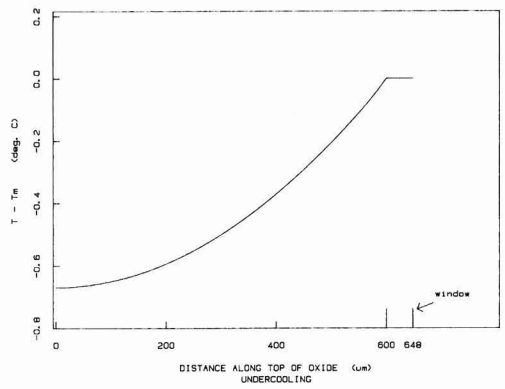


Fig. 15. Deviation of temperature from T_m at the top of the oxide strip during undercooling.

plot the temperature profile $\overline{T} - T_m$ along the top of the oxide strip. It decreases rapidly with distance away from the window, leveling out at the center of the oxide strip.

In many respects, the undercooling results are nearly symmetric to the superheating results. Some differences are worth noting. The curve in Fig. 12 dips before rising (as a function of distance away from the window), while that in Fig. 15 does not rise before dipping. We do not have a good physical interpretation for this effect; however, it is the behavior far away from the window which interests us most here. Also, although the superheating and undercooling at the bottom or top of the oxide at the left-hand side in the two computations are approximately of the same magnitude, the regions affected by superheating or undercooling are quite different. Since the thermal gradient in liquid silicon is approximately a factor of three smaller than that in solid silicon, the region affected by undercooling is larger. In Fig. 14, a substantial portion of the liquid layer, including most of the surface, is undercooled. A significantly smaller portion of the region in Fig. 11 experiences superheating.

Parameter variations.—We now investigate the sensitivity of the superheating or undercooling to variations in several parameters.

The most critical parameter is w_1, the half-width of the oxide layer. Using the dimensions of our usual computational domain (d_1 = 160 μm, d_2 = 4 μm, d_3 = 60 μm, d_2 = 48 μm), setting P/P_2 = 1.05, and varying w_1, we show in Fig. 16 the magnitude of the superheating at the left edge of the region, under the oxide. The superheating increases substantially, in fact, nearly exponentially, with oxide width. Similarly, with P/P_2 = 0.95 and all other parameters as above, we show in Fig. 17 that undercooling, measured at the left edge of the region, over the oxide, also varies nearly exponentially with the oxide width. Notice that, all else being equal, the magnitude of superheating and undercooling are nearly the same for the same amount (5%) of excess or deficit power from equilibrium.

Computations were performed on a limited domain because of storage constraints on the Cray-1. Using a relatively thin substrate d_1 was justifiable earlier (*cf.* Fig. 3, 4) when the lower portion of the computational domain exhibited a nearly planar behavior. When superheating or undercooling is present (*cf.* Fig. 11, 14), this is no longer true. In Fig. 17, we include the results of a few calculations using thicker substrates. They indicate that the amount of undercooling in a region with a thicker substrate is somewhat less than was previously calculated,

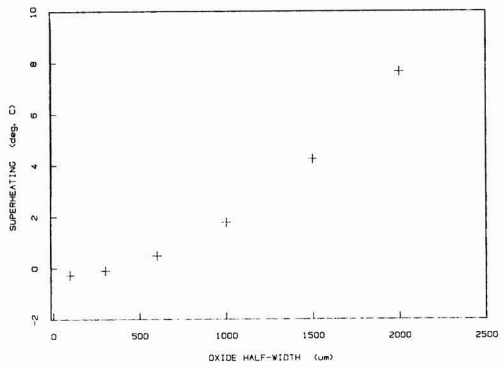


Fig. 16. Magnitude of superheating directly under the center of the full oxide strip as a function of the half-width w_1.

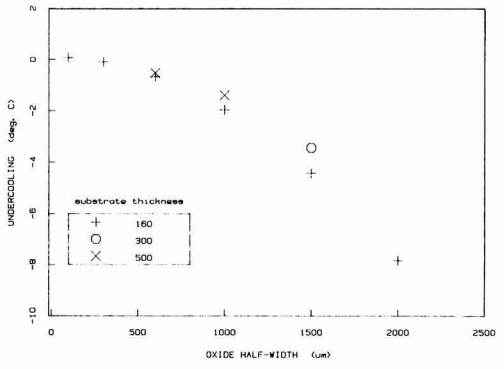


Fig. 17. Amount of undercooling directly over the center of the full oxide strip as a function of the half-width w_1, for various substrate thicknesses.

and that the discrepancy increases with oxide width w_1. Symmetric results were obtained for superheating, where our thin substrate calculations overestimate the amount present.

For similar reasons, we expect the thickness d_3 of the polycrystalline layer to play an important role in determining the amount of superheating or undercooling, and it does. In Fig. 18, we illustrate what happens if the thickness of the layer is reduced from 60 to 30 μm, with $P/P_2 = 0.95$ (note the change of scale from Fig. 17). Reducing the thickness of the polycrystalline layer can increase the undercooling significantly, particularly when the oxide strip is long. In a symmetric fashion, reducing the thickness increases the superheating by approximately the same amount when $P/P_2 = 1.05$.

Varying the oxide thickness or the window width within reasonable limits produces comparatively small effects.

Finally, suppose that the domain is fixed (we used $w_1 = 1000$ μm, $w_2 = 48$ μm, $d_1 = 160$ μm, $d_2 = 4$ μm, and $d_3 = 60$ μm) and that the power input is varied. Figure 19 indicates that, for small deviations of P from the threshold P_2, the amount of superheating or undercooling (measured at the left edge, below or above the oxide, as usual) varies linearly with the power input.

Dynamic picture.—We now sketch briefly what happens dynamically as the melt or solidification front passes in the vicinity of the oxide layer and the seeding window.

If melting is taking place and the melt front is above the oxide layer (*cf.* Fig. 3), the silicon below the oxide is solid and is below the melting temperature. The isotherms directly underneath the oxide, away from the window, are nearly horizontal. As the front starts to intersect the oxide and subsequently move through the seeding window, the temperature under the oxide increases. If the power input is sufficiently greater than the threshold P_2, the region under the oxide becomes superheated. The superheating starts under the center of the entire oxide strip, far away from the seeding window(s). It then spreads out, extending horizontally under more of the oxide layer and penetrating more deeply into the substrate (*cf.* Fig. 11). As the melt front proceeds along the bottom of the oxide layer, the superheated region diminishes in size and eventually disappears.

A similar sequence of events, involving undercooling above the oxide layer, happens when the solidification front proceeds through the window.

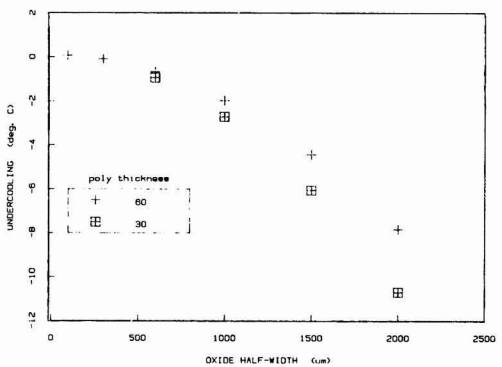


Fig. 18. Amount of undercooling directly over the center of the full oxide strip as a function of the half-width w_1, for various thicknesses of the polycrystalline layer.

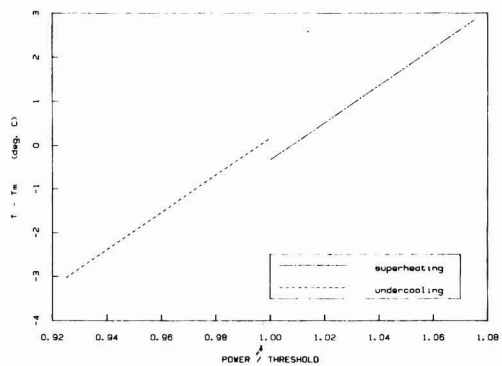


Fig. 19. Amount of superheating or undercooling as a function of power input, normalized by P_2.

Experimental Results

Experimentally, we can verify some aspects of the calculations presented above. The temperature is measured with an optical pyrometer at one spot of ~1 mm diam at the back side of the irradiated wafer. The temperature of the front side is determined by extrapolation, using known values of thermal conductivities and sample thickness. Of course, during most of the process cycle, the front surface temperature is pinned near T_m, with the back side temperature lower by 3-7°C, depending on the depth of melt. A small transient temperature rise and dip are detected when the liquid-solid interface passes through the oxide; they reflect the occurrence of superheating and undercooling, respectively.

The position and shape of the interface cannot be measured directly, but we can detect the maximum melt depth by examining cross sections of recrystallized samples. A series of such cross sections is retraced in Fig. 20. The shape of the interface at various depths is quite similar to those plotted in Fig. 7, and the interface flip in the window is clearly seen.

We already mentioned that superheating and undercooling can be discerned from pyrometer measurements. Superheating at the buried oxide-Si interface also leads to melting of the cooler back side of the sample, away from the heat source. To assure that silicon on this surface melts when T_m is reached, the surface is sandblasted to introduce a high density of crystalline defects. (It should be mentioned here that although a free, clean surface cannot be superheated, the SiO_2 provides excellent passivation of the broken Si bonds and makes superheating possible in defect-free layers.) When samples with a continuous buried oxide are irradiated, molten droplets and voids appear on the back side and vertical molten channels can be detected in cross sections (20).

In samples with windows in the oxide, superheating is a function of the oxide width and position with respect to the windows. When we used wafers with oxide of a half-

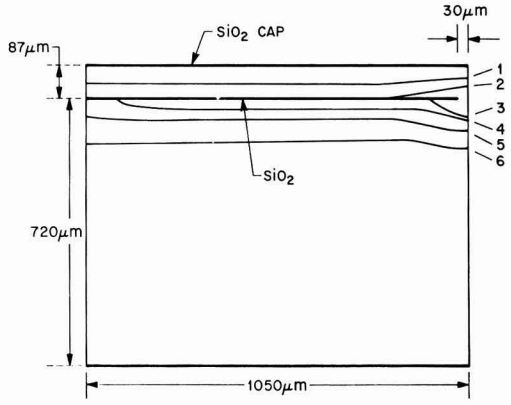


Fig. 20. Composite picture of maximum melt penetrations found experimentally for a series of irradiation energies.

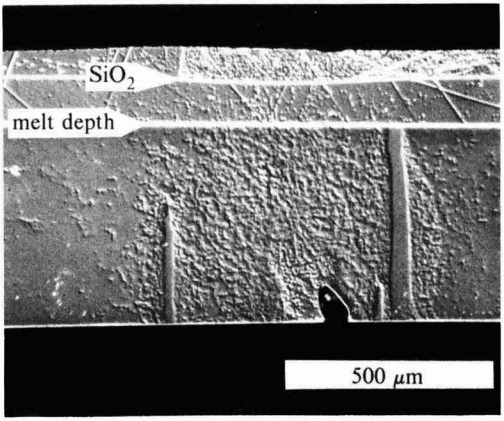


Fig. 21. Etched cross section of a recrystallized sample, showing the depth of the planar melt and the localized melt spikes originating from the superheated back surface.

width $w_1 = 920$ μm over part of the area and $w_1 = 1840$ μm over the rest, traces of melting appeared only under the centers of the wide stripes. A cross section of an area with melt spikes emanating from the back side is shown in Fig. 21. For $d_1 = 600$ μm distance between the buried oxide and the back surface, the temperature drop

$$\Delta T = \frac{d_1}{K} \epsilon_R \sigma T_m^4$$

is about 7°C. This is in excellent agreement with calculated superheating values of ~2° and ~7°C for 920 and 1840 μm half-widths, as plotted in Fig. 16.

It should be noted that the presence of molten regions at specific locations on the back surface is a positive proof of superheating. If melting were induced by impurities on the back surface, the correlation between the melt sites and the pattern in the buried oxide would be entirely different.

Discussion

We have presented a detailed numerical study of radiative melting and recrystallization of Si structures containing a patterned buried oxide layer. All modeling had to be in a two-dimensional domain because of the presence of slit-shaped seeding windows in the oxide that profoundly modified the shape of isotherms. The numerical results are consistent with the experimental data and provide insight into the details of melting and crystallization processes that cannot be measured directly.

We determined that the velocity of the melt front is 5-10 μm/s for the representative input power of $1.05P_2$. Similarly, the vertical component of the solidification velocity is ~20 μm/s when the input power is ramped down in 60s. The top surface directly above the SiO_2 window is always slightly cooler because of the heat sinking effect of the window, but the temperature of the bottom surface is essentially uniform except during brief superheating and undercooling phases.

We found that superheating and undercooling of silicon reach maximum values at the time when the solid-liquid interface passes through the SiO_2 windows. The regions most removed from the windows deviate most from the melting temperature. Superheating is of little practical consequence even though it may cause some undesirable melting at the bottom side of the wafers. Control of undercooling, on the other hand, is essential in achieving successful epitaxial crystallization, since excessive undercooling causes formation of polycrystalline Si. Undercooling increases approximately exponentially with the spacing between the seeding windows and can reach 10°C for $w_1 = 2000$ μm. Thicker polysilicon over the oxide reduces somewhat the amount of undercooling, and so does a thicker substrate. Undercooling is less when the input power P is close to the threshold P_2 (slow motion of the interface through the window region).

The numerical results indicate that the crystallization velocity has a very large vertical component. The actual physical regrowth is likely to differ somewhat from its numerical counterpart because the directional anisotropy of crystallization was not included in the calculation. It is known that growth of Si crystals is slowest along the <111> axis, and this leads to faceting in the (111) planes. Therefore it is likely that the solidification front is approximately parallel to the (111) plane and forms ~55° angle with the surface.

In any case, the propagation is slower than 100 μm/s and has a significant vertical component. This may explain why low angle grain boundaries (subboundaries) that are notorious in thin films (21) are not observed in our experiments. The crystallization front in thin films propagates strictly in the lateral direction, and any impurities present in the melt tend to accumulate ahead of the interface. This builds up their concentration and likely leads to defect formation. In our configuration, the impurities are continuously zone refined toward the top surface, preventing any large buildup at the solid-liquid interface.

Acknowledgments

We gratefully acknowledge contributions of Lee Trimble to the experimental part of the paper and of Kent Smith, Eric Grosse, and Norm Schryer to the numerical part.

Manuscript submitted May 17, 1985; revised manuscript received July 30, 1985.

AT&T Bell Laboratories assisted in meeting the publication costs of this article.

REFERENCES

1. G. W. Cullen, (Issue Editor), *J. Cryst. Growth*, **63,** 429 (1983).
2. K. E. Bean and W. R. Runyan, *This Journal*, **124,** 5C (1977).
3. G. K. Celler, McD. Robinson, and D. J. Lischner, *Appl. Phys. Lett.*, **42,** 99 (1983).
4. G. K. Celler, McD. Robinson, L. E. Trimble, and D. J. Lischner, *This Journal*, **132,** 211 (1985).
5. D. J. Lischner and G. K. Celler, *Mater. Res. Soc. Symp. Proc.*, **4,** 759 (1982).
6. G. K. Celler, L. E. Trimble, and L. O. Wilson, *ibid.*, **35,** 635 (1985).
7. E. Yablonovitch, *J. Opt. Soc. Am.*, **72,** 899 (1982).
8. G. K. Celler, McD. Robinson, L. E. Trimble, and D. J. Lischner, *Appl. Phys. Lett.*, **43,** 868 (1983).
9. L. O. Wilson, G. K. Celler, and L. E. Trimble, In preparation.
10. M. E. Glicksman and P. Voorhees, *J. Electron. Mater.*, **12,** 161 (1983).
11. A. Bell, *RCA Rev.*, **40,** 295 (1979).
12. L. O. Wilson, *This Journal*, **129,** 831 (1982).
13. N. L. Schryer, AT&T Bell Laboratories CSTR no. 115 (1984).
14. P. A. Fox, A. D. Hall, and N. L. Schryer, Bell Laboratories CSTR no. 47 (1976).
15. R. E. Bank, W. M. Coughran, Jr., W. Fichtner, D. J. Rose, and R. K. Smith, In preparation.
16. W. Fichtner, L. W. Nagel, B. R. Penumalli, W. P. Petersen, and J. L. d'Arcy, *Proc. IEEE*, **72,** 96 (1984).
17. R. E. Bank and A. H. Sherman, "PLTMG User's Guide," CNA152, Center for Numerical Analysis, University of Texas, Austin, TX (1979).
18. B. S. Baker, E. Grosse, and C. S. Rafferty, Submitted to *SIAM J. Algabr. Discrete Methods.*
19. L. O. Wilson, Submitted to *SIAM J. Algabr. Discrete Methods.*
20. G. K. Celler, K. A. Jackson, L. E. Trimble, McD. Robinson, and D. J. Lischner, *Mater. Res. Soc. Symp. Proc.*, **23,** 409 (1984).
21. J. C. C. Fan, B.-Y. Tsaur, and M. W. Geis, *J. Cryst. Growth*, **63,** 453 (1983).

The Analysis of Diffusion Data by a Method of Moments

R. Ghez,* J. D. Fehribach,[1] and G. S. Oehrlein*

IBM T. J. Watson Research Center, Yorktown Heights, New York 10598

ABSTRACT

We develop a method for extracting diffusivities from concentration profiles that uses the moments of these profiles. We show that these moments are coefficients of polynomial equations in the fitting parameter Dt; these equations are easily solved. The method does not rely on the estimation of slopes or of functional values; it is therefore both accurate and simple to use. We apply this method to the case of P redistribution by rapid thermal annealing of ion-implanted Si.

A Basic Diffusion Problem

The analysis of diffusion data requires fitting procedures that are often nonlinear. For example, if the data are representable by a given functional form $C(x, t)$ of the concentration, then the diffusivity D often enters that function parametrically in a nonlinear way. One then needs minimization schemes such as the Davidon-Fletcher-Powell algorithm (1) to determine D. The Boltzmann-Matano analysis (2), sometimes applicable when D is a function of C, provides another example of nonlinear analysis. In this case, the functional form of C is not even required: one operates directly on the diffusion equation. It is well known, however, that this method can handle only very few types of initial and boundary conditions, and that the procedure relies heavily on the accurate estimation of slopes from numerical data. Consequently, we are driven to look for methods for extracting diffusivities from experimental data that are only mildly nonlinear, that do not require curve-fitting, and that do not depend on a given functional form, *i.e.*, one need not even have a solution, analytic or numerical, of the diffusion equation.

A few years ago, one of us (3) proposed a method for the analysis of diffusion data when these are representable by error functions. That method depended on the calculation and numerical estimation of moments of these functions. It was then shown that the unknown parameters could be easily obtained through a simple iterative scheme. Further, that paper offered the pious hope that such methods could be extended to functions outside the class of error functions. Such is the object of this paper.

Our method is best illustrated through the following simple problem; it arose in connection with a study of dopant redistribution in ion-implanted semiconductors (4)

$$\frac{\partial C}{\partial t} = D\,\frac{\partial^2 C}{\partial x^2} \quad \text{for } x > 0,\ t > 0 \qquad [1]$$

and

$$C(x, 0) = C_0(x) \qquad [2]$$

$$\partial C/\partial x = 0 \text{ at } x = 0 \qquad [3]$$

$$C(\infty, t) = 0 \qquad [4]$$

The first equation simply states that the mobile species diffuses without any internal loss mechanisms and that the diffusivity D is independent of location x (and of concentration C). The diffusivity, however, can depend[2] on time t through a temperature schedule $T(t)$. Equation [2] means that the initial condition is an arbitrary profile C_0. Equations [3] and [4] are boundary conditions: the first assumes that the free surface is insulated (no loss); the second condition states that the concentration, deep inside the material, is negligible.

This problem has an exact solution [Ref. (5), p. 56], namely, a convolution of the initial profile with gaussians centered at "source" points $x = \pm x'$

$$C(x, t) = \frac{1}{2\sqrt{\pi Dt}} \int_0^\infty [e^{-(x-x')^2/4Dt} + e^{-(x+x')^2/4Dt}]\, C_0(x')\, dx' \qquad [5]$$

This formula allows the explicit computation of concentration distributions, regardless of the initial profile C_0. In practice, however, the integral [5] must be evaluated numerically for each value of D. Data fitting can therefore become quite tedious.[3] The method that follows is far more direct.

Diffusivity Measurements from Moments of Concentration Profiles

Consider the (nonnormalized and noncentered) moments at time t

$$M_n(t) = \int_0^\infty x^n C(x, t)\, dx \qquad [6]$$

of the concentration distribution, much as one defines moments of probability distributions (6). For any positive integer n, these quantities are easy to evaluate from numerical data if the data are measured over a wide enough range and if the concentration, far from the surface, decays sufficiently rapidly. The following steps are quite simple. Take the derivative of Eq. [6] with respect to time, use Eq. [1] to get

$$\frac{dM_n}{dt} = D \int_0^\infty x^n\, \frac{\partial^2 C}{\partial x^2}\, dx \qquad [7]$$

and integrate by parts, taking the boundary conditions [3] and [4] into account. One obtains easily integrable differential equations, and thus the relations

$$M_0(t) = M_0(0) \qquad [8a]$$

$$M_1(t) = M_1(0) + D \int_0^t C(0,t')\, dt' \qquad [8b]$$

$$M_n(t) = M_n(0) + n(n-1)\, D \int_0^t M_{n-2}(t')\, dt', \quad n \geq 2 \qquad [8c]$$

The first relation [8a] is nothing but a statement of mass conservation. The second, [8b], expresses the first moment (proportional to the centroid or mean of the distribution) in terms of the time-integral of the surface concentration. The third and most important, [8c], is a recursion between moments. For example, for $n = 2, 4, 6$, we get successively

$$M_2(t) = M_2(0) + 2M_0(0)Dt \qquad [9a]$$

* Electrochemical Society Active Member.

[1] On leave from Department of Mathematics, Duke University, Durham, North Carolina 27706

[2] In that case, the diffusion equation [1] reduced to one having constant coefficients through Kirchhoff's transformation [*cf.* Ref. (4) or Ref. (5), p. 11]: $t \to \vartheta = \int D\, dt$. Equations [5]-[10] remain formally unchanged except for the substitution of ϑ for Dt. The variable ϑ was labeled λ^2 in Ref. (4) because it has dimensions of length squared. One can also interpret this integral as a time average or effective value of D. Thus, $\vartheta = D_{\text{eff}}t$ is proportional to the diffusion time, where it must be understood that D_{eff} is generally a function of time.

[3] Even in those cases where the integral [5] can be performed exactly [*e.g.*, in Ref. (4)], one must still evaluate transcendental functions in which the diffusivity occurs nonlinearly.

$$M_4(t) = M_4(0) + 12[M_2(0)Dt + M_0(0)(Dt)^2] \quad [9b]$$

$$M_6(t) = M_6(0) + 30[M_4(0)Dt + 6M_2(0)(Dt)^2 + 4M_0(0)(Dt)^3] \quad [9c]$$

We thus see that the moments of even order $2n$ yield polynomial expressions of order n in the variable Dt (or, more generally, in the Kirchhoff variable ϑ, *cf.* footnote 2), whose coefficients are all measurable. In particular, Eq. [9a] shows that the second-order moment (proportional to the moment of inertia or "dispersion") increases linearly with Dt. Data fitting, *i.e.*, the determination of D [4] then reduces to finding roots of polynomials. This will be illustrated in the next section. On the other hand, no such simple relations exist between the odd-ordered moments because Eq. [8b] expresses M_1 as a time integral over the surface concentration whose values are often difficult to measure. Of course, one can always evaluate the integral in [8b] with the help of Eq. [5]. Thus, we have

$$M_1(t) = M_1(0) + 2\sqrt{Dt}\int_0^\infty C_0(x)i^1\,\mathrm{erfc}\left(\frac{x}{2\sqrt{Dt}}\right)dx \quad [10]$$

A moment's reflection, however, shows that all the odd moments are still expressed in terms of transcendental functions of the diffusivity, and that definitely defeats our purpose.

Before applying this method to experimentally determined concentration profiles,[5] we should make the following remarks. First, the formulas [8]-[10] are independent of the origin of time, *i.e.*, one can evaluate the moments between any two values of time for which the profiles are known. Second, the polynomials [9] have positive coefficients except for the constant term, which is always negative. It easily follows that each of these expressions has only one positive root, namely, the value of Dt that we are seeking. Last, we emphasize that the numerical estimation of moments represents a smoothing operation, as contrasted with point-wise or slope estimates.

A Numerical Example

We use the same data as in Ref. (4); a B-doped (100) Si wafer was P-implanted (energy 50 keV, dose 2×10^{15} cm^{-2}) and then short-time annealed (1100°C, 10s). The profiles were acquired by secondary ion mass spectroscopy (SIMS), and they are shown again in Fig. 1. The as-implanted and annealed data are represented by triangles and circles, respectively. The analysis in Ref. (4) was based on the assumption of a gaussian representation of the initial profile (triangles). This is a fair assumption for concentrations greater than 10^{19} cm^{-3}. The integral [5] can then be performed exactly, and the resulting expression, shown as a dotted line, fits well the annealed data, at least for the higher concentrations. As we pointed out, however, such expressions are nonlinear in the diffusivity; fitting thus requires minimization schemes. The simplicity of our present method will now be illustrated.

The data are sufficiently dense to provide reasonable estimates of the moments [6]. These were computed from the raw data using the trapezoidal rule, and they are recorded in Table I. These moments form the coefficients of the polynomial equations [9] which are trivially solved for Dt. The corresponding values for the orders 2, 4, and 6 are also recorded in Table I. The values of Dt corresponding to the second and fourth moments are close to one another and to the value 2.98×10^{-11} cm^2 found earlier (4). On the other hand, the sixth-order moments yield an overestimate of *ca.* 20%, which can be traced back to a poor resolution of the higher-order moments. It should always be remembered that the calculations assume integrations [6] over an infinite range. Since the higher-order moments (in this instance, the sixth) tend to weight the tail of the distributions, these tend to amplify experimental uncertainties. Some improvement is possible if one can fit the tail of the distributions to sufficiently rapidly decreasing functions or if one can subtract out the background. The moments can then be estimated more precisely, but our experience with such procedures[6] indicates but minor shifts in the values of Dt. Finally, we merely insert the measured value of Dt into the integral [5] and evaluate it numerically to obtain the solid line on Fig. 1. Here, we choose the value corresponding to $n = 2$; the curve corresponding to the fourth-order calculation is hardly distinguishable from this case. We note that the solid line represents the data better than the dotted one. This is easily understood since the latter calculation (4) does not take the channeling tail of the initial implant into account.

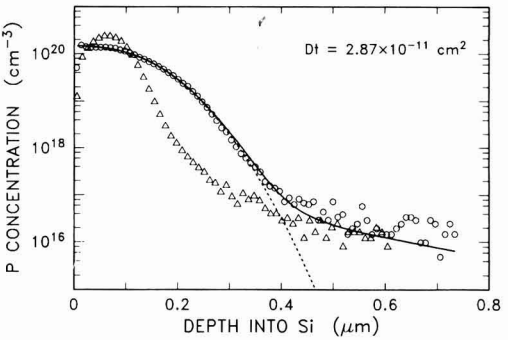


Fig. 1. Time development of an initial P implant in Si. The triangles and circles represent the as-implanted and annealed data, respectively. The solid line represents the best fit by our method of moments, and the dotted line shows the same fit by our former analytic approximation (4).

We should point out that our method may not be entirely applicable to the present experimental data, because P diffusion in Si, at impurity levels greater than 10^{20} cm^{-3}, cannot be fully described by the simple diffusion Eq. [1]. [Reference (9) gives a review of this topic.] Therefore, the specific solution provided by our method of moments cannot give a completely accurate description in the case of high level P diffusion. For example, the systematic deviation of the full line from the experimental data in the concentration tail appears physically significant, and it is, most likely, related to the enhanced tail diffusion observed in high dose P experiments (9). Nevertheless, our solution is a very good approximation of a more rigorous treatment, as is clear from Fig. 1, because concentration enhancement effects are only beginning to become significant for our experimental conditions of dose and temperature.

Generalization to Other Diffusion Problems

Our method, as described, appears limited to conservative systems. We now show that it also applies to more general situations, for sources and sinks are a very real

[4] We emphasize that any analysis of diffusion profiles yields values of ϑ and not of D, except in ideal cases when the $T(t)$ schedule is either "rectangular" or its rise and decay times are short in comparison with the time at temperature. The extraction of the diffusivity $D(T)$ then requires further information on the $T(t)$ schedule. See also Ref. (7) for an asymptotic analysis of the variable ϑ.

[5] The present method for extracting effective diffusivities from concentration profiles has been extensively used by Oehrlein *et al.* (8).

[6] For example, subtracting a 10^{16} cm^{-3} background level from our data reduces the values of Dt in Table I by 0.3, 1.5, and 4.7% for $n = 2$, 4, 6, respectively. Interestingly, such corrections tend to bring the measured values of Dt into closer agreement.

Table I. Initial and final moments of even orders and corresponding values of Dt computed through Eq. [9]

Order n	$M_n(0)$	$M_n(t)$	$Dt \times 10^{11}$ cm^2
0	2.14×10^{15} cm^{-2}	2.14×10^{15} cm^{-2}	—
2	1.25×10^{5} cm^{0}	2.48×10^{5} cm^{0}	2.87
4	1.71×10^{-5} cm^{2}	8.49×10^{-5} cm^{2}	2.99
6	1.08×10^{-14} cm^{4}	7.32×10^{-14} cm^{4}	3.69

possibility. For example, a dopant that precipitates is described by an internal sink in the diffusion equation. Likewise, a surface sink characterizes a lossy surface.

Consider then a mild generalization of our previous problem. The diffusion equation [1] is replaced by

$$\frac{\partial C}{\partial t^2} = D\frac{\partial^2 C}{\partial x^2} - \sigma_v \quad \text{for} \quad x > 0, t > 0 \qquad [11]$$

and the boundary condition at the surface becomes

$$D\frac{\partial C}{\partial x} = \sigma_s \quad \text{at} \quad x = 0 \qquad [12]$$

The other conditions [2] and [4] remain unchanged. Here, $\sigma_v(x,t)$ and $\sigma_s(t)$ represent volume and surface sinks, respectively. They are assumed to be known functions. Defining moments of the concentration C as in Eq. [6], and, similarly, moments

$$\mu_n(t) = \int_0^\infty x^n \sigma_v(x,t)\, dx \qquad [13]$$

of the volume sink σ_v, we perform the same steps that led to Eq. [8]

$$M_0(t) = M_0(0) - \int_0^t \sigma(t')\, dt' \qquad [14a]$$

$$M_1(t) = M_1(0) + D\int_0^t C(0,t')\, dt' - \int_0^t \mu_1(t')\, dt' \qquad [14b]$$

$$M_n(t) = M_n(0) + n(n-1)D\int_0^t M_{n-2}(t')\, dt' - \int_0^t \mu_n(t')\, dt', \quad n \geq 2 \qquad [14c]$$

For brevity, we have defined the total "surface-equivalent" sink

$$\sigma(t) = \sigma_s(t) + \int_0^\infty \sigma_v(x,t)\, dx = \sigma_s(t) + \mu_0(t) \qquad [15]$$

that occurs in Eq. [14a] and in the subsequent calculations. It represents the degree to which mass conservation, due to diffusion alone, does not hold. Nonetheless, Eq. [14a] is still a statement of global mass balance in the sense that the mass at time t is strictly accounted for by the initial mass and the total losses. Likewise, Eq. [14b] and [14c] generalize the corresponding Eq. [8] when sinks are present. It is now easy to write polynomial expressions analogous to [9]. For example, evaluating [14c] for $n = 2$, we get

$$M_2(t) = M_2(0) + 2M_0(0)\, Dt - \int_0^t [\mu_2(t') + 2D(t - t')\sigma(t')]\, dt' \qquad [16]$$

which is again a linear equation in D if all other terms are measurable.

Summary

We have developed a method of data analysis that is based on the computation of moments of the concentration distribution. We have shown that these quantities form the coefficients of polynomials in the fitting parameter Dt. Since the moments are easily evaluated numerically from experimental data, it follows that data fitting reduces to finding roots of polynomials. Not only is this procedure much simpler than the usual minimization schemes, but also it must be remembered that the estimation of moments introduces a measure of smoothing. Nowhere is it necessary to estimate slopes or functional values. One can therefore expect increased accuracy in the measurement of diffusivities. It should also be appreciated that the initial profile can be arbitrary, a condition in line with most experimental situations.

We have also demonstrated the method's applicability in the practical case of impurity redistribution in ion-implanted material, but it can be applied equally well to other physical cases that satisfy essentially the same boundary conditions. Although the method requires that the diffusivity be concentration independent and that the boundary conditions be quite simple (given flux, *i.e.*, a Neumann condition), one can anticipate its extension to more complex cases.

Manuscript submitted Feb. 15, 1985; revised manuscript received June 24, 1985.

IBM Corporation assisted in meeting the publication costs of this article.

REFERENCES

1. G. Dahlquist and A. Björk, "Numerical Methods," pp. 438-446, Prentice-Hall, Englewood Cliffs, NJ (1974).
2. B. Tuck, "Introduction to Diffusion in Semiconductors," pp. 199-203, Peter Peregrinus Ltd., Stevenage, England (1974).
3. R. Ghez and M. B. Small, *This Journal*, **128,** 1468 (1981).
4. R. Ghez, G. S. Oehrlein, T. O. Sedgwick, F. F. Morehead, and Y. H. Lee, *Appl. Phys. Lett.*, **45,** 881 (1984).
5. H. S. Carslaw and J. C. Jaeger, "Conduction of Heat in Solids," Clarendon Press, London (1959).
6. W. Feller, "An Introduction to Probability Theory and Its Applications," John Wiley and Sons, New York (1957).
7. J. D. Fehribach, R. Ghez, and G. S. Oehrlein, *Appl. Phys. Lett.*, **46,** 433 (1985).
8. G. S. Oehrlein, R. Ghez, J. D. Fehribach, E. F. Gorey, T. O. Sedgwick, S. A. Cohen, and V. R. Deline, in "Proceedings of the Thirteenth International Conference on Defects in Semiconductors," L. C. Kimmerling and J. M. Parsey, Editors, pp. 539-546, The Metallurgical Society of AIME, Warrendale, PA (1984).
9. S. M. Hu, P. Fahey, and R. W. Dutton, *J. Appl. Phys.*, **54,** 6912 (1983).

Comparisons of GaAs, Tungsten, and Photoresist Etch Rates and GaAs Surfaces Using RIE with CF_4, $CF_4 + N_2$, and $SF_6 + N_2$ Mixtures

Nobuhiko Susa

Nippon Telegraph and Telephone Corporation, Musashino Electrical Communication Laboratory, Musashino-shi, Tokyo 180, Japan

ABSTRACT

Etch rates for GaAs, tungsten, and photoresist were compared using CF_4, $CF_4 + N_2$, and $SF_6 + N_2$ gases. Etch rate ratio between the W and photoresist can be increased by N_2 gas addition, with a negligibly low GaAs etch rate. GaAs surfaces exposed to $CF_4 + N_2$ or $SF_6 + N_2$ plasmas were characterized by means of photoluminescence (PL), Schottky contacts, secondary ion mass spectroscopy (SIMS), and Auger electron spectroscopy (AES). The PL intensity measurements and Schottky characteristics revealed that the damage to the GaAs surface was somewhat smaller than that caused by pure CF_4 gas. The AES and SIMS measurements showed that the change in Ga/As composition after reactive ion etching was negligibly small. Results of heat-treatment are also described. Curious annealing characteristics were observed in the $CF_4 + N_2$, suggesting the existence of GaN.

As the sizes of high speed electronic devices are scaled down to the submicrometer level, dry processes such as reactive ion etching (RIE) become essential in the development of microdevices. This is because undercutting occurs in fabrication of such devices when conventional wet etching is employed. On the other hand, since RIE is an anisotropic etching method due to the formation of volatile compounds by plasma species and also due to the accelerated ion bombardment in the plasma sheath, high grade photolithography without undercutting is obtained. The energetic ions, electrons, ultraviolet photons, and x-rays in the plasma, however, produce degradation in semiconductor surfaces exposed to it.

Recently, Bozler *et al.* (1) and Asai *et al.* (2) developed a permeable base transistor (PBT), consisting of submicrometer tungsten gratings embedded in a GaAs epitaxial layer. RIE is a suitable technique for patterning the submicrometer W grating on GaAs, because there is no undercutting. In this case, the plasma is required to etch only the W films and not the GaAs layer. Moreover, GaAs surface damage caused by exposure to the plasma must be minimized, because a second GaAs epitaxial layer is grown on the first epitaxial layer after the W photolithography and a damage-free process is needed for the W photolithography to realize a high performance PBT. Although RIE has been extensively studied for application to GaAs etching, few reports on W dry etching, which meets these requirements, have been published (3-5). We have tried several mixtures of several gases to realize W etching without surface damage while maintaining the GaAs etching rate at a negligibly low level. Finally, fluoride gases mixed with nitrogen were found to be suitable for W film etching on GaAs, because the use of these gases resulted in a higher etching rate for the W film than for the photoresist (AZ-1350). Detailed results on the etching rate and conditions with various kinds of gases will be published elsewhere (6). Here, only the etching rates with N_2 gas mixtures will be mentioned briefly in the Etching Rate section.

Surface degradation caused by exposure to $CF_4 + N_2$ or $SF_6 + N_2$ plasma was characterized by means of carrier concentration, photoluminescence, and Schottky characteristics and was compared with that caused by exposure to pure CF_4 plasma. Changes in surface composition and contamination on the plasma-exposed GaAs surfaces were analyzed by means of Auger electron spectroscopy (AES) and secondary ion mass spectroscopy (SIMS). The results of annealing experiments on the damaged samples are also described in this paper.

Experimental Procedures

The W films used were deposited by conventional RF diode sputtering on (100) GaAs substrates. Since the etching rate for the W film depends on the sputtering pressure, the pressure was fixed at 4×10^{-2} torr, where the resistivity of the deposited W film was minimal. Details on the deposition conditions and the properties of the W films will be reported elsewhere (7).

The GaAs crystals used were sulfur-doped epitaxial layers 2.6 μm thick grown by conventional vapor phase epitaxy on (100) 2° off GaAs substrates doped with silicon. Their carrier concentrations were 1×10^{17} and above 10^{18} cm^{-3} for the epitaxial layers and the substrates, respectively. The surfaces of the epitaxial layers were exposed to CF_4, $CF_4 + N_2$, and $SF_6 + N_2$ plasmas for 15 min and characterized by various methods. Since 300-2000Å thick W films (usually used for the PBT) deposited on GaAs were etched within 10 min under the present RIE condition, the plasma exposure time of 15 min was enough to study the GaAs surface damages.

The RIE apparatus used was a commercially available parallel-plate reactor. It consists of a stainless steel chamber and SiO_2 electrodes of 28 cm diam. The chamber can be evacuated to less than 1×10^{-5} Pa with an oil diffusion pump having a liquid N_2 cold trap. All of the RIE experiments in the present paper were done at an RF frequency of 13.56 MHz for 15 min and an input power of 50W (which corresponded in our system to a power density of 0.081 W/cm²). No substrates were intentionally heated, and their temperatures were apparently near room temperature during the plasma etching. Purities of CF_4, SF_6, and N_2 were 99.9999, 99.99, and 99.999%, respectively. The gas flow rates of gases were controlled by mass flow meters.

Etching rates for W films on GaAs were measured for the films etched through 100×200 μm windows in the AZ-1350 photoresist mask. After removing the photoresist, the step was measured with a Talystep meter.

The carrier concentration profiles of plasma-exposed GaAs were obtained from the C-V characteristics. The Schottky diodes for the C-V measurements were fabricated by evaporation of Au dots with an area of 1.26×10^{-3} cm^{-2}, and the C-V measurements were done by using a capacitance meter at 1 MHz.

The photoluminescence (PL) intensity was measured at 77 K by illuminating the RIE-processed surfaces with a He-Cd laser (4416Å), and was detected with a cooled S-1 type photomultiplier. The penetration depth at the laser wavelength of 4416Å is about 300Å.

Schottky characteristics, such as barrier height, ideality factor, and leakage current, were evaluated for diodes with Au-Schottky contacts vacuum evaporated on the plasma-exposed surfaces. The diameter of the Schottky contact was 400 μm. Ohmic contacts of alloyed Au-Ge-Ni were made by vacuum evaporation and annealing at 430°C for 150s in H_2 gas flow.

The Ga/As composition ratio and contamination elements, (C, O, F, N) supplied from etching gases and air were analyzed with AES. The in-depth profile was measured by sputtering the GaAs with Ar^+ ion at an etching

rate of about 5 Å/min. The SIMS profiles of C, F, O and N atoms were measured by Cs^+ ion sputtering with the modified CAMECA IMS-3F.

Etching Rate

When CF_4 gas is employed in RIE, one may expect the etching rate for a W film will be large, while that for GaAs will be negligibly small, because of the volatility of gallium fluoride (GaF_3, bp > 950°C) is lower than that of gallium chlorides ($GaCl_3$, bp = 201.3°C) and because the volatility of tungsten hexafluoride (WF_6, bp = 17.5°C) is higher than that of tungsten chlorides (WCl_6, bp = 346.7°C).

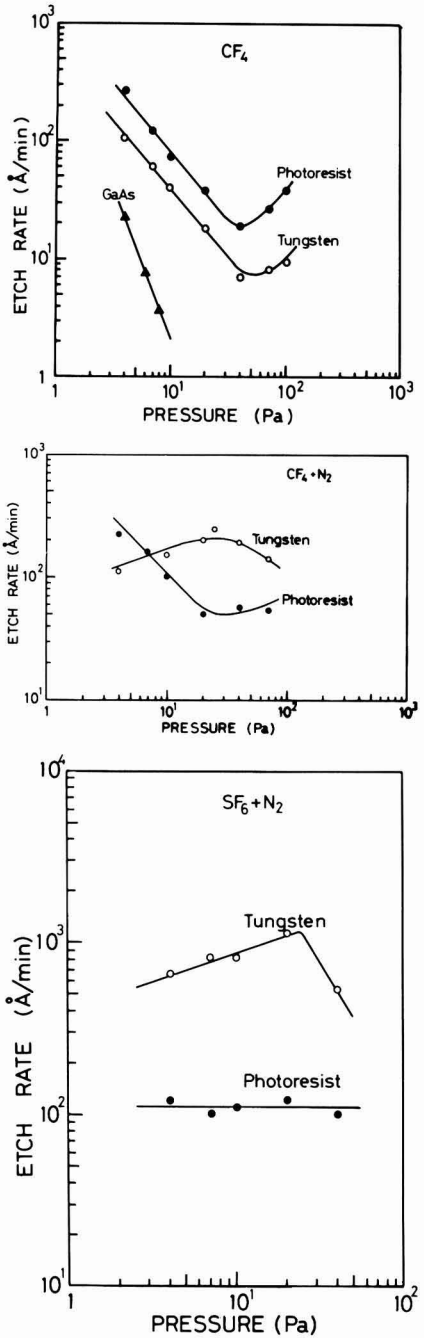


Fig. 1. Etch rate of tungsten, photoresist (AZ-1350), and GaAs as a function of pressure with (a,top) pure CF_4, (b, middle) 90% CF_4 + 10% N_2, and (c, bottom) 80% SF_6 + 20% N_2.

However, the GaAs etching rate in our experiments was rather high, as shown in Fig. 1a. Usually, CF_4 gas mixed with O_2 or Ar is used in RIE to change the etching characteristics. We studied these mixtures mainly with respect to the etching selectivity of the W film to the photoresist (AZ-1350). However, these trials resulted in an inadequate etching rate ratio between the W film and the photoresist. Next, CF_4 and SF_6 gases mixed with nitrogen were tried because no reports had been published on these mixtures for either W, GaAs, or photoresist etchings.

The etch rates for the W film, photoresist (AZ-1350), and GaAs as a function of pressure are shown in Fig. 1a, 1b, and 1c for pure CF_4, 90% CF_4 + 10% N_2, and 80% SF_6 + 20% N_2 gases, respectively. Total gas flow rate was fixed at 35 sccm for each case. Input power was 50W, and other etching conditions were identical to those described in the Experimental Procedures section.

Etching rates for GaAs with CF_4 + N_2 and SF_6 + N_2 were found to be negligibly low compared with those for pure CF_4 and SF_6. On the other hand, the etch rate for the W film was rather high when N_2 was added to pure CF_4 and SF_6. In CF_4 + N_2, the etching rates for the photoresist decreased with an increase in the pressure, while in SF_6 + N_2 the etching rates for the photoresist were independent of the pressure. The maximum etching rate ratios of the W film to the photoresist were 4 for CF_4 + N_2 and 10 for SF_6 + N_2. Therefore, the addition of N_2 to CF_4 and SF_6 was concluded to be suitable for etching the W film under the gas mixtures examined, while maintaining a practical, useful high etching rate ratio of the W to the photoresist. Moreover, the GaAs etching rate was negligibly low under these conditions.

More precise studies on the etching conditions and characteristics with various kinds of gases will be published elsewhere (6) as mentioned in the introductory section.

Surface degradation of the GaAs was evaluated in the CF_4 + N_2 and SF_6 + N_2 mixtures. Since the data for the SF_6 + N_2 were similar to those for the CF_4 + N_2, only the results for the CF_4 + N_2 will be described in the following sections.

Carrier Concentration Profiles

Carrier concentration profiles calculated from the C-V characteristics for the GaAs epitaxial layers exposed to pure CF_4 and 90% CF_4 + 10% N_2 plasmas are shown in Fig. 2a and 2b, respectively. The pressure was 25 Pa, and the other RIE conditions were the same as those described in the Experimental Procedures section. The GaAs surfaces were exposed to the plasmas for 15 min. In CF_4, the plasma-induced defects were large enough to diminish carriers near the surfaces. Similar carrier concentration reduction has been reported in RIE when 55% CF_4 + 45% H_2 (8) or pure H_2 (9) was used. On the other hand, no carrier concentration reduction was observed for the CF_4 + N_2, as shown in Fig. 2b. This implies that the surface damage due to CF_4 + N_2 was smaller than that due to pure CF_4.

Since the plasma- or ion-bombardment-induced damage can be repaired by a conventional annealing process (8, 10, 11), annealing experiments were performed in the present study. Carrier concentration profiles for the GaAs epitaxial layers exposed to the pure CF_4 or 90% CF_4 + 10% N_2 plasma are shown in Fig. 2a and 2b, respectively. The carrier concentration profiles for samples annealed in the 10% H_2 + 90% Ar gas flow at 430°C are also shown in the figures. The Au-Schottky contacts were deposited after the annealing, while the Au-Ge-Ni-alloyed ohmic contacts were made before the annealing. Surface deterioration due to exposure to the CF_4 plasma was found to have been repaired by the heat-treatment, as

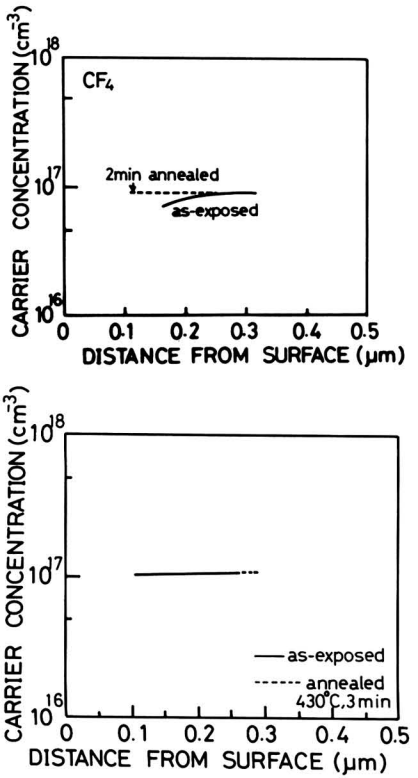


Fig. 2. Carrier concentration profiles for the GaAs epitaxial layers exposed to (a, top) CF_4 and (b, bottom) 90% CF_4 + 10% N_2 plasmas and annealed in H_2 + Ar at 430°C.

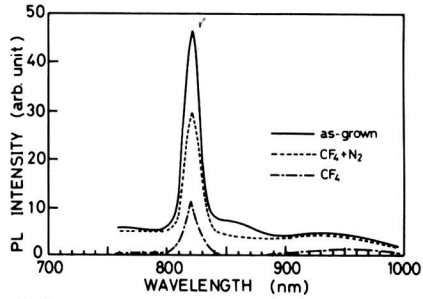


Fig. 3. Photoluminescence (PL) intensity for as-grown epitaxial GaAs and GaAs exposed to CF_4 or CF_4 + N_4, as a function of wavelength.

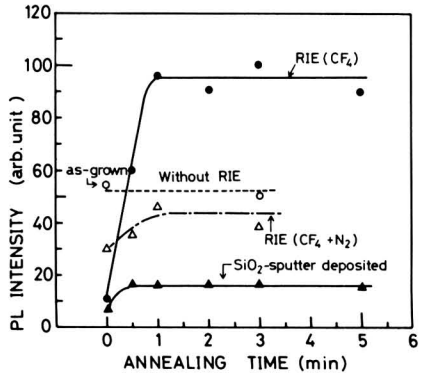


Fig. 4. PL intensity as a function of annealing time at 430°C for as-grown GaAs, GaAs exposed to CF_4 or CF_4 + N_2, and SiO_2 sputter-deposited GaAs.

shown in Fig. 2a. On the other hand, in the CF_4 + N_2, the carrier concentration profile was not affected by annealing.

Photoluminescence

Since photoluminescence (PL) spectra and intensity are affected by defects, they are sometimes used to study surface damage induced by ion irradiation. The PL spectra were measured before and after RIE to evaluate the degree of surface deterioration. The PL intensity as a function of wavelength at 77 K for as-grown GaAs and GaAs exposed to the CF_4 + N_2 or CF_4 plasma are shown in Fig. 3. The RIE conditions were identical to those in the carrier concentration measurements. Carrier concentration of the as-grown epitaxial layer was 1×10^{17} cm^{-3}, and its thickness was 2.6 μm.

When the surfaces were exposed to the plasmas, the PL intensity at an 820 nm peak was reduced by defects produced which acted as nonradiative surface recombination centers. The use of pure CF_4 resulted in a drastic reduction in the PL intensity compared with that of the CF_4 + N_2 mixtures, as shown in Fig. 3. This result agrees with the noticeable reduction (Fig. 2a) in the carrier concentration of the GaAs layer exposed to the CF_4 plasma.

Annealing experiments were carried out at 430°C in 10% H_2 + 90% Ar gas flow for the damaged GaAs surfaces, and a recovery process by the capless heat-treatment was observed by means of PL measurement. The PL intensities as a function of annealing time at the 820 nm peak at 77 K are shown in Fig. 4. The samples measured were the GaAs epitaxial layer exposed to the CF_4 or CF_4 + N_2 plasma, and as-grown GaAs. Data for SiO_2 sputter-deposited GaAs is also shown in Fig. 4 for comparison. In this case, a SiO_2 film with 700Å thickness was deposited by Ar sputtering for 15 min at 6×10^{-2} torr at an input power of 50W. This film deposited on the GaAs epilayer was then removed by wet etching with buffered HF solution before the PL measurement.

Interestingly, the values of PL intensity for the samples exposed to the pure CF_4 plasma and then annealed increased until they were nearly double that for the as-grown crystal, even though the PL intensity decreased considerably immediately after exposure to the CF_4 plasma. On the other hand, the PL intensity for the CF_4 + N_2 was somewhat larger than that for the CF_4 before heat-treatment. In the CF_4, the reason for the abrupt increase in the PL intensity due to the annealing is not clear at present. The As vacancies produced by the ion irradiation due to the CF_4 plasma may be occupied by donor impurities such as sulfur (dopant in the epitaxial layer) which migrated during the heat-treatment. This would cause the carrier concentration near the GaAs surface and the PL intensity to increase. If this is the case, the increase in carrier concentration should occur only near the surface, since it cannot be detected by means of the carrier concentration profile described in the previous section. However, this increase in the carrier concentration can be estimated from a value of capacitance at 0 bias voltage, as will be described in the Capacitance section.

The surface deposited with the sputtered SiO_2 film suffered the most serious damage, as shown in Fig. 4. This is because the GaAs surface was deteriorated seriously by Ar ion bombardment rather than by ion radiation due to the CF_4 plasma. This damage cannot be corrected by the present annealing process.

Schottky Characteristics

In order to characterize the damaged surfaces of GaAs epitaxial layers, Schottky diodes were fabricated by Au vacuum evaporation on the plasma-exposed surfaces. The GaAs surfaces were exposed to pure CF_4, CF_4 + N_2, or SF_6

+ N_2 plasma at 25 Pa at 50W for 15 min. Barrier heights were obtained from two different methods which are C-V and forward I-V characteristics (12) and were compared. Ideality factors were also calculated from the forward I-V characteristics (12). Effects of the 430°C heat-treatment on the leakage current, barrier height, and ideality factor were also examined. In these experiments, the Au Schottky contacts of 400 μm diam were evaporated after the annealing, while Au-Ge-Ni alloyed ohmic contacts were formed before the plasma exposure, as in the measurements of the carrier concentration profiles.

Barrier height and ideality factor.—Barrier heights and ideality factors for CF_4 and CF_4 + N_2 are shown in Fig. 5a and 5b, respectively. In the CF_4, a large difference in barrier height between the C-V and I-V characteristics was observed before the heat-treatment, as shown in Fig. 5a. This is because a thin insulator layer or a thin layer with low carrier concentration was formed as a result of the CF_4 plasma exposure, as deduced from the carrier concentration profile shown in Fig. 2a. The barrier heights measured from the I-V characteristics provided more reasonable values than those obtained from C-V measurements. It was found that the short annealing period was sufficient to correct the GaAs surface deterioration caused by the CF_4 plasma.

In CF_4 + N_2, it is interesting to note that the difference in barrier heights obtained from the two methods increased with an increase in the annealing time. This suggests that a higher resistive layer was formed during the heat-treatment. Such a layer, however, cannot be detected in the carrier concentration profile shown in Fig. 2b, probably because the layer was too thin (< 0.1 μm thick). In the present experiment, the barrier heights calculated from the forward I-V characteristics gave a rather exact value.

Ideality factors n for the Au-GaAs Schottky contacts before and after the present RIE process were nearly identical, as shown in Fig. 5a and 5b. This was in contrast to the results in previous reports where the n factor increased from 1.09 to 1.32 after 700Å GaAs etching for 15 min with 55% CF_4 + 45% H_2 (8), or from 1.1 to 1.2-1.5 after GaAs RIE for 1 min with pure CF_4 (13). This is also due to the lower input power density in the present experiment.

Capacitance.—Capacitances of the Schottky diodes at 0 V bias for the CF_4 and CF_4 + N_2 are shown as a function of annealing time in Fig. 6. Capacitances for the as-grown epitaxial layers are also shown for comparison.

Values of capacitances for CF_4 showed a reduction in carrier concentration due to damage, as shown in Fig. 6. After annealing, the capacitance for the pure CF_4 increased from 89 to 140 pF. The value of 140 pF corresponded to an average carrier density of 1.2×10^{17} cm^{-3} and was higher than that for the as-grown epitaxial layer (129 pF). However, the increase in carrier concentration by annealing occurred only near the surface and could not be detected with the carrier concentration profiles. On the other hand, the capacitance for the CF_4 + N_2 after annealing was 120 pF, which corresponded to a carrier concentration of 8.8×10^{16} cm^{-3} when uniform carrier distribution was assumed.

In the CF_4, the carrier concentration variation induced by the heat-treatment was in qualitative agreement with the variation in PL intensity shown in Fig. 4. However, this was not the case for CF_4 + N_2.

Leakage current.—Leakage currents (backward I-V characteristics of the Au-Schottky diodes) were measured for various kinds of Schottky diodes. Since results for CF_4 + N_2 were similar to those for pure CF_4, only experiments with CF_4 will be mentioned in this section. Leakage currents for as-grown, as-plasma-exposed, and annealed (in 10% H_2 + 90% He gas for 2 min) GaAs epitaxial layers are shown as a function of the reverse bias voltage in Fig. 7. Although reduction of the carrier concentration due to surface damage was observed as shown in Fig. 2a, leakage current did not increase after plasma exposure and was comparable to that for the as-grown epitaxial layer.

Surface Contamination and Composition

Surface contamination and changes in surface composition (Ga/As ratio) caused by RIE were analyzed. Contamination elements such as C, F, N, and O which were supplied from the CF_4, CF_4 + N_2, and air were detected mainly with SIMS. Surface composition (= Ga/As) was measured with AES. The results are described below.

Surface contamination.—Since it has been reported that Si surfaces etched with RIE using CF_4 were contaminated by the composition elements such as C and F contained in the etching gases (14, 15), GaAs surfaces exposed to CF_4 and CF_4 + N_2 plasma were analyzed with respect to C, F, N, and O in the present experiment. In-depth profiles of $^{19}F^-$ for surfaces exposed to CF_4 plasma at 50W and 25 Pa for 15 min are shown in Fig. 8. Data for

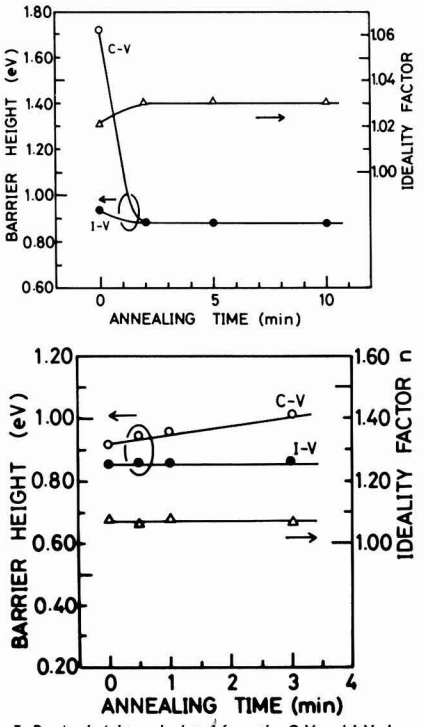


Fig. 5. Barrier heights calculated from the C-V and I-V characteristics, and ideality factor n as a function of annealing time at 430°C for samples etched with (a, top) CF_4 and (b, bottom) CF_4 + N_2.

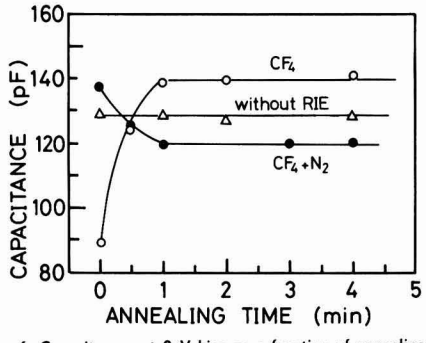


Fig. 6. Capacitances at 0 V bias as a function of annealing time (430°C) for samples etched with CF_4 and CF_4 + N_2. Capacitances of the as-grown GaAs are shown for comparison.

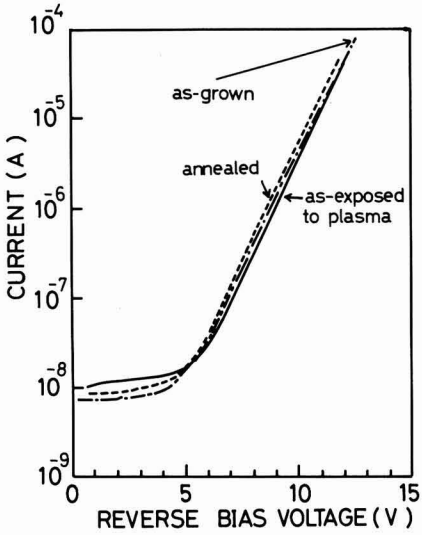


Fig. 7. Leakage currents as a function of reverse bias voltage for as-grown GaAs, and samples as exposed to plasma and then annealed at 430°C.

samples annealed in 10% H_2 + 90% Ar at 430°C for 2 min with and without RIE are also shown for comparison. F contamination was observed after RIE. However, the F on the surface can be easily removed by a simple heat-treatment, as shown in Fig. 8. No C or O contamination was detected on the GaAs surface after RIE in either the CF_4 or CF_4 + N_2 gases.

Changes in composition.—Surface composition change (Ga/As ratio) due to the plasma exposure was analyzed with AES. We measured several kinds of GaAs samples: the epitaxial layer exposed to the CF_4 or CF_4 + N_2 plasma, the layers exposed to these gases and then annealed in 10% H_2 + 90% Ar at 430°C for 3 min, and the as-grown epitaxial layer. In-depth profiles of Ga, As, C, and O for the as-grown and CF_4 plasma-exposed samples are shown in Fig. 9a and 9b as examples. Data for other samples, such as the annealed one, were similar to those shown in Fig. 9a and 9b. Neither AES nor SIMS revealed any C or O contamination due to RIE, although C and O signals due to GaAs surface oxidation and air exposure were always observed, as shown in Fig. 9a and 9b. It has been reported that GaAs surfaces become As or Ga rich as a result of RIE with CF_4 or CCl_4, respectively (16). However, in the present study, no changes in the Ga/As ratio were observed in any of the samples examined. This is probably due to the input power density of 0.081 W/cm², which is lower than that for GaAs etching by about one order.

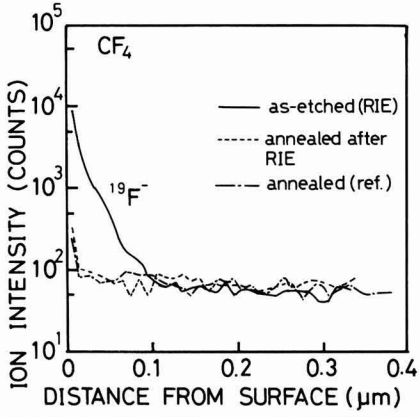


Fig. 8. In-depth profiles of $^{19}F^-$ measured with SIMS for GaAs as exposed to CF_4 plasma, and samples annealed at 430°C with and without CF_4 plasma exposure.

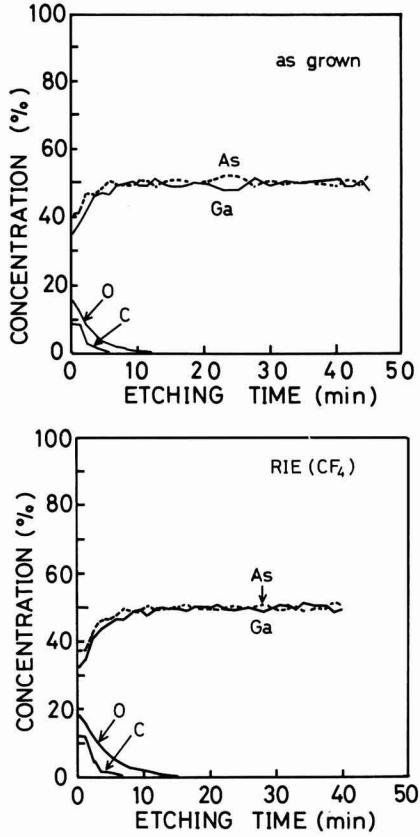


Fig. 9. In-depth profiles of Ga, As, C, and O measured with AES for (a, top) as-grown GaAs and (b, bottom) GaAs exposed to CF_4 plasma.

Discussion

In order to etch W films while keeping the GaAs etching rate negligibly low and to achieve practical etching selectivity of the W film to the photoresist (AZ-1350), the addition of nitrogen gas to CF_4 or SF_6 was found to be essential in the present experiment. The PL measurements, further, revealed that GaAs surface damage caused by exposure to CF_4 + N_2 or SF_6 + N_2 plasma was somewhat less than that caused by exposure to CF_4 plasma.

Interestingly, these results suggested that GaAs surface treatment with nitrogen plasma should reduce the surface damage. Similar results have been reported by Pankove *et al.* (17) and Matsumoto (18). They concluded that GaN (which has a wider bandgap than GaAs) formation due to the N plasma diminishes the surface recombination velocity for photogenerated carriers and that the PL intensity does not decrease much. Accordingly, the process of immersing the GaAs into nitrogen plasma is a useful method for surface passivation. In their studies, H_2 plasma was used to simultaneously remove As from the GaAs surface as AsH_3 and to produce an As vacancy in parts occupied by a N atom. Nitrogen was detected on the GaAs surface with AES in their experiments. On the other hand, no GaN was detected on the GaAs surface with either SIMS or AES in the present experiment. However, it was observed that the addition of N_2 gas to pure

CF_4 or SF_6 had a noticeable effect on surface damage, as shown in Fig. 2a and 2b and also in Fig. 3. It has been reported that the As was removed preferentially from the surface rather than the Ga when CF_4 was used as the etching gas in RIE (16). Therefore, the GaN formed by replacement of As with N probably prevents the increase in surface recombination velocity, though no Ga-rich layer could be detected in the present experiment (Fig. 9b) owing to the lower input power density and the excessive thinness of the layer.

It is interesting to note that, after annealing, the PL intensity for the GaAs exposed to the CF_4 plasma became about twice as large as that for the as-grown or annealed GaAs which was not exposed to the plasma, as shown in Fig. 4. This is probably because vacancies (probably As vacancies) produced by the ion bombardment were occupied partly by the S donor near the surface through the annealing, causing the PL intensity to increase as a result of the increase in carrier concentration. This increase in carrier concentration for the CF_4 was estimated from the somewhat larger capacitance than that of the as-grown GaAs epitaxial layer with 1×10^{17} cm^{-3} carrier concentration, as shown in Fig. 6. On the other hand, the capacitance for $CF_4 + N_2$ was slightly smaller than that of the as-grown crystal after annealing. This is probably because the As vacancies produced by the plasma were partially occupied by N rather than S and a surface layer with lower carrier concentration was formed.

From the results for CF_4 shown in Fig. 2a and 5b, the abnormally large barrier height value obtained from the C-V characteristics is concluded to be due to the formation of an insulator layer or a highly resistive layer between the Au-Schottky contact and the undamaged GaAs. In contrast, for $CF_4 + N_2$, the difference of the barrier height calculated from the C-V and I-V characteristics increased with an increase in annealing time, as shown in Fig. 5b. This suggests the existence of an insulating or highly resistive layer, or GaN after annealing. The existence of such layers can be estimated from the value of capacitance at 0 bias voltage shown in Fig. 6, although it cannot be detected with the carrier concentration profile, SIMS, or AES.

These results indicated that a W film deposited on the GaAs can be successfully etched in $CF_4 + N_2$ or $SF_6 + N_2$ with a negligibly small GaAs etching rate, minimizing the surface damage caused by exposure to the plasma.

Conclusion

A tungsten film was successfully etched on a GaAs substrate in $CF_4 + N_2$ or $SF_6 + N_2$ mixtures, with a negligibly low GaAs etching rate. PL intensity measurements revealed that surface damage caused by exposure to the plasma was considerably less than that caused by exposure to pure CF_4 gas. This is probably due to the formation of GaN on the GaAs surface and resultant suppression of surface recombination velocity. Schottky characteristics such as barrier height, ideality factor, and leakage current did not deteriorate much as a result of the low power density employed in the present study.

The GaAs surface was contaminated by F from the CF_4 compound. However, it was found that this F could be easily removed from the surface by annealing at 430°C. The levels of C and O contamination due to RIE were comparable to those for as-grown crystals. Changes in the Ga/As composition ratio after RIE could not be detected with AES or SIMS as a result of the low power density employed and thinness of the damaged layer.

The addition of N_2 to CF_4 or SF_6 gas was revealed to be essential in the W photolithography necessary for the fabrication of microdevices such as PBT's.

Acknowledgments

The authors would like to express their gratitude to Dr. Kenji Kumabe, Dr. Kiyomasa Sugii, Dr. Hideo Sugiura, Dr. Yoshifumi Takanashi, and Dr. Sadao Adachi for their constant encouragement and support. They are also grateful to Yoshikazu Homma for the SIMS measurements and Hamao Okamoto for the AES measurements.

Manuscript submitted March 19, 1985; revised manuscript received June 23, 1985.

Nippon Telegraph and Telephone Corporation assisted in meeting the publication costs of this article.

REFERENCES

1. C. O. Bozler and G. D. Alley, *IEEE Trans. Electron Devices*, **ed-27,** 1128 (1980).
2. H. Asai, S. Adachi, S. Ando, and K. Oe, *J. Appl. Phys.*, **55,** 3868 (1984).
3. C. C. Tang and D. W. Hess, *This Journal*, **131,** 115 (1984).
4. J. N. Randall and J. C. Wolfe, *Appl. Phys. Lett.*, **41,** 247 (1982).
5. K. Tsujimoto, S. Tachi, T. Mizutani, and S. Okudaira, *Proceedings of the Technical Meeting of the Institute of Electrical and Communication Engineers of Japan*, **ssd-84,** 45 (1984).
6. S. Adachi and N. Susa, *This Journal*, To be published.
7. N. Susa, S. Ando, and S. Adachi, *This Journal*, To be published.
8. Y. Yamane, K. Yamasaki, and T. Mizutani, *Jpn. J. Appl. Phys.*, **21,** L537 (1982).
9. Y. Chung, D. W. Langer, R. Becker, and D. Look, *IEEE Trans. Electron Devices*. **ed-32,** 40 (1985).
10. M. Kawabe, N. Kanzaki, K. Masuda, and S. Namba, *Appl. Opt.*, **17,** 2556 (1978).
11. C. Chen and K. D. Wise, *IEEE Trans. Electron Devices*, **ed-10,** 1522 (1982).
12. S. M. Sze, "Physics of Semiconductor Devices," pp. 279-293. Wiley-Interscience, New York (1981).
13. T. Terada, Y. Kitaura, T. Mizoguchi, and K. Hojo, in "Proceedings of the 1983 Spring Meeting of the Japan Society of Applied Physics," 7a-D-4, p. 454 (1983).
14. M. Oshima, *Surf. Sci.*, **86,** 858 (1979).
15. G. S. Oehrlein, R. M. Tromp, Y. H. Lee, and E. J. Petrill, *Appl. Phys. Lett.*, **45,** 420 (1984).
16. N. Yabumoto, M. Oshima, and S. Maeyama, in "Proceedings of the 1982 Dry Process Symposium," Tokyo, III-2, p. 73.
17. J. I. Pankove, J. E. Berkeyheiser, S. J. Kilpatric, and C. W. Magee, *J. Electron. Mater.*, **12,** 359 (1983).
18. M. Matsumoto, "Proceedings of the Technical Meeting of the Institute of Electrical Engineers of Japan," **emf-84-17,** 59 (1984).

Electrodeposition of Cadmium Telluride Using Phosphine Telluride

Andrzej Darkowski[1] and Michael Cocivera*

Guelph-Waterloo Centre for Graduate Work in Chemistry, University of Guelph, Guelph, Ontario, Canada N1G 2W1

ABSTRACT

Cadmium telluride is electrodeposited on a titanium cathode in a new process that employs tri-n-butylphosphine telluride and cadmium ion dissolved in propylene carbonate at about 100°C. Smooth gray films have been obtained with thicknesses up to 5.4 μm. The Te/Cd atomic ratio depends on applied potential and solution composition with values ranging between 0.63 and 1.1. X-ray data indicate that the as-deposited film is amorphous but becomes polycrystalline (cubic) upon annealing at 400°C. The as-deposited film can be deposited as either p or n type, and heat-treatment converts p to n. In photoelectrochemical cells, photocurrents up to 4.2 mA/cm^2 have been obtained for p-type at −1200 mV *vs.* Ag/AgCl.

Cadmium telluride is a semiconductor that has been considered as a candidate for solar energy conversion because it has a suitable bandgap. Studies using single-crystal CdTe indicate that solar conversion efficiencies near 10% are possible (1). Preparation of thin film semiconductors by electrodeposition could provide a substantial cost reduction in the manufacture of solar cells if they can replace the single-crystal material. A number of workers have studied the electrodeposition of thin film CdTe using tellurium dioxide as the tellurium source (2). It has been found that the film can be obtained from this process as either n- or p-type, depending on the potential applied (2a). In a more recent paper, tellurocyanide has been explored as a source of tellurium for electrodeposition of the film (3). Possible advantages are that this tellurium source, being in a lower valency, is less likely than tellurium dioxide to oxidize the telluride ion that is produced electrochemically because the free energy difference between oxidized and reduced species is diminished. Also, this source is more soluble than tellurium dioxide (3).

We have been exploring the use of other tellurium compounds as possible tellurium sources for the electrodeposition of thin film CdTe. In particular, we wanted the tellurium in a low valency, and we wanted the compound to be soluble in organic solvents. For these reasons, we have chosen trialkyl- or triarylphosphine tellurides. In this paper, we report the cathodic electrodeposition of thin film CdTe using tri(n-butyl)phosphine telluride in propylene carbonate. We have studied the deposition under various conditions of temperature, potential, and solution composition. At a given temperature, the Cd-to-Te ratio in the film depends on the applied potential. Data from x-ray diffraction indicate that the as-deposited film is amorphous. However, it becomes polycrystalline (cubic) when annealed at 400°C in Ar. High temperature annealing also converts p- to n-type.

Experimental

Materials.—Tri(n-butyl)phosphine telluride was prepared according to the procedure described earlier (4). Propylene carbonate was distilled from calcium oxide under vacuum. Lithium perchlorate, cadmium perchlorate, and trifluoromethane sulfonic acid were obtained from commercial suppliers. Sodium trifluoromethane sulfonate and cadmium trifluoromethane sulfonate were prepared from the acid and the corresponding base. The salts were vacuum dried at 100°C prior to use.

Substrate.—Titanium substrates were abraded with no. 400 emery paper, sonicated in warm Decon, and rinsed in distilled water. Prior to electrodeposition, the substrate was etched in 5% hydrofluoric acid and sonicated in distilled water.

Electrodeposition.—A cell in which the anode and cathode compartments were separated by a glass frit was employed to avoid contaminants from the anodic process. A Pt anode was used. The solution was kept under a nitrogen atmosphere during electrodeposition. Various temperatures ranging from 50° to 120°C were used. Depositions were performed galvanostatically and potentiostatically using a PAR 173 potentiostat/galvanostat. A silver/silver chloride reference electrode was employed for the constant potential deposition. The solutions contained 2-10 m*M* cadmium perchlorate or trifluoromethane sulfonate, 120 m*M* lithium perchlorate or sodium trifluoromethane sulfonate, and 7-26 m*M* phosphine telluride. Current density ranged from 0.1 to 0.5 mA/cm^2 for constant current deposition, and potential ranged from −650 to −1600 mV(Ag/AgCl) for constant potential deposition.

Chopped light.—In most cases, the majority carrier was determined in a photoelectrochemical cell (PEC) consisting of the photoelectrode, an Ag/AgCl reference electrode, and a Pt counterelectrode immersed in the deposition solution. Dark and light induced current as a function of applied potential was measured using chopped illumination from an ELH lamp. Current and potential were measured using the PAR 173 potentiostat/galvanostat. In some cases, the majority carrier of the film was determined using a PEC that consisted of the thin film photoelectrode and a cuprous sulfide-on-brass counterelectrode (5) immersed in a sulfide/polysulfide solution (3.0*M* sodium sulfide, 1.3*M* sulfur, and 0.8*M* NaOH in water).

X-ray diffraction.—Data were obtained using a Rigaku x-ray diffraction system (a Geigerflex D/Max Model 1A) operating with copper radiation. Data were collected for 2θ from 20° to 80° with a counting rate of 1000 counts.

Composition of films.—Polarographic analysis was used to determine the absolute amounts of cadmium and tellurium in the film. For this purpose, the film was dissolved in concentrated nitric acid at 25°C. We could find no polarographic evidence that the titanium substrate was dissolved using this procedure (6). We investigated two approaches for the polarographic analysis. The first, which we subsequently discarded, involved separation of cadmium and tellurium by base precipitation of cadmium hydroxide followed by separate analysis of the two elements in acid solutions. We found the separation cumbersome, and we found that analysis of Te(IV) in 0.01*M* nitric acid (7) was not sufficiently accurate because the Te(IV) wave at −1.25V was distorted due to hydrogen evolution.

A more convenient method, which allowed analysis for both Cd(II) and Te(IV) in the same solution, involved the use of an ammonia solution at *p*H 10 (6). After dissolution in nitric acid, the solution was diluted with 1*M* sulfuric acid and the excess HNO_3 was evaporated. The concentrated solution was diluted with deionized water and ammonia was used to adjust the *p*H and prevent the precipitation of cadmium hydroxide. Under these conditions, the Cd(II) and Te(IV) waves are well separated, −0.61 and −0.80V *vs.* Ag/AgCl, respectively (Fig. 1). At concentrations between 5×10^{-4} and 5×10^{-3}*M*, the Te(IV) wave represents a four-electron reduction, and the tellurium concentration can be determined without using either the

*Electrochemical Society Active Member.

[1]On leave from Department of Chemistry, Warsaw Technical University, Warsaw, Poland.

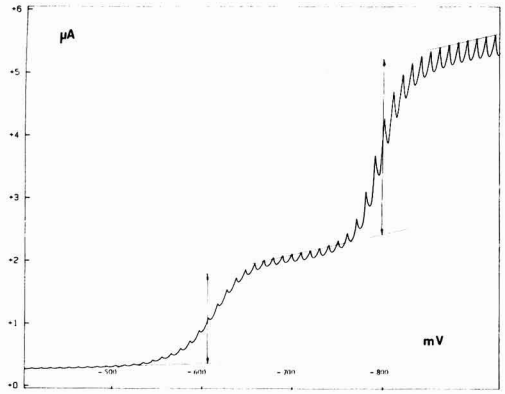


Fig. 1. Polarographic waves due to Cd(II) and Te(IV) with $E_{1/2}$ at −610 and −800 mV *vs.* Ag/AgCl, respectively. The solution contained 1 × 10^{-4}M Cd(II), 1 × 10^{-4}M Te(IV), and 0.1M ammonium sulfate. Obtained for a drop time of 2s.

standard addition technique or standard curves. Accordingly Te(IV) appears to be reduced to elemental tellurium.

Results and Discussion

Cyclic voltammetry for a solution containing Cd(II) alone, phosphine telluride alone, and Cd(II) plus phosphine telluride is presented in Fig. 2 for a titanium working electrode. The Cd(II) wave occurs at a more negative potential than the one for phosphine telluride. In the mixture, the cathodic currents are larger, and the phosphine telluride wave is shifted slightly in the positive direction. It would appear that phosphine telluride interacts weakly with Cd(II).

The composition of the electrodeposited film was determined by polarography. To test the accuracy of the analysis, the procedure was applied to an authentic sample of 99.99% CdTe. This analysis gave a Te/Cd ratio of 1.00 ± 0.01 (Fig. 1) (6).

The cathodic deposition of thin film CdTe on titanium was carried out both potentiostatically and galvanostatically, and the composition and photoresponse were monitored. For potentiostatic deposition at temperatures between 50° and 100°C, films were deposited at potentials between −650 and −1600 mV *vs.* Ag/AgCl. Table I lists the Te/Cd atomic ratio as a function of applied potential and temperature for solutions containing 0.003*M* Cd(II) and 0.012 and 0.018*M* phosphine telluride. At temperatures between 95° and 100°C, the tellurium content increases as the potential is made more negative, and the Te/Cd ratio appears to level off at about 1.0. At a given potential, this ratio and the deposition current also appear to depend somewhat on the relative Cd(II) and phosphine telluride concentrations. A detailed study is underway. The fact that Te/Cd ratios less than 1.0 can be obtained at more positive potentials indicates that two competing processes may be occurring

$$Cd^{2+} + 2e \rightarrow Cd \qquad [A]$$

$$(\text{n-butyl})_3\text{PTe} + 2e \rightarrow (\text{n-butyl})_3\text{P} + Te^{2-}$$
$$Cd^{2+} + Te^{2-} \rightarrow CdTe \qquad [B]$$

The reduction step in process [B] may, in fact, involve a complex series of equilibria because cadmium ion causes a positive shift in the reduction wave assigned to the phosphine telluride (Fig. 2). In addition, excess phosphine also affects this reduction wave.

As the deposition at constant potential progresses, the current density decreases monotonically. For example, at −1100 mV (Ag/AgCl) and 100°C, the current density decreases from an initial value of 1.5 mA/cm² to 0.08 mA/cm² after 20 min for 0.003*M* Cd(II) and 0.018*M* phosphine telluride. The rate of current decrease is affected by the concentration of the cadmium ion relative to that of the phosphine. For example, with 0.026*M* phosphine telluride, the deposition current decreases with time, but the rate of decrease is smaller for 0.006*M* Cd(II) than 0.003*M* Cd(II). Thus, for 0.006*M* Cd(II), the current density decreases from an initial value of 0.75 mA/cm² to 0.50 mA/cm² after 9 min, whereas this decrease takes only about one minute for 0.003*M* Cd(II) at the same potential. This concentration effect may be an indication that the mechanism for the deposition of CdTe is more complicated than that suggested above. One possibility under investigation is that a cadmium-phosphine telluride complex is involved. Such complexes are known to exist in the case of phosphine selenides (8). The p-type conductivity of the as-deposited film as well as its resistivity may also be partly responsible for the decrease in current with time. At potentials negative of −600 mV, p-type films are deposited as discussed below.

Although the current decreases with time, it is possible to obtain fairly thick films in reasonably short times. Films as thick as 5.4 μm have been obtained in 1h using appropriate Cd(II) concentrations. Film thickness was calculated from the mass of the film (determined by polarography) using the surface area of the film and the reported density for CdTe (9).

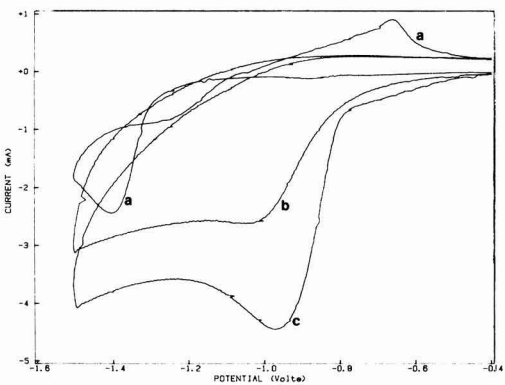


Fig. 2. Cyclic voltammetry in propylene carbonate under N_2 at 100°C and a scan rate of 100 mV/s for 0.003M Cd(II) and 0.10M $LiClO_4$ (a), 0.018M tri-n-butylphosphine telluride and 0.10M $LiClO_4$ (b), and 0.003M Cd(II), 0.018M tri-n-butylphosphine telluride, and 0.10M $LiClO_4$ (c).

Table I. Effect of applied potential on composition and photoresponse of CdTe films

Potential[a] (mV)	Composition[b] (Te/Cd)	Conductivity[c]	Deposition temperature (°C)	Photocurrent[d] (mA/cm²)
−650	0.68	p	95	
−700	0.63	p	95	
−800	0.70 ± 0.05	p	95	0.13
−1000	0.80 ± 0.07	p	100, 95	0.40
−1100	0.8 ± 0.1	p	100, 95	0.63
−1200	0.95 ± 0.05	p	100, 95	—
−1300	1.05 ± 0.05	p	100, 95	—
−1400	1.08 ± 0.08	p	100, 95, 50	0.80[e]
−1500	1.1	p	100, 95, 50	
−1600	0.9	p	100	
[f]		n	95	

[a] *vs.* Ag/AgCl.
[b] By polarography.
[c] Determined by chopped light using the deposition solution in PEC.
[d] Determined at −800 m*V vs.* Ag/AgCl.
[e] Determined at 95°C.
[f] Constant current deposition at 0.50 mA.

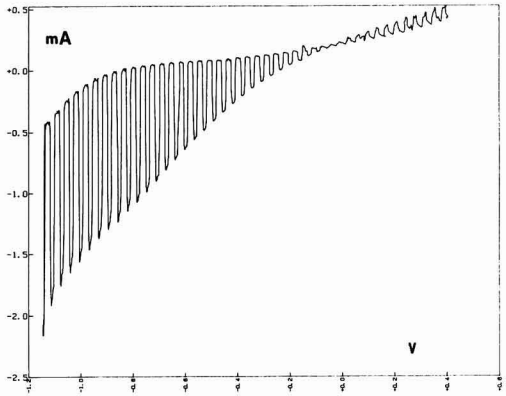


Fig. 3. Photoresponse at 100°C of electrodeposited CdTe film in PEC containing 0.003M Cd(II), 0.018M tri-n-butylphosphine telluride, and 0.10M $LiClO_4$ in propylene carbonate under nitrogen with no stirring.

Figure 3 illustrates the typical chopped light response of CdTe films deposited potentiostatically. This film was prepared by deposition at −1100 mV and 100°C in the dark. In this experiment, the deposition cell was used as the PEC cell. Thus, immediately after completion of the deposition, the film was subjected to chopped light in the same cell and solution, which contained 3.0 m*M* cadmium perchlorate, 17.5 m*M* phosphine telluride, and 100 m*M* lithium perchlorate. Because of the geometry of the cell, it was not possible to determine the light intensity accurately. However, based on the distance of the ELH lamp from the film, the power of the illumination is estimated to be less than 70 mW/cm². Since a cathodic photocurrent is observed, the film is p-type. To assure that the light-induced current is due to photogeneration of minority carriers rather than merely to an increase in photoconductivity, the potential scan was extended to 500 mV positive of the shutoff potential, and the photoanodic current was found to be negligible. Furthermore, in sulfide/polysulfide solution, the as-deposited film, which exhibited a photocathodic current, was found to exhibit a photoanodic current at potentials positive of −500 mV *vs.* Ag/AgCl after it had been annealed at 400°C. Consequently, the chopped light response appears to be a valid indicator of the type of conductivity.

The photocurrent is a factor of eight the value of the dark current since only one side is illuminated. This result is not unusual; enhancements ranging from six to 20 times the dark current have been observed for a large number of films grown under various conditions. The large increase in cathodic current upon illumination indicates that illumination can be used to avoid the large decrease in current that accompanies potentiostatic deposition in the dark (10). In Fig. 3, the potential is scanned from −1113 to +500 mV and the photocurrent is very close to zero at 0 mV (shutoff potential). Correcting for the liquid junction potential using ferrocene [E^0, +0.34V *vs.* SCE (11)], the shutoff potential becomes −80 mV *vs.* SCE. For CdS, the shutoff potential has been found to correlate well with the Mott-Schottky flatband potential in both water and acetonitrile (12). For comparison, values of −30 (13a), +210 mV (13b), and +100 mV (13c) *vs.* SCE have been reported for p-type CdTe single crystals in water.

Chopped light studies of the film while it is grown have proved to be a great advantage. Thus, by means of these studies, we can monitor the effect of various deposition conditions on the quality of the film without having to remove it from the electrochemical cell. Consequently, time is saved since each film does not have to be incorporated into either a photovoltaic cell or another PEC. Likewise, since the films are not modified in any way for the photoresponse studies, their compositions may be determined, and the photoresponse may be correlated with the composition and thickness of the film. Finally, it is possible to check the effect of aging and exposure to air on the photoresponse of the film. In this regard, we find that exposure of the dried film to air causes a decrease in the photocurrent. Preliminary results indicate that this decrease is time dependent but stabilizes at about 50% of the original value after 24h. A detailed study is under way.

The observed photocurrents of up to 4.2 mA/cm² for films with surface areas of 1.2 cm² seem promising in view of the poor cell geometry employed. The cell consisted of two compartments separated by a frit, which no doubt caused a large cell resistance. Furthermore, the solution concentrations were quite low, as indicated above. Work is under way to devise a more efficient cell that contains a more suitable redox couple. It should be noted that these photocurrents are obtained at 100°C at applied potentials between −800 and −1300 mV *vs.* Ag/AgCl.

To date, the conditions providing the p-type film that has the best photocurrent density are 0.003*M* Cd(II), 0.012*M* phosphine telluride, 0.10*M* lithium perchlorate, and a potential of −1200 mV *vs.* Ag/AgCl. These conditions are being used to make films for photovoltaic cells (14). It is interesting to note that the photocurrent obtained from our as-deposited films is substantially larger than that reported recently for as-deposited thin film p-CdTe obtained by electrolysis of aqueous TeO_2 (2e, 2f). X-ray diffraction data (see below) indicate that both films may be amorphous. Consequently, the difference lies either in the nature of the two films or in the medium and temperature employed (for the TeO_2 grown film, the PEC cell contained aqueous sodium hydroxide at room temperature). These possibilities are under investigation.

A study of the relation between the composition of the film and its conductivity indicates that p-type CdTe is obtained even when the film contains an excess of cadmium. Thus films deposited at potentials in the range from −650 to −1200 mV *vs.* SCE exhibit p-type conductivity and have Te/Cd ratios of 0.95 or less (Table I). Since a CdTe film containing an excess of cadmium is expected to exhibit n-type behavior (15), we conclude that the excess cadmium is not distributed uniformly throughout the film. Instead, it may be present as small pockets of cadmium metal. Films deposited at −600 mV *vs.* SCE do not exhibit appreciable photocurrent in the deposition solution.

Preliminary work indicates that the deposition temperature may affect the nature of the conductivity of the film. It is also possible to convert the CdTe film from p- to n-type by annealing it at 400°C in an argon atmosphere for 30 min. In addition, heat-treatment at 400°C converted the film from an apparently amorphous material to a polycrystalline material. X-ray diffraction indicates that the average crystal diameter is about 50 nm in the heat-treated film. The diffraction angles correspond well to those reported for cubic CdTe (Table II). This film had a Cd/Te ratio of 1.0, and no peaks due Cd metal were detected.

In general, the visible appearance of the film depended on the deposition potential employed. Those with the

Table II. Comparison of x-ray diffraction data for thin film CdTe with literature values

Observed		Reported[a] Cubic		Hexagonal	
2θ	I/I_0	2θ	I/I_0	2θ	I/I_0
23.7	1.00	23.75	1.00	23.70	1.00
—	—	—	—	25.27	0.80
39.3	0.46	39.28	0.60	39.25	1.00
—	—	—	—	45.42	0.75
46.4	0.27	46.42	0.30	—	—

[a] ASTM x-ray powder diffraction file numbers 19-193, 4-0554, and 15-770.

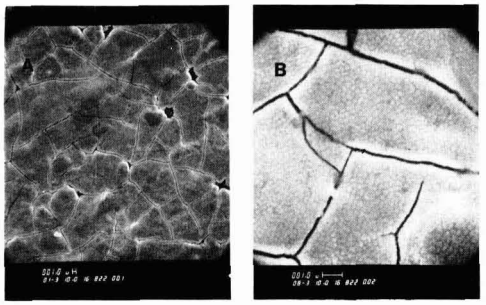


Fig. 4. SEM of thin film CdTe electrodeposited in the dark on titanium at 100°C. The film thickness and Te/Cd ratio are 2.4 μm and 1.0, respectively. Magnification: A:B = 1000:8000.

best appearance were grown at potentials ranging from −1000 to −1300 mV *vs.* Ag/AgCl. They appear smooth, uniform to the eye, and dark gray in color. At −1600 mV, the film is thin and is not uniformly gray. A SEM of a film grown at constant potential (−1100 mV) is presented in Fig. 4. Cracks are clearly visible. These appear to be a function of the thickness. For thinner films (*ca.* 0.5 μm), the cracks are fewer and thinner.

Acknowledgment

This work is funded in part by a grant to M. C. from the Natural Sciences and Engineering Research Council of Canada. We are indebted to Professor R. T. Oakley for making us aware of phosphide tellurides.

Manuscript submitted April 8, 1985; revised manuscript received July 10, 1985.

The University of Guelph assisted in meeting the publication costs of this article.

REFERENCES

1. K. Yamaguchi, N. Nakayama, H. Matsumoto, and S. Ikegami, *Jpn. J. Appl. Phys.*, **16,** 1203 (1977).
2. (a) M. P. R. Panicker, M. Knaster, and F. A. Kroger, *This Journal*, **125,** 566 (1978); (b) G. Fulop, M. Doty, P. Meyers, J. Betz, and C. H. Liu, *Appl. Phys. Lett.*, **40,** 327 (1982); (c) J. Llabres, *This Journal*, **131,** 464 (1984); (d) R. N. Bhattacharya, K. Rajeshwar, and R. N. Noufi, *ibid.*, **131,** 939 (1984); (e) K. Uosaki, M. Takahashi, and H. Kita, *Electrochim. Acta*, **29,** 279 (1984); (f) M. Takahashi, K. Uosaki, and H. Kita, *This Journal*, **131,** 2034 (1984).
3. M. Skyllas-Kazacos, *J. Electroanal. Chem.*, **148,** 233 (1983).
4. R. A. Zingaro, B. H. Steeves, and K. Irgolic, *J. Organomet. Chem.*, **4,** 320 (1965).
5. G. Hodes, J. Manassen, D. Cahen, and M. David, *This Journal*, **127,** 2252 (1980).
6. A. Darkowski and M. Cocivera, *Talanta*, To be published.
7. D. C. Whitnack, T. Donovan, and M. H. Ritchie, *J. Electroanal. Chem.*, **14,** 205 (1967).
8. (a) P. A. Dean and M. K. Hughes, *Can. J. Chem.*, **58,** 180 (1980); (b) P. A. Dean and L. Polensek, *ibid.*, **58,** 1627 (1980).
9. "CRC Handbook of Chemistry and Physics," 46th ed., R. C. Weast, Editor, p. B161, Chemical Rubber Co., Cleveland, OH (1965).
10. A. Darkowski, J. von Windheim, and M. Cocivera, *This Journal*, To be published.
11. M. E. Langmuir, P. Hoenig, and R. D. Rauh, *This Journal*, **128,** 2357 (1981).
12. J. H. Reeves and M. Cocivera, *ibid.*, **131,** 2042 (1984).
13. (a) J. F. McCann and J. Pezy, *ibid.*, **128,** 1735 (1981); (b) J. O'M. Bockris and K. Uosaki, *ibid.*, **124,** 348 (1977); (c) J. L. Sculfort, R. Triboulet, and P. Lemasson, *ibid.*, **131,** 209 (1984).
14. A. Darkowski and M. Cocivera, *This Journal*, To be published.
15. D. de Nobel, *Philips Res. Rep.*, **14,** 361 (1959).

Thermodynamic Properties of Potassium Polyphosphide KP_{15}

H. S. Marek, C. G. Michel, J. A. Baumann, and M. A. Kuck

Stauffer Chemical Company, Eastern Research Center, Elmsford, New York 10523

ABSTRACT

The equilibrium vapor pressure of phosphorus over crystalline KP_{15} has been measured in the temperature range of 305°-530°C by means of a Bourdon gauge. The reaction of 6/19 KP_{15} (s) = 2/19 K_3P_7 (s) + P_4 (g) is described by the equation

$$\ln p \text{ (atm)} = -\frac{14{,}849 \pm 340}{T} + 19.35 \pm 0.5$$

The calculated standard enthalpy and entropy of this reaction are

$$\Delta H^\circ_{298} = 118.8 \pm 2.9 \text{ kJ/mol}$$

$$\Delta S^\circ_{298} = 159.0 \pm 4.2 \text{ J/mol-K}$$

The standard enthalpy for the formation of KP_{15} from the elemental gases

$$K\text{ (g)} + 15/4\ P_4\text{ (g)} = KP_{15}\text{ (s)}$$

was found to be $\Delta H^\circ_{v,298} = -651.0 \pm 3.3$ kJ/mol. Our data show that the thermal stability of KP_{15} is greater than that of crystalline red phosphorus. In addition, the kinetics of dissociation of KP_{15} were found to be significantly faster than the kinetics of vaporization of crystalline red phosphorus.

The useful semiconductor properties of polyphosphide materials have been recently reported (1). These materials were prepared in our laboratory by several processes. However, until now, very little has been known about their thermodynamic properties.

Metal polyphosphides having the formula MP_{15} (M = alkali metal) constitute a family of P-rich materials with structural units which are derivatives of Hittorf's phosphorus. These polyphosphides, first reported (2, 3) by von Schnering, have a unique atomic framework: a one-dimensional polymer-like structure consisting of parallel phosphorus tubes of pentagonal cross section linked by M-P bridges.

The crystalline metal polyphosphides (MP_{15}) and Hittorf's phosphorus (4) both contain layers of P tubes. In Hittorf's phosphorus, two consecutive layers of P tubes are aligned crosswise. In the metal polyphosphides, the layers are aligned parallel to each other.

The vapor pressure of various modification of solid red phosphorus has been previously studied as a function of temperature (5). In this paper, we report the equilibrium vapor pressure of phosphorus over crystalline KP_{15}.

Standard enthalpies for the dissociation reaction and for the formation of KP_{15} from the elemental gases were calculated from our pressure-temperature data and compared with the thermodynamics of red phosphorus.

Experimental Technique

The tensimetric apparatus used in this work consists of a quartz Bourdon gauge of the spoon type used as a null-point instrument and controllers to monitor pressure-temperature as shown in Fig. 1. Gauges of various sensitivity were obtained by varying the size and thickness of the spoon. A 25 cm quartz rod pointer was attached to the top of the spoon. Deflection of the rod caused by the vapor pressure in the reaction chamber was detected by observing the displacement of the pointer image from a fixed reference using an optical system. The displacement caused by the vapor pressure on the sample side of the Bourdon gauge was countered by applying argon gas pressure. The argon pressure was measured with a mercury manometer, having an accuracy of 1 torr over a range from 3 to 800 torr. Eleven different Bourdon gauges of various size spoons were used.

Before each experiment, the empty gauge chamber was baked at approximately 550°C with continuous pumping at $\sim 10^{-5}$ torr for several hours. The apparatus was tested using 6*N* red phosphorus secured from United Mineral and Chemical Corporation. The vapor pressure data of Ref. (5) for material IV were reproduced within 3%.

The sample of KP_{15} (~ 0.1-0.5g) was introduced into the reaction chamber at room temperature under nitrogen. The sample was degassed by pumping for several hours at 150°C and then sealed.

During the experiments, the temperature was varied in steps of ~ 20°C and maintained constant at sufficiently high temperatures to prevent any condensation of phosphorus.

Sample Preparation

The crystalline KP_{15} materials used in this study were prepared by three different methods. Raman and x-ray powder diffraction spectra shown in Fig. 2 were used as fingerprints to identify these materials. Raman characterization of KP_{15} crystals has been discussed in detail in Ref. (6). Slight differences were observed in the line broadening of the x-ray diffraction peaks, suggesting a variation in the degree of crystallinity of the KP_{15} materials according to the method of preparation. The DTA curve of the crystalline KP_{15} used in the study consists of a single sharp endotherm at 640°C. Repeated heatings of the same sample resulted in virtually identical DTA curves. Samples of commercially available red phosphorus exhibited a sharp endotherm in the 590°-600°C region.

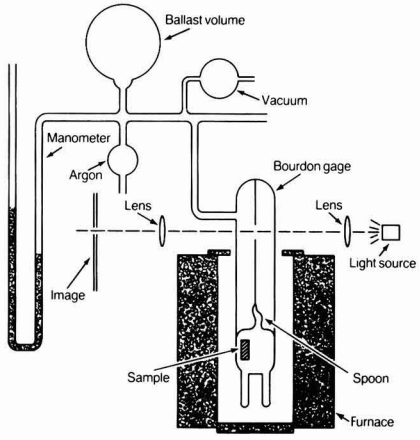


Fig. 1. Schematic of the tensimetric apparatus

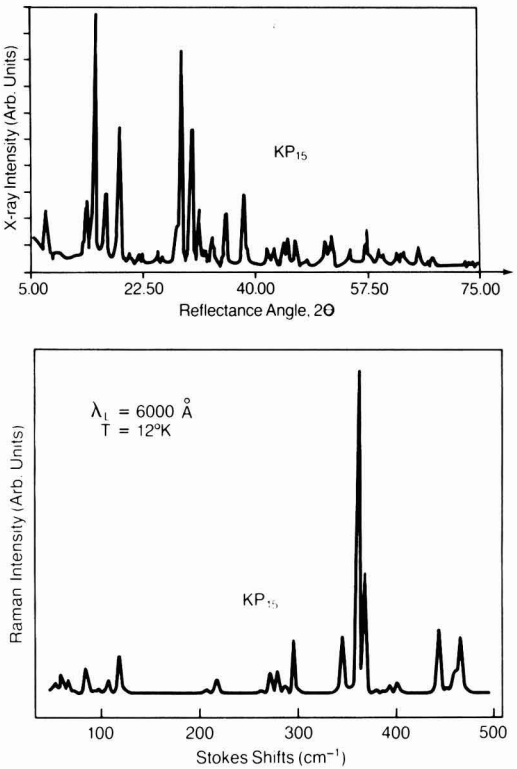


Fig. 2. a: X-ray powder diffraction pattern of KP_{15} whiskers obtained by VT process (Cu-K_α radiation). b: First-order Raman spectrum of crystalline KP_{15}.

The different processes used for the synthesis of KP_{15} crystalline materials are described below.

Condensed phase (CP).—Polycrystalline KP_{15} materials were synthesized by the direct solid-state reaction of potassium and red phosphorus. The initial stoichiometric mixture consists of high purity potassium (4*N*) and electronic grade red phosphorus (6*N*) ball milled under a nitrogen atmosphere for 48h at 70°-80°C. The resulting mixture was transferred under nitrogen to a Pyrex reaction tube. The tube was heated at 450°C for 100h. Based on the absence of a peak at 590°-600°C in the DTA data, these materials did not contain red P. The DTA results indicated a solid-state conversion from the elements into KP_{15}. However, the broadening of the x-ray powder diffraction peaks was found to be significant for this KP_{15} material. These data suggest that polycrystalline KP_{15} prepared by the CP process have small crystallite size with a low degree of crystallinity.

Vapor transport (VT).—In this process, the KP_{15} samples were synthesized by vapor transport in a sealed quartz ampul by heating the metal and red phosphorus according to the method described by von Schnering *et al.* (2). Modifications were made in our system in order to optimize the yield and to improve the control in the deposition zone of the KP_{15} whiskers.

Large quantities of dark-red, long (> 1 cm) KP_{15} whiskers were obtained by monitoring the heating cycle of the K and P charge and by controlling the temperature (~ 450°C) in the reaction zone over a large area. The basic structural framework of this material defined by x-ray single-crystal study was found to be the same as that of the KP_{15} structure previously reported (2). However, we obtained the best least squares refinement of x-ray results by lowering the symmetry of the space group in the

triclinic cell from $P\bar{1}$ to P1, corresponding to P tubes slightly shifted from their centrosymmetric positions.

Liquid phase (LP).—KP_{15} crystalline materials were prepared in quasi-equilibrium conditions from the liquid phase (LP) in a sealed tube system. In the LP process, large KP_{15} crystals were grown by slow cooling (1°C/min) from 660° to 630°C in a specially designed LP apparatus. The volume-to-charge ratio was calculated to maintain the melt composition of KP_{15-x} within the limit $x < 2$ during the growth cycle. The LP growth was terminated at ~ 630°C by using a tilting furnace.

Unlike CP and VT materials, these LP samples exhibited sharp x-ray diffraction peaks. This feature is characteristic of high quality crystals and suggests that, of the three processes, KP_{15} materials prepared from the liquid phase have the highest degree of crystallinity.

Results

Mass spectral analyses, performed on KP_{15} whiskers in a Knudsen cell, indicated that P_4 was the only significant vapor species present between 280°-450°C. In this temperature interval, the ion current increased rapidly with a change to a higher isotherm and then slowly tapered off. The observed P_4 evolution suggests that the kinetics of the process is diffusion controlled. In the tensimetric experiment, the composition of the solid phase can be calculated, provided that the composition and the mass of the initial phase and the volume of the reaction chamber are known. The P:K ratio of the final solid product was 2.3:1. Chemical analysis confirmed this ratio. Powder diffraction x-ray analysis also indicated the absence of KP_{15} in the solid product and the presence of a new phase. From the calculated composition of the final solid product in the tensimetric experiment and considering the mass spectral results, the reaction equation can be formulated as follows

$$6KP_{15}\,(s) = 2K_3P_7\,(s) + 19P_4\,(g) \qquad [1]$$

This equation is in agreement with the observations from Santandrea *et al.* obtained (7) with their Knudsen effusion technique.

Figure 3 gives the measured vapor pressure as a function of temperature for KP_{15} decomposition obtained from 33 independent data points. In spite of the fairly high temperatures, about 24h were usually required for equilibrium to be established at each temperature step. Approximately 95% of equilibrium was usually established within ~ 2h. Data were taken only when the measured pressure did not change more than 2 mm in 10h. The time to obtain this equilibrium was faster by about one order of magnitude for KP_{15} than for red phosphorus.

All vapor pressure measurements were taken in the $KP_{15} + K_3P_7$ two-phase region as indicated by the constant pressure at any one isotherm throughout the experiment.

The tensimetric data were obtained during heating. When the system was cooled, the rate of the reverse reaction decreased rapidly and equilibrium was not established even after 100h.

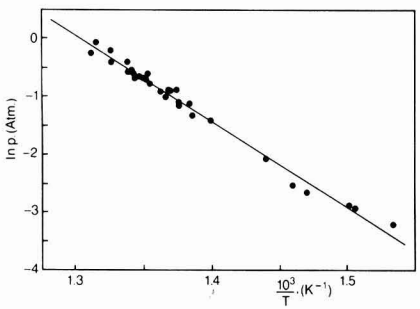


Fig. 3. Measured equilibrium vapor pressure of P_4 over crystalline KP_{15} as a function of temperature.

The pressure data obtained from the KP_{15} crystalline materials prepared from condensed phase, vapor transport, and liquid phase were found to be slightly different. A trend was observed which suggests an inverse correlation between vapor pressure and degree of crystallinity. Therefore, LP materials with the highest degree of crystallinity were used to establish the *P-T* dependence at low pressure in the plot shown in Fig. 3.

For the reaction

$$6/19\ KP_{15}\,(s) = 2/19\ K_3P_7\,(s) + P_4\,(g) \qquad [2]$$

the following equation was obtained from a least squares fit of the experimental data

$$\ln p\ (\text{atm}) = -\frac{14{,}849 \pm 340}{T} + 19.35 \pm 0.5$$

Using elemental heat capacities from the literature (8), the standard enthalpy and entropy of the reaction [2] were calculated. They are

$$\Delta H^\circ_{298} = 118.8 \pm 2.9\ \text{kJ/mol}$$

$$\Delta S^\circ_{298} = 159.0 \pm 4.2\ \text{J/mol-K}$$

Since the reaction took place in the two-phase region, $KP_{15} + K_3P_7$, pressures of P_4 at any isotherm were constant. Thus, the enthalpy of formation of KP_{15} can be calculated by a method analogous to that used by Schiffman (9) for binary compounds.

In the present calculation, the activity of P_4 was obtained from the experimental measurements, the activity of K is estimated using the Gibbs-Duhem equation, and it is assumed that the range of homogeneity of KP_{15} is small. For the following reaction

$$K\,(g) + 15/4\ P_4\,(g) = KP_{15}\,(s) \qquad [4]$$

the enthalpy of formation from the elemental gases, calculated by the third law method, is

$$\Delta H^\circ_{v,298} = -651.0 \pm 3.3\ \text{kJ/mol}$$

Discussion

Vaporization of both KP_{15} and crystalline red P yields P_4 vapor. The structural units of these two substances consist of the similar infinite P tubes with pentagonal cross section (2, 3). Thus, it can be expected that the decomposition and vaporization of these substances would have approximately the same enthalpy and entropy changes.

In the temperature range investigated (305°-530°C), we have found for the reaction [2]

$$\Delta H_T = 123.4 \pm 2.1\ \text{kJ/mol}$$

and

$$\Delta S_T = 160.7 \pm 4.2\ \text{J/mol}$$

The values of thermodynamic functions are comparable with those reported (5) for the crystalline modification of red P in about the same temperature range

$$\Delta H_T = 133.5\ \text{kJ/mol}$$

$$\Delta S_T = 186.2\ \text{J/mol}$$

Recent studies also showed a similarity in the temperature dependence of the heat capacity between KP_{15} (10) and crystalline red P (11). These data demonstrate that the same basic structural units of covalently bonded P tubes dominate the thermodynamic properties of the metal polyphosphides and crystalline red P.

Figure 4 is a comparative plot of the temperature dependence of the vapor pressure for crystalline KP_{15} and the various crystalline modifications of red P (5) referred to as forms I, II, IV, and Hittorf's P. An increase in the degree of crystallinity from form I to form IV is inferred from the methods of preparation of these materials and their corresponding x-ray powder diffraction patterns.

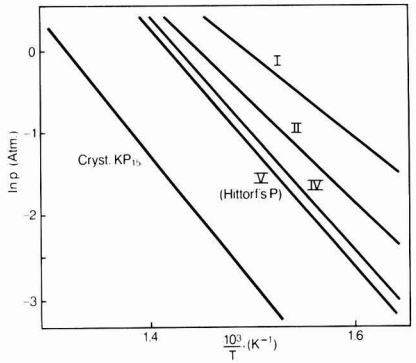


Fig. 4. Plot of the temperature dependence of the vapor pressure for crystalline KP_{15} and the various crystalline modifications of phosphorus I, II, IV, and V.

The Gibbs free energies for the various modifications of red P calculated for the average temperature of our experiment (T = 683 K) are[1]

$$\Delta G_T \text{ (I)} = -2385 \text{ J/mol}$$

$$\Delta G_T \text{ (II)} = 397 \text{ J/mol}$$

$$\Delta G_T \text{ (IV)} = 2582 \text{ J/mol}$$

$$\Delta G_T \text{ (V)}^1 = 3335 \text{ J/mol}$$

$$\Delta G_T \text{ } (KP_{15}) = 13{,}690 \text{ J/mol}$$

These data indicate that increases in the degree of crystallinity of the various modifications of red P are directly correlated with lower vapor pressure at any given temperature and, accordingly, an increase in thermal stability as shown in Fig. 4.

The calculated values of the Gibbs free energies indicate that the presence of a K-P bridge within the one-dimensional structure of KP_{15} increases its thermal stability as compared with crystalline P. In addition, analysis of our tensimetric data shows that the kinetics of dissociation of KP_{15} is much faster than the kinetics of vaporization of red P. Hence, at low pressure, KP_{15} appears to be a more suitable source of P_4 than red P (5), especially in processes where the control of P_4 (g) evolution is required.

Enthalpy of formation is calculated from data for the elemental gases instead of from the solid elements. This is because subtracting the elemental gas-solid enthalpy results in the difference between two large numbers which is smaller than the standard deviation of the components and is greatly dependent upon the source used for the elemental enthalpies. However, if the data of Hultgren *et al.* (8) are used for the enthalpy of potassium, the reaction

$$KP_{15(s)} = K_{(s)} + 15/4\ P_4 \text{ (g)}$$

$$\Delta H^\circ_{298} = 35.10 \text{ kJ/mol}$$

can be compared with the enthalpy of vaporization of red phosphorus (8) of ΔH°_{298} = 32.13 kJ/mol.

[1] ΔG_T (V) stands for Hittorf's P.

Enthalpy of formation for KP_{15} from the elemental gases was also calculated by the second law method, with the 33 data points giving

$$\Delta H^\circ_{v,298} = -657.7 \pm 21.3 \text{ kJ/mol}$$

Within the standard deviation, this agrees with the value from our third law calculation of −651.0 ± 3.3 kJ/mol. The larger deviation in the second law result is to be expected within the restricted temperature range of this investigation. The third law value is preferred since it is less sensitive to temperature errors.

Summary

We have studied the thermodynamic properties of KP_{15} prepared by different processes. The equilibrium vapor pressure of phosphorus P_4 (g) over KP_{15} solid was measured in the temperature range of 305°-530°C by using a Bourdon gauge tensimetric apparatus. The standard enthalpy and entropy for the dissociation reaction and for the formation of crystalline KP_{15} were calculated from the P-T data. We have shown that the thermodynamics of KP_{15} dissociation and of crystalline red P vaporization are comparable. The rate of dissociation of KP_{15} crystalline materials was found to be significantly faster than the rate of vaporization of crystalline red P. Our data show that the presence of a K-P bridge within the one-dimensional structure of parallel P pentagonal tubes is correlated with the greater thermal stability of the polyphosphide compounds compared to the crystalline modification of red phosphorus.

Acknowledgments

We would like to thank L. Polgar and P. Raccah for helpful discussions and comments on this paper and D. Olego for taking Raman spectra.

Manuscript submitted April 25, 1985; revised manuscript received July 19, 1985.

Stauffer Chemical Company assisted in meeting the publication costs of this article.

REFERENCES

1. R. Schachter, C. G. Michel, M. A. Kuck, J. A. Baumann, D. J. Olego, L. G. Polgar, P. K. Raccah, and W. E. Spicer, *Appl. Phys. Lett.*, **45,** 277 (1984).
2. H. G. von Schnering and H. Schmidt, *Angew. Chem.*, **79,** 323 (1967).
3. H. G. von Schnering, "Homoatomic Rings, Chains and Macromolecules of Main-Group Elements," p. 317, Elsevier, New York (1977).
4. H. Von Thurn and K. Krebs, *Act. Crystallogr. B*, **125,** 125 (1969).
5. K. J. Bachmann and E. Buehler, *This Journal*, **121,** 835 (1974).
6. D. J. Olego, *Phys. Rev. B*, **31,** 2240 (1985).
7. R. P. Santandrea and H. G. von Schnering, in "8 ETPC Abstracts," p. 279, 27/9-1/10 (1982).
8. R. Hultgren, P. P. Desai, D. T. Hawkins, M. Gleiser, K. K. Kelley, and A. D. Wagman, "Selected Values of the Thermodynamic Properties of the Elements," American Society for Metals, Metal Park, OH (1973).
9. R. A. Schiffman, *J. Phys. Chem.*, **86,** 3855 (1982).
10. R. Santandrea, E. Gmelin, C. Santandrea, and H. G. von Schnering, *Thermochim. Acta*, **67,** 296 (1983).
11. C. C. Stephenson, R. L. Potter, T. G. Maple, and J. C. Morrow, *J. Chem. Thermodyn.*, **1,** 59 (1969).

Lift-Off Patterning of Sputtered SiO_2 Films (LOPAS) and Its Application to Recessed Field Isolation

T. Yachi and T. Serikawa

Nippon Telegraph and Telephone Public Corporation, Musashino Electrical Communication Laboratory, 3-9-11 Midoricho, Musashino-shi, Tokyo 180, Japan

ABSTRACT

The lift-off patterning of sputtered SiO_2 films (LOPAS) and its application to a new recessed field isolation technique are described. The LOPAS is performed through the following steps: (*i*) SiO_2 film is sputter-deposited on the photoresist pattern; (*ii*) slight etching with buffered hydrofluoric acid to remove SiO_2 films on the photoresist sidewalls is done, and (*iii*) the photoresist is removed. Successful pattern formation using LOPAS strongly depends on the sidewall angle of the under pattern. Recessed field isolation is performed by using LOPAS and silicon substrate oblique ion milling. This recessed field isolation is free of bird's beaks and minimizes the narrow-channel effect.

The field isolation of devices on silicon substrate is of primary importance in fabricating LSI circuits. One well-known technique for defining the field oxide patterns is known as LOCOS (1), in which a nitride film is masked and etched to form the desired pattern, followed by a long high temperature oxidation. The LOCOS process, however, has several disadvantages, such as resulting in bird's beak formation and lateral diffusion of the channel stopper dope into active device areas owing to the oxidation. To overcome these problems, other isolation techniques requiring extra processes, such as two nitride masks (2) and an aluminum mask to etch a silicon groove and lift off plasma-deposited SiO_2 (3), have been reported. Few approaches have been reported to overcome the problems in the LOCOS process through a simple and straightforward process (4).

In a previous paper (5), the authors reported a new simple and straightforward field isolation technique utilizing lift-off patterning of sputtered SiO_2 films (LOPAS) (6). This paper reports the details of this LOPAS process and its application to a new recessed field isolation technique jointly utilizing silicon grooving by oblique ion milling. Combining silicon grooving by oblique ion milling and LOPAS result in isoplanar field oxide formation, which is self-aligned to the channel stop region at a low temperature. With this technique, recessed field isolation, which is suitable for high yield LSI circuits processing, is easily realized through a simple and straightforward fabrication process. Moreover, bird's beaks and lateral channel stopper dope diffusion are not observed.

Experimental

The silicon grooving was performed using a Kaufmann-type ion milling apparatus. Argon ions were accelerated with 600V acceleration voltage and 0.5 mA/cm^2 ion current density. The substrate holder inclination angle (ion beam incident angle) was changed in the range of 0°-60°. The substrate holder also rotated at 1 rpm during ion milling. Photoresist AZ-1350J 1.3 μm thick was used as an etching mask.

Field oxide film was deposited using an RF planar magnetron sputtering apparatus (7). The target was a SiO_2 sheet, 5 × 15 in. and 1/8 in. thick. The sputtering was carried out at 0.4 Pa in a 95% argon-5% hydrogen mixture. The barrel-type substrate holder of 500 mm diam and 530 mm height had a 10 rpm rotation rate during deposition. The minimum spacing between the substrate and the target was 50 mm. The sputtering power was fixed at 1.5 kW. The substrate temperature was kept below 150°C during sputtering.

The SiO_2 films on the photoresist sidewalls were selectively removed by slight etching in buffered hydrofluoric acid (6). Unwanted SiO_2 film was removed along with the photoresist patterns by dipping the substrates in photoresist strip.

MOS devices were fabricated with a new recessed-isolation technique utilizing silicon grooving by oblique ion milling and LOPAS. The starting wafers were (100)-oriented p-type silicon with resistivity of 4 Ω-cm. A 50 nm thick gate oxide film was grown in an oxidation ambient with trichloroethylene as an HCl source. Phosphorus-doped polysilicon was chemically vapor deposited, and gate electrodes were defined by plasma etching. Phosphorus was implanted for source/drain formation. Subsequently, the intermediate insulator film was chemically vapor deposited. After annealing at 1000°C for 20 min, windows were formed on the polysilicon and source/drain region. Aluminum metallization was performed for the contact on the polysilicon and source/drain. Finally, annealing was carried out in forming gas at 450°C for 20 min.

In control devices using the LOCOS technique, the field oxide was formed by high temperature oxidation at 1000°C for 6h.

Scanning electron microscopy (SEM) was used to evaluate the various device cross sections. MOSFET threshold voltage was determined using the turn-on voltage in the transconductance-gate voltage curve.

LOPAS

Lift-off process.—SEM photographs at various steps of lift-off patterning of sputtered SiO_2 films (LOPAS) are shown in Fig. 1. As shown in Fig. 1A, the SiO_2 film is fully deposited on the photoresist sidewalls by the planar magnetron sputtering. With slight etching, however, the SiO_2 film on the photoresist sidewall is removed selectively because of the extremely high etching rate, and a narrow groove is formed on the photoresist sidewall (Fig. 1B) (6). The thickness of the SiO_2 on the flat surface, on the other hand, decreased by only about 50 nm. Soaking the sample in a solution to dissolve photoresist material was carried out removing the unwanted SiO_2 film along with the photoresist pattern. Figure 1C shows the final structure.

The successful formation of the SiO_2 pattern depends on the sputtering conditions. SEM photographs of the LOPAS process are given in Fig. 2, following SiO_2 film deposition on an Al-Si pattern. The Al-Si pattern exhibits cylindrical sidewalls, in which the sidewall angle changes from 0° to 90°. During the process, the SiO_2 film is first uniformly deposited on the cylindrical sidewalls of the Al-Si pattern, as shown in Fig. 2A. After slight etching and aluminum removal, the SiO_2 pattern is then formed with a slight projection boarding both sides (Fig. 2B). This formation indicates that the SiO_2 removal by slight etching strongly depends on the sidewall angle of the under pattern. Here, the critical angle for successful SiO_2 pattern formation is determined to be approximately 60°. Additionally, this angle is also strongly dependent on the sputtering conditions, especially the sputtering gas (argon/hydrogen composition) used (7).

In a planar magnetron sputtering deposition system, SiO_2 film properties depend on sputtering conditions, *e.g.*, argon pressure and target-substrate arrangement (8, 9). The SiO_2 thickness and etching rate as a function of the

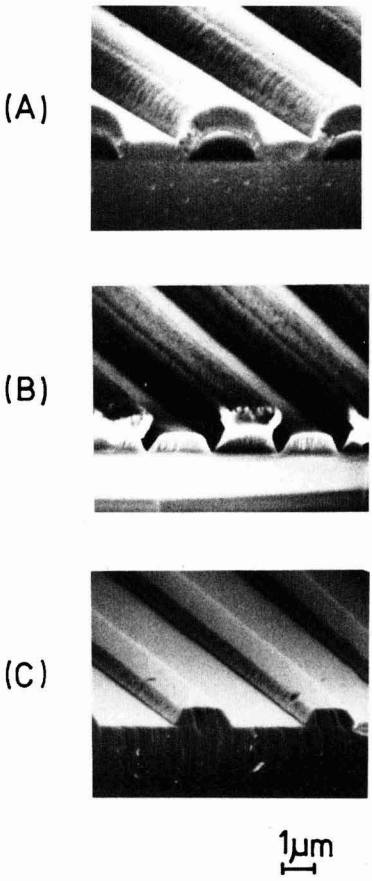


Fig. 1. SEM photographs at various steps of lift-off patterning of sputtered SiO_2 films (LOPAS). A: SiO_2 film deposited on a resist pattern. B: After slight etching. C: Final structure.

position on the substrate holder are shown in Fig. 3 for when the SiO_2 film was deposited at substrate holder stopping. The SiO_2 thickness changes depending on the position. The SiO_2 etching rate also changes extremely depending on the position. For example, on the substrate b parallel to the target, which SiO_2 particles reach with a small incident angle, the SiO_2 etching rate is about 80 nm/min, comparable to that of the thermal oxide film. On each of the side substrates a and c, which SiO_2 particles reach with a large incident angle, on the other hand, the SiO_2 etching rate increases radically to about ten times higher than that for the film deposited on the substrate paralleled to the target. SiO_2 films deposited with a large incident angle were shown to contain microvoids by observing the surface replica with a transmission electron microscope. This microvoid formation is caused by self-shadowing, which is in turn due to large incident angle (10). Owing to etching along microvoids, the SiO_2 films deposited with a large incident angle have a markedly high etching rate.

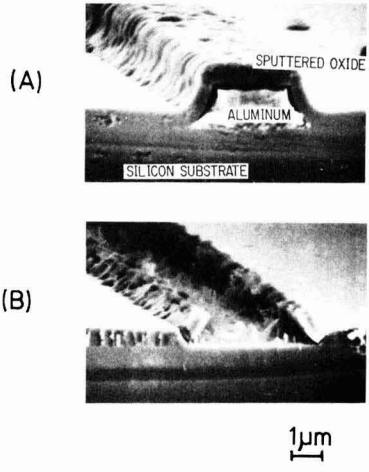


Fig. 2. SEM photographs of LOPAS process using aluminum alloy film. A: SiO_2 film deposited on an aluminum pattern with cylindrical sidewall. B: After lift-off patterning.

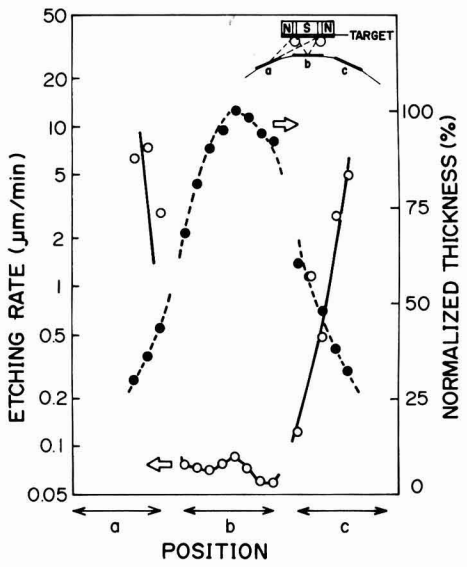


Fig. 3. SiO_2 film deposition rate and etching rate over substrates a, b, and c when the substrate holder was stopped during the deposition.

Figure 4 demonstrates the incident direction of particles sputtered onto a step profile during substrate rotation in the experimental apparatus having a barrel-type substrate holder. In the calculation, it was assumed that the sputtered particles are emitted from the target, follow the cosine emission distribution, and reach the substrate nearly free of collisions with the argon atoms. This process is thought to be correct at low sputtering gas pressure (11). Although the SiO_2 particles reach the resist sidewall having a steep incident angle in spite of the rotational barrel-type substrate holder, they contain microvoids and are etched at an extremely high rate. This situation is quite similar to that for the side-angled substrates a and c shown in the inset in Fig. 3.

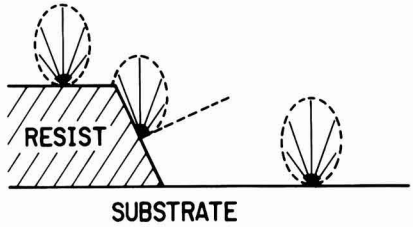


Fig. 4. Incident direction of sputtered particles on a step profile during substrate rotation in the experimental apparatus having a barrel-type substrate holder.

As described above, in planar magnetron sputtering the SiO_2 film on the under pattern sidewall, whose angle is greater than the critical angle, is easily removed by slight etching. This sidewall SiO_2 removing by slight etching successfully performs the lift-off patterning without pattern width reduction. The SiO_2 removing by slight etching is caused by the arrival of the sputtered particles with large incident angle on the under-pattern sidewall.

Recessed LOPAS.—The SiO_2 film on the under-pattern sidewall is removed by slight etching when the under-pattern sidewall angle is greater than the critical angle, as described in the preceding paragraph. Recessed patterning can be performed by SiO_2 sputtering on the silicon groove with two-step sidewall angle, one angle less than the critical angle and the other angle greater than the critical angle. The silicon groove with two-step sidewall angle is easily formed by oblique ion milling (12).

SEM photographs at steps of recessed lift-off patterning of sputtered SiO_2 films (recessed-LOPAS) are shown in Fig. 5. The substrate holder inclination angle is 40° during ion milling. The sidewall angles of the silicon groove are 30° and 80°, respectively (Fig. 5a). The SiO_2 films on the under-pattern with sidewall angle 80° are removed selectively because of the high etching rate. On the other hand, the SiO_2 films on the under-pattern with sidewall angle 30° are not removed, similar to what occurs with a flat surface, as shown in Fig. 5b.

The sidewall angle in the silicon groove depends on the substrate-holder inclination angle during ion milling (12). SEM photographs are shown in Fig. 6 for samples etched with ion beam incident angles of 0° (A), 20° (B), 40° (C), and 60° (D). The samples milled by ion beam incident angles of 40° and 60° have a clear two-step sidewall angle and are formed recessed SiO_2 patterns. With ion beam incident angles of 0° and 20°, the samples do not have a two-step sidewall angle, however, but have, rather, deep ditches in the pattern edge. The horn at pattern edge in a sample milled by incident angle 0° is caused by redeposition during ion milling.

Figure 7 shows the normalized depth of recession (s/d) as a function of the ion beam incident angle. The s/d markedly decreases as the ion beam incident angle increases. The s/d is about 30% for the samples milled by ion beam incident angles 40° and 60°. The two-step sidewall angle formation in silicon groove contributes to the s/d decreasing.

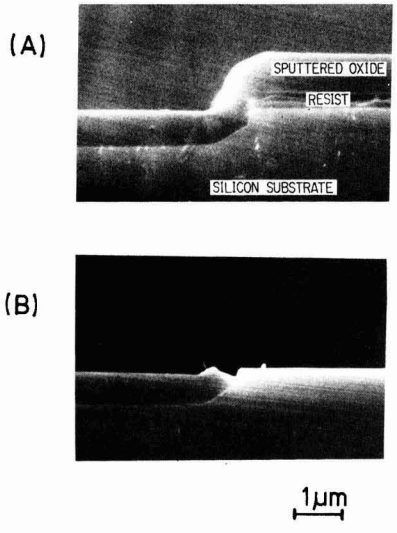


Fig. 5. SEM photographs of LOPAS process on the silicon groove with two-step sidewall angle forming by oblique ion milling. A: SiO_2 deposited on the groove. B: Final structure. The substrate-holder inclination angle is 40° during ion milling.

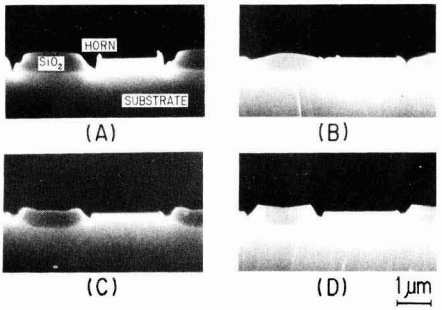


Fig. 6. SEM photographs of the samples that were etched with ion beam incident angles of 0° (A), 20° (B), 40° (C), and 60° (D).

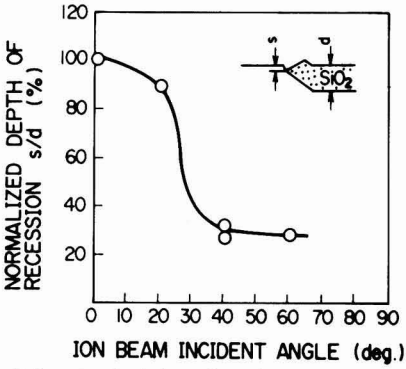


Fig. 7. Recession depth change by ion beam incident angle. Silicon groove depth is 0.6 μm.

Figure 8 shows the normalized side etching x/d by ion milling as function of ion beam incident angle. The x/d decreases with increasing incident angle. In the case of incident angles 40° and 60°, the x/d is about 20%. This small side etching is caused mainly by etching rate angular dependency (12).

As described above, the recessed SiO_2 patterns are formed by the LOPAS technique and oblique ion milling. At ion incident angle 40°, pattern edge recession and side etching are small.

Application to MOS devices

The recessed-field isolation is performed using recessed LOPAS as described in the preceding paragraph.

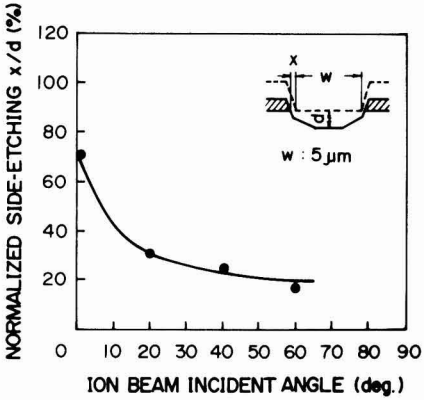


Fig. 8. Side etching change by ion beam incident angle. Silicon groove depth is about 0.6 μm.

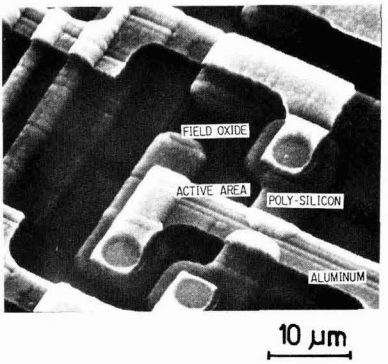


Fig. 9. SEM photograph of the MOS device fabricated using the recessed-field isolation technique.

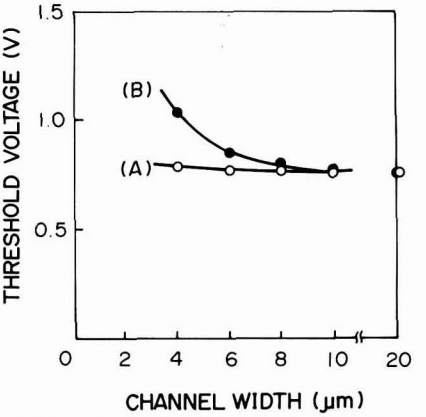


Fig. 10. Changes in threshold voltage with channel width. A: Using recessed field isolation. B: Using LOCOS.

The process sequence is as follows. (*i*) Photoresist patterns are formed on the silicon substrate with a thin thermal oxide to protect against contamination. (*ii*) Silicon grooves are formed by ion milling. (*iii*) Implantation for channel stopper dope is performed. (*iv*) SiO_2 films are deposited by planar magnetron sputtering at < 150°C. (*v*) The samples are dipped in buffered hydrofluoric acid to selectively etch the films on the under-pattern sidewalls at a steep angle. (*vi*) The photoresist is then removed with resist pattern. In this way, recessed-field isolation free of bird's beaks can form through the low temperature process.

An SEM photograph of MOS device using the recessed field isolation is shown in Fig. 9. The minimum feature size is 2.5 μm. The aluminum line step coverage is better on the recessed-field isolation pattern edge than on the polysilicon gate pattern edge.

Figure 10 shows threshold voltage for MOSFET's using the recessed-field isolation curve (A) and using the LOCOS isolation curve (B) as a function of channel width. In the LOCOS isolation, the threshold voltage shows a markedly narrow channel effect. On the other hand, in the recessed field isolation using LOPAS, the narrow channel effect is minimized by mainly eliminating lateral channel stopper dope diffusion through the low temperature process. The mobilities of the MOSFET's using the recessed-field isolation are similar to those of the control MOSFET's using the LOCOS isolation.

Summary

The lift-off patterning of sputtered SiO_2 films (LOPAS) and its application for a new recessed-field isolation technique have been described. The following results are demonstrated. (*i*) The successful pattern formation using LOPAS depends on the sidewall angle of the under-pattern. The critical angle is about 60° in sputtering with 95% argon-5% hydrogen mixed gas. (*ii*) Recessed patterning is easily performed by sputtering on the silicon groove with two-step sidewall angle forming by oblique ion milling. (*iii*) The recessed-field isolation using LOPAS is free of bird's beaks and minimizes the narrow-channel effect as a result of the elimination of lateral channel stopper dope diffusion.

Acknowledgment

The authors would like to thank Akiteru Ishimoto, Deputy Director of Division, and Tutomu Wada, Staff Engineer, Electrical Equipment Division, Musashino ECL, NTT, for their helpful suggestions and encouragement. The authors would also like to thank Akio Okamoto, Engineer, Musashino ECL, NTT, and Noriyoshi Yamauchi, Staff Engineer, Ibaraki ECL, NTT, for assistance with MOS device fabrication.

Manuscript submitted March 11, 1985; revised manuscript received July 19, 1985.

Nippon Telegraph and Telephone Public Corporation assisted in meeting the publication costs of this article.

REFERENCES

1. E. Kooi, J. G. van Lierop, and J. A. Appels, *This Journal*, **123**, 1117 (1976).
2. K. Y. Chin, R. Fang, J. Lin, and J. L. Moll, in "Proceedings of the 1982 Symposium on VLSI Technology," (Oiso, Japan), p. 28 (1982).
3. K. Kurosawa, T. Shibata, and H. Iizuka, *IEDM Tech. Dig.*, 384 (1981).
4. J. Y. Chen, R. C. Henderson, J. T. Hall, and J. W. Peters, *This Journal*, **131**, 2146 (1984).
5. T. Yachi, T. Serikawa, and T. Wada, *IEEE Trans. Electron Devices*, **ed-31**, 1748 (1984).
6. T. Serikawa and T. Yachi, *This Journal*, **128**, 918 (1981).
7. T. Serikawa and T. Yachi, *ibid.*, **131**, 2105 (1984).
8. T. Yachi and T. Serikawa, *ibid.*, **131**, 2720 (1984).
9. K. Hara, Y. Suzuki, and Y. Taga, *Jpn. J. Appl. Phys.*, **18**, 2027 (1979).
10. N. G. Nakhodkin and A. I. Shaldervan, *Thin Solid Films*, **10**, 109 (1972).
11. R. E. Jones, Jr., *IBM J. Res. Dev.*, **16**, 27 (1972).
12. N. Yamauchi, T. Yachi, and T. Wada, *J. Vac. Sci. Technol. A*, **2**, 1552 (1984).

Kinetics and Mechanism of Selective Tungsten Deposition by LPCVD

Y. Pauleau* and Ph. Lami

Centre National d'Etudes des Télécommunications, 38243 Meylan, France

ABSTRACT

Tungsten films have been deposited selectively on oxide-patterned silicon wafers by the H_2 reduction of WF_6 in WF_6-H_2 and WF_6-H_2-Ar gas flow systems. The deposition rate of films was investigated as a function of reactant partial pressures. The reaction orders with respect to WF_6 and H_2 are zero and one-half, respectively. Under given experimental conditions, the growth rate of the selectively deposited W films was reduced by 32% when the deposition area increased by a factor of 10-100. This decrease in growth rate can be attributed to the effect of HF on the surface reaction. The selective nature of the process deteriorates with increasing deposition rate, WF_6 partial pressure, H_2 partial pressure, or deposition time. The loss of selectivity seems to be linked to an increase in HF partial pressure in the reactor.

Since the 1960's, the potential advantages of vapor-deposited tungsten as a metallization and interconnection material for silicon devices have become well-known (1). Tungsten is a promising candidate for contact and diffusion barriers, low resistance gates, and interconnect lines in VLSI circuits. W films have been prepared by chemical vapor deposition (CVD) in several gas systems (2). The hexafluoride vapor, WF_6, is currently used as a starting material. Under appropriate experimental conditions, W can be deposited selectively on oxide-patterned silicon wafers via the H_2 reduction of WF_6, *i.e.*, the metal can grow on monocrystalline and polycrystalline silicon surfaces while the surrounding oxide regions remain free of any deposit. Several etching and lithography steps are eliminated using the selective process to deposit tungsten on source, drain, and gate regions of MOS circuits. Owing to the advantages of selective deposition and the requirements for VLSI technology, the interest in vapor-deposited tungsten films has been revived (3, 4).

The growth rate of CVD tungsten metallurgical coatings by reduction of WF_6 with hydrogen has been investigated as a function of deposition temperature and reactant partial pressures (5, 6). Lately, the kinetics of W deposition has been examined at lower temperature-pressure combinations compatible with the selective process (7). The deposition rate dependence on the substrate temperature and the partial pressures of WF_6 and H_2 has been found consistent with the results obtained for deposition of tungsten metallurgical coatings. The selective nature of the W deposition process is dependent on various parameters such as deposition temperature, composition of WF_6-H_2 gas mixtures, and total pressure (8). However, the relationships between selectivity and processing parameters remain essentially qualitative.

The purpose of our experiments was to investigate the kinetics of W deposition via the H_2 reduction of WF_6 and the effect of H_2 and WF_6 partial pressures on selectivity. The metal was deposited on oxide-patterned silicon wafers in two stages. In a first step was grown a self-limiting layer of W via the Si reduction of WF_6 under fixed and constant experimental conditions. Then the growth of metallic films is continued via the H_2 reduction of WF_6 carried out under variable experimental conditions. The deposition rate of metal produced by the H_2 reduction of WF_6 and the selectivity of the deposition process have been determined as a function of the deposition parameters. The growth mechanism of tungsten films will be discussed in the following sections.

Experimental Procedure

The deposition of tungsten films was carried out in a low pressure CVD system with a three-zone resistance-heated horizontal furnace. This experimental setup is quite similar to systems described in previous papers (7-9). The reaction chamber was evacuated with a Roots blower backed by an oil rotary pump. To maintain the total pressure in the reactor constant, the pumping capacity of the vacuum system could be adjusted by introducing an argon stream at the entrance of the Roots blower. So, total pressure and gas flow could be varied independently of one on another. The temperature setting of the reactor was calibrated with an internal thermocouple, at the same pressure and gas flow as those used during the experiments. The temperature difference across the length of the boat was less than 1°C. The purities of WF_6, hydrogen, and argon gases were 99.8, 99.9995, and 99.9995%, respectively. The deposition process was controlled and monitored by a microprocessor.

20-40 Ω-cm p-type (100)-oriented single-crystal silicon wafers of 100 mm diam were used. These wafers were coated with a 40 nm thick thermal oxide layer. Then, a 800 nm thick undoped low temperature oxide (LTO) was deposited on top of the thermal oxide via LPCVD at 430°C. The test pattern for W selective deposition (Fig. 1) was delineated by standard photolithographic methods; the oxide layers were etched by dipping in a buffered HF solution. After photoresist stripping, a lot of 25 substrates was cleaned in a mixture of (2.5:1) H_2SO_4:H_2O_2 for 15 min, rinsed in deionized water, and nitrogen spin dried before storage in dust-proof containers. In the reactor, a quartz boat containing 80 wafers is positioned so that the substrate surface is parallel to the gas stream. The wafers are placed in eight rows (A to H) comprising five slots spaced 12 mm apart; two wafers are placed back to back in each slot. Only three or four wafers per deposition run were used as samples; the others were thermally oxidized dummy wafers. Prior to loading in the quartz boat, the test wafers were chemically etched to remove the native oxide layer on the bare silicon regions. This chemical treatment consisted of etching in a (10:1) HF solution for 20s, rinsing in deionized water, and a nitrogen spin dry.

Some W films were prepared via the Si reduction of WF_6. The substrate temperature was fixed at 285°C. The partial pressures of WF_6 and argon were 0.005 and 0.245 torr, respectively. The sheet resistance of films was determined as a function of the reaction time which varied between 2 and 12 min. This deposition process comprises several sequences. After loading the quartz boat into the furnace, which is at deposition temperature, the reactor is evacuated, purged with nitrogen at a pressure of 0.25 torr for 10 min, and again evacuated to a base pressure of 5×10^{-3} torr. The argon flow rate corresponding to the deposition conditions is established for 10 min to allow the substrate temperature to stabilize, and then WF_6 is introduced into the reactor for 2-12 min for W deposition on monocrystalline silicon.

The W deposition experiments via the H_2 reduction of WF_6 were carried out in two successive stages. The first stage consisted in the Si reduction of WF_6 performed under the experimental conditions described above. After this step, the reactor is purged with argon for 2 min, and the second stage of deposition via the H_2 reduction of WF_6 proceeds according to the following sequences. The ar-

*Electrochemical Society Active Member.

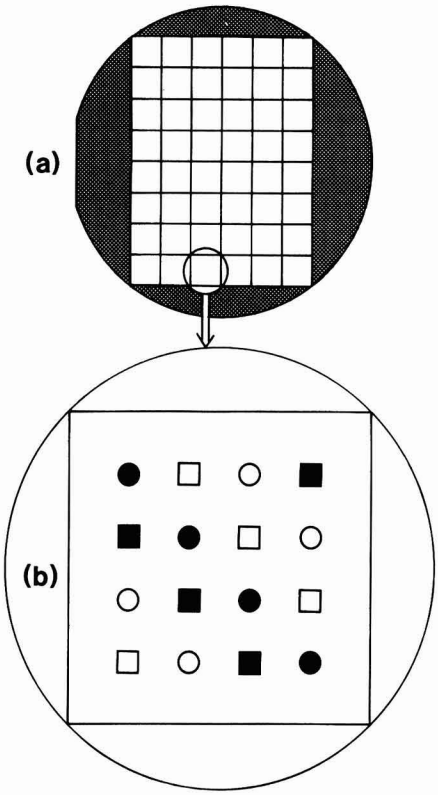


Fig. 1. a: Test pattern for selective deposition of tungsten on silicon wafers. Si (dark areas); SiO_2 (light areas). b: Magnification of 1 cm^2 of SiO_2 showing square windows of different sizes. Solid squares: 600 μm. Open squares: 400 μm. Solid circles: 200 μm. Open circles: 100 μm.

gon and hydrogen flow rates are established for 10 min, and then the deposition occurs when WF_6 is introduced into the reaction chamber. The deposition duration is fixed at 15 min. The gas flow rates and partial pressures of WF_6, hydrogen, and argon were varied as given in Table I. In all these experiments, the deposition temperature was maintained at 285°C since at this low temperature encroachment problems are suppressed (10) and excellent selectivity can be obtained (8).

The thickness of W films was measured using a stylus profilometer. Tungsten steps were etched in the large deposition zones near the wafer edges (Fig. 1). To delineate the steps, after coating with a protective wax layer, the samples were dipped in a $KOH(0.24M)$-$KH_2PO_4(0.25M)$-$K_3Fe(CN)_6(0.1M)$ solution for 1 min (2) after which the wax was stripped in trichlorethylene. The W deposition rate was derived from thickness measurements. To evaluate the selectivity of the process, the test wafers were observed by dark field optical microscopy at a magnification of 500. When a failure of selectivity occurred, minute shiny dots of tungsten could be detected on the oxide regions. Selectivity is less good at the edges of the large surfaces of deposition than in the center of samples. To characterize the quality of selectivity, different symbols are used in Fig. 3-5; the meaning of these symbols is shown in Table II.

Table I. Processing parameters for selective tungsten deposition at 285°C. (1torr = 133 Pa)

	H_2	WF_6	Ar	Total
Flow rate (liter/min)	1-4	0.015-0.300	1-4	4-7
Pressure (mtorr)	180-1400	3-55	0-1200	250-1400

Table II. Symbols used to characterize the selective nature of the tungsten deposition process

△	Selective deposition
	Failure of Selectivity
◮	W dots on SiO_2 up to 1 mm from the edge of the large deposition zones.
◭	W dots on SiO_2 up to 10 mm from the edge of the large deposition zones.
▲	Non-selective deposition

Results

Si reduction of WF_6.—The Si reduction of WF_6 proceeds according to the reaction (2, 9)

$$WF_6 + 3/2\ Si \rightarrow W + 3/2\ SiF_4$$

Tungsten films can form only on silicon regions, and this process is strictly selective. At 285°C and under the partial pressures of WF_6 and argon used, encroachment of W films along the SiO_2-Si interface does not occur. This result is consistent with that obtained by Moriya *et al.* (10). At the initial stage, the reaction of WF_6 with silicon is very fast. The sheet resistance of W films has been found to decrease very rapidly during the first 3 min; for reaction times longer than 3 min, the sheet resistance reaches a constant value (Fig. 2). The minimum resistivity is 30 $\mu\Omega$-cm, which is in good agreement with values reported in the literature (2). The metallic layers reach a limit in thickness once silicon is completely covered with a continuous, compact W layer. 15 nm thick W films were deposited during this step. The thickness of silicon consumed was about 30 nm. These thickness values deduced from scanning electron microscopic observations of samples are consistent with the data previously published (7, 9, 10).

H_2 reduction of WF_6.—When a WF_6-H_2 gas mixture is introduced into the reactor to deposit W on silicon, Si and H_2 react simultaneously with WF_6 (7, 10) and it is impossi-

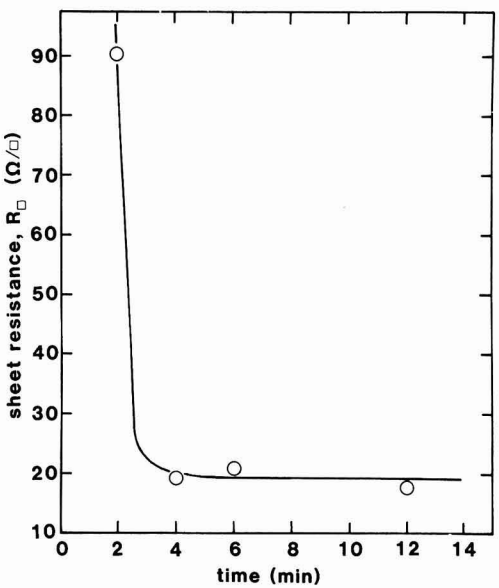


Fig. 2. Sheet resistance of W films vs. reaction time for films produced via the Si reduction of WF_6. Argon pressure = 0.245 torr; WF_6 pressure = 5 mtorr; deposition temperature = 285°C. (1 torr = 133 Pa.)

ble to determine accurately the thickness of W films grown via the H_2 reduction of WF_6 (2, 11)

$$WF_6 + 3H_2 \rightarrow W + 6HF$$

To eliminate this uncertainty, a first deposition step consisting in the Si reduction of WF_6 was systematically carried out under the experimental conditions already described. W films prepared by the H_2 reduction of WF_6 were deposited on 15 nm thick tungsten layers formed during the first step. To determine the deposition rate, 15 nm of tungsten have been deducted from the total thickness of films obtained by α-step height measurements.

The growth rate of W films on wafers closest to the tube wall (positions 1 and 10 in rows A to H) was zero or very slight compared with the deposition rate on wafers placed within a row. Consequently, the results obtained on the outermost test wafers have been disregarded and only those found for wafers in an internal position (no. 2 to 9 in a row) are reported. The deposited material was determined to be polycrystalline W by x-ray diffraction techniques. In Fig. 3 is plotted the deposition rate of films produced from WF_6-H_2-Ar or WF_6-H_2 gas systems *vs.* WF_6 partial pressure. The hydrogen partial pressure was varied between 0.18 and 0.81 torr, and the argon partial pressure was adjusted to maintain a constant total pressure of 1.4 torr. The growth rate of W films is essentially independent of the WF_6 partial pressure with or without argon in the gas phase.

The deposition rate of W films prepared from WF_6-H_2-Ar gas mixtures under a constant total pressure of 1.4 torr was examined as a function of the H_2 partial pressure. During these experiments, the WF_6 partial pressure could be varied in a wide range (5-50 mtorr) without showing any effect on the deposition rate. The dependence of the growth rate on the H_2 partial pressure is shown in Fig. 4. The deposition rate of W films is proportional to the square root of H_2 partial pressure. The curve (C1) has been plotted using the kinetic data resulting from experiments carried out when the quartz tube, quartz boat, and dummy wafers were clean. Under these experimental conditions, the total surface area of W deposition was about 60 cm^2, *i.e.*, the deposition area was limited to the silicon area left exposed on the test wafers. The rate constant deduced from the slope of the straight line (C1) is equal to 8.12 $nm\text{-}min^{-1}\text{-}torr^{-1/2}$. With the processing parameters used, the quartz ware remains free of any W deposit during 20-25 runs; the cumulated thickness of metal deposited on silicon regions of the test wafers is between 1.5 and 2 μm. After about 25 runs, a W deposit could be detected on the quartz boat near the test wafer positions and on its downstream part. The quartz tube wall and some dummy wafers were also partially covered with a W deposit. The W layer formed progressively; nevertheless, it spread more and more rapidly during further runs.

Curve (Di) corresponds to kinetic data obtained for experiments performed with dirty quartz ware, *i.e.*, when a slight deposit of metal could be detected on the quartz

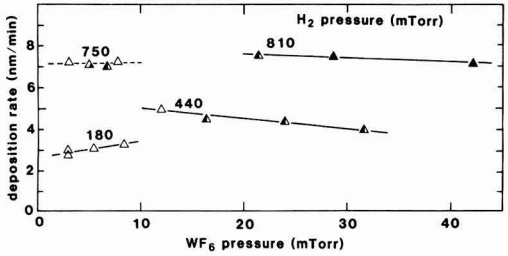


Fig. 3. Deposition rate *vs.* WF_6 partial pressure for W films deposited at 285°C from WF_6-H_2-Ar (solid line) or WF_6-H_2 (dotted line) gas systems. In WF_6-H_2-Ar mixtures, the total pressure was 1.4 torr; the H_2 partial pressures were 180, 440, and 810 mtorr. (1 torr = 133 Pa.) The meanings of symbols used for data points are given in Table II.

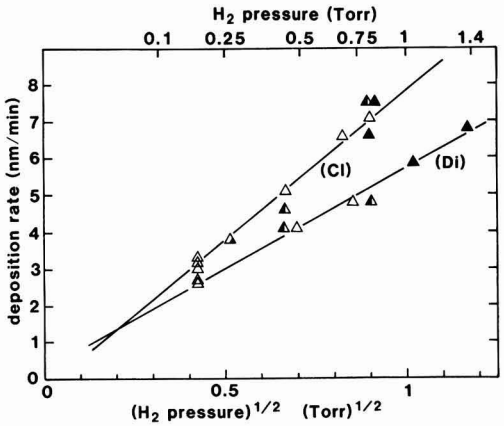


Fig. 4. Deposition rate *vs.* square root of H_2 partial pressure for W films deposited at 285°C from WF_6-H_2-Ar gas mixtures. Total pressure = 1.4 torr. (1 torr = 133 Pa.) Curve C1 results from experiments performed with a clean quartz ware; curve Di is obtained from experiments carried out with a W deposit on the quartz ware. The meanings of symbols used for data points are given in Table II.

boat in proximity to the test wafer positions. Under these conditions, the surface area of W deposition can be estimated at several hundred cm^2. The rate constant calculated from the slope of the straight line (Di) is 5.47 $nm\text{-}min^{-1}\text{-}torr^{-1/2}$. In other words, when a W deposit appears and can be detected on the quartz ware, the growth rate of metal on the test wafers is reduced by 32% whatever the number of selective deposition runs already performed. Nevertheless, the reaction order with respect to hydrogen remains equal to one-half.

The deposition rate of W films prepared from WF_6-H_2 gas mixture has been determined as a function of H_2 partial pressure (Fig. 5). Curve (C1) shown in Fig. 5 represents the kinetic data obtained for deposition experiments carried out with WF_6-H_2-Ar mixtures (Fig. 4). The WF_6 partial pressure was relatively low (3-8 mtorr). Two kinetic regimes can be distinguished. First, under hydrogen partial pressures higher than 0.7 torr, the deposition rate of W films is quite similar to that obtained with argon in the gas phase. Thus, the growth rate displays no

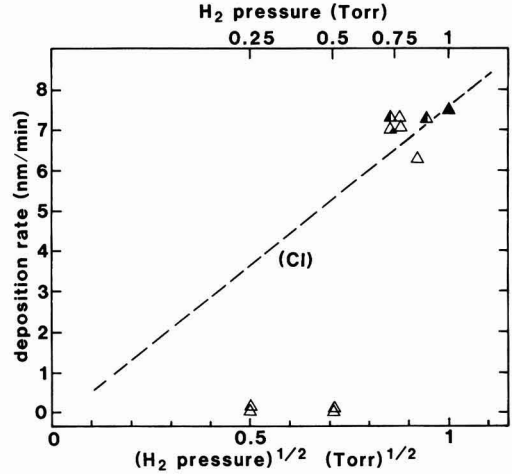


Fig. 5. Deposition rate *vs.* square root of H_2 partial pressure for films deposited at 285°C from WF_6-H_2 mixtures. (1 torr = 133 Pa.) WF_6 partial pressure = (3-8) mtorr. Curve C1 (dashed line) reports the data given in Fig. 4. The meanings of symbols used for data points are given in Table II.

dependence on changes in the argon partial pressure. Second, when the hydrogen partial pressure is less than 0.6 torr, the thickness of W films is limited to 15 nm, *i.e.*, the metal can be deposited only via the Si reduction of WF_6 occurring during the first step and the growth rate of W films via the H_2 reduction of WF_6 is about zero.

Selectivity.—The Si reduction of WF_6 yields perfect selectivity since no reaction can take place on SiO_2.

The symbols in Fig. 3-5 show the selective nature of deposition via the H_2 reduction of WF_6 as a function of WF_6 and H_2 partial pressures. Selectivity dependence on gas partial pressures is valid only for a deposition time of 15 min. For longer deposition times or thicker W films, selectivity would in all likelihood be lost owing to the development of W nuclei on the SiO_2 surface.

Selectivity deteriorates with increasing WF_6 partial pressure (Fig. 3). Under a hydrogen partial pressure of 0.44 torr, deposition remains selective at WF_6 partial pressures of less than 15 mtorr and W films will grow at a rate of only 15 nm/min. Selectivity is preserved at higher deposition rates: under an H_2 partial pressure of 0.75 torr with or without argon in the gas phase, 120 nm thick selective W films have been routinely deposited.

The correlation between selectivity and hydrogen partial pressure is shown in Fig. 4. Failure of selectivity occurs more frequently with increasing hydrogen partial pressure. For a given H_2 partial pressure (0.5 torr, for example), selectivity depends only on WF_6 partial pressure, *i.e.*, a failure of selectivity is observed under a WF_6 partial pressure higher than 15 mtorr. When a W deposit appears on the quartz boat, not only does the deposition rate fall off rapidly, but selectivity is more often lost. Consequently, after ten or 15 deposition runs, the quartz boat and reactor were cleaned in $HF\text{-}HNO_3$ solution to etch an eventual W deposit and oxidized dummy wafers were renewed.

Discussion

Reaction mechanism.—The kinetics of the chemical vapor deposition of W films via the H_2 reduction of WF_6 have been already extensively studied and Bryant (6) has analyzed experimental rate data. The reaction mechanism comprises five main sequences: (*i*) diffusion of reactants to the surface, (*ii*) adsorption of reactants on the surface, (*iii*) reaction in the adsorbed phase on the surface, (*iv*) desorption of gas products, and (*v*) diffusion of gas products from the surface.

At high substrate temperatures ($T > 700$°C), relatively low reactant flow rates, and high total pressure, the mass transport process by diffusion in the gas phase is the rate-controlling step (12). Throughout the temperature and pressure ranges investigated for selective tungsten deposition, the kinetic data may be interpreted on the basis of the Langmuir-Hinshelwood model which is currently used in heterogeneous catalysis. In previous studies (5-7), the dissociative adsorption of hydrogen on tungsten was considered as the rate-limiting step. This assumption does not account for the large decrease in deposition rate observed when W deposits on the quartz ware. Nor can this decrease in deposition rate be explained by a depletion of reactant gases due to the large increase in deposition area. Indeed, hydrogen consumption is only 0.4 cm^3/min when 60 cm^2 of metal are deposited at a rate of 10 nm/min. In the reaction scheme proposed in the present work (see Appendix), HF has been considered to affect the surface reaction rate in the adsorbed phase. Details of the procedure used to establish the expression of growth rate of the W films are given in the Appendix.

The actual HF partial pressure, P_C, in the reactor is proportional to the growth rate of tungsten, *i.e.*, to the square root of hydrogen pressure, $(P_B)^{1/2}$, and to the surface area of W deposition; therefore

$$P_C = \beta(a_0 + a_1)(P_B)^{1/2} \quad [1]$$

where a_0 is the surface area for selective deposition and a_1 is the surface area of deposition when a W deposit is detected on the quartz ware, $a_1 >> a_0$.

Using the value of HF partial pressure given by Eq. [1], the expression [A-15] for the growth rate becomes

$$G_R = [k_R\alpha(1 - \epsilon)N_s\epsilon K_B - k'_R N_s^2\epsilon^2 K_C\beta(a_0 + a_1)](P_B)^{1/2} \quad [2]$$

Therefore, the reaction orders with respect to WF_6 and H_2 (zero and one-half, respectively) provided by Eq. [2] are in good agreement with the experimental values determined during this study as well as with the findings of other investigators (5-7). By plotting G_R *vs.* $(P_B)^{1/2}$, two curves can be obtained. When the quartz ware is clean, the surface area, a_1, is zero and the slope of the straight line (C1) is given by

$$S_{(C1)} = k_R\alpha(1 - \epsilon)N_s\epsilon K_B - k'_R N_s^2\epsilon^2 K_C\beta a_0 \quad [3]$$

After several runs, when the metal is deposited on the quartz tube, boat, and dummy wafers, the deposition rate decreases and the slope of the straight line (Di) is given by

$$S_{(Di)} = S_{(C1)} - k'_R N_s^2\epsilon^2 K_C\beta a_1 \quad [4]$$

Thus, the experimental results as given in Fig. 3 and 4 can be described by Eq. [2].

The effect of HF partial pressure on the H_2 reduction of WF_6 has been studied in the past. Berkeley *et al.* (13) have shown that a concentration of HF equal to about 25% of the volume of reactants was sufficient to inhibit the deposition of tungsten from static reacting gases. On the contrary, according to Cheung (5), the addition of up to 40% HF to the WF_6-H_2 gas flow system did not have more than a dilution effect on the deposition rate. This apparent discrepancy can be explained on the basis of the mechanism proposed (see Appendix) according to which a blocking effect of HF on the deposition process occurs in step [R]. Under relatively high WF_6 partial pressures, such as those used by Cheung, the value for ϵ^2 will be very small. Therefore, Eq. [A-15] can be simplified by neglecting the second term in the right member, which gives

$$G_R = k_R\alpha(1 - \epsilon)N_s\epsilon K_B(P_B)^{1/2} \quad [5]$$

And by neglecting ϵ with respect to unity, the expression becomes

$$G_R = k_R N_s\epsilon K_B\alpha(P_B)^{1/2} \quad [6]$$

Thus, it can be established that the growth rate of W films is independent of HF partial pressure but only under HF pressures higher by a factor of 100-1000 than those used in the present study.

Under hydrogen partial pressures of less than 0.6 torr, the growth rate of W films produced in WF_6-H_2 gas systems has been found dependent on the orientation of the wafer surface with respect to the gas flow. With the wafer surface parallel to the gas flow, the growth rate is zero (Fig. 5). On the other hand, with the wafer surface perpendicular to the gas flow and under analogous reactant partial pressures, W films were deposited (7, 8). The deposition rate dependence on wafer surface orientation may be linked to the hydrodynamics of the gas system. This point remains the focus of continuing studies.

Selectivity.—The processing conditions leading to the loss of selectivity given in Fig. 3-5 are in good agreement with those put forward by Saraswat *et al.* (8). Losses in selectivity can be linked to an increase in HF partial pressure in the reactor. The selective nature of the W deposition process deteriorates when the growth rate (or HF pressure) is increased and also specially at the edges of the large deposition zones, *i.e.*, in the areas of highest HF pressure. As has already been reported by Cuomo (14), the glass substrate is etched around the W deposition zone by HF liberated from the reduction reaction. In this ablative zone, water vapor is formed on the SiO_2 surface and WF_6 can be hydrolyzed to form tungsten oxyfluoride, WOF_4. A tungsten compound containing fluorine atoms has been detected by x-ray probe analysis around the ablative zone on the glass substrate (14). At low temperature

(285°C), the etching of SiO_2 due to HF formed by the H_2 reduction of WF_6 is very slight. Nevertheless, water vapor is probably formed on the SiO_2 surface and WF_6 may be locally converted into tungsten oxyfluoride. This compound serves as a nucleating site for W deposition. Hydrolysis is favored under relatively high WF_6 partial pressure and selectivity is reduced with increasing WF_6 pressure (Fig. 3). The nuclei grow slowly during the first minutes of the deposition process; their development thereafter accelerates, and, for longer periods, the selective nature of the deposition process becomes entirely lost.

The advantage of deposition with the wafer surface parallel to the gas flow is a shortening of the HF residence time on the SiO_2 surface. This ought to improve selectivity with respect to wafers placed perpendicular to the gas flow. This point, however, remains to be ascertained by comparative experiments. A parallel configuration implies a higher total pressure than if the wafers are perpendicular to the gas flow. This increase in total pressure has been achieved in the present study by adding argon to the gas system.

Selectivity of W deposition can be further improved by various other means: both deposition area and W growth rate must be as small as possible; a low deposition temperature minimizes the interaction between HF and SiO_2.

Conclusion

The kinetic data for selective tungsten deposition via the H_2 reduction of WF_6 can be interpreted on the basis of the Langmuir-Hinshelwood model. The surface reaction between fluorine and hydrogen atoms in the adsorbed phase is considered as the rate-controlling step. The deposition rate is dependent on the HF partial pressure and, consequently, on the surface area of W deposition. To minimize this surface area and obtain a good reproducibility on the deposition rate, the quartz tube, boat, and oxidized dummy wafers have to be free of any W deposit. The selectivity of the deposition process deteriorates with increasing WF_6 partial pressure and deposition rate. The loss of selectivity seems to be linked to an increase in HF partial pressure in the reactor. The selective nature of the process can certainly be preserved under processing conditions in which HF partial pressure in the reactor and the interaction between HF and SiO_2 are minimized.

Manuscript submitted April 9, 1985; revised manuscript received July 12, 1985.

Centre National d'Etudes des Télécommunications assisted in meeting the publication costs of this article.

APPENDIX

The different steps of the reaction mechanism for the H_2 reduction of WF_6 can be schematically represented as follows.

1. Adsorption of WF_6

$$WF_6\,(g) + s \underset{k'_A}{\overset{k_A}{\rightleftarrows}} WF_6\text{-}s \rightarrow W + \ldots \rightarrow F\text{-}s \qquad [A]$$

2. Dissociative adsorption of hydrogen

$$1/2\ H_2\,(g) + s \underset{k'_B}{\overset{k_B}{\rightleftarrows}} H\text{-}s \qquad [B]$$

3. Surface reaction in the adsorbed phase

$$F\text{-}s + H\text{-}s \underset{k'_R}{\overset{k_R}{\rightleftarrows}} HF\text{-}s + s \qquad [R]$$

4. Desorption of HF

$$HF\text{-}s \underset{k'_C}{\overset{k_C}{\rightleftarrows}} HF\,(g) + s \qquad [C]$$

where k and k' are the rate constants of the direct and reverse reactions, respectively. K is the equilibrium constant with $K = k/k'$.

The Langmuir-Hinshelwood model is based on three main assumptions. First, the adsorption sites, s, on the surface of tungsten are equivalent and the adsorption of different gases (WF_6, H_2, and HF) is a competitive process. Second, the rate-limiting step is the surface reaction in the adsorbed phase; thus, the other surface processes are in equilibrium. Moreover, the surface reaction is assumed to be an opposing reaction, *i.e.*, the adsorbed species, F-s and H-s, can be formed by the adsorption of HF vapor on the tungsten surface. Nevertheless, the overall reduction reaction is not a reverse process. Third, the rate of the surface reaction, [R], is proportional to the concentrations of adsorbed species.

In order to establish an expression describing the growth rate of W films from WF_6-H_2 systems, some additional assumptions have been considered. The adsorption of WF_6 on tungsten produces fluorine atoms, called F-s in reaction [A], which are strongly adsorbed on the surface, *i.e.*, the equilibrium constant, K_A, in process [A] is very high. Some support for this assumption is provided by experimental data on the interactions between tungsten and WF_6 molecules or fluorine atoms (15-17). However, neither the stages from adsorbed fluorine atoms to WF_5 or WF_6 gas molecules nor the steps in the reverse processes have been completely understood. Finally, hydrogen and HF are assumed to be weakly adsorbed on tungsten, *i.e.*, the equilibrium constants, K_B and K_C, are very low.

To simplify the formalism of the rate equations, the subscripts A, B, and C will be used to designate the gases WF_6, H_2, and HF, respectively.

Let N_s be the total number of surface sites per square centimeter and let Θ_s, Θ_A, Θ_B, and Θ_C be the fractions of the surface sites which are free and covered by A, B, and C, respectively. In other words, Θ_s, Θ_A, Θ_B, and Θ_C are the mole fractions of free sites and adsorbed species, WF_6-s, H-s, and HF-s, *i.e.*, $\Theta_s = 1 - \Theta_A - \Theta_B - \Theta_C$. The concentrations of the adsorbed species and free sites on the W surface are given by

$$|WF_6\text{-}s| = N_s\Theta_A \qquad [A\text{-}1]$$

$$|H\text{-}s| = N_s\Theta_B \qquad [A\text{-}2]$$

$$|HF\text{-}s| = N_s\Theta_C \qquad [A\text{-}3]$$

$$|s| = N_s\Theta_s \qquad [A\text{-}4]$$

Since the adsorption step [A] is in equilibrium, the fraction of the surface sites occupied by WF_6 molecules can be expressed as a function of gas pressures (P_A, P_B, and P_C) using the steady-state equation (18)

$$\Theta_A = \frac{K_A P_A}{1 + K_A P_A + K_B (P_B)^{1/2} + K_C P_C} \qquad [A\text{-}5]$$

where K_A, K_B, and K_C are the equilibrium constants of the processes [A], [B], and [C], respectively.

Since H_2 and HF are weakly adsorbed and WF_6 strongly adsorbed on the W surface, the equilibrium constants K_B and K_C are very small and can be neglected with respect to K_A. Equation [A-5] can be simplified, and the term Θ_A is almost equal to unity. Setting

$$\epsilon = 1 - \Theta_A \qquad [A\text{-}6]$$

the value of ϵ will be very small.

The concentration of adsorbed fluorine atoms is assumed to be proportional to Θ_A and can be expressed by the following equation

$$|F\text{-}s| = \alpha(1 - \epsilon) \qquad [A\text{-}7]$$

Consequently, the concentration of fluorine atoms adsorbed on the W surface is independent of gas pressures. The terms Θ_B and Θ_C can be calculated in the same way as Θ_A (18). Since the sum $[K_B(P_B)^{1/2} + K_C P_C]$ is negligible with respect to unity, the simplified expressions of Θ_B, Θ_C, and Θ_s are the following

$$\Theta_B = \epsilon K_B (P_B)^{1/2} \qquad [A\text{-}8]$$

$$\Theta_C = \epsilon K_C P_C \qquad [A\text{-}9]$$

$$\Theta_s = \epsilon \qquad [A\text{-}10]$$

Furthermore, the concentrations of the adsorbed species and free sites on the W surface become

$$|H\text{-}s| = N_s \epsilon K_B (P_B)^{1/2} \qquad [A\text{-}11]$$

$$|\text{HF-s}| = N_s\epsilon K_C P_C \quad [A\text{-}12]$$

$$|\text{s}| = N_s\epsilon \quad [A\text{-}13]$$

The growth rate of W films, G_R, is equal to the rate of the surface reaction [R] which is considered to be the rate-limiting process. This surface reaction is an opposing reaction, and its rate is given by

$$G_R = k_R|\text{F-s}||\text{H-s}| - k'_R|\text{HF-s}||\text{s}| \quad [A\text{-}14]$$

Using Eq. [A-7] and Eq. [A-11]-[A-13], this rate equation takes the form

$$G_R = k_R\alpha(1-\epsilon)N_s\epsilon K_B(P_B)^{1/2} - k'_R N_s^2\epsilon^2 K_C P_C \quad [A\text{-}15]$$

REFERENCES

1. J. M. Shaw and J. A. Amick, *RCA Rev.*, **31,** 306 (1970).
2. Y. Pauleau, *Thin Solid Films*, **122,** 243 (1984).
3. N. E. Miller and I. Beinglass, *Solid State Technol.*, **23,** 79 (1980).
4. N. E. Miller and I. Beinglass, *ibid.*, **25,** 85 (1982).
5. H. Cheung, in "Proceedings of the Third International Conference on Chemical Vapor Deposition," F. A. Glaski, Editor, p. 136, The American Nuclear Society, Hinsdale, IL (1972).
6. W. A. Bryant, *This Journal*, **125,** 1534 (1978).
7. E. K. Broadbent and C. L. Ramiller, *ibid.*, **131,** 1427 (1984).
8. K. C. Saraswat, S. Swirhun, and J. P. McVittie, in "VLSI Science and Technology/1984," K. E. Bean and G. A. Rozgonyi, Editors, p. 409, The Electrochemical Society Softbound Proceeding Series, Pennington, NJ (1984).
9. K. Y. Tsao and H. H. Busta, *This Journal*, **131,** 2702 (1984).
10. T. Moriya, K. Yamada, Y. Tsunashima, S. Nakata, and M. Kashiwagi, Extended Abstracts of the 15th Conference on Solid State Devices and Materials, p. 225, Tokyo (1983).
11. Y. Pauleau, *Bull. Soc. Chim. France*, **4,** 583 (1985).
12. W. R. Holman and F. J. Huegel, *J. Vac. Sci. Technol.*, **11,** 701 (1974).
13. J. F. Berkeley, A. Brenner, and W. E. Reid, Jr., *This Journal*, **114,** 561 (1967).
14. J. J. Cuomo, in "Proceedings of The Third International Conference on Chemical Vapor Deposition," F. A. Glaski, Editor, p. 270, The American Nuclear Society, Hinsdale, IL (1972).
15. L. V. McCarty, W. E. Reith, and M. T. Simon, *This Journal*, **121,** 1372 (1974).
16. J. L. Philippart, J. Y. Caradec, B. Weber, and A. Cassuto, *ibid.*, **125,** 162 (1978).
17. M. Metlay and G. E. Kimball, *J. Chem. Phys.*, **16,** 779 (1948).
18. G. W. Castellan, "Physical Chemistry," 2nd ed., p. 795, Addison-Wesley, New York (1971).

A Diffusion Model for Electron-Hole Recombination in Zn_2SiO_4:(Mn,As) Phosphors

D. J. Robbins,*,[1] N. S. Caswell,* Ph. Avouris, E. A. Giess,* I. F. Chang,* and D. B. Dove

IBM Thomas J. Watson Research Center, Yorktown Heights, New York 10598

ABSTRACT

Optical techniques have been used to study the extended persistence of luminescence in willemite phosphors coactivated with Mn and As. Absorption and photoluminescence excitation spectroscopy establish that the Mn_{Zn}^{2+} impurity ground state lies 3.9 ± 0.1 eV below the conduction bandedge in willemite. Laser pulse excitation at energies > 3.9 eV has been used to generate Mn_{Zn}^{2+} luminescence decay curves. At short times (t < 100 ms), the shape of these decay curves depends strongly on both temperature and As concentration in the samples (N_{As}). These pulse response curves have been analyzed using a bimolecular kinetic model. The behavior of the model parameters as a function of N_{As} is interpreted in terms of a diffusion-controlled recombination between trapped electrons and ionized Mn centers. When $N_{As} < 1 \times 10^{19}$ cm^{-3}, the recombination is dominated by thermal emission of electrons to the conduction band. When $N_{As} > 2 \times 10^{19}$ cm^{-3}, diffusion by intertrap tunneling is dominant.

Manganese-activated willemite (Zn_2SiO_4:Mn), when coactivated with As, forms the phosphor system designated P39 (1). The active luminescence is the $^4T_1 \rightarrow {}^6A_1$ intracenter d electron relaxation of the Mn_{Zn}^{2+} impurity with lifetime $\tau_e \sim 10$ msec (2). The addition of As introduces a long nonexponential afterglow to the decay. This extended persistence of the P39 phosphor system makes it of considerable current interest as an antiflicker phosphor in displays where the refresh rate must be minimized, such as computer data display.

The Zn_2SiO_4:(Mn,As) phosphor was originally reported by Frohlich and Fonda (3). They investigated a number of approaches to increasing the persistence of Mn_{Zn}^{2+} luminescence in willemite, including quenching from high temperature, variation of stoichiometry, and incorporation of many coactivator impurities. Of these, the addition of As impurity to Zn_2SiO_4:Mn was found to be most effective in extending persistence. Improved methods of synthesizing the coactivated phosphor have recently been reported (4). In addition, the effects of $AlPO_4$ substitution in the willemite lattice have been investigated (5), although it is not yet clear that significant improvements in brightness and persistence can be achieved in this way (6).

There has been considerable effort devoted to studying the physics of the phosphorescence process in Zn_2SiO_4:(Mn,As). Most of these studies have involved measurement of thermal glow curves (7-14). More recently, photostimulated luminescence and conductivity measurements have been carried out (15-18). However, as yet, there is no general agreement about the recombination mechanism in this phosphor.

It is known empirically that for maximum enhancement of persistence in P39 phosphor the concentrations of Mn and As must be controlled within definite limits. State-of-the-art antiflicker performance is achieved when Mn is ~0.1%, substituted for Zn, and the As concentration is somewhat lower. The Mn concentration is about ten times lower than that used in the Zn_2SiO_4:Mn (P1) phosphor system which does not exhibit extended persistence, so that the overall efficiency of the P39 phosphor is reduced. However, there is no quantitative model which can be used to assess whether the presently favored composition of P39 is indeed optimal, or to guide the development of new phosphor systems.

In order to improve our understanding of the mechanism of this phosphor's operation, it is necessary to have more quantitative information about the impurity energy levels in the bandgap of the willemite lattice, about the partitioning of excitation energy between electron traps

*Electrochemical Society Active Member.
[1]On leave from Royal Signals and Radar Establishment, Malvern, England WR14 3PS.

and Mn_{Zn} impurities, and about the rates of recombination between separated electrons and holes in Zn_2SiO_4:(Mn,As) phosphors of different compositions. In this paper, we report the results of various spectroscopic measurements designed to provide this quantitative information. The samples used were either single crystals (19) with varying concentrations of Mn and As impurities or commercial powder phosphors. The techniques employed include absorption and photoluminescence excitation spectroscopy to determine the Mn_{Zn}^{2+} impurity level energy, and time-resolved luminescence to provide information on energy partitioning and recombination rates. Trap population parameters and recombination rate constants were obtained from the time-resolved measurements by computer fitting of the experimental curves with a bimolecular kinetic model. The behavior of these model parameters as a function of As concentration is consistent with recombination occurring by diffusion of trapped electrons, in contrast to conclusions reached in recent work.

The paper is organized as follows. In the second section, the experimental techniques are described, and in the third the results are summarized. The fourth section covers the energy levels for both As and Mn impurities in relation to the bandedges in willemite. The next section develops the simplified diffusion model used to describe electron-hole recombination in the P39 phosphor, and interprets the parameters obtained by numerical fitting of this model to the decay curves. The sixth section is a consideration of the general significance of the power law decay often observed at long times in these phosphors, and the difficulties which prevent firm conclusions about recombination mechanisms being drawn solely from such long-time decay curves. Finally, the last section discusses the optimal composition of the P39 phosphor system in the light of the diffusion-controlled recombination suggested by our results.

Experimental

Spectroscopic measurements have been made on both the Zn_2SiO_4:Mn and Zn_2SiO_4:(Mn,As) systems. The samples used were either commercial powder phosphors or single crystals grown in this laboratory as previously reported (19). The Mn and As impurity concentrations in the single crystals were determined by x-ray microanalysis in a JEOL electron microscope. The Mn concentration in the powder materials was determined using atomic absorption spectroscopy and the As concentration using a colorimetric technique. The impurity concentrations, represented as atoms per formula unit of willemite, are given in Table I. Where a particular crystal was not directly analyzed, the impurity concentration in a crystal grown from a melt of identical composition is indicated; these concentrations are shown in parentheses in the table.

Absorption measurements on single crystals were made using a Cary 17 spectrophotometer with the sample mounted in a variable-temperature He cryostat. For photoluminescence excitation (PLE) spectra, the samples were mounted on a copper block in an evacuable Dewar. The crystals were mounted directly on the copper block using thermal paste, while the powders were first spread as a thin layer on a copper disk. The temperature of the block was controlled by a combination of liquid N_2 cooling and resistance heating. The PLE source was a 150W Hg lamp in conjunction with a broad UV bandpass filter. The excitation wavelength was selected by a Bausch and Lomb monochromator. The luminescence was passed through a low fluorescence edge filter to remove scattered excitation light, and then through a second monochromator acting as a tunable filter at 525 nm near the peak of the Mn^{2+} luminescence spectrum. The signal was detected with an S-20 response phototube and electrometer. The PLE spectra were recorded point by point to allow those phosphor systems with long time constants to reach a steady state. The excitation lamp and monochromator combination was calibrated against a thermopile to allow correction of the PLE spectra.

Table I. Impurity atoms per formula unit of willemite[a]

Sample	Mn	Ar
	Crystals	
2173H	(0)	(0.0030)
2348A	0.0015	0.0009
2349A	0.0016	0.0018
2350A	0.0012	0.0041
2279A	(0.0140)	(0.0017)
2159E	(0.0240)	(0)
2228A	0.063	0.0017
	Powders	
U-P1	0.0220	(0)
U-P39	0.0012	0.0002_3
G-P39	0.0014	0.0011_3

[a] Nonstoichiometric formula unit $Zn_{1.96}Si_{1.04}O_{4.04}$ [Ref. (19)].

Luminescence rise and decay curves of the phosphors in response to long (2 ms) excitation pulses were measured by introducing a mechanical shutter into the excitation beam. The signal was summed over repeated pulses using a Nicolet 1174 signal averager.

The response to very short (< 10 ns) pulses was measured using two different excitation systems. The first was a Molectron DL II N_2-pumped dye laser using either a stilbene dye lasing at 440 nm to generate local excitation of the Mn^{2+} centers without ionization, or the output of a rhodamine 6G dye lasing at 576 nm and frequency doubled to 288 nm by a KDP crystal. The second pulse excitation source was a Lambda Physik excimer laser producing emission at 248 and 193 nm using KrF and ArF, respectively. The repetition rate for both pulse systems was ~0.1 Hz, and repeated pulses were again summed with the Nicolet signal averager.

Results

Room temperature absorption spectra for three crystals are shown in Fig. 1. The absorption strength in the visible region (Fig. 1a-1c) increases with increasing Mn concentration in the crystals; this absorption is due to intracenter d electron transitions of Mn_{Zn}^{2+} impurities on the two inequivalent zinc sites in the willemite lattice (20, 21). Figure 1d compares the absorption spectra of the three crystals in the near-UV region. It is evident that the presence of Mn in the crystal induces absorption. Hence, incorporation of Mn^{2+} in the willemite lattice introduces relatively weak intracenter d electron transitions in the visible region of the spectrum and a strong electronic transition in the near UV. Any optical effects due to As incorporation occur at higher energy and are relatively small by comparison (22).

Figure 2 illustrates the temperature-dependence of the absorption spectrum for crystal 2228A, which has the

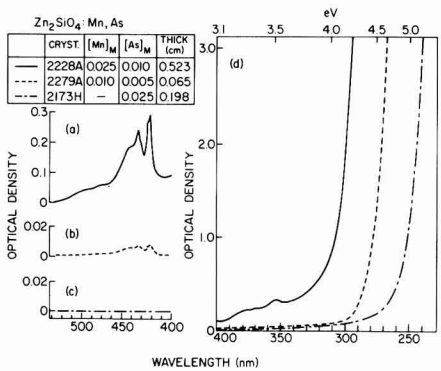


Fig. 1. Room temperature absorption spectra for willemite single crystals. Melt composition and optical path length are given in the key. The incorporated impurity concentrations are given in Table I.

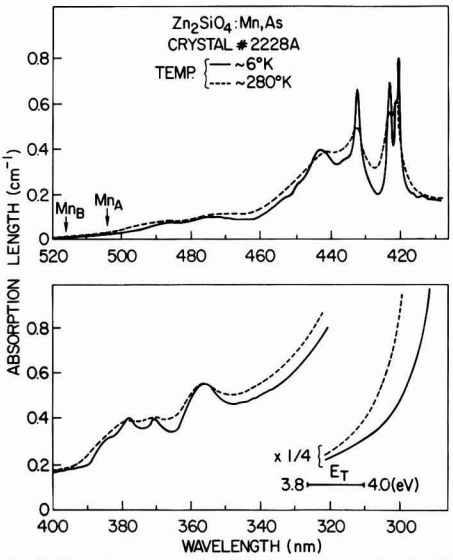


Fig. 2. Absorption spectra of a willemite crystal at ~6 and ~280 K. Mn_A and Mn_B are the zero phonon line positions for the $^6A_1 \rightarrow {}^4T_1$ transitions of Mn^{2+} ions on the two inequivalent Zn sites of willemite. E_T is the estimated threshold for ionization of $Mn_{Zn}{}^{2+}$. Crystal composition is given in Table I.

highest Mn concentration. The d electron transitions in the upper figure show some sharpening at low temperature. The zero phonon line positions for the $^6A_1 \rightarrow {}^4T_1$ transitions of the two inequivalent $Mn_{Zn}{}^{2+}$ centers, Mn_A and Mn_B, are indicated; these lines are too weak to be detected in absorption even at ~6 K, although they are easily observable in luminescence (23, 24). The onset of the strong Mn-induced absorption edge is evident near 330 nm (~3.8 eV). The intensity of absorption in this edge region clearly increases with increasing temperature.

The threshold for the Mn-induced absorption edge can be more easily determined from the PLE spectrum of the Mn^{2+} luminescence. The spectra in Fig. 3 were taken point by point and corrected as described in the previous section. Figure 3a gives the room temperature PLE spectra for three samples of composition Zn_2SiO_4:(Mn,As) (P39), both crystal and powder; Fig. 3b gives the corresponding PLE spectra for a Zn_2SiO_4:(Mn) (P1) powder sample at 300 and 470 K. It is evident from Fig. 3a and 3b that the form of the room temperature PLE spectrum in the energy range 3.8-5 eV is not very sensitive to the presence of As

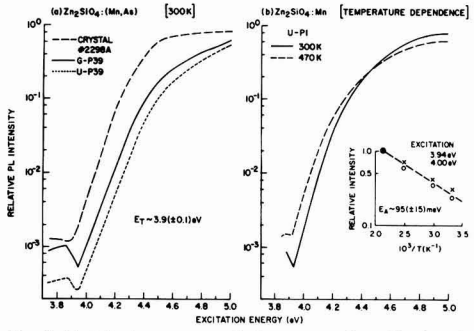


Fig. 3. Photoluminescence excitation spectra for willemite phosphors. The detected signal is the $^4T_1 \rightarrow {}^6A_1$ luminescence of $Mn_{Zn}{}^{2+}$ at 525 nm. The lines are drawn through data taken point by point. a: Room temperature spectra of crystal and powder of composition equivalent to P39. b: Temperature dependence of a powder P1 phosphor. The inset shows the activated form of the spectrum near threshold E_T.

impurity. The sharp increase in the PLE intensity can be used to estimate the threshold for the process leading to Mn^{2+} luminescence, and this is found to be $E_T \sim 3.9 \pm 0.1$ eV. This threshold is marked on the lower part of Fig. 2 and is seen to correspond with the onset of the Mn-induced absorption edge.

The PLE intensity near threshold increases with increasing temperature, as illustrated in Fig. 3b. This behavior parallels the increase in absorption with increasing temperature shown in Fig. 2. The inset to Fig. 3b suggests an activation energy of ~95 ± 15 meV for the PLE threshold. This is within the upper range of vibrational energies of the $SiO_4{}^{2}$ anion (25) and is consistent with a phonon-assisted absorption process near threshold in willemite.

Although the incorporation of As impurity does not affect the form of the PLE and absorption spectra in the range 2.5-5 eV, the presence of As has a profound influence on the measured decay curve for the Mn^{2+} luminescence. The results of a series of measurements of luminescence decay using an electrical shutter to interrupt the excitation beam are summarized in Fig. 4. As the excitation energy increased, it was found that the measured decay curves showed an initial fast decaying component which possibly arose from relaxation at some defect native to the willemite lattice (9, 17). The detected signal was, therefore, gated with a 2 ms delay to allow the fast component to disappear before measuring the Mn^{2+} decay curves. The time to decay to 1/e of the intensity observed at the end of the gate pulse is shown as a function of excitation energy in Fig. 4. Figure 4a gives the results for powder and crystal samples coactivated with Mn and As, and Fig. 4b for powder and crystal samples activated with Mn alone.

In Fig. 4b, the 1/e decay time over the whole excitation energy range is close to 10 ms, the value expected for the intrinsic $^4T_1 \rightarrow {}^6A_1$ decay of Mn_A and Mn_B centers in willemite at room temperature and with low Mn concentration (23, 24). However, the situation is very different when As is included in the lattice as in Fig. 4a. In this case, the intrinsic decay of ~10 ms is observed only for excitation energies < 3.9 eV, *i.e.*, below the absorption threshold E_T determined from the PLE spectra in Fig. 3. At energies above this threshold, the decay time increased to a value > 20 ms and close to 30 ms in the powder sample G-P39. It is important to note that this marked increase in decay time is only observed when two conditions are fulfilled: (*i*) the excitation occurs above the Mn-induced threshold, ~3.9 eV, and (*ii*) As impurity is present in the crystal. When these conditions are met, the decay shows the extended persistence characteristic of P39 phosphor systems.

The effect of As incorporation on the Mn^{2+} luminescence decay can also be studied using very short excitation pulses from a dye laser or excimer laser at energies above the threshold E_T. Families of decay curves at a series of temperatures in the range 270-390 K were measured for several of the samples listed in Table I. A typi-

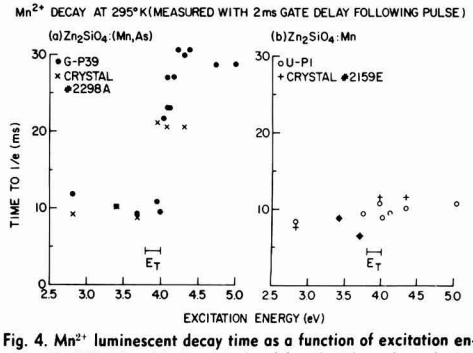


Fig. 4. Mn^{2+} luminescent decay time as a function of excitation energy for Zn_2SiO_4:Mn with As codoping (a) and without As codoping (b).

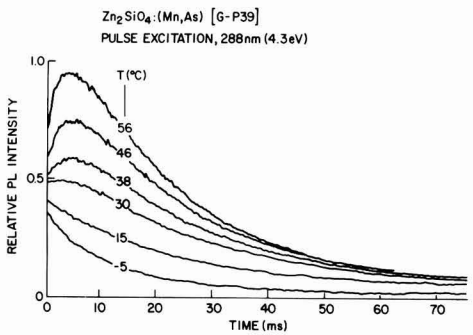


Fig. 5. Pulse response of Mn^{2+} luminescence in a P39 phosphor at different temperatures. The laser pulse was ~5 ns. Similar families of curves were obtained with 248 and 193 nm excimer laser pulses.

cal set, for the powder sample G-P39 and taken with a frequency-doubled dye laser at 288 nm (4.3 eV), is shown in Fig. 5. This was the weakest of the pulse excitation sources used; the signal/noise ratio for decay curves measured with the excimer laser at 248 nm (5 eV) and 193 nm (6.4 eV) was always better than that evident in Fig. 5. The dependence of the luminescence intensity on excitation density was checked by attenuating the dye laser beam with neutral density filters; Fig. 6 shows the response to be linear over the measured range.

On the time scale of Fig. 5, the excitation pulses from both the dye laser and the excimer laser correspond to δ-functions at the origin. The appearance of a delayed maximum in the decay curves was only observed for those samples which were simultaneously doped with Mn and As, and then only for pulse excitation above the threshold E_T, *i.e.*, only when conditions (*i*) and (*ii*) above were met. Samples without As addition showed a decay curve close to the intrinsic Mn^{2+} decay at all temperatures and no delayed maximum. These pulse decay curves have been fitted numerically to obtain kinetic parameters describing the decay for several of the powder and crystal samples. The details of the fitting, and the correlation between the kinetic parameters and the chemical composition of the samples, are discussed in the fifth section.

Impurity Energy Levels in Zn_2SiO_4

The chemical form in which the As impurity is incorporated in Zn_2SiO_4 is not known. However, the idea that As acts as an electron trap in willemite is supported by electrical measurements on As^+-implanted SiO_2 (26). These show that As^+ implantation produces a dominant electron trap with capture cross section (1-2) × 10^{-15} cm^2 and a gaussian distribution around a median thermal trap energy E_m = 1.2-1.3 eV with standard deviation ~0.2 eV. The results of thermal glow measurements on Zn_2SiO_4:Mn, with and without As addition, have been summarized by Yang *et al.* (27) and Avouris *et al.* (12). The willemite lattice shows glow peaks indicating at least four distinct trap distributions, characterized by trap energies ~0.15, ~0.25, ~0.55, and ~0.9 eV. When As is added to the lattice, the glow peak near 273 K (~0.55 eV) is greatly enhanced and dominates the thermal glow spectrum, and a new peak is detected near 553 K with activation energy ~1.9 eV. This latter peak appears to correlate with the introduction of impurity atoms, the effect of As being particularly large (10); the two dominant peaks may be due to As impurity centers or may represent native defects of the willemite lattice whose concentration is greatly enhanced by the presence of As. These various energy levels are represented as "electron traps" in Fig. 7, the trap energy being measured downward from the conduction band (CB) edge.

In contrast to the situation for As, much is known about the incorporation of Mn^{2+} in willemite. It is incorporated substitutionally at the two inequivalent Zn sites forming the Mn_A^{2+} and Mn_B^{2+} centers (20, 23, 24). The way in which simultaneous doping with As affects the Mn_{Zn}^{2+} luminescence decay, evident in Fig. 4 and 5, is most easily explained if it is assumed that the near-UV threshold E_T corresponds to the impurity → CB charge transfer transition

$$Mn_{Zn}^{2+}(d^5) \rightarrow Mn_{Zn}^{3+}(d^4) + e_c \qquad [1]$$

The free CB electrons can be efficiently trapped in the presence of a high concentration of As-related centers, leading to slow recombination and enhanced persistence. For excitation below E_T, no ionization is possible and only intracenter excitation occurs to produce the intrinsic Mn^{2+} decay with no enhanced persistence. The threshold E_T, therefore, defines the position of the Mn^{2+} impurity level in the gap as being ~3.9 ± 0.1 eV below the CB edge. This is illustrated in Fig. 7 together with the estimated position of the $^4T_1$ excited level. This positioning of the Mn^{2+} level, deduced from the absorption and PLE spectra in Fig. 2 and 3, is consistent with earlier estimates of ~3.96 eV below the CB by Chang and Sai-Halasz (15) based on photostimulated luminescence measurements, and ~4 eV by Dove *et al.* (11) based on the threshold for trap filling. In fact, there are two impurity levels corresponding to

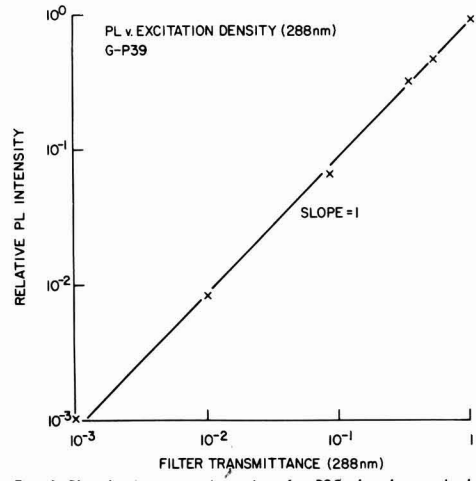


Fig. 6. Photoluminescence intensity of a P39 phosphor excited by 288 nm laser pulses transmitted through attenuating filters. The response is linear with excitation density.

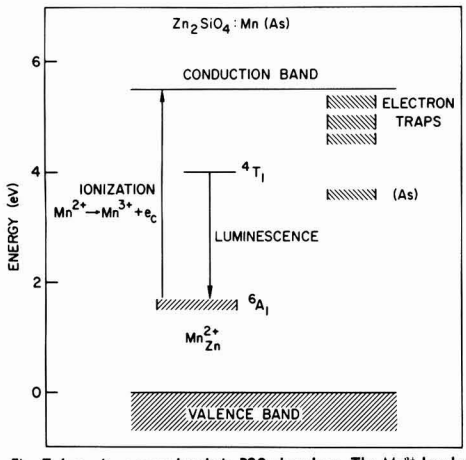


Fig. 7. Impurity energy levels in P39 phosphors. The Mn^{2+} levels are estimated from absorption and PLE spectra. The electron trap levels are taken from thermal glow data.

Mn_A and Mn_B centers; the present experiments detect mainly the lower energy threshold corresponding to the center lying higher in the forbidden gap. This does not affect the arguments presented below.

The assignment of the near-UV absorption edge as an impurity → CB charge transfer process implies that the transition occurs from a d-like orbital to an s-like orbital and is, therefore, parity forbidden. This would be quite consistent with the observation that the absorption process is phonon assisted near threshold.

A Recombination Model

Previous work.—The enhanced persistence of the P39 system is due to the slow recombination of spatially separated charges, *viz.*, trapped electrons and ionized Mn_{Zn}^{3+} centers. At long times after the cessation of excitation, it is quite generally found that the decay of inorganic phosphors can be described by an equation of the form (9, 28)

$$I(t) = I_0 \left(\frac{\beta}{\beta + t}\right)^m \quad [2]$$

where the parameters β and m depend on the particular system studied, the excitation density, the time elapsed since cessation of excitation, temperature, and so on.

Kinetic models attempting to describe this decay behavior were developed initially by Randall and Wilkens (7) using first-order kinetic equations, and extended by Garlick and Gibson (8) to include retrapping effects. Medlin (28) subsequently introduced second-order equations to describe the recombination, but found that the behavior of the parameters β and m predicted by the second-order equations was consistent with the experimental data only at temperatures above the glow peak maximum for any trap. At lower temperatures it was necessary to revert to the idea that a first-order trap emptying process was rate limiting. Medlin was then able to obtain a numerical fit to the experimental data by assuming that the trap levels were spread in energy according to a gaussian distribution (28).

More recently, the concept of a quantum-mechanical tunneling recombination between trapped electrons and ionized luminescent centers has been introduced into the kinetic models (12-14, 18). Tunneling from the ground state of an electron trap is a nonthermally activated process. Examples are found in the radiative recombination of donor-acceptor pairs in semiconductors (29) and in the temperature-independent afterglow observed between 4 and 77 K in irradiated KCl:M (M = Ag, Tl) (30). This afterglow is attributed to radiative tunneling recombination between holes trapped as V_k centers and electrons trapped at neutral metal atom sites.

Avouris and co-workers (12, 13) have applied the concept of tunneling recombination to the Zn_2SiO_4:Mn,As system. In this case, however, the proposed tunneling process has an activated form. It is assumed that recombination occurs between a fixed distribution of trapped electrons and the ionized Mn_{Zn}^{3+} centers and that the tunneling process involves thermal activation of a trapped electron to a shallow excited state of large radius. This model is adequate to fit the shape of the glow curves on the low temperature side of the maximum, but above the glow peak it is necessary to assume that thermal emission to the conduction band dominates in the recombination. However, the usefulness of the activated tunneling model is suggested to lie in the explanation which it offers for the form of the phosphorescence decay and the decay of photostimulated luminescence, both of which can show a t^{-1} behavior in Zn_2SiO_4:Mn,As materials. In this context, the model has been further developed by Chang and coworkers (14, 18).

A diffusion model.—There is a need to develop a model for recombination in the P39 phosphor system which can be related to the chemical composition of the material and which can be used as an aid to optimization of the phosphor properties. Attempts to model the long-time decay behavior of the Zn_2SiO_4:Mn,As materials, outlined above, have not produced agreement on the most appropriate description of the recombination process. In particular, they have not provided quantitative information on decay rates of the kind necessary to develop a useful predictive model of phosphor properties.

We have therefore approached the problem in a different way. First, we have made a systematic comparison of the recombination processes in a series of samples in which the concentration of Mn^{2+} centers is roughly constant, whereas the concentration of As atoms introducing electron traps is increased by more than an order of magnitude. This series includes the powder samples U-P39 and G-P39 and the crystal samples 2348A, 2349A, and 2350A listed in Table I. By this means it is possible to determine whether electrons trapped at As-related centers can become mobile in the lattice by tunneling from trap to trap; the probability of such tunneling increases exponentially with increasing trap concentration. Second, we have studied the recombination mechanism by exciting the phosphors with laser pulses of nanosecond duration and recording the luminescent response over relatively short periods, up to ~100 ms. In this way, it proves possible to extract information on the initial partitioning of the excited electrons and on the rates of recombination. Both parameters are essential for a quantitative understanding of the phosphor properties. The remainder of this section outlines the basic theoretical model which is used to analyze the experimental data.

It will be assumed that the traps constitute a disordered system of impurity levels. In the normal way (31), the distribution of trap levels can be described by a density-of-electronic-states function, the width of the distribution arising from differences in charge compensation for the trap centers, random fields, and other sources of inhomogeneity. As mentioned previously, thermally stimulated luminescence data for P39 phosphors suggest the presence of two dominant trapping centers, corresponding to glow peaks near 273 and 553 K. The electron density-of-states (DOS) function will therefore show two major peaks within the willemite bandgap, E_g, as illustrated in Fig. 8.

The effect of a very short laser pulse with energy $E_T < h\nu < E_g$ is to ionize some fraction of the Mn_{Zn}^{2+} centers in the willemite lattice, producing instantaneously equal concentrations of ionized Mn_{Zn}^{3+} centers and free CB electrons. These free electrons rapidly relax to different centers in the lattice. Some recombine immediately with ionized Mn_{Zn}^{3+} centers producing an initial population of excited Mn_{Zn}^{2+} centers in the $^4T_1$ excited state; the remainder of the CB electrons are captured by traps. If the initial electron population is normalized to unity, and the concentration of electrons in the CB is assumed to be negligible, the following relationships hold

$$M_0^* + n_0 \approx 1 \text{ and } M_0^+ \approx n_0 \quad [3]$$

where M^+ is the population of ionized Mn_{Zn}^{3+} centers, M^* is the concentration of excited Mn_{Zn}^{2+} centers, n is the concentration of trapped electrons, and the subscript o denotes the concentration at time $t = 0$ immediately following the laser pulse.

Assuming for simplicity that the electron capture rate is independent of trap depth, and neglecting trap saturation, the initial distribution of the trap population will follow the DOS function

$$n_0(E) = \frac{n_0 N(E)}{N} \quad [4]$$

where $N(E)$ is the DOS function and N is the total trap concentration.

The time dependence of the luminescence obeys the equation

$$\dot{M}^* = -\dot{M}^+ - bM^* \quad [5]$$

where b^{-1} is the measured lifetime for the $^4T_1 \rightarrow {}^6A_1$ transition of Mn_{Zn}^{2+}. It will be assumed that at low concentrations of Mn impurity the ionized Mn_{Zn}^{3+} centers are immo-

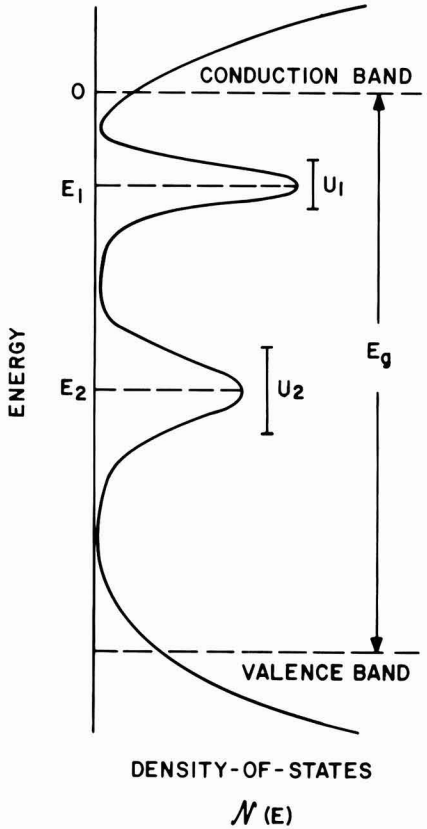


Fig. 8. A schematic representation of the electron trap distribution in P39 phosphors with two dominant trap levels, E_1 and E_2, corresponding to glow peaks near ~273 K and ~583°C. The widths of the peaks in the DOS function are U_1 and U_2, respectively.

bile; recombination is then assumed to occur by diffusion of the trapped electron population. The rate of recombination by diffusion is given by (32)

$$-\dot{M}^{+} = 4\pi D'R\left[1 + \frac{R}{(\pi D't)^{1/2}}\right] \cdot M^{+}n \qquad [6]$$

where D' is a diffusion coefficient and the radius R defines a sphere of influence for the ionized Mn_{Zn}^{3+} centers such that an electron impinging on the surface of this sphere undergoes recombination with a probability of unity. To simplify the analysis, we shall neglect the second term in the brackets (which should be important only at very short times) and rewrite Eq. [6] as

$$-\dot{M}^{+} \approx (DR)M^{+}n \qquad [7]$$

where $D = 4\pi D'$.

Following the usual analysis for such disordered systems (31), the diffusive motion of the electrons can take place by two main mechanisms. (i) The first process is a thermally activated emission to the CB followed by diffusion of the free electron. This process is denoted by the diffusion coefficient D_T. (ii) The second is a nonactivated tunneling transfer of an electron from the ground state of one trap to the ground state of another trap. This is denoted by the diffusion coefficient D_N. The observed diffusion coefficient represents the sum of these two processes. If diffusion of trapped holes (*i.e.*, Mn_{Zn}^{3+} centers) occurs at high Mn concentration, the effect will simply be to add an extra component to the overall diffusion coefficient (32).

Thermal emission.—For a single trap level of depth E, the thermal emission rate to the CB is given by (33)

$$P_T(E) = \sigma < v > N_c e^{-E/kT} \qquad [8]$$

where σ is the capture cross section for the trap, $<v>$ is the thermal velocity, and N_c an effective density of states in the CB. The mean distance traveled between emission and recapture, L, is given by $L = : (\sigma N)^{-1}$ and the activated diffusion coefficient by

$$D_T(E) = \frac{1}{6} P_T L^2$$

$$= \frac{<v>N_c e^{-E/kT}}{6\sigma N^2} \qquad [9]$$

It should be noted that the thermal diffusion coefficient is inversely proportional to the square of the trap concentration, reflecting the fact that retrapping effects inhibit this thermal diffusion motion.

Tunneling transfer.—The rate of tuneling from trap to trap within a particular DOS peak will have the form (31)

$$P_N = \nu e^{-2\alpha\gamma} e^{-W/kT} \qquad [10]$$

where ν is some phonon frequency, γ is the distance between centers, and W is a small activation energy which depends on the width, U, of the DOS peak. The parameter α depends on wavefunction overlap; for deep centers, with localized wave functions, α is large. The term $e^{-2\alpha\gamma}$ therefore ensures short range hops, primarily to nearest-neighbor trap levels. This near-neighbor transfer may require an activation energy approaching the distribution width, $W \sim U$. At the temperatures of interest ($\gtrsim$ 300 K), this thermal energy is available so that the $e^{-2\alpha\gamma}$ term should dominate. If the trap sites are randomly distributed, an effective mean hop length, γ_m, can be defined as a function of concentration and the hopping rate becomes

$$P_N \approx \nu e^{-2\alpha\gamma_m} e^{-U/kT} \qquad [11]$$

The length γ_m decreases, and hence P_n increases, as trap concentration increases. The diffusion coefficient for tunneling transfer is then given by (32)

$$D_N \approx \frac{1}{6} P_n \gamma_m^2 \qquad [12]$$

In contrast to the thermal motion, the diffusion coefficient for the tunneling transport increases as the trap concentration increases. This simply reflects the fact that wave function overlap, and hence the tunneling rate, increase as the distance between traps decreases. The activation energy U is small compared with the trap depth appearing in the thermal diffusion coefficient, a typical DOS peak having a width ~0.1-0.2 eV. In principle, the tunneling diffusion coefficient is a function of trap depth, there being a different coefficient for each DOS peak in the trap distribution.

In order to calculate the recombination, it is now necessary to make some assumption about the energy distribution of the trapped electrons as a function of time. For simplicity, we shall assume that both the processes of thermal emission and recapture, and of nearest-neighbor hopping, tend to randomize the electron population so that at all times the electron distribution follows the DOS function

$$n(E, t) = \frac{n(t)N(E)}{N} \qquad [13]$$

The rate of recombination can then be written using Eq. [7] and [13] as

$$(DR)M^{+}n \approx RM^{+} \cdot \int_E [D_T(E) + D_N(E)]n(E)\, dE$$

$$\approx \frac{RM^{+}n}{N} \cdot \int_E [D_T(E) + D_N(E)]N(E)\, dE \qquad [14]$$

The integral in this equation defines the effective diffusion coefficient D which represents the sum of thermally activated and nonthermal tunneling processes

$$D = \frac{1}{N} \cdot \int_E [D_T(E) + D_N(E)]N(E)\, dE \qquad [15]$$

The temperature dependence of the effective diffusion coefficient D will depend upon the overall trap concentration as indicated schematically in Fig. 9 for three trap concentrations, $N_3 > N_2 > N_1$. For the low concentration, N_1, $D_T > D_N$ at all temperatures so that the observed diffusion coefficient D will show simple activated behavior. However, for the highest concentration, N_3, $D_T < D_N$ at all temperatures and the observed diffusion coefficient will be dominated by the tunneling process showing essentially nonactivated behavior. At the intermediate concentration, N_2, the diffusion coefficients due to thermal emission and tunneling are comparable so that the observed diffusion coefficient will show a more complicated behavior with some intermediate value for the apparent activation energy.

Fitting to a bimolecular rate equation.—It is a central part of the recombination model developed in the previous section that, throughout the decay, the concentration of ionized Mn_{Zn}^{3+} centers is balanced by an approximately equal concentration of trapped electrons, *i.e.*, we have the conditions

$$M^{\cdot} \approx n,\ \dot{M}^{\cdot} \approx \dot{n} \qquad [16]$$

Substituting these equalities in Eq. [7] gives

$$-\dot{n} \approx (DR)n^2 = kn^2 \qquad [17]$$

where $k = DR$ is a bimolecular rate constant. Thus, the various assumptions and approximations introduced into the model have resulted in a description of electron-hole recombination at ionized Mn_{Zn}^{3+} sites in terms of a bimolecular rate equation. The physical picture underlying this description is that the electrons are isotropically distributed in the lattice and are able to diffuse through it. The kinetics of this system consist of two independent parts, the capture of an electron at a Mn^{3+} site, as discussed above, and its subsequent decay by photon emission. These processes are governed by two rate constants, the bimolecular rate k and the intrinsic Mn_{Zn}^{2+} decay rate b, giving the overall kinetic equation

$$\dot{M}^* = kn^2 - bM^* \qquad [18]$$

The solution to Eq. [17] is

$$n = \left(kt + \frac{1}{n_0}\right)^{-1} \qquad [19]$$

Substituting Eq. [19] into [18] and solving yields

$$M^*(t) = (M_0^* + n_0)e^{-bt} - \left(kt + \frac{1}{n_0}\right)^{-1} + \frac{b}{k}\, e^{-(bt + b/kn_0)} \cdot [Ei(bt + b/kn_0) - Ei(b/kn_0)] \qquad [20]$$

where $Ei(x)$ is the exponential integral. The luminescence intensity as a function of time is proportional to the excited state population, $M^*(t)$. Equation [20] has been used to generate computer fits to families of luminescence pulse response curves of the kind illustrated in Fig. 5.

The decay rate, b, for each sample was obtained experimentally by measurement of the luminescence decay curve at a series of temperatures using laser pulses at 440 nm to produce only localized, intracenter excitation of the Mn_{Zn}^{2+} ions. These measured decay curves were then approximated by a simple exponential decay. Using the measured values for b, the fitting procedure involved two main parameters, the bimolecular rate constant k and the initial trap population n_0, together with a normalization factor to scale the fit. Best values of k and n_0 were obtained for each experimental pulse response curve using a nonlinear least squares fitting algorithm developed by Marquardt (35).

The fitted curves reproduced the main features of the experimental data: in particular, the appearance of a delayed maximum in the pulse response curve. However, there was some tendency towards a systematic deviation from the form of the experimental data. A fairly typical result is shown in Fig. 10, which gives the best fit function for one data curve together with the deviation between that fitted curve and the experimental data. This deviation was always significant at short times and may reflect, at least in part, the neglect of the higher-order term in the diffusion (Eq. [6]). This point will be addressed elsewhere (36). In general, however, we feel that the simple bimolecular fitting procedure reported here is quite adequate to establish semiquantitatively the main trends in the recombination rate and trap population as they are influenced by changes in chemical composition in Zn_2SiO_4:(Mn,As) phosphors.

The results of fitting pulse response curves measured over a range of temperatures are summarized in Fig. 11, which shows the best fit values for the bimolecular constant k, and in Fig. 12, which shows the corresponding best fit values for the trap population parameter n_0. The parameters k and n_0 are normalized to the initial total ex-

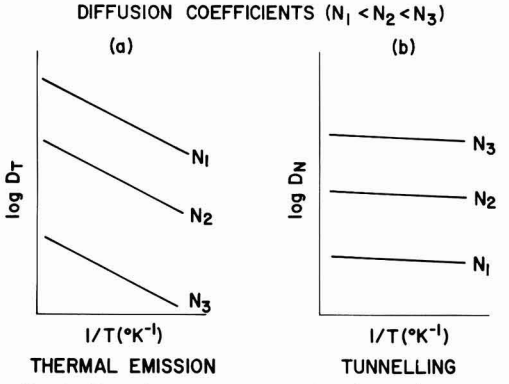


Fig. 9. The schematic temperature dependence of processes contributing to electron diffusion in different P39 phosphors. The relative As concentration in the phosphors is $N_1 < N_2 < N_3$. a: The thermal diffusion coefficient D_T, showing strongly activated behavior favored by low As concentration. b: The tunneling diffusion coefficient D_N, showing weakly activated behavior favored by high As concentration.

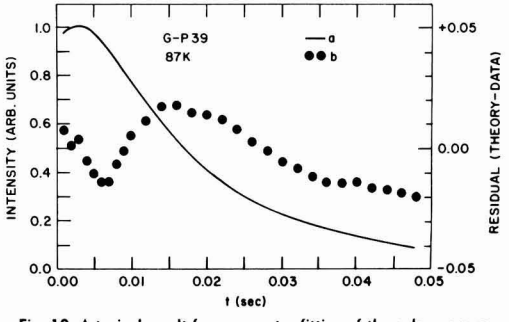


Fig. 10. A typical result from computer fitting of the pulse response curves according to Eq. [21]. a: The solid line (left ordinate) is the calculated function and experimental curve. They are indistinguishable on the scale of this drawing. b: The open circles represent the difference between the calculated function and the experimental curve (right ordinate). The oscillation in the difference curve at short time is a systematic feature of the fitting.

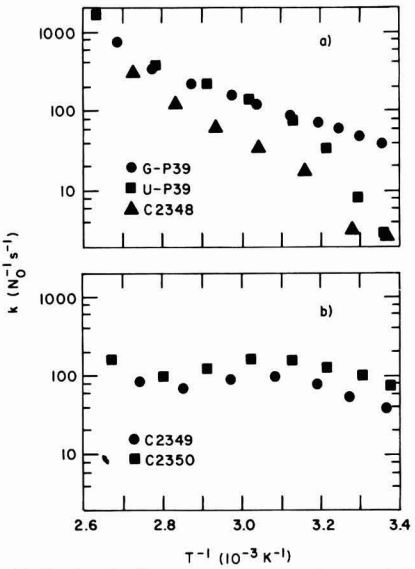


Fig. 11. The bimolecular rate constant k as a function of temperature derived from fitting Eq. [21] to the pulse response curves. Note that the units of k are normalized to the initial concentration of ionized electrons N_0.

cited state population $N_0(= M_0^* + n_0)$ which, for numerical convenience, is set to one. As a result, the units of k are N_0^{-1}-s^{-1}, while n_0 is a dimensionless fraction. It is assumed that N_0, which is proportional to the Mn^{2+} absorption cross section, is not a strong function of temperature. The experimental data were obtained from samples U-P39, G-P39, 2348A, 2349A, and 2350A listed in Table I. For all the samples, decay curves were taken using KrF excitation at 248 nm; in addition, the decay of the powder phosphors U-P39 and G-P39 was measured at 193 nm using ArF. No significant differences between these two excitation wavelengths were observed.

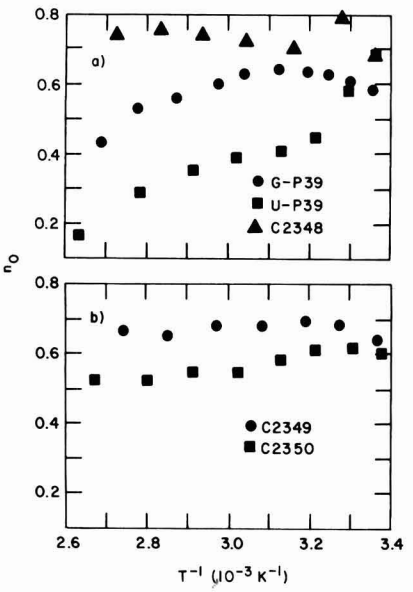


Fig. 12. The initial trap population fraction, n_0, as function of temperature derived from fitting Eq. [21] to the pulse response curves. The key to the data points is given in the caption to Fig. 11.

Table II. Activation energies and impurity separation

Sample	Activation Energy (eV)	N_{As} (cm^{-3})
U-P39	~0.6	2.6×10^{18}
G-P39	~0.4	1.3×10^{19}
2348A	~0.6	1.0×10^{19}
2349A	Very small	2.1×10^{19}
2350A	Very small	4.7×10^{19}

Table II lists the approximate activation energy for the bimolecular rate constant derived from Fig. 11 for each of the samples, together with the As impurity concentration. The spread in value of n_0 is shown as a function of As concentration in Fig. 13. The behavior of the model parameters divides into two regions as a function of As concentration, the transition occurring when $N_{As} \sim 1\text{-}2 \times 10^{19}$ cm^{-3}.

Region 1 is when $N_{As} \leq 1 \times 10^{19}$ cm^{-3}. (*i*) k is activated, $\Delta E \sim 0.6$ eV

$$k(300\text{ K}) \leq 10\ N_0^{-1}\text{-s}^{-1}$$

$$k(370\text{ K}) \sim 10^3\ N_0^{-1}\text{-s}^{-1}$$

(*i*) n_0 increases as N_{As} increases.

Region 2 is when $N_{As} \geq 2 \times 10^{19}$ cm^{-3} (*i*) k is not activated

$$k(300\text{ K}) \sim 10^2\ N_0^{-1}\text{-s}^{-1}$$

$$k(370\text{ K}) \sim 10^2\ N_0^{-1}\text{-s}^{-1}$$

(*ii*) n_0 decreases as N_{As} increases.

The sample G-P39 falls in the transition region. It shows an activated recombination, but $\Delta E < 0.6$ eV. The bimolecular rate constant at 300 K is $k \sim 50\ N_0^{-1}$-s^{-1}, approaching the nonactivated rate at low temperature. The rate constant at 370 K is $k \sim 10^3\ N_0^{-1}$-s^{-1}, similar to the activated rate at high temperature.

This behavior of the model parameters can be interpreted in terms of the diffusion model developed in the previous section. From Eq. [18], and assuming the radius R to be a constant, the bimolecular rate constant k is proportional to the effective diffusion coefficient D for each sample; in particular, the temperature dependence of k will reflect that of D. In Region 1, the rate constant is activated and the diffusion is dominated by the thermal emission process, D_T, which is favored by low trap concentration, *e.g.*, N_1, depicted in Fig. 9. The observed activation energy, $\Delta E \sim 0.6$ eV, corresponds to a weighted average of thermal trap depths for centers which contribute to trapping and diffusion. This observed value lies within the range of trap energies determined from thermal glow

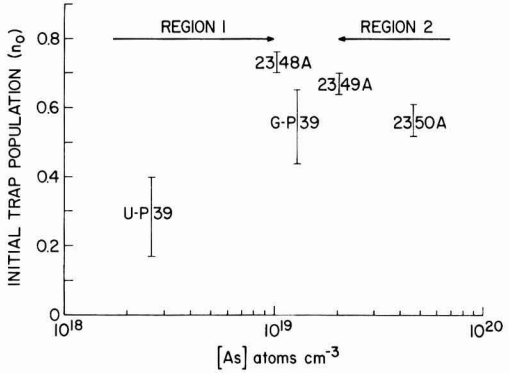


Fig. 13. The initial trap population fraction, n_0, as a function of As concentration in the samples indicated. The error bars represent the limits of n_0 values obtained by fitting Eq. [21] to the pulse response curves. The significance of Regions 1 and 2 is discussed in the text.

measurements on the dominant glow peak of P39 phosphors center at ~273 K.

In Region 2, the rate constant is not activated and the diffusion is dominated by the intertrap tunneling process, D_N, which is favored by high activator concentration. This concentration range would correspond to the high trap concentration, N_3, depicted in Fig. 9. The sample G-P39 falls in the transition region in which the contributions of thermal emission and tunneling are comparable, analogous to the intermediate trap concentration N_2 depicted in Fig. 9. The diffusion coefficient for this sample is limited by tunneling at low temperature and by thermal emission at high temperature. The effect of comparable contributions from tunneling and thermal emission processes is to reduce the apparent activation energy for the diffusion process.

The behavior of the parameter n_0 can be explained in the following way. The excitation photons excite electrons from the Mn_{Zn}^{2+} centers into the CB with considerable excess energy, *e.g.*, at 248 nm the photon energy, $h\nu$ = 5 eV, would ionize the electrons with (5-3.9) ~ 1.1 eV excess kinetic energy. This kinetic energy propels the electrons through the lattice and affects the distribution of electrons immediately following the excitation pulse.

In the simplest case, we suppose that each ionized Mn_{Zn}^{3+} center is surrounded by its sphere of influence of radius R and that, if the excited electron comes to rest within this sphere, the recombination with Mn_{Zn}^{3+} center is extremely fast. This would represent a geminate recombination process (37). The parameter n_0 represents the fraction of electrons on As-related traps immediately following the excitation pulse. Thus

n_0 = (probability that an ionized electron escapes the sphere of influence)

× (probability of a CB electron being captured by a trap)

$$= (\text{probability of escape}) \times \left[\frac{\sigma N}{\sigma N + \sigma' M'}\right] \qquad [21]$$

where σ is the capture cross section for traps of concentration N, and σ' is the cross section for ionized Mn_{Zn}^{3+} centers. In the absence of As impurity, the probability of escaping the Mn_{Zn}^{3+} sphere of influence will be denoted by p_0. We shall assume that in the presence of As, electron trapping within the radius R will still produce geminate recombination; hence, the probability of escape in the presence of As, denoted p_{As}, depends upon the probability that an ionized electron is not trapped in traversing the distance R

$$p_{As} = p_0 e^{-\sigma NR} \qquad [22]$$

Combining Eq. [21] and [22] gives

$$n_0 = p_0 e^{-\sigma NR}\left[\frac{\sigma N}{\sigma N + \sigma' M'}\right] \qquad [23]$$

The exponential term will be close to unity at low trap concentration, so the behavior of n_0 will be determined by the term in brackets. This term increases as trap concentration N increases, and explains the increase in n_0 with increasing N at low concentrations (Region 1) in Fig. 13. At high trap concentrations, however, the term in brackets will approach unity, and the behavior of n_0 will be determined by the exponential term. This term decreases as N increases, which explains the decrease in n_0 with increasing N at higher concentrations (Region 2) in Fig. 13. Estimating crudely from Fig. 13 that the exponential term $e^{-\sigma NR} \sim 0.6$ when $N \sim 5 \times 10^{19}$ cm^{-3}, gives $(\sigma R) \sim 10^{-20}$ cm^3. Assuming $R \sim 2$ nm, the distance at which intertrap tunneling becomes significant, allows the trap capture cross section to be estimated

$$\sigma \sim \frac{10^{-20}}{2 \times 10^{-7}}\ \text{cm}^2 \sim 5 \times 10^{-14}\ \text{cm}^2 \qquad [24]$$

This value for the cross section of the As-related traps, which depends upon the estimate of R, would be typical for coulombic trapping centers, although it is larger than the value $\sigma \sim$ 1-2 × 10^{-15} cm^2 reported for As-induced traps in SiO_2 (26).

The Power Law Decay

The expression for the recombination rate contained in Eq. [14] assumes that throughout the decay the trap population $n(E)$ remains proportional to the DOS, $N(E)$. This assumption leads to the definition of the effective diffusion coefficient D in Eq. [15] and thence to Eq. [20], which gives the luminescence intensity as a function of time based on bimolecular recombination kinetics. It is of interest to consider the long-time behavior of Eq. [20] since there have been many attempts to deduce the mechanism of recombination from the form of the decay curves at long times. In the limit $t >> 1/kn_0$, the asymptotic behavior of the exponential integral is

$$Ei(x) \simeq \frac{e^x}{x}\left[1 + \frac{1}{x} + \frac{2}{x^2} + \ldots\right] \qquad [25]$$

Substituting in Eq. [20] and retaining only first-order terms gives

$$M^* \simeq -\frac{1}{bt} + \frac{1}{bt} + \frac{1}{bt^2} \propto \frac{1}{t^2} \qquad [26]$$

The t^{-2} behavior at long times is characteristic of bimolecular recombination. Measurements of long-time decay on some of the samples studied have shown t^{-2} behavior over extended periods of time (36), consistent with the description in terms of the simplified diffusion model.

On the other hand, it is clear from measurements on many different systems that while the extended decay follows a power law, $I \propto t^{-m}$, the exponent m can vary throughout the decay, taking a wide range of values from $m < 0.5$ to $m > 2$. This exponent varies with temperature and excitation intensity in addition to time elapsed from the cessation of excitation. There are many examples, including P39 and P1 phosphors, in which a t^{-1} behavior is observed over considerable periods in both luminescence decay and the decay of photostimulated luminescence. This t^{-1} behavior has been variously interpreted in terms of trap levels distributed in energy (7, 28) and as evidence of tunneling recombination between Mn_{Zn}^{3+} centers and a fixed spatial distribution of trapped electrons (12-14).

Considering the diffusion model of the previous section, such complexity in the decay behavior might be expected when some of its simplifying assumptions break down. The most important is likely to be the assumption that $n(E) \propto N(e)$ throughout the decay. Since thermal emission is favored for shallower centers over deeper ones, there will be a tendency for the population to accumulate in the deeper levels as the decay proceeds. When this effect is significant, the integral $\int_E [D_T(E) + D_N(E)]n(E)\, dE$ will no longer be simply proportional to the total trap population $n(t)$, and simple bimolecular kinetics with t^{-2} decay at long times is no longer to be expected. In addition, as the mean depth of the trapped electrons increases with time, the balance of contributions from thermal diffusion, D_T, and tunneling diffusion, D_N, will change, leading to a time-dependent rate coefficient in the kinetic equations.

Conclusions

Absorption and photoluminescence excitation spectra have confirmed that the Mn_{Zn}^{2+} ground state impurity level in willemite lies 3.9 ± 0.1 eV below the conduction bandedge. The ionization cross section for Mn_{Zn}^{2+} shows activated behavior near the threshold, $E_T \sim 3.9$ eV, which can lead to variations in the efficiency of exciting thermally-stimulated glow curves when UV wavelengths near threshold are used to excite the system at different temperatures.

The luminescence pulse response curves for Zn_2SiO_4:(Mn,As) phosphors with varying As concentration have been analyzed in terms of a simplified diffusion model. The effective diffusion coefficient D is found to

be activated when the As impurity concentration $N_{As} \lesssim 1 \times 10^{19}$ cm^{-3}, suggesting that the electron motion is dominated by thermal emission to the conduction band. However, D is nonactivated when $N_{As} > 2 \times 10^{19}$ cm^{-3}, suggesting that tunneling between traps is then the dominant mechanism for electron motion; in this limit the recombination rate at 300 K is larger than is the case for activated diffusion. The fraction of excited electrons captured by As-related traps initially increases with increasing N_{As} and then decreases. This effect is explained in terms of competition between geminate recombination at ionized Mn_{Zn}^{3+} centers and electron capture at traps. The general validity of the simplified diffusion model, which leads to a bimolecular decay law, is supported by the observation of t^{-2} decay behavior at long times (36). However, this simplified model, while giving reasonable quantitative fits to the experimental data, also shows evidence of systematic deviations which may arise from neglect of higher-order terms in the diffusion equation. The observation of more complex power law decay at long times is probably the result of redistribution of the trapped electron population.

The form of the luminescence pulse response curve, Fig. 5, is insensitive to excitation energy above threshold E_T, and, indeed, we have observed essentially similar behavior for electron beam excitation. From a practical point of view, the optimization of an extended persistence P39 phosphor for CRT displays requires that as large a fraction of excited electrons as possible be captured and stored in traps while the recombination rate should remain as low as possible without introducing "smearing" in refreshed displays. From Fig. 11 and 13, it is evident that for the phosphors studied here with Mn_{Zn}^{2+} concentration $\sim 1.6 \times 10^{19}$ cm^{-3}, the optimum As concentration is $N_{As} \sim 1\text{-}2 \times 10^{19}$ cm^{-3}. At this concentration, the trapped electron fraction is maximum, $n_0 \sim 0.6$, and the recombination rate constant at the phosphor operating temperature, ~300 K, is low, $k < \sim 50$ cm^3-s^{-1}. If N_{As} is increased above this level, the fraction n_0 decreases, probably due to an increased rate of geminate recombination, and the recombination rate increases rapidly because of the onset of intertrap tunneling.

Finally, it should be noted that we have studied recombination in P39 phosphor systems over a temperature range approximately 0°-100°C, which corresponds to the high temperature side of the principal glow peak for P39. This temperature range shows the strongest variation in the shape of the luminescence decay curves and is the one of most practical relevance in operation of the phosphor in data displays. We describe the recombination in terms of a diffusive motion of the trapped electrons, this diffusion occurring by thermal emission and intertrap tunneling, the dominant process being determined by the trap concentration. This model correctly predicts the observed change in the kinetics of recombination from activated to nonactivated behavior as N_{As} increases, and is further supported by the observation of t^{-2} decay at long times (36). This recombination model is quite different from the activated tunneling model proposed by Avouris and co-workers (12, 13), who have described the luminescence decay on the low temperature side of the glow peak (*i.e.*, below 0°C) in terms of a tunneling transfer of electrons from excited states of traps in a fixed spatial distribution to the ionized Mn_{Zn}^{3+} centers. The Avouris and Morgan model proposes that at temperatures below the glow peak maximum the electrons distributed on trap sites are immobile before recombination by tunneling, whereas at temperatures above the glow peak maximum the trapped electrons are thermally emitted to the conduction band and can recombine with Mn_{Zn}^{3+} centers by diffusion. From our results, we expect intertrap tunneling between As centers to be an important factor affecting electron motion at low temperatures, and we have no evidence to suggest a marked change in recombination mechanism at the temperature of a glow peak maximum. The significance of these differences will be discussed in a later paper.

Acknowledgments

The authors are grateful to Y. Thefaine and J. Wilson for assistance in making some of the experimental measurements, to C. F. Guerci for assistance in sample preparation, and to F. Cardone, J. Kuptsis, and R. Savy for the chemical analyses.

Manuscript submitted Jan. 26, 1984; revised manuscript received July 31, 1985.

IBM Corporation assisted in meeting the publication costs of this article.

REFERENCES

1. "Optical Characteristics of CRT Screens," JEDEC Publication 16-C, Electronic Industries Association, Washington, DC (Nov. 1975).
2. D. S. McClure, "Electronic Spectra of Molecules and Ions in Crystals," Academic Press, New York (1959).
3. H. C. Froelich and G. R. Fonda, *J. Phys. Chem.*, **46,** 878 (1942).
4. J. M. Brownlow and I. F. Chang, in "SID/IEEE Display Research Conference Proceedings," p. 66, IEEE, New York (1982).
5. I. F. Chang and M. W. Shafer, *Appl. Phys. Lett.*, **35,** 229 (1979).
6. T. E. Peters and J. R. McColl, Abstract 151, p. 379, The Electrochemical Society Extended Abstracts, Vol. 81-1, Minneapolis, MN, May 10-15, 1981.
7. J. T. Randall and M. H. F. Wilkins, *Proc. R. Soc. London, Ser. A,* **184,** 390 (1945).
8. G. F. J. Garlick and A. F. Gibson, *Proc. Phys. Soc.*, **60,** 574 (1948).
9. H. W. Leverenz, "Luminescence of Solids," John Wiley and Sons, New York (1950).
10. U. Kummel, E. Krantz, and R. Knutter, *Phys. Status Solidi A,* **11,** 181 (1972).
11. D. B. Dove, T. Takamori, I. F. Chang, P. Thiolouse, E. E. Mendez, and E. A. Giess, *J. Lumin.*, **24/25,** 317 (1981).
12. Ph. Avouris, I. F. Chang, D. B. Dove, T. N. Morgan, and Y. Thefaine, *J. Electron. Mater.*, **10,** 887 (1981).
13. Ph. Avouris and T. N. Morgan, *J. Chem. Phys.*, **74,** 4347 (1981).
14. P. Thioulouse, I. F. Chang, and E. A. Giess, *This Journal,* **130,** 2065 (1983).
15. I. F. Chang and G. A. Sai-Halasz, *ibid.*, **127,** 2458 (1980).
16. I. F. Chang, P. Thioulouse, E. E. Mendez, D. B. Dove, and T. Takamori, *J. Lumin.*, **24/25,** 313 (1981).
17. H. Hess and E. Krautz, *ibid.*, **24/25,** 321 (1981).
18. I. F. Chang and P. Thioulouse, *J. Appl. Phys.*, **53,** 5873 (1982).
19. E. A. Giess, C. F. Guerci, J. D. Kuptsis, I. F. Chang, and D. J. Robbins, *J. Cryst. Growth,* **60,** 219 (1982).
20. H. K. Perkins and M. J. Sienko, *J. Chem. Phys.*, **46,** 2398 (1967).
21. D. T. Palumbo and J. J. Brown, *This Journal,* **117,** 1184 (1970).
22. R. Fern and I. F. Chang, Unpublished work.
23. A. L. N. Stevels and A. T. Vink, *J. Lumin.*, **8,** 443 (1974).
24. D. J. Robbins, E. E. Mendez, E. A. Giess, and I. F. Chang, *This Journal,* To be published.
25. K. Nakamoto, "IR Spectra of Inorganic and Coordination Compounds," John Wiley and Sons, New York (1963).
26. R. F. DeKeersmaecker and D. J. DiMara, *J. Appl. Phys.*, **51,** 1085 (1980).
27. E. S. Yang, D. B. Dove, M. W. Shafer, and I. F. Chang, *J. Electron. Mater.*, **10,** 423 (1981).
28. W. L. Medlin, *Phys. Rev.*, **122,** 837 (1961); *ibid.*, **123,** 502 (1961).
29. P. J. Dean, *Prog. Solid State Chem.*, **8,** 1 (1973).
30. C. J. Delbecq, Y. Toyozawa, and P. H. Yuster, *Phys. Rev. B,* **9,** 4497 (1974).
31. N. F. Mott and E. A. Davis, "Electronic Processes in Non-crystalline Materials," Clarendon Press, Oxford, England (1971).
32. S. Chandrasekhar, *Rev. Mod. Phys.*, **15,** 1 (1943).
33. S. M. Sze, "Physics of Semiconductor Devices," John Wiley and Sons, New York (1981).
34. R. M. Fuoss, *Trans. Faraday Soc.*, **30,** 967 (1934).
35. D. W. Marquardt, *J. Soc. Ind. Appl. Matl.*, **2,** 431 (1963).
36. N. S. Caswell, D. J. Robbins, and I. F. Chang, Unpublished work.
37. L. Onsager, *Phys. Rev.*, **54,** 554 (1938).

Backgating in Ion-Implanted GaAs MESFET

Wade C. Tang,* Kerry S. Lowe,*,[1] I. Abdel-Motaleb, and Lawrence Young*

Department of Electrical Engineering, University of British Columbia, Vancouver, British Columbia, Canada V6T 1W5

Modification of MESFET drain current characteristics by varying the (negative) voltage applied to a nearby electrode on the semi-insulating substrate is known as backgating (1-5) and is potentially a serious dysfunction for GaAs integrated circuits. Although the name implies an electrostatic field effect which causes a modulation of the channel, the substrate does not normally act simply as a dielectric through which a field is generated by the backgate. Lee *et al.* (3) and Miers *et al.* (4) found that a threshold voltage was required to produce the effect and that a sharp increase in the current drawn by the backgate occurred at the same threshold. This suggested a trap-filled limit (6) above which injected electrons cause the substrate to become sufficiently conducting to transfer a sufficient part of the applied voltage to the junction of the n-channel with the substrate. In a more recent paper, Blum and Flesner (7) found little or no threshold with devices made using capless proximity annealing of the implanted silicon in contrast to the use of a Si_3N_4 cap in the previous work. They suggested the presence of a p-like layer produced by the outdiffusion of EL2, an idea previously mooted by Chang *et al.* (8) to explain cross talk between devices. Ogawa and Kamiya (10) have now re-

* Electrochemical Society Active Member.

[1] Present address: Bell Northern Research Laboratories, Ottawa, Ontario, Canada K1Y 4H7.

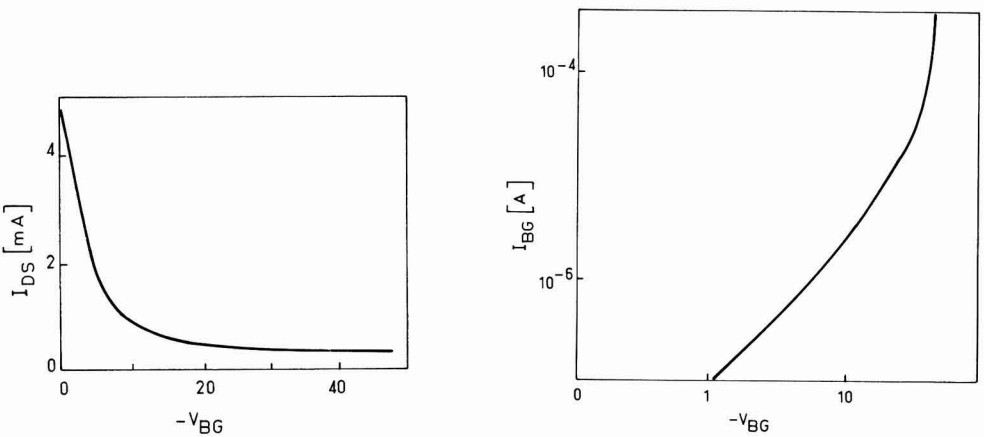


Fig. 1. MESFET annealed under SiO_2 cap. a(left): I_{DS} vs. V_{BG} for $V_{GS} = 0$ showing no threshold. b(right): I_{BG} vs. V_{BG} showing sudden increase in I_{BG} at $V_{BG} \sim -30V$.

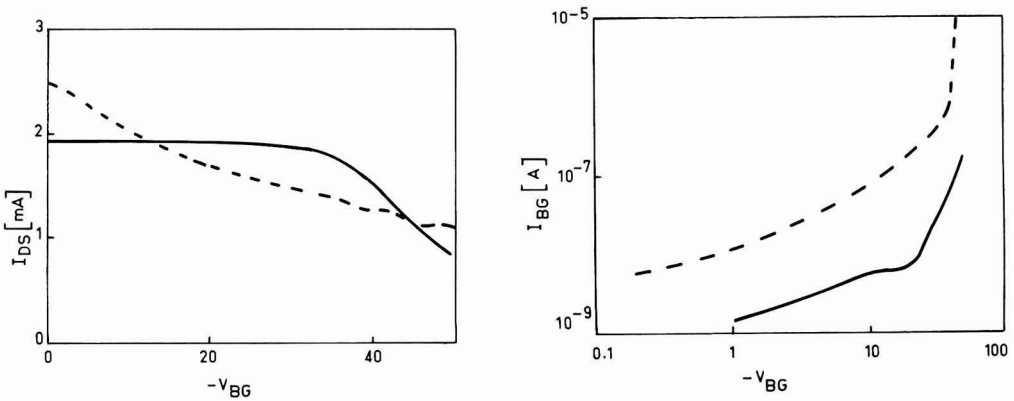


Fig. 2. MESFET annealed under Si_3N_4 cap. a(left): I_{DS} vs. V_{BG} for $V_{GS} = 0$. b(right): I_{BG} vs. V_{BG}. Solid lines: implanted directly. Broken lines: implanted through thin Si_3N_4.

ported that with Cr-doped wafers the backgating occurred gradually but that there was a threshold for undoped wafers.

In the present communication, we wish to report having obtained a result similar (9) to that of Blum and Flesner with devices made in our laboratory. In one set of MESFET's with 3 and 20 μm long Al gates, 3×10^{12} cm^{-2} ^{29}Si was directly implanted at 100 keV (at OPTOTEK, Ottawa, Canada) and annealed under a 170 nm RF-sputtered SiO_2 cap at 850°C for 20 min under N_2. These devices did not require a threshold voltage for backgating (Fig. 1a). Figure 1b shows how I_{BG} rose sharply at (typically) −30V. It was proposed (9) that the model of Chang *et al.* (8) applied to our device. The n$^+$ layer (due to indiffused Ge under the Au + Ge electrode) with the p-surface conversion layer (due to loss of EL2) and the n-channel form an n + p-n structure. The sharp increase in I_{BG} may perhaps be due to the reverse breakdown of the p-n junction part of this structure.

Results are also given (Fig. 2) for I_{DS} *vs.* V_{BG} (MESFET gate grounded) for samples on two slices both annealed with a 90 nm PECVD Si_3N_4 cap (deposited with a Plasmatherm Multiversion system). One slice was directly implanted with 2.2×10^{12} cm^{-2} ^{29}Si, and the other was implanted through 40 nm of Si_3N_4 with 3.4×10^{12} cm^{-2}, both at 100 keV, using the EXTRION 200-20 implanter in our laboratory. This 40 nm was increased to 90 nm before annealing. A "fat FET" mobility profile (5) was done. The devices implanted through Si_3N_4 gave a mobility decreasing with depth. The other gave increasing mobility. As found by Immorlica *et al.* (5), the decreasing mobility profile gave more backgating.

It is clear that the backgating effect can be strongly dependent on the details of the fabrication process and that more than one mechanism can produce the effect.

Acknowledgments

This work was supported by the B. C. Science Council and by the National Science and Engineering Research Council of Canada. We thank OPTOTEK Limited, Ottawa, for their courtesy in doing implants for us before we had the necessary equipment.

Manuscript submitted April 3, 1985; revised manuscript received June 17, 1985.

The University of British Columbia assisted in meeting the publication costs of this article.

REFERENCES

1. T. Itoh and H. Yanai, *IEEE Trans. Electron Devices*, **ed-27,** 1037 (1980).
2. H. Goronkin, M. S. Birrittella, W. C. Seelbach, and R. L. Vaitkus, *ibid.*, **ed-29,** 845 (1982).
3. C. P. Lee, S. J. Lee, and B. M. Welch, *IEEE Electron Dev. Lett.*, **edl-3,** 97 (1982).
4. T. H. Miers, W. M. Paulson, and M. S. Birrittella, in "GaAs and Related Compounds," Institute of Physics Conference Series 65, p. 339, Institute of Physics, London (1982).
5. A. A. Immorlica, D. R. Ch'en, D. R. Decker, and R. D. Fairman, in "GaAs and Related Compounds," Institute of Physics Conference Series 65, p. 423, Institute of Physics, London (1980).
6. M. A. Lampert and P. Mark, "Current Injection in Solids," Academic Press, New York (1970).
7. A. S. Blum and L. D. Flesner, *IEEE Electron Dev. Lett.*, **edl-6,** 97 (1985).
8. M. F. Chang, C. P. Lee, L. D. Hou, R. P. Vahrenkamp, and C. G. Kirkpatrick, *Appl. Phys. Lett.*, **44,** 869 (1984).
9. W. C. Tang, M.A.Sc. Thesis, University of British Columbia, Vancouver, B.C., Canada (1984).
10. M. Ogawa and T. Kamiya, *IEEE Trans. Electron Devices*, **ed-32,** 571 (1985).

Precipitation in Fe-Doped Semi-Insulating InP Epitaxial Layer Grown by Metalorganic Chemical Vapor Deposition (MOCVD)

S. N. G. Chu,* S. Nakahara,* J. A. Long, V. G. Riggs, and W. D. Johnston, Jr.*

AT&T Bell Laboratories, Murray Hill, New Jersey 07974

Growth of semi-insulating InP bulk crystals by the liquid-encapsulated-Czochralski (LEC) technique has been achieved routinely by doping with iron (1-8). Resistivity greater than 10^7 Ω-cm can be attended. However, due to the low segregation coefficient ($k_{eff} = 2 \times 10^{-4}$) of Fe in InP (8), the pile-up of Fe in the vicinity of the growing solid-liquid interface leads to the formation of a eutectic phase, FeP_2, which in turn is trapped randomly in the crystal as the growth proceeds (6, 7). Needle- and block-shaped particles 100 μm in size have been observed (7). The estimated dopant concentration at which the particles begin to incorporate into the crystal is around 1×10^{19} cm^{-3} (6). Recently, Smith *et al.* have also observed a spongelike rod-shaped particle which was identified to be FeP (8).

More recently, Long *et al.* (9) have demonstrated the growth of Fe-doped semi-insulating InP on (001) InP substrates by metalorganic chemical vapor deposition (MOCVD) using Me_3In-PMe_3 adduct as the In source and $Fe(C_5H_5)_2$ and $Fe(CO)_5$ as dopant sources. Resistivity as high as 2×10^8 Ω-cm can be achieved at a dopant level of $\sim 2 \times 10^{18}$ cm^{-3}. The semi-insulating InP epitaxial layer has been used as the current confinement layer for buried heterostructure lasers (10). Potential applications for the material, such as its use as the base material for microwave devices and as the isolation layer for vertical integration of optoelectronic devices, can also be envisaged. Since the perfection of the epitaxial layer is crucial to the ultimate performance of the device, the possibility of precipitation in semi-insulating InP grown by MOCVD needs to be explored. In this study, we report the observation of a precipitate in the Fe-doped epitaxial layer by transmission electron microscopy. The composition and structure of the precipitate will be investigated by x-ray energy dispersive analysis and TEM microdiffraction.

Experimental

Fe-doped semi-insulating InP epitaxial layers used in this study were grown by MOCVD on S-doped (001) InP substrates, using Me_3InPMe_3 adduct as the In source and $Fe(C_5H_5)_2$ and (COT)$Fe(CO)_3$ (COT = cyclooctatetraene) as dopant sources. Details of the MOCVD reactor and the growth procedure were described elsewhere (9). The layers were grown at 650°C with a growth rate ranging from ~3 to 10 μm/h. The defect structure of the as-grown layer was characterized by transmission electron microscopy (TEM) on a (110) cross-section sample. The cross-section TEM (XTEM) sample preparation technique, using a grid masking method, was described previously (11). SIMS depth profiling of the Fe-concentration distribution was done by Charles Evans, Incorporated, using a calibrated standard with known Fe concentration. The composition and structure of the precipitate were investigated by x-ray energy dispersive analysis and electron diffraction. Detailed TEM diffraction study on particles extracted by dissolving the epilayer and particles collected using nitro-

*Electrochemical Society Active Member.



Fig. 1. Nomarski interference photomicrograph of as-grown surface of Fe-doped InP epitaxial layer.

cellulose film (1% amyl acetate) will be discussed elsewhere (14).

Results and Discussion

Although the surface of as-grown Fe-doped InP is highly specular under reflected light, detailed surface morphology is not smooth as revealed by Nomarski interference contrast microscopy (see Fig. 1).

A desert-like surface is typical for a vapor-grown InP layer. The Fe-concentration distribution determined by SIMS depth profiling is shown in Fig. 2. Two peaks near the interface are present. The Fe peak located at the interface (3.20 μm) is similar to those observed at substrate/epi layer interfaces regardless of the dopant types. The possible causes have been attributed to surface contamination introduced during wafer handling or out-diffusion of background Fe concentration from the substrate material (12, 13). The appearance of a second peak indicates a transient period in Fe incorporation during the initial stage of epitaxial growth. The average Fe concentration away from the interface is $\sim 1.2 \times 10^{18}$ cm^{-3}, and the resistivity of the layer is 2×10^{8} Ω-cm.

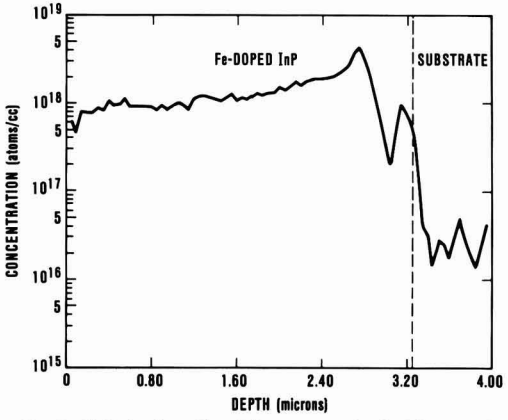


Fig. 2. SIMS depth profile of Fe concentration in InP grown by MOCVD.

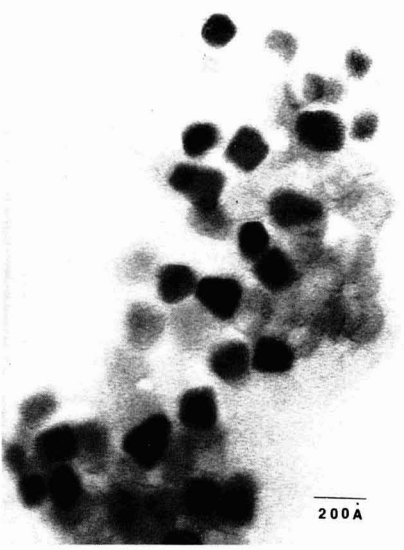


Fig. 3. TEM micrograph of precipitates in Fe-doped InP

Small precipitates of 100-250Å in size are observed by transmission electron microscopy in the (110) cross-section sample. They appear in the form of clusters as shown in Fig. 3. A close examination reveals Moirè fringes associated with most of the particles (see Fig. 4), which indicates that the particles are actually lying on the surface of the sample.

The chemical constituents of the particle were determined by x-ray energy dispersive analysis using a fine electron probe 20Å in size. The spectra taken inside and outside the particle are shown in Fig. 5. Since the detection limit of Fe concentration in InP by this technique is $\sim 5 \times 10^{20}$ cm^{-3}, a dopant level of 10^{18} cm^{-3} cannot be ob-

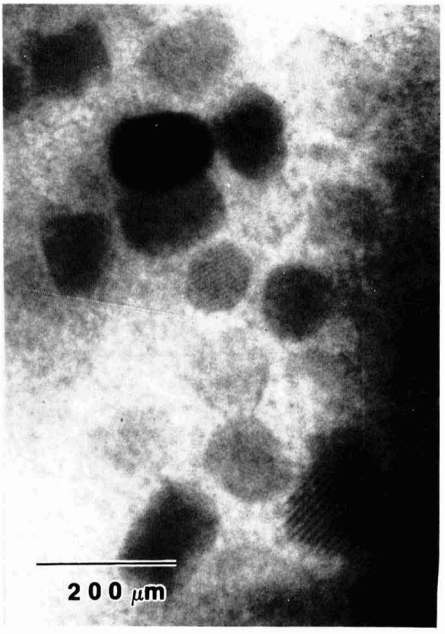


Fig. 4. TEM micrograph showing Moirè fringes associated with the particles.

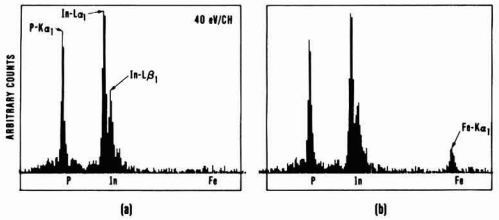


Fig. 5. X-ray energy dispersive spectra taken outside (a) and inside (b) the precipitate.

served. The spectrum taken outside the particles shows only In L lines and P K_α lines (see Fig. 5a). However, an FeK_α peak does appear in the spectrum taken inside the particle (see Fig. 5b). X-ray line scan across the particle further confirms that the iron detected is confined inside the particle. Since the Fe_mP_n compounds have lattice structures different from InP, the type of compound which constitutes the particle can be determined by electron diffraction on extracted particles. The details of the electron-diffraction analysis on the extracted particles will be described elsewhere (14). The major result is shown in Fig. 6, where the electron diffraction pattern is compared with the calculated pattern for FeP_2 and FeP. A careful examination confirms that the particles are FeP.

Since the majority of the precipitates observed in the MOCVD layer are coherent to the InP lattice, the minimization of the strain energy associated with the mismatch thus plays a major role in determining the type of Fe-P compound to be precipitated out. Although the lattice structure of both FeP and FeP_2 are orthorhombic, the difference in lattice constants results in a closer match of FeP (a = 5.794, b = 5.187, and $2c$ = 6.190) to InP (a = 5.869) as compared to FeP_2 (a = 5.460, b = 4.985, and $2c$ = 5.668) to InP.

Occasionally, dislocation structures are observed in conjunction with the particles, of which one is shown in Fig. 7. The strong strain contrast associated with the particle is an indication that the high stress concentration developed around the particle is likely to be the cause for dislocation generation. Furthermore, most of the bow-out dislocations contain cusps along the dislocation line, which indicates that the dislocations are pinned by the precipitates during their slipping.

Finally, the density of the precipitates are compared for layers at two different dopant concentrations, *i.e.*, 3×10^{17} and 2×10^{19} cm^{-3}. The corresponding XTEM micrographs are shown in Fig. 8. In spite of the fact that the majority of the precipitates are lying on the surface of the sample, the drastic increase in the density of the precipitates at a doping level of 2×10^{19} cm^{-3} is clearly demonstrated. The size of the precipitates, however, is more or less constant, which is expected if it is determined by the misfit strain energy.

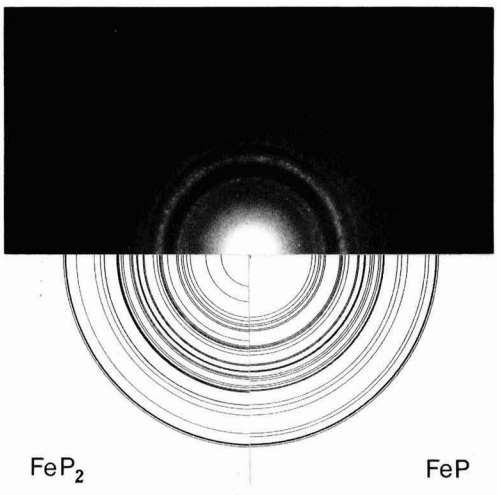


Fig. 6. Comparison of electron diffraction pattern from extracted particles with calculated diffraction patterns from FeP_2 and FeP powders.

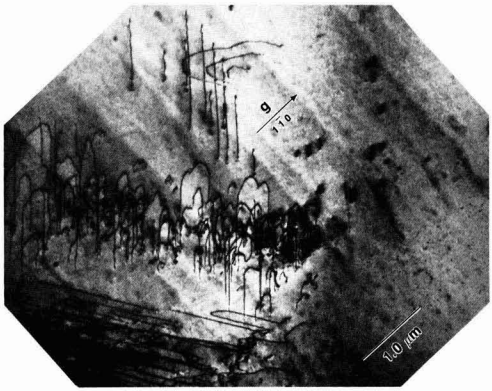


Fig. 7. Dislocation structure in Fe-doped InP epitaxial layer. The dark spots are precipitates.

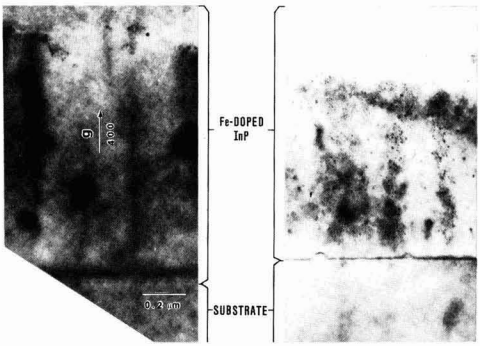


Fig. 8. (110) TEM cross-sectional view of Fe-doped InP epilayers showing particle density at Fe concentrations of 3×10^{17} cm^{-3} (a) and 2×10^{19} cm^{-3} (b).

Conclusion

We have reported the observation of small coherent precipitates in Fe-doped semi-insulating InP epitaxial layer grown by MOCVD on S-doped (001) InP substrate. Within the iron concentration range of 3×10^{17} to 2×10^{19} cm^{-3}, the density of precipitate increases with increasing iron concentration, while the size of precipitates (100-250Å) remains more or less constant. These are identified as FeP. Due to the differences in lattice structures, precipitation of FeP instead of FeP_2 observed in bulk crystal can be rationalized in terms of the minimization of the misfit strain energy. Occasionally, slip-type dislocation structures were observed associated with the precipitates.

Acknowledgment

The authors would like to thank A. F. Bloemeke and A. T. Macrander for the resistivity measurements. Thanks are also due to Dr. Richard McConville, who kindly took the x-ray line scan shown in Fig. 5. The support and encouragement of J. V. DiLorenzo, L. C. Feldman, and G. Y. Chin for this work are appreciated.

Manuscript received March 29, 1985.

AT&T Bell Laboratories assisted in meeting the publication costs of this article.

REFERENCES

1. O. Mizuno and H. Watanabe, *Electron. Lett.*, **11,** 5, 118 (1975).
2. D. Rumsby, R. M. Ware, and M. Whitaker, *J. Cryst. Growth*, **54,** 32 (1981).
3. C. R. Zeisse, G. A. Antypas, and C. Hopkins, *ibid.*, **64,** 217 (1983).
4. E. Kubota, Y. Ohmori, and K. Sugii, *Inst. Phys. Conf. Ser.*, **n63,** 31 (1982).
5. M. Morioka, K. Kikuchi, K. Kohe, and S. Akai, *ibid.*, **n63,** 37 (1982).
6. S. Miyazawa and H. Koizumi, *This Journal*, **129,** 2335 (1982).
7. R. N. Lee, M. K. Norr, R. L. Henry, and E. M. Swiggard, *Mater. Res. Bull.*, **12,** 651 (1977).
8. N. A. Smith, I. R. Harris, B. Cockayne, and W. R. MacEwan, *J. Cryst. Growth*, **68,** 517 (1984).
9. J. A. Long, V. G. Riggs, and W. D. Johnston, Jr., *J. Cryst. Growth*, **69,** 10 (1984).
10. D. P. Wilt, J. A. Long, W. C. Dautremont-Smith, and M. W. Focht, Unpublished work.
11. S. N. G. Chu and T. T. Sheng, *This Journal*, **131,** 2663 (1984).
12. J. Chevrier, M. Armand, A. M. Huber, and N. T. Link, *J. Electron. Mater.*, **9,** 745 (1980).
13. S. N. G. Chu, F. A. Stevie, A. T. Macrander, R. F. Karlicek, C. C. Chang, C. M. Jodlauk, K. E. Strege, D. L. Mitcham, and W. D. Johnston, Jr., *This Journal*, **132,** 1187 (1985).
14. S. Nakahara, S. N. G. Chu, J. A. Long, V. G. Riggs, and W. D. Johnston, Jr., *J. Cryst. Growth*, To be published.

Color and Efficiency of Neodymium Iodide Discharges

W. A. McAllister*

North American Philips Lighting Corporation, Bloomfield, New Jersey 07003

Atomic radiation from a number of metals, added as iodides to the high intensity mercury discharge, has provided light sources of exceptional efficiency (100 lm/W) and some improvement in color rendering properties (1). An exception, the tin iodide-mercury discharge has the color rendering characteristics of an incandescent source (2), some Sn-I molecular species being held responsible for the continuum radiation associated with this color improvement (3). Since both continuum and line spectra have been noted in rare earth iodide discharges (4), attractive combinations of efficiency and color rendition might be attainable at the color temperature (2900 K) of an incandescent source. One such material, neodymium iodide, alone or in combination with alkali iodides, has been examined in this work.

Experimental

Arc tubes (400W) were baked at 1050°C under vacuum, electrodes flashed in argon, and raw materials added in a commercial dry train under argon. After evacuation, 20 torr of argon was introduced, and the completed arc tube end coated using a zirconia suspension before mounting in a quartz-jacketed assembly. This evacuated unit was then used for measurement of the spectral power distribution in an integrating enclosure, and the other parameters of interest determined using a computer program formulated for this purpose. When results were attractive, the arc tube was mounted in outer bulb coated with CaS;Eu phosphor in organic lacquer, the resultant change in spectral and other properties were determined as above.

Neodymium was added as wire (99.9% pure, United Mineral) to react *in situ* with mercuric iodide, both the latter and the alkali iodides being introduced as spherical pellets (Anderson Physics Laboratories). A slight excess of neodymium metal over that required for complete reaction with the iodide was found necessary to improve starting. The mercury concentration was 2.5×10^{-4} mol, neodymium iodide 2.5×10^{-5} mol; alkali iodide concentrations are listed in Table I.

Results

The efficiencies and the color characteristics of neodymium iodide discharges are listed in Table I, with the voltage and current values for operation at 400W; included for comparison are figures for bare mercury and sodium-scandium iodide discharges evaluated in the same decountable configuration. Neither efficiency nor color temperature is changed from that of the mercury discharge on inclusion of neodymium iodide alone; the improvement in color rendering index (CRI) is associated with continuum radiation throughout the visible (Fig. 1), particularly in the 600-700 nm region. This feature is enhanced considerably upon addition of cesium iodide with the rare earth halide (Fig. 2), with both CRI and efficiency now improving and color temperature remaining at the mercury discharge level (Table I). Use of sodium iodide (4×10^{-5} mol) instead of the cesium salt brought the color temperature down to 4580 K, efficiency and CRI values being lower than those noted with cesium iodide. Addition of 2×10^{-5} mol cesium iodide at this so-

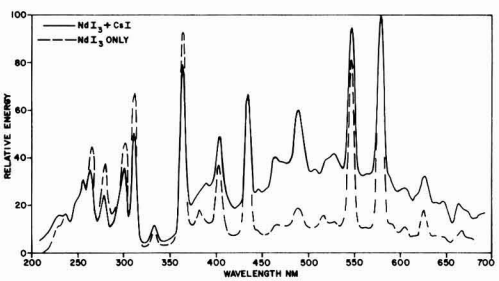


Fig. 1. Spectra of neodymium iodide discharges. Dashed line: NdI_3 only. Solid line: NdI_3 + CsI.

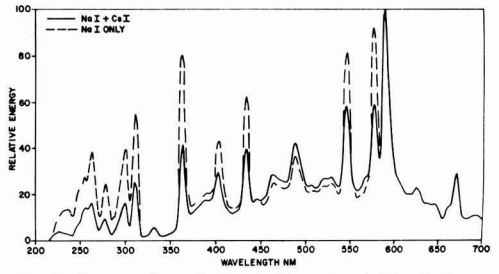


Fig. 2. Spectra of neodymium iodide-cesium iodide discharges. Dashed line: NaI only. Solid line: NaI + CsI.

* Electrochemical Society Member Representative.

Table I. Efficiency and color characteristics of neodymium iodide discharges (lamps)

Additive concentration (mol × 10^{-5}) CsI	NaI	Efficiency (lm/W)	Color rendering index	Color temperature (K)	Voltage (V)	Current (A)
—	—	56	57	5490	145	3.05
2.0	—	81 (52.0)	72 (86)	6220 (4280)	138 (140)	3.7 (3.7)
2.0	—	81 (51.8)	73 (89)	6136 (4250)	130 (127)	3.4 (3.7)
—	4.0	73	66	4580	175	3.6
2.0	4.0	84 (69)	69 (59)	5029 (3350)	136 (125)	3.14 (3.3)
2.0	2.7	81 (60)	72 (80)	5080 (3360)	132 (137)	3.2 (3.2)
2.0	1.4	82 (54)	73 (80)	5180 (3480)	150 (150)	2.55 (2.87)
1.0	2.0	87 (63)	76 (88)	5360 (3380)	165 (160)	2.76 (2.8)
Mercury		50	20	5800		
Sodium						
Scandium		100	65	3900		

dium iodide concentration increased the efficiency to 84 lm/W, CRI to 69 and CCT to 5029 K, with the spectral shifts given in Fig. 2. Only slight changes in these values could be effected by altering the CsI/NaI ratios or concentrations (Table I).

Further discharge-related color improvements being unattainable, conversion of ultraviolet to visible red emission was accomplished through use of CaS:Eu,Sn (6) phosphor (λ_{peak} = 650 nm) coated on the outer bulb for some arc tubes, the lamps burned for 100h, after which time the data in Table I were assembled. Those with lamps having neodymium and cesium iodides had CRI values near 90, but color temperature was that of cool white source and efficiency that of the mercury discharge. While additions of sodium iodide increased the latter figure and lowered color temperature to values approaching the 2900 K of an incandescent source, color rendition dropped as sodium iodide concentration increased. Then with lower concentrations of the two alkali iodides, efficiency and color rendition improved but color temperature was again near 4000 K; application of a more dense phosphor coating lowered the latter to 3380 K, efficiency now being 63 lm/W and CRI = 80. The spectral changes occurring as phosphor coating weight increased are depicted in Fig. 3, the most dense coating weight providing a trace similar to that of an incandescent source with mercury and sodium lines superimposed.

Discussion

The large increases in efficiency and improvement in color rendition on adding both neodymium and cesium iodides to the mercury discharge are due to greater continuum radiation intensities with insignificant change in the mercury line intensities (Fig. 1). This suggests that the neodymium contribution has been enhanced by formation of a complex with higher vapor pressure than that for the rare earth salt alone (7).

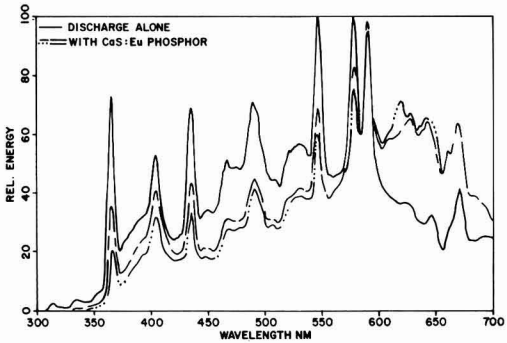


Fig. 3. Spectra of neodymium iodide · cesium iodide · sodium iodide discharge lamps. Solid line: discharge only. Dashed line: discharge + CaS:Eu,Sn phosphor (light density). Dot-dashed line: discharge + phosphor (heavier density).

The continuum radiation (Fig. 2) is not as intense relative to the mercury and sodium lines when sodium iodide is the only added halide and is not altered significantly in absolute terms on addition of cesium iodide. The latter's presence is associated with considerable suppression of mercury line intensities without effect on the sodium line intensity. Thus, the continuum becomes a greater fraction of the overall radiated energy, giving the better color and efficiency characteristics cited above. The mercury line suppression may be due to the formation of $NdI_3 \cdot CsI \cdot Hg$ complex, as postulated by Liu and Zollweg (8). Some support for this speculation is supplied by the facts that (*i*) the spectra, efficiency, and color properties are unchanged with a three-fold change in sodium iodide concentration, cesium iodide being held constant at 2×10^{-5} mol, and (*ii*) the mercury lines regain their prominence, and continuum contribution improves, when the cesium iodide concentration is halved at 2×10^{-5} mol sodium iodide.

The bandpass used for these figures made for ease in the analog-to-digital conversion required for the application of correction factors to the raw data and derivation of the efficiency and chromatic parameters. Closer inspection at higher resolution revealed the presence of many lines ascribed to Nd atomic transitions in the band envelopes depicted, yet the continuum persisted even at high resolution (1 nm) slit width. Although some of the continuum below 405 nm has been associated with electron attachment to halogen atoms (9) and the 444 nm band is due to Hg-I (10), most is doubtless due to some molecular neodymium-iodine species, or combinations thereof with the monovalent iodides. Since NdI_3 can dissolve neodymium metal, in excess here, to form $NdI_{1.95}$ (11) with lower melting point (562°C) than NdI_3, a contribution from the reduced iodide to the molecular radiation would be expected. However, absorption measurements by others showed no spectral difference in vapor over $NdI_3 \cdot CsI$ and $NdI_2 \cdot CsI$ mixtures (8). Uncertainty surrounding the geometry of $NdI_3 \cdot CsI$ complexes, or for that matter NdI_3 itself (8, 12), makes further speculation on the molecular species involved somewhat presumptuous.

Acknowledgments

The writer gratefully acknowledges the discussions with, and measurements provided by, W. A. Thornton as well as the technical assistance of D. Rachko and E. Chen.

Manuscript submitted Feb. 8, 1985; revised manuscript received *ca.* July 1, 1985. This was Paper 584 presented at the Hollywood, Florida, Meeting of the Society, Oct. 5-10, 1980.

North American Philips Lighting Company assisted in meeting the publication costs of this article.

REFERENCES

1. See, for example, J. F. Waymouth, "Electric Discharge Lamps," MIT Press, Cambridge, MA (1971).
2. T. Higashi, L. Mori, and S. Nagano, Paper presented at the CIE Conference, Washington, DC (1967).
3. D. M. Speros, R. M. Caldwell, and W. E. Smyser, *High Temp. Sci.*, **4**, 99 (1972).

4. W. Pilz and H. P. Popp, in "Proceedings of the International Conference on Phenomena Ionized Gases (Prague)," p. 409, Czechoslovakian Academy of Science, Prague, Czechoslovakia (1973); D. A. Larson and W. A. Thornton, Final Report, ECOM Contract DAAB07- 72-C-0091 (1973).
5. W. A. Thornton, *This Journal*, **116,** 286 (1969).
6. W. Lehmann and F. M. Ryan, *ibid.*, **118,** 477 (1971).
7. C. Hirayama, C. S. Liu, and R. J. Zollweg, in "High Temperature Metal Chemistry," D. L. Hildenbrand and D. D. Cubicciotti, Editors, p. 95, The Electrochemical Society Softbound Proceedings Series, Princeton, NJ (1978).
8. C. S. Liu and R. J. Zollweg, *J. Chem. Phys.*, **60,** 2384 (1974).
9. D. A. Rothe, *Phys. Rev.*, **177,** 93 (1969).
10. R. W. B. Pearse and A. G. Gaydon, "The Identification of Molecular Spectra," 3rd ed., Chapman and Hall, London (1965).
11. L. F. Druding and J. C. Corbett, *J. Am. Chem. Soc.*, **83,** 2462 (1961).
12. J. C. Wells, J. B. Gruber, and M. Lewis, *Chem. Phys.*, **24,** 391 (1977).

JOURNAL OF THE ELECTROCHEMICAL SOCIETY

COMMENTS

NOVEMBER 1985

Each issue of the **Journal** will have a section of "Comments." In this section, we provide a means via short pieces, *i.e.*, one column or less, to applaud, dispute, or otherwise discuss the papers published in the **Journal.** Space will be provided for one response by the paper's author(s) to each comment.

Since space available in each issue for the "Comments" section is limited; it is important to be concise.

Comments should be sent to the Editor, Dr. Norman Hackerman, Department of Chemistry, Rice University, P.O. Box 1892, Houston, TX 77251.

Norman Hackerman
Editor

Adsorption of Hydroxide and Sulfide Ions on Single-Crystal n-CdSe Electrodes

K. W. Frese, Jr. and D. G. Canfield

(pp. 2614-2618, Vol. 131, no. 11)

S. Licht:[1] The attempt to determine equilibrium and free energy constants for hydroxide and hydrosulfide/sulfide adsorption onto CdSe in this study is commendable, although certain anomalies render the data uninterpretable.

(*i*) Surface adsorption of charged particles changes the free energy and potential over that surface.[2] Hence the equilibria "constant" and free energy for adsorption are potential (*i.e.*, concentration dependent), and it was inappropriate to determine constants for these processes.

(*ii*) The measured CdSe flatband potentials, V_{FB}, variation of 240 mV/log [OH^-] and approximately 90 mV/log [HS^-], even upon assumption of large interaction parameters between adsorbed particles, are inconsistent with their proposed adsorption of monovalent species onto the electrode surface. Regeneration of their data, using their adsorption isotherm, provides a poor fit of their measured data. Hence by rearrangement of their Eq. [8], [OH^-] in solution may be computed from θ, the relative extent of hydroxide adsorbed on the surface, using their equilibria constant, $K = 50.4$ and their interaction parameter, $f = 1.7$. These computations are presented in Fig. 1 and are compared to their experimental data; their adsorption isotherm fits only at $\theta = 0.5$. An alternate, charge- and potential-consistent model for adsorption onto semiconductors has recently been proposed.[3]

(*iii*) Time-dependent chemical substitution reactions occur in the dark between CdSe and alkali polysulfide electrolytes[4] and will presumably occur to a greater degree in the less stabilizing sulfate and sulfide electrolytes used in the study of Frese and Canfield. Assuming a time- and concentration-dependent modification of the CdSe electrode in sulfate electrolyte to $Cd(OH)_2$, or in the sulfide solution to CdS, it becomes unclear on which semiconductor their V_{FB} and adsorption properties were characterized.

(*iv*) Variation in the redox potential of the electrolyte can have a large effect on measured V_{FB}.[5] The alkaline sulfate and sulfide electrolytes employed in the study were made without added sulfite or sulfur. From the Nernst equation, the sulfate/sulfite and the polysulfide redox couples both have undefined potentials in the respective absence of

[1] Department of Materials Research, The Weizmann Institute of Science, Rehovot 76100, Israel.

[2] S. R. Morrison, "Electrochemistry at Semiconductor and Oxidized Metal Electrodes," pp. 60-64, Plenum Press, New York (1980).

[3] S. Licht and V. Marcu, Submitted to *J. Electroanal. Chem.*

[4] D. Cahen, G. Hodes, and J. Manassen, *This Journal*, **125**, 1623 (1978).

[5] S. U. M. Khan and J. O'M. Bockris, *J. Appl. Phys.*, **52**, 7270 (1981).

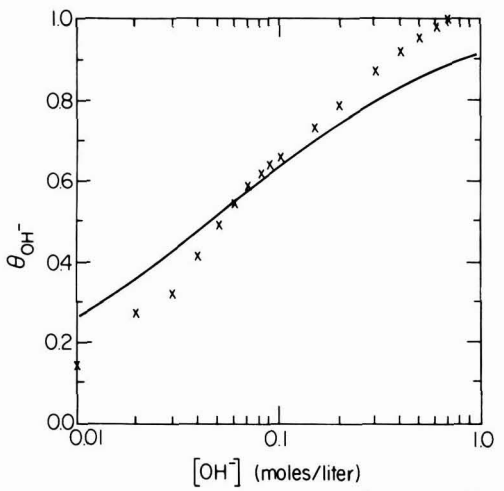


Fig. 1. Extent of hydroxide surface coverage on CdSe, θ, vs. log of hydroxide concentration in solution for n-CdSe (1120) in 0.1M Na_2S_4. Experimental data (points) are from Frese and Canfield. Solid curve: this work. Hydroxide concentrations are calculated upon rearrangement of Eq. [8] in Frese and Canfield, using $K = 50.4$ and $f = 1.7$.

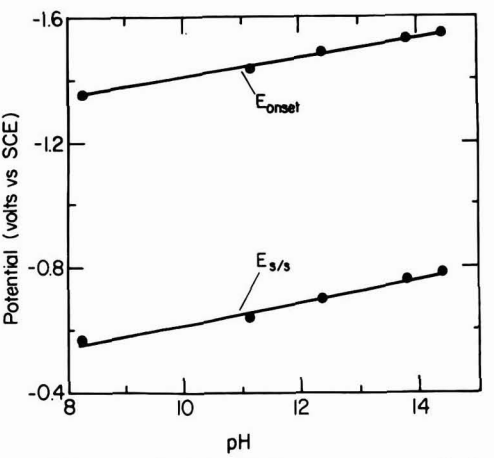


Fig. 2. The measured variation with pH, at room temperature, of polysulfide redox potential (vs. standard calomel electrode) and of the photocurrent onset potential (vs. standard calomel electrode) for a 0.15 cm^2 $CdSe_{0.65}Te_{0.35}$ single-crystal immersed in an aqueous solution containing 1.8*m* in CsHS and 3*m* in sulfur, and various concentrations of CsOH, under tungsten halogen lamp illumination of 75 mW/cm^2.

significant quantities of sulfite or sulfur. In both cases, impurities and oxidation products of these materials will greatly effect the electrolyte redox potential, which, in turn, may create significant errors in measured V_{FB}.

The differential change of V_{FB} with $[OH^-]$ might be expected to be similar for the other cadmium chalcogenides. An attempt at measuring cadmium sulfide flatband potential variation with $[OH^-]$ and $[HS^-]$ had experimental deficiencies which also rendered the data uninterpretable. That study concluded a 60 mV/pH unit slope for V_{FB};[5] however, their measured pH values were inconsistent by up to 2.2 pH units with pH values readily calculated from their initial concentrations of alkali hydroxide and alkali sulfide added to solution (total hydroxide = alkali hydroxide + hydrolyzed alkali sulfide).[6] In Fig. 2, my measurements in polysulfide solution of the pH variation of $CdSe_{0.65}Te_{0.35}$ V_{FB}, as reflected by trends in photocurrent onset potential, show a slope of 30 mV/pH unit. Note that this slope approximates the observed pH variation of the polysulfide redox potential.

Systematic and consistent application of solution chemistry is vital to the fundamental understanding of CdX/aqueous polysulfide photoelectrochemical solar cells. A recently developed model for the complex distribution of species within aqueous polysulfide solution is useful in understanding these processes.[7] This correspondent has recently proposed an overall mechanism for the photooxidation of polysulfide in CdX/polysulfide PEC's in which $S_4^=$, OH^-, and HS^- are shown to be the preferential participants in the reaction process.[8]

K. W. Frese, Jr.:[9] We are aware that the free energy of adsorption and the apparent equilibrium constant are coverage dependent. This was demonstrated by our Eq. [8]-[10] in the paper under discussion. The isotherm we used accounts for this dependence in an approximate way; that is, it assumes that the free energy of adsorption varies linearly with coverage. We disagree that our results are not interpretable, because in the very least the apparent free energy of adsorption can be extrapolated to zero coverage to obtain a meaningful result.

In the case of adsorption of OH^-, we calculated the apparent free energy of adsorption at each coverage up to $\theta = 0.6$. The value of ΔG of -1.7 kcal/mol was found for $\theta < 0.2$, which corresponds to $K = 18$. A slightly more negative value of -2.3 kcal/mol was reported in our paper.

A new feature was revealed by the additional analysis of the OH^- adsorption data. The apparent ΔG becomes negative as coverage increases up to $\theta = 0.6$. This behavior suggests that f in the Frumkin isotherm is actually negative. A possibly similar effect was mentioned in our paper in the discussion of sulfide adsorption. In that case, surface compound formation (CdS) is strongly suspected. Because f appears to be small (about -0.9), we could not distinguish the correct sign in our original analysis. Perhaps compound formation as cadmium hydroxide is suggested by our data.

The use of photocurrent onset potentials to measure the flatband potential as suggested by Licht is not without difficulties. The onset potential depends on light intensity, is influenced by the magnitude of the forward current, and probably depends on the amount of dissolved sulfur. The parallelism between the onset potential and the redox potential in Licht's Fig. 2 probably means that the Helmholtz potential drop is changing due to Fermi level pinning. This means that variations such as the 30 mV/pH of the onset potential reflect the metallic character of the surface (high surface state density) rather than adsorption properties. Our unpublished measurements of the surface state density on n-CdSe in 1*M* NaOH show that there are only about 1×10^{11} state/cm^2 in the upper part of the gap. On the contrary, more than 1×10^{14} state/cm^2 were found in the upper part of the bandgap of CdSe in contact with alkaline sulfide solutions.

[6] D. S. Ginley and M. A. Butler, *This Journal*, **125**, 1968 (1978).
[7] S. Licht, J. Manassen, and G. Hodes, Submitted to *Inorg. Chem.*
[8] S. Licht, Submitted to *J. Phys. Chem.*
[9] SRI International, Menlo Park, California 94025.

Electrochemical Behavior of Passive Iron in Acid Medium
II. The Passive Film/Solution Interface

M. Keddam and C. Pallotta

(pp. 781-787, Vol. 132, no. 4)

V. Jovancicevic:[10] In this paper, the authors raise two interesting questions relating to the passive iron/solution interface. The first one is the relationship between electron and ion charge transfer at the interface, and the second one is about the effect of anions on the kinetics of charge transfer on the film surface. The interpretation of the results involving a loosely structured boundary layer on the top of the inner solid layer needs some remarks.

Keddam and Pallotta argue that the redox reactions, with opposite anion effect on $Fe(CN)^{4-}$ and Fe(II) oxidation on the passive layer, are allowed by the good electron conductivity of the inner layer and controlled by mass transfer across the transition layer. The effect of anion in the increasing interaction sequence, perchlorate, sulfate, and phosphate, on the passive current is described in terms of the adsorption and subsequent penetration of anions into the loosely structured layer, affecting its passive properties. This model has some similarity to the "chemiconductor" model of the passive film regarding its conductivity.[11]

The mass-transfer properties and anion interaction with the passive layer are studied by using the angular velocity transient and composition transient of the passive current. Both transients show similar features: first, fast change of the current (minutes), followed by slow attainment of the steady state (hours). Even though the observed effects are similar in these transients, they are interpreted differently. The short-time response is explained as a "mass-transfer-limited process," whereas the long-time response as a decrease of the thickness of the film in the case of tha angular velocity transient. In the case of the composition transient, the fast response corresponds to anion adsorption, while the slow response to anion penetration into the film. Recently, similar effects have been obtained with the pH transient where both changes in the thickness and in the surface composition of the layer were suggested.[12,13]

The adsorption of anions on the surface of the passive layer supported by the results on the colloidal iron oxide is a first step in the formation of Fe(III)-anion soluble complexes.[14] It is well known that Fe(III) forms in acid solution stable octahedral aquo complexes where water molecule(s) are substituted by the anion ligands.[15] The stability of the complexes depends on the pH and on the type of anions increasing in the sequence, perchlorate, sulfate, phosphate, as discussed by Keddam and Pallotta. Thus, under steady-state conditions, at constant potential, the different currents correspond to different thicknesses of the film in equilibrium with the solution. When various transients are applied, the passive current increases or decreases, depending on whether more stable or less stable complexes are being formed.

The authors studied kinetics and mass transfer at the passive film/solution interface without clearly giving the reasons for the increase or decrease of the current with the change of the composition of the solution or angular velocity of the electrode. Both effects as well as pH effect can be attributed to the change of the thickness of the passive layer.[16]

A relevant aspect of the passive film behavior has been neglected in the study of the current transients which is its potential dependence. Besides the change of the thickness, the potential variation may cause some change in the com-

[10] Department of Chemistry, Texas A&M University, College Station, Texas 77843-3255.
[11] B. D. Cahan and C. T. Chen, *This Journal*, **129**, 17, 474, 921 (1982).
[12] O. Reies Iola, A. M. Sukhotin, and L. N. Gerasimenko, *Electrokhimiya*, **18**, 723 (1982).
[13] V. Jovancicevic and J. O'M. Bockris, Submitted to *This Journal*.
[14] K. J. Vetter and F. Gorn, *Electrochim. Acta*, **18**, 321 (1973).
[15] F. A. Cotton and G. Wilkinson, "Advanced Inorganic Chemistry," Interscience Publishers, New York (1980).
[16] V. Jovancicevic, In preparation.

position and structure of the passive layer. Thus, using the pH, abrupt change in the solution the relative concentration of Fe(II) in the passive layer could be estimated.[16]

S. Kapusta:[17] The dependence of the anodic current measured on passive iron electrode in acid solutions on rotational speed and the correlation of these results with erosion-corrosion phenomena deserve some comments. For the systems under consideration, fluid flow can either promote the transport of matter to and from the surface (convective mass-transfer-controlled dissolution) or it can cause stresses on the surface that may shear the passive film or the metal (corrosion-erosion).

The shear stress on a rotating disk electrode is[18]

$$\tau\omega = \rho r \nu^{1/2} \omega^{3/2} G'(0) \quad [1]$$

where ρ is the density of the solution, r the radius of the electrode, ν the kinematic viscosity, ω the angular frequency, and $G'(0)$ a function described elsewhere.[18] One disadvantage of the rotating disk (as compared, *e.g.*, to the rotating cylinder) is that the shear stress depends on position, being maximum at the border of the electrode and (virtually) vanishing at the center. Another often overlooked problem is that the shear stress values obtainable on a practical RDE are small, usually of the order of a few dynes per square centimeter. For instance, for $r = 0.25$ cm and $\omega = 100$ rpm, $\tau\omega = 0.5$ dyn/cm^2. These stresses may become two to three times larger if the disk is suddenly started, although the stress transients are short.[18]

It is doubtful that these small stresses could shear a passive film, since this would imply that the forces bonding the film to the metal surface (or to other, "inner" films) are very weak (less than 1 kcal/mol, *i.e.*, at or below the range of physical adsorption). As an example, we have all experienced the difficulty in removing nitrogen bubbles that tenaciously remain on the center of a RDE even at relatively high speeds. The bubbles are held mainly by buoyancy. One can calculate that even though the bonding forces are very small, rotation alone cannot dislodge these bubbles. To consider such a loosely attached layer part of the passivation film is, at best, arbitrary. However, the authors have based many of their conclusions precisely on this approach.

The stresses involved in actual erosion-corrosion are several orders of magnitude higher, since they may inflict damage to the passive film or the metal itself. These stresses can usually be achieved in multiphase flow, *e.g.*, by particle impact, or, more recently, by focused ultrasonic waves.

Several criteria can be used to distinguish between convective mass transfer and erosion effects. In a first approximation, we may assume that film shearing occurs above a certain threshold shear stress. An increase in ω then should lead to a corresponding decrease in the coverage of the electrode above a certain radius from the center, as can be calculated from Eq. [1] setting $\tau\omega$ = const. If we further assume that the passive current I_p is proportional to the uncovered area, we obtain

$$I_p \propto 1 - \omega^{-3} \quad [2]$$

i.e., a much higher functional dependence of current on ω than reported (*i.e.*, 1/2). Usually, with direct erosion the current varies with the third to sixth power of velocity, while with convective mass transport, the order is ≤ 1.0.[19]

A second difference between convective mass transfer and erosion-controlled reactions is that, with the former, the current follows almost instantaneously any changes in rotational speed and is reversible towards reversal of these changes, while the latter may show an induction period and a certain degree of hysteresis on returning to the starting conditions.

[17] Shell Development Company Westhollow Research Center, Houston, Texas 77001

[18] "Hydrodynamic Resistance and the Heat Loss of Rotating Solids," L. A. Dorfman, Editor, Oliver and Boyd, London (1963).

[19] V. Lotz and E. Heitz, *Werkst. Korros.*, **34**, 454 (1983).

The "staircase" shape of the current transient at constant potential and ω, observed in H_3PO_4 solutions, seems like an experimental artifact, since electrochemical systems do not usually show this type of "digital" behavior.

All this evidence suggests that, indeed, a loosely adherent layer may form, under these experimental conditions, on top of the true passive film. However, dissolution of this layer is to some extent mass-transfer controlled. It is further suggested that this layer is formed by dissolution and reprecipitation, from a saturated solution, of the phosphate and sulfate iron salts. As mentioned earlier, this outer salt layer is not part of the true passive film, but it is rather loosely attached by weak forces and easily overcome (*e.g.*, by rotation). In addition, the anions may also be incorporated into the passive film, as is the case with borate ions, or may otherwise induce localized film breakdown.[20] These are, however, well known and documented effects, and I fail to see any new facts in the paper under discussion.

The kinetics of redox reactions on passive electrodes has received considerable attention, and the present results are very interesting. The absence of one of the components of the redox couple, however, introduces some ambiguities in the results, because the system is "unbuffered," *i.e.*, large potential changes occur near the surface as one of the species in the redox couple is generated in the course of the reaction. These potential changes may affect both the conductivity and the composition of the film.

I wish the authors had published some of their polarization curves. In fact, even some old-fashioned exchange current densities and Tafel slope values would have served the purpose. It is frustrating trying to obtain any correlation between reported currents measured at different potentials.

Unexpectedly, the diffusion coefficients of the ferrocyanide ion measured on passive electrodes are consistently lower (approximately 1/2-1/3) than those measured on platinum (although the authors claim that they are similar), even in $HClO_4$ solutions where passive iron shows a "metallic" (in what sense?) behavior. Was a similar effect observed with Fe^{2+}? If not, it could be a specific $Fe(CN)_6^{4-}$ effect caused by diffusion through a thin and rotation-dependent layer of $[Fe(CN)_6]_2Fe_3$ deposited on the surface, as briefly indicated by the authors. If this is the case, however, the ferrocyanide may also interfere with the formation of the overlying salt film, considerably complicating the analysis of ac impedance diagrams.

The EHD diagrams are somehow misleading: Contrary to appearance and expectations, the results for H_3PO_4 solutions, where the more stable "porous" film is formed, fall between those of $HClO_4$ and H_2SO_4 solutions, instead of being the furthest removed from the ideal diffusion case. This, again, suggests some leveling effect perhaps caused by interference of the $Fe(CN)_6^{4-}$ with the normally deposited salt film. Moreover, mechanical removal of this porous film should eliminate the shift towards lower p values, which it does not. Therefore, the evidence overwhelmingly negates any mechanical effect on film stability, while it indicated a mass-transfer-controlled mechanism.

It should be obvious by now that electrochemical techniques alone cannot uniquely define the film composition, and, lacking some independent analytical result, all speculations in this respect will remain just that. Since the films grown in H_3PO_4 solutions may incorporate significant amounts of phosphate ions, it is questionable that the β-FeOOH composition is a valid model. On the other hand, it is to a certain point arbitrary and even confusing to attribute a particular bulk oxide composition to a thin film, (about 40Å in 1*M* $HClO_4$),[21] especially since compositional gradients are unavoidable and interfaces are not well defined.

In particular, the structure and properties of passivation films grown on stainless steels is strongly influenced by the presence of chromium, and any extrapolation from pure iron is not only unwarranted, but is also probably

[20] See, *e.g.*, Z. Szklarska-Smialowska, in "Proceedings of the 9th ICMC, Toronto (June 1984)," Vol. 2, p. 112.

[21] B. P. Lochel and H. H. Strehblow, *Electrochim. Acta*, **28**, 565 (1983).

wrong. Therefore, to attribute the protective effect of molybdenum to intercalation or modification of the iron oxide requires further justification.

M. Keddam:[22] We think that this comment brings about some interesting points and deserves the following remarks.

As has been pointed out by Keddam *et al.*,[23] the way in which we have depicted the passive film has some similarity with the chemiconductor model in the sense that the high field transport across the inner part of the film is anion dependent. However, our results tend to prove that the anion contents of the inner layer, determining the passive current, is controlled by the highly hydrated outer part of the film. The properties of the latter are determined by the adsorbability of anions on the oxide's surface and by their interaction with the solvent structure.

Regarding the nextcoming papers announced in this comment, we would like to emphasize that, according to data we will show in Fig. 5 of our paper,[23] the film thickness at a given potential, referred to the Flade potential in the same solution, is practically independent of pH and anions. These parameters seem to modify the passive behavior through compositional effects (*e.g.*, ferric to ferrous oxide ratio[24]) in the inner layer and structural change in the outer layer. Even in the limit, long-term aging changes hardly the thickness but rather proceeds by water out-take and progressive appearance of crystalline iron oxides.[24]

With respect to pH transients published by Soviet authors and apparently repeated by Dr. Jovancicevic, the short-time response is considerably faster than with anion transient. A likely explanation is to consider that the film/electrolyte potential is determined by pH through an equilibrium between OH and iron oxides. Therefore, pH transients are equivalent to a transient of electrical field strength across the film and induce a fast current step. According to our own experiments, the direction of this step *vs.* pH step is consistent with this explanation.

[22] Physique des liquides et électrochimie, l'Université Pierre et Marie Curie, 75230 Paris Cedex 05, France.

[23] M. Keddam, J. F. Lizée, C. Pallotta, and H. Takenouti, *ibid.*, **131,** 2016 (1984).

[24] A. Hugot-Le Goff and C. Pallotta, *ibid.*, To be published.

Regarding the comments of Dr. Kapusta on mechanical disturbances of the passive film, we have never meant that our rotating disk experiments could reproduce the high stresses or solid impacts involved in actual erosion-corrosion. This situation has been dealt with elsewhere.[25] Undoubtedly, the shear at the disk is by several orders of magnitude too low for destroying the passive film. However, the argument of a bubble at the very center of the disk submitted to a zero resulting radial force is not convincing.

Owing to the very low passive c.d., mass-transfer control by convective diffusion in its usual sense cannot be accepted as an explanation of the observed response. Therefore, an interpretation must be looked for in a weak hydrodynamical interaction with the passive film. As recognized finally in the comment, the existence of a loosely adherent layer constitutes a satisfactory model. In contrast with Dr. Kapusta's statement, there is no reason at all for thinking of this layer in terms of the salt film which precipitates during fast metal dissolution. In the case of phosphate, *in situ* Raman spectroscopy evidences iron phosphates on top of the passive film.[24] Washing out these products removes the corresponding spectrum but does not modify the passive current.

Regarding the RED-OX kinetics, most of the data have been completed and numerically processed since the time of publication of this paper. In fact diffusivities on Pt and on the passive film in $HClO_4$ are very close. "Metallic" does not refer to the type of conductivity but only to the fast charge transfer ensured by the film.

EHD data fit correctly to a model incorporating diffusion through a "solid" layer[26] which persists at high rotation speeds hence explaining the remanent shift towards low p values, for phosphate solution, as pointed out in the comment. We agree with the comment that ferrous ferricyanide is able to complicate the interpretation, Fe(II) shows a more complex behavior due to strong interference with the inner film structure. As explained in this paper, it tends to favor the formation of magnetite followed by Raman spectroscopy.

[25] J. C. Colson, A. Desestret, M. Keddam, and R. Oltra, *Corros. Sci.*, **23, 441** (1983).

[26] C. Deslouis, M. Keddam, C. Pallotta, and B. Tribollet, "Electrochemical Methods in Corrosion Research," Toulouse, France (July 1985).

JOURNAL OF THE ELECTROCHEMICAL SOCIETY

ACCELERATED

BRIEF COMMUNICATIONS

NOVEMBER 1985

In Situ Raman Spectroscopy for the Study of Iron Passivity in Relation to Solution Composition

A. Hugot-Le Goff

LP 15 "Physique des Liquides et Electrochimie," associé à l'Université Pierre et Marie Curie, Tour 22, 75230 Paris Cedex 05, France

C. Pallotta

Faculdad de Ciencias Exactas, Ciudad Universitaria, 1428 Nunez, Buenos Aires, Argentina

One of the most complicated topics in metal passivity is the chemical identification of thin films grown on iron electrodes. They are too thin to be analysed by X-rays, and in-situ methods such as Mossbauer spectroscopy or ellipsometry give only indirect results. RHEED (or LEED) which require that the sample be put in vacuum, are not suited to the problem. This explains why several structures, involving some of the numerous possible oxides or oxihydroxides, have been proposed. Raman Spectroscopy has become a useful tool for obtaining chemical and crystallographic identification (1,2).

In this paper, we will try to answer the following two questions :

- Is a defined film composition detectable by Raman Spectroscopy when the passive current, Ip, attains its steady-state value ?
- If a composition is defined, does it depend on the anion composition of the electrolyte ?

Previously we obtained spectra of each compound likely to appear in the passivity state, oxides or oxihydroxides, either as powder, or in single crystal form, together with thermal oxide films of easily controlled thickness (2). We studied the stability of these compounds under exposure to the laser beam. The oxihydroxides undergo a modification leading to the stable forms : hematite α-Fe_2O_3, and magnetite Fe_3O_4. However, when the samples were covered by a thin liquid layer during illumination (which reproduces the electrolysis conditions), each of them gave its proper spectrum.

EXPERIMENTAL

Iron electrodes (Johnson Matthey) carefully prepared, as previously described (3), and polished to 1200 grade emery paper, were polarised at different potentials in the full passive range in 1N H_2SO_4 solutions. These samples were placed flat in the cell under the objective of a microscope which served to focus the laser beam (514 nm) on a small area of the sample. This allowed study of local composition changes, and verification that the impact point was not damaged by the laser beam. The front length of objective is about 0.3 mm, permitting good optical yield, and room for a layer of electrolyte sufficient to ensure stability of the electrochemical process. The spectroscope, DILOR OMARS 89, has a diode array detection system which permits addition of spectra and collection of data over long periods. This improves the signal to noise ratio. All potentials are referred to the saturated sulfate electrode (vs SSE).

Manuscript submitted Jan. 28, 1985; revised manuscript received Sept. 10, 1985.

RESULTS

When the passive potential is more anodic than 0.6 V, even if the current attains its steady-state value (5 $\mu A.cm^{-2}$), a Raman spectrum is observed only after about 12 hours of polarisation. However, it has been shown that a passive film is formed at shorter times (4). The thickness of this "detectable" film was estimated by the amount of O^{16} in the film, as determined by nuclear reaction (5). The thickness was between 10 nm and 17 nm after three days of polarisation, whereas the thickness of the passive film observed after the first hour of polarisation was about 4 nm. Furthermore, for polarisation potentials more cathodic than 0.5 V, no Raman spectrum was observed even for long polarisation times (i.e. 90 hours).

Figure 1 represents two spectra : spectrum a is obtained in-situ after 12 hours of polarisation. Spectrum b corresponds to the same sample taken out of the electrolyte after a longer polarisation time. The electrolyte has an intense spectrum (due to SO_4^{2-} ions) in the 900-1000 cm^{-1}, but in the useful range for iron oxides, the in-situ identification is easy.The species identified under these experimental conditions were a mixture of magnetite (659, 544 cm^{-1}) and hematite (221, 253, 290, 406, 498, 616 cm^{-1}) γ-ferric oxide, as α - or γ - hydrated modifications, which are often assumed to appear, give quite different patterns and one can affirm that they are not present.

However, if the presence of hematite can be conclusively established, the existence of magnetite is not so evident. For the shortest polarisation times, the 544 cm^{-1} peak was not always present ; in this case, one cannot distinguish between the spectrum of magnetite,

CNRS assisted in meeting the publication costs of this article.

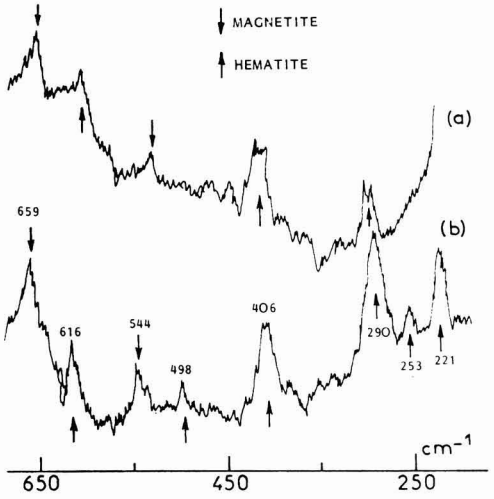


Figure 1 : 1a : in-situ 1b : ex-situ

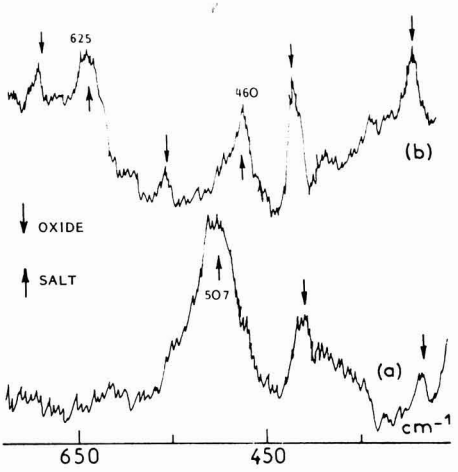


Figure 2 : 2a : 2N H_3PO_4 2b : 1N $HClO_4$

and that of the short-range oxihydroxide, a-FeOOH, which as the β- and δ-modifications, gives a single faint peak at 670 cm^{-1}. The existence of an amorphous film at the beginning of the passivation is supported by the long ageing necessary under potentiostatic polarisation to obtain Raman spectra. If the lack of a spectrum during the first hours was simply due to the insufficient film thickness, it would be possible to detect some signal by increasing the laser power and the accumulation time. This was not observed. It can be assumed that, during this period, a qualitative change of the initial material, together with a slow thickening takes place. Furthermore, the oxides are detected only if the passivation potential is more anodic than 0.6 V, which is the thermodynamic potential for the formation of iron oxides.

The anions, at constant pH, have a definite effect in determining the Ip value (3). In the case of electrodes passivated for about 15 hours it was shown that the current responds reversibly to a rapid change of the electrolyte composition (6). In order to better understand the role of anions, the solution was rapidly changed (either to 2N H_3PO_4 or to 1N $HClO_4$). In the first case, when the current attained its new steady-state value (50 $\mu A.cm^{-2}$), the Raman spectrum was recorded, as shown in Fig. 2a. The intensity of the peaks related to hematite is increased, and a new peak at 507 cm^{-1}, corresponding to ferric phosphate, is observed. After several hours of polarisation, only the peaks of hematite remain along with a very intense salt peak.

In the second case, the oxide peaks remain unchanged (Fig. 2b), and two peaks of iron perchlorate are seen at 460 and 625 cm^{-1}. The salt layer is tightly fixed on the film : and in spite of the solubility of the salt in water, it is necessary to wash the film for a long time to remove it. When the electrode is immersed again, the absence of the salt does not alter the current. From these experiments, it is possible to conclude that :

- The existence of a constant passive current is not related to the presence of species detectable by Raman Spectroscopy.
- The ratio between α-Fe_2O_3 and Fe_3O_4 depends on anions and, like the value of steady-state current, increases from H_2SO_4 to H_3PO_4.

This work has to be pursued by further measurements just below the range where the hematite/magnetite mixture is formed. From the present measurements, it is possible to conclude that the presence of crystalline oxide or oxihydroxide in α- or γ- modification in the young passive film is not probable. The structure of this young passive film may be polymeric, like with a-FeOOH structure containing, as proved in(4)a certain amount of Fe(II) ions.

REFERENCES

1. J. Dünnwald, A. Otto, Fresenius Z. Anal. 319 (1984) 742.
2. M. Froelicher, A. Hugot-Le Goff,C. Pallotta, R. Dupeyrat, M. Masson "Passivity of metals and Semiconductors", Froment Ed. Elsevier Science Pub. (1983) 101.
3. M.Keddam,J.F. Lizee,C.Pallotta,H.Takenouti, J. Electrochem. Soc. 131 (1984) 2016.
4.M.Froelicher,A.Hugot-Le Goff,V.Jovancicevic, R. Dupeyrat, M.Masson, J.Phys. C10 (1983) 187.
5. B. Agius, S. Siejka, J. Electrochem. Soc., 122 (1975) 723.
6. M. Keddam, C. Pallotta, J. Electrochem.Soc. 132 (1985) 781.

The Analysis of Silver in Germanium Selenide Photoresist by Anodic Stripping Voltammetry

P. G. Huggett[1] and J. Greenaway

RCA Laboratories, CH-8048 Zurich, Switzerland

M. L. Hitchmen

Department of Pure and Applied Chemistry, University of Strathclyde, Glasgow, Scotland G1 1XL

ABSTRACT

Germanium Selenide (Ge_zxSe_{1-x}, x=0.1-0.3) has shown considerable promise as a very high resolution photoresist when sensitized with silver deposited from an aqueous solution. However, the sensitization step has been found to be irreproducible for films prepared in different batches. It is therefore necessary to assess the silver uptake rate for each production batch. This paper will demonstrate how it is possible to assay absolutely the deposited silver by anodic stripping voltammetry. The technique is shown to be much quicker than the currently accepted analysis by X-ray fluorescence spectroscopy and also to be of reasonable accuracy and precision, provided background currents are subtracted from the voltammogram.

INTRODUCTION

The silver sensitized germanium selenide/polymer, bilevel photoresist system offers considerable advantages over conventional photoresists by extending the capabilities of optical lithography into the submicron regime (1,2). Sensitization of the films is performed by immersion in a solution of $AgNO_3$ or $KAg/CN)_2$ which deposits silver. However, this reaction is very dependent upon the nature of the surface of the germanium selenide and this leads to variations from batch to batch in the reaction rates and induction times, even when films are evaporated under very stringent process parameters (3,4). Therefore it is necessary to assess each batch of films produced for the silver uptake rate in order to achieve reproducible photolithographic sensitivity. This has previously been done by X-ray fluorescence spectroscopic analysis (XRF) of sacrificial samples (3), but this technique, whilst highly accurate, requires calibrated sub-standards and is capital intensive and slow.

We have investigated the electrochemistry of the sensitizing reaction, in an attempt to measure the amount of silver deposited and to elucidate the mechanism of the reaction, by potentiometry and anodic stripping voltammetry. This communication describes the analysis technique and compares results with those from XRF spectroscopy. The method is shown to be a fast, reliable and absolute method of adequate precision for the assay of silver in germanium selenide photoresist films. A full discussion of the mechanism of the reaction will appear in a forthcoming paper (5).

EXPERIMENTAL

Approximately 250nm thick germanium selenide ($Ge_{15}Se_{85}$) films were prepared, as described earlier (4), by evaporation onto scrupulously clean substrates. Substrates for XRF analyses consisted of 2 inch silicon wafers. Electrodes for electrochemical analyses consisted of a polymer coated 25x10mm quartz chip with a 100nm layer of sputtered gold and a top coating of germanium selenide. Electrical connection was made by a gold plated clip which punched through the underlying gold film. The edges of the chip and the atmosphere/electrode/electrolyte triple interface were coated with PMMA to avoid edge effects.

Sensitizing and stripping was carried out in 0.1M $KAg(CN)_2$ buffered at ph10 and thermostatted at 25°C. The counter electrode consisted of a 10x25mm platinum foil held 20mm away and parallel to the germanium selenide electrode. The reference electrode was a saturated calomel electrode (SCE) separated from the working solution by a tube with a frit filled with 0.1M KCN solution to prevent the SCE clogging with AgCl. An air ambient was employed since no differences were found when the experiments were carried out with degassed solvents under nitrogen atmosphere. Electrical measurements were performed with in-house instrumentation. Stripping voltammetry was commenced at the rest potential of the system (ca -0.275V vs SCE) and then the potential was increased by a linear ramp to +1V with respect to the SCE at a rate of 13mV/s.

RESULTS

Two typical traces of current vs voltage with respect to the SCE are shown in Figure 1. Each plot shows 3 peaks which are all assignable to forms of silver; the exact assignment of the peaks will be discussed in a forthcoming paper. The absolute amount of silver stripped off can be determined from the area under the peaks. However, it is clear from the figure that background currents vary from sample to sample. Therefore, in order to subtract the background, it is necessary to apply a different correction for every run. We tried several protocols for background subtraction. The only successful method was to extrapolate the peak flanks to the base line as represented by the shaded areas in Figure 1(a).

The amounts of silver represented by the shaded areas are shown in the Table together with the results of the XRF analyses on the same evaporation batches. The Table shows the results from seven batches, each sample being sensitized for 3 minutes. The XRF data are the mean of 2 samples with an estimated error of better than $\pm 0.5 \mu g/cm^2$. The electrochemical data are the mean of 6 samples and at the 95% confidence level, there is an error of $\pm 2.0 \mu g/cm^2$ when total areas under the curves are taken, and of $\pm 0.9 \mu g/cm^2$ when the background current is subtracted. The larger error for the data using the total area probably represents the variability of the background current. For the corrected values of the silver content the agreement with the XRF values is good.

CONCLUSIONS

We have shown that stripping voltammetry is a useful technique for the absolute assay of silver in germanium selenide photoresist films. Unlike the established XRF and wet chemical analyses, the method offers a fast turn around with sufficient reliabilty for analyses of silver, which would be essential should germanium selenide photoresist be implemented on a wafer fabrication line.

REFERENCES

1. A D Doare, A Heller (eds), Proc.Symp. Inorg. Resists, ECS-82-9, (1982).

2. K L Tai, W R Sinclair, R G Vadimsky, J M Moran, J.Vac.Sci.Technol. 16, 1977 (1979).

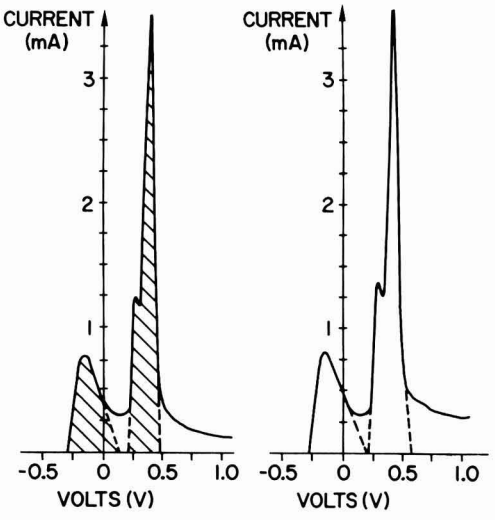
3. S M Vincent, T Y Kometari, Proc.Symp. Inorg. Resists, ECS-82-9, 169, (1982).

4. P G Huggett, K Frick, H W Lehmann, Appl. Phys.Lett., 42, 592, (1983).

5. P G Huggett, J Greenaway and M L Hitchman, results to be published.

Table Comparing Silver Analyses by XRF and Stripping Voltammetry

Evaporation Batch No.	Silver Content ($\mu g/cm^2$) XRF	Voltammetry Uncorrected	Voltammetry Background Subtracted
1	12	17	13
2	16	24	18
3	14	24	17
5	13	17	13
6	15	22	16
7	13	16	14



Voltammograms for stripping silver from silver sensitised germanium selenide

Note: differences in the contributions of the background currents

[1]Present address: Plessey Research (Caswell) Limited, Caswell, Towcester, Northants, England NN12 8EQ.

Manuscript received Aug. 19, 1985.

Laboratories RCA Limited assisted in meeting the publication costs of this article.

Alkenylsilane Sulfone Copolymers and Terpolymers as Electron-Beam-Sensitive Positive Resists for Two-Layer Systems

Antoni S. Gozdz, Harold G. Craighead, and Murrae J. Bowden

Bell Communications Research, Incorporated, Murray Hill, New Jersey 07974

The continuing trend towards higher resolution and smaller feature sizes in integrated circuitry has led to the development of multi-layer resist processing schemes to achieve submicron resolution on topographical features [1]. A variety of organosilicon polymers have been investigated in the past decade as potential oxygen reactive ion etching (O_2 RIE) resistant resists for such applications. Although sensitive negative resists for two-layer applications have been developed [2], the sensitivity of similar positive resists is low [3].

Several years ago researchers at RCA reported [4] that poly(vinyltrimethylsilane sulfone) (PVTMSS) is a sensitive positive resist useful as a reactive ion etching (RIE) mask in two-layer resist systems. However, we found that this polymer is difficult to prepare in a soluble form and in a satisfactory yield. In this communication, we report an efficient synthesis, properties and lithographic performance of soluble poly(silane sulfone)s in which the silicon-bearing group is separated from the main chain by one or more methylene groups.

EXPERIMENTAL

Polymers suitable as e-beam resists were obtained by a UV-initiated terpolymerization of allyltrimethylsilane (ATMS) with at least a 6-fold molar excess of 1-butene and sulfur dioxide or in a similar reaction between 3-butenyltrimethylsilane (BTMS) and sulfur dioxide used as a solvent and monomer at −20°C. The polymerization was carried out in sealed Pyrex glass ampoules into which the monomers were transferred using vacuum line techniques. Resist films ca. 3000 Å thick were spun from 3.5% solutions of the polymers in cyclopentanone, and after soft-baking at 120°C they were exposed at 20 keV. Patterns were developed with 1:5 amyl methyl ketone/amyl alcohol solutions and transferred into 1.2 μm-thick hard-baked HPR-204 photoresist by O_2 RIE.

RESULTS AND DISCUSSION

Although poly(olefin sulfone)s are easily degraded upon irradiation, only poly(1-butene sulfone) (PBS) has found wide application as a sensitive, positive e-beam resist [5]. In spite of its many unique properties, its major drawback is its lack of resistance to the various plasma etching techniques used in integrated circuit manufacturing. The introduction of silicon into its structure as reported by the RCA group [4], was expected to increase its O_2 RIE resistance because of the formation of an SiO_x layer on top of the resist. Unfortunately, we were unable to reproduce the results reported by the RCA group. By following the reported procedure, we could obtain only small amounts of insoluble polymer. However, we prepared and isolated a soluble material under conditions different from those reported in the mentioned patent. After precipitation into methanol, the polymer became insoluble due to hydrolysis of the trimethylsilyl group [6].

Since the solubility of poly(olefin sulfone)s is known to increase with increasing side chain length [7], and an increased reactivity of allylsilanes is well documented [8], we decided to synthesize poly(allyltrimethylsilane sulfone) (PATMSS). This copolymer is insoluble, as is its carbon analog, poly(4,4-dimethyl-1-pentene sulfone) [7]. However, we found that PATMSS may be solubilized by introducing at least 25−30 mol-% of 1-butene into the polymer chain by a UV-initiated terpolymerization of ATMS, 1-butene and SO_2 at below-ambient temperatures, preferably below −10°C. Modeling studies and chemical analyses indicate that ATMS is ca. 9 times more reactive towards SO_2 or SO_2-capped growing radicals at −20°C than is 1-butene, while vinyltrimethylsilane (VTMS) is ca. 6 times less reactive. Therefore, the successful preparation of a soluble terpoly(ATMS butene sulfone) requires that 1-butene be present in at least a 6-fold molar excess vs. ATMS and that UV radiation be used to initiate the polymerization. If *tert*-butylhydroperoxide is used, an insoluble fraction, enriched in ATMS, was always obtained. Moreover, the polymerization should be carried out to low conversion (10−15%), to avoid an unacceptably heterogeneous terpolymer with inferior lithographic properties.

Very recently, we have found that 3-butenyltrimethylsilane forms a soluble and stable polysulfone which contains 14.6 wt-% Si. In view of the problems associated with PVTMSS and terpoly(ATMS butene sulfone)s, this material is being studied as a very promising poly(silane sulfone) for two-layer applications.

The low reactivity of VTMS may be explained by a steric hindrance caused by a relatively bulky trimethylsilyl group attached to the double bond. The *t*-butyl group in 3,3-dimethyl-1-butene is bulkier and this compound does not copolymerize with SO_2. Also, the previously reported insolubility of poly(olefin sulfone)s

obtained from lower and branched olefins was explained as a result of their high cohesive energy density [7]. Bowden et al. [5] have found that polymerization of a 1:1 molar mixture of 1-hexene and SO_2 at O°C gave a product containing a gel fraction which was attributed to cross-linked polymer formed via hydrogen abstraction and chain transfer reaction. Similar arguments may be invoked to explain the insolubility of PATMSS.

The terpoly(ATMS butene sulfone)s containing less than 70 mol-% of ATMS (vs. butene) are high-molecular weight polymers ($M_n > 2-3*10^5$, M_w/M_n = 2–2.5 by GPC, $[\eta]$ = 150–250 cm^3/g in MEK at 30°C), soluble in a wide range of organic solvents. Their solubility varies with the ATMS/butene ratio. The terpolymers are thermally stable in air up to 170–180°C (TGA) and their T_g was 99±1°C (DSC). Initial data indicate that poly(3-butenyltrimethylsilane sulfone) (PBTMSS) has similar properties.

Lithographic sensitivity of the terpolymers containing 60–70 mol-% of ATMS (12–13.5 wt-% Si) and of PBTMSS to a 20 keV e-beam was 1.2–2.5 $\mu C/cm^2$, dependent on the substrate and development conditions. The terpolymers were used as top imaging layers for O_2 RIE pattern transfer into a thick planarizing layer of a conventional photoresist. Scanning Auger spectroscopic studies showed that they degraded rapidly under O_2 RIE conditions to a 10–100 Å thick SiO_x layer on top of degraded polysulfone. This layer was sufficient to provide protection against O_2 RIE for the underlying planarizing layer. Submicron resolution with vertical walls was readily attained (Fig. 2). However, the O_2 RIE processing latitude of these terpolymers is rather narrow, since their final performance is the result of two competitive processes: oxidative degradation and vaporization, and SiO_x protective layer formation. Thus, under harsher RIE conditions the first group of processes prevail and the resulting patterns contain many defects.

In conclusion, we have synthesized soluble poly(alkenylsilane sulfone)s by a UV-initiated copolymerization of 3-butenyltrimethylsilane with SO_2 or terpolymerization of allyltrimethylsilane with an excess of 1-butene and sulfur dioxide. Their sensitivity to a 20 keV e-beam is ca. 1.5 $\mu C/cm^2$ and contrast ca. 1.5–2.5. They are promising for use as sensitive, positive imaging layers for two-layer pattern transfer techniques.

REFERENCES

1. B.J. Lin, in: L.F. Thompson, C.G. Willson and M.J. Bowden, eds., Introduction to Microlithography, ACS Symp. Series No. 219, Washington, D.C. 1983, p.287-350
2. M. Morita, A. Tanaka, S. Imamura, T. Tamamura, and O. Kogure, Japanese J. Appl. Phys., *22*, L-659 (1983)
3. E. Reichmanis and G. Smolinsky, in: C.G. Willson, ed., Adv. Resist Technol., Proc. SPIE *469*, 1984, p.38
4. K.B. Kilichowski and T.R. Pampalone, U.S. Pat. 4,357,369 (1982); N.V. Desai, E.S. Poliniak, U.S. Pat. 4,396,702 (1983)
5. M.J. Bowden and L.F. Thompson, J. Appl. Polym. Sci., *17*, 3211 (1973)
6. A.S. Gozdz and M.J. Bowden, submitted to Polymer Communications
7. K.J. Ivin, H.A. Ende and G. Meyerhoff, Polymer *3*, 129 (1962)
8. H. Sakurai, A. Hosomi and M. Kumada, J. Org. Chem., *34*, 1764 (1969)

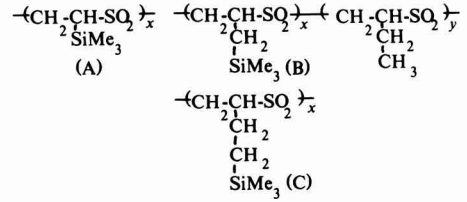


Fig. 1. Structural formulas of PVTMSS (A), terpoly(ATMS butene sulfone) (B) and PBTMSS (C)

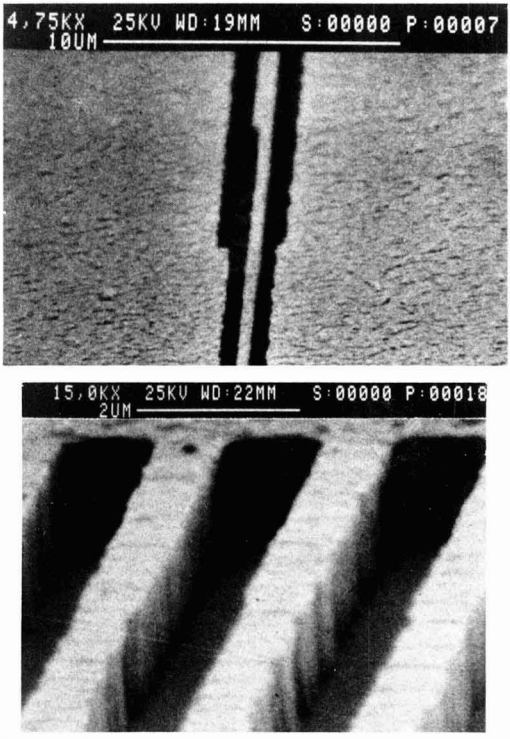


Fig. 2. Submicron pattern O_2 RIE'd into 1.2 μm-thick HPR-204 using terpoly(ATMS butene sulfone) as a top imaging layer

Manuscript received July 25, 1985.

Bell Communications Research assisted in meeting the publication costs of this article.

Microphotoelectrochemical Etching of n-GaAs Using a Scanned Focused Laser

R. D. Rauh* and R. A. LeLievre

EIC Laboratories, Incorporated, Norwood, Massachusetts 02062

Localized photoelectrochemical reactions at semiconductor-electrolyte interfaces have been employed for producing photographic images, diffraction gratings, optical lenses, and metal contacts (1). Generally, fabrication of microetched structures have been accomplished at low light intensities (<100 mW/cm^2) by projecting an image onto the electrode surface and allowing anodic dissolution to occur preferentially in illuminate portions of n-type crystals. An alternative method to forming an etched structure is to guide a focused laser beam in a predefined pattern along the electrode surface. In this way, the etched figures might be "micromachined" with micron scale features without using projection masks. Potential applications include customized marking of semiconductor wafers incorporating integrated circuits, micromachining of sensor elements such as very small scale gas chromatographic columns (2), and direct ruling of grating structures. However, high photoetching rates are necessitated by this approach in order to complete an etched image in a reasonable time.

In this communication, we demonstrate high rate photoassisted etching of <100> n^+-GaAs (N_d = 1.5 x 10^{18} cm^{-3}, Laser Diode, Inc.) using a scanned focused laser. The etching solution is 10% aqueous KOH, in which oxidative dissolution of III-V compounds is mediated by holes (3). The process is accelerated in n-type crystals by holes provided by above bandgap light and the resulting photovoltage that develops between dark and illuminated regions (4).

The experimental arrangement is a variation of that described previously (5). The output of a 1 mw HeNe laser (Uniphase Model 1301) was spatially conditioned, reflected vertically through a cube beam splitter and focused through the etching solution onto the crystal surface using a microscope objective (Melles Griot, 20X, N.A. = 0.5). An eyepiece with reticle placed above the beam splitter permitted visual observation of the focused spot and estimation of its diameter, about 2 μm. The total intensity of the unattenuated beam exiting the objective was determined radiometrically to be 480 μW. A knife edge measurement of the focused beam profile revealed a nearly Gaussian intensity distribution, with a small amount of anomalous "tailing" out to about 15 μm diameter, accounting for <1% of the total intensity. The crystal's position was controlled by two stepper motors operating at an x-y translation stage in 1 μm increments at rates up to 350 Hz. Computer control of the stage motion and of an electronic shutter were employed to "write" figures produced on the monitor directly onto the crystal with user specified x and y scaling.

Holes were etched in the n^+-GaAs surface with the focused beam at a variety of light intensities (16 W/cm^2 to 16 kW/cm^2) and exposure energies (5 to 1.6 x 10^5 J/cm2). The resulting hole diameters and, where possible, hole profiles were determined using optical microscopy and a Sloan Dektak mechanical profilimeter. Figure 1 shows that the etched hole diameters become progressively larger with increasing energy. To first order, this effect is independent of laser intensity, at least within the intensity region investigated. The same result was obtained with dilute H_2O_2/H_2SO_4 and with Br_2/methanol etchants as well as with crystals of different orientation and doping level.

The theoretical hole diameters expected for etching with a Gaussian beam of several ($1/e^2$) diameters, W_o, are superimposed on Figure 1. Evidently, the experimental hole diameters increase much too sharply with energy to be explained by this mechanism. Furthermore, measurement of the hole profiles revealed conical depressions rather than holes with narrow centers and a shallow "halo". The latter shape might be expected for our slightly nonideal Gaussian beam. Explanations for Figure 1 involving localized heating are not consistent with the independence of the result on light intensity. Indeed, it can be shown by simple theoretical considerations (6) that the local temperature rise will be less than 3°C for the highest

*Electrochemical Society Active Member.

Manuscript received Aug. 12, 1985. This was Paper 454 presented at the Las Vegas, Nevada, Meeting of the Society, Oct. 13-18, 1985.

intensity used. An explanation which is consistent both with the observed broadening and hole profile is the diffuse scattering of the focused light within the growing hole. This might be expected under many conditions of "high rate" etching, where revealed surfaces can have a rough microstructure (4,7). The scattered light would be absorbed by the walls, thus causing their erosion by photoetching.

An example of high resolution etching of a character set is shown in Figure 2, demonstrating that this method can be used for the custom marking of wafers. In this case, the characters are formed from an array of pits 0.3-0.5 μm deep, photoetched at 32 J/cm^2. The smallest alphanumeric characters that we have etched in n$^+$-GaAs using this apparatus had an average unit size of 4 x 4 μm, equivalent to a character density of 7 x 10^6/cm^2.

The directed laser etching process would find increased utility if higher aspect ratios could be attained without loss of spatial resolution. Significantly, Podlesnik and coworkers (8) recently reported on photoelectrochemical hole drilling in n-GaAs using focused laser light and several different etchants. Using a frequency doubled Ar$^+$ laser operating at 257 nm, these authors produced holes >100 μm deep and 1-4 μm in diameter, but only at power densities of ≈0.1 W/cm^2. At this power, etch rates were about 0.003 μ/sec, compared to >10 μ/sec in the present work. At low etching rates, specular features are produced, and the hole grows by "light guiding". In order to get the same effect at high intensities, conditions of high rate photoelectrochemical polish-etching must be developed. Work is continuing along these lines in our laboratory.

Acknowledgment

This work was supported by the Office of Naval Research.

EIC Laboratories, Incorporated, assisted in meeting the publication costs of this article.

REFERENCES

1. T. Inoue, A. Fujishima and K. Honda, This Journal, 127, 1582 (1980); R.M. Osgood, Jr., A. Sanchez-Rubio, D.J. Ehrlich and V. Daneu, Appl. Phys. Lett., 40, 391 (1982); F.W. Ostermeyer, Jr., P.A. Kohl and R.H. Benton, ibid., 43, 642 (1983); R.H. Micheels, A.D. Darrow III and R.D. Rauh, ibid., 39, 418 (1981).
2. S.C. Terry, J.H. Jerman and J.B. Angell, IEEE Trans. Electron Devices, ED-26(12), 1880 (1979).
3. H. Gerischer and W. Mindt, Electrochim. Acta, 13, 1329 (1968).
4. F. Kuhn-Kuhnenfeld, This Journal, 119, 1063 (1972).
5. C.A. Kavassalis, D.H. Longendorfer, R.A. LeLievre and R.D. Rauh, Mat. Res. Soc. Symp. Proc., Vol. 29, 151 (1984).
6. M. Lax, J. Appl. Phys., 48, 3919 (1977).
7. P.A. Kohl, C. Wolowodiuk and F.W. Ostermeyer, Jr., This Journal, 130, 2288 (1983).
8. D.V. Podlesnik, H.H. Gilgen and R.M. Osgood, Jr., Appl. Phys. Lett., 45, 563 (1984).

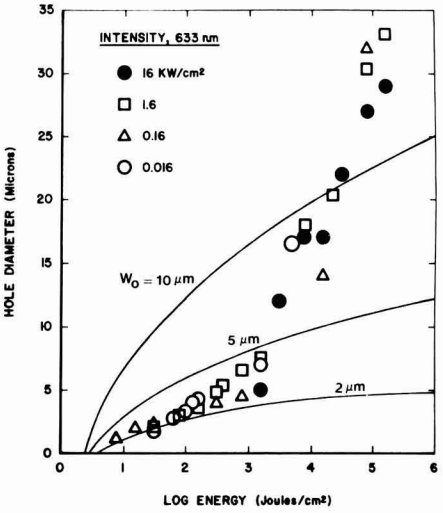


Fig. 1. Etched hole diameters vs. exposure energy for 2 μm diameter laser spot on n$^+$-GaAs in 10% KOH; also, theoretical diameters at >0.1 μm depth for a Gaussian beam profile.



Fig. 2 Photoelectrochemically etched character set in n$^+$-GaAs using scanned 2 μm diameter HeNe laser spot (160 W/cm^2, 0.2 sec/point). Holes appear raised due to illusion from reflected light.

Elimination of Flux Transients in Molecular Beam Epitaxy

P. A. Maki,* S. C. Palmateer, A. R. Calawa,† and B. R. Lee

General Electric Company, Electronics Laboratory, Syracuse, New York 13221

Film thickness reproducibility in the growth of group III-V compounds by molecular beam epitaxy (MBE) depends on the substrate temperature and on the temperature stability of the group III source. The In, Ga or Al melts are contained in pyrolytic boron nitride (PBN) crucibles of various shapes and sizes. The basic concepts of crucible design for achieving uniform deposition over 2 or 3 inch diameter wafers are well understood. [1,2] Unfortunately for many of these cell configurations the melt temperature is affected by the radiation shielding provided by the beam shutter [3]. A flux transient typically lasting 1-3 minutes occurs when the shutter is opened and the cell establishes a new equilibrium temperature. In this letter, we report on a unique PBN crucible which simultaneously exhibits a low flux transient and provides excellent beam uniformity.

Uniformity of molecular beam patterns depends on the source to substrate spacing and the angular flux distribution at the source. The best uniformity is obtained with a large source to substrate spacing and an emitting flux distribution at the cell orifice which is isotropic in the solid angle subtended by the substrate [2]. A conically shaped crucible has these flux characteristics as well as a large cell orifice for high flux density. Flux uniformity at the source is attained by allowing a direct path to the entire substrate from each point on the melt surface. The atoms which escape the crucible without wall collisions are the main component of the flux. The cone angle and hence depth of the crucible is determined by the solid angle subtended by the cell orifice and substrate peripheries. This depth limits the cell volume and reduces practical usage between fillings. Schaff found that partially filled deep crucibles exhibit a smaller flux transient while retaining a large volume [4]. This is because the melt temperatures deep within the furnace are less sensitive to changes in radiation shielding at the cell orifice. Deep crucibles tend to collimate the beam, however, which limits uniformity. [2,4]

Our approach to improving the flux transient behavior is to use a two crucible configuration which takes advantage of a deeply recessed melt while maintaining flux uniformity through the use of a beam shaping conical insert. The crucible arrangement is shown in Figure 1. The cell is assembled from a conventional Varian GEN II furnace equipped with a short thermocouple and a 40cc crucible which holds the group III melt [5]. A 16cc conical crucible with its bottom ground off is centered within the 40cc crucible so that intimate contact occurs near their rims.

In our initial studies, we have implemented this cell as a gallium source. Figure 2 shows a plot of the Ga beam equivalent pressure (P_{BE}) versus time for both the new cell and a conventional conical cell. The double crucible cell exhibits only 5% transient over 4 minutes while the conventional cell exhibits a 32% transient over the same time period. A uniformity map of a Si-doped GaAs film grown on a 2 inch diameter substrate is shown in Figure 3. The doping and thickness uniformity is less than ± 2%. Our initial studies indicate that the GaAs material quality is equivalent to that obtained in our machine from the conventional furnace design [6]. The oval defect density is also comparable ($<500/cm^2$).

The small flux transient observed from this cell reflects a more stable melt temperature. This is attained both as a result of the melt location deep in the furnace and through the additional radiation shielding provided by the crucible insert. Beam uniformity is maintained because the recessed aperture of the crucible insert presents a constant melt area to all points on the substrate. A further desirable feature of this cell is its lower operating

* School of Electric Engineering, Cornell University, Ithaca, New York 14853

† Cornell Lecturer. Permanent Address: Lincoln Laboratory, Massachusetts Institute of Technology, Lexington, Massachusetts 02173

temperature. Using the cells as Ga sources, the temperatures required for a GaAs growth rate of 1 μm/hr are 1100°C for the new cell, 1000°C for the deep crucible cell and 1200°C for the standard conical cell. The temperatures cannot be directly compared since the thermocouple touches the bottom of each cell and is therefore at a different position for the shallower conical cell. However, we have observed that the power requirements are slightly lower than for the conventional conical cell. We believe this reflects an overall cell temperature which is lower than a conical cell. The lower cell temperature is significant since hot cell parts are thought to be a source of impurities in the MBE environment.

We have demonstrated a practical crucible combination which produces excellent film uniformity with little transient. The usable cell capacity is increased by approximately two times. While demonstrated for gallium, this approach should work equally well for other group III elements.

ACKNOWLEDGEMENTS

We would like to thank J. Berry, JCM Hwang, and R. Finicle for helpful discussions and assistance in this work.

REFERENCES

(1) For a discussion of cell design, see for example K. Ploog, "Molecular Beam Epitaxy of III-V Compounds," Crystal Growth Properties and Applications, 1980, Vol. 3, Springler-Verlag.

(2) P.E. Luscher and D.M. Collins, "Design Considerations for Molecular Beam Epitaxy Systems," Progress in Crystal Growth and Characterization, 1979, Vol. 2, pp. 15-32, Pergamon Press Ltd.

(3) The authors are most familiar with the problem on the Varian GEN II system. Private communications with colleagues indicates that the problem exists to varying degrees on other machines.

(4) W. Schaff, PhD Thesis, Cornell University, 1984.

(5) This work was performed on a Varian GEN II. For details on the machine and cell configuration refer to the Varian GEN II operators manual.

(6) S.C. Palmateer, PhD Thesis, Cornell University, 1985.

Manuscript received June 13, 1985.
General Electric Company assisted in meeting the publication costs of this article.

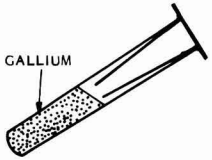


Figure 1. Diagram of Crucible Assembly

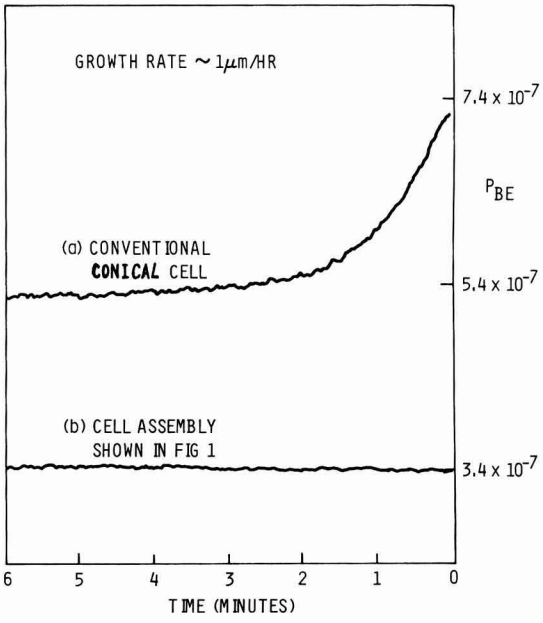


Figure 2. Comparison of Gallium Cell Transient as Measured with Beam Flux Monitor

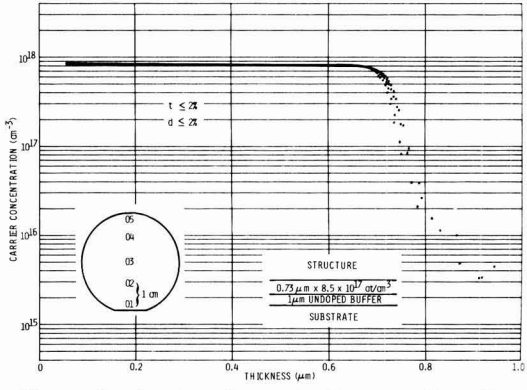


Figure 3. Doping Concentration as a Function of depth from the surface of a Si-doped GaAs Film Grown at 600°C with the Substrate Rotated at 10 RPM

A Measurement of the Effect of Intrinsic Film Stress on the Overall Rate of Thermal Oxidation of Silicon

J. K. Srivastava* and E. A. Irene*

Department of Chemistry, University of North Carolina, Chapel Hill, North Carolina 27514

The effects of intrinsic film stress on Si oxidation kinetics has been receiving considerable attention in recent years(1-5). Oxidation models have appeared that relate the Si-SiO_2 interfacial intrinsic stress to both the interface reaction between oxidant and Si and to a stress altered oxidant transport. The experimental measurement of the film stress itself has been reported, although to date the data is rather sparse(1,6). Recently, in our laboratory more extensive intrinsic stress measurements have been made and these measurements will be reported separately. So while the existence of a compressive intrinsic SiO_2 film stress has been experimentally verified, the experimental verification of the effects of the stress on oxidation kinetics remains a matter of speculation within the various models.

Along with the development of an intrinsic film stress due to the molar volume change during the oxidation of Si, a SiO_2 film density increase occurs and has been measured (6, 10, 11). The density increase of 2-3% is too large to have arisen from the stress optical constant and has therefore been attributed to an accomodation of system to the buildup of stress (6). We consider the intrinsic stress and density increases to have a common origin in the nature of the Si oxidation process on a single crystal Si surface. The present communication provides a rather direct experimental measurement of the effect of the compressive intrinsic film stress and/or oxide density on the Si oxidation kinetics.

We report the result of a simple but careful experiment that shows the parallel between stress and/or density and kinetics in the thicker film regime of Si oxidation where the film thickness, L, is greater than 100nm, and at an oxidation temperature of 800°C. In this thickness range, the transport and interfacial effects are nearly equivalent. The results show a decrease in the rate of oxidation as had been anticipated for a compressive stress and/or for a higher density film.

EXPERIMENTAL PROCEDURES

All the Si wafers used were lightly P doped n-type (100) oriented commercially available high quality single crystal Si slices. The wafers were cleaned by a slightly modified RCA procedure(7) and followed with an HF dip and thorough deionized H_2O rinse. A batch of ten wafers was oxidized in pure dry O_2 at 800°C to an oxide thickness of between 100-110nm. This thickness was chosen to be near a half of an ellipsometric period (about 140nm for 632.8 nm light) so that both SiO_2 film thickness and refractive index could be accurately measured. The batch was then split in half with one half receiving a one hour 1000°C anneal in pure Ar so as to relieve the stress. This anneal was found to be more than adequate for this purpose(6). At this point all the wafers were measured by ellipsometry. The ellipsometer was of research quality with the capability of polarizer and analyzer resolution to 0.01° and was carefully aligned prior to use. The Δ and Ψ values were converted to SiO_2 thickness and refractive index using a modified version of McCrackin's program(8). We conservatively estimate a thickness and index accuracy of better than 2% and 0.005, respectively. The batch halves were recombined and then the entire batch was oxidized at 800°C in pure O_2. Wafers were selected from each half batch (the annealed and unannealed halves) at various oxidation times so that film thickness and refractive indices could be remeasured.

EXPERIMENTAL RESULTS AND DISCUSSION

Table 1 shows a comparison of the

film thicknesses and refractive indices after the final 800°C oxidation for the oxidation time noted in the left most column. The SiO_2 film thickness is reported as the difference between the initial 800°C oxidation to produce the 100-110nm samples and the final oxidation at 800°C to compare the unannealed and annealed samples. In all cases the stress annealed samples grew oxide more rapidly than the stressed samples. The refractive indices indicate that the unannealed samples had the higher density and stress throughout the final oxidation as had been previously reported (6).

Within the Deal and Grove model(9) the transport of oxidant is governed by the parabolic rate constant, k_p and is given as:

$$k_p = 2CD/\rho \qquad [1]$$

where C is the dissolved oxidant in SiO_2, D is the oxidant diffusivity and ρ is the SiO_2 density. The transport term can then be reduced by either a decrease in D or an increase in ρ or both. Recently, several studies have shown the likelihood of the intrinsic compressive SiO_2 film stress decreasing D (4,5). Also several studies have shown that the oxide density, ρ, increases with decreasing oxidation temperature(10,11). The experiments reported herein cannot distinguish between these two factors, as both stress and density increase with decreasing oxidation temperature and both anneal out with high temperature treatment (6).

For the interface reaction, a revised formulation now includes the effect of film stress and oxide viscosity (6, 12). In this model (12), the interface reaction constant k_1 is given as:

$$k_1 = kC_oC_{Si}\sigma/\eta \qquad [2]$$

where k is a constant, C_o and C_{Si} are the oxygen and silicon concentrations, σ is the intrinsic stress and η is the viscosity of SiO_2. The compressive SiO_2 stress is tensile in Si thereby stretching the Si - Si bonds and increasing the likelihood for oxidation. At low temperatures σ is larger (1, 6) but so is η hence we can neither distinguish σ from η effects nor k_1 from k_p effects. Despite these difficulties, we have demonstrated that the overall rate of oxidation of Si is reduced in low temperature grown thermal oxide films on Si, and the reduction is linked to the intrinsic film stress. At the present time, more detailed studies aimed at separating film stress and density effects are in progress in our laboratory.

*Electrochemical Society Active Member.
Manuscript received Aug. 9, 1985.

Acknowledgment

This work was supported in part by the Office of Naval Research (ONR).

The University of North Carolina assisted in meeting the publication costs of this article.

REFERENCES

1. E.P. EerNisse, Appl. Phys. Lett., 35, 8(1979).
2. W.A. Tiller, J Electrochem. Soc., 127, 625(1980).
3. E.A. Irene, J. Appl. Phys., 54, 5416(1983).
4. A. Fargeix, G. Ghibaudo and G. Kamarinos, J. Appl. Phys, 54, 2878(1983).
5. R.H. Doremus, Thin Solid Films, 122, 191(1984).
6. E.A. Irene, E. Tierney, and J. Angillelo, J. Eelectrochem. Soc., 129, 2549(1982).
7. W. Kern and D.A. Puotinen, RCA Review, 31, 187(1970.
8. F.L. McCrackin, NBS Technical Note 499, U.S. Government Printing Office, Washington, D.C.
9. B.E. Deal and A.S. Grove, J. Appl. Phys., 36, 3770(1965).
10. E.A. Taft, J. Electrochem. Soc., 125, 968(1978).
11. E.A. Irene, D. Dong, and R.J. Zeto, J. Electrochem. Soc., 127, 396(1980).
12. E.A. Irene, J. Appl. Phys. 54, 5416 (1983).

Table I

SiO_2 Film Thickness and Refractive Index Comparsion for Annealed and Unannealed Samples

Oxidation Time of Second Oxidation (hrs.)	Unannealed Thickness (Å)	Unannealed Ref. Index	Annealed Thickness (Å)	Annealed Ref. Index
1	9	1.474	23	1.463
2	15	1.475	44	1.465
4	30	1.475	83	1.465
9	78	1.474	163	1.466
19	178	1.473	267	1.466

JOURNAL OF THE ELECTROCHEMICAL SOCIETY

REVIEWS AND NEWS

NOVEMBER 1985

Abstracts of Recent News Papers

Presented at the Las Vegas, Nevada, Meeting of the Society, October 13-18, 1985

573 RNP Laser Electrochemical Etching of Semiconductors: *G. Valasco* and *J. Ph. Schnell*, Thomson-CSF/LCR, Corbeville, France

Laser electrochemical etching of semiconductors is increasingly involved in the design of high speed electronics and optical devices such as millimeter wave electron oscillators, holographic gratings and patterns, integral lenses for diode lasers, and submicron gratings for DFB lasers. In this paper, some problems associated with the basic process of photoelectrochemical etching, including methods of improving spatial resolution toward submicron patterns and reduction of surface roughness are discussed. These can be partly overcome by a proper choice of the etching solution, electrical polarization, semiconductor nature, and by modifying the photogenerated carriers lifetime by techniques such as ion implantation. Current results on these topics are reviewed.

574 RNP Surface Raman Microscopy as an *In Situ* Probe of Laser Microfabrication Processes: *R. P. Van Duyne, R. A. Altkorn*, and *K. L. Haller*, Dept. of Chemistry, Northwestern University, Evanston, IL 60201

The intensity of a surface Raman spectrum is independent of the area illuminated. As a result, surface Raman and related spectroscopies form a family of *in situ* diagnostic techniques for laser microchemical fabrication processes. A combined surface Raman microprobe and laser microfabrication apparatus is discussed. Applications will center on laser direct-write processes for the deposition of Ag, Cu, and Au metallization. Since these materials support surface enhanced Raman scattering, unprecedented mass sensitivity can be obtained. The detection of adsorbates at the attomole level is described.

575 RNP Laser-Induced Metallization from Electrolytic Solutions on Semiconductor and Polymer Substrates: *J. Zahavi* and *S. Tamir*, Israel Institute of Metals, Technion, Haifa 32000, Israel, *M. Halliwell*, Wright Patterson Air Force Base OH 45433

This work is aimed at studying the feasibility of laser-induced high speed, highly selective direct plating of metals and alloys on semiconductor and polymeric substrates immersed in plating solutions without external electric current and masking procedures. A Q-Switch Nd/YAG pulse laser was used together with a commercial gold plating solution to obtain gold deposition at laser-irradiated zones on the surfaces of silicon and GaAs semiconductors and on polymide polymeric substrates. Processes and possible mechanisms involved are discussed.

576 RNP Initial Characterization of Low Temperature, Chemical Vapor Deposited Silicon Epitaxial Films: *L. S. Mason*, Dept. of Materials Science and Engineering, MIT, Cambridge, MA 02139, *R. Reif*, Dept. of Electrical Engineering and Computer Science, MIT, Cambridge, MA 02139

A low pressure CVD reactor is being used to deposit epitaxial films from a silane source gas in the temperature range of 700°-800°C. The effects of growth conditions and subsequent annealing cycles on the structural and electrical character of the films are under investigation in order to optimize the growth process. Structural information, obtained with defect etching and SIMS, has been compared with free carrier profiles obtained with spreading resistance measurements for films grown at a base pressure of 10 mtorr both with and without plasma enhancement.

577 RNP Kinetics of Titanium Silicide Formation during Rapid Thermal Processing: *P. Davies, U. Mitra, R. Shukla*, and *J. Multani*, Intel Corp., Livermore, CA 94550

The reaction of sputtered titanium thin films with single-crystal silicon substrates during rapid thermal annealing (RTA) has been investigated. The reaction products and kinetics of silicidation were characterized using TEM, ESCA, SIMS, Auger, RBS, and electrical sheet resistance measurements. The study identifies the different phases of titanium silicide formed as well as the influence and redistribution of dopants and impurities during silicidation. In addition, the strong dependence of the reaction kinetics on the ambient atmosphere as well as on the titanium film thickness has been characterized. The electrical resistance of the films produced under different RTA conditions is rationalized in terms of the materials properties and reaction kinetics of the titanium-silicon system.

578 RNP The Effect Of Intrinsic Film Stress on the Thermal Oxidation of Silicon: *J. K. Srivastava* and *E. A. Irene*, Dept. of Chemistry, University of North Carolina, Chapel Hill, NC 27514

The effect of intrinsic film stress on the thermal oxidation of Si has recently received considerable attention (1). Not only has the stress been related to a change in the oxide properties, but also to one on oxidation kinetics. Most of the available literature present models for this relationship but not experimental verification. The present work experimentally demonstrates that intrinsic stress variations parallel measureable changes in oxidation kinetics. For oxide films containing intrinsic stress as well as relaxed films, we report the difference in oxidation kinetics and film properties. (Acknowledgment: This work was supported in part by the Office of Naval Research.)

1. E. P. EerNisse, *Appl. Phys. Lett.*, **35,** 8 (1979); E. A. Irene, *J. Appl. Phys.*, **54,** 5416 (1983); A. Fargeix, G. Ghibaudo, and G. Kamarinos, *ibid.*, **54,** 2878 (1983); R. H. Doremus, *Thin Solid Films*, **122,** 191 (1984).

579 RNP XPS Studies on Surface Oxidation of Silicon by Some Cleaning Procedures: *C. Y. Wong* and *S. P. Klepner*, IBM, T. J. Watson Research Center, Yorktown Heights, NY 10598

X-ray photoelectron spectroscopy was used to analyze silicon surfaces after some standard cleaning procedures. Buffered hydrofluoric acid (BHF), RCA clean, and back-door etch (BDE) result in less than one monolayer of oxide coverage. RCA clean without BHF, heat-treatment in nitrogen ambient, and prolonged exposure to air at room temperature all result in thicker self-passivating suboxides. Wafers with arsenic ion implantation yield thicker oxides even immediately after BHF or BDE clean. Arsenic ion implantation also causes additional chemical shift of 0.3 eV on Si peak. The possible causes for these observations are discussed.

580 RNP Analysis of the Lowered Barrier Height (LB) Oxide: *N. Matsukawa, S. Morita, K. Shinada*, and *H. Nozawa*, Toshiba Corp., Semiconductor Device Engineering Lab., Komukai Toshiba-cho, Saiwai-ku, Kawasaki-shi 210, Japan

I-V characteristics of the oxide which was grown on heavily arsenic or phosphorus ion-implanted Si substrate show low barrier height of about 1.7 eV with respect to silicon conduction band. The conduction mechanism was investigated by various methods, such as temperature dependence of I-V curve, XES, SEM, and cross-sectional TEM. The results rejected possibilities of trap-assisted Frenkel-Poole-type conduction and field enhancement by rough surface asperity. The most probable mechanism is sequential direct tunneling through precipitated Si or impurity clusters.

581 RNP Circuit for Measuring Trapped Charge Produced by Avalanche Hole Injection Into SiO_2: *E. H. Nicollian*, Dept. of Electrical Engineering, University of North Carolina, Charlotte, NC 28223

A feedback circuit is described that generates an output voltage proportional to the trapped hole charge necessary to keep the injected gate current constant. Instability problems are addressed.

582 RNP Electrochemical Studies of Dendritic Failure in Electronic Devices: *B. D. Yan, G. W. Warren*, and *P. Wynblatt*, Dept. of Metallurgical Engineering and Materials Science, Carnegie-Mellon University, Pittsburgh, PA 15213

Dendritic failure of Cr-Cu-Cr metallization on alumina substrates has been studied by using a potential bias step test in bulk solutions with different pH. The short-circuit potential was observed to increase with increasing pH as a result of a decrease in dendrite growth rate. Cyclic voltammetry studies were performed on both the Cr-Cu-Cr metallization and pure metals. Electrochemical reactions were identified, and the relationship between the cyclic voltammetry experiments and the potential step tests is discussed.

583 RNP Fracture Strength of Silicon *vs.* Etched Depth: *L. D. Dyer*, Texas Instruments, Inc., Sherman, TX 75080

The purpose of this study was to measure the fracture strength of silicon *vs.* quantity etched away. A simple bending test was chosen for the strength measurement. In sawed (100) slices, both acid and base etching showed a slight initial strength decrease and a region of large scatter, coupled with differences between first- and last-cut sides. Deepest damage persisted to at least 2.5 mil. Acid etching showed an earlier increase in strength than KOH etching.

584 RNP Nucleation of CVD Tungsten Films on Insulators: *D. Bradbury* and *T. Kamins*, Hewlett-Packard Laboratories, Technology Research Center, Palo Alto, CA 94304

A major advantage of low pressure CVD tungsten films compared to sputtered aluminum films for IC metallization is the ability to deposit tungsten selectively on silicon without depositing on the insulator in the field. One area of concern when applying selective tungsten to an IC containing one or more insulating materials used to planarize high density IC's is the nucleation rate of tungsten on the various insulators exposed during the deposition. In this study, a quantitative comparison was made. Nucleation rates were found to vary widely and depended on the insulator material and the method of surface treatment prior to deposition. For example, the nucleation rate of CVD tungsten on LPCVD silicon nitride is much higher than it is on phosphorus-doped low temperature CVD oxide.

585 RNP Metal-to-Metal Capacitors for VLSI Using Plasma-Deposited Dielectrics: *B. Gorowitz, T. B. Gorczyca*, and *D. M. Brown*, General Electric Co., Corporate Research and Development, Schenectady, NY 12301

Thin (< 1000Å) silicon dioxide and silicon nitride films and combinations thereof have been used as dielectric layers of on-chip, metal-to-metal capacitors for VLSI applications. The dielectric films are formed by plasma-enhanced deposition in a hot wall, longitudinal reactor. Typical capacitance values are in the range of 5-10 × 10^4 pF/cm²; leakage current at 10V is less than 5 μA/cm²; breakdown voltage is in excess of 15V; and the deviation of capacitance within a die is less than 0.5%. The relationship of deposition parameters to properties is discussed.

586 RNP Analysis of Polymer-Based Spin-On Dopant Sources: *M. Rivera* and *E. W. Maby*, Rensselaer Polytechnic Institute, Troy, NY 12180-3590, *S. K. Gupta*, Allied Chemical Corp., Buffalo, NY 14210

Polymer-based (Accuspin) phosphorus and boron spin-on dopants have been evaluated to determine if these sources can be used in conventional semiconductor fabrication processes without compromising the electrical performance of the final product. Both p+/n and n+/p diodes have been fabricated using spin-on and ion-implantation processes. For the polymer-doped diodes, the polymer-based dopant was spun at 3000 rpm for 40s and then diffused. For the p+/n diodes, the dopant was driven in at 1050°C for 1h in a 1% oxygen/nitrogen atmosphere; for the n+/p diodes, the dopant was driven in at 1000°C for 30 min in an oxygen atmosphere. No further processing to remove polymer residue was required prior to contact metallization. Forward and reverse current-voltage characteristic were measured, and the low voltage ideality factor was calculated. The data thus obtained were nearly identical for both processes and suggest that undesired impurities from the polymer base are not present. These results have been confirmed by DLTS analysis.

587 RNP *In Situ* Doping of Polysilicon Using Boron Trichloride: *D. W. Freeman*, Texas Instruments, Inc., Dallas, TX 75265

In situ doped polysilicon films are finding greater use in VLSI processing. Boron trichloride was introduced to an LPCVD reactor during a polysilicon deposition. Gas flows, pressure, temperature, and gas ratios were varied to determine optimum deposition and doping parameters. Resistivities of 4000 μΩ-cm can be obtained at optimum processing parameters. Sheet and thickness measurements display excellent uniformity across the slice, while SIMS measurements show uniform doping throughout the film profile.

588 RNP Average Conductivity of the Silicon Layers Doped by Boron Diffusion from An Infinite Source: *F. Gaiseanu*, Research and Development Centre for Semiconductors, R 72996 Bucharest, Romania

On the basis of the previous statement showing a variation of the boron diffusion coefficient with the square root of the boron concentration, an explicit expression of the average conductivity of the silicon layers doped by boron diffusion is given. It is known that this expression consists of two terms. One of them, defined as the correction term, determines a predictable deviation from a linear law of the average conductivity as a function of the surface boron concentration exhibited by the other one. The approximation limits and the agreement with some collected experimental data are also discussed.

589 RNP An Improved Terbium-Activated Single-Crystal Phosphor for Head-Up Display Cathode Ray Tube: *G. W. Berkstresser, J. Shmulovich, D. T. C. Huo, G. Matulis, C. D. Brandel*, and *A. J. Valentino*, AT&T Bell Laboratories, Murray Hill, NJ 07974

We report a new efficient GA^{3+} substituted single crystal phosphor $(Y_{3-x-y}Tb_xLu_y)(Al_{5-w}Ga_w)O_{12})$ grown epitaxially on $Y_3Al_5O_{12}$ substrates. Gallium substitutions up to $w \simeq 2$ were made, with $y \simeq 1.4w$. We observed a 60% increase in the light output at high power density excitation regime over that achievable with the best $Tb:Y_3Al_5O_{12}$ films. The phosphor composition optimization with respect to Tb^{3+} and Ga^{3+} concentration is reported. Our results do not confirm data in the literature on the detrimental effect of Ga^{3+} substitution in epitaxial single crystal phosphors. (This work was partially supported by Air Force Contract no. F33615-83-C-1072).

590 RNP Highly Stable and High Performance Amorphous-Silicon MOS Transistors for Active Matrices: *Y. Uchida* and *M. Matsumura*, Dept. of Physical Electronics, Tokyo Institute of Technology, Oh-okayama, Meguro-ku, Tokyo 152, Japan

Nearly ideal amorphous-silicon planar MOS transistors have been proposed and demonstrated. The transistor has the native silicon dioxide gate thermally grown at 250°C inside the original amorphous silicon layer and also on the highly conductive source and drain of microcrystal silicon covered by the thick silicon-dioxide layer. Thus, it can be fabricated by only four photomasks and has negligibly few parasitic elements. The prototype transistor had a lifetime of as long as 10^{16} yr and a mobility of more than 0.6 cm²/V-s.

Corrosion Division Award
for
Summer Study in Corrosion Science

The Corrosion Division of The Electrochemical Society is offering its new Award for Summer Study in Corrosion Science to a qualified graduating senior or advanced undergraduate for the summer of 1986. This award provides a minimum grant-in-aid of $1000 and travel expenses toward a summer's (at least two months) research and study in a laboratory of a recognized institute or institution of higher learning.

The objectives of this award are as follows.

1. To stimulate and encourage active and continued participation in the field of corrosion science and corrosion protection by outstanding students of science and engineering.

2. To encourage education in this field for a student likely to attend graduate school for an advanced degree.

To be eligible for the award, the entrant must qualify in at least one of two following categories. He or she must be either (1) a graduating senior of demonstrated ability, regularly enrolled in any recognized college, university, or institute of technology in the United States or Canada, who intends to seek an advanced degree, or (2) an advanced undergraduate similarly enrolled, within six months of graduation who intends to seek an advanced degree. No limitations of sex, race, nationality, or religion are to be imposed by the Award Committee in determining the recipient of the Award.

The award shall be presented on the basis of the following material.

1. A complete transcript of the student's academic record.

2. The original and two copies of a letter, over the signature of the head of the college or department in which the student is enrolled, describing briefly the student's academic work, campus activities, and abilities.

3. The original and two copies of a letter, over the student's signature, containing a brief biographical sketch, a detailed description of the nature and extent of the student's academic work, particularly as it may relate to the field of the Award, and an outline of future plans. The student shall suggest the topic and site for the intended research and his or her basis for this choice. The student's letter should also contain a statement signifying willingness to fulfill the requirements of the Award as described in the Award Rules.

Application forms are available from the Executive Secretary, V. H. Branneky, The Electrochemical Society, 10 South Main St., Pennington, NJ 08534-2896. Deadline for receipt of completed applications is December 1, 1985, and the award winner will be announced by April 1, 1986.

SECTION NEWS

Southern California-Nevada Section



This year's recipient of the Graduate Student Research Award is Dr. Stephen L. Gipson, a 1985 Ph.D. recipient and a student of Professors Fred C. Anson and T. J. Collins, Division of Chemistry and Chemical Engineering of the California Institute of Technology, Pasadena, California.

Gipson's thesis, "Electrochemical Studies of New Inorganic Oxidants," was one of the papers at the Section's first mini-symposium for nominees for the Award. Before beginning his studies at the Institute, Gipson was introduced to electrochemical research at Baylor University as a student of Professor Thomas C. Franklin. At Baylor, he graduated *Summa cum Laude* with a B.S. degree in May 1981. His honors include *Phi Betta Kappa*, the American Institute of Chemists Award for Outstanding Senior Undergraduate in Chemistry (1981), and IBM and NSF Graduate Fellowships. He is currently a senior chemist at Union Carbide's Technical Center in South Charleston, West Virginia.

The Section sponsored a mini-symposium for all of the nominees for this year's Award. The session was held at the Athenaeum at the California Institute of Technology on June 11, 1985. In addition to Dr. Gipson's presentation, the mini-symposium included the following presentations:

Robert J. Cave, California Institute of Technology: "Molecular Orientation Effects on the Rates of Electron Transfer Reactions"

Thomas C. Banwell, California Institute of Technology: "Mechanisms Induced by Heavy Ion Radiation"

John L. Stickney, University of California at Santa Barbara: "Electrodepositions on Well Defined Surfaces"

Shaiu-Yih Yin, University of Southern California: "Electron and Ion Microprobe Studies of GaAs and Its Oxides"

OBITUARY

Warren D. Sherrow, Past Chairman of the Industrial Electrolytic Division, died on July 9, 1985, in Youngstown, New York. He was 63.

Sherrow was born in Fordland, Missouri, and received a certificate in chemistry from Marion Military Institute, Marion, Alabama, in 1941. After leaving Marion, he worked for two years with the Chemical Warfare Service in Huntsville, Alabama. In 1944, Sherrow joined the U.S. Army Air Corps as a navigator, and served with the Ninth Air Force in the European, African, and Middle East campaigns.

After leaving the military, Sherrow began working for the Hooker Electrochemical Company in Niagara Falls, New York, on experimental projects and in sales work. In 1950, Sherrow moved to Great Lakes Carbon, where he was to remain for 29 years, beginning as a sales representative and eventually becoming a general sales manager. Before retiring in 1984, Sherrow acted as a general sales manager for Grelcon Company, a subsidiary of Great Lakes, for three years.

Sherrow joined The Electrochemical Society in 1950. From 1954 to 1958, he served as the Secretary-Treasurer for the Industrial Electrolytic Division. In 1958, he was elected Vice-Chairman of the Division, and from 1960 to 1962 he acted as Chairman of the Divison.

Call for Papers
Symposium on
Silicon on Insulators
169th Meeting of The Electrochemical Society
Boston, Massachusetts
May 4-9, 1986

Focus will be placed on recent advances in the various approaches to the formation of device-quality silicon on insulating substrates.

Approaches to be discussed:
- Lateral growth from the melt and by CVD and SPE.
- Buried insulating layer formation.
- Growth on patterned relief structures.
- Heteroepitaxial growth.

Topics to be included:
- Preparative procedures.
- Properties crystalline and electronic.
- Characterization.
- Advantages and limitations.
- Applicability to device structures.

Invited Speakers

H. Baumgart, Philips Laboratories
M. Bomchil, CNET
J. B. Butcher, Middlesex Polytechnics
S. Furukawa, Tokyo Institute of Technology
P. Hemment, University of Surrey
L. Jastrzebski, RCA Laboratories
J-P. Joly, LETI
T. I. Kamins, Hewlett-Packard
H. W. Lam, Texas Instruments
S. Muramoto, NTT Atsugi Laboratory
I. Ohdomori, Waseda University
L. Pfeiffer, AT&T Bell Laboratories
N. Sasaki, Fujitsu Semiconductor Division
H. Tango, Toshiba VLSI Laboratory
L. E. Trimble and G. K. Celler, AT&T Bell Laboratories
B-Y. Tsaur, MIT Lincoln Laboratory
G. Zimmer, Fraunhofer Institute

Symposium Co-Chairmen

G. W. Cullen, RCA Laboratories, Princeton, NJ 08540; J. Butcher, Microelectronic Center, Middlesex Polytechnic, London, England N11 1NQ; G. K. Celler, AT&T Bell Laboratories, Rm. 6F-217, Murray Hill, NJ 07974; J. C. C. Fan, MIT Lincoln Laboratory, 244 Wood St., Lexington, MA 02173; S. Furukawa, Dept. of Applied Electronics, Tokyo Institute of Technology, Nagatsuta, Midori-ku, Yokohama 227, Japan; V. A. Wells, Sandia National Laboratories, Div. 2147, Albuquerque, NM 87175.

Extended and 75-word abstracts must be received by **December 1, 1985** by The Electrochemical Society, 10 South Main St., Pennington, NJ 08534-2896.

$LiAsF_6$

(Lithium Hexafluoroarsenate)

USS LECTRO-SALT®

The superior electrolyte salt for nonaqueous lithium cells. Available in commercial quantities.

Pure $LiAsF_6$ is not toxic by dermal absorption, and is only slightly toxic when ingested. Ames test results indicate $LiAsF_6$ is not a carcinogen.

ELECTROCHEMICAL GRADE 99.9+%

1. Less than 100 ppm H_2O
2. Completely soluble in organic solvents
3. Acid equivalent near zero

For technical bulletins, and price information, call or write:

USS Agri-Chemicals
Division of United States Steel

Atlanta Technical Center
685 DeKalb Industrial Way
Decatur, GA 30033
Phone: 404/292-2525

PEOPLE

Florian Mansfeld has accepted a position as Professor of Materials Science at the University of Southern California at Los Angeles. In his new position, beginning this month, he will establish a Corrosion and Environmental Effects Laboratory and continue his research in corrosion science with emphasis on studies of electrochemical kinetics and mechanisms of corrosion phenomena.

Prior to joining USC, he spent 16 years at the Rockwell International Science Center in Thousand Oaks, California, where his most recent position was manager of the Surface and Electrochemical Processes Department.

Mansfeld is a member of The Electrochemical Society (Past Chairman of the Corrosion Division), the International Society of Electrochemistry (Co-chairman of the Corrosion Division), NACE (member of the Research Committee), ASTM (Past Chairman of GO1.11), and Sigma Xi.

NEW MEMBERS

It is a pleasure to announce the following new members of The Electrochemical Society as recommended by the Admissions Committee and approved by the Board of Directors in August 1985.

Active Members

Alamgir, M., Norwood, MA
Batista, J. M., Eatontown, NJ
Berger, H., Research Triangle Park, NC
Dion, J. B., Methuen, MA
Dun, J., Eagan, MN
Forgerson, D., Camarillo, CA
Hariri, A., Mountain View, CA
Jarrett, Q. T., Orlando, FL
Josowicz, M., Salt Lake City, UT
Kadono, K., Kanagawa-ken, Japan
Kantamneni, C. S., Eagan, MN
Kerrigan, R., DeLeon Springs, FL
Kychakoff, G., Stanford, CA
Lauria, D. A., Raritan, NJ
Lee, K. W., Newport News, VA
Liu, H.-Y., Dallas, TX
Marolf, J., Boise, ID
Martinez, R., Torrance, CA
Mazurk, G. W., Willoughby, OH
Olds, R. S., St. Louis, MO
Rath, H. J., Burghausen, Germany
Sen, P. N., Ridgefield, CT
Sizemore, J. T., San Diego, CA
Tseng, S. C., Santa Clara, CA
Volpe, L., San Jose, CA
Walker, M. L., San Jose, CA
White, J. R., Yorktown Heights, NY

Student Members

Dean, M. H., Elizabeth, NJ
Ferry, L. L., Stanford, CA
Foral, M., Madison, WI
Fritts, S. D., Akron, OH
Johnson, R. W., Auburn, AL
Lindsey, S. E., Evanston, IL
McCluskey, F. P., Bethlehem, PA
Nolen, T. R., Raleigh, NC
Richards, A. D., Cambridge, MA
Romano, L., Urbana, IL
Spears, S. G., Houston, TX
Vutetakis, D. G., Columbus, OH
Yoon, S., Los Angeles, CA

Reinstatement

Wang, T. E., Milpitas, CA

REVIEWS & NEWS INDEX

Abstracts—Recent News Papers 445C
Section News 447C
Obituary 447C
People 448C
New Members 448C
Meetings Calendar 449C
Positions Wanted 449C
Call for Papers—Boston, Massachusetts, Meeting 459C-464C

ADVERTISERS' INDEX

ElectroCell AB 456C
Electrosynthesis Company 458C
Epid, Inc. 450C
Princeton Applied Research 457C
University of Wisconsin 449C
USS Agri-Chemicals 448C

Nominations Invited for Edward Goodrich Acheson Award and Prize

The Edward Goodrich Acheson Award and Prize was established in 1928 to recognize a person who, in the judgment of the directors of the Society, has made contributions to the advancement of any of the objects, purposes, or activities of The Electrochemical Society as to merit the award. Such contributions may consist of, but shall not be limited to, (a) a discovery pertaining to electrochemistry, electrometallurgy, or electrothermics, (b) an invention of a plan, process, or device, or research evidenced by a paper embodying information useful, valuable, or significant in the theory or practice of electrochemistry, electrometallurgy, or electrothermics, and/or (c) distinguished services rendered to the Society.

The Award consists of a gold medal, a bronze replica, and two thousand dollars ($2000). The following have received the Award:

1929—Edward G. Acheson
1931—Edwin F. Northrup
1933—Colin Garfield Fink
1935—Frank J. Tone
1937—Frederick M. Becket
1939—Francis C. Frary
1942—Charles F. Burgess
1944—William Blum
1946—H. Jermain Creighton
1948—Duncan A. MacInnes
1951—George W. Vinal
1953—J. W. Marden
1954—George W. Heise
1956—Robert M. Burns
1958—William J. Kroll
1960—Henry B. Linford
1962—C. L. Faust
1964—Earl A. Gulbransen
1966—Warren C. Vosburgh
1968—Francis L. LaQue
1970—Samuel Ruben
1972—Charles W. Tobias
1974—Cecil V. King
1976—N. Bruce Hannay
1978—David A. Vermilyea
1980—Ernest B. Yeager
1982—Harry C. Gatos
1984—Norman Hackerman

Nominations for the next Award to be presented at the Fall Meeting of the Society in 1986 in San Diego, California, are invited. Nominees do not have to be members of the Society to be considered. Furthermore, there are no distinctions, restrictions, or reservations regarding age, sex, race, citizenship, or place of origin or residence.

Please send nominations before March 1, 1986 with supporting documents to Wayne L. Worrell, Dept. of Metal and Materials Science, University of Pennsylvania, 3231 Walnut St., K1, Philadelphia, PA 19104.

MEETINGS CALENDAR

Materials Research Society
Spring Meeting
April 15-18, 1986
Palo Alto, California
For further information, contact J. B. Ballance, Executive Director, Materials Research Society, 9800 McKnight Rd., Suite 327, Pittsburgh, PA 15237. Telephone: (412) 367-3003.

Deutsch Bunsen-Gesellschaft für
Physikalische Chemie
on
"Structure and Dynamics of Solid/
Electrolyte Interfaces"
September 2-5, 1986
Fritz-Haber-Institut
Berlin, Germany
For further information, contact H. Gerischer, Fritz-Haber-Institute der Max-Planck-Gesellschaft, Faradayweg 4-6, D-1000 Berlin 33, Federal Republic of Germany.

The Adhesion Society
Tenth Annual Meeting
February 22-27, 1987
Williamsburg, Virginia
For further information, contact L. T. Drzal, Dept. of Chemical Engineering, Michigan State Univeristy, East Lansing, MI 48824-1226.

POSITIONS WANTED

Please address replies to the box number shown, c/o The Electrochemical Society, Inc., 10 South Main Street, Pennington, NJ 08534-2896.

Ph.D. Electrochemist—15 years experience in applied electrochemical R&D. Recent experience in corrosion measurement, electrochemical instrumentation and sensor development for high temperature aqueous environments, modeling of corrosion environment in SCC cracks, and electrochemistry of ceramics. Desires university or industrial R&D position. Reply Box C-257.

Senior Electrochemist—Ph.D. industrial/academic background. Industrial electrolytes, chlor-alkali, fused salt electrolysis, hydrometallurgy, electrodeposition, metal finishing, speciality and electronic materials, plasma chemistry. R&D as well as plant support and operation experience. Versatile, innovative, and highly self-motivated. Patents and Publications. Reply Box C-258.

Electrochemist—Ph.D. Twenty years experience. Development of secondary batteries, lithium batteries, fuel cells, electrochemical sensors. Hardware, material and process development. Extensive management expertise. Patents and publications. Seeking challenging technical or management position. No agencies. Reply Box C-259.

Ph.D. Electrochemical/Chemical Engineer—Seeks industrial/university R&D. Presently postdoctoral fellow. Research experience in laboratory-scale electrolysis, chlor-alkali, reactor analysis, ion transport in diaphragm and membrane, mass-transfer measurement, computer simulation, electrode gas evolution, electroless plating, metal recovery, EC techniques, and proposal writing. Reply Box C-260.

POSITION AVAILABLE

Materials Engineering/Science—Faculty Position—University of Wisconsin-Madison. The University of Wisconsin-Madison is looking for candidates who are interested in a teaching/research career in the general areas of processing, characterization (electrical, chemical, thermal, magnetic, optical, etc.), and microscopy with emphasis in metals, alloys, ceramics, or semiconductors. Academic rank is open depending on candidate's qualifications. The Department of Metallurgical and Mineral Engineering and the College of Engineering have research activities in the areas of metals, semiconductors, and polymers. We have recently added two new faculty in the ceramic area in our department and intend to add additional faculty if exceptional candidates are found. The person must have the capability of developing an active research program and interact effectively with others. Interested persons should submit an application including a resume and a list of three references to: Professor Y. Austin Chang, Dept. of Metallurgical and Mineral Engineering, University of Wisconsin-Madison, 1509 University Ave., Madison, WI 53706. The University of Wisconsin is an equal opportunity employer.

The Electrochemical Society, Inc. Society Awards

The Edward Goodrich Acheson Award

Given for distinguished "contributions to the advancement of any of the objects, purposes, or activities of The Electrochemical Society."

Presented in the Fall of even-numbered years.

The Vittorio de Nora-Diamond Shamrock Award

Given for distinguished "contributions to the field of electrochemical technology."

Presented in the Spring of even-numbered years.

The Henry B. Linford Award for Distinguished Teaching

Given for "excellence in teaching in subject areas of interest to the Society."

Presented in the Spring of even-numbered years.

The Olin Palladium Award

Given for distinguished "contributions to the field of electrochemical science and corrosion."

Presented in the Fall of odd-numbered years.

The Electrochemical Society Award in Solid State Science and Technology

Given for distinguished "contributions to the field of solid state science."

Presented in the Spring of odd-numbered years.

The Electrochemical Society Carl Wagner Memorial Award

Given to "recognize mid-career achievement and excellence in research in areas of interest of the Society, and significant contributions in the teaching or guidance of students or colleagues in education, industry, or government."

Presented in the Fall of odd-numbered years.

PHYSICS SECTION HEAD

We are EPID, Inc. (an Exxon Enterprises affiliate), a dynamic, well-funded corporation developing display products at the forefront of technology. We seek a technical leader to fill an immediate opening for Device Physics Section Head in our Technology Department.

Your responsibilities will include technical direction of a small group of Ph.D. level professionals involved in the development of a second-generation electro-phoretic display, from concept to lab prototype. Also, preparation of proposals, plans, and documentation. Technical participation in fundamental characterization and modelling of device properties, display addressing, and prototype design and fabrication.

Qualified applicants will have a Ph.D. in Physics, Electrical Engineering, or related field and 5+ years experience in applied research or advanced product development, a minimum of one year of which has been spent in technical management. Experience in display science, semiconductor devices preferred.

We offer an excellent compensation and benefits package, including an individual incentive bonus program. Your immediate reply will be held in the strictest confidence. Please send your resume or curriculum vitae, including salary history, to EPID, Inc., 3099 Orchard Drive, San Jose, CA 95134. An EOE M/F/H/V.

EPID INC.

An Affiliate of Exxon Enterprises

Workshop Announcement

Electronic Materials: A Key to U.S. Competitiveness?

Sponsored by the Federation of Materials Societies

February 26 and 27, 1986

Capital Holiday Inn
Washington, DC

A position paper will be developed that will be made available (through the FMS and FMS member societies) to individuals in academia, government, and industry who are in policy-making positions in research and development. It is an overall emphasis that an increase in focus by U.S. policy makers on the importance of research and development would be appropriate. Separate Workshop sessions will take place to develop answers to the following.

- Why are electronic materials a key to U.S. competitiveness?
- What is the present position of U.S. electronic materials technology?
- What can we do in the U.S. to maintain (regain?) our competitive position in electronic materials technology?

The Workshop will be divided into three parts:

February 26, afternoon:	Presentations by keynote speakers.
February 27, morning:	Development of position papers.
February 27, afternoon:	Presentation of the positions and discussion.

The first and third sessions are open to all interested individuals. The second session is open to participants only.

Participation is by application to ensure a balance of interests and backgrounds and to facilitate planning. Applications can be obtained from

Mrs. Betsy Houston
Federation of Materials Societies
1901 L Street, N.W., Suite 804
Washington, DC 20036

For further information, contact one of the Workshop Cochairmen:

G. W. Cullen
RCA Laboratories
Princeton, NJ 08540
(609) 734-2851

R. Laudise
AT&T Bell Laboratories
Murray Hill, NJ 07974
(201) 582-6220

D. Richman
RCA Laboratories
Princeton, NJ 08540
(609) 734-3207

The Electrochemical Society, Inc.

CALL FOR PAPERS

State-of-the-Art Program on Compound Semiconductors (SOTAPOCS IV)

Sheraton Boston Hotel, Boston, Massachusetts, USA
May 4-9, 1986

The **SOTAPOCS** series has already become a forum for the presentation and discussion of the **latest** developments in areas involving Compound Semiconductor Processing and related fields.

SOTAPOCS IV continues this series of **special** Symposia established by the Electronics Division of The Society.

As in the past, of particular interest are talks and papers in the following general areas:

- **Materials Preparation and Growth Technologies**
- **Processing related characterization studies**
- **Metal-Semiconductor Interactions:** Schottky barriers, ohmic contacts
- **Dielectrics/Passivation**
- **Ion Implantation:** isolation, activation
- **Fine Feature Patterning:** Lithography, etching
- **Gate and Interconnect Technologies**
- **Heterojunction Devices**

Original papers and reviews are solicited. In recognition of the interdependence between processing, materials properties and device characteristics, talks which correlate these topics for high-speed, microwave, photonic, opto-electronic and sensing devices (discrete and integrated devices) are welcome.

The Symposia are also aimed at providing a forum for synergistic interactions between those working in compound semiconductors and those involved in silicon technologies.

To ensure the **timely** nature of the **SOTAPOCS** effort, a **special** deadline has been set. Abstracts will be accepted until February 1, 1986. The standard 75-Word Electrochemical Society Abstract is sufficient for paper presentation at **SOTAPOCS.** There is no need to submit an Extended Abstract.

Suggestions, inquiries and Abstracts should be sent to the Program Co-Chairmen:

S.N.G. Chu
Room 7C-304A
AT&T Bell Laboratories
Murray Hill, New Jersey 07974
(201) 582-7318

C.E. Weitzel
Motorola Inc.,
5005 East McDowell Rd.,
Phoenix, Arizona 85008
(602) 244-4421

(See other side for 75-word abstract form)

R.E. Enstrom
RCA Laboratories
Princeton, New Jersey 08540
(609) 734-2309

75-Word Abstract Form

(Submit by February 1, 1986)
(This Deadline Date for SOTAPOCS ONLY)

Sheraton Boston Hotel, Boston, Massachusetts, USA — MAY 4-9, 1986

Submit to: Program Co-Chairmen
(See other side for names and addresses)

Abstract No. .....
(to be assigned by the Society)

SOTAPOCS IV

Schedule for .....
(Title of Symposium)

Sponsored by **Electronics, Dielectrics & Insulation & Luminescence & Display Materials**
(Division/Group)

Title of paper .....

.....

Authors (Underline name of author presenting paper) .....

.....

Business affiliation and address .....

.....

.....
(State or Country) (Zip Code) (Telephone No.)

(Type abstract in this area - double-spaced.)

Do you require any audiovisual equipment?

☐ **35 mm (2 x 2 in.) slide projector**

☐ **Vu-Graph**

☐ **other (specify)**

Has the information in this abstract been presented verbally, submitted for publication, or published?
☐ **Yes** ☐ **No**
If the answer is yes, please provide the reference (except in the case of invited review presentations). _____

Is a full length paper on this work to be submitted for Society Journal publication? ☐ **Yes** ☐ **No**

Papers presented before a Society technical meeting become the property of the Society and may not be published elsewhere without written permission of the Society. Papers presented at Society technical meetings must be authored by a member or sponsored by an active member.

.....
Insert name of Society member author or sponsor

The Electrochemical Society, Inc.
10 South Main Street, Pennington, New Jersey 08534 • Telephone: 609-737-1902

Instructions to Authors

The **JOURNAL OF THE ELECTROCHEMICAL SOCIETY** is the official monthly journal of the Society. It contains three sections: Electrochemical Science and Technology, Solid-State Science and Technology, and Reviews and News. Technical Papers, Technical Notes, and Accelerated Brief Communications are published in the first two sections and Review Papers in the third. **All manuscripts (in English) submitted are considered for publication, with the understanding that they have not been submitted, accepted for publication, or published elsewhere. Material, e.g., figures and tables, may not be reproduced from another publication unless it absolutely cannot be described in words. If this material must be used, it must be properly referenced and acknowledged, and permission to reproduce it must be obtained from the publisher.** A wide range of subject matter is acceptable. Manuscripts can be handled promptly and efficiently if these instructions are followed.

TYPES OF PAPERS

Technical Papers describe fundamental or applied studies in depth. They contain new data and/or new interpretations of existing data. Abstracts summarizing the results are required.

Technical Notes report briefly on limited research or development that is not being pursued further. No abstracts are required.

Accelerated Brief Communications present, in camera-ready format of limited length, scientific or technological information warranting rapid dissemination. No abstracts are required.

Review Papers furnish critical analyses of topical subjects. Abstracts are required.

SUBMISSION

Submit three complete, clear copies of each manuscript and the originals of all figures and illustrations to:

Editorial Office
The Electrochemical Society, Inc.
10 South Main Street
Pennington, New Jersey 08534

A letter accompanying the manuscript should give (a) the name and mailing address of the author to whom correspondence should be sent, (b) reference to any presentation of the work at a meeting of The Electrochemical Society, (c) the Division or Group of the Society or the Divisional or Group Editor (both are listed in the front of each issue of the Journal) whose interests are most closely related to the work being discussed, (d) the section of the Journal in which the work should appear, and (e) the names and addresses of people able to act as reviewers.

EDITORIAL PRACTICES

Following receipt by the Editorial Office, each manuscript is sent to a Divisional or Group Editor with knowledge of the subject matter. This editor arranges for review of the manuscript and communicates with the author(s) regarding revisions. Final acceptance or rejection of a manuscript is determined by the Editor.

Accelerated Brief Communications are handled as rapidly as possible, ordinarily with a response to the author(s) from the Divisional Editor, the Group Editor, or the Editor within three weeks of their arrival at Pennington. Response to the authors of other manuscripts usually takes place within six weeks. Following acceptance, authors are notified of the Journal issue in which publication is scheduled; about one month before publication, page proofs and an order blank for reprints are provided. Proofs must be promptly corrected and returned. Extensive alterations by the author may delay publication; their cost will be billed to the author(s).

PUBLICATION CHARGE

To help meet publication costs, a payment of $65.00 per printed page is requested for the publication of technical material. If at least one author is a Society member or an employee of a Patron or Sustaining member, a 10% reduction is allowed. Acceptance of manuscripts for publication is, however, based on merit and is in no way dependent on such payment, which may be waived in individual cases upon request.

PRESENTATION

Organization and clarity are essential elements of successful written communication. Identify the subject matter in the title, using words useful in indexing. State the purpose of the work early in the text. Avoid introductory and explanatory material that is overly familiar to those in the field. Present the work and the arguments in an order that leads naturally to clearly specified conclusions. Provide enough information for the work to be reproduced and the logic behind it to be understood. Identify and justify any assumptions that are made; avoid tacit assumptions. Omit details that are generally known or that can be covered by reference to other publications. Give the magnitude and define the significance of experimental errors. Use headings and subheadings as appropriate. Avoid proprietary and trade names, but capitalize them where their use is necessary. Define unusual technical terms and abbreviations. Where symbols are used extensively, list them with their definitions at the end of the paper. Avoid repetition in the text and duplication of material in figures and tables. Be brief but clear.

Edit and proofread the manuscript carefully; these are not the responsibilities of the editors or reviewers.

MANUSCRIPT PREPARATION

Accelerated Brief Communications must be typewritten or printed on standard forms obtained, with detailed instructions for their use, from the Pennington Editorial Office.

All other manuscripts must be typewritten or printed, double-spaced throughout, on one side only of white 21.6 x 27.0 cm paper, with 2.5-3.8 cm margins. Do not use single spacing anywhere, in title, abstract, text, references, tables, or figure captions.

For general matters of style and format, see papers in recent issues of the **Journal** and consult a style manual such as that of the American Chemical Society or that of the American Institute of Physics. These also provide lists of common abbreviations and units. The following specific items should be noted:

(a) Système Internationale (SI) units are to be used; a description may be found in NBS Special Publication 330 or ASTM Metric Practice Guide E-380-72.

(b) The signs of cell and electrode potentials are to follow the IUPAC conventions of 1953.

(c) **Mathematical equations** should be written on a single line, if possible, using parentheses, brackets, the solidus, negative exponents, etc.

(d) **References** are to be listed separately at the end of the paper in the order they are cited in the text, being sure that each listed reference is cited. Authors' initials must be given, and Chemical Abstracts abbreviations must be used. Citations of other than the generally available literature should be avoided if possible.

(e) **Tables** are to be presented on individual sheets, with both captions and body double-spaced.

(f) **Figure captions** and numbers are to be included on a separate sheet and must not appear in the body of any figure or illustration.

(g) **Drawings** and **graphs** will ordinarily be reduced to column width (8.3 cm) and after such reduction should have lettering at least 0.15 cm high. Lettering must be of letter-guide quality. Originals in India ink on tracing cloth or paper are preferred, but India ink on coordinate paper with blue ruling is acceptable. When several curves are shown, each may be lettered and identified in the caption. The Editorial Office will not make corrections or additions to figures.

(h) **Photographs** should be used sparingly. The originals supplied must be glossy prints and should be protected against bending. Micrographs must have a labeled unit length within the body of the picture; reduction for printing makes magnifications meaningless.

Revised August 1, 1984

Printed in the United States of America

OUT-OF-PRINT SOCIETY VOLUMES

The following volumes sponsored or published by The Electrochemical Society, Inc., are now out of print. Xerographic copies* or reprints† of these volumes are available.

* **Vapor Plating.** C. F. Powell, I. E. Campbell, and B. W. Gonser, Editors. A 1955 symposium. 158 pages.
* **The Structure of Electrolytic Solutions.** W. J. Hamer, Editor. A 1957 symposium. 441 pages.
* **Technology of Columbium (Niobium).** B. W. Gonser and E. M. Sherwood, Editors. A 1958 symposium. 120 pages.
* **Surface Chemistry of Metals and Semiconductors.** H. C. Gatos, J. W. Faust, Jr., and W. J. LaFleur, Editors. A 1959 symposium. 526 pages.
* **Electrode Processes,** First Conference. E. Yeager, Editor. A 1959 symposium. 374 pages.
* **Mechanical Properties of Intermetallic Compounds.** J. H. Westbrook, Editor. A 1959 symposium. 435 pages.
* **Zirconium and Its Alloys.** J. P. Pemsler, E. C. W. Perryman, and W. W. Smeltzer, Editors. A 1965 symposium. 205 pages.
† **Measurement Techniques for Thin Films.** B. Schwartz and N. Schwartz, Editors. 1965 and 1966 symposia. 347 pages.
† **Electrode Processes,** Second Conference. E. Yeager, H. Hoffman, and E. Eisenmann, Editors. A 1966 symposium. 190 pages.
* **Electrolytic Rectification and Conduction Mechanisms in Anodic Oxide Films.** P. F. Schmidt and D. M. Smyth, Editors. A 1967 symposium. 230 pages.
* **Electrets and Related Electrostatic Charge Storage Phenomena.** L. M. Baxt and M. M. Perlman, Editors. A 1967 symposium. 150 pages.
* **Dielectrophoretic and Electrophoretic Deposition.** E. F. Pickard and H. A. Pohl, Editors. A 1967 symposium. 138 pages.
* **Electron and Ion Beam Science and Technology,** Third International Conference. R. Bakish, Editor. A 1968 symposium. 725 pages.
* **Optical Properties of Dielectric Films.** N. Axelrod, Editor. A 1968 symposium. 325 pages.
* **Thin Film Dielectrics.** F. Vratny, Editor. A 1968 symposium. 680 pages.
* **Ohmic Contacts to Semiconductors.** B. Schwartz, Editor. A 1968 symposium. 356 pages.
* **Semiconductor Silicon.** R. R. Haberecht and E. L. Kern, Editors. A 1969 symposium. 750 pages.
* **Chemical Vapor Deposition,** Second International Conference. J. M. Blocher, Jr. and J. C. Withers, Editors. A 1970 symposium. 872 pages.
* **Marine Electrochemistry.** J. B. Berkowitz, M. Banus, M. J. Pryor, R. Horne, P. L. Howard, G. C. Whitnack, and H. V. Weiss, Editors. A 1972 symposium. 416 pages.
* **Semiconductor Silicon 1973.** H. R. Huff and R. R. Burgess, Editors. A 1973 symposium. 936 pages.
* **High Temperature Oxidation of Metals.** By P. Kofstad. The Corrosion Monograph Series. 340 pages.
* **Chemical Vapor Deposition,** Fourth International Conference. G. F. Wakefield and J. M. Blocher, Jr., Editors. A 1973 symposium. 595 pages.
* **Electrets, Charge Storage and Transport in Dielectrics.** M. M. Perlman, Editor. A 1973 symposium. 675 pages.
* **Corrosion Problems in Energy Conversion and Generation.** C. S. Tedmon, Editor. A 1974 symposium. 484 pages.
* **Electrocatalysis.** M. W. Breiter, Editor. A 1974 symposium. 378 pages.
* **Electron and Ion Beam Science and Technology,** Sixth International Conference. R. Bakish, Editor. A 1974 symposium. 594 pages.
* **Energy Storage.** H. P. Silverman and J. B. Berkowitz, Editors. A 1975 symposium. 258 pages.
* **Chemical Vapor Deposition, Fifth International Conference.** J. M. Blocher, Jr., H. E. Hintermann, and L. H. Hall, Editors. A 1975 symposium. 848 pages.
* **Etching.** H. G. Hughes and M. J. Rand, Editors. A 1976 symposium. 203 pages.
* **Electrode Materials and Processes for Energy Conversion and Storage.** J. D. E. McIntyre, S. Srinivasan, and F. G. Will, Editors. A 1977 symposium. 340 pages.
* **Electron and Ion Beam Science and Technology,** Eighth International Conference. R. Bakish, Editor. A 1978 symposium. 297 pages.
* **International Symposium on Solar Energy.** J. B. Berkowitz and I. A. Lesk, Editors. A 1976 symposium. 372 pages.
* **High-Temperature Metallic Corrosion of Sulfur and Its Compounds.** Z. A. Foroulis, Editor. A 1969 symposium. 276 pages.
* **Properties of Electrodeposits—Their Measurement and Significance.** R. Sard, H. Leidheiser, Jr., and F. Ogburn, Editors. A 1974 symposium. 430 pages.
* **Chemical Vapor Deposition, Sixth International Conference.** L. F. Donaghey, P. Rai-Choudhury, and R. N. Tauber, Editors. A 1977 symposium. 596 pages.
* **The Electrocatalysis of Fuel Cell Reactions.** W. E. O'Grady, S. Srinivasan, and R. F. Dudley, Editors. A 1978 workshop. 228 pages.
* **Electron and Ion Beam Science and Technology,** Fourth International Conference. R. Bakish, Editor. A 1970 symposium. 680 pages.
* **Plasma Processing.** R. G. Frieser and C. J. Mogab, Editors. A 1980 symposium. 360 pages.
* **Oxide-Electrolyte Interfaces.** R. S. Alwitt, Editor. A 1972 symposium. 312 pages.
* **Industrial Water Electrolysis.** S. Srinivasan, F. J. Salzano, and A. R. Landgrebe, Editors. A 1978 symposium. 297 pages.
* **Semiconductor Characterization Techniques.** P. A. Barnes and G. A. Rozgonyi, Editors. A 1978 symposium. 532 pages.
* **Fundamentals of Electrochemical Machining.** A 1970 symposium. 365 pages.
* **Electron and Ion Beam Science and Technology,** Seventh International Conference. R. Bakish, Editor. A 1976 symposium. 632 pages.
* **Thin Film Phenomena—Interfaces and Interactions.** J. E. E. Baglin and J. M. Poate, Editors. A 1977 symposium. 525 pages.
* **Electrochemical Contributions to Environmental Protection.** T. R. Beck, O. B. Cecil, C. G. Enke, J. McCallum, and S. T. Wlodek, Editors. A 1972 symposium. 173 pages.
* **Chemical Vapor Deposition, Seventh International Conference.** T. O. Sedgwick and H. Lydtin, Editors. A 1979 Symposium. 658 pages
* **Battery Design and Optimization.** S. Gross, Editor. A 1978 symposium. 486 pages.
* **Chemical Vapor Deposition, Eighth International Conference.** J. M. Blocher, Jr., G. E. Vuillara, and G. Wahl, Editors. A 1981 symposium. 836 pages.

* Order from University Microfilms, Inc., 300 North Zeeb Street, Ann Arbor, MI 48106. Specify an Electrochemical Society volume.

† Order from Johnson Reprint Co., 355 Chestnut St., Norwood, NJ 07648. Specify an Electrochemical Society volume.

4/85

THE ELECTROCHEMICAL SOCIETY BOOKS IN PRINT

Society Proceedings Series
1972-1979

The following softbound proceedings volumes are sponsored and published by The Electrochemical Society, Inc., 10 South Main Street, Pennington, NJ 08534-2896. Orders filled at the list price given, subject to availability. Enclose payment with order.

Electron and Ion Beam Science and Technology, Fifth International Conference. R. Bakish, Editor. A 1972 symposium. 420 pages, **$5.50.**

Electrochemical Bioscience and Bioengineering. H. T. Silverman, I. F. Miller, and A. J. Salkind, Editors. A 1973 symposium. 268 pages, **$8.00.**

Chlorine Bicentennial Symposium. T. C. Jeffery, P. A. Danna, and H. S. Holden, Editors. A 1974 symposium. 404 pages, **$11.00.**

Fine Particles. W. E. Kuhn and J. Ehretsmann, Editors. A 1974 symposium. 352 pages, **$15.00.**

Metal-Slag-Gas Reactions and Processes. Z. A. Foroulis and W. W. Smeltzer, Editors. A 1975 symposium. 1032 pages, **$20.00.**

Chemistry and Physics of Aqueous Gas Solutions. W. A. Adams, G. Greer, J. E. Desnoyers, G. Atkinson, G. S. Kell, K. B. Oldham, and J. Walkley, Editors. A 1975 symposium. 522 pages, **$11.00.**

Thermal and Photostimulated Currents in Insulators. D. M. Smyth, Editor. A 1975 symposium. 215 pages, **$7.00.**

International Symposium on Molten Salts. J. P. Pemsler, J. Braunstein, K. Nobe, D. R. Morris, and N. E. Richards, Editors. A 1976 symposium. 632 pages, **$16.00.**

Properties of High Temperature Alloys. Z. A. Foroulis and F. S. Pettit, Editors. A 1976 symposium. 851 pages, **$12.00.**

Semiconductor Silicon 1977. H. R. Huff and E. Sirtl, Editors. A 1977 symposium. 1100 pages, **$15.00.**

A History of The Electrochemical Society. The first 75 years. R. M. Burns with E. G. Enck, 160 pages. **$5.00.**

Semiconductor-Liquid Junction Solar Cells. A. Heller, Editor. A 1977 symposium. 340 pages, **$10.00.**

Load Leveling. N. P. Yao and J. R. Selman, Editors. A 1977 symposium. 412 pages, **$13.00.**

High Temperature Metal Halide Chemistry. D. L. Hildenbrand and D. D. Cubicciotti, Editors. A 1977 symposium. 678 pages, **$17.00.**

Selected Topics in the History of Electrochemistry. George Dubpernell and J. H. Westbrook, Editors. A 1977 symposium. 523 pages, **$11.00.**

Laser and Electron Beam Processing of Electronic Materials. C. L. Anderson, G. K. Celler, and G. A. Rozgonyi, Editors. A 1979 symposium. 560 pages, **$13.00.**

Thin Film Interfaces and Interactions. J. E. E. Baglin and J. M. Poate, Editors. A 1979 symposium. 536 pages, **$16.00.**

Electrode Processes. S. Bruckenstein, J. D. E. McIntyre, B. Miller, and E. Yeager, Editors. A 1979 symposium. 500 pages, **$21.00.**

Power Sources for Biomedical Implantable Applications and Ambient Temperature Lithium Batteries. B. B. Owens and N. Margalit, Editors. A 1979 symposium. 652 pages, **$18.00.**

Monograph Series

The following hardbound volumes are sponsored by The Electrochemical Society, Inc. and published by John Wiley & Sons, Inc. Members who wish to receive a discount must send their orders to the Society Headquarters, 10 South Main St., Pennington, NJ 08534-2896. The books will be shipped by John Wiley & Sons, Inc. Invoices for the cost of the volume plus postage and handling will be sent by Society Headquarters. Terms: Payment upon receipt of invoice. All others should send their orders directly to John Wiley, 1 Wiley Dr., Somerset, NJ 08873. All prices are subject to change without notice.

Corrosion Handbook, edited by Herbert H. Uhlig (1948). 1188 pages, **$79.95.**

Alkaline Storage Batteries, by S. Uno Falk and Alvin J. Salkind (1969). 656 pages, **$91.95.**

Handbook on Corrosion Testing and Evaluation, edited by W. H. Ailor (1971). 873 pages, **$99.50.**

Modern Electroplating, edited by Frederick A. Lowenheim. Third Edition (1974). 801 pages, **$59.95.**

Marine Corrosion, by Francis L. LaQue (1975). 332 pages, **$48.95.**

The Primary Battery, Volume II, edited by George W. Heise and N. Corey Cahoon (1975). 528 pages, **$82.50.**

Thin Films—Interdiffusion and Reactions, edited by J. M. Poate, K. N. Tu, and J. W. Mayer (1978). 576 pages, **$69.95.**

Corrosion of Stainless Steels, by J. A. Sedriks (1979). 282 pages, **$48.95.**

Corrosion of Nickel and Nickel-Base Alloys, by Wayne Z. Friend (1980). 460 pages, **$72.95.**

Atmospheric Corrosion, edited by W. H. Ailor (1982). 1028 pages, **$172.50.**

Lithium Battery Technology, edited by H. Venkatasetty (1984). 247 pages, **$42.50.**

The following volume, sponsored by The Electrochemical Society, Inc., should be ordered directly from the publisher, Plenum Publishing Corporation, 233 Spring St., New York, NY 10013.

Adhesion Aspects of Polymeric Coatings, edited by K. L. Mittal (1983). 658 pages, **$85.00.**

The following hardbound volumes are sponsored by and published by The Electrochemical Society, Inc. They should be ordered from: The Electrochemical Society, Inc., 10 South Main St., Pennington, NJ 08534-2896. Remittance must accompany order for these volumes.

Society Published Monograph Series

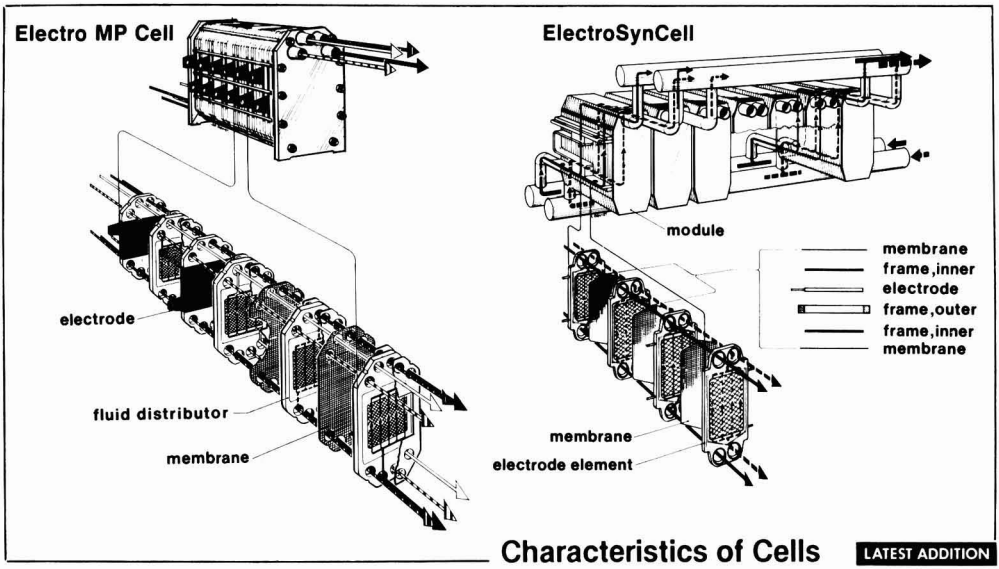
Passivity of Metals (proceedings of The Fourth International Symposium on Passivity). R. P. Frankenthal and J. Kruger, Editors. A 1977 symposium. 1078 pages, **$65.00**

Other Society Books

Bibliography of Electro-Organic Syntheses, by Sherlock Swann, Jr. and Richard C. Alkire, 755 pages, **$35.00**

Off-the-shelf electrochemical cells for lab, pilot plant and production are now available for a variety of applications.

Expertly designed and engineered flow cells are available for applications including chloralkali and synthesis of a wide range of inorganic and organic chemicals. These modular membrane cells have found application world-wide! Start with a laboratory unit as small as 0.01 m^2 (Electro MP Cell) or 0.04 m^2 (ElectroSynCell) and expand to a pilot scale module, and then to production plant size by adding on modules, or installing the NEW Electro Prod Cell especially designed for production. Injection molded cell parts are available in a wide range of inert materials. Electrodes can be of DSA^R, Pt on Ti, PbO_2on Ti, graphite and many others. Further advantages: leakproof, uniform hydrodynamics and current distribution, and narrow inter-electrode gap.



Characteristics of Cells

LATEST ADDITION

	Electro MP Cell	ElectroSynCell	ElectroProdCell
Electrode area (min):	0.01 m^2	0.04 m^2	0.4 m^2
(max):	0.2 m^2/module	1.04 m^2/module	16.0 m^2/module
Current density (max):	4 kA/m^2	4kA/m^2	4 kA/m^2
Interelectrode gap:	6-12 mm	5 mm	0.5-4 mm
Electrolyte flow, per cell:	1-5 l/min	5-15 l/min	10-30 l/min
Flow Rate in each cell:	0.03-0.15 m/s	0.2-0.6 m/s	0.15-0.45 m/sek

Write or call for further technical information and a quotation.

AB

ElectroCell AB

P.O. Box 34,
S-184 00 Akersberga,
Sweden.
Int. + 46 764-600 40
Telex 15313 ECAB S

REPRESENTATIVES:

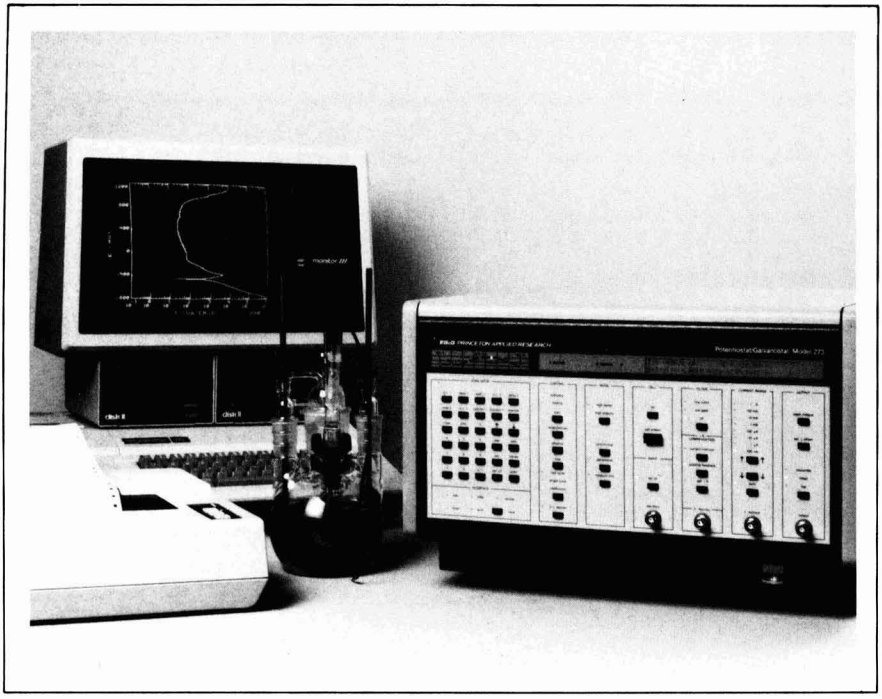
USA, Canada:
THE ELECTRO SYNTHESIS CO., INC.
P.O. Box 16,
E. Amherst, N.Y.,
14051 U.S.A.
(716)684-0513.

France:
SORAPEC.
192 rue Carnot,
94120 Fontenay
Sous-Bois,
France.
(1) 8774959

Germany:
SIGRI ELEKTROGRAPHIT GMBH
Werner-von-Siemens
Strasse 18
D-8901 Meitingen
West Germany
(08 271) 83-0

Spain:
AFORA S.A.
Aribau 240
Barcelona-6
Spain
(93) 200 9911

Southeast Asia:
SHOKO CO. LTD.
8-3 Nishi Shimabashi,
3-chome, Minato-ku,
Tokyo 105,
Japan.
(03) 459-5280~6



The Corrosion Measurement System for Electrochemists

The Model 332 Corrosion Measurement System provides fully automatic operation via our unique SoftCorr program for the Apple IIe computer. The software performs nine different corrosion measurement techniques from test definition through data evaluation and documentation of results. It includes PARCalc, a sophisticated and highly effective corrosion rate calculation routine.

The Model 332-1 is based on our new Model 273 Potentiostat/Galvanostat which has been optimized for computer-assisted electrochemistry. The Model 273 represents the ultimate in flexibility and is ideal for many other types of experiments. User programming is an efficient process since the Model 273 has a "vocabulary" of over 80 dedicated commands, and our new Free-Form Experiment disk (for the Apple IIe) makes it simple. All you do is assemble a list of commands, initiate the experiment, and obtain the data plot.

AC Impedance experiments can easily be performed with the addition of the Model 5301EC Lock-In Amplifier and our Model 368 AC Impedance Software.

If versatility is a primary requirement, then the Model 332 is the system of choice. For more details write or call our Applications Group.

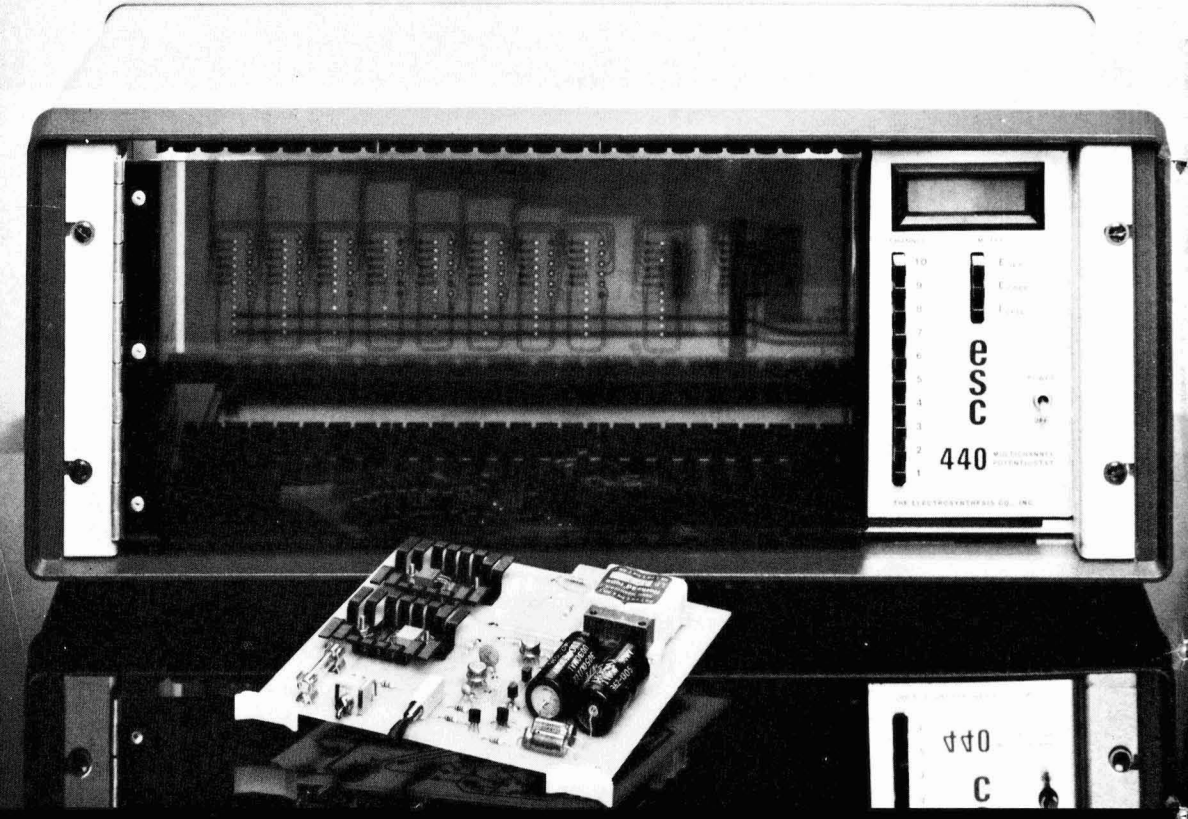
EG&G PRINCETON APPLIED RESEARCH
P.O. BOX 2565 • PRINCETON, NJ 08540, U.S.A. • 609/452-2111 • TELEX: 843409

If you're doing multi-sample corrosion research . . . the ESC 440 MULTICHANNEL POTENTIOSTAT should be in your lab . . .

Ten independent potentiostats for control of corrosion coupons during extended testing. The ESC 440 is *the* most cost effective method for individual control of multiple samples.

Interchangeable electronic modules for each channel. Separate current monitor outputs for connection to your data collection system.

Call us today for the details.



THE ELECTROSYNTHESIS CO., INC.

P.O. Box 16, E. Amherst, N.Y. 14051 • 716-684-0513

Call for Papers
169th Meeting
Boston, Massachusetts, May 4-9, 1986

Selected symposium topics and planned General Sessions are described in the following pages.

Procedure for Submitting Papers

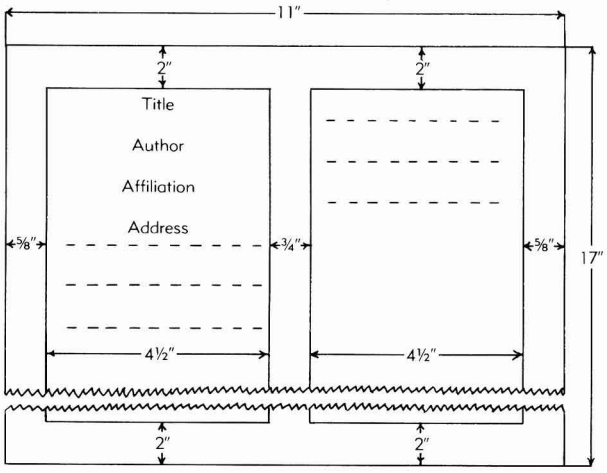
1. Submit one original 75-Word Abstract on the attached form or a facsimile together with one original Extended Abstract to The Electrochemical Society, Inc., 10 South Main St., Pennington, NJ 08534-2896. The deadline for receipt of **both** the 75-Word and Extended Abstract at The Electrochemical Society Headquarters Office is **December 1, 1985.**

2. Send a copy of **both** the 75-Word and Extended Abstract to the appropriate organizing symposium or General Session chairman listed. **No paper will be considered unless both the 75-Word and Extended Abstract are received at Society Headquarters by December 1, 1985. Both abstracts and the oral presentation are required in English.**

Instructions for Preparation of Extended Abstract

1. New Deadline—Extended Abstract must be submitted with the 75-Word Abstract by **December 1, 1985.**

2. All scheduled papers will be published in the EXTENDED ABSTRACTS volume for this meeting. The volume is published photo-offset directly from typewritten copy submitted by the author. The volume will be 7 × 10 in.; therefore, it is essential that the typing be clear and all lettering should be the size of ordinary type or at least 1/16 in. high so that it will be legible after reduction. The EXTENDED ABSTRACTS volume is in a double-column format. Camera-ready typing mats may be obtained from The Electrochemical Society, Inc., 10 South Main St., Pennington, NJ 08534-2896, or you may use any white bond paper 11 × 17 in. The diagram below gives the dimensions of the Extended Abstract form.



A. Use black typewriter ribbon only; type single-spaced.

B. Opaque lacquer may be used for corrections.

C. Type title, author(s), affiliation(s), and address(es) at top of first column (see diagram).

D. Tables and figures must be securely mounted within the margins with rubber cement.

E. Place references and figures after text.

3. The text of the abstract, including references, must not exceed one page (two columns) in length. An additional two columns are permitted for figures, if necessary. Papers exceeding this limit will be returned or rejected.

Mailing Instructions

Mail the original Extended Abstract together with the original 75-Word Abstract to The Electrochemical Society, Inc., 10 South Main St., Pennington, NJ 08534-2896 and a copy to the organizing chairman **for receipt before December 1, 1985.**

Notification of Paper Acceptance

Programming for this meeting will occur in early January. Organizing chairmen will notify those authors whose papers have not been accepted. In early March, a complete packet of program materials, including an Advance Program, will be sent to the presenting authors. Coauthors will receive a meeting packet without an Advance Program.

Manuscript Publication in the JOURNAL OF THE ELECTROCHEMICAL SOCIETY

Upon presentation, all meeting papers become the property of The Electrochemical Society, Inc. However, presentation incurs no obligation to publish. If publication in the JOURNAL OF THE ELECTROCHEMICAL SOCIETY is desired, papers should be submitted as promptly as possible in full manuscript form in order to be considered. "Instructions to Authors" for JOURNAL publication are available from the Society Headquarters office and are published monthly in the JOURNAL. If publication elsewhere is desired after presentation, written permission from Society Headquarters is required.

Boston, Massachusetts, Meeting Symposia Plans—Spring 1986
May 4-9, 1986

Extended Abstract must be submitted with the 75-Word Abstract by December 1, 1985.

CORROSION

General Session

Papers on all aspects of low and high temperature corrosion and associated phenomena will be considered. Experimental techniques for the study of corrosion processes and corrosion products are also of interest.

Suggestions and inquiries should be sent to the Session Chairman: E. McCafferty, Code 6314, Naval Research Laboratory, Washington, DC 20375-5000.

DIELECTRICS AND INSULATION/ELECTRONICS

Electrochemistry in Electronic Packaging

Papers on electrochemical process are solicited in areas of: 1. microwave as well as electronic packaging; 2. electroless copper catalysis and deposition on insulators; 3. metallization of silicon; 4. photoenhanced metal deposition; 5. materials and processing considerations in high density/high frequency packaging; 6. sensor (biomedical, pressure, etc.) packaging; 7. corrosion mechanisms and failure testing; 8. electromigration, with special attention to fundamentals and scientific understanding.

Suggestions and inquiries should be sent to the Symposium Chairman: E. A. Giess, IBM T. J. Watson Research Center, P.O. Box 218, Yorktown Heights, NY 10598.

DIELECTRICS AND INSULATION/ ELECTRONICS/CORROSION

Aluminum Surface Treatment Technology

This symposium is for people who are involved with the diverse products that are made from oxide-coated aluminum. It will be a forum for the exchange of ideas and information concerning the electrochemical and related chemical processing of aluminum surfaces, as well as the properties of the finished surface or device. The goal will be technology transfer between different applications through consideration of common fundamental aspects.

Presentations on recent advances, either from a scientific or an engineering viewpoint, are encouraged. Principal areas of interest are as follows. 1. Adhesive bonding of aluminum alloys. The relationship of anodic oxide film structure and composition to the integrity of the adhesive bond; aging, humidity, and other environmental effects; failure mechanism and evaluation of accelerated test methods. 2. Electrolytic capacitors, both wet and solid types. New processes and materials for ac and dc etching; improved types of oxide dielectrics; mechanisms of aluminum dissolution and oxide growth; novel capacitor materials such as Ti-Al sintered bodies and TCNQ solid electrolyte; capacitor performance related to use of advanced materials. 3. Lithographic plate. Relationship of surface roughness, texture, and anodic oxide properties to image quality and plate life; etch and anodizaton processes for high speed production lines; plate surfaces for new printing technologies. 4. Porous anodic oxide coating for architectural, corrosion protection, electrical insulation, decorative, and wear-resistant applications. Fundamental aspects of oxide growth, structure and environmental effects; improved processes, new products, shifting markets. 5. Surface treatments of new aluminum alloys and composites. 6. Emerging applications such as electrochromic and luminescent displays, memory storage disks, and solar heat collector panels.

Publication of a proceedings volume is planned. Papers published in a proceedings volume may also be submitted to the **Journal**, but must be received no later than 6 months after the date of the symposium at which the paper was presented.

Suggestions and inquiries should be sent to the Symposium Co-Chairman: R. S. Alwitt, Boundary Technologies, Inc., 3000 Dundee Rd., Suite 309, Northbrook, IL 60062; or G. E. Thompson, Corrosion and Protection Centre, University of Manchester Institute of Technology, P.O. Box 88, Manchester, England M60 1QD.

DIELECTRICS AND INSULATION/ ELECTRONICS/LUMINESCENCE AND DISPLAY MATERIALS

Patterning Science and Technology

Papers on advances in the technology of pattern transfer in the optical, E-beam, and x-ray regimes are solicited. Relevant ion beam topics will also be considered.

The emphasis will be on materials, and processes, to maximize the fidelity of the pattern-transfer step (in the radiation-sensitive layer) both by incremental improvements in current technology and by novel systems. Modeling papers to increase understanding and predict performance are also invited.

Suggestions and inquiries should be sent to the Symposium Co-Chairmen: A. W. McCullough, Shipley Co., Inc., 2300 Washington St., Newton, MA 02162; or M. J. Watts, AZ Corp., 615 Palomar Ave., Sunnyvale, CA 94086.

ELECTRONICS/DIELECTRICS AND INSULATION

Silicon on Insulators

In this symposium, focus will be placed on recent advances in the various approaches to the formation of device-quality silicon on insulating substrates. This forum should provide the opportunity to develop a perspective on the advantages and limitations of the individual approaches with respect to preparative procedures, crystalline and electronic properties, applicability to various device configurations, and economics. An important aspect of the symposium will be the crystalline and electronic characterization of SOI materials. SOI approaches to be discussed include: 1. lateral growth from the melt (seeded and unseeded); 2. lateral growth by solid phase epitaxy; 3. lateral growth by CVD; 4. the formation of an insulating layer beneath a layer of bulk silicon; 5. oriented growth induced by a patterned relief structure; and 6. the heteroepitaxial growth of silicon on single-crystal insulating substrates.

Suggestions and inquiries should be sent to the Symposium Co-Chairmen: G. W. Cullen, RCA Laboratories, Princeton, NJ 08540; J. Butcher, Microelectronic Center, Middlesex Polytechnic, London, England N11 1NQ; G. K. Celler, AT&T Bell Laboratories, Rm. 6F-217, Murray Hill, NJ 07974; J. C. C. Fan, MIT Lincoln Laboratory, 244 Wood St., Lexington, MA 02173; S. Furukawa, Dept. of Applied Electronics, Tokyo Institute of Technology, Nagatsuta, Midori-ku, Yokohama 227, Japan; or V. A. Wells, Sandia National Laboratories, Div. 2147, Albuquerque, NM 87175.

Electrochemical Sensors for Biomedical Applications

This symposium will explore a variety of novel electronic and electrochemical sensors important in biology and medicine. Presentations will address sensor fabrication, principles of operation, applications, and measurement sensitivities. The types of sensors to be discussed include, but are not limited to, 1. solid-state chemical sensors, 2. membrane electrodes, 3. potentiometric sensors of immunological reactions, 4. electronic detectors of nucleic acids, and 5. enzyme-mediated electrochemical detectors.

Publication of a proceedings volume is being considered. Papers published in a proceedings volume may also be submitted to the **Journal**, but must be received no later than 6 months after the date of the symposium at which the paper was presented.

Suggestions and inquiries should be sent to the Symposium Chairman: C. Li, Cambridge Research Laboratory, 195 Albany St., Cambridge, MA 02139.

Tutorial on Medical Electronics

This symposium will be presented for the benefit of the nonexpert. Its focus is on implanted devices. Topics to be covered include the following: 1. implantable electronics, sensors, and actuators in acute and long-term use; 2. neural prostheses; 3. electronic interface with physical prostheses; 4. the interface between electronic components and body fluids, both acute and long term; 5. electrical stimulation; 6. regulatory issues and processes; 7. safety issues; 8. body response to materials and stimulation, including biocompatibility, induced bone growth, and excapsulation; 9. materials: polymers, metals, and substrates; 10. testing and reliability; 11. percutaneous and transcutaneous signal transmission: leads, coupling methods; 12. passivation and protection of unencapsulated integrated circuits. Topics specifically excluded are imaging systems and electronics not related to implanted devices.

Some contributed papers may be included. Publication of a proceedings volume is being considered. Papers published in a proceedings volume may also be submitted to the **Journal**, but must be received no later than 6 months after the date of the symposium at which the paper was presented.

Suggestions and inquiries should be sent to one of the Symposium Co-Chairmen: P. W. Barth and L. A. Roberts, Integrated Circuits Laboratory, Stanford University, Stanford, CA 94305; or R. J. Huber, Dept. of Electrical Engineering, University of Utah, Salt Lake City, UT 84112.

Fifth International Symposium on Silicon Materials Science and Technology

The symposium will cover a wide range of topics related to silicon material phenomena accompanying the fabrication of advanced devices, integrated circuits, and, in particular, very large scale integration (VLSI). This includes the preparation, properties, and characterization of silicon crystals and thin films, as well as the chemical impurities and structural imperfections accompanying VLSI processing. Particular emphasis will be accorded the manifold interactive effects of silicon starting material properties and the multiple IC processing steps on VLSI circuit performance.

Initial plans call for a selection of papers to be comprehensive reviews of fundamental research as well as items of technological importance. The remainder of the papers will be selected from a representative sampling, but not necessarily inclusive of, contributed original research papers not previously published in the areas listed below. Authors are encouraged to recommend the appropriate session for their submitted abstracts.

The sessions will include: 1. crystal growth; 2. thin film and interfaces; 3. oxidation and nitridation; 4. diffusion and ion implantation; 5. silicon defects; 6. gettering phenomena; and 7. silicon materials/IC process failure analysis.

Suggestions and inquiries should be sent to the Symposium Co-Chairmen: H. R. Huff, Monsanto Electronic Materials Co., P.O. Box 10123, Palo Alto, CA 94303; T. Abe, SEH R&D Center, Shin-Etsu Handotai Co., Ltd., 2-13-1 Isobe, Annaka-Shi, Gunma-Ken 379-01, Japan; or B. O. Kolbesen, Siemens AG, Zentralbereich Technik, Zentrale Forschung und Entwicklung, Postfach 832729, D-8000 Muenchen 83, Germany.

Detailed instructions concerning participation in this symposium appear in the special Call for Papers in the **Journal of the Electrochemical Society,** April 1985, p. 183C.

Joint General Session

Papers are solicited on all aspects of electronic materials and processing technologies except those covered by special symposia. Topics of interest include electronic materials preparation, characterization, interactions, and device applications, basic chemistry and physics of materials processing, process and device modeling, sensor technology, and computer-aided manufacturing of electron devices. Of particular interest are new or novel materials and processes.

Suggestions and inquiries should be sent to the Session Co-Chairmen: W. M. Bullis, Siltec Silicon, 423 National Ave., Mountain View, CA 94043; H. R. Huff, Monsanto Electronic Materials Co., P.O. Box 10123, Palo Alto, CA 94303; or G. C. Schwartz, IBM Corp., Dept. 206, Bldg. 300-48A, Hopewell Junction, NY 12533.

Joint Recent News Papers Session

Recent News Papers and Extended Recent News Papers consisting of topics covered by the symposia and sessions being sponsored or cosponsored by the Electronics and Dielectrics and Insulation Divisions are invited for presentation.

A special Call for Recent News Papers will appear in the January, February, and March 1986 issues of the **Journal**.

Suggestions and inquiries should be sent to the Session Chairman: W. A. Pliskin, IBM Corp., Dept. 04A, Zip 48A, Hopewell Junction, NY 12533.

ELECTRONICS/DIELECTRICS AND INSULATION/LUMINESCENCE AND DISPLAY MATERIALS

State-of-the-Art Program on Compound Semiconductors (SOTAPOCS IV)

SOTAPOCS IV is the fourth of a new series of special symposia intended to provide a forum for discussion on the latest developments in areas involving compound semiconductors. Original papers and reviews relating to all aspects of compound semiconductor processing are solicited and welcomed. Of particular interest are papers which correlate materials properties with fabrication processes for high speed, microwave, photonic, optoelectronic and sensing devices, and integrated circuits.

The symposia are also aimed at providing a forum for synergistic interactions between those working in compound semiconductors and those involved in silicon technologies. A recent example of such synergism in materials research is the new area of silicon/compound semiconductor heteroepitaxy.

To ensure the timely nature of the SOTAPOCS IV effort, a special deadline has been set. Abstracts will be accepted until February 1, 1986. The standard 75-word Electrochemical Society abstract (refer to form in this Call for Papers) is sufficient for paper presentation at SOTAPOCS. There is no need to submit an extended abstract.

Suggestions, inquiries, and the abstracts should be sent to the Symposium Co-Chairmen: S. N. G. Chu, AT&T Bell Laboratories, Rm. 7C-226, Murray Hill, NJ 07974; R. E. Enstrom, RCA Laboratories, Princeton, NJ 08540; or V. G. Keramidas, Bell Communications Research, Rm. 7B-402, Murray Hill, NJ 07974.

ELECTRONICS/PHYSICAL ELECTROCHEMISTRY/ENERGY TECHNOLOGY/NEW TECHNOLOGY

Organic Semiconductors at the Molecular Level

This symposium will be devoted to the fundamental physical, chemical, and electrochemical properties of organic semiconductors and related electroactive organic materials. Contributions relating to the synthesis, oxidation-reduction, charge transport, charge compensation and stability properties, theory and potential use of these materials in sensors, photovoltaics, molecular electronics, and other nonbattery applications are invited. Papers on structure-property relationships, the design synthesis of large organic molecules with significantly delocalized pi networks and organic superconductors are welcome. Emphasis will be on results which provide an understanding of the fundamental principles governing the structures, properties, and behavior of the materials and mechanisms involved in their electrochemically important characteristics.

Publication of a proceedings volume is being considered. Papers published in proceedings volumes may also be submitted to the **Journal**, but must be received no later than 6 months after the date of the symposium at which the paper was presented.

Suggestions and inquiries should be sent to the Symposium Co-Chairmen: D. S. Ginley, Sandia National Laboratories, Org. 1154, Albuquerque, NM 87185; or J. J. Smith, Office of Naval Research, Chemistry Div., Arlington, VA 22217-5000.

ENERGY TECHNOLOGY

General Session

Papers are solicited in the fundamental and applied aspects of energy conversion, storage, and transmission not covered by current symposia. Of particular interest are new developments in photoelectrochemistry and novel methods for energy storage, conversion, and transmission. Papers on the application of electrochemistry for environmental cleanup are also welcome.

Suggestions and inquiries should be sent to Session Co-Chairmen: H. C. Maru, Energy Research Corp., 3 Great Pasture Rd., Danbury, CT 06810; or D. S. Ginley, Sandia National Laboratories, Div. 1154, Albuquerque, NM 87185.

ENERGY TECHNOLOGY/ DIELECTRICS AND INSULATION/ELECTRONICS

Materials and New Processing Technologies for Photovoltaics VI

This symposium will focus on the new developments in the rapidly growing field of photovoltaics with special emphasis on processing techniques that help lower the cost of manufacturing PV modules and approaches that are needed to develop high efficiency solar cells.

Papers are solicited on the following main topics: 1. thin film amorphous silicon solar cells; 2. thin film polycrystalline solar cells; 3. crystalline silicon solar cells; 4. tandem-structure solar cells; 5. new materials and advanced concepts in photovoltaics. Papers that deal with the material properties and characterization, growth mechanisms, structure of thin films, nature of interfaces, stability of photoactive materials, defects that affect the performance of solar cells, and papers on processes for uniform deposition of thin films, and monolithic integration of solar cells and silicon sheet growth are welcome.

Publication of a proceedings volume is planned. Camera-ready copies of manuscripts must be provided at the time of presentation. Papers published in a proceedings volume may also be submitted to the **Journal**, but must be received no later than 6 months after the date of the symposium at which the paper was presented.

Suggestions and inquiries should be sent to the Symposium Co-Chairmen: V. K. Kapur, International Photovoltaic Systems, 9540 Donna Ave., Northridge, CA 91324; P. Rai-Choudhary, Westinghouse Research and Development Center, 1310 Beulah Rd., Pittsburgh, PA 15235; or S. Pizzini, Dept. of Physical and Electrochemistry, University of Milan, Via Golgi-20133, Milan, Italy.

ENERGY TECHNOLOGY/ ELECTRODEPOSITION/ ELECTRONICS

Electrodeposition of Semiconductors

This symposium will focus on mechanism, applications, and end use of electrochemically deposited semiconductor thin films and on electrochemical deposition of thin films on semiconducting substrates.

Papers are solicited in the following areas: 1. mechanisms, including correlation of solid-state properties of the deposit and solution chemistry, correlation between deposition parameters and the electronic and optical properties of the film, control of stoichiometry and doping, and correlations between the mechanism of the deposition and the morphology of the film; 2. photoelectrochemical and photothermal deposition; 3. electrodeposition of organic semiconductors; 4. post-treatment including nonelectrochemical post-treatment to electrochemical deposits and electrochemical post-treatment to thin films in general; 5. adhesion; and 6. economic analysis, utilization, and comparison of electrochemical and nonelectrochemical deposition methods.

Suggestions and inquiries should be sent to the Symposium Co-Chairmen: M. Tomkiewicz, Dept. of Physics, Brooklyn College of CUNY, Brooklyn, NY 11210; R. Noufi, Solar Energy Research Institute, 1617 Cole Blvd., Golden, CO 80401; or G. Hodes, Dept. of Plastic Research, The Weizmann Institute of Science, Rehovot 76100, Israel.

ENERGY TECHNOLOGY/ PHYSICAL ELECTROCHEMISTRY

Strong Metal-Support Interaction in Electrocatalysis

There are many scattered evidences of metal-support interactions in electrocatalysis, such as enhanced activity and reduced degradation, the causes of which have been postulated to be simple physical attraction, electronic interaction, and even chemical reaction between metal and support. Even for gas phase catalysis, on which a considerable amount of research has been reported, no comprehensive understanding of metal-support interaction exists. This symposium will attempt to bring together researchers in the catalyst field, to produce a common forum for discussion, and to guide future advances in electrocatalysis.

Topics of interest include catalysis in electrochemical energy conversion, industrial electrolytics, electrometallurgy, and organic and biological electrochemistry. The proposed papers may cover all studies ranging from preliminary experiments to commercial processes and theoretical considerations.

Suggestions and inquiries should be sent to the Symposium Co-Chairmen: V. M. Jalan, Giner, Inc., 14 Spring St., Waltham, MA 02154; or J. A. Horsley, Exxon Research and Engineering Co., Corporate Research-Science Laboratories, Annandale, NJ 08801.

HIGH TEMPERATURE MATERIALS/CORROSION

Fundamental Aspects of High Temperature Corrosion II

This is the second in a series of symposia that will deal with the mechanistic aspects of high temperature corrosion. Papers are solicited in the following areas: 1. fundamental mechanisms of scale growth in single or multiple gaseous oxidants; 2. fundamental mechanisms of complex scale growth on alloys; 3. fundamental mechanisms of reaction product growth on nonmetallics, structural ceramics; 4. chemical and electrochemical mechanisms of hot corrosion; 5. studies of the relationship of alloy or scale microstructure to corrosion; 6. studies of the development of growth stresses, thermal stresses, and/or cracking of scale; and 7. theoretical considerations in high temperature corrosion.

Publication of a proceedings volume is being considered. Papers published in a proceedings volume may also be submitted to the **Journal**, but must be received no later than 6 months after the date of the symposium at which the paper was presented.

Suggestions and inquiries should be sent to the Symposium Co-Chairmen: D. A. Shores, University of Minnesota Corrosion Research Center, 221 Church St., Minneapolis, MN 55455; or G. Yurek, Massachusetts Institute of Technology, 77 Massachusetts Ave, Rm. 4-136, Cambridge, MA 02139.

HIGH TEMPERATURE MATERIALS/CORROSION/ DIELECTRICS AND INSULATION

Surface Modification of High Temperature Materials

Oxidation, corrosion, erosion, and wear of materials modified by surface treatment are to be covered. Examples of such surface treatments could include ion implantation, ion plating, ion mixing, coatings effected by sputtering, electron-beam-physical vapor deposition (EB-PVD), plasma spraying, chemical vapor deposition (CVD), and diffusion processes, as well as modifications produced by laser and electron-beam techniques.

Suggestions and inquiries should be sent to the Symposium Co-Chairmen: J. G. Smeggil, United Technologies Research Center, M/S 22, Silver Lane, East Hartford, CT 06108; or K. Grabowski, Naval Research Laboratory, Code 6671, 4555 Overlook Ave. SW, Washington, DC 20375.

HIGH TEMPERATURE MATERIALS/DIELECTRICS AND INSULATION

Contemporary Film Structures and Their Properties

This symposium will focus on recent advances in multicomponent thin film structures that owe their unique properties in part to the geometry of their individual components. Modulated thin metal film structures, as well as multilayered Langmuir-Blodgett-type films, and composite thin film structures, such as metal dispersions in dielectric thin film matrices, will be considered. Contributions are being solicited that deal with novel synthetic or characterization techniques with emphasis on microstructure/physical property correlations, both theoretical and experimental. Discussions of existing or unique potential applications are welcome.

Suggestions and inquiries should be sent to the Symposium Co-Chairmen: E. Kay, IBM Research Laboratory, Dept. K33/281, 5600 Cottle Rd., San Jose, CA 95193; or J. Susko, R. D. 1, Box 401, Owego, NY 13827.

High-Technology Silicon-Based Structural Ceramics

This symposium will focus on physical, chemical, mechanical, and tribological properties of SiC, Si_3N_4, and related compounds. Topics include powder synthesis, processing characterization, and microstructure-property relationships. There is interest in applications, manufacture, and design of ceramic components for use in high performance turbine engines, automobile engines, and cutting tools. Contributions may be state-of-the-art review articles or from research in a related field.

Suggestions and inquiries should be sent to Symposium Co-Chairmen: K. S. Mazdiyasni, AFWAL/MLLM, WPAFB, Dayton, OH 45433; or T. Johansson, KemaNord, S-840 10, Ljungaverk, Sweden.

INDUSTRIAL ELECTROLYTIC

Nonaqueous Electrolytic Processes

This symposium focuses on the industrial applications of nonaqueous systems in electrolysis and related electrochemical processes. A broad spectrum of contributions is being sought, with special emphasis on nonaqueous electrolytic areas such as molten salts, organic solvents, solid electrolytes, membranes, and room temperature ionic liquids. Metal electrowinning, electrorefining, electroplating, nonmetallic production processes, and surface treatment are particularly solicited. The chemistry, design, development, current and

potential distribution, optimization, and economic evaluation are among the various aspects of the symposium.

Publication of a proceedings volume is planned. Papers published in a proceedings volume may also be submitted to the **Journal**, but must be received no later than 6 months after the date of the symposium at which the paper was presented.

Suggestions and inquiries should be sent to the Symposium Co-Chairmen: J. Jorne, Dept. of Chemical Engineering, University of Rochester, Rochester, NY 14627; or K. Hanson, AT&T Bell Laboratories, Rm. 7D-208, Murray Hill, NJ 07974.

General Session

Papers are solicited in the areas of industrial electrochemistry or electrochemical engineering not covered by the special symposia. Of particular interest are papers concerning the application of statistics, parameter estimation, or experimental design to industrial electrochemical systems.

Suggestions and inquiries should be sent to the Session Chairman: J. Van Zee, Dept. of Chemical Engineering, University of South Carolina, Columbia, SC 29208.

INDUSTRIAL ELECTROLYTIC/BATTERY/ ENERGY TECHNOLOGY

Load Leveling and Energy Conservation in Industrial Processes

The objective of this symposium is to bring together the technical experts who are working on electrochemical energy storage and energy conservation in industrial electrochemical processes. The spectrum of the symposium covers the research and development, conceptual design, economic analysis, prototype test, and operating results of full-scale installations.

Papers are solicited on the following or related areas: 1. secondary batteries for energy storage and on-site load leveling applications; 2. fuel cells for power generation; 3. solar and photovoltaic energy conversion systems; 4. hydrogen energy storage and utilization in the process industry; 5. on-site power generation and storage using wing, geothermal, and small hydroelectric energy resources; 6. depolarized air or oxygen cathode for industrial electrolysis; 7. electrocatalysis and development of energy efficient electrodes; 8. novel cell design, cell separator and membrane for energy savings; 9. use of pulsating or alternating current in industrial electrolysis; 10. other energy conservation measures in industrial electrochemical processes including electro-organic synthesis, electroplating, electrowinning, etc.; 11. cost analysis, mass and energy balance, and optimization of electrochemical energy storage systems.

Publication of a proceedings volume is being considered. Papers published in a proceedings volume may also be submitted to the **Journal**, but must be received no later than 6 months after the date of the symposium at which the paper was presented.

Suggestions and inquiries should be sent to the Symposium Chairman: D.-T. Chin, Dept. of Chemical Engineering, Clarkson University, Potsdam, NY 13676.

INDUSTRIAL ELECTROLYTIC/BATTERY/ PHYSICAL ELECTROCHEMISTRY

Diaphragms, Separators, and Ion-Exchange Membranes

Papers are solicited for this symposium which deal with separators for batteries, fuel cells, or electrochemical cells used for the production of chemicals. Papers that deal with the preparation techniques, characterization methods, transport properties, applications, and, especially, ones that combine these aspects will be of interest. Papers should contain both theoretical and experimental work, but papers dealing with either will be considered.

Publication of a proceedings volume is being considered. Papers published in a proceedings volume may also be submitted to the **Journal**, but must be received no later than 6 months after the date of the symposium at which the paper was presented.

Suggestions and inquiries should be sent to the Symposium Co-Chairmen: R. E. White, Dept. of Chemical Engineering, Texas A&M University, College Station, TX 77843; H. S. Burney, Dow Chemical Co., B-2234, Freeport, TX 77541; or K. Kinoshita, Applied Science Div., 90-3026, Lawrence Berkeley Laboratory, Berkeley, CA 94720.

ORGANIC AND BIOLOGICAL ELECTROCHEMISTRY

Electrochemical and Ionic Mechanisms in Electromagnetic Cell Stimulation

Electromagnetic stimulation has been found useful in certain forms of therapy. There have also been reports of harmful effects in living systems due to exposure to electromagnetic radiation. Papers in this symposium should be devoted to elucidating the basic electrochemical and ionic mechanisms involved in these effects.

Suggestions and inquiries should be addressed to the Symposium Chairman: G. Rein, Dept. of Orthopedic Surgery, Mt. Sinai Medical School, New York, NY 10029.

Organic Reaction Mechanisms

Papers devoted to studies of organic reactions accompanying electron transfers using electrochemical and auxiliary techniques are solicited. Biochemically important and catalytic reactions will also be considered.

Suggestions and inquiries should be addressed to the Symposium Co-Chairmen: J. F. Russling, Dept. of Chemistry, University of Connecticut, Storrs, CT 06268; or P. Zuman, Dept. of Chemistry, Clarkson University, Potsdam, NY 13676.

PHYSICAL ELECTROCHEMISTRY

Electrode Processes IV

The symposium will consist primarily of invited papers. The focus is on aspects of structure and microscopic dynamics influencing processes at electrochemical interfaces. Subtopics that will receive emphasis include kinetics of simple systems, interfacial structure, spectroscopic probes of electrode processes, electrochemical microstructures, and organic and inorganic mechanisms. Persons interested in contributing papers to this symposium should contact one of the organizers.

Suggestions and inquiries should be sent to the Symposium Co-Chairmen: B. E. Conway, Dept. of Chemistry, University of Ottawa, Ont., Canada K1N 9B4; M. J. Weaver, Dept. of Chemistry, Purdue University, West Lafayette, IN 47907; or L. R. Faulkner, Dept. of Chemistry, University of Illinois, Urbana, IL 61801.

General Session

Papers concerning any aspect of physical electrochemistry not included in the topic areas of the symposia are welcome.

Suggestions and inquiries should be sent to the Session Chairman: B. Miller, AT&T Bell Laboratories, Rm. 1D-350, Murray Hill, NJ 07974.

PHYSICAL ELECTROCHEMISTRY/ ORGANIC AND BIOLOGICAL ELECTROCHEMISTRY

Ion Transfer at Liquid-Liquid Interfaces

This symposium will provide a forum for discussion of theoretical and applied research on ion-transport kinetics and mechanisms at immiscible electrolyte interfaces (ITIES). Among the relevant topics are: 1. single ion partition equilibrium theory; 2. double layer structures; 3. double layer potential profiles in relation to kinetics of single-ion transfers; 4. ionophore/carrier-induced ion transport; 5. ITIES in relation to ion transport through lipid bilayers; 6. metal ion/chelate interfacial transport; 7. electrolyte/ion-exchanger interfacials transport; 8. protein-modified interfacial transport; and 9. heterophase catalysis mechanisms. New points of view, new applications, new techniques and instrumentation from a variety of interdisciplinary specialists will be welcomed in this symposium.

Suggestions and inquiries should be sent to the Symposium Chairman: R. P. Buck, Dept. of Chemistry, University of North Carolina, Chapel Hill, NC 27514.

NEW TECHNOLOGY SUBCOMMITTEE

Electrochemistry and Solid-State Science Education at the Graduate and Undergraduate Level

The advancement and accomplishment of electrochemical and solid-state science and engineering are objectives of The Electrochemical Society. The goal of this symposium is to identify means of enhancing the role of education in achieving these objectives. Batteries, electronics, corrosion, dielectrics, insulation, electrodeposition, high temperature materials, energy technology, industrial electrolytic, luminescence and display materials, organic, biological, and physical electrochemistry have developed rapidly and successfully as major areas of interest of this Society. Maintaining the breadth of these multidisciplinary fields and increasing their applications are extremely important pedagogical aims of this symposium. The progress of theoretical and applied science and engineering in the coming decades will be connected with the underlying need for acquiring greater and deeper knowledge. Both theoretical and experimental topics are requested that will advance the process of educating scientists and engineers in electrochemistry and solid-state science.

Publication of a proceedings volume is being considered. Papers published in a proceedings volume may also be submitted to the **Journal**, but must be received no later than 6 months after the date of the symposium at which the paper was presented.

Suggestions and inquiries should be sent to the Symposium Co-Chairmen: W. H. Smyrl, Dept. of Chemical Engineering and Materials Science, University of Minnesota, Minneapolis, MN 55455; A. Landgrebe, Dept. of Energy, MS 5E052, Washington, DC 20585; R. C. Alkire, Dept. of Chemical Engineering, University of Illinois, Urbana, IL 61801; F. McLarnon, Applied Science Div., Lawrence Berkeley Laboratory, University of California, Berkeley, CA 94720; G. C. Farrington, Dept. of Materials Science, University of Pennsylvania, Philadelphia, PA 19104; E. H. Nicollian, Dept. of Mechanical Engineering and Engineering Science, University of North Carolina, Charlotte, NC 28223; or L. R. Faulkner, Dept. of Chemistry, University of Illinois, 1209 West California St., Urbana, IL 61801.

NEW TECHNOLOGY SUBCOMMITTEE/CORROSION/ BATTERY

Electrochemistry of Reactive Metal Electrodes in Aqueous Solution

Papers are solicited concerning the aqueous electrochemistry of reactive metal electrodes such as aluminum and alkali or alkaline earth metals. Relevant topics include ionic and electronic transport in surface films, physical and morphological properties of films, kinetics or mechanisms of competing reactions (*e.g.*, metal dissolution and water reduction) and technological applications in energy storage, corrosion protection, etc.

Suggestions and inquiries should be sent to the Symposium Co-Chairmen: J. F. Cooper, Lawrence Livermore National Laboratory, L-490, P.O. 808, Livermore, CA 94550; or S. Gross, 7201 26th NE, Seattle, WA 98115.

Extended Abstract must be submitted with the 75-Word Abstract by December 1, 1985.

75-Word Abstract Form

Extended Abstract must be submitted with the 75-Word Abstract by December 1, 1985

Boston, Massachusetts—May 4-9, 1986

Submit to: The Electrochemical Society, Inc.
10 South Main Street, Pennington, NJ 08534-2896

Abstract No. .....
(to be assigned by the Society)

Schedule for .....
(Title of Symposium)

Sponsored by .....
(Division/Group)

Title of paper .....

.....

Authors (Underline name of author presenting paper.) .....

.....

Business affiliation and address .....

.....

.....
(State or Country) (ZIP Code) (Telephone No.)

(Type abstract in this area—double-spaced.)

Do you require any audiovisual equipment?

☐ **35 mm (2 x 2 in.) slide projector**

☐ **Vu-Graph**

☐ **other (specify)**

Has the information in this abstract been presented verbally, submitted for publication, or published?
☐ **Yes** ☐ **No**
If the answer is yes, please provide the reference (except in the case of invited review presentations). _____

Is a full length paper on this work to be submitted for Society Journal publication? ☐ **Yes** ☐ **No**

Papers presented before a Society technical meeting become the property of the Society and may not be published elsewhere without written permission of the Society. Papers presented at Society technical meetings must be authored by a member or sponsored by an active member.

.....
Insert name of Society member author or sponsor

This form should accompany your Extended Abstract.

SUSTAINING MEMBERS (CONTINUED)

Fairchild Camera & Instrument Corp.
Research & Development Laboratory
Palo Alto, CA

Focus Semiconductor Systems, Inc.
Sunnyvale, CA

Ford Motor Co.
Dearborn, MI

The Gates Corporation
Denver, CO

General Motors Corp.
Delco-Remy Div., Anderson, IN
Research Laboratories Div.
Warren, MI

Gould Inc.
Gould Research Center
Rolling Meadows, IL

GTE Laboratories
Waltham, MA

GTE Sylvania Inc.
Chemical & Metallurgical Div.
Towanda, PA

Heliotronic GmbH
Burghausen, Germany

Hewlett Packard Co.
Loveland, CO

Hewlett Packard Laboratories
Palo Alto, CA

Hill Cross Co., Inc.
West New York, NJ

Hitachi, Ltd.
Central Research Laboratory
Tokyo, Japan

Hoechst-Uhde Corp.
Englewood Cliffs, NJ

Honeywell, Inc.
Power Sources Center
Horsham, PA

Hughes Research Laboratories
Div. of Hughes Aircraft Co.
Malibu, CA

IMI Marston Limited
Wolverhampton, England

International Lead Zinc Research Organization, Inc.
New York, NY

Johnson Controls, Inc.
Milwaukee, WI

Kaiser Aluminum & Chemical Corp.
Pleasanton, CA

KBI
a division of Cabot Corp.
Boyertown, PA

Kerr-McGee Chemical Corp.
Oklahoma City, OK

Lockheed Missiles & Space Co., Inc.
Research Laboratory
Palo Alto, CA

LSI Logic Corp.
Santa Clara, CA

Marathon Battery Co.
Waco, TX

Medtronic Energy Technology
Minneapolis, MN

Mepco/Electra, Inc.
Columbia, SC

Microwave Associates, Inc.
Burlington, MA

Molycorp, Inc.
New York, NY

Monsanto Co.
St. Louis, MO

Motorola Inc.
Phoenix, AZ

M&T Chemicals Inc.
Detroit, MI

NEC Corporation Central Research Laboratories
Kawasaki, Japan

Nippon Telegraph and Telephone Public Corporation
Tokyo, Japan

Noranda Research Centre
Pointe Claire, Que., Canada

North American Philips Lighting Corp.
Bloomfield, NJ

Northern Telecom
Ottawa, Ont., Canada

Occidental Chemical Corporation
Research & Development
(2 memberships)
Grand Island, NY

Olin Corp.
Metals Research Laboratories
New Haven, CT

OMI International Corp.
Udylite/Sel-Rex
Warren, MI

Ovonic Battery Co.
Troy, Michigan

Perkin-Elmer Corp.
Norwalk, CT

Philips Laboratories, Inc.
Briarcliff Manor, NY

Prototech Co.
Newton Highlands, MA

Public Service Electric and Gas Co.
PSE&G Research Corp.
Newark, NJ

Rayovac Corp.
Madison, WI

RCA Corp.
Color Picture Tube Div.
Lancaster, PA

Reynolds Metals Co.
Reduction Research Div.
Sheffield, AL

Rockwell International
El Segundo, CA

SAB NIFE AB
Oskarshamn, Sweden

SAFT America, Inc.
Power Sources Division,
Valdosta, GA
Advanced Battery Systems Division,
Cockeysville, MD

Sandia National Laboratories
Albuquerque, NM

Sanyo Electric Co., Ltd.
Osaka, Japan

Schlumberger-Doll Research
Ridgefield, CT

J. C. Schumacher Co.
Oceanside, CA

Shipley Company, Inc.
Newton, MA

Siemens Aktiengesellschaft
Munich, Germany

Siltec Corp.
Menlo Park, CA

Sonnenschein GmbH
Budingen, Germany

Sprague Electric Co.
North Adams, MA

Standard Telecommunication Laboratories Ltd.
Essex, England

St. Joe Minerals Corp.
Monaca, PA

Tektronix, Inc.
Beaverton, OR

Texas Instruments Inc.
Attleboro, MA
Dallas, TX

Toshiba Corp.
Toshiba Research and
Development Center
Kawasaki, Japan

Toyota Central Research and Development Labs, Inc.
Nagoya, Japan

Tracor Applied Science, Inc.
Alexandria, VA

Varian Associates
Palo Alto, CA

VARTA Batterie AG
Kelkheim, Germany

Wacker Chemitronic
Burghausen, Germany

Wilson Greatbatch Ltd.
Clarence, NY

Xerox Corp.
Webster Research Center
Rochester, NY

Yardney Corp.
Pawcatuck, CT

Yuasa Battery Co., Ltd.
Osaka, Japan

THE ELECTROCHEMICAL SOCIETY PATRON MEMBERS

AT&T Bell Laboratories
Murray Hill, NJ

Dow Chemical Co.
Inorganic Chemicals Dept.
Midland, MI

ELTECH Systems Corp.
Chardon, OH

Exxon Research and Engineering Co.
Corporate Research
Advanced Energy Systems Laboratory,
Materials and Catalysis Sciences Laboratory
Linden, NJ
Technology Department
Chemical Engineering Technology Div.
Materials Technology Div.
Florham Park, NJ

Fujitsu Limited
Tokyo, Japan

General Electric Co.
Chemical Laboratory, Knolls Atomic Power Laboratory,
Schenectady, NY
Chemical Products, Engineering
& Technical Support, Cleveland, OH
Materials & Process Laboratory, Large Steam
Turbine-Generator Dept., Schenectady, NY
Research and Development Center,
Inorganic Materials Laboratory
Schenectady, NY

General Electric Co. (continued)
Signal Processing & Communication Laboratory,
Schenectady, NY
Semiconductor Products Dept.,
Syracuse, NY

International Business Machines Corp.
New York, NY

Olin Corp.
Chemicals Div.
Charleston Technology Center
Charleston, TN

Philips Research Laboratories
Eindhoven, The Netherlands

Tadiran, Israel Electronics Industries, Ltd.
Tel Aviv, Israel

Union Carbide Corp.
Battery Products Div.
Corporate Research Dept.
Danbury, CT

Westinghouse Electric Corp.
Electronic Tube Div., Elmira, NY
Nuclear Center, Monroeville, PA
Semiconductor Div., Youngwood, PA
Research Laboratories, Pittsburgh, PA

THE ELECTROCHEMICAL SOCIETY SUSTAINING MEMBERS

The Aerospace Corp.
Los Angeles, CA

Airco Industrial Gases
Murray Hill, NJ

Allen Clark Research Centre
Plessey Research (Caswell) Ltd.
Towcester, Northants, England

Allied Corporation
C&D Power Systems
Plymouth Meeting, PA

Aluminum Co. of America
New Kensington, PA

AMAX Inc.
Greenwich, CT

AMP Inc.
Harrisburg, PA

Analog Devices, Inc.
Norwood, MA

Applied Materials, Inc.
Santa Clara, CA

ASARCO, Inc.
South Plainfield, NJ

AT&T Technologies
Princeton, NJ

AT&T Teletype Corp.
Skokie, IL

Ballard Research, Inc.
North Vancouver, B.C., Canada

Battelle Memorial Institute
Columbus, OH

Bioanalytical Systems Inc.
West Lafayette, IN

Boeing Co.
Seattle, WA

BP Research Centre
Middlesex, England

Brown, Boveri & Co., Ltd.
Research Center
Baden, Switzerland

C-I-L Inc.
Industrial Chemicals Div.
Montreal, Que., Canada

Comdial Semiconductor, Inc.
Sunnyvale, CA

Cominco Ltd.
Trail, B.C., Canada

Corning Glass Works
Corning, NY

Crawford & Russell Inc.
Stamford, CT

CSIRO Division of Mineral Chemistry
Port Melbourne, Victoria, Australia

Diamond Shamrock Chemicals Co.
Painesville, OH

Duracell Inc.
A Division of Duracell International
Tarrytown, NY (2 memberships)

Duro-Test Corp.
North Bergen, NJ

Eagle-Picher Industries, Inc.
Electronics Div.
Joplin, MO

Eastman Kodak Co.
Rochester, NY

ECO Energy Conversion
Newton, MA

EG&G Princeton Applied Research Corp.
Princeton, NJ

Elcap Electronics Ltd.
Tai Po, Hong Kong

Electric Power Research Institute
Palo Alto, CA

Electrochemical Technology Corp.
Seattle, WA

Energy Conversion Devices, Inc.
Troy, MI

Energy Development Associates
A Gulf and Western Co.
Greensboro, NC

Engelhard Corp.
Engelhard Industries Div.
Iselin, NJ

Ever Ready Co. (Holdings) Ltd.
Whetstone, London, England

Exide Corp.
Yardley, PA

Exmet Corp.
Bridgeport, CT